U.S. DEPARTMENT OF
ENERGY

Office of
ENERGY EFFICIENCY &
RENEWABLE ENERGY

Materials

2017 Annual Progress Report

Vehicle Technologies Office

(This page intentionally left blank)

Disclaimer

Acknowledgements

First and foremost, the Principal Investigators from industry, academia, and national laboratories who supplied the content of these reports are to be acknowledged and commended. It is their work that moves our nation forward to improved and more affordable transportation, as well as increased energy security.

Thank you to the project managers at the National Energy Technology Laboratory for continued support administering these projects.

We would also like to acknowledge Energetics, Inc., for their help in preparing and publishing this report.

Felix Wu, Ph. D

Materials Technology Program Manager

Vehicle Technology Office

Jerry Gibbs

Technology Manager, Propulsion

Vehicle Technology Office

Sarah Kleinbaum

Technology Manager, Joining

Vehicle Technology Office

Carol Schutte, Ph. D

Technology Manager, Carbon Fiber

Vehicle Technology Office

Acronyms and Abbreviations

symbols

β phase	In Mg-Al alloy, $Mg_{17}Al_{12}$, the main precipitate and reinforced phase
2T	two thickness
3D	three-dimensional
3T	three thickness
4130	grade of steel with alloying elements of chromium and molybdenum, often informally referred to as chromoly steel, with an excellent strength to weight ratio and considerably stronger and harder than standard 1020 steel, but not easily welded (requiring thermal treatment both before after welding to avoid cold cracking)
5055-C	a non-corrosive, low viscosity, ultraviolet/visible light curing silicone adhesive
5xxx	series designation of Al alloyed with Mg
6xxx	series designation for Al alloyed with Mg and Si
7xxx	series designation for Al alloyed with Zn
η	incoherent precipitates
η’	coherent precipitates
ΔH_{rx}	change in heat of reaction
Ω·m	ohm-meter
α phase	yarn angle (when referring to fabrics)
ε	strain
ε_{LS}	lattice strain
λ	wavelength
μ	micron
μm	micrometer
μs	microsecond
μA	microampere or microfarad
θ	inter-yarn angle or fiber misalignment angle
σ	tensile stress (or strength)
σ_{UTS}	ultimate tensile strength
σ_{ys}	yield strength

A

a	amplitude
A11	designation for tool steel with high carbon and vanadium composition having good wear resistance, toughness and strength for cold work tooling applications
AA	Aluminum Association

AA2014	a copper-based wrought Al alloy with very high strength together with excellent machining characteristics in the 2000 series containing 4.40% Cu, 0.80% Si and 0.50% Mg
AA3003	aluminum alloy with moderate strength, which and be increased by cold working, and good corrosion resistance
AA5082	aluminum alloy with quantities of magnesium to cause substantial lowering of the melting point without producing brittleness and is moderate-to-high strength non-heat treatable with very good weldability, good corrosion resistance
AA5754	wrought aluminum alloy containing 94.2 to 97.4% Al, 0.3% max Cr, 0.1% max Cu, 0.4% max Fe, 2.6 to 3.6% Mg, 0.5% max Mn, 0.4% max Si, 0.15% max Ti, 0.2% max Zn and 0.15% max residuals formed by rolling, extrusion, and forging, but not casting that can be cold worked to produce tempers with a higher strength but a lower ductility
AA6005	an alloy in the wrought aluminum-magnesium-silicon family commonly heat treated to produce tempers with a higher strength at the expense of ductility
AA6022	heat treatable low copper precipitation hardenable Al sheet alloy containing 0.8 to 1.5% Si and 0.45 to 0.70% Mg
AA6061	precipitation hardening Al alloy containing 0.8 to 1.2% Mg and 0.4 to 0.8% Si as its major alloying elements
AA6111	wrought alloy that is a heat treatable and possesses high strength and excellent stretch-forming characteristics
AA7055	aluminum alloy used in the aerospace sector and other high strength requirement areas
AA7075	aluminum alloy with strength comparable to many steels, good fatigue strength, and average machinability
AA7085	an aerospace grade Al alloy containing 7.15% Al, 1.75% Mg, 1.45% Cu, 0.12% Zr, 0.06% Fe, and 0.02% Si.
Abaqus	software suite for finite element analysis and computer-aided engineering
ACEM	aberration corrected electron microscope
AFS	American Foundry Society
AHSS	advanced high-strength steel
AISI	American Iron and Steel Institute
Al	aluminum
Al 3003	alloy in the wrought Al-Mn family (3000 or 3xxx series)
Al 6013	weldable high strength 6XXX series alloy exhibiting 7XXX strength levels in the T6 temper
Al:Cu_2O	aluminum: copper (I) oxide
Al_2O_3	alumina
alumina	aluminum-based protective oxides
AM	Mg alloy designation with Al and Mn as principal alloying metals

AM50	Mg alloy 5.0% Al and less than 0.5% Mn
AM60	Mg alloy 5.6 to 6.5% Al and less than 0.25% Mn
AMO	Advanced Manufacturing Office
AMP	Advanced Manufacturing Program
ANL	Argonne National Laboratory
ANR	ammonia to NO_x ratio
ANSYS	specialists in finite element analysis, computational fluid dynamics, electronics, semiconductors, embedded software and design optimization
ARB	accumulative roll-bonding
Arconic	company specializing in lightweight metals engineering and manufacturing
ASPPRC	Advanced Steel Processing and Products Research Center
ASTM	American Society for Testing and Materials International
at.%	atomic percent
AT72	magnesium alloy comprised of 7% Al and 2% Sn
ATS	aftertreatment system
Aural 2	aluminum alloy used for thin wall structural components
Autodesk	Autodesk, Inc.—a multinational software corporation that makes software for the architecture, engineering, construction, manufacturing, media, and entertainment industries
AWD	all-wheel drive
AZ31B	most widely available Mg grade alloy, high strength to weight ratio with 2.5 to 3.5% Al and 0.7 to 1.3% Zn
AZ91	Mg alloy with 9 weight percent Al and 1 weight percent Zn

B

B	boron
BASF	largest chemical company in the world
BEI	backscattered electric images
BES	Basic Energy Sciences
BIW	body-in-white
BM	ball milled
BM+D	ball milled with diluent added
BMW	Bayerische Motoren Werke AG; a German luxury automobile, motorcycle, and engine manufacturing company
BP	budget period
BSE	backscattered electron

C

C	carbon
Ca	calcium
CAD	computer-aided design
CAE	computer-aided engineering
CAFE	Corporate Average Fuel Economy
CALPHAD	CALculation of PHAse Diagrams
CAMECA	supplier of microanalytical and metrology instrumentation for research and process control in end markets that include semiconductor, nanotechology, biology, environment, geology, nuclear and material sciences
CATIA	computer aided three-dimensional interactive application
CCT	cyclic corrosion testing
Ce	cerium
CEC	cyclic extrusion-compression
CETP	corrosion evaluation test procedure
CF	carbon fiber
CFD	computational fluid dynamics
CFR	Code of Federal Regulations
CFRP	carbon fiber reinforced polymer
CFTF	Carbon Fiber Technology Facility
CGI	compacted graphite iron
Chomarat	international, privately-owned, textile group producing textile and plastic coatings, textile finishing, and special reinforcement materials
chromia	chromium-based protective oxides
cm^2	square centimeter
CNMS	Center for Nanophase Materials Sciences
CO	carbon monoxide
CO_2	carbon dioxide
CompuTherm	University of Wisconsin-Madison spin-off company
Cosma	Cosma International (an operating unit of Magna International) provides a comprehensive range of body, chassis and engineering solutions to original equipment manufacturers
CPEC	close proximity electromagnetic carbonization
CPM® 10V®	tool steel made by the Crucible Particle Metallurgy process with optimized vanadium content to provide superior wear resistance while maintaining toughness and fabrication characteristics (AISI A11)
Cr	chromium
CRADA	Cooperative Research and Development Agreement

C-RTM	continuous (or compression) resin transfer molding
CSP	Continental Structural Plastics
CTE	coefficient of thermal expansion
CTS	cross-tension strength
Cu	copper
CUDA	Compute Unified Device Architecture
CUV	crossover utility vehicle

D

d	yarn width (when referring to fabric)
D	deuterium
DAR	double acetone rubs
DCB	double cantilever beam
DEF	diesel exhaust fluid
DIC	digital image correlation
DICTRA	DIffusion-Controlled TRAnsformations in multicomponent systems, a software diffusion module within Thermo-Calc for accurate simulation of diffusion-controlled reactions in multicomponent alloy systems
Digimat®	nonlinear multi-scale material and structure modeling platform by MSC Software
DIW	door in white
DOC	diesel oxidation catalyst
DOE	U.S. Department of Energy
DoE	design of experiments (when referring to experimental procedures)
Dow	Dow Chemical Company
DowAksa	large-scale, full-service, fully integrated provider of carbon fiber solutions for industrial applications
DP	dual-phase
DP1180	high-ductility, dual-phase, ultra-high-strength steel with an ultimate tensile strength greater than or equal 1180 MPa
DP590	advanced high-strength formable steel for inner body side, inner quarter panel, rear rails, and rear shock reinforcements
DP980	dual-phase steel consisting of a ferrite matrix containing a hard second phase
DPF	total denier (linear mass density of fibers) per quantity of uniform filaments
DR	diffuse reflectance
DRIFTS	diffuse reflectance infrared Fourier transform spectroscopy
DS	door sag
DSC	differential scanning calorimetry
DSpace	open source, turnkey, online repository application

DTA	differential thermal analysis

E

e.g.	abbreviation meaning “for example”
E717	high formability magnesium sheet by Magnesium Elektron North America
EBSD	electron backscatter diffraction
ECAP	equal channel angular pressing
E-coat	electrophoretic coating
EDAX	energy dispersive analysis x-ray
EDS	energy dispersive spectroscopy
EDXS	energy dispersive x-ray spectroscope
EELS	electron energy loss
EERE	Office of Energy Efficiency and Renewable Energy
EGR	exhaust gas recirculation
EL	electrode life
Eng.	abbreviation for engineering
EP	equilibrium partitioning
EPA	Environmental Protection Agency
EPDM	ethylene propylene diene monomer
EPMA	electron probe microanalysis
EPRI	Electric Power Research Institute
EPSC	Elasto-Plastic Self-Consistent
Equi.	equivalent
ESC	externally solidified crystal
ESE[T]	eccentrically loaded single edge notch tension
ESI	Engineered Solutions, Inc. Group
ESTECO	an independent technology provider with software solutions aimed at perfecting the simulation-driven design process
et al.	abbreviation meaning “and others”

F

F	fluorine
FBJ	friction bit joining
FCA	Fiat Chrysler Automobile, U.S., LLC
FDS	flow-drill screw
Fe	iron
FE	finite element

FEA	finite element analysis
FEM	finite element method
FIB	focused ion beam
FLD	forming limit diagram
FMVSS	Federal Motor Vehicle Safety Standards
FOA	funding opportunity announcement
Ford-HPDC	Ford High-Pressure Die Cast
Ford-SPMC	Ford Semi-Permanent Mold Cast
FSLW	friction stir lap welding
FSN	filter smoke number
FSS	friction stir scribe
FSSJ	friction stir scribe joining
FSSW	friction stir spot welding
FSW	friction stir welding
ft	foot or feet
FTIR	Fourier Transform Infrared
FTP	federal test procedure
FY	fiscal year
f_γ	volume fraction
f_γ^{max}	maximum volume fraction
f_γ^{RT}	room temperature volume fraction

G

g	gram(s)
g/cc	gram(s) per cubic centimeter
G’	storage modulus (when referring to rheology)
Gd	gadolinium
GEN	generation
gf	grams-force
GHG	greenhouse gas
GM	General Motors
GMW14872	an accelerated laboratory corrosion test method to evaluate assemblies and components and provides a combination of cyclic conditions (salt solution, various temperatures, humidity and ambient environment)
GMW-15282	standard developed for corrosion/undercutting scribe creepback

GMW15356	a sheet metal rating scale developed by GM to allow comparison between vehicles and consistency between personnel for rating corrosion, which involves subjective perception of an objectionable surface
G-NAC	GTEKT North American Corporation
Go/No-Go	determination to proceed with or abandon a plan or project
GP	Guinier-Preston
GPa	gigapascals
GPU	Graphics Processing Unit

H

h or hr	hour(s)
H	hydrogen (when referring to the element)
H	latent heat
H/D	ratio of hydrogen to deuterium
H13	versatile chromium-molybdenum steel for hot and cold work tooling applications
H_2	molecular hydrogen
H_2O	the chemical symbol for water
HAADF-STEM	high-angle annular dark field-scanning transmission electron microscope
HAZ	heat-affected zone
HBM	company providing sensors, transducers, strain gauges, amplifiers, data acquisition systems, and software for structural durability investigations, tests, and analysis
HC	hydrocarbons
HCF	high-cycle fatigue
HD	heavy-duty
HDF	hierarchical data format
HE	hydrogen embrittlement
HER	hole-expansion ratio
HEXRD	high energy x-ray diffraction
HPC	high-performance computing
HPC4Mfg	high-performance computing for manufacturing
HPDC	high-pressure die casting
HP-RTM	high-pressure resin transfer molding
HR-STEM	high-resolution scanning transmission electron microscope
HRA	Honda R&D Americas
HRC	Hardness, Rockwell, C-scale—a scale that expresses hardness of a material as an arbitrary dimensionless number
HSA	high-strength aluminum (Al) alloy
HSLA	high-strength low-alloy

HT	high temperatures
HTC	high-temperature carbonization
HyperMesh	multi-disciplinary finite element pre-processor with advanced model assembly tools

I

i3	five-door urban electric vehicle
i8	coupe with an advanced plug-in hybrid drivetrain
IA	inter-critical annealing
ICME	integrated computational materials engineering
ICNIRP	International Commission on Non-Ionizing Radiation Protection
ICSD	inorganic crystal structures database
ICWE	integrated computational welding engineering
ID	identification
IEEE	Institute of Electrical and Electronics Engineers
IM	intermetallic
IMC	intermetallic compound
in situ	onsite or in place
INFUCOMP	simulation-based software for industrial manufacture of large-infusion composite parts
INS	inelastic neutron scattering
IPS	initial plastic strain
ISO 2808:2007	standard by the International Organization of Standards that describes various methods that are applicable to the measurement of the thickness of coatings applied to a substrate for determining wet-film thickness, dry-film thickness and the film thickness of uncured powder layers

J

JAC270C	commercial quality galvannealed steel
JAC980	multi-phase galvannealed steel
JMAK	Johnson-Mehl-Avrami-Kolmogorov

K

K	potassium
kA	kiloampere
Kevlar®	registered trademark for a para-aramid synthetic fiber
kg	kilogram
kJ	kilojoules
kN	kilonewtons
kpsi	kilopound per square inch

Ksi or ksi	kilopound per square inch
KUKA	KUKA Robotics Corporation—Chinese-owned German manufacturer of industrial robots and solutions for factory automation

L

L&L Products	technology driven business-to-business company with unique expertise in static sealing, acoustics, vibration reduction, structural reinforcements, and composite components
LabVIEW	Laboratory Virtual Instrument Engineering Workbench
lb	pound(s)
LBNL	Lawrence Berkeley National Laboratory
LBS100	value for 100 lb of weight reduction in crash models
LCCF	low-cost carbon fiber
LCF	long carbon fiber
LDH	limiting dome height
LEAP	local electrode atom probe
LFT	long fiber-reinforced thermoplastic
Li	lithium
LIN	local interconnected network
LLC	Limited Liability Company
LSDC	liquid-solid diffusion couple
LS-DYNA	advanced, general-purpose, multi-physics simulation software package
LSF	Load Sharing Facility - a workload management platform and job scheduler for distributed high performance computing
LSTC	Livermore Software Technology Corporation
LSW theory	Lifshitz, Slyozov, and Wagner theory
LT	light truck
LTC	low-temperature carbonization
LT-SCR	low temperature selective catalytic reduction

M

MAGMASOFT®	modular simulation software for casting process simulation
Magna	Magna International Inc.
Mag-tec	company offering full service die casting in Mg, Al, and Zn
MAT_COMPRF or MAT_293	software in LS-DYNA for woven pattern prepreg composite preforming simulation
MATLAB	MATrix LABoratory, a multi-paradigm numerical computing environment and programming language
MDA	molecular dynamic analysis

MDO	multidisciplinary design optimization
MDS	multiscale design system
MEF	mobility enhancement factor
MeV	million electron volts
Mg	magnesium
$Mg(OH)_2$	magnesium hydroxide
MgH_2	magnesium hydride
MGI	Materials Genome Initiative
MgO	magnesium oxide
Micromill™	Alcoa-patented process for changing the microstructure of the metal and producing an Al alloy that has 40% greater formability and 30% greater strength
mil or mils	unit of length equal to one thousandth (10^{-3}) of an inch
min	minute(s)
ml/sec	milliliters per second
mm	millimeters
mm/min	millimeters/minute
MMHF	MicroMill™ high form
Mn	manganese
MOBFE3	TCS Steels/Fe-Alloys Mobility Database, Version 3
modeFRONTIER®	software for streamlining the design process with workflows, innovative algorithms, and sophisticated post-processing tools
MPa	megapascals
mpg	miles per gallon
mph	miles per hour
MRD	Moldflow Rotational Diffusion
MRI	Major Research Instrumentation
MSC-Simufact	software to simulate complex welding processes that may involve multiple welding sequences and to predict distortions of the components, while considering phase transformations occurring during the process
MSI or Msi	million pounds per square inch
MTS	MTS Systems Corporation
MY	model year

N

N	newtons
Nano-Al	nanostructured aluminum
NASTRAN	multidisciplinary structural analysis application for performing static, dynamic, and thermal analysis across the linear and nonlinear domains

NCF	non-crimped fabric
nCode	engineering data analysis tool with special concentration in fatigue and durability
Nd	neodymium
NETL	National Energy Technology Laboratory
NH_3	ammonia
NH_4NO_3	ammonia nitrate
NHTSA	National Highway Traffic Safety Administration
Ni	nickel
NIST	National Institute of Standards and Technology
nm	nanometers
Nm	newton metre
NO_x	nitrogen oxides (NO and NO_2)
NSC	NO_x storage converter
NSLS	National Synchrotron Light Source
NU	Northwestern University
NVH	noise, vibration, and harshness

O

OEM	original equipment manufacturer
OLCF	Oak Ridge Leadership Computing Facility
OptiStruct	structural analysis solver for linear and nonlinear problems under static and dynamic loadings supplied by Altair
ORNL	Oak Ridge National Laboratory
OSHA	Occupational Safety and Health Administration
OSU	The Ohio State University
OVERWT00	value for mass reduction in heavier-than-average cars

P

Pa s	pascal-second (unit of viscosity)
PAM DISTORTION	software package for prediction of manufacturing-induced residual stresses and shape distortion of composites parts
PAM-FORM	software program enabling realistic and predictive simulation of dry textiles or prepregs forming processes
PAM-RTM	pluggable authentication module-resin transfer molding
PAN	polyacrylonitrile
PanPrecipitation	module in the Pandat™ software simulating precipitation kinetics during heat treatment process

PBS-Pro	Portable Batch System, Professional Edition™ - workload manager software designed to improve productivity, optimize utilization and efficiency, and simplify administration for high performance computing clusters, clouds and supercomputers
PCBN	polycrystalline cubic boron nitride
PCE	polynomial chaos expansion
PCP	peak cylinder pressure
Pd	palladium
PD	plunge depth
PDV	photonic doppler velocimeter
PGM	platinum-group minerals
PI	principal investigator
PlastiComp	supplier of stronger, tougher, and lighter benefits of long fiber reinforcement technology
PM	particulate matter
PNNL	Pacific Northwest National Laboratory
PP	polypropylene (when referring to polymers)
PP	pararequilibrium partitioning (when referring to metallurgical processes)
PPG	Pittsburgh Plate Glass
ppm	parts per million
PRISMS	PRedictive Integrated Structural Materials Science
ProCAST	simulation software for predicting distortions and residual stresses and more specific processes like semi-solid, core blowing, centrifugal, lost foam and continuous casting
Pt	platinum
PTFE	polytetrafluoroethylene
PVD	physical vapor deposition (used in vapor phase processing)

Q

QoI	quantities of interest
QT	QuesTek Innovations, LLC

R

R&D	research and development
RA	retained austenite
RAVF	retained austenite volume fraction
RCS	robot controller software
RE	rare-earth
Redox	reduction-oxidation
RFL	random fatigue limit

Rh	rhodium
RIVTAC®	a high-speed process supplied by Bollhoff for joining aluminum, steel, plastics and non-ferrous metals as well as for mixed joints, multilayer joints and hybrid joints of these materials
RMX	RMX Technologies, an advanced materials technology company with ceramics and various commercialized products
RPM or rpm	revolution(s) per minute
RSC	reduced strain closure
RSR	resistance spot rivet
RSW	resistance spot weld
RT	room temperature
RTM	resin transfer molding
RVE	Representative Volume Element
R4-3GA	designation for a rivet 4mm in length and 3 gauge (0.2294-inch diameter)
R4-6GA	designation for a rivet 4mm in length and 6 gauge (0.1620-inch diameter)

S

S	yarn spacing (when referring to fabric weave)
SAE	Society of Automotive Engineers
SAERTEX	a multi-axial warp knit carbon fiber fabric
SAS	originally “statistical analysis system”; herein, the name of a company that provides software for statistical analyses
SAXS	small angle x-ray scatter
SCA	self-consistent clustering analysis
SCC	stress corrosion cracking
Scheil Model	model for describing the microsegregation present in primary phase dendritic growth and directional solidification
SCR	selective catalytic reduction
SDAS	secondary dendrite arm spacing
SECO	Scientific Equipment Company
SEM	scanning electron microscopy
SEM-EDAX	scanning electron microscopy and energy dispersive spectroscopy
ShAPE™	shear-assisted processing and extrusion
Si	silicon
SIMS	secondary ion mass spectrometry
SINCAP	Side Impact New Car Assessment Program
SKP	scanning Kelvin probe
SKPFM	scanning Kelvin probe force microscopy

SLME	self-learning metabasin escape
SLTNR	sustained low temperature NO_x reduction
SMC	sheet molding compound
Sn	tin
SNS	spallation neutron source
SPR	self-pierce rivet
Sr	strontium
SR	sash rigidity
SSDC	solid-solid diffusion couple
STEM	scanning transmission electron microscope
STEM-EDS	scanning transmission electron microscope-energy-dispersive X-ray spectroscopy
SVDC	super vacuum die casting

T

T	temperatures
T4	temper designation for a solution heat-treated material used for castings which require high strength and maximum toughness
T5	temper designation for material cooled from hot working and artificially aged (at elevated temperature)
T6	temper designation for solution heat-treated and artificially aged alloy
TCFE8	TCS Steels/Fe-Alloys Database, Version 8.0
TEM	transmission electron microscope (or microscopy)
T_g	glass transition temperature
TGA	thermogravimetric analysis
T_h	holding temperature
Thermo-Calc	software package for thermodynamic
Ti	titanium
Ti:2B	a mixture of one part titanium and two parts boron
TiB_2	titanium boride
TiC	titanium carbide
TiO_2	titania
TMD	theoretical maximum density
TMK-3012	tungsten carbide tool material supplied by TechMet Carbides, Inc. with a combination of high hardness, high strength and wear resistance
TOF	time-of-flight
TP	thermoplastic
TPI	TPI Composites, Inc.

TRIP	transformation-induced plasticity
TRL	technology readiness level
TSS	tensile shear strength
TWB	tailor-welded blanks
TWC	three-way catalyst

U

UD	unidirectional
UD-CCM	University of Delaware Center for Composite Materials
UHS	ultra-high strength
UHSS	Ultra High-Strength Steel
ULSD	ultra-low sulfur diesel
UM	University of Michigan-Dearborn
UNDRWT00	value for mass reduction in lighter-than-average cars
Usibor®	a hardenable boron alloyed steel coated with Al-Si coating used in automotive components when high strength is required
UTS	ultimate tensile strength
UV	ultraviolet

V

V	volt
VASP	Vienna Ab initio Simulation Package
VCCD	virtual cast component development
V_f	volume fraction
VFAW	vaporizing foil actuator welding
VFT	virtual fabrication technology
vis	visible spectroscopy
VISION	highest resolution broadband inelastic neutron scattering spectrometer in the world designed to study the vibrational dynamics of atoms in molecules and solids and by combining a series of diffraction banks, their structure
viz	synonym for “namely,” “that is to say,” and “as follows”
VMT	vehicle mile(s) of travel
VrWeld	software by Goldak Technologies used to simulate the transient 3D temperature field, the evolution of microstructure in low alloy steel welds, transient 3D displacement, stress and strain in the structure being welded
vs	versus
VTO	Vehicle Technologies Office
VUMAT	vectorized user material – a subroutine to define material behavior in Abaqus/Explicit software

W

W/g	watts per gram (heat flow)
WARP3D	software used for the investigation of fracture in metals include a robust finite strain formulation, a general J-integral computation facility (with inertia, thermal, face loading), interaction integrals for computation of linear-elastic fracture parameters (stress intensity factors and T-stress), very general element extinction and node release facilities to model crack growth, nonlinear material models including viscoplastic and cyclic, cohesive elements and cohesive constitutive models, hydrogen effects on plasticity, Norton creep, and the Gurson-Tvergaard dilatant plasticity model for void growth
W_b	surface structure value for appearance from 0.3-1 mm
W-C-Co	tungsten-carbon-cobalt (type of tool steel)
WE43	high strength casting alloy used in temperatures of up to 300°C (572°F)
WHO	World Health Organization
WPI	Worcester Polytechnic Institute
WSS M2G575	material specification by Ford specifying material that is a pumpable, one component, thermal curing, weldable epoxy resin base and a structural adhesive for steel with bondline spacers for bonding metal in hem applications
wt%	percent by weight

X

XPS	x-ray photoelectron spectroscopy
XRD	x-ray diffractometer
XTALIUM™	aluminum-based nanostructured alloys for coating metals to add strength, corrosion and scratch resistance to other lightweight materials and for forming discrete articles via electrodeposition and electroforming

Y

Y	yttrium
YS	yield strength

Z

ZEK100 (ZE10A)	novel magnesium alloy with reduced content of rare-earth metals
ZK60	magnesium wrought alloy consisting of primary matrix α (Mg) and the eutectic
Zn	zinc
Zr	zirconium
ZrH_2	zirconium(II) hydride

Executive Summary

The Materials Technology subprogram supports the Vehicle Technology Office's mission to help consumers and businesses reduce their transportation energy costs while meeting or exceeding vehicle performance expectations. The Propulsion Materials research portfolio seeks to develop higher performance materials that can withstand increasingly extreme environments and address the future properties needs of a variety of high efficiency powertrain types, sizes, fueling concepts, and combustion modes. Advanced Lightweight Materials research enables improvements in fuel economy by providing properties that are equal to or better than traditional materials at a lower weight. Because it takes less energy to accelerate a lighter object, replacing cast iron and traditional steel components with lightweight materials such as high-strength steel, magnesium (Mg), aluminum (Al), and polymer composites can directly reduce a vehicle's fuel consumption. Materials technology activities focus on the following cost and performance targets: (1) enable a 25 percent weight reduction for light-duty vehicles including body, chassis, and interior as compared to a 2012 baseline at no more than a $5/lb-saved increase in cost; and (2) validate a 25 percent improvement in high temperature (300°C) component strength relative to components made with 2010 baseline cast Al alloys (A319 or A356) for improved efficiency light-duty engines.

Propulsion Materials

In fiscal year (FY) 2017, the Propulsion Materials portfolio included research in three main areas: (1) use of integrated computational materials engineering (ICME) to predict materials properties needed to achieve increases in brake thermal efficiency for heavy duty vehicles; (2) development of advanced cast aluminum alloys for high-temperature engine components; and (3) development of catalyst materials for energy recovery and aftertreatment.

Heavy-duty (HD) internal combustion engines for use in the transportation sector are operating at increasingly high peak cylinder pressure (PCP) to achieve required increases in brake thermal efficiency. One project in the propulsion materials portfolio is using ICME to estimate combustion intensity and heat transfer and to evaluate the thermo-mechanical effects on materials. In this way, it is possible to identify properties requirements of materials suitable to withstand a lifetime of operation at the elevated temperatures and pressures in future higher-efficiency HD engines.

To increase engine efficiency in light-duty vehicles, the maximum operating temperature of engine components has increased from approximately 170°C in earlier engines to peak temperatures well above 200°C in current engines. This increase in operational temperatures requires a material with optimized properties in terms of tensile, creep, and fatigue strength. Several projects focus on developing advanced cast Al alloys for automotive engine applications to meet these challenging requirements. Another potential approach to achieving improved combustion engine efficiency and specific power is by retaining more heat in the exhaust gas to recover in a turbocharger. However, higher exhaust gas temperatures increase the operational temperature requirements of structural components in the exhaust gas path, particularly the exhaust valves. Identifying a structural engine material with adequate high-temperature mechanical properties and oxidation resistance to enable the projected engine operating parameters without exceeding the cost constraints is the focus of another Propulsion Materials project in this report.

Finally, the goal of several projects in the Propulsion Materials portfolio is to develop and test new catalysts for gasoline and diesel engines at lower operating temperatures that may occur with future, more efficient vehicles. Specifically, the goal is to achieve conversion efficiencies of 90% at temperatures as low as 150°C. This will enable the deployment of lean combustion powertrains with significantly increased fuel efficiencies, but lower exhaust temperatures. In addition, current aftertreatment technologies, such as exhaust gas recirculation (EGR), are being studied in order to provide information to industry about the properties of

deposit buildup so as to enable improved models and potential design improvements to reduce fouling and its impact on the performance of EGR coolers.

Lightweight Materials

In FY2017, the Lightweight Materials portfolio included research in the following three areas: (1) improving the manufacturability of light metals, such as advanced high strength steel (AHSS), Al, and Mg; (2) reducing the cost of carbon fibers and creating ICME models for the manufacturing of carbon fiber composites; and (3) developing novel joining methods to enable multi-material systems.

Substitution of light metals for mild steel can result in weight savings of 25-60% per component, which increases fuel efficiency. However, there are several challenges to the increased use of light metals including material cost, room temperature formability, and limitations within the existing manufacturing infrastructure. During cold-stamping of AHSS parts, the most commonly observed failure mode is edge-splitting, and the sheared-edge stretchability appears to depend on a complex combination of factors. One light metals project is working to enhance the sheared-edge stretchability of AHSS by developing quantitative and predictive understanding of the microstructure effects on sheared-edge fracture and stretchability, hence enabling implementation of AHSS in vehicle structures. Two projects are pursuing unique pathways to develop a high strength 7xxx series Al alloy and demonstrate its ability to replace an ultra-high strength automotive component at a cost of less than $2 per pound saved. Addressing the affordability of high-strength Al will accelerate their adoption in the automotive market. Similarly, the use of high-performance Mg alloys in the automotive industry is currently limited due to the addition of costly rare-earth (RE) elements and the slow rate of the manufacturing components. One project in this report aims to eliminate the need for RE additives, while simultaneously improving the processing rate and energy efficiency to manufacture Mg components.

Carbon fiber reinforced polymer (CFRP) composites also have the potential to reduce component weight by more than 60%. One of the main barriers to widespread implementation is the high cost of carbon fiber, which is due in large part to the cost of input material (precursor) and the carbonization process. One project is addressing this challenge by developing higher throughput, low-temperature carbonization of carbon fiber, thus lowering manufacturing costs and increasing production rates. Another challenge that the Lightweight Materials subprogram is addressing is the lack of predictive modeling available, which is necessary to accelerate development to deployment of CFRP automotive components. Two projects are creating ICME models in order to predict the manufacturing and structural performance of carbon fiber (CF) composites. Material design and manufacturing process information, such as geometric dimension, fiber layout, and fiber orientation, are inputs for multiscale models to generate local material constitutive relations used in following noise, vibration, harshness, crash safety, and durability analyses. The integrated tools are being applied to component design and optimization, demonstrating that the ICME approach generates powerful tools for the most efficient usage of CFRP, leading to optimized weight savings with minimum cost increase.

The most effective way to reduce the overall weight of a vehicle is to tailor the material selection to each component's needs. However, joining dissimilar materials to create a multi-material structure is a significant challenge. Several projects in this area investigate the use of friction-based solid state welding processes to join Al to steel, Al to CF reinforced composites, as well as dissimilar Al alloy combinations. Solid-state welding allows for joining materials with vastly different melting temperatures, which is not possible with fusion welding. Two projects incorporate fasteners into welding processes, both solid-state and fusion, in order to provide a strong spot joint comparable to resistance spot welds in steel to steel joints. Research in this portfolio also includes adhesives that address concerns with the coefficient of thermal expansion mismatch seen in dissimilar material joints, as well as a novel joining process being developed based on impact welding.

Table of Contents

List of Figures

List of Tables

Vehicle Technologies Office Overview

Vehicles move our nation. Vehicles transport more than $36 billion worth of goods each day[1] and move people more than 3 trillion vehicle-miles each year.[2] Growing our national economy requires transportation and transportation requires energy. The average U.S. household spends nearly one-fifth of its total family expenditures on transportation,[3] making transportation the most expensive spending category after housing. The transportation sector accounts for 70% of U.S. petroleum use. The United States imports 25% of the petroleum consumed – sending more than $10 billon per month[4] overseas for crude oil.

To strengthen national security, enable future economic growth, and increase transportation energy efficiency, the Vehicle Technologies Office (VTO) funds early-stage, high-risk research on innovative vehicle and transportation technologies. VTO leverages the unique capabilities and world-class expertise of the national laboratory system to develop innovations in electrification, advanced combustion engines and fuels, advanced materials, and energy efficient mobility systems.

VTO is uniquely positioned to address early-stage challenges due to strategic public-private research partnerships with industry (e.g. U.S. DRIVE, 21st Century Truck Partnership). These partnerships leverage relevant expertise to prevent duplication of effort, focus DOE research on critical research and development (R&D) barriers, and accelerate progress. VTO focuses on research that industry does not have the technical capability to undertake on its own, usually due to a high degree of scientific or technical uncertainty, or it is too far from market realization to merit industry resources. VTO's research generates knowledge that industry can advance to deploy innovative energy technologies to support affordable, secure, and efficient transportation systems across America.

Vehicle Technologies Office Organization Chart

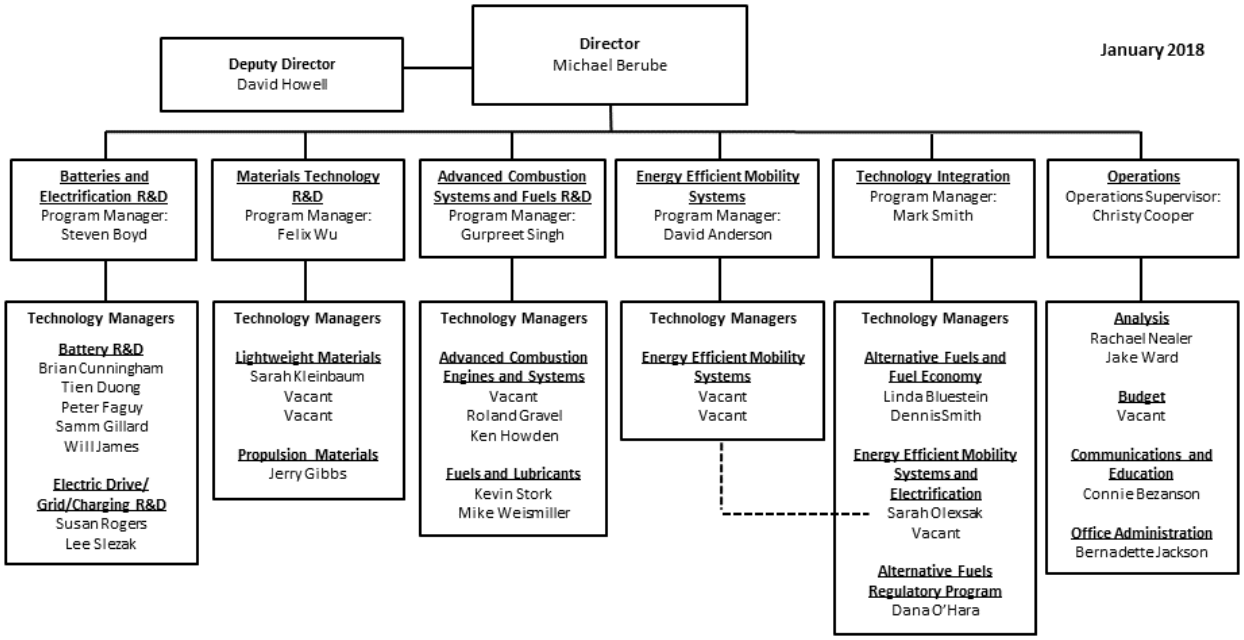

[1] https://ops.fhwa.dot.gov/publications/fhwahop16083/ch1.htm#t1.
[2] https://www.fhwa.dot.gov/policyinformation/statistics/2015/vm1.cfm.
[3] https://www.bls.gov/cex/2015/standard/multiyr.pdf.
[4] Transportation Energy Data Book Edition 34, ORNL, Table 1.7 and Table 10.3; Overseas includes countries and territories outside the 50 States and the District of Columbia.

Materials Program Overview

Introduction

The Materials Technology subprogram supports vehicle lightweighting and improved propulsion (powertrain) efficiency through early-stage R&D to increase understanding of novel materials and to enable industry to develop and deploy more fuel efficient light- and heavy-duty vehicles. The research focus is on activities that have a high degree of scientific or technical uncertainty, or that are too far from market realization to merit sufficient industry focus and critical mass. The Materials Technology subprogram accomplishes its technical objectives through research programs with academia, national laboratories, and industry.

The Propulsion Materials portfolio is closely aligned with other VTO subprograms to identify critical materials needs for next generation high-efficiency powertrains for both light- and heavy-duty vehicles. Strategies for achieving high-efficiency powertrains include improved powertrain thermal efficiency, increased power density resulting from lightweighting, and petroleum displacement through fuel substitution strategies. In FY 2017, the Propulsion Materials portfolio included research in three main areas: (1) use of ICME to predict materials properties needed to achieve increases in brake thermal efficiency for HD vehicles; (2) development of advanced cast Al alloys for high-temperature engine components; and (3) development of catalyst materials for energy recovery and aftertreatment.

The Lightweight Materials team works closely with industry through the USDRIVE partnership to understand both light- and heavy-duty vehicle structural weight reduction goals and to identify technical challenges that prevent the deployment of lightweight materials. The most promising and likely approach for lightweighting is a multi-material approach that focuses on the use of the right material for the application. The Lightweight Materials research portfolio addresses significant technology gaps for each family of structural materials: Mg, advanced high-strength steel, Al, and CF composites. In addition, there is a growing focus on dissimilar material joining in order to enable the reliable assembly of these multi-material systems.

Goals

The Materials Technology subprogram supports the VTO's mission to help consumers and businesses reduce their transportation energy costs while meeting or exceeding vehicle performance expectations. Lighter vehicles with more efficient engines reduce fuel use and save consumers money. The structural and powertrain systems that we target to improve are limited by materials performance. By improving the properties of powertrain and structural materials, we can enable a significant improvement in fuel economy for future vehicles. Increasing the strength and oxidation resistance of high-temperature materials will enable new combustion strategies while improving properties in structural materials such as stiffness, strength, join-ability, and crash energy absorption—all with lower cost, and will accelerate the deployment of lightweight materials in the automotive market.

The specific performance and cost targets for the Materials Technology subprogram are:

- Validate a 25 percent improvement in high-temperature (300°C) component strength relative to components made with 2010 baseline cast Al alloys (A319 or A356) for improved efficiency light-duty engines.
- Enable a 25 percent weight reduction for light-duty vehicles including body, chassis, and interior as compared to a 2012 baseline at no more than a $5/lb-saved increase in cost.

State of the Art

Automakers are seeking to improve fuel economy while maintaining or improving vehicle performance and safety. Reducing the weight of a vehicle's structure improves fuel economy and reduces the strain on a vehicle's powertrain, allowing for further fuel savings. For structural components, the market is shifting from traditional steel components to lighter weight materials such as advanced high-strength steels, Al alloys, Mg alloys, and CF composites. Lighter structures allow for downsizing engines and increasing power density, which requires lightweight materials with low-density, high-strength, and high-stiffness at elevated temperatures.

In order to meet property requirements in increasingly severe combustion environments, new cast Al alloys are needed. This is due, in part, to inadequate thermal performance, as well as very high PCPs in advanced engine applications. As engine thermal efficiency improves, the temperature experienced by downstream exhaust components is decreased. This leads to a need for low-temperature catalyst development in order to maintain effective reduction of tailpipe emissions. Moreover, inadequate databases, modeling, and design tools are significant barriers for further development of new materials. By evaluating existing computational tools, identifying gaps that must be overcome to achieve seamless integration across multiple-length scales, and increasing understanding of the basic behavior of the material (e.g., effects of solute at the atomistic level, microstructural development, microstructure/property relationships, fracture and failure mechanisms, durability, temperature dependent behavior, etc.), more accurate design tools and predictive models can be established. High-quality, consistent, and accessible databases are needed to support this development.

Advanced high-strength steel is the most mature lightweight material in terms of widespread use in industry due to its compatibility with existing manufacturing infrastructure and vehicle materials. Application of third generation high-strength steel has the potential to reduce component weight by up to 25%, particularly in strength-limited designs. However, technical challenges remain to achieve room temperature formability, improved weldability, and reliable and accurate predictive performance models. Al continues to see steady growth in market share in the automotive industry despite issues with material cost, room temperature formability, and limitations within the existing manufacturing infrastructure. This is due to the 40% weight savings that can be achieved with Al along with the well-established domestic supply chain. Mg has the potential to significantly reduce vehicle component weight by 55% or greater; however, there are several significant technical barriers preventing the increased use of this material in vehicle designs. Mg has high raw material costs and price volatility, relatively low specific stiffness, difficulty in forming sheets at low temperatures, low ductility of finished components, and a limited alloy set, among other challenges. CF composites have the potential to reduce component weight by more than 60%. The main barriers to widespread CF use are the high cost to manufacture the CF, lack of high volume composite manufacturing methods, and a need for reliable predictive tools for both part design and performance prediction.

When combinations of the above lightweight materials are used, the resulting multi-material structures have challenges of their own. Traditional joining methods used in automotive assembly, such as resistance spot welding and riveting, are inefficient for joining of dissimilar metals and for some combinations, infeasible. In the near term, friction-stir scribe welding and resistance spot riveting are showing promising advances for joining of advanced high-strength steel and Al (e.g., the more mature lightweight metals). An additional challenge posed by multi-material structures is the increased risk of corrosion due to galvanic coupling. As barriers to the introduction of Mg and CF are overcome, breakthroughs in joining technology will also be necessary.

Program Organization Matrix

The Materials Technology subprogram is led by Program Manager, Felix Wu:

- Lightweight Materials consists of three research portfolios:
  - Light Metals (open position) includes research on property improvement and processing advances for advanced high-strength steel, Al, and Mg.
  - Carbon Fiber Composites (Carol Schutte) includes research on low-cost production of CF and predictive performance models of CF composites.
  - Joining of Dissimilar Materials (Sarah Kleinbaum) includes research on solid-state and mechanical joining methods, as well as galvanic corrosion mitigation.
- Propulsion Materials consists of two research portfolios:
  - High Temperature Materials (Jerry Gibbs) includes research on the material characteristics that influence temperature dependent behavior, as well as alloy development.
  - Materials for Aftertreatment and Emissions Control (Jerry Gibbs) includes the development of new catalyst materials that operate in a low-temperature environment.

All of the activities within the Materials Technology subprogram utilize computational methods for material discovery, prediction of structure, understanding failure mechanisms, including corrosion and the effects of processing on properties.

I. Propulsion Materials

I.1 Integrated Computational Materials Engineering

I.1.A Development and Integration of Predictive Models for Manufacturing and Structural Performance of Carbon Fiber Composites in Automotive Applications (General Motors)

Charles E.A. Finney, Principal Investigator
Fuels, Engines, and Emissions Research Center
National Transportation Research Center
2360 Cherahala Blvd.
Knoxville, TN 37932
Phone: 865-946-1243
E-mail: finneyc@ornl.gov

Jerry L. Gibbs, Technology Manager
E-mail: jerry.gibbs@ee.doe.gov

Start Date: October 1, 2014 End Date: September 30, 2018
Total Project Cost: $815,000 DOE share: $815,000 Non-DOE share: $0

Project Introduction

HD internal combustion engines for the transportation sector are operating at increasingly high PCP to achieve required increases in brake thermal efficiency. Current operating ranges are 75-190 bar PCP, and the next decade could see over 300 bar PCP. The current generation of engine structural materials, such as gray cast iron, is widely considered inadequate for the projected elevated-pressure environment of future higher-efficiency engines. Although candidate replacement materials, such as compacted graphite iron (CGI), are being developed and evaluated for use in intermediate-term applications, a robust understanding of near-cylinder stresses and temperatures, and the future materials properties necessary to enable desired engine efficiency and power densities of future higher-PCP HD engines, is lacking.

Numerical simulations offer insight into the cylinder environment at such elevated operating cylinder pressures and can help identify design needs and changes more comprehensively than can be identified experimentally. The current practice of simulation can achieve low- or high-dimensional modeling of the combustion environment or the cylinder/engine structure, but a fully coupled, high-dimensional computational fluid dynamics - finite element analysis (CFD-FEA) simulation of combustion, heat transfer and consequential material temperatures, and stresses is a fundamental development need.

Part of this limitation is the time and level of detail required to set up simulations. For FEA particularly, a proper meshing of complex geometries for high-fidelity calculation of materials stresses with conjugate heat-transfer can be very labor-intensive. However, with simplifications, a sufficient first-order estimate of future required materials properties can be gauged with simulations. This project is employing an incremental process for this problem, starting with the use of CFD results as inputs to FEA simulations of an actual production scale HD diesel engine.

Objectives

- Study the effects of operating HD internal combustion engines at higher PCP to increase engine thermodynamic efficiency.
- Evaluate the performance of currently available materials at current and projected future PCP conditions.
- Identify properties requirements of materials suitable to withstand a lifetime of operation at the elevated temperatures and pressures in future higher-efficiency HD engines.

Approach

- Use computational simulations to estimate combustion intensity and heat transfer (mapping local heat fluxes) using CFD software and evaluate the thermo-mechanical effects on materials using finite element method (FEM) software.
- Focus on three conditions: 190 bar [1 bar = 105 Pa] (current baseline), 250 bar (current stretch), and 300 bar (projected future) PCP.
- Experimentally measure relevant mechanical, thermal, and physical properties over a range of temperatures for an intermediate-grade material (CGI-450) for use as the next generation material in the models, including creep and fatigue loading in the higher temperature range.
- Evaluate materials stresses, temperatures, and design safety factors with current materials and engine design, with a focus on the cylinder head, valve faces, liner, and piston.
- Use the established HD Federal certification cycle to estimate loading conditions over a lifetime of operation where critical fatigue and creep would be expected based on measured properties.
- Partner with two HD engine original equipment manufacturers (OEMs) for material specimens and for the design and operating data of baseline targets.

Results

Activity this year focused on two efforts: (1) continuation of experimental measurement of relevant mechanical properties of an advanced, engine-grade material; and (2) numerical simulation of combustion at different operating conditions. The materials properties will be used for numerical simulations of thermal and mechanical stresses in the engine at the three PCP conditions. The combustion simulations will be used to provide boundary conditions for FEM of the engine to evaluate suitability of materials for a lifetime of commercial operation under different conditions.

In the previous year, an OEM partner supplied a sufficient quantity of one grade of CGI-450, where the following properties were measured:

- tensile strength
- thermal diffusivity
- coefficient of thermal expansion (CTE)
- critical temperatures
- specific heats
- short-term creep.

These measurements were obtained over a range of ambient temperatures, from room temperature up to 650–800°C. This temperature range greatly expanded the knowledge of CGI properties into temperature ranges relevant to modern engine operation.

This year, short-term, step-load creep measurements were completed, while measurements of long-term creep under isothermal, constant-loading were initiated. Such materials performance properties are important to evaluate suitability for long-term operation of a lifetime of commercial engine operation. The results of one isothermal, constant-load creep test are seen in Figure I.1.A.1, where a creep rupture life was measured at 211 hours at 500°C and 20 ksi loading. More tests are planned once the range of operating environments is defined.

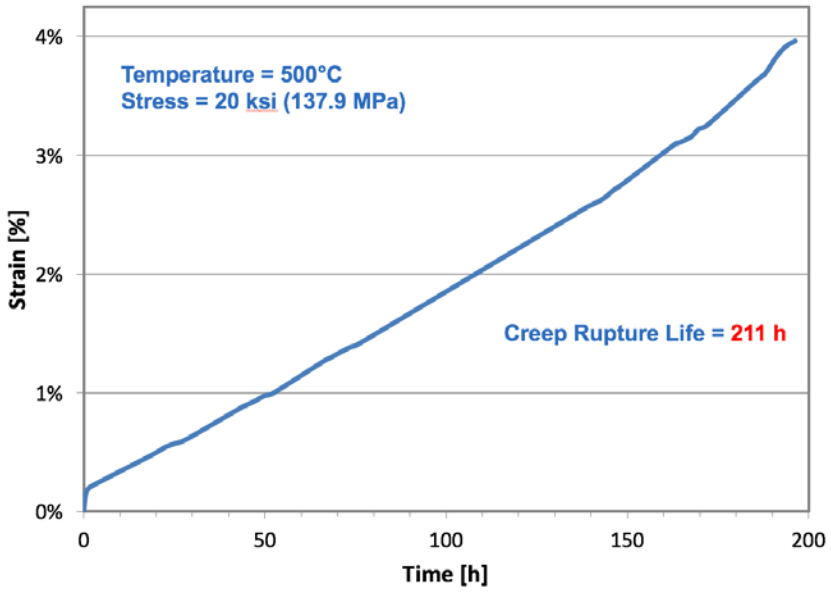

Figure I.1.A.1. Creep strain in CGI-450 specimen under isothermal constant loading.

In the CFD simulations of engine combustion, progress this year included the continuation of the tuning of conjugate heat transfer and thermal boundary conditions. In consultation with a HD OEM, the baseline operating target conditions were changed from earlier targets to match operating states more relevant to the practical engine operation. Previous simulations had used static temperatures for the head, liner, valve-face, and piston crown, but these temperatures are presently undetermined at the operating conditions in this study. Advanced conjugate heat transfer simulations were employed to tune the combustion to achieve target engine performance at the three PCPs of interest. The resulting temperature distributions and heat flux maps through the cylinder walls give the most accurate estimates of temperatures and thermal stresses available and provide high-fidelity inputs for the stress and fatigue models.

The thermal diffusivity of the material is expected to have a significant impact on heat flux from the cylinder and on the resulting materials temperature, which in turns affects the suitability of the material to withstand the mechanical stresses during engine operation. As seen in Figure I.1.A.2, the thermal conductivities of the current standard head material—gray cast iron, using publicly available data—and the advanced material—CGI-450, using Oak Ridge National Laboratory (ORNL)-measured data—differ significantly over a wide temperature range. These thermal-property differences affect materials temperatures over the engine cycle. Although the CGI material has improved fatigue resistance over gray cast iron, the thermal response is less ideal.

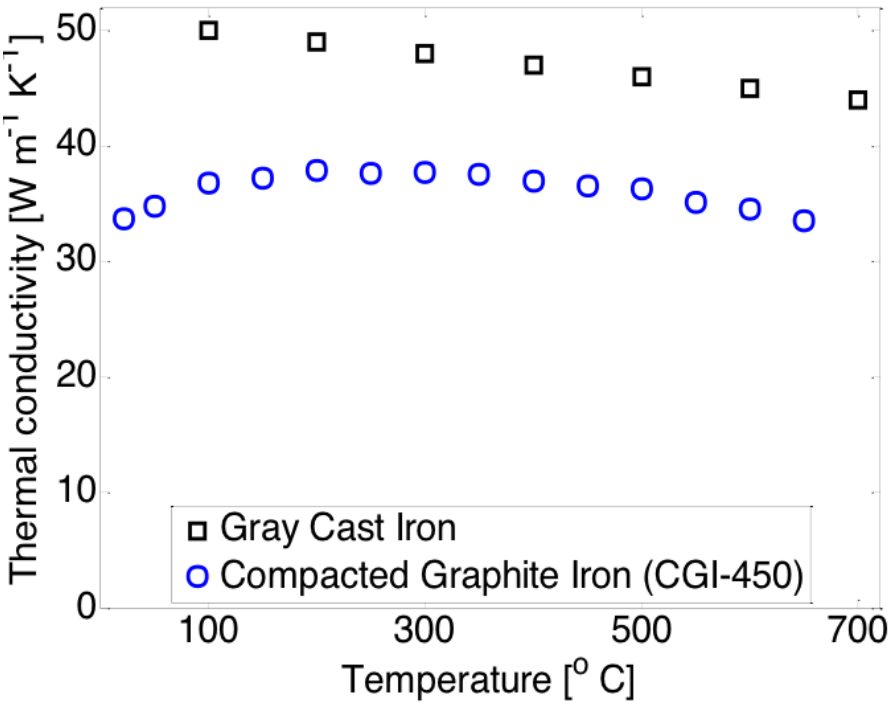

Figure I.1.A.2. Thermal conductivities of gray cast iron and CGI-450 over a range of temperatures.

Figure I.1.A.3 shows the calculated materials temperature distributions, on a cycle-averaged basis, on the fire side of the cylinder head and valves, comparing a gray cast iron and a CGI-450 cylinder head. Here, the bridge between the exhaust valves experiences significantly higher temperatures (e.g., 50–75°C or more) with CGI-450. This bridge area in the head is prone to cracking in current operation, so accurate evaluation of stresses at more extreme operating points is a necessity. Simulations are being adapted to reflect current best practices in conjugate heat transfer and combustion for an accurate calculation of cylinder heat fluxes for use in pending materials stress and fatigue evaluations.

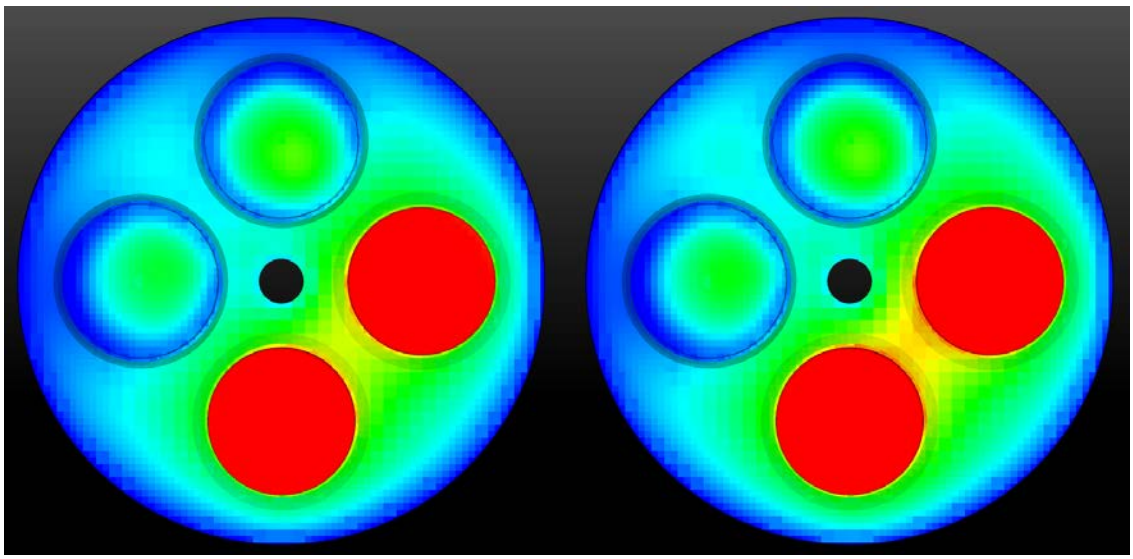

Figure I.1.A.3. Head and valve temperature distributions using different head materials: gray cast iron (left) and CGI (right). Note the higher peak temperature at the valve bridge in the CGI material with lower thermal conductivity, as shown in Figure I.1.A.2.

Conclusions

An integrated experimental and computational approach shows promise for the virtual evaluation of materials properties in the absence of an extensive experimental program; this approach also can provide guidance for future materials research. The strategies employed in the project are evolving to reflect best practices to provide the most confidence in simulated results.

Ongoing activities should include the following:

- Evaluate thermal and mechanical stresses in selected engine components at the three PCP conditions using finite-element analysis.
- Identify properties needed for prospective materials to be suitable for future production environments.
- Develop a constitutive model for CGI-450 to assist in engine analysis and design.
- Extend this methodology to light-duty engine applications.

Key Publications

Finney, C. E. A., G. Muralidharan, J. A. Haynes, and S. Simunovic, 2017, "Future Engine Requirements," U.S. Department of Energy (DOE) Vehicle Technologies Office (VTO) Annual Merit Review, PM057.

I.2 High Temperature Engine Materials

I.2.A ICME Guided Development of Advanced Cast Aluminum Alloys for Automotive Engine Applications (Ford Motor Company)

Mei Li, Principal Investigator
Ford Motor Company
2101 Village Rd., RM 2014
Dearborn, MI 18124
Phone: 313-206-4219
E-mail: mli9@ford.com

Jerry L. Gibbs, Technology Manager
E-mail: jerry.gibbs@ee.doe.gov

Start Date: February 1, 2013 End Date: August 31, 2018
Total Project Cost: $4,630,000 DOE share: $3,240,000 Non-DOE share: $1,390,000

Project Introduction

Recently legislated fuel economy standards require new United States (U.S.) passenger vehicles to achieve at least 34.1 miles per gallon (mpg) on average by model year 2016 and 58 mpg by 2030, up from 28.8 mpg today. Two major methods of achieving improved fuel economy in passenger vehicles are reducing the weight of the vehicle and developing high-performance engines. To increase engine efficiency, however, the maximum operation temperature of these components has increased from approximately 170°C in earlier engines to peak temperatures well above 200°C in current engines. This increase in operational temperatures requires a material with optimized properties in terms of tensile, creep, and fatigue strength. This program focuses on developing advanced cast Al alloys for automotive engine applications to meet these challenging requirements.

Several alloy compositions have been proposed in the past four years. Among them, Heat 17, which is 319-based (i.e., Al-silicon [Si]-copper [Cu]-magnesium [Mg] systems) with alloying of novel additions, shows higher 300°C yield strength (YS) and ultimate tensile strength (UTS) than DOE targets, even after 100 hour pre-exposure at testing temperature. In addition, this alloy has a large elevated temperature (e.g., 120°C) endurance limit that includes more important properties for automotive engine applications. Based on Heat 17, two different alloys were developed this year, which show a promising application in automotive engines. The Ford Semi-Permanent Mold Cast (Ford-SPMC) alloys utilizing a three-stage heat treatment are applicable for cylinder heads, while Ford High-Pressure Die Cast (Ford-HPDC) alloys with traditional T5 heat treatment is applicable for the engine block. In this report, the mechanical properties—including the tensile properties and endurance limits—of these two alloys will be presented to demonstrate their application prospects as an automotive engine component. The ICME tools for the simulation of post-solidification precipitation and their gaps will also be discussed.

Objectives

- To develop a new class of advanced, cost-competitive Al casting alloys providing a 25% improvement in component strength relative to components made with A319 or A356 alloys using sand- and semi-permanent casting processes for high-performance engine applications.
- To demonstrate the power of ICME tools for accelerating the development of new materials and processing techniques, as well as to identify the gaps in ICME capabilities.

- To develop comprehensive cost models to ensure that components manufactured with these new alloys do not exceed 110% of the cost using incumbent alloys A319 or A356.
- To develop a technology transfer and commercialization plan for the development of these new alloys in automotive engine applications.

Approach

- Start the alloy design process with a baseline alloy in line with 356/319 alloys with well quantified properties.
- Evaluate the heat treatment response and strengthening effect of some heat resistance elements of interest in simple model alloys, particularly at high temperatures (e.g., 300°C).
- With the aid of ICME tools, design and optimize the chemical composition and heat treatment process of the baseline alloys with novel alloying additions.
- Demonstrate new alloys' performance at both room and elevated temperature by a series of mechanical tests, including YS, UTS, endurance limits, and so on.
- With the aid of ICME tools, develop a commercialization prototyping plan, and investigate the performance of new alloys as automotive engine components by this prototyping plan.

Results

Two proposed alloys—Ford-SPMC and Ford-HPDC—and two benchmark alloys—AA319, which is the baseline alloy of the proposed alloys, and AS7GU, which is a currently used alloy for high performance automotive engines—are cast into torpedo shape. Heat-treatment for these torpedo samples are performed in a fan-assisted resistance furnace, followed by quenching into water. The quasi-static tensile test results of these alloys from room temperature to 300°C are summarized in Figure I.2.A.1. As is shown in Figure I.2.A.1.a, 300°C YS tests of these alloys exhibit a significant decrease after 100 hours of pre-exposure at this temperature. It is obvious that YS of AA319-T7 after pre-exposure cannot meet DOE requirements, while YS of Ford-SPMC with both T7 and three-stage heat treatment are still above the DOE target. The pre-exposure is always necessary for elevated temperature mechanical tests. Figure I.2.A.1.b and I.2.A.1.d indicate that both YS and UTS of the test alloys decrease with an increase in temperature. The decreasing of Ford-HPDC-T5, however, is much slower than the other alloys. Although Ford-HPDC-T5 has the lowest YS and UTS at room temperature, which is due to the lack of solution treatment in T5 heat treatment, its YS and UTS are higher than the other alloys once the testing temperatures are above 250°C. At 300°C, YS and UTS of Ford-HPDC-T5 exhibit a 30% increase, as compared to the other alloys.

It is well known that the strengthening precipitates of AA319 type alloys are mainly Θ'-Al2Cu forming during artificial aging and they coarsen rapidly when exposed to 300°C. Two different morphologies of Θ'-Al2Cu precipitates, however, are observed in the transmission electron microscopy (TEM) imaging of Ford-HPDC-T5 after 300°C quasi-static tensile test, as shown in Figure I.2.A.2. The precipitates circled by the red line have already coarsened and do not provide any degree of strength, while the precipitates circled by the blue line are still small and coherent with an Al-matrix. These coherent small Θ'-Al2Cu precipitates result in the superior 300°C YS and UTS of Ford-HPDC-T5. According to the Langer-Schwartz model, several factors are possible to slow down the precipitation kinetics of Θ'-Al2Cu, such as the diffusivity of Cu in Al, interfacial energy and strain energy between the Θ'-Al2Cu and Al-matrix. It is believed that the alloying of novel additions can prevent Θ'-Al2Cu precipitates from coarsening through one of these factors. The investigation is on-going to figure out how the novel additions affect the precipitation kinetics of Θ'-Al2Cu. Finally, although the Ford-HPDC-T5 has a superior YS and UTS above 250°C, this alloy is not applicable for cylinder head application because the elongation for cylinder head alloys are required to be above 2% and the ductility of Ford-HPDC-T5 cannot meet this requirement, as is shown in Figure I.2.A.1.d. On the other hand, as the candidate of cylinder head alloy, Ford-SPMC alloy's elongation is above 2%.

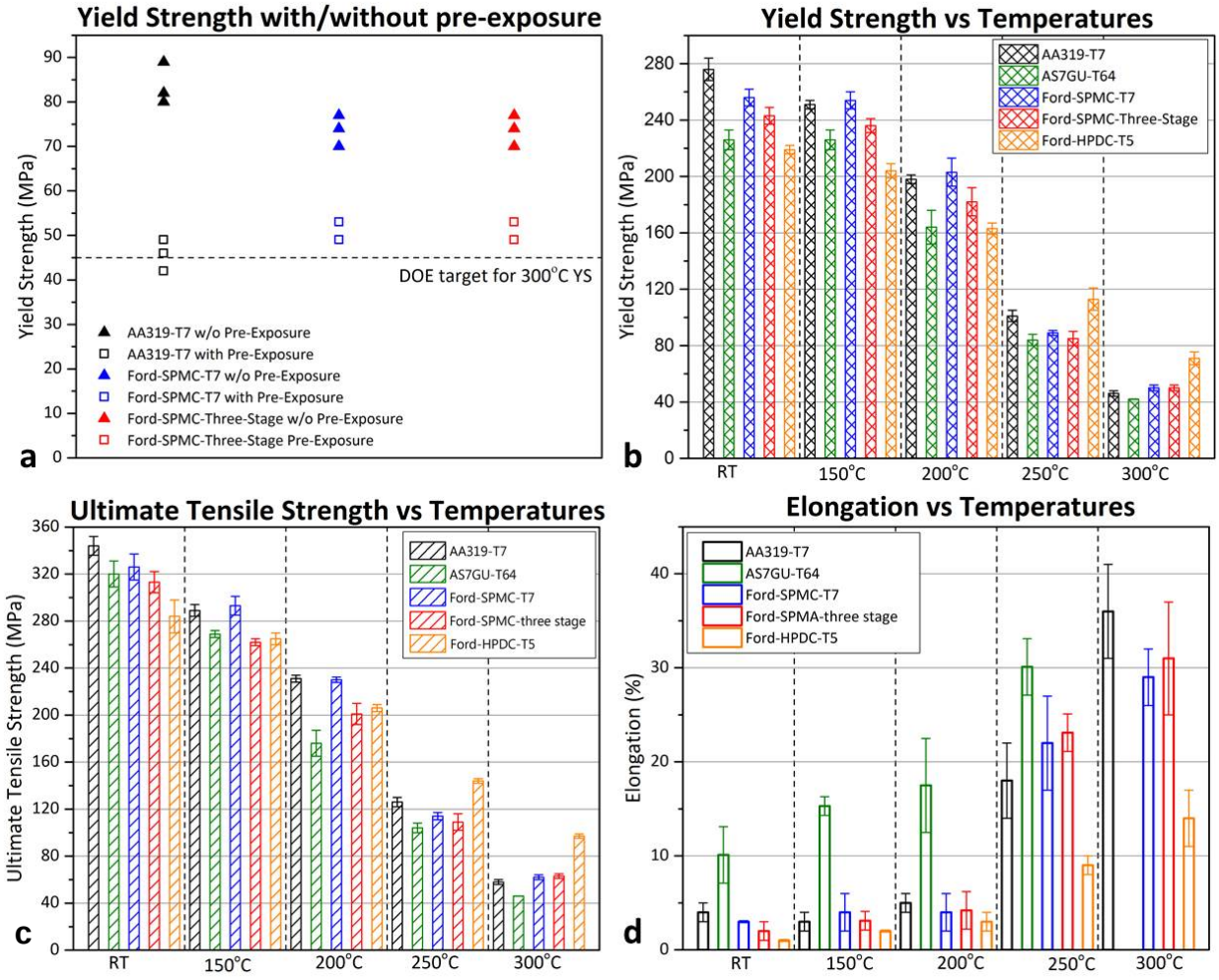

Figure I.2.A.1. Graphical representation of quasi-static tensile test results of AA319-T7, AS7GU-T64, Ford-SPMC-T7, and Ford-SPMC-Three-Stage, and Ford-HPDC-T5 from room temperature to 300°C.

According to Figure I.2.A.1, the improvement of both YS and UTS of Ford-SPMC with T7 and novel three-stage heat treatment is limited, as compared to AA319. Although it is hard for YS of AA319-T7 to meet the DOE requirement of 300°C, its YS and UTS are higher than that of Ford-SPMC at low temperatures. In the most situations, however, the failure of automotive cylinder heads are typically dominated by fatigue crack growth. As a result, the high-cycle fatigue (HCF) strength is a more important mechanical parameter than YS and UTS for cylinder head alloys, especially at temperatures above 120°C. The HCF tests were performed on a servo-hydraulic testing machine at 70 Hz. The stress ratio for all HCF tests is -1 and the criterion for HCF life is the final fracture of the sample. The HCF data are processed by the random fatigue limit (RFL) model and HCF strength predicted by this model is summarized in Table I.2.A.1. First, although no improvement is observed in room temperature HCF strength, the Ford-SPMC-three-stage has a much higher 120°C HCF strength than AA319-T7 and Ford-SPMC-T7. This result indicates that elevated temperature HCF strength benefits from novel additions only through the designed heat treatment. No enhancement is achieved through the chemistry solely, since both AA319-T7 and Ford-SPMC-T7 have comparable HCF strength at 120°C. Second, the enhanced HCF fatigue of Ford-SPMC-three-stage is maintained at least to 180°C. Thus, the Ford-SPMC-three-stage has better elevated temperature HCF performance than AS7GU-T64, because HCF strength of AS7GU drops from 83±11 megapascals (MPa) at 120°C to 62±6 MPa at 150°C. Finally, the Ford-HPDC-T5 also has excellent HCF strength at elevated temperatures. To the knowledge of the authors, the Ford-SPMC-

three-stage and Ford-HPDC-T5 have the best HCF performance at elevated temperatures (>150°C) in all of the Al alloys intended for engine applications.

To summarize, the proposed alloys—Ford-SPMC-three-stage and Ford-HPDC-T5—present significant improvements on the elevated temperature HCF strength of currently available alloys for cylinder head and engine block applications. Though this superior elevated-temperature performance is obtained at the expense of reduced tensile strength at lower operating temperatures, the performance of the proposed alloys surpass requirements at all temperatures. Comparisons to existing alloys, such as AS7GU-T64, and other heat treatments, such as Ford-SPMC-T7, through the testing of the various mechanical properties, as well as microstructural features, have established the unique features of this alloy system that lead to the dramatic increase in performance.

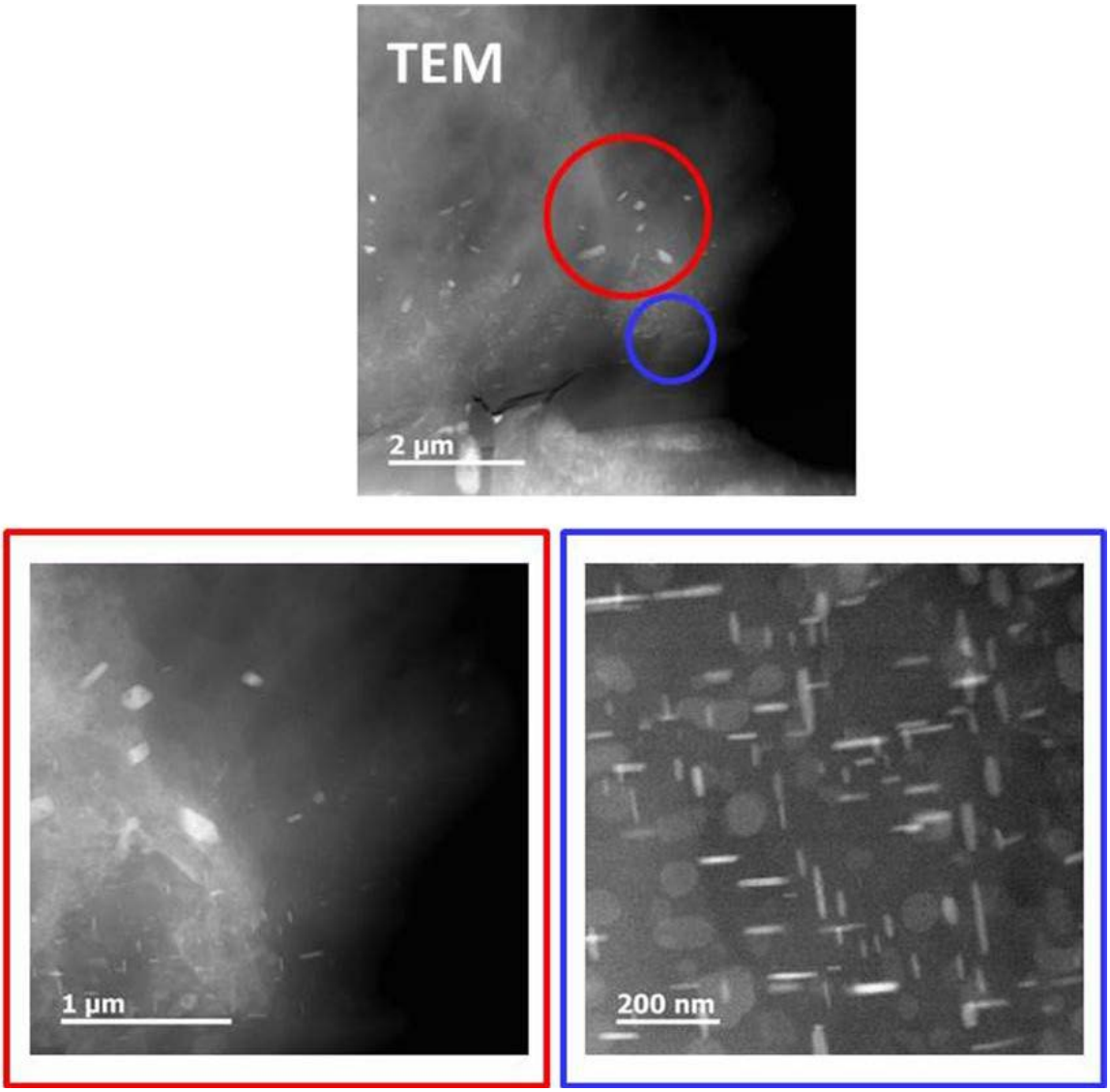

Figure I.2.A.2. Graphical representation of TEM imaging of Ford-HPDC-T5 showing lots of small and coherent Θ'-Al_2Cu precipitates with plate shape are observed after 300°C pre-exposure for 100 hours.

It has been proven that the Ford-SPMC-three-stage and Ford-HPDC-T5 alloys have superior mechanical properties as torpedo-shape samples prepared at laboratory conditions. A prototyping plan is ongoing to

demonstrate the mechanical properties reported above can be achieved as engine components. The Ford-SPMC alloy is being prototyped into two different cylinder heads: 1.5L Dragon GTDI (Dragon) and 6.7L V8 Scorpion TDI 4V Diesel (Scorpion). Meanwhile, the Ford-HPDC alloy is being prepared by a high-pressure die-cast method using I4-Bearing-Beam die to test the alloy's performance under a high-pressure die-cast condition. The testing samples will be sectioned from them and heat-treated with corresponding heat treatment. Then, quasi-static tensile tests and endurance limit tests at different temperatures will be conducted on these samples.

Table I.2.A.1. Endurance Limit of Test Alloys at Different Temperatures Calculated by RFL Model.

	RT	120°C	150°C	180°C
AA319-T7	88±6 MPa	64±6 MPa	< 64 MPa	<<64 MPa
AS7GU-T64	89±6 MPa	83±11 MPa	62±6 MPa	<62 MPa
Ford-SPMC-T7	N/A	68±17 MPa	<68 MPa	<<68 MPa
Ford-SPMC-Three-Stage	N/A	91±12 MPa	91±12 MPa	92±12 MPa
Ford-HPDC-T5	N/A	N/A	97±7 MPa	98±9 MPa

ICME has been demonstrated to be quite efficient in the development of cast Al alloys. It is based on a series of advanced materials models that bridge the many key dimensional scale from the atomistic level (~Å) to the microstructure level (~µm) and even to the component level (~m), as Figure I.2.A.3 shows. It is well known that the mechanical properties of these alloys are mainly determined by precipitates forming during artificial aging. With the aid of some theories, like the phase-field model and the Langer-Schwartz model, the precipitation behavior can be calculated. In the past four years, we have evaluated two commercial software products—TC-PRISMA developed by Thermo-Calc and Pan-Precipitation developed by CompuTherm—on their capability in simulating precipitation behavior. We have also worked with the developers to improve their software.

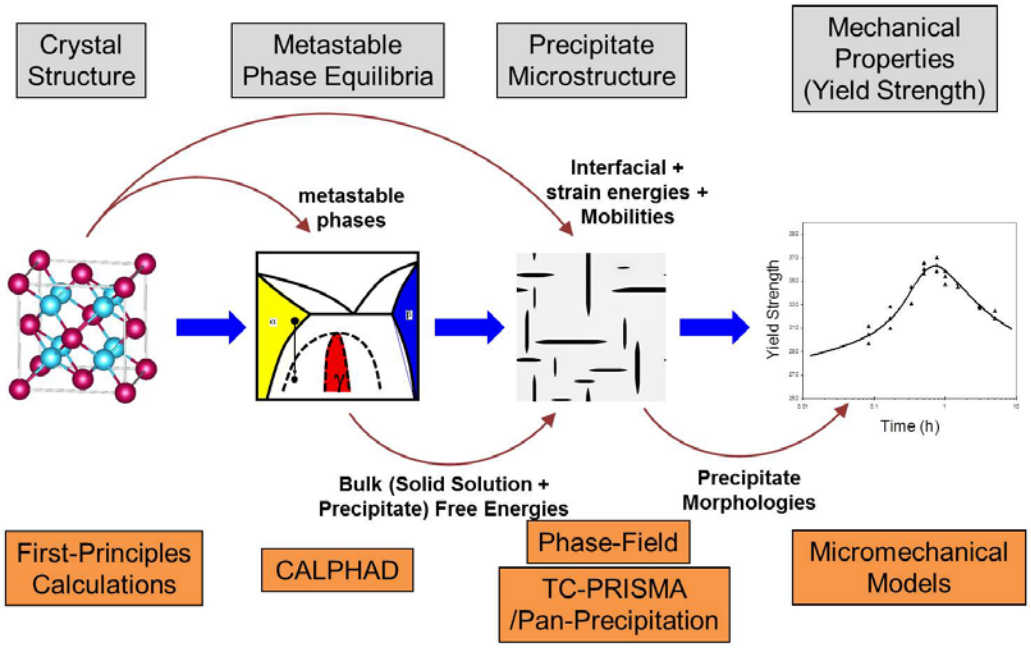

Figure I.2.A.3. Graphical representation of the various linked models needed in ICME to predict the mechanical properties of a precipitates-hardened alloy, starting from the system's fundamental microstructure and materials properties.

To evaluate the capability of TC-PRISMA and PanPrecipitation, the aging response of an Al-Si system with alloying of novel additions at 400°C were experimentally studied by TEM at the University of Michigan and small angle x-ray scatter (SAXS) at the University of Manchester. The results are shown as scatter symbols in Figure I.2.A.4. Then, the simulation with the same experimental condition, including alloy composition and aging temperature, was performed using the software mentioned above. In addition to the thermodynamic and mobility databases (i.e., TCAL4 and MOBAl3 for TC-PRISMA and PanAl2016 TH+MB for PanPrecipitation), kinetic databases were also developed for this simulation. The common parameters in a kinetic database include interfacial energy, strain energy, nucleation site parameters, and molar volume. In addition to these common parameters, a mobility enhance parameter is used in the kinetic database because it is found that the kinetics of novel additions containing precipitates in an Al-Si system are much faster than those in a system without Si by the literature and our experimental data. In fact, this observation of different precipitation kinetics should have been taken into account through the mobility database rather than the kinetic database. Thus, a gap in precipitation simulation is presented here that a reliable thermodynamic and mobility database should be developed, prior to precipitation simulation. As shown in Figure I.2.A.4, the simulated results (solid lines) with enhanced mobility show well agreement with the TEM and SAXS experiments (scatter symbols). Thus, both TC-PRISMA and PanPrecipitation work well as ICME tools to predict the precipitation behavior. It is noted that there is an unrealistic inflection locating at the aging duration of three hours in the curve simulated by PanPrecipitation. This is due to numerical issues and the software developer is trying to fix it. The next step is to use the software to predicate the precipitation behavior of Θ'-Al2Cu with plate morphology. Unfortunately, another gap is that both TC-PRISMA and PanPrecipitation cannot deal with two-dimension morphology, since they are based on the Langer-Schwartz model, which is one dimensional. We are working with the software developer to fill this gap now. In addition, the phase-field model is under evaluation as an ICME tool to simulate the aging response of precipitates with complicated morphologies.

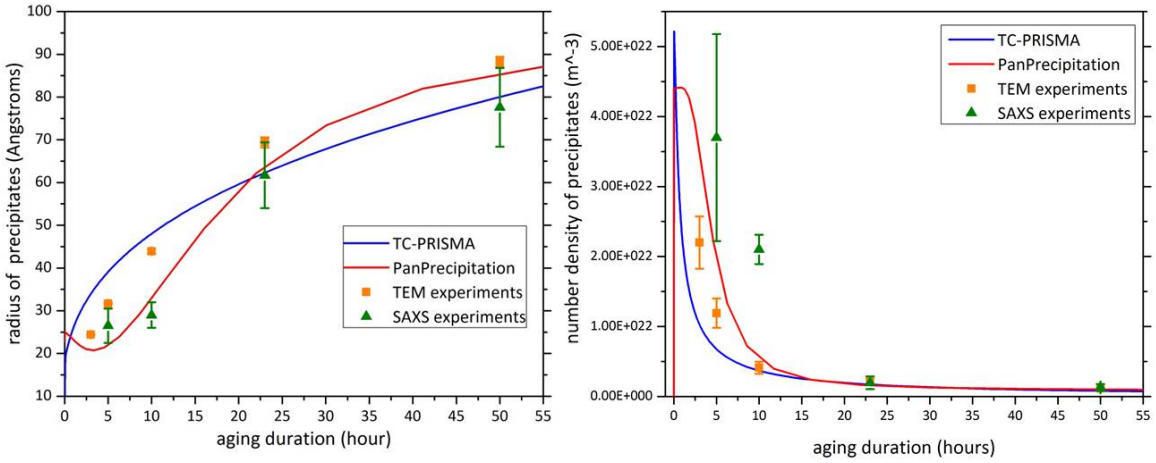

Figure I.2.A.4. Graphical representation of radius and number density of precipitates in Al-Si-TMs systems calculated by TC-PRISMA (blue) and PanPrecipitation (red) compared with the experimental data from TEM and SAXS (scatter symbols).

Conclusions

Five conclusions are drawn as follows:

1. Two Al alloys—Ford-SPMC with a novel three-stage heat-treatment process and the Ford-HPDC with a T5 heat treatment process—have been developed, which are applicable for cylinder head and engine block application, respectively.
2. Ford-SPMC with both T7 and three-stage heat-treatment can meet the DOE requirement for 300°C YS, while the baseline alloy, AA319, and current used cylinder head alloy, AS7GU, cannot meet this requirement after 100 hours at pre-exposure. In addition, Ford-HPDC with T5 heat treatment shows around a 30% increase in YS and UTS at 300°C, when compared to other alloys.

3. 150°C HCF strength of Ford-SPMC-three-stage and Ford-HPDC-T5 is above 90 MPa, which is much higher than that of AS7GU. To the knowledge of the authors, these two alloys have the best HCF performance at elevated temperatures (>150°C) in all the Al alloys intended for engine application.
4. A prototyping plan is on-going to test the mechanical properties of Ford-SPMC and Ford-HPDC as an automotive engine component.
5. TC-PRISMA and PanPrecipitation are evaluated with TEM and SAXS experimental data in an Al-Si system with alloying of novel addition. Although some gaps still exist, they have been proven to work well, and the ICME tools predict positive precipitation behavior.

Key Publications

One patent filed.

One paper to be submitted to *Scripta Materialia*.

One paper to be submitted to *Acta Materialia*.

I.2.B Computational Design and Development of a New, Lightweight Cast Alloy for Advanced Cylinder Heads in High-Efficiency, Light-Duty Engines (General Motors)

Mike J. Walker, Principal Investigator
General Motors Research and Development Center
30470 Harley Earl Blvd.
Warren, MI 48090-9055
Phone: 586-651-3757
E-mail: Mike.J.Walker@gm.com

Qigui Wang, Co-Principal Investigator
General Motors Global Propulsion Systems
800 North Glenwood Ave.
Pontiac, MI 48340-2925
Phone: 248-762-6332
E-mail: Qigui.Wang@gm.com

Jerry L. Gibbs, Technology Manager
E-mail: jerry.gibbs@ee.doe.gov

Start Date: February 1, 2013 End Date: June 30, 2018
Total Project Cost: $5,145,073 DOE share: $3,498,650 Non-DOE share: $1,646,423

Project Introduction

DOE's Office of Energy Efficiency and Renewable Energy (EERE) is targeting a 25% lighter powertrain by 2025 and a 40% lighter powertrain by 2050. As a result, the engine power density will be increased significantly. This will result in higher exhaust temperatures and a doubling of the cylinder peak pressures by 2050. To meet these requirements and achieve the stated goals, the properties of the state-of-the-art materials, like cast aluminum alloys, must increase substantially. Today, methods such as the ICME and advanced experimental analytical tools, such as the focused ion beam (FIB) microscope, high-resolution scanning transmission electron microscope (HR-STEM), and local electrode atom probe (LEAP), are now available to accelerate the timeframe usually required to develop new alloys. Combining ICME tools with expert knowledge from the field and judicious experiments for verification and validation is the quickest and most effective way to achieve the goals of developing a new high-temperature-capable Al alloy for cylinder head production.

Objectives

The objective of this project is to develop an alloy capable of handling higher temperatures and pressures experienced in smaller, more efficient engines with a material and production cost penalty of no more than 10% above current production alloys and methods. Room temperature tensile strength is to exceed current baseline aluminum alloys by 25% and 300°C, while tensile strength is to exceed by 25% and 250°C. The project will utilize state-of-the-art computational methods, analytical tools, and experimental validation to assess the true capabilities of these methods and define gaps that should be filled in the future to accelerate alloy development.

Approach

This collaborative project between General Motors (GM), QuesTek Innovations LLC (QT), Northwestern University (NU), Camanoe Associates, the American Foundry Society (AFS), and Dr. Fred Major will use ICME tools, expert knowledge, and experimental validation to identify coarsening resistant precipitate structures in the alloy to meet the high-temperature requirements. QT's proprietary iCMD™ platform is a core modeling software system that integrates proprietary and commercial mechanistic modeling tools to facilitate rapid design and development of new materials. NU has advanced microstructure characterization equipment and facilities such as TEM, atom probe, and differential scanning calorimetry (DSC), in addition to software for phase property calculations, phase field modeling, and ICME methodologies and tools. As a world manufacturer of automobiles, GM LLC has vast knowledge in the design and manufacture of engines and cylinder heads. In addition to GM's casting experience, the company utilizes many computational methods for engine design and manufacture. GM's Virtual Cast Component Development (VCCD) system interface with commercial software, such as MagmaSoft, Flow-3D, ABAQUS, FE-safe, Pandat, iSIGHT, and UGNX to integrate manufacturing processes with component design to produce reliable and high-quality cast structural components with minimum lead-time and cost. AFS and Dr. Fred Major are long-time experts in casting processing and Al alloys. Thus, the strong collaboration will utilize state-of-the-art ICME tools, such as first principles calculations, computational thermodynamic and kinetic models, virtual casting modules, and commercially available casting process simulation and structural and durability analysis software to design a new, lightweight cast-alloy with ideal multi-scale microstructures and minimum tendency for casting defects to achieve the desired high-temperature strength and fatigue performance requirements in complex castings.

Results

Mechanical Properties of Cylinder Heads Made of the Newly Developed Alloys

In 2016, the first head casting trial was carried out. Because of the extensive time required to carry out HCF results, the samples became available in 2017. Analysis of these results became the focus of 2017. Yield strength and plastic elongation results for the deckface and combustion chamber regions, where the highest temperatures are seen, are plotted in Figure I.2.B.1. Each data point represents the average of nine samples. All of the alloys are based on Q-phase precipitation hardening. Alloy l is the baseline Q-phase alloy, while Alloy 2 increases the amount of Q-phase forming elements, as well as Si, manganese (Mn), and strontium (Sr). Alloy 3 consists of the Alloy 2 composition, plus specific minor elements that are slow diffusers, segregate to the Q-phase, and have been shown to inhibit Q-phase growth. As observed in Figure I.2.B.1, increasing the amount of Q-phase and Si increases the overall strength of the alloys at all temperatures. However, at 300°C, only the addition of the minor Q-phase stabilizing elements contributes to a significant improvement in strength. In contrast to the benefit of improving yield strengths, the increased volume fraction of intermetallic phases is partially responsible for the reduction of ductility. As with composite materials, increasing the volume fraction of strengthening particles usually decreases ductility of the material. However, the loss in ductility of Alloy 3 at 300°C appears anomalous and needs to be investigated further. Without this loss of ductility, the strengths of this alloy at high temperatures could be improved further.

Scanning electron microscopy (SEM) images of fracture surfaces of the tensile specimens support the observed mechanical behavior in the three alloys. Backscattered electric images (BEI) from tensile sample fracture surfaces show an increase in intermetallic phases with the increased elements from Alloy 1 to Alloy 2 to Alloy 3. Porosity is commonly known as the most important factor affecting the ductility and fatigue of cast Al alloys. Pores are stress risers and act as crack initiators. Along with cracked Si and intermetallic particles, porosity provides weak paths for crack propagation. In general, the area fraction of porosity observed on the fracture surfaces can be more than ten times higher than the volumetric fraction of porosity in the bulk material. Figure I.2.B.2 shows the relationships between ductility and the area fraction of porosity observed on the fracture surfaces of the tensile samples of the three alloys. In general, ductility decreases with the increase of porosity observed on the fracture surfaces, particularly for Alloy 1 and Alloy 2. However, for Alloy 3,

ductility appears independent of porosity and other microstructure characteristics, presumably the oxides and intermetallic phases that dominate the effect of porosity on the loss of the ductility of Alloy 3.

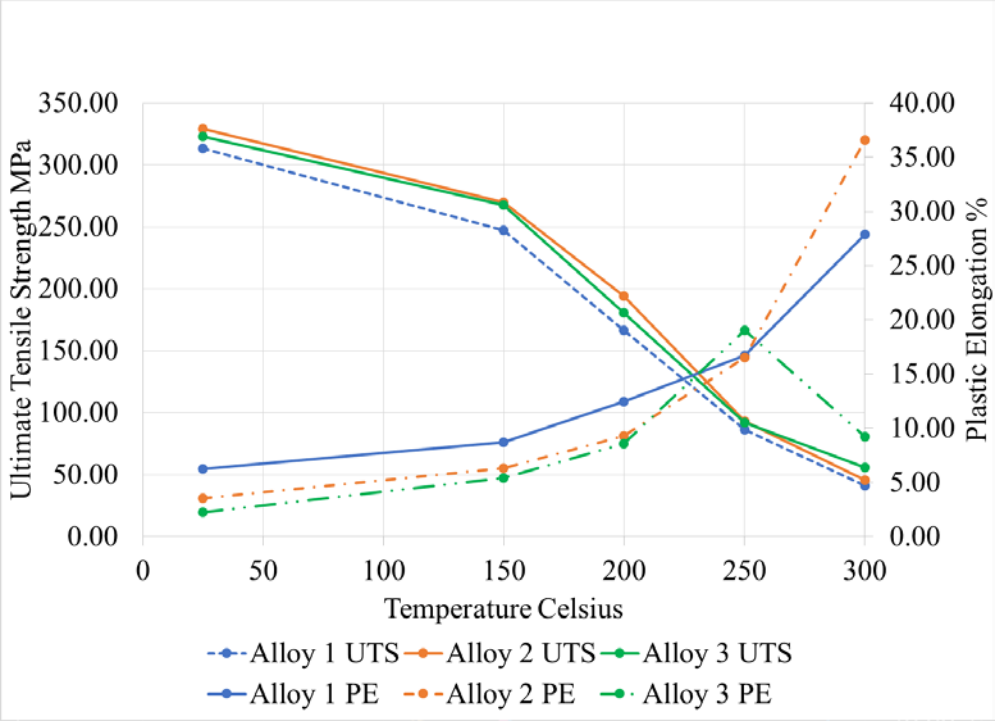

Figure I.2.B.1. UTS and plastic elongation of the deckface and combustion chamber specimens of engine cylinder heads. All samples above 150°C were conditioned for 100 hours at temperature.

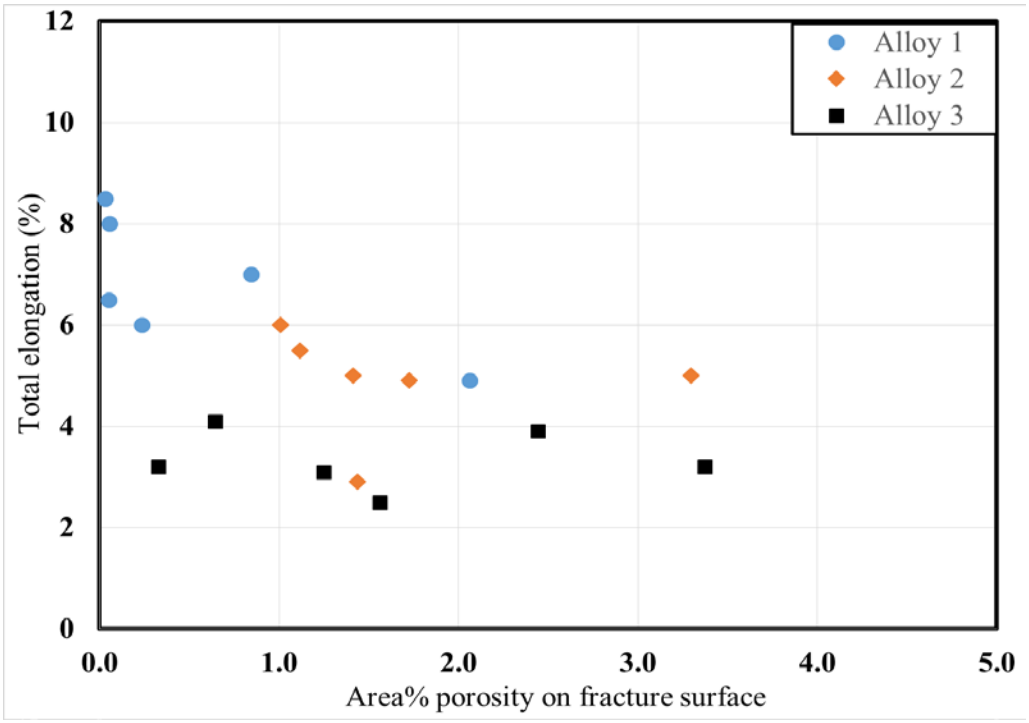

Figure I.2.B.2. Relationship between tensile ductility (elongation) and area fraction of porosity on the tensile fracture surfaces of three alloys.

The size and volume fraction of porosity in Al castings is strongly related to melt treatment, casting process, and alloy composition. For a given casting process and melting practice, a small variation of alloying elements can play an important role in porosity as they affect castability of the material, including freezing range, fluidity, feeding capability, hot tearing, etc. In comparison with Alloy 1, both Alloy 2 and Alloy 3 have a higher area fraction of porosity. A similar increase in pore sizes is seen in both Alloy 2 and Alloy 3, as shown in Figure I.2.B.3.

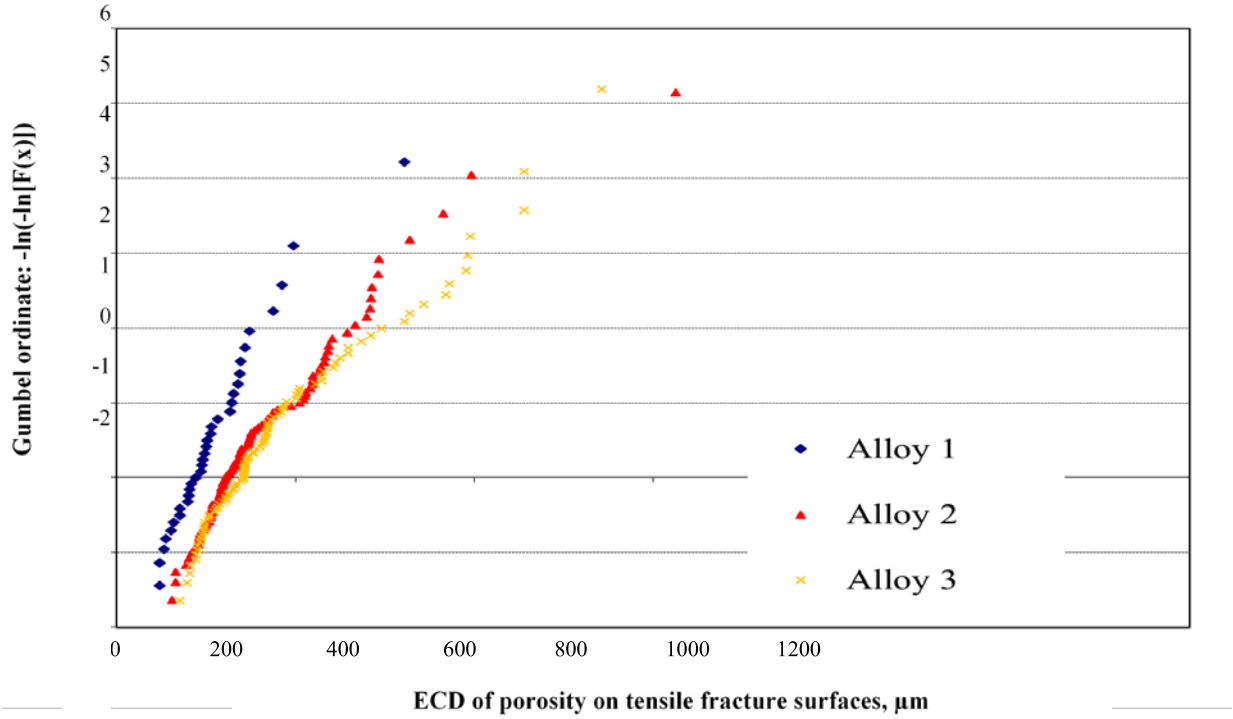

Figure I.2.B.3. Gumbel distribution of the pore sizes of three alloys.

The improvement in tensile strength of Alloy 3 over Alloy 1 and Alloy 2 can be directly attributed to the size and misorientation of Q-phase precipitates in the three alloys. The measurements of the Q-phase dimensions are shown in Table I.2.B.1. TEM images of the tree alloys preconditioned at 300°C for 100 hours are shown in Figure I.2.B.4. Further measurements are ongoing and the data will be used to improve the strength models.

Table I.2.B.1. Q-Phase Precipitate Size Measured in Head Castings Samples Conditioned for 100 Hours at Test Temperature.

	Alloy 1		Alloy 2		Alloy 3	
Temperature (°C)	Length nm	Radius nm	Length nm	Radius nm	Length nm	Radius nm
200	148± 50		164 ± 54		141 ± 51	
250			449 ± 184		358 ± 129	
300		67 ± 23		55 ± 16		26 ± 11

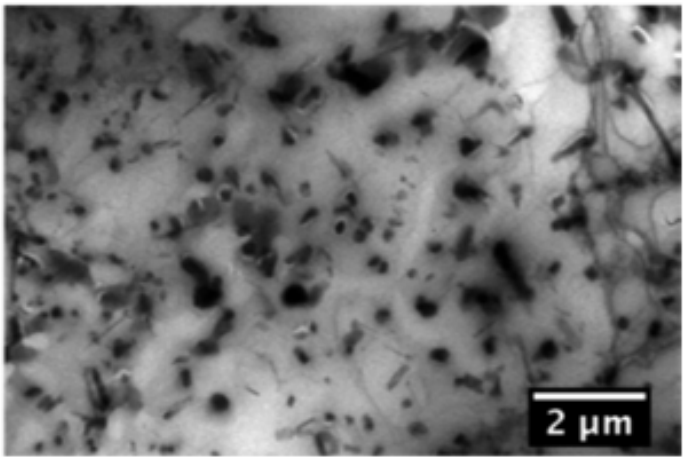

(a)

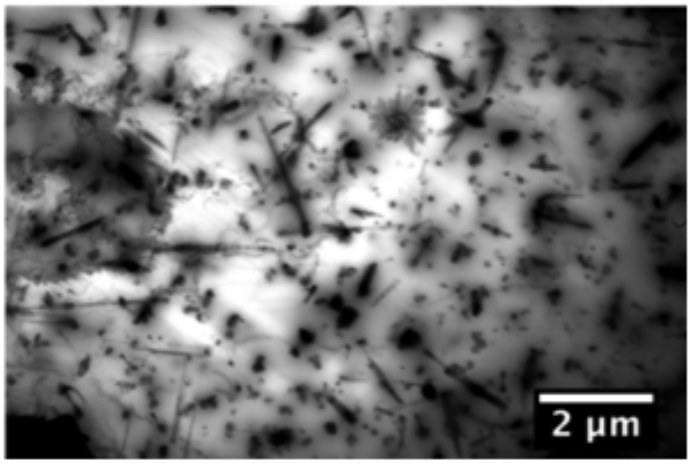

(b)

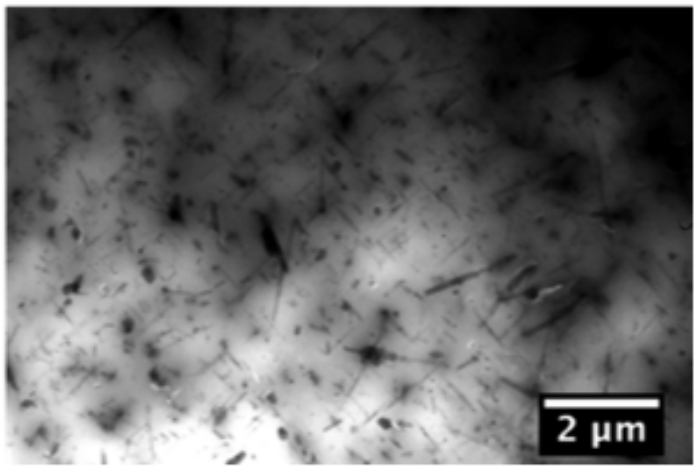

(c)

Figure I.2.B.4. TEM micrographs of cylinder head samples conditioned at 300°C for 100 hours (a) Alloy 1, (b) Alloy 2, and (c) Alloy 3.

Both high cycle (10^7 cycles) and low cycle (10^4 cycles) fatigue testing has been completed. A comparison of HCF results for the deckface and combustion chamber areas among the three alloys is shown in Table I.2.B.2.

Table I.2.B.2. HCF (107 cycles) Results for Three Alloys in Combustion Chamber and Deckface Areas.

Temperature (°C)	Alloy 1 HCF (MPa)	Alloy 2 HCF (MPa)	Alloy 3 HCF (MPa)
Room	65.5	58.5	90.3
150	63.6	59.7	67.2
250	48.7	51.2	52.7

SEM image analysis of fracture specimens from HCF samples reveal a distinct difference between the crack initiation sites of Alloy 1 and Alloy 3. Alloy 1 initiation sites are dominated by microporosity, while Alloy 3 initiation sites are dominated by oxide inclusions. Thus, similar to tensile specimens, alloy chemistry, and process conditions used to produce the third alloy resulted in fatigue failure more by oxides and inclusions. Despite this fact, overall tensile and fatigue values of Alloy 3 exceeded the other alloys because of the reduction in coarsening of the Q-phase precipitate.

A second casting trial on engine cylinder heads was carried out in 2017. The aim of this trial is to continue to improve on the mechanical properties of the Q-phase alloy. Properties of these castings and subsequent microstructural analysis will be carried out in 2018. Methods to improve on the processing of the coarsening resistant alloy are being investigated.

Alloy Strength Model

A YS model that takes into account the base material strength, solid-solution strengthening, dislocation strengthening, grain-size strengthening, and precipitation strengthening due to rod-shaped Q-phase and plate-shaped Θ phase (at both peak-aged and over-aged conditions) and the effect of the Al-Si eutectic has been developed. For solid-solution strengthening, two models have been implemented—empirical models and the Feltham Trough model. The major contribution to strength was observed to be due to precipitation strengthening. A rod-shaped strengthening model for Q-phase was developed, predicting both peak-aged and over-aged strength of the alloy. The model was extended to include the strength contribution of plate-shaped Θ phase for strength predictions in alloys containing dual-precipitation of the Q-phase and the Θ phase. Based on the TEM results and the literature survey, it was assumed that Q-phase precipitates (like Θ phase) are not shearable and strengthening contributions can be completely modeled by Orowan equations. Coarsening of precipitates was modeled according to Lifshitz, Slyozov, and Wagner (LSW) theory by predicting the coarsening rate of precipitates based on the Lee coarsening model. The model has been compared to high-temperature tensile tests and shown to have a mean average error of 18.6 MPa and a Pearson correlation coefficient of 0.97 for a series of six different Al alloys with a variety of Q-phase and Θ phase strengthening. The YS models do not currently reflect the effects of misorientation, but developments in this area are being investigated. The model predictions and measured tensile YS data taken at various temperatures are plotted in Figure I.2.B.5.

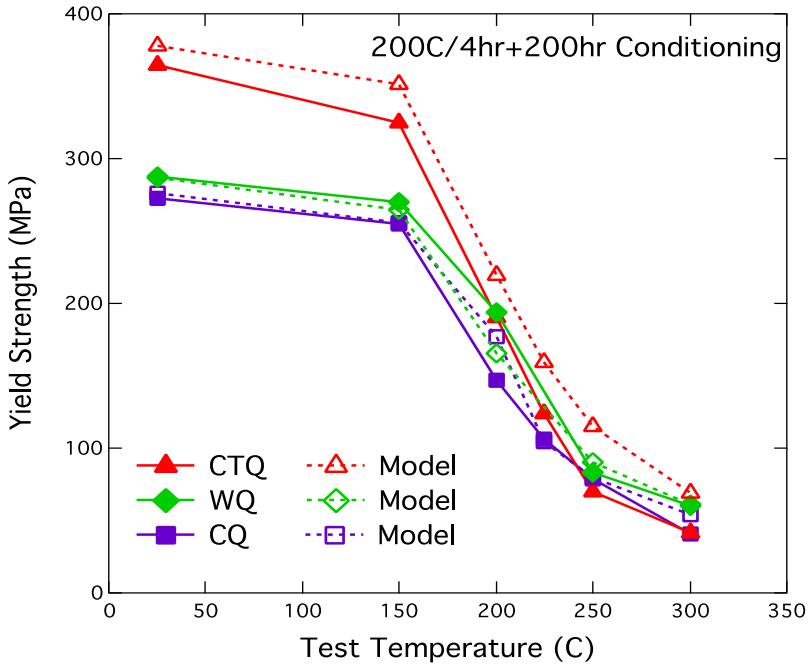

Figure I.2.B.5. Measured and predicted YS of Q and Θ + Q alloys.

Conclusions

A heat-resistant Q-phase-based alloy has been developed and cast into engine cylinder heads with current production tooling. Properties of the alloy meet most of the program targets. However, microstructural analysis has also revealed that the alloy's properties in cylinder heads are significantly affected by process conditions that limits its ductility and overall strength. Methods to improve the process are being developed that could further increase the strength and ductility of the alloy, while maintaining the excellent castability already achieved.

Key Publications

Bobel, A. C., M. J. Walker, and G. Olson, 2017, "Strengthening model to optimize coarsening resistant Q- and θ phase precipitates in Al-Si-Mg-Cu cast alloys," presented at TMS 2017 Annual Meeting and Exhibition, February 2017.

Bobel, A., K. Kim, C. Wolverton, M. Walker, G. Olson, 2017, "Equilibrium composition variation of Q-phase precipitates in Al alloys," submitted to *Acta Materialia*.

Kim, K., A. Roy, M. P. Gururajan, C. Wolverton, and P. W. Voorhees, 2017, "First-principles/phase-field modeling of equilibrium Theta' precipitation in Al-Cu alloys," submitted to *Acta Materialia*.

Patent Application Filed 04/07/17: "Methods to increase solid solution zirconium in aluminum alloys."

Walker, M., A. Bobel, N. Hatcher, A. Saboo, D. Frankel, K. Kim, and C. Wolverton, 2017, "Progress and gaps in thermodynamic modeling for the development of advanced cast aluminum alloys using integrated computational materials engineering," presented at the Materials, Metals, & Minerals Society (TMS) 2017 Annual Meeting and Exhibition, February 2017.

I.2.C High Performance Cast Aluminum Alloys for Next Generation Passenger Vehicle Engines (Oak Ridge National Laboratory)

Amit Shyam, Principal Investigator
Oak Ridge National Laboratory
1 Bethel Valley Rd.
Oak Ridge, TN 37831
Phone: 865-576-2894
E-mail: shyama@ornl.gov

J. Allen Haynes, Co-Principal Investigator
Oak Ridge National Laboratory
1 Bethel Valley Rd.
Oak Ridge, TN 37831
Phone: 865-576-2894
E-mail: haynesa@ornl.gov

Jerry L. Gibbs, Technology Manager
E-mail: jerry.gibbs@ee.doe.gov

Start Date: November 15, 2013 End Date: December 31, 2017
Total Project Cost: $5,500,000 DOE share: $3,500,000 Non-DOE share: $2,000,000

Project Introduction

The cast Al alloys that are standard across the automotive industry for cylinder heads, such as Al 319 and Al 356, have now been available for several decades. The design and implementation of higher efficiency passenger automotive engines is currently limited by the absence of economical lightweight materials with improved castability, higher temperature strength, and fatigue performance. The next generation of lightweight alloys must allow a significant reduction in the total weight of automobiles, while still maintaining vehicle performance and safety. The electrification of transportation vehicles has accorded an additional emphasis on lightweighting because of the additional weight of power systems, such as batteries.

The development of new cast Al alloys that allow improved performance will be dictated to a large extent by the ability to manipulate and enhance the desirable features of microstructural constituents. The alloy system, however, is too complex to undertake this development process by trial and error. Indeed, a trial and error alloy development approach is inefficient and expensive in the long run. In this regard, predictive modeling and ICME provide powerful tools to accelerate the development and deployment of new cast Al alloys. In this project, we performed ICME-based iterative design and development of new cast Al alloys with improved performance characteristics compared to industry standard Al 319/356 alloys. The new family of cast Al alloys provides a significant opportunity for the automotive industry to increase engine and vehicle efficiency.

Objectives

- Develop high-performance cast Al alloys with improved castability, high-temperature strength, and fatigue performance compared to industry standard Al 319 and 356 baseline alloys. Engine cylinder heads cast with the new alloys will have a minimum of 25% strength improvement compared to those cast from the baseline alloys. The cost of engine cylinder heads manufactured by the new alloys will be less than 110% of heads manufactured by Al 319 or 356. Effectively, the new alloys will allow a 50°C increase in maximum operating temperature of cylinder heads to 300°C.

- Evaluate the adequacy of existing ICME models and codes for the prediction of properties and development of cast Al alloys. A gap analysis report for existing ICME codes for cast Al alloy development will be generated prior to the project end date of December 31, 2017.

Approach

- Industry partners were Fiat Chrysler Automobile, U.S., LLC (FCA) and Nemak U.S.A. Inc.
- Special facilities included the characterization and computational facilities at ORNL, including but not limited to the aberration corrected electron microscope (ACEM), the Oak Ridge Leadership Computing Facility (OLCF), the Center for Nanophase Materials Sciences (CNMS), and the spallation neutron source (SNS). A complete list is provided in Table I.2.C.1.
- Developed microstructure property maps for baseline compositions.
- Predictive modeling and ICME approach was taken for alloy development and material/component property prediction.
- Casting and mechanical property measurements were performed for selected compositions.
- Components were cast for materials that met cost and property requirements.
- Engine testing for components in progress.
- Cost analysis for the production of hundreds of thousands of components is complete.
- Commercialization plan is in progress.

Results

The major goal of this project was to develop and implement cost-effective and improved cast Al alloys that will enable the design of higher efficiency light-duty passenger vehicle engines. The developed alloys needed to have improved high-temperature strength, fatigue performance, and castability compared to industry standard 319 and 356 alloys. A traditional physical metallurgy-based approach, as well as a computational materials science-based approach, was taken to identify promising new candidate alloying elements that could be added to improve the castability and elevated temperature microstructural stability/mechanical properties of Al alloys. The additional or substitutional elements needed to result in an alloy within acceptable cost constraints as stated earlier. Models for metal casting, microstructure evolution, residual stress, and mechanical property prediction were implemented. Several identified alloys were cast in small batches and standard test specimens were harvested from the batch castings for property measurements. The differences in the measured and predicted properties will serve as a basis to identify the gaps in existing ICME codes. The gap analysis report will be provided before the end date of the project (December 31, 2017) and will include the following: (a) a list of predictive modeling tools and grade them in terms of investment needs (e.g., short and long term); (b) a list of tools that can be led by industry; and (c) a list of tools in terms of their impact.

Previous annual reports have included information regarding our progress on the characterization of alloys. Significant progress was achieved in the development of alloys with improved tensile properties up to 300°C. It was demonstrated previously in the present project that the high-temperature performance of Al alloys is limited by the stability of their microstructure at elevated temperature. The new alloys have stable microstructures up to a temperature of 350°C and three joint patent applications from our team describe the composition range of these new alloys. In previous years, it was reported that components have been successfully cast with selected alloy compositions. This FY, our work focused on engine testing of components cast with one of our alloys and a cost model for the new alloy family, development of a commercialization plan, and a gap analysis report. In addition, complex cylinder heads were cast with the new Al-Cu-Mn-Zr (zirconium) alloys. Figure I.2.C.1 gives an example of this new alloy with 8 wt% Cu.

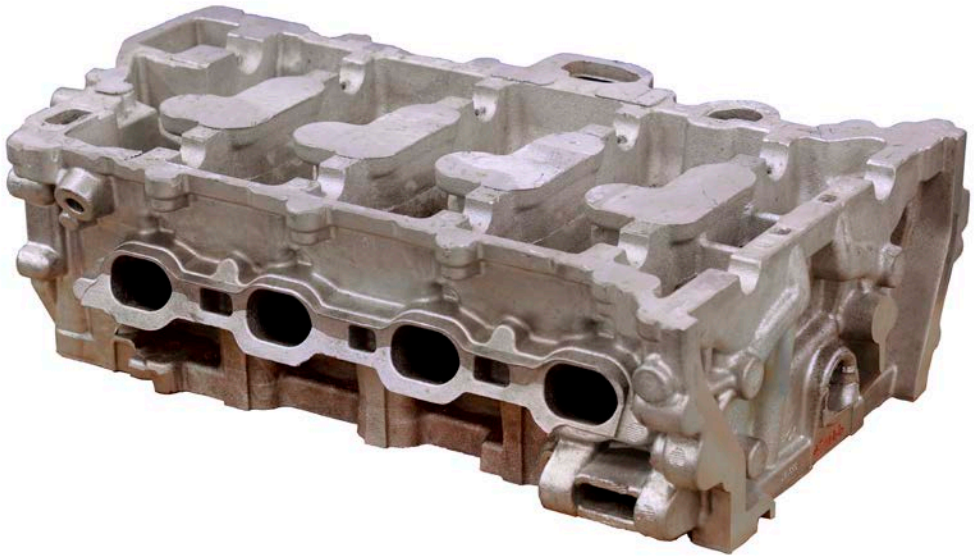

Figure I.2.C.1. A cylinder head sand-cast with one of the new Al-Cu-Mn-Zr alloys. An identical cylinder head is presently undergoing engine testing at a dyno at the OEM partner.

Table I.2.C.1. A List of Facilities and Tools that Were Utilized in the Course of Our Four Year Effort.

Facility/Tool Name	Context of Use
Aberration Corrected Electron Microscope	Look at precipitate microstructures, atomic scale imaging and analysis.
Brookhaven's National Synchrotron Light Source (NSLS)	Phase identification in cast alloys.
Center for Nanophase Materials Science	Atom probe tomography.
Mechanical, x-ray diffractometer (XRD), SEM, Electron Probe Microanalysis (EPMA), and thermal property characterization	Characterization of baseline and new alloys at ORNL.
Spallation Neutron Source	Residual stress measurements on engine cylnder heads.
Worcester Polytechnic Institute (WPI) Casting Facility	To determine the hot tearing resistance of new alloys.
ProCast	Simulation of casting and thermal and mechanical properties of baseline alloys (ORNL License).
Vienna Ab initio Simulation Package (VASP)	Density functional theory calculations (ORNL License).
Element	Constrained thermal fatigue testing and some of the aging-dependent hardness studies.
Scientific Equipment Company (SECO)	Machinability studies on new alloys.
Nemak Casting Facility	Larger scale castings and hot tear studies. Casting of tensile and fatigue testing coupons and cylinder heads.
ORNL Casting Facility	Smaller scale castings for alloy development and hardness testing coupon.
FCA Corrosion Evaluation	Evaluation of baseline and new alloys in representative corrosive environments.
FCA Engine test Evaluation	Engine testing of components cast from new alloys.

In this reporting period, over 120 cylinder heads were cast in multiple successful casting trials using the existing commercial gravity sand-casting processes common for high-volume cylinder heads. Residual stress was measured with neutron diffraction techniques at an experiment performed at ORNL's SNS in November 2016. The measurements were performed on cylinder heads cast with both the commercial diesel alloy (e.g., A356 + 0.5Cu) and one of our new alloys. The first stress invariant (e.g., MPa) as a function of relative distance across the combustion cylinder face of a sample A356 + 0.5 Cu cylinder head was reported. More work was performed on characterizing the cylinder heads, developing appropriate heat treatments, and the characterization of machinability, thermal conductivity, corrosion resistance, and thermomechanical fatigue resistance. Most of this work was led by the industry partners through their cost-shared effort.

An engine test of one of the Al-Cu-Mn-Zr alloys was initiated in the reporting period. A preliminary cost model of our new cast Al alloy family was developed. A 7% estimated increase in material costs for the new alloys was within the 10% total increase in cost that was stipulated in the original funding opportunity announcement (FOA).

Overall, this was a very successful collaborative effort between ORNL and the industry partners. A summary of the outcomes from this project in relation to the key FOA targets are summarized in Table I.2.C.2. Table I.2.C.3 provides a summary of the project output to date. It should be noted that the ORNL/FCA/Nemak team received a 2017 R&D 100 award for the new Al-Cu-Mn-Zr alloy technology developed under the VTO Propulsion Materials program. A commercialization plan will be outlined by FCA and presented to DOE in the last quarter of the Cooperative Research and Development Agreement (CRADA) project in the first quarter of FY 2018 (e.g., by November 30, 2017). ORNL will also provide a Gap Analysis Report to DOE upon project completion.

Table I.2.C.2. Outcomes of Current Project Compared to Targets in FOA.

Property	Cast Alloy Targets	Outcomes
Tensile Strength @ 300°C	9.5 ksi @ 300°C	19.8 ksi @ 300°C (>2X target and ~3-4X of baseline 319 and 356 type alloys).
Hot Tearing Resistance and Castability	Excellent	Excellent (Improved hot tearing resistance compared to 319 type alloys).
Thermal Fatigue Performance	@ 300°C	>10 X compared to A356 and >3X compared to 319 type alloys.
Cost	$ 1.1x/lb	Cost of alloys within 10% of baseline alloy cost (~1.07x).
Thermal Conductivity	No target in FOA	Improved thermal conductivity compared to 319 alloys and close to that of A356 + 0.5 Cu alloy.
Machinability	No target in FOA	Excellent and comparable to baseline alloys such as A356 + 0.5 Cu.

Table I.2.C.3. Summary of Project Output to Date.

Activity	Outcome
Joint Patent Applications	3
Invention Disclosures	4
Invited talks	10
Publications	10
Awards	ORNL Significant Event Award, December 2016; Distinguished Researcher Award for team member Lawrence Allard; 3rd Place - Best Poster Award; 2nd Place – Best Poster Award, ASM Students Poster Competition; R&D 100 Award 2017.

Conclusions

High temperature Al alloys were developed by a team of researchers from ORNL with FCA and Nemak. These new Al alloys are affordable, lightweight, and capable of withstanding temperatures almost 100°C higher than current commercial alloys while providing exceptional thermomechanical performance and hot-tear resistance. Common commercial alloys soften rapidly at high temperatures, limiting their use in next-generation vehicles, while other alloys that can withstand elevated temperatures are cost-prohibitive and difficult to cast. The Al-Cu-Mn-Zr alloys were developed using a suite of atomic-level characterization and computation tools, resulting in a strong, stable, and versatile material capable of withstanding the stressful conditions of next-generation high-efficiency combustion engines. The alloys are currently being engine-tested at FCA and could be commercially available through our industry partners as early as 2019. The unique properties of this new family of alloys were also recognized with a 2017 R&D 100 Award.

Key Publications

Cooper, R. C., S. Roy, A. Sabau, C. S. Hawkins, and A. Shyam, 2015, "Defect modeling and endurance limit prediction for cast aluminum alloys," *TMS Annual Meeting*, March 16, 2015, Orlando, FL, USA (**Invited**).

Milligan, B., S. Roy, C. S. Hawkins, P. Shower, and A. Shyam, 2017, "Creep behavior of cast Al-Cu alloys at 300°C," (Poster Presentation) *TMS Annual Meeting*, San Diego, CA, USA.

Roy, S., C. S. Hawkins, D. McClurg, G. Muralidharan, L. F. Allard, A. Rodriguez, and A. Shyam, 2014, "Microstructure-mechanical property correlation in several cast Al alloys," *Materials Science and Technology (MS&T) 2014*, October 12–16, 2014, Pittsburgh, PA, USA.

Roy, S., L. F. Allard, A. Rodriguez, T. R. Watkins, and A. Shyam, 2017, "Comparative evaluation of cast Al alloys for automotive cylinder heads: Part I – Microstructure evolution," *Metallurgical and Materials Transactions A*, Vol. 48, No. 5, pp. 2529–2542.

Roy, S., L. F. Allard, A. Rodriguez, W. D. Porter, and A. Shyam, 2017, "Comparative evaluation of cast Al alloys for automotive cylinder heads: Part II – Mechanical and thermal properties," *Metallurgical and Materials Transactions A*, Vol. 48, No. 5, pp. 2543–2562.

Roy, S., L. F. Allard, and A. Shyam, 2015, "Nano-scale strength modeling of cast Al alloys," *TMS Annual Meeting*, March 16, 2015, Orlando, FL, USA.

Sabau, A. S., 2015, "Modeling of casting defects in an integrated computational materials engineering approach," *2015 TMS Annual Meeting & Exhibition*, Proceedings: Advances in the Science and Engineering of Casting Solidification: An MPMD Symposium Honoring Doru Michael Stefanescu, Orlando, FL, USA.

Sabau, A. S., 2015, "Modeling of casting defects in an integrated computational materials engineering approach," in Nastac, L., B. Liu, H. Fredriksson, J. Lacaze, C.-P. Hong, A. V. Catalina, A. Buhrig-Polacez, C. Monroe, A. S. Sabau, R. E. L. Ruxanda, A. Luo, S. Sen, and A. Diószegi (eds.) Advances in the Science and Engineering of Casting Solidification: An MPMD Symposium Honoring Doru Michael Stefanescu, John Wiley & Sons, Inc., Hoboken, NJ, USA. doi: 10.1002/9781119093367.ch28.

Sabau, A. S., 2016, "Modeling of interdendritic porosity defects in an integrated computational materials engineering approach for metalcasting," *International Journal of Cast Metals Research*, accepted for publication in February 2016.

Sabau, A. S., S. Mirmiran, C. Glaspie, S. Li, D. Apelian, A. Shyam, J. A. Haynes, and A. F. Rodriguez, 2017, "Hot-tearing of multi-component Al-Cu alloys-based casting load measurements in a constrained permanent mold," *TMS Annual Meeting*, San Diego, CA, USA.

Sabau, A. S., W. D. Porter, S. Roy, and A. Shyam, 2014, "Process simulation role in the development of new alloys based on an integrated computational materials engineering approach," paper IMECE2014-37982, Proceedings of the *ASME 2014 Int. Mech. Eng. Congress & Exposition IMECE2014*, Volume 14: Emerging Technologies; Engineering Management, Safety, Ethics, Society, and Education; and Materials: Genetics to Structures, November 14–20, 2014, Montreal, Quebec, Canada (**Invited**).

Shin, D., 2014, "High-performance cast Al alloys for next generation passenger vehicle engines," *Materials Genome Initiative: Materials Data Workshop*, July 15–16, 2014, Dayton, OH, USA (**Invited**).

Shin, D., 2015, "Solute cluster and vacancy interaction in multi-component Al alloys," *TMS Annual Meeting*, March 16, 2015, Orlando, FL, USA.

Shin, D., A. Shyam, S. Lee, Y. Yamamoto, and J. A. Haynes, 2017, "Solute segregation at the Al/θ'-Al2Cu interface in Al-Cu alloys," *Acta Materialia*, Vol. 141, pp. 327–340.

Shin, D., S. Lee, A. Shyam, and J. A. Haynes, 2017, "Petascale supercomputing to accelerate the design of high-temperature alloys," *Science and Technology of Advanced Materials*, Vol. 18, No. 1, pp. 828–838 (invited article).

Shin, D., S. Roy, L. F. Allard, J. A. Haynes, and A. Shyam, 2017, "Solute segregation in Al alloys" *TMS Annual Meeting*, San Diego, CA, USA.

Shin, D., S. Roy, T. R. Watkins, and A. Shyam, 2017, "Lattice mismatch modeling of Al alloys," *Computational Materials Science*, Vol. 138, pp. 149–159.

Shower, P. T., B. Radhakrishnan, J. R. Morris, and A. Shyam, 2017, "The evolution of θ′ precipitates in an Al-Cu alloy investigated with phase field theory," *TMS Annual Meeting*, San Diego, CA, USA.

Shower, P., S. Roy, C. S. Hawkins, and A. Shyam, 2017, "The effects of microstructural stability on the compressive response of two cast Al alloys up to 300°C," *Materials Science & Engineering A*, Vol. 700, pp. 519–529.

Shyam, A., D. Shin, S. Roy, A. Sabau, Y. Yamamoto, and J. A. Haynes, 2017, "An assessment of modeling tools for high-temperature Al alloy development: The good, the bad and the ugly," (**Invited**) *TMS Annual Meeting*, San Diego, CA, USA.

Shyam, A., D. Shin, S. Roy, L. F. Allard, Y. Yamamoto, T. R. Watkins, and J. A. Haynes, 2017, "High-temperature Al alloy development: Computational thermodynamics and kinetics," (**Invited**) *TMS Annual Meeting*, San Diego, CA, USA.

Shyam, A., J. A. Haynes, A. Rodriguez, J. A. Gonzalez, S. Mirmiran, C. Glaspie, and G. Black, 2017, "Heat-treatments for high-temperature cast Al alloys and components fabricated from them," U.S. Patent Application Number 62/577,324, Filed October 26, 2017.

Shyam, A., S. Roy, D. Shin, L. F. Allard, Y. Yamamoto, J. R. Morris, B. Mazumder, J. Poplawsky, J.-C. Idrobo, A. Rodriguez, T. R. Watkins, and J. A. Haynes, 2017, "Cast Al alloys with extreme microstructural stability at elevated temperature," (in review).

Shyam, A., Y. Yamamoto, D. Shin, J. A. Haynes, A. Sabau, A. Rodriguez, J. A. Gonzalez, S. Mirmiran, and C. Glaspie, 2017, "Al alloy compositions and methods of making and using the same," U.S. Patent Application Number 15/594,434, Filed May 12, 2017.

Shyam, A., Y. Yamamoto, D. Shin, S. Roy, J. A. Haynes, P. Maziasz, A. Sabau, A. Rodriguez, J. A. Gonzalez, J. Talamantes, L. Zhang, S. Mirmiran, and C. Glaspie, 2016, "Al alloy compositions and methods of making and using the same," U.S. Patent Application Number 15/160,926, Filed May 20, 2016.

Watkins, T. R., S. Roy, L. F. Allard, A. Shyam, D. Shin, and J. A. Haynes, 2017, "X-ray and microstructural study of a set of cast Al alloys," (Poster Presentation) *TMS Annual Meeting*, San Diego, CA, USA.

I.2.D Computation-Guided Development of Lower Cost Alumina-Forming Alloys (Oak Ridge National Laboratory)

Govindarajan Muralidharan, Principal Investigator
Oak Ridge National Laboratory, Materials Science and Technology Division
1 Bethel Valley Rd.
Oak Ridge, TN 37831
Phone: 865-574-4281
E-mail: muralidhargn@ornl.gov

Jerry L. Gibbs, Technology Manager
E-mail: jerry.gibbs@ee.doe.gov

Start Date: October 1, 2015 End Date: September 30, 2019
Total Project Cost: $800,000 DOE share: $800,000 Non-DOE share: $0

Project Introduction

Improving the engine efficiencies of passenger and commercial vehicles is a major goal of the VTO and materials play a significant role in achieving this objective. One potential approach to achieving improved combustion engine efficiency and specific power, in engines with high-manufacturing volumes, is through retaining more heat in the exhaust gas to recover in a turbocharger. Higher exhaust gas temperatures increase the operational temperature requirements of structural components in the exhaust gas path, particularly the exhaust valves. It has been projected that exhaust gas temperatures would increase from a 2012 value of 760°C to values of at least 870°C and very likely reach as high as 1000°C in the long-term (DOE-EERE 2013a, DOE-EERE 2013b). Availability of structural engine materials with adequate high-temperature mechanical properties and oxidation resistance to enable the projected engine operating parameters without exceeding the cost constraints is a barrier to the adoption of new higher-efficiency powertrain technologies. In particular, at higher temperatures, YS and oxidation resistance in a water vapor-containing environment become more critical for materials exposed to exhaust gases.

High-performance exhaust valves currently used at temperatures up to ~760°C are fabricated using nickel (Ni)-based alloys, such as alloy 751. Other higher-performance Ni-based alloys primarily developed for aerospace applications have the potential to operate at temperatures of up to 1000°C with desired strength, but are too expensive for automotive applications and may be difficult to fabricate into desirable shapes. Additionally, at temperatures greater than 850°C, achieving good oxidation resistance in exhaust gases containing water vapor may be challenging for existing high-strength alloys such as alloy 751 that depend on the formation of chromium (Cr)-based protective oxides (chromia) for their oxidation resistance. Hence, new alloys with appropriate strength, oxidation resistance, and formability are necessary for the operating characteristics and lifetime expectations for automotive valves in next-generation powertrains. This project is focused on a lower technology readiness level (TRL) development of alloys that form Al-based protective oxides (alumina), which are more stable than chromia at higher temperatures, and thus have the potential for improved oxidation resistance in water-vapor containing environments when compared to chromia-forming alloys. However, it is more challenging to establish higher strengths at elevated temperatures in conventionally formed alumina-forming alloys.

Objectives

The primary objective of this project is the identification and research development of materials for alumina-forming exhaust valves that could operate at temperatures of up to 1000°C. These alloys should have the appropriate combinations of cost, high-temperature mechanical properties, and oxidation resistance required for exhaust valve applications for on-road powertrains.

Approach

The overall approach used in this project focuses on identifying affordable alloys with an appropriate combination of two-key properties—oxidation resistance and mechanical properties. Required materials properties are being identified, baseline material properties are evaluated, and the development of new materials are targeted and characterized with the goal of achieving required properties at a lower cost.

A recently concluded alloy development project by this team successfully addressed the development of new lower cost chromia-forming Ni-iron (Fe)-Cr alloys for use in exhaust valves at temperatures up to 870°C through a synergistic approach that included computational modeling and selected experimental evaluation of properties (Muralidharan 2017a, Muralidharan 2017b). The premise behind this approach has been that mechanical properties can be correlated with microstructure and the fractions of microstructural constituents can be predicted as a function of composition through thermodynamic modeling. Different phase fractions of strengthening phases and their compositions can be achieved through alloying element additions, thermomechanical processing, and heat-treatment. Microstructural characteristics of existing alloys can be correlated with their mechanical properties to identify desirable compositions and microstructures. Once such correlations are established, computational modeling of untested compositions can be used to identify compositions that have the potential for improved properties. Small heats of targeted materials can then be processed to confirm the modeled properties and broaden the correlation database.

In an earlier study on automotive valves for performance at 870°C and 950°C, synergistic computational and experimental aspects were used to develop cost-effective Ni-based alloys (Muralidharan 2017a, Muralidharan 2017b). A range of Ni-based alloys with potentially varying weight fractions (or volume fractions) of the key γ'-Ni_3Al strengthening phase were identified in efforts to correlate the high-temperature fatigue properties with the microstructure of the alloys. The selection of nine commercial Ni-based alloys included Alloy 751, Waspaloy, Udimet 520, and Udimet 720. The Ni+Co contents ranged from 66–76 wt %. To obtain initial information on the microstructures of these alloys at equilibrium, thermodynamic calculations were carried out. Comparison of the results of the calculations showed that all alloys have a matrix of γ with the major strengthening phase as γ'. One or more carbide phases such as $M_{23}C_6$, MC, and M_7C_3 may also be present in different alloys. The primary difference between the microstructures of the various alloys was the weight percent of the γ' phase at a given temperature and the highest temperature at which the γ' phase is stable in the different alloys. Since the size of the strengthening precipitates is also critical, it was anticipated that the kinetics of coarsening of this phase would also be influential in the long-term performance of the alloys in this application. Using the microstructures of these alloys as a guide, computational thermodynamics was used to design new alloys with microstructure similar to the commercial alloys in an effort to obtain materials with desirable properties. In contrast to the commercially available alloys with Ni+Co contents greater than 66 wt%, the Ni+Co content in these newly identified candidate alloys was lower than 50 wt % (i.e., Ni being replaced with other elements such as Fe) with the potential to achieve comparable properties. While it has been shown that strength targets are achievable, the oxidation resistances at 950°C of the newly developed alloys were limited to short peak exposure times. This stems from the fact that this previous study focused on alloys that achieve oxidation resistance through the formation of chromia scales. Alloys that rely on the formation of an alumina scale have the potential for improved oxidation resistance and the focus of the current work is alumina-forming alloys. The focus of the current work is to use a similar approach to develop new alloys that are alumina-formers, with significantly improved oxidation resistance at 950°C and beyond.

Results

Figure I.2.D.1 shows a comparison between the oxidation resistance of two commercial alumina-forming alloys—Haynes HR-214® (Ni-16Cr-3Fe-4.5Al-0.01Y-0.04C) and Haynes HR-224®(Ni-20Cr-27.5Fe-3.6Al-0.3Si-0.3Ti-0.05C)—with that of two commercially available chromia-forming alloys—IN®751 and Udimet®520. Note that at 950°C in air + 10% water vapor environment, the chromia-forming alloys show a significantly larger positive mass change (e.g., weight gain), followed by a rapid loss of mass indicative of spallation and/or volatilization. In contrast, the alumina-forming alloys show a small mass gain over extended periods of time (in this case, 1750 hours) indicating very good oxidation resistance at these temperatures. Note that the presence of water vapor creates a more aggressive test and also effectively simulates the exhaust environment.

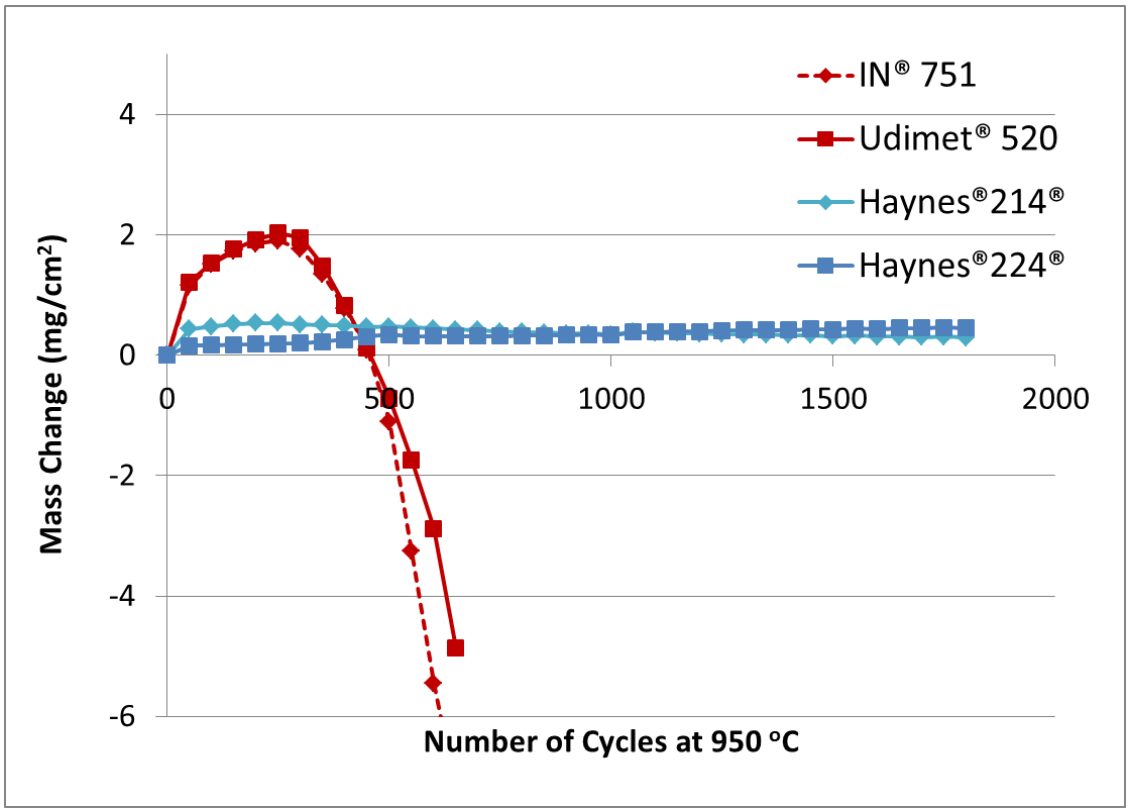

Figure I.2.D.1. Mass change of selected commercial chromia-forming and Al-forming alloys during exposure to an air + 10% water vapor environment at 950°C.

Figure I.2.D.2 shows the mass change at 950°C in air + 10% water vapor environment for Udimet®520—a commercial chromia-forming alloy, two commercial alumina-forming alloys, and three ORNL-developed alumina-forming alloys with lower Ni-levels than the commercial alumina-forming alloys. Note that the ORNL-developed alloys show good oxidation behavior similar to that of the commercial alumina-forming alloys for times up to 1500 hours. These are very encouraging results.

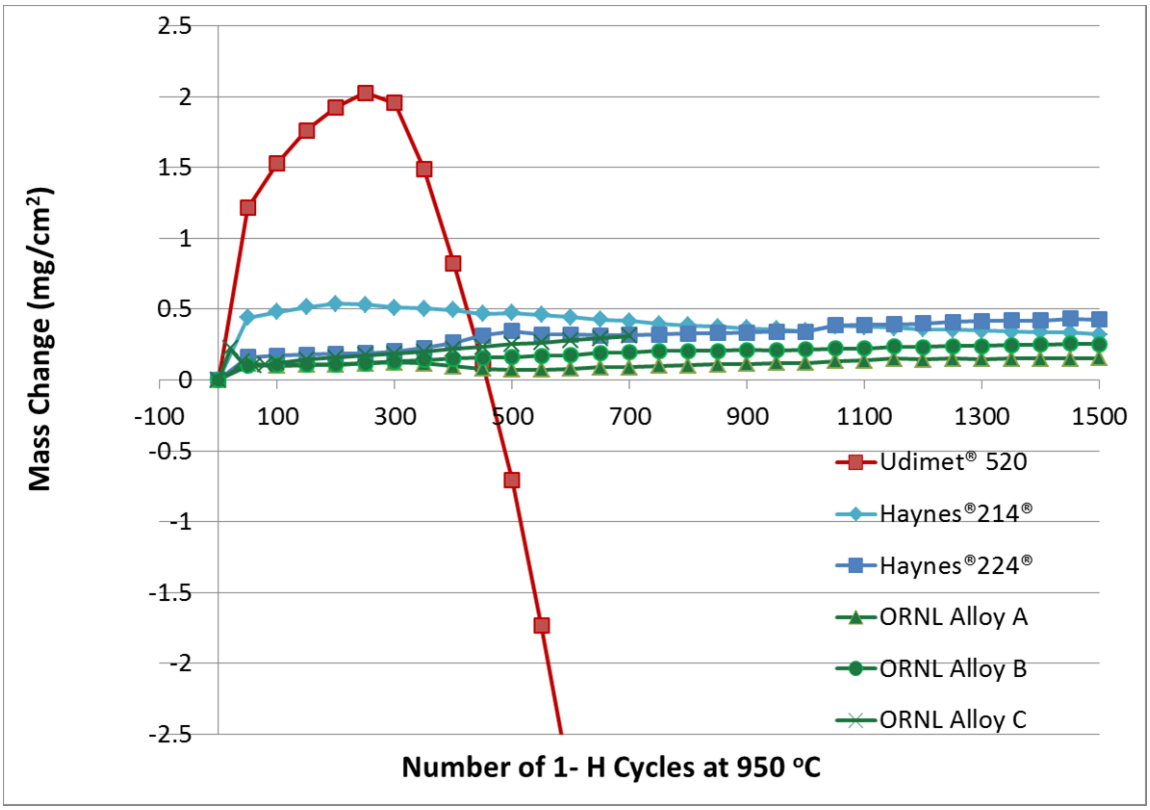

Figure I.2.D.2. Mass change of selected commercial Al-forming alloys compared to ORNL developed Al-forming alloys during exposure to an air + 10% water vapor environment at 950 °C.

Figure I.2.D.3 shows the YSs at 950°C of two commercial chromia-forming alloys and two chromia-forming alloys with lower Ni contents developed at ORNL (Muralidharan 2017a, Muralidharan 2017b) compared with that of two commercially available alumina-forming alloys. Note that all of the commercial alumina-forming alloys have significantly lower strength at 950°C when compared to the commercial and ORNL-developed chromia-forming alloys.

Thus, a significant target and challenge for the current project is the development of alumina-forming alloys with a significantly higher YS at 950°C, without compromising the oxidation resistance of these alloys. Figure I.2.D.4 shows the YSs of several new alumina-forming alloys developed at ORNL compared with that of commercial alumina-forming alloys. These alloys also use lower Ni levels in an effort to lower the overall cost of the alloys. Note that significant improvements have also been achieved in the YS measured at 950°C. Further alloy development and microstructural characterization in collaboration with Argonne National Laboratory (ANL) is in progress to improve the strength of alumina-forming alloys (Andrews et al. 2017).

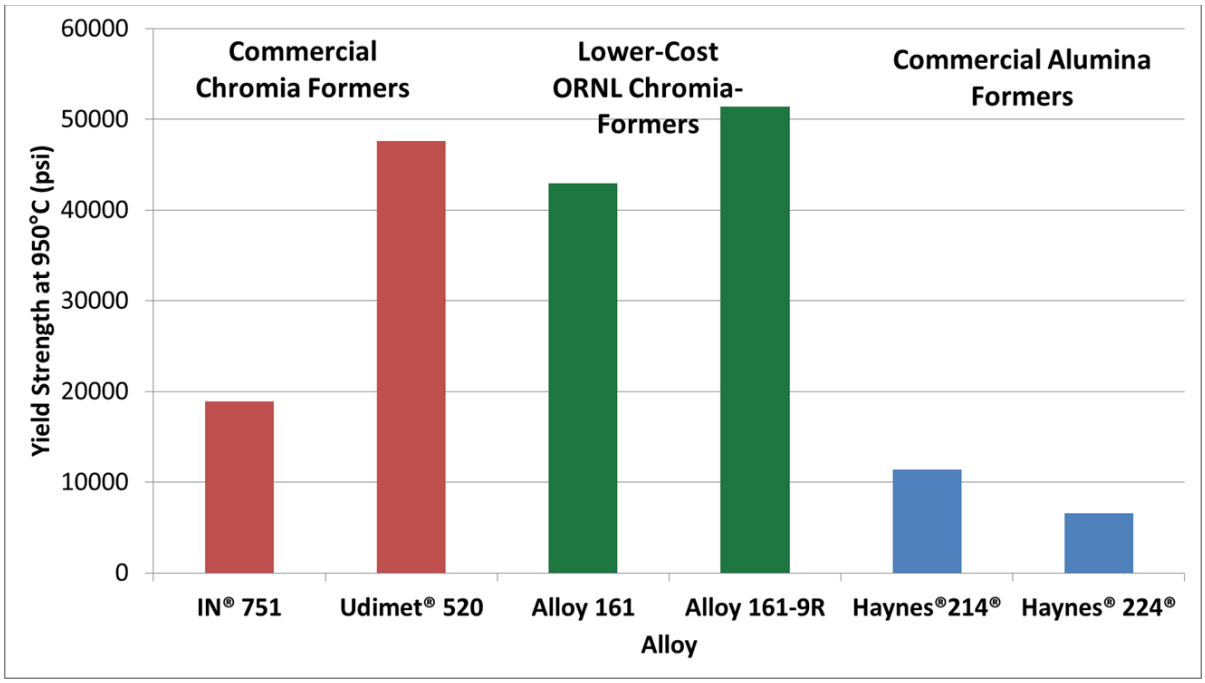

Figure I.2.D.3. YS at 950°C of selected commercial chromia-forming and alumina-forming alloys.

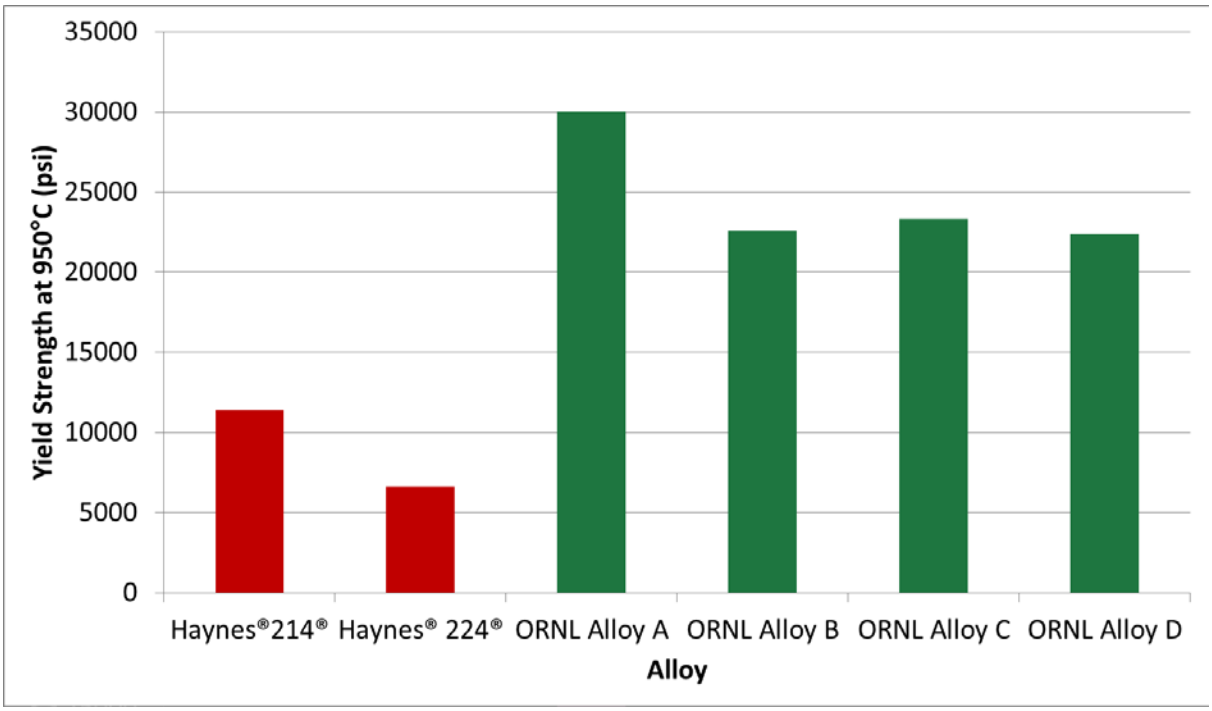

Figure I.2.D.4. YS at 950°C of ORNL-developed alumina-forming alloys show significant improvement over commercial alumina-forming alloys.

Conclusions

A computationally guided approach is being used to develop affordable new higher strength alumina-forming alloys at 950°C for future exhaust valves for advanced combustion engines. New alumina-forming alloys with oxidation resistance comparable to commercial alumina-forming alloys, but with greater YS at 950°C are being developed. Further alloy development is in progress to improve the high-temperature YS of the new alloys, while also maintaining superior oxidation resistance.

References

Andrews, R. N., J. Serio, G. Muralidharan, and J. Ilavsky, 2017, "An in situ USAXS-SAXS-WAXS study of precipitate size distribution evolution in a model Ni-based alloy," *Journal of Applied Crystallography*, Vol. 50, pp. 734–740. https://doi.org/10.1107/S1600576717006446.

DOE-EERE, 2013a, "DOE Vehicle Technologies Workshop Report: Light-Duty Vehicles Technical Requirements and Gaps for Lightweight and Propulsion Materials, February 2013." https://www.energy.gov/sites/prod/files/2014/03/f13/wr_ldvehicles.pdf.

DOE-EERE, 2013b, "DOE Vehicle Technologies Workshop Report: Trucks and Heavy-Duty Vehicles Technical Requirements and Gaps for Lightweight and Propulsion Materials, February 2013." https://www.energy.gov/sites/prod/files/2014/03/f13/wr_trucks_hdvehicles.pdf.

Muralidharan, G., 2017a, U.S. Patent No. 9,605,565, "Low-cost Fe-Ni-Cr alloys for high-temperature valve applications," March 28, 2017.

Muralidharan, G., 2017b, U.S. Patent No. 9,752,468 B2, "Low-cost, high-strength Fe-Ni-Cr alloys for high-temperature exhaust valve applications," September 5, 2017.

I.2.E Lightweight High-Temperature Alloys Based on the Al-Fe-Si System (University of Florida)

Michele V. Manuel, Co-Principal Investigator
University of Florida
549 Gale Lemerand Dr.
Gainesville, FL 32611
Phone: 352-846-3780
E-mail: mmanuel@mse.ufl.edu

Richard Hennig, Co-Principal Investigator
University of Florida
549 Gale Lemerand Dr.
Gainesville, FL 32611
Phone: 352-392-7327
E-mail: rhennig@mse.ufl.edu

Jerry L. Gibbs, Technology Manager
E-mail: jerry.gibbs@ee.doe.gov

Start Date: October 1, 2016 End Date: September 30, 2019
Total Project Cost: $1,102,081 DOE share: $991,873 Non-DOE share: $110,208

Project Introduction

Automotive applications need low-cost, lightweight, high-temperature alloys to enhance efficiencies in systems such as internal combustion engines. The Al-Fe-Si system provides an opportunity to develop such a material, as it comprises all of the three low-cost elements that are abundant in nature. Specifically, the τ_{10}-Al-Fe-Si (Al_4-$Fe_{1.7}$-Si) ternary intermetallic phase is a lightweight and low-cost phase that exhibits excellent mechanical properties at high-temperatures. However, the τ_{10}-Al_4-$Fe_{1.7}$-Si phase has an extremely small compositional range, which should be expanded in order to use this alloy at commercial scale. To increase this compositional range, the equilibrium phase boundaries can be manipulated and expanded- via alloy design and non-equilibrium processing, while the parts can potentially be fabricated by additive manufacturing.

Objectives

The objective of this project is to design alloy chemistries to create phases with an excellent combination of mechanical properties and to 3D laser print them to exploit the nearly non-equilibrium nature of the total melting and solidification process. Additions of a quaternary solute X to an Al–Fe–Si system will be examined. It is expected that alloys produced will have three times the tensile strength of competing intermetallics and have a density comparable to Ti–Al alloys.

Approach

The recipient will use an integrated computational approach spanning electronic structure calculations to thermodynamic models that are paired with strategic experiments for alloy characterization, and thereby, validation to produce revolutionary automotive components that will supersede current commercial and research-grade high-temperature alloys.

The project will be conducted in 3 budget periods:

Budget Period 1: The recipient will identify candidate solute elements that may have the potential to increase the compositional range over which the τ10-Al_4-$Fe_{1.7}$-Si phase is stable. Ternary and quaternary alloys will be cast via arc melting.

Go/No-Go: Deliver alloys that have the potential to display a stable τ10 Al-Fe-Si-X phase.

(Go) This deliverable was achieved through the experimental demonstration of the desired τ10 phase in the Al-Fe-Si-Ni alloy system (where X = Ni).

Budget Period 2: For the candidate solute elements, the recipient will expand the compositional range of the τ10 phase by computationally evaluating its energetic and thermodynamic stability.

Go/No-Go: Creation of a list of chemistries suitable for powder processing via 3D printing.

Budget Period 3: Component manufacturing: Specimens for mechanical and microstructural characterization will be produced using 3D powder bed processing.

Go/No-Go: Production of mechanical test samples using additive manufacturing.

Results

Al-Fe-Si alloys were successfully fabricated via arc melting. The presence of τ_{10}-Al_4-$Fe_{1.7}$-Si phase in these alloys was confirmed by energy-dispersive spectroscopy (EDS) and XRD. After annealing the samples at different temperatures, the τ_{10}-$Al_4Fe_{1.7}Si$ phase of had a volume fraction in the range of 60 to 100%. The alloys resulting in single phase τ_{10}-Al_4-$Fe_{1.7}$-Si (100v%) after homogenization have a nominal composition of $Al_{24.5}$-$Fe_{10.2}$-Si (at%) and $Al_{26.0}$-$Fe_{9.0}$-Si (at%). All compositions in this report are presented in at%. SEM backscattered electron (BSE) images of the two alloys are shown in Figure I.2.E.1.a and Figure I.2.E.1.b. Figure I.2.E.2 shows XRD patterns of the as-cast and homogenized alloy with a nominal composition of $Al_{26.0}$-$Fe_{9.0}$-Si. The results confirmed the homogenized $Al_{26.0}$-$Fe_{9.0}$-Si alloy is the τ_{10}-Al_4-$Fe_{1.7}$-Si single phase.

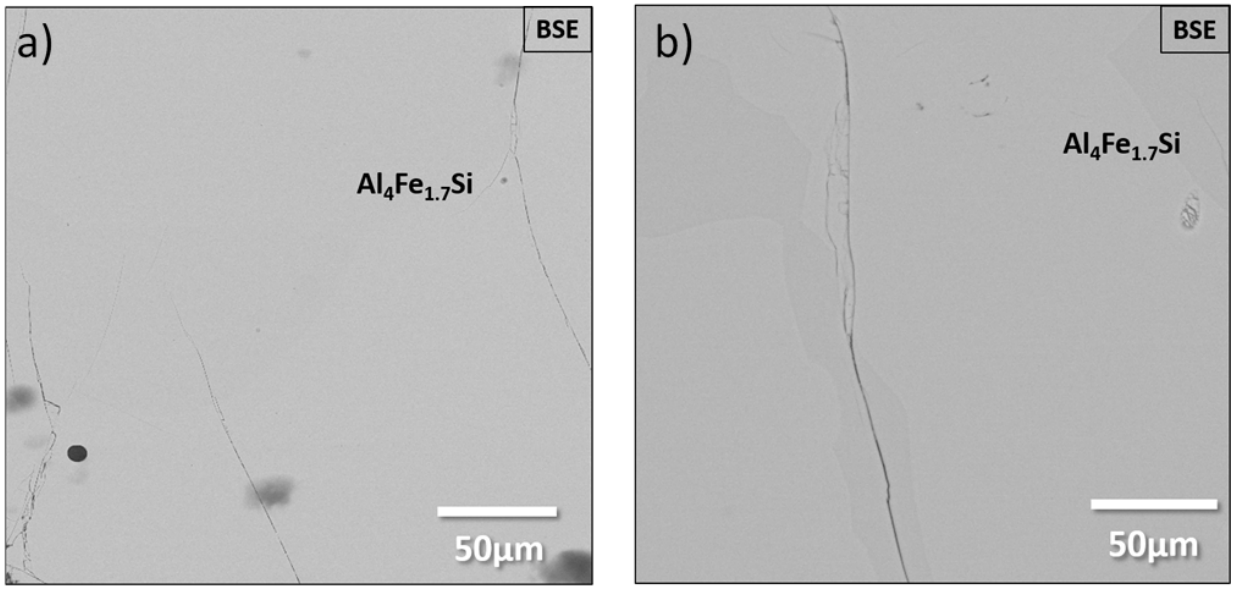

Figure I.2.E.1. SEM BSE images of homogenized (a) $Al_{24.5}$-$Fe_{10.2}$-Si; and (b) $Al_{26.0}$-$Fe_{9.0}$-Si alloys after a heat treatment at 950°C for 100 hours.

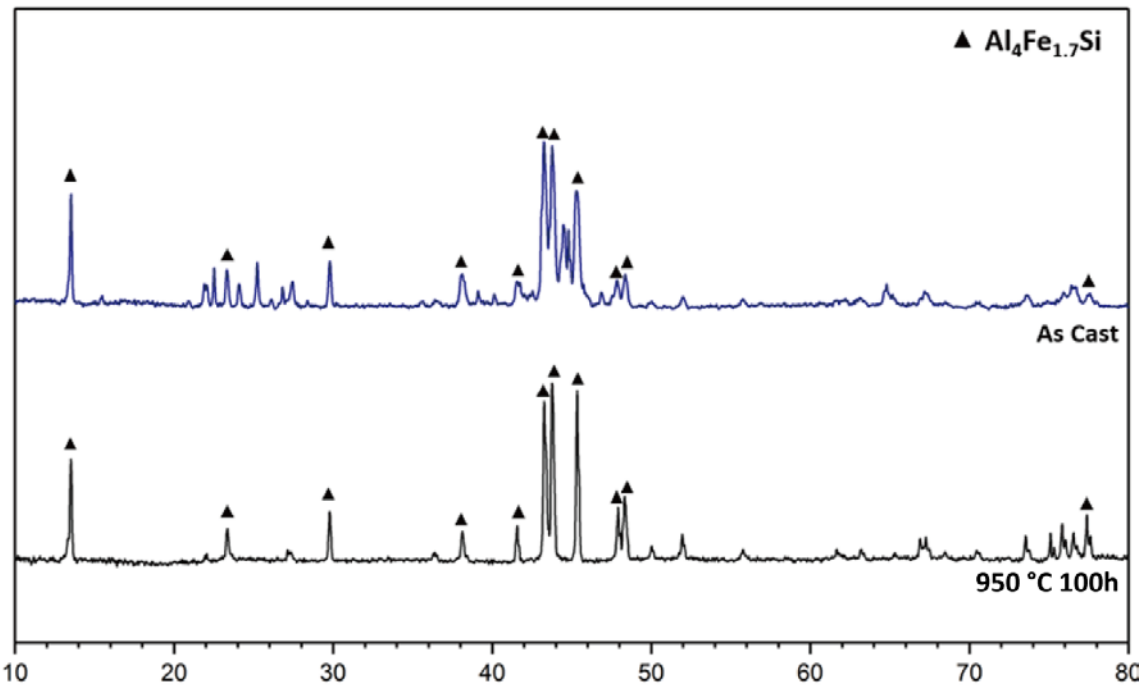

Figure I.2.E.2. XRD diffraction patterns of as cast and homogenized Al-26.0Fe-9.0Si alloy after a heat treatment at 950°C for 100 hours.

Computationally, the energetics of the τ_{10}-Al_4-$Fe_{1.7}$-Si has been evaluated with the use of cluster expansions. Due to the potential for partial site occupancies in this phase, allowing for multiple species to occupy on the same sublattice, clustered expansion of various configurations and compositions of Al, Fe, and Si was employed to calculate the energetics in the τ_{10}-Al_4-$Fe_{1.7}$-Si phase to determine the site occupancy of each element. We found that in 2d Wycoff position, vacancy is energetically favorable than Fe. Likewise, in 6h position, Al is more favorable than Si. In 12k position, Al is more favorable. However, in 2a position, Si is more energetically favorable. We conducted Monte Carlo simulations to identify the relative energetics of the phases at higher temperatures for binary compounds. We performed the energetic and elastic constants calculations for ternary compounds that have similar structure to the τ_{10} phase and explore potential quaternary alloying elements. Since cluster expansion and Monte Carlo simulation to get the energetics at higher temperature in system with larger number of atoms is difficult, breaking down the problem to find the site occupancy for a binary Nb-Sn system was conducted. This is to develop the method to determine the solubility of Nb in Sn and vice versa. This method will be transferred to learn about the Al-Fe-Si system, which is a more complex system. It is envisioned that as we explore additional Al-Fe-Si-based systems, this method will allow for the reliable and rapid calculation of phase diagrams and other relevant phase equilibria schematics.

To stabilize the τ_{10}-Al_4-$Fe_{1.7}$-Si phase and expand its phase boundaries, there are a large number of possible alloying additions. A two-step down-selection was carried out to identify the potential quaternary solute alloying additions. A first down-selection to 28 elements was made based on the following criteria:
1) impossibility, based on transience or man-made nature; 2) infeasibility, based on gaseousness, radioactivity, or high reactivity; and 3) cost, aiming for elements with a bulk price of >$100/kg. The second down-selection consisted of identifying elements with potential to stabilize the τ_{10}-Al_4-$Fe_{1.7}$-Si phase and expand its compositional range. The approach was to mine the inorganic crystal structures database (ICSD) to search for phases with a crystal structure similar to the τ_{10}-Al_4-$Fe_{1.7}$-Si phase, since the elements in these systems will be the prime candidates to stabilize the τ_{10} phase, as well as to expand its compositional range. This led us to

explore the Al-Mn-Si and Al-Fe-Ni ternary systems, which form intermetallic phases τ_2-Al_{10}-Fe_3-Ni and τ_8-Al_9-Mn_3-Si with same structure as τ_{10}-Al_4-$Fe_{1.7}$-Si phase. Based on this information, $Al_{21.5}$-$Fe_{7.0}$-Ni and $Al_{23.1}$-$Mn_{7.7}$-Si alloys were fabricated and the presence of τ_2-Al_{10}-Fe_3-Ni and τ_8-Al_9-Mn_3-Si was confirmed by EDS and XRD. Figure I.2.E.3 shows a SEM BSE image of the $Al_{21.5}$-$Fe_{7.0}$-Ni alloy after homogenization comprising of τ_2-Al_{10}-Fe_3-Ni as a single-phase, illustrating the presence and stability of the desired τ_{10}-Al_4-$Fe_{1.7}$-Si phase.

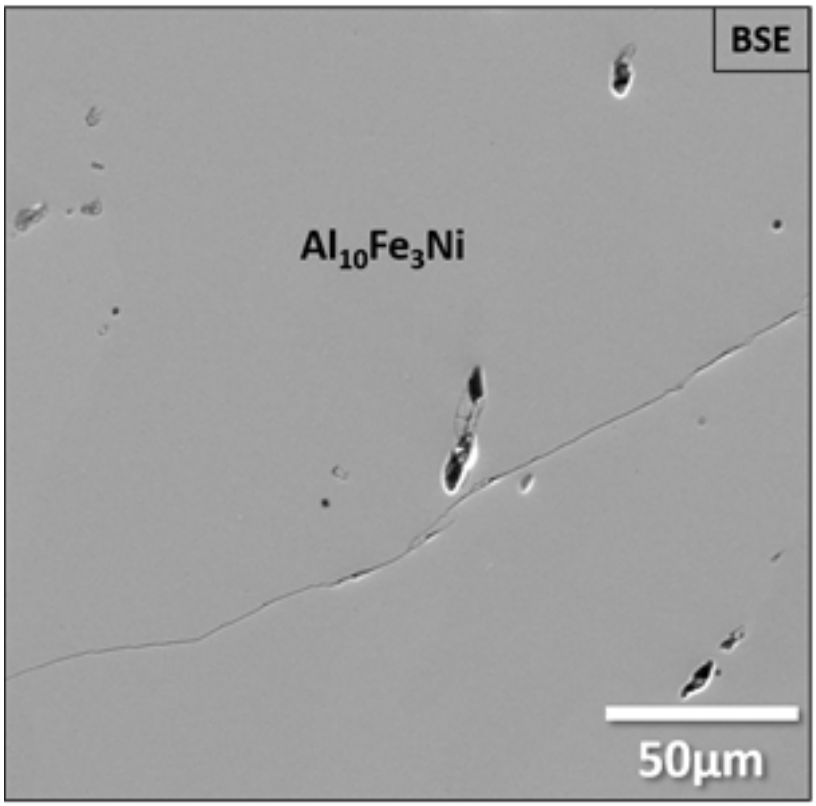

Figure I.2.E.3. SEM BSE images of $Al_{21.5}$-$Fe_{7.0}$-Ni alloy homogenized after a heat treatment at 950 °C for 100 hours showing the τ_2-Al_{10}-Fe_3-Ni phase.

Based on the ICSD search and the above preliminary experimental results, Ni and Mn were selected as the first potential quaternary solute elements for the Al-Fe-Si-X alloys. In order to determine the solubility of Ni in the τ_{10}-Al_4-$Fe_{1.7}$-Si phase, and thereby, its potential as a phase stabilizer, diffusion couples consisting of $Al_{24.5}$-$Fe_{10.2}$-Si alloy and pure Ni as end members were annealed at 800°C for 336 hours, as shown in Figure I.2.E.4.a. Concentration profiles, shown in Figure I.2.E.4.b, obtained using EPMA line scan across the diffusion region, indicate that the maximum solubility of Ni in τ_{10}-Al_4-$Fe_{1.7}$-Si phase at 800°C is 2 at% Ni. Based on the data from the diffusion couple, Al-Fe-Si-based alloys with up to 2 at% Ni were fabricated. Figure I.2.E.5 shows the microstructure of $Al_{24.5}$-$Fe_{8.2}$-$Si_{2.0}$-Ni alloy after annealing at 950°C for 100 hours. As can be seen, the alloy is the τ_{10}-Al_4-$Fe_{1.7}$-Si single phase at 950°C.

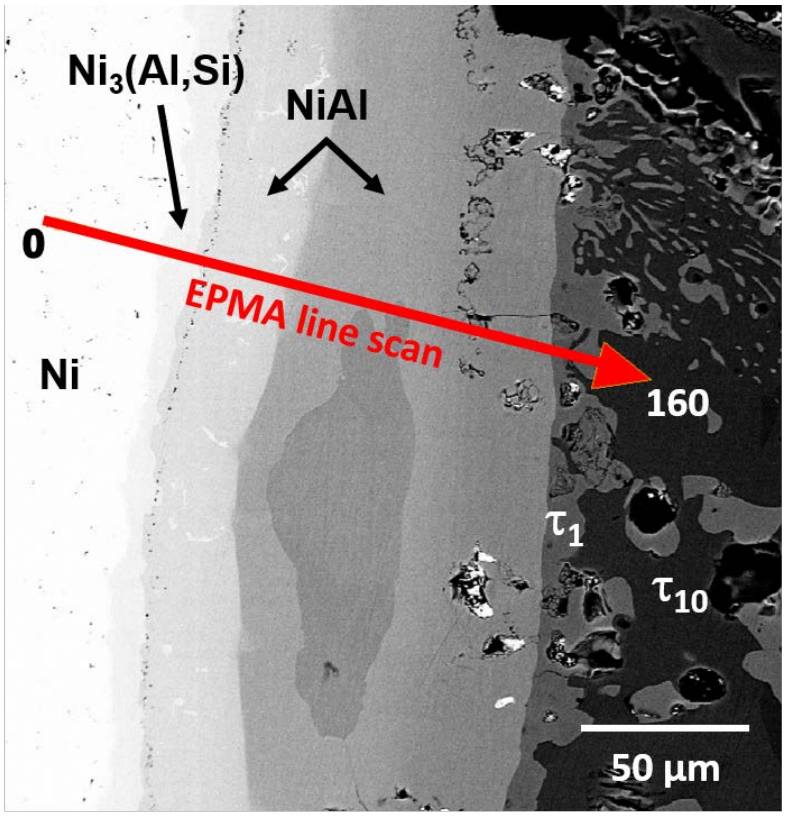

(a)

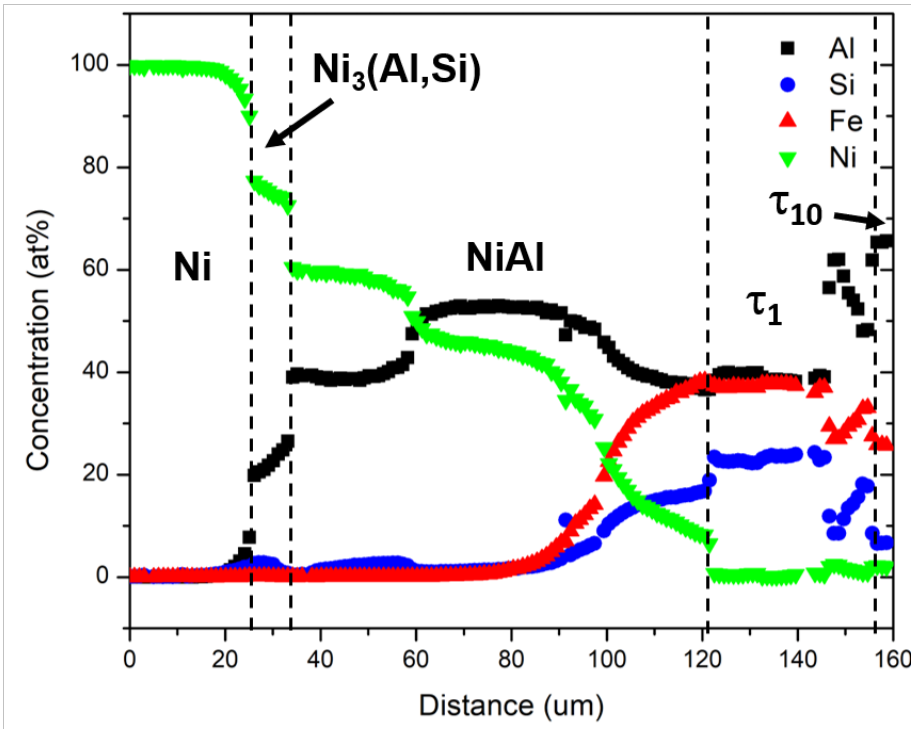

(b)

Figure I.2.E.4.(a) SEM BSE image of the Ni/Al-24.5Fe-10.2Si diffusion couple after being annealed at 800°C for 336 hours showing the phase formation by interdiffusion; and (b) concentration profiles obtained by performing EPMA line scan across the diffusion region shown in (a).

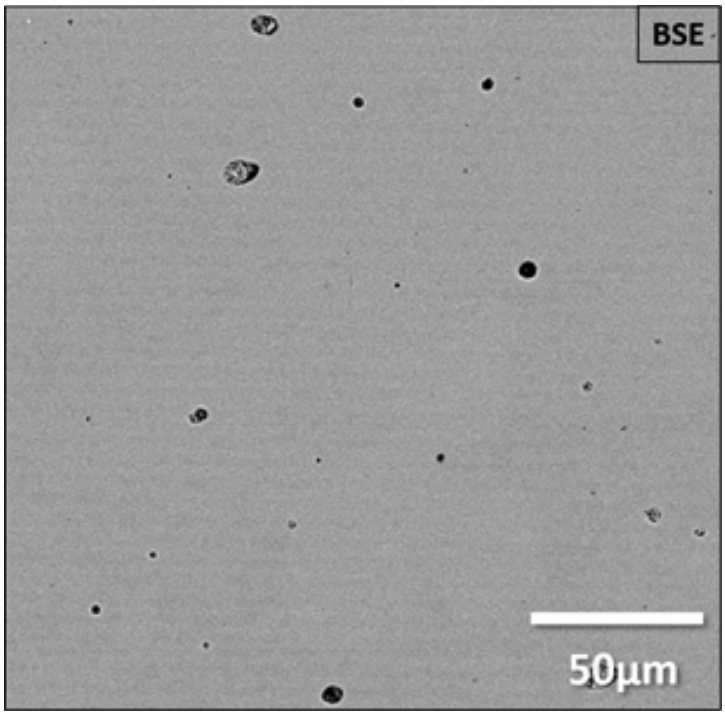

Figure I.2.E.5. SEM BSE image of $Al_{24.5}$-$Mn_{8.2}$-$Si_{2.0}$-Ni alloy homogenized after a heat treatment at 950°C for 100 hours.

All milestones have been completed for Budget Period 1. Alloys having τ_{10}-Al-Fe-Si-Ni single phase with Ni additions to Al-Fe-Si system were obtained. Next, we will focus on exploring the compositional range and thermal stability of these alloys with Ni, Mn, Co, and Ti as quaternary solutes. In order to accelerate this experimental process, a high-throughput diffusion multiple approach will be employed. These experimental results will reveal the accurate solubility limits of those quaternary solutes in the τ_{10} phase, while suppressing the formation of other phases. The next step in the computational side would be to create the convex hull of the binary system, transfer the method in the Al-Fe-Si system to develop the phase diagram for the system, and use data from Monte Carlo to create phase diagrams. The experimental data will validate and optimize the calculated phase diagrams. The data obtained from the diffusion multiple can directly be used for Al-Fe-Si-X alloy design, and can also be used to test and improve current Al thermodynamic database for computational design of materials.

Conclusions

Al-Fe-Si alloys were successfully fabricated via arc melting. $Al_{24.5}$-$Fe_{10.2}$-Si and $Al_{26.0}$-$Fe_{9.0}$-Si alloys were homogenized to obtain samples with 100v% τ_{10} phase. The presence of τ_{10} in these alloys was confirmed by EDS and XRD. After data mining using ICSD database, two intermetallic phases τ_2-Al_{10}-Fe_3-Ni and τ_8-Al_9-Mn_3-Si with the same structure as Al_4-$Fe_{1.7}$-Si were found in the Al-Fe-Ni and Al-Mn-Si systems, respectively. Al-Fe-Ni and Al-Mn-Si alloys were fabricated and the presence of τ_2 and τ_8 were confirmed by EDS and XRD. Based on the ICSD search and the results obtained experimentally from Al-Fe-Ni and Al-Mn-Si alloys, we selected two elements, Ni and Mn, as the first potential quaternary elements for the Al-Fe-Si-X alloys. $Al_{24.5}$-$Fe_{8.2}$-$Si_{2.0}$-Ni alloys were fabricated and 100v% τ_{10} were obtained in these alloys after homogenization. Early indications show that Al-Fe-Si-Ni and Al-Fe-Si-Mn have the greatest potential for the alloy developed in Budget Period 2.

I.3 Materials for Energy Recovery and Aftertreatment

I.3.A Innovative SCR Materials and Systems for Low Temperature Aftertreatment (Pacific Northwest National Laboratory)

Yong Wang, Co-Principal Investigator
Pacific Northwest National Laboratory
902 Battelle Blvd.
Richland, WA 99354
Phone: 509-371-6273
E-mail: yong.wang@pnnl.gov

Craig DiMaggio, Co-Principal Investigator
Fiat Chrysler Automobile, U.S., LLC
1000 Chrysler Dr.
Auburn Hills, MI 48326-2766
Phone: 248-576-5741
E-mail: cld62@chrysler.com

Jerry L. Gibbs, Technology Manager
E-mail: jerry.gibbs@ee.doe.gov

Start Date: July 1, 2015 End Date: June 30, 2018
Total Project Cost: $2,000,000 DOE share: $1,500,000 Non-DOE share: $500,000

Project Introduction

The key focus of this program is to further develop newly invented materials for the selective catalytic reduction (SCR) of nitrogen oxides (NO_x) by ammonia (NH_3) that show promise for significantly reducing 'light-off' temperatures compared to current commercial catalysts. Specifically, the goal of the proposed work is to achieve 'light-off' of NH_3 SCR at 150°C in order to realize conversion efficiencies of 90% at these low temperatures. This will enable the deployment of lean combustion powertrains with significantly increased fuel efficiencies, but lower exhaust temperatures. To accomplish these overall goals, it will be essential to also identify an appropriate NH_3 supply strategy for the SCR aftertreatment device that can controllably deliver NH_3 at these low temperatures.

Objectives

- Enabling SCR catalyst system that will function at very high efficiency to attain the most demanding emissions regulations and thereby facilitate the market introduction of advanced powertrains that will support domestic energy independence and security.
- Further develop newly invented materials for the SCR of NO_x by NH_3 that show promise for significantly reducing 'light-off' temperatures compared to current commercial catalysts. Specifically, the goal of the proposed work is to address the challenge of 'light-off' of NH_3 SCR at 150°C in order to realize conversion efficiencies of 90% at these low temperatures.

Approach

This project adapts a newly developed SCR material to function with high-efficiency under conditions consistent with low temperature portions of drive cycles. We will demonstrate the SCR catalyst, aged under realistic conditions (lean or stoichiometric), will provide 90% conversion efficiency at/near 150°C. For the aftertreatment system, we will demonstrate that a SCR catalyst system will attain Tier III and SULEV30 emissions using an engine or simulated engine federal test procedure (FTP) cycle. We will evaluate SCR catalyst system activity using alternate upstream NO_x control and NH_3 generation strategies to achieve Tier 3 criteria emissions control and greenhouse gas (GHG) emissions minimization, and to estimate the fuel penalty, control/OBD complexity, and component/system cost.

Results

Key accomplishments for FY 2017 include:

- Initiated realistic aging studies of the optimized first generation catalysts that have been washcoated onto a monolith substrate.
- Determined an optimized composition of the second generation low temperature selective catalytic reduction (LT-SCR) catalyst.
- Verified sufficient hydrothermal stability of the first generation catalyst formulation.
- Downselected passive NH_3 dosing technology.

A large batch of the first generation powder sample was prepared and washcoated on a monolith substrate. Core samples were hydrothermally aged at 600°C and 700°C, respectively. Both samples were tested under both the fast and standard SCR conditions. Figure I.3.A.1 shows there is no difference in NO_x reduction efficiency for samples hydrothermally aged at 600°C and 700°C. NO_x conversion efficiency reaches 75–80% at 175°C, which very well reproduced the performances of the powder catalysts and demonstrated successful transfer of powder catalyst formulation to monolith catalysts. More importantly, high-temperature NO_x reduction efficiency was not compromised. Additional tests also showed that the pretreatment of the monolith sample at 700°C showed increased NH_3 storage and decreased NH_3 oxidation compared to that at 600°C. This is likely due to the fact that more $Cu(OH)^+$ sites are converted to Cu^{+2}. These are desired features for SCR, which were achieved after aging at 700°C, as opposed to 600°C.

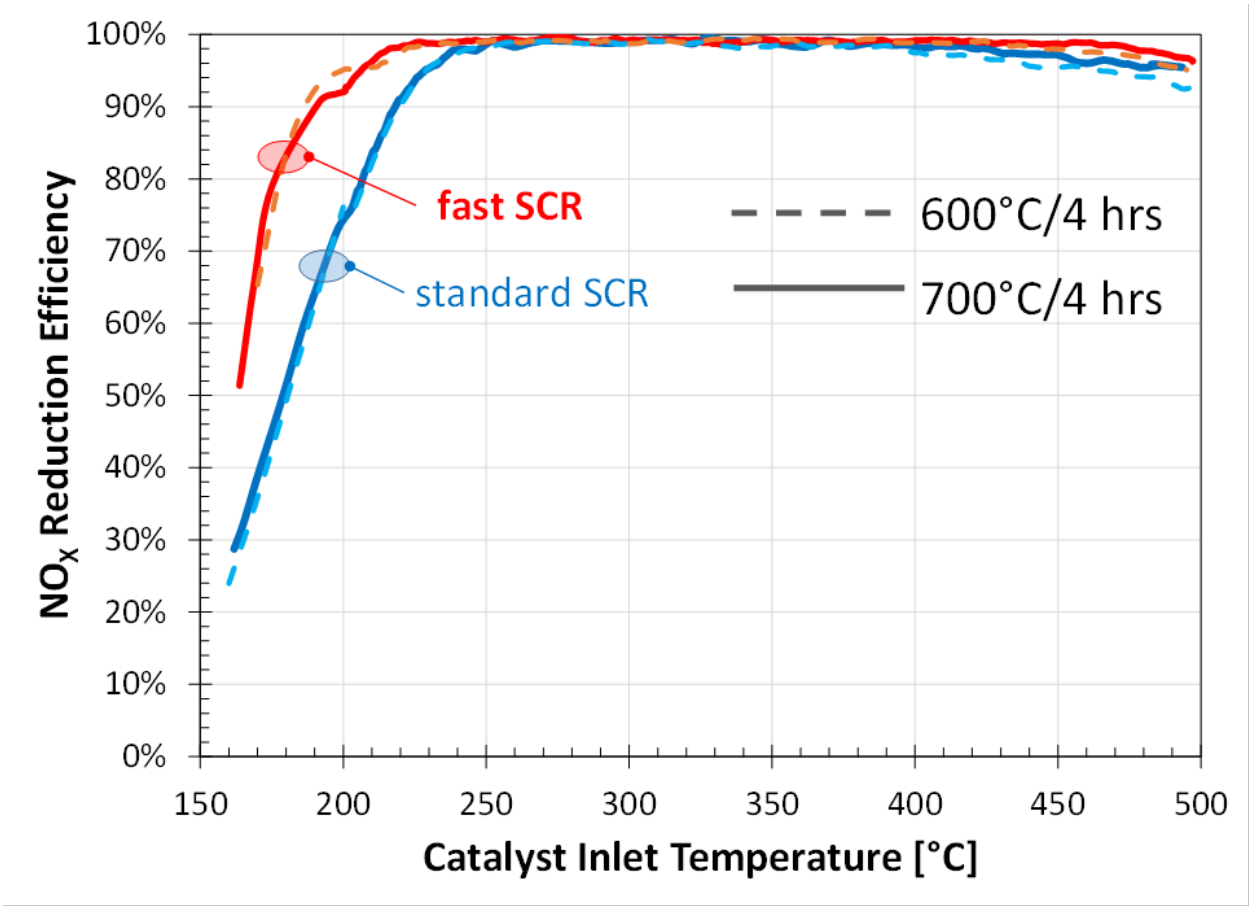

Figure I.3.A.1. NO_x reduction efficiency as a function of catalyst inlet temperature on a core sample, which was hydrothermally aged at 600°C and 700°C, respectively.

Continued efforts were made to improve the first generation of catalyst formulation. The new ion-exchange method and a different Cu precursor were used to prepare a second generation catalyst in order to further improve the low temperature NO_x reduction. The new Cu SCR catalyst provides additional active sites and continues to maintain high Cu dispersion. As shown in Figure I.3.A.2, the second generation catalysts with high Cu loading lead to ~80% NO conversion at 150°C, while the 1st generation was ~40%.

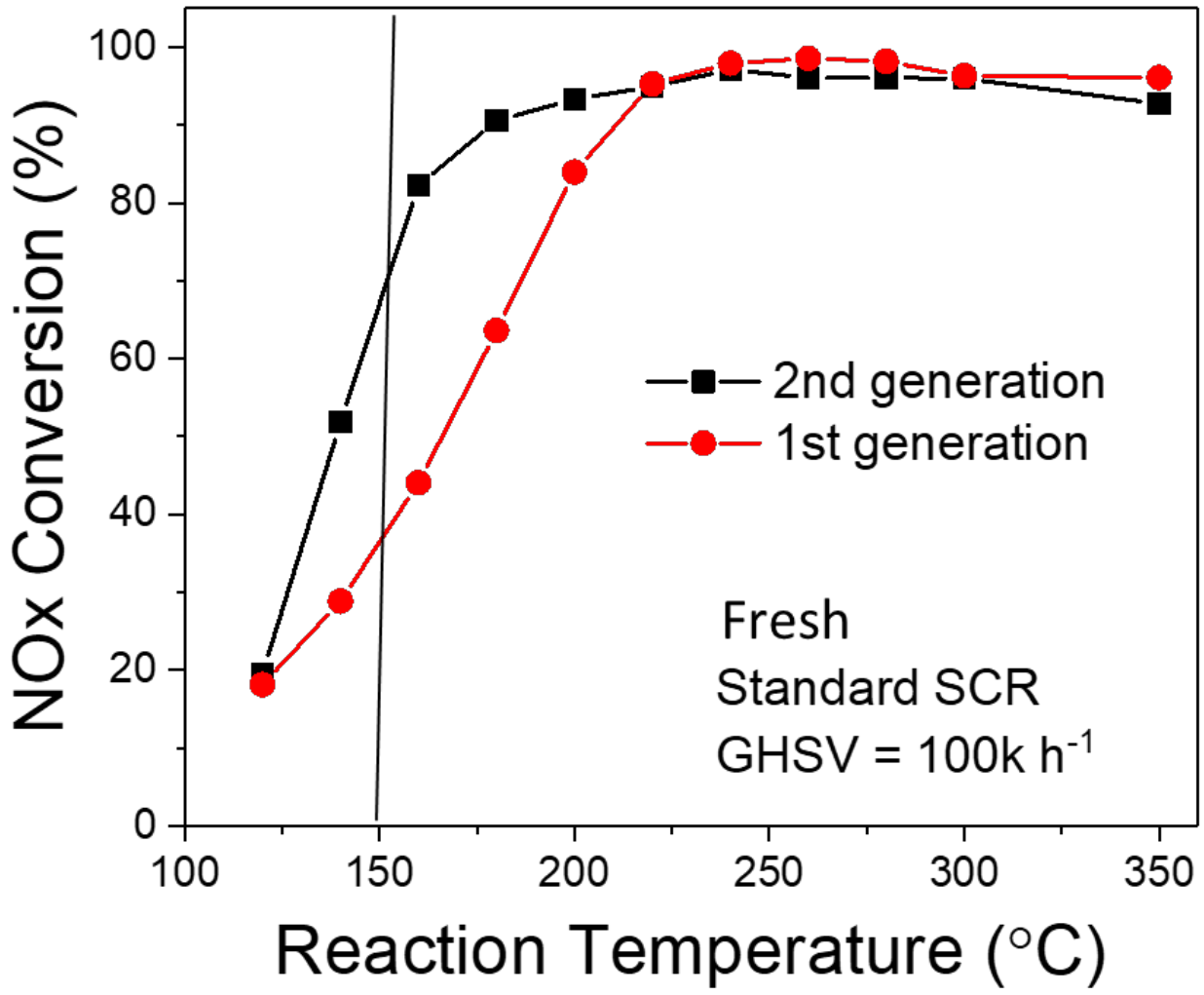

Figure I.3.A.2. Comparison of NO_x conversion as a function of reaction temperature on both the first and second generation catalysts.

Conclusions

- Demonstrated lightoff of the first generation SCR catalyst is improved over the industry standard (>75% NO_x @ 175°C).
- Successfully synthesized a large batch of Cu/SSZ catalyst and transferred the material to a monolith for pre-vehicle evaluation.
- Bench reactor testing of SCR monolith confirmed performance.
- Identified and successfully applied a research direction for development of a second generation SCR catalyst (80% conv. @150°C).
- Down-selected alternatives to urea NH_3 generation.
- Derived a kinetic model to predictively control the function of a three-way catalyst (TWC) + NO_x storage converter (NSC) catalyst technology for NO_x control & NH_3 generation.
- Established dyno-test baseline system (TWC/NSC + SCR).

I.3.B Next Generation Three-Way Catalysts for Future, Highly Efficient Gasoline Engines (Ford Motor Company)

Christine K. Lambert, Co-Principal Investigator
Ford Motor Company
2101 Village Rd.
Dearborn, MI 48121
Phone: 313-323-1038
E-mail: clamber9@ford.com

Todd J. Toops, Co-Principal Investigator
Oak Ridge National Laboratory
2360 Cherahala Blvd.
Knoxville, TN 32932
Phone: 865-946-1207
E-mail: toopstj@ornl.gov

Johannes Schwank, Co-Principal Investigator
The University of Michigan
2300 Hayward St.
Ann Arbor, MI 48109
Phone: 734-764-3374
E-mail: schwank@umish.edu

Jerry L. Gibbs, Technology Manager
E-mail: jerry.gibbs@ee.doe.gov

Start Date: October 1, 2014 End Date: December 31, 2017
Total Project Cost: $1,090,470 DOE share: $752,376 Non-DOE share: $338,094

Project Introduction

Ford Motor Company has successfully used catalysts on cars and trucks to control emissions for over 40 years. Changes in gasoline engine technology have allowed the use of "high tech" TWCs to simultaneously control HC (hydrocarbons), CO (carbon monoxide), and NO_x at nearly 100% efficiency. Waste heat is used on engine start to bring the catalyst up to its full operating temperature of greater than 350°C, thereby lowering fuel economy and creating particulate matter. The goal of this project is to develop and test new catalysts for lower operating temperatures that may occur with future, more efficient gasoline-powered vehicles. The work includes laboratory preparation, aging, and poisoning of catalyst materials, activity tests, and chemical analyses. The objective is to make progress toward the USDRIVE goal of achieving durable 90% conversion of HC, CO, and NO_x at 150°C.

Objectives

Develop new TWC materials that show progress towards durable 90% conversion of CO, HC, and NO_x at 150°C (T90).

Approach

- Establish common test protocols between the project partners.
- Identify and characterize known, proven exhaust catalyst materials in new ways.
- Develop new catalyst formulations that improve platinum-group minerals (PGM) dispersion and promote activity after aging.
- Predict vehicle performance and finished catalyst cost.
- Leverage cross-laboratory analytical capabilities, including the Talos electron microscope at ORNL.

Results

The project partners focused on several supported metal catalyst structures to promote lower light-off temperatures, enhance metal-support interaction, and improve durability. The raw materials (oxides of Al, cerium [Ce], Si, titanium [Ti], and Zr) were not new, but were used in novel ways. Palladium (Pd) or rhodium (Rh) were supported either on layered metal oxide supports, on nanoparticles, or used in various core@shell configurations. Ford had the most success with Rh on a layer of titania (TiO_2) on a stabilized alumina (Al_2O_3) support, as shown in Figure I.3.B.1.a. Similar structural confirmation was completed on ORNL's deposition of Pd on Ce-Zr nanoparticles onto an alumina support using a strong electrostatic adsorption method, as shown in Figure I.3.B.1.b).

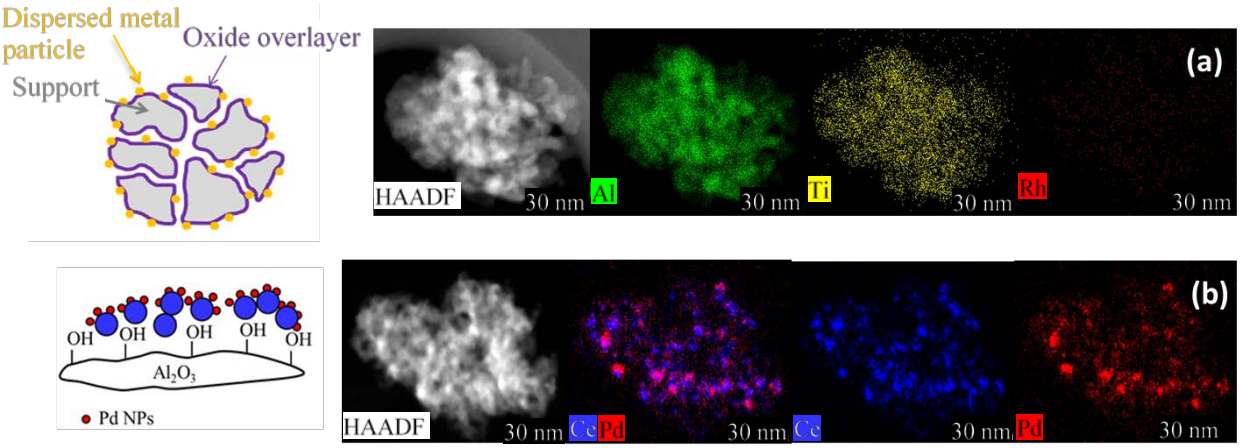

Figure I.3.B.1. Two most successful approaches to depositing highly dispersed precious metals on metal oxide supports: (a) Rh/Ti/Si-alumina; and (b) Pd on ceria-zirconia nanoparticles supported on alumina. (Images obtained using the Talos F200X STEM at ORNL, provided by DOE, Office of Nuclear Energy, Fuel Cycle R&D Program and the Nuclear Science User Facilities).

The Rh-Ti-Si-alumina materials showed promise for lower light-off of CO, HC, and NO_x after aging to represent high mileage. Table I.3.B.1 compares T90s for new catalysts versus a commercial sample. The commercial TWC contained 1.7% Pd and was aged on a four-mode cycle (lean, stoichiometric, rich, exothermic) with peak temperatures of about 960°C. Most notably, the 0.5% Rh-Ti-Si-Al_2O_3 sample aged in the same manner displayed 90% CO conversion below 200°C, and the total HC and NO T90s were 253°C and 222°C, respectively. This represented 55°C to 108°C lower T90s than the commercial catalyst while using a much lower precious metal loading. Smaller improvements in CO and HC T90s and a larger improvement in NO were seen with 0.6 wt% Rh on the zirconia overlayer on Si-alumina. Alternatively, samples with higher metal content (2 wt% Pd or 1 wt% platinum [Pt]) on Ce-Zr nanoparticles reduced the HC and NO_x T90s by 32°C to 65°C. While none of these samples achieved 150°C aged T90s, results showed meaningful progress towards this goal.

Table I.3.B.1. Temperatures for 90% Conversion of CO, HC, and NO_x.

	1.7% Pd commercial TWC (960°C 4-mode)	0.5% Rh-Ti-Si-Al_2O_3 (960°C 4- mode)	0.6% Rh-Zr-Si-Al_2O_3 (960°C 4-mode aged)	2% Pd-Ce-Zr-Al_2O_3 (900°C stoich. aged)	1% Pt-Ce-Zr-Al_2O_3 (900°C stoich. aged)
T90 CO	245°C	190°C (-55°C)	201°C (-44°C)	245°C (0°C)	252°C (+7°C)
T90 HC	345°C	253°C (-92°C)	256°C (-89°C)	305°C (-40°C)	280°C (-65°C)
T90 NO	330°C	222°C (-108°C)	202°C (-128°C)	298°C (-32°C)	277°C (-53°C)

The loading of titania as an overlayer was studied in the range of 0–12 wt% at a 0.5 wt% Rh level; 8 wt% Ti was found to be the optimum, as shown in Figure I.3.B.2.a). Likewise, the Rh loading was varied from 0.1–1.0 wt%; the 0.5 wt% was found to be the optimum, as shown in Figure I.3.B.2.b.

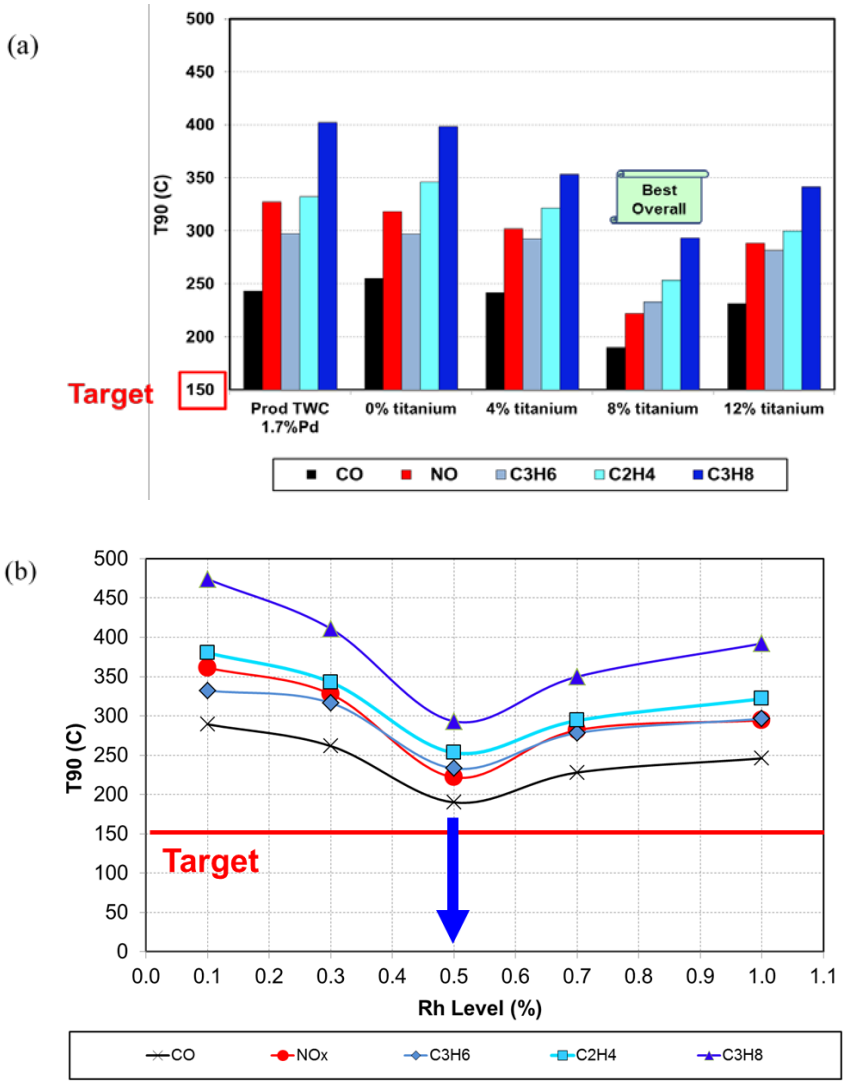

Figure I.3.B.2. Optimization of the (a) Ti; and (b) Rh loading in the Rh/Ti/Si-Al_2O_3 TWC samples.

The potentially damaging effects of sulfur were studied for the 0.5 wt% Rh / 8 wt% Ti-Si-Al_2O_3 material. For all constituents except propane, the T90s were unchanged by sulfur exposure. Only the propane conversion suffered from exposure to SO_2 in the gas stream. Increasing the catalyst temperature to 600°C under normal operating conditions was sufficient to regain the initial activity for propane. Analogous testing performed on the zirconia version resulted in more significant deterioration and full recovery was not achieved, implying titania offered more resistance to sulfur poisoning.

To further understand the physical location of titania in the 0.5 wt% Rh / 8 wt% Ti-Si-Al_2O_3 material, the titania band gap energy was determined by diffuse reflectance (DR) ultraviolet (UV) visible spectroscopy (vis) (DR-UV-vis). This technique can provide information about the degree of dispersion of the metal oxide, with isolated metal atoms having higher band gaps than particles composed of many atoms. Analysis of a sample containing 8 wt% Ti overlayer on Si-alumina revealed a higher band gap than that of bulk titania, suggesting that the Ti overlayer consisted of metal oxide clusters of < 100 atoms, and possibly fewer than 10 atoms.

As explained in Figure I.3.B.3, the band gap of the sample containing 10 wt% colloidal anatase in alumina was 3.22 eV, consistent with the known 3.2 eV band gap of bulk anatase. The band gap of the 8 wt% titania overlayer support was higher at 3.46 eV. Since DR-UV-vis averages over all absorbers in the sample and alumina does not absorb UV light below 5.5 eV, it could be concluded that the large majority of the titania in the overlayer was present in particles smaller than 2 nm. This was consistent with previous failures to observe these particles by XRD is generally limited to particles > 5 nm, as well as the observed high dispersion in the TEM image in Figure I.3.B.1.a.

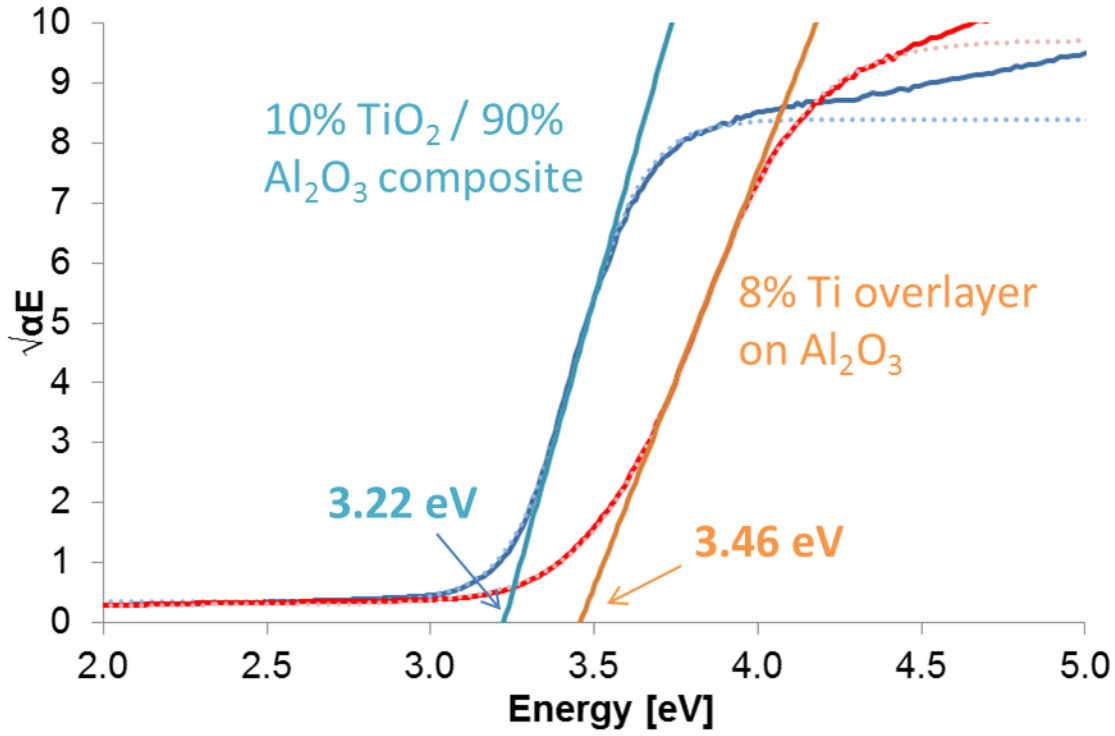

Figure I.3.B.3. DR-UV-vis on 8% Ti overlayer on stabilized alumina (red) and on a sample containing 10 wt% of colloidal anatase physically mixed with alumina (blue). Straight lines are extrapolated band gap energies. Dotted lines are fits to the adsorption edge.

Conclusions

Further understanding of the catalyst architecture provided additional confidence to move forward with a scale-up of 0.5 wt% Rh-Ti-Si-Al_2O_3 and 0.6 wt% Rh-Zr-Si-Al_2O_3, along with 2 wt% Pd-Ce-Zr-Al_2O_3 and 1% Pt-Ce-Zr-Al_2O_3 to coated monolith laboratory cores for further evaluation. The third and last year of the project involves work with a major catalyst manufacturer, Johnson Matthey.

Key Publications

Binder, A. J., T. J. Toops, and J. E. Parks II, 2017, "Cu-Co-Ce ternary oxide as an additive to conventional Pt-Al_2O_3 catalyst for lean exhaust catalysis," 25th North American Catalysis Society Meeting, June 4–9, 2017, Denver, CO, USA.

Getsoian, A., J. Theis, and C. Lambert, "Low temperature three-way catalysts for future gasoline engines," 25th North American Catalysis Society Meeting, June 4–9, 2017, Denver, CO, USA.

Kyriakidou, E. A., T. J. Toops, M. J. Lance, J.-S. Choi, and J. E. Parks II, 2017, "Advanced support modifications to improve the low-temperature activity and durability of Pd-based emissions control catalysts," 25th North American Catalysis Society Meeting, June 4–9, 2017, Denver, CO, USA.

Lambert, C., 2017, DOE Annual Merit Review, June 2017.

Seo, C. Y., L. F. Allard, C. Kokenoz, G. B. Fisher, and J. W. Schwank, 2017, "Facile synthesis of Pd@SiO_2/CeO_2 core@shell catalysts with tunable core and shell sizes: Improved thermal stability and catalytic activity," 25th North American Catalysis Society Meeting, June 4–9, 2017, Denver, CO, USA.

Seo, C., E. Yi, M. Nahata, R. M. Laine, and J. W. Schwank, 2017, "Facile, one-pot synthesis of Pd@CeO_2 core@shell nanoparticles in aqueous environment by controlled hydrolysis of metalloorganic cerium precursor," *Materials Letters*, Vol. 206, pp. 105.

Theis, J., A. Getsoian, and C. Lambert, "Impact of promoters and air-fuel ratio on light-off performance of Rh/Al_2O_3 model TWCs," 2017 CLEERS Workshop, October 3–5, 2017, Ann Arbor, MI, USA.

Theis, J., A. Getsoian, and C. Lambert, 2017, "The development of low temperature three-way catalysts for high efficiency gasoline engines of the future," SAE 2017-01-0942.

Toops, T. J., E. A. Kyriakidou, A. J. Binder, M. J. Lance, J.-S. Choi, and J. E. Parks II, 2017, "Approaches to treating emissions at low temperatures," 2017 CLEERS Workshop, October 3–5, 2017, Ann Arbor, MI, USA.

I.3.C Sustained Low Temperature NO_x Reduction (Cummins, Inc.)

Yuhui Zha, Principal Investigator
Cummins, Inc.
1900 McKinley Avenue
Columbus, IN 47201
Phone: 812-322-0935
E-mail: yuhui.zha@gmail.com

Jerry L. Gibbs, Technology Manager
E-mail: jerry.gibbs@ee.doe.gov

Start Date: February 1, 2015 End Date: December 31, 2017
Total Project Cost: $2,400,000 DOE share: $1,200,000 Non-DOE share: $1,200,000

Project Introduction

There are two competing drivers in the diesel engine aftertreatment market today. On one hand, many efforts have been taken to improve engine efficiency to lower GHG emissions, as stated in the Super Truck Program. This approach drives decreases of the average exhaust temperature during the cert cycle and many other operational duty cycles as well. On the other hand, led most aggressively by Europe and growing worldwide are stricter requirements for in-use compliance. This will require aftertreatment capable of tailpipe NO_x control in real world operations, where the exhaust temperature could be much colder than cert cycles, which add more challenges to aftertreatment to meet tailpipe NO_x emissions. All of these drive the direction of aftertreatment system (ATS) performance improvement towards low temperature conditions under sustained operation conditions. Many current aftertreatment development work has been focused on the "cold start." The sustained low temperature NO_x reduction shares some common enablers, such as low temperature reduction introduction, but also pose distinct challenging situations. The most challenging one is how to minimize ammonia nitrate (NH_4NO_3) inhibition in a sustained low-temperature operation.

The NH_4NO_3 is typically formed by a reaction of NO_2 and NH_3 in the ratio of 1:1 at temperatures below 200°C (R1). The NH_4NO_3 deposit is white crystal material that could cause fouling or masking of the pore channels of the catalyst and inhibit the SCR reaction, leading to its temporary deactivation. There are at least three reactions for NH_4NO_3 removal: (1) NH_4NO_3 sublimation (R2); (2) thermal decomposition (R3); and (3) reaction with NO (R4). The common enabler for all three removal mechanisms is temperature (e.g., higher temperature will promote the removal).

$$2NO_2+2NH_3 \rightarrow NH_4NO_3+N_2+H_2O \quad \text{(R1)}$$

$$NH_4NO_3 \leftrightarrow NH_3+HNO_3 \quad \text{(R2)}$$

$$NH_4NO_3 \rightarrow N_2O+2H_2O \quad \text{(R3)}$$

$$NH_4NO_3+NO \rightarrow NO_2+2H_2O+N_2 \quad \text{(R4)}$$

Therefore, the accumulation of NH_4NO_3 is favored by low temperature where the formation rate is higher than the removal rate of NH_4NO_3; therefore, NO_x reduction performance in the sustained low temperature operation is expected to suffer the most from the inhibition of NH_4NO_3 over NOx conversion. Although many researchers have discussed NH_4NO_3 impact on Cu, Fe-based zeolite, and V-based SCR catalysts, few have been focused systematically to explore the design levels to minimize the NH_4NO_3 impact over NO_x conversion in low temperature operation, especially in the operation region of 150°C.

Cummins decided to take ownership of this challenging task and co-funded this program with DOE. With the collaboration of Johnson Matthey and Pacific Northwest National Laboratory (PNNL), this program was kicked off in 2015 and is currently nearing the end of the three-year contract period.

Objectives

In this program, we set up a bold target to achieve sustained 90% NO_x conversion at the SCR inlet of 150°C. The technology development commitments involved:

- Developing integrated high NO_2 system that can deliver favorable NO_2/NO_x in the feed gas of SCR at low temperature operation condition where SCR inlet is around 150°C.
- Developing an SCR component and system solution that can achieve 90% NO_x reduction at the SCR inlet of 150°C.
- Developing reductant delivery system that can deliver reductant at the SCR inlet of 150°C.

Approach

- Test the developed system on engine for performance demonstration.
- Develop component models for the unique components.
- Identify the technical challenges of developed components to be resolved towards commercialization.

Results

In this year, we mainly focus on reversible deterioration study of SCR and on-engine performance evaluation of the sustained low temperature NO_x reduction (SLTNR) aftertreatment.

1. *The developed SLTNR diesel oxidation catalyst (DOC) and SCR system meets program target 90% NO_x conversion at steady-state SCR 150°C condition; in low temperature transient cycle testing, it delivers ~85% NO_x conversion in a 9-hour duration test*

NO_2/NO_x sweep testing was conducted on a reactor core to evaluate the sustainability and capability of the NO_x reduction. Figure I.3.C.1 shows examples of results collected on: (a) a commercial Cu-SCR; and (b) one of the generations of the developed SLTNR-SCR formulation. At NO_2/NO_x <0.5, Cu-SCR is able to maintain NO_x conversion at 163°C at 66%; however, at 0.5, it shows performance degradation, which indicates the NH_4NO_3 inhibition occurs at NO_2/NO_x 0.5 and 163°C. At NO_2/NOx <0.6, the SLTNR-SCR is able to maintain NO_x conversion at 86% at 150°C. So NO_2/NO_x 0.6 is taken as the upper limit of NO_2/NO_x at 150°C for this formulation to be sustained and free of an NH_4NO_3 deposit and plotted in Figure I.3.C.1.c, which summarizes the maximum NO_2/NO_x as a function of temperature where the SCR reaction could reach steady-state and no noticeable NH_4NO_3 deposition over two commercially available Cu-SCR and two developed low temperature SLTNR-SCR after different heat treatments. The area above each line illustrates the poison zone where that catalyst is at high risk of NH_4NO_3 inhibition and observed the accumulation of NH_4NO_3 during the SCR reaction; while the area below each line indicates the sustainable zone where that catalyst has less of a risk of an NH_4NO_3 inhibition and observed SCR reaction reach steady-state. It is noticed that with the developed SLTNR-SCR catalyst after activation, it shows more tolerance toward higher NO_2/NO_x and lower temperature than the degree of the SLTNR-SCR and two types of commercial Cu-SCRs that were provided by Johnson Matthey. The pink dot is the targeted SLTNR condition where NO_2/NO_x is at 0.5 and temperature is at 150°C, which shows that the developed SLTNR-SCR after activation has the potential to achieve sustained performance at SLTNR condition with minimal NH_4NO_3 inhibition effect.

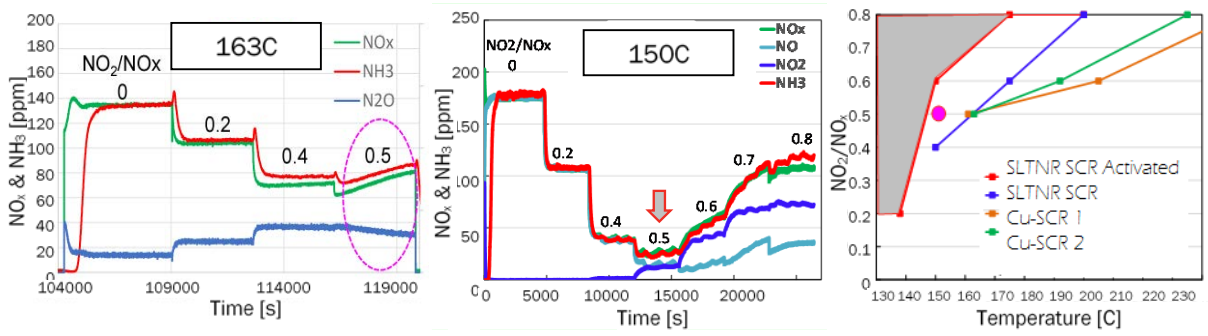

Figure I.3.C.1. NO_2/NO_x sweep testing on: (a) a commercial Cu-SCR; (b) one of the SLTNR-SCRs coated by JM [testing condition: SV 40k/hr, Temperature 150°C, NO_x 180 parts per million (ppm), NH3: NOx = 1:1]; and (c) ammonia nitrate poison zone mapping and comparison.

Engine operation conditions were selected to simulate sustained low temperature operation where exhaust gas temperature at the SCR inlet is around 150°C, at the turbo outlet it is around 200°C, and at the turbo inlet it is around 240°C, as illustrated in Figure I.3.C.2. The operation continues for ~16 hours, followed by 30 minutes of regeneration to clean up soot in the filter and any other possible deposition in the system. The SCR system includes SLTNR SCR followed by a commercial Cu-SCR.

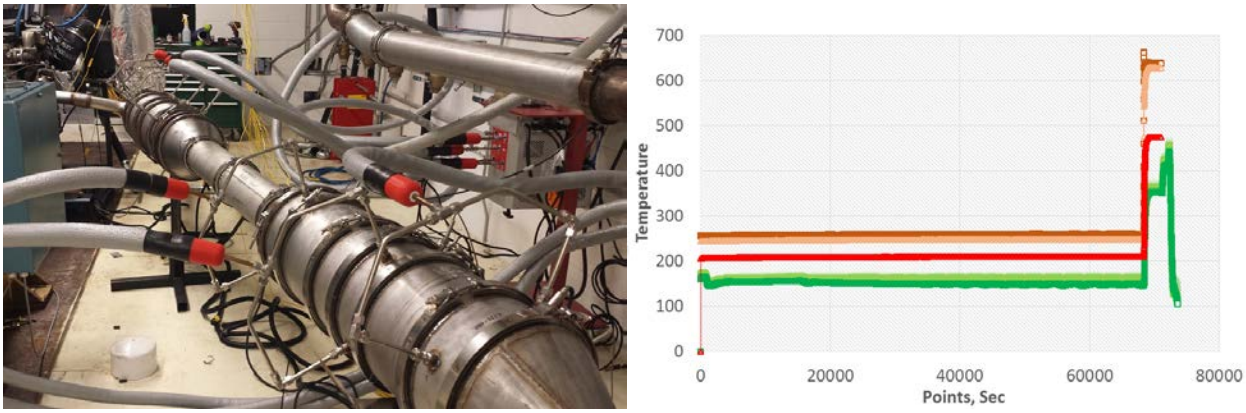

Figure I.3.C.2. A typical temperature profile through a 16-hour steady-state engine test [brownish: turbo inlet; red: turbo outlet; greenish: SCR brick].

The NO_x conversion is calculated by using NO_x concentration at the inlet of SCRs and the outlet of SCRs. Ammonia to NO_x ratio is set at 1:1. The EGR fraction swings from 0–0.2. In Figure I.3.C.3.a, a sustained low temperature operation was tested with EGR 0. It shows that with baseline DOC set 1 and baseline Cu-SCR, the NO_2/NO_x at the SCR inlet at the beginning of testing is around 0.2 and then progressively drops to 0.1, while NO_x conversion is 75% at the beginning and then drops to 60% in 16 hours of steady-state testing. This indicates that the baseline DOC could not provide favorable NO_2/NO_x fraction at this low temperature operation condition and even with such low NO_2/NO_x, Cu-SCR could not reach steady-state NO_x conversion and got inhibition from NH_4NO_3 accumulation. With the introduction of SLTNR SCR set 2 and integrated high NO_2/NO_x DOC set 2, the NO_2/NO_x is increased and stabilized above 0.2 and NO_x conversion increase to 80%. With DOC set 3 and SCR set 2, NO_2/NO_x is improved and stabilized at 0.4 and ~89% NO_x conversion is achieved at end of 16 hour steady-state testing.

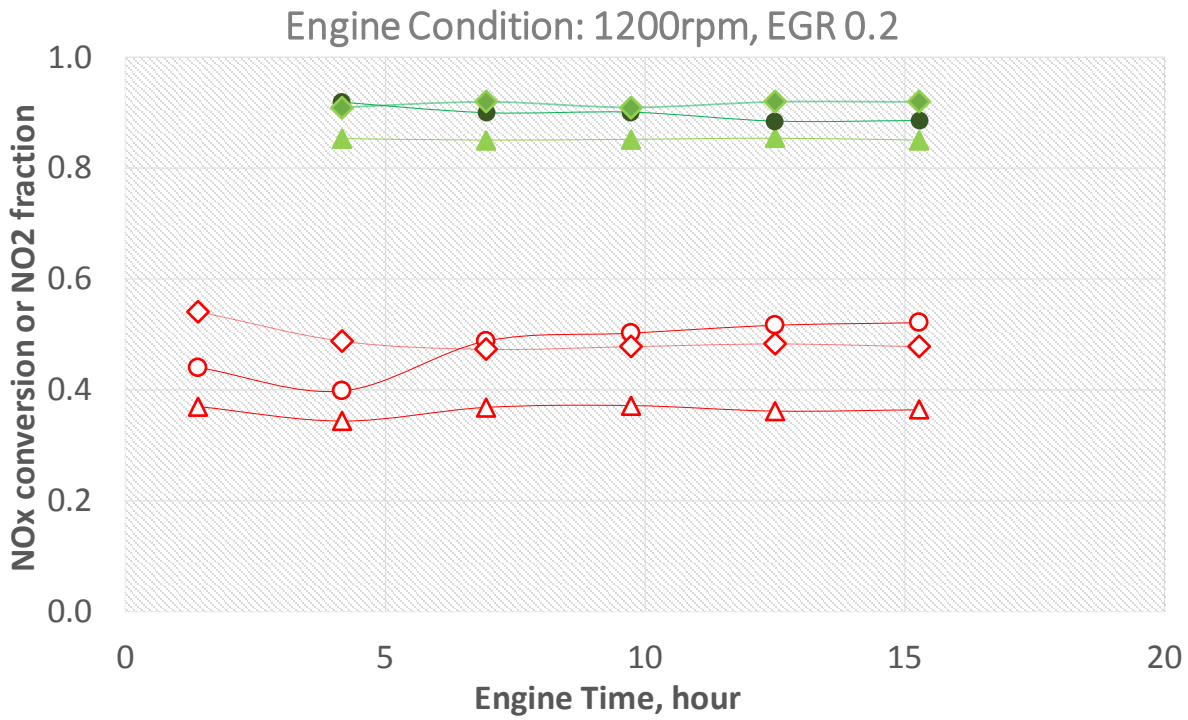

(a)

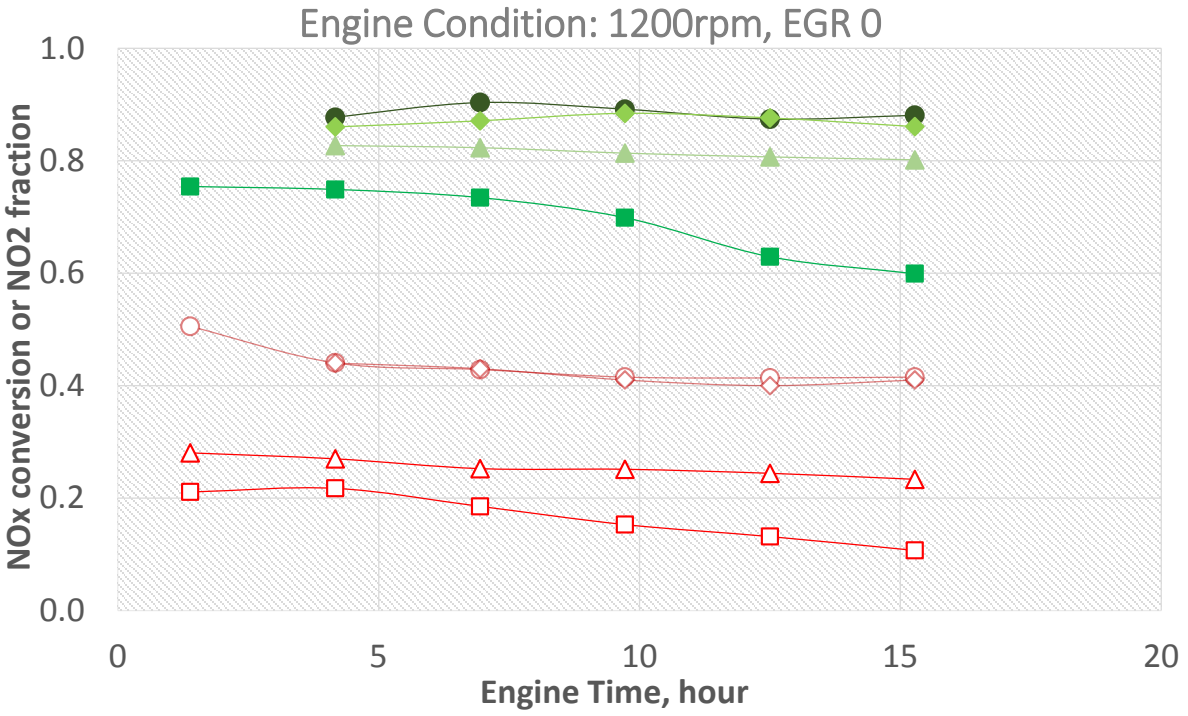

(b)

Figure I.3.C.3. Incremental performance improvement along with feed gas NO_2/NO_x increase and SCR formulation and system design changes: (a) EGR=0; and (b) EGR=0.2 [red: NO_2/NO_x of SCR feed gas; green: NO_x conversion; square: Cu-SCR with baseline DOC set 1; triangle: SLTNR SCR1 with integrated high NO_2/NO_x set 2; circle: SLTNR SCR2 with integrated high NO_2/NO_x set 3; and diamond: SLTNR SCR3 with integrated high NO_2/NO_x set 3].

The same engine testing is conducted again with EGR 0.2. Both of the DOC and SCR performance shows improvements. The best stable performance is observed with DOC set 3 and SCR set 3, where NO_2/NO_x is ~0.5 and NO_x conversion is above 90% at the end of 16 hours of steady-state low temperature operation.

Figure I.3.C.4 shows an example of a NO_x trace long SCR system in architecture (DOC set 3 + SCR set 3) at the end of 16 hours of steady-state low temperature operation with EGR 0.2. In this architecture, the SCR system includes two SCRs with SLTNR-SCR in front followed by a Cu-SCR. It is observed that the SLTNR-SCR catalyst shows stable performance in this duration test and reduces the most NO_x (~84%) in the exhaust, indicating a minimal impact from the NH_4NO_3 inhibition, which protects the downstream component (Cu-SCR) from the exposure of the high NO_2 and NH_3 flux; therefore, it minimizes the risk of NH_4NO_3 inhibition over Cu-SCR.

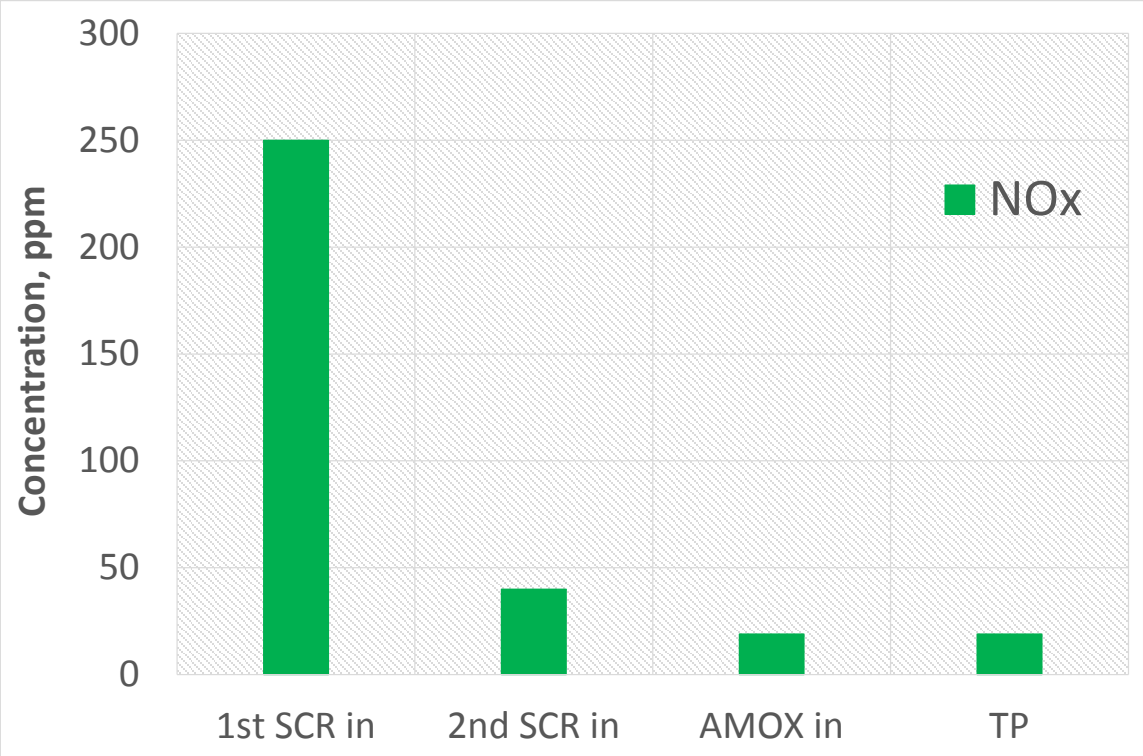

Figure I.3.C.4. NO_x concentration by Fourier Transform Infrared (FTIR) at each components inlet and outlet at end of 16 hours of steady-state low temperature operation with EGR 0.2.

Figure I.3.C.5 summarizes the incremental improvements along with progressive introduction of SLTNR integrated high NO_2/NO_x DOC architecture and SLTNR low temperature SCR architecture. It shows that in order to maximize SLTNR aftertreatment performance, engine calibration (e.g., EGR) needs to be tuned to optimize DOC and SCR performance.

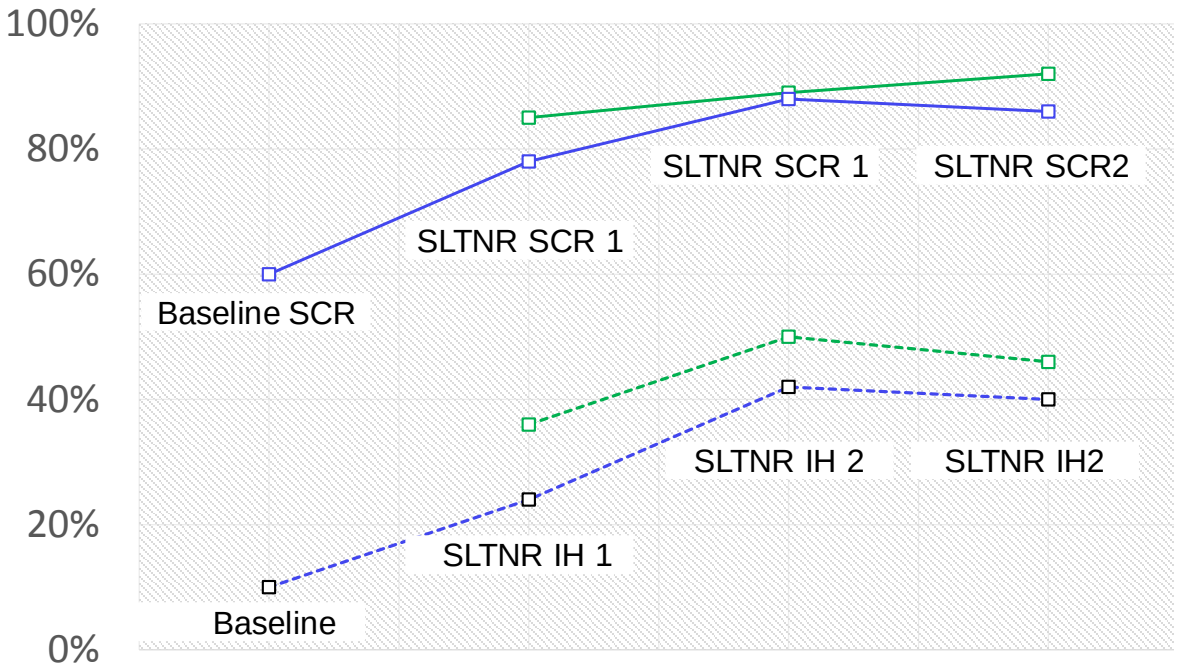

Figure I.3.C.5. Summary of performance incremental gain along with progressive SLTNR technology introduction step-by-step [blue dotted line: NO_2/NO_x in feed gas at SCR inlet with EGR 0; blue solid line: NO_x conversion with EGR 0; green dotted line: NO_2/NO_x in feed gas at SCR inlet with EGR 0.2; green solid line: NO_x conversion with EGR 0.2; IH: integrated high NO_2/NO_x set].

A reversible deterioration was observed in both the reactor test and the engine test. Performance can be recovered by an appropriate hydrothermal treatment (e.g., 4 hour @600°C). It is believed that this is caused by the accumulated changes of catalyst active sites associated with ammonia nitrate formation at low temperature events (<200°C). Further investigation is to be conducted to evaluate and simulate this performance in modeling for better understanding of its application and integration requirements.

The developed SLTNR DOC and SCR system was also tested with transient cycles to understand its real world operation capability. A city bus cycle was selected for this test based on its exhaust condition where turbo out-temperature is close to 200°C and the SCR is 145°~170°C for the whole cycle. The cycle was conducted on both the Cu-only architecture and the Fe-Cu architecture and with the EGR default and the EGR 0 for about 8~9 hours. Figure I.3.C.6 shows that Fe-SCR provides better tolerance to higher NO_2/NO_x and could deliver lower tail pipe NO_x over the same time period as Cu-SCR, where AN becomes a signification inhibitor at higher NO_2/NO_x testing; while at lower NO_2/NO_x, the SLTNR system shows comparable performance with the baseline system, as is shown in Figure I.3.C.7.

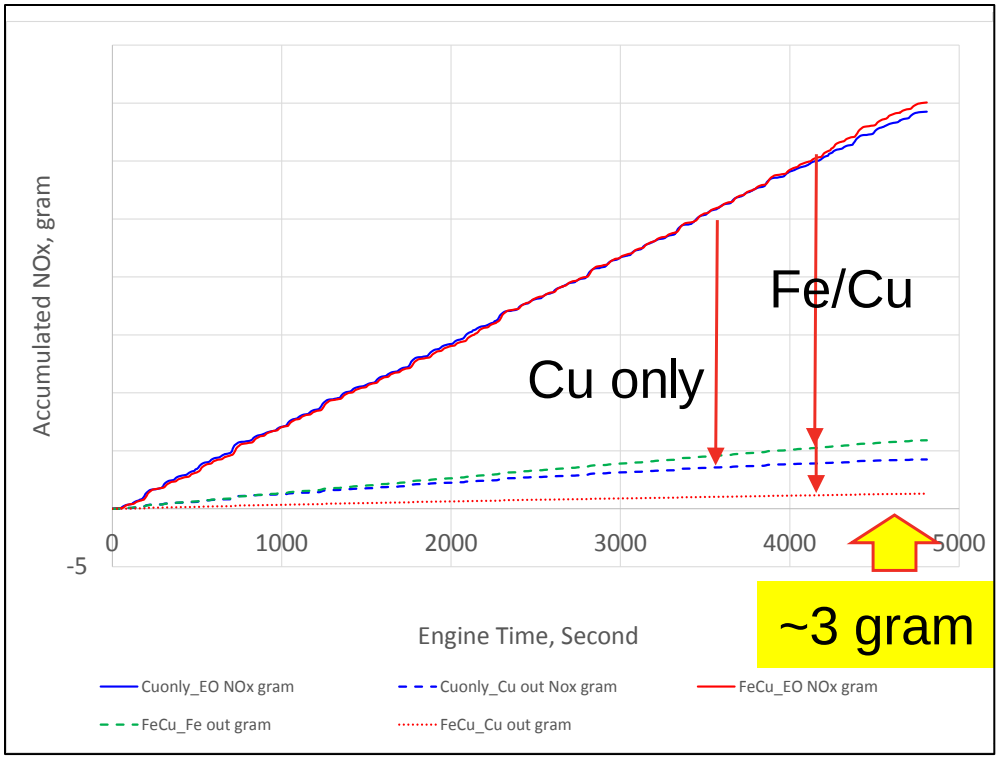

(a)

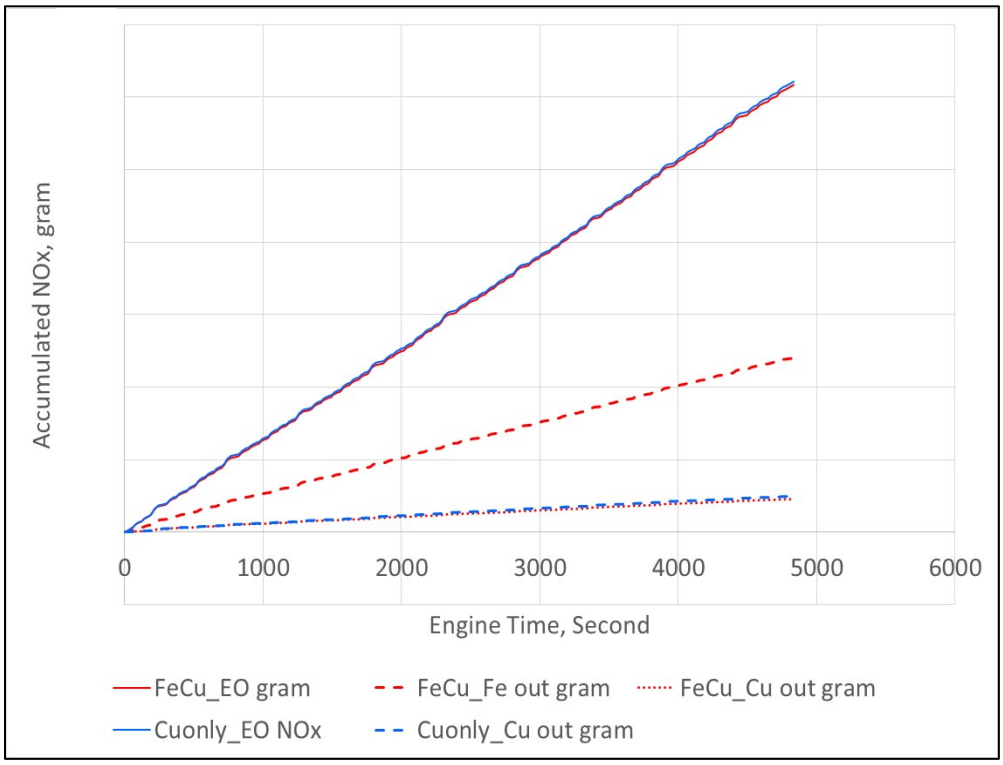

(b)

Figure I.3.C.6. Accumulative NO_x at engine out and tailpipe comparison: Cu-only architecture versus Fe-Cu-architecture with: (a) EGR default; and (b) EGR=0.

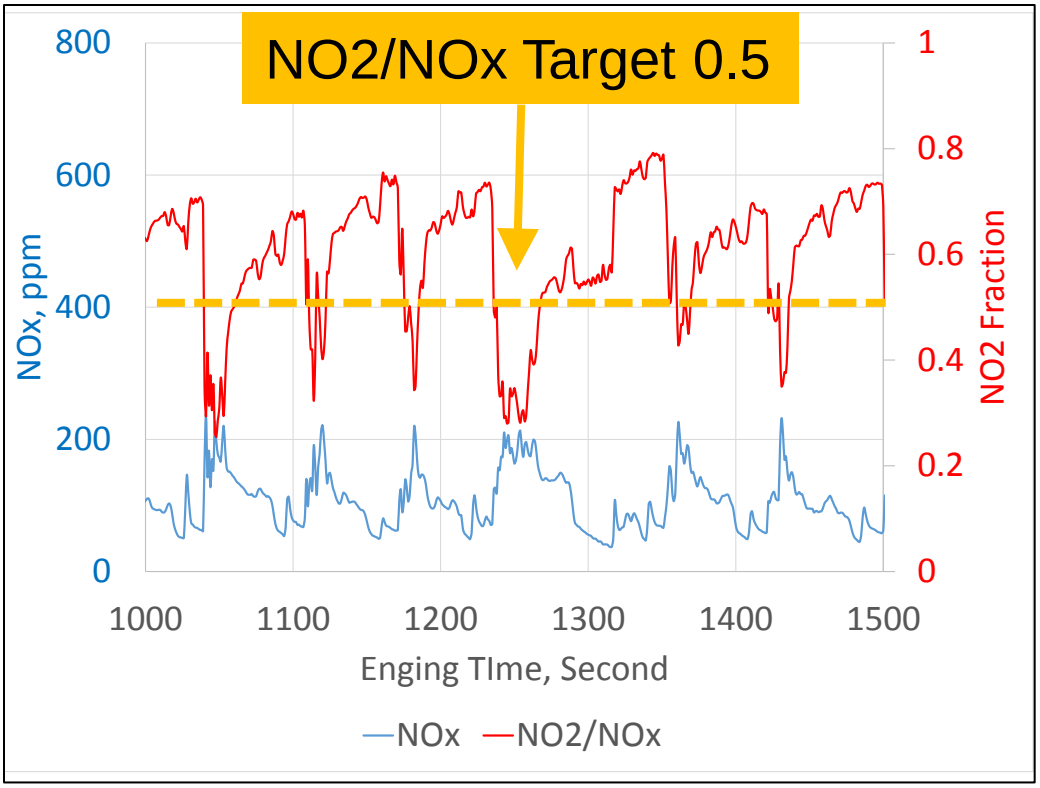

(a)

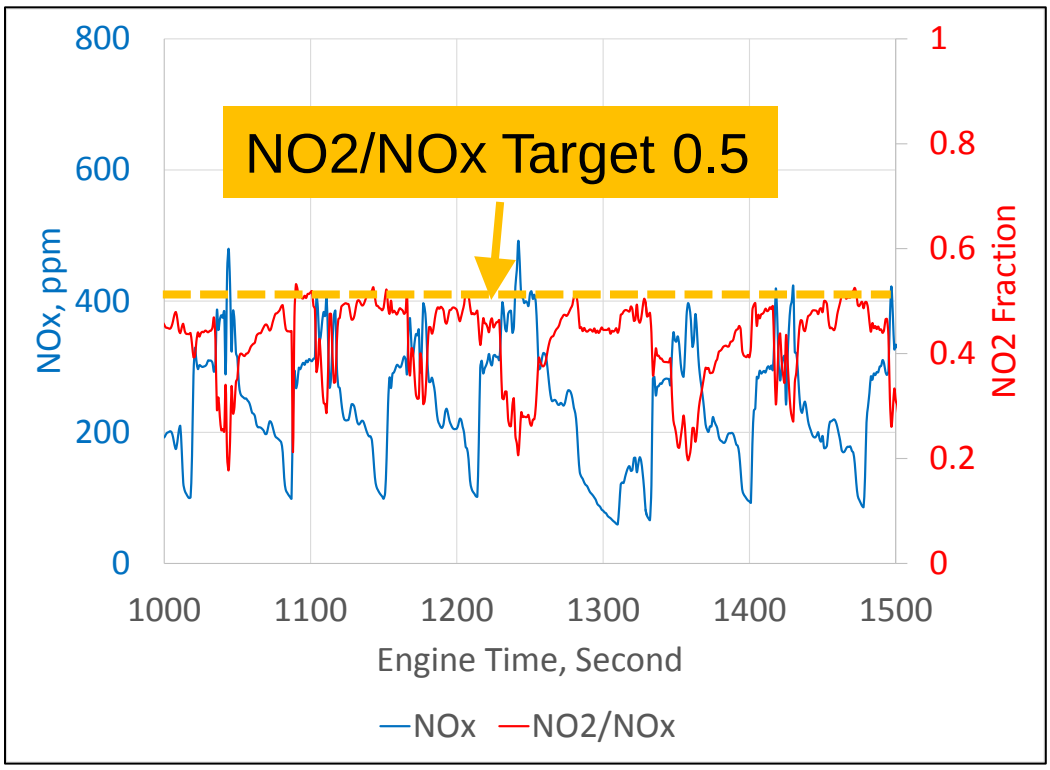

(b)

Figure I.3.C.7. NO_2/NO_x at SCR inlet with: (a) EGR default; and (b) EGR=0.

2. *The developed SLTNR-DOC prototype provides the capability to meet NO_2/NO_x target at SLTNR condition, but two challenges were observed: 1) there is space claim challenge of packaging the pre-turbo DOC in the engine compartment; and 2) there is an expected challenge of a negative impact to the transient response of the engine. Mitigation plans are under discussion and evaluation.*

For a turbocharged diesel engine, there is a known lag in acceleration performance due to the time it takes to get the work out of the turbocharger. Putting a large volume of gas upstream of the turbocharger will delay the time that it takes to get the energy to and from the turbocharger system. An initial study was completed in order to determine the impact of the pre-turbo catalyst on the transient response of the engine. It should be noted that the use of a bypass control valve around the pre-turbo catalyst during significant transient events may be a way to mitigate any negative effects. It should also be noted that the air-handling calibration or turbocharger were not re-optimized for the pre-turbo configuration so there may be some improvement opportunities to consider.

Two conceptual design developed to mitigate the above two challenges. One of them was able to build into prototype part and tested behind the engine. The performance is in the process of evaluation. Due to confidentiality issues, these will not be elaborated on further here.

3. *An initial concept design and on-engine demonstration was conducted on diesel exhaust fluid (DEF) ultrasonic technology with intention to deliver fine droplets and therefore minimize the potential deposit at SLTNR conditions. The developed prototype DEF ultrasonic device shows the capability to achieve NO_x conversion 98% at 300°C, but a few challenges were observed: 1) significant solid deposits are found inside the ultrasonic device; and 2) dosing rate control needs to be improved.*

As shown in Figure I.3.C.8, with gaseous NH_3 and baseline ATS, NO_x conversion is calculated at ~50% at ammonia to NOx ratio (ANR) 0.5, 70% at ANR 0.8, and 78% at ANR 1.0 at SCR inlet ~ 160°C, which is considered to be the entitlement of reductant delivery system performance. In the same testing with the 2017 production dosing system, NO_x conversion is at 35% for ANR 0.5, 45% for ANR 0.8, and 50% at ANR 1.0. The doser efficiency (normalized by performance with gaseous NH_3) is calculated at 64~70% for this ANR sweep 0.5~1.0, which indicates that about 1/3 of reductant did not contribute to SCR reaction due to the inefficient dosing capability that specifically correlated to the large droplets and low temperature.

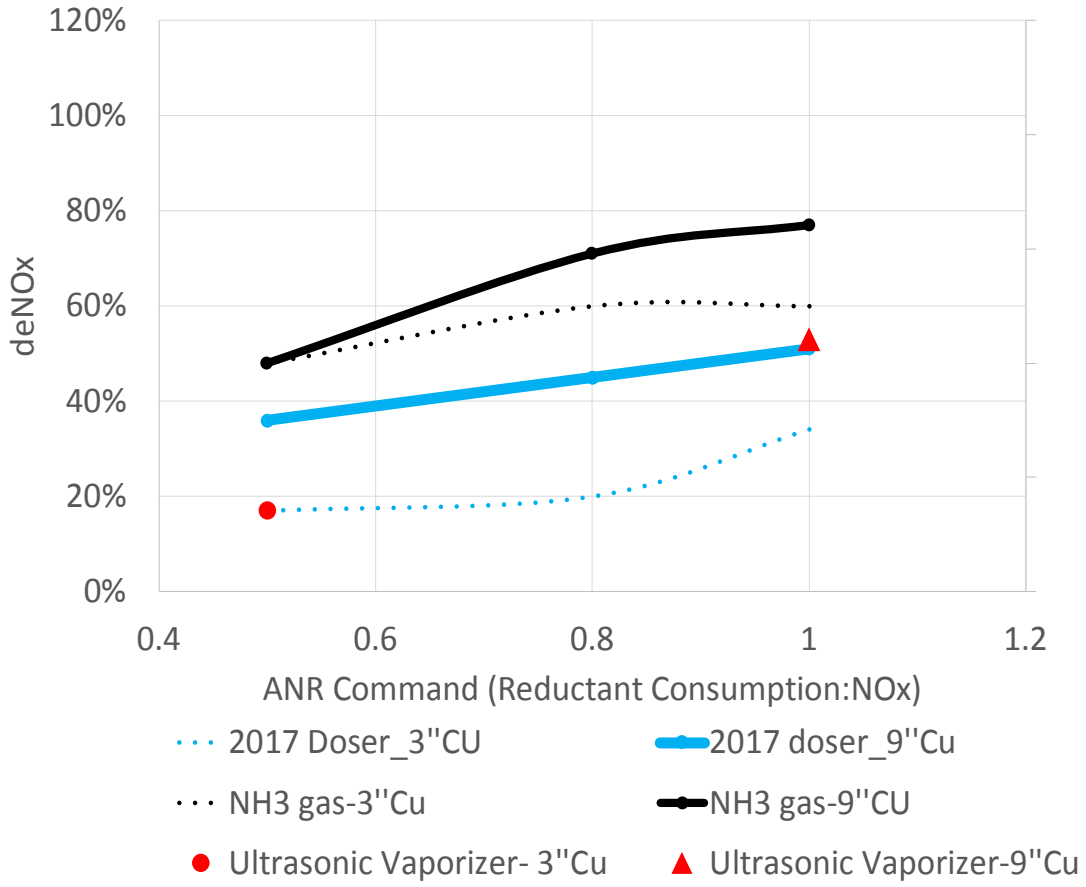

Figure I.3.C.8. Performance comparison of various reduction introduction technology: Gaseous NH3, 2017 Production Doser, and Ultrasonic Vaporizer.

The ultrasonic vaporizer was also tested under the same engine condition; only limited data were available for this comparison upon the submission of this annual report. It shows an equivalent performance with the 2017 doser from the NO_x conversion performance. However, the calculated ANR for the vaporizer was based on the pump stroke rate; a significant amount of DEF was observed staying inside the DEF ultrasonic device and dried out along the time-forming deposit inside the vaporizer chamber. So the actual ANR if using the DEF that was able to get into the exhaust to do the calculation will be much less than what is reported in Figure I.3.C.9. So the red dots are expected to shift to the right, which will put them in between the solid blue line (2017 Production doser) and solid black line (Gaseous NH_3 dosing). This testing will be repeated with improved control strategy to mitigate the potential deposit inside chamber and confirm the benefit of the DEF ultrasonic vaporizer over the 2017 production mechanical doser.

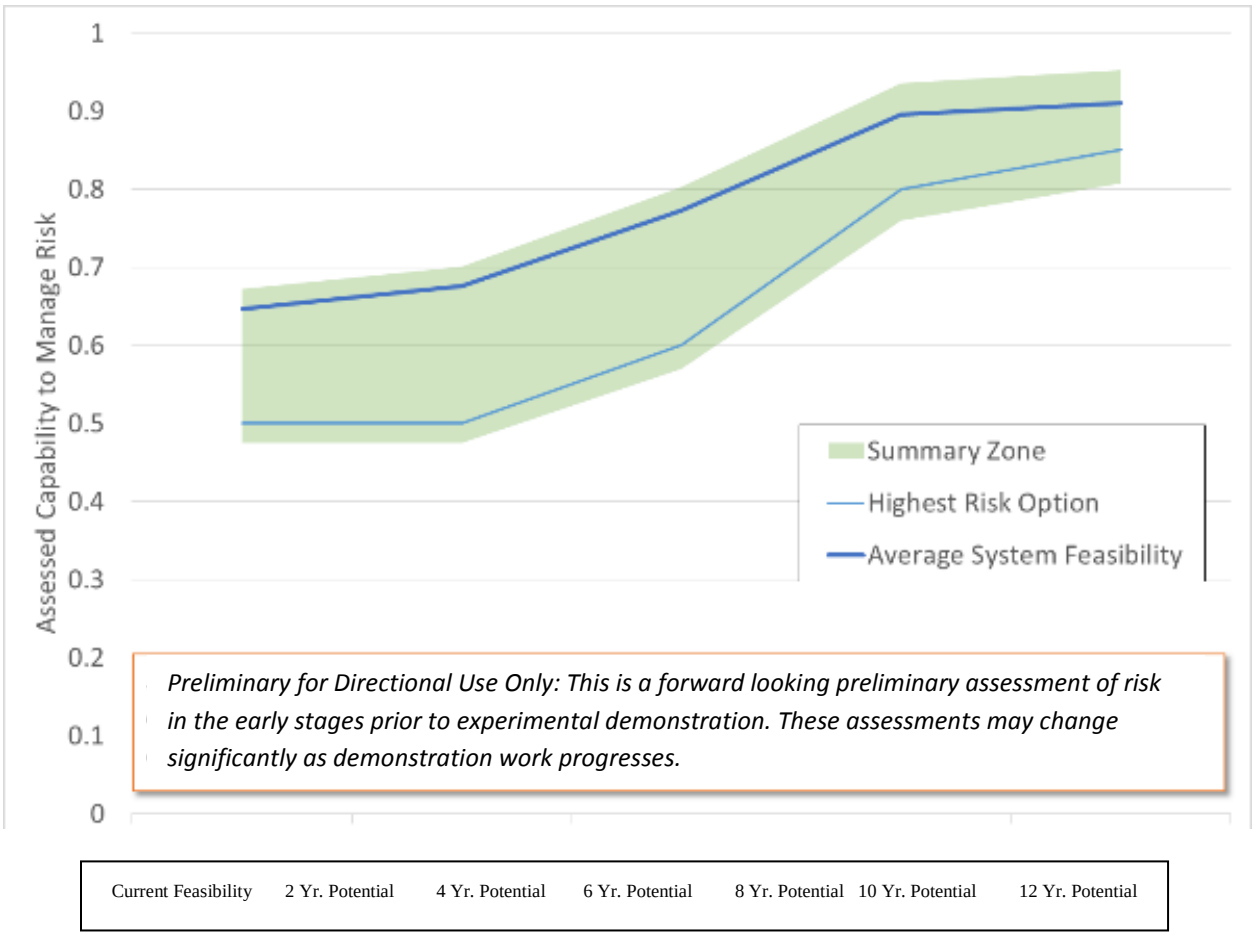

Figure I.3.C.9. Graphical illustration of the summary of the assessed capability to manage risk for the complete system.

The commercial assessment of SLTNR technology includes four categories:

1. Assessment of material cost.
2. Assessment for operating cost (impact on engine efficiency and GHG, specifically at high-load operation condition).
3. Assessment of maintenance cost (technology risk management capability).
4. Assessment for OEM development cost (packaging impact).

The average curve summarizes the various items assessed at this point in the project. The green shaded zone shows a pretty steady maturity growth rate with most technologies needing about 8–12 years to ensure the risks can be understood and managed. The average also comes in around 90% after 12 years of development, with the zone between 80–90%, which suggests that additional maturity may be required for some components in order for this type of system to be ready to implement in a commercially viable solution. Again, this will need to be re-assessed as additional information is gained through development and demonstration work.

Conclusions

The flow charts in Figures I.3.C.10, I.3.C.11, and I.3.C.12 highlight the process of each technology development work, including low temperature SCR formulation development, integrated high NO_2 system development, and low-temperature reductant delivery ultrasonic vaporizer technology development.

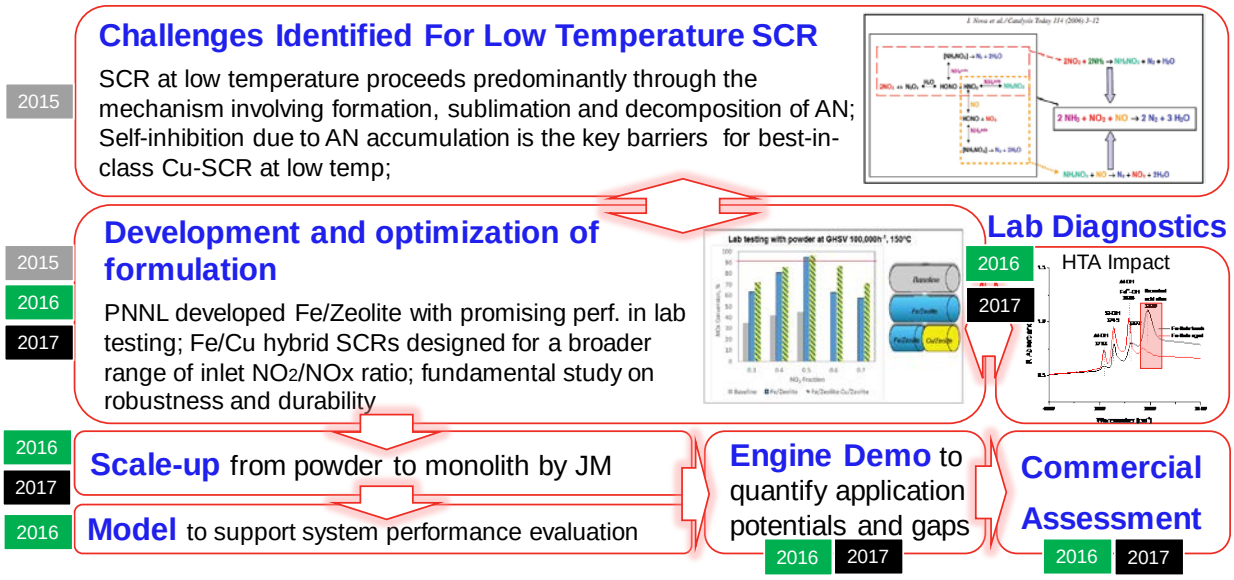

Figure I.3.C.10. Development path and process for SCR formulation and system.

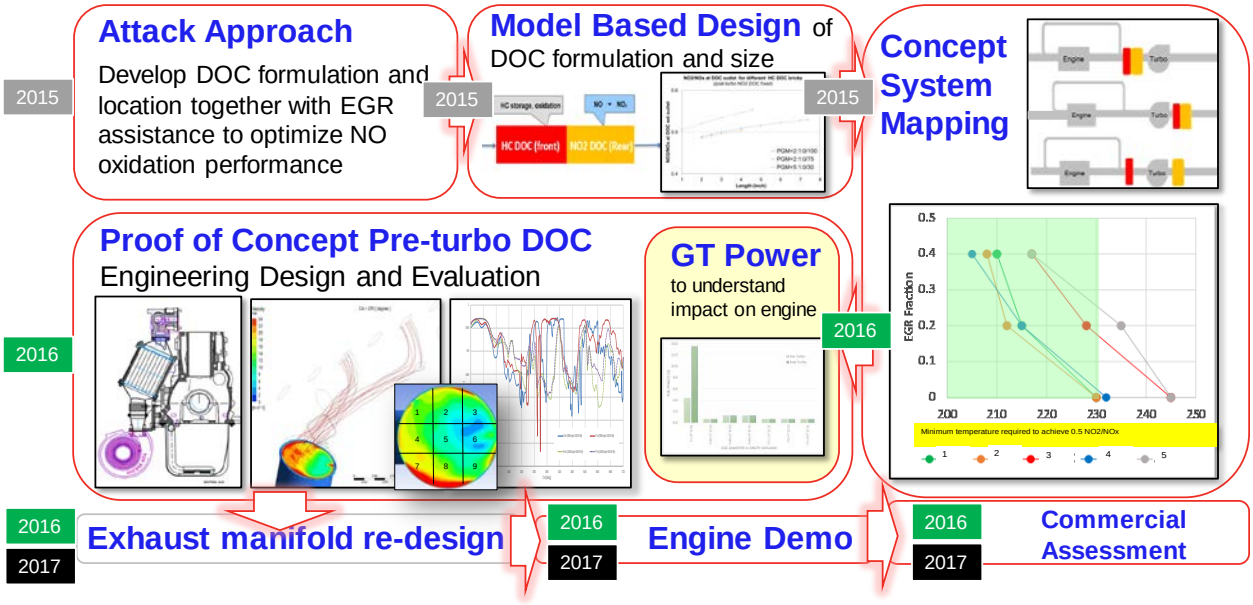

Figure I.3.C.11. Development path and process for integrated high NO_2 system.

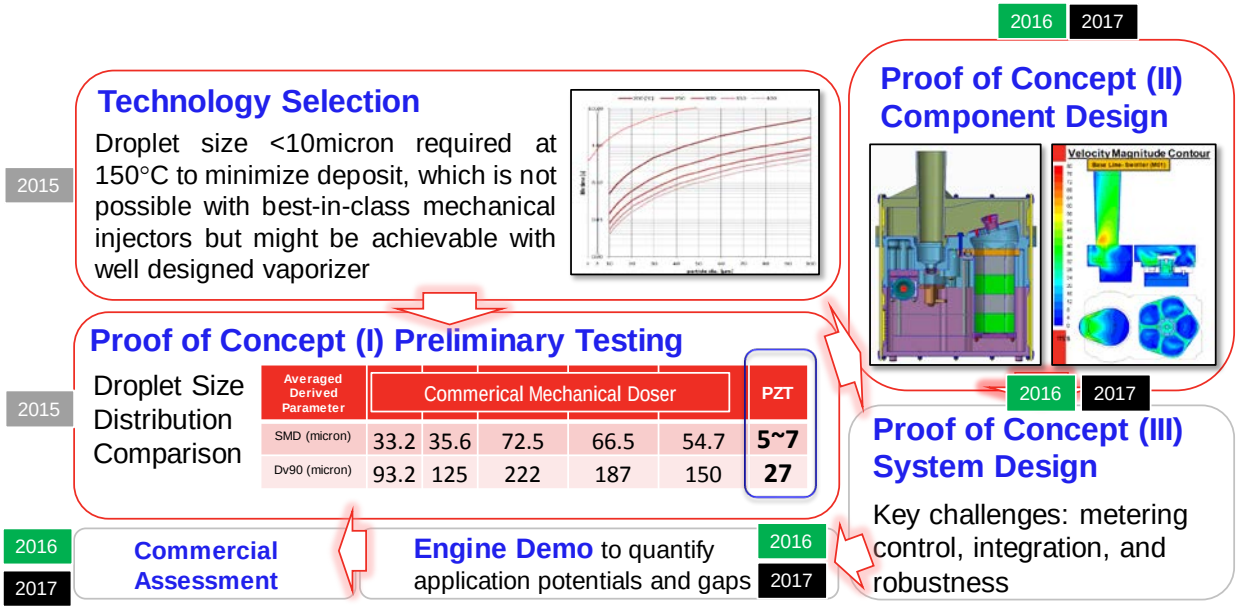

Figure I.3.C.12. The development path and progress of DEF Ultrasonic Vaporizer Technology.

Key Findings #1

The developed SLTNR DOC and SCR system meets the program target of 90% NO_x conversion at steady-state SCR 150°C condition. In low-temperature transient cycle testing, it delivers ~85% NO_x conversion in a 9-hour duration test.

Key Findings#2

The developed SLTNR DOC prototype provides the capability to meet the NO_2/NO_x target at the SLTNR condition, but two challenges were observed: 1) there is a space claim challenge of packaging the pre-turbo DOC in the engine compartment; and 2) there is an expected challenge of a negative impact to the transient response of the engine. Mitigation plans are under discussion and evaluation.

Key Findings#3

An initial concept design and on-engine demonstration was conducted on DEF ultrasonic technology with the intention to deliver fine droplets and therefore minimize potential deposits at SLTNR conditions. The developed prototype DEF ultrasonic device shows the capability to achieve NO_x conversion ~50% at 160°C, which is at comparable levels with gaseous NH_3, but a few challenges were observed: 1) significant solid deposits develop inside the ultrasonic device; 2) the dosing rate control needs to be improved; and 3) there is significant gaseous NH_3 generated by the front few inches of the SCR, which indicates that a hydrolysis catalyst might be necessary to promote system performance at such a low-temperature operation region.

The maturity assessment of the SLTNR system takes each individual component/technology into account and is estimated at about 12 years of dedicated development effort with additional maturity required for some components in order for this type of system to be ready to implement in a commercially viable solution.

Key Publications

Reports

"Sustained low temperature NO_x reduction," 2017 SAE Global Conference.

"Sustained low temperature NO_x reduction," 2017 AMR Conference.

Patents

62 / 368,470 and 15 / 663,457, "Concept for increasing NO_2 fraction at low temperature operation condition by placing specialty PGM containing components at pre-turbo location and secondary specialty PGM containing component at post-turbo location."

I.3.D Materials Issues Associated with EGR Coolers (Oak Ridge National Laboratory)

Michael J. Lance
Oak Ridge National Laboratory
1 Bethel Valley Rd.
Oak Ridge, TN 37831-6068
Phone: 865-241-4536
E-mail: lancem@ornl.gov

Jerry L. Gibbs, Technology Manager
E-mail: jerry.gibbs@ee.doe.gov

Start Date: October 1, 2009 End Date: September 30, 2017
Total Project Cost: $2,245,000 DOE share: $2,245,000 Non-DOE share: $0

Project Introduction

Throughout the developed world, strict regulations have been enacted to reduce the emission of harmful pollutants, such as NO_x, CO, HC, and particulate matter (PM) produced by diesel engines. For NO_x emissions, the limits have decreased from 9.2 g/kW-hr in 2002 to just 0.40 g/kW-hr in 2014 for many classes of non-road compression-ignition engines in the U.S. This has placed increased importance on engine technologies for preventing NO_x formation, as well as technologies for removing NO_x from exhaust gases. A commonly used method to control NO_x formation is exhaust gas recirculation (EGR) whereby a fraction of the engine exhaust is recirculated back to the combustion chambers. The introduction of inert exhaust gas, which is composed primarily of nitrogen, CO, and water vapor, increases the heat capacity of the cylinder contents. This increased specific heat acts to reduce combustion temperatures, thereby decreasing the formation of oxides of nitrogen. Before being re-introduced into the cylinder, the exhaust gas is normally cooled in a heat-exchanger or cooler, which enhances the EGR effect.

Some PM and HC present in exhaust gas will form a deposit inside the EGR cooler through thermophoresis and condensation, respectively. Due to the high concentrations of PM and HC in the exhaust gas, the formation of these deposit layers can form rapidly. Furthermore, under most conditions, this deposit is an excellent thermal insulator (Lance et al. 2009), causing it to significantly decrease the effectiveness of the EGR cooler. The reduced effectiveness of the cooler leads an increase in the temperatures of the exhaust gas re-introduced into the engine cylinders and, in turn, NO_x pollutants generated during combustion. In addition, as the deposit thickens, it will impede the flow of exhaust through the cooler, thereby causing an increase in the pressure drop across the cooler. This results in a loss in fuel efficiency as more energy must be expended to drive the exhaust gas through the cooler. Previous studies have focused on deposit formation and removal on flat tubes (Abarham et al. 2013, Sluder et al. 2014), but less work has been reported on substrates with turbulated structures that are typically used in production EGR coolers. Field-returned coolers have been observed to have microstructural features on the deposit surface, which suggests that deposit removal is occurring on the upstream side of the fins during operation where shear stresses are high (Lance et al. 2010). Previous attempts to image EGR deposits nondestructively and characterize how the turbulation structures impact deposition and removal using neutron tomography was successful for high-HC plugging deposits, but produced mixed results for low-density deposit layers that are far more common in the field (Lance et al. 2014). In this report, we describe a new approach for measuring deposit thickness along the cooler turbulation structure using structured light imaging and our investigations of the effect of varying engine operating conditions on deposit thickness.

At the start of this project, an advisory team consisting of engineers responsible for EGR systems was assembled from nine diesel engine manufacturers: Caterpillar, Cummins, Detroit Diesel, Ford, GM, John Deere, Navistar, DAF Trucks, Volvo/Mack, and one heat exchanger supplier, Modine. They were asked what

the biggest problem facing EGR cooling systems is and the clear winner was fouling. Over the course of this project, the EGR team has been notified of the results generated and have contributed coolers for forensic analysis of fouling deposits.

Objectives

To provide information to industry about fouling deposit properties so as to enable improved models and potential design improvements to reduce fouling and its impact on the performance of EGR coolers.

Approach

One of the members of the EGR Team, John Deere, was gracious enough to provide 20 coolers that were fouled using different operating conditions at a cost that must have exceeded $1,000,000. John Deere used a 9-L HD engine and ultra-low sulfur diesel (ULSD) fuel to foul 20 EGR tube-in-shell coolers by varying five factors: (A) EGR flow rate; (B) EGR inlet gas temperature; (C) coolant temperature; (D) smoke level (e.g., filter smoke number [FSN]); and (E) HC concentration. Table I.3.D.1 shows the target operating conditions. A five-factor, two-level design-of-experiments (DoE) required 16 coolers to test all combinations, but an additional 4 coolers were operated using midpoints for some or all the factors for a total of 20 coolers. Coolers were run until the effectiveness stabilized (typically 40-70 hours), were cooled down to room temperature, and then run again for an additional few hours to measure the change in effectiveness due to shut-down. High HC could not be achieved with high EGR inlet gas temperatures due to the burning of the HC prior to entering the cooler.

Table I.3.D.1. Target Operating Conditions for the EGR Coolers.

Factor	Low	Midpoint	High
A. EGR Rate (g/s)	83.3	118.1	152.8
B. EGR Inlet Gas Temperature (°C)	350	450	550
C. Coolant Temperature (°C)	85	92.5	100
D. Smoke Level (FSN)	0.5	1.25	2.0
E. Hydrocarbon Concentration (ppm)	25	50	75

Each cooler had 12 oblong tubes bundled in a 6 by 2 pattern all inside a shell that contained the coolant. Each tube was 48 cm long, 4.4 cm tall, and 0.76 cm wide. There were 20 fins inside each tube spaced ~0.2 cm apart from one another. Along the flow direction, the fins formed a sinusoidal wave with a wavelength of 1 cm and an amplitude of ~0.065 cm.

In order to measure the true deposit thickness and how it varies across a sinusoidal fin, measurements were performed using a Keyence VR-3100 optical profilometer. This instrument measures height by illuminating bands of structured light on the surface. When the reflected light is collected from another angle, height differences on the surface appear as distortions of the shapes of the incident light bands. Triangulation calculations are then performed to measure the surface height at each point to a resolution of ~1 µm across a field-of-view 17 by 2.4 cm, thereby allowing the entire three-dimensional (3D) surface profile of the sample to be acquired in less than one minute.

Sections near the inlet, center, and outlet of a single channel in each of the 20 coolers were prepared for measurement by milling two lines running parallel to the exhaust flow on either side of the section to a depth of ~25 µm. The samples were then carefully peeled open along these two lines, thereby exposing the undisturbed deposit surface. In order to measure the true deposit thickness and how it varies across the sinusoidal fin, height maps of the surface before and after removing the deposit were collected. Figure I.3.D.1.a shows the height map obtained with the optical microscope of a single fin coated with

deposits, while Figure I.3.D.1.b shows that of the same region after the deposit was cleaned off with a lint-free swab and a vacuum. The sample was held in place with a vice that was affixed to the microscope stage to ensure that it did not move during cleaning. The deposit thickness, shown in Figure I.3.D.1.c, was obtained from the difference of the two surface heights. All of the height maps captured at least one complete wavelength of the sinusoidal fin, as well as the entire fin width (0.76 cm).

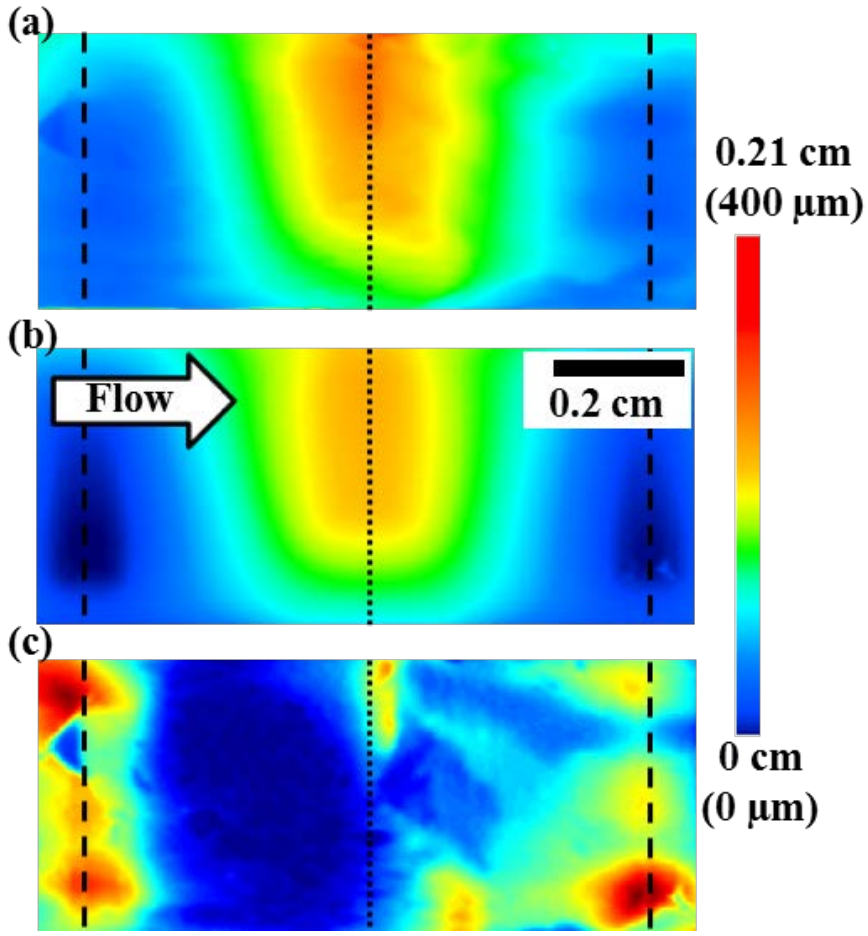

Figure I.3.D.1. Height maps of: (a) a fouled fin surface; (b) the fin surface after deposit removal; and (c) the deposit thickness calculated from the difference of the fouled and cleaned surfaces. The scale bar applies to (a) and (b) with 0.21 cm as the maximum height and to (c) with (400 µm) as the maximum thickness. Dashed and dotted lines indicate the location of the fin peak and trough, respectively.

Results

In all 20 fouled coolers, the deposit maintains the same general shape across each period over the entire length of the channel, as shown in Figure I.3.D.2. The deposit was thinnest and thickest on the upstream and downstream sides of the fin peak, respectively. This is due to the fin geometry, which coupled with the high flow rates, is sufficient to produce the shear necessary to inhibit deposit growth along the upstream side of the fin for all flow rates investigated. Although the same general deposit shape was found for all conditions, the overall average thickness across each period varies. Furthermore, the engine operating conditions that influence the average thickness varied with position along the length of the channel.

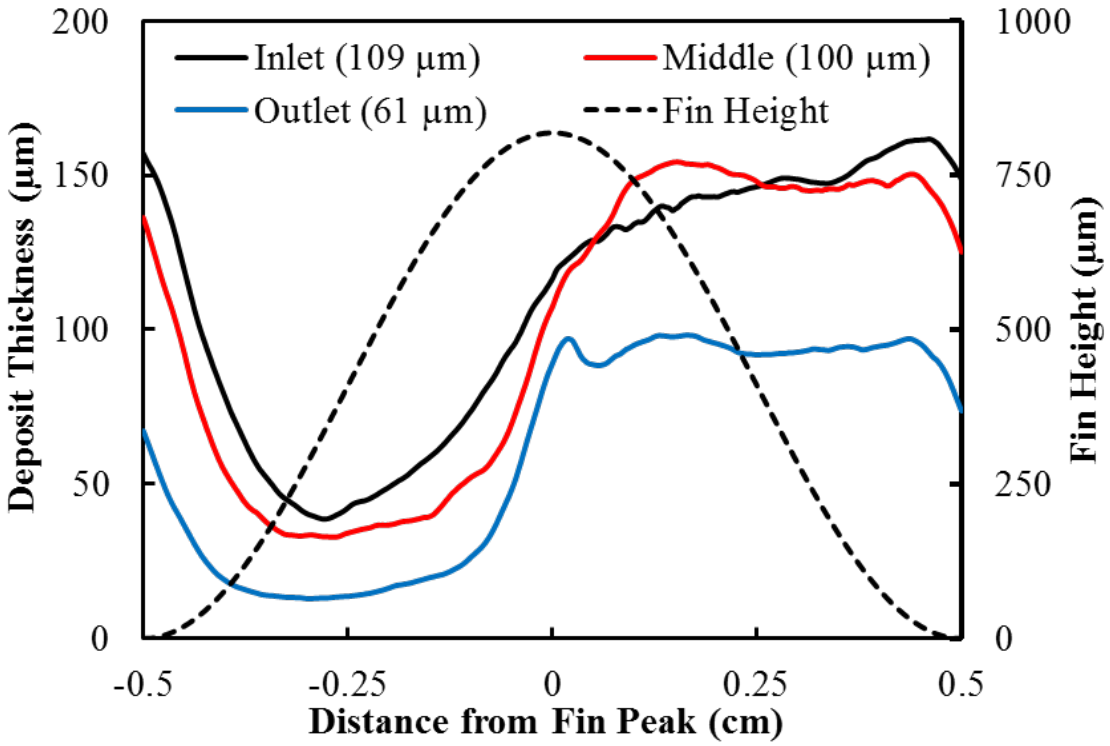

Figure I.3.D.2. Average deposit thickness of all 20 coolers along one period near the inlet, middle, and outlet of the cooler. The average thickness at each location is provided in the legend.

As the hot exhaust gas enters the cooler channel, it comes into contact with cooled walls, allowing for volatile species of HCs to condense. Additionally, the large temperature gradients near the wall induce significant thermophoretic velocities in soot particles entrained in the flow. This results in the rapid formation of the fouling layer and, subsequently, causes the temperature at the surface of the layer to quickly approach that of the exhaust gas. As the deposit thickens, the surface will remain at the gas temperature, but the deposit in contact with the metal wall will be at the coolant temperature creating a thermal gradient across the deposit layer. Condensed HCs in the deposit begin to evaporate from the deposit surface, where it is hottest, and less so near the metal wall, resulting in an HC concentration gradient across the deposit (Lance et al. 2010). This evaporation causes the deposit to shrink at the surface eventually leading to the formation of mud-cracks.

Mud-cracks have been observed in both field-aged and laboratory-generated samples and is thought to aid in the removal of large regions of the deposit through spallation (Lance et al. 2013). Furthermore, the similar effect of water vapor condensation on mud-cracking and spallation at lower coolant temperatures has been investigated as a strategy for regeneration of fouled coolers. When the inlet temperature of the exhaust gas is increased, the magnitude of the variation in temperature in the fouling layer increases as well. This leads to increased devolatilization rates, increasing the shrinkage of the deposit layer near the surface, which enhances the effect of mud cracking and, in turn, the removal of deposits.

The influence of the inlet gas temperature on the deposit thickness through mud-cracking can be seen in Figure I.3.D.3, which contains the average thickness of the fouling layer across a single period near the inlet of each of the 20 coolers. As the inlet temperature increases, the average thickness of the deposit decreases due to the effect of mud-cracking. Figure I.3.D.4 shows a SEM image of the deposit near the inlet of a cooler with both high inlet temperature and EGR rate set points. Because of the high inlet temperatures, the fouling layer underwent significant mud-cracking, which allowed for the removal of large regions of the deposit through spallation.

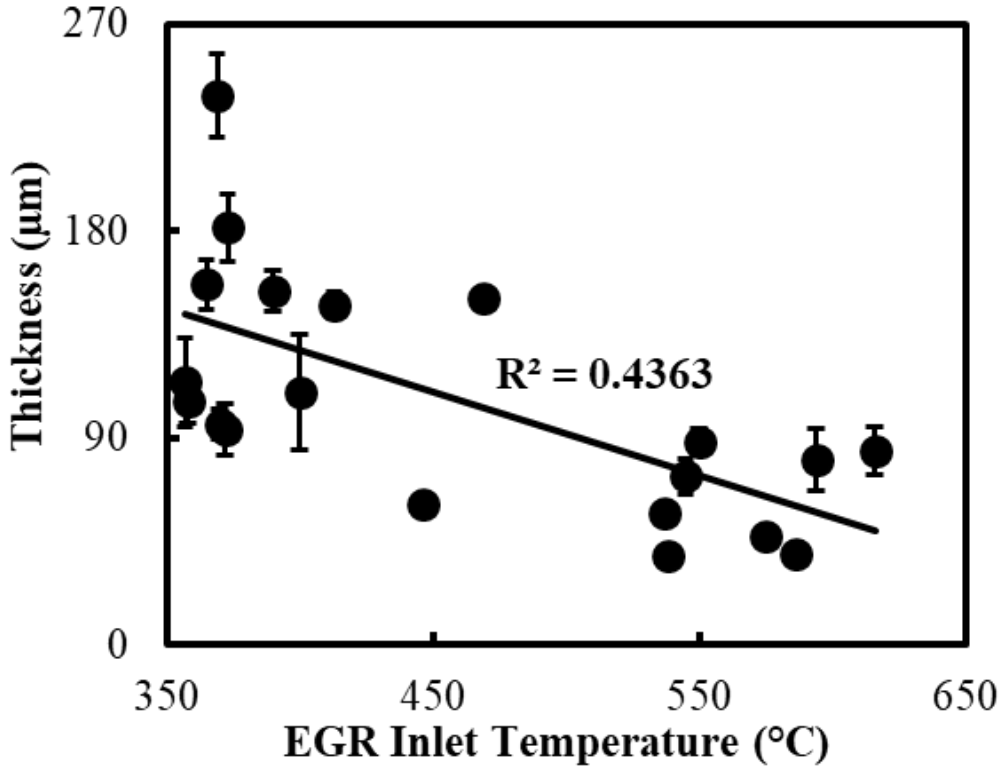

Figure I.3.D.3. Average deposit thickness for a single fin period near the inlet of the cooler versus the EGR inlet temperature. Error bars represent the mean value of the standard deviation in the thickness across the width of the channel at each measurement location along the length.

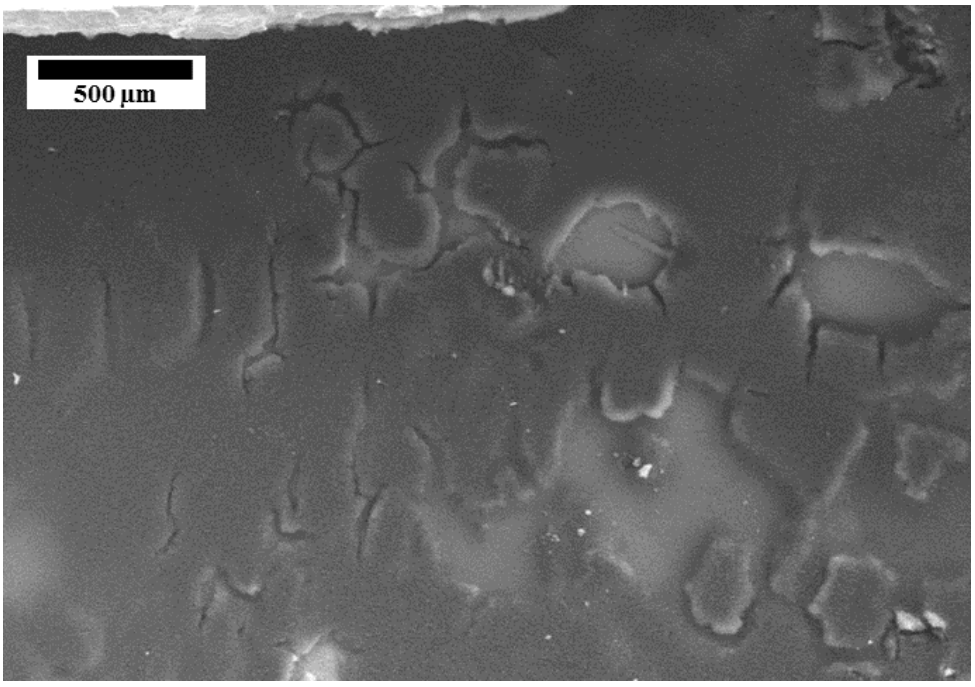

Figure I.3.D.4. A SEM image of deposit from the cooler with a high EGR rate and inlet temperature showing mud-cracking and spallation near the peak of the sinusoidal fin. The scale bar is 500 µm.

In addition to performing linear regression on each of the individual parameters, a multiple regression analysis was also conducted. In this analysis, a best fit was obtained from a combination of any of the five parameters and their two-way interactions. Near the inlet of the cooler, the multiple regression analysis indicates that the inlet gas temperature is the dominant factor influencing average deposit thickness. This can be seen in Figure I.3.D.5, which shows that the inlet temperature (effect B), has the largest absolute coefficient and is the only single factor found to be the best fit for the data. The two remaining coefficients belong to the two-way interactions of the inlet temperature with the EGR rate (effect A) and the coolant temperature (effect C). The negative values of these interaction coefficients indicate that the effect of the inlet temperature increases with both decreasing coolant temperature and EGR rate.

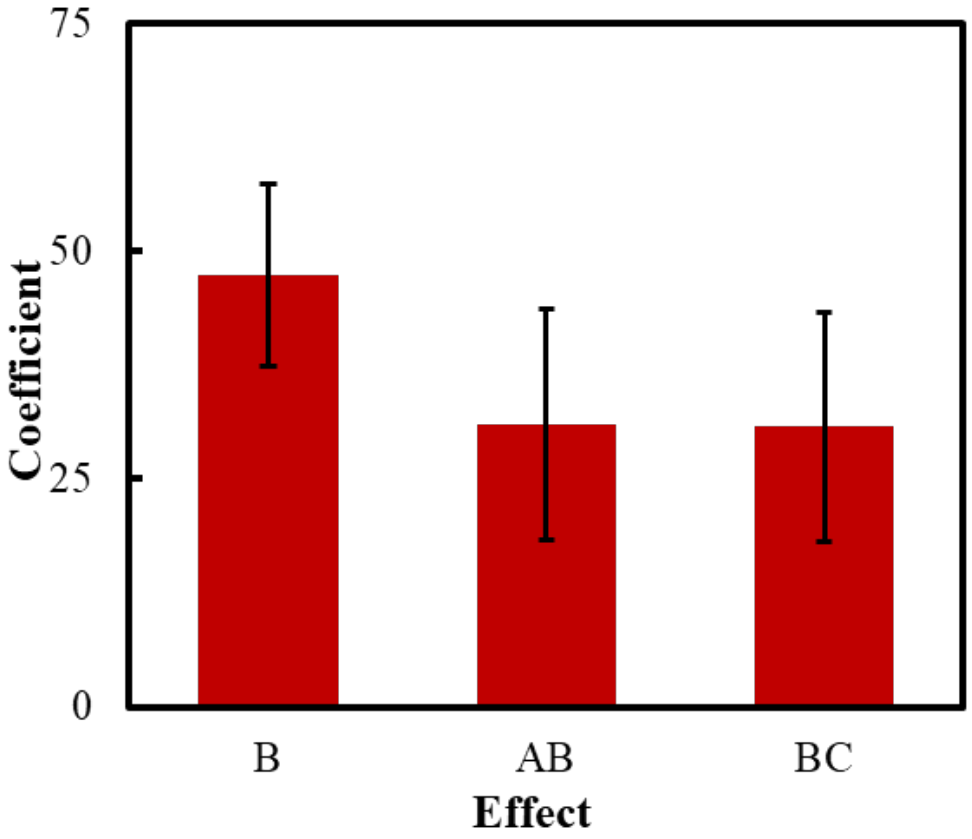

Figure I.3.D.5. Bar chart showing the absolute value of the multiple regression coefficients with variables A, B, and C, representing the flowrate, inlet temperature, and coolant temperature, respectively. The red bars indicate negative values of the coefficients.

Half-way downstream near the middle of the channel, the temperature of the exhaust gas has been sufficiently reduced, which mitigates the formation of mud-cracks in the deposit. As a result, the influence of the EGR inlet temperature on the deposit thickness is negligible. Without the removal of deposits through mud-cracking and spallation, the average thickness of the fouling layer becomes determined by the magnitude of thermophoretic deposition. Because the magnitude of the thermophoretic deposition scales with the thermal gradients near the wall, the average deposit thickness scales linearly with the temperature difference between the exhaust gas and the coolant. Furthermore, the temperature of the exhaust gas at this location is highly dependent on the flow rate rather than the inlet temperature due to its effect on the residence times of the fluid in the channel. As a result, the thickness of the deposit near the middle of the cooler is most influenced by the EGR rate. At low flow rates, the increased residence time reduces the temperature difference between exhaust and the coolant, leading to the formation of a thinner deposit. Increasing the flow rate and, subsequently, decreasing the residence time of the exhaust results in larger temperature differences, which produces a thicker

deposit. Results from a multiple regression analysis confirms that the EGR rate is indeed the largest influencing factor on deposit thickness midway down the channel. Additionally, the analysis indicates that an interaction between the soot and HC concentrations influences the average thickness. This is due to the ratio of condensed HC to soot particles in the deposit influencing the deposit density, and in turn, its thickness.

Near the outlet of the channel, the difference between the temperature of the fluid and that of the coolant ranges between 4°C and 24°C for all 20 coolers. As discussed previously, increased flowrates lead to reduced residence times of the fluid in the channel. As a result, the flowrate has a greater influence on the temperature difference near the outlet than near the inlet. Because the rate of the thermophoretic deposition of particles onto the wall scales with this temperature difference, the EGR rate also influences deposit thickness with increasing flowrates increasing the deposit thickness. In addition to the decreased thermophoretic deposition associated with smaller thermal gradients, the lower temperatures near the outlet allow for more rapid condensation of HCs along the wall. This results in an increased influence of the HC concentration on deposit thickness. Like the EGR rate, deposit thickness increases with increasing HC concentration. The influence of these two factors are confirmed by a multiple regression analysis. As with the middle of the cooler, the regression model also indicates a large interaction between the soot and HC concentrations. At the outlet, however, high soot concentrations act to decrease the resulting deposit thickness, while higher HC concentrations act to increase the thickness.

Conclusions

EGR coolers were fouled by varying five engine operating conditions using a 9-L HD engine. An optical profilometer was used to measure the thickness of the deposit along a single channel near the inlet, middle, and outlet of each of the 20 fouled EGR coolers. Using statistical methods, engine operating conditions influencing deposit thickness near the inlet, middle, and outlet sections of the cooler were investigated.

It was found that as inlet temperature increases, the deposit thickness near the inlet of the channel decreases. This is due to the higher gas temperatures inducing mud-cracking in the deposit layer, allowing for the removal of deposits through spallation. Halfway down the length of the channel, the influence of the inlet temperature is negligible as the reduced temperatures are insufficient to induce mud-cracking. At this location, the thickness of the fouling layer is driven by the magnitude of the thermophoretic deposition. Because of its effect on residence time, and therefore the temperature of the gas, the EGR flow rate has the largest influence on the deposit thickness at this location. Lastly, near the outlet of the cooler, the HC concentration begins to have an influence on deposit thickness. This is because the temperatures are sufficiently low for significant condensation of HC species, which acts to form a denser deposit. The higher thermal conductivity of the dense HC-rich deposit allows for continued thermophoretic deposition, increasing the thickness of the deposit.

Key Publications

Lance, M. J., Z. G. Mills, J. C. Seylar, J. M. E. Storey, and C. S. Sluder, “The effect of engine operating conditions on exhaust gas recirculation cooler fouling,” to be submitted.

Uy, D., G. Pranis, A. Morelli, A. Gangopadhyay, and M. J. Lance, 2017, “Correlating laboratory oil aerosol coking rig tests to diesel engine tests to understand the mechanisms responsible for turbocharger compressor coking,” SAE Technical Paper 2017, doi:10.4271/2017-01-0887.

References

Abarham, M., P. Zamankhan, J. W. Hoard, D. Styles, C. S. Sluder, J. M. E. Storey, M. J. Lance, and D. Assanis, 2013, “CFD analysis of particle transport in axi-symmetric tube flows under the influence of thermophoretic force,” *Int J Heat Mass Tran*, Vol. 61, pp. 94–105.

Lance, M. J., C. S. Sluder, H. Wang, and J. M. E. Storey, 2009, “Direct measurement of EGR cooler deposit thermal properties for improved understanding of cooler fouling,” in *SAE International*.

Lance, M. J., C. S. Sluder, S. Lewis, and J. M. E. Storey, 2010, "Characterization of field-aged EGR cooler deposits," *SAE Int. J. Engines*, Vol. 3, No. 2, pp. 126–136.

Lance, M. J., J. M. E. Storey, C. S. Sluder, H. Meyer III, B. Watkins, M. Kaiser, and P. Ayyappan, 2013, "Microstructural analysis of deposits on heavy-duty EGR coolers," in *SAE International*.

Lance, M. J., H. Bilheux, J.-C. Bilheux, S. Voisin, C. S. Sluder, and J. Stevenson, 2014, "Neutron tomography of exhaust gas recirculation cooler deposits," in *SAE International*.

Sluder, C. S., J. M. E. Storey, and M. J. Lance, 2014, "Effectiveness stabilization and plugging in EGR cooler fouling," in *SAE International*.

(This page intentionally left blank)

II. Lightweight Materials

II.1 Automotive Metals

II.1.A Advancing Properties, Processes, and Enabling Tools for Lightweight Metals (Pacific Northwest National Laboratory)

Darrell Herling, Field Technical Monitor
Pacific Northwest National Laboratory
902 Battelle Blvd.
Richland, WA 99352
Phone: 509-375-6905
E-mail: darrell.herling@pnnl.gov

Will James, Technology Manager
E-mail: charles.james@ee.doe.gov

Start Date: October 1, 2014 End Date: September 30, 2018
Total Project Cost: $4,020,000 DOE share: $4,020,000 Non-DOE share: $0

Executive Summary

The Advancing Properties, Processes, and Enabling Tools for Lightweight Metals Project consists of four tasks that are focused on early-stage research in pursuit of advancing the basic mechanical properties, manufacturability, and addressing the affordability of lightweight materials. These tasks have the common goal to reduce the technical risk of implementing lightweight material systems and accelerating the adoption into the automotive market. The specific tasks include the following:

1. Enhancing Sheared-Edge Stretchability of Advanced High-Strength Steel/Ultra High-Strength Steel (AHSS/UHSS) through Integrated Manufacturing Process Simulations
2. Cost-Effective Magnesium Extrusion
3. Optimizing Heat-Treatment Parameters for Third Generation AHSS with High Throughput in-situ Experiments and Integrated Modeling Frameworks
4. Room Temperature Stamping of High-Strength Al Alloys

The following sections of this report outline the specific task work conducted at PNNL in the areas of predictive engineering, process development, and enabling technologies for lightweight metals and associated manufacturing processes. Each task supports one or more goals within the VTO mission of achieving better fuel-efficiency through lighter weight vehicle structures.

II.1.A.1 Enhancing Sheared-Edge Stretchability of Advanced High-Strength Steel/Ultra High-Strength Steel through Integrated Manufacturing Process Simulations

Kyoo Sil Choi, Principal Investigator
Pacific Northwest National Laboratory
902 Battelle Blvd.
Richland, WA 99352
Phone: 509-372-6967
E-mail: kyoosil.choi@pnnl.gov

Project Introduction

During cold-stamping of AHSS/UHSS parts, the most commonly observed failure mode is edge-splitting, and the sheared-edge stretchability appears to depend on a combination of factors including edge-stretching mode and edge-shearing/trimming conditions, as well as the initial sheet properties defined by microstructural characteristics and damage occurrence in the steel sheets. The contributions of these various factors to the material edge stretchability are not well understood due to the complex interactions of these factors during edge preparation and subsequent forming operations.

The edge damage caused by a piercing operation depends upon the microstructure of the material and the difference in the edge-stretching limit between different dual-phase (DP) steels of the same UTS level could be due to different levels of edge damage produced by the hole-piercing operation. But quantitative and predictive capabilities linking the microstructure characteristics to the sheared-edge stretchability under different loading modes (i.e., tensile stretching or hole-expansion) are not available. Moreover, the experimental data available from the open literature are typically only valid for the specific material under the specific combination of edge-preparation and stretching conditions due to the lack of fundamental understanding of microstructure effects on sheared-edge stretchability. There is a keen interest from the steel producers for more fundamental understandings on the key microstructure features influencing the macroscopic properties (i.e., tensile properties, hole-expansion ratio [HER], and localized formability of AHSS/UHSS) in the steel development process. On the other hand, there is an urgent need from automotive OEMs in obtaining a quantitative and predictive understanding on whether a specific type of macroscopic test result can be used to infer these steels' in die behaviors in their efforts to establish robust manufacturing processes for the new generations of AHSS/UHSS.

The purpose of this project is to enhance the sheared-edge stretchability of AHSS/UHSS by developing quantitative and predictive understandings of the microstructure effects on sheared-edge fracture and stretchability, hence accelerating the development of next generation advanced high-strength steels and enabling a rapid and cost-effective implementation of AHSS/UHSS in vehicle structures for substantial mass savings.

Accomplishments

- Examined the effects of microstructure features on the sheared-edge stretchability using two different DP980 steels (i.e., DP1, DP2):
  - Performed various mechanical tests and microstructural examinations with DP1 steel for its material characterization.
  - Performed hole-piercing/extrusion tests with the two steels for various cutting clearances.
  - Measured the edge characteristics along the circumferences of the pierced hole for the two steels.
  - Performed shearing and tensile edge stretchability tests with two steels for various cutting clearances.

- Validated and upgraded the computational models and schemes with the new experimental results for DP1 and DP2 steels:
    - Developed 3D one-stroke finite element (FE) model to simulate the hole-piercing/extrusion process.
    - Performed the submodeling simulations using the microstructure-based FE models to qualitatively examine the effects of microstructure features on the shearing-induced edge damage.
    - Estimated the phase fracture strain curves and the void volume fraction as a function of plastic-strain for the two steels using the microstructure-based FE models.
    - Performed parametric studies to find the key microstructure features influencing on the shearing-induced edge damage.

Technology Assessment

- Target: Enhance the sheared-edge stretchability of AHSS/UHSS by developing quantitative and predictive understandings of the microstructure effects on sheared-edge fracture and stretchability.
- Gap: The experimental data currently available from open literature are typically only valid for the specific material under the specific combination of edge preparation and stretching conditions due to the lack of fundamental understandings of the microstructure effects on sheared-edge stretchability.

Approach

In this project, a combined experimental and modeling approach has been adopted to develop a quantitative understanding and predictive capability on the effects of microstructure features on sheared-edge fracture and stretchability for AHSS/UHSS sheet steels with UTS of 980 MPa. We proposed to focus on two or three UHSS sheets with minimum UTS of 980 MPa (referred as DP980 hereafter) as our example material systems, but the overall approach should be extendable to other AHSS/UHSS grades.

For the experimental approach in FY 2017, hole extrusion tests were first performed for assessing the effects of different microstructure features (i.e., microstructure, constituent phase properties, etc.) on the sheared-edge stretchability. For this purpose, two different DP 980 steels (i.e., DP1 and DP2) were obtained from different suppliers. Various experiments (e.g., the tensile test, high-energy X-ray diffraction [HEXRD] test, etc.) were subsequently performed with these materials for material characterization. Tensile stretchability tests were also performed with these steels to assess the effects of microstructure features and cutting clearance on the edge stretchability of their sheared samples. For the modeling approach, two different modeling methods have been adopted in order to simulate the processes of the hole-piercing/extrusion test and tensile stretchability test. The computational models for hole-piercing/extrusion are being upgraded with fine calibration to match the experimental observations on the hole extrusion tests. For the modeling of the tensile stretchability test, the computational scheme previously developed in FY 2016 has been under a validation process against the new experimental data with DP1 and DP2 steels.

Technology Transfer Path

Technology transfer of this project will be directly through Ford Motor Company and their Tier 1 suppliers. The broader commercialization of the technology through the Tier 1 suppliers will reach the entire automotive OEM industry. We also plan to present and publish our findings as a Society of Automotive Engineers Technical Paper and/or in other engineering journals to further disseminate our research results.

Results

Two DP980 steels from different suppliers (i.e., DP1 and DP2) were used to examine the effects of different microstructure features on the performance in the hole extrusion test and tensile stretchability test. Figure II.1.A.1.1(a) and Figure II.1.A.1.1(b) compare the SEM images for microstructures of the two steels. As shown in the two images, the microstructures are quite different, especially in terms of grain size (i.e., ~10 µm vs. ~5 µm), although they appear to have similar martensite volume fractions. These two steels show similar UTS levels (i.e., ~1000 MPa), as shown in Figure II.1.A.1.1(c); however, their uniform elongations and total elongations are different due to their varied microstructure features.

Figure II.1.A.1.2 compares the large-strain flow stresses and constituent-phase properties between the two DP980 steels. Here, the large-strain flow stresses were obtained from the accumulated rolling and tension tests and constituent-phase properties were estimated from the HEXRD test with an Elasto-Plastic Self-Consistent (EPSC) model (Hu et al. 2016). Similar to Figure II.1.A.1.1(c), the large-strain flow stresses of the two steels are also similar to each other as compared in Figure II.1.A.1.2(a) and Figure II.1.A.1.2(c), although the DP1 steel shows a slightly lower strength level. Note here that these large-strain flow stresses are used as the input properties in the macro-shearing model in this study. In Figure II.1.A.1.2(b) and Figure II.1.A.1.2(d), the DP1 steel shows less strength disparity between the two phases than the DP2 steel, which is probably due to their different chemical compositions and heat treatments during the manufacturing process.

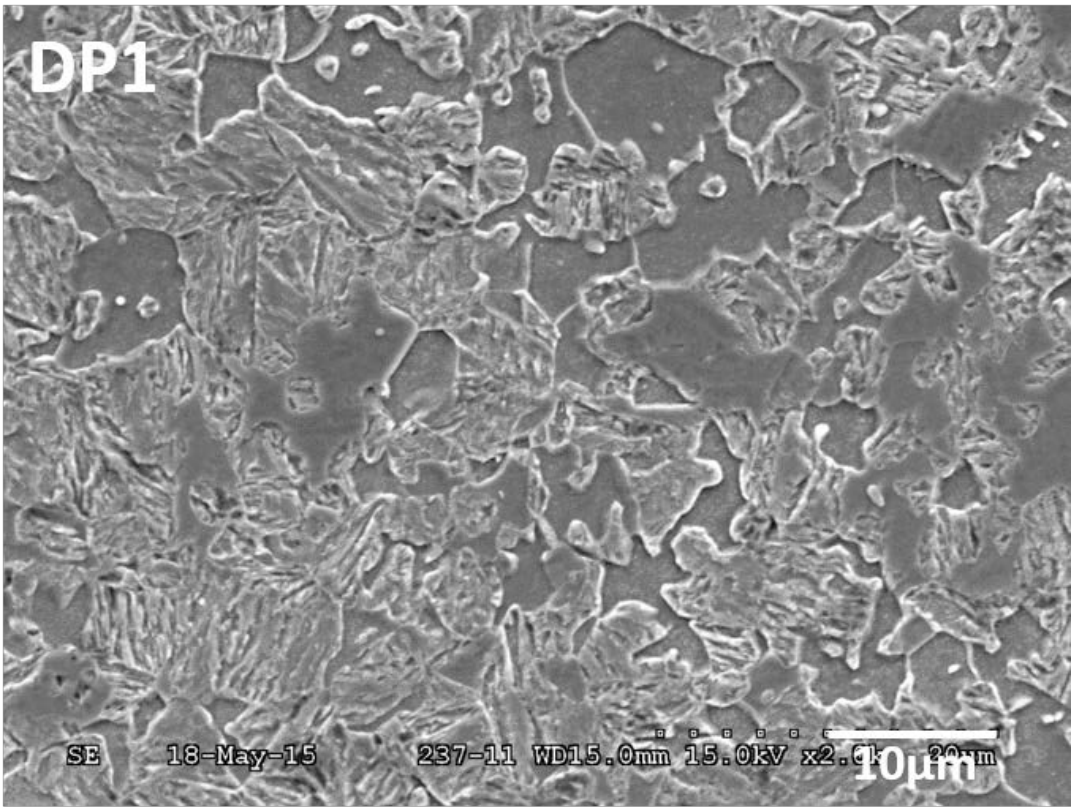

(a)

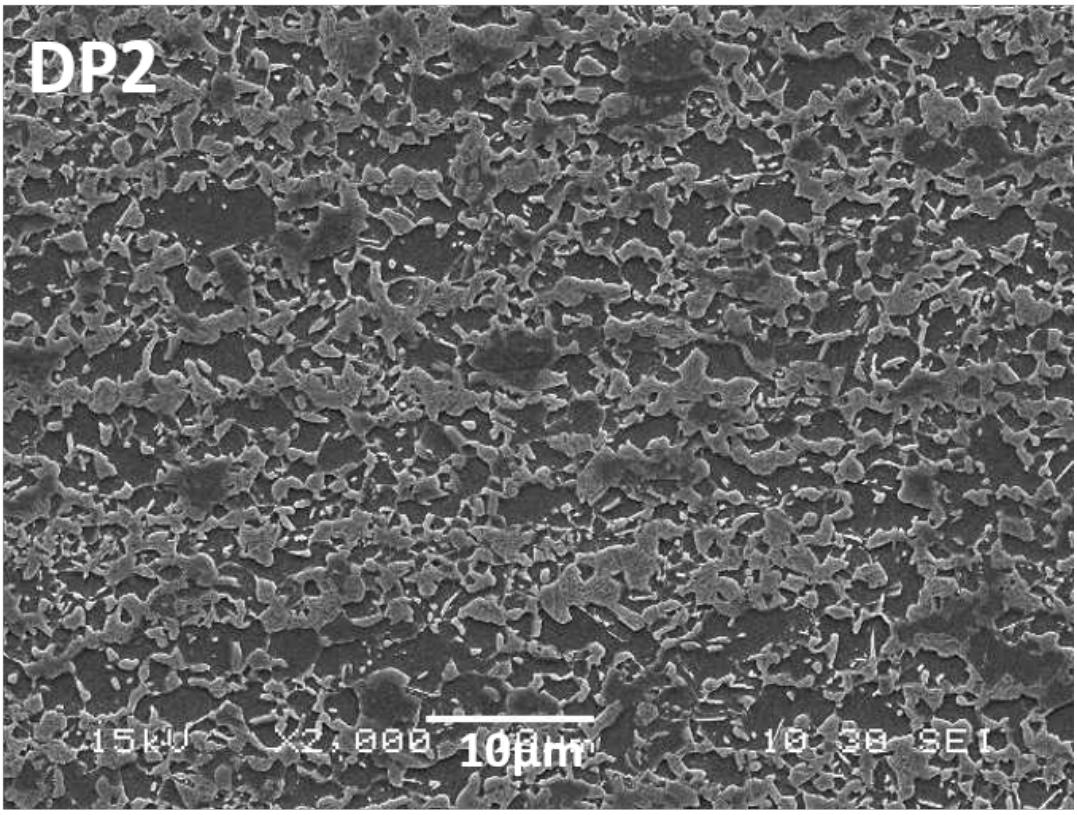

(b)

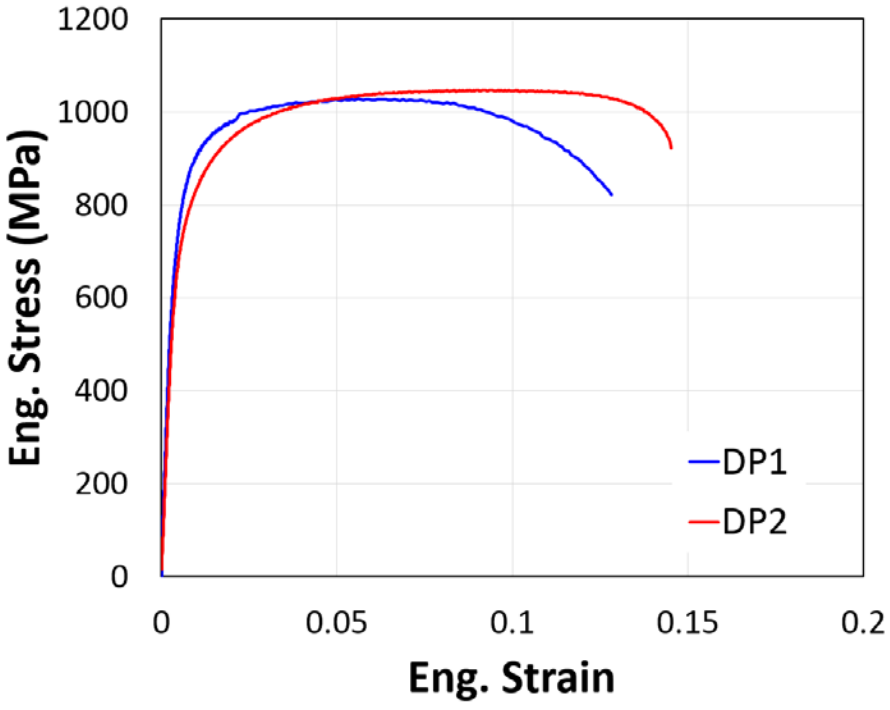

(c)

Figure II.1.A.1.1. SEM micrograph of (a) DP1 and (b) DP2 steels. (c) Stress-strain curves for the two DP980 steels. Source: PNNL.

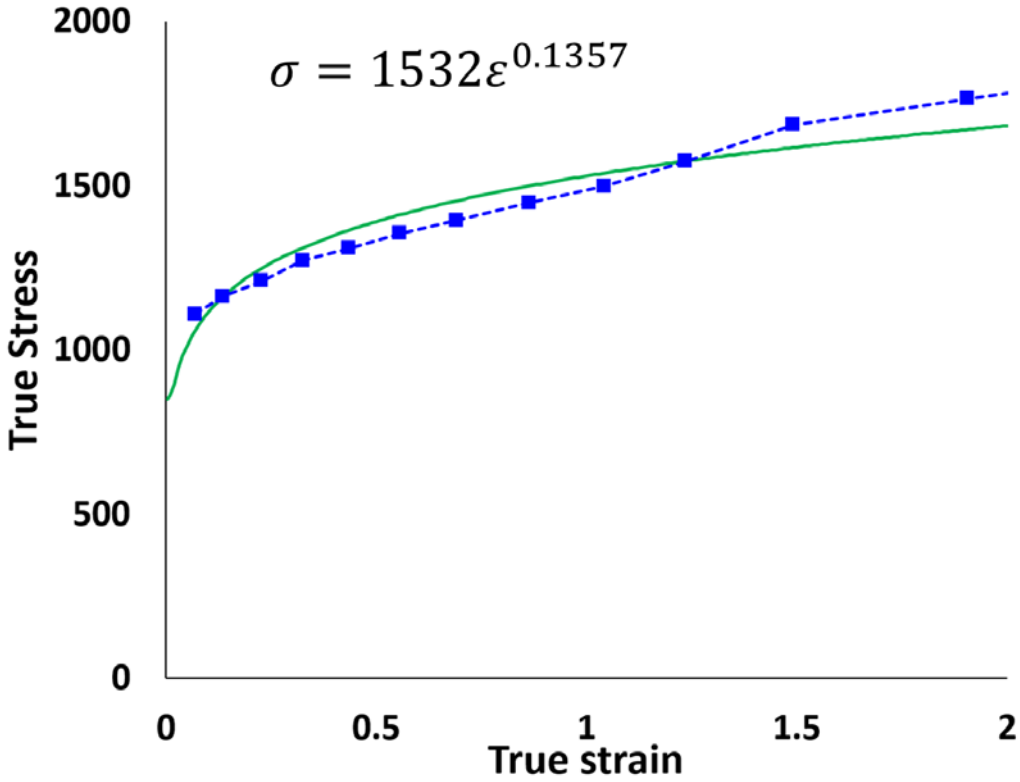
$\sigma = 1532\varepsilon^{0.1357}$
True Stress
True strain
2000
1500
1000
500
0
0
0.5
1
1.5
2

(a)

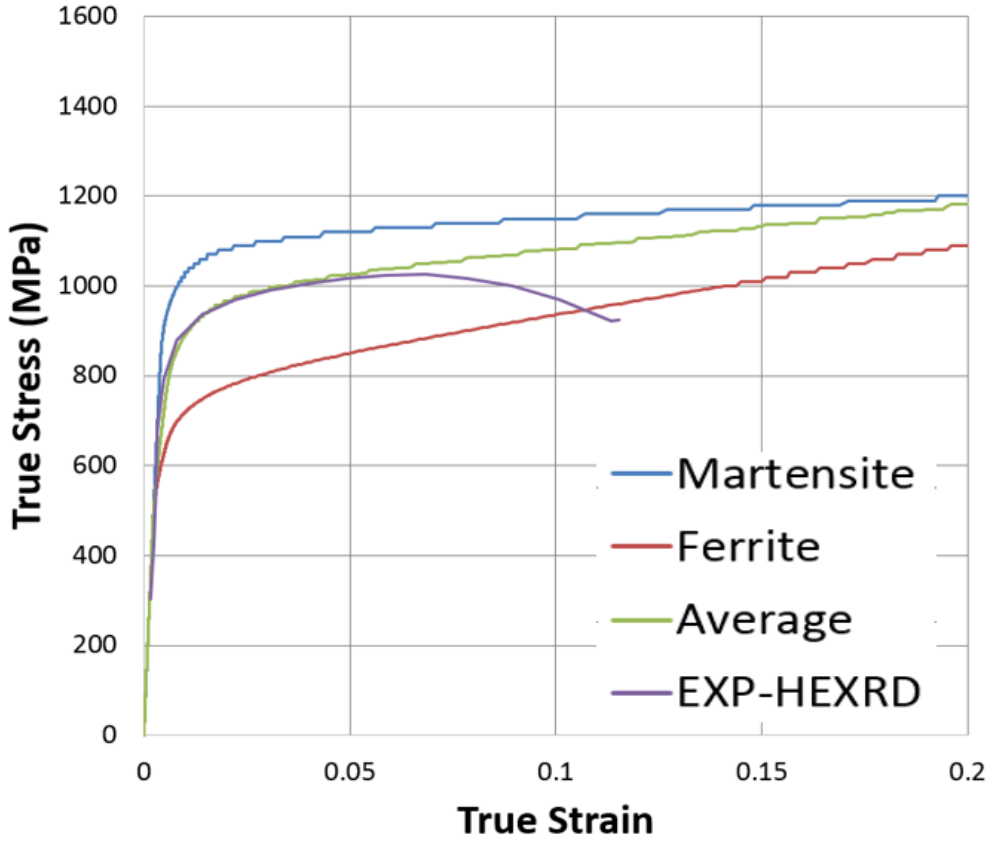
True Stress (MPa)
True Strain
1600
1400
1200
1000
800
600
400
200
0
0
0.05
0.1
0.15
0.2
Martensite
Ferrite
Average
EXP-HEXRD

(b)

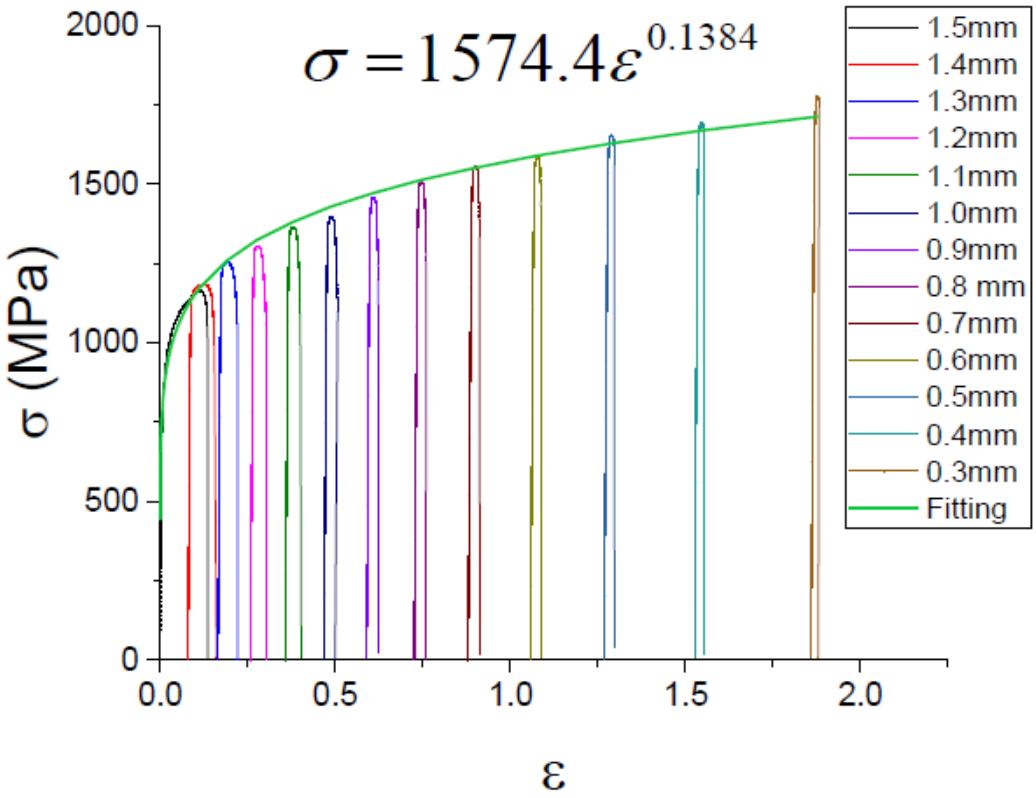

(c)

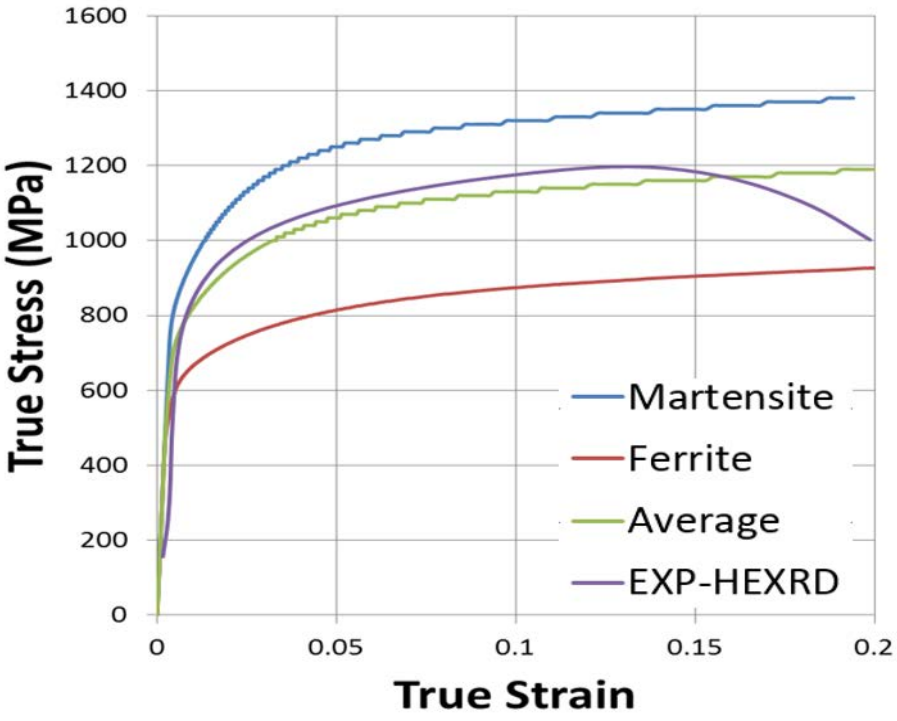

(d)

Figure II.1.A.1.2. Flow stresses at large strain and individual phase properties of (a) and (b) DP1 and (c) and (d) DP2 steels. Source: PNNL.

Hole extrusion tests with a 10-mm diameter hole were performed for the DP1 and DP2 steels. In the tests, a conical die extrudes the pierced blank with the burr away from the punch until a through-thickness crack is observed. HER is then defined as the percentage change in the diameter of the pierced hole. The width of each individual split along the fractured perimeter was measured and excluded from the overall length of the fractured perimeter to provide the information of HER at which the fracture just started. Note that the broad range of cutting clearance was adopted in the test to reflect more realistic cutting conditions. Figure II.1.A.1.3 compares the HER between the two steels. As shown in Figure II.1.A.1.3(b) and Figure II.1.A.1.3(c), the DP1 steel shows much higher HER compared to the DP2 steel. The higher HER with DP1 may be due to the lower strength disparity between the constituent phases as shown in Figure II.1.A.1.2. Lower phase-strength disparity may contribute to less shearing-induced edge damage (e.g., cracking, void) during the punching process.

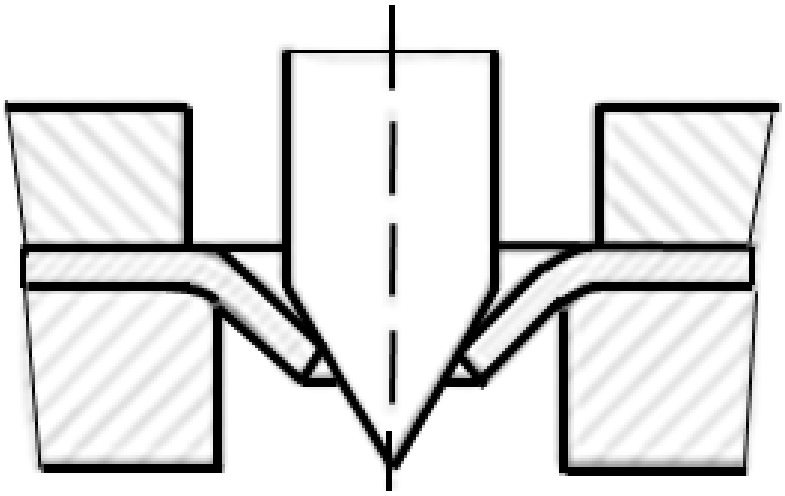

(a)

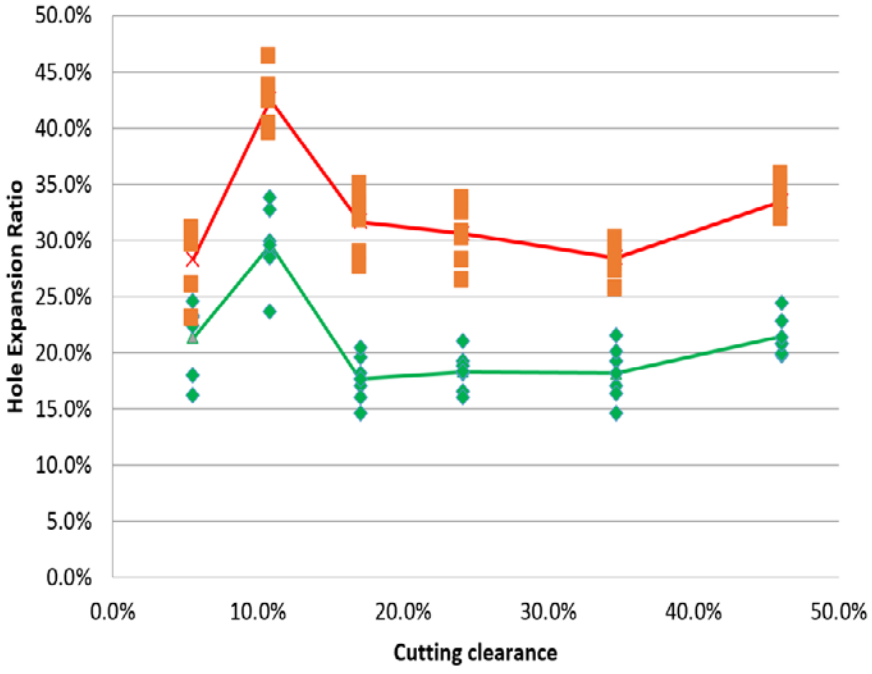

(b)

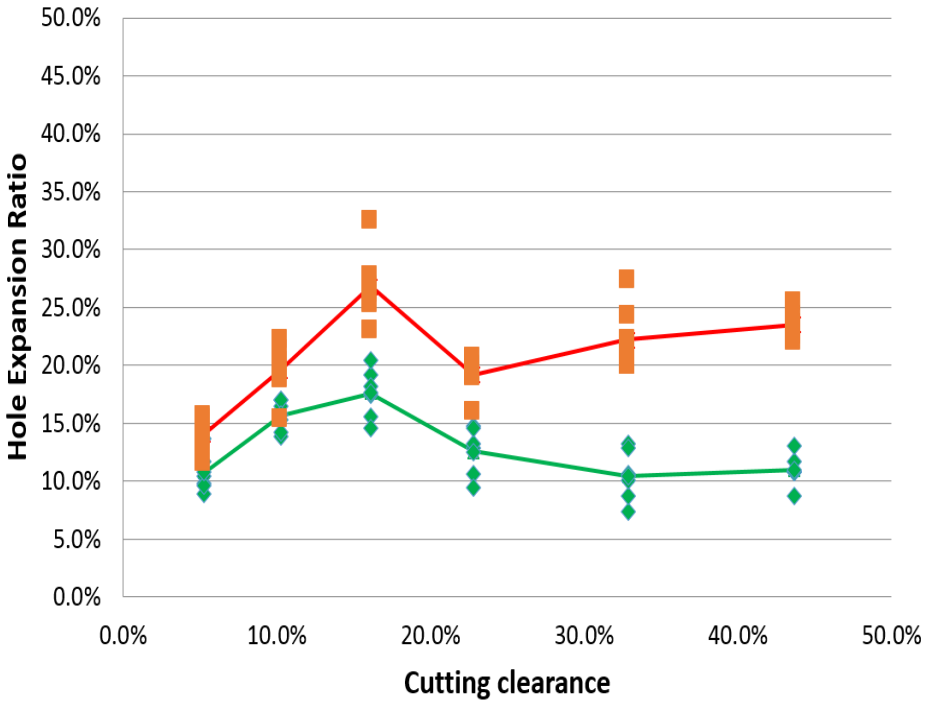

(c)

Figure II.1.A.1.3. (a) Schematics of the hole extrusion test. HER for various cutting clearances for (b) DP1 and (c) DP2 steels. (Orange symbols and red lines drawn through the average values represent HER in the fracture zone. Green symbols and a green line drawn through the average values represent HER around the blank where no fracture was observed.) Source: PNNL.

Before the hole extrusion test, the edge characteristics (i.e., the sizes of rollover, burnish, fracture, and burr) were also measured at eight different locations along the punched hole circumference for different cutting clearances in order to examine the effects of edge characteristics on the HER. Figure II.1.A.1.4(a) shows the eight locations selected for measuring the edge characteristics, while Figure II.1.A.1.4(b) shows the photographs taken for the eight locations of a punched hole. It is observed in Figure II.1.A.1.4(b) that the edge characteristics are varied along the hole circumference. Specifically, Figure II.1.A.1.4(c) and Figure II.1.A.1.4(d) show the examples of burr height variation along the hole circumference, obtained from the edge characteristics measurement and 3D microscope, respectively. The results here indicate the cutting clearance may not be uniform along the circumference of these small diameter holes and a slight off-center punching may have occurred during the punching process.

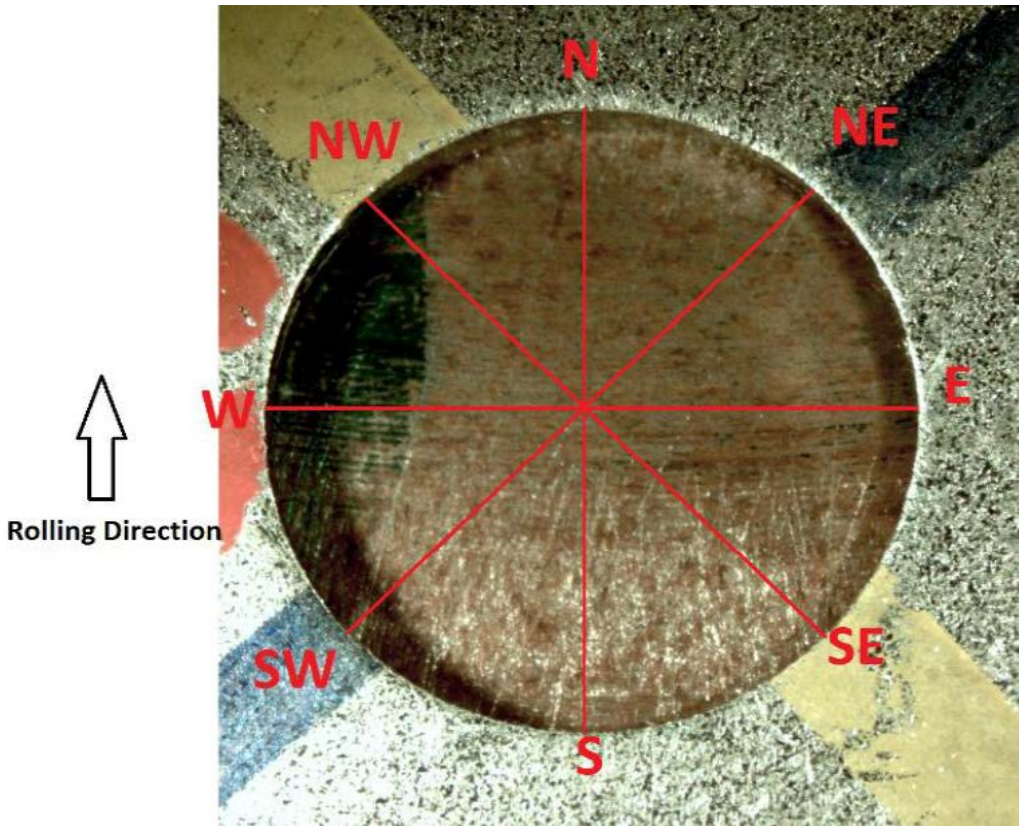

(a)

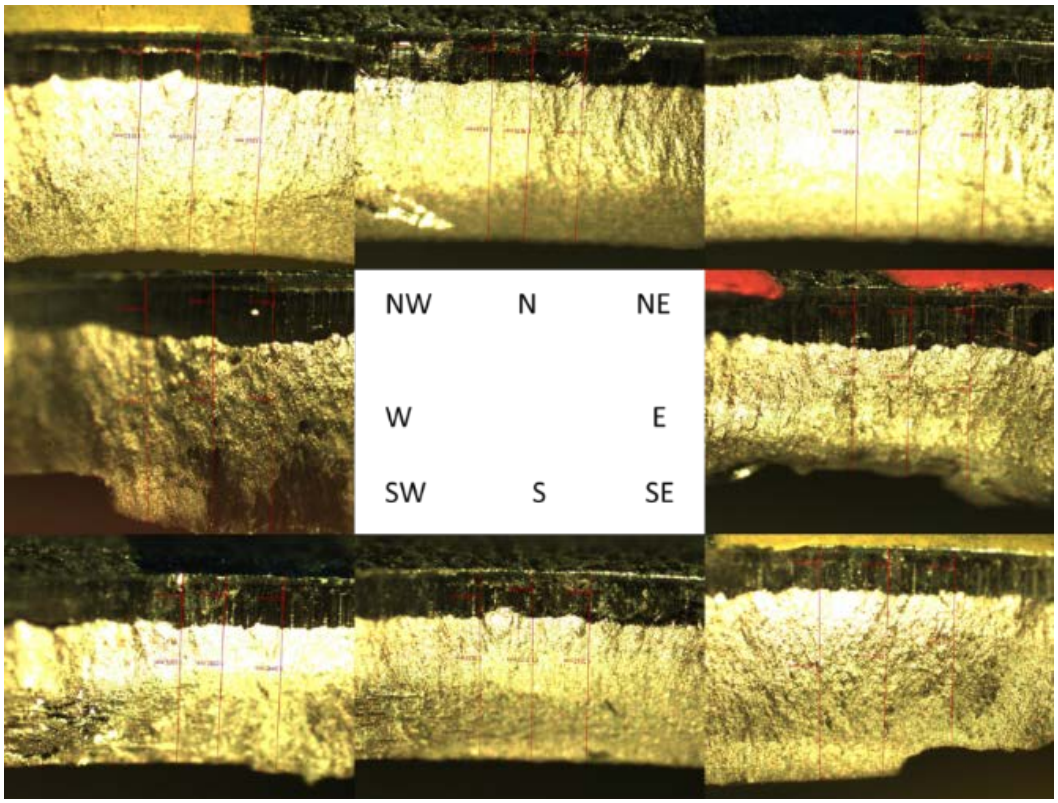

(b)

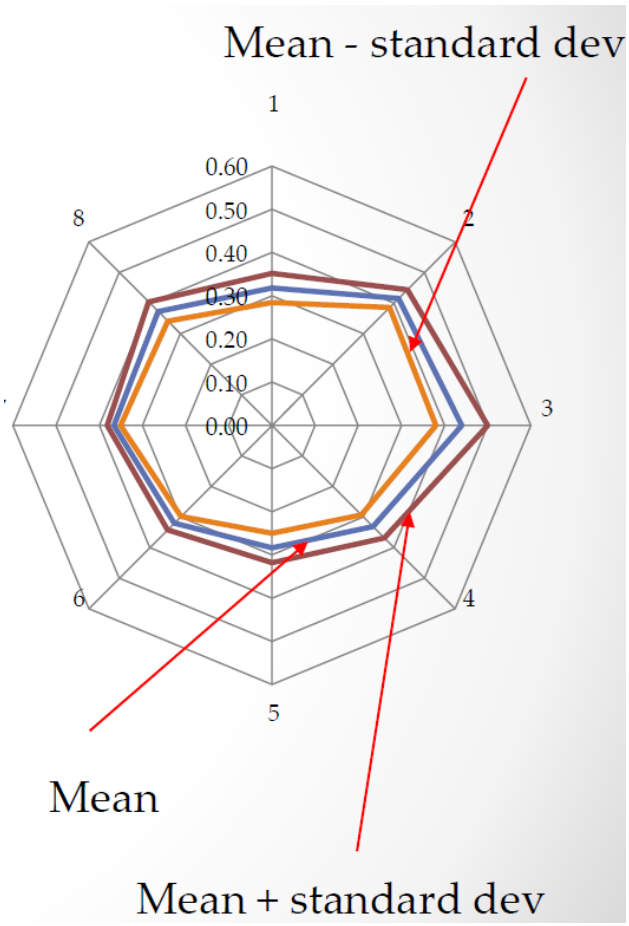

(c)

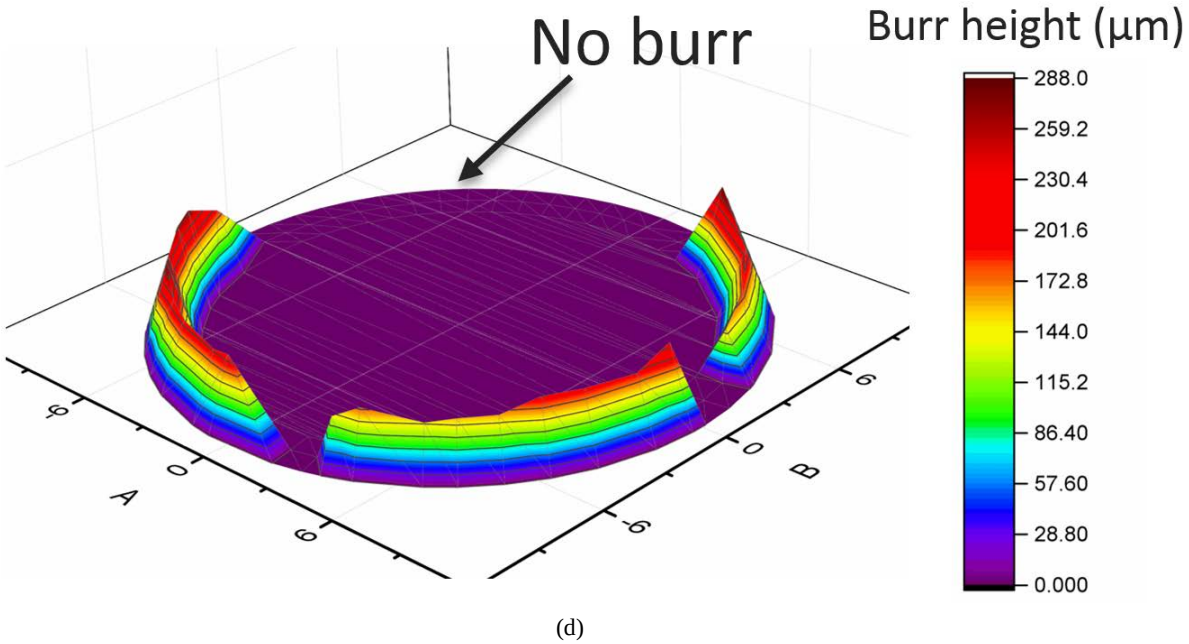

(d)

Figure II.1.A.1.4. (a) Eight locations along the hole circumference selected for measuring the edge characteristics, (b) example photographs of the sheared edges at the eight locations, (c) burr height measurement at the eight locations, and (d) burr height variation along the hole circumference detected using a 3D microscope. Source: PNNL.

Figure II.1.A.1.5 shows the measured edge characteristics for different cutting clearances, obtained by averaging all of the eight locations of the punched holes. Interestingly, Figure II.1.A.1.5(c) shows that the burr may not be observed for cutting clearances, approximately between ~10% and ~20% for both steels. These cutting clearances are consistent with those showing the highest HER for the two steels as shown in Figure II.1.A.1.3(b) and Figure II.1.A.1.3(c). Note that for the 5% cutting clearance, a substantial-sized burr was observed along some portion of the hole circumference possibly due to off-center punching effects. The existence of a burr from this off-center punching appears to have contributed to decrease the HER, even for this lowest cutting clearance. The results here indicate that the existence of a burr, even along a small portion of the hole circumference, may be detrimental to the HER.

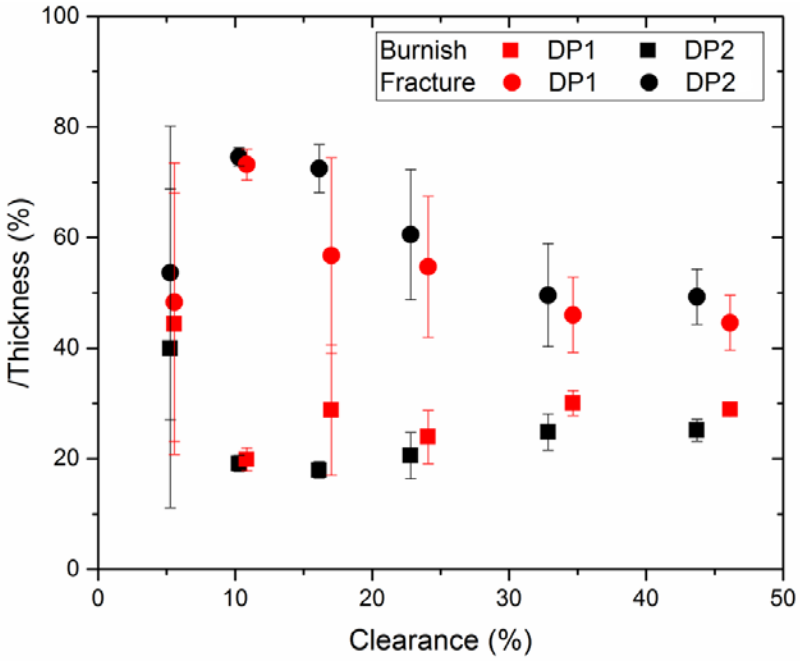

(a)

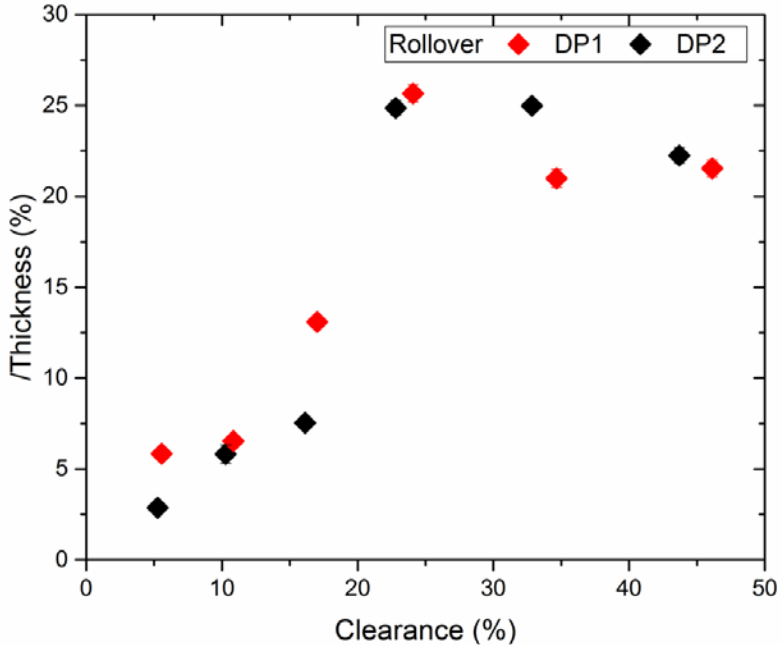

(b)

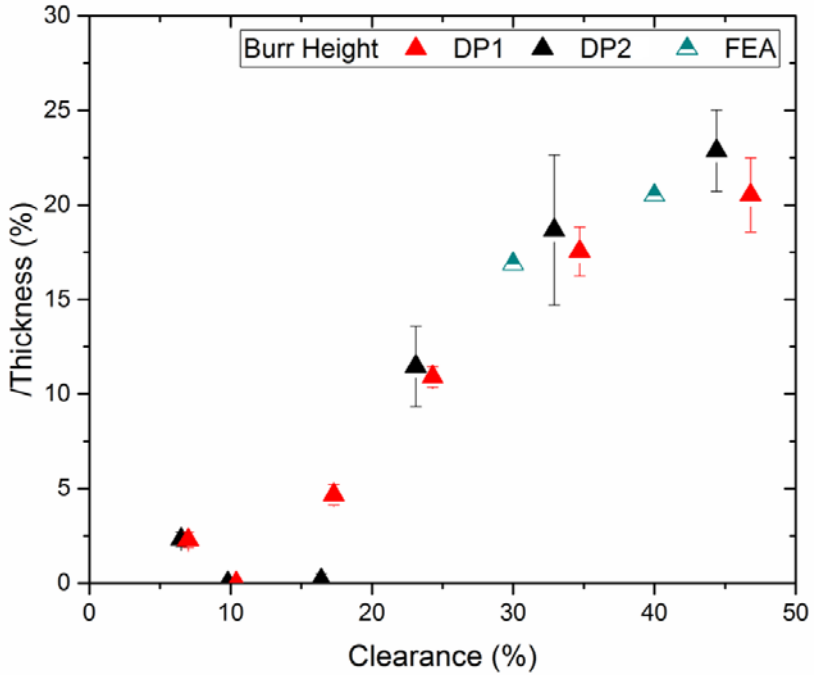

(c)

Figure II.1.A.1.5. Measured edge characteristics: (a) Burnish and fracture zones, (b) rollover zone, and (c) burr height for various cutting clearances for DP1 and DP2 steels. Source: PNNL.

In order to consider the effects of off-center punching during the hole-piercing/extrusion test, a 3D one-stroke FE model was generated, as is shown in Figure II.1.A.1.6(a). Figure II.1.A.1.6(b) shows an example of simulation results for off-center punching and extrusion for 20% cutting clearance, while Figure II.1.A.1.6(c) shows preliminary results on the effects of off-center punching on the HER for different cutting clearances. As is also shown in Figure II.1.A.1.6(c), the off-center punching may significantly decrease the HER compared to the center punching (i.e., blue symbol vs. red symbol). The computational method for hole-piercing/extrusion is being further upgraded and refined with consideration of more factors to match the experimental data from the hole extrusion test (i.e., the black symbols in Figure II.1.A.1.6(c)). For example, the Gurson model for porous material may be adopted in the one-stroke simulation to consider the piercing-induced voids near the hole edge. A two-step computational scheme, as in the tensile stretchability modeling, can also be under consideration.

A tensile stretchability test was also performed with the DP1 and DP2 steels. Figure II.1.A.1.7(a) shows the schematics of the conventional shearing process, while Figure II.1.A.1.7(b) shows three different in-plane failure modes usually observed from DP steels (Golovashchenko 2008). Depending on the distance of the grid from the fracture, the measured local strains may be classified as fractured, safe, and outside necking (Le et al. 2014). Figure II.1.A.1.7(c) and Figure II.1.A.1.7(d) show the tensile stretchability for the two steels in the form of major strain as a function of cutting clearance. Here, the lower boundary of all fractured data points may represent the fracture limit (red line) and the upper boundary of all safe data points may represent the safe forming limit (green line). As shown in Figure II.1.A.1.7(c) and Figure II.1.A.1.7(d), DP1 steels usually show good tensile stretchability for a wide variety of clearances as the splitting from the sheared edge occurs during the necking stage of the tensile test. DP2 steels exhibit substantially different behavior such that the visible effect of the cutting clearance was seen for the cutting clearances starting from 20%. By further increasing the clearance, a more substantial reduction in fractured and safe strains occurred. DP2 steels appear to have more shearing-induced edge damage (e.g., crack, voids).

As the shearing-induced edge damage, especially cracks and voids, can have dominant effects on the subsequent edge stretchability, those damages need to be considered in the modeling of edge stretchability prediction. A computational scheme was developed in FY 2016 with consideration of the effects of shearing-induced voids on the tensile edge stretchability. In FY 2017, this computational scheme has been under validation against the new experimental data with DP1 and DP2 steels. Figure II.1.A.1.8(a) and Figure II.1.A.1.8(b) show the macroscopic/phase stress-strain curves and fracture strain curves used in this modeling method for the two steels. Here, the stress-strain curves in Figure II.1.A.1.8(a) are based on the experimental data presented in Figure II.1.A.1.2, and the macroscopic fracture strain curves in Figure II.1.A.1.8(a) were determined by comparing the sheared edge shapes between the experiments and two-dimensional (2D) shearing simulations (Hu et al. 2014). Note that the phase fracture strain curves in Figure II.1.A.1.8(b) were estimated based on the microstructure-based FE simulations such that they result in the macroscopic fracture strain curves when they are employed in the microstructure-based FE models. Figure II.1.A.1.8(c) shows the concept about submodeling simulation using microstructure-based FE models for prediction of shearing-induced cracks and voids. As shown in the figure, some major internal cracks are observed from the submodels representing highly deformed regions. In general, more cracks were observed in DP2 models than in DP1 models. Various aspects were examined using submodeling simulations. The results from these examinations showed that the phase strength disparity might have primary effects on the number of shearing-induced cracks. Note that the submodeling approach can only be used to understand the qualitative effects of microstructure features on shearing-induced cracks as the simulations results highly depend on the adopted microstructures and boundary conditions.

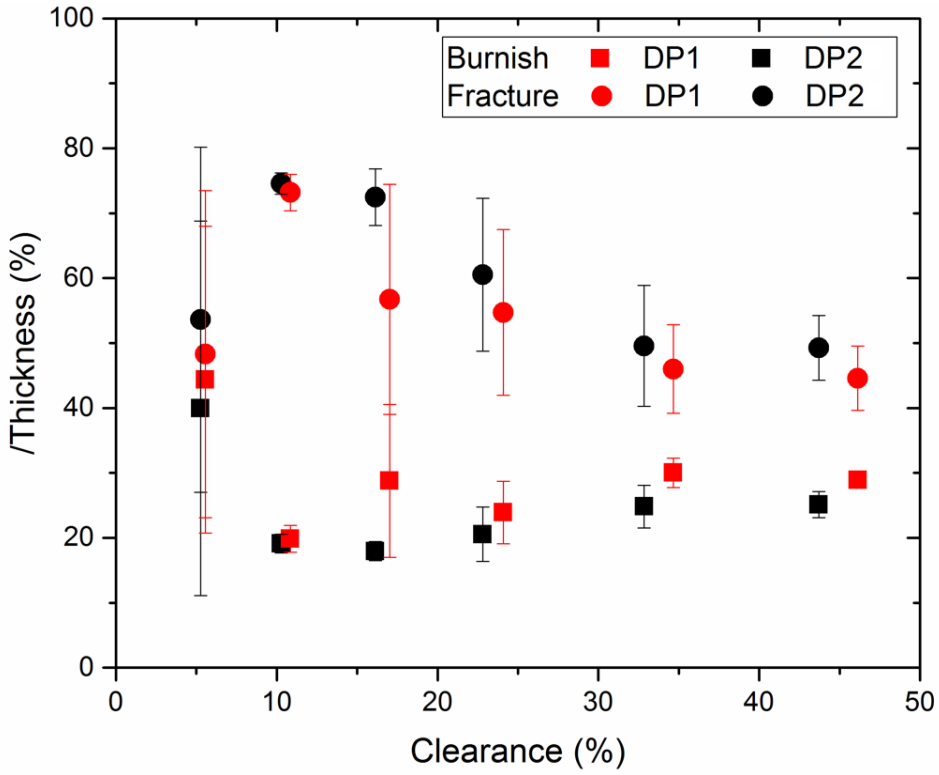

(a)

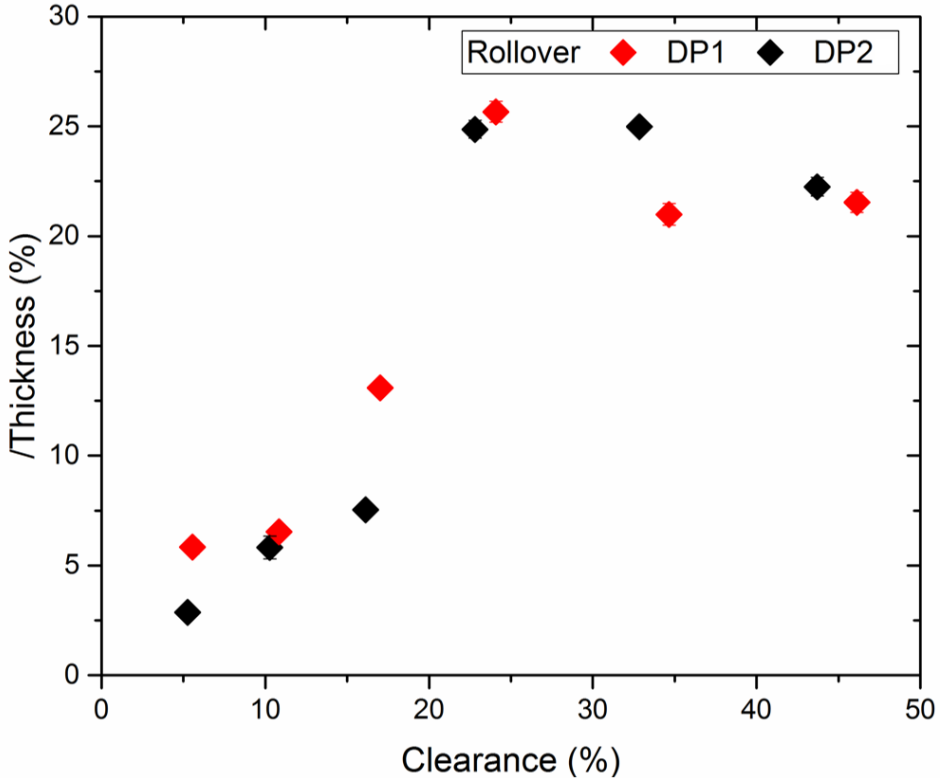

(b)

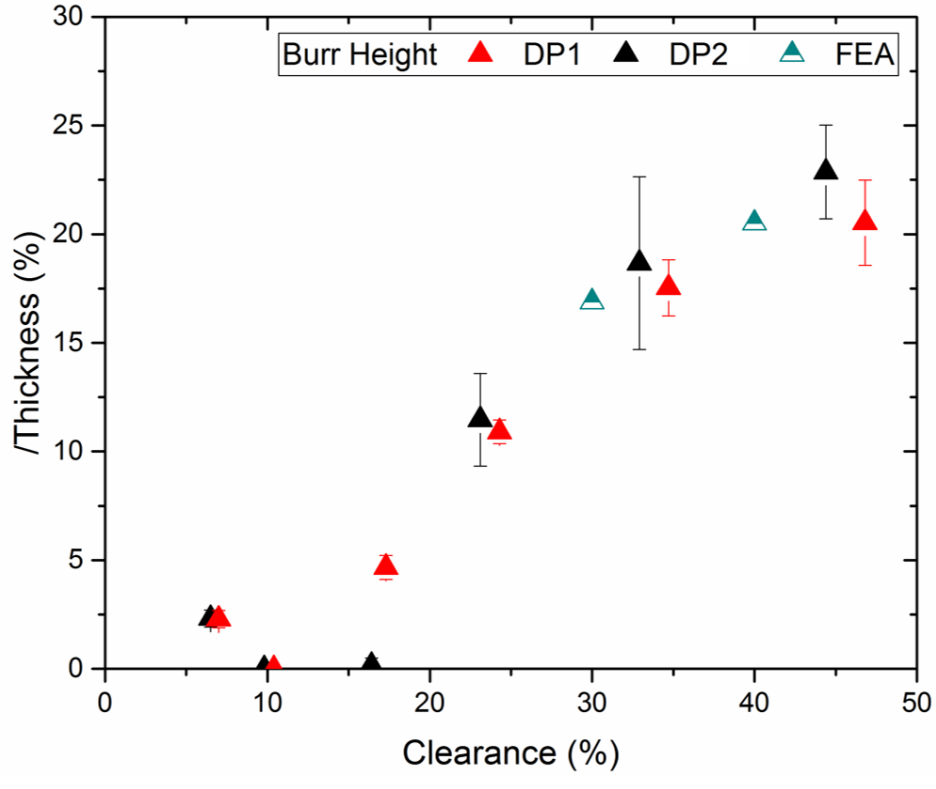

(c)

Figure II.1.A.1.6. (a) 3D one-stroke FE model for hole-piercing/extrusion simulation, (b) an example of simulation result for off-center punching, and (c) preliminary examination on the effects of off-center punching on HER. Source: PNNL.

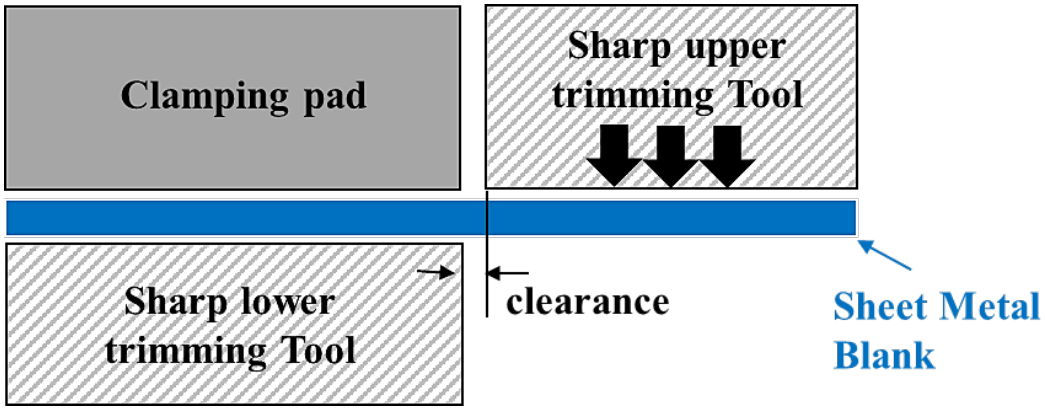
Clamping pad
Sharp upper trimming Tool
Sharp lower trimming Tool
clearance
Sheet Metal Blank

(a)

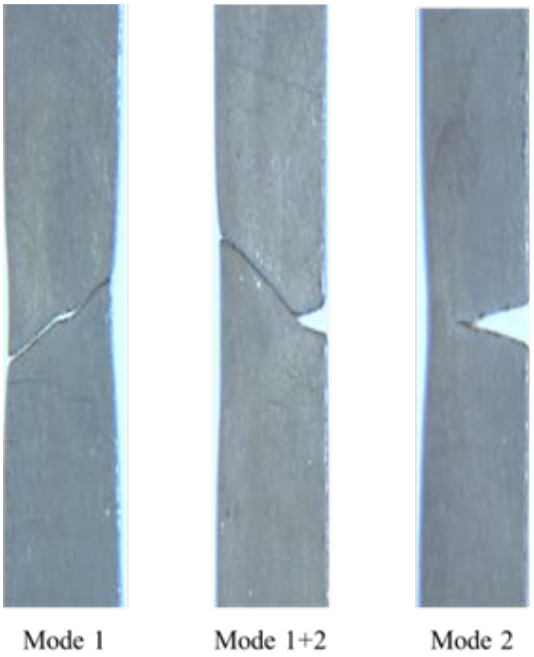
Mode 1
Mode 1+2
Mode 2

(b)

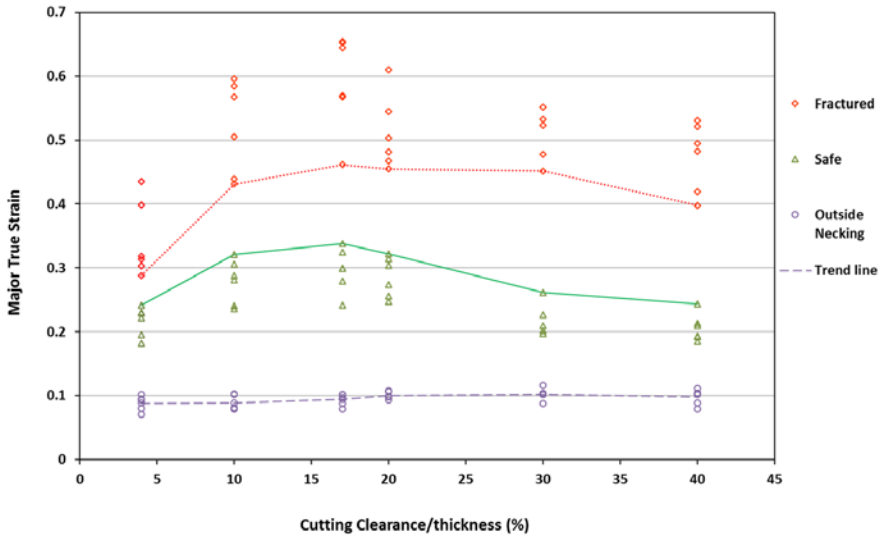
Major True Strain
Cutting Clearance/thickness (%)
Fractured
Safe
Outside Necking
Trend line
0
0.1
0.2
0.3
0.4
0.5
0.6
0.7
0
5
10
15
20
25
30
35
40
45

(c)

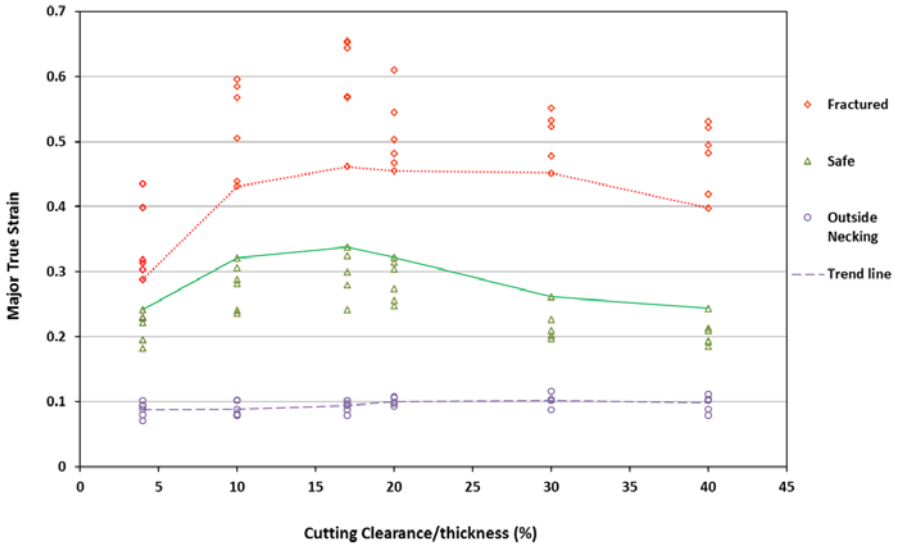

(d)

Figure II.1.A.1.7. (a) Schematics of the conventional shearing process, (b) failure modes under tension of sheared samples. Tensile stretchability for the sheared (c) DP1 and (d) DP2 steels as a function of cutting clearance. Source: PNNL.

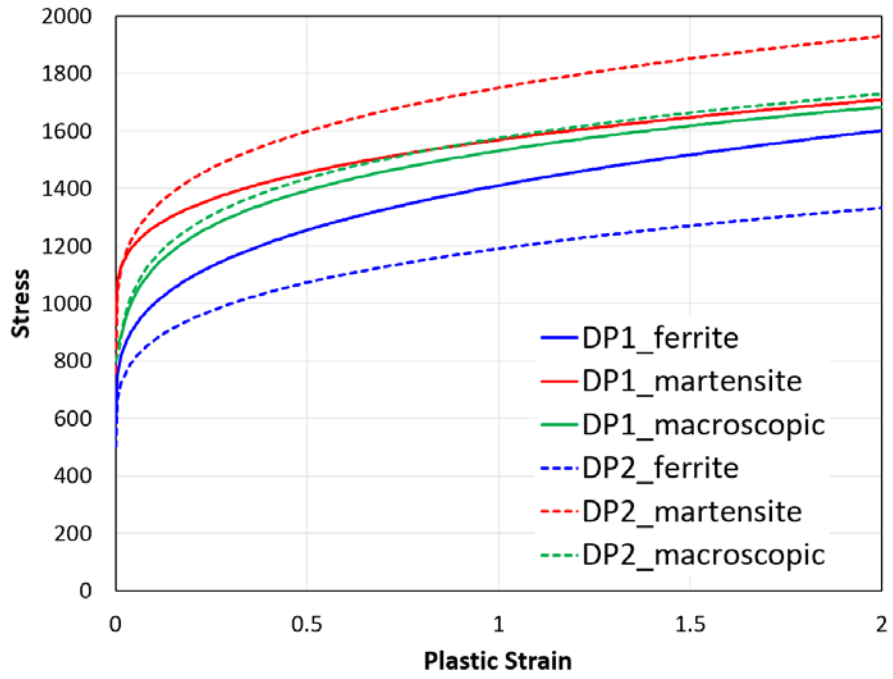
2000
1800
1600
1400
1200
1000
800
600
400
200
0
Stress
0
0.5
1
1.5
2
Plastic Strain
DP1_ferrite
DP1_martensite
DP1_macroscopic
DP2_ferrite
DP2_martensite
DP2_macroscopic

(a)

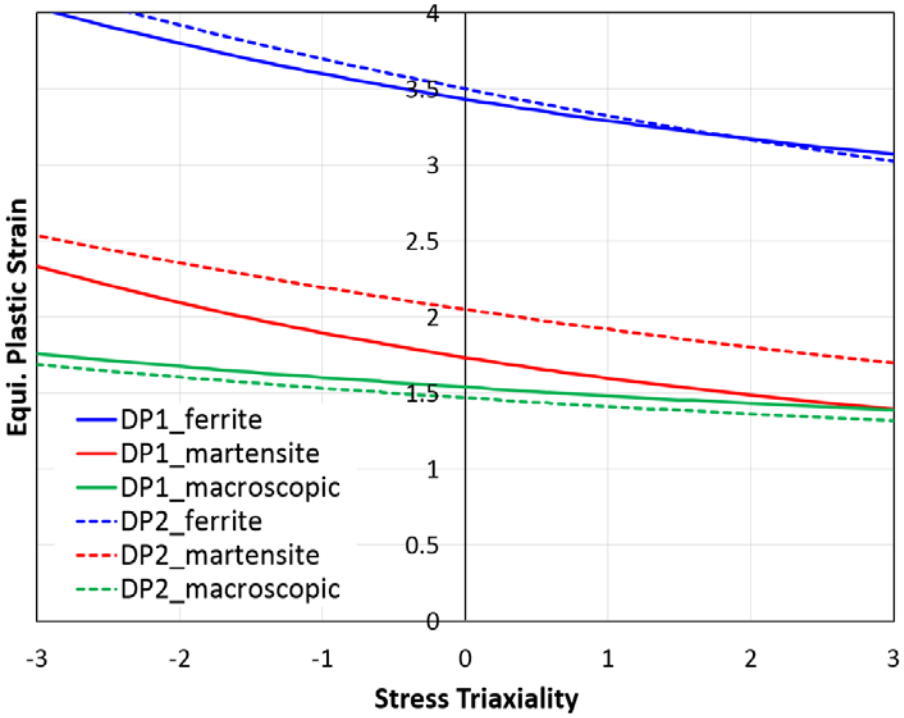
4
3.5
3
2.5
2
1.5
1
0.5
0
Equi. Plastic Strain
-3
-2
-1
0
1
2
3
Stress Triaxiality
DP1_ferrite
DP1_martensite
DP1_macroscopic
DP2_ferrite
DP2_martensite
DP2_macroscopic

(b)

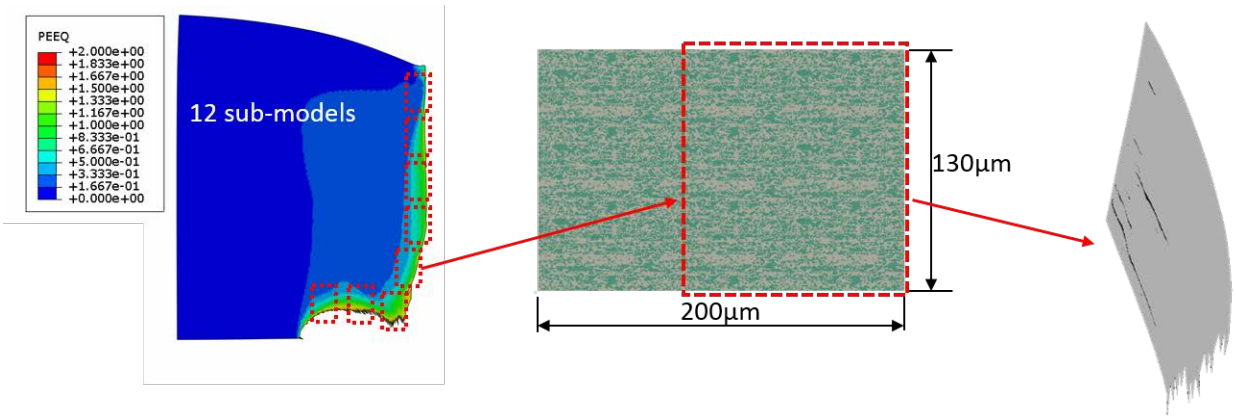

(c)

Figure II.1.A.1.8. (a) Phase stress-strain curves and (b) phase fracture-strain curves used in the microstructure-based FE model for DP1 and DP2 steels. (c) Example of submodeling simulation using microstructure-based FE models for predicting the shearing-induced internal cracking/void. Source: PNNL.

In order to obtain the quantitative information on the shearing-induced damage, a different approach was developed using microstructure-based FE models, as shown in Figure II.1.A.1.9(a) and Figure II.1.A.1.9(b). Note that the size of the microstructure-based FE models is the same as that of the element size of the two-dimensional macro-shearing model. The evolutions of void volume fraction as a function of equivalent plastic-strain of the model under tensile and compressive-loading conditions were estimated for DP1 and DP2 steels, as shown in Figure II.1.A.1.9(c). The curves in Figure II.1.A.1.9(c) can be used as a baseline in estimating the amount of shearing-induced voids near the edge. It is also observed in Figure II.1.A.1.9(c) that DP2 can have more voids than DP1 for the same deformation levels. Further parametric studies with this approach also showed that the phase-strength disparity could be a primary factor in determining the amount of shearing-induced voids.

3D tensile stretchability models were generated with consideration of shearing-induced damage. For example, Figure II.1.A.1.10(a) and Figure II.1.A.1.10(b) show a 3D tensile stretchability model for DP2 with 40% cutting clearance, where some shearing-induced plastic-strain and voids were incorporated based on the results of a two-dimensional macro-shearing simulation. Note that the amount of damage was varied along the length of the tensile sample to consider the microstructural inhomogeneity. Further parameters (i.e., the fracture strain curve, initial/critical void growth for 3D model, etc.) need to be determined to perform the simulations. With determination of those parameters, simulation results as shown in Figure II.1.A.1.10(c) and Figure II.1.A.1.10(d) will be obtained, and the effects of shearing-induced damage will then be assessed. This task is currently underway.

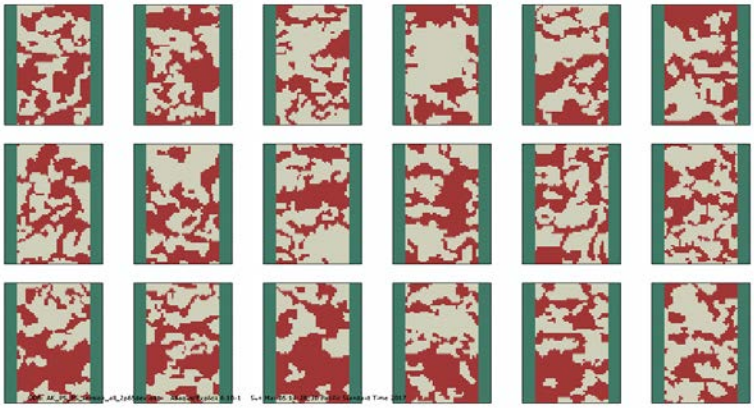

(a)

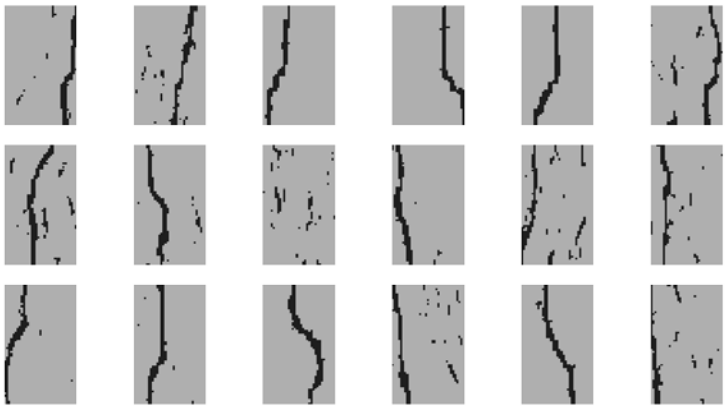

(b)

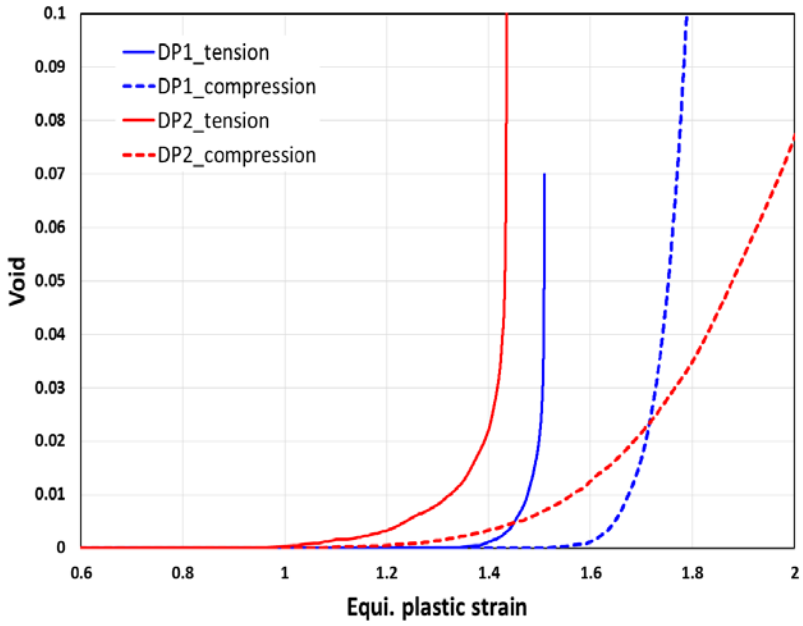

(c)

Figure II.1.A.1.9. (a) Microstructure-based FE models used for estimating the evolution of void volume fraction as a function of equivalent plastic-strain of the model, (b) example of crack/void distributions (i.e., black-colored region) within the models at a certain stage under tensile loading, and (c) estimated void volume fraction evolution as a function of equivalent plastic-strain under compressive and tensile loadings for DP1 and DP2 steels. Source: PNNL.

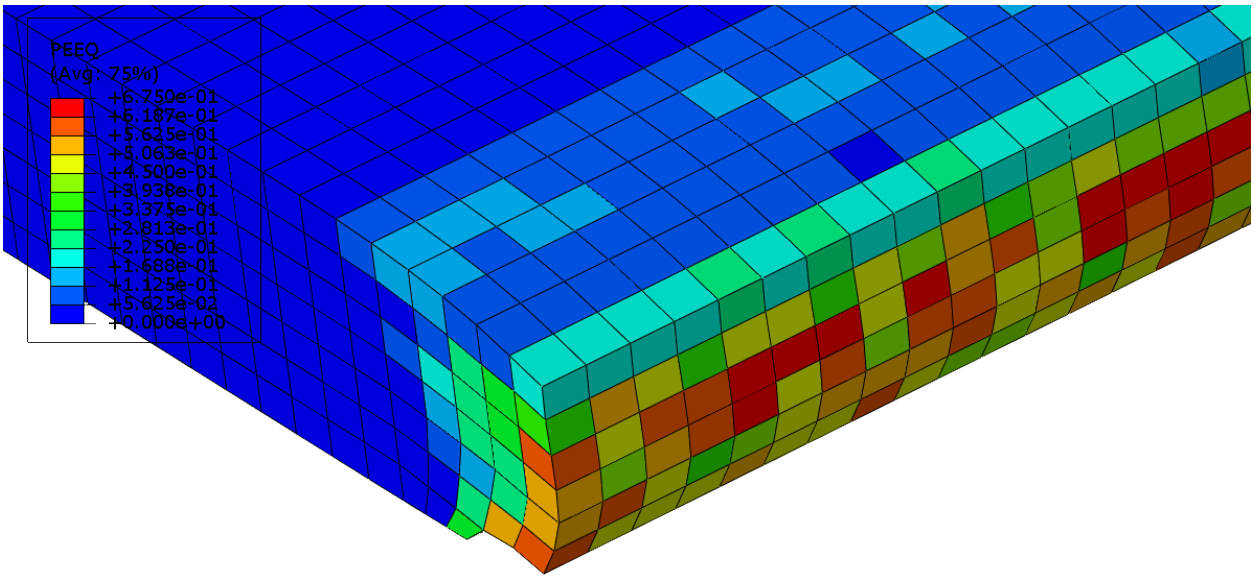
PEEQ
(Avg: 75%)
+6.750e-01
+6.187e-01
+5.625e-01
+5.063e-01
+4.500e-01
+3.938e-01
+3.375e-01
+2.813e-01
+2.250e-01
+1.688e-01
+1.125e-01
+5.625e-02
+0.000e+00

(a)

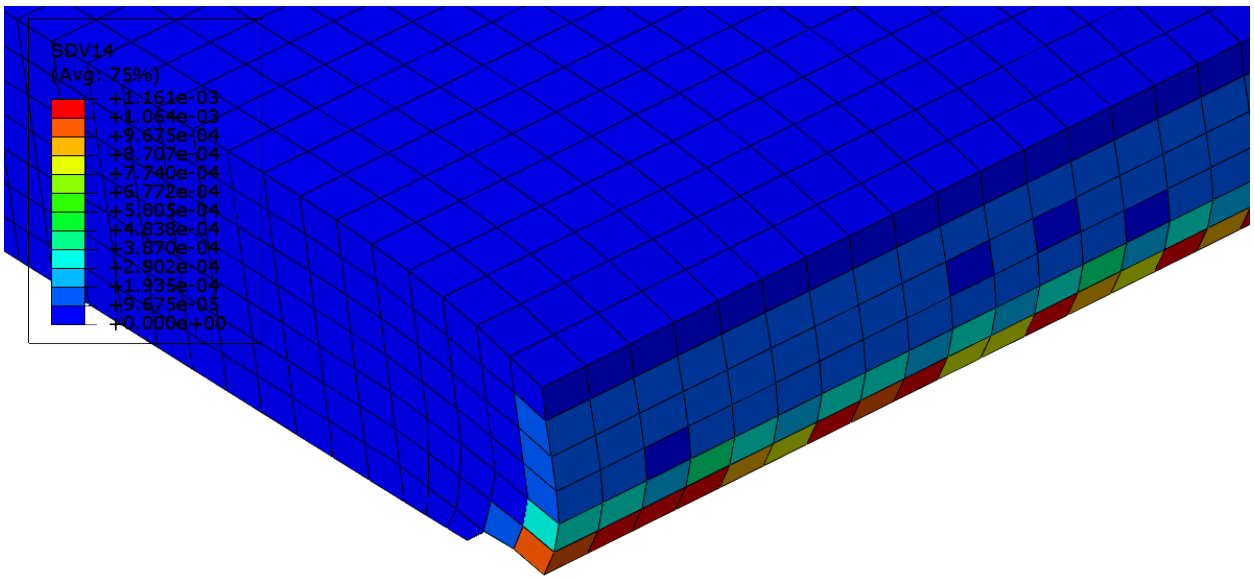
SDV14
(Avg: 75%)
+1.161e-03
+1.064e-03
+9.675e-04
+8.707e-04
+7.740e-04
+6.772e-04
+5.805e-04
+4.838e-04
+3.870e-04
+2.902e-04
+1.935e-04
+9.675e-05
+0.000e+00

(b)

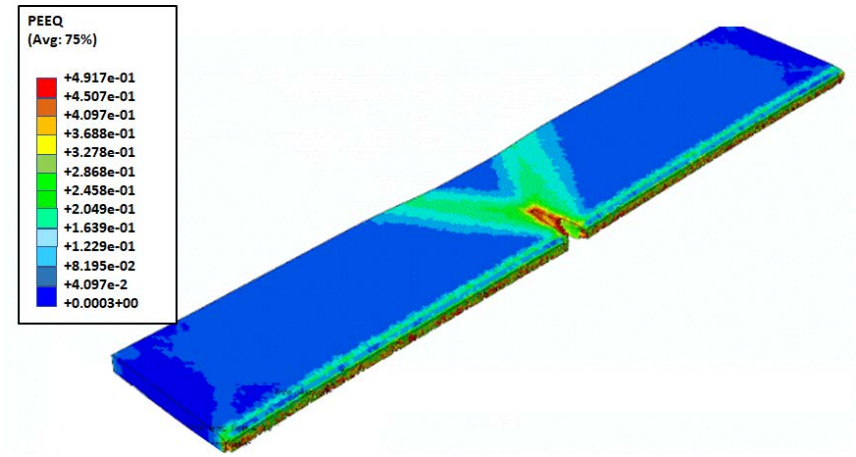
PEEQ
(Avg: 75%)
+4.917e-01
+4.507e-01
+4.097e-01
+3.688e-01
+3.278e-01
+2.868e-01
+2.458e-01
+2.049e-01
+1.639e-01
+1.229e-01
+8.195e-02
+4.097e-2
+0.0003+00

(c)

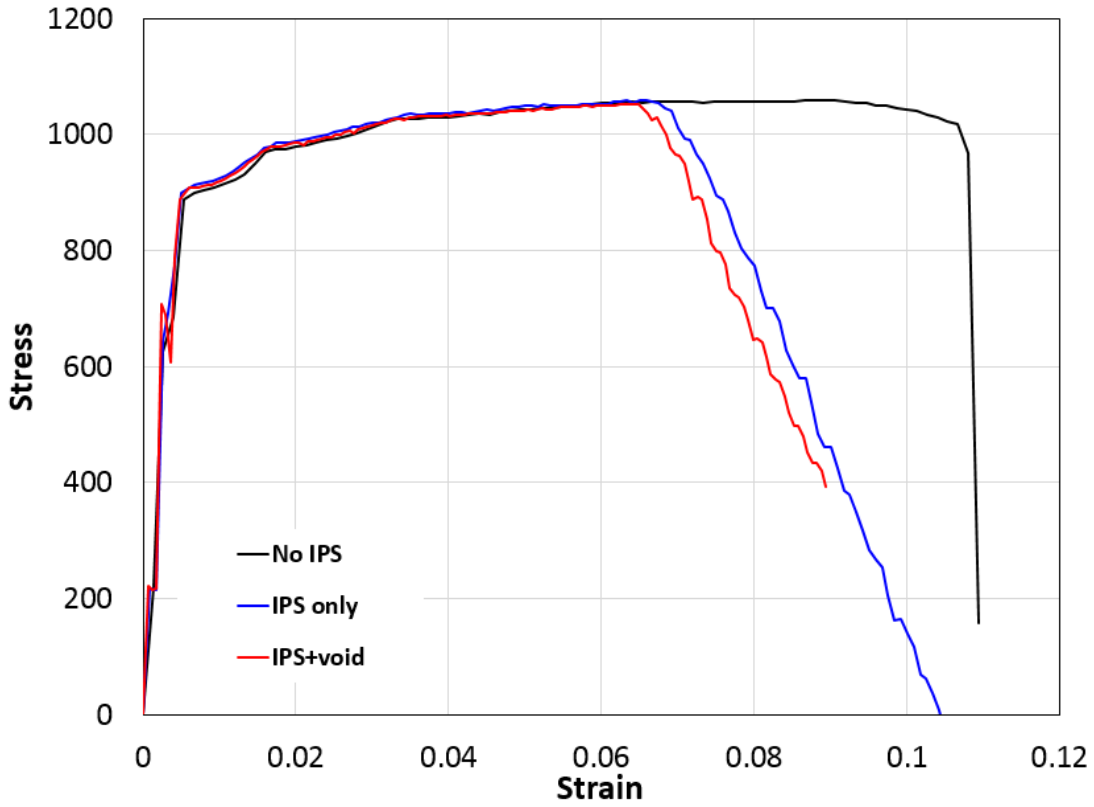

(d)

Figure II.1.A.1.10. Integration of the two-dimensional shearing simulation results into three-dimensional tensile stretchability model. Examples of (a) equivalent plastic-strain distribution mapped from two-dimensional-shearing simulation results and (b) void distributions mapped based on the void vs. equivalent plastic-strain relation shown in Figure II.1.A.1.9(c). (c) and (d) Examples of simulation results (i.e., failure mode and stress-stain curves) for the case of 40% clearance (IPS represents initial plastic-strain). Source: PNNL.

Conclusions

Effects of different microstructure features on the edge stretchability were examined using two DP980 steels (i.e., DP1 and DP2) from different suppliers. Hole extrusion tests and tensile stretchability tests were performed with the two steels for a wide range of cutting clearance. In general, DP1 steels show better sheared-edge stretchability as compared to DP2 steel possibly due to less phase-strength disparity. A substantial difference in the effect of cutting clearance between the tensile test and hole expansion test was also observed, which can be attributed to the difference in cutting conditions between punching of 10 mm in diameter hole and cutting along the straight line. Another contributing factor can be a non-uniform distribution of cutting clearances along the hole circumference, which is very typical for punching of small diameter holes. It should be noted that both tests provide the information essential for designing the stamping dies. Stretchability in the tensile test is more applicable to trimming along the perimeter of the blank while hole expansion test data could be applied for die design in punching holes.

Previously developed computational models and schemes for simulating the hole extrusion and tensile stretchability tests are being upgraded and are also under validation against the new experimental data with the DP1 and DP2 steels. Once validated, the computational models are expected to provide more fundamental understanding on the key factors influencing the edge stretchability of DP980 steels. Interim results from the modeling work indicate that phase-strength disparity can be a primary factor in determining the amount of shearing-induced damage near the edge.

References

Golovashchenko, S. F., 2008, "Quality of trimming and its effect on stretch flanging of automotive panels," *Journal of Materials Engineering and Performance*, Vol. 17, pp. 316–325.

Hu, X., K. S. Choi, X. Sun, and S. F. Golovashchenko, 2014, "Edge fracture prediction of traditional and advanced trimming processes for AA6111-T4 sheets," *Journal of Manufacturing Science and Engineering*, Vol. 136, pp. 021016–1.

Hu, X., K. S. Choi, X. Sun, Y. Ren, and Y. Wang, 2016, "Determining individual phase flow properties in a quench and partitioning steel with *in situ* high-energy x-ray diffraction and multiphase elasto-plastic self-consistent method," *Metallurgical and Materials Transactions A*, Vol. 47, pp. 5733–5749.

Le, Q. B., J. A. deVries, S. F. Golovashchenko, and J. J. F. Bonnen, 2014, "Analysis of sheared edge formability of aluminum," *Journal of Materials Processing Technology*, Vol. 214, pp. 876–891.

II.1.A.2 Cost Effective Magnesium Extrusions

Curt A. Lavender, Co-Principal Investigator
Pacific Northwest National Laboratory
902 Battelle Blvd.
Richland, WA 99352
Phone: 509-372-6770
E-mail: curt.lavendar@pnnl.gov

Tim Skszek, Co-Principal Investigator
Magna International, Inc.
750 Tower Dr.
Troy, MI 48098
Phone: 248-631-5375
E-mail: tim.skszek@cosmaeng.com

Project Introduction

PNNL and Magna International, Inc. (Magna) have been actively collaborating on technologies relevant to the automotive industry that support DOE's mission of improving process and product efficiencies while reducing the weight of the automobiles. The use of high-performance Mg alloys in the automotive industry is presently limited due to the addition of costly RE elements and the slow rate of the processing (i.e., conventional extrusion techniques). Current work aims at eliminating the need for RE additives, while simultaneously improving the processing rate and energy efficiency.

The application of Mg alloys in bumper beams, crush tips, and intrusion beams would result in significant vehicle weight savings. However, new cost-effective extrusion methods are necessary to increase the structural use of Mg alloys. A primary challenge for Mg extrusions is low room temperature ductility due to limited slip systems being activated during compression and tension in the extrusion direction. Mg alloys also suffer from excessive grain growth due to elevated process temperature, which reduces strength. This project aims to develop low-cost extruded Mg alloys that do not rely on RE alloying elements for their strength, ductility, and energy absorption properties. A novel low-cost, high-speed, processing method, in conjunction with Mg alloys containing RE substitutes, will be developed to produce the microstructure and properties needed for the automotive applications in a cost-effective manner.

Accomplishments

- Filed non-provisional patent, "Shear Assisted Processing and Extrusion (ShAPE™)," 15/351,201 on 11/14/2016.
- Filed provisional patent, "Functionally Graded Coatings and Claddings and Through-Wall Texture Control," 62/460,227 on 2/17/2017.
- Published "Scaled-Up Fabrication of Thin-Walled Magnesium ZK60 Tubing using Shear Assisted Processing and Extrusion (ShAPE)," Magnesium Technology, Feb 16, 2017, 315-321, DOI: 10.1007/978-3-319-52392-7_45.
- Issued press release, "*ShAPEing the Future of Magnesium Car Parts*," on Aug. 22, 2017, which was picked up by 30+ domestic and international media outlets, including R&D Magazine, ASM International, The Engineer, Light Metal Age, The Engineer (UK), IOM3 (UK), Phys.org, and Science Dailey. 3K+ hits on Youtube video. https://www.pnnl.gov/news/release.aspx?id=4452.

- Authored Wiki page, “Friction Extrusion,” where images and accomplishments from this project are highlighted. https://en.wikipedia.org/wiki/Friction_extrusion.
- Transferred fixtures, tooling, and process parameters from friction stir welding (FSW) machine to newly installed ShAPE™ machine.
- Achieved 9.6% concentricity (difference between max and min wall thickness) for ZK60 tubing have 2.00” outer diameter and 0.06” nominal wall thickness.
- Achieved 1.3% concentricity for ZK60 tubing, which has a 2.12 in. outer diameter and a 0.120 in. nominal wall thickness.
- Heat-treated ZK60 tubing to T4 and T5 conditions and measured subsequent hardness.
- Demonstrated the ability of scroll designs to affect through-wall texture alignment and the extent of grain refinement.

Approach

In this project, shear-assisted processing and extrusion (ShAPE™) is being developed to fabricate extruded parts with improved material properties and process efficiency. In ShAPE™, the extrusion die and Mg billet are rotated counter to one another and significant heating occurs due to friction at the billet/die interface as shown in Figure II.1.A.2.1. In this schematic, the extrusion die rotates but does not traverse. Instead, the non-rotating Mg billet traverses from right to left and presses against the rotating extrusion die. In this configuration, the tube is extruded in the direction of billet translation, thus being classified as a direct extrusion. The amount of heat generation is proportional to the applied torque and rotational speed of the die. As temperature increases, the billet face softens and plastically flows through the spiral scroll features inward toward the extrusion orifice. Material flowing out of the individual scroll is consolidated between the mandrel and die-bearing surface prior to exiting through the die relief.

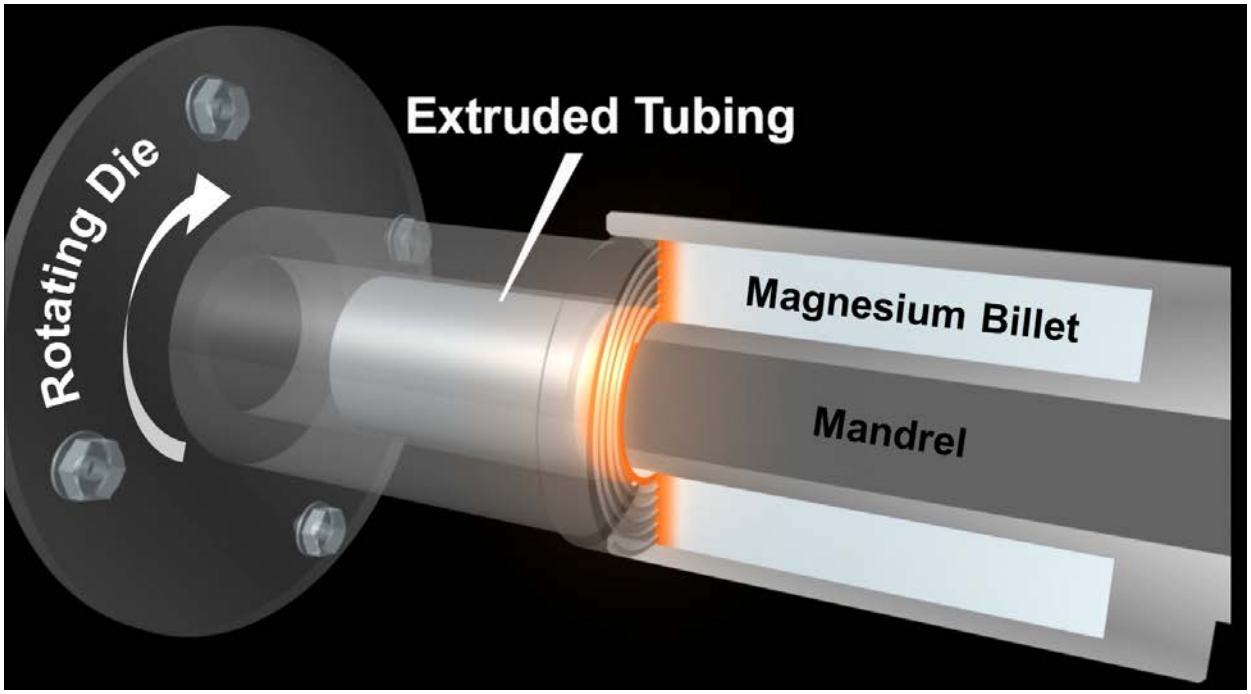

Figure II.1.A.2.1. Cross-section of tooling showing a direct extrusion embodiment of the ShAPE™ process. Source: PNNL.

Recrystallization occurs within the deforming material and when shear and temperature are suddenly reduced, a refined microstructure can be obtained in the extrudate. Due to the complex shear and thermal conditions present during ShAPE™, crystallographic texture is thought to develop as a combination of recrystallization mechanisms due to the interplay between rotational speed, extrusion rate, and thermal conditions. Advantages of ShAPE™ may include enhanced grain refinement leading to better material properties, the ability to align crystallographic texture, lower extrusion forces leading to smaller tonnage equipment, and lower process energy consumption.

Technology Transfer Path

Discussions with multiple industrial companies regarding the licensing of intellectual property began in FY 2017. Additional patent filings are anticipated in FY 2018. Process development will continue until defect-free tubes of sufficient length can be evaluated by Magna in FY 2018. Tubes of this quality will lead to additional exposure for the technology and new interest from industry.

Results

Research during FY 2015 and FY 2016 was conducted on PNNL's FSW machine, which resulted in the exciting material properties described in previous annual reports. Although successful from a scientific standpoint, it became difficult to demonstrate industry-relevant scalability, achieve any semblance of dimensional control, or to consider alternate die configurations. The FSW machine performed admirably in the exploratory stage of the project, but it was simply not designed to perform ShAPE™ at the level required for the ultimate objectives of this project. The capability and configuration of the FSW machine posed four primary challenges for the project:

1. Vertical orientation of the FSW motor limited the extrusion length to approximately 12 inches.
2. Inability to spin the die resulted in tubes with unsatisfactory straightness.
3. Low FSW machine stiffness resulted in tubes with highly non-uniform wall thickness.
4. FSW machine torque limit restricted the diameter of tubing that could be considered.

A new custom designed ShAPE™ machine capable of addressing these challenges was procured using internal PNNL funds during the third quarter of FY 2016. As a result of FSW machine limitations, the decision was made in the fourth quarter of FY 2016, in collaboration with the VTO program manager, to curtail spending on this project until the new ShAPE™ machine was installed and functioning at PNNL. Unfortunately, it took approximately 12 months for the new ShAPE™ machine, shown in Figure II.1.A.2.2, to get up and running, which led to a substantial delay in the project and necessitated the carrying over of funds into FY 2018. We see this as a positive in that the remainder of the work will now be able to be completed using a machine designed for this very purpose. The new ShAPE™ machine was up and running in the mid fourth quarter of FY 2017. As such, we have already been able to make good technical progress during that time, which is reported herein.

Figure II.1.A.2.2. Customized ShAPE™ machine installed at PNNL. Source: PNNL.

This new ShAPE™ machine was used to extrude ZK60 tubing, as is shown in Figure II.1.A.2.3. Tubes were nominally 2.0-in. in diameter with wall thicknesses of 0.60-in. and 0.120-in. Process parameters such as extrusion force, torque, rpm, feed rate, and temperature were similar to tubes reported in FY 2016. Noteworthy differences for tubes fabricated on the new ShAPE™ machine are described in more detail below.

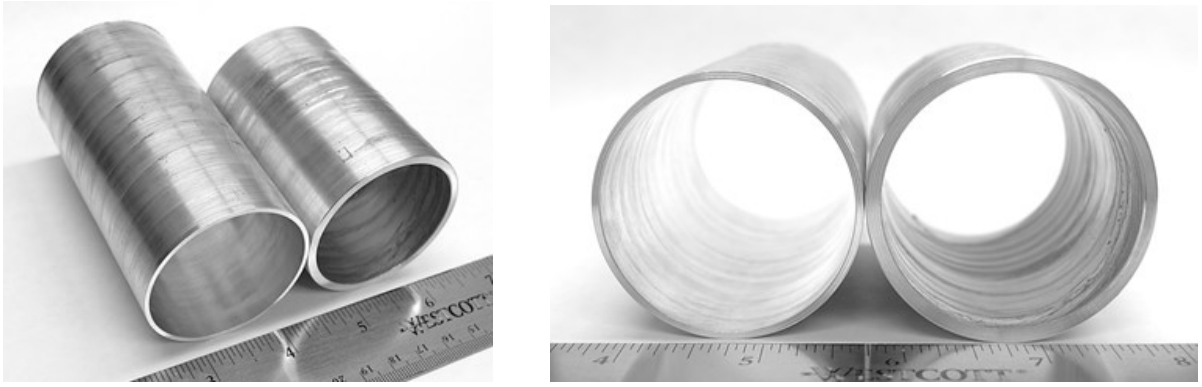

Figure II.1.A.2.3. ZK60 tubing fabricated using the new ShAPE™ machine. Source: PNNL.

A significant improvement in the tubes made using the ShAPE™ machine (compared to the FSW machine) is the concentricity of the inner and outer diameters as show in Figure II.1.A.2.4. For the 0.060-in. thick tube, the minimum and maximum wall thickness ranged from 0.0570-in. to 0.625-in., a difference of 9.6%. For the 0.120-in. thick tube, the minimum and maximum wall thickness ranged from 0.1135-in. to 0.1150-in., a difference of 1.3%. A 1.3% variation in wall thickness (e.g., a difference of merely 1.5 mils, or 0.0015-in.) is considered a very high concentricity tube by industry. This dimensional control is attributed to the new ShAPE™ machine being much stiffer than the FSW machine. In addition to concentricity, the straightness of the tubes (e.g., a few tens of mils over a length of one foot) are dramatically improved compared to those made previously on the FSW machine (e.g., a few tenths of inches, or more, over a length of one foot). There is still much work to be done on straightness and eliminating defects that occur periodically along the length of the tube, but the concentricity achieved in FY 2017 was a major step forward for ShAPE™. Surface finish was

also improved with less galling and scoring, since we were able to: 1) rotate the die rather than the billet/tube; and 2) eliminate machine stiffness "walking," which was present using the FSW machine.

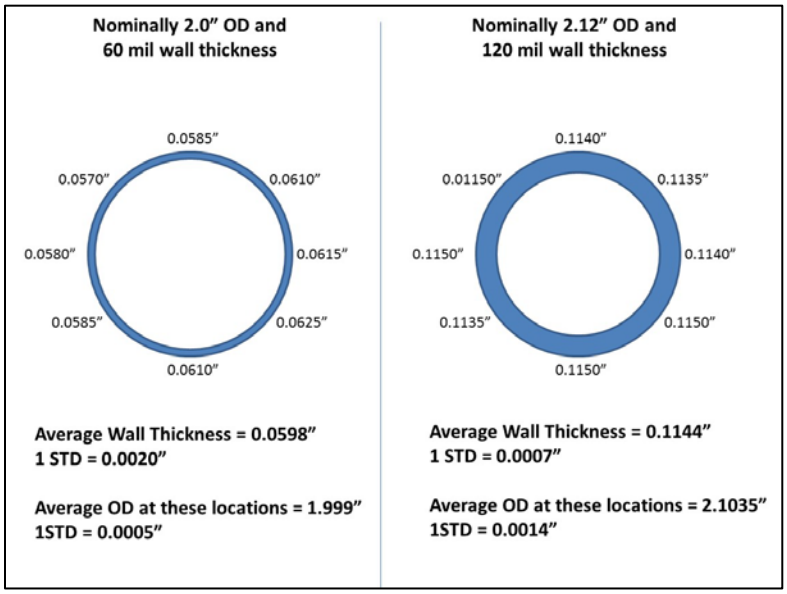

Figure II.1.A.2.4. The concentricity of ZK60 tubing fabricated using the new ShAPE™ machine. Source: PNNL.

The effect of scroll design on texture development and grain refinement was explored during FY 2017 for ZK60 tubing and resulted in the patent filing described in the accomplishments section. The 2-start, 4-start, and 16-start scroll patterns, shown in Figure II.1.A.2.5, were tested with each scroll having a width of 2.72 mm, a depth of 0.47 mm, and a pitch of 4.04 mm. Process parameters were held constant for each trial and tubes with a 0.060-in. wall thickness were fabricated for all three scroll patterns.

Figure II.1.A.2.5. 2-start, 4-start, and 16-start scroll patterns tested in the ShAPE™ process for ZK60. Source: PNNL.

Following extrusion of the three tubes, SEM and electron backscatter diffraction (EBSD) was performed to determine grain size and texture alignment through the wall thickness. This data is plotted in Figure II.1.A.2.6 and shows that grain size and basal texture alignment can be affected by the scroll pattern. Compared to the 2-start pattern, the 4-start and 16-start patterns result in larger grain size and significant variation in texture through the wall thickness. The ability to control texture through the wall thickness of a tube could be very advantageous depending on the end-use application. We hypothesize that the different shearing conditions imparted by the different scroll patterns are responsible for the changes in grain size and texture. Modeling would be required to assess this theory but is beyond the scope of this project.

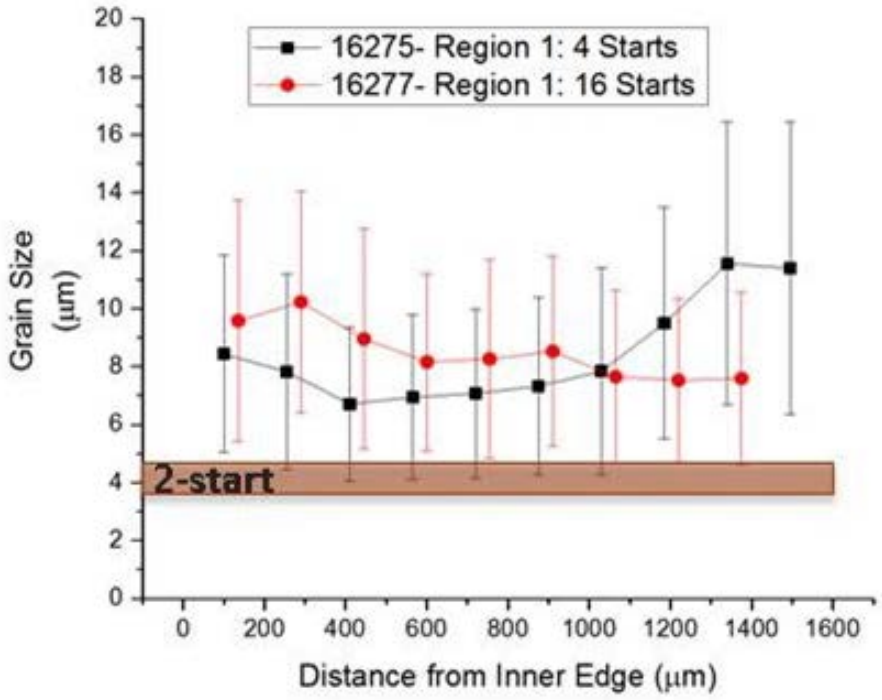

(a)

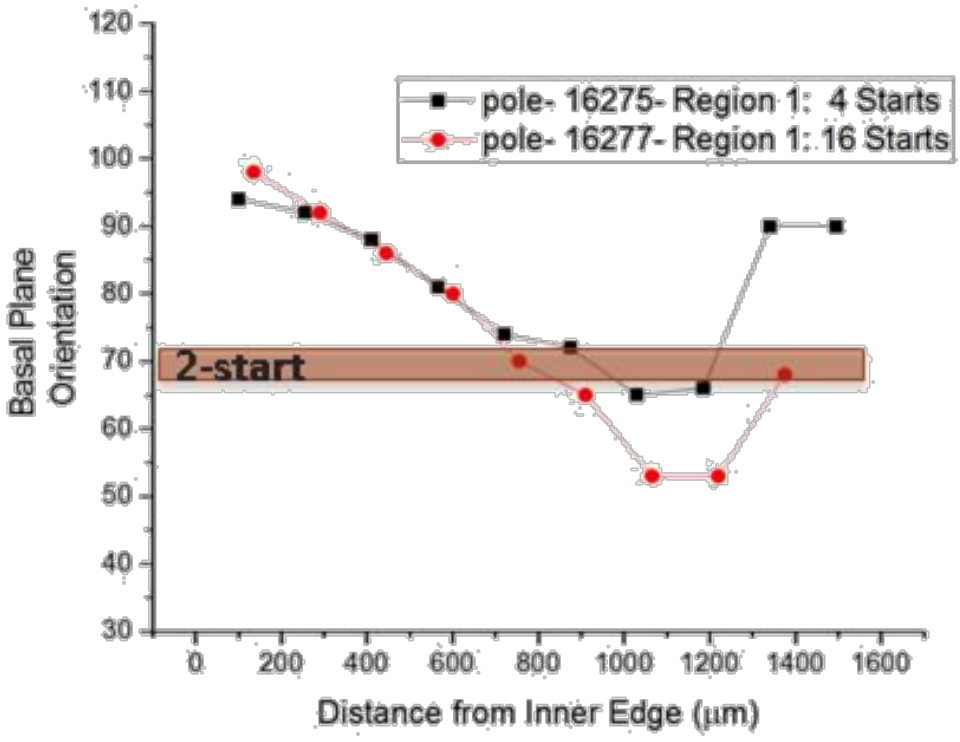

(b)

Figure II.1.A.2.6. (a) Grain size; and (b) orientation of the (0001) basal plane as a function of scroll pattern.

For the 0.060-in. and 0.120-in. thick tubes, the scrolled die was rotated at 250 rpm and rammed against the ZK60 billet at a constant rate of 3.81 mm/min. Tool speed was reduced incrementally during the process, while the thermocouple temperature eventually stabilized at 450–500°C with a final tool speed of 100 rpm. Ram force and torque build rapidly, as is shown in Figure II.1.A.2.7, after contact is made between the billet and die. During this initial phase, the scroll is essentially machining the billet, creating shavings with a "steel wool" consistency and no extrusion is formed. Once the temperature elevates, the material softens and begins to plastically deform within the scrolls and extrudes through the die. The force and torque required to extrude the 0.120-in. tube was noticeably less than 0.060-in. tube, due to the difference in extrusion ratio. The high frequency oscillations in the torque and force data are attributed to small amounts of non-uniform, intermittent flashing observed between the die outside diameter and container inside diameter.

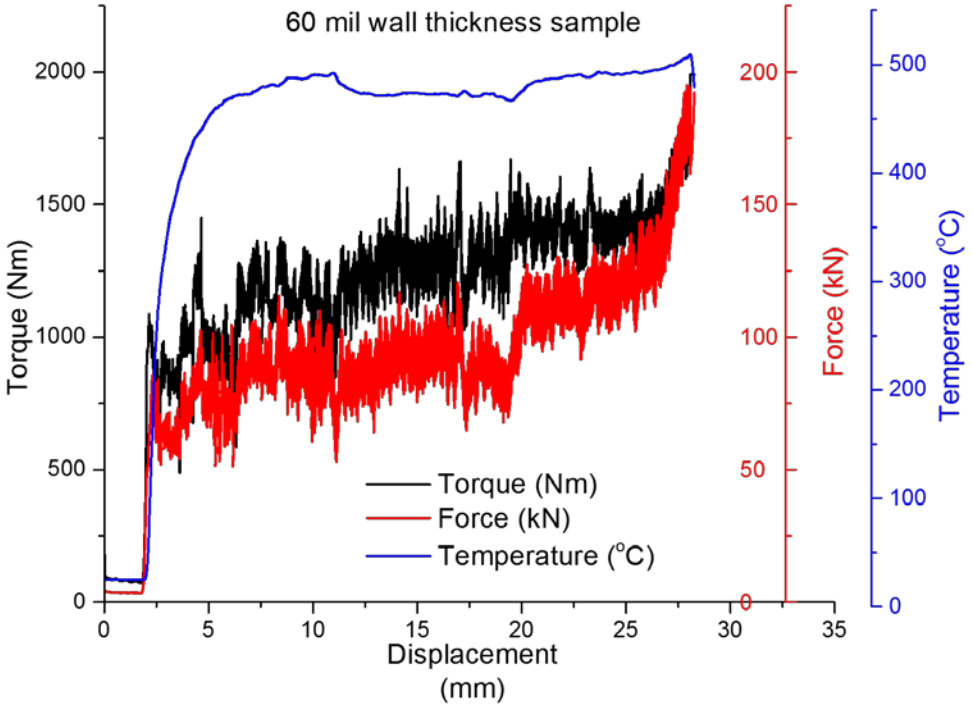

(a)

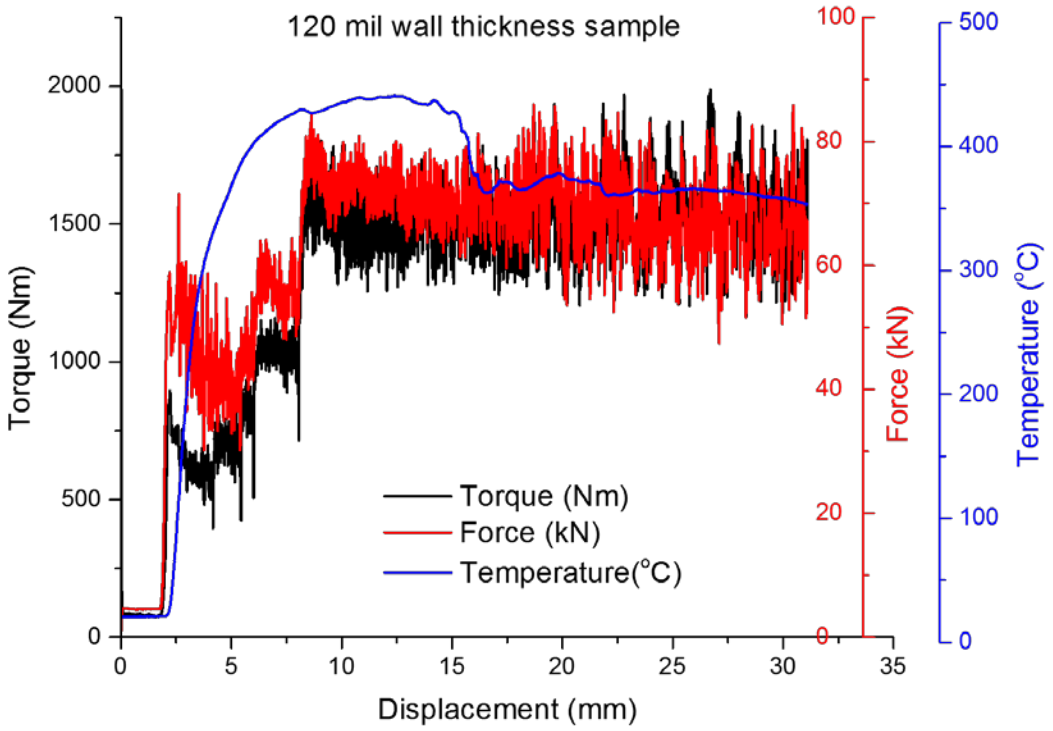

(b)

Figure II.1.A.2.7. Force in kilonewtons (kN), torque in newton meter (Nm), and temperature in degrees Centigrade (°C) data for (a) 0.060-in. wall thickness; and (b) 0.120-in. wall thickness while extruding ZK60 tubing using the ShAPE™ process.

Heat-treatment studies were performed to determine the time and temperature to achieve T5 conditions with ShAPE™ processed ZK60 tubes. Specimens from the 0.060-in. wall thickness, 2-start tubes were used in this study. Specimens were encapsulated in quartz tubes filled with inert Argon cover gas as shown in Figure II.1.A.2.8.

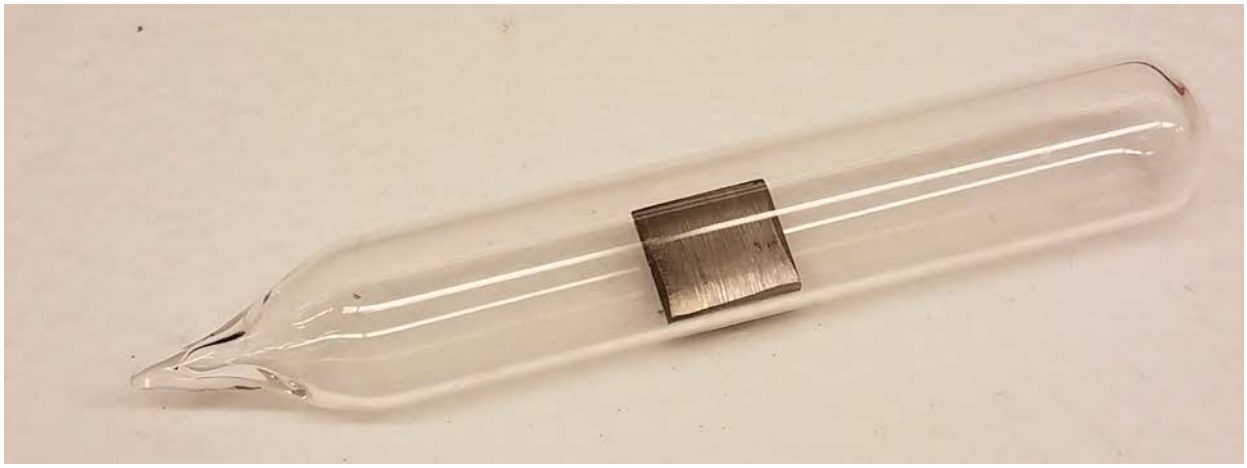

Figure II.1.A.2.8. A specimen of ZK60 tubing extruded by ShAPE™ using a 2-start scroll encapsulated in a quartz tube filled with Argon. Source: PNNL.

Specimens were heated at 150°C, 175°C, and 200°C at 1, 10, 25, 50, 75, and 100 hours to determine T5 heating conditions. Hardness reached a maximum of 84 HV after ~5 hours at 175°C, which is consistent with literature values. SEM and EBSD were performed and did not show any measurable grain growth under these heat-treatment conditions. This is a promising result; therefore, fully extruded tubes will be heat-treated to the T5 condition and then tested for strength and ductility in the longitudinal and circumferential directions. The results will be compared with those reported in FY 2016 for tubes that were not heat-treated.

Conclusions

There are several advantages of the ShAPE™ process that lend well to potential cost reduction and scale-up for industry. First, the ram force required is >10 times lower than is required for similarly sized tubing fabricated using conventional direct extrusion. This is because material flow induced by the scroll pattern plays an important role in feeding material into the extrusion orifice. Such a large reduction in force would enable substantially smaller machinery, thus lowering capital expenditure and operational costs. An additional advantage of the ShAPE™ process is that the frictional heat generated at the billet/die interface is the only process heat required to soften the material and maintain temperature. As such, the overall energy input to the process, and therefore the cost, may be reduced as compared to conventional heating approaches such as billet preheating or container heating.

Transfer of the process from the FSW machine to the dedicated ShAPE™ machine resulted in ZK60 tubes with dramatically improved concentricity and straightness. This was demonstrated for nominally 2.0-in. OD tubes with 0.060-in. and 0.012-in. wall thicknesses. 2-start, 4-start, and 16-start dies were then used to demonstrate the influence of scroll patterns on grain refinement and though-wall texture development. Two patents were filed in FY 2017 covering the ShAPE™ technology.

Finally, ShAPE™ is a single-step process that can lead to cost reduction as compared to other multi-step severe plastic deformation processes such as equal channel angular pressing, accumulative roll-bonding, and cyclic extrusion-compression. In fact, the authors are exploring the possibility of going directly from castings to a final extruded product using the ShAPE™ process. In addition to these potentially significant cost and scalability advantages, the ShAPE™ process also holds promise for improved mechanical properties.

II.1.A.3 Optimizing Heat-Treatment Parameters for Third Generation Advanced High-Strength Steel with High Throughput in-situ Experiments and Integrated Modeling Frameworks

Xiaohua Hu, Co-Principal Investigator
Pacific Northwest National Laboratory
902 Battelle Blvd.
Richland, WA 99352
Phone: 509-375-6681
E-mail: xiaohua.hu@pnnl.gov

Emmanuel De Moor, Co-Principal Investigator
Advanced Steel Processing and Products Research Center
Colorado School of Mines
1500 Illinois St.
Golden, CO 80401
Phone: 303-273 3624
E-mail: edemoor@mines.edu

Project Introduction

Medium Mn transformation-induced plasticity (TRIP) steels represent potential important products to achieve the performance requirements of third generation AHSSs in an effort to make vehicles more lightweight for improved fuel-efficiency while meeting or exceeding safety regulations.

Medium Mn steels typically contain 5-10 wt. % Mn and other alloying elements like those used in current selected AHSS grades. It is well known that the mechanical properties of these steels are extremely sensitive to chemical compositions (e.g., carbon (C) and Mn content) and inter-critical annealing (IA) temperatures, which in turn determine the volume fraction and thermodynamic stability of the retained austenite (RA) in corresponding microstructures. Given a certain microstructure of the multiphase steel (i.e., volume fraction, morphology, and stability of the RA), our team's previous work established an integrated experimental and computational approach linking the microstructures to corresponding mechanical properties (Choi et al. 2008, Choi et al. 2010).

However, traditional experimental heat-treatment and characterization techniques applied in optimizing heat-treatment parameters for strength and ductility combinations are often laborious and time-consuming. Complete descriptions, efficient experimental characterization techniques and predictive capabilities and the applications of these to describe relationships between chemical compositions, initial microstructures, heat-treatment parameters, and subsequent RA volume fraction, RA stability, and mechanical properties have not been established.

Accomplishments

- Scanning electron microscopy and energy dispersive analysis x-ray (SEM-EDAX) microstructural and composition analysis has been performed on as-received 7 wt. % Mn (7 Mn) and 10 wt. % Mn (10 Mn) steels to obtain information of Mn, Al, and Si partitioning in austenite and ferrite phases.
- High throughput *in-situ* HEXRD measurement technique has been developed to obtain austenite transformation kinetics and lattice parameter changes during IA heating and cooling cycles of 7 Mn and 10 Mn steels.
- *In-situ* HEXRD room temperature tensile tests have been performed to understand the deformation mechanism, transformation kinetics, and lattice distortions.

- Dilatometry tests have been performed using identical thermal cycles as the *in-situ* HEXRD IA cycles.
- Thermo-Calc/DICTRA simulations for 5 Mn and 7 Mn steels have not been performed to study martensitic transformation and C/Mn partitioning during high-temperature holding.

Technology Assessment

- Target: Obtain thermodynamic parameters for model predictions of transformation kinetics, microstructures of constituent phases for the Thermo-Calc and phase-field modeling.
- Gap: The links correlating the lattice parameters obtained from HEXRD to the chemical composition in the ferrite-like phases and austenite are not well known. There is a lack of correlation between HEXRD measured transformation kinetics, dilatometric measurement, and traditional experimental heat-treatment and metallography.

Approach

In this project, the following approaches are proposed: 1) Perform conventional experimental mechanical and microstructural characterization and heat-treatment experiments to study the RA volume fraction and alloy elements partitioning for as-received and heat-treated medium Mn steels; 2) Develop an *in-situ* characterization technique to determine the austenite formation kinetics of medium Mn TRIP steels on heating and during IA to enable the accelerated development of future third generation AHSS; 3) Develop a Thermo-Cal/DICTRA and phase-field based modeling capability to predict the volume fraction, morphology (including grain size), and stability (C and Mn concentration) of the austenite formed during the IA process; 4) Link the predicted microstructures, including the austenite volume fraction retained after cooling, stability, and morphology to the mechanical properties; and 5) Optimize the strength and ductility of medium Mn TRIP steels by judicious IA temperature selection.

Technology Transfer Path

The deliverables of this project will be transferred to OEM companies and steel producers during regularly scheduled semi-annual review meetings of the Advanced Steel Processing and Products Research Center (ASPPRC), an industry/university cooperative research center at the Colorado School of Mines. The modeling methodology and modeling results will also be published in peer-reviewed technical journals so that they are freely available to a broader engineering community.

Results

The as-received 7 Mn and 10 Mn steels from an ASPPRC sponsor has been characterized by SEM and EDAX composition analysis. *In-situ* HEXRD tensile tests were also performed to study the transformation kinetics and individual phase lattice distortion information during deformation.

The as-received 7 Mn steel has a nominal chemical composition of 0.14 C, 0.2 Si, and 7 Mn in weight percentage and is produced by a continuous annealing process, while 10 Mn material is hot-dip galvanized after IA. The 10 Mn steel has a nominal composition of 0.14 C, 0.2 Si, 10 Mn, and 1.5 Al in weight percentage. The microstructure of as-received 7 Mn consists of lamellar structures consisting of alternative ferrite/austenite lamellae, as shown in Figure II.1.A.3.1, in sub-micron range in size, while 10 Mn consists of mixed microstructure, which consists of both areas of lamellar microstructures and grains of small aspect ratios.

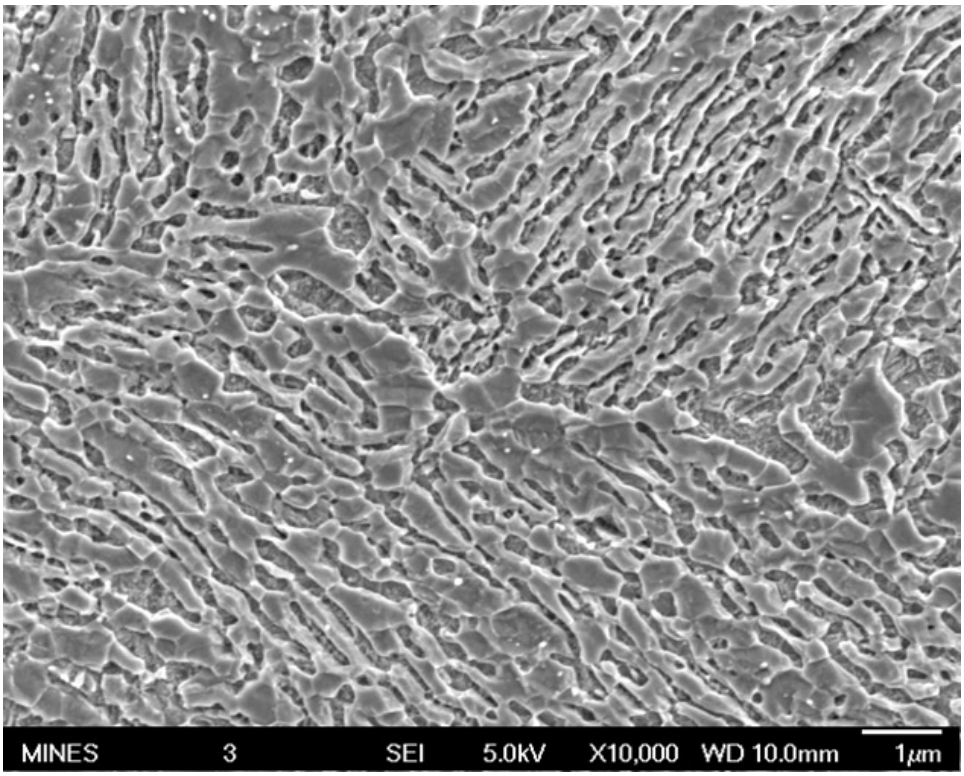

(a) 7 Mn Steel

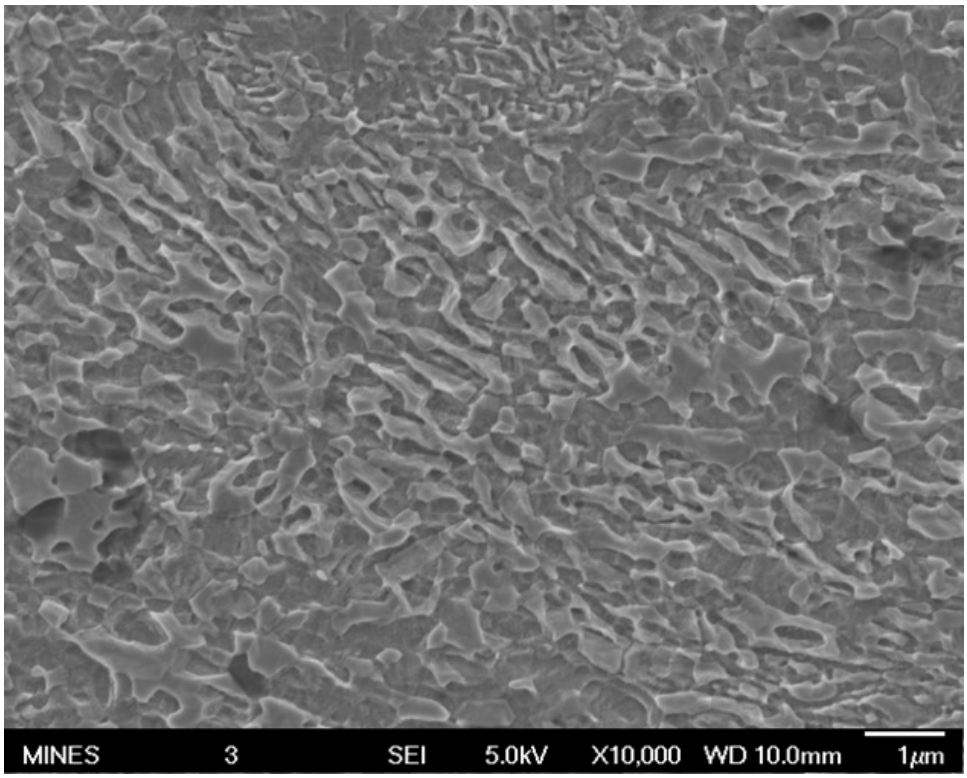

(b) 10 Mn Steel

Figure II.1.A.3.1. SEM microstructures of (a) 7 Mn; and (b) 10 Mn steels. Source: PNNL.

EDAX compositional analysis has been performed on alloy elements such as Mn, Al, and Si for both 7 Mn and 10 Mn steels, as shown in Figure II.1.A.3.2(a) and Figure II.1.A.3.2(b). It can clearly be seen that much higher Mn content in the area that has darker colors for both 7 Mn and 10 Mn. Based on phase transformation analysis, the darker area should at least be part of the austenite lamellae. The range of Mn content in the 7 Mn steel line scan is 3-11 wt. %, while that for 10 Mn steel is 0-26 wt. %. With no exception, there is low Al content in the areas with high Mn content for Al containing 10 Mn steel; this is consistent with Al having little solubility in austenite Fe from the Fe-Al binary phase diagrams.

As shown in the SEM-EDAX microstructure and composition examination in Figure II.1.A.3.2, the Mn or Al are partitioned between the austenite and ferrite phase after continuous annealing and/or galvanizing process. Due to the relatively short time of continuously annealing or hot-dip galvanizing process and much slower than C, we believe that the Mn and Al are not fully partitioned during those processes (Han et al. 2017), while C might have been fully partitioned (Muller and Moor 2017). The high Mn (low Al) region should be the region of austenite near the austenite grain boundaries. The information of alloy elements partitioning will provide important input data for the later thermodynamic microstructural modeling, which will simulate similar 7 Mn and 10 Mn steels that have heating, holding, and cooling cycles in the *in-situ* HEXRD heat-treatment or dilatometry experiments.

To further characterize the 7 Mn and 10 Mn steel, in-situ HEXRD tensile tests were performed where kinetics of deformation-induced phase transformation from austenite to martensite transformation and associated lattice parameter changes during deformation are carefully analyzed with the use of fit by two-dimensional and origin software to obtain volume fraction variation of various phases (Hu et al. 2016, Hu et al. 2017). The results for the 10 Mn steel are similar to that observed in similar steels from the prior integrated computational materials engineering project (Abu-Farha 2017), which shows large-yield point elongation and Luders band, followed by dynamic Portevin–Le Chatelier banding behavior. The 7 Mn steel, on the other hand, shows mostly Luders banding behavior and several long plateaus in the curve of austenite volume fraction variation with macroscopic strain, as shown in Figure II.1.A.3.3(a). This phenomenon has been supported by digital image correlation techniques (Abu-Farha 2017). The lattice strain data, as shown in Figure II.1.A.3.3(b) of ferrite-like phases is shown to increase stepwise for new martensite, while those of original ferrite-like phases show little changes, as shown in Figure II.1.A.3.3(b). These lattice strain data will be helpful information for understanding the peculiar dynamic banding behavior of medium Mn steels.

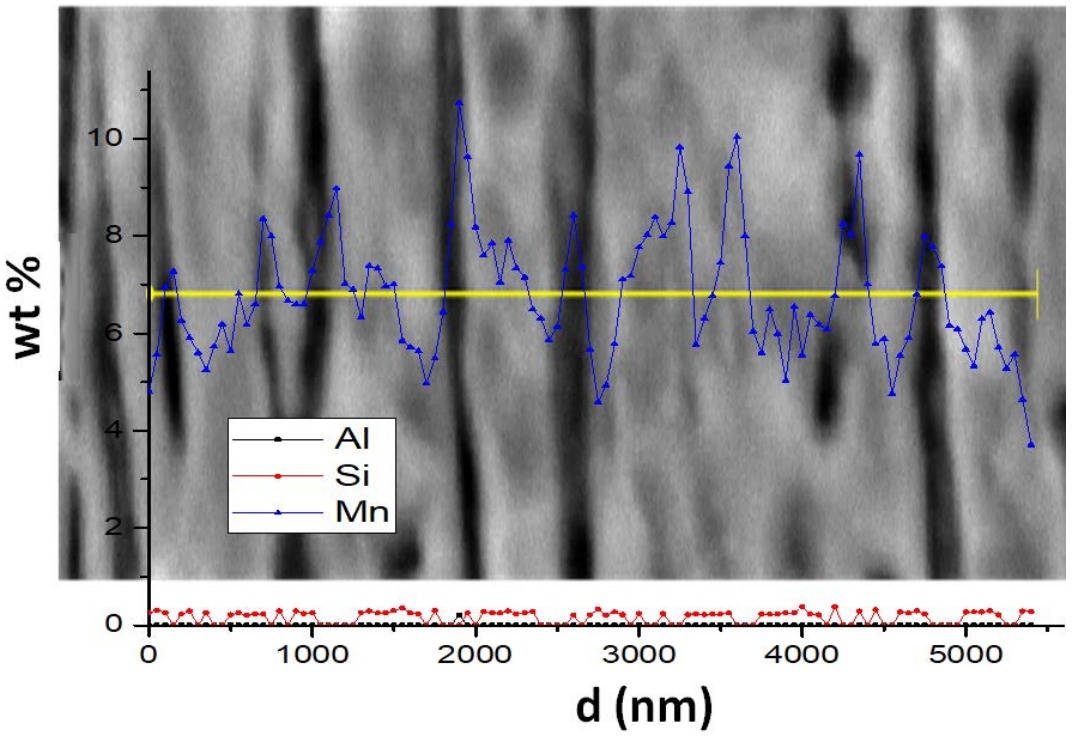

(a)

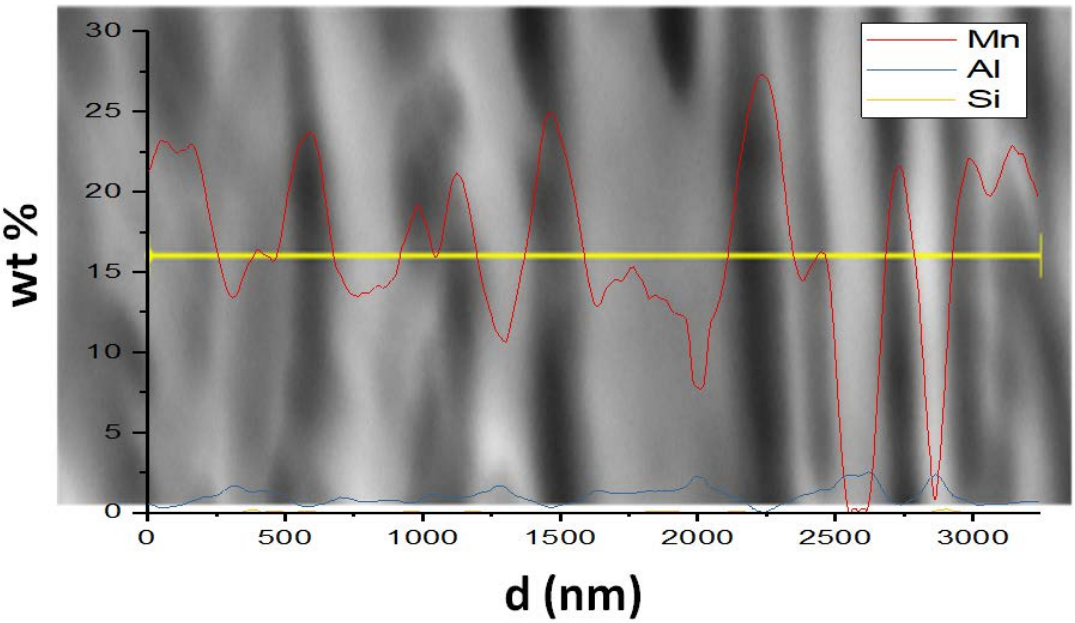

(b)

Figure II.1.A.3.2. The SEM-EDAX Mn, Al, and Si composition analysis of the (a) 7Mn and (b) 10Mn steel. Source: PNNL.

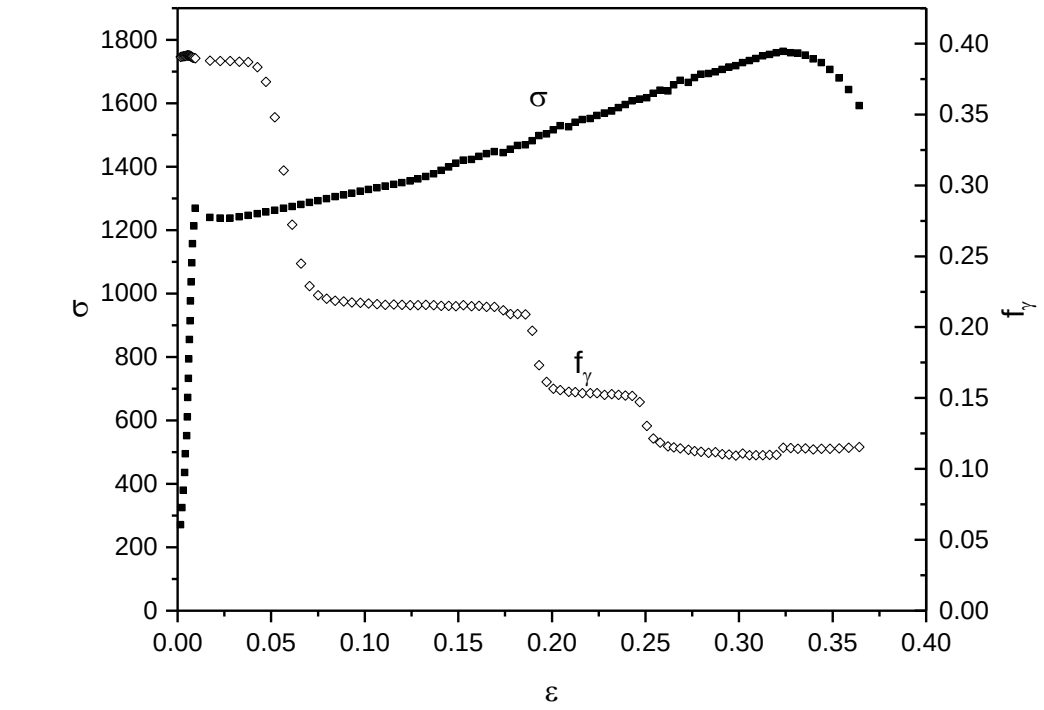

(a)

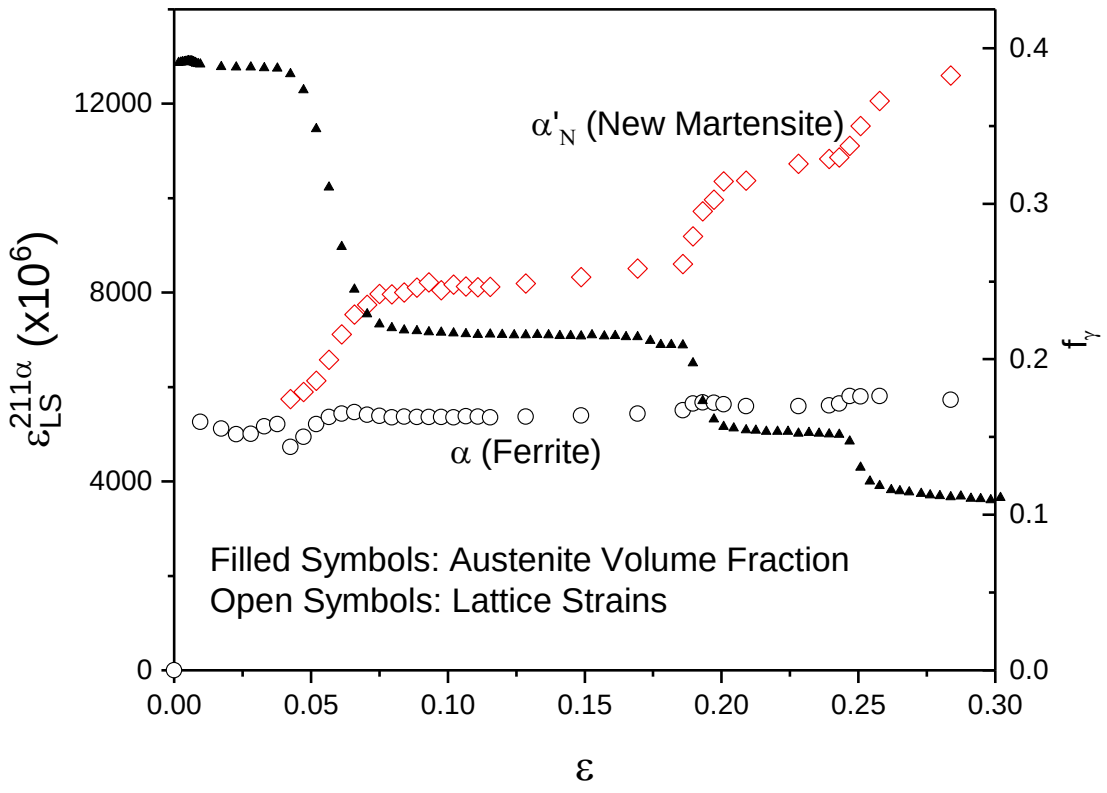

(b)

Figure II.1.A.3.3. The variation with macroscopic strains (ε) of (a) the tensile stresses (σ) and austenite volume fractions (f_γ); and (b) the austenite volume fractions and ferrite-like phase (α) lattice strains (ε_{LS}).

For the as-received 7 Mn and 10 Mn steels, the high throughput *in-situ* HEXRD experimental procedure was developed to obtain the kinetics of phase transformations during heating and cooling cycles of 7 Mn and 10 Mn steels under different IA heat-treatment. This experiment utilized the high-energy synchrotron source at beamline 11-D-C at the advanced photon source at Argonne National Laboratory and a Linkam Scientifc TS1500 heating stage. In the experiment, a small sample is placed inside the chamber of the Linkam Scientific heating device with argon as the inert gas to protect the sample from oxidation during experiments. The heating cycle consists of heating, holding, and cooling stages. The sample is heated at a heating rate of 100°C/min, then held at an IA temperature for one hour, followed by cooling to room temperature at the 120°C/min cooling rate. The selected IA temperatures ranges from 600°C to 750°C for 7 Mn steel and 650°C to 800°C for 10 Mn steel. During the thermal cycle, the synchrotron beam keeps radiating the center of the sample and the diffraction patterns are recorded at a set interval of time.

Results of the obtained phase volume fractions and lattice parameters will be used to calibrate the thermodynamic parameters, such as temperature-dependent C and Mn diffusivity in various phases, as well as energy criteria for phase transformations, which will be used in subsequent tasks of materials by design in selecting the chemistry and associated thermomechanical processes in achieving the performance requirements of third generation AHSS. Figure II.1.A.3.4(a) shows the results of austenite volume fraction changes with time of 7 Mn steel for four different holding temperatures (T_h). For T_h=600°C, the austenite f_γ increases when the temperature rises. At the T_h, f_γ increases slightly from about 39% and then decreases when cooling down, returning to almost the initial level at room temperature; contrarily, while at other temperatures, f_γ would increase with time during holding and decrease when cooling down to room temperature. The final value of f_γ at room temperature is about 0.5 and 0.62 for T_h=650°C and 700°C, respectively, as shown in Figure II.1.A.3.4(b). As for T_h=800°C, on the other hand, the austenite increases quickly with time during holding, with the material almost fully austenized after ~12 min of holding. The austenite f_γ, however, drops to 0.2 after cooling down to room temperature, which is believed to be the martensitic transformation.

To understand phase transformation behaviors during IA thermal cycles, it is also helpful to consider the lattice parameter variation with time and temperatures, as shown in Figure II.1.A.3.4. For all IA cycles, the lattice parameters for both austenite and ferrite increase quickly during heating and drop quickly during cooling. This is due to thermal expansion during heating and thermal contraction during cooling. During holding at 600°C, the lattice parameter of austenite slightly increased and is slightly higher than as-received material after cooled down to room temperature, indicating there are alloy elements (C or Mn) partitioning during holding where the austenite should have slightly higher C or Mn content after the IA cycle. Corresponding well with lattice parameter changes in austenite, the lattice parameter of ferrite decreases during holding at 600°C, but looks less sensitive to partitioning.

On the other hand, when holding temperatures are at 700°C and 750°C, lattice parameters decrease with time during holding, which are coincident with rapidly rising austenite volume fractions. The rate of the lattice parameters decreasing correspond well with the speed of the increasing austenite volume fractions. The explanation for this phenomenon is that the dilution of austenite C and Mn content due to the transformation of ferrite with low C and Mn content into austenite. The decreasing austenite lattice parameter does not mean the opposite trend of ferrite lattice parameters. The results shown in Figure II.1.A.3.4(b) actually saw the decrease of ferrite lattice parameters during holding as well, which could be explained that those grains with slightly higher C and Mn content are preferentially transformed to austenite. The lattice parameters after cooling down to room temperature for T_h=600°C is slightly higher than that for the as-received condition, and slightly lower for T_h=700°C.

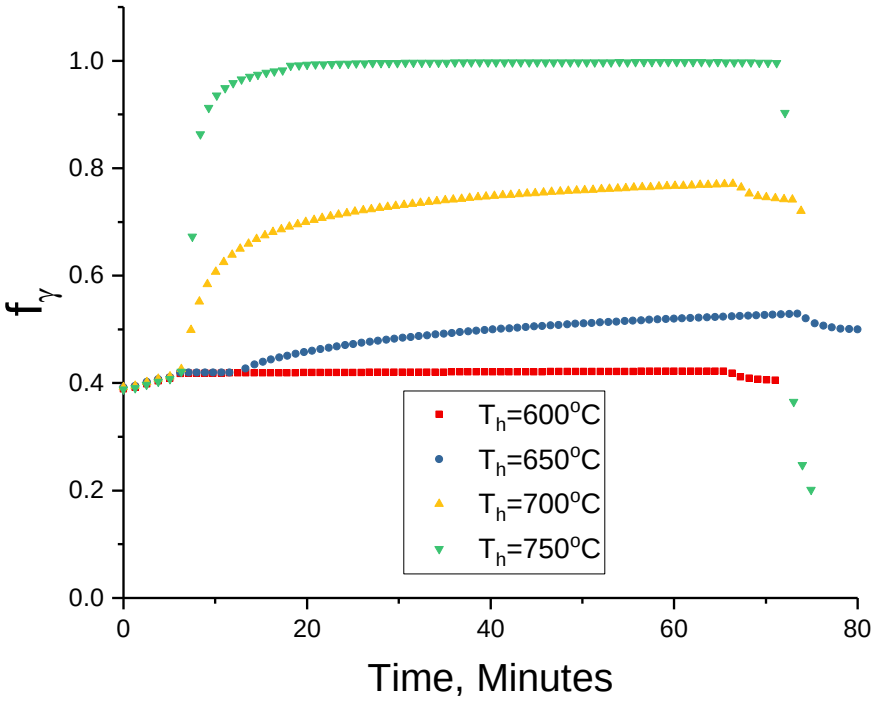

(a)

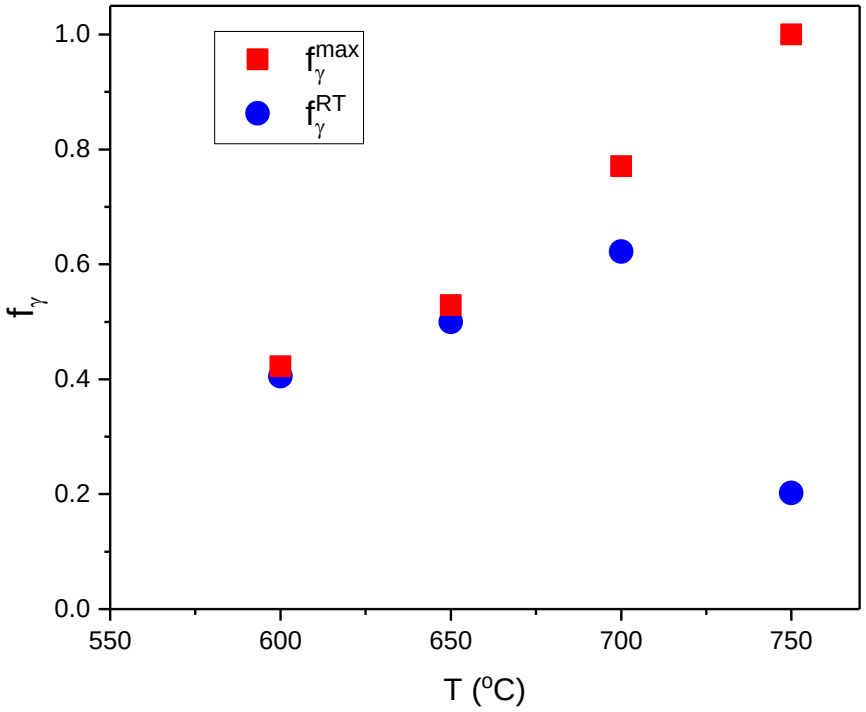

(b)

Figure II.1.A.3.4. The results for *in-situ* HEXRD heat-treatment experiments of a 7 Mn steel with four IA temperatures (T): (a) austenite volume fraction changes with time; and (b) maximum austenite volume fraction (f_γ^{max}) at high temperatures and the austenite volume fraction when it is cooled down to room temperature (f_γ^{RT}).

As for T_h=750°C, the lattice parameter of austenite during holding does not change anymore when the material is fully austenized. The austenite decreases to a level that is much lower than that of as-received, indicating a much lower level of C and Mn content during high temperature dilution of C and Mn from the austenite transformed from ferrite-like phases, which has much less C and Mn content. On the other hand, a new ferrite-like phase, fresh martensite, formed after cooling down to about 300°C, the lattice parameter of this phase is much higher than that of as-received one. Figure II.1.A.3.5(a) shows a higher ferrite-like phase lattice parameter, while Figure II.1.A.3.5(b) shows there is no lattice parameter data for ferrite when the material is fully austenized.

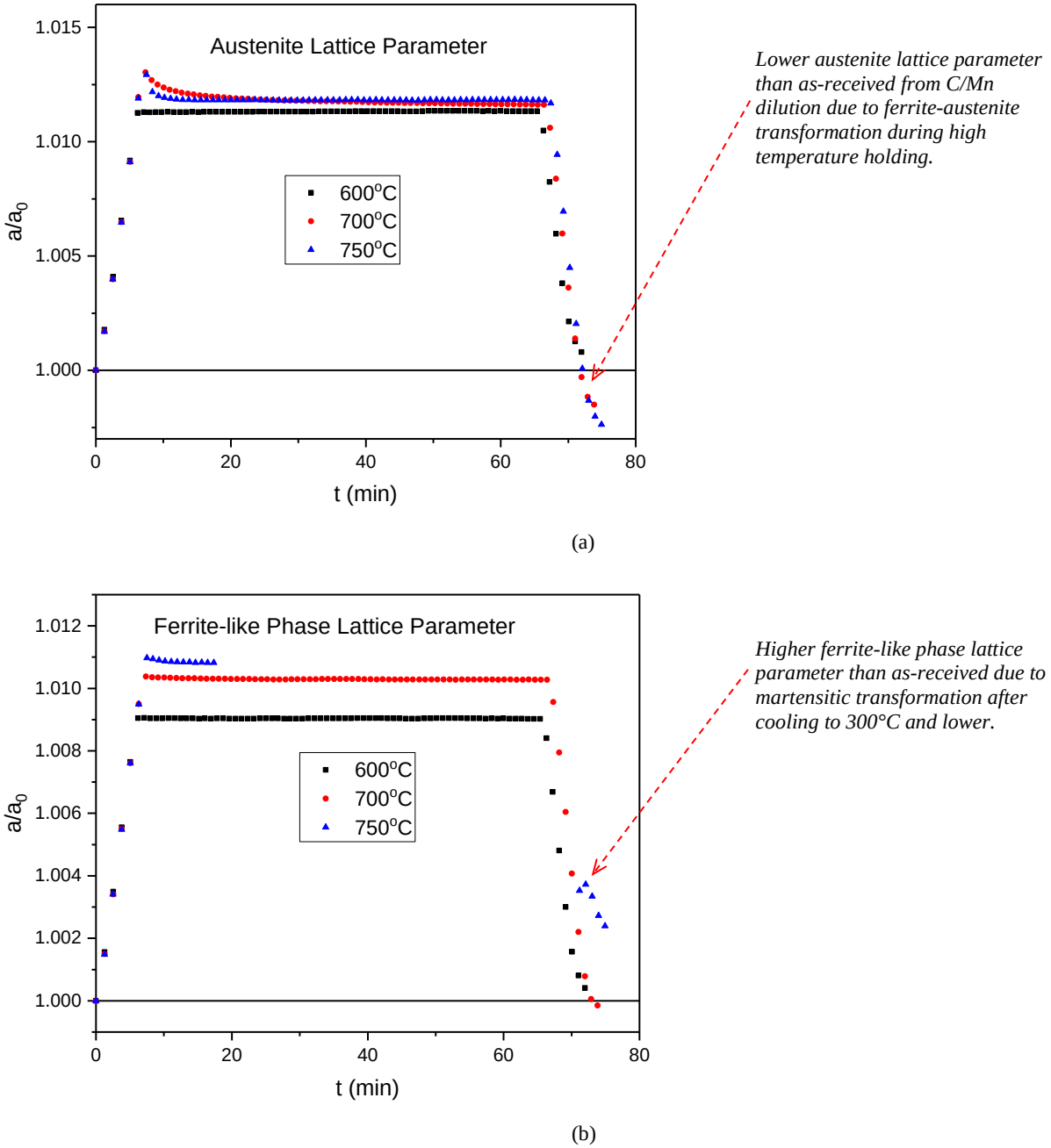

Figure II.1.A.3.5. The results of normalized lattice parameter variation with time for *in-situ* HEXRD heat-treatment experiments of a 7 Mn steel with four IA temperatures for: (a) austenite; and (b) ferrite-like phase.

Similar phenomenon seen in 7-Mn steel for the phase transformation and lattice parameter changes are observed in 10 Mn steel, as shown in Figure II.1.A.3.6 and Figure II.1.A.3.7. The quantitative values, however, are different. The case for T_h=650°C of 10 Mn steel is similar to T_h=600°C of 7 Mn steel, where the austenite volume fraction increases with temperature during heating, decreases with temperature during cooling, and have similar volume fractions as the received condition after cooling down to room temperature. The cases for T_h=700°C and 750°C of 10 Mn steel are similar to T_h=650°C and 700°C of 7 Mn steel. When T_h=750°C, the austenite volume fraction of austenite reaches at 92% and slightly reduces to 89% after cooling to room temperature. The lattice strain of austenite is quite lower than as-received due to reduced C and Mn content due to the dilution from the ferrite-austenite transformation during holding. The 10 Mn steel is almost fully austenized during holding at 800°C, with a tiny amount of remaining ferrite. During cooling, no transformation from austenite to ferrite happens only after the temperature is reduced to 150°C, as shown in Figure II.1.A.3.6(b), which sees a sudden jump of lattice parameter of ferrite-like phase, as shown in Figure II.1.A.3.7(b).

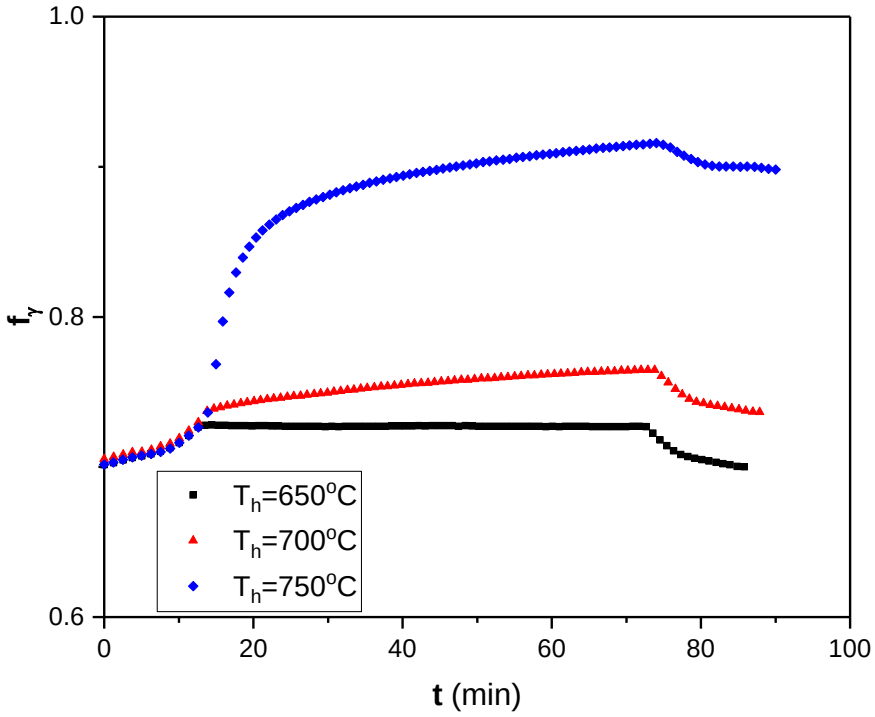

(a)

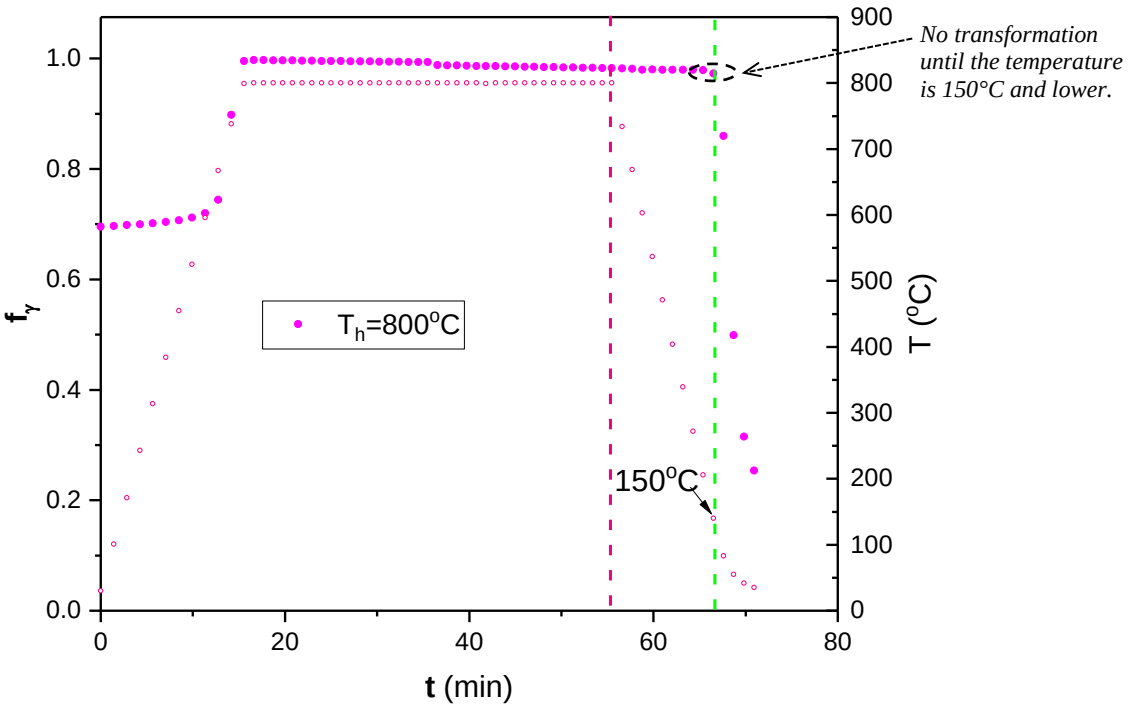

(b)

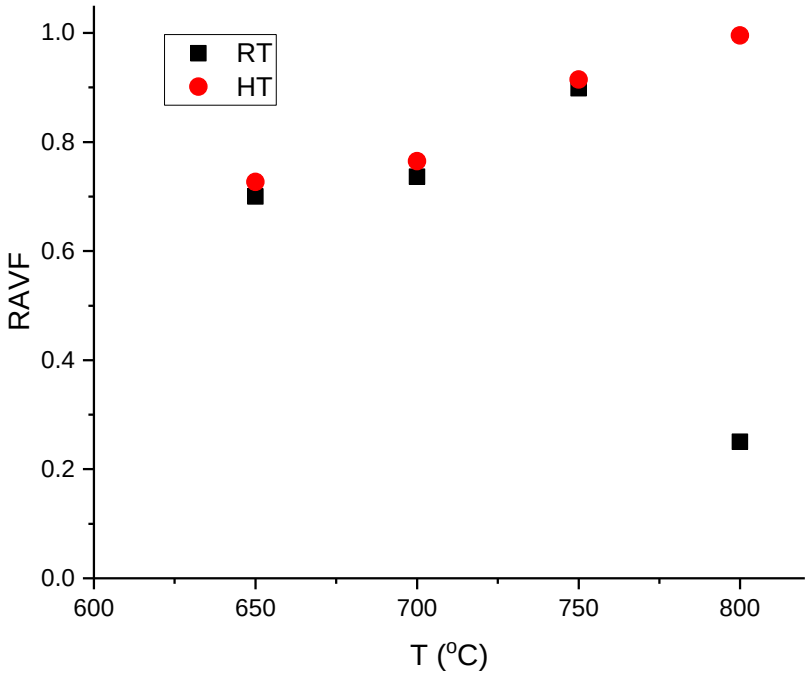

(c)

Figure II.1.A.3.6. The results for in-situ HEXRD heat-treatment experiments of a 10 Mn steel with 4 IA temperatures: (a) and (b) austenite volume fraction changes with time; and (c) maximum austenite volume fraction at high temperatures (HT) and the retained austenite volume fraction (RAVF) when it is cooled down to room temperature (RT).

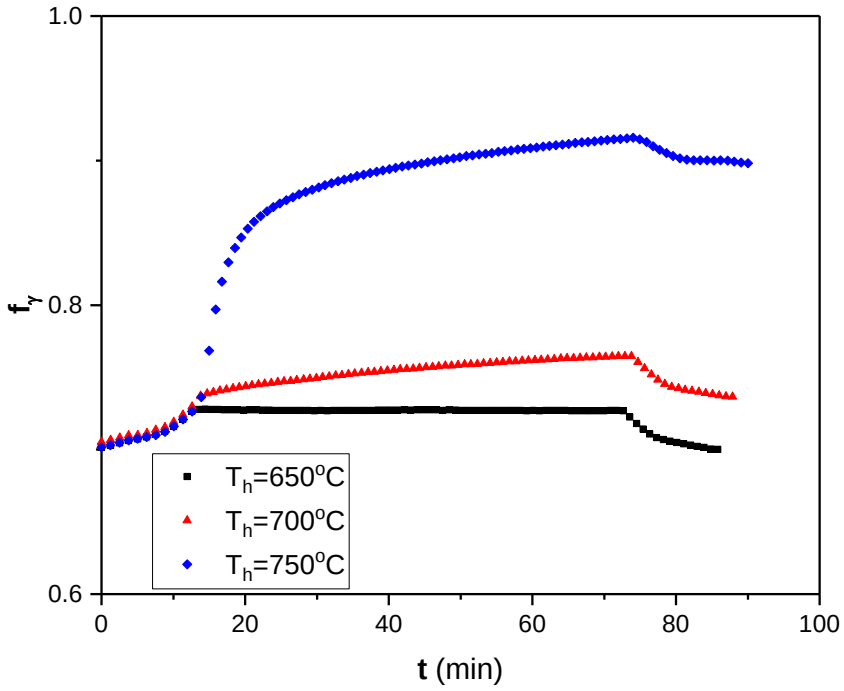

(a)

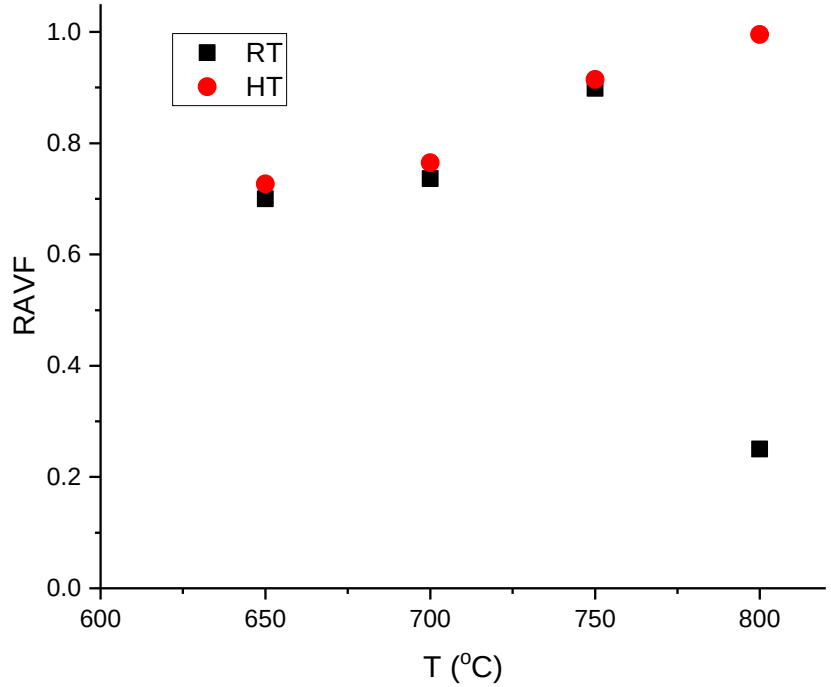

(b)

Figure II.1.A.3.7. The results of normalized lattice parameter variation with time for *in-situ* HEXRD heat-treatment experiments of a 7 Mn steel with four IA temperatures for: (a) austenite; and (b) ferrite-like phase where a/a0 is the ratio of the lattice parameters.

It should be noted that all of the data obtained from *in-situ* HEXRD heat-treatment experiments for austenite volume fraction and lattice distortion data cannot be obtained in alternative approaches and will provide comprehensive data for the validation and determination of thermodynamic parameters with thermodynamics-based, phase-field-based, and microstructure-based models.

Apart from the *in-situ* HEXRD experiments, dilatometry experiments are also performed by the use of similar heating and cooling cycles for comparison. Figure II.1.A.3.8 shows the examples for 7 Mn steel with holding temperatures to be 600°C and 700°C, respectively. The former shows a much smaller volume decrease than the latter, which is consistent with the HEXRD results showing a much faster ferrite/martensite to austenite transformation, while holding at 700°C, as shown in Figure II.1.A.3.4.

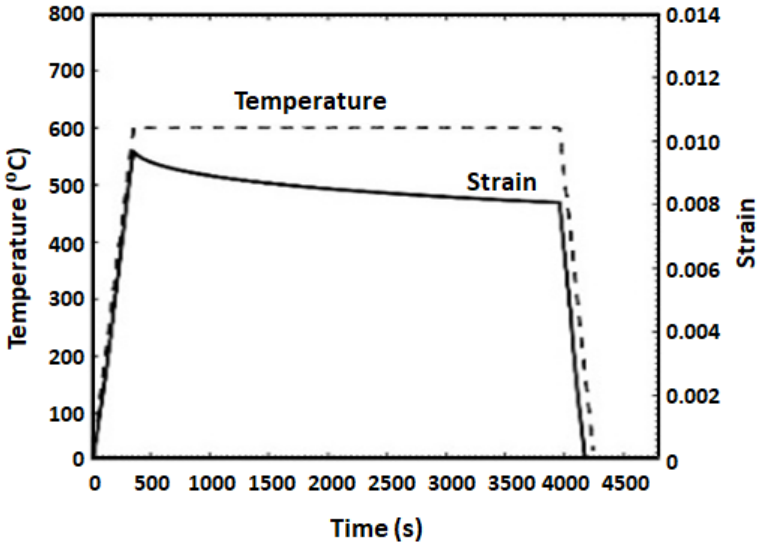

(a)

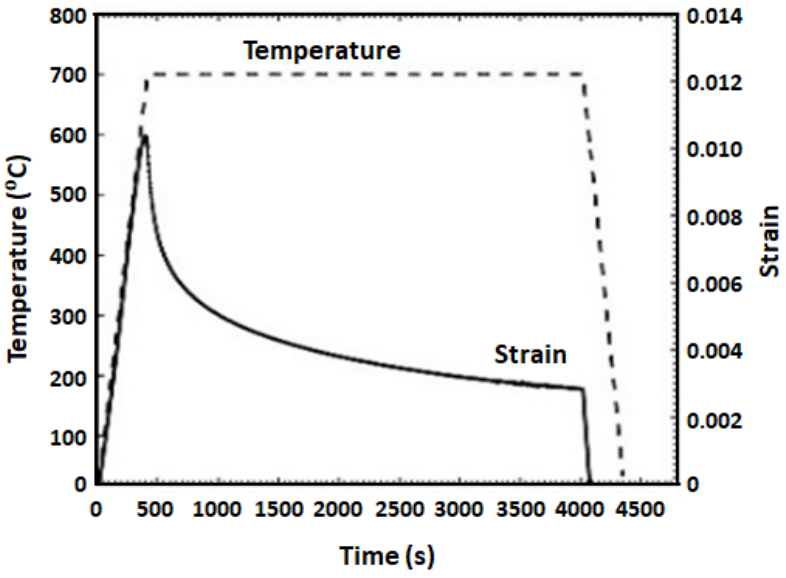

(b)

Figure II.1.A.3.8. The dilatometry results for 7 Mn steels with the use of similar IA cycles with HEXRD: (a) T_h=600°C; and (b) T_h=700°C.

DICTRA was used to model austenite growth during IA. Simulations were conducted to compare how some variables relevant to IA of medium Mn steels affected the simulation results. The simulation work was presented at the Materials Science and Technology 2017 Conference in Pittsburgh, PA, and published in its conference proceedings (Zhao 2014). All simulations were conducted with a moving interface to simulate austenite film growth during IA. The thermodynamic and mobility databases used for all simulations are TCS Steels/Fe-Alloys Database, Version 8.0 (TCFE8) and TCS Steels/Fe-Alloys Mobility Database, Version 3 (MOBFE3), respectively. All simulations consider an isothermal hold at an annealing temperature of 650°C for 0.2C-5Mn steel.

The first simulation considers austenite film growth from an initial microstructure prior to IA consisting of martensite with inter-lath austenite films. The width of a martensite lath is assumed to be 400 nm (Roberts 1970), while the width of the retained austenite film was calculated by estimating the fraction of martensite formation upon cooling to room temperature from the fully austenitic region using and assuming the untransformed fraction to be retained austenite. The extent of martensite formation upon cooling to room temperature was calculated with the Koistinen-Marburger equation (Koistinen and Marburger 1959). Half-widths of the dimensions for martensite and austenite are used in the DICTRA simulations to reflect identical growth of the austenite film in two directions. Calculated half-widths for martensite and austenite in the initial microstructure are 200 nm and 10 nm, respectively.

The second simulation uses the same initial microstructure as the first, but also considers the effect of increased Mn mobility. While the initial microstructure is assumed to be martensite and austenite, DICTRA databases do not presently have mobility data for martensite. The simulations in this report, as well as several others (Kamoutsi et al. 2015, De Moor et al. 2015, Wei et al. 2013, Dmitrieva et al. 2011), model martensite as ferrite when using DICTRA. However, it has been suggested that the mobility of Mn in martensite is significantly greater than in ferrite due to the high defect density present in martensite (De Moor et al. 2015, Dmitrieva et al. 2011). To overcome this, DICTRA allows the user to apply a mobility enhancement factor (MEF) to a species in a phase. In a study by Dmitrieva et al. (2011), it was found that for a DICTRA model to corroborate with atom probe tomography results for austenite film growth in a 12 wt. % Mn managing-TRIP steel aged at 450°C, a MEF of 45 was required to be applied to the mobility of Mn in ferrite. Figure II.1.A.3.9 shows the predicted carbon and Mn concentration profiles along the distance of the simulation cell after annealing times of 0.001 s, 1,000 s, and 1,000,000 s for the first and second simulations. Figure II.1.A.3.10 shows predicted austenite growth during IA plotted against anneal time for both simulations.

The progression of the composition profiles with increased annealing times indicates two regimes of austenite growth—pararequilibrium partitioning (PP) growth followed by equilibrium partitioning (EP) growth. At very short annealing times, the austenite grows from only C partitioning during PP growth, creating a region of austenite that has no Mn enrichment (Note the initial austenite film width is 10 nm). During intermediate annealing times, austenite growth occurs from equilibrium Mn partitioning; however, the low mobility of Mn in austenite prohibits the development of a homogenous Mn concentration profile in the austenite. After very long annealing times, the Mn profile is predicted to equilibrate in the austenite, which is accompanied by a slight decrease in austenite fraction. The paraequilibrium and equilibrium growth regimes are also identified in Figure II.1.A.3.10 (Note the initial fraction of austenite upon annealing is 0.048). The second simulation (e.g., MEF of 45) predicts a substantial decrease in anneal time required to reach the EP growth regime.

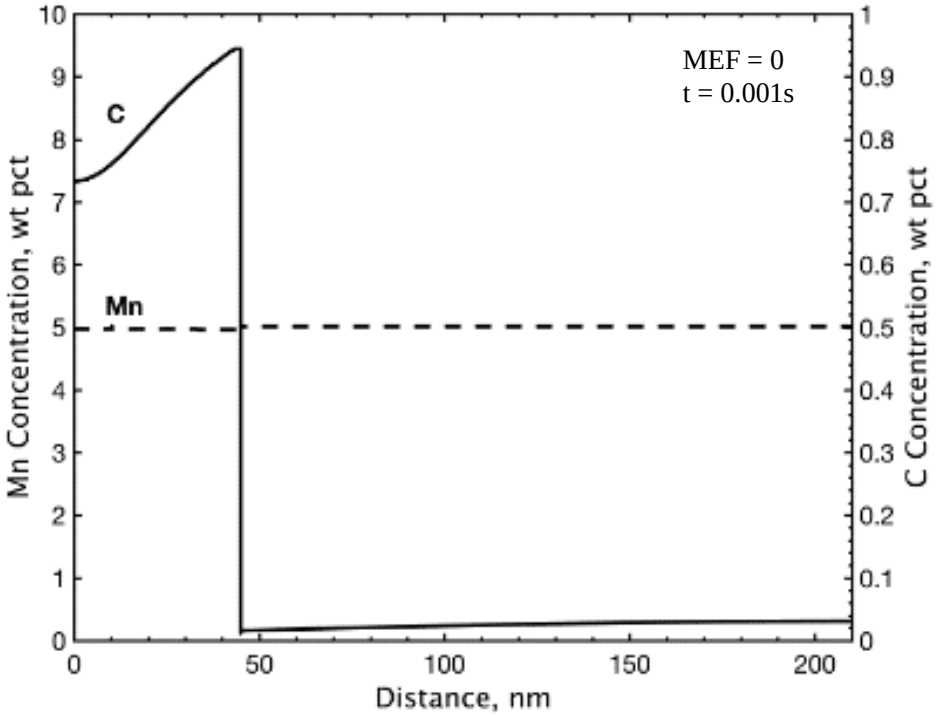
MEF = 0
t = 0.001s
C
Mn
Mn Concentration, wt pct
C Concentration, wt pct
Distance, nm
0
50
100
150
200
0
1
2
3
4
5
6
7
8
9
10
0.1
0.2
0.3
0.4
0.5
0.6
0.7
0.8
0.9

(a)

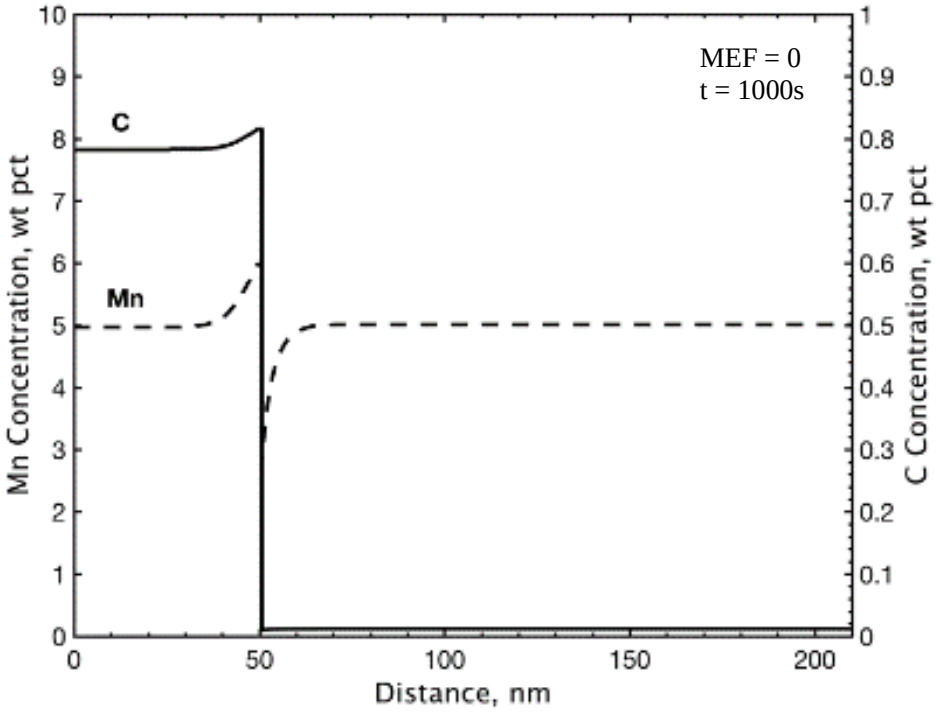
MEF = 0
t = 1000s
C
Mn
Mn Concentration, wt pct
C Concentration, wt pct
Distance, nm
0
50
100
150
200
0
1
2
3
4
5
6
7
8
9
10
0.1
0.2
0.3
0.4
0.5
0.6
0.7
0.8
0.9

(b)

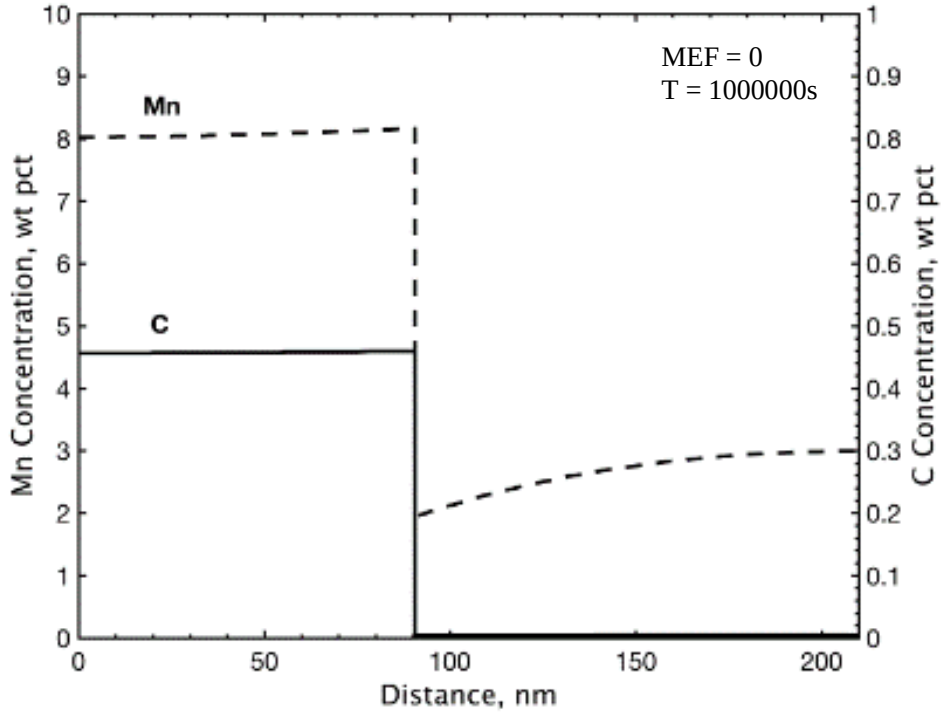
MEF = 0
T = 1000000s
Mn
C
Mn Concentration, wt pct
C Concentration, wt pct
Distance, nm
0
50
100
150
200
0
1
2
3
4
5
6
7
8
9
10
0.1
0.2
0.3
0.4
0.5
0.6
0.7
0.8
0.9

(c)

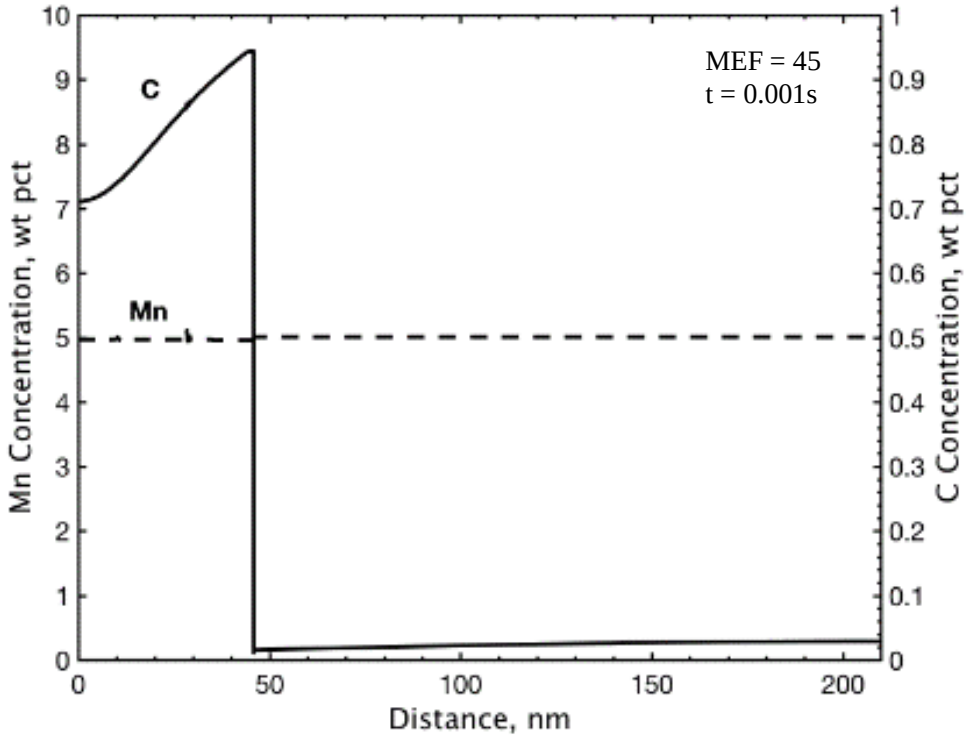
MEF = 45
t = 0.001s
C
Mn
Mn Concentration, wt pct
C Concentration, wt pct
Distance, nm
0
50
100
150
200
0
1
2
3
4
5
6
7
8
9
10
0.1
0.2
0.3
0.4
0.5
0.6
0.7
0.8
0.9

(d)

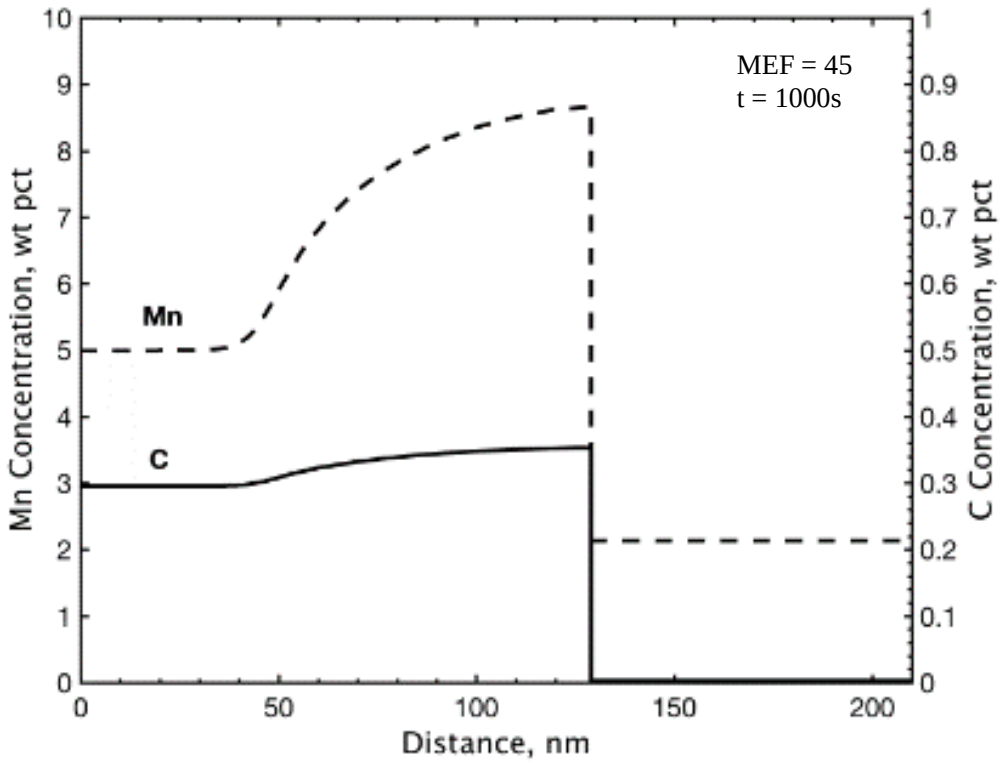

(e)

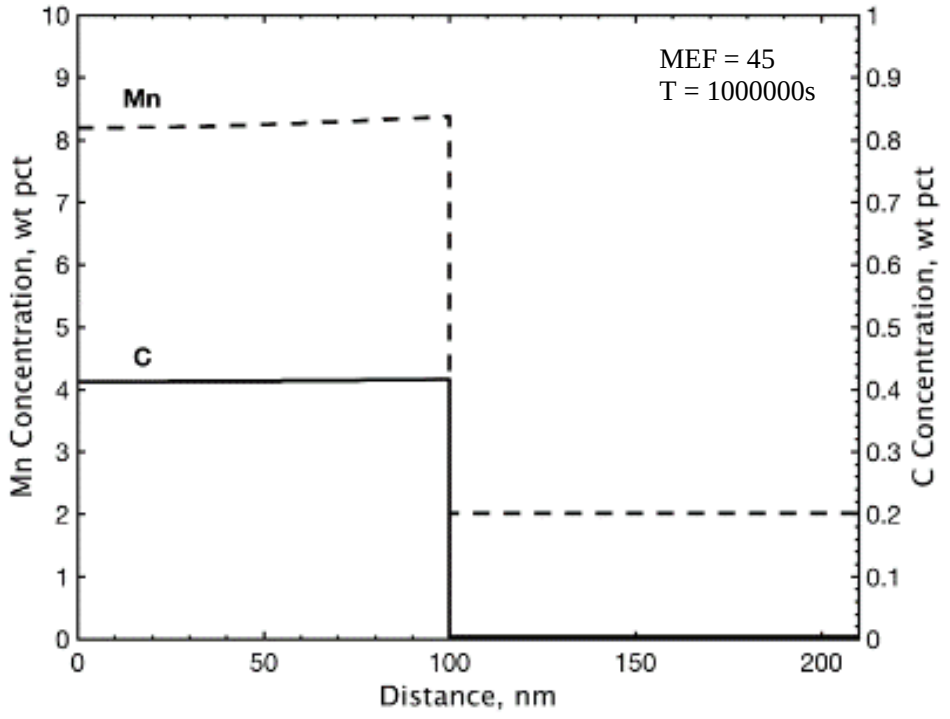

(f)

Figure II.1.A.3.9. (a)-(f) Predicted C and Mn concentration profiles along the distance of the simulation cell after anneal times of 0.001 s, 1,000 s, and 1,000,000 s for simulations without a MEF and with a MEF of 45 for Mn in ferrite.

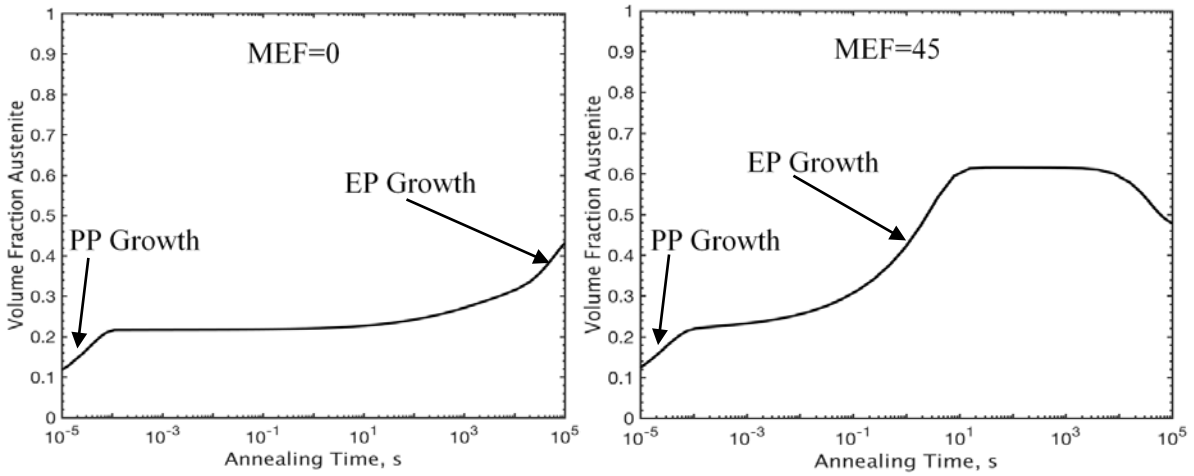

Figure II.1.A.3.10. Austenite volume fraction plotted against annealing time without any MEF (left) and with a MEF of 45 for Mn (right) in ferrite.

The third simulation is identical to the second, but also considers the effect of cementite precipitation and carbon partitioning upon heating. The first and second simulations consider the solute concentration to be identical in the initial austenite and ferrite (e.g., martensite). However, it is not unreasonable to consider processes that alter the carbon concentration profile during heating to the annealing temperature. Carbon partitioning from martensite to austenite and carbide precipitation in martensite during heating are two processes that are presently considered. Carbon partitioning during heating would increase the carbon concentration in the austenite upon IA, while carbide precipitation in the martensite would reduce the solute carbon available to partition to the austenite during IA until carbide dissolution takes place. An IA simulation was conducted to approximate these effects. The simulation includes a MEF of 45 for Mn in ferrite and considers initial solute carbon concentrations in the austenite and martensite to be 0.95 wt. % and 0.01 wt. %, respectively. Figure II.1.A.3.11 shows the predicted carbon and Mn concentration profiles along the distance of the simulation cell after annealing times of 0.001 s, 1,000 s, and 1,000,000 s. Figure II.1.A.3.12(a) shows predicted austenite growth during IA plotted against annealing time.

The progression of the concentration profiles during IA exhibits only EP growth. At very short annealing times, the austenite growth is negligible due to the lack of solute carbon available in the martensite. During intermediate annealing times, austenite growth occurs by equilibrium Mn partitioning. After very long annealing times, the Mn profile is predicted to equilibrate in the austenite, which is accompanied by a slight decrease in austenite fraction. Because the PP growth region is essentially nonexistent, there is little development of a Mn deficient region in the austenite. The predicted austenite growth during IA shown in Figure II.1.A.3.12(a) also does not exhibit two-regime growth, as seen in Figure II.1.A.3.10. Because EP growth occurs without prior PP growth, the maximum amount of austenite formed during annealing is reduced, compared to the predictions shown in Figure II.1.A.3.10.

The third simulation shows good agreement with experimental observations. Figure II.1.A.3.12(b) shows the predicted retained austenite content from the third DICTRA simulation, as well as experimentally observed retained austenite content from similar IA medium-Mn steels. Currently, IA is being conducted of 0.2C-5 Mn steel specimens via dilatometer so that the predicted retained austenite content for increasing annealing times can be compared to experimental observations.

Future simulations will directly include the presence of cementite, as well as the heating portion of thermal processing (current models only consider the isothermal anneal). Phase-field modelling will also be conducted, which will predict a microstructure and provide a picture of a simulated microstructure.

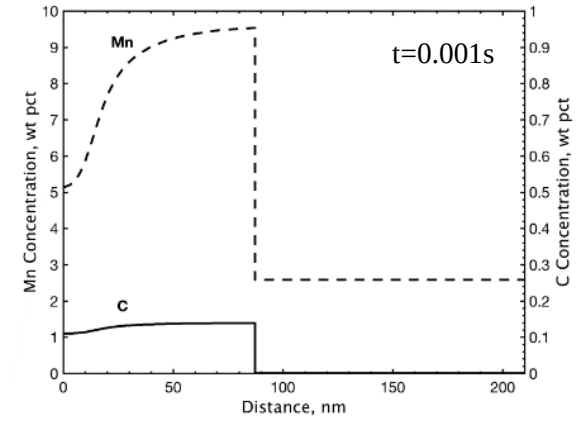

(a)

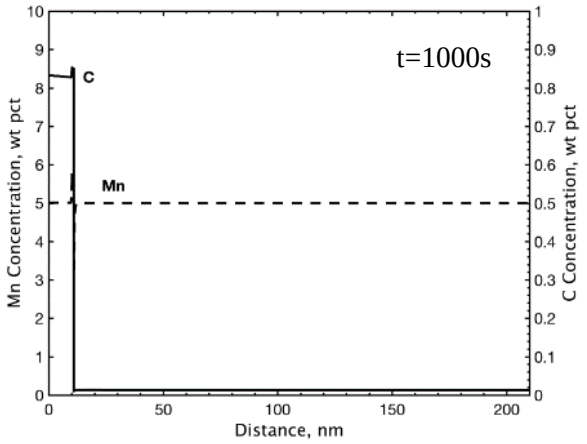

(b)

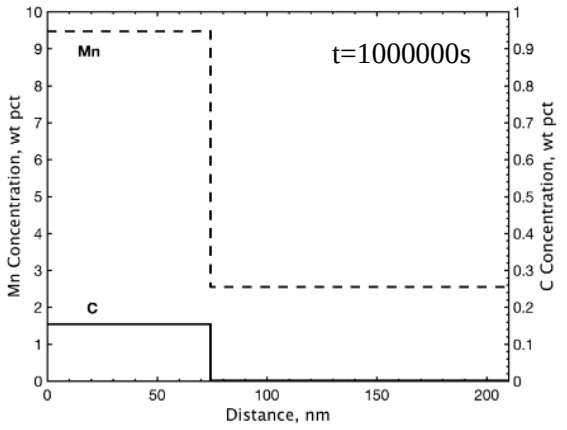

(c)

Figure II.1.A.3.11. (a)-(c) Predicted carbon and Mn concentration profiles along the distance of the simulation cell after anneal times of 0.001 s, 1,000 s, and 1,000,000 s for a simulation with a MEF of 45 for Mn in ferrite and initial solute carbon concentrations in the austenite and martensite to be 0.95 wt. % and 0.01 wt. %, respectively.

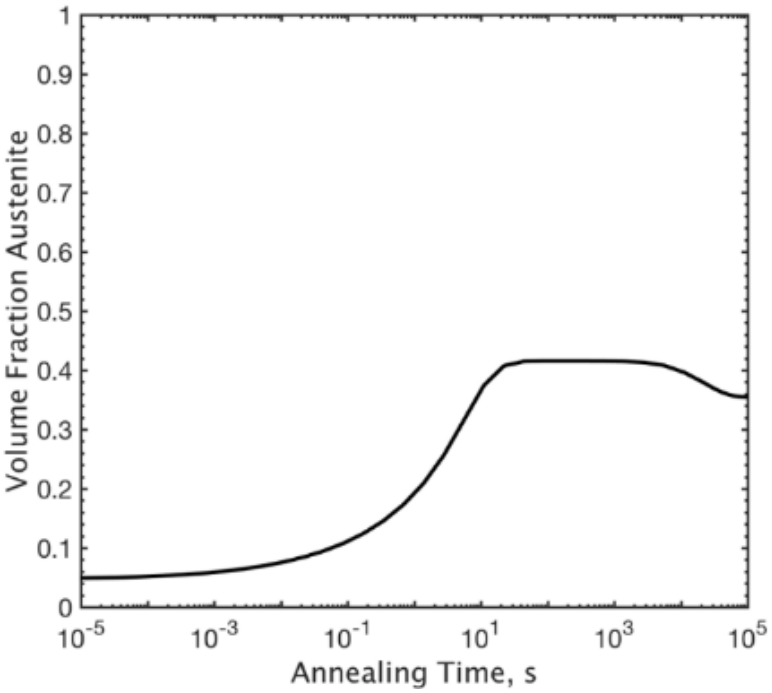

(a)

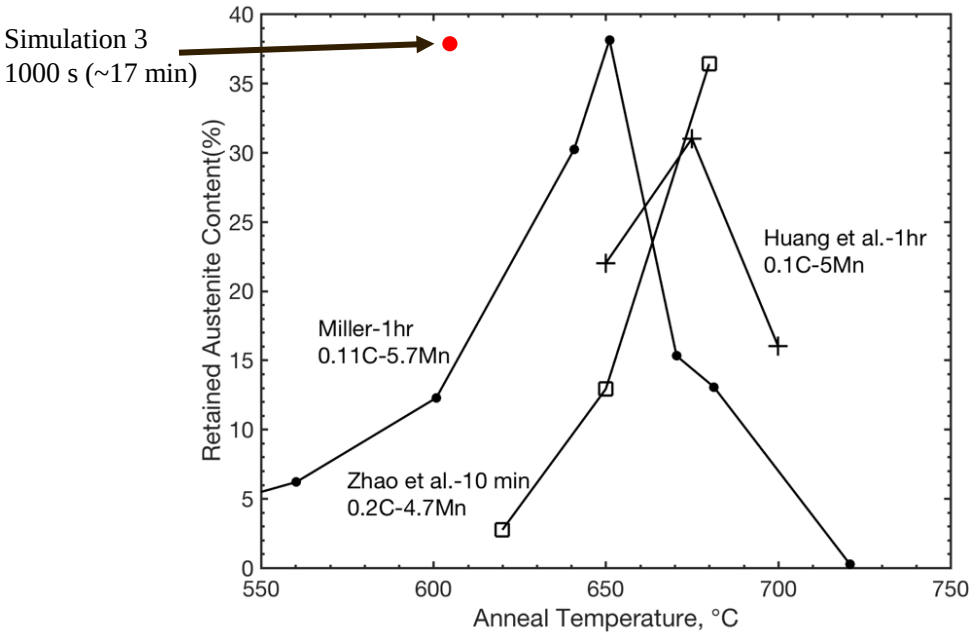

(b)

Figure II.1.A.3.12. (a) Austenite volume fraction plotted against annealing time for a simulation with a MEF of 45 for Mn in ferrite and initial solute carbon concentrations in the austenite and martensite to be 0.95 wt. % and 0.01 wt. %, respectively; and (b) Experimentally observed retained austenite content plotted against IA temperature. Prediction from third DICTRA™ simulation is included for comparison (Zhao et al. 2014, Miller 1972, and Huang et al. 1974).

Conclusions

Medium Mn TRIP steel was selected as the model steel for the development of an integrated experimental and modeling framework in optimizing the heat-treatment parameters for third generation AHSS. Once developed, the proposed work will not only gain predictive understanding in the phase transformation and diffusion processes during IA process for medium Mn steels, but it is also expected to provide a general capability in high-throughput characterization and prediction of evolving phase boundaries and carbon concentration gradients during other thermomechanical processes, such as the quenching and partitioning process.

References

Abu-Farha, F., X. H. Hu, Y. Ren, X. Sun, L. G. Hector, G. Thomas, and T. W. Brown, 2017, "In-situ local measurement of austenite mechanical stability and transformation behavior in third generation advanced high strength steels." *Metallurgical and Materials Transactions A*, in press.

Choi, K. S., W. N. Liu, X. Sun, M. A. Khaleel, Y. Ren, and Y. D. Wang, 2008, "Advanced micromechanical model for transformation-induced plasticity steels with application of in-situ high-energy x-ray diffraction," *Metallurgical and Materials Transactions A*, Vol. 39A, No. 13, pp. 3089–3096.

Choi, K. S., A. Soulami, W. N. Liu, X. Sun, and M. A. Khaleel, 2010, "Influence of various material design parameters on deformation behaviors of TRIP steels." *Computational Materials Science*, Vol. 50, No. 2, pp. 720–730.

De Moor, E., S. G. Kang, J. G. Speer, and D. K. Matlock, 2015. "Manganese diffusion in third generation advanced high strength steels," International Conference on Mining, Material, and Metallurgical Engineering, Singapore, SG (March).

Dmitrieva, O., D. Ponge, G. Inden, J. Millàn, P. Choi, J. Sietsma, and D. Raabe, 2011, "Chemical gradients across phase boundaries between martensite and austenite in steel studied by atom probe tomography and simulation." *Acta Materialia*, Vol. 59, No. 1, pp. 364–374.

Han, J., A. K. da Silva, D. Ponge, D. Raabe, S. M. Lee, Y. K. Lee, S. I. Lee, and B. Hwang, 2017, "The effects of prior austenite grain boundaries and microstructural morphology on the impact toughness of intercritically annealed medium Mn steel." *Acta Materialia*, Vol. 122, pp. 199–206.

Hu, X. H., K. S. Choi, X. Sun, Y. Ren, and Y. D. Wang, 2016, "Determining individual phase flow properties in a Quench and Partitioning steel with in-situ high energy X-ray diffraction and multi-phase elasto-plastic self-consistent method." *Metallurgical and Materials Transactions A*, Vol. 47, No. 12, pp. 5733–5749.

Hu, X. H., X. Sun, J. Hector, and Y. Ren, 2017, Individual phase constitutive properties of a TRIP-assisted QP980 steel from a combined synchrotron X-ray diffraction and crystal plasticity approach, *Acta Materialia*, Vol. 132, pp. 230–244.

Huang, H., O. Matsumura, and T. Furukawa, 1994, "Retained austenite in low carbon, manganese steel after intercritical heat-treatment." *Materials Science and Technology*, Vol. 10, No. 7, pp. 621–626.

Kamoutsi, H., E. Gioti, G. N. Haidemenopoulos, Z. Cai, and H. Ding, 2015, "Kinetics of solute partitioning during intercritical annealing of a medium-Mn steel." *Metallurgical and Materials Transactions A*, Vol. 46, No. 11, pp. 4841–4846.

Koistinen, D., and R. Marburger, 1959, "A general equation prescribing the extent of the austenite-martensite transformation in pure iron-carbon alloys and plain carbon steels." *Acta Metallurgica*, Vol. 7, No. 1, pp. 59–60.

Miller, R. L., 1973, "Ultrafine-grained microstructures and mechanical properties of alloy-steels." *Metallurgical Transactions*, Vol. 3, No. 4, pp. 905–912.

Muller, J. J., and E. De Moor, 2017, "Austenite growth and retention simulations in inter-critically annealed medium manganese steels." *Materials Science & Technology*, October 8–12, Pittsburgh, PA, USA.

Roberts, M. J., 1970, "Effect of transformation substructure on the strength and toughness of Fe−Mn alloys." *Metallurgical Transactions*, Vol. 1, No. 12, pp. 3287–3294.

Wei, R., M. Enomoto, R. Hadian, H. S. Zurob, and G. R. Purdy, 2013, "Growth of austenite from as-quenched martensite during inter-critical annealing in an Fe–0.1C–3Mn–1.5Si alloy." *Acta Materialia*, Vol. 61, No. 2, pp. 697–707.

Zhao, C., W. Cao, C. Zhang, Z. Yang, H. Dong, and Y. Weng, 2014, "Effect of annealing temperature and time on microstructure evolution of 0·2C–5Mn steel during intercritical annealing process." *Materials Science and Technology*, Vol. 30, No. 7, pp. 791–799.

II.1.A.4 Room Temperature Stamping of High-Strength Al Alloys

Aashish Rohatgi, Principal Investigator
Pacific Northwest National Laboratory
902 Battelle Blvd.
Richland, WA 99352
Phone: 509-372-6047
E-mail: aashish.rohati@pnnl.gov

Project Introduction

This project is addressing the challenge that Al sheet alloys possess limited formability at room temperature and under high-strength conditions; i.e., it is difficult to stamp a high-strength Al sheet at room temperature into a structural component with complicated geometry because the sheet is unable to deform uniformly, thereby leading to cracks during forming/stamping. Room temperature formability of Al alloys is further lowered if they are stamped in high-strength condition. Warm/hot-forming can increase the formability of Al, but is expensive due to the added costs of heated dies, forming lubricants, lubricant clean-up, etc. Unlike hot-stamped steels that undergo austenite to martensite phase transformation during quenching and achieve high-strength at the end of the stamping process itself, Al alloy matrix does not undergo such phase transformation upon quenching. Hence, warm/hot-forming results in lower post-formed strength, such as heat-treatment in addition to paint-bake, is needed (adding cost) to regain the strength. Thus, the use of Al sheet is limited to lower-strength Al alloys and simple shapes (e.g., hood, deck lids, door inner, etc.) and many sheet components are still stamped in steel in the high-volume automotive industry. As such, the ability to form high-strength Al alloys cost effectively, such as at room temperature, will expand Al use for structural components as well (e.g., crash beams, B-pillars, etc.) and has the potential to result in significant lightweighting.

Accomplishments

- Surveyed technical literature and identified potential components that could provide weight savings if made of high-strength Al alloys (FY 2017).
- Investigated the formability of Al 7075 alloy sheet and performed finite element modeling to evaluate the effect of friction on formability (FY 2017).

Technology Assessment

- Target: Develop a cost-effective forming approach that can simultaneously achieve high formability and high-strength (ultimate tensile strength ~600 MPa) in Al alloys.
- Gap: High-strength Al alloys have poor formability at room temperature.
- Gap: Warm/hot-forming can increase formability, but at the expense of increased component cost and lower strength.

Approach

This project aims to develop processing techniques that will overcome the formability limitations of high-strength Al alloys and enable their room temperature forming. Thus, we will focus on understanding the microstructure-formability-strength interplay in high-strength Al alloys with the expectation that microstructural control during processing could enable sufficient formability and strength in the formed part. The project is structured to be performed in three phases over a duration of three years.

In the first phase of the project in FY 2017, we will perform a qualitative assessment of the commercial potential of stamped high-strength 7xxx Al alloys. This involves a survey of literature and discussions with

industry partners to identify potential components that, if made of high-strength Al, will provide sufficient weight savings relative to high-strength steel.

In the second phase of the project in FY 2017–2018, we will determine the feasibility of achieving both high-strength and room temperature formability in high-strength Al alloys for a selected automotive component. This will involve identifying high-strength Al alloys and determining their strengthening potential and formability in different temper conditions. Solutionization and aging heat-treatments will be performed to determine the aging behavior; quasi-static tension tests will be performed to determine the stress-strain curves; and limiting dome height (LDH) tests will be performed to determine the forming limit diagrams for the selected alloy(s). This data will be used to determine the constitutive relations that can then be used as an input to the models to perform stamping simulations and ascertain the feasibility of room temperature forming of the selected component.

In the third phase of the project in FY 2018–FY 2019, we will develop microstructure and mechanical property models of the selected high-strength Al alloy. Microstructural evolution (e.g., precipitation kinetics) during aging will be determined. Analytical models from the literature will be used to correlate microstructural evolution (e.g., precipitation nucleation and growth) and mechanical properties (e.g., strength and fracture) to understand the resulting strength and formability of the alloy. The models, in turn, will guide the stamping approach. We will work with industry partners to design a die and stamp a prototypical component in 7xxx Al alloy at room temperature. The stamped component will be characterized for formability and strength to evaluate our stamping approach towards meeting the target properties.

Technology Transfer Path

While the technology for stamping Al alloys exists commercially, the main hurdle in greater implementation of high-strength Al alloys is the lack of cost-effective approaches that can achieve the desired formability and strength in the post-formed part. Therefore, this project will develop and transfer to industry, the understanding of the microstructure-formability-strength correlation in high-strength Al alloys. Industry partners will guide the selection and design of a prototype component of interest to them and PNNL will guide the materials processing to achieve the required combination of formability and strength. Finally, we will work with OEM and tier-1 industry partners to design the die and stamp a prototypical part to validate the approach developed in this project.

Results

The project started in FY 2017. In the first phase, several industry reports and recently published literature (on the use of Al sheet components for automotive lightweighting) were reviewed (Lotus Engineering Inc. 2010, Lutsey 2010, Skszek et al. 2015, Plourde et al. 2015, Kerns et al. 2015) to understand the potential of the use of high-strength Al alloys. We conclude that while the 5xxx or 6xxx Al alloys are typically used for Al automotive components, the use of high-strength 7xxx alloys is only starting to appear. For example, an AA7075-type proprietary Al alloy has been used to warm-form (at 200°C) a side impact beam (Austria Metal AG 2014). In another recent example, a light-weight door was designed and fabricated using warm-formed 7xxx Al for the door beam and cold-stamped 5xxx and 6xxx Al for the inner and outer panels, respectively (Reaburn 2017). Thus, it appears that while the automotive industry has made efforts to incorporate high-strength 7xxx (or their variants) Al alloys as a replacement for steel in structural components, these high-strength Al components are typically produced by warm-forming. Two commercial compositions, AA7075 and AA7055, have typically been used or cited as the alloys when demonstrating a processing technology suitable for high-strength 7xxx Al alloys. Of these, AA7075 was found to be most easily commercially-available in automotive relevant thickness, and is a good representative of the limited room temperature formability of high-strength Al alloys, as well. Therefore, AA7075 Al was selected as the test material for this project and a T6 temper, 2.5 mm thick sample was purchased from a commercial vendor. Table II.1.A.4.1 shows the handbook composition of AA7075 alloy.

Table II.1.A.4.1. Standard composition in wt. % of AA7075 Al alloy (Davis 1993).

Si	Fe	Cu	Mn	Mg	Cr	Zn	Ti	Others (Total)	Al
0.40	0.50	1.2 - 2.0	0.30	2.1 - 2.9	0.18 - 0.28	5.1 - 6.1	0.20	0.15	Balance

The as-received AA7075 Al (T6 temper) was machined into ASTM-E8 specimen geometry and tested in quasi-static tension to establish the baseline stress-strain behavior. Figure II.1.A.4.1 shows the resulting stress-strain curves measured along different in-plane directions. The stress-strain curves indicate that the sheet is fairly isotropic in the in-plane directions. The average yield and ultimate tensile strength are 515 MPa and 575 MPa, respectively, while the average strain to failure is ~13%.

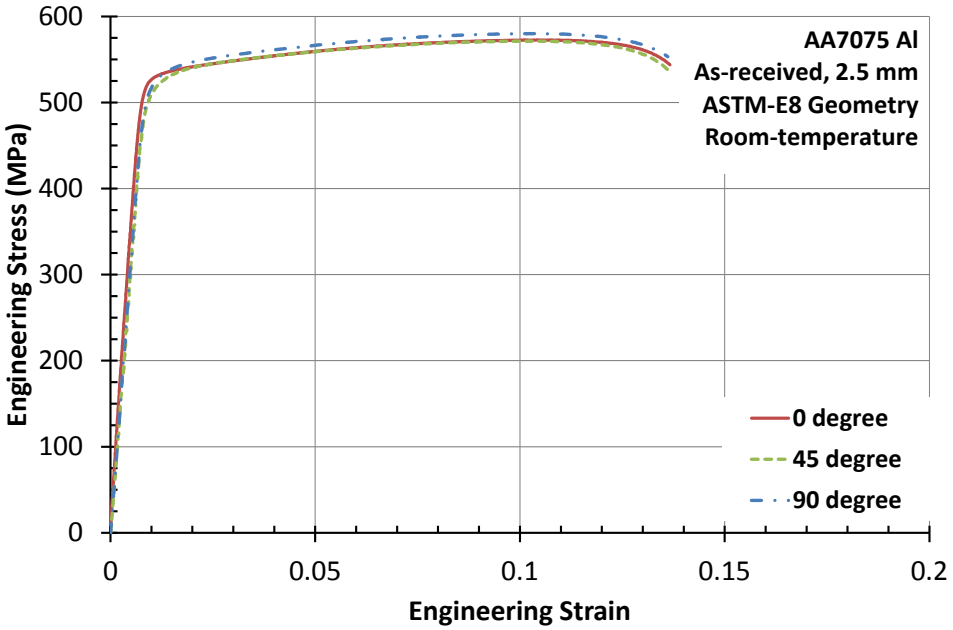

Figure II.1.A.4.1. Quasi-static stress-strain curves for as-received AA7075 Al (T6 temper) tensile tested at room temperature. 0 and 90 degree in the legend refer to the sheet rolling and transverse directions, respectively.

Test coupons of as-received materials were solutionized at 480°C for 40 minutes and given different tempering treatments. Figure II.1.A.4.2 shows the hardness evolution of the material when it was allowed to naturally age at room temperature. The natural aging curve shows that this alloy rapidly hardens at room temperature within a matter of several hours and subsequently, the rate of hardening slows down. Such age-hardening characteristics of the 7075 Al is indicative of the important role of precipitation strengthening in the 7xxx Al alloys—the Al-Zn-Mg-Cu system, together with small amounts of Cr and Mn, result in the highest strength Al-base alloys commercially available. The Zn and Mg control the aging process, while Cu increases the aging rate by increasing the degree of supersaturation (during solutionizing) and perhaps through nucleation of the Cu-Mg-Al_2 phase (Davis 1993). The precipitation sequence in the 7xxx Al alloys (e.g., 7075 Al) typically involves the formation of Guinier-Preston (GP) zones, followed by coherent precipitates (η') that are then followed by stable, incoherent precipitates (η) (Totten and Mackenzie 2003). Peak strength is associated with the GP zones and coherent precipitates, while the subsequent decrease in strength upon over-aging is attributed to the loss of coherency of the precipitates. Thus, the strength and ductility in 7075 Al (or 7xxx Al alloys, in general) can be understood and controlled through an understanding of the interplay between the solutes, precipitate volume fraction, and precipitation sequence.

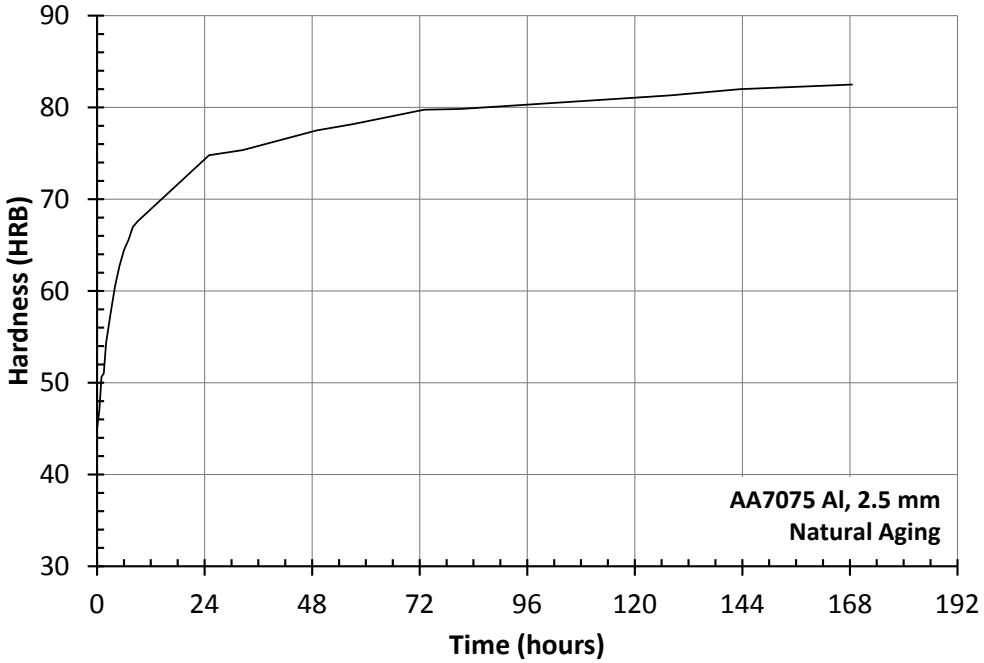

Figure II.1.A.4.2. Natural aging curve of AA7075 Al showing the hardness evolution (Rockwell B scale) following solutionization and quenching.

The formability of 7075 Al was investigated through limiting LDH tests using a 4-in. diameter hemispherical punch. The as-received material was heat-treated to produce various tempers, and then sheared into rectangular coupons for LDH tests. Results are being analyzed and will be reported at a future time.

Considering that friction plays an important role during the stamping operation, the experimental work was complemented by a FE modeling study to understand the role of friction in influencing formability. Commercial FE software LS-DYNA was used to simulate the LDH tests using shell elements for the Al blanks and selecting a friction coefficient between the Al coupon and the steel punch of 0.3 (high friction) or 0.08 (low friction). The stress-strain data for a selected temper and measured along three directions (rolling direction, 45° and 90°), was used as an input to simulate the plastic deformation of the blanks. Different failure criteria have been used in the literature. For example, one study used a stress-based criterion to identify localization/necking and predict the forming limit diagram (FLD) of AA2014 Al alloy (Kumar et al. 2016). In another study, an approach based on the Hutchinson-Neale model taking into account the strain rate sensitivity was used (Părăianu et al. 2017). Using complex plasticity and failure models, such as those discussed in the literature, to predict the FLD require a large number of experiments to determine multiple "calibration" parameters (Părăianu et al. 2017). Therefore, for the sake of simplicity, we adopted a strain-based criterion to track localization and used the maximum equivalent plastic-strain during tension as the limit strain criterion to demarcate the "safe" and "unsafe" (i.e., necking) regions of the FLD. Thus, quasi-static stress-strain curves, such as those shown in Figure II.1.A.4.1, were sufficient for our modeling work. Figure II.1.A.4.3(a) and Figure II.1.A.4.3(b), respectively, show the simulated dome profiles of an equi-biaxial and a biaxial geometry (rectangular) specimen that have been deformed by the punch. Figure II.1.A.4.4(a) and Figure II.1.A.4.4(b) show a top-view of the location of limit strains on an equi-biaxial specimen for the case of high and low friction coefficient, respectively. The simulations show that for the LDH test, a higher friction coefficient shifts the failure location away from the dome apex as well as to a lower strain. Finally, Figure II.1.A.4.5 plots the predicted FLD and shows that a "high" friction coefficient can effectively lower the limit strains of this material. In other words, too high a friction coefficient could limit the geometries that the 7075 Al could be stamped into.

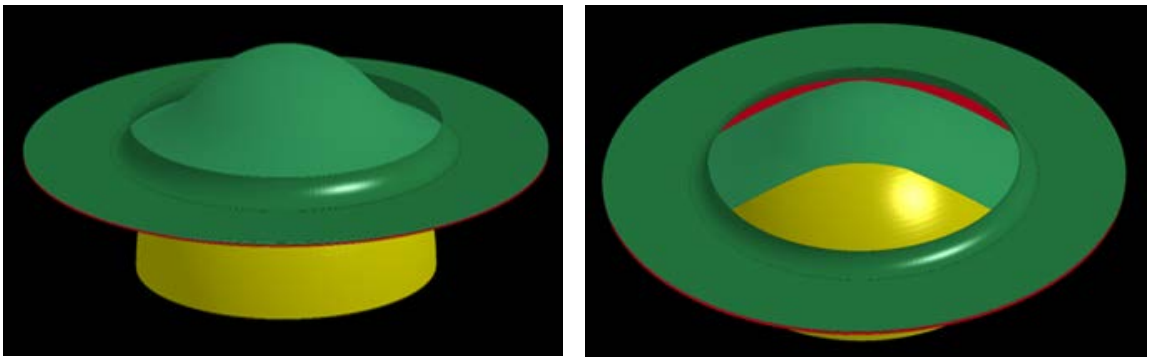

(a) (b)

Figure II.1.A.4.3. Simulated dome shapes of 7075 Al for (a) equi-biaxial; and (b) biaxial geometry. Source: PNNL.

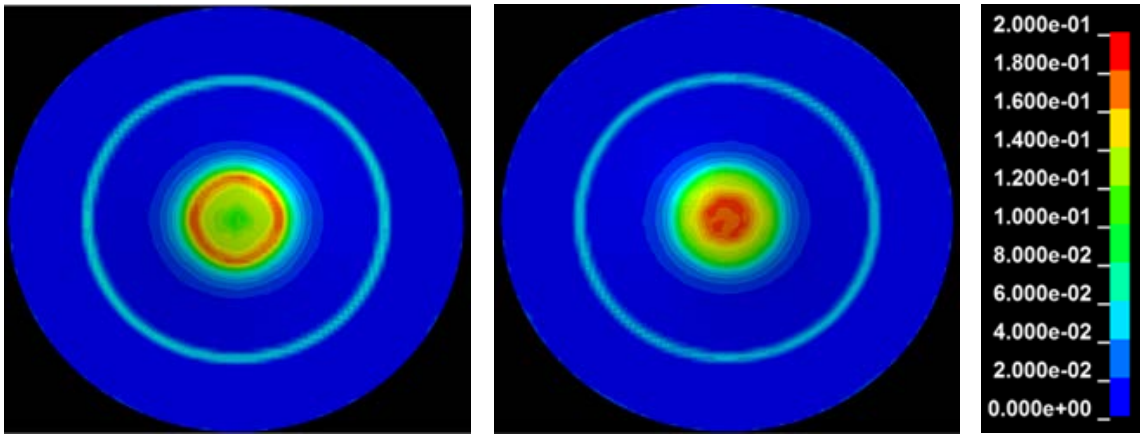

(a) (b)

Figure II.1.A.4.4. Location of simulated limit strains at failure (red color region/band) in an equi-biaxial specimen in an LDH test for the coefficient of friction (between the Al coupon and steel punch) of (a) 0.30; and (b) 0.08. Source: PNNL.

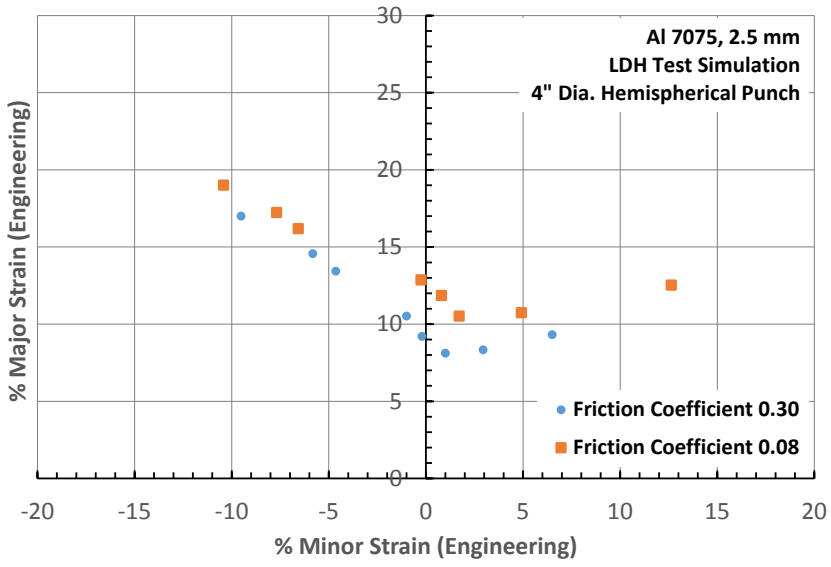

Figure II.1.A.4.5. Predicted FLD for 7075 in a selected temper for "high" (0.30) and "low" (0.08) values of coefficient of friction. Source: PNNL.

Conclusions

This project is addressing the challenge of achieving sufficient room temperature formability, as well as high-strength in post-formed parts, when stamping components out of high-strength Al alloys. The automotive industry has typically used warm/hot-forming to fabricate components in high-strength 7xxx Al alloys. However, a room temperature forming approach is more cost-effective, and therefore, desirable since warm/hot-forming approach entails additional costs. Therefore, this project will develop an understanding of the microstructure-formability-strength correlation in high-strength Al alloys to overcome the challenges associated with stamping components out of high-strength Al alloys.

In FY 2017, we selected AA7075 as a representative high-strength Al alloy and purchased 2.5 mm thick sheets from commercial vendor for subsequent testing. We determined the tensile stress-strain curves that show that the as-received material is relatively isotropic in the in-plane directions. Such in-plane isotropy may simplify the development of constitutive models, component design and the corresponding stamping simulations. We determined the natural aging curve of 7075 Al, which shows continued hardening/aging at room temperature even after seven days. Thus, any future heat-treatment process that is eventually implemented in a forming operation needs to consider the unstable temper produced in 7075 Al when it is held at room temperature. Finally, we performed FE modeling simulations of LDH tests and determined that depending upon the strain-state, a relatively higher coefficient of friction can lead to somewhat reduced formability. This understanding of the relationship between friction and formability will be important in designing a component and controlling the lubrication (and hence, coefficient of friction between the Al blank and the die) during stamping.

References

Austria Metal AG (AMAG) Aluminum Report. 2014. https://www.amag.at/fileadmin/user_upload/amag/Downloads/AluReport/EN/AR-2014-3-EN-S14-15.pdf. Accessed 29th Nov. 2016.

Davis, J. R., 1993, Aluminum and Aluminum Alloys – ASM Specialty Handbook edition. ASM International, Materials Park, OH, USA.

Kearns, J., S. Park, J. Sabo, and D. Milacic, 2015, "MMLV: Automatic Transmission Lightweighting," SAE Technical Paper 2015-01-1240, doi:10.4271/2015-01-1240.

Kumar, S. D., T. R. Amjith, and C. Anjaneyulu, 2016, "Forming limit diagram generation of Al alloy AA2014 using Nakazima test simulation tool," *Procedia Technology*, Vol. 24, pp. 386–393.

Lotus Engineering Inc., 2010, "An Assessment of Mass Reduction Opportunities for a 2017 – 2020 Model Year Vehicle Program." Submitted to: The International Council on Clean Transportation, (March) Accessed on 1st Dec. 2016 from http://altairenlighten.com/wp-content/uploads/2016/03/Mass-Reduction-Opportunities-for-a-2017-2020-Model-Year-Vehicle-Program.pdf.

Lutsey, N., 2010. "Review of technical literature and trends related to automobile mass-reduction technology." Institute of Transportation Studies, University of California, Davis. UCD-ITS-RR-10-10. http://pubs.its.ucdavis.edu/publication_detail.php?id=1390.

Părăianu, L., D. Comşa, J. Gracio, and D. Banabic, 2007, "Modelling of the Forming Limit Diagrams using the Finite Element Method." Advanced Methods in Material Forming. Springer, Berlin, Heidelberg, GE.

Plourde, L., M. Azzouz, J. Wallace, and M. Chellman, 2015, "MMLV: Door Design and Component Testing," SAE Technical Paper 2015-01-0409, 2015, doi:10.4271/2015-01-0409.

Reaburn, R., 2017, "Ultra-light Door Design," presentation given at the DOE VTO and Hydrogen and Fuel Cells Program Annual Merit Review and Peer Evaluation Meeting, Washington, D.C. https://energy.gov/sites/prod/files/2017/06/f35/lm120_skszek_2017_o.pdf.

Skszek, T., M. Zaluzec, J. Conklin, and D. Wagner, 2015, "MMLV: Project Overview," SAE Technical Paper 2015-01-0407, doi:10.4271/2015-01-0407.

Totten, G. E., and D. S. Mackenzie, 2003, Handbook of Aluminum, Vol. 2 – Alloy Production and Materials Manufacturing editions, Marcel Dekker.

Overall PNNL Project Conclusions

The Advancing Properties, Processes, and Enabling Tools for Lightweight Metals Project is focused on research and development activities for advancing the basic mechanical properties, manufacturability, and cost of lightweight materials toward levels needed for increased implementation in automotive applications.

Highlights of these tasks, as well as conclusion of results from the FY 2017 activities, were captured in the previous sections. Ultimately these four tasks, with unique scope and leadership, each addresses an aspect of the materials challenges limiting implementation of advanced high-strength steels and Mg as lightweight metals solutions for future automotive applications.

II.1.B Development of Low Cost High Strength Automotive Aluminum Sheet (Arconic)

Russell Long, Co-Principal Investigator
Arconic
100 Technical Dr.
New Kensington, PA 15069
Phone: 724-337-5420
E-mail: russell.long@arconic.com

John Newman, Co-Principal Investigator
Arconic
100 Technical Dr.
New Kensington, PA 15069
Phone: 724-337-2689
E-mail: john.newman@arconic.com

Will James, Technology Manager
E-mail: charles.james@ee.doe.gov

Start Date: October 1, 2014 End Date: December 31, 2018
Total Project Cost: $2,820,115 DOE share: $1,344,252 Non-DOE share: $1,475,863

Executive Summary

The goal of the project is to develop an automotive high strength 7xxx Al alloy and demonstrate its ability to replace an ultra-high strength component with significant weight savings at a cost of less than $2 per pound saved.

Arconic, in partnership with ORNL and our industrial partners—Honda R&D Americas, Inc. (Honda), and Cosma—leads this project to productively reduce weight in vehicles in a cost-effective manner. This effort, to increase the strength of 7xxx material while reducing the costs, can only be successfully performed by a team that includes a Tier 1 automotive supplier (Cosma), an OEM (Honda), and an Al producer. Honda will provide the requirements for the component in the vehicle, while Cosma will develop the warm-forming tooling and procedures for forming the baseline component. ORNL will develop the method required to develop tailor-welded blanks to further reduce the material usage. The proposed alloy developments will be done initially on a laboratory scale and then in full-scale trials at Arconic. Once the full-scale trial material is available, full-scale forming trials will be conducted with and without tailor-welded blanks. The material will be evaluated for strength, formability, and corrosion based upon stringent Honda requirements.

Accomplishments

- The warm-forming trials were conducted using 7055 and four new 7xxx alloys. This included optimizing the blank shape.
- The forming trials were repeated with 7055 and three new alloys using the modified tooling. The forming process was optimized with heated blanks while using room temperature tooling.
- Forming trials were repeated on 7055 and three new alloys using heated blanks and heated tooling.
- Arconic conducted another full-scale trial to provide additional material for the next forming trial.
- Strength of all new alloys were evaluated using samples cut from the formed parts before and after a paint-bake cycle.

- Corrosion testing of FSW test samples was completed.
- The initial trials of full-size tailor FSW blanks were carried out.
- The project was presented during the 2017 DOE Annual Merit Review in Washington, DC.
- A paper summarizing the results of the project was published in the *Journal of The Minerals, Metals, & Materials Society*.

Technology Assessment

- Target: Achieve the targets of 600 MPa ultimate strength and 8% elongation following warm-forming simulation and paint-bake cycles on several ingot casts and Micromill™-produced experimental alloys.
- Gap: The 600 MPa ultimate strength and 8% elongation target has not been reached on samples cut from warm-formed parts.
- Target: Development of robust warm-forming procedures, including the effect of die and blank temperature changes.
- Gap: The formability of the material is increased with higher forming temperatures; however, the higher temperatures can over-age the material, thereby resulting in lower strength.
- Target: Produce sound tailor-welded blanks on sample materials using FSW and successfully form the parts without weld fracture.
- Gap: Tailor welded blanks may be difficult to form with weld splitting.

Project Introduction

The initial phase of this project has been based on alloy development to reach the stated targets. Corrosion and forming requirements are being developed by Honda and Cosma, respectively. The alloy development trials targeted the properties stated along with the added corrosion and formability requirements.

The team has also defined a demonstration part, which includes the critical features in the current production hot-stamped steel component. The geometry of this demonstration part has been evaluated in forming simulations using the material properties developed during the alloy development phase. The demonstration part tooling has been built, as well as the oven to heat the blanks. The tooling and oven are installed in a press line. Several forming trials of the new alloys have also been completed.

ORNL has evaluated the properties in tailor-welded blanks produced using friction-stir welding in these experimental alloys. ORNL procedures will be used to produce a large number of full-size tailor-welded blanks of these alloys for forming trials next year.

Approach

The first year of the contract provided definition of the detailed requirements. These specifications were targeted during the alloy development phase. Multiple new alloys were produced at a laboratory scale. These alloy development trials were used to define a number of alloys that were produced at full-scale in existing Arconic facilities. A demonstration part, developed by Honda and Cosma, which includes all the critical features needed for the current ultra-high strength steel production part, is shown in Figure II.1.B.1.

The forming tooling was designed and built to form this part at elevated temperatures. A warm-forming oven that can heat a single blank with rapid heat-up times was built as part of the project.

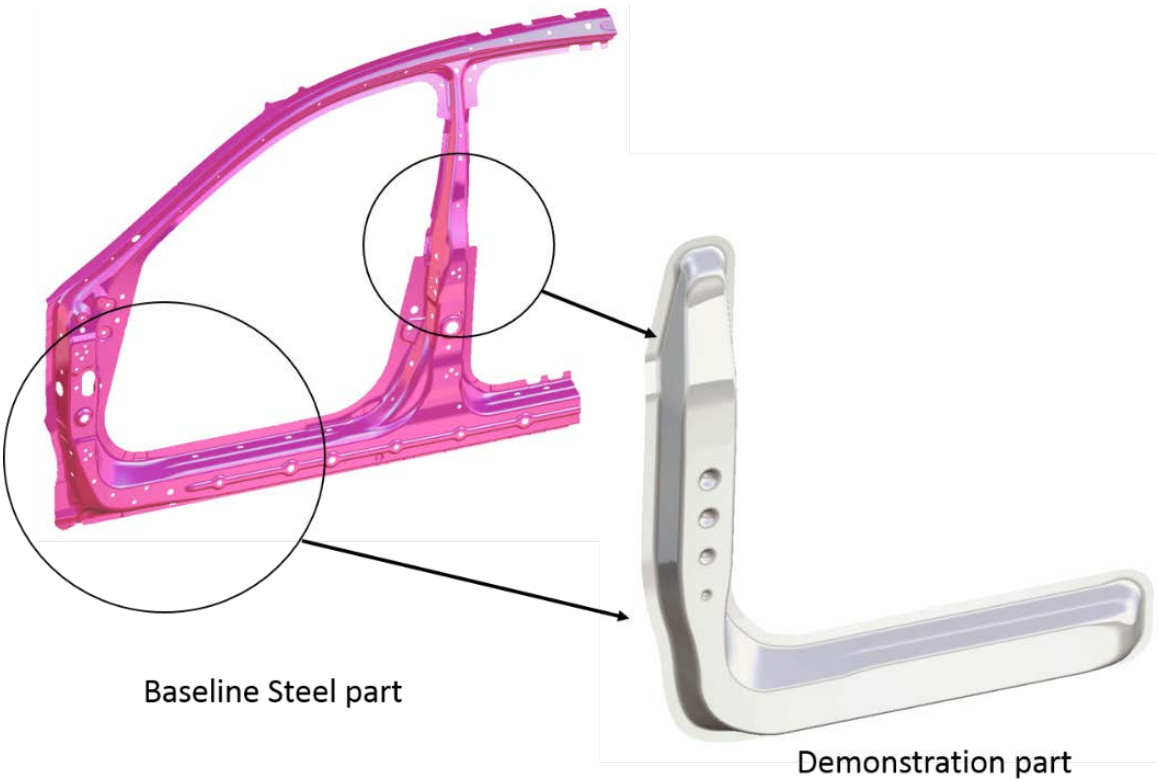

Figure II.1.B.1. Demonstration part geometry. Source: Honda.

Technology Transfer Path

The project is based upon an existing ultra-high strength door-ring in Honda vehicles. The project will demonstrate the weight reduction, production method, and cost implications of converting this component to high strength Al. The new alloy will be produced at existing production facilities at Arconic. The forming trials will be conducted at Cosma, which is the current production supplier of hot-stamped steel components. Both Arconic and Cosma are committed to the production of high strength Al components. This project serves as a means of developing the part requirements with Honda, as well as the information needed to demonstrate the feasibility of this approach. Arconic will produce the experimental alloy for supply to the automotive industry once the strength, formability, and cost-feasibility is demonstrated.

Results

There are several paths that can be used to form 7xxx materials. For roll-formed or simple shapes, a room temperature forming path can be used on tempered materials. The complex stamped shape of the baseline steel parts cannot be formed at room temperature in these alloys. This shape could be hot-formed using procedures similar to those used for hot-forming steel, but at much lower temperatures. The other alternative is to warm-form, which means that the material forming temperature is significantly lower than the solution heat-treating temperature of the alloy. This project also stipulated that the forming be done at a maximum temperature of 225°C, which falls more into the warm-forming range.

A forming cell consisting of a press, an oven for blank heating, a robotic transfer system, and tooling has been set up in an existing press line at Eagle Bend Manufacturing. This forming cell is shown in Figure II.1.B.2.

Figure II.1.B.2. Forming cell. Source: Cosma.

This cell was used to explore the impact of blank shape, blank temperature, lubricant, and tooling temperature on each alloy. The goal of the trial is to develop robust procedures to produce this part and then evaluate the performance of each alloy. Initial trials indicated a need for tooling modifications. The tooling was removed, modified, and reinstalled in the press. The blank shape was optimized during the forming trial of the 7055 baseline alloy. This blank shape was used for forming experimental alloys. Forming trials were conducted on each alloy with increasing blank temperatures, which were measured in the oven and were discovered to lose 6–8°C during transfer to the press. The forming result for one of the experimental alloys is shown in Figure II.1.B.3. The part was successfully formed in three of four experimental alloys. Forming improved with increasing blank temperature with successful parts being formed at 220–230°C. Parts produced with each alloy were gridded for strain measurement. Once the measurements are complete, the strain maps will be used to correlate with the forming simulation.

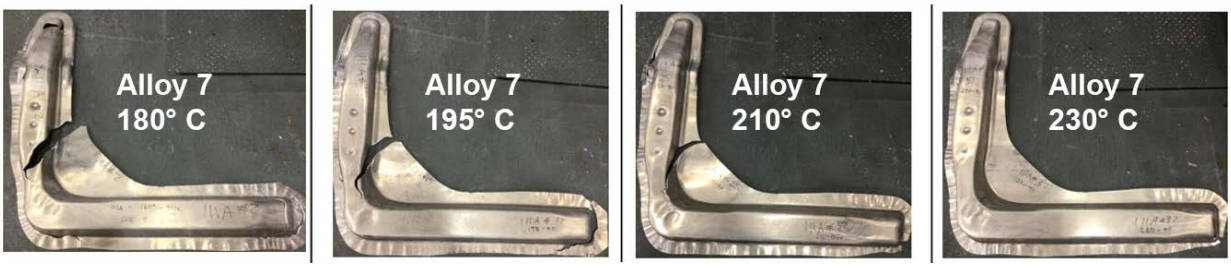

Figure II.1.B.3. Selected results from forming trial. Source: Cosma.

Parts formed from all of the experimental alloys were given a paint-bake cycle of 185°C for 20 minutes. Samples were then cut from the formed parts to measure their mechanical properties. The strengths of the formed parts were then measured with and without this paint-bake cycle. Those results are shown in Figure II.1.B.4. The strengths of each alloy are increasing with the addition of the paint-bake cycle, so the warm-forming step is not resulting in over-aging in the 220–230°C blank temperature for a 90-second cycle. It should be noted that increasing the blank temperature to 250° for 120 seconds did reduce the overall strength. The ultimate strengths after the paint-bake cycle ranged from 560–580 MPa. This is 20–40 MPa below the project target.

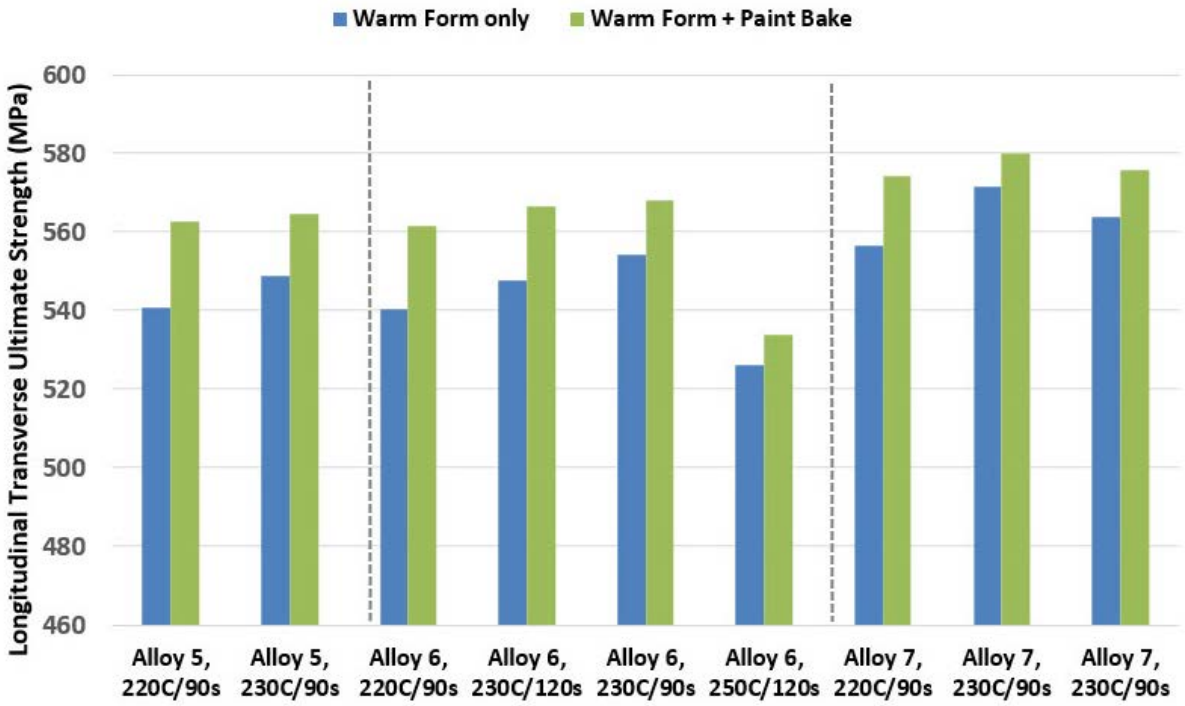

Figure II.1.B.4. Strengths measured from formed parts. Source: Arconic.

The project target is to maintain at least 8% elongation at ultimate strength levels at or approaching 600 MPa. The elongations measured from warm-formed parts both with and without the paint-bake cycle are shown in Figure II.1.B.5. Elongation values were all above project targets.

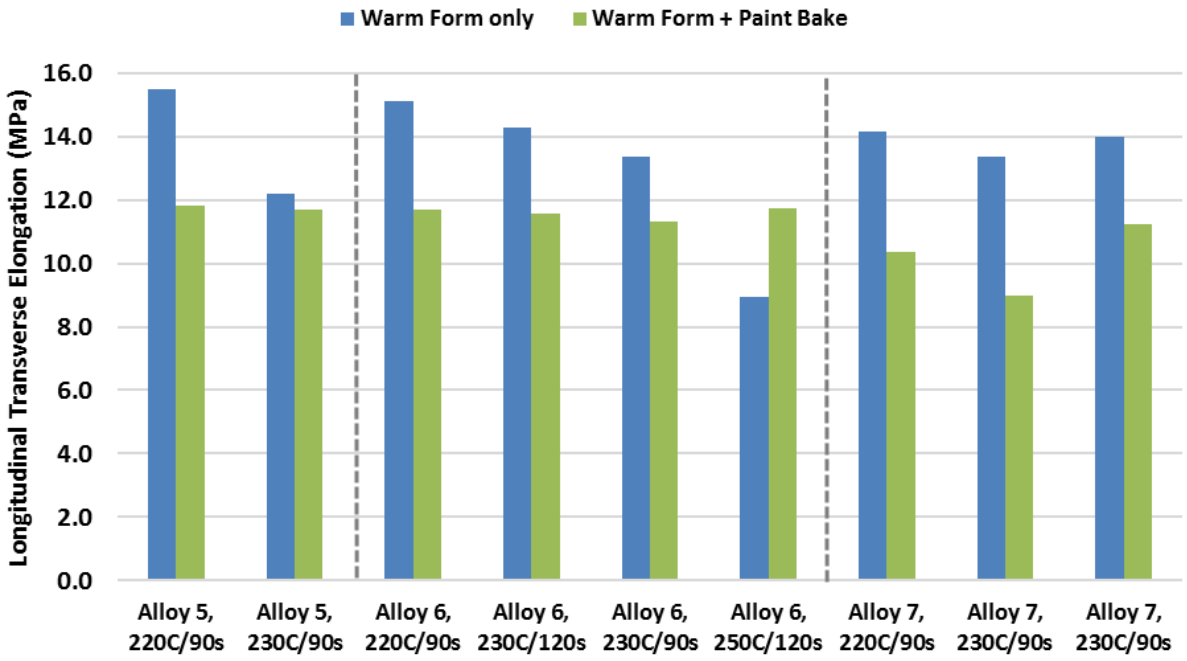

Figure II.1.B.5. Elongations measured from formed parts. Source: Arconic.

An additional alloy full-scale trial was conducted at the San Antonio Micromill™ facility to provide additional material that could assist in reaching the ultimate strength target. These materials will be tested after a simulated warm-forming and paint-bake cycle to determine the strength.

Tailor-welded blanks will be used to increase material usage. ORNL has produced sound tailor-welded samples earlier in the project. The next step is to scale-up to full-size blanks. ORNL has produced some full-size blanks, as shown in Figure II.1.B.6.

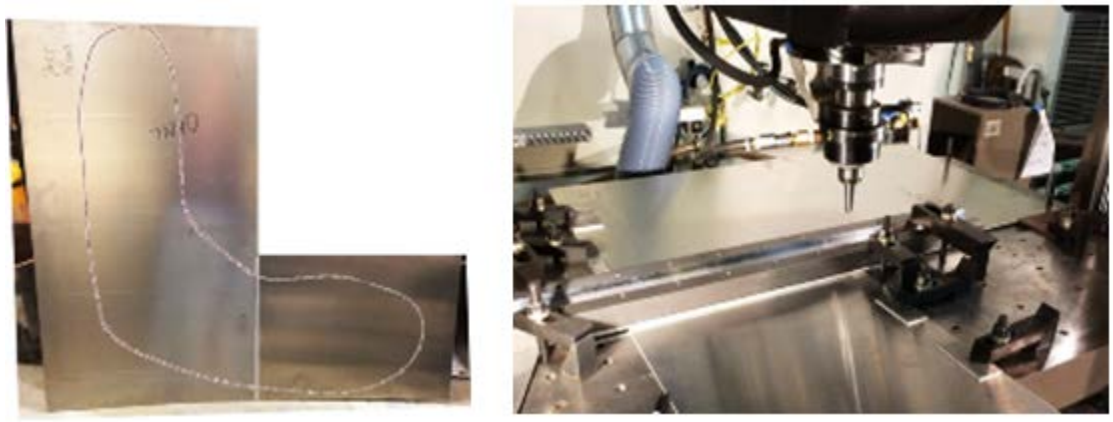

(a) (b)

Figure II.1.B.6. (a) Tailor welded blank; and (b) FSW setup and blank. Source: ORNL.

Due to the number of blanks required for the forming trials, the TWB Company in Monroe, MI, has been contracted to produce the remaining blanks. TWB Company has participated in other DOE programs producing tailored-welded blanks.

Conclusions

In the third year of the contract, the demonstration part was successfully formed using multiple experimental alloys. The forming trial better defined the temperature profile needed for successful forming. The part must be formed at production rates approaching 60–80 parts per hour and have uniform properties over the full part. Estimates of cycle time will be completed as a part of the cost study. The strains in the formed parts are being measured to provide input to improve the forming simulation. Properties from many locations within the part will be measured. Samples from these parts are undergoing corrosion testing. Full-scale tailor-welded blanks will be produced for the forming trials next year.

The properties within the formed part were measured both with and without the paint-bake cycle. The ultimate strengths reached 580 MPa, which is slightly lower than the 600 MPa strength target. All alloys had elongations that exceeded the target. The tensile strength and elongation targets are required by DOE, but part requirements from Honda are more complex. The lower portion of the demonstration part is simulating the rocker in the vehicle. This part will be dynamically loaded in a side impact. Likewise, the A-pillar will also be impacted and will be loaded at the door hinge locations during impact. Arconic and Honda are currently working on a three-point bend test to simulate the final part performance, which will be completed in the fourth year of the contract. This bending performance must be predictable analytically during the design phase of the vehicle. This must also account for the presence of the FSW.

Key Publications

Long, R., E. Boettcher, and D. Crawford, 2017, "Current and future uses of aluminum in the automotive industry," *Journal of The Minerals, Metals, & Materials Society*, Vol. 69, No. 12, pp. 2635–2639.

II.1.C High-Strength Electroformed Nanostructured Aluminum for Lightweight Automotive Applications (Xtalic Corporation)

Robert Hillty, Principal Investigator
Xtalic Corporation
260 Cedar Hill St.
Marlborough, MA 01752
Phone: 508-804-7265
E-mail: bhilty@xtalic.com

Will James, Technology Manager
E-mail: charles.james@ee.doe.gov

Start Date: October 1, 2014 End Date: December 31, 2018
Total Project Cost: $5,064,543 DOE share: $2,500,000 Non-DOE share: $2,564,543

Executive Summary

The overall project goal is to electroform high-strength nanostructured aluminum (nano-Al) alloys for lightweight automotive applications. During FY 2017, we successfully plated full-size 6-in. by 6-in. panels with nano-Al alloys. The single-sided plating cell was qualified, successfully meeting our go/no-go criteria. We then applied the capabilities of the cell into a new double-sided plating cell design. This new plating cell has been built and is ready for installation. We conducted a 468-position Design of Experiments (DoE) to quantify plating parameter effects on surface morphology, quality, and overall plating rate. We have made significant progress to understand the key variables affecting cost and our ability to meet the $2 per pound saved metric.

Accomplishments

- Qualified and tested a 6-in. by 6-in. plating cell used to produce double-sided nano-Al samples (FY 2017).
- Developed a shaped anode design using COMSOL simulation and verified the performance experimentally in a 50-mm by 50-mm format (FY 2017).
- Redesigned and fabricated an improved plating cell that allows for continuous and double-sided plating of a 7-in. wide strip of nano-Al on an Al core. The system is built and ready for installation in the first quarter of FY 2018.
- Designed and executed on a 468-position DoE intended to improve the fundamental understanding of plating process control parameters, which can be used to increase the plating rate and plating quality. Both the speed and quality of plating have a strong influence on the overall cost of the final strip material, and hence, directly impact our ability to achieve the $2 per pound saved target.
- The cost model was further refined, and key targets identified.
- The supply chain was developed to further reduce the cost of the ionic liquid electrolyte. A key development here was the identification and qualification of a large-scale (> 6.5 metric ton capable supplier of ionic liquid).

Technology Assessment

- Target: Achieve 600 MPa ultimate strength with 8% elongation. We achieved this using a composite of nano-Al over a core of commercial-wrought Al sheet.

- Gap: Our cost model is most effective when the strength of the nano-Al is 900 MPa or more; however, at these strengths, we have not been able to achieve the desired ductility of 8% elongation.
- Target: Achieve a mass production cost of $2 per pound saved.
- Gap: We reduced the cost of the ionic liquid electrolyte by five times in FY 2017 by qualifying a new and large-scale chemical supplier. However, this cost remains two times the aspirational cost used in our cost model.

Project Introduction

Xtalic's electrodeposition process is a transformative, disruptive technology that has produced nano-Al alloy sheet materials, which dramatically outperform traditional high-strength Al alloys. These new materials can enable weight reductions of 50% or more in strength-critical applications. The nano-Al alloy, XTALIUM™, utilizes core technology related to creating thermodynamically stable alloys. This is achieved by understanding the enthalpy of mixing and segregation for alloys and the resulting atomic configurations that naturally occur under the correct process conditions.

Approach

Our basic approach is to use a 200μm core material of commercially available aluminum alloy onto which we plate 400μm layers of nano-Al alloy on both sides of the substrate. This creates a three-layer composite structure that is 1mm thick with outstanding mechanical properties.

During this FY, our approach was to qualify the 6-in. by 6-in. plating cell, proving the ability to scale-up the process. We then needed to focus on the economic feasibility of the overall process. We leveraged the economic model developed in budget period (BP) 2 to identify the best opportunities for improvement. The strongest factors were then researched for improvement. These include the plating rate, plating quality, process risk reduction, and building a viable large-scale supply chain.

Technology Transfer Path

Xtalic's business model includes working with manufacturing partners to produce nano-crystalline electrodeposited metal products by providing manufacturing process design specifications and onsite engineering support and raw materials to its manufacturing partners. Xtalic will work with Tri-Arrows Aluminum, Inc., or another manufacturing partner to fabricate, install, and operate the nano-Al sheet lines.

Xtalic is actively working with top-tier automotive OEM suppliers to identify suitable entry-point applications. For this project, Xtalic is collaborating with FCA to simulate the formation of prototype component parts. This project is the first step in the process of technology development within FCA. Throughout the duration of this project, FCA will monitor technical progress, experimental results, and economic analysis to evaluate the technology's potential to meet their product performance requirements and economic goals for future vehicle applications. FCA will determine the technology's suitability to proceed to the next phase of their internal technology development stage-gate process.

Results

6-in. by 6-in. Sheet Plating

The 6-in. by 6-in. plating cell is constructed of polytetrafluoroethylene (PTFE) to make it compatible with the plating electrolyte. This introduces some challenges, such as welding and leakage, which can be overcome through engineering design.

Figure II.1.C.1 shows a successful plating run of the 6-in. by 6-in. substrate using the new plating cell. The brown liquid is the plating solution. In this run, a brass substrate was used as part of the qualification of the plating cell. Spots can be seen on the plated surface, which reflect the localization of both flow and current density. In this test, the substrate is static, so the impact of the flow nozzles can be most clearly quantified. In a production process, the strip will be moving across the cells, leading to more homogeneity to the plating fields and flow. Figure II.1.C.1 also shows a small region (bottom right corner) where the flow rate was insufficient to fully coat the surface during plating. We adjusted the flow rate and weir covers at the top of the cell to control the direction of flow laterally across the cathode interface. We were able to experiment with various weir positions and flow nozzle heights to find a combination that fully wets the surface and produces a desirable coating.

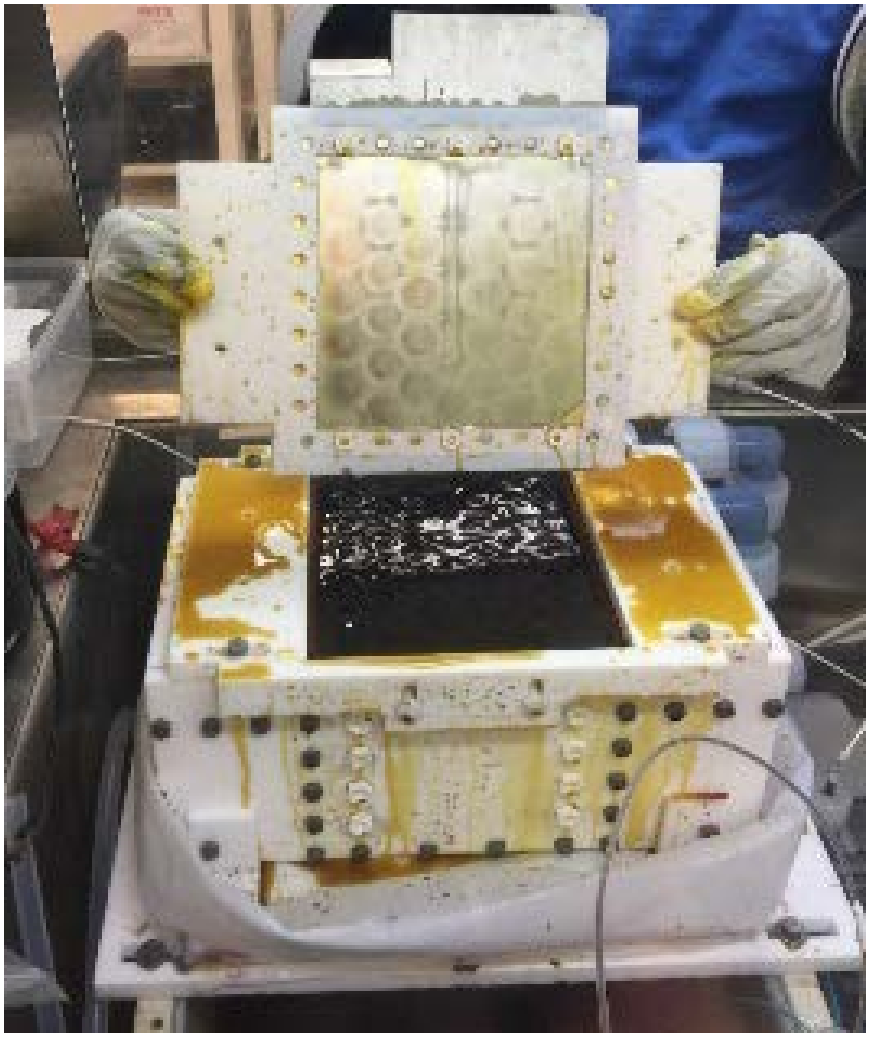

Figure II.1.C.1. 6-in. by 6-in. plating cell used to produce nano-Al. Source: Xtalic.

An early qualification plating run is shown in Figure II.1.C.2, where plating thickness varied from 37–57 µm across the area of the 6-in. by 6-in. surface. We found moderate thickness variations between the center of the flow (e.g., circular areas) and the interstitial regions where the anode is located, and hence, the electric field is more highly concentrated. As expected, the locations with a higher electric field (e.g., interstitial regions) plated faster than in the locations where the flow was high, but the electric field was low.

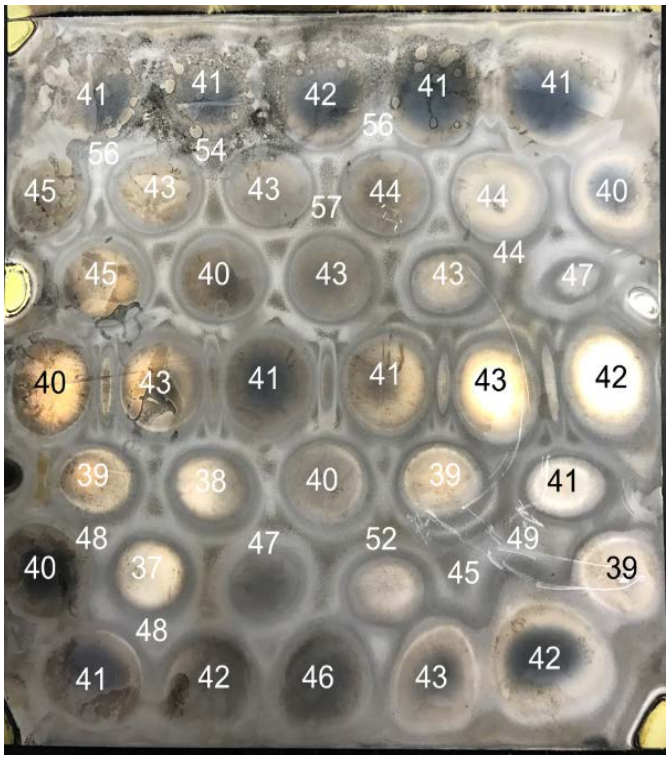

Figure II.1.C.2. Plating thickness distribution in early qualification testing. Measurements are in µm and are single-sided measurements. Source: Xtalic.

The nozzle heights were varied to help qualify the effects of flow and direction on the thickness uniformity across the sheet sample. The Mn concentrations were generally flat across the sample, varying less than 0.5 at.% from location to location. Figure II.1.C.3 shows some of the sample variants produced during these tests.

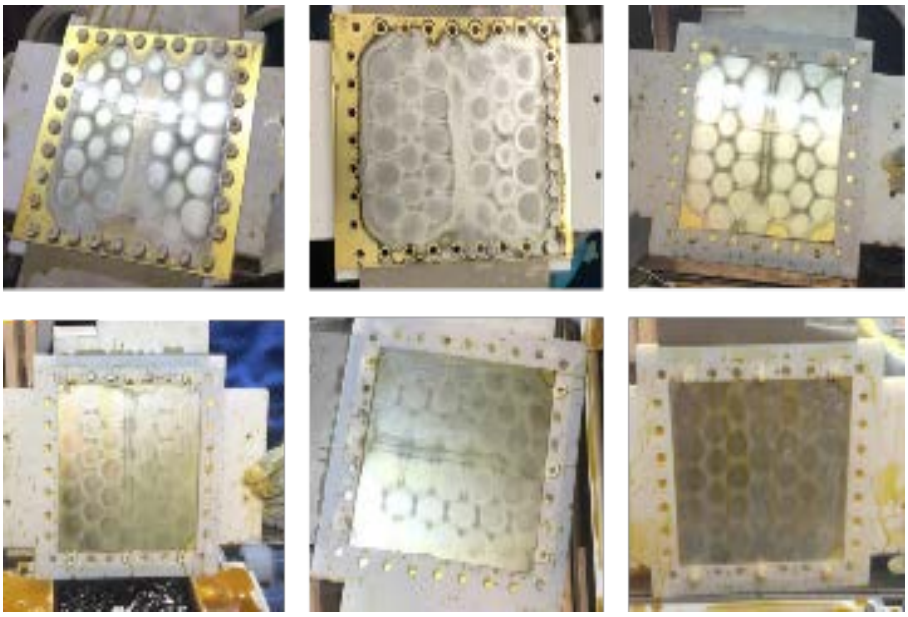

Figure II.1.C.3. Plating qualification test runs with variable pump pressure, flow rates, weir gaps, and substrates. Source: Xtalic.

We prepared AA 6061 alloy sheets for use in the plating cell. Our previously developed activation methods (Freydina et al. 2017) worked well in producing good adhesion across the surface with limited modifications necessary. We produced samples of nano-Al on both sides of the Al 6061 as evidence of the qualification and manufacturability of the tool. The plating cell as constructed now is a single-sided plate, such that the substrate is manually flipped halfway through the plating run. The new surface is reactivated and plated to reach the desired thickness. We also produced samples with 50 µm of nano-Al plated onto both sides of Al 6061. We limited the thickness due to limitations in the thermal control of the plating bath. In order to maximize the plating rate additional chilling will be required in the plating cell.

Plating Optimization: 50-mm. by 50-mm

As an intermediate step to full-scale-up plating, we can easily modify parameters in our 20-liter reactor with a 50-mm by 50-mm (2-in. by 2-in.) substrate. This form factor has proven effective at establishing plating chemistry and process parameters critical to successful sheet formation.

The existing plating chemistry includes a co-solvent to adjust the viscosity of the electrolyte. The co-solvent can introduce other variabilities to the process and an additional cost. We also built a new ionic liquid bath without the co-solvent, which we then experimented with at 45°C and 60°C. As the plating tests continued, we introduced an additive system in doses to determine its efficacy. Additional work is needed on the non-co-solvent bath to ensure that dendrites can be suppressed, and that color can be maintained as we scale-up.

The uniformity thickness of the sheet is also an area of engineering concern for production. Typical-wrought sheet stock has tight tolerance on thickness uniformity due to the nature of the rolled product. In the electroformed version, significant factors that control the plating rate are the electric field and flow. Our plating cell can provide some balance to the flow field and provides an option for variable flow across the workpiece.

We tested changes to the shape of the anode, which has a direct effect on the applied electric field that is developed between the anode and cathode. The edges of the sample, especially a square sample, can have a high flux density due to the transition between the conductive cathode and the insulating fixtures. Conversely, the center of the sample can have a uniform, but relatively depleted flux field producing a lower plating rate. If the anode and cathode are parallel and flat, then the resulting electric field produces a thickness variability of about 55% across a 50-mm by 50-mm sample. That is to say, the center may have a target thickness of 400 µm, while the edges are closer to 500 µm.

The electric field can be flattened by shaping the anode such that the anode is closer to the cathode in areas where the deposition rate is too low. This aligns the flux isobars and evens out the plating. A diagram of the anode and cathode configurations is shown in Figure II.1.C.4. The existing anode and cathode configurations are flat and parallel. The new configurations use a domed or paraboloid shaped anode which directs more of the plating energy towards the center of the workpiece, evening out the thickness.

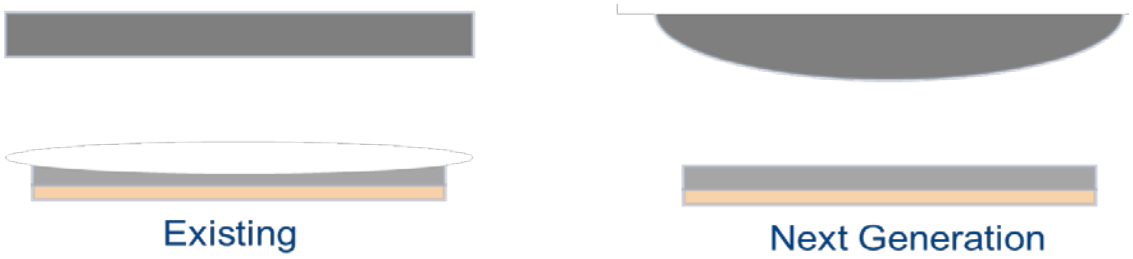

Figure II.1.C.4. Anode evolution to address uneven plating thickness development for thicker samples. Source: Xtalic.

Several anode configurations were tested to check efficacy. Figure II.1.C.5 shows the evolution of thickness and composition as the anode is changed. The left image shows the standard flat anode and cathode condition. In this case, the outer regions are much thicker than the center by 55%. In the center condition, the anode has a curvilinear shape that can be approximated as the curved surface of a half cylinder. This can make the thickness distribution worse since the anode is closer to the cathode along the major axis of the anode, which is confounded by the proximity of the insulating fixture. As such, the thickness distribution is wider than in the flat anode case. In the image on the right, the anode is a partial domed shape with a diameter of 4-in. The apex of the dome is placed closest to the cathode, while the thickness uniformity is significantly improved with a 25% variation.

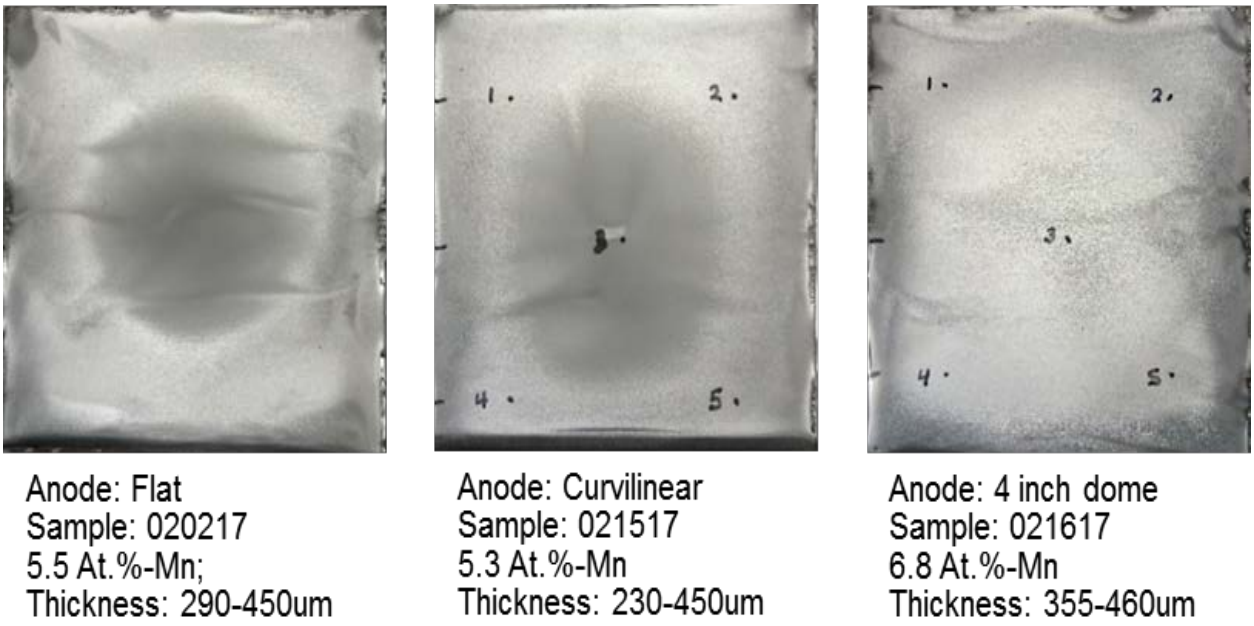

Figure II.1.C.5. Improvement in thickness uniformity using different anode configurations. The left image is for flat anodes; the center image is for curvilinear anodes; and the right is for domed shape anodes. Source: Xtalic.

Plating Optimization: Design of Experiments

The cost/lb.-saved of the plated nano-Al is strongly a function of the strength, plating rate, electrolyte cost, and quality (yield). We have executed a large design of experiments intended to boost speed and improve surface roughness.

The DoE included 468 specimens, where many of the primary input parameters could be varied to determine and quantify the output. These are shown in Figure II.1.C.6, while the input and output variables forming the DoE are summarized in Table II.1.C.I.

Round 1	Run Conditions
Mn conc in bath (g/kg)	2, 3.5, 6, 10
Temp (C)	35, 80
Agitation (rpm)	3000, 1000, 500
Waveform	Waveform 1, waveform 2, waveform 3
Current (mA)	5, 50, 100
Number of runs	101 tabs

Round 2a	Run Conditions
Mn conc in bath (g/kg)	3.5, 6
Additive	B
Additive Conc (g/kg)	1, 3, 18
Temp (C)	35, 80
Agitation (rpm)	3000, 500
Waveform	Waveform 1, waveform 3
Current (mA)	5, 50, 100
Number of runs	125 tabs

Round 2b	Run Conditions
Mn conc in bath (g/kg)	3.5, 6
Additive	A
Additive Conc (g/kg)	5
Temp (C)	35, 80
Agitation (rpm)	3000, 500
Waveform	Waveform 1, waveform 3
Current (mA)	5, 50, 100
Number of runs	48 tabs

Round 2c	Run Conditions
Mn conc in bath (g/kg)	3.5, 6
Additive	S
Additive Conc (g/kg)	20
Temp (C)	35, 80
Agitation (rpm)	3000, 500
Waveform	Waveform 1, waveform 3
Current (mA)	5, 50, 100
Number of runs	48 tabs

Round 4	Run Conditions
Mn conc in bath (g/kg)	3.5, 6
Additive	B A S
Additive Conc (g/kg)	18, B 5, A 20, S
Temp (C)	35, 80
Agitation (rpm)	3000, 500
Waveform	Waveform 1, waveform 3
Current (mA)	50, 100
Number of runs	57 tabs

Figure II.1.C.6. The design of experiments experimental plan. Round 1 focused on plating parameters. Rounds 2a, 2b, and 2c focused on the additives. Round 4 focused on making thicker deposits to consider the evolution of surface morphology under optimized conditions.

Table II.1.C.1. Summary of Input and Output Variables of the DoE.

Inputs	Outputs
Mn concentration in the bath	Mn Composition in coating
Additives	Roughness
Temperature	Grain size
Rotation speed	Grain orientation
Waveforms	Topography
Current Density	Thickness
	Hardness

The Mn content variations are critical to achieving optimum performance from the deposits. Figure II.1.C.7 shows the variation in Mn content in the deposit in at% as the plating conditions are changing during the DoE. Two outputs were given—one at 35°C and the other at 80°C. The surface morphology changes are evident as we work to target a Mn content in the range of 7.5 at%.

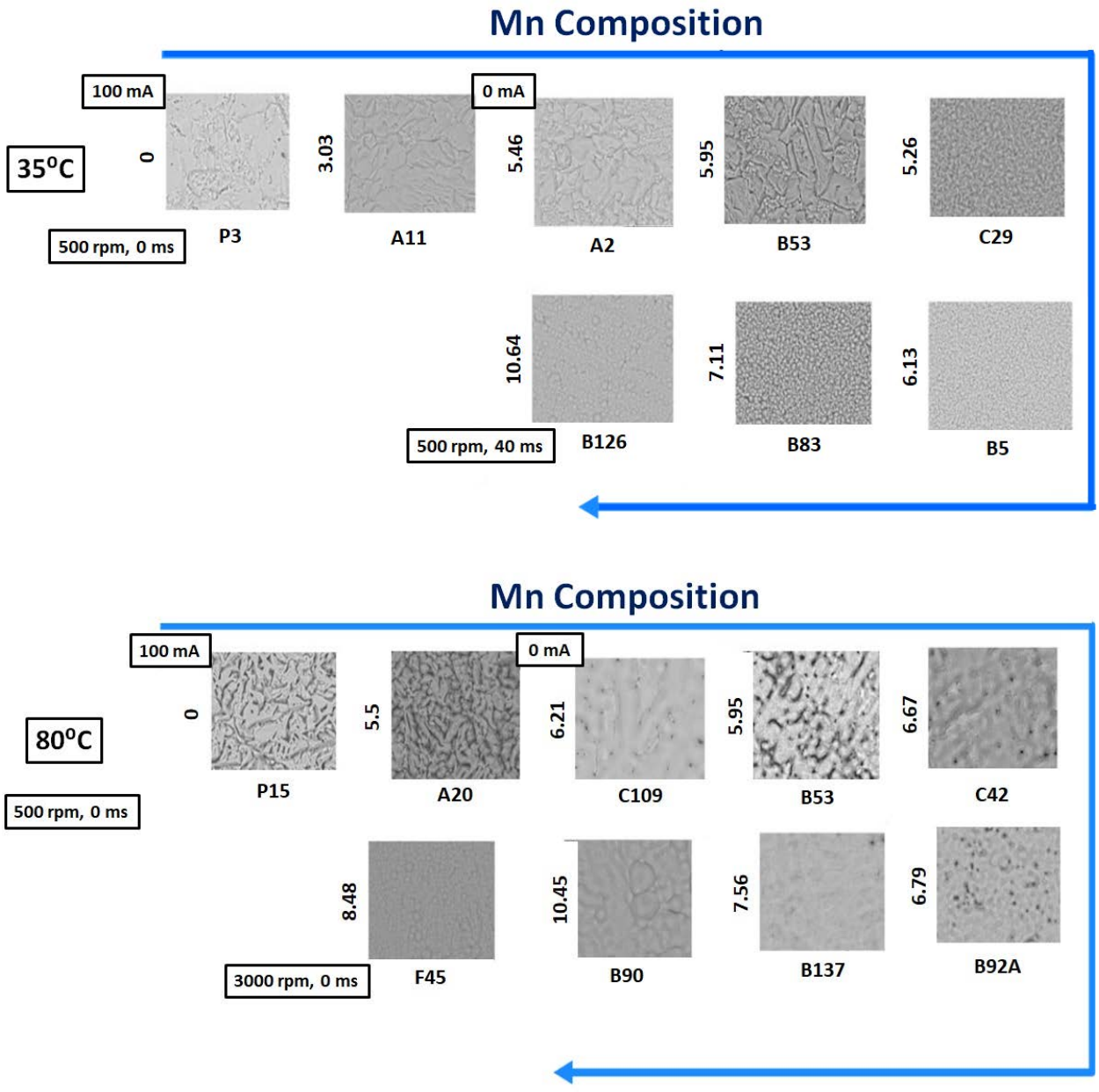

Figure II.1.C.7. Mn composition output from a DOE cell at 35 °C (top) and 80 °C (bottom). The Mn content increases can be seen and related to the surface morphology. Source: Xtalic.

From the DoEs, several results were observed about the factors most affecting performance.

Kinetics for flux are the most important for:

- Current density
- Temperature
- Agitation:
    - Additives are effective at reducing dendrites at lower temperature
    - Mn content between 6 and 9 at% is preferred
    - Pulse waveform can affect kinetics and Mn content
    - Scaling to larger substrates is required to verify performance.

Supply Chain Development

The two most important raw materials for this process are aluminum core sheet stock and ionic liquid. As part of the supply chain management process and cost model effort, we need to establish viable partners and suppliers.

Tri-Arrows Aluminum, Inc. is a valued partner in this project. They have provided insight regarding the processes and markets for new nano-Al. Tri-Arrows has also been working on the supply of 200 µm core material onto which we will deposit 400 µm (per side) of the nano-Al material to achieve the final thickness of 1 mm. The core materials for scale-up will be AA 5082 and AA 6005, which have reasonable strength and are readily available in 200 µm thicknesses. Tri-Arrows has completed the heat treatments and the samples are ready to ship to Xtalic.

The other core input material is 1-ethyl-3-methylimidazolium chloride ionic liquid base. Over the course of the project, we have purchased this material from two suppliers. One is no longer offering it as a product, while the other provides high-quality material, but in limited volumes. In order to scale to automotive volumes, we need a supplier capable of producing many tons of ionic liquid at a reasonable cost. We have found a new supplier who is now scaling to a 1-metric-ton batch size and has the capacity to scale to batches on many metric tons as needed. We have performed initial quality control testing on lots of ionic liquid to verify purity, chemistry, and performance. The quality looks acceptable and we are negotiating sales and supply terms for scale-up quantities. We expect to purchase a larger quantity of ionic liquid from them as we scale the bath to a larger volume and replenish baths that are no longer viable for development.

Electroforming System

The plating cell design from BP2 is single-sided. To boost efficiency, the plating cell has been redesigned to be double-sided and to boost flow rate. Flow of the electrolyte across the cathode interface is critical to ensure adequate mass transport, which ensures fresh electrolytes and additives are presented at the electrode.

The new cell design has incorporated many refined design characteristics from our initial cell designs. The new cell uses a more laminar flow configuration. The previously used jet configuration provided an abundance of mass transport, but led to non-uniform plating. The new design employs a series of weirs and flow constrictors that guide the flow across the plating interface. The new cell, like the old cell, uses aluminum-shot anode material for easy maintenance and regeneration of the anode supply. Each of the anode compartments utilize an anode bag to contain the anode, which reduces the risk of small particles in the bath as the anode dissolves.

The cell includes three stations: 1) activation; 2) plating; and 3) rinsing. The activation station uses a similar ionic liquid plating electrolyte. The substrate is configured as the anode for this portion of the cell, such that applied current will reduce the oxides on the surface of the incoming sheet stock. Figure II.1.C.8 shows an overall view of the plating cell and strip configuration. The plating cell is double-sided and includes a flow-through mechanism to ensure adequate solution transfer to the anodes and the strip. Anodes will be bagged in Kevlar® to reduce the risk of particulate contamination as the anodes dissolve. Rectifier connections to each anode container are not shown in Figure II.1.C.8.

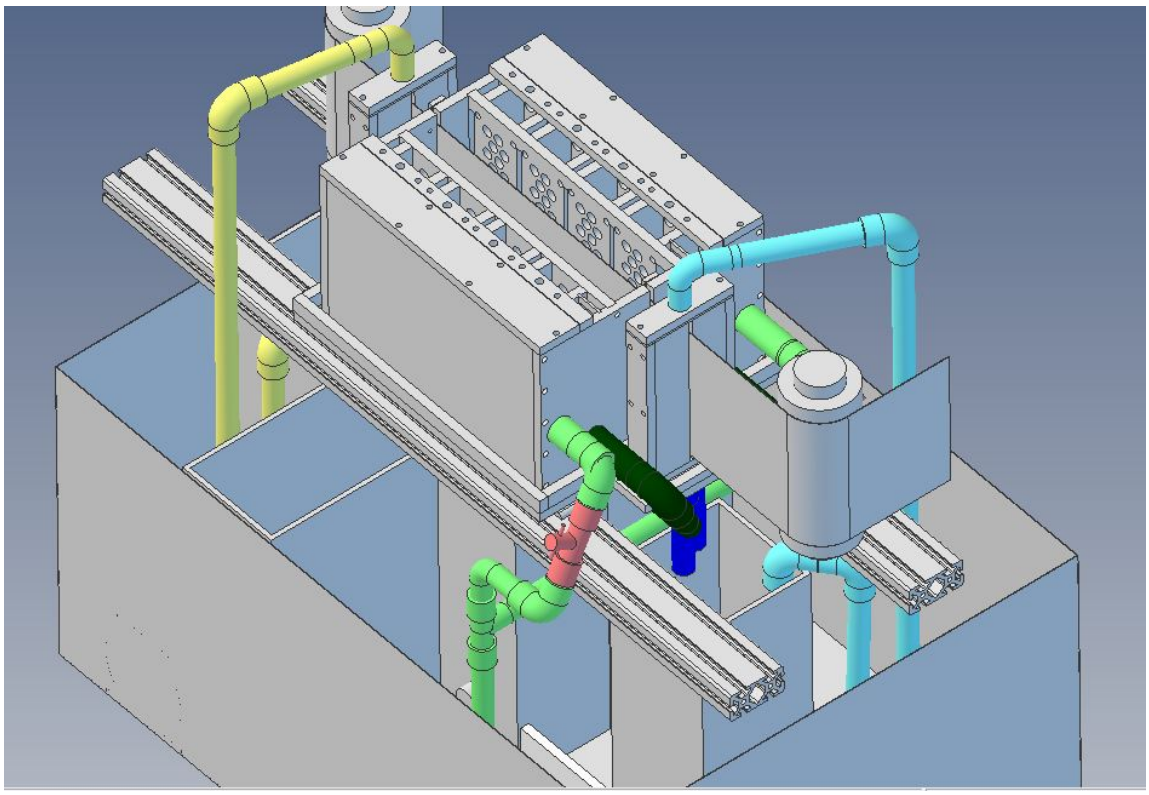

Figure II.1.C.8. Isometric view of the plating cell showing the three cells—activation, plating, and rinse (top left to bottom right). Green pipes feed and return the electrolyte for plating. Blue pipes feed and return toluene for rinsing. Yellow pipes feed and return the electrolyte for activation. Each liquid has its own sump and pump system. Red control valves are included on the electrolyte feed system to balance the flow to each side of the plating cell. Source: Xtalic.

Feed pipes for each of the solutions are shown. Lighter-colored pipes are the supply feeds, while the darker-colored pipes are the returns. Valves are available on each feed line to control the flow rate and balance to each portion of the cell. Additional flow control is available on each pump controller. The strip and roller assembly can be seen as well. An activation station is the first step and is 1 cm long with a separate ionic liquid cell and electrolyte sump and pump. We have designed flexible wiper assemblies on the exit portals of the cells to reduce drag-out of the electrolyte on the strip. Leakage containment systems are included to capture drips and leaks, and then return those to the capture sump. The plating cell is 30 cm long and includes double-sided plating with variable flow control through a weir system. Weirs can be adjusted to compensate for loss of pressure across the cathode interface. Again, wipers are used at the exit portal to reduce drag-out. Lastly, a 1 cm toluene rinse station follows plating.

The plating system design is targeted at producing either a 1-mm sheet or coatings of nano-Al onto a strip where the coating may be thinner, as small as 30 µm. This latter capability will be useful for other DOE-related applications, namely nano-Al plating onto a Mg sheet.

The plating cell has been constructed as shown in Figure II.1.C.9. The existing frame and feed system was able to be re-used with a reconfigured feed and a new cell. The pay-off coil has been reconfigured to accommodate a larger starting coil, which will reduce feed stock changeover needs and reduce the risk for damage to the plating wipers. The plating cell has been built from PTFE. Eight anode cavities will produce a large plating area with a sufficient anode area to optimize the chemistry of the reactions. Each cavity will be lined with an anode bag made from Kevlar®, which is compatible with the plating chemistry. The activation and rinse stations are smaller than the main plating tank, as these regions require less dwell time. Each of the sump tanks have also been built (not shown in this picture) with PTFE liners. The plumbing system has been built to allow flow from each of the pumps, filters, and reservoirs. The electrical contacts were reconfigured to attach at the top of the device to simplify the connection and remove the electrical wiring from the working area.

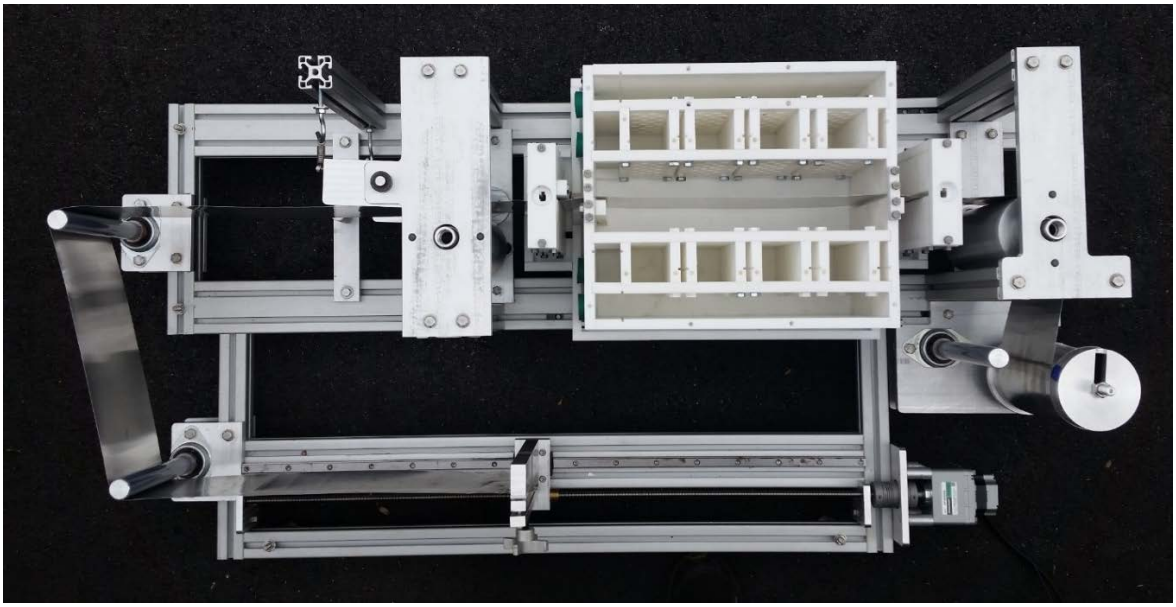

Figure II.1.C.9. Top view of double-sided plating cell. Source: Xtalic.

Conclusions

We have successfully plated full-size 6-in by 6-in panels with nano-Al alloys. The single-sided plating cell was qualified, then the capabilities were incorporated into a new double-sided plating cell design. This new plating cell has been built and is ready for installation. We conducted a 468-position design of experiments to quantify plating parameter effects on the overall plating rate, surface morphology and quality.

Key Publications

Hilty, R. D., and L. J. Masur, 2017, "On the formation of lightweight nanocrystalline aluminum alloys by electrodeposition," *The Journal of The Minerals, Metals & Materials Society (TMS)*, Vol. 69, No. 12, pp. 2621–2625. DOI: 10.1007/s11837-017-2499-z.

References

Freydina, E., S. Ruan, C. A. Schuh, and A. C. Lund, 2017, U.S. Patent 9758888, September 12, 2017. Preparation of metal substrate surfaces for electroplating in ionic liquids. U.S. Patent 9,758,888, filed May 6, 2014.

II.1.D High-Throughput Study of Diffusion and Phase Transformation Kinetics of Magnesium-Based Systems for Automotive Cast Magnesium Alloys (The Ohio State University)

Alan A. Luo, Co-Principal Investigator
The Ohio State University
137 Fontana Labs, 116 W. Nineteenth Ave.
Columbus, OH 43210
Phone: 614-292-5629
E-mail: luo.445@osu.edu

Ji-Cheng Zhao, Co-Principal Investigator
The Ohio State University
286 Watts Hall, 116 W. Nineteenth Ave.
Columbus, OH 43210
Phone: 614-292-9462
E-mail: zhao.199@osu.edu

Jerry L. Gibbs, Technology Manager
E-mail: jerry.gibbs@ee.doe.gov

Start Date: October 1, 2013 End Date: March 31, 2017
Total Project Cost: $800,000 DOE share: $600,000 Non-DOE share: $200,000

Executive Summary

The objective of this study was to establish the scientific foundation on the kinetic modeling of diffusion, phase precipitation, and casting/solidification in to accelerate the design and optimization of cast Mg alloys for weight reduction of the U.S. automotive fleet. The team has: 1) studied diffusion kinetics of six Mg-containing binary systems using high-throughput diffusion multiples to establish reliable diffusivity and mobility databases for the Mg-Al-zinc (Zn)-tin (Sn)-calcium (Ca)-strontium (Sr)-Mn system; 2) studied the precipitation kinetics (e.g., nucleation, growth, coarsening) using both innovative dual-anneal diffusion multiples and cast model alloys to provide large amounts of kinetic data (including interfacial energy) and microstructure atlases to enable implementation of the Kampmann-Wagner numerical model to simulate phase transformation kinetics of non-spherical/non-cuboidal precipitates in Mg alloys; 3) implemented a micromodel to take into account back diffusion in the solid phase in order to predict microstructure and microsegregation in multicomponent Mg alloys during dendritic solidification, especially under high-pressure die casting (HPDC) conditions; and 4) widely disseminated the data, knowledge, and information using the Materials Genome Initiative (MGI) infrastructure (http://www.mgidata.org), as well as publications and digital data sharing, to enable researchers to identify new pathways/routes to better cast Mg alloys.

Accomplishments

- Mg-Al, Zn, Sn, and yttrium (Y) systems diffusion data were critically evaluated with all other available literature data. The best-judgment diffusion coefficients as a function of temperature are determined. All the diffusion data are used as inputs to establish the Mg mobility database. Diffusion couples including Mg-Ce, gadolinium (Gd), Mn, and lithium (Li) systems were prepared and subjected to heat-treatment at various temperatures to study the diffusion and generate a series of composition profiles.
- Considering the back-diffusion and geometric of solidification dendritic structures, CALculation of PHAse Diagrams (CALPHAD)-based micromodels were used to simulate the microstructure evolution of die-casting AT72 alloy. A large difference exists between the simulations and the experimental measurements. TEM was used to reveal the details associated with die-casting Mg alloy microstructure.

- PanPrecipitation coupling with the Mg thermodynamic database and a new mobility database was used to simulate the evolution of concurrent precipitation microstructure in Mg-Al-Sn-based alloys. The simulation of precipitation kinetics in ternary Mg-Al-Sn system shows that the precipitation kinetics of Mg_2Sn phase in a ternary system is much faster than that in binary Mg-Sn systems, indicating alloying may be an effective method to speed up the precipitation kinetics in Mg-Sn systems.

Technology Assessment

- Target: Experimentally establish a complete Mg diffusivity/mobility database, including key alloying elements—Al, Zn, Sn, Ca, Mn, Sr, Zr—as well as RE elements—Y, Ce, Gd.
- Gap: Some elements are difficult to deal with in experiments. Reliable diffusion profiles cannot be measured using the EPMA due to extremely low solubility of Sr in Mg. The interaction between elements with high melting points and Mg is weak at the interface, since Mn and Zr do not form eutectic with Mg. RE elements are prone to oxidation and master Mg-RE alloys are needed.
- Target: Develop the PanSolidification module to simulate the solidification of multi-component Mg alloys and die-casting conditions.
- Gap: Issues such as applicability of the models to simulate alloys prepared by industrial solidification process with higher cooling rate need to be investigated and solved.
- Target: Investigate the precipitation of AT72 alloy during aging by a combination of experiment and simulation.
- Gap: Further optimize the PanPrecipitation module to achieve reliable simulation of concurrent precipitation microstructure.

Project Introduction

The lack of diffusivity data for Mg alloys is hindering the computational design of high performance Mg alloys using the Integrated Computational Materials Engineering approach. Compared with Al alloys, information on precipitation kinetics (e.g., nucleation, growth, and coarsening) of Mg alloys is not sufficient and needs to be investigated by a combination of experiments and simulations. A micromodel considering back diffusion and cooling rate is important for accurately simulating the solidification of Mg alloys, especially prepared by casting conditions. Solid-liquid diffusion couples for Mg-MgY, MgGd, MgCe, MgMn, and Li systems were prepared, and heat treatments were conducted at various temperatures to generate diffusion profiles for EPMA measurement. The diffusivities for Al, Zn, Sn, Ca, and Y were extracted from diffusion profiles by the forward simulation method (Zhang and Zhao 2013). Using the CALPHAD approach (Saunders and Miodownik 1998), the first version of a CALPHAD-type Mg atomic mobility database within this project was finished and used in the design of the solution treatment schedule, precipitation, and solidification simulations. The simulations on the microstructure evolutions of AZ91 and Mg-Sn alloys during aging were updated with the new database. AT72 alloy was microalloyed with Zn, Ag, Ca, and Cu, and the aging hardening responses were measured. The microsegregation data for Mg-Al, Mg-Al-Ca, and Mg-Al-Ca-Sn alloys from literature and current experiment were compiled. The PanSolidification module was used to simulate the solidifications of several binary Mg-Al and ternary Mg-Al-Ca alloys prepared by directional solidification. The HPDC AT72 alloy was prepared to provide microsegregation data for further development of the PanSolidification module.

Approach

Diffusion Study

Two types of diffusion samples are employed in this work to study the diffusion in Mg-based systems. The first type is the diffusion multiple, which is a highly-efficient technique to study solid diffusion. Another novel liquid-solid diffusion couple (LSDC) developed in this project is used to study the diffusion at elevated temperatures above eutectics of Mg binary systems. Figure II.1.D.1 shows an example of LSDC for studying diffusion in Mg alloys. The detailed procedures for preparing LSDC are as follows (Zhong and Zhao 1989): A ~5-mm diameter hole with a screw thread at the upper neck and a flat bottom was made to ~18 mm depth in a pure Mg (99.95 wt. %) block of ~20×20×25 mm. Pure Mg, Zn (99.95 wt. %), Sn (99.95 wt. %), Fe (99.9 wt. %), and a Mg-25 wt. % Y master alloy were prepared to required pellets (~5 mm in diameter and 3–5 mm in height) using mechanical machining or electrical discharge machining followed by grinding to a fine surface finishing. A steel screw was used to tighten the assembly after the prepared pellets were put in sequence into the hole of Mg blocks inside an argon protected glove box. The whole assembled LSDC was then sealed in a quartz tube with 1/5 atm pressure of backfilled argon. The samples were then subjected to designed heat treatments. The Mg-M (M refers to Zn, Sn, or Mg-25Y) region was then melted at annealing temperatures and diffusion took place between the melt and the surrounding pure Mg to form a Mg solid solution adjacent to the liquid pool formed in the center as schematically shown in Figure II.1.D.1(c). The LSDC samples were then quenched and sectioned through a center line, followed by metallographic preparation for microscopy characterization. The EPMA was employed to collect the diffusion profiles using a CAMECA SX100 electron microprobe with operation condition of 15 keV accelerating voltage, 30 nA beam current, and a 40° take-off angle at various step sizes. The forward-simulation analysis (Saunders and Miodownik 1998) was employed to extract both the impurity and interdiffusion coefficients.

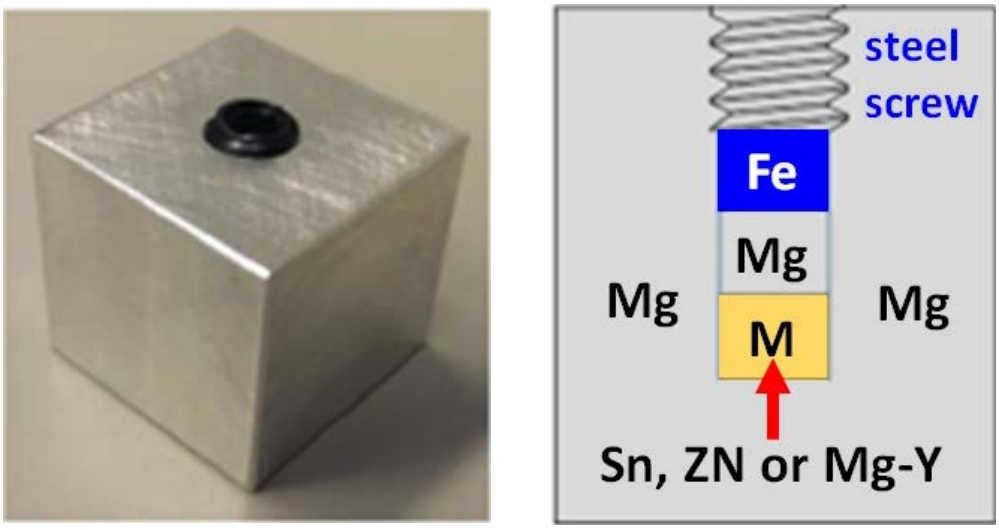

(a) (b)

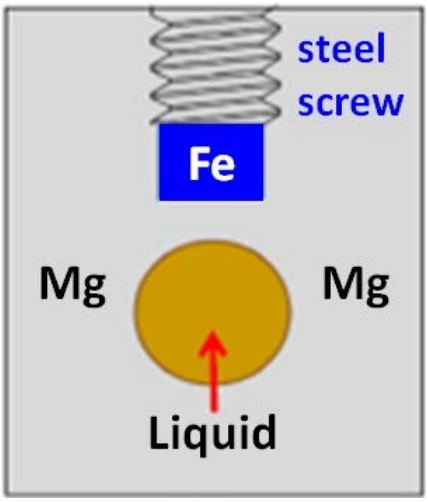

(c)

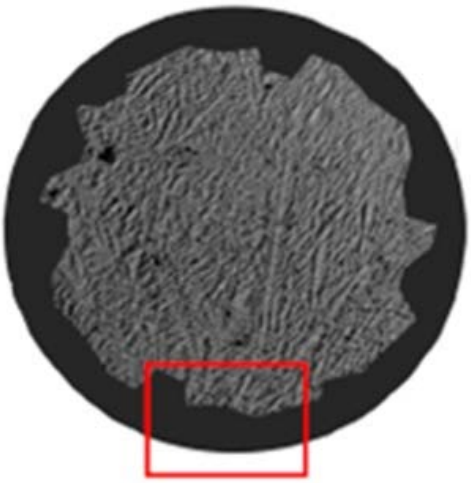

(d)

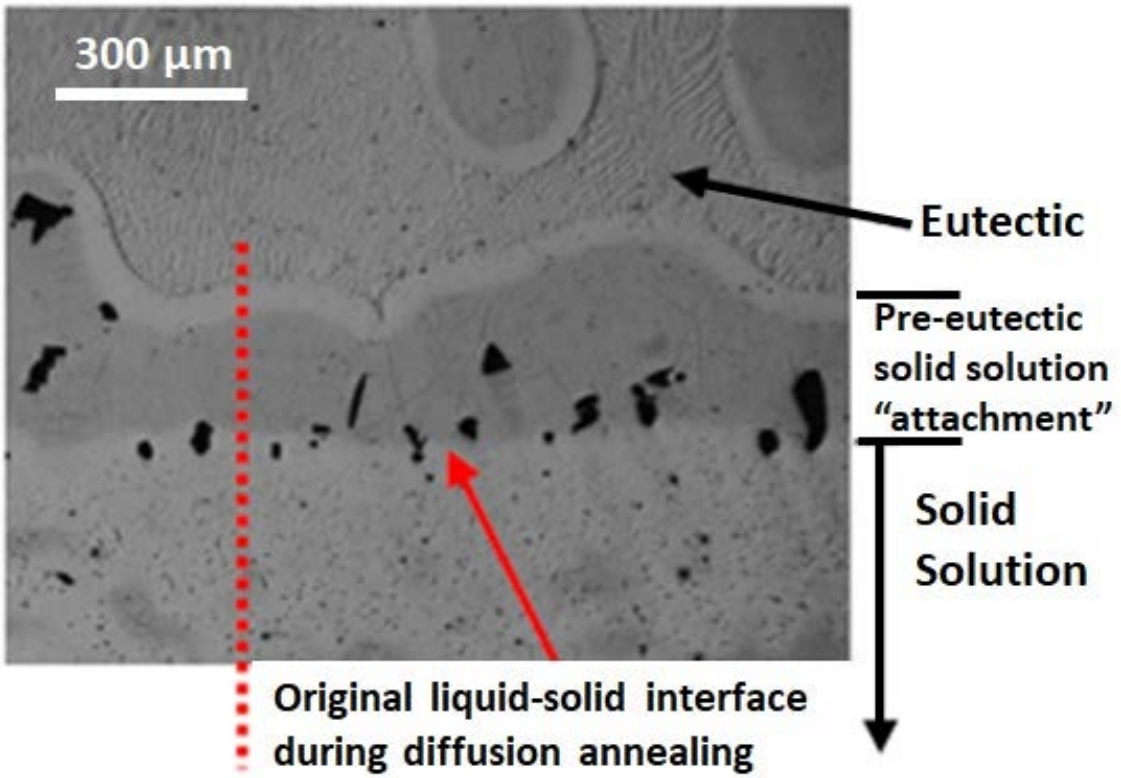

(e)

Figure II.1.D.1. Geometry of a LSDC and interaction of the molten/liquid phase with the solid solution: (a) photo of a sample LSDC (~ 20×20×25 mm); (b) schematic of a cross section; (c) schematic of the molten liquid in the middle to diffuse against the solid solution surrounding it at the annealing temperature; (d) schematic showing the formation of pre-eutectic solid solution ''attachment'' to the original solid solution during quenching to room temperature; and (e) Optical image of ''attachment'' to the original solid solution in the Mg-Y LSDC that was annealed at 630°C for 8 hours and then quenched to room temperature. The dotted line in (e) schematically denotes the EPMA line-scan orientation, while the rectangle location in (d) schematically shows the attachment layer location relative to the original solid solution. Source: The Ohio State University.

Solidification Modeling and Experimental Study

The microsegregation behavior of Mg alloys can be quantitatively characterized using EPMA. To achieve statistical results of microsegregation of different alloying elements, testing grids consisting of 400 data points with an inter-space ranging from 10–20μm were uniformly placed in a sample area covering several grains. At each grid point, the chemical compositions of alloying elements were measured using EPMA. Figure II.1.D.2(a) shows an example of such a testing grid overlapped on a backscattered electron SEM image of the microstructure of a directional solidification Mg-8.12Al-1.55Ca-2.91Sn alloy. The collected compositions of different alloying elements can be further sorted using the Flemings-Gungor method (Gungor 1989). Figure II.1.D.2(b) shows an example of sorted composition profile of Al in the directional solidification Mg-8.12Al-1.55Ca-2.91Sn alloy.

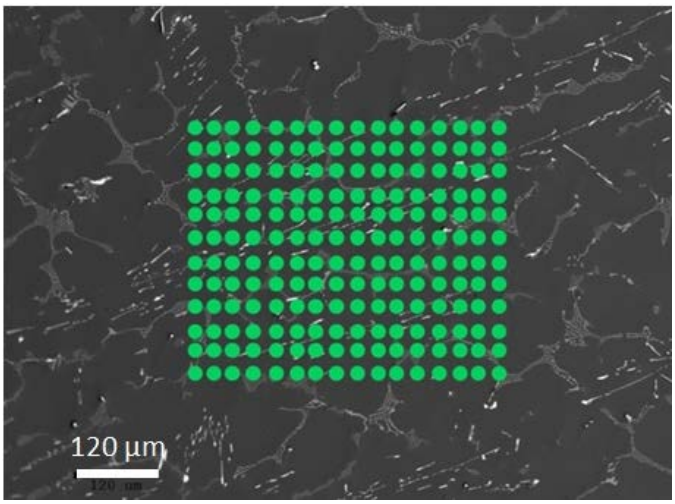

(a)

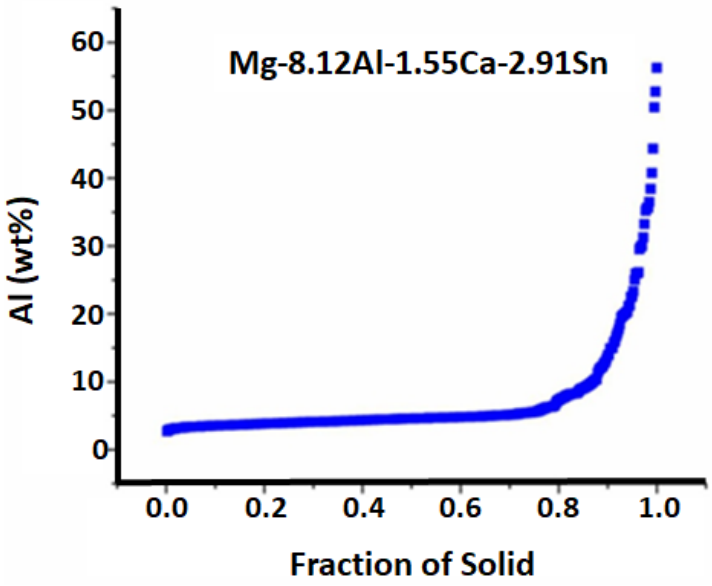

(b)

Figure II.1.D.2. Quantitative characterization of microsegregation of alloying elements in Mg alloys: (a) an example of EPMA testing grid overlapped on a backscattered electron SEM image; and (b) an example of a sorted composition profile of Al based on quantitative EPMA analysis. Source: The Ohio State University.

Precipitation Modeling and Experimental Study

The evolution of precipitation microstructure in Mg alloys was characterized using advanced electron microscopy techniques. Figure II.1.D.3(a) shows the high-angle annular dark field-scanning transmission electron microscope (HAADF-STEM) image of the AT72 (Mg-7, Al-2, Sn, wt. %) sample aged for 72 hours. Scanning transmission electron microscope-energy-dispersive X-ray spectroscopy (STEM-EDS) maps were used to distinguish two group precipitates in this alloy: Mg_2Sn and $Mg_{17}Al_{12,}$ as shown in Figure II.1.D.3(b) through Figure II.1.D.3(d). The foil thickness for calculating the number density is measured using zero-loss electron energy loss (EELS) spectrum. Figure II.1.D.3(e) shows an example of zero-loss EELS spectrum obtained from an AT72 TEM specimen.

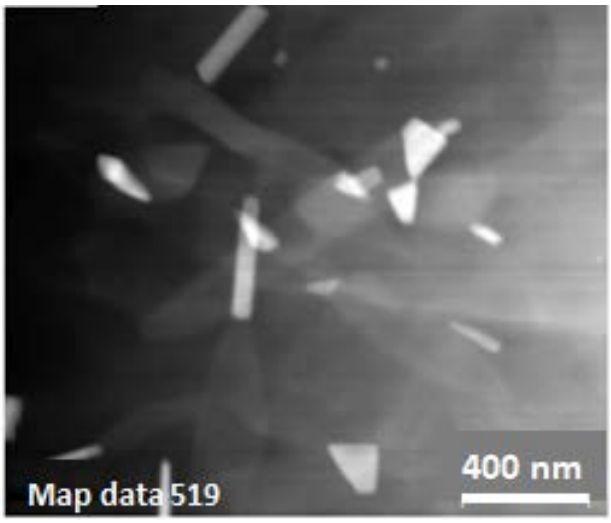

(a)

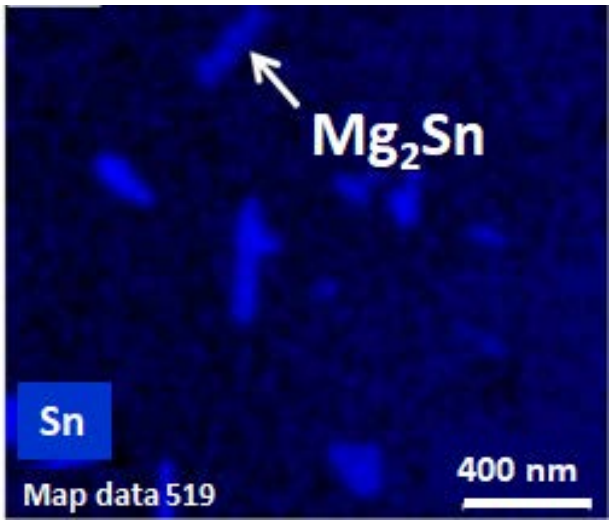

(b)

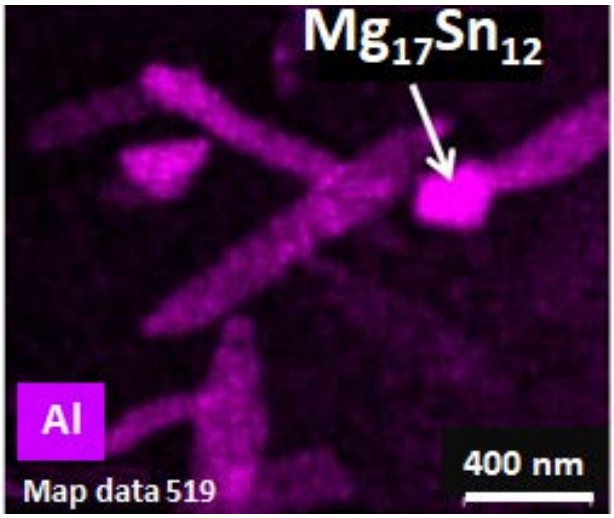

(c)

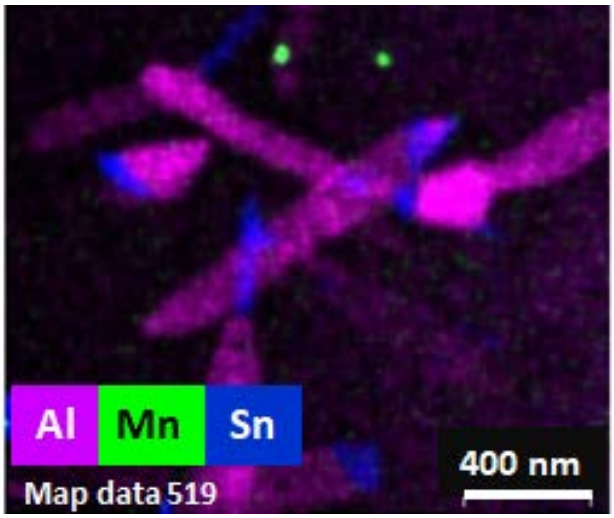

(d)

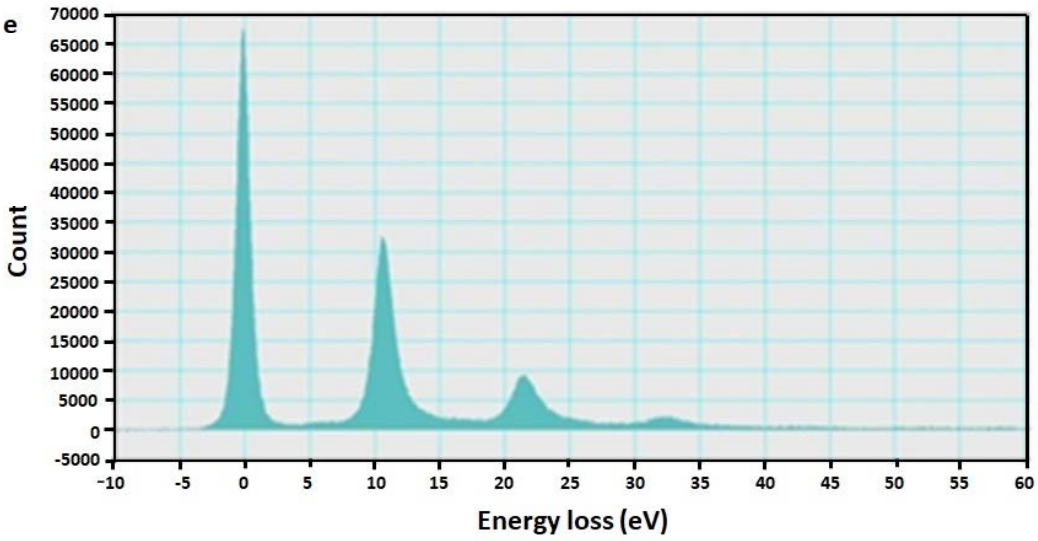

(e)

Figure II.1.D.3. STEM/STEM-EDS characterization of AT72 microstructure aged at 200°C for 72 hours: (a) HAADF-STEM image, (b) Sn-EDS map; (c) Al EDS map; (d) overlapped elements map; and (e) zero-loss EELS spectrum. Source: The Ohio State University.

Technology Transfer Path

The diffusivities measured in this work significantly improve the Mg alloy diffusivity database, which is rather inadequate compared with that of Al alloys. These experimental data lay the foundation for investigation of diffusion of alloying element in Mg and can assist the design of high performance Mg alloys using an Integrated Computational Materials Engineering approach.

Through coupling to Mg thermodynamic database, the established CALPHAD-type Mg atomic mobility database can conveniently calculate or extrapolate composition and temperature dependent diffusion coefficients for precipitation and solidification simulations or other process design.

The PanSolidification module can be used to predict more accurate microstructure evolution of Mg alloys during casting process such as solidification path, microsegregation and second arm spacing once fully developed.

The research on the precipitation and micro-alloying of AT72 alloy can help further improve and optimize the aging hardening response of AT72 alloy.

Results

Three Mg-Zn LSDCs were annealed at 450°C for 8 hours, 500°C for 6 hours, and 550°C for 6 hours, respectively. The solubility values at these temperatures are determined to be 3.5, 2.6, and 1.7 wt. % Zn, respectively. In Figure II.1.D.4(a), forward-simulation analysis was used to obtain the interdiffusion and impurity diffusion coefficients on the LSDC profiles. As shown in Figure II.1.D.4(b) and Figure II.1.D.4(c), the results from this work are comparable with those from literatures. Additional data from one diffusion multiple containing a Mg-Zn solid-solid diffusion couple (SSDC) annealed at 275°C for 1760 hours are also included in Figure II.1.D.4(b) and Figure II.1.D.4(c) to extend the reliability of the diffusion coefficients to lower temperatures. Our results agree very well with those of Kammerer et al. (2014). As shown in Figure II.1.D.4(c), the diffusion coefficient values obtained by Das et al. (2013) are significantly lower than all other datasets: our data, the results obtained by Kammerer et al. (2014), as well as data from tracer experiments

performed by Lal (1967) and Čermák and Stloukal (2006). By fitting four datasets with remarkable agreement, our data, results from Kammerer et al. (2014), and tracer experiments by Lal (1967) and Čermák and Stloukal (2006), the best-judgement/consentaneous impurity diffusion coefficient of Zn in Mg is determined as the solid line in Figure II.1.D.4(c).

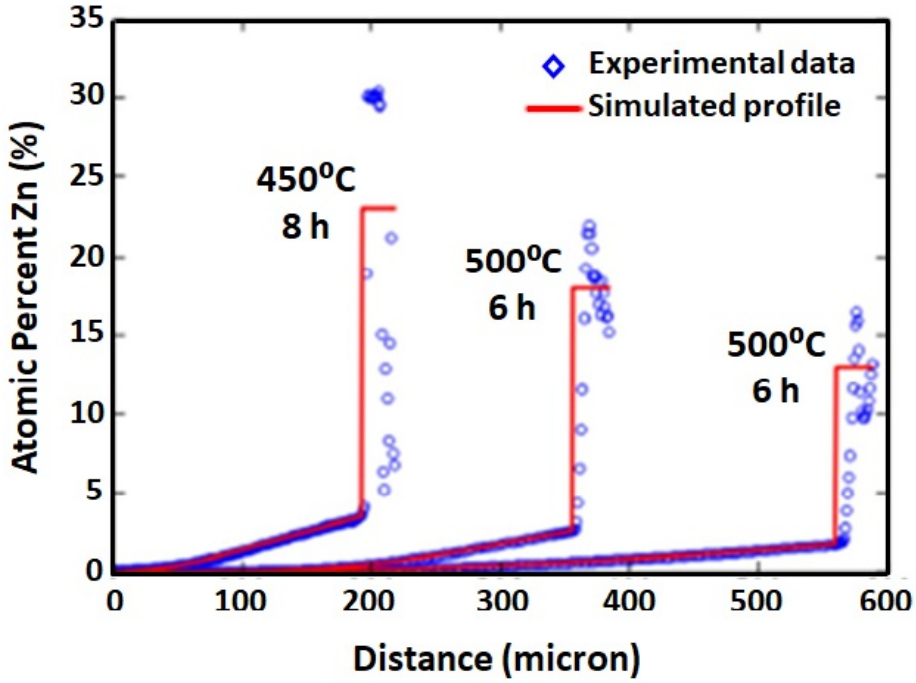

(a)

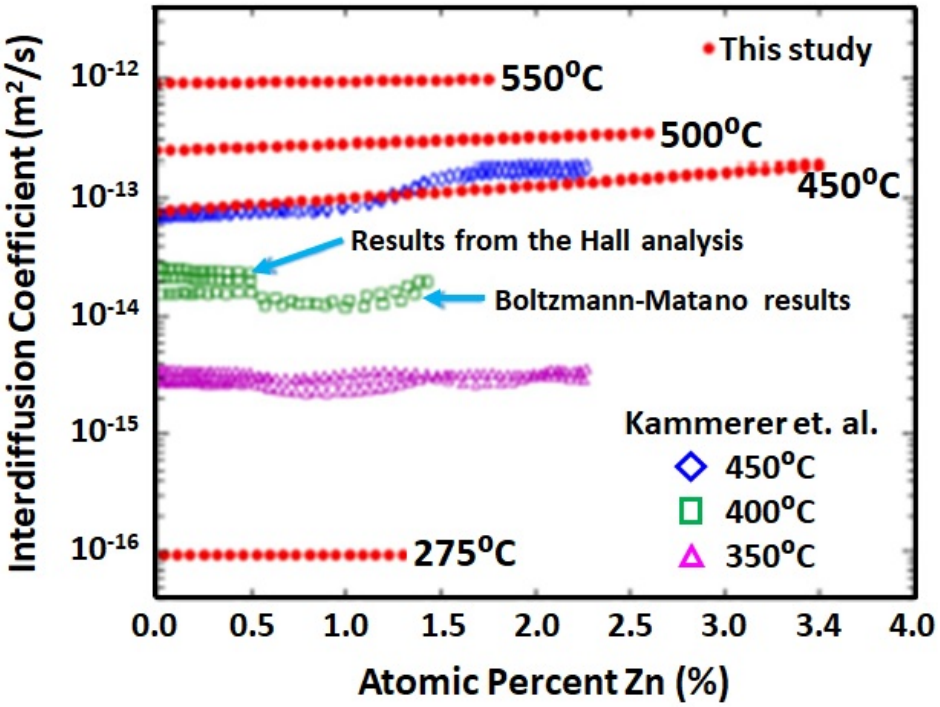

(b)

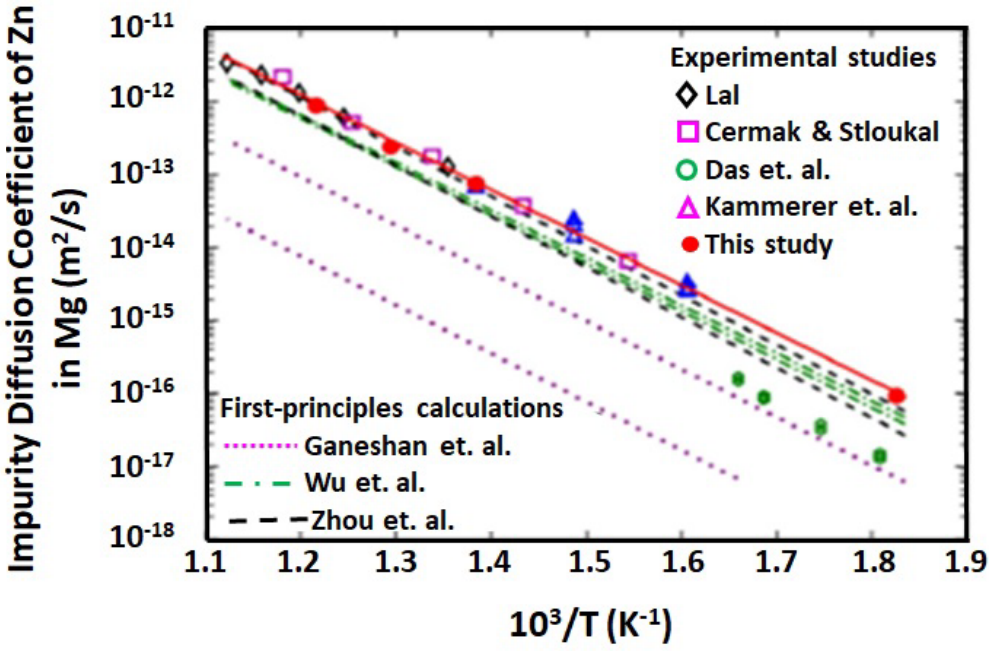

(c)

Figure II.1.D.4. Results for the Mg-Zn system: (a) experimental and simulated LSDC profiles; (b) interdiffusion coefficients for the hcp phase of the Mg-Zn system; and (c) comparison of experimental impurity diffusion coefficients of Zn in Mg with first-principle calculation results (Zhou et.al. 2016, Ganeshan et.al. 2011, and Wu et al. 2016).

Similarly, LSDCs and diffusion multiples were used for studying interdiffusion and impurity of Sn in Mg alloys. Figure II.1.D.5(a) shows experimentally measured concentration profiles, as compared with forward-simulation analysis results. The optimized Sn interdiffusion coefficient obtained in this work at different temperatures is given in Figure II.1.D.5(b). The Sn interdiffusion coefficient has no strong dependence on composition. Impurity diffusion coefficients of Sn in Mg are also shown in Figure II.1.D.5(c), as compared with results from both experimental results and first principle calculations from the literature.

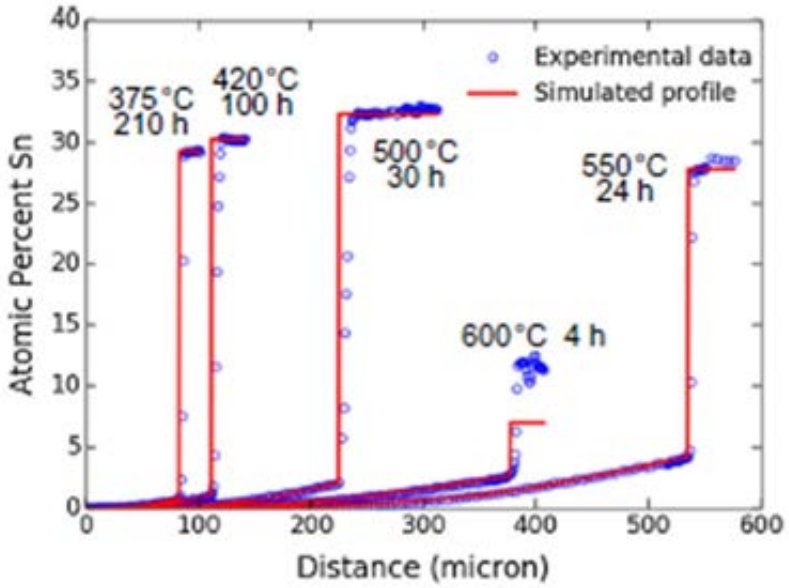

(a)

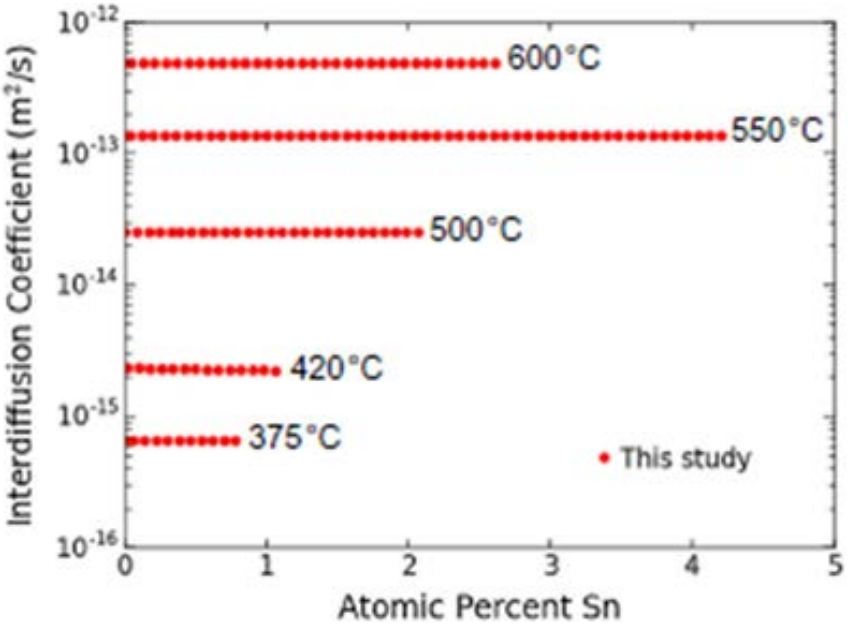

(b)

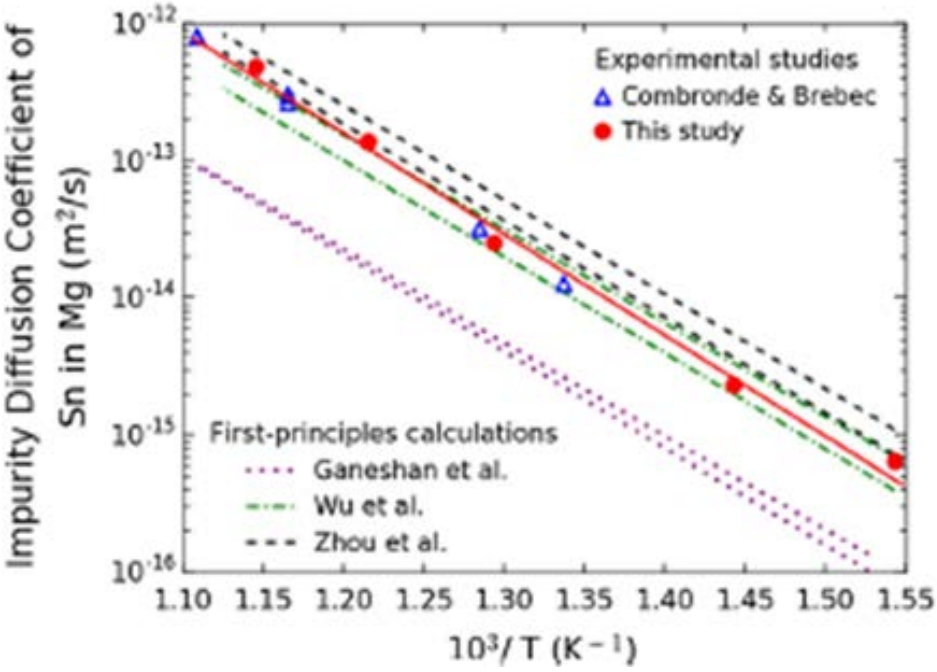

(c)

Figure II.1.D.5. Results for the Mg-Sn system: (a) experimental and simulated diffusion profiles; (b) interdiffusion coefficients for the hcp phase of the Mg-Sn system; and (c) comparison of experimental impurity diffusion coefficients of Sn in Mg with first-principle calculation results (Zhou et.al. 2016, Ganeshan et.al. 2011, and Wu et al. 2016).

Diffusion samples of Mg-Nd, Sr, Gd, Li, Ce, and Mn systems were also prepared. There were some difficulties in studying the diffusion behavior in these systems. Sr is a very reactive element and has very low solubility in Mg. Although Mg-Sr LSDCs were successfully annealed in our work, the diffusion profiles cannot be reliably determined due to the measurement limit of EPMA. Li is also a very active element and liquefies easily. The Mg-Li liquid-solid diffusion couples were thus assembled in a glove box with a high purity argon atmosphere. The atom of Li is so light that the composition of Li in the obtained diffusion samples cannot be measured by EPMA. Therefore, the diffusion profiles of Mg-Li are determined by measuring the Mg composition in the couple. Mn and other RE elements have relatively high melting points compared to Mg, as well as other solutes in Mg. Therefore, the Mg binary alloys with these elements were used to assemble the LSDCs. Some diffusion profiles obtained are shown in Figure II.1.D.6. The diffusion coefficients will be extracted using forward-simulation analysis afterwards.

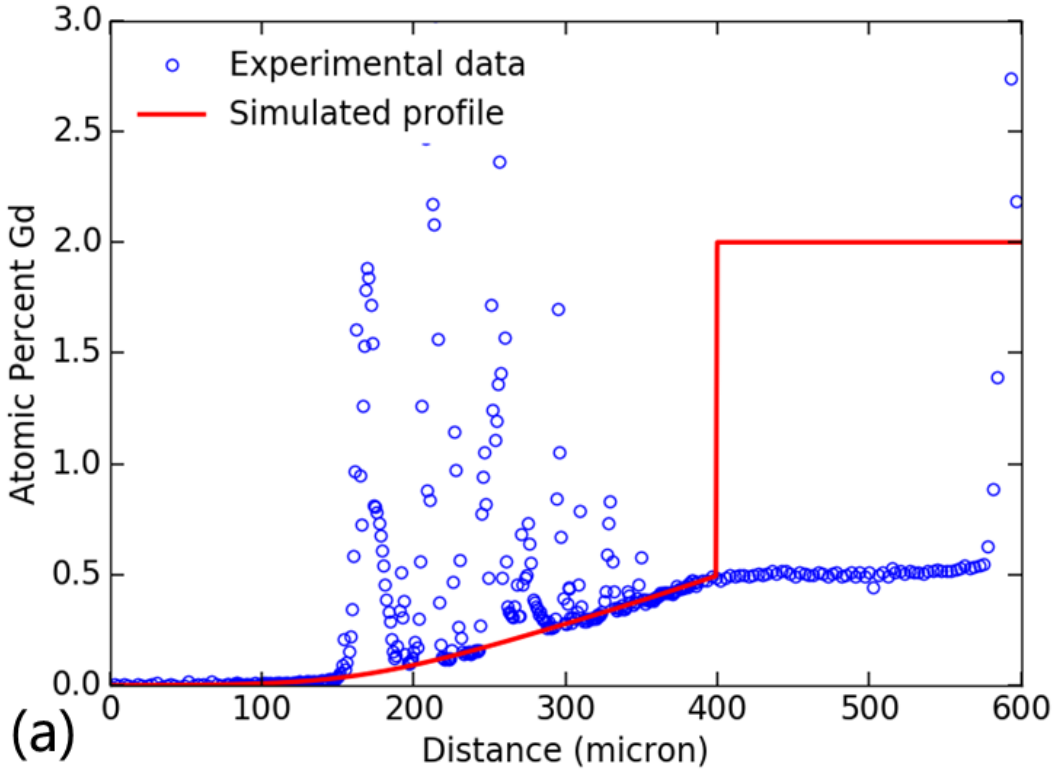

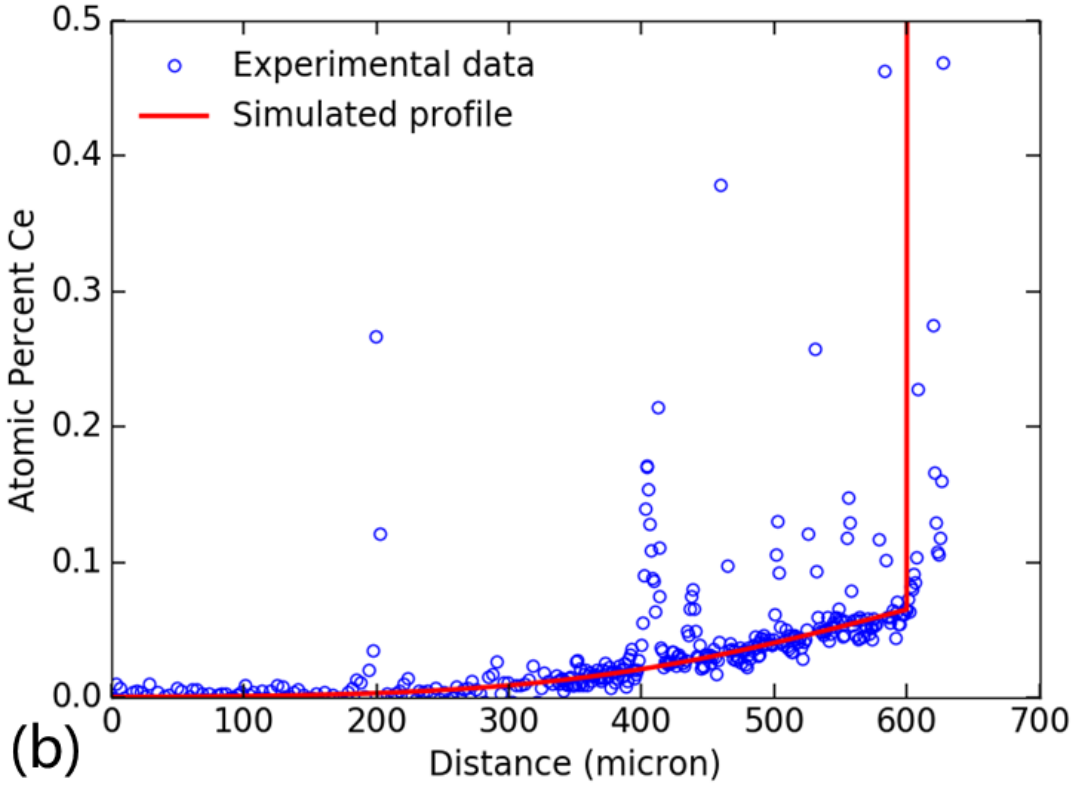
Experimental data
Simulated profile
Atomic Percent Ce
Distance (micron)
0.0
0.1
0.2
0.3
0.4
0.5
0
100
200
300
400
500
600
700
(b)

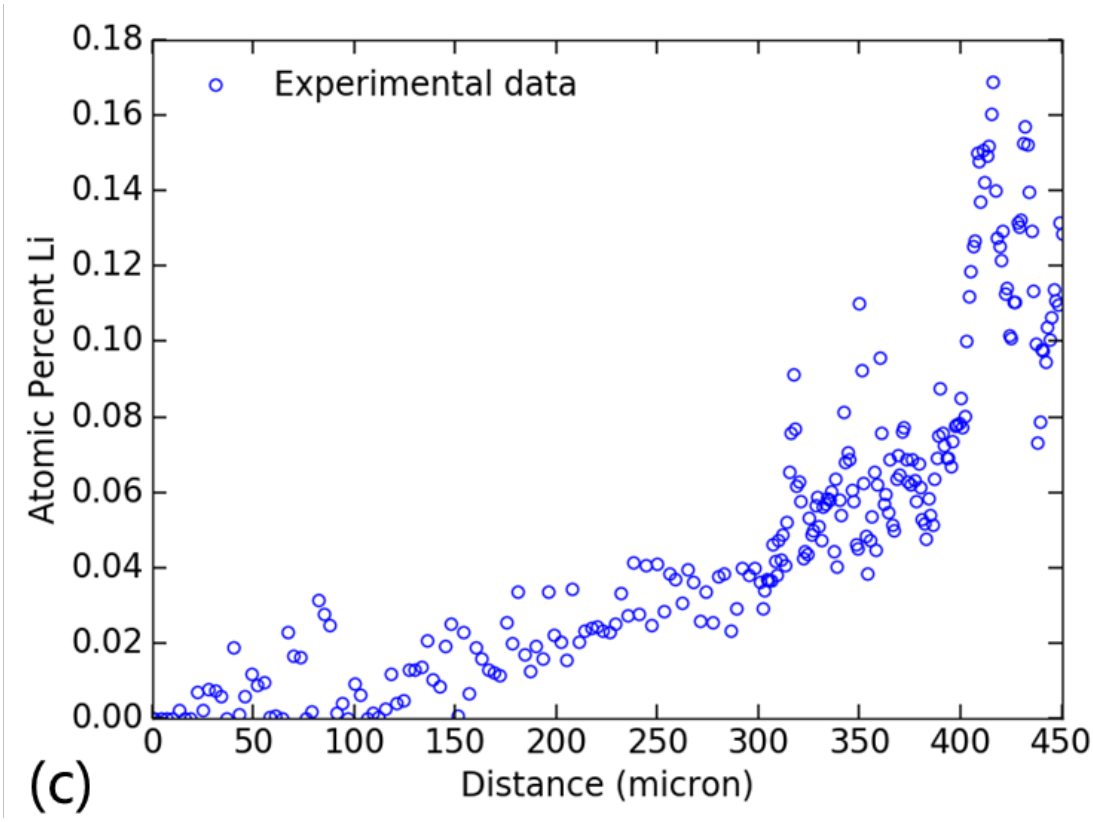
Experimental data
Atomic Percent Li
Distance (micron)
0.00
0.02
0.04
0.06
0.08
0.10
0.12
0.14
0.16
0.18
0
50
100
150
200
250
300
350
400
450
(c)

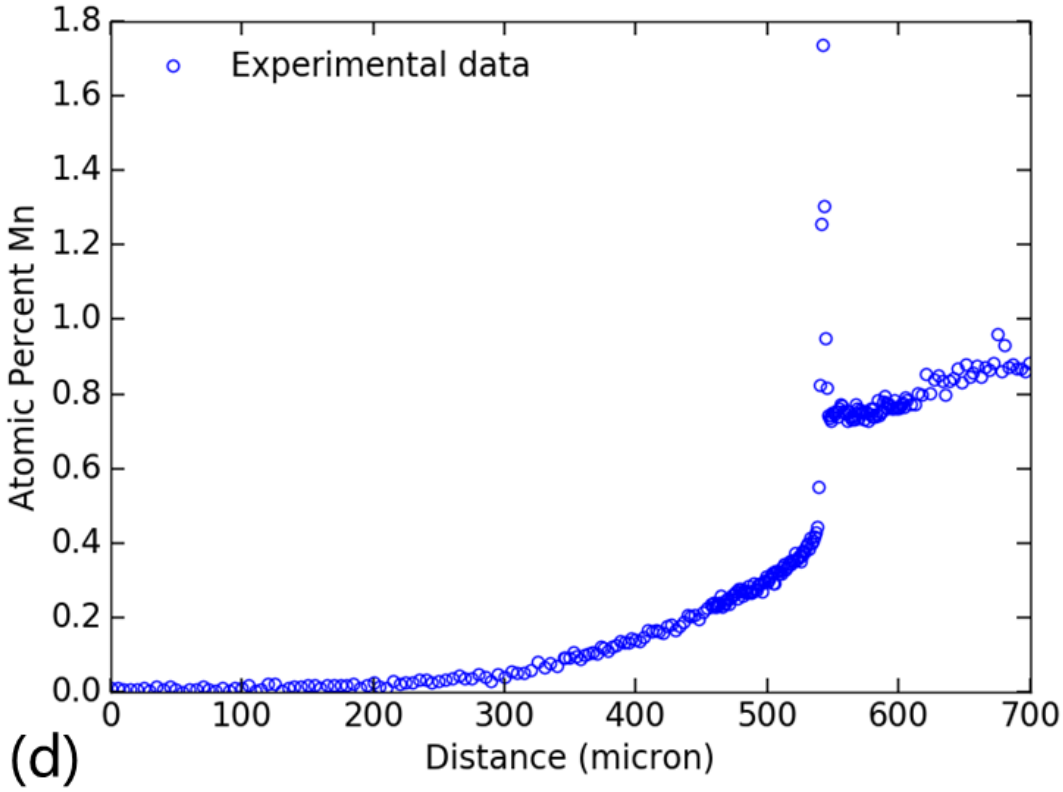

Figure II.1.D.6. Diffusion profiles: (a) Mg-Gd; (b) Mg-Ce; (c) Mg-Li; and (d) Mg-Mn systems.

The PanSolidification module was employed to simulate microsegregation behavior associated with the die casting process. AT72 Mg test samples were prepared using die casting. The cooling curve associated with the solidification were experimentally measured at the center of casting ingot and also simulated using ProCAST software. Figure II.1.D.7 shows both the experimental measurement and simulation results of cooling curves. It can be seen that ProCAST simulations can successfully capture main features of the experimental cooling curve. However, the simulation curve shifts to the right in Figure II.1.D.7 with respect to the experimental cooling curve. This is possibly due to the fact that in simulation, it needs about 0.5 sec. to allow the molten alloy to fill the center location of casting mold. The measured cooling curve may provide accurate inputs for PanSolidification modeling.

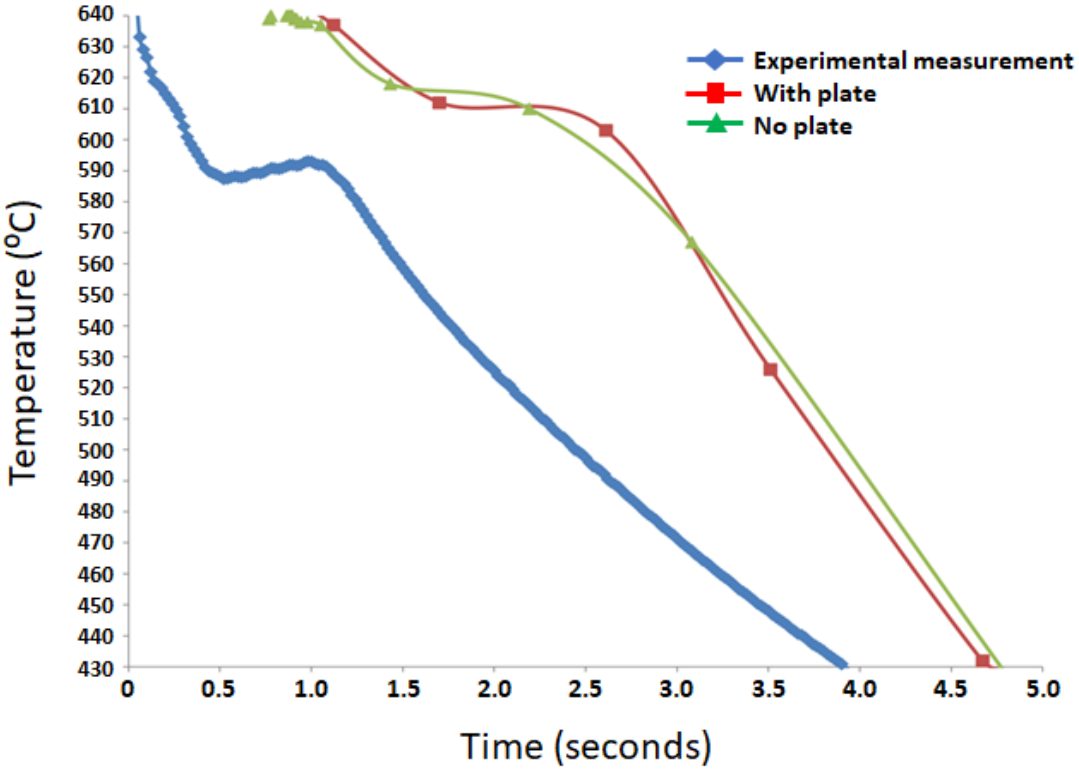

Figure II.1.D.7. Experimental measurement of cooling curve and ProCAST simulation with or without consideration of the effect of cooling plate beneath the casting mold.

Figure II.1.D.8(a) shows the as-cast microstructure of AT 72 Mg alloy. Due to fast cooling rate associated with solidification process, the microstructure has fine primary α cell in the order of a few microns. Figure II.1.D.8(b) shows the calculated concentration profiles of Al and Sn for AT72 alloy. The solid lines are calculated using the Scheil model for both Al and Sn, and the results calculated using the Lever-rule model are shown in dashed lines. EPMA measurements are also shown in the figure for comparison. As mentioned above, the AT72 sample was prepared using die-casting. The cooling rate involved in die-casting is much higher than those in directional solidification tests. Based on experience, this experimental data should be much closer to the results of the Scheil prediction than the Lever-rule prediction. However, large discrepancies are found between the experimental data and calculated results. There are several possibilities from either experimental measurement and/or calculation. Here, we would like to mention the EPMA measurement for the die casting sample is extremely difficult due to the relatively small sizes of primary Mg cells. There is an interaction volume when electron beam interacts with specimens. The size of interaction volume depends on accelerating voltage: the higher accelerating voltage, the larger interaction volume which usually ranges from 1–10 µm in diameter. For die-casting microstructure with fine primary α cells, during EPMA data collection, the electron beam has more of a chance to hit the inter-dendritic region than the primary hexagonal close-packed (Mg) phase. Thus, the statistical approach used in the work to normalize the measured results linearly within 0 to 1 may not be reasonable and the contribution from the inter-dendritic region could be over-counted. STEM-EDS was employed to further study the as-cast microstructure. Figure II.1.D.9(a) shows a HAADF-STEM image of an as-cast microstructure of AT72 alloy. EDS element maps of Mg, Al, and Sn are given in Figure II.1.D.9(b) to Figure II.1.D.9(c), respectively. It can be seen that Al and Sn are mainly partitioned to the cell boundaries. Such segregation may impose large impact on mechanical properties of Mg alloys. Figure II.1.D.10 shows the microstructure of AT72 alloy after directly aging at 200°C without solution treatment. There is high density of $Mg_{17}Al_{12}$ and Mg_2Sn precipitates at cell boundaries, while the density of precipitates within the interior of the cell is very low.

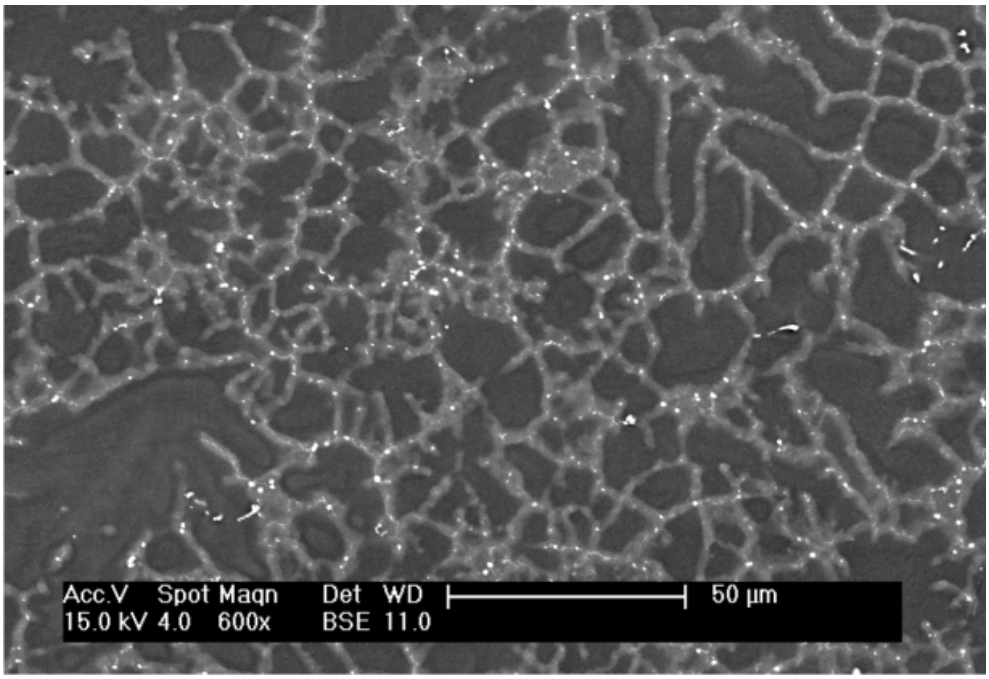

(a)

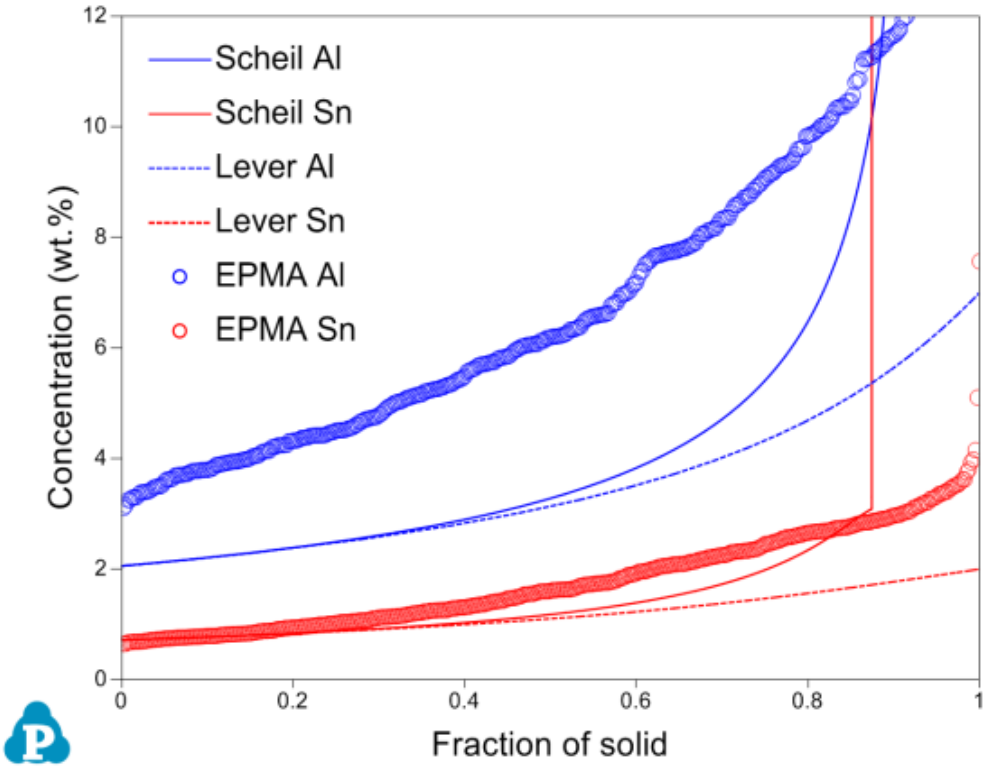

(b)

Figure II.1.D.8. (a) The microstructure of die-casting AT72 alloy; and (b) the calculated concentration profiles of Al and Sn for AT72 alloy using both Scheil and Lever-rule models as compared with experimental results. Source: The Ohio State University.

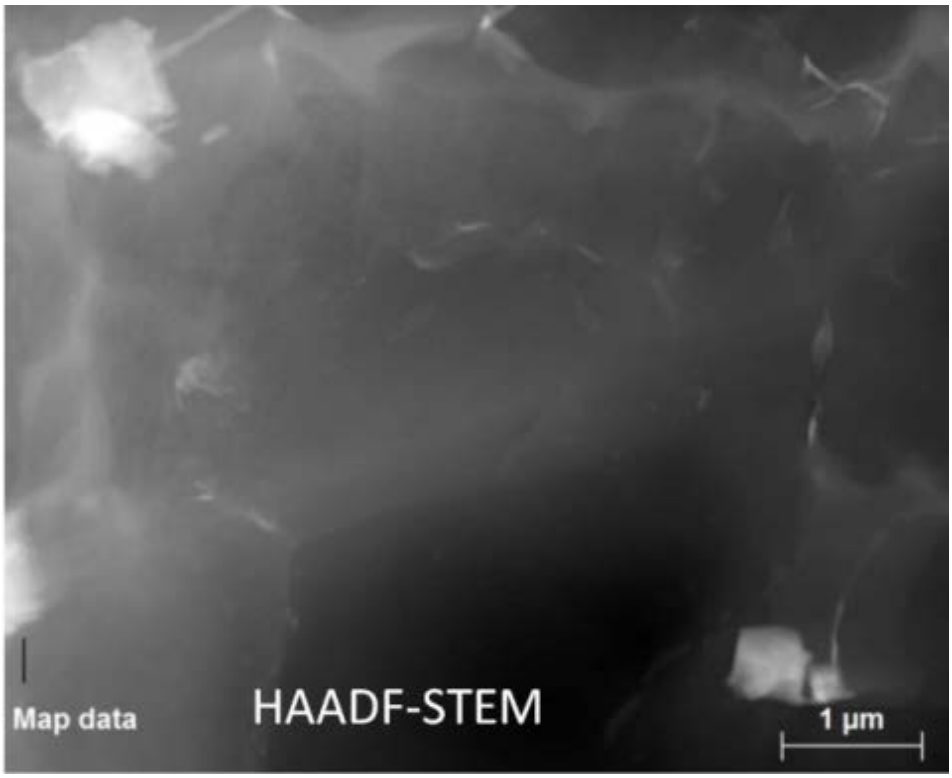

(a)

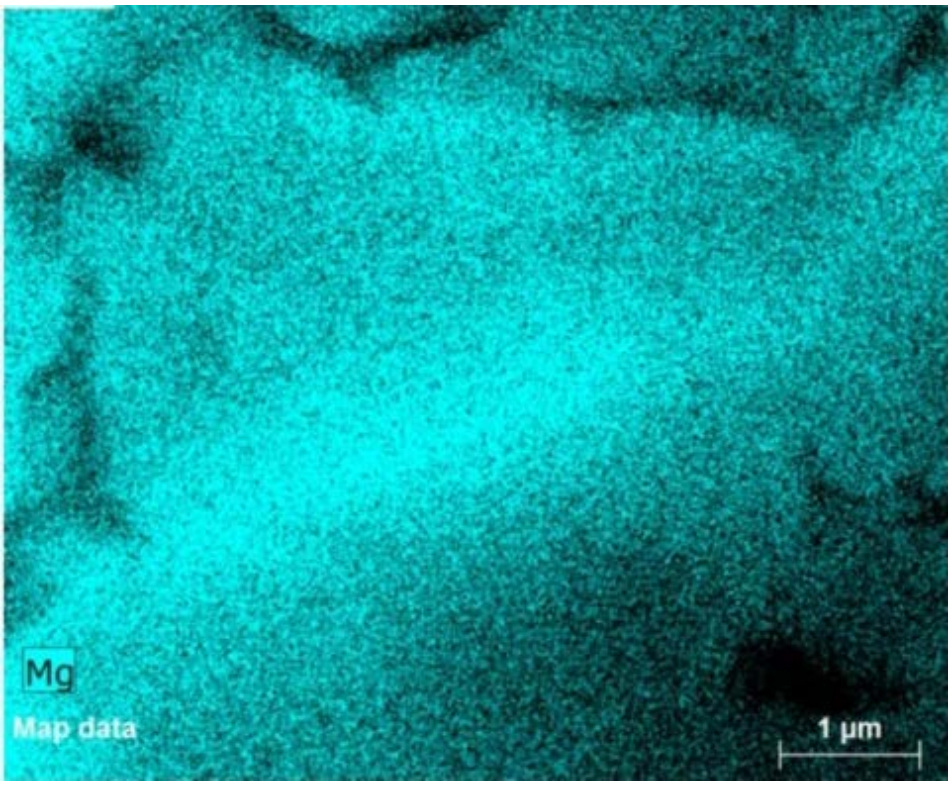

(b)

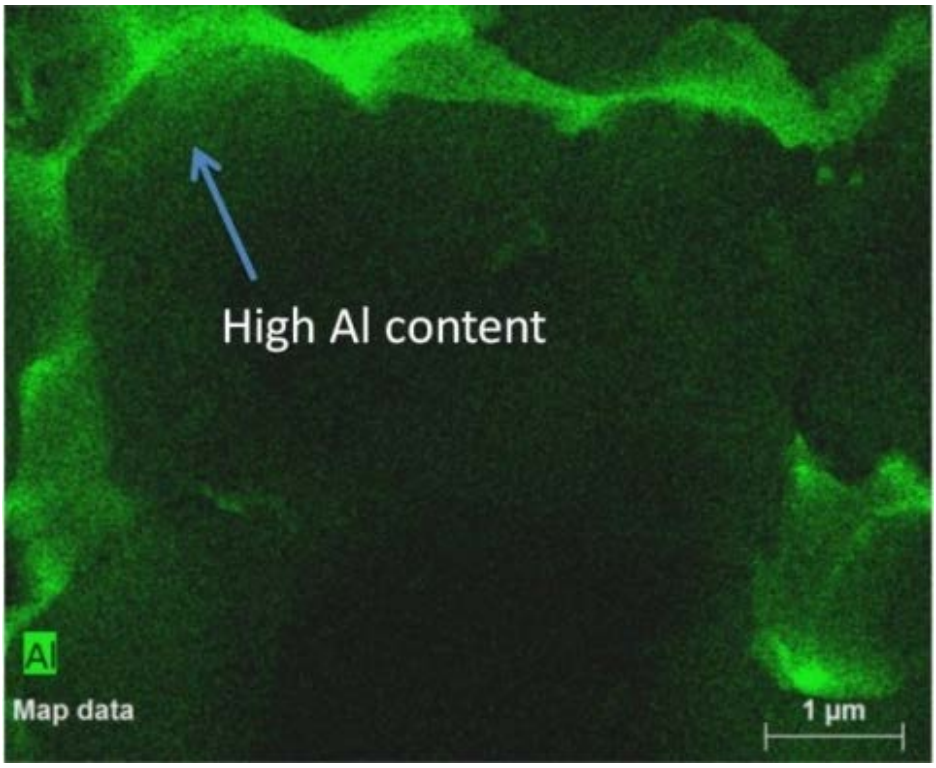

(c)

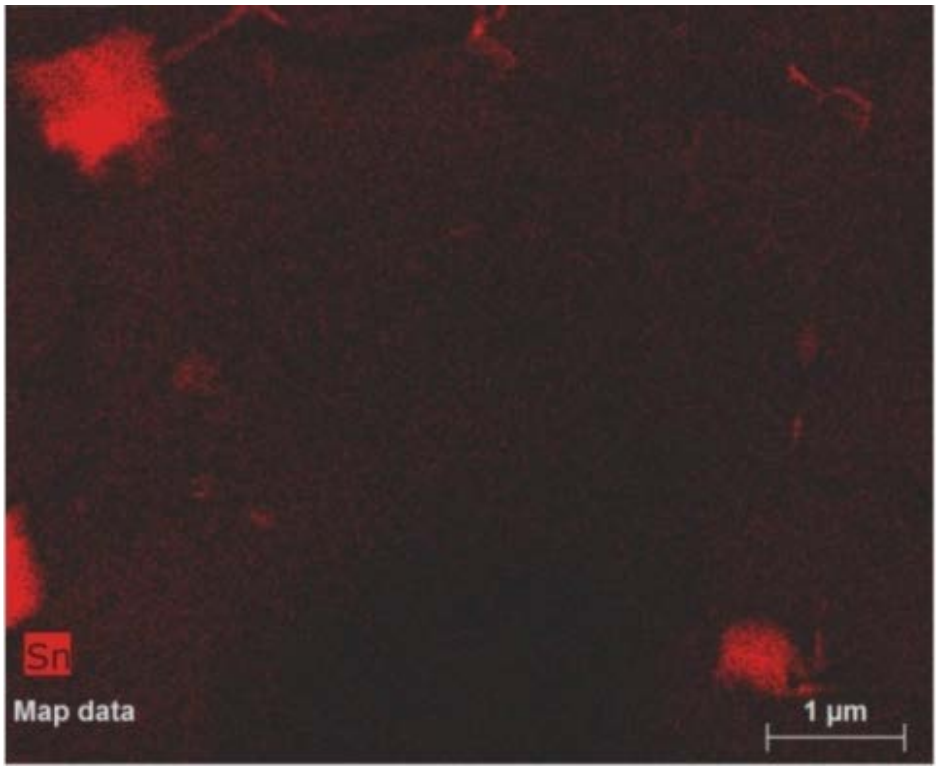

(d)

Figure II.1.D.9. STEM characterization of HPDC microstructure: (a) HAADF-STEM image; (b) Mg map; (c) Al map; and (d) Sn map. Source: The Ohio State University.

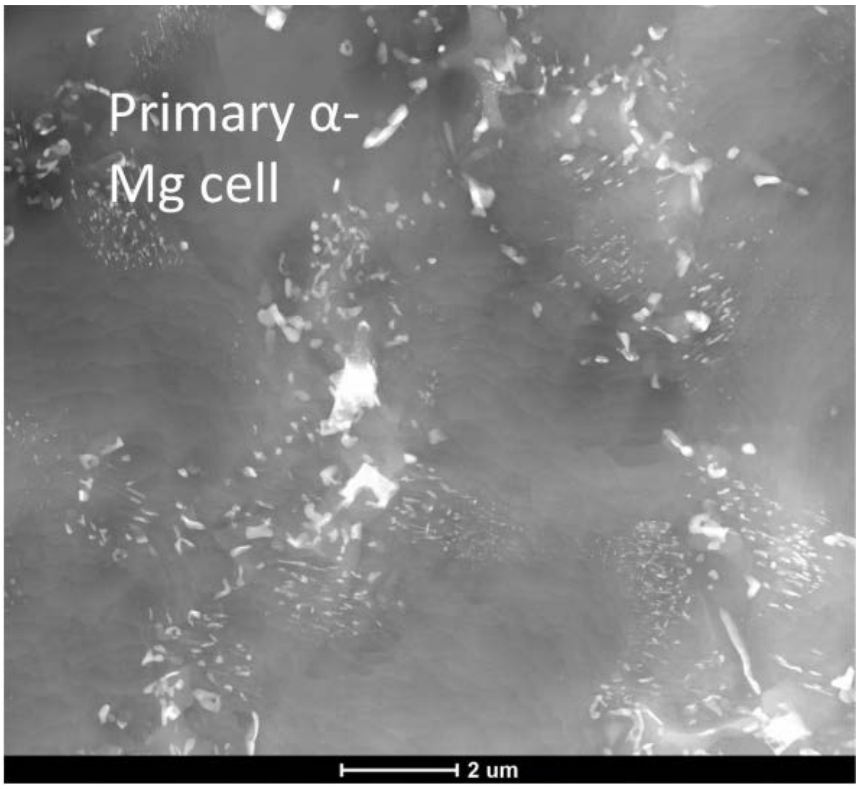

(a)

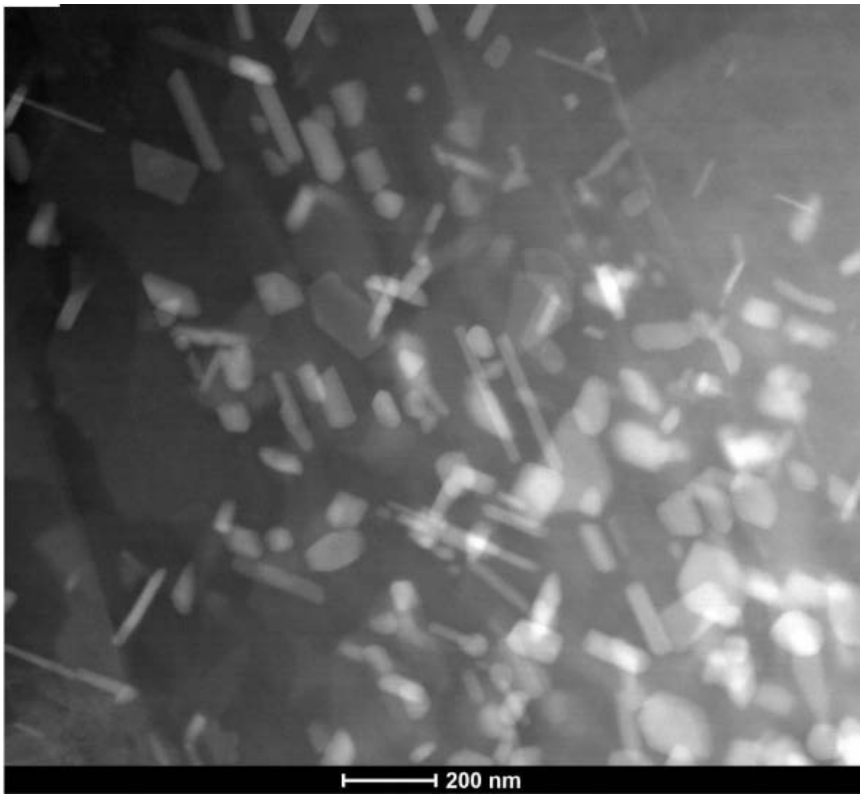

(b)

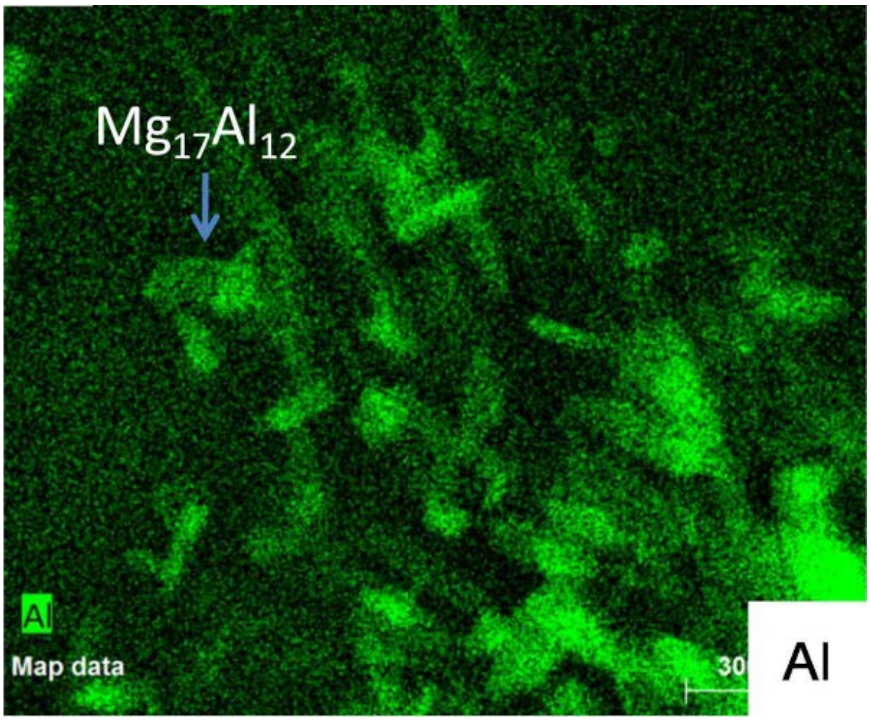

(c)

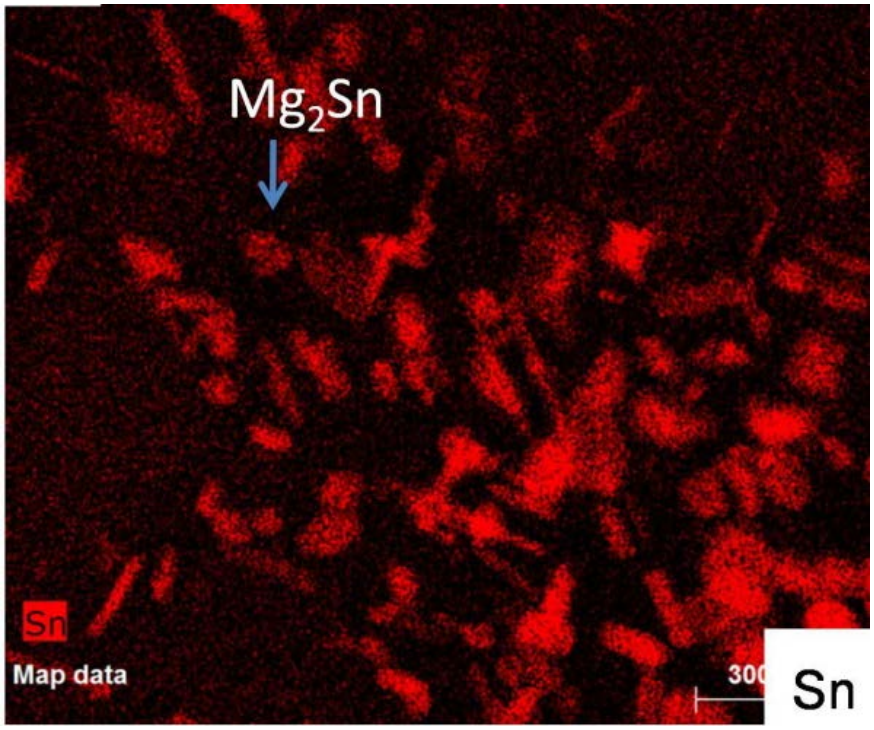

(d)

Figure II.1.D.10. STEM characterization of AT72 microstructure after aging treatment at 200 °C without solution treatment: (a) low magnification HAADF-STEM image; (b) high magnification HAADF-STEM image showing the formation of high density of precipitation microstructure at primary cell boundaries; (c) corresponding Al map of the region in (b); and (d) corresponding Sn map of the region showing in (b). Source: The Ohio State University.

Concurrent precipitation of $Mg_{17}Al_{12}$ and Mg_2Sn in Mg-7Al-2Sn (wt. %) alloys is simulated using Panprecipiation combining with the newly developed Mg mobility database. Figure II.1.D.11 shows the predicted microstructure evolution of Mg_2Sn and $Mg_{17}Al_{12}$ as compared with the measured number density of each precipitates. The number density of Mg_2Sn precipitates predicted by simulation is lower than that experimentally measured (the blue triangle). Therefore, in Figure II.1.D.11(a), the blue triangle (experimental measurement) is above the lower line (simulation results) rather than on it. From simulation, it is concluded that the precipitation of $Mg_{17}Al_{12}$ is much faster than that of Mg_2Sn. As compared with precipitation kinetics of Mg_2Sn in Mg-Sn binary alloy, the precipitation of Mg_2Sn in the ternary alloy was greatly accelerated. Further alloying may be an effective way to optimize the properties of AT72 alloy.

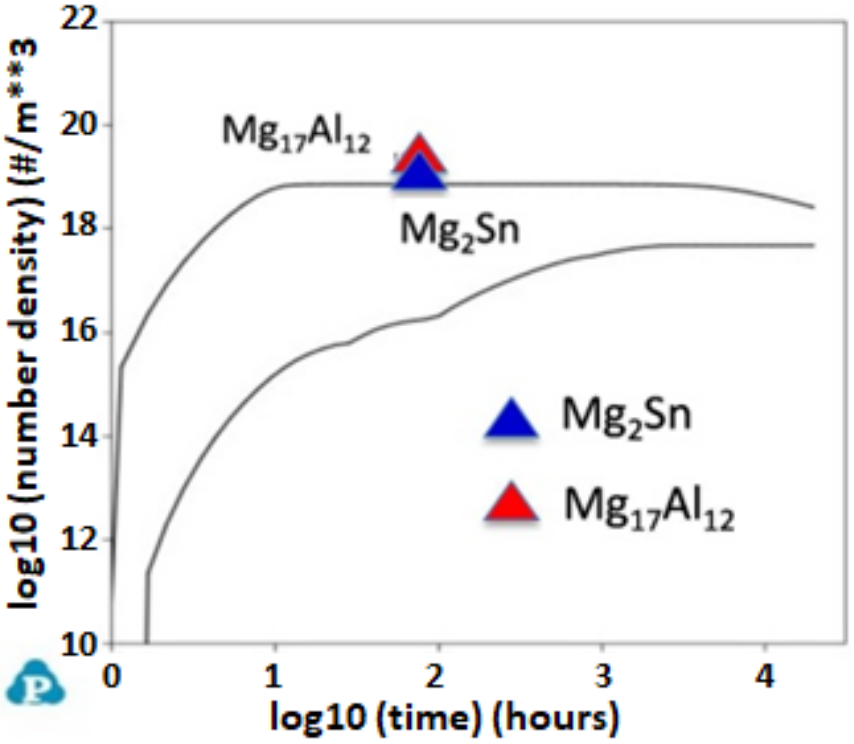

(a)

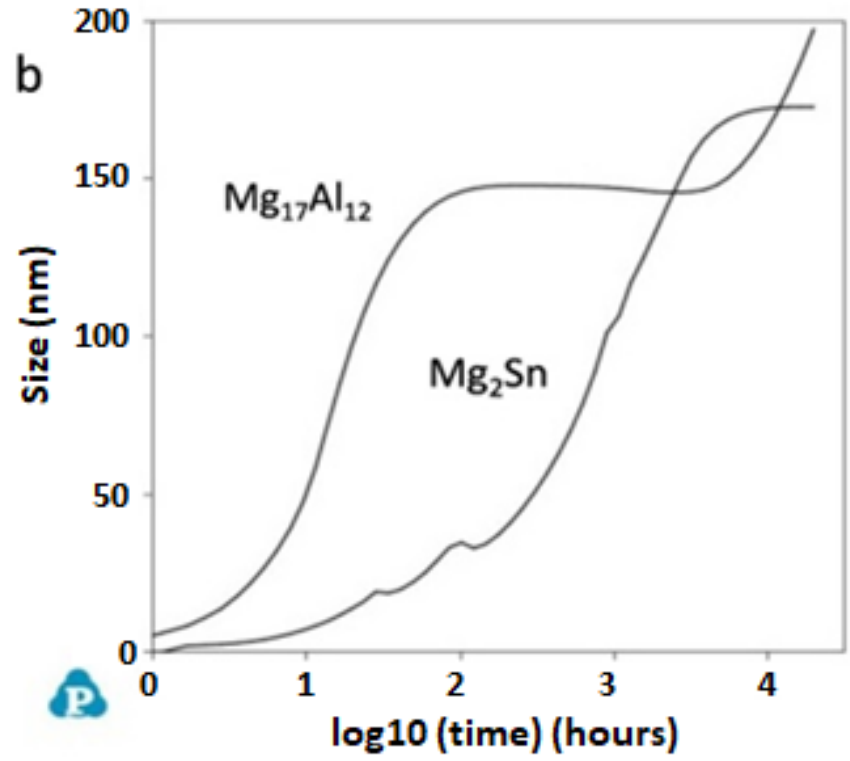

(b)

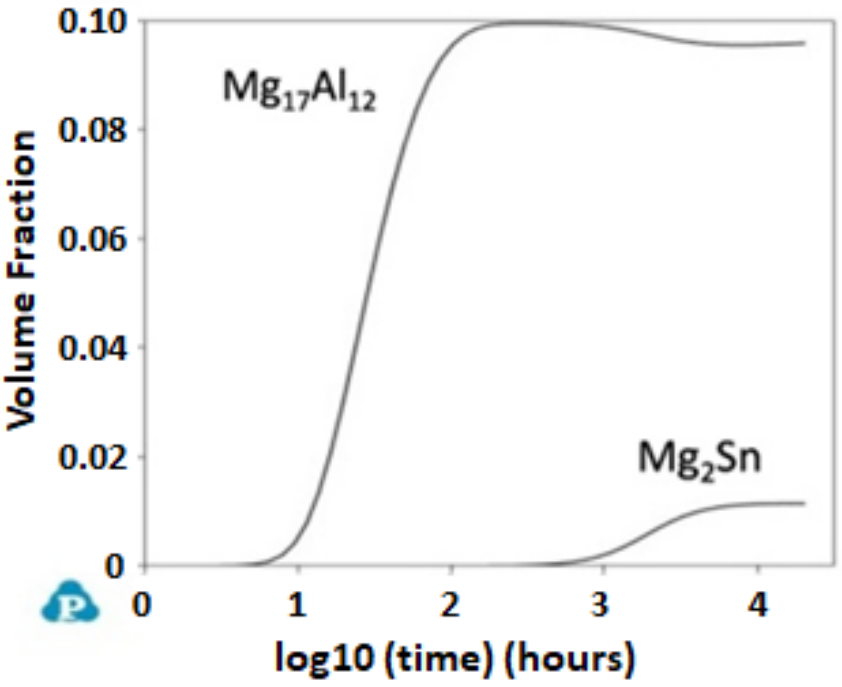

(c)

Figure II.1.D.11. Modeling of concurrent precipitation microstructure in AT72 alloys using PanPrecipitation coupling with the newly developed Mg mobility database developed in this work: (a) number density as compared with experimental density; (b) precipitate sizes; and (c) volume fraction of precipitates.

Conclusions

Reliable diffusivities for Mg-Al, Zn, Sn, Ca, and Y systems were obtained by a combination of diffusion multiples/LSDCs and forward simulation analysis. LSDCs, including Mg-MgNd, MgY, MgGd, MgCe, MgMn, Li, and Sr systems were prepared and diffusion profiles obtained.

PanSolidification, which takes into account both back diffusion in the solid phase and the geometrical dendrite structure, were used to modeling solidification microstructures in die-casting conditions. The difference between simulation results and experimental results obtained from EPMA study was analyzed. Microstructure details of die-casting AT72 microstructure was further characterized using a STEM-based technique.

PanPrecipitation coupling with the mobility database developed in this work was used to simulate the precipitation evolution in AT72 alloy. The simulation results show that addition alloying elements may improve the precipitation kinetics in Mg-Al-Sn-based alloys.

Key Publications

Sun, W.; C. Zhang, W. Zhong, J. Miao, R. Zhang, J. C. Zhao, and A. Luo, 2017, "Modeling solidification process and precipitation evolution in Mg alloys—Application of a new Mg mobility database," NIST 2017 Diffusion Workshop, Gaithersburg MD (September).

Zhong, W., and J. C. Zhao, 2017, "First experimental measurement of calcium diffusion in magnesium using novel liquid-solid diffusion couples and forward-simulation analysis," *Scr. Mater.*, Vol. 127, pp. 92-96.

Zhong, W., and J. C. Zhao, 2017, "First reliable diffusion coefficients for Mg-Y and additional reliable diffusion coefficients for Mg-Sn and Mg-Zn," *Metallurgical and Materials Transactions A*, Vol. 48, No. 12, pp. 5778-5782.

References

Čermák, J., and I. Stloukal, 2006, "Diffusion of 65Zn in Mg and in Mg–x Al solid solutions." *Physica Status Solidi A*, Vol. 203, No. 10, pp. 2386-2392.

Das, S. K., Y. M. Kim, T. K. Ha, and I. H. Jung, 2013, "Investigation of anisotropic diffusion behavior of Zn in HCP Mg and interdiffusion coefficients of intermediate phases in the Mg–Zn system," *Calphad*, Vol. 42, pp. 51-58.

Ganeshan, S., L. G. Hector, and Z. K. Liu, 2011, "First-principles calculations of impurity diffusion coefficients in dilute Mg alloys using the 8-frequency model," *Acta Materialia*, Vol. 59, No. 8, pp. 3214-3228.

Gungor, M. N., 1989, "A statistically significant experimental technique for investigating microsegrgation in cast alloys," *Metallurgical and Materials Transactions A*, Vol. 20, No. 11, pp. 2529–2533.

Kammerer, C. C., N. S. Kulkarni, R. J. Warmack, and Y. H. Sohn, 2014, "Interdiffusion and impurity diffusion in polycrystalline Mg solid solution with Al or Zn," *Journal of Alloys and Compounds*, Vol. 617, pp. 968-974.

Lal, K, 1967, "L'Étude de la diffusion de quelques éléments dans le magnésium." Ph.D. Dissertation. Paris, France: University of Paris.

Saunders, N., and A. P. Miodownik, (eds.), 1998, CALPHAD (Calculation of Phase Diagrams): A Comprehensive Guide, Oxford: Pergemon Press.

Wu, H., T. Mayeshiba, and D. Morgan, 2016, "High-throughput ab-initio dilute solute diffusion database," arXiv preprint, arXiv:1602.01725.

Zhang, Q., and J. C. Zhao, 2013, "Extracting interdiffusion coefficients from binary diffusion couples using traditional methods and a forward-simulation method," *Intermetallics*, Vol. 34, pp. 132–141.

Zhong, W., and J. C. Zhao, 2017, "First reliable diffusion coefficients for Mg-Y and additional reliable diffusion coefficients for Mg-Sn and Mg-Zn," *Metallurgical and Materials Transactions A*, Vol. 48, No. 12, pp. 5778-5782.

Zhou, B. C., S. L. Shang, Y. Wang, and Z. K. Liu, 2016, "Diffusion coefficients of alloying elements in dilute Mg alloys: A comprehensive first-principles study," *Acta Materialia*, Vol. 103, pp. 573-586.

II.1.E Phase Transformation Kinetics and Alloy Microsegregation in High Pressure Die-Cast Magnesium Alloys (The University of Michigan)

John Allison, Principal Investigator
Materials Science & Engineering
The University of Michigan
2200 Bonisteel Blvd.
Ann Arbor, MI 48104
Phone: 734-971-3989
E-mail: johnea@umich.edu

Sarah Kleinbaum, Technology Manager
E-mail: sarah.kleinbaum@ee.doe.gov

Start Date: October 1, 2013 End Date: September 30, 2018
Total Project $600,000 DOE share: $600,000 Non-DOE share: $0

Executive Summary

HPDC is the predominant manufacturing method for Mg alloy automotive components; however, the phase transformation kinetics that occur in this process are, at best, poorly understood. The cooling rates during solidification in HPDC are far from equilibrium and have not been the subject of significant quantitative research. Improved understanding of microstructural kinetics and alloy segregation are required to refine industrial processes and to develop new alloy systems. Improvements in this understanding will be accomplished by combining systematic and quantitative experiments and state-of-art modeling and simulation.

The primary objective of this project is to conduct a systematic, quantitative study of phase transformation kinetics and microsegregation in HPDC Mg alloys is both as-cast and heat-treated conditions. These results will be used to develop and validate physics-based phase transformation kinetics micromodels that quantitatively capture microstructural evolution and microsegregation during HPDC and heat-treatment of Mg alloys. Finally, this knowledge will be transferred to industry and the wider research community through these micromodels and the experimental data that will be stored in the NIST-DOE-EERE Advanced Automotive Cast Mg Alloys Repository and in a new repository, the University of Michigan – Department of Energy (DOE) – PRedictive Integrated Structural Materials Science (UM DOE PRISMS) Materials Commons. To accomplish these goals, a systematic and comprehensive experimental study is being combined with computational modeling and simulation.

UM is conducting all experimental characterization of microstructures and microsegregation in the HPDC/super vacuum die casting (SVDC) materials. The microstructure and chemical compositions of as-cast HPDC Mg alloys are being quantitatively and systematically characterized using a combination of methods including EPMA, optical, SEM, and TEM. This comprehensive characterization has been initiated in AM60 and AZ91 cast at Tsinghua University and in Al-Mg-Mn ternaries (i.e., Al-Mn alloy [AM] series) and Mg-Al binary plates provided by the Ford Research and Innovation Center at Mag-Tec Corporation. These initial results have shown that while Scheil solidification kinetics appear to describe the Al segregation profile at mid-thickness in 2.5 mm and 5.0 mm plates, Scheil models do not describe the microsegregation that occurs during rapid solidification at the edge of the plate. Continued characterization will provide new insights in understanding phase transformation kinetics during high cooling rate solidification, micro-segregation of different alloying elements, and the impact of casting parameters like cooling rate and casting thickness on as-cast microstructure and microstructure evolution during subsequent heat treatment processes.

Based on quantitative experimental results, a solidification micromodel is being developed in collaboration with Dr. Mei Li at Ford Motor Co to predict the evolution of the primary microstructure features of as-cast HPDC Mg alloys. Micromodels will also be developed to predict the dissolution of eutectic phases and redistribution of alloying elements during solution treatment and the precipitation of strengthening phases during aging. These micromodels will be validated using quantitative results obtained on complex-shaped HPDC/SVDC casting of AM50 and AZ91.

The experimental data and models will be made available to the technical community via the NIST DOE-EERE Advanced Automotive Cast Mg Alloys Repository and the UM-DOE Materials Commons, a new knowledge repository under development within the UM Center for PRISMS funded by DOE-Basic Energy Sciences (BES).

This project is planned to span six years and will be conducted in one phase consisting of six tasks.

Accomplishments

- Completed study of phase transformation kinetics and microsegregation in as-cast Mg-Al binaries (FY 2017).
- Completed study of dissolution phase transformation and changes in microsegregation during heat treatment of Mg-9wt. %Al and developed models to describe the evolution (FY 2017).
- Began calibration of the micromodel to predict microsegregation in as-cast Mg-Al binaries (FY 2017).
- Completed micromodel to predict changes in microsegregation and dissolution phase transformation in Mg-Al binaries (FY 2017).
- Developed an empirical relationship to predict grain size as a function of the local cooling rate (FY 2017).

Technology Assessment

- Target: Improved predictive capabilities for HPDC Mg alloy microstructures and precipitation kinetics.
- Gap: There is a lack of quantitative information on phase transformations and microsegregation in HPDC Mg alloys.

Project Introduction

HPDC is used to manufacture over 90% of the commercial Mg products (Slade 2010). This process is fast, economical, and produces complex thin-wall Mg components that cannot be fabricated by other means. The cooling rate involved in HPDC and SVDC are extremely high and range from 10–1000°C/s (Gjestland and Westengen 2007, Kim et al. 2004). The solidification processes experienced in this region are far from equilibrium conditions. Under such extreme conditions, the solidification kinetics, phase transformations, and the redistribution of alloying elements cannot be predicted using equilibrium thermodynamics or the typical modifications to predict alloy partitioning, such as those represented by a Scheil model (Porter and Easterling, 2014). There is essentially no systematic, quantitative information on eutectic phase formation or microsegregation in this region. This represents a major and distinct gap in our scientific understanding of this important manufacturing process.

The redistribution of alloying elements during non-equilibrium solidification leads to microscale segregation across the dendrite/cell and this microscale segregation is strongly dependent on the cooling rate. Although microsegregation has been the subject of a limited number of investigations in Mg alloys (Mirković and Schmid-Fetzer 2009, Terbush et al. 2010, Zheng et al. 2012, Zhang et al. 2007, Paliwal et al. 2014, Liu et al. 2014, and Khan et al. 2014), there is no known microsegregation study for Mg alloys under HPDC conditions in the open literature. Previous studies of microsegregation in Mg alloys have been obtained in directionally solidified castings or in samples cast under moderate cooling rate conditions.

Research on heat treatment of die-cast Mg alloys has been limited due to the blistering that occurs when entrapped air expands during solution treatment. A new processing technology, SVDC for Al and Mg alloy components (Sadayappan et al. 2009, Luo et al. 2010), significantly reduces or eliminates air entrapment thus enabling heat treatment of die-casting alloys and components. This advanced processing route offers new approaches for alloy development and improved Mg component properties. To date, studies of the dissolution of eutectic phases and precipitate evolution during heat treatment of die-cast alloys has been very limited (Li et al. 2010, Miao et al. 2012, and Wang et al. 2012), and there has been no systematic investigation of alloying and processing effects.

Precipitation hardening has the potential to be a major strengthening mechanism in heat treatable SVDC Mg alloys; however, SVDC Mg alloys have not yet been the subject of extensive studies. Gradients in alloy microsegregation and eutectic phase transformation that will be exhibited during SVDC will likely have a key influence on the development of new alloy systems. In addition, quantitative characterization of precipitation microstructure under different heat-treatment condition is crucial to optimize the effects of precipitation strengthening and building physics-based strengthening models.

Approach

Manufacture of HPDC Plates and Complex-Shaped Castings and Simulation

The target alloy compositions used in this study are shown in Table II.1.E.1. The alloy matrix was selected to include a wide range of compositions that will provide for optimization of current commercial alloys AM50/AM60 and AZ91. The castings are being provided the Ford Research and Innovation Center at Mag-Tec Corporation. These castings are being processed using SVDC casting procedures.

Table II.1.E.1. Target alloy compositions used in this study (wt. %).

Mg	Al	Zn	Mn
Balance	3		
Balance	5		
Balance	9		
Balance	12		
Balance	4		0.5
Balance	5		0.5
Balance	6		0.5
Balance	7		0.5
Balance	9	0.5	
Balance	9	1	
Balance	9	2	
Balance	5		
Balance	5		

Note: Balance refers to the Mg content in the alloy and is determined by subtracting the solute content (e.g. 3%) from 100%.

Die-casting process controls linked with precision MAGMASOFT® HPDC simulations are being used to provide an estimate of the cooling rate as a function of location in casting and casting geometry. The simulations use a fine finite difference mesh (e.g., at least 5–10 elements through the cross-section, though some have been completed with 30–45 elements) and high-fidelity HPDC interfacial heat transfer coefficients for HPDC developed by Li and Allison and co-workers (Zhi-pen et al. 2008; Li et al. 2010; Guo et al. 2008) to estimate cooling rate as a function of location.

Quantitative Characterization of Phase Transformation Kinetics and Microsegregation in HPDCs

Solidification phase transformation kinetics are being quantified using comprehensive microstructural characterization, including optical metallography and SEM coupled with advanced image analysis. The primary characteristics that are being quantified are eutectic volume fraction and size and grain size as a function of alloy, location, sample thickness, and process condition. Microsegregation profiles of alloying elements (e.g., Al, Mn, Zn) versus solidification fraction are being quantitatively characterized using the EPMA scan method (Mirković and Schmid-Fetzer 2009, Terbush et al. 2010, and Zheng et al. 2012). These microsegregation results are being compared with CALPHAD-based Scheil solidification estimates of alloy partitioning. Phase transformation kinetics and microsegregation profiles will also be quantified in a complex casting of both AM50 and AZ91 to confirm the experimental findings and to validate the phase transformation kinetics micromodels described below.

Quantitative Characterization of Phase Transformation Kinetics and Microsegregation during Heat Treatment of SVDCs

This task is to quantitatively characterize phase transformation kinetics and changes in microsegregation profiles during heat treatment of SVDC plates. Eutectic phase dissolution and changes in microsegregation are being characterized as a function of solution treatment time and temperature. Phase transformation kinetics are being quantified using quantitative microstructural characterization, including x-ray diffraction, optical metallography, and SEM. The primary characteristics that are being quantified are changes in eutectic volume fraction and size as a function of alloy, location, sample thickness, and process condition. Solution treatment induced changes in microsegregation profiles of alloying elements (e.g., Al, Mn, Zn) are being quantitatively

characterized using the electron microprobe area scan method. Precipitate evolution will be characterized in selected alloys using quantitative TEM techniques (Miao et al. 2012). Precipitate evolution will be captured in the form of isothermal transformation curves. Beta-phase dissolution kinetics and changes in microsegregation profiles will also be quantified in complex castings of AM50 and AZ91 to validate the phase transformation kinetics micromodels.

Develop Physics-Based Phase Transformation Kinetics Micromodels that Quantitatively Capture Microstructural Evolution and Microsegregation during HPDC and Heat-Treatment

The quantitative and systematic results described above are being used to develop state-of-the-art phase transformation kinetics micromodels for HPDC alloys. A comprehensive "solidification kinetics micromodel" is being developed, which considers solute trapping, dendrite arm coarsening, and dendrite tip undercooling and couples these calculations directly with multicomponent phase diagram computations. Given solidification conditions and alloy compositions, this micromodel will can predict secondary dendrite arm spacing, types and fractions of various non-equilibrium phases, liquid concentrations, and solute concentration profiles in the primary Mg phase under the extreme high-heat extraction conditions that exist in HPDC and SVDC. A "dissolution kinetics micromodel" will be developed to account for eutectic phase dissolution and compositional homogenization. In addition, an analytical "precipitation kinetics micromodel" for predicting precipitate kinetics will also be developed.

Technology Transfer Path

Project knowledge, including experimental data and micromodels, will be transferred to industry and the research community through the NIST DOE-EERE Mg Kinetics Repository and UM DOE PRISMS Materials Commons. The database structure and content used for The Materials Commons is being constructed in coordination with national Materials Genome Initiative repository efforts lead by NIST. The project team has had extensive discussions with key repository experts. This will ensure that the information developed in this program will be broadly accessible to the technical community. Templates specific to the EPMA data acquisition and analysis and EBSD data collection have been implemented into Material Commons. A dataset describing the microstructure and microsegregation in the as-cast HPDC Mg-Al-Mn alloys was published on the Materials Commons Public Data site.

Results

The focus this past year has been on collecting all the experimental microsegregation data in a set of HPDC AM series and Mg-Al binary plate in both as-cast and solution-treated conditions. In addition, physics-based micromodel characterizing the phase transformation kinetics and microstructure evolution has also been productively developed.

Microsegregation was characterized in nearly one hundred samples. At present, three hundred high quality EPMA scans of both microsegregation and macrosegregation have been generated for this project. For the as-cast alloys alone, there are 48 conditions that are characterized as a function of alloy (e.g., AM40, AM50, AM60, AM70, Mg-3wt. %Al, Mg-5wt. %Al, Mg-9wt. %Al, or Mg-12wt. %Al), plate thickness (2.5 or 5.0mm), and distance from the casting surface (e.g., edge, near edge, and center). Solution treatments performed to characterize though-thickness macrosegregation of Al resulted in an additional 48 conditions. Finally, an additional 45+ conditions are being measured to study changes in microsegregation and phase transformation kinetics during heat-treatment of Mg-9%Al. Scripts that were written last year work well for rapid consolidation and analysis of the microsegregation data and to export the data/curves into an appropriate format for incorporation into the Materials Commons and the NIST DSpace Repository.

One goal of this project is to model the homogenization of microsegregation and phase transformation kinetics during solution treatment. Heat treatments have been performed at 380°C, 400°C, and 420°C for 2 min, 5 min, 10 min, 30 min, 1 hr., and 2 hr. on the Mg-9wt. %Al alloy. The factors that will influence the homogenization process include solution treatment temperature, duration, and the fraction of externally solidified crystals (ESCs). Figure II.1.E.1 gives example EPMA results on a 2.5mm Mg-9wt. %Al plate solution treated at 420°C for different duration. Figure II.1.E.1(a) illustrates the microsegregation behavior at the center of the samples. The Al concentration profile shows that for 2 min and 10 min, the microsegregation still exists, and it becomes more homogenized when solution treatment duration increases. After a 60-minute solution treatment at 420°C, microsegregation at the center of 2.5 mm plate disappears. The average grain size at edge and near edge is smaller than the size at center; therefore, the microsegregation in these locations should be homogenized more quickly. This is validated by the EPMA results from edge and near edge locations. Macrosegregation still can be observed after complete homogenization; however, the macrosegregation is reduced with a longer solution treatment. Results from Figure II.1.E.1(b) indicates that concentration profiles at the edge are very similar between 60 min and 120 min; while the profiles at the center show obvious differences. For a longer solution treatment, difference between the concentration profiles at the edge and center is smaller due to a longer time for Al diffusion between grains.

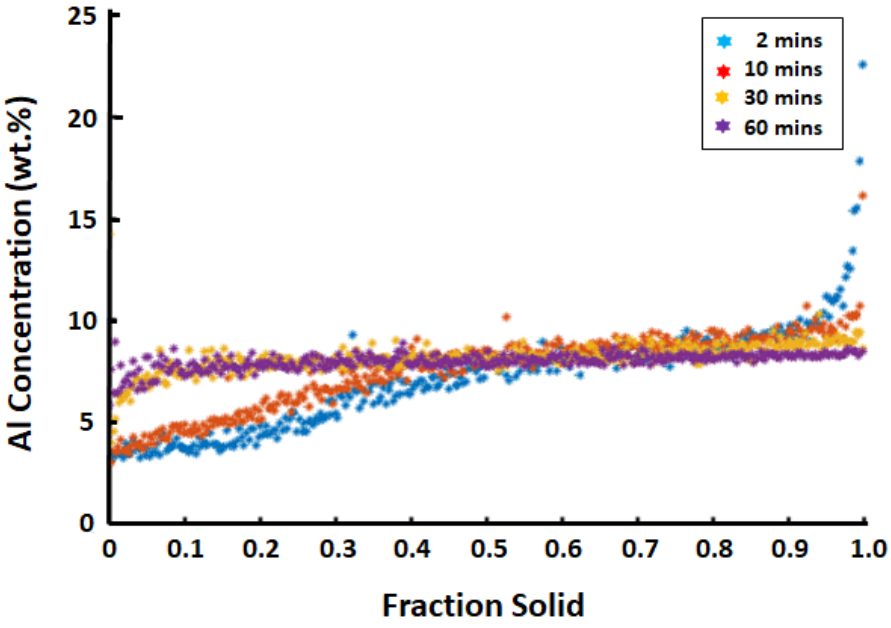

(a)

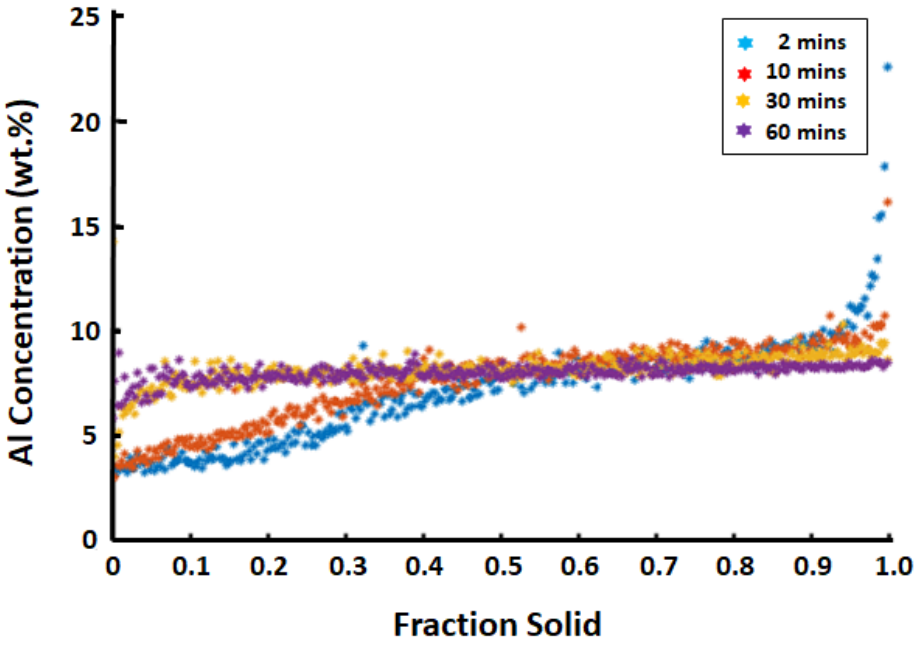

(b)

Figure II.1.E.1. EPMA results of 2.5 mm Mg-9Al solution treated at 420°C: (a) microsegregation of Al profile for various durations; and (b) macrosegregation behavior between edge and center of the sample.

Additional investigation is needed to determine the minimum treatment time for homogenization at different temperatures. The time needed for homogenization is less at the edge due to the smaller average grain size. For a higher treatment temperature, less time is needed to complete homogenization due to a larger diffusion rate. Hence, it can be observed that at 420°C, it only takes 1 hr for a complete homogenization; while at 380°C, some microsegregation can still be observed after 2 hr. The initial curvature at the beginning of the profile from Figure II.1.E.1(a) is due to the existence of the ESCs, which are lower in Al concentration and have a larger size than the in-mold grains. The ESCs are formed during the casting process, and most of them are located at the center of sample. Due to their larger size, a longer treatment is required to homogenize the Al concentration distribution in the center location.

In Mg-Al binaries, $Mg_{17}Al_{12}$ (e.g., β phase) exists as microstructural inhomogeneity and affects the Al content in the matrix for solid solution strengthening during aging. The dissolution model is used to characterize the volume fraction of the β phase after different solution treatment. Experimental results from SEM imaging characterization are compared with the simulation results from the DIffusion-Controlled TRAnsformations (DICTRA) software.

SEM microstructure characterization was conducted to determine the volume fraction of β phase in samples which were solution treated at 420°C for various durations. The MATrix LABoratory (MATLAB) algorithm was used to calculate the volume fraction of β phase; the results of this analysis are shown in Figure II.1.E.2. Additional characterization will be performed to decrease the standard deviation for some positions. Overall, the volume fraction of β phase decreases as treatment time increases and 5 mm plate has a higher volume fraction at each position compared with 2.5 mm plate. Notice that the β phase dissolves dramatically at the beginning of the solution treatment, and then dissolution occurs at a slower rate with additional time at the solution treatment temperature. Experimentally, the volume fraction does not appear to decrease to zero even after a 2 hr treatment. We attribute this to the inability of the current MATLAB algorithm to discriminate between the Al-Mn intermetallic phases, which does not dissolve at this temperature, and the β phase.

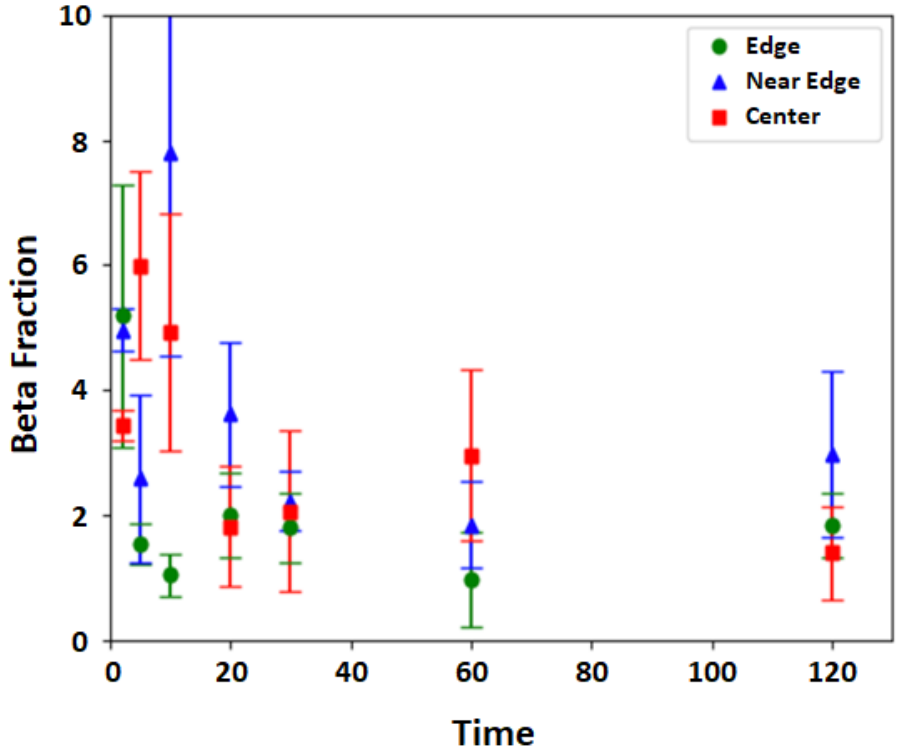

(a)

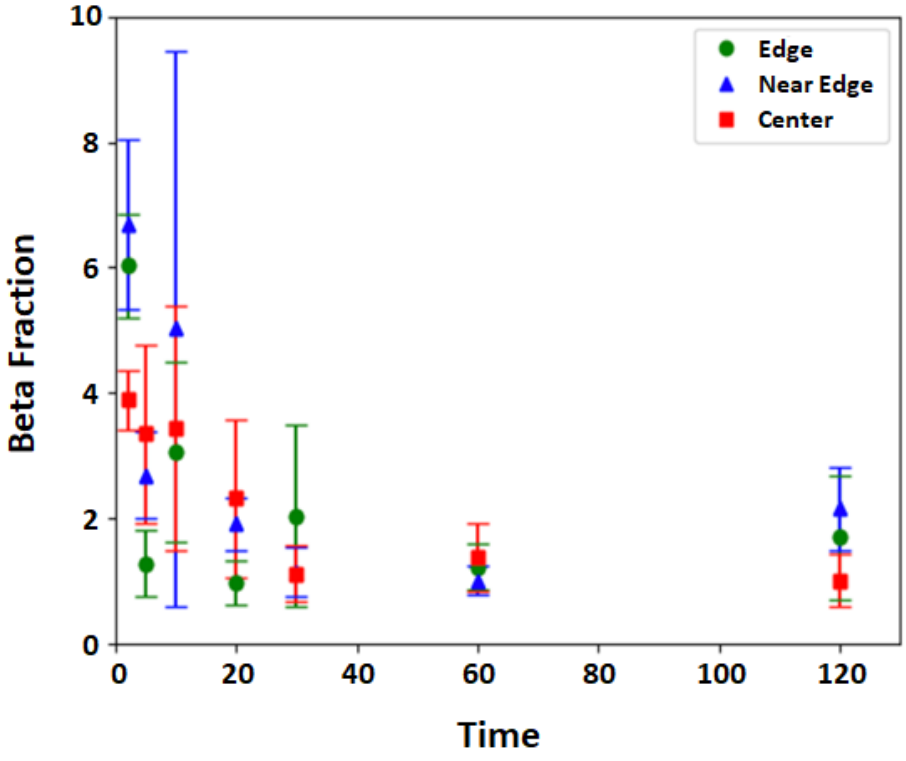

(b)

Figure II.1.E.2. Volume fraction of β phase characterization after solution treatment at 420°C: (a) 5 mm plate; and (b) 2.5 mm plate.

A physics-based micromodel (Zuo 2014; Samaras and Haidemenopoulos 2007) and a CALPHAD-based DICTRA computational simulation have been used to predict the β phase volume fraction. The micromodel combines the classical diffusion-controlled mechanisms during solution treatment with a Johnson-Mehl-Avrami-Kolmogorov (JMAK)-relationship to predict the volume fraction change of the secondary phase. A schematic representation of the model setup for the DICTRA simulation is shown in Figure II.1.E.3. The β phase is located at the center of the cell model and surrounded by the α-Mg matrix/secondary Mg-phase with an annular radius of Rα. The volume fraction of β phase is calculated based on the spherical cell model assumption, Equation (1), is:

$$\frac{R_{\beta}^{3}}{R_{tot}^{3}} = \frac{V_{\beta}}{V_{tot}} = V_{\beta}^{f} \quad (1)$$

where R_β and R_{tot} are the initial radius of β phase and the radius of the grain, respectively; V_β and V_{tot} are the volume of the β phase and grain, respectively; and V_β^f is the volume fraction of the β phase. $R_\beta$can be determined by the initial volume fraction of β phase from as-cast sample.

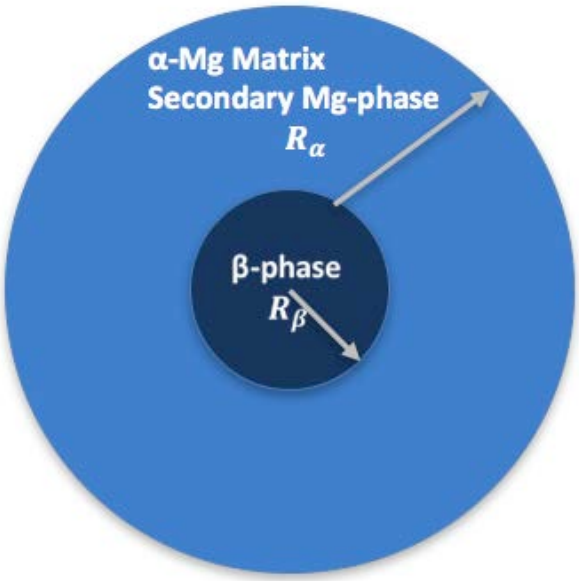

Figure II.1.E.3. β phase dissolution model. Source: University of Michigan.

The results of the DICTRA simulation are provided in Figure II.1.E.4(a). The volume fraction of the β phase decreases as the solution treatment time increases. After 20 minutes, the simulation suggests that the β phase is completely dissolved. The micromodel prediction, DICTRA simulation results, and SEM experimental results of β phase are shown in Figure II.1.E.4(b), respectively. The micromodel matches the SEM results, which shows the model's capability of capturing the dissolution of β phase. Furthermore, the DICTRA simulation results also closely follow the decreasing trend of the β phase volume fraction. Both model and simulation can quantitatively predict the volume change of the secondary phase, which provides the capability of quantitative study of phase transformation kinetics during the dissolution evolution. Further improvement in this model will be to improve the accuracy and reproducibility and apply this micromodel in more complicated alloy systems like Mg-Al-Mn ternaries.

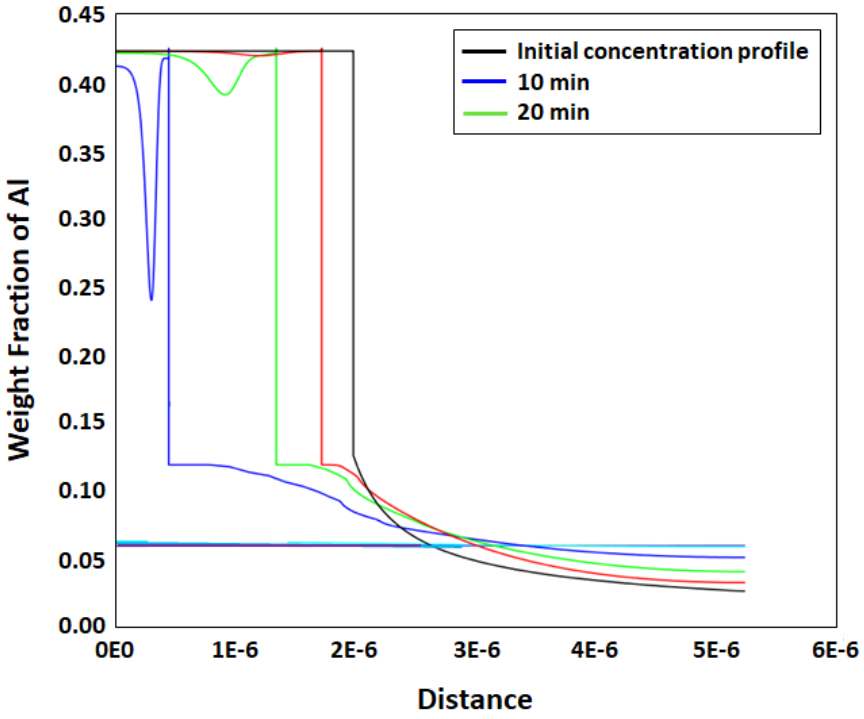

(a)

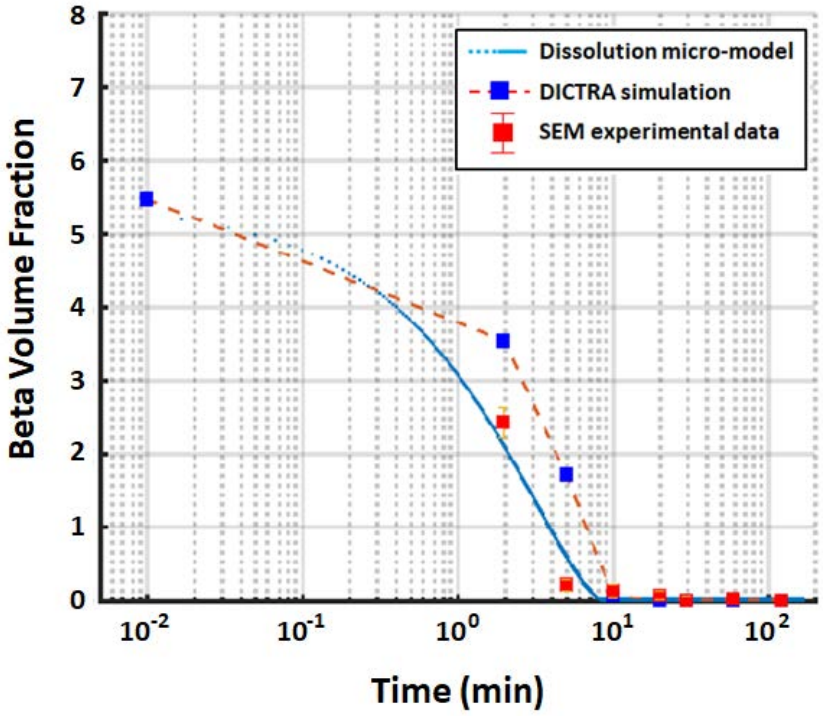

(b)

Figure II.1.E.4. (a) DICTRA simulation results for 420°C solution treatment and 5.47 μm grain size; and (b) comparison between experimental results, micromodel, and DICTRA simulation results of β-phase volume fraction.

The local grain size, d_{grain} in the HPDC Mg alloys can be predicted from MAGMASOFT® solidification modeling by a power law relationship in the form of Equation (2):

$$d_{grain} = \alpha R^{-\beta} \quad (2)$$

where α and β are empirical constants. The local cooling rate, R, is calculated as the derivative of the cooling curve just below the liquidus temperature. For a Mg-7Al alloy, a liquidus temperature of ~613°C was calculated using ThermoCalc. The cooling rate at the near edge (~300 µm from the surface of the plate) and center (half-thickness) locations is shown in Table II.1.E.2 for both the 2.5 mm and 5 mm thick plates. It is also common to calculate the cooling rate as the difference between the liquidus and solidus compositions divided by the solidification time; these values are included in Table II.1.E.2 as well. The inversion in values for the 2.5 mm and 5 mm plates below liquidus and during solidification is a MAGMASOFT® prediction and presumably relates to differences in heat evolved during solidification.

Table II.1.E.2. Local Cooling Rates and in-Mold Grain Size.

Location	Grain radius (µm)	R (°C/s) (below liquidus)	R (°C/s) (average during solidification)
2.5 mm – near edge	5	456	836
2.5 mm – center	6	337	927
5.0 mm – near edge	5.5	591	536
5.0 mm – center	7	225	603

Both methods indicate more rapid cooling in the thinner plates; however, using the average cooling rate during solidification results in a larger difference between the two thicknesses. The average method also suggests a higher cooling rate in the center than at the near edge. The cooling rates calculated just below the liquidus suggest a faster cooling rate at the near edge than in the center, which is more consistent with the solidification process, and therefore, these are the rates used for the empirical model.

Data from several pieces of literature (Paliwal et al. 2014, Khan et al. 2014, Labrecque et al. 1997, Petersen 1990, and Caceres 2002), along with data from the HPDC Mg-Al alloys, were used to relate the cooling rate to secondary dendrite arm spacing (SDAS)/grain radius using Equation (2). The relationship between data in the literature and results from obtained during the current effort are shown in Figure II.1.E.5. The best-fit parameters were found to be 46 for α and 0.32 for β.

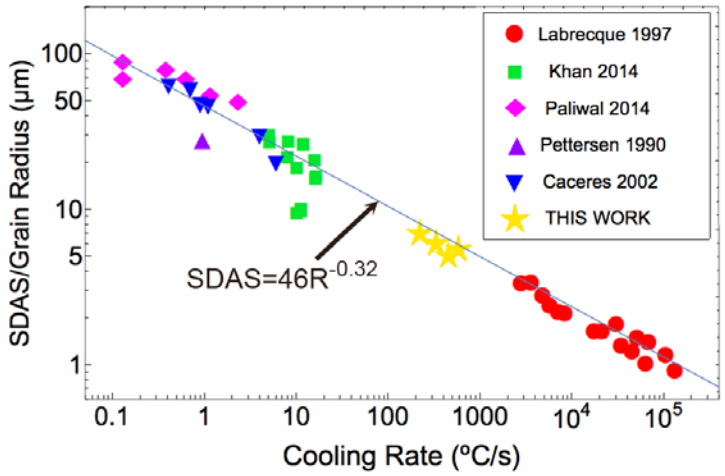

Figure II.1.E.5. SDAS/grain size as a function of cooling rate in AZ and AM series alloys with the empirical fit.

Conclusions

Systematic experimental measurements have been used to quantify both microsegregation and macrosegregation under as-die cast and solution treated conditions. A physics-based solidification model combining the velocity-dependent partition coefficient with the actual elemental microsegregation behavior was developed and has been validated with the actual EPMA data. The model results give a better quantitative understanding of how solidification velocity is related to the microsegregation in as-die cast samples. The EPMA and SEM experimental data reveal that solution treatment temperature and duration strongly affect the dissolution of secondary phase and elemental homogenization process. The dissolution micromodel predicts the volume change of the secondary phase and the DICTRA simulation shows the capability of predicting the homogenization evolution process. The experimental analysis and computational models of microsegregation gives a better understanding of phase transformation kinetics during solution treatment. This will help to optimize the solution and aging treatments in super vacuum HPDC Mg alloy components.

Key Publications

Berman, T. D., M. Li, and J. Allison, 2017, "Microsegregation in High Pressure Die Cast Mg Alloys," invited keynote presentation at *2017 TMS Annual Meeting & Exhibition*, February 28, 2017, San Diego, CA, USA.

Berman, T. D., M. Li, and J. Allison, 2017, "Microsegregation in High Pressure Die Cast Mg Alloys," *Magnesium Technology 2017*, Part of The Minerals, Metals & Materials Series. Springer, Cham, pp. 73–78. https://link.springer.com/chapter/10.1007/978-3-319-52392-7_13.

References

Càceres, C. H., C. J. Davidson, J. R. Griffiths, and C. L. Newton, 2002, "Effects of solidification rate and ageing on the microstructure and mechanical properties of AZ91 alloy," *Mater. Sci. Eng. A*, Vol. 325, pp. 344–355.

Gjestland, H., and H. Westengen, 2007, "Advancements in high pressure die casting of magnesium." *Adv. Eng. Mater.*, Vol. 9, pp. 769–776.

Guo, Z. P., S. M. Xiong, B. C. Liu, M. Li, and J. Allison, 2008, "Effect of process parameters, casting thickness, and alloys on the interfacial heat-transfer coefficient in the high-pressure die-casting process," *Metall. Mater. Trans. A Phys. Metall. Mater. Sci.*, Vol. 39, pp. 2896–2905.

Khan, M. I., A. O. Mostafa, M. Aljarrah, E. Essadiqi, and M. Medraj, 2014, "Influence of cooling rate on microsegregation behavior of magnesium alloys," *J. Mater.* Vol. 2014, Article ID 657647, 18 pages. http://dx.doi.org/10.1155/2014/657647.

Kim, J. S., M. Isac, and R. I. L. Guthrie, 2004, "Metal-mold heat transfer and solidification of magnesium alloys in belt casting processes." *Magnes. Technol.*, pp. 247–255.

Labrecque, C., R. Angers, R. Tremblay, and D. Dubé, 1997, "Inverted disk centrifugal atomization of AZ91 magnesium alloy," *Can. Metall. Q.*, Vol. 36, pp. 169–175.

Li, M., R. Zhang, and J. Allison, 2010, "Modeling casting and heat treatment effects on microstructure in super vacuum die casting (SVDC) AZ91 magnesium alloy," *Magnes. Technol.*, pp. 623–627.

Li, S., S. Xiong, B. Liu, M. Li, and J. E. Allison, 2010, "Numerical simulation of flow-induced air entrapment defects in the high pressure die casting process." *Magnes. Technol.*, pp. 613–616.

Liu, S., G. Yang, and W. Jie, 2014, "Microstructure, microsegregation, and mechanical properties of directional solidified Mg-3.0Nd-1.5Gd alloy," *Acta Metall. Sin. English Lett.*, Vol. 27, pp. 1134–1143.

Luo, A. A., A. K. Sachdev, and B. R. Powell, 2010, "Advanced casting technologies for lightweight automotive applications," *China Foundry*, Vol. 7, pp. 463–469.

Miao, J., M. Li, and J. E. Allison, 2012, "Microstructure evolution during heat treatment in a super vacuum die casting Az91 alloy," *Mg2012 9th Int. Conf. Magnes. Alloy. Their Appl.*, pp. 493–498.

Mirković, D., and R. Schmid-Fetzer, 2009, "Directional solidification of Mg-Al alloys and microsegregation study of Mg alloys AZ31 and AM50: Part II. Comparison between AZ31 and AM50," *Metall. Mater. Trans. A*, Vol. 40A, pp. 974–981.

Paliwal, M., D. H. Kang, E. Essadiqi, and I. H. Jung, 2014, "The evolution of as-cast microstructure of ternary Mg-Al-Zn alloys: An experimental and modeling study," *Metall. Mater. Trans. A Phys. Metall. Mater. Sci.*, Vol. 45, pp. 3596–3608.

Pettersen, K., O. Lohne, and N. Ryum, 1990, "Dendritic solidification of magnesium alloy AZ91," *Metall. Trans. A*, Vol. 21, pp. 221–230.

Porter, D. A., and K. E. Easterling, 2014, *Phase Transformations in Metals and Alloys*, Third Edition. CRC Press, 138. doi:10.1146/annurev.ms.03.080173.001551.

Sadayappan, K., W. Kasprzak, Z. Brown, L. Quimet, and A. A. Luo, 2009, "Characterization of magnesium automotive components produced by super-vacuum die casting process," *Mater. Sci. Forum*, Vol. 618–619, pp. 381–386.

Samaras, S. N., and G. N. Haidemenopoulos, 2007, "Modelling of microsegregation and homogenization of 6061 extrudable Al-alloy," *J. Mater. Process. Technol.* 193: 63–73.

Slade, S., 2010, "Magnesium: Bridging diverse metal markets," *Magnes. Technol.*, pp. 91–95.

Terbush, J. R., N. D. Saddock, J. W. Jones, and T. M. Pollock, 2010, "Partitioning of solute to the primary a-Mg phase in creep-resistant Mg-Al-Ca-based cast alloys," *Metall. Mater. Trans. A*, Vol. 41, pp. 2435–2442.

Wang, J., et al., 2010, "A microstructural evolution model for Mg17Al12 precipitates in AZ91," *Magnes. Technol.*, pp. 163–170.

Zhang, C. et al., 2007, "Microstructure and microsegregation in directionally solidified Mg-4Al alloy," *Intermetallics*, Vol. 15, pp. 1395–1400.

Zheng, X., A. A. Luo, C. Zhang, J. I. E. Dong, and R. A. Waldo, 2012, "Directional solidification and microsegregation in a magnesium-aluminum-calcium alloy," *Metall. Mater. Trans. A*, Vol. 43A, pp. 3239–3248.

Zhi-peng, G., X. Shou-mei, L. Bai-cheng, M. Li, and J. Allison, 2008, "Determination of the heat transfer coefficient at metal-die interface of high pressure die casting process of AM50 alloy," *Int. J. Heat Mass Transf.*, Vol. 51, pp. 6032–6038.

Zuo, Q., F. Liu, L. Wang, C. F. Chen, and Z. H. Zhang, 2014, "An analytical model for secondary phase dissolution kinetics," *J. Mater. Sci.*, Vol. 49, pp. 3066–3079.

II.2 Carbon Fiber and Polymer Composites

II.2.A Close Proximity Electromagnetic Carbonization (Oak Ridge National Laboratory)

Felix L. Paulauskas, Principal Investigator
Materials Science and Technology Division
Oak Ridge National Laboratory
1 Bethel Valley Rd.
Oak Ridge, TN 37831–6053
Phone: 865-574-8257
E-mail: paulauskasfl@ornl.gov

Will James, Technology Manager
E-mail: charles.james@ee.doe.gov

Start Date: October 1, 2015 End Date: September 30, 2018
Total Project Cost: $4,570,000 DOE share: $4,500,000 Non-DOE share: $70,000

Executive Summary

The close proximity electromagnetic carbonization (CPEC) project is a joint development project between RMX Technologies (RMX) and ORNL funded by DOE. Preliminary work on electromagnetic carbonization was jointly conducted by both institutions starting in 2013. This previous work was the impetus for the CPEC project. This report outlines the progress of the work on the CPEC project over FY 2017, building upon significant progress from FY 2016. By the end of FY 2017, CPEC-3 was operating on a continuous basis, producing fiber capable of withstanding high-temperature carbonization, and exhibiting properties exceeding those required by the FY 2017 milestones.

Accomplishments

- Completed construction of the physical setup of CPEC-3, as well as the operational test phase and the continuous operation phase. This is the third iteration of the CPEC furnace, and is referred to in this report as CPEC-3 (FY 2017).
- Completed first performance assessments with static batches of fiber to determine energy field distribution (FY 2017).
- Produced the first continuously processed samples by the end of December 2016 to demonstrate scalability (FY 2017).
- Completed system modification to prevent reoccurrences of electrical system breakdown and then began producing fibers meeting milestone requirements (FY 2017).

Technology Assessment

- Target: Develop higher throughput (30% faster) low-temperature carbonization (LTC) of CF, thus lowering CF manufacturing costs and increasing the material throughput and production rates.
- Target: Reduce the unit energy consumption (in kilowatt-hours per kilogram) by 50%.
- Target: Reduce operational cost by 25% by limiting equipment downtime.
- Gap: Operation of conventional furnaces requires heating a large thermal medium.

- Gap: The CPEC process has been successfully demonstrated in the laboratory, but has not yet been demonstrated while integrated with other parts of the CF conversion process or at speeds and reliability levels required for industrial adoption of the technology.

Project Introduction

During FY 2017, the technology was capable of producing CF on a continuous basis with direct electromagnetic radiation alone. The carbonized fiber was measured to have a density of 1.5 g/cc; however, the sample that was originally produced was a damaged tow not capable of surviving high-temperature carbonization (HTC). The project team then proceeded to isolate and mitigate the root cause of the tow damage.

During this investigation, it was discovered that CPEC-3 was damaged and required repair. This break in operation facilitated restructuring the application method and producing a more robust system to avoid future equipment failures, but this did create some schedule "slip." The project team successfully negotiated a path forward that allowed the CPEC project to complete 110 operational runs in FY 2017. With the modifications in place, CPEC-3 is now able to produce undamaged fiber capable of withstanding HTC. This resulted in preliminary results showing good fiber characteristics that surpass the final milestone of FY 2017, while processing the fiber in residence times lower than required and maintaining the cost benefits of energy savings.

Modeling the next phase of the CPEC system—CPEC-4—is now under way. CPEC-4 will be a highly tunable and agile system that will lead to even higher energy savings per kilogram of CF while producing an undamaged tow and low resident times. The CPEC-4 is capable of processing four times the amount of fiber that is currently processed in CPEC-3. CPEC-4 will be fully scalable to typical industrial production tow widths. The fully scaled version will be a direct drop-in replacement for conventional ovens in existing CF processing lines.

Approach

The CPEC project is split into four major design and construction phases, with each phase related to a separate experimental setup. These phases are reported in Table II.2.A.1, which encompasses the project from its preliminary work in FY 2013 to its desired end state in FY 2018. This report highlights the tasks accomplished in FY 2017. The main tasks over this FY were the commissioning and operation of CPEC-3. This is the third iteration of the electromagnetic LTC furnace that was jointly developed by ORNL and RMX. Other tasks accomplished in FY 2017 include experimental work to refine processing parameters and the preliminary design of CPEC-4. These tasks are encompassed in phase 3 and phase 4.

Table II.2.A.1. Detail of the Major Phases of the CPEC Project.

Phase	Name	Date	Status (Sept. 2016)	Description
1	CPEC-1	FY 2013	Completed	Demonstration of feasibility (static mode).
2	CPEC-2	FY 2016	Aborted	Upgrade of CPEC-1 (with automatic impedance matching); abandoned in favor of CPEC-2V.
	CPEC-2V	FY 2016	Completed	Optimization of the CPEC concept using a computational model.
3	CPEC-3	FY 2016	Completed	Physical construction of CPEC-2V (continuous process at lab-scale).
4	CPEC-4	FY 2017 FY 2018	To be done	Scale-up of CPEC-3 to a 1 ton/year furnace.

Technology Transfer Path

RMX is partnered on this project as a joint developer and joint inventor. RMX will scale up this technology to the pilot and production levels after completion of this work and will sell commercial furnaces to CF manufacturers. RMX has a track record of successful scale-up having commercialized the advanced oxidation technology, which was previously developed by this team.

Results

CPEC-3 Design, Build, and Check-Out

At the end of FY 2016, some parts were still expected, but the setup of CPEC-3 was almost complete. The furnace and all its subcomponents were assembled and operational by October 15, 2016.

The setup is designed within the Occupational Safety and Health Administration (OSHA), Institute of Electrical and Electronics Engineers (IEEE) Standards Association (IEEE 2014), and the World Health Organization (WHO) International Commission on Non-Ionizing Radiation Protection (ICNIRP) population exposure limits (Sage Associates 2007, WHO 1998). The radiative equipment is enclosed in a shielded cavity. The main openings are secured with interlocks, while the radiation level is continuously measured at the location of the operator and consistent with operational safety mechanisms and interlocks, such as outlined in applicable sections within the Code of Federal Regulations (CFR). Other locations are occasionally checked for safety and quality purposes. To date, external emissions have not exceeded 20% of the general population exposure limits.

Multiple tests have been performed on static fiber batches (e.g., the exposed material does not move) and thermal paper to confirm the field distribution within the furnace. The static tests revealed that the power input has a sufficient footprint of carbonization to accomplish what CPEC-3 was designed for. Compared to the computational model, the level of input power that is required is lower than predicted due to conservative modeling practices. When input power is set too high, the tow is severed in several regions. This test is sufficient to prove that carbonization occurs at or below expected power levels, which indicates an additional energy savings over what was originally proposed. As the amount of converted material was limited and density measurement requires 1–2 g of material, electrical measurements were more reliable to check the progress of conversion.

Figure II.2.A.1 is an example of electrical measurement on a static batch run. This measurement shows that the fiber became conductive. The values reported on this plot are encompassed in the range 10^{-4} to 10^{-2} Ω·m. This has to be compared to the 4×10^{6} Ω·m measured on oxidized polyacrylonitrile fiber. According to our reference, this process would be equivalent to a conventional process at about 900°C. These measurements are

based on 48,000 filaments per tow and do not take the damaged fiber portions into account. The most conductive portions are the most completely processed, but are also the most damaged. As a consequence, the most conductive parts may contain 48,000 or less. At those points, the resistivity could be lower than reported.

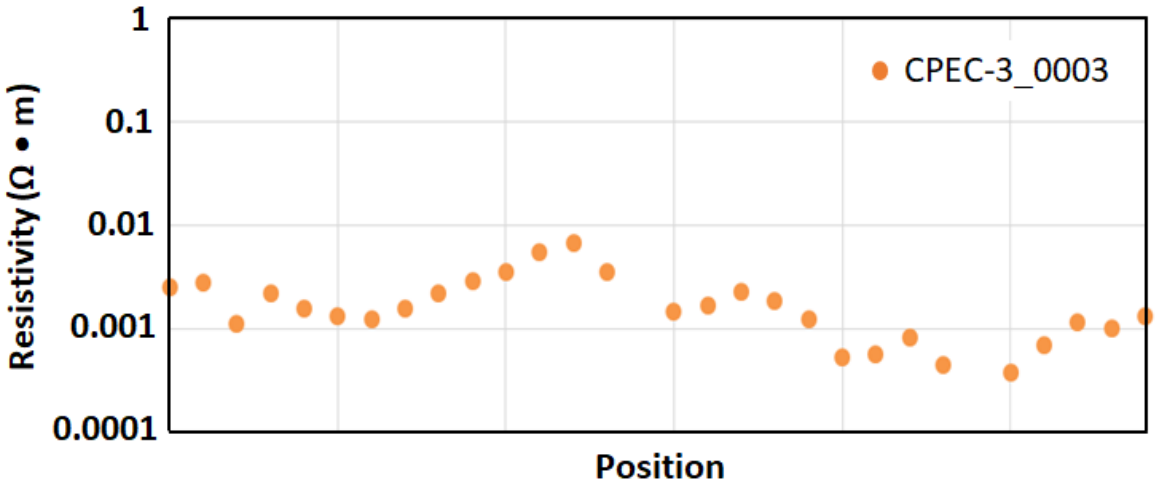

Figure II.2.A.1. Example of electrical measurements on the best static batch on run "CPEC-3_0003."

The first observations from these preliminary runs were as follows:

- CPEC-3, as designed and modeled in December 2016, was capable of converting oxidized polyacrylonitrile fiber into partially carbonized fiber that would have experienced an equivalent exposure of about 900°C of a conventional treatment at its best points in processing. (Note: In this test, the residence time was longer than what it usually is in conventional processes.)
- The profile of electrical measurements on the fiber in Figure II.2.A.1 closely resembles predicted operation without any required alteration of the design. This validates the model developed during FY 2016 in terms of location of the high intensity field and in terms of impedance matching vs. relative distance to source parameters.

CPEC-3 Operational Stability Tests

The first continuous runs with the CPEC-3 setup showed good equipment stability with no unexpected interruption, temperature elevation of specific subcomponents, or some other sort of failure. This allowed rapid performance of continuous runs with minimal time constraints. Results from these first continuous tests are reported in Figure II.2.A.2. The goal of this first continuous test was an evaluation of the response to the system's furnace and feedstock material when exposed to 80% or more of the available power. The power was set at 80% or greater of the unit's capability for about 22 min while the material was in motion at a constant line speed. When set to 95% of its capability, a zone of process instability was noticed, forcing an end to the test. After investigation of the processed material, it was found that two continuous portions of almost 1 ft each were carbonized. Those two portions were separated by a distance of about 1 ft. The most processed of the two portions showed a density of 1.60 g/cc and a resistivity between 1 $\Omega \cdot cm^{-1}$ and 500 $\Omega \cdot cm^{-1}$. This particular run was deliberately interrupted because of a sudden change in the pattern of reflection that is continuously measured when the equipment is operating. The reflection waveform (continuously monitored on an isolated port) was later determined to be caused by two types of electrical breakdowns which were arcing between the tow and the cavity of the furnace and a breakdown between the filaments in the tow itself.

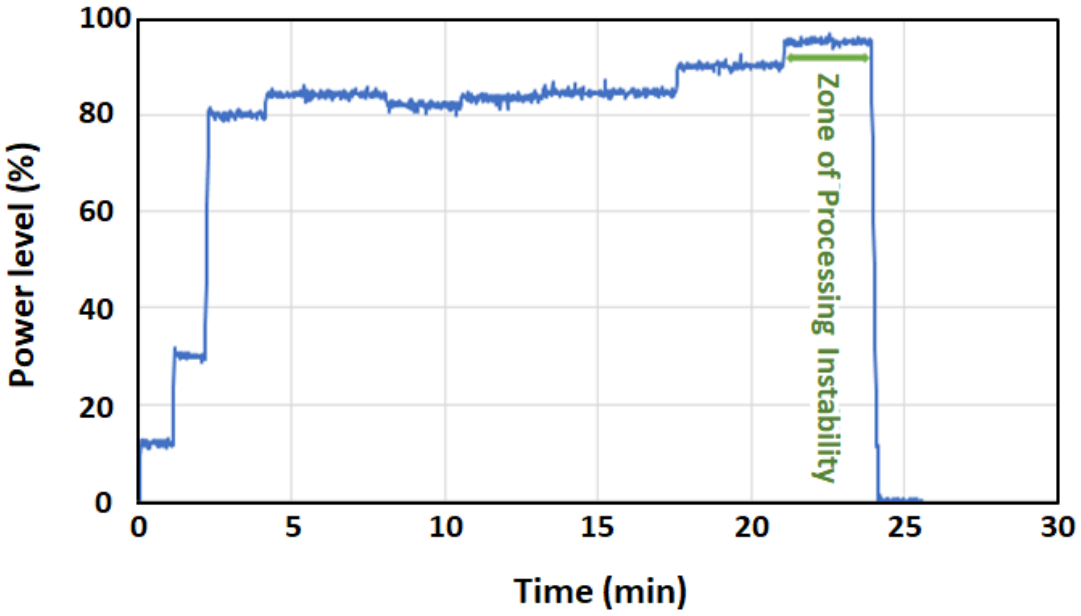

Figure II.2.A.2. Profile of the power setting over time on run "CPEC-3_0009."

Production of Carbonized Material with Damage

The CPEC-3 was rapidly able to produce continuous carbonized material with densities above the objective of 1.50 g/cc. An example of such results is shown in Table II.2.A.2, where a sample 120 in. long was analyzed by sections of 24 in. in length after LTC using CPEC-3 only. By visual examination, this sample was homogeneous, but with damage. It was divided into five even sections of 24 in. for density measurements. In this test, the input power was maintained at a constant level. The average density was 1.64 g/cc, with a standard deviation of 0.07 g/cc. Note that in section E, which had a density of 1.75 g/cc, the sample was severely damaged. It was suspected that this singularity was due to arcing. The best result from this sample is presented in Figure II.2.A.3, while the mechanical properties for a similar sample are reported in Table II.2.A.3. Not all of the material in sample 0030 was used for density measurements. Density characterization requires twisting the samples, thereby disqualifying the analyzed material for subsequent mechanical tests. Consequently, another sample was produced using identical experimental parameters for the mechanical testing. All samples produced, however, exhibited severe damage, leading to a substantial reduction or a breaking of the tow. The standard deviation in peak stress is large due to the early stage development of this technology as processing parameters and influencing parameter sensitivities are being identified.

Table II.2.A.2. Density Measurements for Continuous Sample 0030.

Sample ID	0030					
Section	A	B	C	D	E	Total
Length (in)	24	24	24	24	24	120
Density (g/cc)	1.61	1.56	1.66	1.63	1.75[1]	1.64[2]

[1] This value is abnormally high and is probably due to arcing. Furthermore, its reliability can be questioned due to the sufficient sample size being on the low end of what is required by the pycnometer.

[2] Average value of all sections over this profile.

Figure II.2.A.3. Two-foot sections of the feedstock material (top) and carbonized material (bottom) from sample 0030. The achieved density is around 1.60g/cc. The tow was damaged by arcing within the furnace. Source: ORNL

Table II.2.A.3. Average Mechanical Properties of 18 Single Filaments Randomly Selected in One Location on a Similar Tow to Sample 0030 (see Figure II.2.A.3).

	Diameter (µm)	Peak load (gf)	Peak stress (ksi)	Modulus (Msi)	Strain at break (%)
Averaged Value	8.95	6.9	162.4	11.54	1.29
Standard Deviation	0.72	2.8	87.9	3.42	0.44

This sample was carbonized at LTC in CPEC-3 only, with a residence time shorter than 1 min.

Considering the severity of the damage to the samples, several actions were undertaken:

- Hardware modifications were performed to redistribute the exposure zones into a more favorable configuration. Despite the rigidity of the enclosure of the furnace, some modification was still possible. This improved the performance and final quality of the fiber, but did not help with the arcing issue.
- A video system was installed, which allowed observation of the phenomenon of arcing, but did not serve to help identify its origin.
- A series of additional hardware upgrades were installed to isolate the cause of the arcing. The source was found to be intra-tow random breakdowns.

At the end of this series of tests, it became clear that the electric breakdown occurred between the filaments of the tow. This phenomenon was exacerbated due to some specificity of the design, which allowed arcing between the vessel and the tow at specific areas.

Elimination of the Random Arcing/Performance Evaluation at the End of FY 2017

The development of a technical solution to eliminate the electrical breakdown between the filaments was by far the largest part of the effort over the last months of the FY. A comprehensive technical solution to completely solve this issue has been found. This solution required some minor hardware modifications. One modification was the installation of a low-temperature conventional heat source. This conventional heat source was planned in the original design to prevent off-gas condensation and facilitate preheating of the feedstock to a background temperature. This background temperature was foreseen as being higher than the oxidation temperature but significantly lower than what is usually applied in LTC. Despite this heat source addition, the projected energy savings will still be achieved. A significant experimental test plan change to include low-temperature preheating of the feedstock was also required. As a result, the CPEC-3 setup is able to produce undamaged partially carbonized fiber capable of going through HTC on a continuous basis.

Performance of CPEC-3 at the End of FY 2017

As of the end of FY 2017, several hours of continuous operation have been performed, showing a sustainable, breakdown-free, reproducible process. The material produced was damage-free in most cases, but exhibited some over-processed areas. The over-processed areas made up a small continuous portion estimated to be about 5% to 10% of the tows. This over-processed fiber looks grey in color, indicating that the temperature experienced by this part of the tow was higher than that experienced by others. It has to be mentioned that this over-processed area is not brittle and can be eliminated by process parameter adjustment, which will be one of the goals of more experimental work. These tows have been fully carbonized through HTC at ORNL. Some of the resulting CFs were mechanically tested, and their mechanical properties exceeded the requirements of the milestone of September 18, 2017. Their properties are reported in Table II.2.A.4.

Table II.2.A.4. Mechanical Properties of Six Fully Carbonized Samples (each about 6 ft. long) after HTC.

Test #	Density (g/cc)	Tensile Strength Avg. (ksi)	Std. Deviation	Modulus Avg. (Msi)	Std. Deviation	Strain %	Residence Time
1	1.8142	215.3	89	20.7	2.8	0.98	Short
2	1.8123	216.4	71.2	20.2	2.2	1.01	Short
3	1.8134	312.2	86.4	20.3	1.9	1.43	Long
4	1.8087	428	129.7	22.2	2.3	1.71	Long
5	1.8047	377.2	114	21.46	3.04	1.57	Short
6	1.8111	379.2	109.8	22.28	3.71	1.52	Long

The six samples were produced using the same feed material. Temperature and residence time with CPEC-3 were the only differences (the power level of the radio-frequency generator was kept unchanged). The temperature of the background heat source increases with the number of the test. The residence time is indicated in the last column as "Long" or "Short," but all residence times were shorter than 90 sec.

In May, a malfunction of CPEC-3 occurred. The origin of this incident was an out-of-design parameter during high-power operation. An evaluation of the "cause and effect" of the incident was carried out with the key technical personnel involved in this project. Possible reasons for the incident were identified. Steps have since been taken to avoid a similar incident. This downtime presented an opportunity to redesign the transmission line of the setup. CPEC-3 was entirely fixed and operational by July 2017; however, the scheduled test plan was delayed in accordance with this downtime.

Progress on CPEC-4: Design and Model

Using experience and data collected from testing in CPEC-3, CPEC-4 will be a more flexible design. Parameters such as polarization, incidence angle, etc., will be introduced to further optimize the process. The use of another type of power supply and redesigned applicators will allow greater degrees of freedom within CPEC-4. Emitters for three different design paradigms have been modeled and are undergoing a technical comparison in terms of operation, lifetime, cost of construction, and scalability. The automated generation script for optimization of the applicator is complete.

Hardware-wise, data will be collected via a reconfigurable input/output control system, managed and saved in a computer running LabVIEW. An uninterruptible power supply will provide several minutes for action to save data in the case of a power outage. This subcomponent from CPEC-3 will be reused.

Video monitoring will also be part of the initial design. In addition, live S-parameter data at the generator reference port will be collected during the run, as well as the reflected waveform. This will allow auto-tuning with all power generated in the tuned operational bandwidth.

Conclusions

During FY 2017, significant progress has been made in CPEC of CFs. It has been shown that intra-tow arcing occurs if the feedstock has not been thermally pretreated. Consequently, a background heat source is required to achieve continuous undamaged partial carbonization using electromagnetic energy in a repeatable and self-consistent manner. At the end of FY 2017, given all the hardware modifications and the new test plan, the way that CPEC-3 was set up made it capable of running without breakdown. The resulting fiber was damage-free; however, the processed material exhibited over-processed areas. This will be addressed in the upcoming experimental work.

Filament characterization is ongoing, but all applicable milestones had been met or exceeded by the end of FY 2017. Final optimization is underway with CPEC-3 to achieve optimal outcomes at energy levels much lower than originally predicted by computational electromagnetic modeling.

CPEC-4 modeling is also underway, and the machine design is leading to a flexible and tunable system that will provide more insight on the CPEC process. The CPEC-4 schedule can be adjusted as required to allow purchasing of a new power supply that will determine the capabilities of the final design.

References

IEEE, 2014, IEEE Recommended Practice for Radio Frequency Safety Programs, 3 kHz to 300 GHz, IEEE Std. C95.7-2014, August 2014, pp. 1–58.

Sage Associates, 2007, *Existing Public Exposure Standards*, prepared for the BioInitiative Group, August 2007.

WHO ICNIRP, 1998, Guidelines for limiting exposure to time-varying electric, magnetic, and electromagnetic fields (up to 300GHz), *Health Physics*, Vol. 74, No. 4, pp. 494–522.

II.2.B Carbon Fiber Technology Facility (Oak Ridge National Laboratory)

Merlin Theodore, Principal Investigator
Energy and Environmental Sciences
Oak Ridge National Laboratory
1 Bethel Valley Rd.
Oak Ridge, TN 37831
Phone: 865-576-6569
E-mail: theodorem@ornl.gov

Will James, Technology Manager
E-mail: charles.james@ee.doe.gov

Start Date: March 1, 2013 End Date: Project continuation evaluated annually
Total Project Cost: $7,744,157 DOE share: $7,744,157 Non-DOE share: $0

Executive Summary

In March 2009, DOE-EERE issued a competitive call for proposals to construct and operate a highly flexible, highly instrumented, low-cost carbon fiber (LCCF) technology facility for demonstrating and evaluating new low-cost manufacturing technologies at a pilot scale. ORNL responded to the call and was awarded the project. Construction of the Carbon Fiber Technology Facility (CFTF) began in March 2011, and the facility was commissioned for operations in March 2013.

CFTF offers a unique, highly flexible, highly instrumented carbon fiber line for demonstrating advanced technology scale-up and for producing market-development volumes of prototypical carbon fibers. CFTF's unique capabilities, including the flexibility to process a range of feedstocks and product forms, are unmatched anywhere in the world. Designed to bridge what has been called the "valley of death" between laboratory research and commercial-scale deployment of LCCF technologies, CFTF fills a critical need for support for industrial competitiveness in the manufacture of carbon fiber in this nation. The objective of this project is to accomplish the safe and reliable operation of CFTF and to further DOE's objectives for large-scale commercialization of LCCFs. CFTF supports EERE's efforts toward transitioning technologies to industry, specifically with respect to cost-effective carbon fiber for composite materials in high-volume energy applications.

The CFTF is a cross-cutting effort between the VTO and Advanced Manufacturing Office (AMO). Activities funded under this project include collaborative research and development (R&D) to further develop LCCF, production of materials for prototyping and composites development, development of alternative textile precursor for commodity grade carbon fibers, and development of process monitoring and data analysis techniques to improve process control and accelerate process optimization. No information in any section of this report is export controlled.

Accomplishments

- In FY 2017, CFTF hosted 635 visitors, representing 132 organizations (FY 2017).
- The ORNL Partnerships Office solicited interest from industry to license intellectual property related to increased throughput of textile acrylic fiber. Five companies were selected for negotiations and four licenses were executed with: (1) LeMond Composites; (2) Plastech Manufacturing; (3) Kaltex America Inc.; and (4) Toho. ORNL executed cooperative research and development agreements with LeMond Composites (FY 2017).

- CFTF presented at the VTO Annual Peer Review in Washington, DC, on June 8–9, 2017, and at the Advanced Manufacturing Office Annual Peer Review in Arlington, VA, on June 13–14, 2017 (FY 2017).
- The rebuild of the high-temperature furnace was successfully completed. The furnace is rated to 2,000°C, but is being operated at a maximum of 1,500°C. Carbon fiber produced with the rebuilt furnace has demonstrated properties comparable to prior experience (FY 2017).
- The CFTF team produced 1,816 kg of LCCF with consistent modulus above 35 Msi. This production schedule required significant upgrades to the CFTF line, including upgrades to the thermal oxidizer and replacement and upgrades to the oven ducts (FY 2017).
- CFTF achieved tensile strength exceeding 300 ksi and modulus exceeding 35 Msi with a textile-based polyacrylonitrile (PAN) precursor from Taekwang (FY 2017).
- CFTF demonstrated high volume oxidation (>100,000 denier/in. width of oven) for an alternate precursor with 2.0 dpf Taekwang textile-based PAN precursor. Four bands were converted into carbon fiber with a target modulus greater than 35 Msi (FY 2017).
- Characterization of fiber off-gas composition within the ovens and furnaces of the continuous carbon fiber manufacturing process was examined as a method of process monitoring and data analysis to improve process control and accelerate process optimization. The diversity of components found indicates that if a correlation could be established between off-gas constituents (and/or constituent ratios) and fiber quality, some online spectroscopy or ruggedized chromatography could be developed to provide feedback control of the line (FY 2017).
- Vibrational spectra were examined as a method of process monitoring and data analysis to improve process control and accelerate process optimization. The diffuse reflectance infrared Fourier transform spectroscopy (DRIFTS) technique demonstrated the capability to measure density during oxidation via analysis of the infrared spectra (specifically in the 2,050–2,300 cm−1 spectral region) measured online at the exit of furnace zone 4 of the oxidation process. DRIFTS was also shown to be able to characterize fiber density at different locations within the oxidation process. Previous studies demonstrated the ability of DRIFTS to monitor fiber density in-process as a function of time on moving tow (FY 2017).
- CFTF demonstrated conversion of a second textile precursor with tow fiber count greater than 300,000 fibers to carbon fiber with a maximum tensile strength > 400 ksi, average tensile strength of 366.2 ksi, average tensile modulus > 35 Msi, and strain to failure > 1% using the ORNL patented process (FY 2017).
- CFTF processed and delivered LCCF for 11 industrial projects in 2017 and has 6 other industrial projects pending approval (FY 2017).

Project Introduction

The goal of the CFTF is to provide the advanced carbon fiber research, development, and demonstration capability necessary to achieve the commercialization of LCCF technologies to support a wide range of clean energy initiatives. CFTF serves as a multi-industry, multi-participant technology demonstration and deployment facility easily accessed by key research and development and industry partners. The main objectives are to translate the science of carbon fiber manufacturing to a scalable, cost-effective, and energy-efficient manufacturing process; demonstrate and deploy a skilled workforce development model; and enable commercialization of LCCF and composites for a broad range of industrial clean energy applications. Key strategies to be implemented by the project are to (1) develop and implement the process science for the conversion of alternative precursor materials into LCCF, (2) produce and disseminate quantities of LCCF to industrial partners for market evaluation in composite components, and (3) enable development of domestic commercial sources for production and demonstrate carbon fiber production using of low-cost carbon fiber.

Approach

CFTF is open for tours so that representatives from industry and others can see the technology and the process science being developed to produce LCCF with industry-appropriate mechanical properties from alternative precursor materials. Currently there is no commercial manufacturer of these particular LCCFs, so CFTF plans to produce enough material for industry to evaluate, thus showcasing the quality of the LCCFs on a multitude of end-user platforms. This work is intended to produce industry demand for the technology. CFTF staff members continue to hold discussions with industry partners that are interested in scaling the processes being developed at CFTF. The financial investment for industry to scale-up the technology is significant and thus not quickly decided upon. One CFTF mission is to transition this technology to industry for scaling, but numerous technical challenges remain that must be overcome to further reduce the risk for industry to implement the technology. These technical challenges are being addressed at CFTF in collaboration with industry to reduce implementation risks. Among these challenges are handling the large tow, increasing throughput, splicing, and splitting the large tow, and developing appropriate sizing for the LCCF for specific composite applications. CFTF continues to be a training ground for technical staff in the production of carbon fiber. Multiple tools were developed to establish a training program for future carbon fiber production facilities.

Technology Transfer Path

Four companies have licensed provisional patents to produce carbon fiber from textile precursors.

Results

Tensile Strength Exceeding 300 ksi and Modulus Exceeding 35 Msi with a Textile-Based PAN Precursor from Taekwang

The CFTF team was able to further optimize the process conditions to improve the tensile modulus and the quality of the carbon fiber produced. There was a slight increase in modulus from 36 Msi to 37 Msi and a slight decrease in the variation of the modulus between samples, as shown in Figure II.2.B.1.

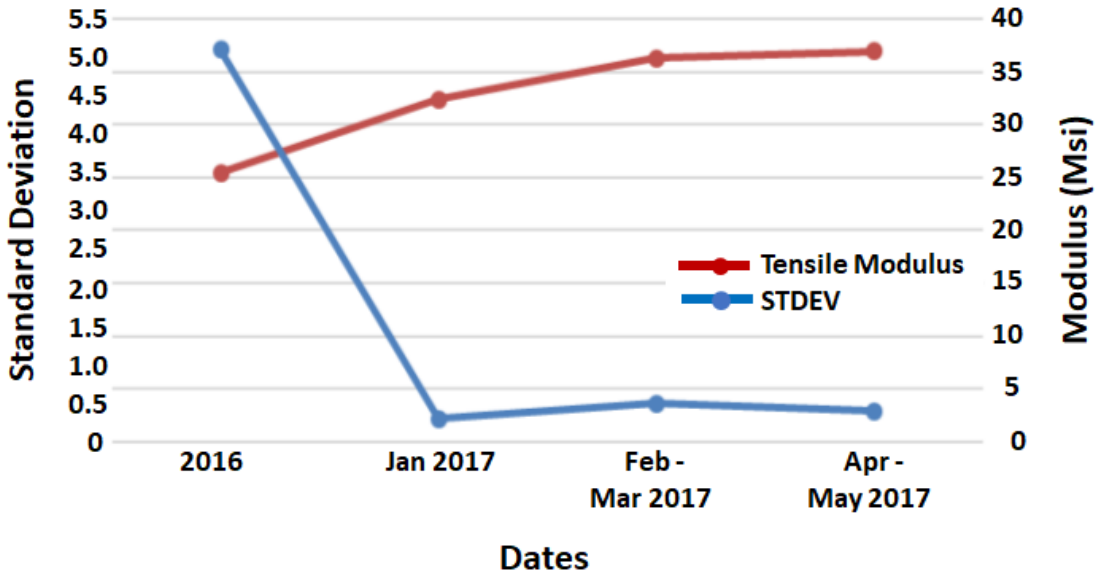

Figure II.2.B.1. Taekwang precursor modulus improvement over time based on trials. Source: ORNL.

Vibrational Spectra Demonstrated as a Method of Process Monitoring

DRIFTS techniques can enable measurement of the specific fiber chemistry associated with crosslinking and cyclization reactions in the carbon fiber production process, as shown in Figure II.2.B.2. These spectroscopy techniques characterize the chemical bonds present in the fiber material and can be applied directly to the fiber

online for nondestructive chemical characterization. The DRIFTS device was installed at the Drive 3 location after Zone 4 oxidation on the CFTF carbon fiber line. Samples were tested for oxidation density using a density column (primary method), and the values were used to draw correlations with data generated from the DRIFTS device. The DRIFTS data correlate extremely well with the sample oxidation density tested in the CFTF laboratory, giving an R-squared of 0.9772 for a linear regression to the data, as shown in Figure II.2.B.3. Based on the data obtained to date, the DRIFTS technique is a viable online process monitoring tool to measure fiber density for the oxidation process.

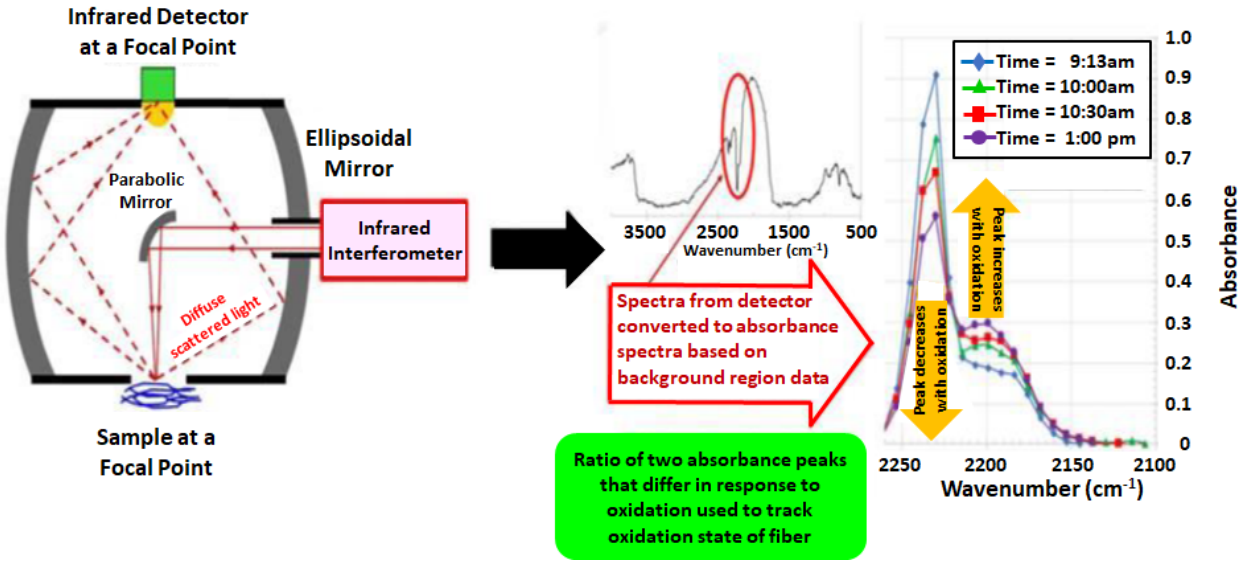

Figure II.2.B.2. The DRIFTS method and conversion of raw spectral data to absorbance spectra. Source: ORNL.

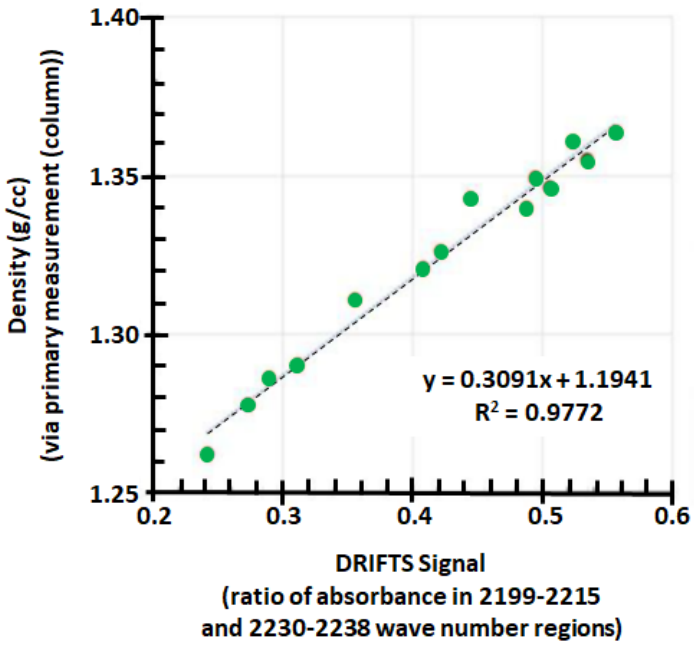

Figure II.2.B.3. DRIFTS data correlation with oxidation density measurements. Source: ORNL.

DRIFTS was next used to measure carbon fiber properties as a function of position in the oxidation process. The DRIFTS instrument was positioned at 22 locations along the oxidation process. Figure II.2.B.4 shows the

density measurements obtained as a function of the number of passes that the carbon fiber tow made through the oxidation furnaces. The four zones of the oxidation furnace are noted on the graph along with the furnace temperature at each zone at the point during shutdown. The results represent a proof-of-principle of the DRIFTS technique for online fiber density measurements. Future studies will seek to repeat the results and expand the calibration correlation across a wider range of fiber densities.

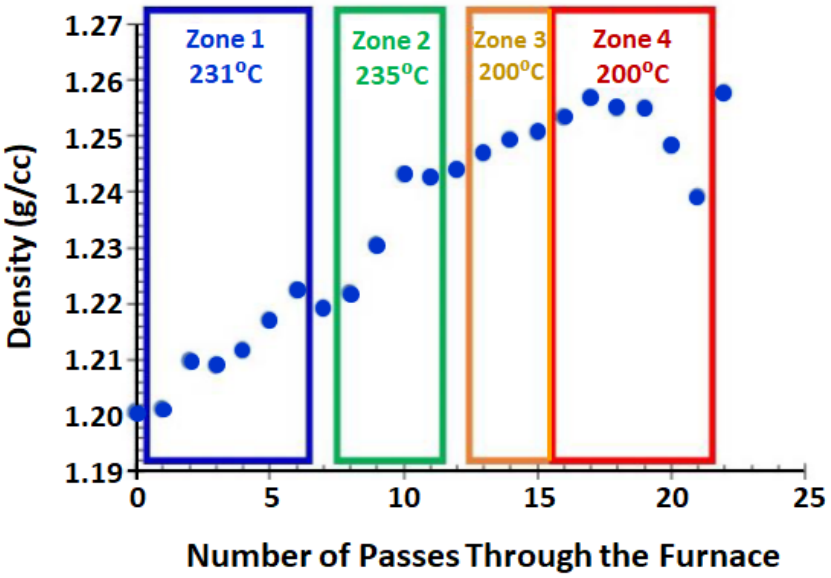

Figure II.2.B.4. Fiber density measured via the DRIFTS technique as a function of the number of passes through the oxidation furnace. The corresponding furnace zones and temperature set points at shutdown are shown on the plot for reference. Source: ORNL.

Conversion of a Second Textile Precursor Meets Target Properties

This annual milestone was met with textile-based PAN precursor from Taekwang. CFTF demonstrated the conversion of a second textile precursor with tow fiber count greater than 300,000 fibers to carbon fiber with tensile strength > 400 ksi, tensile modulus > 35 Msi, and strain to failure > 1% using the ORNL patented conversion process. The tensile strength and modulus values are listed in Table I. The overall tensile strength value is for all fibers that have been processed to date using the Taekwang precursor and is not directly related to the standard and intermediate modulus values shown for some of the fibers. Values in the table are averages.

Table II.2.B.1. Tensile Strength and Modulus for Textile-Based Precursor.

	Overall Tensile Strength	Standard Modulus (Msi)	Elongation (%)	Intermediate Modulus (Msi)	Elongation (%)
Average	Text	Text	Text	Text	
Standard Deviation	Text	Text	Text	Text	
Maximum	Text	Text	Text	Text	
Minimum	Text	Text	Text	Text	
Number	Text	Text	Text	Text	

Conclusions

Significant progress was made in developing processes to convert textile acrylic fiber to carbon fiber with mechanical properties suitable for use in vehicles and other industrial products. Four companies have licensed provisional patents to produce carbon fiber from textile precursors. Although much process development work

remains to enable commercial production of carbon fiber using textile precursors, a clear pathway to the reduction of up to 50% of the cost of production relative to existing commercial operations has been established.

II.2.C Integrated Computational Materials Engineering Development of Carbon Fiber Composites for Lightweight Vehicles (Ford Motor Company)

Xuming Su, Co-Principal Investigator
Ford Research and Advanced Engineering
Ford Research and Innovation Center
2101 Village Rd.
Dearborn, MI 48124
Phone: 313-845-5643
E-mail: xsu1@ford.com

David Wagner, Co-Principal Investigator
Ford Research and Advanced Engineering
Ford Research and Innovation Center
2101 Village Rd.
Dearborn, MI 48124
Phone: 313-845-2547
E-mail: dwagner6@ford.com

Will James, Technology Manager
E-mail: charles.james@ee.doe.gov

Start Date: October 1, 2014 End Date: December 31, 2018
Total Project Cost: $8,580,000 DOE share: $6,006,000 Non-DOE share: $2,574,000

Executive Summary

The project will develop ICME techniques of CFRP composites and use ICME tools to design a structural carbon fiber composite subframe to support immediate weight reduction in light-duty vehicles and reduce development-to-deployment lead time.

This four-year project is currently in its third year. The ICME models developed in the first two years have been further improved, validated, and integrated in FY 2017. The integrated tools are being applied to the subframe design and optimization, demonstrating that the ICME approach generated powerful tools for the most efficient usage of CFRP, leading to optimized weight savings with minimum cost increase.

The validated and integrated ICME tools include a non-orthogonal material model for preforming analysis, compression molding simulations of sheet molding compound (SMC), multiscale models of constitutive behavior of unidirectional (UD) and woven continuous fiber composite and chopped fiber SMC, crash analysis models, and fatigue models. It was shown by comparing to measured data from respective tests that the errors of the predictions of fiber orientations from both preforming analysis and compression molding analysis are less than 15%. The errors of multiscale model predictions of elastic parameters are less than 10%. The accuracy of simulations of impact tests of CFRP is comparable to that of conventional structures. Accuracy of fatigue models is currently under evaluation. We are challenged in achieving a valid tension-compression fatigue test as test results are specimen-size-dependent. The issue is expected to be resolved in the next set of experiments.

ModeFRONTIER® has been chosen as the platform for ICME tool integration and design optimization. Existing capabilities and added scripts enables a seamless integration of manufacturing simulation and vehicle performance analysis. Material design and manufacturing process information, such as geometric dimension,

fiber layout, and fiber orientation, are inputs for multiscale models to generate local material constitutive relation used in following noise, vibration, and harshness (NVH), crash safety, and durability analyses. The success of the integration has been validated by an optimization of design analysis of a hat section. Currently, it is being used for the design of the CFRP subframe.

Building on the above achievements, the ICME project is expected to be successfully completed on time by the end of 2018.

Accomplishments

- Met and exceeded all milestones of the project: validated and implemented non-orthogonal model for preforming; validated SMC molding simulation methodology; validated multiscale Representative Volume Element (RVE) models for UD, woven, and chopped fiber composites; validated computer-aided engineering (CAE) models for crash analysis; implemented models for fatigue life prediction; and integrated all models for design optimization (FY 2017).
- Molded 70 UD plaques with fiber volume fraction (V_f) of 45% and 55%. Tensile tests were completed for the new molded material. The data will further validate the robustness of the multiscale models (FY 2017).
- Produced over 100 hat section parts of UD and woven composites for crash and fatigue validation tests (FY 2017).
- Molded 50 plaques of non-crimped fabric (NCF) for quasi-static and fatigue characterization. Preliminary tensile tests were completed. The study of NCF was added to the project as it is widely used in the industry (FY 2017).
- Conducted round-robin tensile test of UD material to study sample preparation and gripping method (FY 2017).
- Completed the implementation of the non-orthogonal material model as MAT_COMPRF (MAT_293) in LS-DYNA and validated the model by simulation of the double-dome preforming process. The predicted fiber orientations are with less than 15% of errors (FY 2017).
- Calibrated the reduced strain closure (RSC) model and the Moldflow Rotational Diffusion (MRD) in Moldflow for SMC compression molding simulation by using measured fiber orientation tensor components at selected locations. Predicted fiber orientation using calibrated model has less than 15% error (FY 2017).
- Completed a modified UD RVE model to consider interphase properties predicted from molecular dynamic analysis (MDA). Improved predictions in stress-strain and failure modes have been obtained (FY 2017).
- Extended the self-consistent clustering analysis (SCA) to UD and woven composites to speed up finite element analysis (FY 2017).
- Completed the hat section side impact and axial crash tests on both UD and woven composites with different fiber layout for validation of crash analysis models. Crash analysis methodology has been established and simulation results are comparable to test measurements at an accuracy acceptable to conventional structural design (FY 2017).
- Completed implementation of a fatigue prediction module on nCode. Completed all UD fatigue tests of specimen in 90° to fiber directions. Tests of 0° and 15° to fiber direction are ongoing (FY 2017).
- Established the framework for uncertainty analysis and characterized material microstructural variations for UD and woven composites. Developed procedures to quantify uncertainty propagation across different length scales (FY 2017).

- ICME integration has been completed and validated against a hat section structure (FY 2017).
- Completed the topology optimization for the front subframe based on stiffness requirements and developed three design concepts based on the topology results: SMC intensive design, UD/NCF intensive design, and aluminum intensive design (FY 2017).

Technology Assessment

- Target: Comprehensive material characterization of the CFRP and ICME databases to establish and validate the ICME models.
- Gap: NCF plaque characterization needs to be completed.
- Gap: Material microstructure characterizations and quantification need to be completed.
- Gap: Design and manufacture specimens with known misalignment and other variations to validate RVE models considering microstructural variations.
- Target: Preforming models accurately predict fiber orientations and wrinkling.
- Gap: Robustness of the established models needs further validation by more experimental cases.
- Gap: The current model is developed specially for woven prepregs. The model needs to be extended for NCF.
- Target: Using MDA to predict the thermomechanical behavior of resins, explore mechanisms of resin and interphase failures and provide key data for micro- and macro-scale material models.
- Gap: Self-learning metabasin escape (SLME) algorithm needs to be further improved to speed up the analysis.
- Gap: Interphase failure mechanisms needs to be further explored and modeled.
- Target: RVE for UD and woven composites relating mechanical properties of the composite to properties of its constituents.
- Gap: Robustness of RVE of the multiscale model needs to be further verified, especially when material microstructural variations are considered.
- Gap: RVE needs to be extended to predict failures.
- Gap: The computational efficiency of multiscale models needs to be further improved.
- Target: Moldflow module for compression molding simulation of chopped fiber SMC.
- Gap: Robustness of the models needs to be established.
- Target: Fracture and energy absorption models for vehicle component safety analysis.
- Gap: Multiscale RVE failure models need to be validated and applied in crash analysis.
- Target: Fatigue and durability models to predict component life.
- Gap: Available test data are not comprehensive. Further test development must be conducted to generate a comprehensive data set.
- Target: Full integration of all ICME models.
- Gap: The process needs to be standardized and made more user-friendly and efficient.
- Target: The design of CFRP subframe using ICME tools.
- Gaps: The subframe design is preliminary.

- Gaps: Simultaneous optimization of subframe design and manufacturing process needs to be developed.
- Gaps: Cost analysis needs to be developed.
- Target: Models capable of characterizing material uncertainty.
- Gap: Validated multiscale models are needed to describe local material microstructure variations.
- Gap: Models of uncertainty propagation from one scale to another is yet to be explored.

Project Introduction

Vehicle lightweighting is a very important concept for automotive manufacturers to consider to meet the ever-increasing demand of fuel efficiency and to reduce greenhouse gas emissions and dependency on foreign oil. CFRP composites, with a density of 1.55 g/cm^3 and a tensile strength of about 2000 MPa in the fiber direction, are among the most promising candidates to replace the metals currently used for structural components. The goal of this project is to design, develop, and optimize, using CAE only, a light-duty vehicle carbon fiber subframe capable of achieving greater than 25% weight reduction with a cost increase of less than $4.27 per pound of weight saved when compared to the baseline technology to be replaced.

Unlike many metals typically used in automotive vehicles, the mechanical properties of CFRP are highly direction-dependent. The strength of the material in fiber-reinforced-direction could be an order of magnitude higher than in the direction perpendicular to it. It is important to note that the fiber orientation in a component is decided not only by the initial fabric layout, but also the preforming and molding processes. An optimized vehicle component design will thus need tools that are capable of predicting the performance of CFRP parts based on fiber architecture, molding process, and curing history, with considerations of uncertainties and probabilistic nature of materials, processes, and in-service conditions. The current project will develop these ICME tools to meet the design challenge.

ICME tools developed in the project will be robust, accurate, and reliable constitutive models for each constituent material, as well as the composite assembly under expected service conditions including high-strain rates utilizing physics-based models. The manufacturing process (including variability from both process and material) is simulated to predict the fiber orientation and other microstructural features of manufactured products. This information is passed to performance analysis. Material design, manufacturing simulation, and performance analysis are integrated. Local material properties are related to the composite architecture and microstructure by multiscale models. Design and manufacturing process are optimized simultaneously to achieve the most efficient usage of the material.

Approach

The project will design, develop, and optimize, by using CAE only, a light-duty vehicle carbon fiber subframe capable of achieving a ≥25% weight reduction with a cost increase of less than $4.27 per pound of weight saved when compared to the baseline technology to be replaced. This objective will be achieved by developing ICME tools and numerical procedures to optimize both the design and the manufacturing process so that CFRP is most efficiently used.

The ICME tools relate performance requirements of a vehicle to material design and processes. While material performances are expressed at the continuum macroscale, they are decided by material microstructures and microstructural features at the microscale and again by molecular bonds and crosslinking at the nanoscale. The material microstructures and microstructural features, bonding, and crosslinking are results of material design and manufacturing processes. ICME tools are thus multiscale models and approaches that bridge the different material scales. These models are based on physical principles, testing measurements, and observations. Test data are also needed in validating material models. Modeling and testing are always hand-in-hand in successful development of ICME tools. The project team consists of Ford Motor Company, an automotive manufacturer;

Dow Chemical, a material manufacturer; NU, an institution of highly regarded academics; and the National Institute of Standards and Technology (NIST), a world-renowned test lab. As such, the team has all of the elements needed to make a breakthrough in developing ICME tools. The research team also includes software developers from Livermore Software Technology Corporation (LSTC) (LS-DYNA), Autodesk (Moldflow), ESTECO (modeFrontier), and HBM (nCode). The ICME tools developed in the project can be numerically implemented and available through popular engineering software and disseminated.

The project will be conducted in four BPs: 1) CFRP material characterization and ICME model development; 2) ICME model database and validation; 3) ICME model integration and validation; and 4) ICME-based design and optimization. The first two BPs constitute Phase I: Model Development and Model-Level Validation. The remaining two BPs constitute Phase II: ICME Integration and System Design. FY 2017 is the first year of Phase II.

Technology Transfer Path

The project team includes primary software developers in every aspect of the ICME application chain. LSTC's LS-DYNA is a popular finite element analysis package for stress analysis. It is especially dominating in vehicle safety analysis. Autodesk Moldflow has the largest user group in polymer molding analysis. The same is true for HBM's nCode for fatigue and ESTECO's modeFrontier for optimization. All models developed by the project are results of cooperation between the abovementioned software developers, researchers in academia, and end-users in original equipment manufacturers and suppliers. These models are being implemented in their respective software when developed and will be available to the general public once validated.

In FY 2017, HMB implemented a CFRP fatigue module in nCode and LSTC LS-DYNA implemented a non-orthogonal model for preforming as MAT_293. Autodesk is developing technologies to resolve issues that we raised when performing the SMC compression molding simulation.

The second path of technology transfer is through infrastructure and methods identified by NIST. All test data and material models are being stored at the datacenter of NIST and will open to the public once the project is completed. Research results are also planned to be published in respective technical journals and conference proceedings.

The third path of technical transfer is the direct usage of the results at Ford and Dow Chemical.

Results

The project is organized in four main tasks: Task 1 consists of CFRP material characterization and ICME database; Task 2 focuses on ICME model development and validation; Task 3 deals with ICME model integration and validation, and Task 4 is centered on ICME-based design and optimization. FY 2017 is the first year of Phase II. All tasks are active during FY 2017.

Task 1: Material Characterization

Most basic tests required to generate and validate material models at the coupon level—including tensile, compression, shear, and fracture tests of resins, UD, woven, and SMC composites—were completed in FY 2015 and FY 2016. The remaining work was completed in the current year (FY 2017). Several new tests (such as UD composites of varying fiber contents, woven composites of different fiber tow sizes and architectures, NCF, etc.) were added to further improve robustness and validate the ICME models.

Resin Characterization

Elevated temperature and high-strain rate tests were conducted at NIST. Tensile specimens were extracted from neat resin plaques produced by Dow Chemical. Tests were conducted at temperatures from ambient up to 135°C (at a strain rate of 10^{-5}/s) and at strain rates from 0.0001/s to 10/s at room temperature.

Carbon Fiber and Fabric Characterization

Key parameters of woven fabric were studied using optical microscope images, as shown in Figure II.2.C.1. Three parameters, inter-yarn angle, θ, yarn width, d, and yarn spacing, s, are used to characterize the fabric. Figure II.2.C.2 is the distribution of the angles θ, which are a Gaussian-like distribution with the mean of 90 degrees. Similar characterizations are also preformed/being performed on fiber misalignments and waviness for UD.

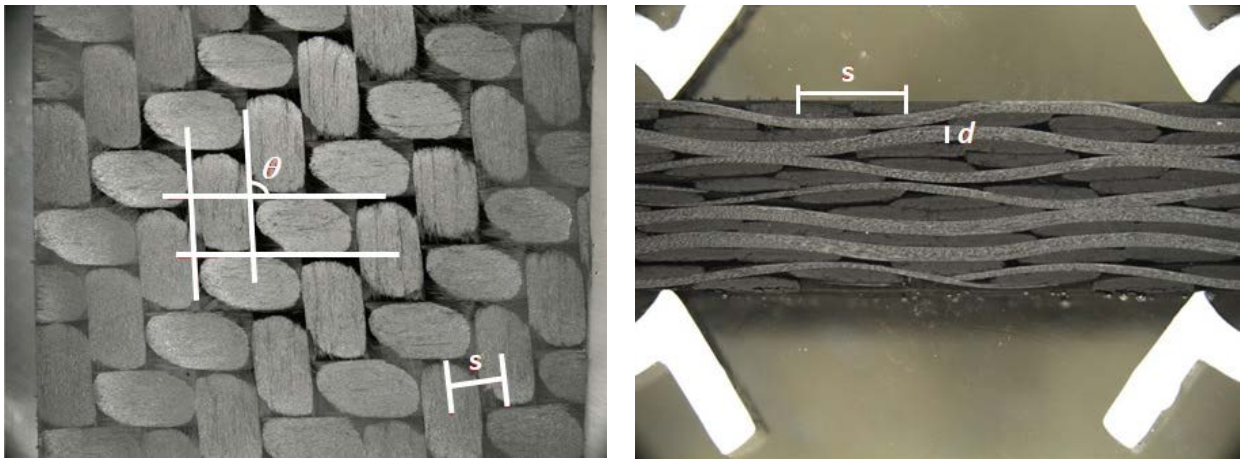

(a) (b)

Figure II.2.C.1. Images of different views (a) in-plane view; and (b) cross-section view. Source: Ford.

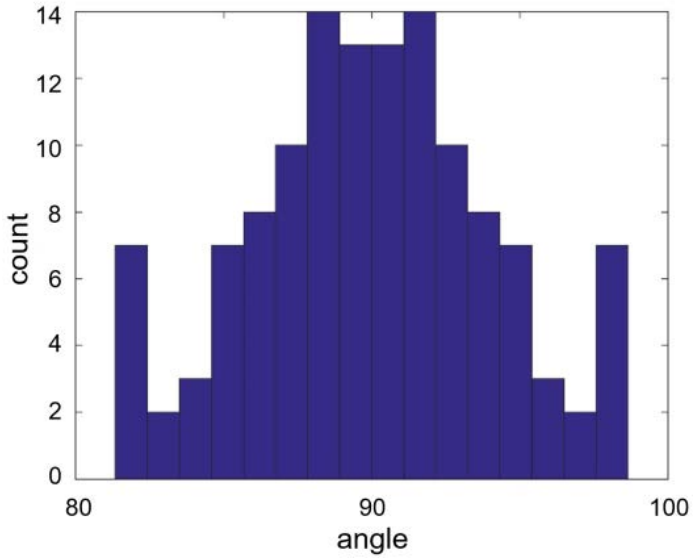

Figure II.2.C.2. Woven yarn angle θ distribution.

Composite Plaque Characterization

Seventy UD plaques were molded at Dow Chemical with 45% and 55% of V_f for validation of the ICME models. The thicknesses of these plaques were 1.2 mm, 2.3 mm, and 5 mm, respectively. Specimens from these plaques were characterized and averaged for elastic modulus (E), strength (F), Poisson's ratio (ν), strain (ε) to failure under tension and compression-loading, shear modulus (G), and shear strain to failure (γ) from 10° off-axis shear tests. Properties were found to vary linearly with V_f. Results of the tests are summarized in Table II.2.C.1, where numbered subscripts refer to a coordinate system with axis 1 in fiber orientation, axis 2 in plaque plane and orthogonal to the fiber direction, and axis 3 orthogonal to plaque plane. Subscript t means tension and c compression. F_6 is in plane shear strength.

Table II.2.C.1. Mechanical Properties Obtained from UD Composites with Varying V_f.

Fiber V_f	E_1 (GPa)	ν_{12}	F_{11} (MPa)	ε_{1tu} (%)	E_2 (GPa)	F_{2t} (MPa)	ε_{2tu} (%)	G_{12} (GPa)	F_6 (MPa)	γ_{6u} (%)
45%	116	0.33	1530	1.24	8.47	75.1	0.99	4.66	81.2	5.62
55%	145	0.32	1960	1.25	9.64	53.2	0.57	5.34	77.2	5.11

Fifty plaques of NCF were molded. The NCF carbon/epoxy plaques were of a $[0/90]_8$ cross-ply construction. Bulk density measurements of NCF material were taken by the water-immersion method of the American Society for Testing and Materials International standard (ASTM D792). Bulk densities were in the range of 1.52-1.54 g/cm^3, close to those of UD material (1.52-1.55 g/cm^3). Tension and compression tests were conducted at Northwestern University, resulting in the measured properties reported in Table II.2.C.2. Ultimate failures were similar in nature to those of the UD coupons. Tests conducted with the fibers aligned ±45° to the loading axis gave results similar to the uniaxial shear tests (45° tests on woven composite, 10° off-axis tests on UD material). Strains at failure (>10%) were significantly larger than in the UD material (~ 5%) due to the cross-ply structure of the NCF material.

Table II.2.C.2. NCF Laminate Properties Obtained from Tension and Compression Tests.

Fiber V_f	E_{1t} (GPa)	V_{12}	F_{1t} (MPa)	G_{12} (GPa)	$F_{45°t}$ (MPa)	E_{1c} (GPa)	F_{1c} (MPa)
Value	74.1	0.042	1142	5.17	112	70.6	557
Coefficient of Variation (%)	3.08	22.2	3.78	2.32	2.06	3.08	7.02

Round-Robin of Tensile Tests for UD

A round-robin of UD tensile tests are performed to study sample preparation and gripping method. The assumption is that the best method should lead to the highest measured strength, which should be closer to the expected theoretical strength for this material. Three sets of samples were prepared and tested, as shown in Figure II.2.C.3.

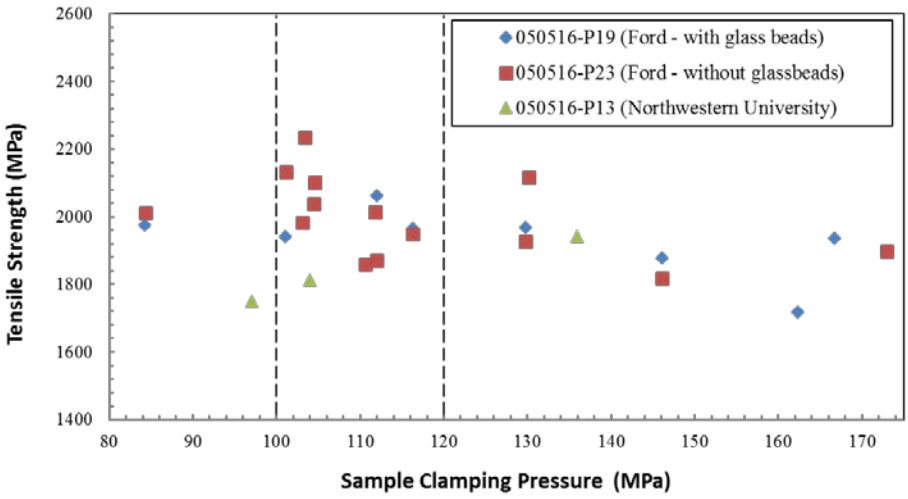

Figure II.2.C.3. Monotonic tensile tests performed in the longitudinal direction for the UD material.

It can be observed from Figure II.2.C.3 that the specimen clamping pressure does indeed affect the tensile test results. If the pressure is too high, the fracture is induced prematurely within or close to the grips, resulting in a lower apparent strength, and if the pressure is too low, the test results are invalid due to slippage of the tabbed area. The optimal clamping pressure depends on the actual tabbing area, but it can be inferred from Figure II.2.C.3that the pressure should be set such as to result in a clamping pressure between 100 and 120 MPa.

Task 2: ICME Model Development and Validation

Atomistically Informed Resin Infusion Models

Major contributions of the MDA in FY 2017 are the improvement in computational speed and modeling of interphase properties. The SLME algorithm was applied to successfully predict material behavior at strain rates achievable in physical tests (10^2/s).

The interphase region includes the fiber surface, sizing of the fiber, and part of the resin matrix. Local properties in the interphase region differ very much from bulk properties. For typical carbon fiber/epoxy system, the thickness of the region is around 200 nm. To predict the interphase properties, the region is simplified as a circular cylindrical shell with an inner radius of fiber radius and thickness of 200 nm. The strength and elastic modulus are modeled as a function of distance from the fiber surface. One assumption is that the strength and modulus at the inner surface of the shell will be those of the fibers and at the outer surface will be those of the matrix. A second assumption is that part of the interphase materials near the matrix would achieve a lower curing degree in the preforming process due to the incompatibility between the sizing and matrix resin chemistry. The average properties for the elastic modulus and strength of the interphase layer should be $\bar{E}_i$~22.5 GPa and $\bar{\sigma}_i$~730 MPa, respectively, in comparison with matrix properties for elastic modulus of $E_m = 3.8$ GPa and compressive strength $\sigma_{fc} = 330$ MPa.

The interphase region with the predicted properties is added to the UD RVE model. The transverse tension and compression results obtained from the three phase RVE model are compared to those from the traditional RVE model where there are only two phases, i.e., matrix and fiber. As shown in Figure II.2.C.4, it is obvious that the stress-strain curves from the modified RVE model are in much better agreement with experiments.

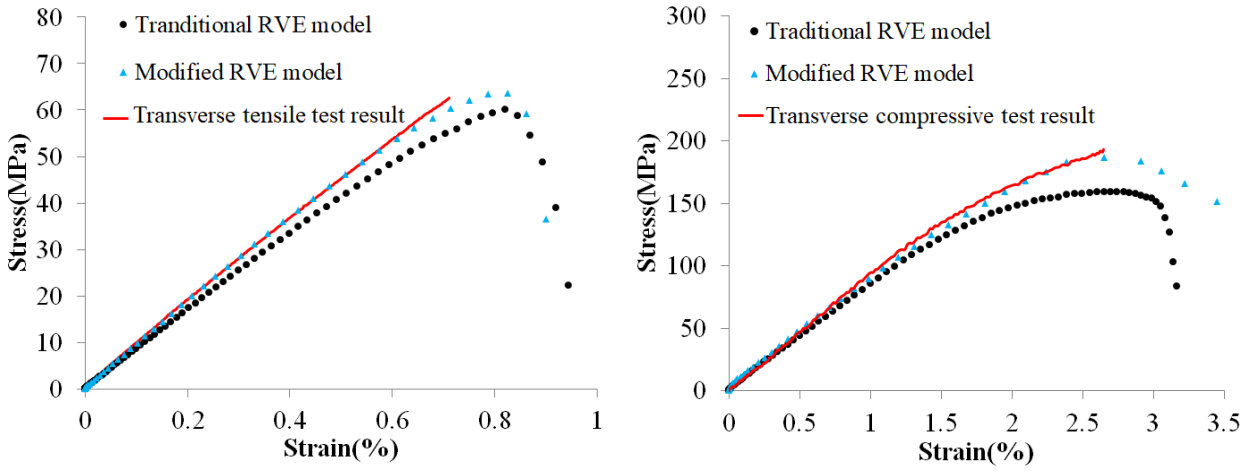

(a) (b)

Figure II.2.C.4. Results from the modified RVE model with interphase region compared with those from the traditional RVE model: (a) transverse tension; and (b) transverse compression.

Preform and Compression Molding Process Models

Prepreg Preforming Modeling

The non-orthogonal model was implemented in LS-DYNA as MAT_COMPRF (MAT_293). The uniaxial tension and bias-extension tests are needed to calibrate the tension and shear parameters, as well as a bending test to reversely calculate the compression modulus of the prepreg material. The double-dome test was conducted to validate the material model. The prepreg for the validation is 2 × 2 twill woven carbon fiber with a unit cell size of about 9 mm × 9 mm. The simulation model was established in LS-DYNA using the explicit integration method. The sheet was modeled by reduced integration shell elements. The punch, binder, and die were modeled by rigid shell elements.

The single layer preforming experiment was conducted with twill woven carbon fiber prepregs at 60°C and the initial yarn direction as ±45°. The simulation results in the upper-right quarter of Figure II.2.C.5 show that the non-orthogonal material model established is capable of accurately predicting the physical experiments regarding the yarn angle distribution and blank draw-ins. For comparison, an orthotropic material model (MAT_002) is also utilized in the same simulation, whose result is shown in the upper-left quarter of Figure II.2.C.5. Table II.2.C.3 compares the resulting shear angles at various locations (A through F) obtained from the experiment and simulations. It shows that the current model has improved the prediction accuracy.

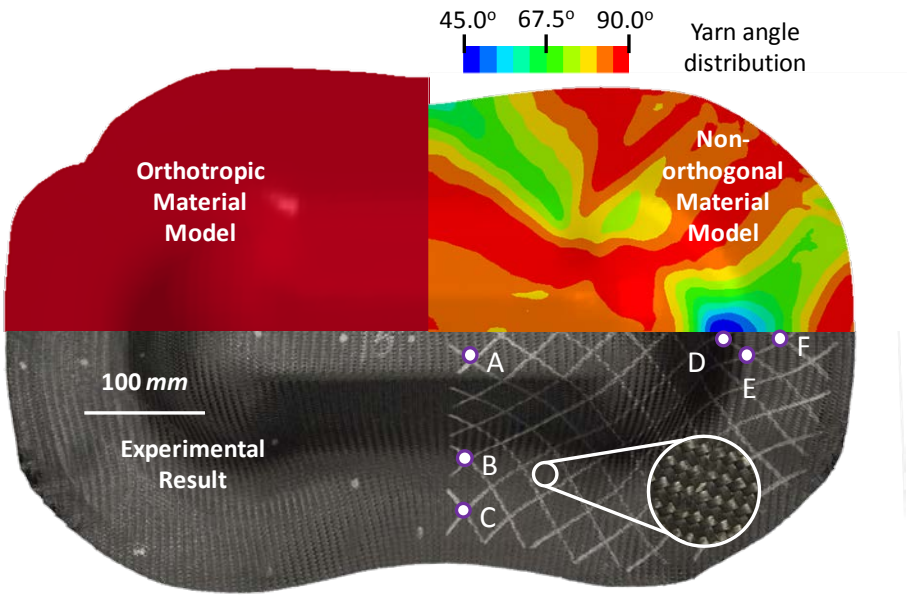

Figure II.2.C.5. Simulation and experimental result comparison of deformed geometry and yarn angle for preformed double-dome of ±45° single-layer woven prepreg. Source: Northwestern University.

Table II.2.C.3. Resulting Yarn Angles from the Single Layer Preforming Case.

Location	A	B	C	D	E	F
Experiment	80°	88°	71°	49°	56°	66°
MAT_293	81°	88°	73°	46°	60°	70°
MAT_002	70°	85°	86°	47°	59°	77°

The double-layer preforming test was also conducted at 60°C with two prepreg sheets as 0°/90° at the outer layer and ±45° at the inner one. These two blanks were modeled by two layers of shell elements with different initial yarn orientations. The simulation predicts the overall geometry and relative motion of two layers of prepreg sheets well.

SMC Compression Molding

Validation of the Moldflow simulation of SMC compression molding is conducted based on the results of the second molding trial. Especially, some of the plaques in the trial are purposely not fully filled to validate filling patterns. The molding process is stopped by shims with different thicknesses inserted between the molds. After the half-filled plaque is taken out of the mold, pictures are taken to quantitatively measure the dimension of the unfilled plaque. The validation work proves that Moldflow can predict filling nicely.

The RSC model was initially selected for SMC compression molding simulation as it can well represent the dynamics in highly concentrated flow in the SMC compression molding. To validate fiber orientation predictions, samples with in-plane dimensions of 1 in. × 1 in. were cut from selected positions of the molded SMC plaque part, as shown in the upper left schematic in Figure II.2.C.6, and fiber orientation components (A11) were measured. A11 characterizes the probability of finding fibers aligning along 1-axis (horizontal direction in upper left schematic in Figure II.2.C.6 in a local region. The comparison between measurement and prediction in Moldflow through sample thickness direction is shown for three test conditions in Figure 6. Additionally, the averaged A_{11} component through thickness is also calculated for both experiment and prediction and shown graphically in the lower right corner of Figure II.2.C.6. The difference between averaged A_{11} in experiment and prediction for tested locations are all within 6%.

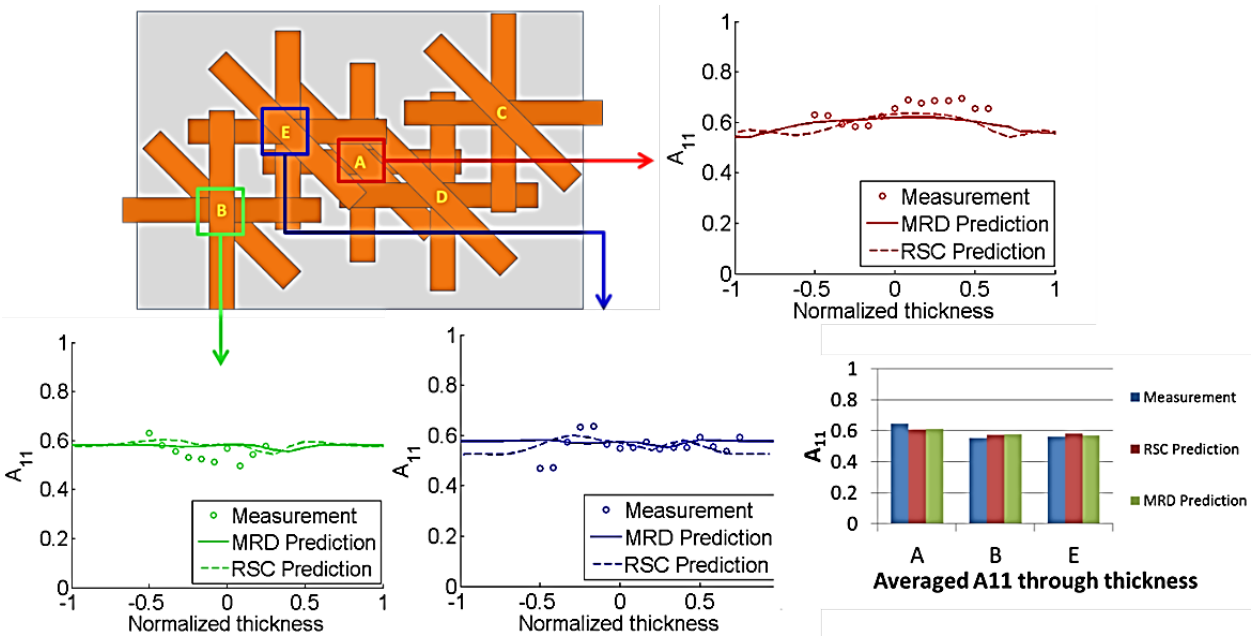

Figure II.2.C.6. A comparison between the fiber orientation tensor component, A_{11}, from the Moldflow prediction using the RSC model with best-fit parameters and measurements from microscopic image analysis.

A new Moldflow model, the MRD model, was also applied to predict the fiber orientation for SMC compression molding in Moldflow, as is shown in Figure 6. While RSC showed good prediction for in-plane component, A_{11}, it would end up with an unrealistically high A_{33} prediction in thickness direction, resulting from lack of consideration of constraints in the fiber tow direction by the part thickness. This issue is fixed in the MRD model, which considers an anisotropic diffusion term. Additionally, local material properties predicted by using the fiber orientation tensor from the MRD model match better with tensile modulus measurements.

Mechanistic Continuum Models for CF Composites

Multiscale models of UD, woven, and SMC composites were developed in FY 2016. The predictions of elastic parameters are less than 10% errors when compared with experimental measurements. In these RVE models, UD RVE is most critical, as woven and SMC RVEs use fiber tow properties derived from UD RVE.

In FY 2017, the developed multiscale models have been used intensively to study various aspects of the material, especially inhomogeneities caused by misalignments of curvature of fibers and fiber tows. Two important improvements (i.e., the introduction of the interphase layer in UD RVE and the implementation of failure analyses in the RVEs) were also made in FY 2017, and will be discussed in the next section. Another development is the SCA method for computationally efficient multiscale modeling.

Improvement of UD RVE Model

An anisotropic failure criterion has been implemented in the UD RVE model in FY 2017(Melro et al. 2013). The Abaqus user subroutine has been modified to include the failure prediction of the resin.

The three phase RVE model, with a 0.2 μm-thick layer of interphase elements between fiber and matrix to account for the strengthening of the material in the interphase, has greatly improved the accuracy of the RVE models as discussed early in the section on MDA. The new UD RVE has been used to study the damage initiation and evolution processes of the UD CFRP composites. Under the transverse tension, interfacial debonding first occurs at the poles of the closely packed fibers where the stress concentration in the

fiber/interphase region are higher, as is shown in Figure II.2.C.7(a). After that, bands of interfacial cracks develop perpendicular to the loading direction. Within these bands of interfacial cracks, the matrix and interphase region are subject to plastic deformation, which further results in the coalescence of neighboring interfacial cracks, as shown in Figure II.2.C.7(b) and Figure II.2.C.7(c). Finally, interfacial cracks and interphase region failure at different locations are connected by matrix cracks through the entire RVE, causing the ultimate fracture of the RVE perpendicular to the loading axis, shown in Figure II.2.C.7(d). The RVE model can also describe other failure modes accurately.

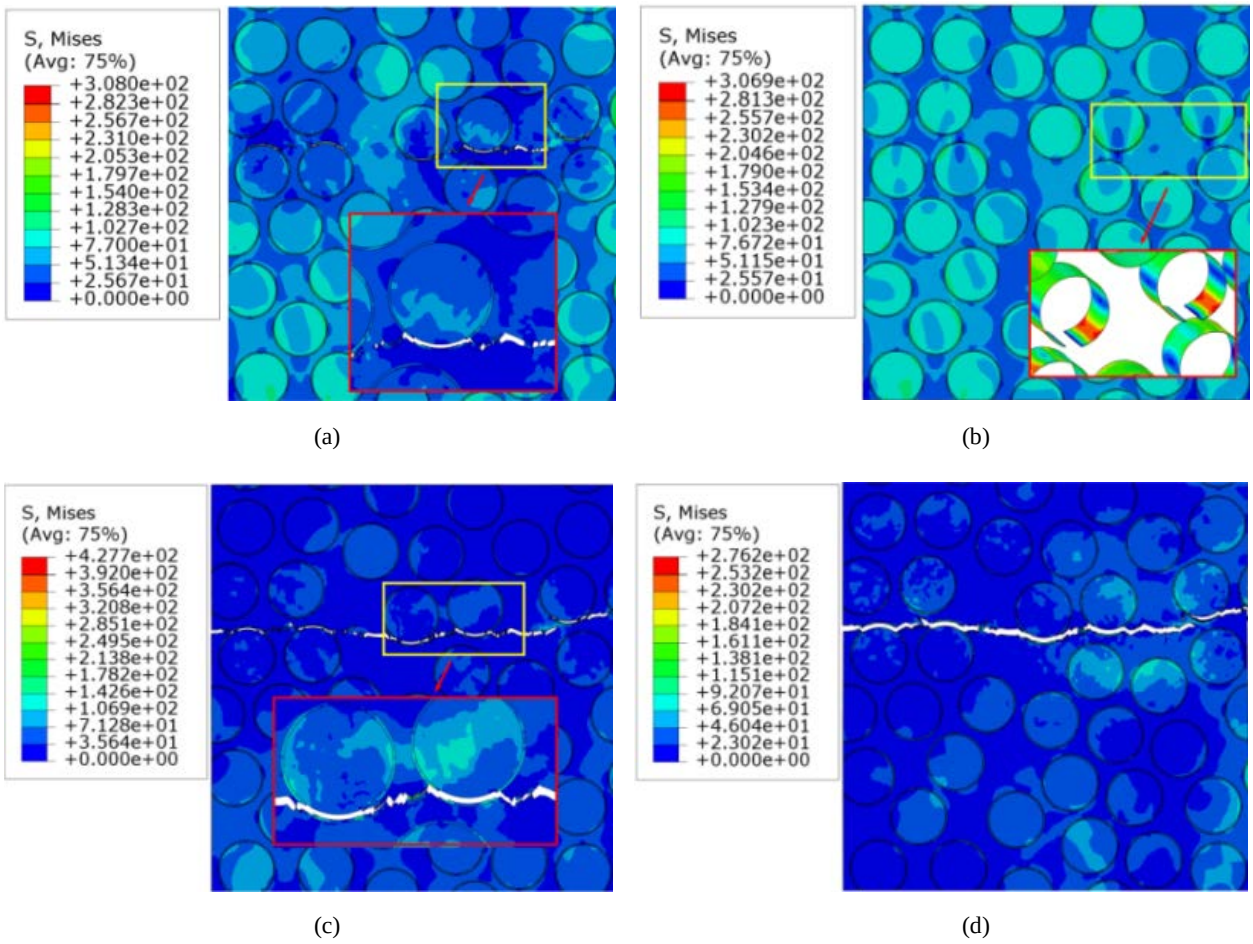

Figure II.2.C.7. Damage initiation and evolution of transverse tension. Source: Ford.

Self-consistent Clustering Analysis (Nonlinear Homogenization)

Multiscale models are accurate in predicting local material properties; however, it is not practical in engineering structural analysis to use RVE directly, as computational efficiency would be an issue. The SCA method is a powerful analysis approach in reducing the size of high-fidelity micro- or meso-scale RVE modeling. Only limited runs of a specific RVE model are required to capture the material's response and generate an equivalent model to represent the material's behavior, without losing any physical details such as void or inclusions.

The SCA method has been extended to both UD and woven composites. The basic framework of SCA stays the same, where the offline stage is proceeded first to obtain the database and a reduced order model is solved in the online stage. The analysis has been integrated into Abaqus as a VUMAT for explicit analysis. Failure of the material is also considered. Discussions are ongoing between Northwestern University and LSTC to implement this procedure in LS-DYNA.

Fracture Models and Energy Absorption Models

LS-DYNA with material models MAT_54 and MAT_58 are used for crash analysis. The focus of FY 2017 is to perform impact tests to calibrate and evaluate the material models. Hat section parts were used for impact tests. Table II.2.C.4 lists the numbers of samples with different lay-ups and loading modes. The two most critical modes in crash safety (i.e., side impact [bending] and axial crash) were also performed.

Table II.2.C.4. Crash Safety Component Test Sheet.

Lay-up		total	crash safety tests	bending		axial crash	
				quasi-static	dynamic	quasi-static	dynamic
UD	[0/90/90/0/0/0]s	36	25	8	6	0	6
	[0/60/-60/0/60/-60]s	36	25	8	6	0	6
Woven	[90/0/90/0]s	12	12	5	4	0	3
	[45/-45/45/-45]s	12	12	5	4	0	3

Simulations of both side impact and axial crash tests were performed with LS-DYNA to calibrate material model inputs. Calibrated material models were able to capture material failure modes and predict load displacement curves with an accuracy that is acceptable in conventional crash analysis. Figure II.2.C.8 shows the results of these axial crash test simulations. One layer of thin shell elements was used in the analysis shown in Figure II.2.C.8(a), with MAT_54. A meso model of multiple thick shell elements and cohesive elements were used in the simulation shown in Figure II.2.C.8(b). The meso model represents delamination better.

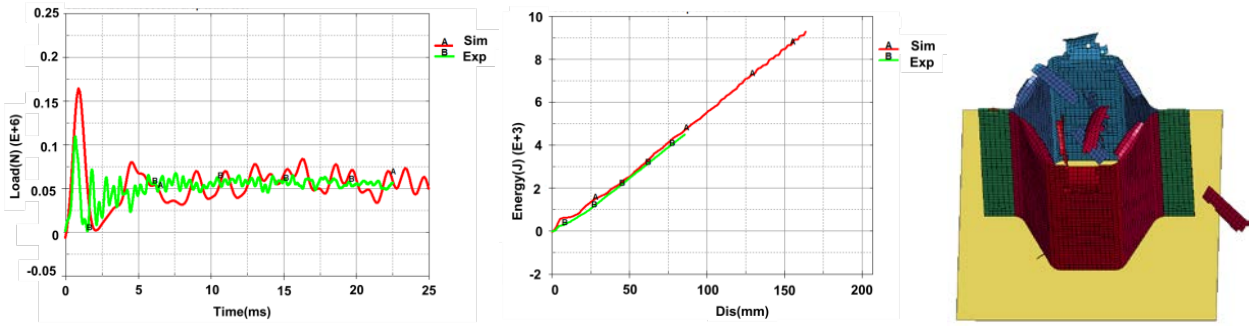

(a) macro model

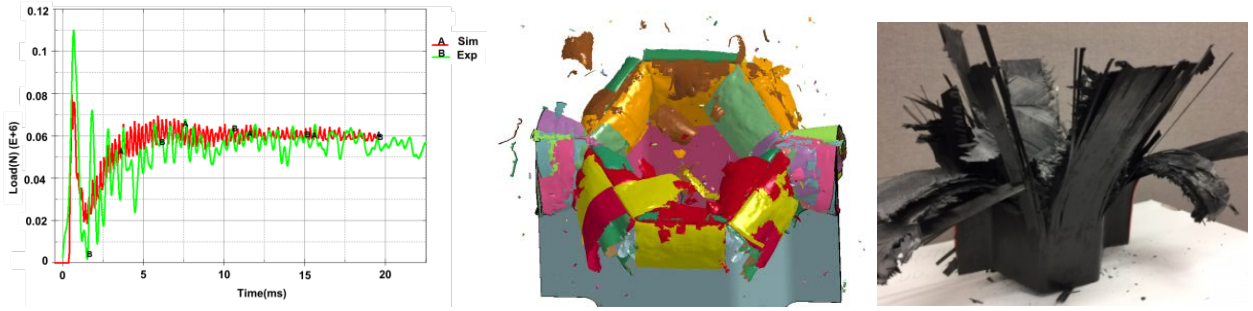

(b) meso model

Figure II.2.C.8. Axial crash simulation with macro and meso models for UD 0-60 lay-up. Source: Ford.

A new element for modeling CFRP material delamination is under development. Dynamic three-point bending tests were carried out to validate the new element.

Fatigue and Durability Models

A new method to calculate the fatigue life of UD and woven CFRP components has been implemented in nCode. This method assumes a first-ply failure approach, which is implemented as an extension of a chosen static failure criterion where multiple choices are available. The fundamental assumption is that the fatigue behavior of a lamina may be used to evaluate the expected durability of a laminated component or structure. An example of the implementation is illustrated as a screenshot in Figure II.2.C.9. Fatigue tests of hat sections under four-point bending are ongoing, and results are being analyzed to validate nCode CFRP fatigue module.

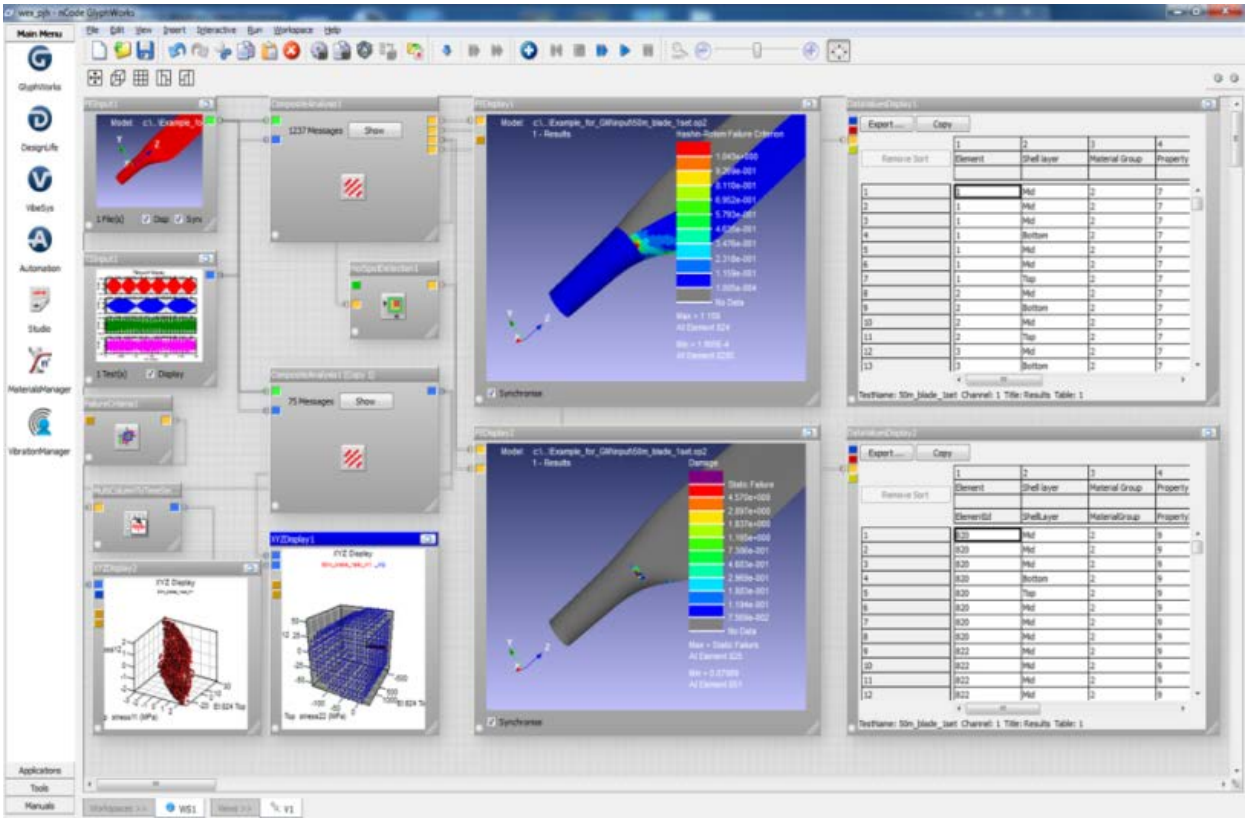

Figure II.2.C.9. Screenshot of multiaxial fatigue analysis of a UD CFRP using the new implemented nCode. Source: Ford.

All tests needed to characterize the fatigue behavior of the UD CFRP material in the transverse direction (90° to fiber orientation) have been completed and the results analyzed. The test results have been used to generate Constant Fatigue Life diagrams for nCode fatigue analysis.

Tests in the 0° orientation have been successfully completed for the tension-tension condition (with minimum-maximum peak stress ratio equal to 0.1). However, tests under tension-compression conditions (with minimum-maximum peak stress ratio less than 0) have not yet been completed as the specimen heats up excessively during the tests and the adhesive used to attach the gripping tabs to the specimen fails prematurely. A series of different adhesive types are currently being tested to determine the best adhesive for this application. At the same time, new specimen geometries will be fabricated combining a dog-bone-shaped geometry with glued tabbed ends, to maximize the surface area of the adhesive within the gripping area. Similar tests for 10° orientation were also performed using an anti-buckling device.

Stochastic Multiscale Characterization

The effect of microstructural correlations and uncertainties at three scales—micro-, meso-, and macro-scale—were investigated. Major sources of uncertainty at each length-scale of the material system of interest were identified. At each particular scale, the spatial correlations among the quantities or parameters of interest are modeled as a function of the spatial coordinates at the next higher scale via a random field. Sensitivity analyses were carried out to make sure that dominant sources of uncertainty at the meso- and macro-scale are identified.

In FY 2017, both UD and woven composites were characterized microscopically to study uncertainty quantification and uncertainty propagation. The thickness variations of hat sections used in validation tests were also studied.

A bias-extension test on woven laminates was modeled to demonstrate the proposed uncertainty propagation method. The sample consists of four identical plies stacked in the same orientation with a total thickness of 2.4 mm. Yarn angle (α), V_f, and fiber misalignment angle (θ) are identified as the main uncertainty sources. Three cases are compared: (1) no spatial variations with V_f=55% and α=90°; (2) only α changes spatially; and (3) α, V_f, and θ change spatially, α changes as in Case 2, V_f varies between 45-65%, and θ from 0–10° with 5° as the mean. The von-Mises stress field for the three cases is compared to illustrate the effect of spatial variations on local behavior, where in Case 3, the field is averaged over 20 simulations. As demonstrated in Figure II.2.C.10(a) through Figure II.2.C.10(c), the spatial variations result in stress concentrations especially near the corners. As shown in Figure II.2.C.10(d), the coefficient of variation across these 20 simulations can be as high as 10% over the composite sample for Case 3. These results indicate that the effect of spatial variations, even in the linear analysis, can be quite significant and must be taken into account for accurate prediction of materials properties and performance.

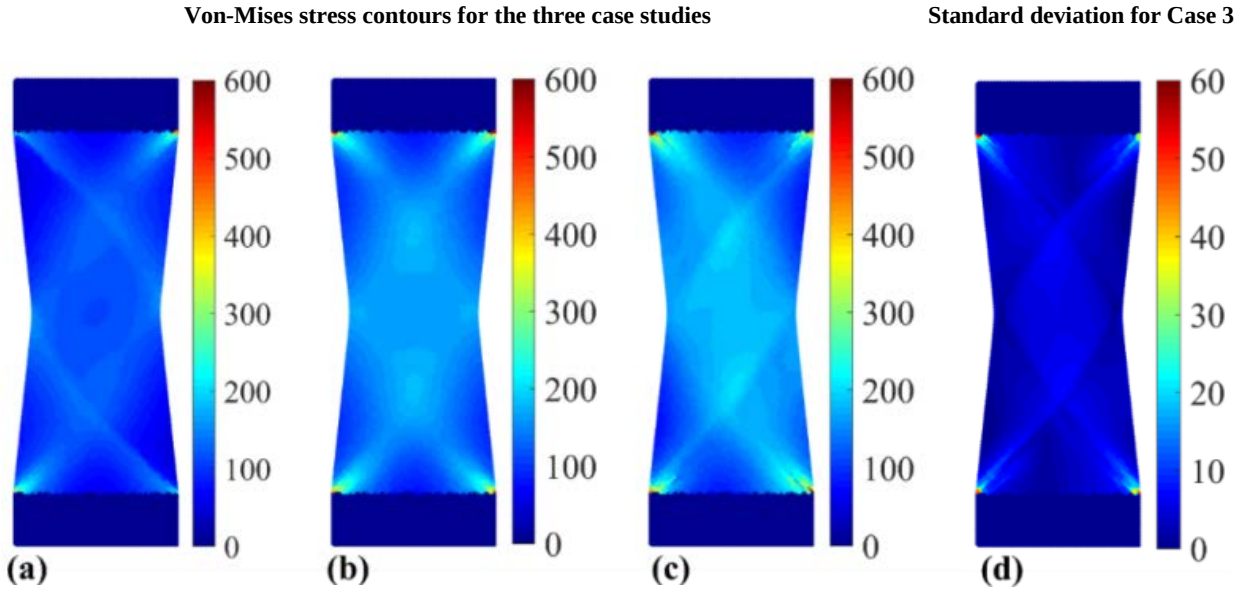

Figure II.2.C.10. Effect of spatial variations on von-Mises stress field (Unit: Mpa). (a) Case 1: No spatial variations. (b) Case 2: Only α changes spatially. (c) Case 3: α, V_f, and θ changes spatially. (d) The standard deviation of the local stress field across the 20 simulations for Case 3.

Task 3: ICME Model Integration and Structure Optimization

The integration of ICME tools was completed in FY 2017.

Three integrated workflows have been developed, respectively for ICME analyses of SMC, woven, and UD composites. There are six major steps in an integrated workflow to enable multidisciplinary design optimization (MDO). They are: (1) perform preforming or compression molding simulation based on initial component geometry; (2) transfer outputs from manufacturing simulation to inputs of structural analysis; (3) generate material constitutive relation based on material design and process simulation; (4) run solver to perform structural stress analysis; (5) complete post processing to estimate structural integrity, such as stiffness, crashworthiness, fatigue life, and compare to design specifications; (6) perform optimization analysis and suggest new component geometry and process parameters for the next run if the design is not optimized.

A hat section part with a close-out flat plate has been created to exercise all aspects of the ICME-based design optimization on a smaller, more tractable example. Figure II.2.C.11 shows the integration and optimization work flow. The design purpose is to minimize the structure weight while satisfying the constraints on stiffness, strength, and impact performance. The following parameters are considered as design variables:

1. The height of the hat section.
2. Two material selection variables: one for the top hat and another for the back plate. The materials can be chosen from five candidates: steel, aluminum, SMC composites, woven composites, and UD composites.
3. One variable for selecting the connection method (adhesive or spot welding).
4. Six variables for the thickness of each part in the structure: five for the top hat (different regions can have different thicknesses) and one for the back plate.
5. Six design variable vectors for the composite layout of each part in the structure (if UD or woven composites are selected for the part). Each vector contains 20 variables, which represent the fiber orientation angles of a maximum number of 20 layers in a composite part.

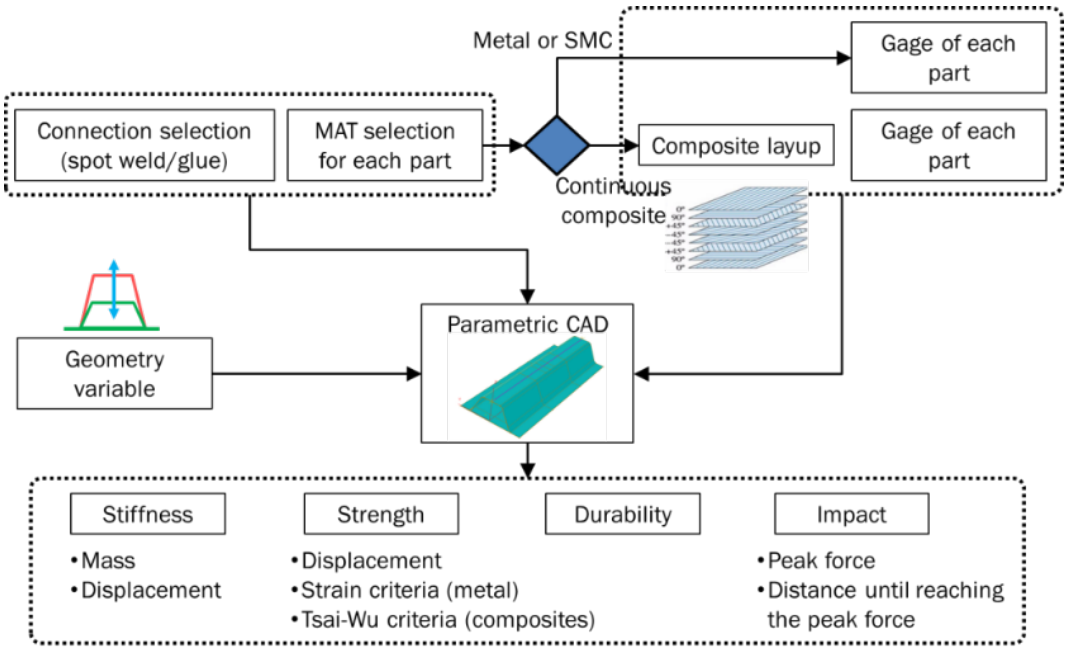

Figure II.2.C.11. Integration and optimization workflow for the hat section example.

In total, there are 130 design variables. During the optimization process, structure geometry and simulation input decks are generated based on the values of the 130 variables. There are three attribute simulations being conducted in parallel: (1) stiffness analysis in NASTRAN; (2) strength analysis in Abaqus; and (3) impact analysis in LS-DYNA. The responses from all these simulations are used for the design constraint check. The optimization objective is to minimize the weight of the structure, while satisfying all the constraints.

A test run has been conducted using this optimization workflow. The preliminary result shows that the optimum design has a weight of 1.496 kg. Compared to the baseline design (pure steel hat section of 2 mm thickness, 3.048 kg), a weight reduction of 50.9% is achieved. The optimum solution is a mixed-material design in which woven composites are selected for the hat section, and aluminum is selected for the back plate. The above MDO process is used for the subframe MDO ICME-Based Design and Optimization in Task 4.

Task 4: Subsystem Design and Analysis ICME-Based Design and Optimization

This task puts the newly developed ICME tools into a test through the exercise of a subframe design and optimization, connecting structure/process/property. In FY 2017, efforts have focused on two main fronts:

1. The topology and initial seed designs for the subframe.
2. The development of a surrogate assembly, the hat section with a back plate as an efficient example to test all the MDO stages.

Figure II.2.C.12 depicts the overall flow of Task 4 to exercise the MDO tools and develop carbon fiber composite intensive front subframes.

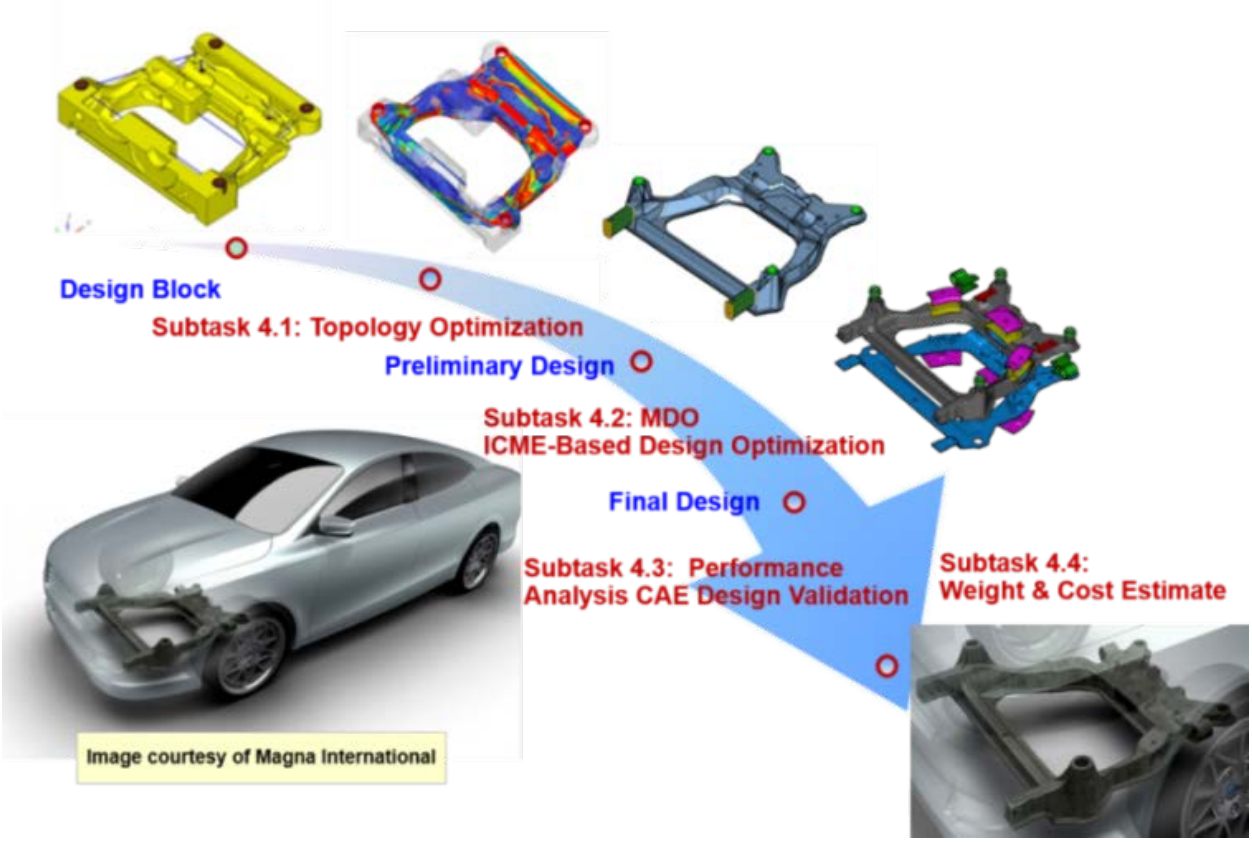

Figure II.2.C.12. Subframe design optimization work flow. Source: Ford, Magna International.

The topology optimization for the front subframe is completed based on stiffness requirements. The subframe design is driven by the 27 stiffness requirements. Three concepts have been developed for the subframe based on the topology results. These concepts are described as follows:

1. SMC Intensive Design –
   This design starts from an initial concept design of a highly ribbed closed section of random chopped SMC with local reinforcements of unidirectional materials and perhaps steel compression limiters at highly loaded bolted connections.
2. NCF/Woven Intensive Design –
   This design starts from an initial concept design of NCF or woven fabric closed section with minor chopped SMC ribbing and perhaps steel compression limiters at highly loaded bolted connections.
3. Aluminum Intensive Design –
   This design starts from an initial concept design of extruded aluminum sections with limited random chopped SMC and NCF or woven fabric reinforcements. This is viewed as the lowest cost subframe with limited carbon fiber composite components.

These three designs will serve as the "seed" initial starting points for the MDO ICME-based Design and Optimization. The parameterized designs are in place for these three starting points. Additionally, the stiffness, strength, and durability are all in place. The safety analyses will be completed soon.

Conclusions

FY 2017 marked the third year of the "Integrated Computational Materials Engineering Development of Carbon Fiber Composites for Lightweight Vehicles" project. The project develops ICME tools for CFRP composites and uses ICME tools to design structural carbon fiber composite subframes to support immediate weight reduction in light-duty vehicles and reduce development-to-deployment lead time.

In FY 2017, all model validation tests have been completed. This is shown by comparing measured data from respective tests, the error of predictions of fiber orientations from both preforming analysis and compression molding analysis is less than 15%, and the multiscale model predictions of elastic parameters are less than 10%. The accuracy of simulations of impact tests of CFRP is comparable to that of simulation in conventional crash analysis. Accuracy of fatigue models is currently under evaluation and is expected to be completed by the end of 2017. We are challenged in achieving a valid tension-compression fatigue test as test results are specimen-size dependent. This issue is expected to be resolved in early FY 2018.

The integration of ICME models has been completed. ModeFrontier is chosen as a platform for ICME tool integration and design optimization. Existing capabilities and added scripts enabled a seamless integration of manufacturing simulation and vehicle performance analysis. Material design and manufacturing process information, such as geometric dimension, fiber layout, and fiber orientation are inputs for multiscale models to generate local material constitutive relation used in following noise, vibration, harshness, safety, and durability analyses. The success of the integration has been validated by an optimization of the design of a hat section. Currently, it is being used for the design of a CFRP subframe.

The developed ICME tools have and will continuously be implemented in popular software packages, such as LS-DYNA for stress and crash analysis, nCode for durability, Moldflow for molding, and modeFrontier for process integration and optimization.

Built on these achievements, this project is expected to be successfully completed on time by the end of 2018.

Key Publications

Bostanabad, R., B. Liang, J. Gao, Z. Liu, P. Cheng, W. Zhang, J. Cao, W. K. Liu, and W. Chen, 2017, "Uncertainty quantification in multiscale simulation of carbon fiber reinforced polymers using additive gaussian processes for top-down sampling," WCX17: SAE World Congress Experience, April 6, 2017, Detroit, MI, USA.

Chen, Z., Y. Li, Y. Shao, T. Huang, H. Xu, Y. Li, W. Chen, D. Zeng, K. Avery, H. T. Kang, and X. Su, 2017, "RVE model for chopped carbon fiber SMC," WCX17: SAE World Congress Experience, April 6, 2017, Detroit, MI, USA.

Chen, Z., T. Huang, Y. Shao, Y. Li, H. Xu, K. Avery, D. Zeng, W. Chen, and X. Su, 2017, "Multiscale finite element modeling of sheet molding compound (SMC) composite structure based on stochastic mesostructure reconstruction," *Composites Part A*, in review, September 2017.

Cheng, H., J. Gao, O. Landauer Kafka, K. Zhang, B. Luo, and W. K. Liu, 2017, "A micro-scale cutting model for UD CFRP composites with thermo-mechanical coupling," *Composites Science and Technology*, Vol. 153, pp. 18–31.

Daniel, I. M., S. M. Daniel, and J. S. Fenner, 2017, "A new yield and failure theory for composite materials under static and dynamic loading," *International Journal of Solids and Structures*, in press, available online 12 September 2017.

Daniel, I. M., J. S. Fenner, and B. T. Werner, 2017, "Characterization and modeling of composite sandwich core foam under static and dynamic loading," Zhu, Y., and A. T. Zehnder (eds.), *Proceedings of the 2016 Annual Conference on Experimental and Applied Mechanics*, Vol. 4, Springer, New York, NY, USA. ISBN-13: 978-3319420271.

Fenner, J. S., and I. M. Daniel, 2017, "Mixed mode and mode II fatigue crack growth in woven composites," Zhu, Y., and A. T. Zehnder (eds.), *Proceedings of the 2016 Annual Conference on Experimental and Applied Mechanics*, Vol. 4, Springer, New York, NY, USA. ISBN-13: 978-3319420271.

Huang, T. Y., H. Xu, and W. Chen, 2017, "Microstructure reconstruction of sheet molding composite using a random chips packing algorithm," WCX17: SAE World Congress Experience, April 6, 2017, Detroit, MI, USA.

Li, Y., Z. Chen, L. Su, W. Chen, X. Jin, and H. Xu, 2017, "Stochastic reconstruction and microstructure modeling of SMC chopped fiber composites," *Composites Part B*, in review, March 2017.

Li, Y., Z. Chen, H. Xu, J. Dahl, D. Zeng, M. Mirdamadi, and X. Su, 2017, "Modeling and simulation of compression molding process for sheet molding compound (SMC) of chopped carbon fiber composites," WCX17: SAE World Congress Experience, April 6, 2017, Detroit, MI, USA.

Lin, S.-P., Y. Chen, D. Zeng, and X. Su, 2017, "Meso-modeling of carbon fiber composite for crash safety analysis," WCX17: SAE World Congress Experience, April 6, 2017, Detroit, MI, USA.

Liu, H., W. Wen, X. Su, and C. Engler-Pinto, 2017, "Study on fatigue behaviors of porous T300/924 carbon fiber reinforced polymer unidirectional laminates," WCX17: SAE World Congress Experience, April 6, 2017, Detroit, MI, USA.

Meng, Z. "Predicting the macroscopic fracture energy of epoxy resins from atomistic molecular simulations," WCX17: SAE World Congress Experience, April 6, 2017, Detroit, MI, USA.

Meng, Z., M. A. Bessa, W. Xia, W. K. Liu, and S. Keten, 2016, "Predicting the macroscopic fracture energy of epoxy resins from atomistic molecular simulations," *Macromolecules*, Vol. 49, No. 24, pp. 9474-9483. DOI: 10.1021/acs.macromol.6b01508.

Powell, L., W. Luecke, M. Merzkirch, K. Avery, and T. Foecke, 2017, "High strain rate mechanical characterization of carbon fiber reinforced polymer composites using digital image correlations," *SAE Int. J. Mater. Manf.*, Vol. 10, No. 2, pp. 138-146. DOI: 10.4271/2017-01-0230.

Ren, H., W. Zhang, Y. Wang, D. Zeng, X. Su, W. Chen, W. K. Liu, and J. Cao, 2017, "Simulation and experimental analysis of the preforming process of the woven composite prepreg," WCX17: SAE World Congress Experience, April 6, 2017, Detroit, MI, USA.

Xu, H., Y. Li, and D. Zeng, 2017, "Process integration and optimization of ICME carbon fiber composites for vehicle lightweighting: A preliminary development," WCX17: SAE World Congress Experience, April 6, 2017, Detroit, MI, USA.

Zhang, W., H. Ren, Z. Wang, W. K. Liu, W. Chen, D. Zeng, X. Su, and J. Cao, 2016, "An integrated computational materials engineering method for woven carbon fiber composites preforming process," ESAFORM 2016.

Zhang, W., Z. Zhang, J. Lu, Q. J. Wang, X. Su, D. Zeng, M. Mirdamadi, and J. Cao, 2017, "Experimental characterization of the interaction between carbon fiber composite prepregs during the preforming process," *ASME 2017 12th International Manufacturing Science and Engineering Conference*, accepted, February 2017.

Zhang, W., H. Ren, B. Liang, D. Zeng, X. Su, J. Dahl, M. Mirdamadi, Q. Zhao, and J. Cao, 2017, "A non-orthogonal material model of woven composites in the preforming process," *CIRP Annals Manufacturing Technology*, accepted, March 2017.

References

Melro, A. R., et al., 2013, "Micromechanical analysis of polymer composites reinforced by unidirectional fibres: Part I–Constitutive modelling," *International Journal of Solids and Structures*, Vol. 50, No. 11, pp. 1897–1905; "Micromechanical analysis of polymer composites reinforced by unidirectional fibres: Part II–Micromechanical analyses," *International Journal of Solids and Structures*, Vol. 50, No. 11, pp. 1906–1915.

II.2.D Development and Integration of Predictive Models for Manufacturing and Structural Performance of Carbon Fiber Composites in Automotive Applications (General Motors)

Venkateshwar Aitharaju, Principal Investigator
Chemical Sciences and Material Systems Laboratory
General Motors R&D Center
MC 480-106-710
30500 Mound Rd.
Warren, MI 48090
Phone: 248-343-9500
E-mail: venkat.aitharaju@gm.com

Carol Schutte, Technology Manager
E-mail: carol.schutte@ee.doe.gov

Start Date: May 1, 2015 End Date: April 30, 2019
Total Project Cost: $8,571,253 DOE share: $6,000,000 Non-DOE share: $2,571,253

Executive Summary

The goal of this project is to develop an integrated suite of state-of-the-art computational modeling tools that are critically needed to enable structural CF applications in automobiles. These tools help to predict the manufacturing and structural performance of CF composites, including stochastic effects. The project team is comprised of researchers from General Motors (GM), Engineered Solutions, Inc. (ESI) Group (i.e., software company owner of composite manufacturing tools PAM-RTM for resin transfer molding and PAM-FORM for forming of composites), Altair (i.e., software company owner of the multi-scale structural performance predictive tool for composites), Continental Structural Plastics (CSP) (i.e., molder/material supplier for composite materials and GM-Corvette composite parts supplier), and the University of Southern California (i.e., leader in uncertainty quantification of DOE's-funded Scientific Discovery through Advanced Computing Institute for Uncertainty Quantification). During the first phase of the project, both the manufacturing and structural performance tools, including a stochastic driver, will be calibrated and validated against coupon and component level tests. The difference between predictions and experimental results is to be limited to less than 15%. During the second phase of the project, the manufacturing and performance tools will be integrated by mapping the manufacturing outcome (e.g., fiber angles, residual stresses, degree of cure, and defects [voids, dry patches, and wrinkles]) into structural models. Further, these integrated manufacturing and structural performance tools will be used to design a composite CF automotive assembly for a high-volume, medium-duty automobile currently made of steel.

Various CF formats friendly to high-volume automotive manufacturing (e.g., non-crimp, woven, and chopped systems) and manufacturing processes (e.g., such as resin transfer molding [RTM] and compression molding) will be studied. Cost models will be developed in parallel for these high-volume manufacturing processes. The total number of parts in the CF assembly will be reduced through part consolidation and weight will be reduced through strategic thickness optimization at critical and noncritical locations for each of the components. Each of the CF composite components in the assembly will be optimized for weight, cost, and performance. The optimized CF automotive assembly will be certified, and the developed numerical models will be validated by comparing the numerical and experimental results for performance of the assembly. Finally, for the optimized CF assembly design, the weight, cost, and performance will be compared with the existing steel design. Availability of integrated computational tools to predict stochastic manufacturing and structural performance of structural composites to an original equipment manufacturer (like GM) can potentially eliminate significant bottlenecks that currently exist with large-scale implementation of CF composites in an automobile.

Accomplishments

- Calibration of PAM-FORM material model for satin and twill fabrics using newly conducted bias-extension experiments (FY 2017).
- Validation of PAM-FORM model for satin and twill fabrics with draping experiments on the truncated pyramid component (FY 2017).
- Validation of PAM-RTM model for filling and curing experiments on the flat plate, including race-tracking effects (FY 2017).
- Validation of enhanced PAM-DISTORTION material model for un-symmetric laminates based on the previous year's research (FY 2017).
- Developed a prototype tool for modeling the compression resin transfer molding (C-RTM) process and validated the model with experiments conducted on the truncated pyramid (FY 2017).
- Developed important manufacturing guidelines for fast curing resins (e.g., maximum thickness, maximum molding temperature) (FY 2017).
- Characterization of non-crimp fabric (NCF) materials, including stitching (FY 2017).
- A mapping capability was developed in Hypermesh software to map the structural outcome on to structural finite element models (FY 2017).
- Validated the multiscale structural model development with crush experiments conducted on flat panel specimens and obtained excellent correlations (FY 2017).
- Demonstrated the integrated computational materials engineering tool development on truncated pyramid component by correlating the prediction of structural performance including the manufacturing outcome (fiber angle changes) with the experimental results (FY 2017).
- Developed cost models for the resin transfer molding of composites (FY 2017).
- Completed polynomial chaos expansion (PCE) models for structural performance prediction under tensile and three-point-bend tests. Ten distinct models have been constructed to-date to keep track of experimental data and updates in the models underlying Multiscale Designer. The update procedure has been automated (FY 2017).
- Completed PCE models for the complete sequence from draping to distortion. Stochastic models for quantities of interest (QoI) for any intermediate quantity can be readily and efficiently evaluated. Also, sensitivities for all QoI with respect to basic random variables can also be readily computed (FY 2017).
- Started the development of a python wrapper that integrates the stochastic modeling, propagation, and updating capabilities for the whole project.

Technology Assessment

- Target: Develop an integrated stochastic manufacturing and structural performance computation tool to design structural automotive composites and predict performance within 15% of experimental results.
- Gap: Unknown manufacturing effects on structural performance of automotive composites.
- Gap: Commercial software package capability to predict combined manufacturing and structural performance, including stochastic effects.
- Gap: Manufacturing process optimized to yield lower costs and higher quality for automotive composites.
- Gap: Certification procedure for an automotive composite assembly based on computer modeling alone.

- Target: Achieve linear performance of design optimization as function of uncertain and design parameters.
- Gap: Uncertain parameters are introduced at different stages in the multiscale multiphysics simulation. Specialized algorithms and interfaces must be developed to meet this requirement.
- Target: Develop and demonstrate probabilistic validation methodology across scales.
- Gap: Modeling errors have been significant and have been reduced through an iterative process and through validation using different data sources including expert opinion from experimentalists.

Project Introduction

GM was the first North American automotive original equipment manufacturer to develop and commercialize CF composites for Class-A body panel (i.e., closure) applications. Going forward, our objective is to look beyond closure components and implement CF composites in body structural panels that undergo the complex loading conditions represented in crash and durability. To enable these broader automotive structural applications of CF composites, three key issues must be addressed. First, significant variability in material properties incurred during the manufacturing process need to be understood and predicted. Second, prediction of the structural performance of composites undergoing complex loading (i.e., crash) and environmental conditions is required. Third, the effect of manufacturing on performance of the final components needs to be understood and predicted. Without a good handle on these issues, automotive designs can be overly conservative, thereby increasing cost significantly and limiting the weight reduction potential of CF composites. The present project addresses these needs by developing a suite of integrated computational tools to predict manufacturing performance and structural performance of CF composites, including stochastic effects.

Approach

Four key components of probabilistic integrated computational materials engineering will be at the core of our approach, namely model *integration*, *optimization*, *validation*, and design *certification*. The computational engine will be constructed by the *integration* of state-of-the-art tools and capabilities from specific domains, namely, composites manufacturing (from GM and Continental Structural Plastics), process simulation software for composites (from ESI), integrated multiscale/multiphysics structural software (using the multiscale design system [MDS] of Altair), probabilistic methods and probabilistic software (from the University of Southern California), and, finally, the largest U.S. automaker with considerable expertise and a record of accomplishment in the design and manufacturing of composite cars (e.g., the Chevrolet Corvette [from GM]) leads the project and integrates these modules. By model *validation*, we refer to making a prediction of the variables of interest and comparing the specific variables under the same conditions. By *certification* of a component, we mean the assurance that once designed, manufactured, and loaded (i.e., crash tested), these components will perform satisfactorily up to preset specifications. Enabling model validation and component certification requires retooling of the deterministic scientific process, specifically by requiring evidential attributes to be attached to model-based predictions. During this project, we will identify the limitations of existing software components comprising the computational engine and offer alternative technologies and solutions that facilitate integration for design *optimization*. Once the computational engine has been developed and validated, the chosen CF assembly will be designed, optimized, tested, and certified, and the resulting composite component will be compared to current steel design.

The present CF integrated computational materials engineering project is organized into 10 tasks executed over a 48-month period. An outline of the tasks carried out during the current FY is given as follows:

Task 1.0: Project planning, coordination, and reporting – ongoing.

Task 2.0: Select the automotive assembly preliminary design – in progress.

Task 3.0: Identify preliminary CF material systems and manufacturing processes – completed.

Task 4.0: Develop and validate the manufacturing and crash simulation engines – in progress.

Task 5.0: Integrate the manufacturing and structural models – started.

Task 6.0: Design and optimize automotive assembly for manufacturing and performance – not started.

Task 7.0: Design and fabricate assembly and the test fixture – completed.

Task 8.0: Manufacture the automotive assembly – not started.

Task 9.0: Certify the automotive assembly – not started.

Task 10.0: Assessment of the assembly: correlation of predictions with experimental results – not started.

Technology Transfer Path

The following technology transfer items are being pursued in FY 2017:

- An application for a patent was jointly submitted between University of California and GM based on findings from this research.
- Mapping of the manufacturing outcome onto structural models developed in this project was implemented in the Hypermesh software commercial program so that users can benefit from it immediately.
- A Python wrapper comprehending tools being developed in this project is being adapted to standard workflow at GM. This is being done in close consultation with GM engineers.

Results

The following sections provide the results for the tasks undertaken during FY 2017 for this project.

Manufacturing Model Development

Draping Calibration and Validation

In FY 2017, the PAM-FORM material model was calibrated for twill and satin fabrics with the final comparisons between tests and simulations for 0/90 and +/-45 single ply fabrics being presented. An alternative test method called “bias-extension” was used to derive shear properties of the dry fabrics.

Bias-extension experiments were carried out at GM’s research and development (R&D) organization using both twill and satin fabrics. Five in.-wide fabric samples with a 1:3 width-to-length ratio were mounted in the Instron machine and evaluated in tension at a constant displacement rate of 30 mm/min. Ten specimens were tested for each fabric type, as shown in Figure II.2.D.1.

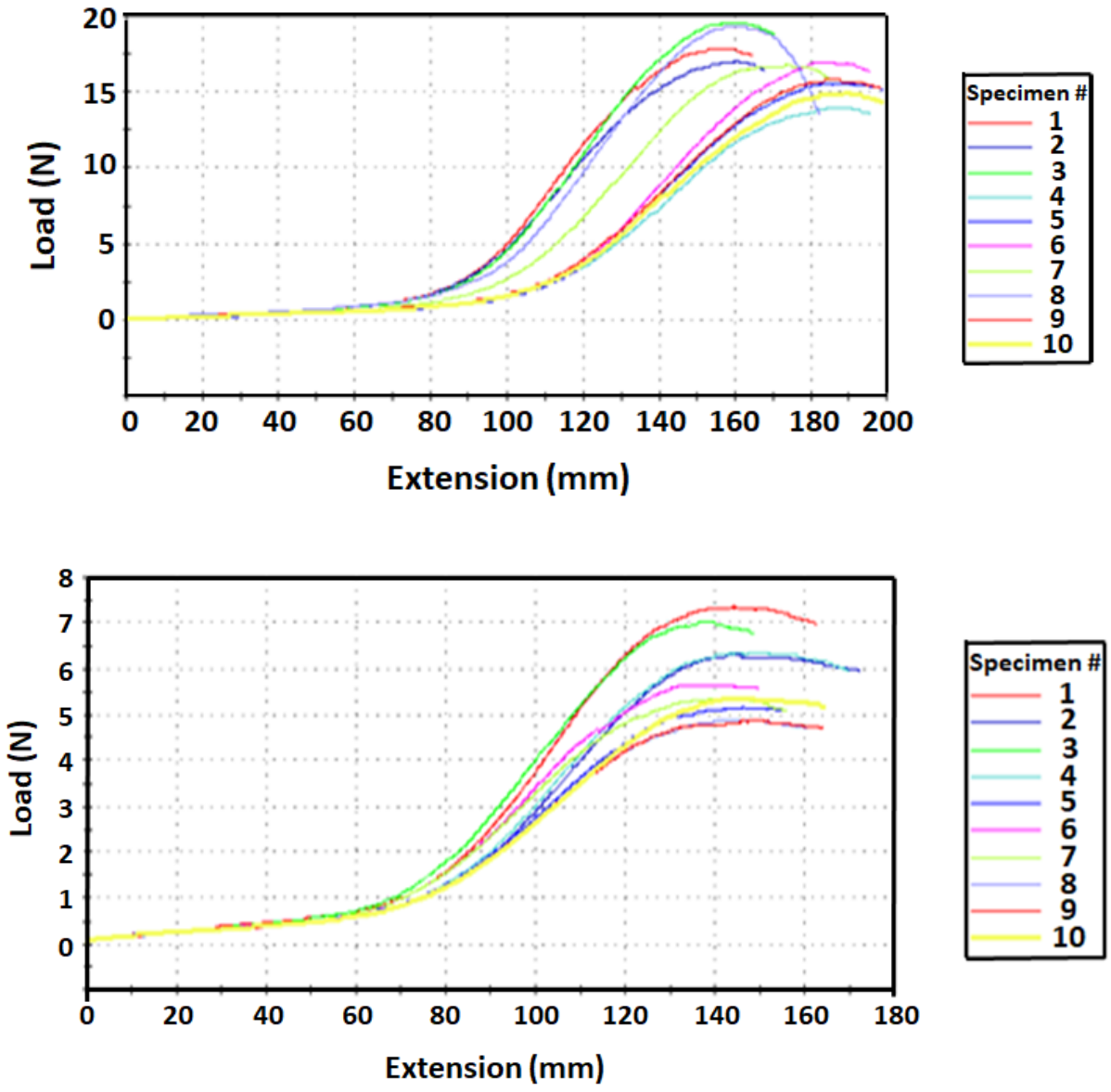

Figure II.2.D.1. Force-deflection curves from bias-extension tests: (top) twill fabric; and (bottom) satin fabric for specimens 1 to 10.

Figure II.2.D.1 shows some scatter in the tests and a median experimenal curve was selected to calibrate the simulation results. A half-symmetry finite element model of the bias-extension coupon, as shown in Figure II.2.D.2, was used to calibrate the shear behavior. Figure II.2.D.3 shows the overlay of the results from the bias-extension experiments.

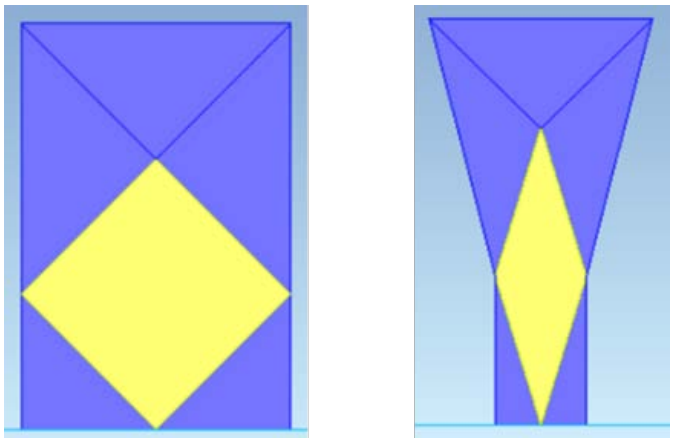

Figure II.2.D.2. Half symmetry model for bias-extension coupon: (left) initial shape; and (right) final deformed shape. Source: General Motors.

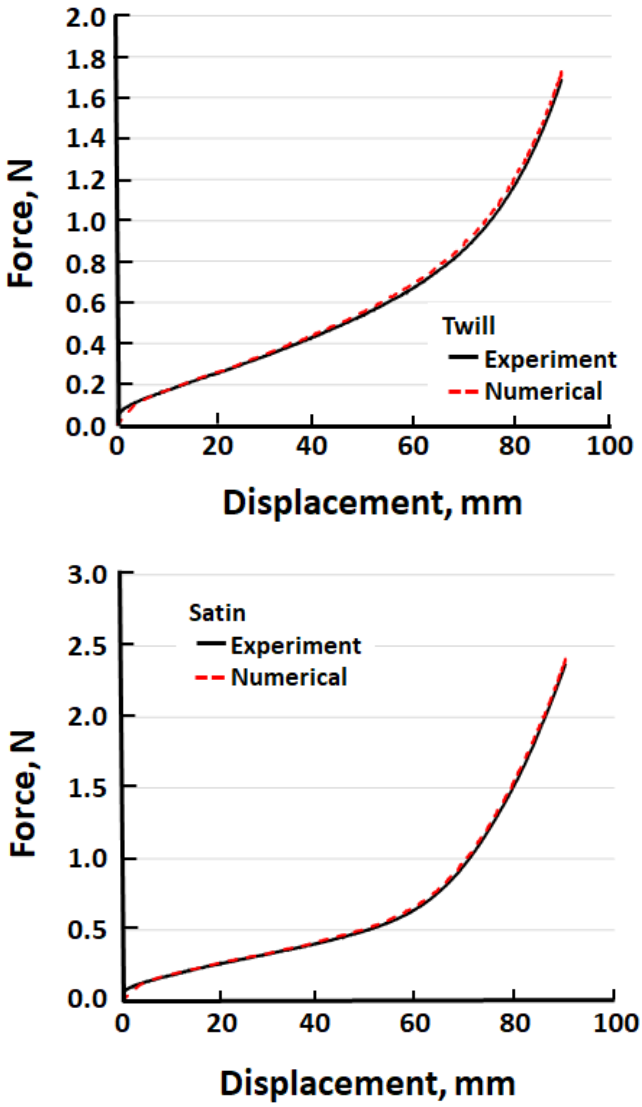

Figure II.2.D.3. Force-deflection overlay of the simulation and the experiment for twill and satin fabric.

The calibrated shear data was then used in the validation of the component draping. A metal preforming tool was used to make a pyramid shape component for validation, as shown in Figure II.2.D.4. The pyramid shape was complex enough to observe fiber angle changes during draping. The ply draw-in shapes of the twill and satin fabrics in 0/90 and +/-45 were captured well by the simulations.

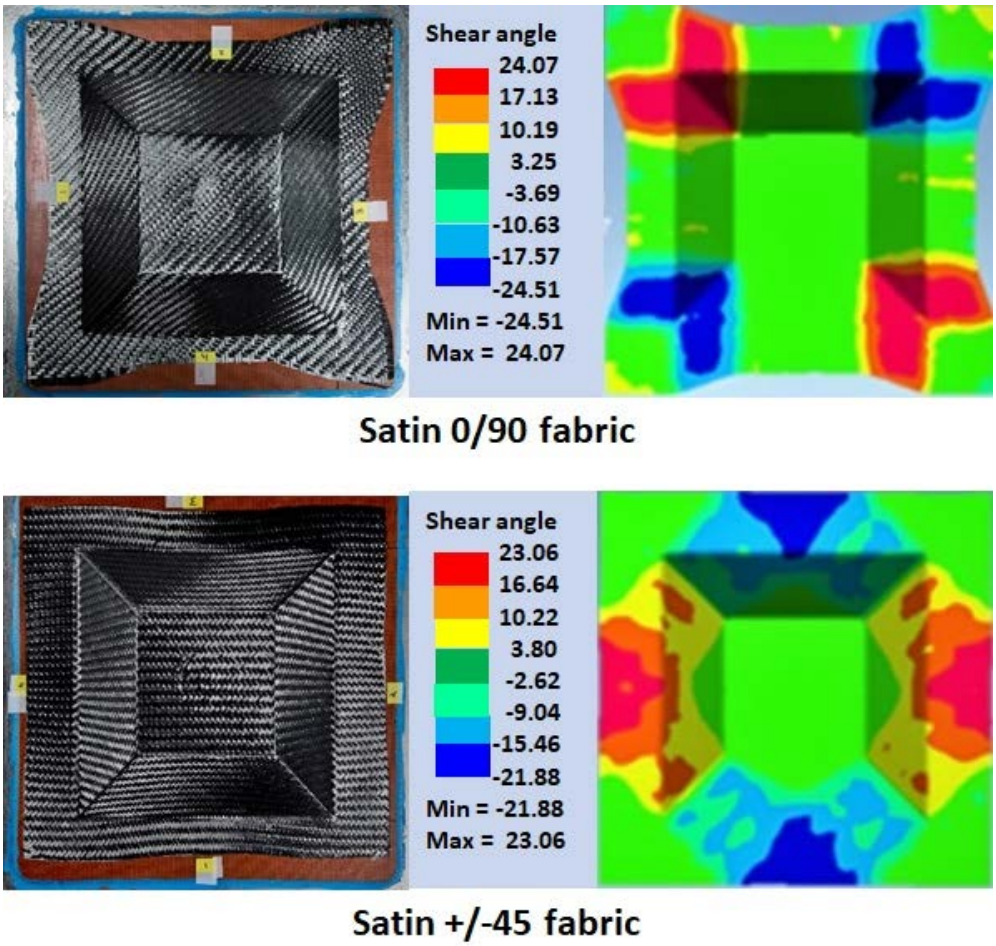

Figure II.2.D.4. Comparative ply draw-in shapes for twill fabric in 0/90 and +/-45 directions. Source: General Motors.

Figure II.2.D.5 shows the comparisons of the experimental data and the simulation of the shear angles for twill 0/90 and satin 0/90 fabrics at different sections along the length of the wall of the truncated pyramid. An overall good agreement was found for both the fabrics with some discrepancy for satin fabrics in the corner.

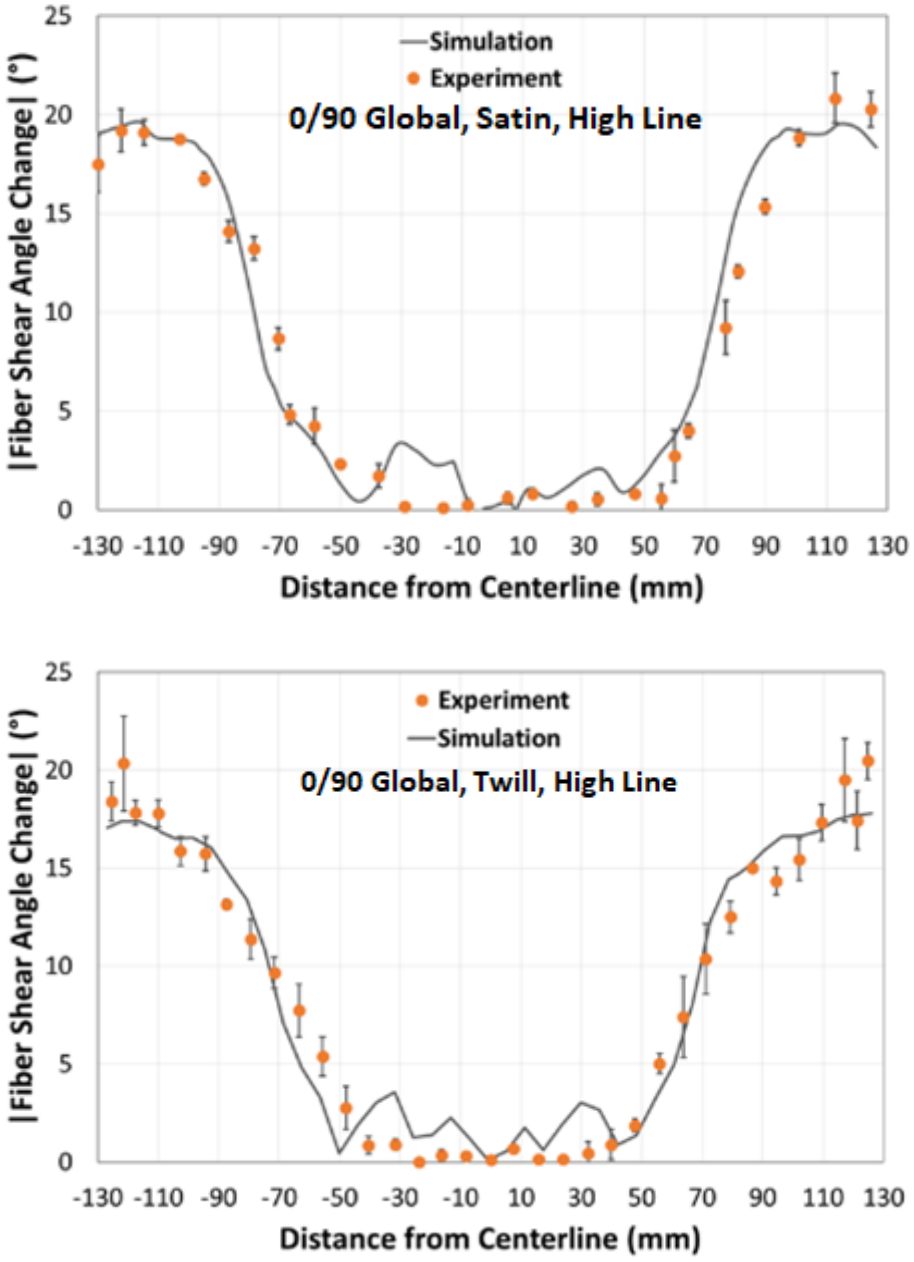

Figure II.2.D.5. Draping 0/90 correlations: (top) satin fabric; and (bottom) twill fabric.

Figure II.2.D.6 shows satin and twill correlations for +/-45 fiber angles at different sections along the length of the wall. A good correlation between simulation and experiments was found.

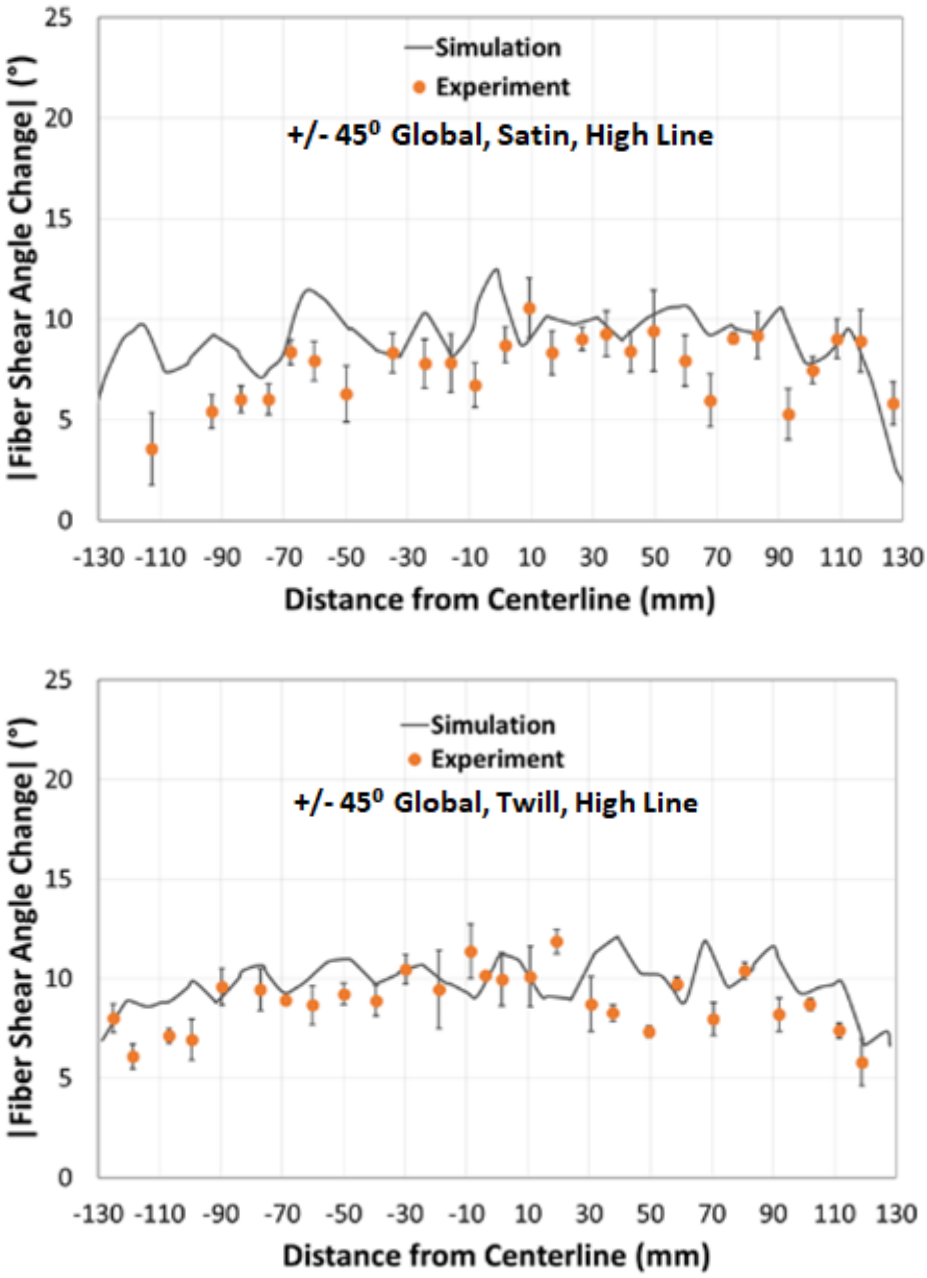

Figure II.2.D.6. Shear angle comparison for satin +/-45 fabric: (top) satin fabric; and (bottom) twill fabric.

This concludes the validation for both woven fabrics in 0/90 and +/-45 global fiber directions. Additionally, a mesh sensitivity analysis was carried out to understand the response of the model to different mesh sizes. Figure II.2.D.7 shows shear angle overlays for different mesh sizes. Though there were some differences, the shear angle distribution for the three different mesh sizes was nearly identical. A target mesh size of 5 mm was found to be the optimum in terms of speed and accuracy of the simulations.

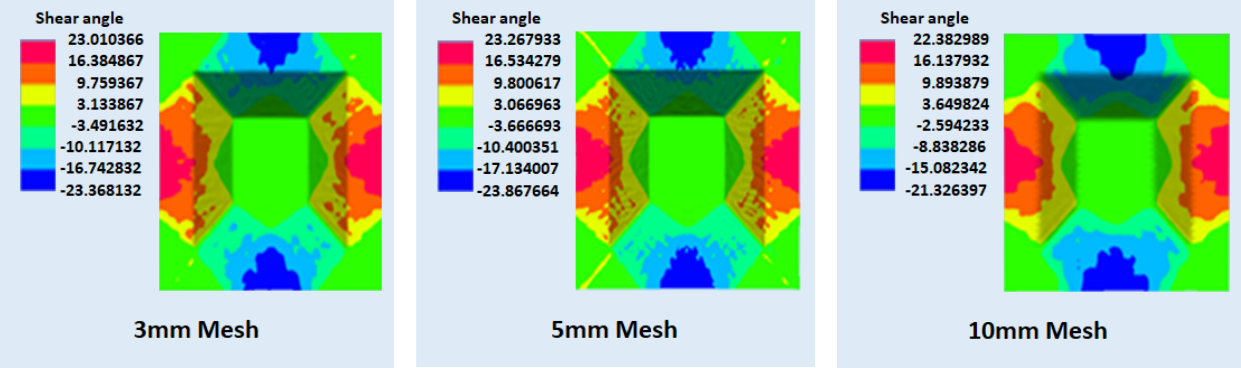

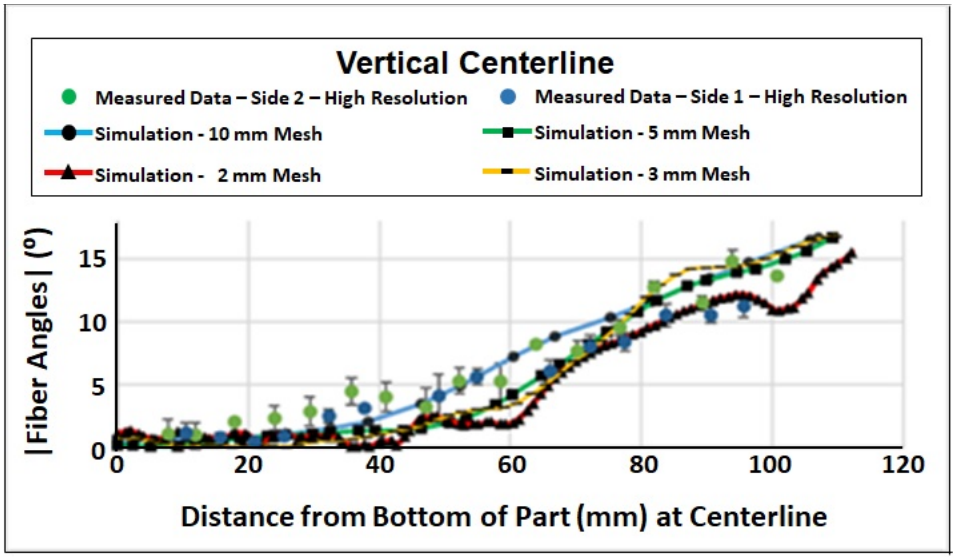

Figure II.2.D.7. Mesh sensitivity analysis for draping. Source: General Motors.

The validated model is now being used to iterate the full scale structural components for various draping scenarios.

C-RTM Simulation Model Validation

ESI continued to perform and demonstrate manufacturing simulation of GM case studies to predict the resin flow for C-RTM process on truncated pyramid geometry.

The C-RTM process consists of two stages, as shown in Figure II.2.D.8:

1. Initial mold opening – mold is opened to a larger thickness than the final target to create a gap that allows resin to flow faster with minimal injection pressure.
2. Mold closing – mold is closed pushing the resin into the fiber bed and compressing the bed to obtain the desired thickness and fiber fraction.

Figure II.2.D.8. C-RTM process illustration. Source: General Motors.

Two main issues need to be addressed in the C-RTM process: (a) the resin gap evolution during tool movement; and (b) preform deformation due to compression and resin flow. Numerically, the analysis is a two-step process. In the first stage, resin is injected into the gap located between mold and the preform; then, in the second stage, resin injection is stopped, and the top mold begins closing the gap and compressing the preform until the final desired thickness is reached.

ESI Group has been working on prototype software for simulation of C-RTM process. The software introduces two new technologies embedded in the PAM-RTM solver:

1. Fluid-Solid mechanics coupling that allows fiber bed deformations during the process.
2. An Inter-Penetrating mesh that allows the handling of gap changes during closing of the mold.

The truncated cone model shown in Figure II.2.D.9 was used to validate the C-RTM process.

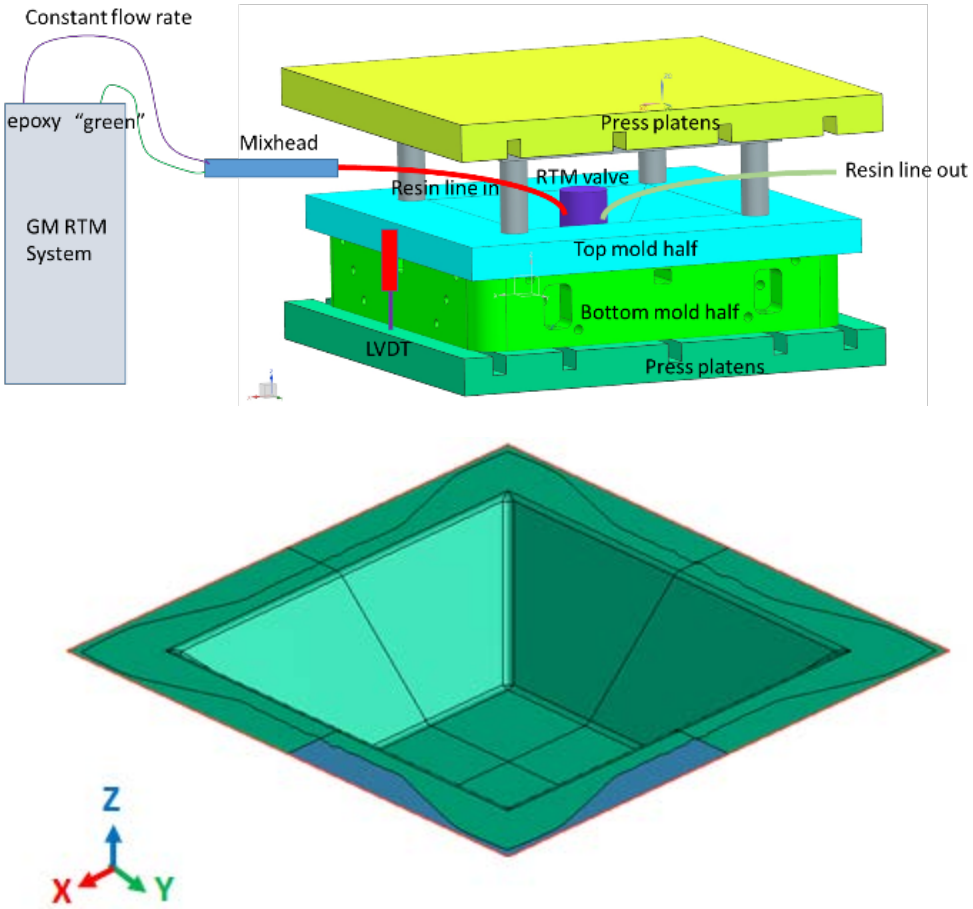

Figure II.2.D.9. Truncated cone geometry for C-RTM: (top) process overview; and (bottom) part geometry overview. Source: General Motors.

Different scenarios of C-RTM were studied as shown in Table II.2.D.1.

Table II.2.D.1. C-RTM Experiments.

Experiment	Ply Number		Mold Opening		Final Thickness (mm)	Preform Thickness (mm)		Initial Fiber Fraction	Flow Rate (m/s)	Injection Time(s)
	preform	patch	flat	tilted		preform	patch	preform		
1	6	N/A	3	2.82	2.4	3	N/A	42%	13.07	20
2	6	2	3.5	3.18	2.4	3	4	42%	13.07	20
3	6	2	3.2	2.97	2.4	3	4	42%	13.07	20
4	9	N/A	4	3.85	3.5	4.5	N/A	48%	9	40
5	9	N/A	4.5	4.21	3.5	4.5	N/A	42%	9	40
6	9	3	5	4.56	3.5	4.5	5.5	38%	9	30
7	9	N/A	6	5.27	3.5	4.5	N/A	32%	9	15
8	9	N/A	8.5	7.04	3.5	4.5	N/A	22%	9	15

Experiment 2: Steel mold with 6-in. patch

Figure II.2.D.10 (left) shows an overview of the different parts that were used for this model. For this case, the initial thickness of the preform was 3 mm in the flat area (green zone) and 3 mm in the tilted area (pink zone) with a targeted final thickness of 2.4 mm. The gap was 3.5 mm (yellow zone) in the flat area and 3.18 mm in the tilted area. The blue part is the punch. A 6-in. patch was modeled on the tilted area, as shown in Figure II.2.D.10 (right). The initial thickness of the patch was modeled as 3.18 mm, which means the tool is already in contact with the patch before the tool starts to close. A total of six layers of fabric were used to model the main truncated cone, while two additional layers were added to the patch area. In terms of the final fiber volume fraction, this results in 52.5% for the main cone area (flat & tilted) and 70.0% for the patch area.

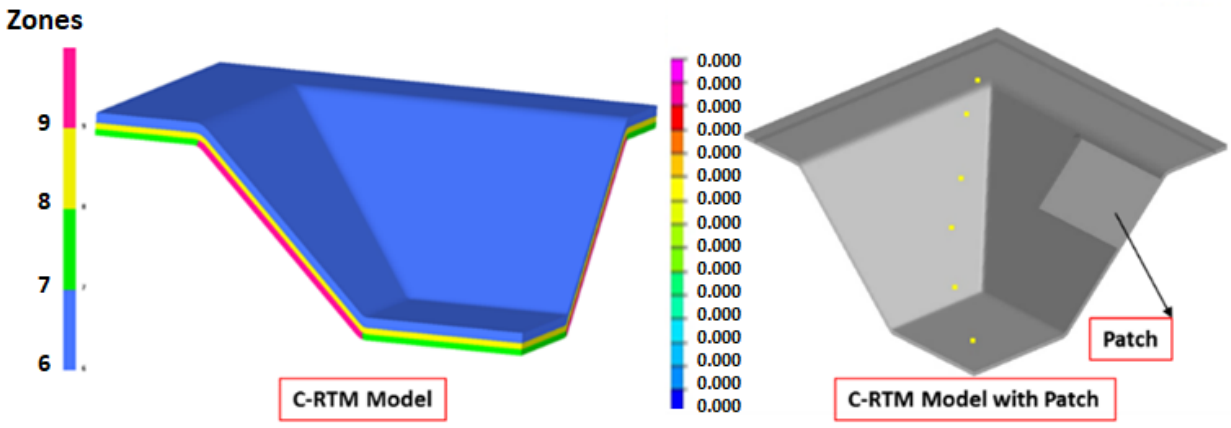

Figure II.2.D.10. C-RTM process: (left) mesh overview of initial truncated cone model; and (right) C-RTM model with 6-in. patch. Source: General Motors.

Resin was injected for 20 seconds at a constant flow rate of 13.07 ml/s. Mold closing velocity was pressure controlled, closing the 3.5 mm gap and compressing the preform to 2.4 mm following the 20-sec injection time. The resin viscosity was assumed to be 0.015 pascal-seconds (Pa s).

Figure II.2.D.11 shows the results of this simulation. During the first 20 seconds, resin is injected into the gap and starts to impregnate the preform. As can be seen in Figure II.2.D.11, due to the high fiber volume content in the patch (hence, low permeability), resin flows much slower into the patch area. After 20 seconds, the mold closes and pushes the resin into the preform. Good agreement was found between the simulation and the experiments with respect to the resin arrival times at different sensor locations as shown in Figure II.2.D.12.

Due to the low permeability in the patch area, resin flows much faster around the patch and creates an air entrapment just on the bottom edge of the flange area, as shown in Figure II.2.D.11 (right). The experiment exhibits a similar air entrapment, although the location of the void is slightly displaced. This may be attributed to the through-thickness permeability assumption made in the modeling, or, other unknown factors at this stage of research.

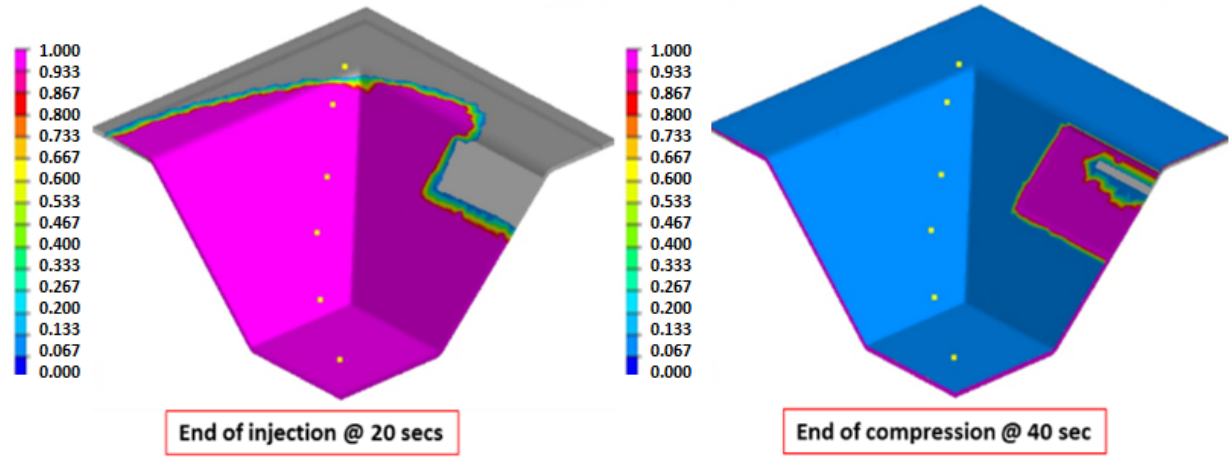

Figure II.2.D.11. C-RTM Simulation: (left) injection phase, 20 seconds; and (right) compression phase, 40 seconds (20 seconds after injection). Source: General Motors.

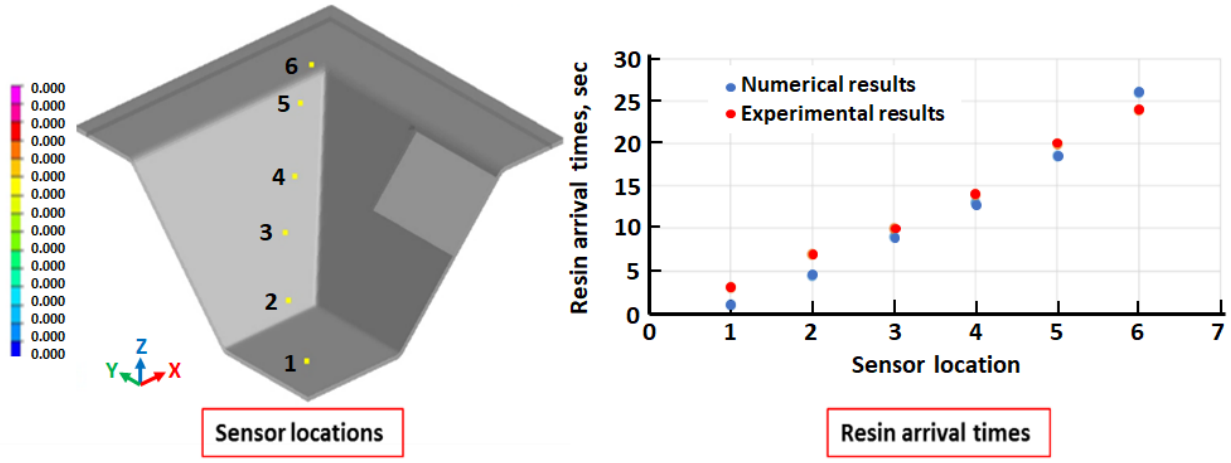

Figure II.2.D.12. Simulation vs Test: (left) sensor locations; and (right) resin arrival times, correlation with test. Source: General Motors.

Effects of Race-Tracking in the Injection Analysis

In FY 2016, the study on injection analysis revealed some discrepancies between the tests and the simulation despite every effort to model as accurately as possible. Upon de-molding, the part exhibited resin rich areas that were likely due to race-tracking. Unfortunately, these race-tracks were not consistent. In FY 2017, the effects of this race-tracking were analyzed. An iterative study was carried out assuming some race-tracks in the mold. An illustration of a possible racetrack on the sides of the plaque, which was created by introducing some high permeability elements, is shown in Figure II.2.D.13.

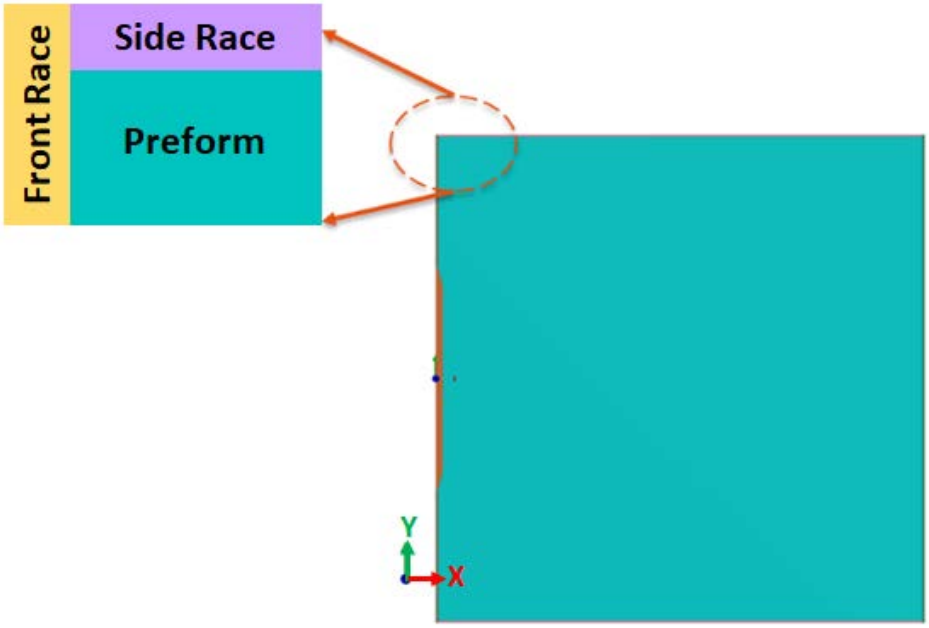

Figure II.2.D.13. Race-tracking region defined in the RTM plate model.

Figure II.2.D.14 shows correlation between tests and simulations with and without race-tracking effects. The pressure deviation observed earlier was corrected after considering race-tracking effects.

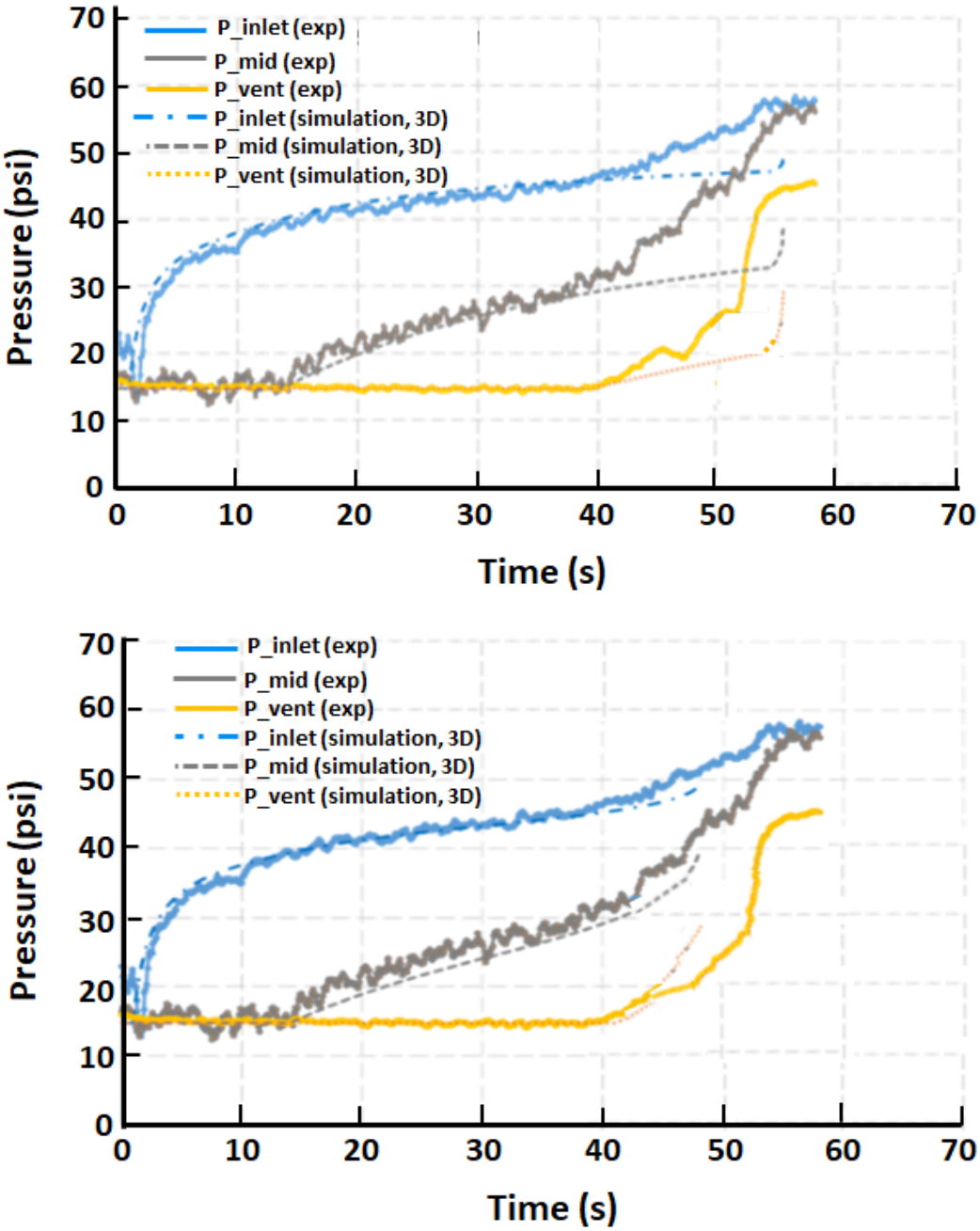

Figure II.2.D.14. Pressure correlation between simulation and experiment: (top) without race-tracking effects; and (bottom) with race-tracking effects.

Distortion Analysis Using Non-Linear Geometric Functionality

An 8-layer laminate plate with an asymmetric stacking sequence [0/45/-45/90/90/45/-45/0] was analyzed for distortion. A 2-stage distortion analysis was carried out using PAM-DISTORTION software. Stage-1 refers to the in-mold curing stage where the part is completely locked in the mold. Stage-2 refers to the demolding stage where the part is ejected, and the mechanical constraints are released.

Prior to this 2-stage distortion analysis, the part was subjected to resin injection and cured. The temperature and degree of cure history from the curing simulation was then used in the distortion analysis. A set of material data, provided by GM describing the cure kinetics, has been used for the distortion analysis. The different properties expected from the different resin phases were also included. Lamina properties are calculated based on a micro-mechanics model. The fiber volume fraction was assumed to be 50%. The expected large deformation due to the asymmetric layup was confirmed by the simulation and the extent was in good agreement with the experiments. The predicted maximum displacement of 20 mm, as shown in Figure II.2.D.15, agrees well with the measured values.

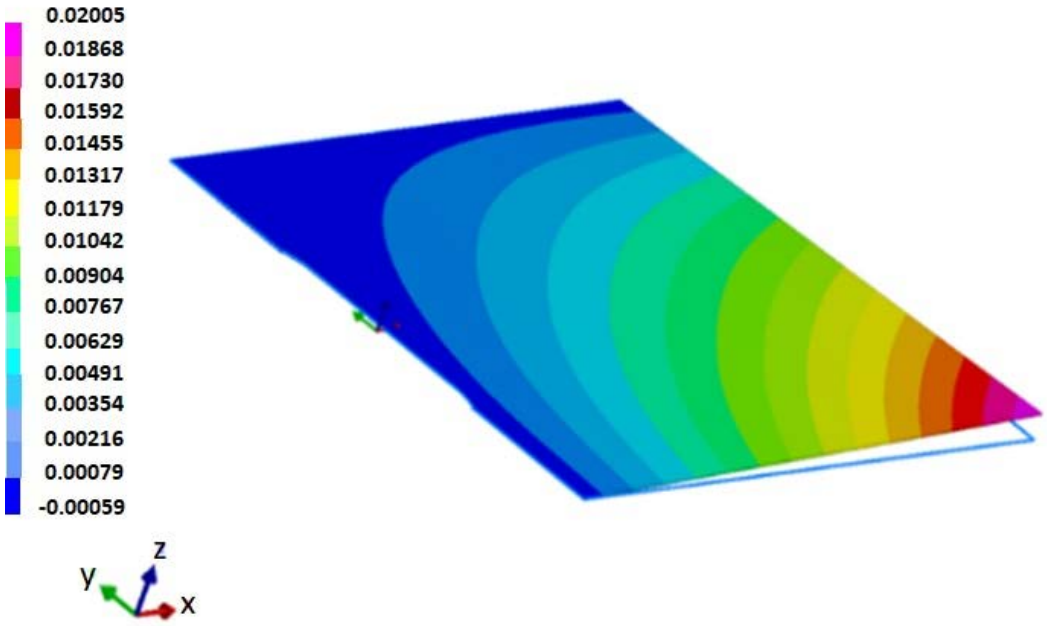

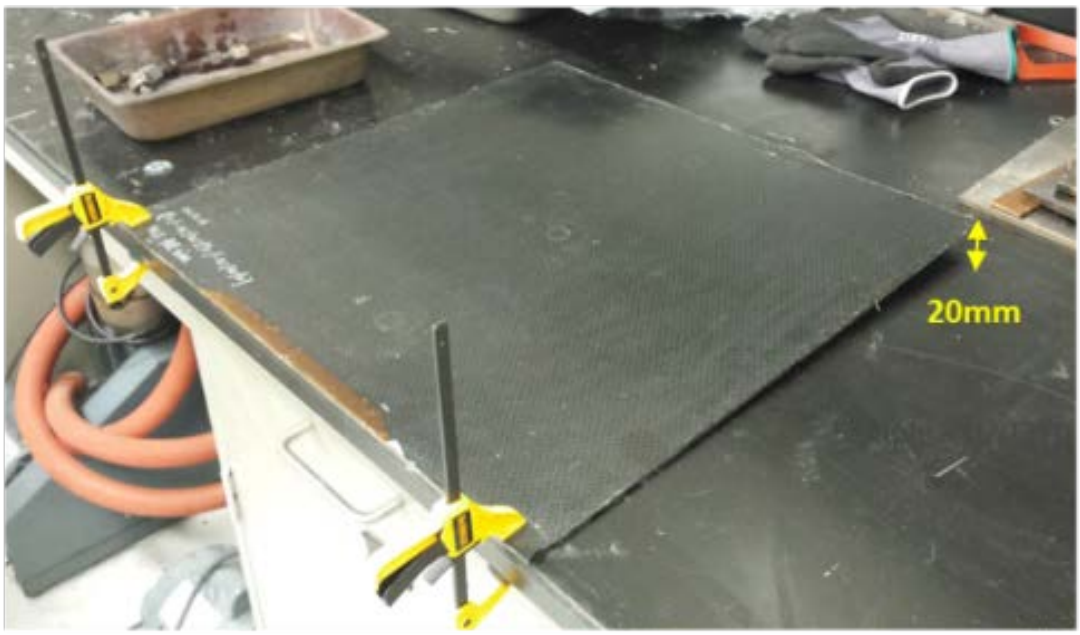

Figure II.2.D.15. Distortion analysis on 8 layers [0/45/-45/90/90/45/-45/0] un-symmetric laminate: (top) simulation result for maximum displacement, units in meters; and (bottom) distorted part after demolding. Source: General Motors.

Development of Manufacturing Guidelines for Fast Curing Resins and Draping of Non-Crimp Fabrics

ESI conducted parametric studies and small-scale simulation (meso-scale) on representative geometries to identify manufacturing guidelines for fast curing resins, such as the maximum thickness of the part that can be molded without resin degradation, acceptable topologies for NCF draping linked to stitching pattern, etc.

Curing of Thick Composites

A fast curing resin is desired to meet mass production requirements; however, this makes filling the part before gelation problematic. Typically, epoxy-based resins undergo exothermic reactions that could potentially generate high internal temperatures leading to degraded mechanical performance. The thicker the parts, the more heat that is generated. To provide manufacturing guidelines for the thickness of the part for a selected thermal cycle and resin system, a simple beam model was created and evaluated at varying thicknesses from 1.8 mm to 5.4 mm for an 8-layer quasi-static $[0/+45/-45/90]_s$ laminate.

Table II.2.D.2 shows the different simulation configurations. For thicker laminates (3.6 mm and 5.4 mm), the internal temperature is quite high (~250°C) with a maximum degree of cure being reached in ~10 seconds. This shows that for the selected resin system and the cure cycle, an optimum thickness exists.

Table II.2.D.2. Curing of Thick Composite Laminates.

Experiment Thickness (mm)	Temperature Before Curing (°C)	Maximum Temperature (°C)	Maximum Cure Time (seconds)
1.8	90	91.9	201
	110	114.4	81
	130	140	35
2.4	90	111.8	158
	110	186.7	43
	130	207.8	11
3.6	90	178.5	82
	110	225.8	21
	130	272.6	11
5.4	90	225.6	49
	110	271.1	21
	130	301	11

Another study was focused on the filling of 5.4 mm thick plate laminates with quasi-isotropic layup for a mold temperature of 110°C with the process conditions shown in Table II.2.D.3.

Table II.2.D.3. RTM Process Conditions for Thick Laminates.

Property/Condition	Value
Thickness	5.4 mm
Fiber Content	0.5
Mold Temperature	110°C
Flow Rate	9.4E-07 m^3/s
Resin Temperature	80°C

Figure II.2.D.16 shows global fill times for the plate model. Figure II.2.D.17 shows maximum cure of 0.63 (63%) at the end of filling (above resin gelation point), which means that the part cannot be filled with this flow rate at this mold temperature.

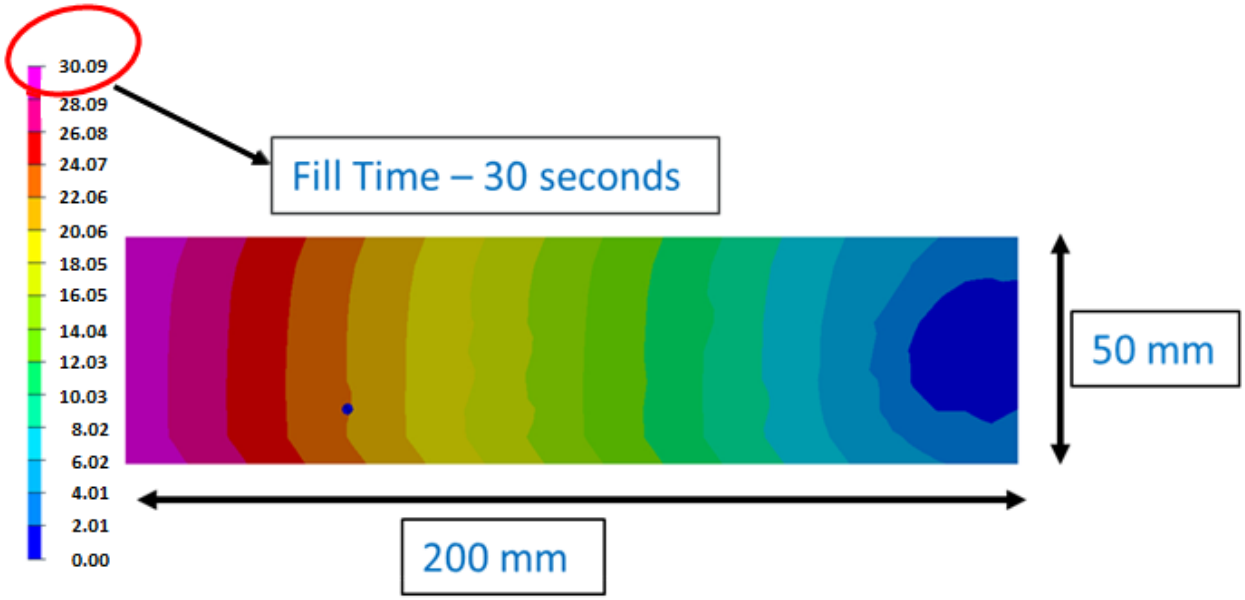

Figure II.2.D.16. Plate dimensions and global fill times. Source: General Motors.

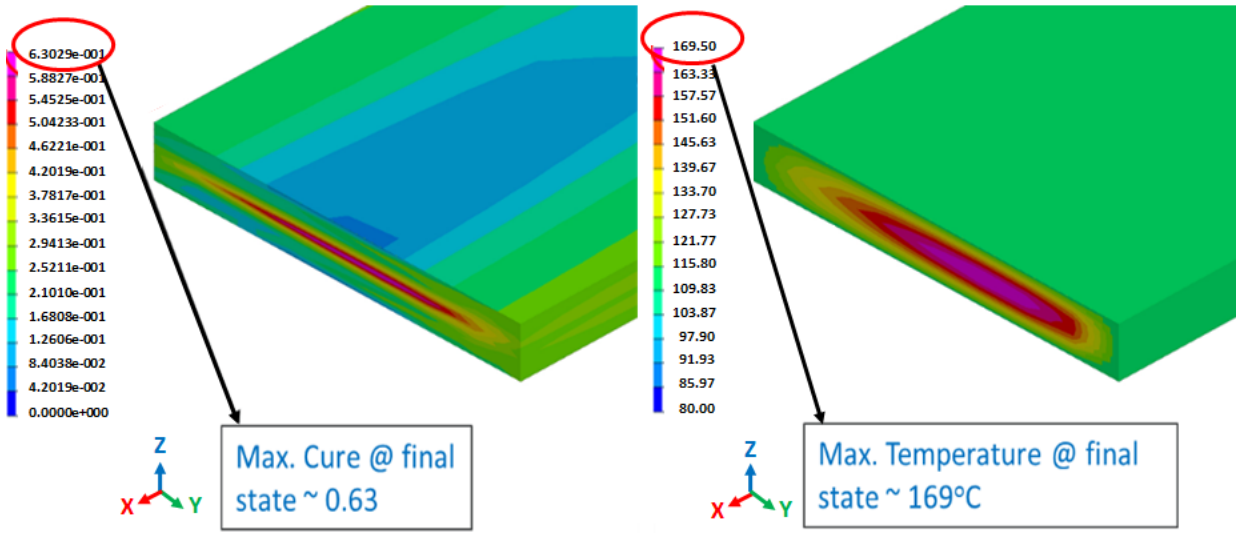

Figure II.2.D.17. Maximum cure and maximum temperature at the end of filling. Source: General Motors.

Meso-Scale Preforming Simulation for NCF

ESI is conducting investigations regarding the meso-scale preforming simulation of dry NCFs. The following three approaches were investigated during FY 2017.

Meso-Scale Approach

The approach is based on the work carried out in a previous European Project (INFUCOMP, FP7 framework). In this approach, the ply model consists of two layers of solid elements representing the yarns surrounded by one-dimensional elements representing the stiches. Material model #30 in PAM-FORM computer program (orthotropic material) was used to represent the yarn behavior, contacts were defined between the yarns and between the yarns and the stiches. Inter-yarn voids were modeled with solid elements associated with material model #99 in PAM-FORM (null material no rigidity), to get a full mesh of the ply that can then be transferred in a deformed shape to PAM-RTM for fluid flow analysis at the meso-scale. Figure II.2.D.18 and Figure II.2.D.19 show one example of this approach.

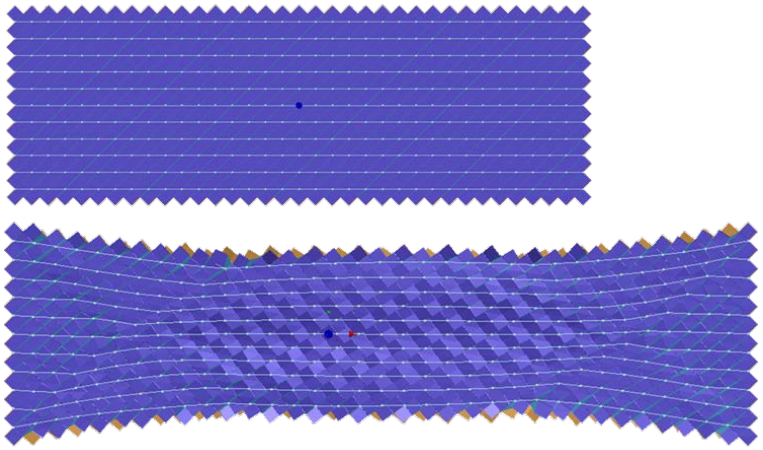

Figure II.2.D.18. Virtual bias-extension calibration model for SAERTEX 20005558 Biax +/-45 NCF. Source: General Motors.

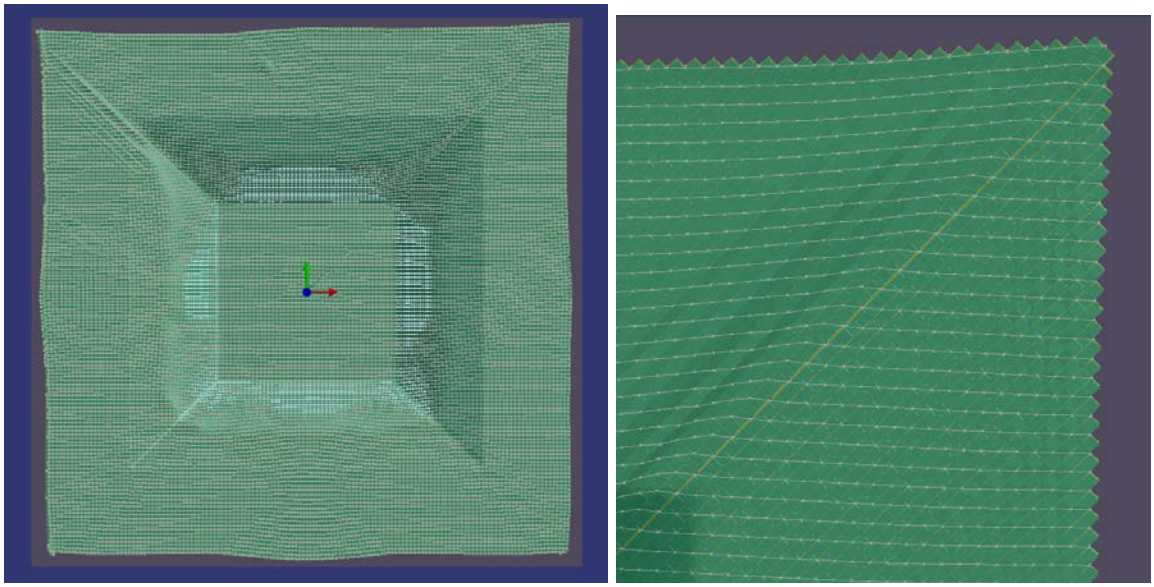

Figure II.2.D.19. Meso-scale preforming of NCF of truncated pyramid model: (left) global overview of deformed shape; and (right) zoom-in view of a corner. Source: General Motors.

However, the material chosen for the automotive assembly selected for this demonstration cannot be modeled with this approach. Basically, it was assumed in the original study that the fibers were clustered in continuous "yarns" across the ply, which was not the case for Chomarat +/-45 spread tows fabrics. Figure II.2.D.20 shows a picture of the Chomarat NCF reference where the fiber bundles were separated and re-clustered into different bundles at each stitch point. As such, it was not possible to consider the yarns as initially proposed in the meso-scale approach.

Figure II.2.D.20. Chomarat spread tow NCF used by GM R&D. Source: General Motors.

Macro-Scale Approach

The macro-scale approach is the approach used by PAM-FORM to perform draping simulations of the truncated pyramid models. In this approach, the ply is considered as one layer of the shell elements with an equivalent orthotropic behavior (ESI MAT140). For NCF, the stitching introduces an unsymmetrical shear behavior, as demonstrated on bias-extension tests performed by GM R&D, as shown in Figure II.2.D.21.

This unsymmetrical behavior can be accounted for in the macro-scale approach by considering negative and positive shear, as shown in Figure II.2.D.22.

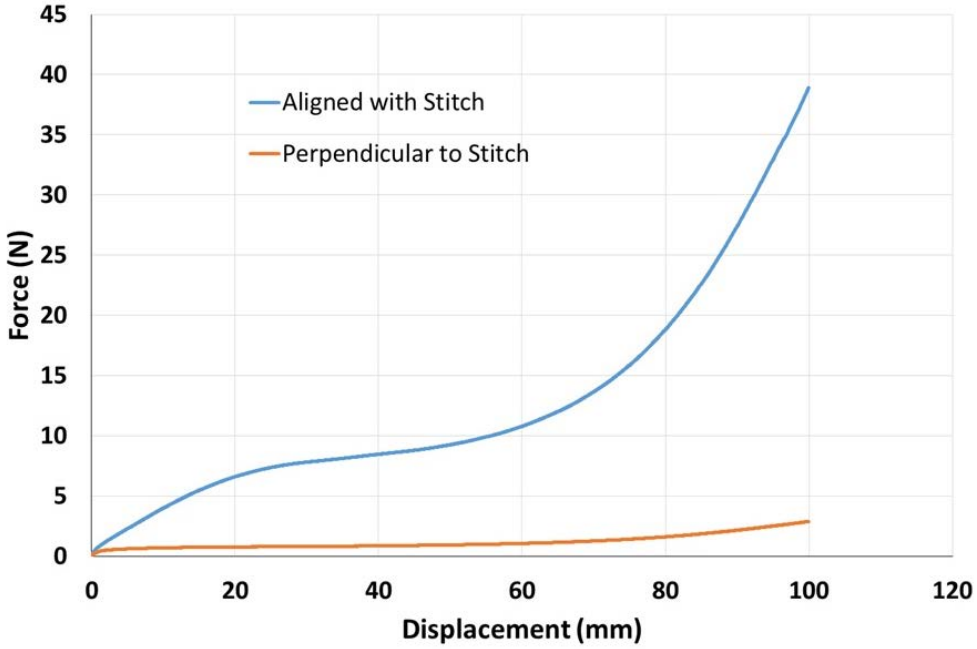

Figure II.2.D.21. Force vs displacement from the bias-extension test.

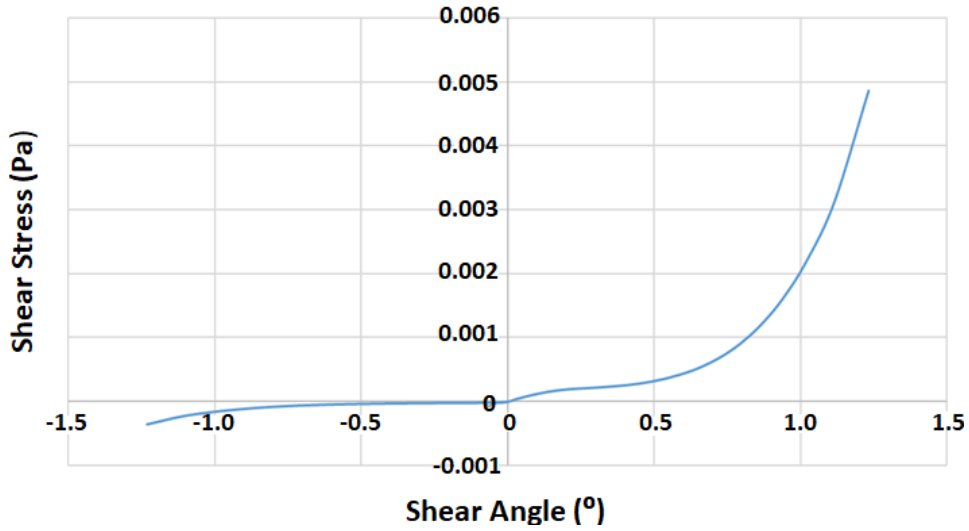

Figure II.2.D.22. Shear stress vs shear angle (input curve for PAM-FORM).

This approach is suitable for large-scale draping simulations; however, it requires characterization tests for each stitching variation, and therefore, does not allow upfront investigations to select and/or suggest stitching patterns. To overcome this issue, ESI proposes a so-called hybrid approach presented in the next section.

Hybrid Approach

The hybrid approach consists of superimposing shell elements (with ESI MAT140) representing the carbon fibers and the beam elements (with ESI MAT205) representing the stiches. In this case, the shear behavior of the shell represents the friction between the layers of carbon, while the elastic tensile behavior of the beam elements represents the stiches. The shells and beams are then linked with kinematic tied elements, which impose the displacements of its projection on the master elements (shell elements) at each slave node (beam element) as a boundary condition inducing a reaction force that introduces the experimentally observed unsymmetrical behavior. Figure II.2.D.23 and Figure II.2.D.24 show results of an example with dummy material parameters.

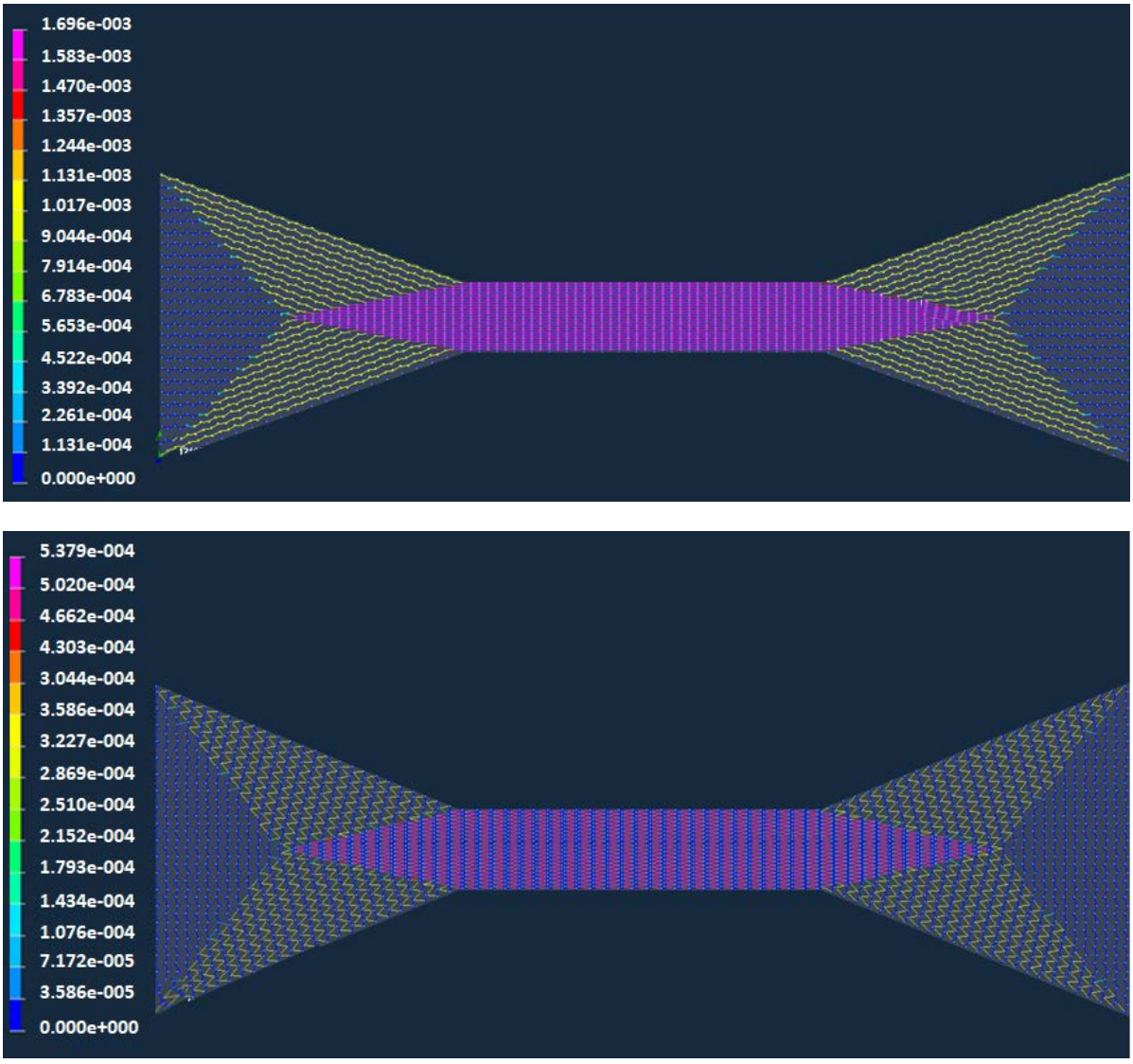

Figure II.2.D.23. Axial force in stitching for a numerical bias-extension test: (top) stitching aligned with force; and (bottom) stitching perpendicular to the force. Source: General Motors.

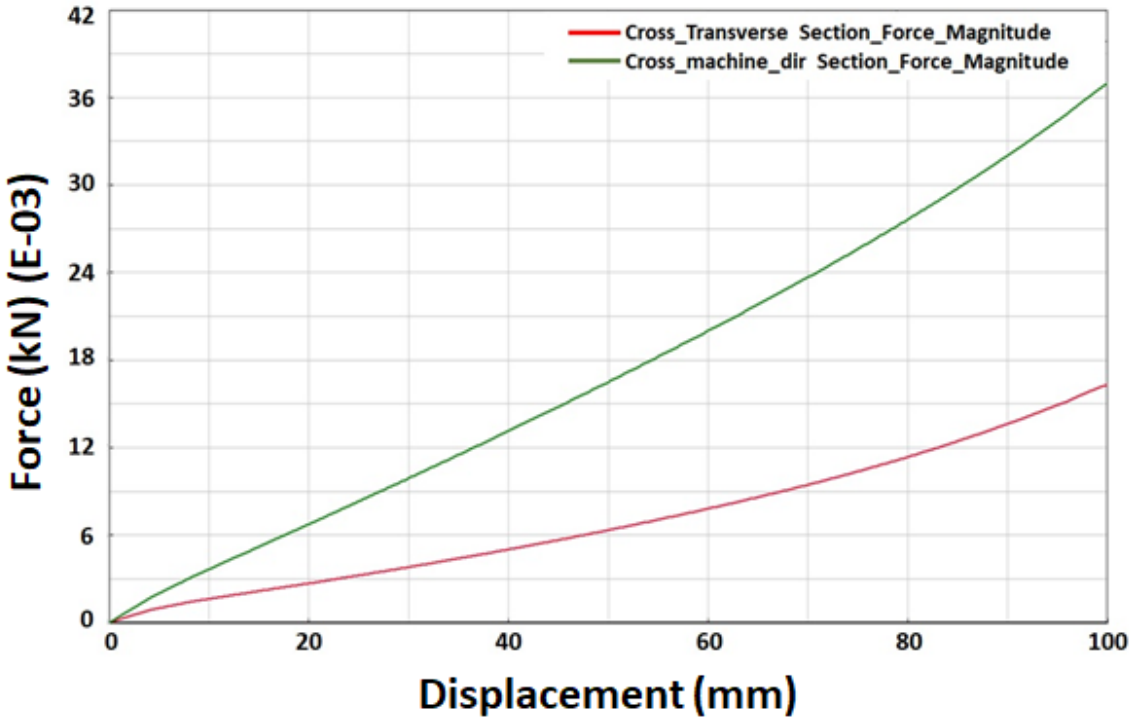

Figure II.2.D.24. Reaction force for numerical bias-extension test: (green) stitching aligned with force; and (red) stitching perpendicular to the force.

Structural Performance Model Development

MDS / LS-DYNA Shared Object Plugin

Development of the MDS shared object plugin for LS-DYNA was crucial in being able to deploy MDS with LS-DYNA on the GM high performance computing (HPC) system or any other large scale HPC system managed with a job scheduler and management system, such as Portable Batch System, Professional Edition™ (PBS-Pro) or platform Load Sharing Facility (LSF).

Previous versions implemented MDS as a user material model subroutine compiled within the LS-DYNA executable. User-level access restrictions and compute system policies only allowed execution on an 8 node, 128 CPU test compute cluster, isolated from the GM HPC system for exclusive use of this project. Job submission requires a customized submission script and manual coordination between users to avoid scheduling conflicts. Running of concurrent jobs was not possible.

The shared object plugin version of MDS with LS-DYNA allows the simulation runs to be submitted on the GM HPC system and fully utilize the LSF job submission and management system. As of the writing of this report, this installation has been installed and verified on a test cluster within the GM HPC system and can subsequently be deployed on the production HPC system at GM.

Mapping Capability

PAM-FORM composite forming simulation software creates fiber orientation direction for each ply after a forming simulation. This data is stored in on a tessellation for each ply in a Hierarchical Data Format – 5 (HDF5) format file. HyperMesh reads this data and maps to structural mesh and creates solver input data files for various structural/ thermal /crash analysis. Herein, we explain the process of mapping the PAM-FORM fiber orientation to a structural mesh model which is different from the mesh used in PAM-FORM simulation. The mapping process is summarized in Figure II.2.D.25.

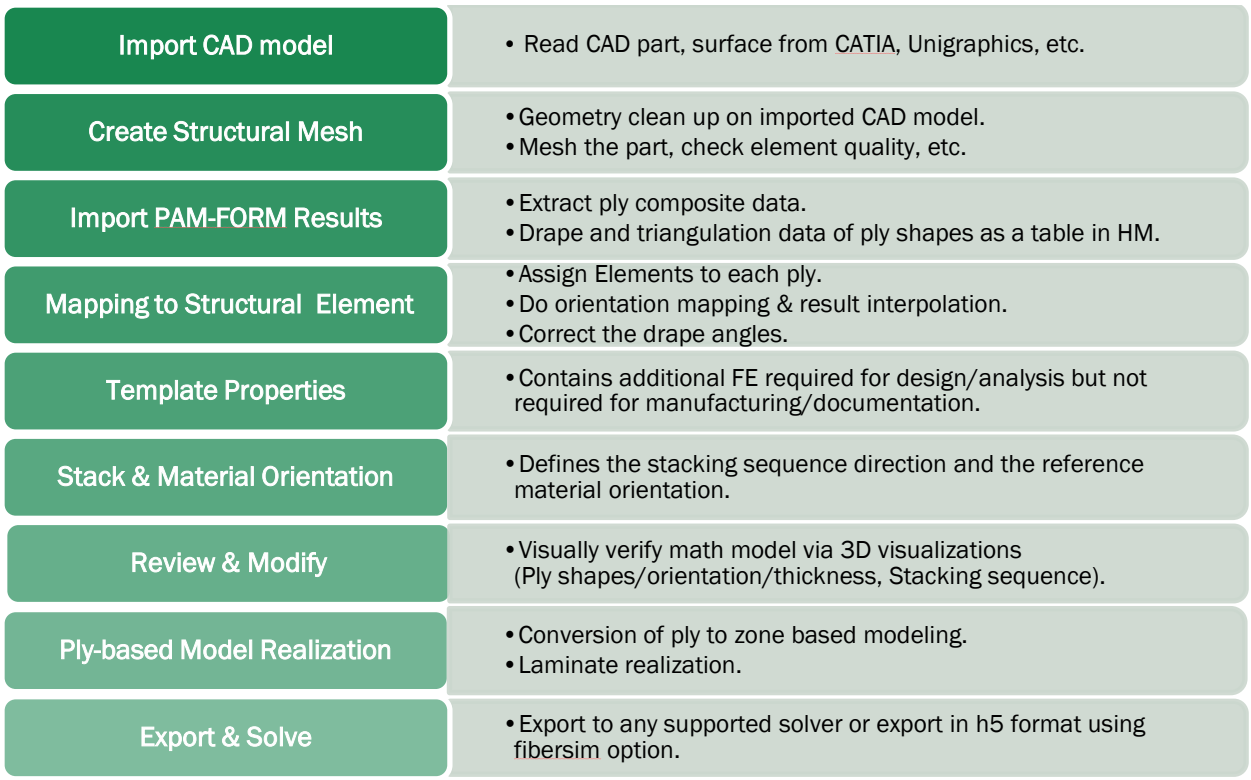

Figure II.2.D.25. Mapping process.

Simulations of Flat Plate Crush Experiments with and Without Guide Pins

Three simulation models were run to correlate the results of the physical test experiments conducted at GM. These included a flat plate crush with guide pins, a flat plate crush without guide pins, and truncated pyramid crush tests. The flat plate crush test, as shown in Figure II.2.D.26, used a test sample of the NCF material with a symmetric 0/-45/45/90 ply layup. The sample dimensions were 39.5 mm wide and 137 mm long. Each ply had a thickness of 0.225 mm. The total thickness was 1.8 mm. The test impactor exerted an impulse of 251.4 kg-m/s onto the test sample. Small serrations were cut into the end of the sample to initiate the crush. Three guide pins 11.5 mm diameter by 10 mm tall were secured to the target plate. The finite element model consisted of 8 node hexahedral elements to model the individual plies. The ply layers were connected using a tiebreak type of contact, which allows for ply-bond failure (delamination). Additional contacts (sliding with friction) were defined for the guide plates and for the target plate/rigid wall.

The flat plate crush model with guide pins was run with MDS / LS-DYNA using the NCF material model developed in the third quarter of 2016. The contact force of the impactor to the test specimen was extracted from the LS-DYNA “binout/rcforce” file. The contact force versus time plot was integrated to generate the energy versus the time plot.

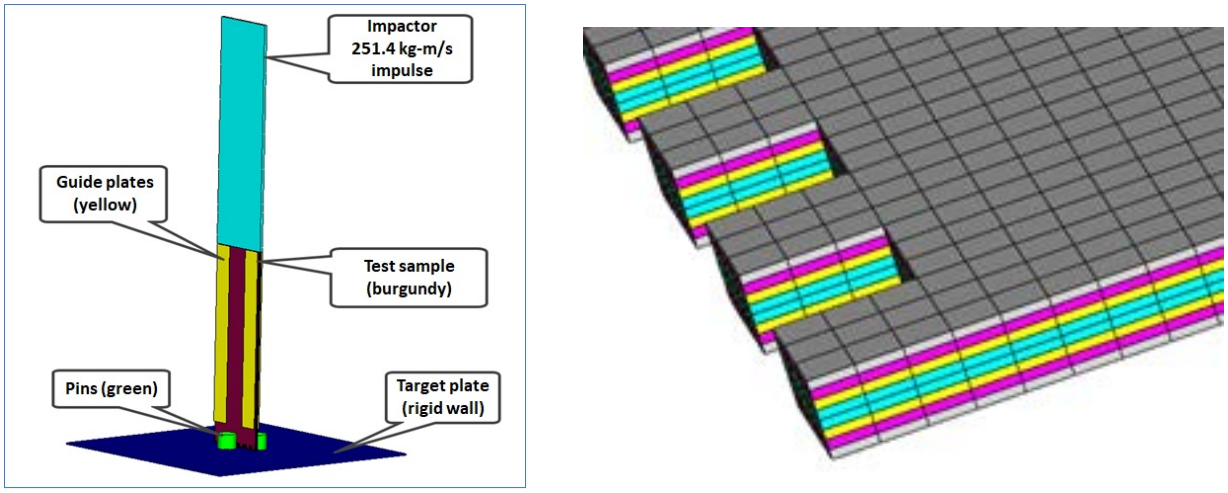

Figure II.2.D.26. Simulation model for flat plate crush with guide pins (left); and detail of plies modeled with hex elements (right). Source: General Motors.

Several variables in the LS-DYNA model were studied to understand the effect on the three correlation targets, including parameters of the inter-laminate contact and friction between the sample and the base plate. No material parameters were adjusted. A study was performed to understand the effect of the friction between the rigid wall (target) and the composite specimen. Three values for the friction coefficient were run — 0.05, 0.15, and 0.30. Force versus time data was provided from six of the physical test experiments carried out in GM laboratories. The plots of the experimental data together with LS-DYNA simulations are shown in Figure II.2.D.27.

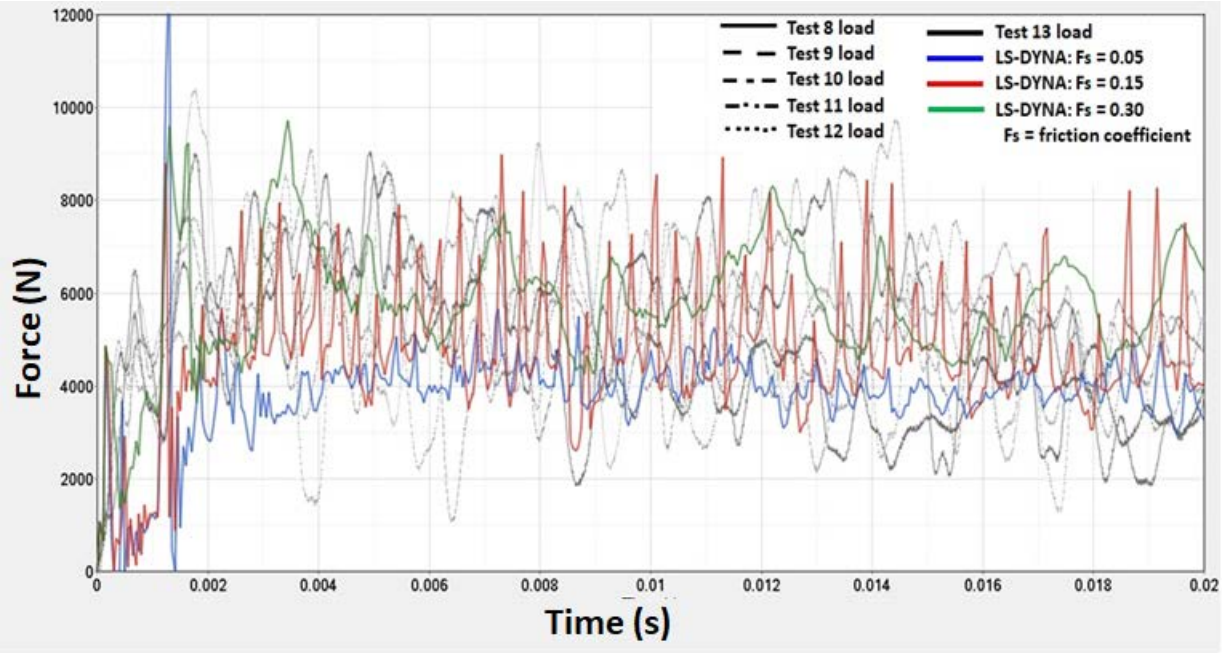

Figure II.2.D.27. Experimental Data overlaid with LS-DYNA results.

Draping Simulations

The truncated pyramid was tested in a universal tension/compression test machine with a complete test setup, as shown in Figure II.2.D.28 (left), while the OptiStruct finite element model is shown in Figure II.2.D.28 (right).

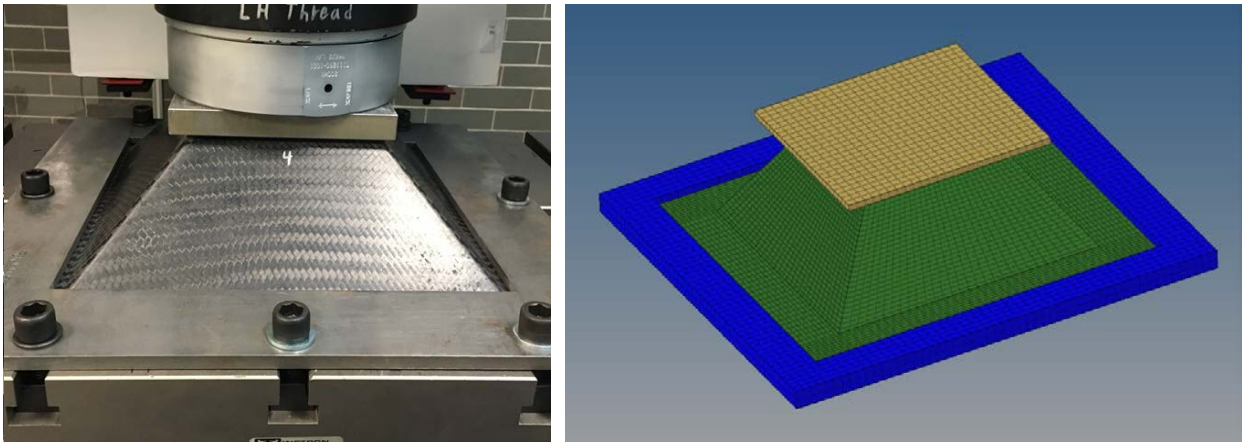

Figure II.2.D.28. The truncated pyramid test setup (left); and the finite element model (right). Source: General Motors.

Note that the data from the weave draping manufacturing simulation, obtained from PAM-FORM, were used to define the TOW-X (warp tow) material direction for each element and the scissor angle (difference between TOW-X and TOW-Y material directions). For the numerical simulation, three different structural models were simulated, one where the principal material direction is assumed to be identical for the whole component (no drape), one where only the special change of the material orientation is considered (drape), and one where both the spatial change of the material orientation as well as the variation of the tow angle (scissor angle) is taken into consideration (drape-scissor). In this way, the effect of accounting for each of these defects can be observed. The truncated pyramid was modeled using 8-node solid elements and a coordinate system was created for each element to account for the change of the principal material orientation due to weave draping. The pyramid is assigned a multiscale material model developed within Multiscale Designer, whereas the bottom and top plates are assigned an elastic material with properties of steel. To account for the gap existing between the lower flange edges and the support fixture plate edges, a contact that allows a small sliding effect needs to be defined. The following results correspond to a gap size of 1.1 mm around all four edges. The load versus deflection and failure loads for the three cases are shown in Table II.2.D.4 and Figure II.2.D.29, respectively.

As it can be seen, the present material model can provide the correct stiffness when compared with the experimental data. The effect of the incorporation of the draping and/or scissor angles is also apparent since, as one would expect when the draping results are incorporated, an increase on the stiffness is observed.

Table II.2.D.4. Truncated Pyramid Experimental and Numerical Results.

Experiment/Simulation	Max Load (kN)	Disp. At Max Load (mm)
Specimen 051117A	53.38	3.08
Specimen 051117B	54.45	2.74
Average	53.91	2.91
MDS (No Draping)	81.14	2.42
MDS (Draping)	86.00	2.30
MDS (Draping & Scissoring)	54.21	1.94

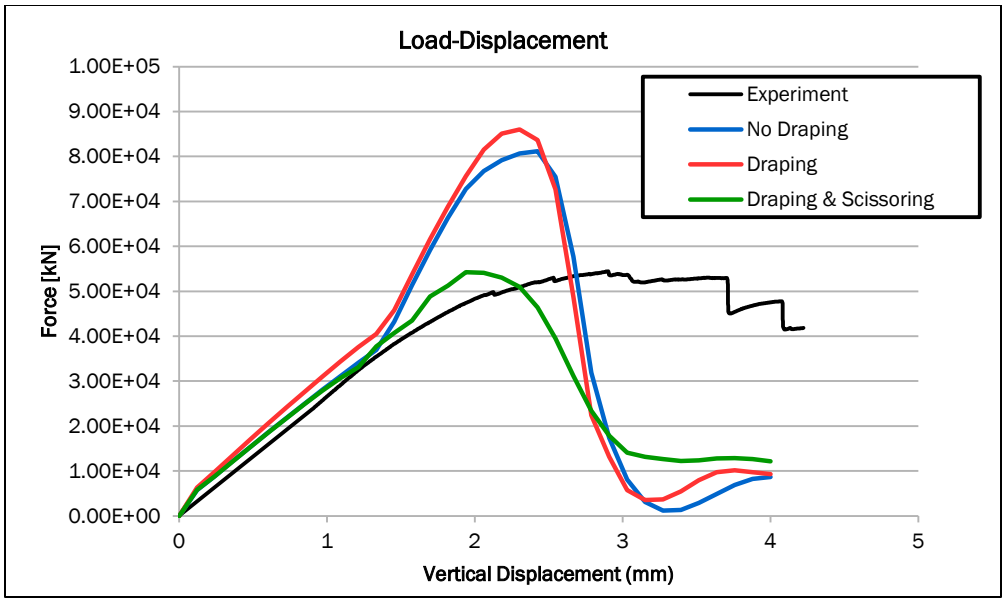

Figure II.2.D.29. Simulation versus experimental load versus displacement curves.

Residual Stress Capability with Reduced Order Homogenization

Among the goals of this project is to link manufacturing simulations with structural performance simulations through residual stress calculations. For composites, residuals are introduced due to thermal expansion in the fiber and matrix, as well as chemical shrinkage in the matrix during cure. Generic non-mechanical strains resulting from the manufacturing process will simply be called expansional strains from here on out. Multiscale Designer employs a material description at the fiber and matrix level, while ESI manufacturing software employs a homogenized, ply-level description. Integrating these two software through expansional strains thus requires recovering the matrix and fiber expansional strains. The Multiscale Designer team has proposed a methodology for recovering these quantities that the ESI group is presently evaluating.

Additionally, the Multiscale Designer group has developed a solution for using reduced order homogenization with residual strains. Model reduction is required to make crash simulation with multiscale analysis feasible, but introduces some difficulty once manufacturing strains are introduced. Namely, the model reduction procedure must account for the state of residual strain in the material, otherwise the material model may exhibit pathological behavior where large stresses remain in the material after it has completely failed. Ideally, model reduction is a preprocessing step that only needs to be done once, but the addition of residuals means model reduction would need to be done for every material point with a different state of residual strain, which could potentially be every single gauss point in a complex model. To avoid this undesirable situation, the Multiscale Designer team has developed a methodology to approximately release the residual stresses as damage in the material progresses. This eliminates the pathological behavior observed due to unreleased residuals at negligible computational expense and model complexity.

The reduced order equations describing micro-scale equilibrium in the presence of generic non-mechanical strains is:

$$\{\varepsilon\}_i^{mechanical} = [A]_i\{\varepsilon\}_{macro}^{mechanical} + \{\varepsilon\}_i^{NM2M} + \sum_{j=1}^{nphase} [P]_{ij}\{\mu\}_j^{mechanical}$$

where $\{\varepsilon\}_i^{NM2M}$ is the mechanical strain in phase i that is induced due to non-mechanical strains in the unit cell. It is defined as:

$$\{\varepsilon\}_i^{NM2M} = -[A]_i[L]_{macro}^{-1}\sum_{j=1}^{nphase}[E]_j\{\mu\}_j^{NonMechanical} + \sum_{j=1}^{nphase}[T]_{ij}\{\mu\}_j^{NonMechanical} - \{\mu\}_i^{NonMechanical}$$

where A is the strain concentration factor for linear problems, i.e., it relates macroscopic strain to strains in the micro-phases for linear problems; L is linear elastic stiffness tensor (Hooke's law); P is mechanical Eigen strain influence function, which means how the unit mechanical Eigen strain in the microphase (that represents the effect of damage and plasticity) influences strains in the unit cell; T is thermal Eigen strain influence function, which means how the unit thermal Eigen strain in the microphase influences strains in the unit cell; and E is a hybrid influence function of T and P, which contains terms due to the macro-level (homogenized) non-mechanical strains, as well as terms that result from the unit cell maintaining equilibrium in the presence of micro-scale non-mechanical strains. Note that because this formulation only requires the phase non-mechanical strain $\{\mu\}_j^{NonMechanical}$, which can come from any number of effects, integration with a manufacturing code is simple as long as phase non-mechanical strains are available. The generic formulation allows us to treat the manufacturing solver as a black box for computing expansional strains and thus leverage sophisticated chemical kinetics models employed by those solvers.

Stochastic Model Development

Introduction to the Model

The objective of the probabilistic component of this effort is to ensure the validity of the predictive simulation used in design optimization. The challenge for this task is two-fold. First, the probabilistic representations must be able to assimilate experimental and simulation data and from multiple scales and multiple simulators modeling distinct physical phenomena and distinct scales. Second, probabilistic calculations must be efficient to accommodate large-scale computational models, updating schemes, credible extreme predictions, and optimization workflows.

Approach to Modeling

The Polynomial Chaos machinery, augmented with basis adaptation and updating schemes is flexible enough to meet all these requirements. It has been demonstrated on each piece of the project and is currently being integrated for demonstration on the design optimization task. Specifically, a probabilistic model for each QoI is constructed in the form of a polynomial function of independent variables representing the fundamental source of uncertainty. All QoI are ultimately functions of the same small subset of fundamental random variables. These are either variables defined at the finest scale, or variables that describe modeling error introduced by some numerical code (and associated theoretical mode/assumptions). The models for the QoI are constructed in two stages, permitting the construction of an adapted model that is not hampered by the curse of dimensionality. This adaptation is repeated for each QoI. A remaining challenge that is being addressed for FY 2018 is to deal with several QoI simultaneously. This is an important situation corresponding to the case where both objective function and constraints, in design optimization, are probabilistic.

Discussion of Results

A PCE model was developed for structural performance considering statistical variations in mechanical properties of fibers and resin, and geometry of tows. The statistical properties of these fine scale variables were calibrated to match predictions from tension tests on the coarse scale. The model was then used in a validation format to predict performance in a three-point-bend test. This exercise (of calibration/validation) was repeated as different data sets for fiber/resin/compression factors were introduced. For each dataset, the range of validity of the three-point-bend test was generally improved. Analysis with the most recent dataset is still underway. Results from this phase will appear in a paper that has been accepted for publication (Meres et.al, 2017) and were presented at the recent ASC conference (Ghanem et.al, 2017). Figure II.2.D.30 and Figure II.2.D.31 show the histogram of elastic modulus and strength of the laminate obtained from an experimental tensile test. On the same plots are superimposed probability density functions of the same quantities obtained through statistical upscaling using PCE constructions with different order approximations. Convergence is clear from a

comparison of the black and red curves in those figures. Figure II.2.D.32 and Figure II.2.D.33 show the sensitivities of modulus and strength with respect to the 11 fundamental variables that entered the PCE approximation. Figure II.2.D.34 shows the joint pdf of two elastic moduli of laminate, obtained from the PCE constructions. It is important to note that this construction permits the construction of joint density functions of various quantities of interest such as upscaled elastic and strength moduli.

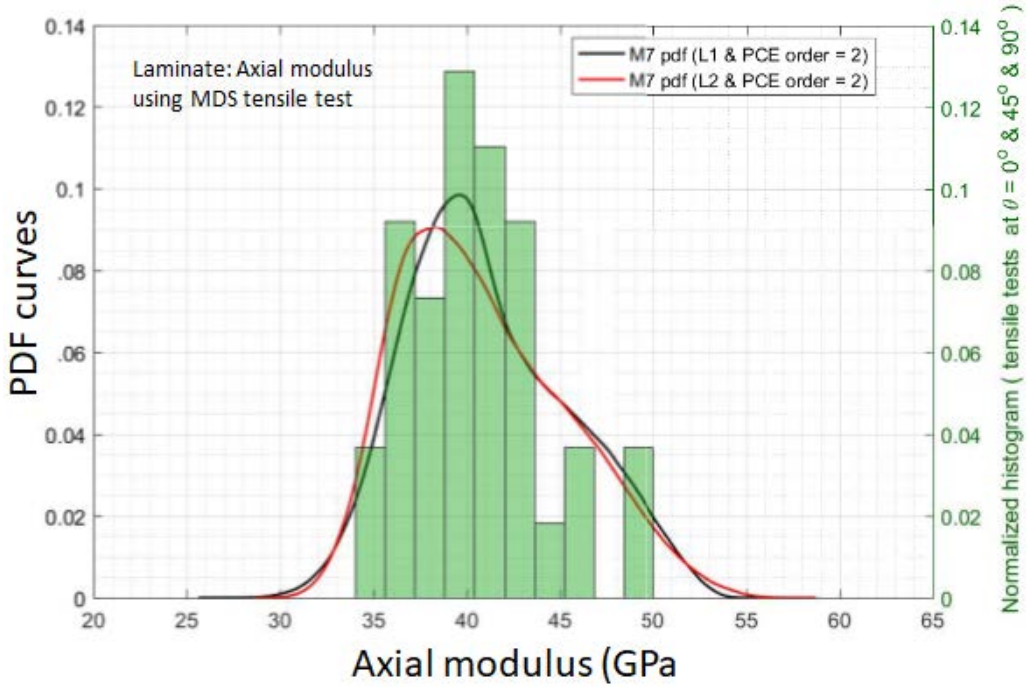

Figure II.2.D.30. Axial modulus of laminate from experimental data and Multiscale Designer simulations.

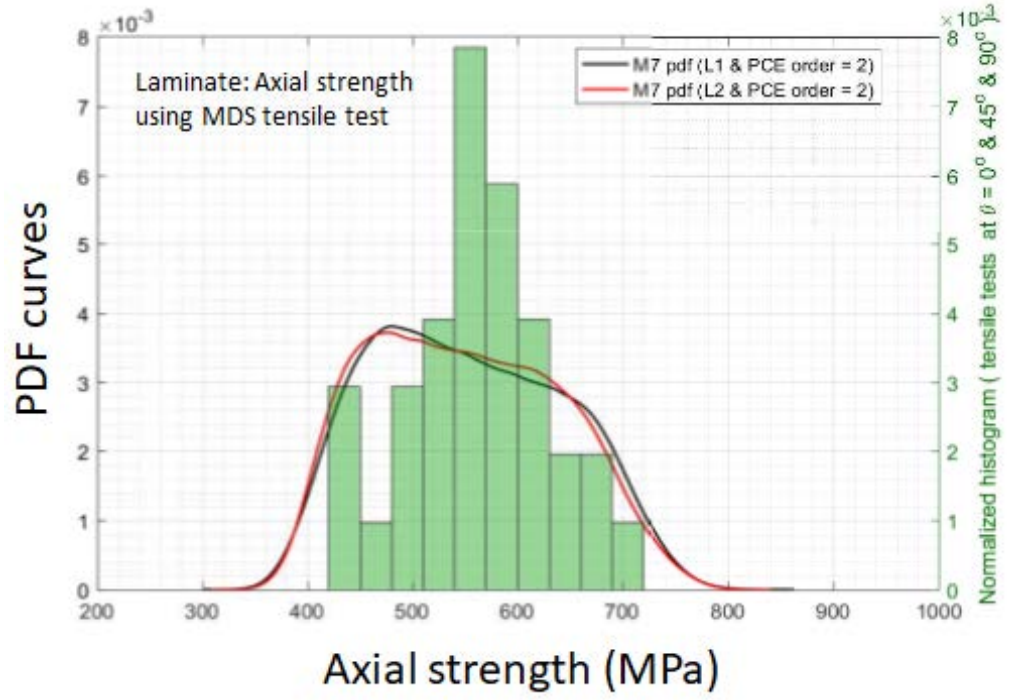

Figure II.2.D.31. Axial strength of laminate using experimental data and of predictions using Multiscale Designer.

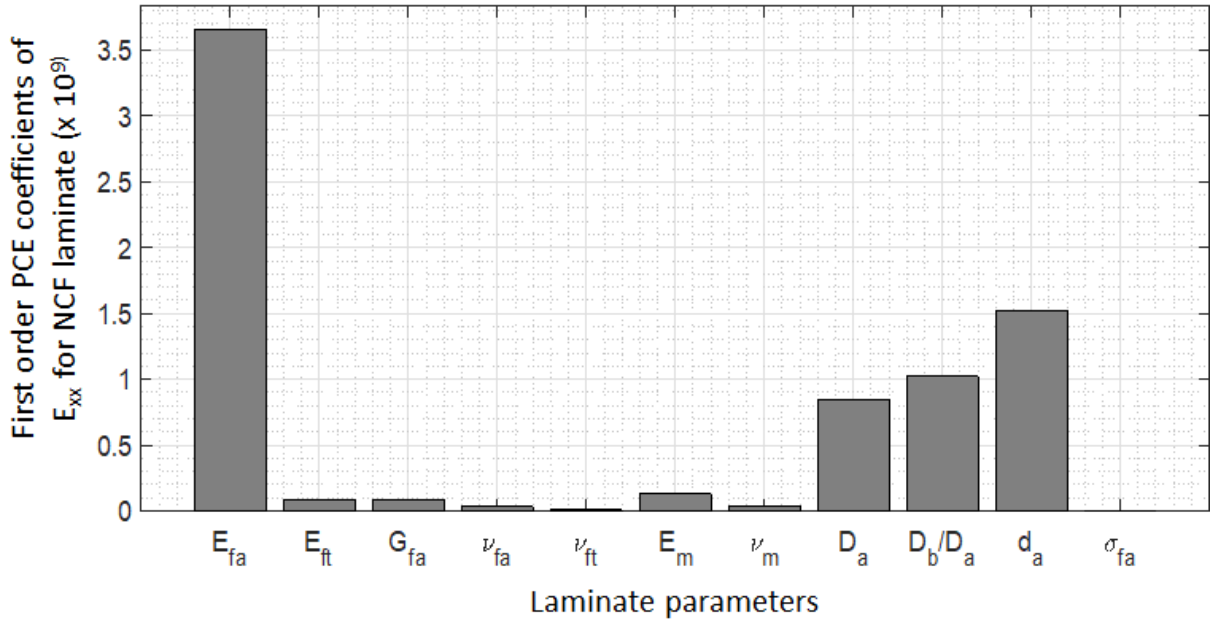

Figure II.2.D.32. Sensitivity coefficients for elastic modulus of laminate with respect to 11 parameters describing fibers, resin, and tow geometry.

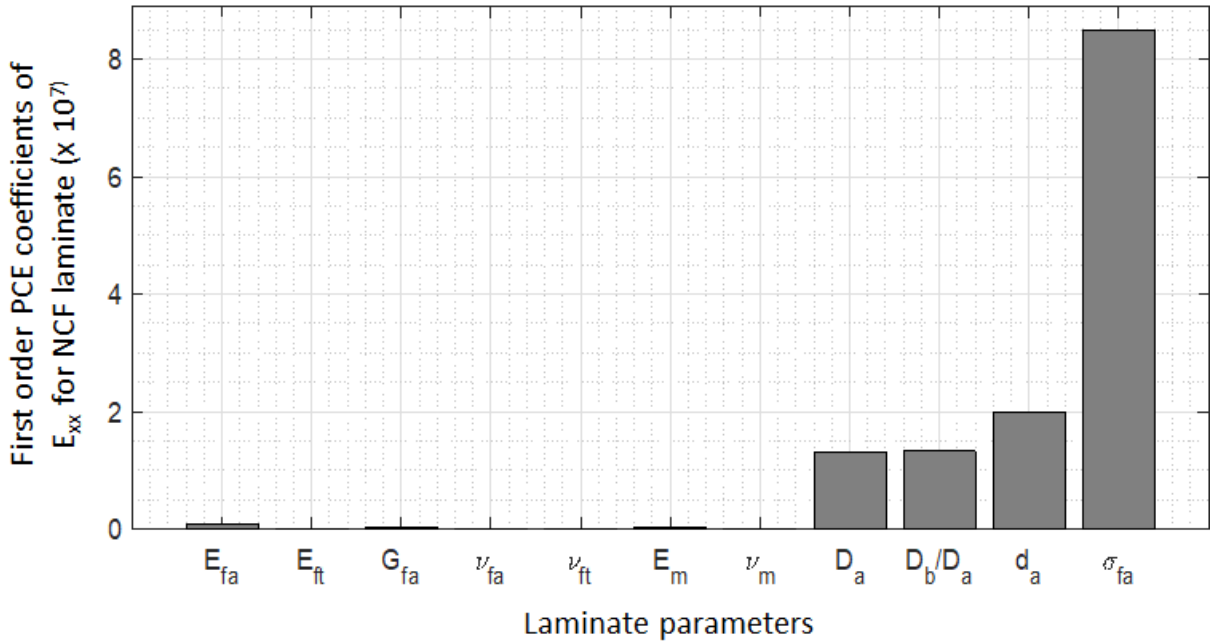

Figure II.2.D.33. Sensitivity coefficients of strength of laminate with respect to 11 parameters describing fibers, resin, and tow geometry.

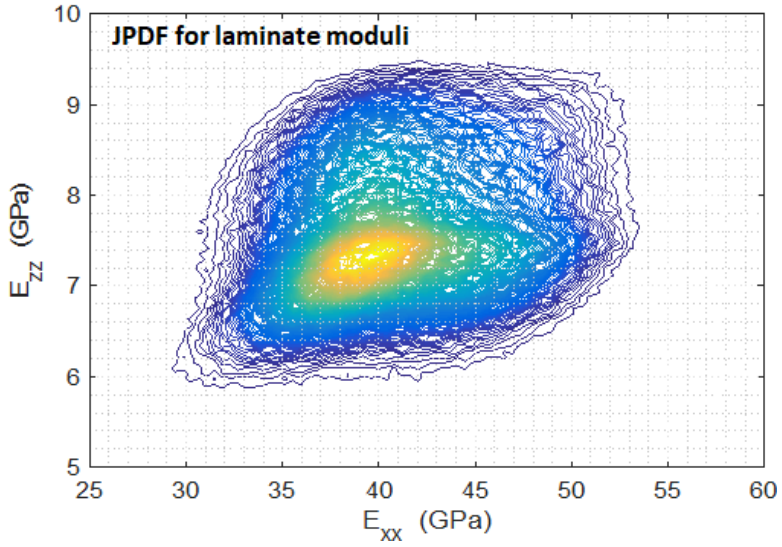

Figure II.2.D.34. Joint density function of elastic moduli in X and Z directions of laminate.

On the manufacturing side, a PCE model for fill time, cure time, and maximum gradient in distortion stress, were constructed in terms of fundamental variables describing the fiber orientation during forming, and fiber elastic and strength moduli, as well as the permeability of race-tracking channel and thermal coefficient during curing. The model was exercised on a rectangular plate and a truncated pyramid model. The output from this model will provide initial stress configuration for the structural performance task. Figure II.2.D.35 shows the orientation angles for the up-scaled shell model used in the forming calculations. These realizations were synthesized starting with an assumed anisotropic covariance function of the orientations. Figure II.2.D.36 shows realizations of the shearing angle after the flat sheet has been draped over a truncated pyramid.

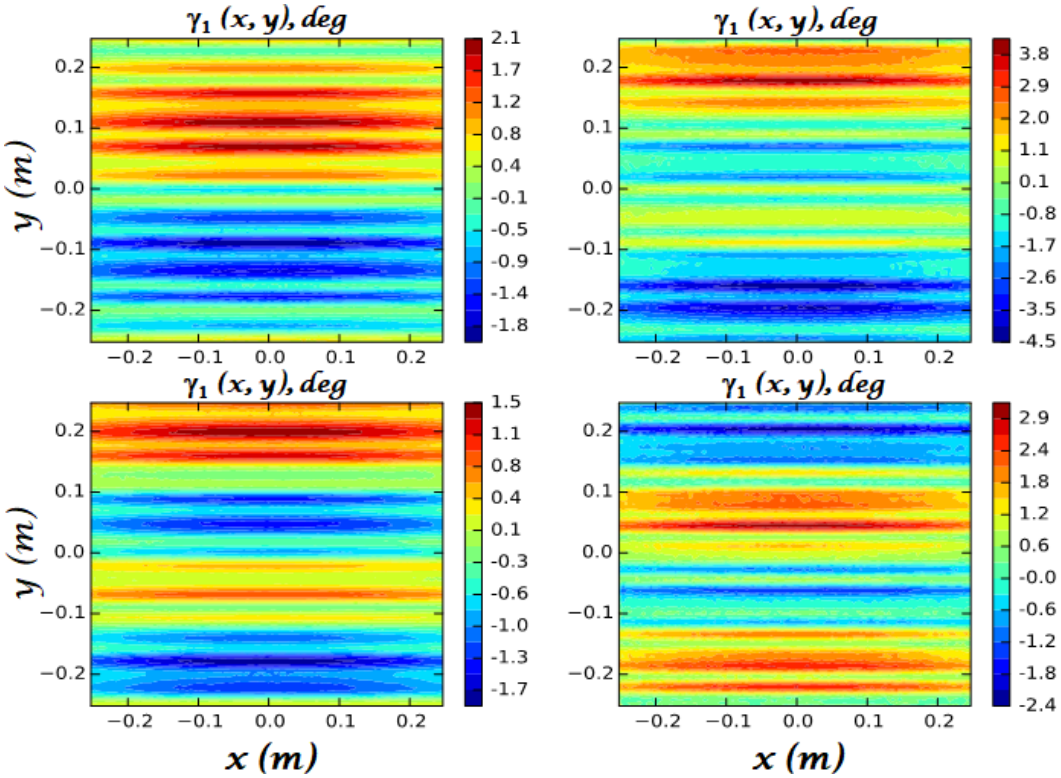

Figure II.2.D.35. Realization of random orientation prior draping.

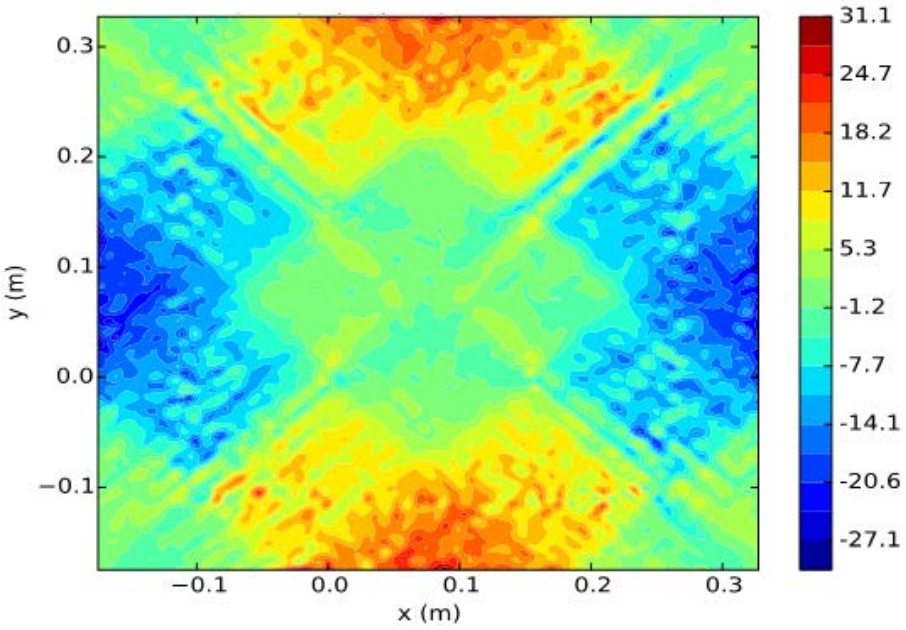

Figure II.2.D.36. Realization of random shearing angle (x, y) after forming on truncated pyramid. Source: General Motors.

Conclusions

During FY 2017, the project team successfully validated the manufacturing and structural performance tools by comparing predictions with experimental results for such parameters as fill time, curing time, and load to failure. In parallel, a new prototype simulation tool was developed for modeling the compression resin transfer molding process—a high-volume composite manufacturing process—very attractive to the automotive industry. Additionally, a mapping tool was developed to transfer the manufacturing outcome onto structural models. The complete integrated tool development was further successfully validated for a truncated pyramid component. Currently, using the tools developed in this project, efforts are underway to design, build, and test an automotive assembly chosen to demonstrate the capability of developed tools for predicting the crashworthiness accurately.

Key Publications

Dereims, A., S. Zhao, H. Yu, P. Pasupuleti, M. Doroudian, W. Rodgers, and V. Aitharaju, 2017, "Accurate compression resin transfer molding (C-RTM) simulation through fluid-solid coupled approach," *American Society of Composites 32nd Technical Conference*, October 19, 2017, West Lafayette, IN, USA.

Pack, S., V. Aitharaju, H. Yu, H. G. Kia, and D. Wilson, 2017, "Integration of cost models and simulation tools for optimum composite manufacturing process," *17th Annual Society of Plastic Engineers (SPE 2017)*, September 6, 2017, Novi, MI, USA.

Rodgers, W. R., P. Pasupuleti, S. Zhao, T. Wathen, M. Doroudian, and V. Aitharaju, 2017, "Numerical simulation with experimental validation of the draping behavior of woven fabrics," *American Society of Composites 32nd Technical Conference*, October 19, 2017, West Lafayette, IN, USA.

Wollschlager, J., D. Plakomytis, J. Fish, and V. Aitharaju, 2017, "Including the effects of weave draping within multiscale simulations," *American Society of Composites 32nd Technical Conference*, October 19, 2017, West Lafayette, IN, USA.

References

Ghanem, R., L. Mehrez, V. Aitharaju, and W. Rodgers, 2017, "Polynomial chaos characterization of uncertainty in multiscale models and behavior of carbon reinforced NCF composites," *American Society of Composites 32nd Technical Conference*, October 19, 2017, West Lafayette, IN, USA.

Mehrez, L., J. Fish, V. Aitharaju, W. Rodgers, and R. Ghanem, 2017, "A PCE-based multiscale framework for the characterization of uncertainties in complex systems," *Computational Mechanics*, in press.

II.3 Multi-Material Joining

II.3.A Understanding Protective Film Formation by Magnesium Alloys in Automotive Applications (Oak Ridge National Laboratory)

Michael P. Brady, Co-Principal Investigator
Materials Science and Technology Division
Oak Ridge National Laboratory
1 Bethel Valley Rd.
Oak Ridge, TN 37831-6156
Phone: 865-425-0231
E-mail: bradymp@ornl.gov

Donovan N. Leonard, Co-Principal Investigator
Materials Science and Technology Division
Oak Ridge National Laboratory
1 Bethel Valley Rd.
Oak Ridge, TN 37831-6064
Phone: 865-241-5493
E-mail: leonarddn@ornl.gov

Sarah Kleinbaum, Technology Manager
E-mail: sarah.kleinbaum@ee.doe.gov

Start Date: October 1, 2015 End Date: September 30, 2018
Total Project Cost: $1,200,000 DOE share: $1,200,000 Non-DOE share: $0

Executive Summary

The objective of this project is to enhance the fundamental understanding of Mg corrosion to provide the basis for designing improved Mg alloys and coatings to permit more widespread automotive adoption of Mg. Two classes of Mg alloys are under study: (1) conventional Mg-Al base alloys; and (2) state-of-the-art RE element-modified Mg alloys of interest for their improved formability characteristics, particularly in sheet form. The project is devoted to understanding the impact of alloying additions on film formation and hydrogen (H) migration into the underlying Mg alloy during aqueous exposures of uncoated (bare) alloys, as well as the impact of substrate alloying segregation tendencies on the formation of surface coatings by electro-ceramic and electro-coating techniques. New insights are achieved through the use of advanced electron microscopy and neutron and isotopic tracer characterization tools not previously widely applied to Mg corrosion. Efforts during FY 2017 transitioned from studies focused on the discovery of unexpected H species penetration into Mg alloys upon aqueous exposure, to study the effects of the substrate alloy on the formation and protectiveness of state-of-the-art electro-ceramic coatings. Inelastic neutron scattering (INS) vibrational spectrometry revealed that enhanced H introduction into Zr and RE-containing Mg alloys as a result of aqueous exposure resulted in molecular H_2 in the alloy. This finding has significant ramifications for understanding and potentially mitigating the susceptibility of Mg alloys to stress corrosion cracking (SCC) and related H embrittlement (HE) phenomena. Cross-section scanning transmission electron microscopy (STEM) analysis of electro-ceramic-coated Mg alloys found an unexpectedly strong impact of the substrate alloy composition on coating thickness and morphology. Such information can be used to optimize coating process parameters for a given alloy and/or aid in designing substrate alloys with increased amenability to coating.

Accomplishments

- Discovered that H introduced into aqueous-exposed Zr and RE-modified Mg alloy ZE10A was present as molecular H_2 within the alloy. This study was accomplished using the VISION INS vibrational spectrometer instrument at ORNL's SNS, the highest-resolution broadband INS spectrometer in the world. To our knowledge, such techniques have not previously been applied in this manner to Mg corrosion (FY 2017).
- Observed an unexpected and significant impact of substrate alloy composition on the subsequent thickness and morphology of state-of the art electro-ceramic coatings for corrosion protection on Mg alloys AZ31B, AZ91, ZE10A, and WE43 (FY 2017).

Technology Assessment

- Target: Gain improved understanding of film and coating formation by Mg alloys as a function of alloy chemistry and microstructure.
- Target: Provide a fundamental basis for designing and optimizing new Mg alloys and/or coating processes to improve corrosion resistance under automotive-relevant conditions.
- Gap: The lack of corrosion prevention strategies is a key factor limiting more widespread use of Mg alloys in automotive applications.
- Gap: Alloying has been shown to modify surface film and coating performance; however, a detailed understanding of how and why it does so is currently lacking. This understanding is needed to develop improved alloys and surface treatments/coatings to permit more widespread adoption of Mg alloys.

Project Introduction

Mg alloys are of great interest to automotive manufacturers because of their attractive combination of low density, good strength, amenability to casting, and ease of recycling. A major obstacle to widespread adoption of Mg alloys is their susceptibility to corrosion (Song and Atrens 2007, Song 2005, and Gray and Luan 2002). Surface treatments and/or coatings are needed for many applications (Gray and Luan 2002); these result in increased cost and can lead to component durability issues. The inability of Mg alloys to establish a continuous and fully protective surface film under many exposure conditions is a key factor underlying their susceptibility to corrosive attack. Alloying has been shown to modify surface film performance and impact the nature and protectiveness of reactive-based coating processes typically used for Mg alloys; however, a detailed understanding of how and why this is the case is currently lacking. This understanding is needed to provide a basis for developing improved alloys and coatings to permit more widespread adoption of Mg alloys in automotive applications.

Approach

This project is using advanced electron microscopy, neutron scattering and spectrometry, and isotopic tracer characterization tools not previously widely applied to Mg corrosion to provide the improved fundamental insights needed to successfully design Mg alloys and coatings with improved corrosion resistance. The project is focusing on select state-of-the-art commercial Mg alloys and coatings relevant to automotive applications and chosen in consultation with project collaboration partners Magnesium Elektron North America (a Mg alloy producer), Henkel Corporation (a coating producer), Magna International (a Tier 1 automotive supplier), McMaster University (for electron microscopy and electrochemistry), McGill University (for developmental Mg sheet alloys), and the University of Manitoba (for secondary ion mass spectrometry [SIMS] sputter depth profile analysis of isotopic tracers). The effort recently pursued film formation and coating studies for a representative alloy from two key classes of Mg alloys:

1. Conventional Mg-3Al-1 Zn (all compositions in weight percent) base alloy AZ31B.

2. State-of-the-art RE- and Zr-modified Mg alloy ZEK100 type (ZE10A) E717 from Magnesium Elektron North America ($Mg_{1.5}Zn_{0.25}Zr_{<0.5}Nd$ base alloy, which is of interest for its improved formability characteristics, particularly in sheet form).

Efforts in FY 2016 to FY 2018 include expansion of the work to permit assessment of the impacts of higher levels of alloying additions and the impacts of second phases on film and coating formation through the study of the automotive-relevant alloys AZ91 (Mg_9Al_1Zn) for comparison with AZ31B, and WE43 ($Mg_{3.7–4.3}Y_{2.3–3.5}RE_{0.2}Zr$) for comparison with ZE10A. This effort is focused on the following two key corrosion aspects:

1. Defining the impacts of Al, Zr, Ca, and RE alloy additions on film structure and enhanced H migration phenomena into Mg alloys during aqueous exposures, which are relevant to SCC/HE susceptibility and dissimilar metal interface corrosion. An understanding of H uptake is also needed to more fully describe and successfully model aqueous corrosion processes for Mg alloys.
2. Establishing the effects of substrate alloying segregation tendencies on state-of-the-art electro-ceramic coating formation and determining performance with an electro-coat top coat to provide a basis for the optimal design of alloys for coating processing. The focus will be on determining why coating protectiveness varies with the substrate alloy in these composition ranges.

Technology Transfer Path

Basic understanding of the aqueous corrosion of Mg alloys will provide insights into how refinements in the design and optimization of new Mg alloys and coatings can improve corrosion resistance under conditions relevant to automotive applications. The current gaps in the basic understanding of the mechanics and kinetics of film and coating formation, and their correlation with alloy chemistry and microstructure, are key factors hindering the improvement of corrosion resistance to permit more widespread use of Mg alloys in automotive applications. Teaming with Magnesium Elektron North America (an Mg alloy producer) and Henkel Corporation (a coating company) provides a direct path for incorporating insights from this effort into practice. Project planning has also benefited from input by Magna International (a Tier 1 automotive supplier).

Results

Efforts during FY 2017 transitioned from studies focused on the discovery of unexpected H species penetration into Mg alloys upon aqueous exposure, to study of the effects of the substrate alloy on the formation and protectiveness of state-of-the-art electro-ceramic coatings. The FY 2015 to FY 2017 H species uptake findings were recently published (portions of this report are taken from that work) (Brady 2017). FY 2015 to FY 2016 project work established that small additions of Zr and neodymium (Nd) to Mg alloys significantly enhanced the penetration of hydrogen to deuterium (H/D) into the alloy upon aqueous exposure, with up to ~100 μm of H/D penetration observed after only 4 hours in room-temperature water (Brady 2017). The enhancement of H penetration by the addition of Zr and Nd is technologically important, as Zr is widely employed as a Mg alloy grain refiner and Nd (and other REs) is used to modify texture to improve manufacturability and improve mechanical properties (Bohlen et al. 2007; Gusieva et al. 2015). INS vibrational spectrometry was used in FY 2016 to FY 2017 to identify the speciation of H introduced into Mg by exposure in water (Brady 2017). This analysis used the VISION instrument at ORNL's SNS. INS is not a surface-limited technique; rather it measures bulk properties, including buried interfaces. To increase the sample volume of H_2O-exposed/H-ingressed metal to aid detection of the H specie(s) present, a ~100 μm thick foil was studied. Forty unexposed, control pieces of ZE10A and 40 foil pieces of unalloyed Mg exposed to H_2O for 4 hours were stacked together for INS analysis. The INS data were acquired at the end of FY 2016 and analyzed in FY 2017. Difference spectra (4 hour H_2O-exposed samples and unexposed control samples) for Mg and ZE10A foils are shown in Figure V.1.A.1 (Brady 2017). Intermixed MgO and $Mg(OH)_2$ films that were on the order of a few hundred nanometers thick were formed on the H_2O-exposed foils of both Mg and ZE10A; the $Mg(OH)_2$ present in the surface film was readily measured by INS (comparison data for an $Mg[OH]_2$ standard is shown in Figure II.3.A.1). A broad peak in the ZE10A INS data at around 15 meV was also observed, which strongly suggests the presence of molecular H in the ZE10A (H_2, first rotational

transition nominally at 14.7 meV in the solid); its breadth is a consequence of strong confinement and/or hindrance. Similar INS peaks have been observed from quantum rattling of H_2 in clathrate hydrate nanocavities (Ulivi et al. 2007). The molecular H peak was larger and more distinct in the ZE10A than in the Mg difference spectra, consistent with the greater H/D penetration observed for H_2O/D_2O-exposed ZE10A in FY 2015 and FY 2016 SIMS studies (Brady 2017).

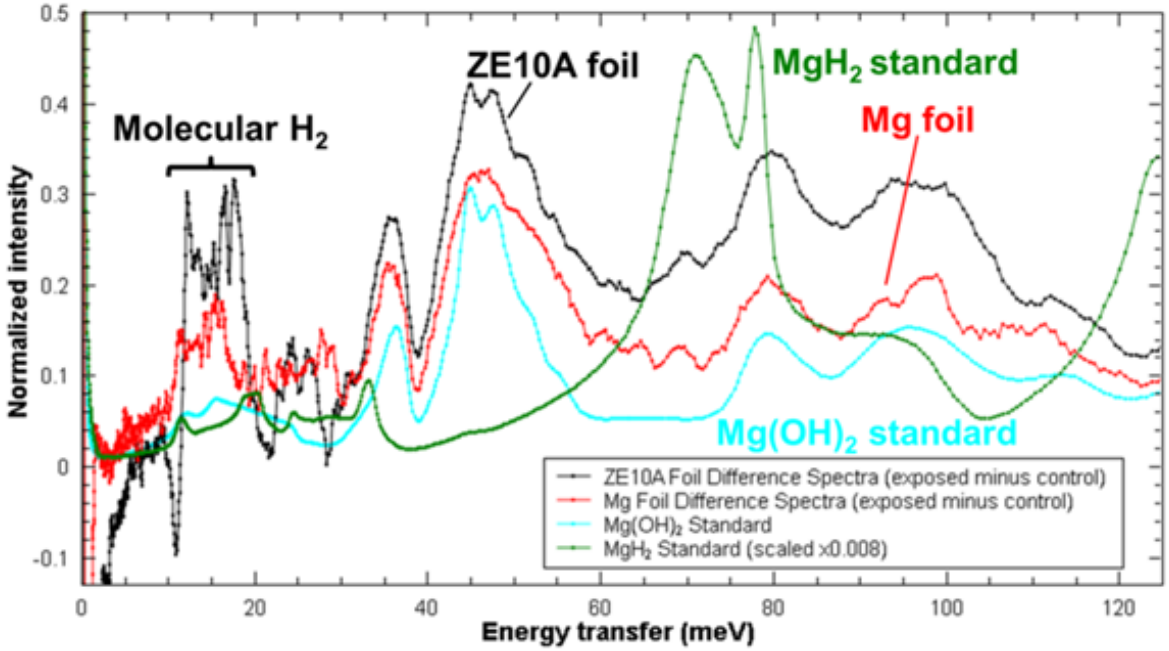

Figure II.3.A.1. INS difference spectra (4 hour H_2O-exposed and unexposed control) for ZE10A and Mg (Brady 2017).

The INS data reflect the entire sample volume and cannot provide information regarding where the detected H species were located. The molecular H_2 was deduced to be associated with Zr/Nd-rich alloy regions in the ZE10A, because no other H species were detected in the INS difference plots and because complementary time-of-flight (TOF)-SIMS studies using D tracers observed preferential segregation of D to a wide range of Zr/Nd-rich nanostructural/microstructural features (Brady 2017). Further, no magnesium hydride (MgH_2) was evident in the INS data for the Mg and ZE10A exposed to H_2O for 4 hours. The INS data did suggest possible trace amounts of zirconium (II) hydride (ZrH_2) in the ZE10A, as shown in Figure II.3.A.2. However, the relevant spectra were quite similar for both the unexposed control and the ZE10A exposed to H_2O for 4 hours, indicating that ZrH_2 was present as an impurity phase—likely from alloy melt processing—and not the result of H_2O exposure (Brady 2017). There was also no evidence of atomic H in the Mg or the ZE10A, typically observed in the 50–90 meV spectra range, although bulk atomic H levels below ~15–25 weight parts per million would not have been detected in the INS measurements (Brady 2017).

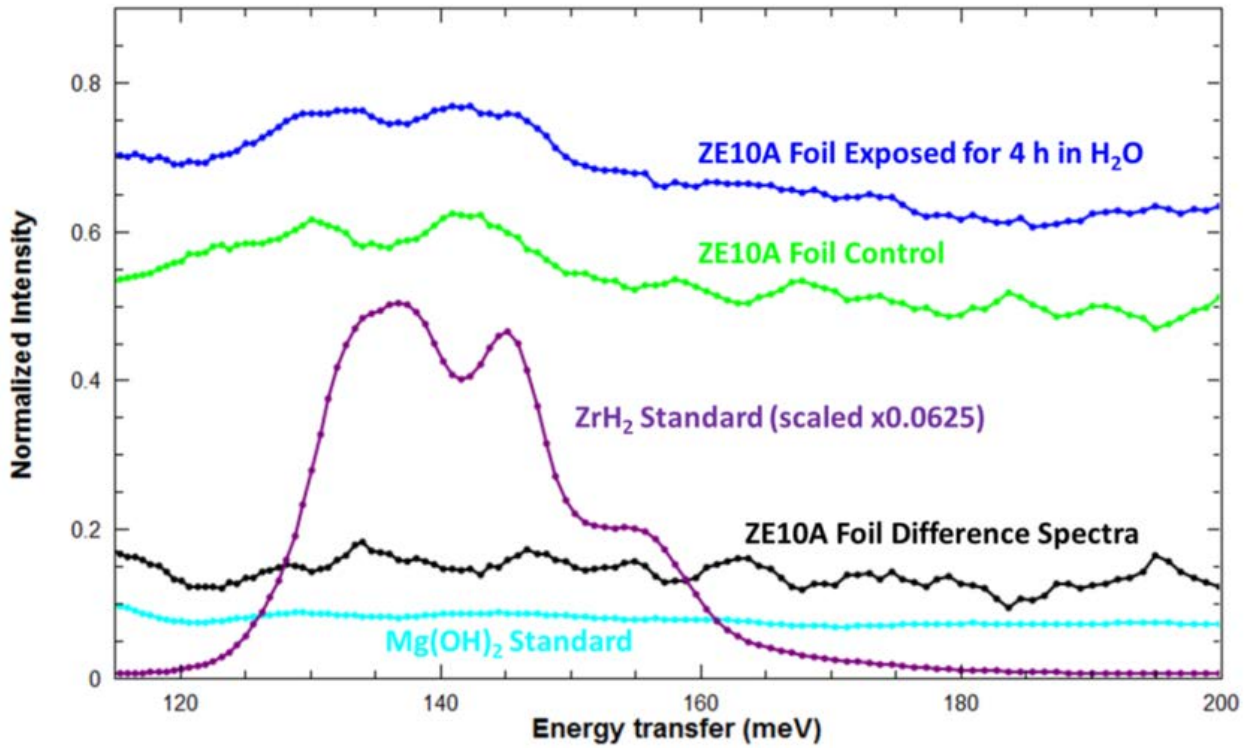

Figure II.3.A.2. ZE10A foil INS spectra and difference spectra (4 hours of H_2O-exposed and unexposed control) compared with a ZrH_2 standard (Brady 2017).

The other major activity in FY 2017 was the study of electro-ceramic coating formation on a series of commercial Mg alloys with low and high levels of Al or RE alloying additions, wrought AZ31B and cast AZ91 for Al effects, and wrought ZE10A and WE43 for RE effects. The coatings were manufactured via collaboration with Henkel Corporation, and the same coating process parameters were used for all four alloy substrate types. SEM images of as-coated cross sections are shown in Figure II.3.A.3. Analysis by x-ray photoelectron spectroscopy (XPS) indicated that the coatings consisted primarily of partially oxidized Mg-fluorine (F) compound(s) and contacting potassium (K) from the coating deposition media. However, the coating thicknesses varied considerably despite the use of the same coating process parameters. Thicknesses were on the order of ~2 μm for the AZ31B and ZE10A, ~10 μm for the high-Al AZ91, and up to ~20–30 μm for the high-RE WE43. The coating morphologies formed on the AZ31B, ZE10A, and AZ91 were similar and consisted of an outer porous layer and a thin (<500 nm) continuous inner layer at the alloy-coating interface. In contrast, although an outer porous coating layer also formed on the WE43, the inner layer was highly striated, consisting of multiple thin, continuous layers.

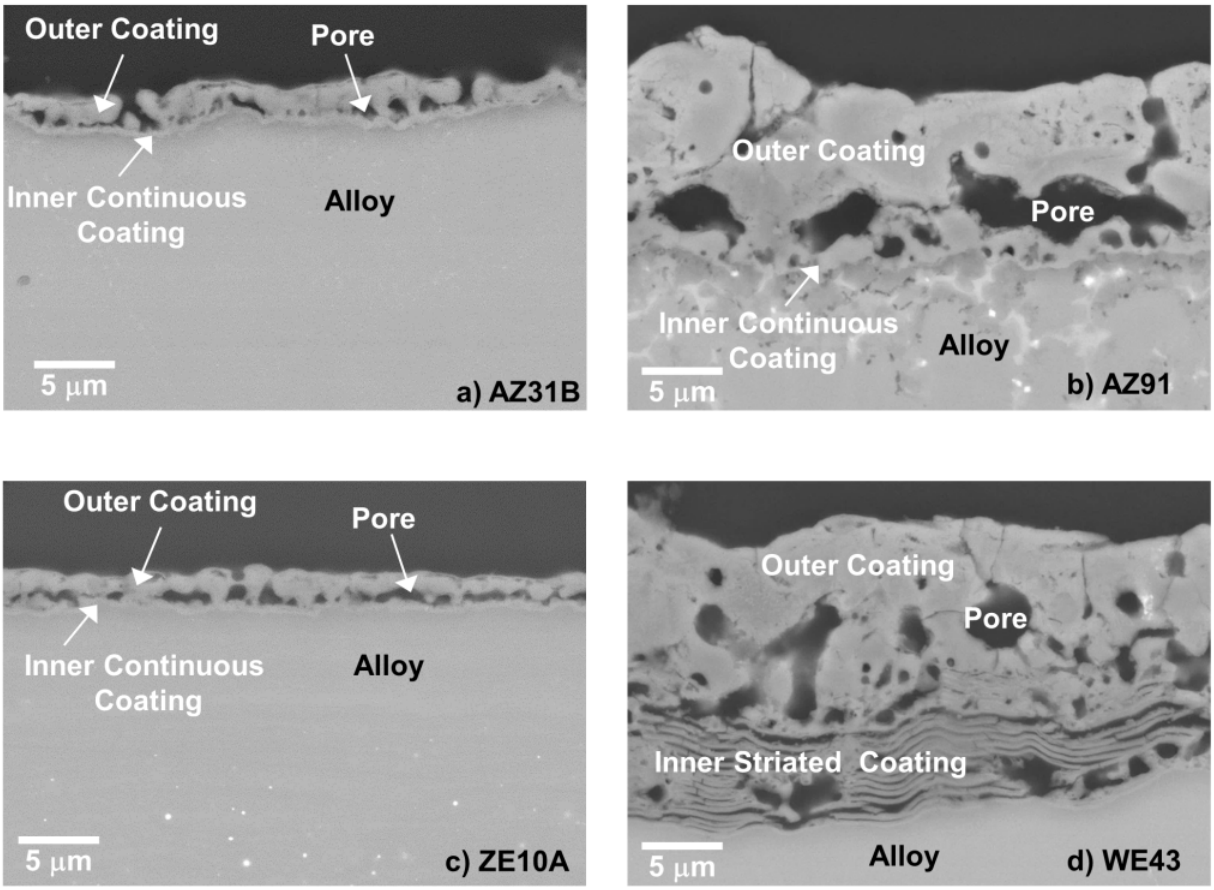

Figure II.3.A.3. SEM backscatter electron mode images of as-coated cross-sections: (a) wrought AZ31B; (b) cast AZ91; (c) wrought ZE10A; and (d) wrought WE43. Source: ORNL.

Figure II.3.A.4 through Figure II.3.A.7 show STEM cross-section images and corresponding energy-dispersive x-ray spectroscopy (EDXS) elemental maps for the alloy-coating interface regions. Consistent with the XPS data, the STEM analysis indicated that the coatings were rich in Mg, F, oxygen (O), and K. For AZ31B, minor amounts of Al and Zn from the alloy substrate were also detected in the coating; whereas the coating on the high-Al AZ91 contained higher levels of Al, and Zn was enriched at the alloy-coating interface. In contrast, neither the ZE10A nor the WE43 showed significant migration of Zr or REs from the alloy substrate and into the coating. The STEM characterization of the as-coated structures will provide a control basis for understanding the corrosion and electrochemical behavior studies planned for the electro-ceramic-coated alloys in FY 2018.

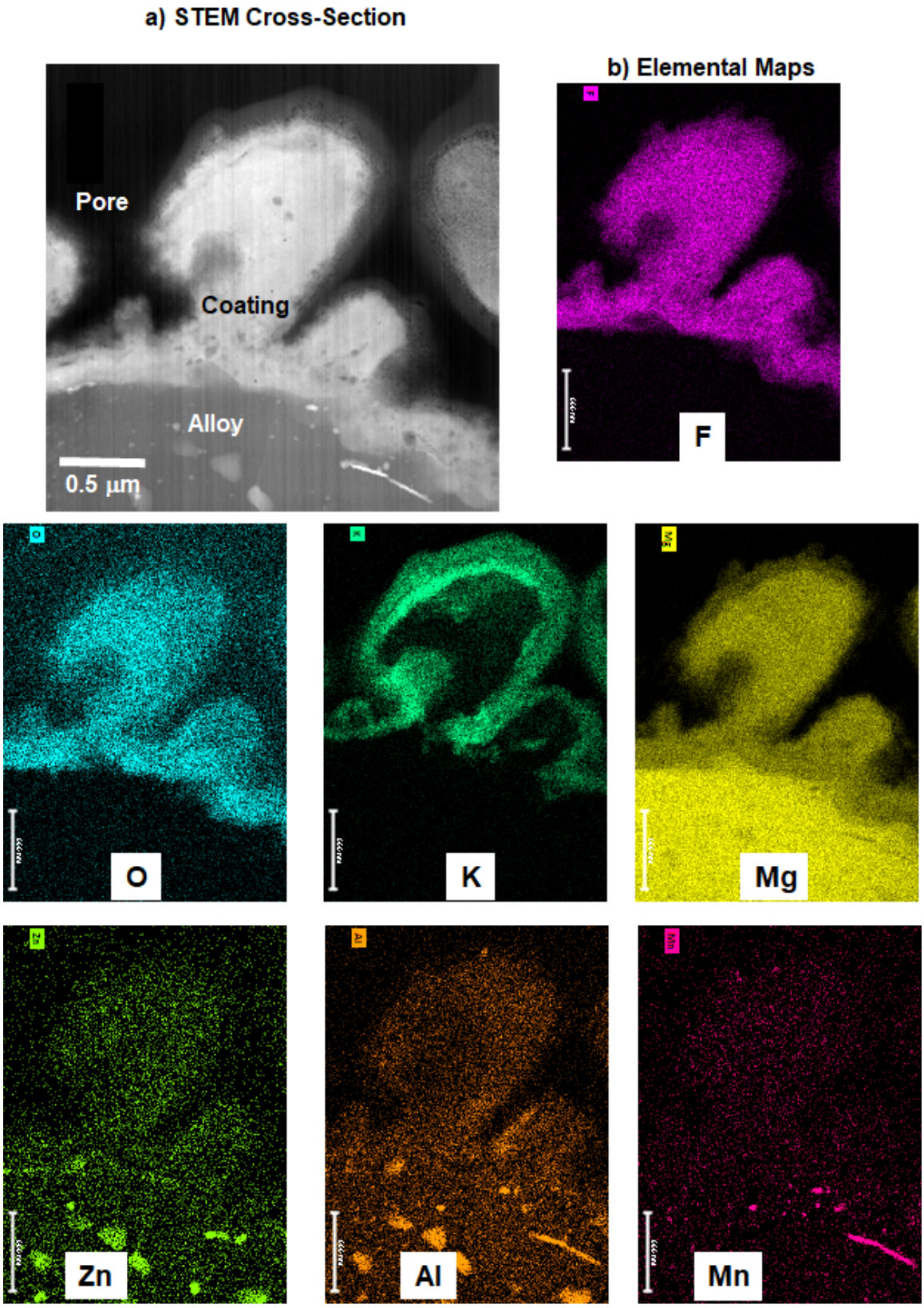

Figure II.3.A.4. STEM Z-contrast cross-section image: (a) corresponding EDXS elemental maps; and (b) of as-coated wrought AZ31B. Source: ORNL.

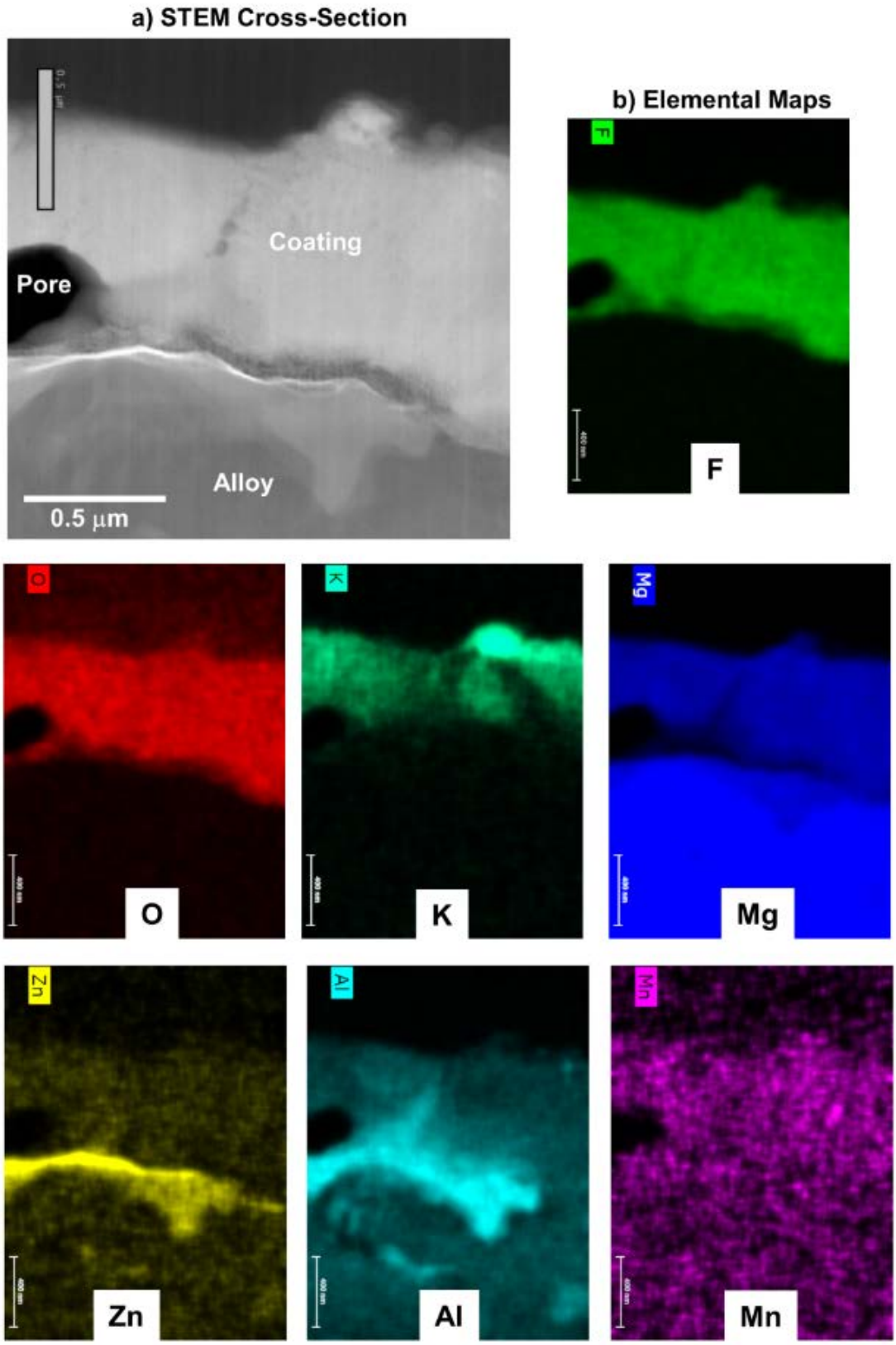

Figure II.3.A.5. STEM Z-contrast cross-section image: (a) corresponding EDXS elemental maps; and (b) of as-coated cast AZ91. Source: ORNL.

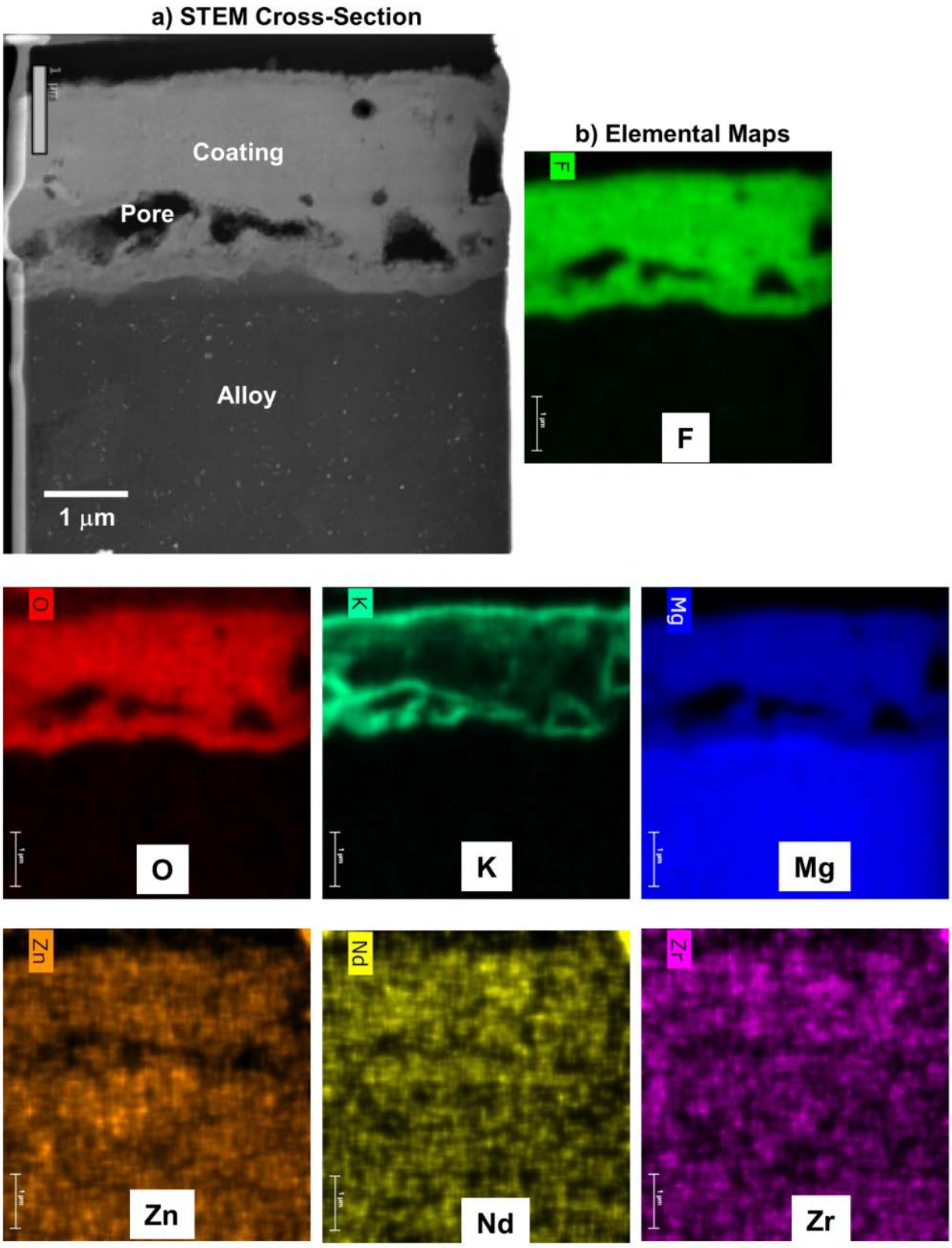

Figure II.3.A.6. STEM Z-contrast cross-section image: (a) corresponding EDXS elemental maps; and (b) of as-coated ZE10A. Source: ORNL.

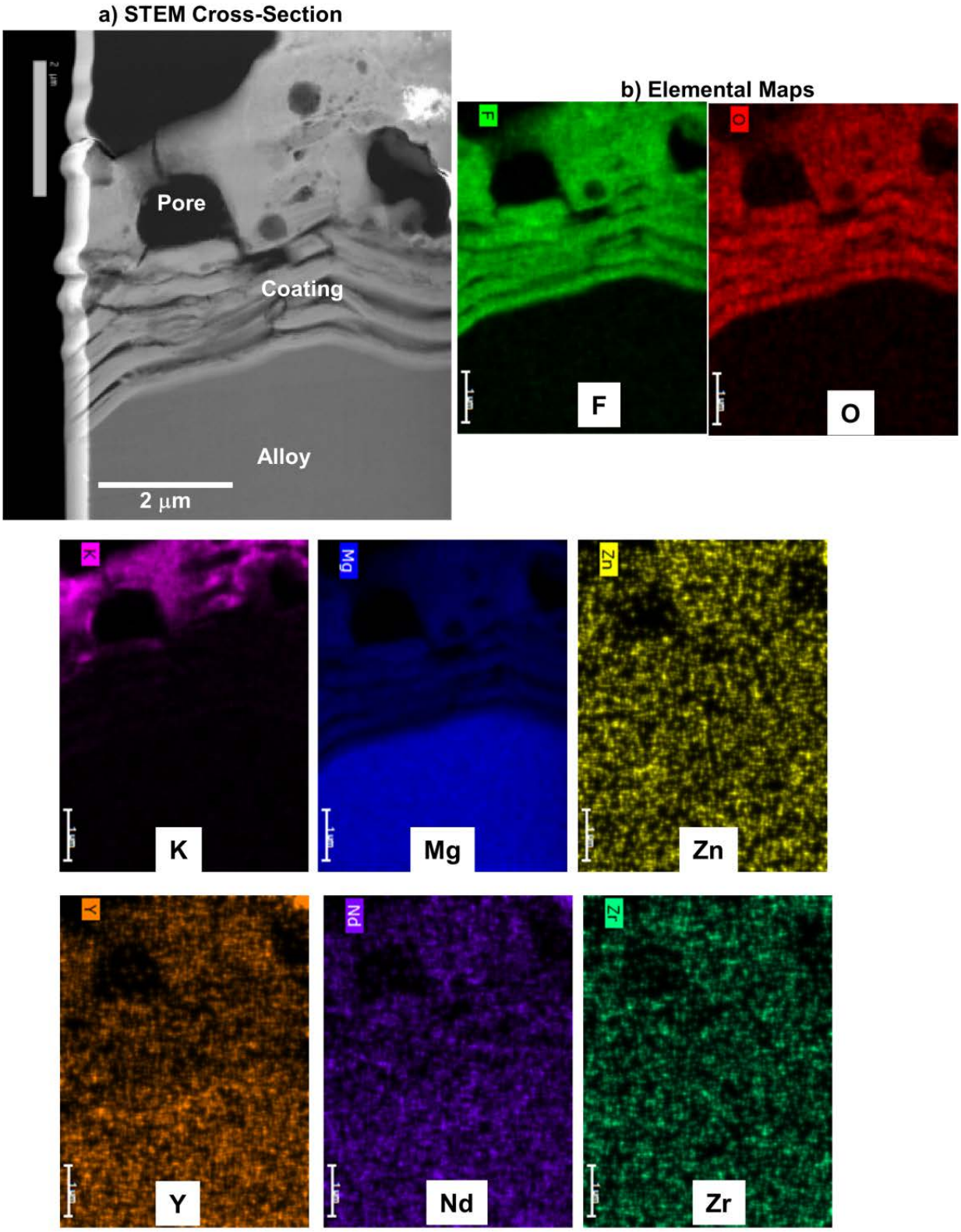

Figure II.3.A.7. STEM Z-contrast cross-section image: (a) corresponding EDXS elemental maps; and (b) of as-coated wrought WE43. Source: ORNL.

Conclusions

During FY 2017, this effort focused on two areas:

1. Identifying the speciation of H penetration into Mg alloys caused by aqueous exposure, to complete the mechanistic understanding of unexpectedly rapid H penetration in Mg alloys containing Zr and RE that were discovered under this project (Brady 2017).
2. Initiating study of the effects of the substrate alloy composition and microstructure on the formation and protectiveness of state-of-the-art electro-ceramic coatings.

Finding molecular H_2 in ZE10A Zr/Nd-rich regions after short-term exposure in water at room temperature was surprising, although internal H_2 has been postulated for Mg alloys after electrochemical charging (Chen et al. 2016). In steels, internal H_2 can result from the recombination of atomic H that enters the alloy during corrosion. It impacts pitting, blistering, and cracking behaviors (Thomas et al. 2017). The enhanced H ingress observed for Zr and Nd additions may not inevitably lead to increased SCC susceptibility or HE. For example, gettering of H to Zr/Nd-rich nanostructure features could potentially act and/or be engineered to reduce the SCC susceptibility of the adjoining Mg matrix phase. It is likely that other H-active alloying additions to Mg—as well as the chemistry, size, and distribution of second phases formed—will significantly impact the H ingress phenomena during aqueous corrosion. Cross-section STEM analysis of electro-ceramic-coated Mg alloys found that the substrate alloy composition had an unexpectedly strong impact on coating thickness and morphology. In particular, substrate alloys with higher levels of Al or RE additions resulted in much thicker coating structures and, in the case of high RE additions in WE43, a striated local layered structure at the alloy-coating interface that may impact coating adherence and/or protectiveness. STEM characterization of the as-coated structures will provide a control basis for understanding the corrosion and electrochemical behavior studies planned for the electro-ceramic-coated alloys in FY 2018. Such information can also be used to optimize coating process parameters for a given alloy and/or aide in designing substrate alloys with increased amenability to coating.

Key Publications

Brady, M. P., et al., 2017, "Insights from a recent meeting: Current status and future directions in magnesium corrosion research," *Corrosion*, Vol. 73, No. 5, pp. 452–462.

Brady, M. P., et al., 2017, "Rapid diffusion and nano-segregation of hydrogen in magnesium alloys from exposure to water," *ACS Applied Materials & Interfaces*, DOI: 10.1021/acsami.7b10750.

Brady, M. P., et al., 2017, "Tracer film growth study of the corrosion of magnesium alloys AZ31B and ZE10A in 0.01% NaCl solution," *Journal of the Electrochemical Society*, Vol. 164, No. 7, pp. C367–C375.

Rossouw, D., et al., 2017, "Characterization of localized filament corrosion products at the anodic head on a model Mg-Zn-Zr alloy surface," *Corrosion*, Vol. 73, No. 5, pp. 518–525.

References

Bohlen, J., et al., 2007, "The texture and anisotropy of magnesium-zinc-rare earth alloy sheets," *Acta Materialia*, Vol. 55, No. 6, pp. 2101–2112.

Brady, M. P., et al., 2017, "Rapid diffusion and nano-segregation of hydrogen in magnesium alloys from exposure to water," *ACS Applied Materials & Interfaces*, DOI: 10.1021/acsami.7b10750.

Chen, J., et al., 2016, "Effect of hydrogen on corrosion and stress corrosion cracking of AZ91 alloy in aqueous solutions," *Acta Metallurgica Sinica (English Letters)*, Vol. 29, No. 1, pp. 1–7.

Gray, J. E., and B. Luan, 2002, "Protective coatings on magnesium and its alloys—a critical review," *Journal of Alloys and Compounds*, Vol. 336, Nos. 1–2, pp. 88–113.

Gusieva, K., et al., 2015, "Corrosion of magnesium alloys: The role of alloying," *International Materials Reviews,* Vol. 60, No. 3, pp. 169–194.

Song, G.-L., 2005, "Recent progress in corrosion and protection of magnesium alloys," *Advanced Engineering Materials*, Vol. 7, No. 7, pp. 563–586.

Song, G.-L., and A. Atrens, 2007, "Recent insights into the mechanism of magnesium corrosion and research suggestions," *Advanced Engineering Materials,* Vol. 9, No. 3, 2007, pp. 177–183.

Thomas, S., et al., 2017, "The effect of absorbed hydrogen on the corrosion of steels: Review, discussion, and implications," *Corrosion*, Vol. 73, No. 4, pp. 426–436.

Ulivi, L., et al., 2007, "Quantum rattling of molecular hydrogen in clathrate hydrate nanocavities," *Physical Review B*, Vol. 76, 161401R.

II.3.B Solid-State Body-in-White Spot Joining of Al to AHSS at a Prototype Scale (Oak Ridge National Laboratory)

Zhili Feng, Principal Investigator
Oak Ridge National Laboratory
1 Bethel Valley Rd.
Oak Ridge, TN 37831-6064
Phone: 865-576-3797
E-mail: fengz@ornl.gov

Sarah Kleinbaum, Technology Manager
E-mail: sarah.kleinbaum@ee.doe.gov

Start Date: November 1, 2014 End Date: September 30, 2018
Total Project Cost: $3,187,000 DOE share: $1,497,890 Non-DOE share: $1,689,110

Executive Summary

This project aims to develop, mature, and validate near-production readiness of a solid-state spot joining technology to join prototype-scale automotive body-in-white (BIW) subsystems made of AHSS and 7000/6000 series high-strength Al alloys (HSA alloys) to meet the dissimilar metal joining challenges in high-volume mass production. Development of the proposed technology is built on the project team's previous success in developing and demonstrating two emerging, solid-state, friction-heating-based spot joining processes—friction bit joining (FBJ) and friction stir spot welding (FSSW)—to join AHSS to Al alloys at a coupon scale. The project is led by ORNL, with participation from Honda R&D Americas, Alcoa, DOW Chemical, L&L, Cosma Engineering, G-NAC, Mega-Stir Technologies, Brigham Young University, and The Ohio State University (OSU).

Accomplishments

- Completed refinement of joining bit geometry, material, and heat treatment combinations for joint strength, cost, and manufacturability (FY 2017).
- Completed joint performance evaluation of FBJ, adhesive bonding, and weld bonding (adhesive + FBJ) on galvannealed DP 1180 (DP 1180GA) and 7xxx series Al alloys at the coupon level (FY 2017).
- Demonstrated the interactive effects of multiple spot welds on mechanical performance with multi-spot-weld large coupons (FY 2017).
- Surpassed the Phase 1 Go/No-Go decision point for the FBJ process by meeting or exceeding all performance targets at the coupon level specified by industry team members (FY 2017).
- Developed a process model of FBJ with reasonable prediction of process conditions and temperature distribution (FY 2017).
- Evaluated corrosion performance of FBJ and Weldbonded (FBJ + adhesive) specimens (FY 2017).
- Refined and demonstrated a prototype automated joining bit feed system (FY 2017).
- Demonstrated FSSW and Weldbonded (FSSW + adhesive) processes for the target material combinations to meet the evaluation criteria (FY 2017).
- Developed an in-situ thermal distortion measurement technique using digital image correlation (DIC) to evaluate and guide a numerical thermal buckling model (FY 2017).

- Demonstrated initial success of a thermal buckling modeling tool to understand and predict thermally induced buckling of spot-welded and adhesively bonded Al-steel components due to the mismatch of the CTE (FY 2017).

Technology Assessment

- Target: Joining of ultra-high-strength steels (i.e., DP1180) with HSAs (i.e., 7xxx series Al alloys) to enable use of the highest strength steel and Al alloys for automotive body light-weighting. Refine and optimize the solid-state spot weld process to meet or exceed all performance targets, including combination with adhesive bonding. Examples of specific performance targets for weld-bonding (i.e., combining solid-state spot welding with adhesive bonding) are 15 kN tensile shear strength (TSS), 4.5 kN cross-tension strength (CTS), 10 million fatigue lifecycles at 0.75 kN, and a 10-week corrosion test per OEM testing specifications. The material combination evaluated will be 1.2 mm DP1180 AHSS and 2.0 mm 7xxx series HSA alloy.
- Gap: Conventional joining processes (i.e., resistance spot welding and self-piecing riveting) are not suitable or feasible for joining these material combinations in a cost-effective manner for high volume production vehicles.
- Gap: Part dimensional changes (i.e., distortion) and damage to joint strength due to thermal expansion mismatch are major technical hurdles that must be solved for successful use of dissimilar materials, such as HSA alloys and AHSSs in auto-body structures.

Project Introduction

This project focuses on developing and demonstrating two emerging solid-state, friction-heating-based spot joining processes—FBJ and FSSW—to join AHSS to HSA alloys from the coupon scale to the prototype part level. Application of these joining processes to HSA and AHSS in the BIW production environment requires further research and development to address several technical obstacles (e.g., joint performance, productivity, maintaining consistency of joint quality under expected dimensional variations of stamped and/or formed parts, and cost-effectiveness).

The project consists of two phases. During Phase 1, both FBJ and FSSW were developed and evaluated at a coupon scale. Furthermore, because corrosion management is a primary concern for joining of dissimilar materials, both FBJ and FSSW were combined with adhesive bonding as an isolation approach to protect the spot joint from galvanic corrosion. Finally, an integrated computational welding engineering modeling framework, developed by the project team over the years, is being adopted, refined, and applied. The purpose of the integrated computational welding engineering model is: (1) to refine and optimize the solid-state joining process; (2) understand microstructure changes in the weld region and their effects on the strength/properties of an individual joint; and (3) optimize joinability and joint performance at the prototype assembly level. During Phase 2, the “winning” process was selected for further development using prototype-scale BIW assembly level joining. Hardware of the winning joining process is being integrated with an assembly-line welding robot. Prototype BIW subsystems, selected by the OEM, will be welded and assembled with the robotic joining system to evaluate and validate production readiness of the joining technology for high-volume mass production BIW assembly. Al-steel joints, at both the coupon and prototype scales, will be tested and characterized to determine performance of the joints in accordance with the requirements in the funding opportunity announcement and a set of process and performance criteria from the OEM, Tier 1 supplier, and industry partners. The project assembled an excellent project team composed of automotive manufacturers and automotive part suppliers to carry out the proposed process research and development; engineering testing; joining system integration; and eventual commercialization and implementation.

Approach

FBJ is a newly invented solid-state joining process particularly suitable for dissimilar materials. FBJ creates a metallurgical bonded spot joint in two or more sheets of dissimilar metals through a combination of frictional drilling and bonding action of a high-strength consumable joining bit. FSSW is a derivative of the FSW process. A rotating fixed-pin tool is plunged into the upper sheet with normal force to generate frictional heat. The heated and softened material adjacent to the tool deforms plastically and a solid-state bond is made between two dissimilar metals, such as Al and steel. Figure II.3.B.1 illustrates both processes.

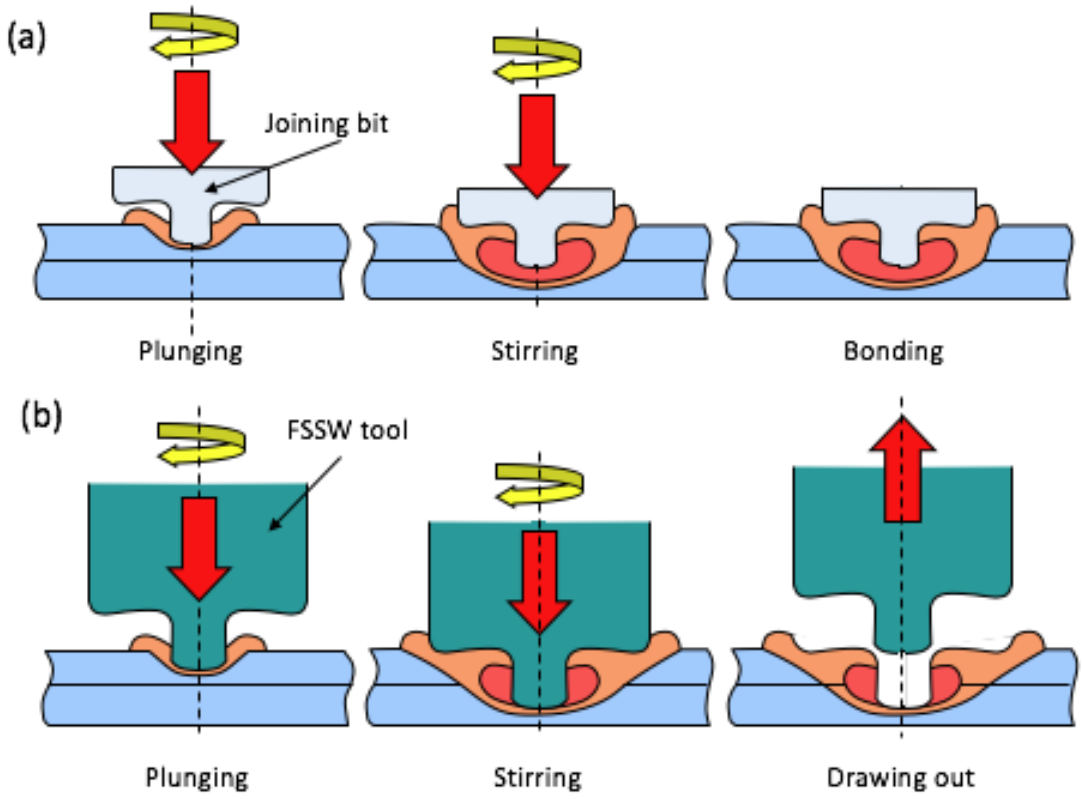

Figure II.3.B.1. Schematic of two emerging solid-state spot joining processes: (a) FBJ; and (b) FSSW. Source: ORNL.

Development of joining technology must be coupled with corrosion management, which is critical for automotive applications, especially for any joint between dissimilar materials. An adhesive was applied at all proposed contact locations between HSA and AHSS components to serve as an insulator. The solid-state joining techniques, adhesive bonding, and combination of the two were initially assessed using laboratory-scale coupons.

Modeling the joining process provides insights on physical phenomena (e.g., thermal and deformation histories) during joining projects. This model is a prerequisite for subsequent weld microstructure and performance modeling and understanding the effect of temperature rise due to joining on the CTE mismatch of two different metals. In addition, component level modeling provides an analytical modeling tool for assisting in design optimization to reduce welding distortion and stresses to an acceptable level. The integrated computational welding engineering approach has been adapted to refine the joining process and to predict joint performance under manufacturing conditions (e.g., paint-baking).

Technology Transfer Path

This project focuses on spot joining—the most common form of joining in BIW structures for high-volume production vehicles. Thus, it enables the broadest insertion of lightweight materials in BIW and has the highest potential among joining technologies for reduction of petroleum consumption, environmental impacts, and costs in the transportation sector.

The project has an excellent team comprising OEM, Tier 1 suppliers, welding equipment manufacturers, national laboratories, and research universities for both technology development and technology transfer. Participation of potential end users, material suppliers, and manufacturers from the outset allows the project to address various hurdles associated with commercialization, while providing a pathway for transfer of results to industry. The vertically integrated team provides an effective channel for technology transfer and commercialization.

Results

FBJ, Adhesive-Bonding, and Weld-Bonding Process Development

FBJ process development focused on the ability for mass production using the final target material combination (7xxx-2 and DP1180GA) identified by project industry partners and the low cost joining bit material. A Design of Experiment (DoE) was used to further refine the FBJ process along with the refined design of the joining bit. Table II.3.B.1 shows a summary of mechanical testing results for FBJ joints, without the use of adhesive bonding, indicating that joints of the final target material combinations have successfully met all the evaluation criteria. The average lap-shear strength of FBJ joints for the target material combinations is 10.7 kN, while the targeted value is greater than 5 kN, CTS and T-peel strength also exceeded the evaluation criteria of 1.5 kN. CTS showed particular progress with a strength nearly two times higher than the previous design's value of 2.54 kN. Finally, the fatigue life of FBJ specimens was evaluated with different fatigue mean loads and we met the evaluation criteria of 10^7 cycles at a suggested testing condition, as shown in Figure II.3.B.2.

Table II.3.B.1. Friction Bit Joining Joint Performance Summary for Final Target Material Combinations (P = pass, F = fail).

Material Combination	Target Strength	Disp. At Max Load (mm)
Thickness (mm)	—	2.0/1.2
FBJ Design/Material	—	3
	Target Value	Test Value
TSS (kN)	>5	10.7 (P)
CTS (kN)	>1.5	4.8 (P)
T-Peel (kN)	>1.5	1.89 (P)
TSS Fatigue (10^7 cycles)	0.75	P

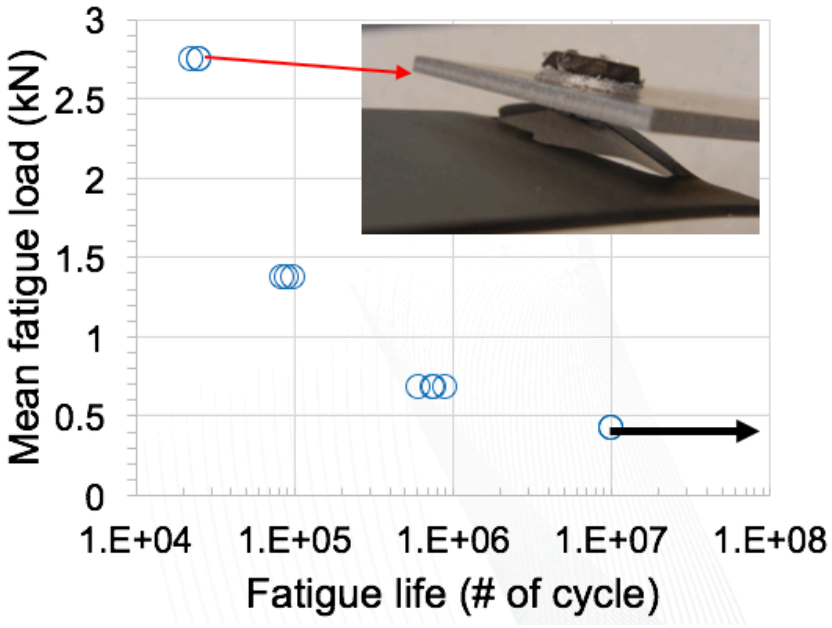

Figure II.3.B.2. Load versus number of cycles for fatigue life of FBJ lap-shear specimens with different mean fatigue loads. Source: ORNL.

After Phase I, FBJ process development with a single weld coupon, we investigated the performance of multiple weld configurations at a scale-up coupon level using the final target material combination. The main purpose of this scale-up coupon testing is to investigate whether there is a joint strength degradation in making multiple spot welds, and whether multiple welds would be additive in peak load. The effect of weld spacing on joint strength was also investigated. This is a necessary learning step before design and fabricating prototype parts in the next phase. For this study, we used the following dimensions of coupons: 120 mm width by 125 mm length with 20 mm overlap, with different weld pitches ranged from 60 mm to 80 mm with a 10-mm increment. Five lap-shear samples were created for each condition. Table II.3.B.2 shows a summary of the overall mechanical joint strength for two-spot weld configurations with different FBJ weld spacing. As can be seen, having multiple welds in a sample has resulted in additive peak loads in lap-shear testing without a joint strength reduction in the prior joint. Also, the average lap-shear failure load per weld ranges from 10 to 11 kN, which is close to the lap-shear failure load of 10 kN for a single FBJ weld coupon in the previous work. We also found that the overall mechanical joint strength didn’t change much as weld pitch increased from 60 mm to 80 mm.

Table II.3.B.2. Summary of Mechanical Joint Performance of Large Coupons with the Target Materials Using Two FBJ Weld Joint Case.

Sample ID	FBJ weld pitch (mm)	Peak lap-shear failure load (kN)	Average lap-shear failure load per weld (kN)
L-2017-02-10-10	60	20.8	10.4
L-2017-02-10-11	60	21.0	10.5
L-2017-02-10-12	60	21.3	10.65
L-2017-02-10-13	60	22.5	11.25
L-2017-02-10-14	60	21.5	10.75
L-2017-02-10-05	70	20.4	10.2
L-2017-02-10-06	70	22.2	11.1
L-2017-02-10-07	70	21.3	10.65
L-2017-02-10-08	70	22.1	11.05
L-2017-02-10-09	70	20.6	10.3
L-2017-02-15-00	80	22.5	11.25
L-2017-02-15-01	80	22.2	11.1
L-2017-02-16-01	80	22.9	11.45
L-2017-02-15-02	80	22.9	11.45
L-2017-02-15-03	80	22.3	11.15

An overall mechanical joint strength for three FBJ weld joint configurations is summarized in Table II.3.B.3. In general, having multiple welds in a sample has resulted in additive peak loads in lap-shear testing. When there were three spot welds in the large coupon with good condition, the average lap-shear failure load of 31.1 kN was achieved. However, two of the samples (marked as *) appear to have at least one bad weld in them, leading to a low average lap-shear load of 24.9 kN. That is, 20% of overall strength reduction was observed. This result will help and guide the design optimization with a reduced number of welds for a prototype part.

Table II.3.B.3. Summary of Mechanical Joint Performance of Large Coupons with Target Materials Using Three FBJ Weld Joint Cases.

Sample ID	FBJ weld pitch (mm)	Peak lap-shear failure load (kN)	Average lap-shear failure load per weld (kN)
L-2016-10-20-00	40	30.8	10.3
L-2016-10-20-01	40	32.5	10.8
L-2016-10-20-02	40	30.1	10
L-2016-10-20-03*	40	24.2	8.1
L-2016-10-20-04*	40	25.6	8.5
(*: has one weak FBJ joint)			

Adhesive bonding has been used increasingly in the automotive industry in the past few years to increase the strength and other performance of automotive body structures made of AHSS. Our previous research also revealed the benefit of using adhesive bonding as an insulation barrier for galvanic corrosion protection in dissimilar metal welds (Lim et al. 2015, Lim et al. 2014). In this project, weld bonding, which combines solid-state spot welding (FBJ or FSSW) with adhesive bonding, is considered essential for meeting performance

requirements at the component level. It is also an effective means for corrosion prevention in joining dissimilar metals. The team evaluated two different types of adhesives from two adhesive suppliers (i.e., DOW Automotive and L&L Products). We evaluated the overall lap joint strength of adhesive bonding and weldbonding (FBJ + adhesive) using a scale-up coupon for the final target material combinations. The optimum bond-line thickness that was found from the small coupon in the previous work was used. Due to an Intellectual Property Management Plan agreement, we cannot disclose the measured mechanical joint strength of each condition in this annual report. The failure mode of adhesive bonded samples shows cohesive failure, which is a failure in an adhesive layer. The failure of Weldbonded specimens had two distinctive stages in lap-shear tests. The first stage was cohesive failure of the adhesive bond, followed by failure in the FBJ joint.

FBJ Process Modeling Development

FBJ process modeling can provide insights on physical phenomena (e.g., thermal and deformation histories) during the joining process. This model is a prerequisite for subsequent weld microstructure and performance modeling and for understanding the effect of temperature rise due to joining and thermal expansion mismatch of two different materials. In this project, the FBJ process model was developed based on Lagrangian finite element formulation. Figure II.3.B.3 shows a comparison of FBJ process modeling (left image) with the experimental result (right image), depicting material flow approximating cross-sectional joint appearance. Furthermore, various FBJ welding conditions with different Z-axis plunge speeds and depths were simulated for process optimization, as shown in Figure II.3.B.4. Peak temperature increases as Z-axis plunge depth increases from 3.73 mm to 4.39 mm at a given Z-axis plunge speed. However, there is a minor effect on temperature change with various Z-axis plunge speeds. The details of the modeling approach and experimental validations are being prepared for a publication.

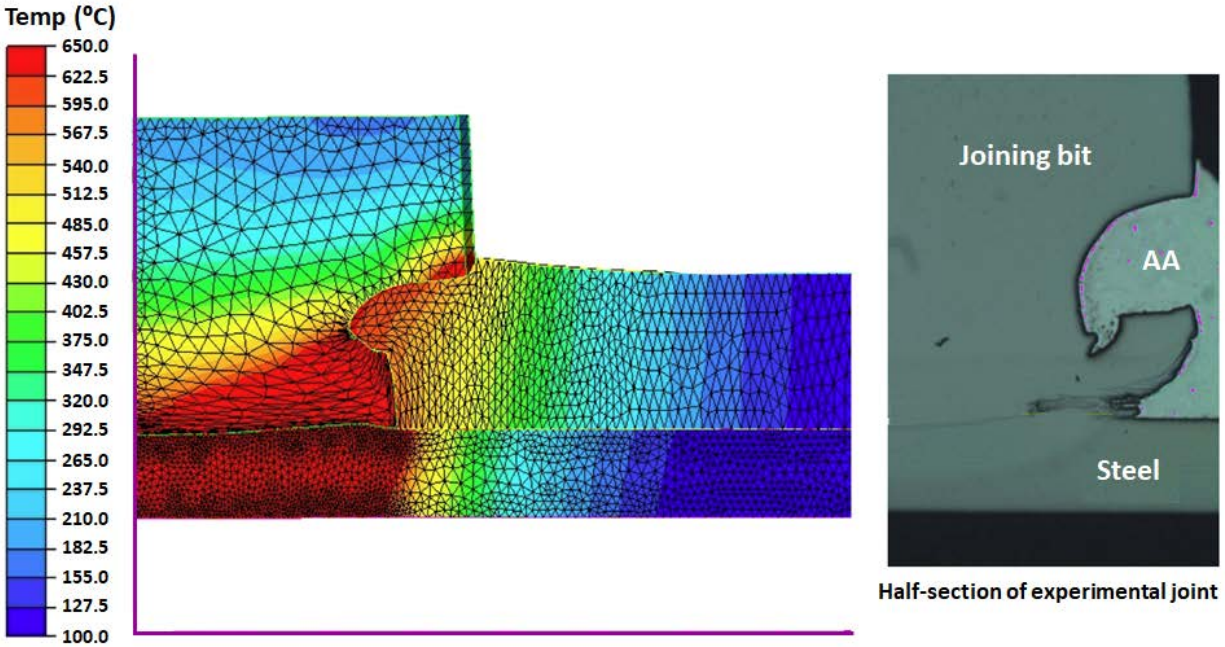

Figure II.3.B.3. Comparison of FBJ simulation (left image) with the experimental result (right image). Source: ORNL.

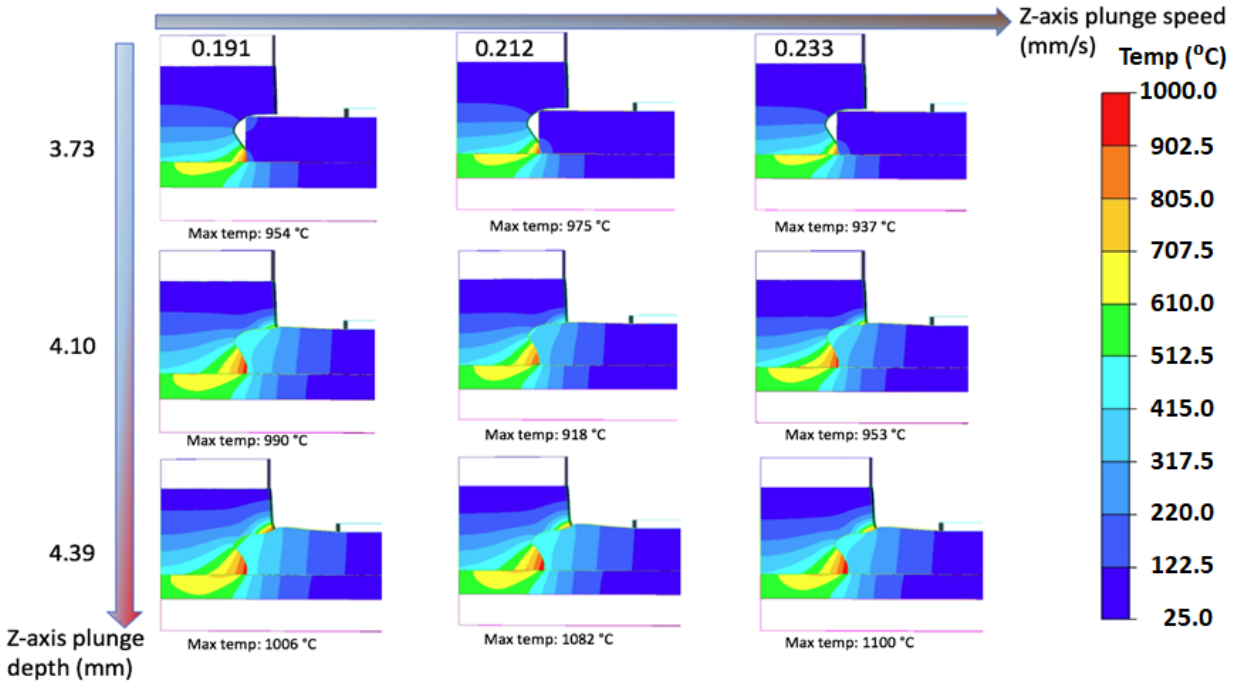

Figure II.3.B.4. FBJ process modeling with different Z-axis plunge speeds and depths. Source: ORNL.

Cyclic Corrosion Testing for FBJ and Weldbonded Specimens

Corrosion studies of dissimilar materials at the small coupon level will provide insight into corrosion behavior and its effective mitigation method. Cyclic corrosion testing (CCT) was used to evaluate the effect of corrosive media on joint strength. CCT was performed by automotive OEM specifications in two rounds. In Round 1 CCT, FBJ only specimens had essentially no remaining strength at the end of CCT, while Weldbonded (FBJ + Adhesive) had 73% and 77% strength reductions for using two different adhesives from two different adhesive suppliers. Based on this examination and the analysis of the failure behavior from Round 1 submission, procedures for sample preparation in Round 2 were modified to eliminate factors not associated with the joining processes developed in this project. Figure II.3.B.5 shows the results of Round 2 CCT—the normalized lap-shear failure load with different adhesives and surface coating/treatment conditions. It is noted that two colors on "control Pre-CCT" (e.g., blue and red) indicate different adhesives from different adhesive suppliers. Post-CCT lap-shear tensile test strength was evaluated at 50% and 48% of original pre-CCT strength, respectively, for the two different adhesives used. The result from Round 2 shows much improved corrosion resistance compared with Round 1. Pre-and post-CCT specimens were evaluated after lap-shear testing. Pre-CCT samples exhibit the ideal "cohesive" failure mode (i.e., the adhesive breaks apart). On the other hand, post-CCT examination revealed that, while the FBJ joint remained essentially at full strength after CCT, exfoliation of the Al substrate surface (underneath the adhesive layer) significantly weakened the adhesive bond. Interestingly, the adhesive maintained connectivity to the Al substrate, based on the findings of Round 2. Further modification of sample preparation was suggested, and weld samples are being prepared for third round of CCT.

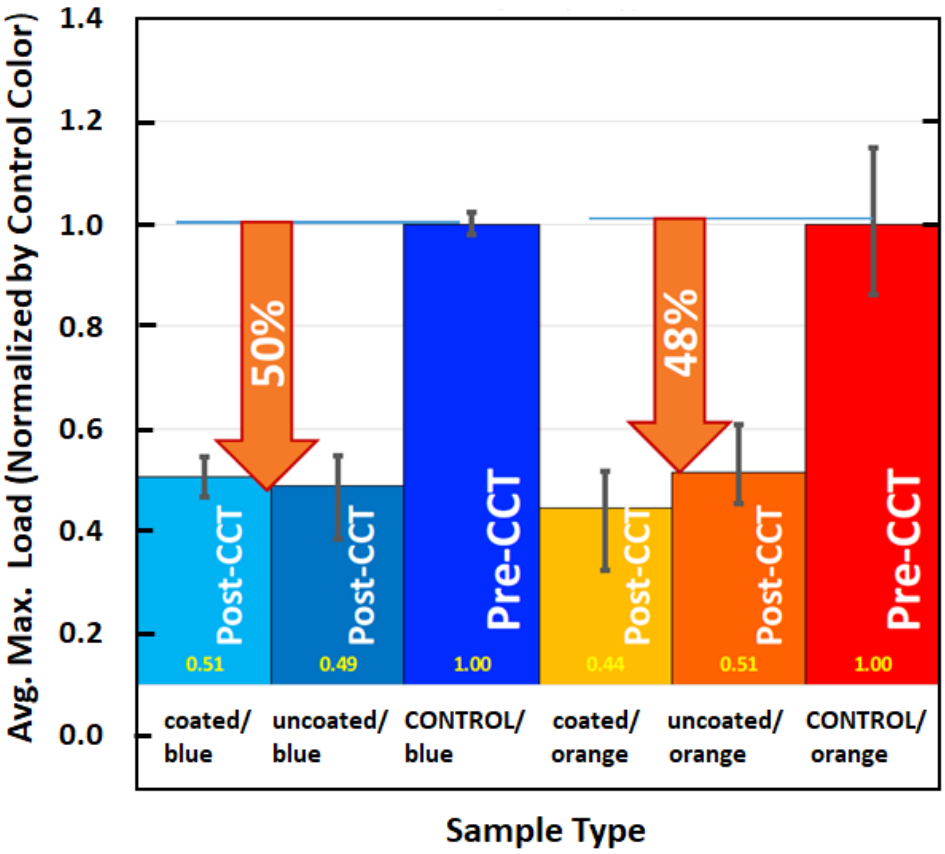

Figure II.3.B.5. Normalized lap-shear failure load with different adhesive and coating conditions for the second round CCT. Source: ORNL.

Automated Joining Bit Feed System Development for FBJ

An automated joining bit feed system is being developed as part of the FBJ system integration for the demonstration of prototype part joining. The conceptualized automated joining bit feed system was fabricated, assembled, and successfully demonstrated. After several design iterations to further simplify the design of the feed system, the project team decided to use a flexible clamping bar to hold and transfer the joining bit from a feed tube to the driver of the welder. This system uses the minimal amount of handling from the feed tube (only the distance that it takes to clear the path of the driver as it comes down to the weld, approximately 1 in.), as opposed to past designs, which transferred to bit between two or three mechanisms and transferred the bit up to 9 in. from the storage area to the welding area. Figure II.3.B.6 presents the refined automated joining bit feed system. This new version relocated the bit tray actuator above the main frame (i.e., the white plastic piece on the left). This new configuration gives us plenty of clearance. The new clamping bar is machined out of a solid piece of steel, as seen in Figure II.3.B.6(b). This monolithic design is also a compliant mechanism that provides enhanced repeatability as the clamp's natural relaxed state is to line up as designed. The bit is held using the spring tension of the metal, as well as a plate on the underside that applies additional clamping pressure. Figure II.3.B.6(b) and (c) show the extended metal tray with a clear plastic feed tube and joining bit siting on the steel clamp. The new bit tray handles bits reliably at the end of the feed tube, which was a prime concern given how fast the bits can come in through a feed tube. We have blown bits into the clamp with 100 psi of compressed air with a blowgun and it has successfully captured and easily released the bit with no damage to the bit or the clamp. Currently, we are working to incorporate a vibratory feed bowl to the system.

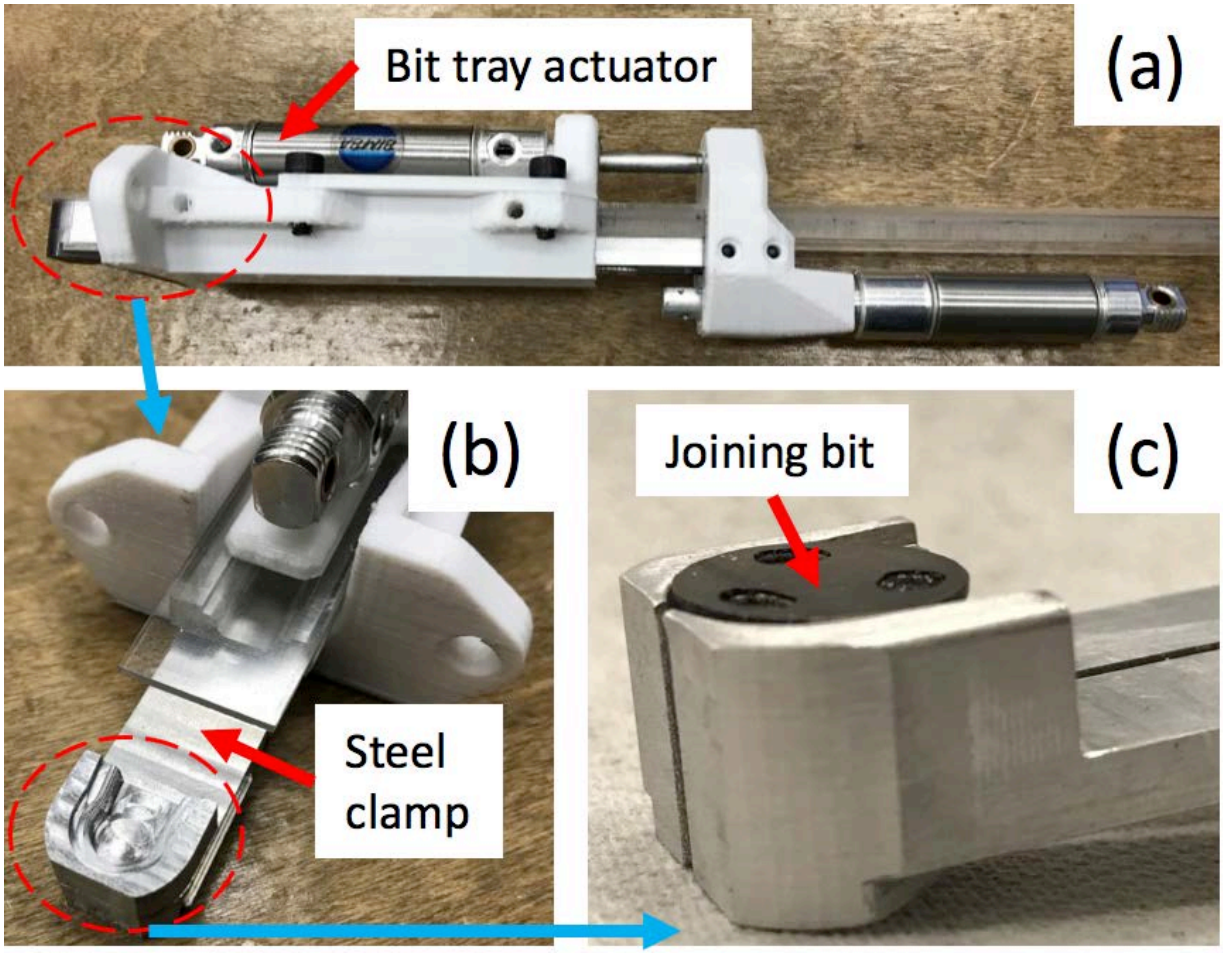

Figure II.3.B.6. Refined automated joining bit feed system: (a) side view; (b) joining bit tray; and (c) joining bit on the bit tray. Source: ORNL.

FSSW, Weldbonding (FSSW + Adhesive) Process Development

In FY 2017, the FSSW process was further optimized to improve mechanical joint strength by refining welding process parameters. Table II.3.B.4 provides a summary of TSS data. A maximum TSS of 7.9 kN was achieved, which is much higher than the strength values of FSSW (ranges from 2.0 to 4.0 kN) in open literature for Al to steel FSSW of similar thicknesses. The average TSS is 6.6 kN, which is about 20% strength improvement compared to the previous result of 5.44 kN. The target TSS strength specified by project OEM was 5.0 kN. Weldbonding (FSSW + Adhesive) was also successful in that it exceeds the strength specified by project OEM, as shown in Table II.3.B.5. Intellectual property protection policy prevents the disclosure of the actual testing results.

Table II.3.B.4. Summary of TSS for FSSW on the Final Target Material Combinations Using Modified FBJ Machine.

Sample ID	Tensile Shear Strength (kN)
20161028#01	6.1
20161122#06	5.3
20161122#07	6.5
20161122#10	7.8
20161122#14	5.0
20161122#15	7.9
20161122#16	7.3
Average	6.6
STDEV	1.2

Table II.3.B.5. Joint Performance Summary of a Weld-Bonded (FSSW + Adhesive) Specimen HSA/AHSS with Different Adhesives (P = pass, F = fail)

Material Combination	Target Strength	Weld Bonding (Adhesive A)	Weld Bonding (Adhesive B)
		7xxx-2–DP1180GA	7xxx-2–DP1180GA
Thickness (mm)	–	2.0/1.2	2.0/1.2
TSS (kN)	>15	P	P

In-situ Distortion Measurement by Digital Image Correlation Technique

The in-situ distortion measurement at the component level is to gain a comprehensive understanding and provide a potential solution for part distortion caused by the mismatch of the thermal expansion of Al and steel during paint-baking and curing of adhesives during the automotive body assembly process. The experiment will guide, improve, and verify the distortion model developed in this project. For FY 2017, a 475-mm long beam component was used to study the distortion. It was made of AA3003 (1.5-mm thick) on the top and DP1180GA (i.e., 1.2 mm thick) on the bottom, fixed by bolts at both ends with pitch distance of 425 mm.

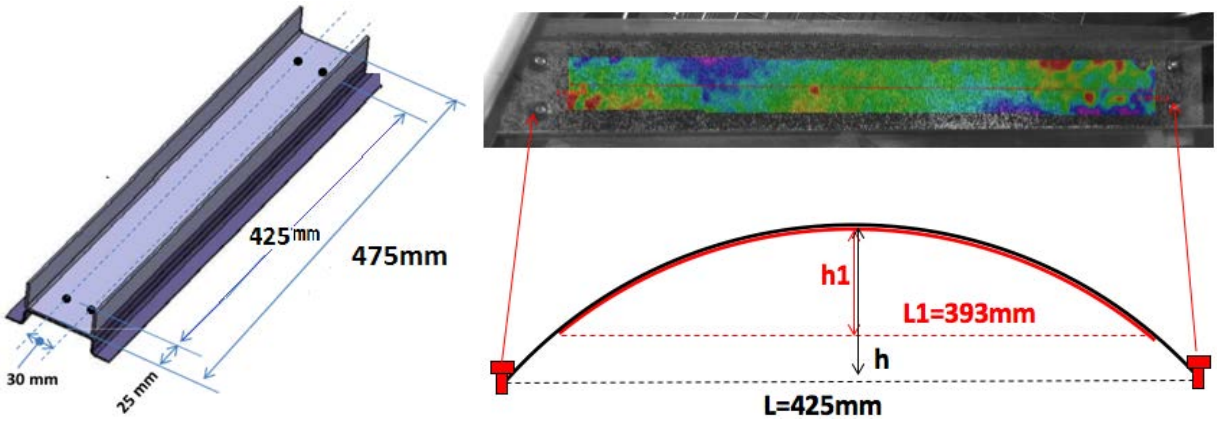

Figure II.3.B.7. A schematic of the component specimen (left) and DIC mapped area between the bolts on the Al part (right). Source: ORNL.

Figure II.3.B.7 schematically shows the geometry of the component and the DIC mapped area between the bolts. Out-of-plane bending distortion of the part was measured in an oven that mimics a paint-baking thermal

cycle. Temperature on the part was monitored and recorded at the three locations along the length direction. The paint-baking condition was achieved by heating the sample to 180°C in 20 min, holding for ~15 min, and cooling to 60°C in 7 minutes. Figure II.3.B.8 summarizes the out-of-plane distortion measurement with heating, holding, and cooling cycles. During the heating cycle, the maximum measured distortion was about 1.42 mm when peak temperature reached 180°C. Then, when the part was held at 180°C for 15 minutes, 1.66 mm was measured as the maximum distortion. The measurement shows residual 0.34 mm distortion in the Al part after the paint-baking condition. The experimental data will be used for comparison with numerical simulation data.

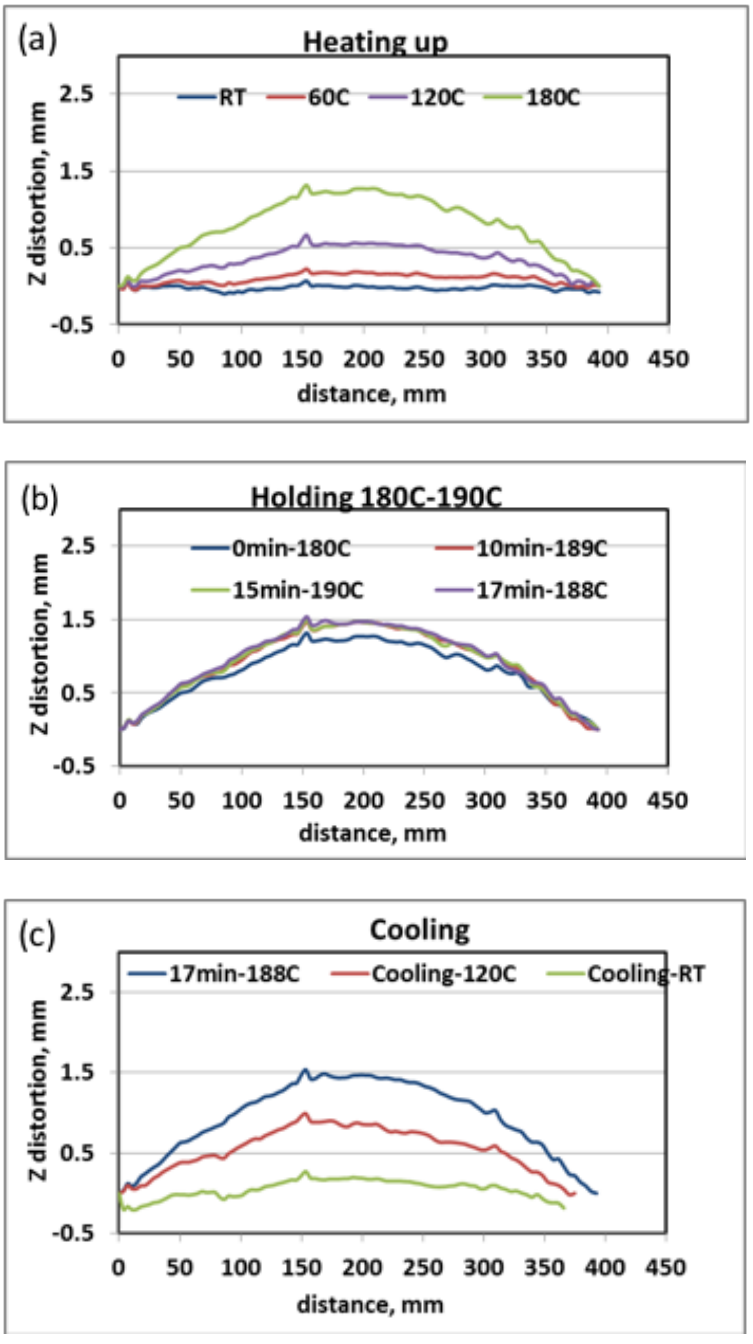

Figure II.3.B.8. Out-of-plane distortion measurement with the paint-baking condition: (a) heating cycle; (b) holding cycle and (c) cooling cycle. Source: ORNL.

Development of Component Level Thermal Distortion Model

The primary objective of component-level modeling is to understand the part distortion of the bi-metallic structure during the paint-bake process. The distortion mode was treated as a thermal buckling problem. Abaqus was used to simulate the thermal buckling. As shown in Figure II.3.B.9(a), the simulation model has two channels—one for Al and another for steel—that were bolted together. To reduce computational time, a quarter of the bi-metallic structure was modeled, as depicted in Figure II.3.B.9(b). Figure II.3.B.10 depicts the deflection profiles along the centerline of the Al piece at the peak temperature (i.e., 180°C) with different configurations. Due to symmetry, only half of the deflection is plotted. The results show a similar deflection profile between the model and the experiment. Given the accuracy of the DIC measurement of around 0.2 mm, reasonable prediction was obtained for this particular part configuration. The modeling effect (i.e., model development and validation) will continue in the next reporting period.

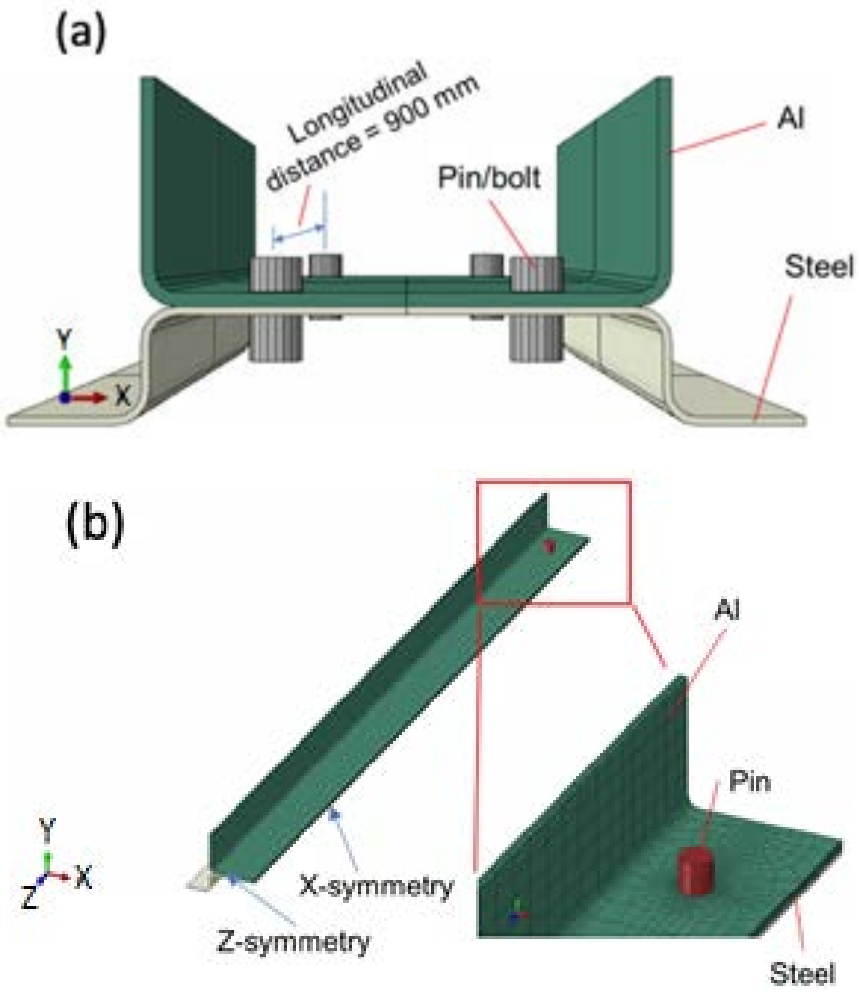

Figure II.3.B.9. Thermal buckling model setup: (a) overview of the entire geometry; and (b) zoomed-in view of the pin region. Source: ORNL.

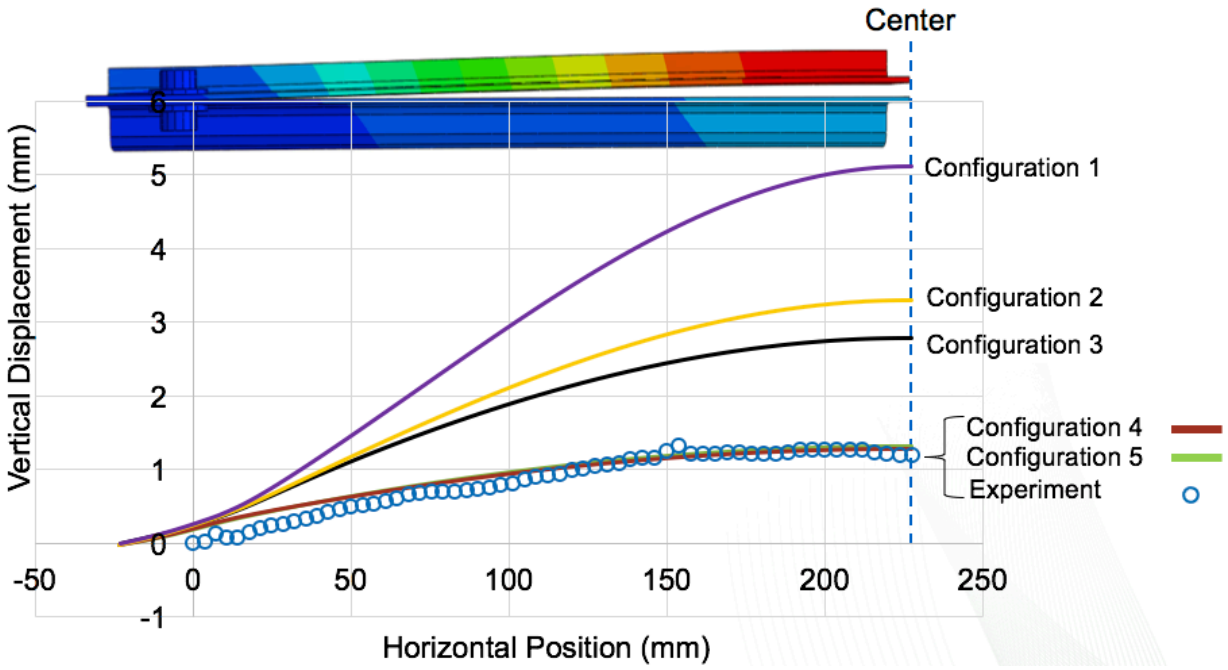

Figure II.3.B.10. Vertical displacement plots of the Al part taken from the centerline of the bi-metallic structure with different configurations. Source: ORNL.

Development of Predictive Model for Adhesive Bonding

The lap-shear model was designed with an Al sheet adhesively bonded on top of a steel sheet. For boundary and loading conditions, the steel's end is fixed, and the Al end pulled with a constant velocity. The adhesive was modeled using cohesive elements with traction and separation failure behavior in Abaqus.

Results calculated using the simulation model are shown in Figure II.3.B.11 and Figure II.3.B.12, where the corresponding experimental data tested are superimposed. It is noted that five colors of data points from experiment are used for comparison only. Due to intellectual property protection policy, the adhesive names are simply referred to as "Adhesive A" and "Adhesive B." Also, force and displacement are normalized. For Adhesive A, the deformation and failure behavior are well captured by the numerical model for both adhesive bondline thicknesses, as seen in Figure II.3.B.11. On the other hand, Adhesive B exhibits more metal-like plasticity, where the slope of force over displacement is tapered down toward failure initiation, as depicted in Figure II.3.B.12. The simulation model was able to capture the initial behavior and the displacement at which the failure initiates. However, it over-predicts the failure peak load. The over-prediction is larger for the case of 500 μm thick adhesive than the 300 μm thick case. In quick summary, this study reveals the complexity in deformation and failure behavior of adhesive material. Further effort is needed in the future to better predict the deformation behavior of more ductile adhesive.

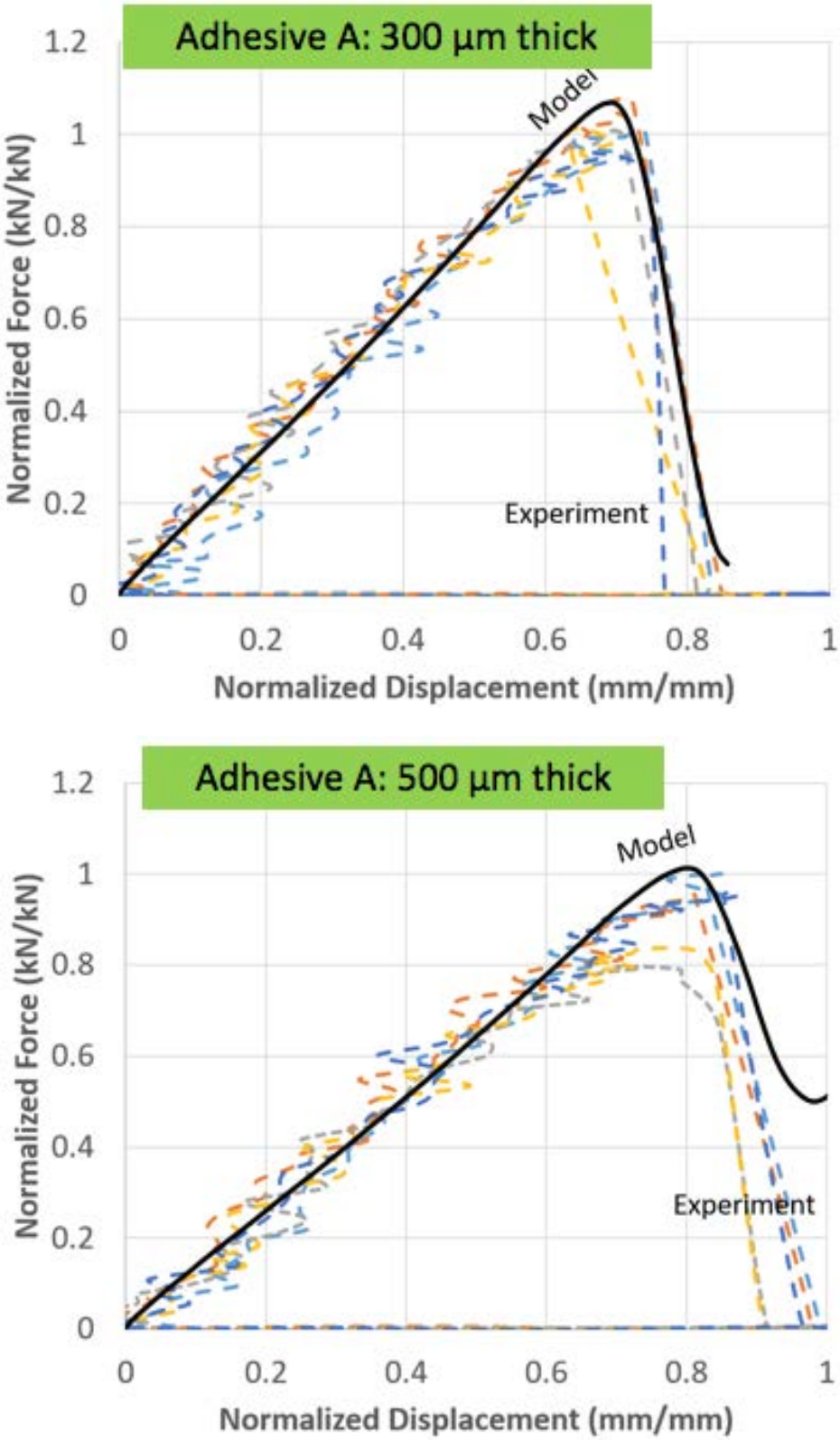

Figure II.3.B.11. Comparison of calculated and experimentally measured load-displacement curves for the lap-shear tensile testing using Adhesive A with different bondline thicknesses. Source: ORNL.

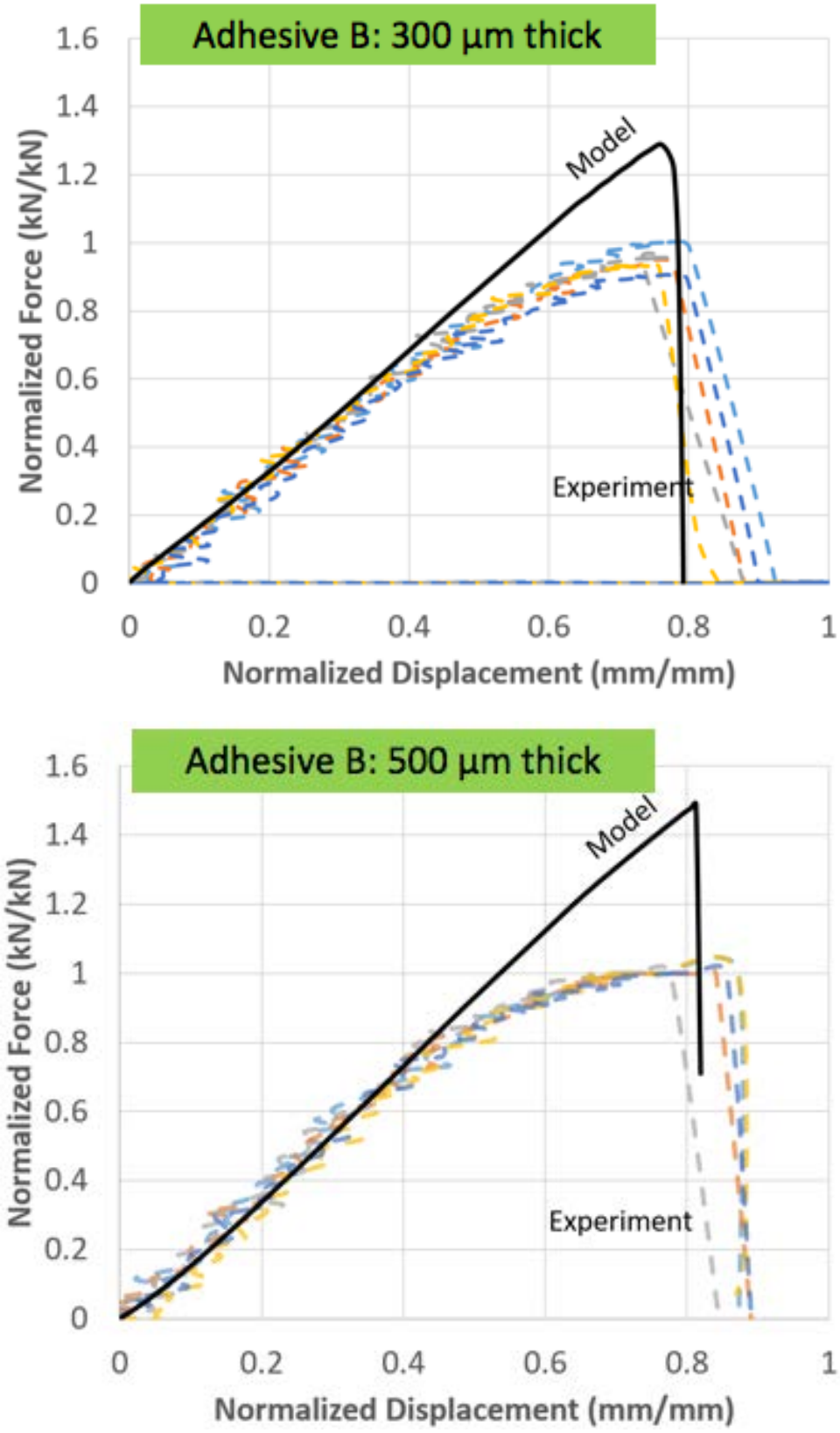

Figure II.3.B.12. Comparison of calculated and experimentally measured load-displacement curves for the lap-shear tensile testing using Adhesive B with different bondline thicknesses. Source: ORNL.

Conclusions

The team completed FBJ, adhesive-bonding, and weld-bonding (FBJ + Adhesive) process development. The target material combination (Al alloy 7xxx-2–DP1180GA) has met or exceeded all coupon-level performance target evaluation criteria set forth by the OEM and industry partners. Also, a significant improvement has been made on FSSW for the target material combination to meet coupon-level evaluation criteria. This is one of the major milestones and deliverables for Phase 1 of the project. Considerable progress has been made on FBJ process modeling, showing good agreement with the experiment. This is critical for microstructural modeling and component-part modeling. A prototype of the automated joining bit feed system was integrated with the FBJ process and successfully demonstrated at the MegaStir Technologies facility. The overall design of the automated joining bit feed system was further refined and finalized and is currently being fabricated and integrated with electronic and control systems. This is a major milestone and deliverable leading to Phase 2 of the project. Significant progress on component level modeling, including distortion and adhesive bonding, has been made.

Key Publications

Feng, Z. (2017). "Solid-State Body-in-White Spot Joining of Al to AHSS at Prototype Scale," *U.S. Department of Energy Hydrogen and Fuel Cells Program and Vehicle Technologies Office Annual Review and Peer Evaluation Meeting*, June 5–9, 2017, Washington, D.C., USA.

Lim, Y. C., L. Atwood, S. Wood, M. P. Miles, Z. Feng, and E. Boettcher, 2017, "Dissimilar materials joining of aluminum alloy and steel by friction bit joining process," *International Welding and Joining Conference*, April 11–14, 2017, Gyeongju, Korea.

Lim, Y. C., L. Squires, T.-Y. Pan, M. Miles, J. K. Keum, G.-L. Song, Y. Wang, and Z. Feng, 2017, "Corrosion behavior of friction bit joined and weld-bonded AA7075-T6/galvannealed DP980," *Science and Technology of Welding and Joining*, Vol. 22, No. 6, pp. 455–464.

Miles, M., L. Atwood, Y. C. Lim, Z. Feng, and E. Boettcher, 2017, "Simulation of friction bit joining of aluminum and steel using a Lagrangian finite element approach," *International Welding and Joining Conference*, April 11–14, 2017, Gyeongju, Korea.

References

Lim, Y. C., L. Squires, T.-Y. Pan, M. Miles, G.-L. Song, Y. Wang, and Z. Feng, 2015, "Study of mechanical joint strength of aluminum alloy 7075-T6 and dual phase steel 980 welded by friction bit joining and weld-bonding under corrosion medium," *Materials & Design*, Vol. 69, No. 0, pp. 37–43.

Lim, Y. C., L. Squires, T.-Y. Pan, M. Miles, Y. Wang, and Z. Feng, 2014, "Mechanical and corrosion properties of aluminum/steel spot welded by friction bit joining process for automotive applications," *67th IIW Annual Assembly & International Conference: Advanced Technology in Welding and Joining for Heavy, Automotive, and Electronic Industries*, July 13–16, 2014, Seoul, South Korea.

II.3.C Friction Stir Scribe Joining of Aluminum to Steel (Pacific Northwest National Laboratory)

Piyush Upadhyay, Principal Investigator
Pacific Northwest National Laboratory
902 Battelle Blvd.
Richland, WA 99352
Phone: 509-375-6591
E-mail: piyush.upadhyay@pnnl.gov

Sarah Kleinbaum, Technology Manager
E-mail: sarah.kleinbaum@ee.doe.gov

Start Date: August 1, 2014 End Date: September 30, 2018
Total Project Cost: $2,500,000 DOE share: $1,300,000 Non-DOE share: $1,200,000

Executive Summary

The purpose of this project is to develop a joining technology to demonstrate the fabrication of dissimilar Al-steel assemblies that can enable direct replacement of steel components with a lightweight Al alternative for high-volume applications. The objectives of the proposed work are to mature friction stir scribe (FSS) technology for implementation and to demonstrate the required Al-steel mechanical properties in industrially relevant components. Specifically, the project will develop the critical process technology, models, and tools necessary to advance the FSS method through experimentation, validation at the laboratory scale, and integration into a production-like environment to demonstrate the viability of FSS technique on industrially relevant components. Additionally, the project also aims to transfer technological understanding, tool designs, and parameters to the participating OEMs and suppliers to aid in the direct joining of Al and steel assemblies and components.

Accomplishments

- Demonstrated the FSS process with an integrated stationary shoulder to produce a joint between AA6022 and mild steel that: (1) demonstrated improved surface finish compared to conventional FSS tooling; and (2) maintained load-bearing capacity greater than 70% of base steel (FY 2017).
- Produced FSS joints between: (1) 3 mm thick cast Al and five sets of progressively harder steel (270 to 1180 MPa); and (2) 1.1 mm thick Surfalex™ 6s to 2.0 mm thick transformation-induced plasticity (TRIP) steel and 2.0 mm thick ultra-high strength (UHS) steel. Supplied joint coupons to corresponding OEM for individual evaluation, including corrosion and impact testing (FY 2017).
- Established welding parameters and tool design to produce FSS joints with adhesives interlayer and spot-welded multilayered steel (FY 2017).
- Completed "structure-property" computational model for Al-steel FSS joint with predictive capability (FY 2017).
- Established the process of technology transfer of the FSS process at KUKA Robotics Corporation (KUKA), a Tier 1 robotic supplier, and an OEM General Motors (GM) facility (FY 2017).

Project Introduction

This project addresses the need to join lightweight dissimilar metal structures made with Al and steel with the aim of achieving DOE's goal of increasing the efficiency of vehicle transportation by enabling more efficient multi-material solutions. Project collaborators include GM, Honda R&D Americas, and FCA. Collaborators

are actively involved in the project by providing materials, demonstration parts, and unique expertise related to the specific hybrid joining needs. KUKA, an automotive supplier and robotic integrator, is another project collaborator that provides a robotic implementation of the FSS technique in the automotive supply chain.

The technology to be developed, if successful, will provide a new method for enabling low-cost joining of Al alloy components to existing steel structures. Success in the project will enable direct replacement of steel components with Al that can achieve a mass savings of more than 40% while maintaining the form and function of existing steel structures. The project provides direct integration of joining technology to participating automotive OEMs for Al-steel assembly. PNNL is responsible for developing, characterizing, and transferring unique joining parameters for specific applications provided by participating collaborators. This includes applications ranging from body structures to assembly of Al chassis components onto a steel substructure. Each specific application will be developed sufficiently to determine the overall properties, welding parameter operating window, tooling and fixture requirements, and computational design specifications. Upon successful completion of development at the laboratory-scale, each participant will demonstrate a prototypical application-specific mockup using the FSS process.

Approach

To develop a joining technology that enables hybrid Al-steel structures and assemblies for high-volume automotive production lines, the project is divided into four main task areas. Task 1 focuses on initial joint development and characterization for each of the selected Al-steel combinations associated with the demonstration needs of each OEM. This includes developing weld parameters, tool design, and other process requirements for achieving acceptable joint performance. Task 2 is designed to expand the overall application of FSS; optimize tooling; introduce stationary shoulder and retractable pin technologies; and provide applicability across numerous alloys, thicknesses, and material combinations. This task ultimately will lead to a decision gate for use of the developed knowledge base in prototypical demonstrations associated with Task 3 by providing the information necessary to justify capital investments and product design using Al-steel joints.

Task 3 is divided into several subtasks that will emphasize the preparation process for commercialization and demonstrate the process in a production-like environment. This task focuses on supporting the transfer of technology into each of the OEM's facilities/suppliers to allow for prototypical demonstrations by each industrial participant. Task 4 will use the information developed in Tasks 1 and 2 to calibrate a numerical modeling tool for prediction of joint performance, failure location, and failure mode, and, finally, to validate the predictive tool against new material combinations and demonstration parts. Figure II.3.C.1 shows the Al-steel combinations selected by each OEM.

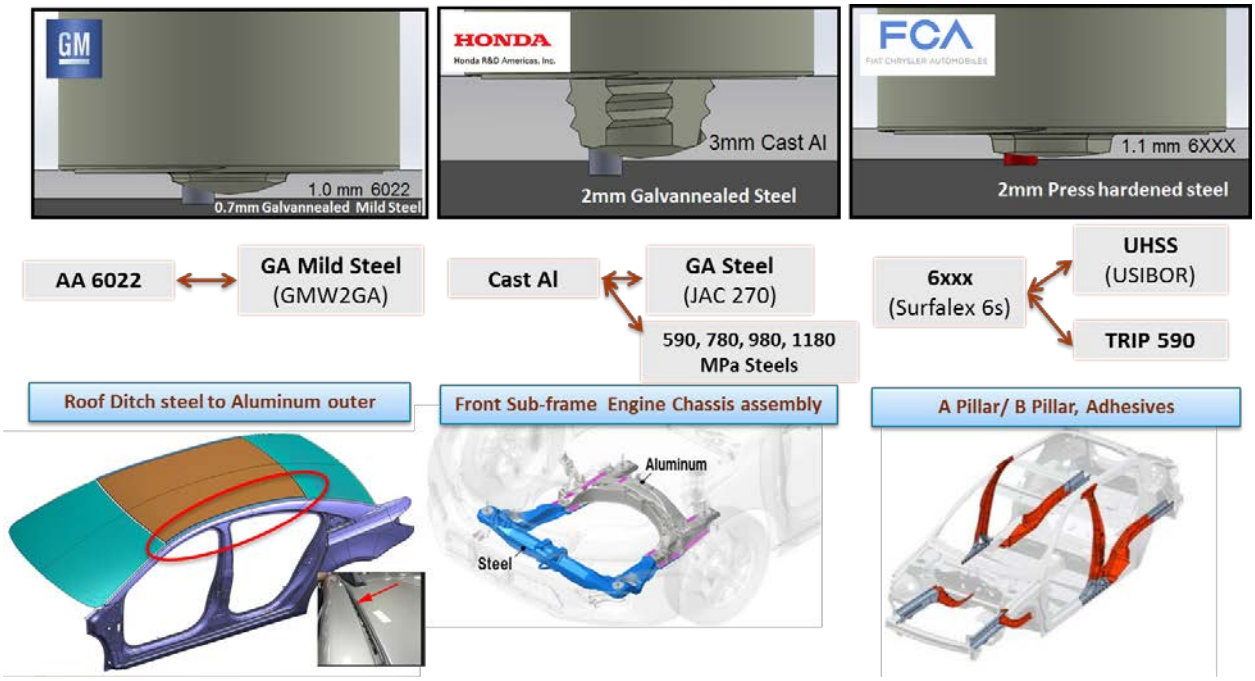

Figure II.3.C.1. Various Al-steel combinations used to evaluate FSS technique for this project. The details of each material combinations and OEM-intended applications are also shown. Source: PNNL, General Motors, Honda R&D Americas, Inc., and FCA, Inc.

Results

As a part of the project milestone in FY 2017, a continuous linear lap joint between a dissimilar pair of materials (e.g., 1 mm AA6022 and 0.7 mm galvannealed mild steel) was demonstrated using integrated tooling designed in previous phases of this project. The joint produced: (1) demonstrated improved surface finish compared to conventional FSS tooling; and (2) maintained load-bearing capacity greater than 70% of base steel. The FSS tool geometry and scribe design developed for conventional rotating shoulder tool and adapted for the stationary shoulder setup at PNNL is shown in Figure II.3.C.2. Consequently, process parameters for stationary shoulder FSS welds between the Al and steel pair were developed. A representative joint coupon from which samples for lap-shear testing were extracted is shown in Figure II.3.C.2, right. The results of the lap-shear test are presented in terms of load per units weld width versus displacement in Figure II.3.C.2. The average load-bearing capacity of the joint for the representative plate reported is 171.6 ± 6 N/mm or ~85% of the corresponding value for the base steel shown by the red dotted line.

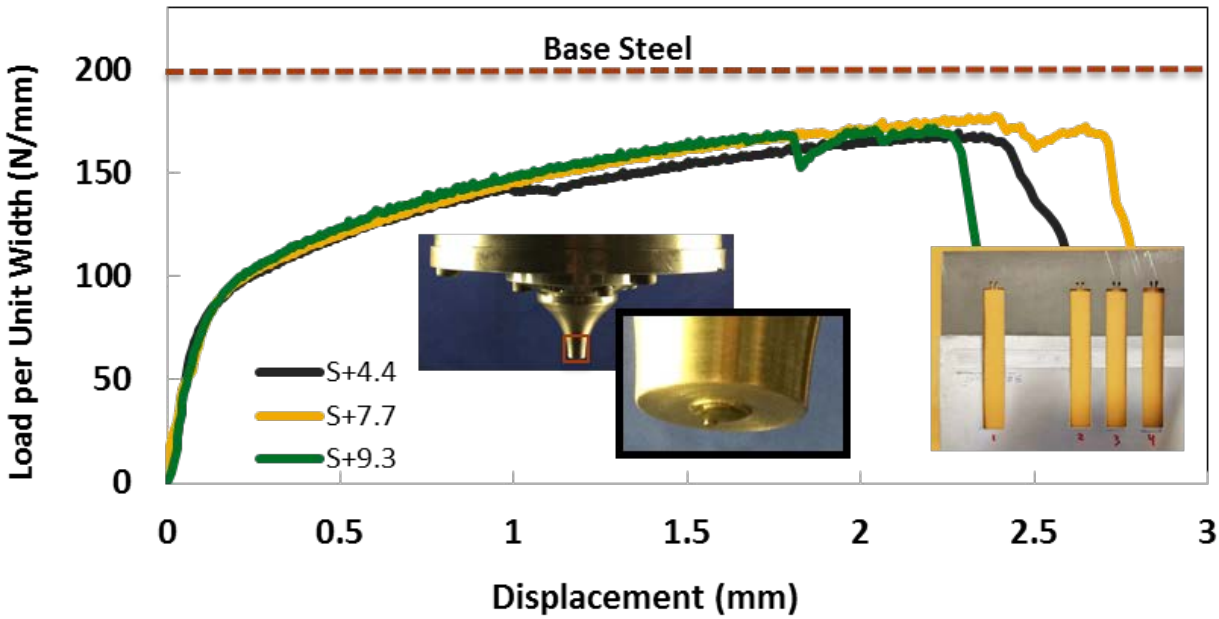

Figure II.3.C.2. Load per unit weld length versus displacement plots obtained from lap-shear testing of Al-steel joints. Legend indicate distance (in inches) of the extracted sample from the weld start. Integrated stationary shoulder and FSS tool (middle inset). Representative joint panel showing water jet cut lap-shear samples (right corner). Source: PNNL.

One of the major advantages of adopting stationary shoulder tooling as opposed to conventional rotating shoulder friction stir is the ability to produce welds with a better surface finish (Hovanski 2017). A significant improvement in weld surface roughness compared to rotating shoulder FSS joints was observed, as shown in Figure II.3.C.3 (Hovanski 2017). This demonstrated ability of dissimilar joining with high-quality surface finish can allow greater flexibility to OEMs like GM, Honda, and Fiat Chrysler Automobiles, particularly in outer body panel applications. It is important to note that since the heat generation from rotating shoulder is absent, the energy input per unit weld length is reduced in stationary shoulder weld assuming all other factors remain constant. Accordingly, there is a need to add heat into the workpiece. This can be accomplished in two ways: (1) by increasing the tool RPMs; or (2) by decreasing the welding speed. In these experiments, the gantry machine at PNNL was already operating at peak RPM so we decreased the welding speed (reduced to 100 mm/min) to accommodate defect-free welds with the stationary shoulder. It is anticipated that this welding speed can be increased with the use of higher RPMs that is typically available on robotic platforms.

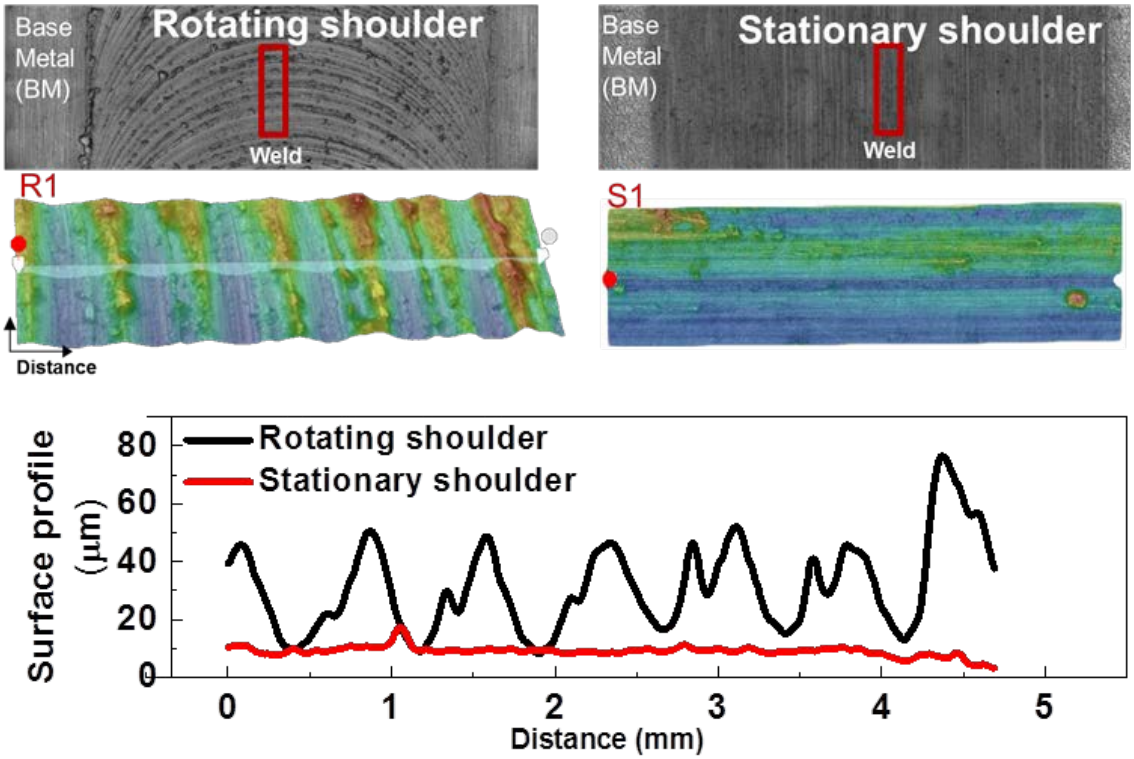

Figure II.3.C.3. Weld surface comparison between the conventional rotating shoulder and integrated stationary shoulder FSS tool. Surface striations associated with advance per revolution of FSS is apparent in rotating shoulder (top left), while smoother surface is obtained with the use of the stationary shoulder tool. Source: PNNL.

In continuation of FY 2016 efforts on developing FSS parameters for joining 3 mm thick cast Al to steel panels, we expanded the FSS process to enable joining of cast Al to a range of progressively harder steels. The steels evaluated were 270 MPa (2 mm), 590 MPa (1.8 mm), 780 MPa (1.6 mm), 980 MPa (1.4 mm), and 1180 MPa (1.2 mm). Figure II.3.C.4 shows representative lap-shear test data from all five of the steel-Al joints. While lap-shear strength values for different steels remained fairly consistent at about 300 N/mm, the measured extension (representative of the energy absorption) decreased gradually with the increase in strength of the steel. For instance, while the elongation measured for 270 MPa steel is close to 1.1 mm, it is almost three times lower for 1180 MPa steel at around 0.45 mm. All the welds shown in Figure II.3.C.4 were made at 500 mm/min. While all the other welding parameters were kept constant between different steels, the required plunge depth (PD) was adjusted with the increase in hardness of the steel.

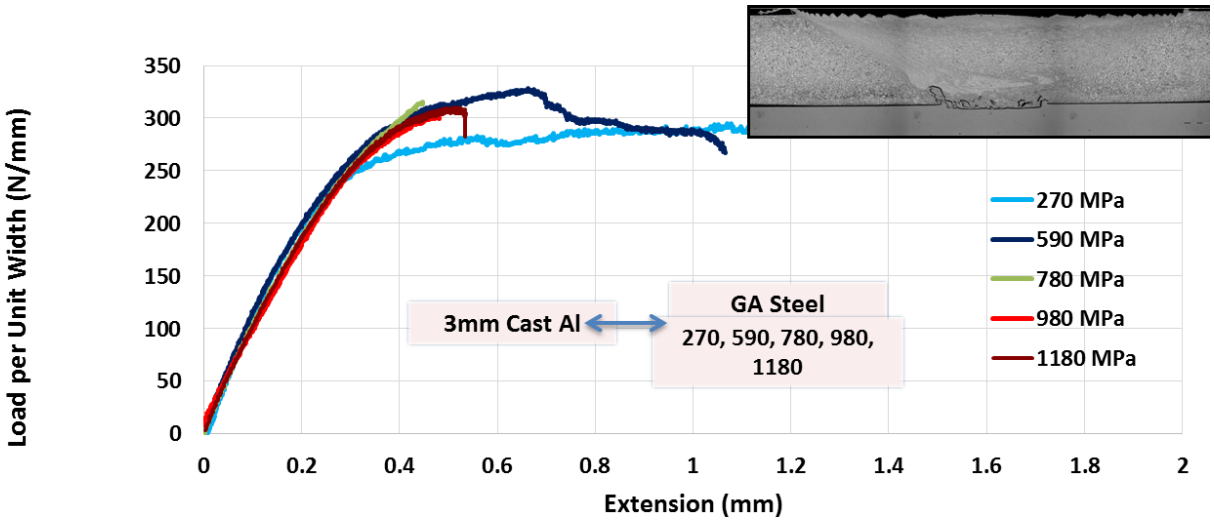

Figure II.3.C.4. Load per unit weld length plotted against measured extension during lap-shear testing of the FSS joint between cast Al (3 mm) to various steels as indicated with their yield strength values. A characteristic joint cross-section is shown in the inset. Source: PNNL.

It is important to note that the extent of scribe engagement into the steel sheet is one of the crucial aspects of the FSS process (Upadhyay 2017, 147-155. This is especially true for relatively thin sheets. Figure II.3.C.5 shows a comparative example of the effect of a small change in the commanded PD in resulting joint interface geometry, lap-shear test results, and fracture modes. The two welds shown in Figure II.3.C.5 were made at 280 mm/min using the identical tool and welding parameters. The only difference between the two is the commanded PD during FSS: PD = 0.8 mm for Figure II.3.C.5(a) and PD = 0.95 mm for Figure II.3.C.5(b).

In the case of a weld made at PD = 0.8 mm, as shown in Figure II.3.C.5(a), all except the sample extracted from the near plunge region of the weld fractured away from the weld region in the base metal resulting in the joint strength close to the base Al. In contrast, a weld shown in Figure II.3.C.5(b) made at PD = 0.95 mm (everything else remaining the same) exhibited poor joint strength. The joint cross sections show that, with a slight increase in PD, the engagement of the scribe into the steel resulted in the formation of a very large hook that penetrated around 80% of the Al sheet thickness. The fracture, in this case, occurred via cracking of the nugget in contrast to base material failure in Figure II.3.C.5(a). This observation shows that maintaining good control over the FSS tool is critical to obtain desired weld quality and joint strength. For a robotic application, this entails the establishment of a “z-negative” limit such that the scribe does not penetrate deeper than designed. Additionally, a force control algorithm can be applied in concert with a z-negative limit to avoid overplunging of the scribe tool into the steel.

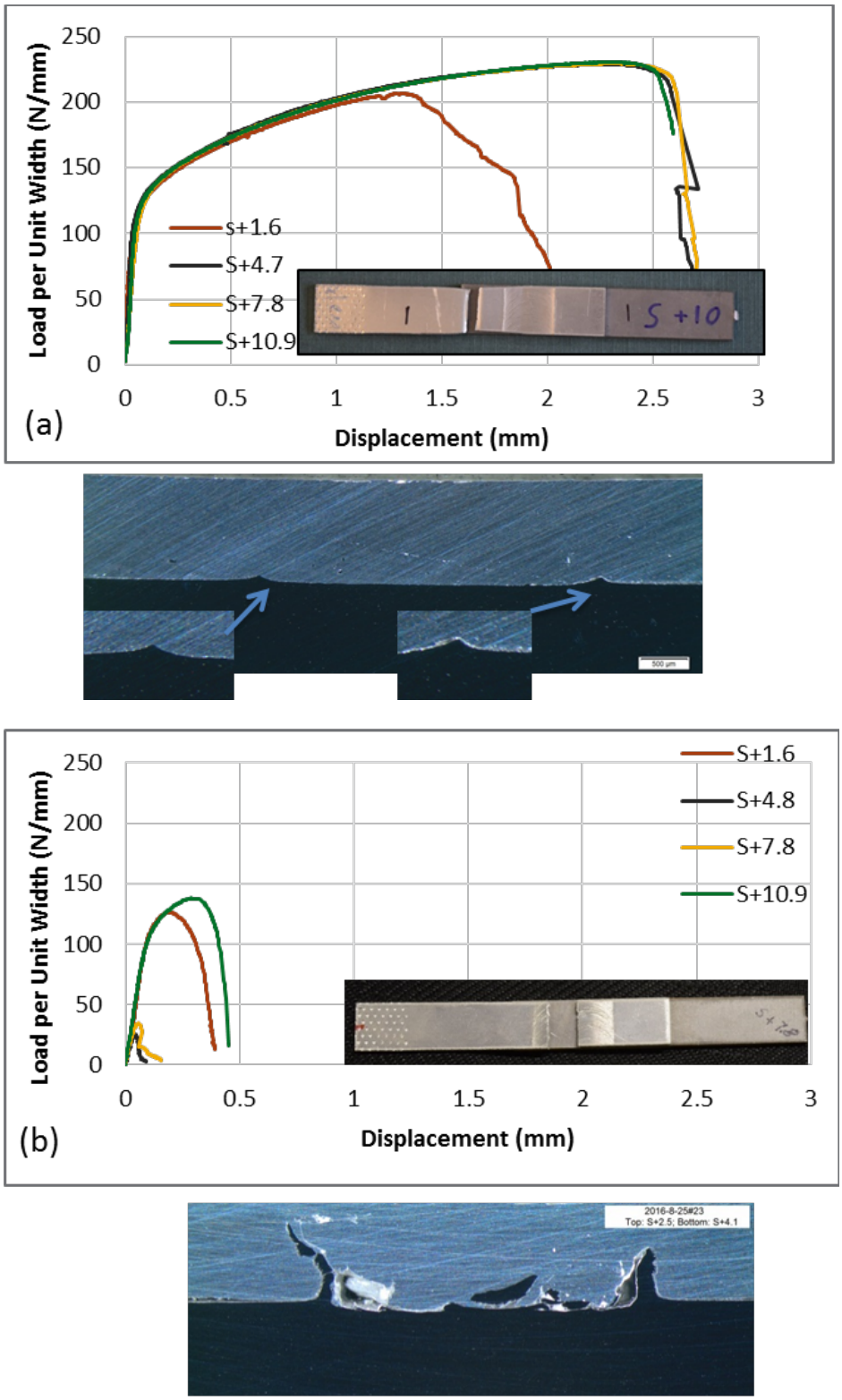

Figure II.3.C.5. A comparison of joint performance (1.1-mm Surfalex™ 6s and 1.6-mm TRIP 590) with changes in welding parameter. Legend indicate distance (in inches) of the extracted sample from the weld start. Results of lap-shear tests and characteristic joint interface and fracture modes are shown for two cases with different PD, but everything else remaining constant. (a) PD = 0.8 mm. (b) PD = 0.95 mm. Source: PNNL.

While coupon level FSS joining, process optimization, and related discovery was the focus of FY 2016 efforts, in FY 2017 a considerable amount of resources moved towards assessment of the FSS process with the added complexity of near-prototype joining requirements. The two added requirements that were evaluated individually and in combination were: (1) the addition of an adhesive interlayer; and (2) joining to a multilayered steel stack joined with resistance spot welds. It is well known that a continuous adhesive interlayer creates an electrical barrier between bare Al and steel which is desirable to prevent galvanic corrosion. After adjustment of welding parameters, effective joints between 1.1-mm Surfalex™ and 1.6-mm TRIP 590 steel with an adhesive interlayer were obtained. The joint was then subjected to a curing regime provided by the relevant OEM. For the case of 1.1-mm Surfalex™ and 1.6-mm TRIP 590 steel, the curing cycle consisted of a standard paint bake cycle followed by the OEM. A joint efficiency of ~80% compared to the adhesive-only joints was demonstrated.

For joining a roof ditch assembly to the roof outer panel, GM desired evaluation of multilayered steel joined with resistance spot welds to be joined to Al using FSS. An adhesive interlayer was also introduced. To this end, a continuous bead of adhesive was applied on the top steel layer and 1 mm thick Al was then overlapped and FSS welded. A welding parameter of 1 m/min at 1950 rpm was used to make a defect-free joint between the Al and steel pair, as shown in Figure II.3.C.6. In cases where the welding speed was higher than 1 m/min (1.5 and 2.0 m/min were tried), intermittent defects associated directly with the location of surface dips corresponding to the resistant spot weld location were observed. In these cases, the adhesive that came in direct contact with the rotating scribe is observed to have ejected up through the weld nugget creating an intermittent crown void in the welded Al/steel joint. Nevertheless, we believe that with increased RPM (>1950 RPM available in the gantry machine at PNNL) this surface breach at higher welding speeds can be avoided.

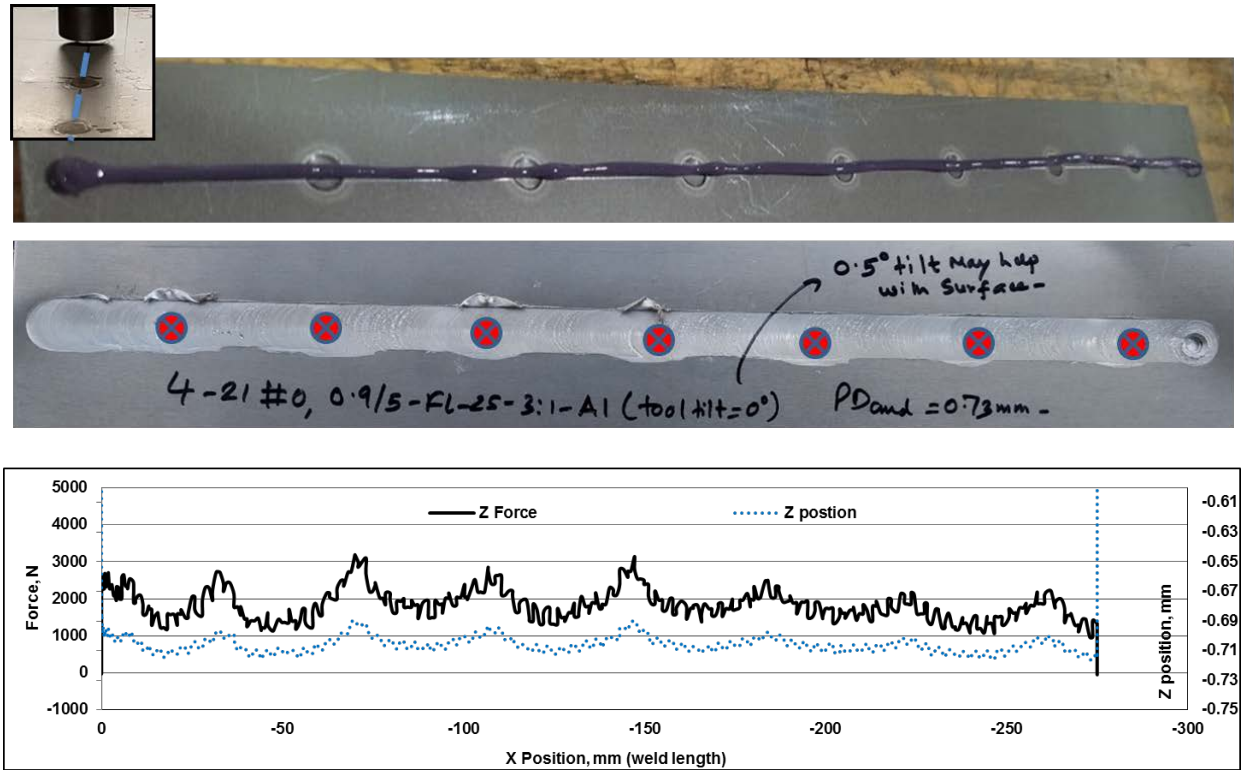

Figure II.3.C.6. Adhesive interlayer applied to spot-welded layer steel sheet (top). Near optimized joint surface for FSS weld performed over spot-welded steel and adhesive interlayer (middle). Z force and z position plotted against the scaled weld length (bottom). Source: PNNL.

It is important to note that the indentation (surface dips), as shown in Figure II.3.C.7, associated with the spot-welded locations are on the order of 50% to 70% of the thickness of the Al sheet, or the length of the FSS tool pin. The direct result of these sudden geometric surface dips, as seen by the approaching tool, can be observed in tool force and displacement plots shown in Figure II.3.C.6. The local peaks in z force observed in this plot are coincident with the location of the indentations in the steel sheet. Thus, the joint characteristics at the spot-welded location might be different than the remainder of the sheet, which is fairly flat. Two 1-in.-wide samples obtained from the weld shown in Figure II.3.C.6 were lap shear tested. Both the extracted samples contained the spot weld near its mid-section. Average lap shear strength of 221 N/mm (75% load-bearing capacity compared to base Al) was observed.

Figure II.3.C.7 shows a representative cross section for a welded joint. The cross section was obtained from a location close to the centerline of the spot-welded indent. As the FSS tool plunged into the stack up with adhesive interlayer, almost all the adhesive from the bottom of the pin and shoulder area (nugget) is squeezed away towards the edges. However, outside the shoulder region on both sides of the Al/steel interface, the presence of continuous adhesive interlayer is confirmed. This provides the evidence that the FSS process can be used in conjunction with an adhesive interlayer to provide a barrier for electrolyte flow and thus prevent susceptibility to bimetallic galvanic corrosion.

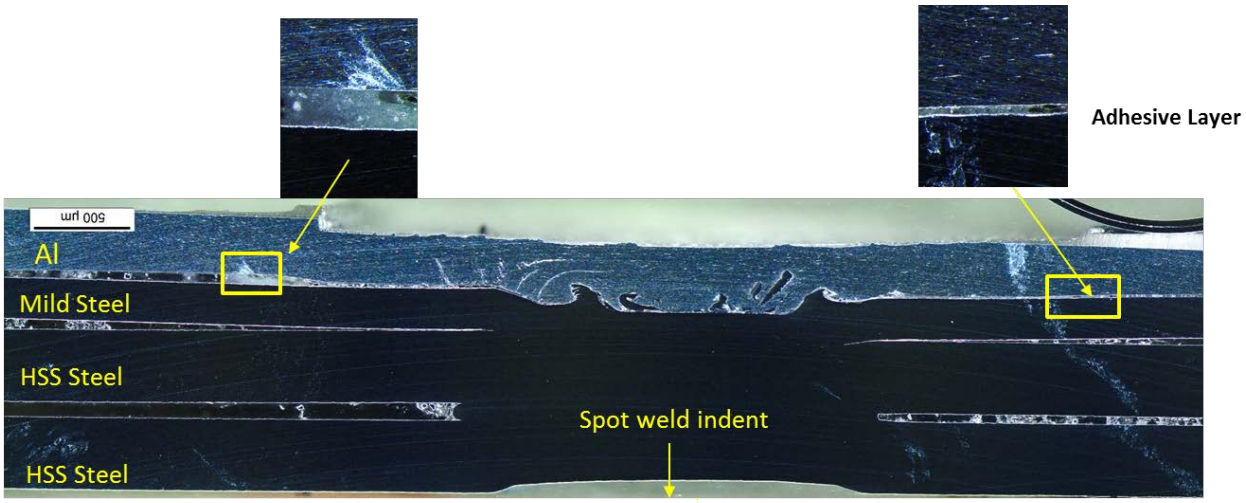

Figure II.3.C.7. Darkfield macro-cross section of FSS Al/steel joint. The steel consisted of three different layers that were spot welded together. The FSS joint between 1-mm-thick Al 6022 and the steel stack was made with the adhesive interlayer. The presence of adhesive interlayer of either side of the weld is shown. The bottom picture shows the relative location of the cross section. Source: PNNL.

Corrosion Testing

In FY 2017, one of the project partners, GM R&D, completed corrosion testing on a batch of Al-steel (1 mm AA6022 and 0.7 mm mild steel, without any adhesive interlayer) FSS joints supplied by PNNL. The following tests were carried out:

1. Panel corrosion testing as per GMW15356.
2. Corrosion/undercutting scribe creep back as per GMW15282.
3. Coating thickness evaluation using ISO 2808:2007.
4. CCT as per GMW14872.

The CCT was performed to assess 15-year durability of bimetallic components. This entailed 43 cyclic exposures as detailed in the GMW14872 standard for materials test procedure. An electrocoated Al/steel joint at the beginning and end of the 15-year accelerated test is shown in Figure II.3.C.8. Film thickness, corrosion ratings, and scribe creepback for the samples are summarized in Table II.3.C.1. As per the pertinent corrosion standard (GMW14872), the tested FSS joint passed the corrosion test administered to the qualifying component.

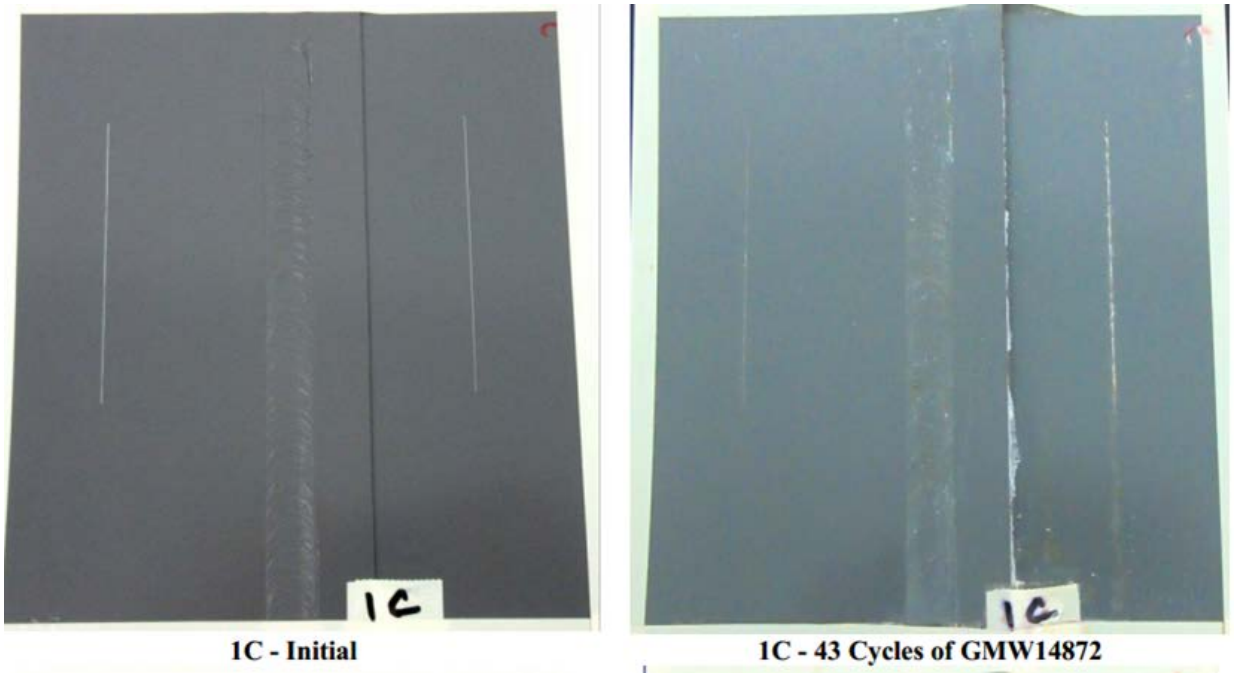

Figure II.3.C.8. Electro-coated Al-steel joint before and after 43 cycles of corrosion testing. The scribe marks in both Al and steel interface do not show any significant corrosion. Source: General Motors.

Table II.3.C.1. CCT Data.

Sample Identification	Test Side	Total Film Thickness (µm)	GMW 15356 Corrosion Rating	Scribe Creepback (mm)			
				$C_{Left, Max}$	$C_{Right, Max}$	C_{Max}	$C_{Average}$
1B	Aluminum	20	10	0			
	Steel		9	2.4	2.4	4.8	2.7
1C	Aluminum	20	10	0			
	Steel			2.1	2.2	4.3	2.6
1D	Aluminum	20	10	0			
	Steel			2.2	2.4	4.6	2.6
1E	Aluminum	20	10	0.5	0.5	1.0	0.5
	Steel		9	1.9	2.2	4.1	2.4

FSS Tool Durability with Ultrahigh Strength Steel

As discussed elsewhere (Upadhyay 2016) we observed a rapid buildup edge formation around the scribe cutter while making welds with UHS (1500 MPa) steel. During this FY research activities, we evaluated some alternative tool materials as a possible alternative to our tool material of choice (H13 for the FSW tool and tungsten-carbon-cobalt (W-C-Co) for the scribe). Figure II.3.C.9 shows the degree of tool degradation after 36 in. of FSS weld using two different uni-body tool designs. The W-C-Co is shown in Figure II.3.C.9(a) and the polycrystalline cubic boron nitride (PCBN) tool is shown in Figure II.3.C.9(b). Unlike conventional

grinding methods, both tools were fabricated using laser cutting of required tool geometry including the cutter scribe. Both the uni-body tools exhibited relatively lesser extent of bonding of machined steel material around the tool and scribe surface, thus resulting in less susceptibility of buildup edge formation. The buildup edge formation in the W-C-Co uni-body tool, for example, was dislodged from the tooltip upon quick chiseling by a sharp edge (e.g., drill bit) as shown in Figure II.3.C.9(a). Compared to the W-C-Co uni-body tool, the PCBN tool exhibited lower extent of buildup edge; however, the scribe appears to have slightly chipped off at the edge. These two candidate materials for the FSS tool and their performance evaluation show that the FSS tool life for significantly hard steels like UHSS (1500 MPa) may be resolved by using proper material selection and uni-body tool design.

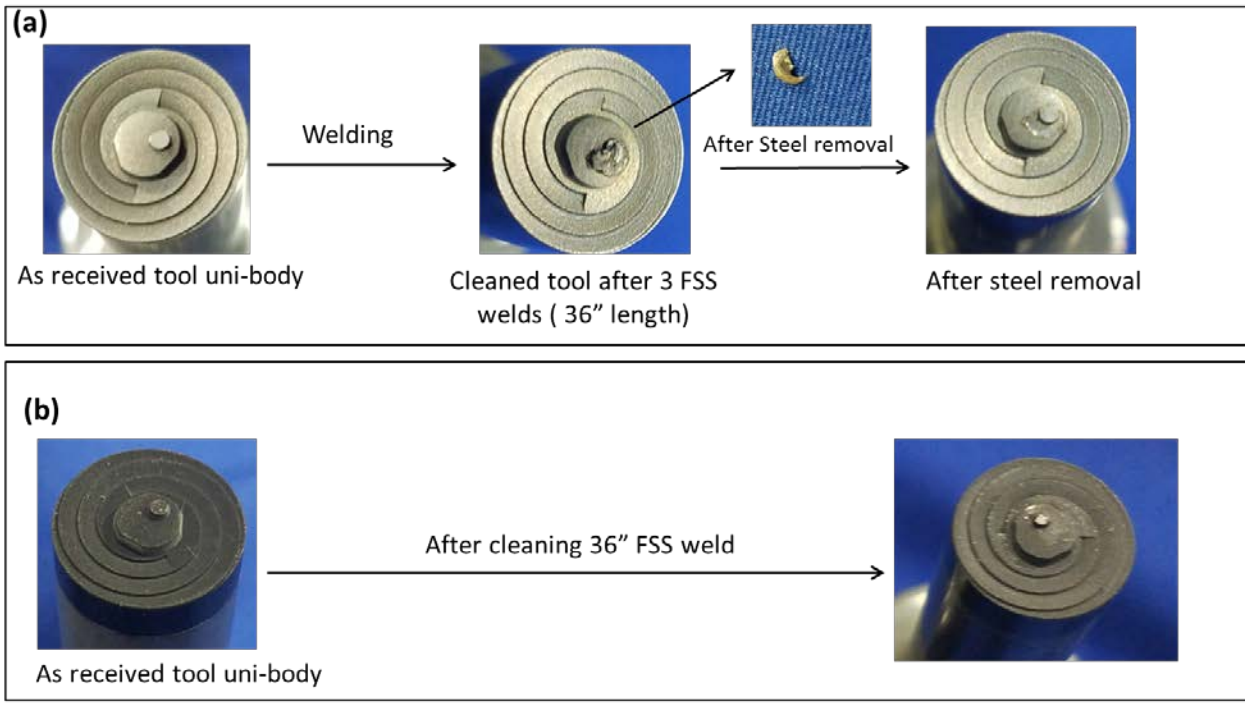

Figure II.3.C.9. Performance of uni-body FSS tool designs. (a) buildup edge formation and removal for FSS tool made from uni-body (W-C-Co [TMK-3012] material. (b) FSS tool made with PCBN brazed over W-C-Co. Source: General Motors.

Characterization of Al/Steel Interface

Figure II.3.C.10 provides a snapshot of the Al/steel interface at various degrees of magnification using advanced characterization techniques. Figure II.3.C.10(a) shows a macro cross section of a typical joint between 1.1 mm Surfalex™ 6s Al joined to UHSS (Usibor® steel). Prior to joining, the Al-Si coating on the UHSS was removed to simplify the characterization process. While four different regions within the interface were characterized during this work only one representative case is presented in this report. The joint interface close to the retreating side hook of the joint, as observed in Figure II.3.C.10(b), is shown in subsequent images and charts in Figure II.3.C.10. Energy dispersive x-ray spectroscopy (EDXS) line scanning at different locations within the interface (not shown) suggested the presence of a diffusion layer (a gradual change in Al content from Al-rich side to the Fe-rich side). This diffusion layer ranges from 4 to 7 µm. A sustained intermetallic (IM) layer was not resolvable by the means of scanning electron microscopy line scanning. To evaluate the presence of an IM compound at higher resolution, transmission electron microscope (TEM) samples were cut from various locations within the interface. As observed in Figure II.3.C.10(c, d, f, and g), a distinct IM layer was observed with a thickness of 190 nm. Figure II.3.C.10(d) shows the Al elemental distribution across the IM layer. Figure II.3.C.10(e) shows EDXS line scan across the identified IM layer. As per the Fe-Al binary phase diagram (Kattner 1990), the IM compound Fe_2Al_5 is hypothesized to be present at the interface. Figure II.3.C.10(f, g) show the magnified interface with the IM layer, Fe-rich side, and Al-rich

side identified. The diffraction pattern shown in the lower right corner of Figure II.3.C.10(g) confirms the IM layer is composed of several distinct grains. A detailed characterization of the joint interface is being prepared for a journal paper submission (Wang 2017). In summary, the interface characterization for the Al-steel interface shows the presence of an IM layer in sub-micron thickness. Characterizations like these can serve as important inputs into a predictive model for dissimilar joints (Barker 2017).

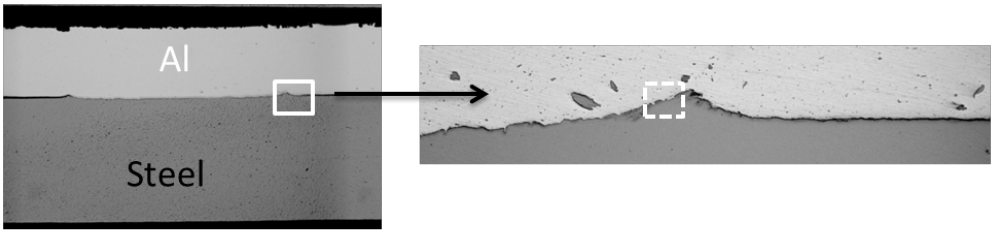

(a) (b)

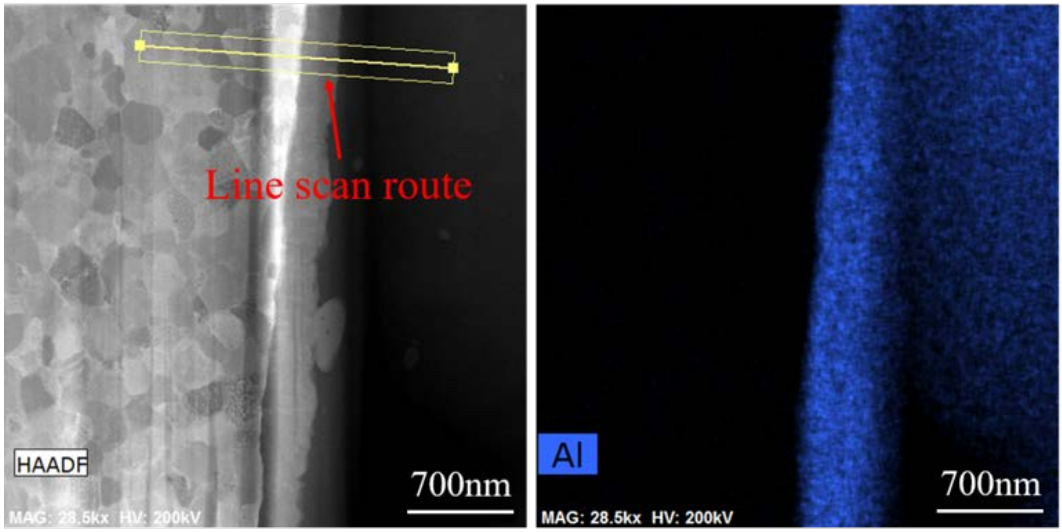

(c) (d)

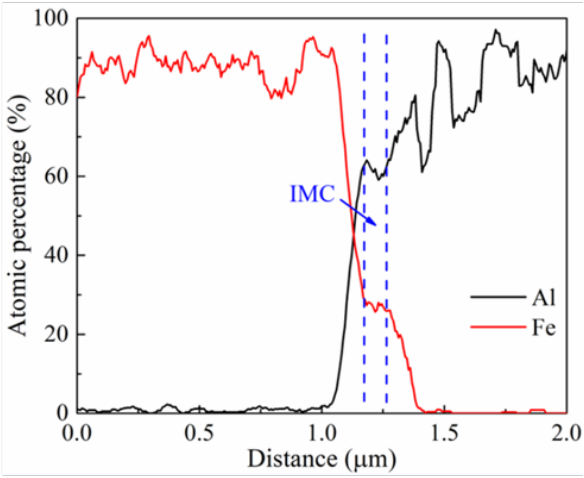

(e)

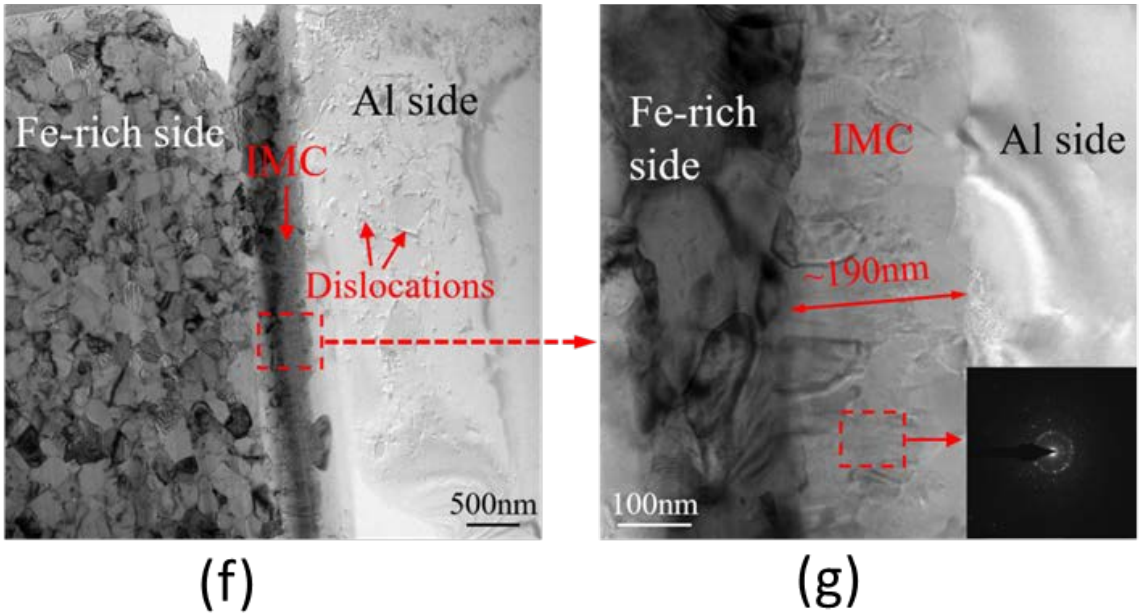

Figure II.3.C.10. Snapshot of advanced characterization performed on Al-steel interface. (a) macrograph of the joint cross section between 1.1-mm-thick Surfalex™ 6s Al to 2-mm-thick UHSS (Usibor®) steel. (b) close-up view of retreating side hook feature. (c) scanning transmission electron microscope image at Al-steel interface in the region marked in (b). (d) Al elemental distribution at the interface. (e) EDXS line scan results showing relative atomic percentage across the observed IMC layer. (f) TEM image of the interfacial microstructure inside the hook. (g) High-magnification TEM image of the IMC layer. Source: PNNL and Pennsylvania State University.

Structure-Property Modeling and Modeling Work

Previous work included developing a two-dimensional finite element model of a FSS lap joint within LS-DYNA. The model was developed for lap joints with a top 1-mm-thick sheet of AA6022 Al and a lower 0.7-mm sheet of galvanized mild steel provided by GM. A series of joint morphologies was created to capture the range of morphologies observed from optical images of joint cross sections. For each sheet, different material regions were determined and assigned specific sets of material properties. The top sheet included the nugget region, heat affected zones on either side of the nugget, and the base material for the rest of the sheet. The bottom sheet was simply assigned the base material properties.

Lap-shear loading was simulated by fixing one end of the joint and applying a strain rate to the opposite end. Initially, models were loaded from the advancing side. These results showed variability in the failure load of the joint due to the different hook morphology. While the modeled joints showed similar yield stress the ultimate strength is over predicted by the model. Except for a sample near the weld start (S+2.5), the elongation values are fairly close to the simulated value for the given sample geometry to the experimental measurements, the simulated failure strain was much lower as seen in Figure II.3.C.11. Loading the advancing side also showed the same failure location as seen experimentally.

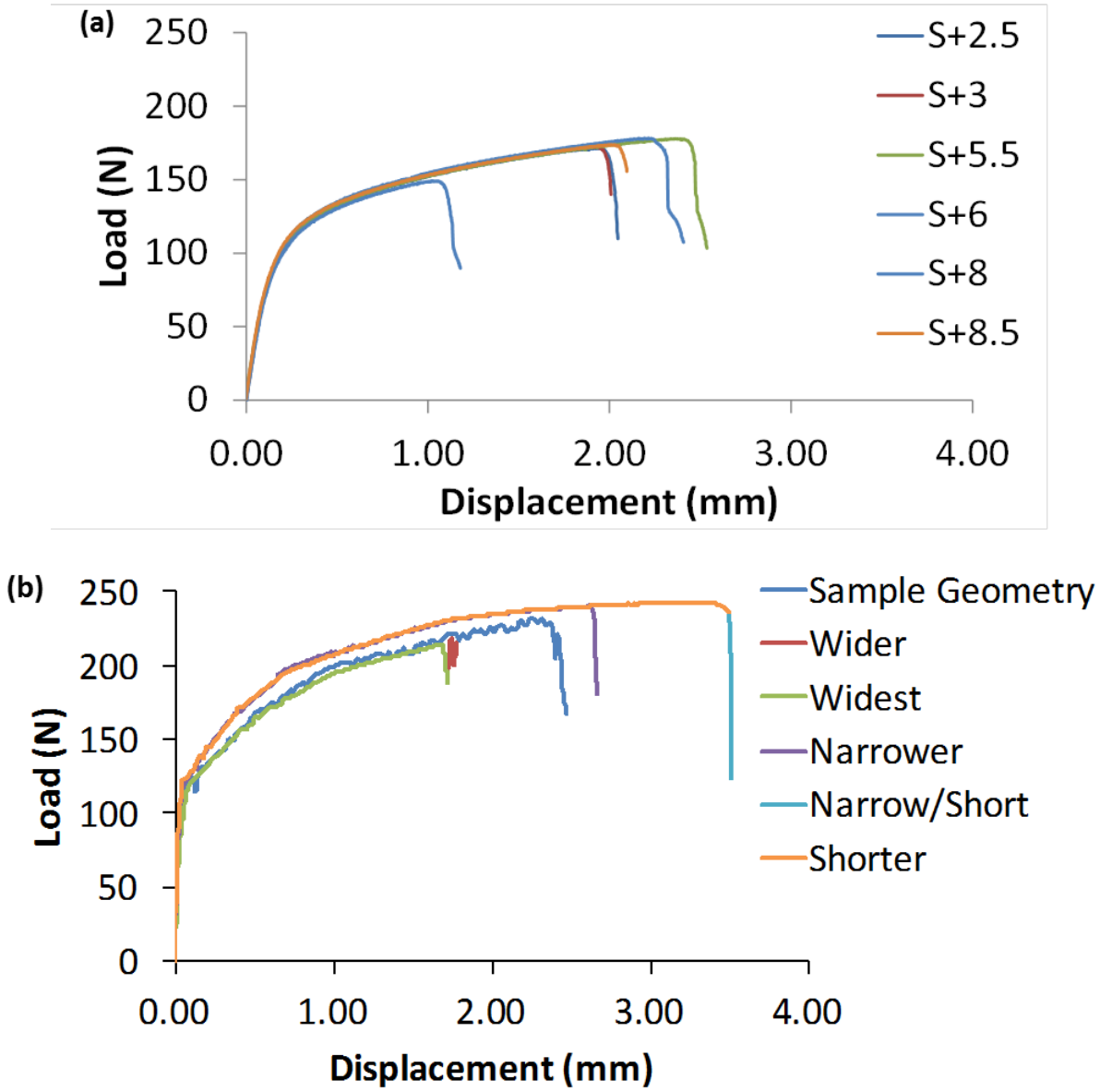

Figure II.3.C.11. (a) Experimental load versus extension results for multiple FSS lap joints; and (b) simulated load versus extension curves for various hook morphologies.

The previous work was extended by also loading from the retreating side. Results showed less variation due to the hook morphology. Examining the deformation and failure location revealed that when loading from the retreating side, the simulated failure location was from the advancing side hook and through the lower steel sheet. This is not the experimentally observed location.

The micro-hardness measurements made of joint cross sections indicate that there is a heat-affected zone in the lower sheet below the nugget. This region exhibits an increase in hardness. The models were updated to include the lower heat-affected zone and executed again. This modification had two impacts on the simulation results. First, the failure location when loading from the retreating side shifted to tearing from the retreating hook up through the top sheet as seen experimentally. Figure II.3.C.12 shows the simulated and experimentally observed failure locations. Second, the variation in failure strains due to hook morphology was reduced.

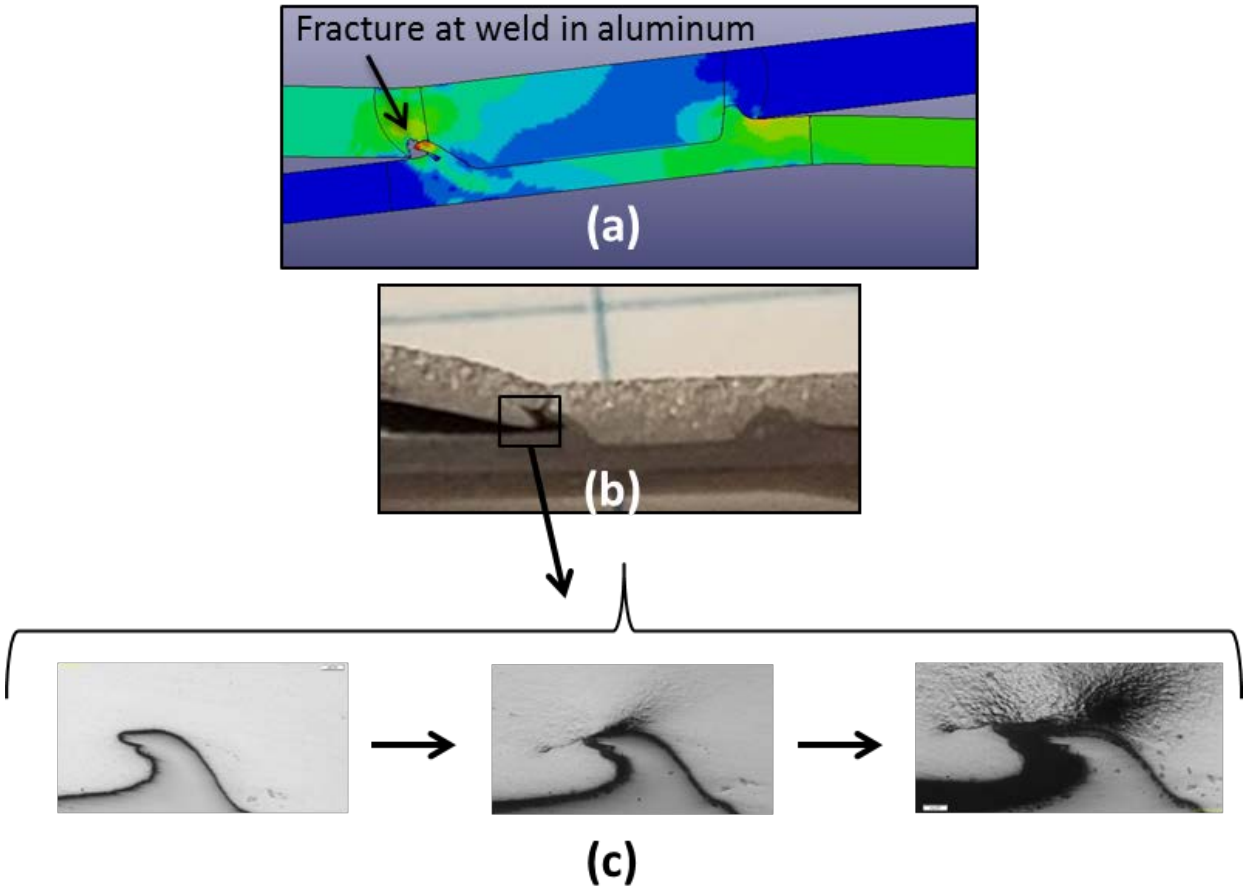

Figure II.3.C.12. Simulated failure location (a) and (b) after including lower heat-affected zone in the steel sheet; and (c) experimentally observed failure location for same loading condition. Source: PNNL.

Next, the base model setup was extended to the Honda material set, which consists of a 3-mm cast Al top sheet and 2-mm bottom sheet of different steels. Initially, the models were set up in the same manner as for the GM material set. A series of hook morphologies was created to capture the range of heights and widths observed in optical images. The same set of material regions were assumed to be present including a heat-affected zone in the lower steel sheet. The specific location and geometry of the regions were determined from optical images of joints along with micro-hardness measurements. Figure II.3.C.13 shows the center region of the lap joint. The material properties of each region were scaled from the base material properties based on the average hardness measured in each region.

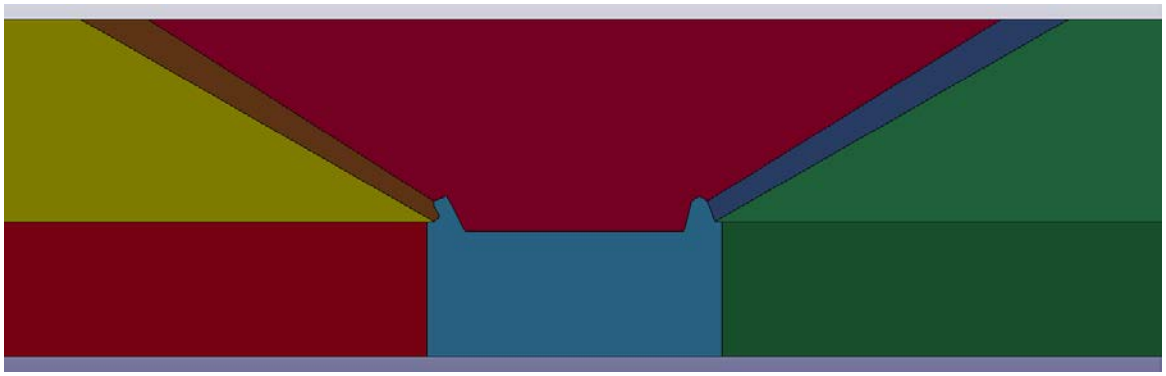

Figure II.3.C.13. Joint geometry and material regions for Honda material set of 3-mm cast Al and 2-mm mild steel.

In generating the finite element meshes for each model geometry, the meshes for the top and bottom sheet are generated separately. This results in no physical connection or interaction between the meshes. To connect the top and bottom sheet meshes, the surface nodes located between the two hook peaks are merged. This models a perfect interface between the top and bottom sheets along the nugget region. Surface nodes from the hook peaks along the outside of each hook are linked through a master-slave contact model. This prevents the meshes from penetrating into the other during the simulation.

For the GM material set, lap-shear tests showed joint failures through the top Al sheet. However, for the Honda material set, interfacial failures were also observed. Simulations only reproduced the failure locations through the top sheet. The simulated load versus extension results, as shown in Figure II.3.C.14, also overestimate the ultimate strength of the joints. This is likely due to overestimation of the strength of the interface in the nugget region. The difference in interface strength is possibly due to the increase in plate thickness and differences in the interfacial chemistry due to the Al being cast rather than wrought. Additional simulations may be needed to determine an interface strength that results in interfacial failure. This will indicate how much lower the interface strength must be to allow for interfacial failure.

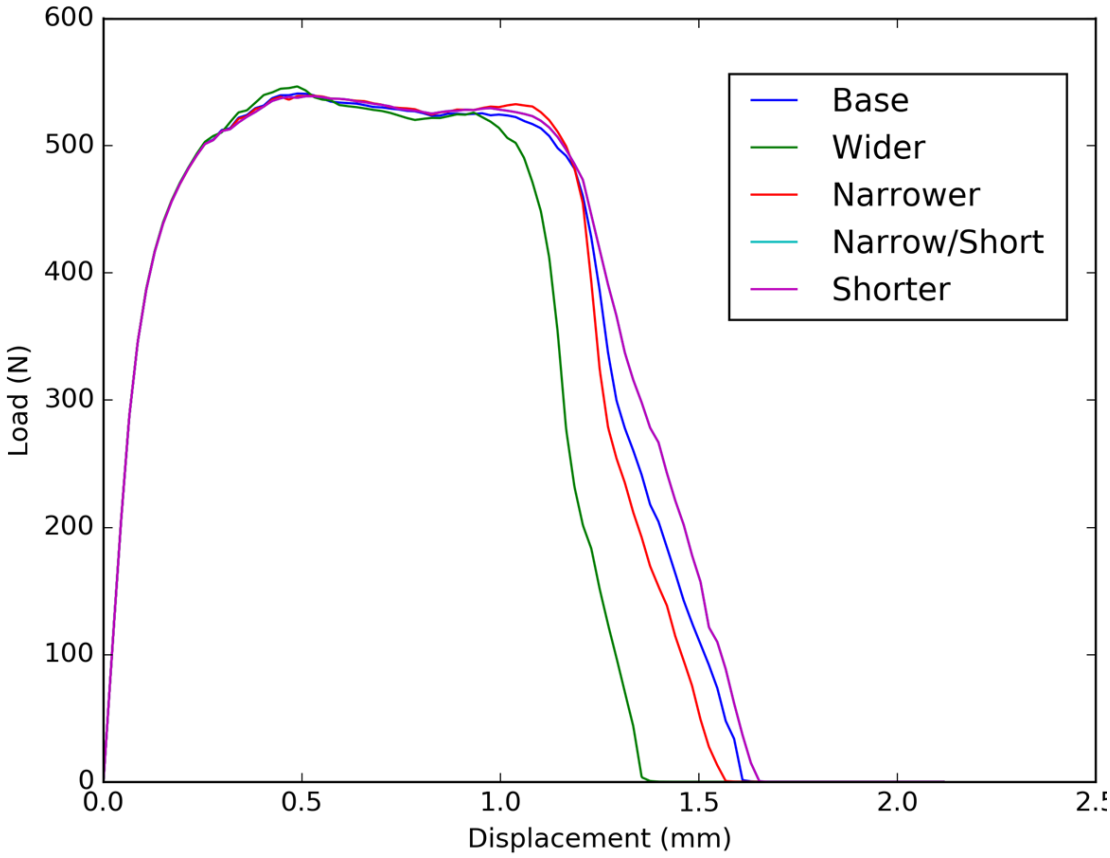

Figure II.3.C.14. Simulated load versus displacement curves for loading the Honda material set on the retreating side.

In FY 2017, we worked with our partners at KUKA (Tier 1 supplier) and an OEM (GM) to provide transfer of the FSS technique and knowledge base to the industry floor. For this purpose, corresponding FSS scribe tools were designed and fabricated that fit into the available FSW machines (both robotic and gantry types). PNNL provided both onsite and offsite guidance to transfer the FSS joining technique into a robotic platform, as shown in Figure II.3.C.15. Engineers at KUKA are now trained to use FSS tooling to make joints between Al and steel components. Additionally, GM is currently in the process of integrating FSS tooling in its gantry and robotic systems. Engineers at GM are working closely with KUKA to complete the technology transfer. The PNNL team continues to provide support in implementation of the FSS tooling and processes.

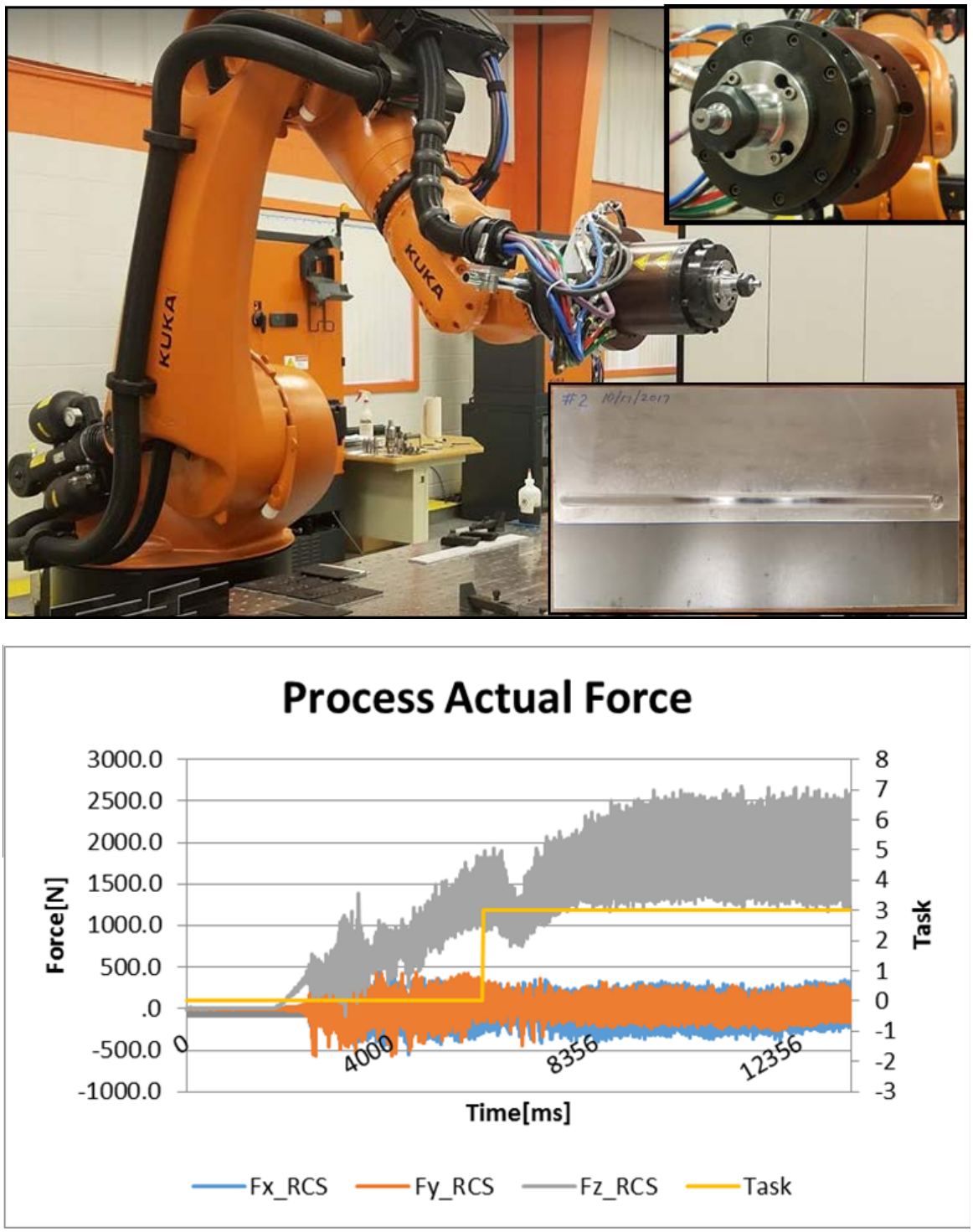

Figure II.3.C.15. Friction stir welding robot at KUKA Systems fitted with FSS tool (left). Al/steel joint recently made using the robot (bottom corner on left). Force versus time chart showing three planar forces during welding (right). RCS stands for Robot Controller Software. Source: KUKA Systems.

Conclusions

Working in association with three automotive OEMs and a supplier, a set of relevant Al and steel components were effectively joined using the FSS technique. During the process, a large collection of data sets, including joint cross sections, resulting hook features, lap shear strength, weld forces, and torque, have been generated and analyzed. The FSS technique was matured from a flat coupon sample to near prototype samples; including evaluation of spot-welded multilayered steel, adhesive interlayers, and steel with coatings. For the material combinations provided by each OEM, the FSS process was able to meet or exceed the static joint strength required by the OEM. The participating Tier 1 robotic supplier has successfully implemented FSS tooling and demonstrated the joining process within its facility. Predictive modeling tools that provide fracture mode and joint strength estimate for a given Al/steel combination have also been developed.

Key Publications

Hovanski, Y., G. J. Grant, S. Jana, and K. F. Mattlin, 2013, "Friction Stir Welding Tool and Process for Welding Dissimilar Materials," US8434661 B2, May 7, 2013.

Upadhyay, P., Y. Hovanski, B. Carlson, R. Ruokolainen, P. Busuttil, and E. Boettcher, 2015, "Solid-State Joining of Aluminum to Steel Using Friction Stir Scribe," *Materials Science & Technology*, Columbus, Ohio.

Wang, T., H. Sidhar, R. S. Mishra, Y. Hovanski, P. Upadhyay, and B. Carlson, 2017, "Friction stir scribe welding technique for dissimilar joining of aluminium and galvanised steel," *Science and Technology of Welding and Joining*, October 4, 2017, http://www.tandfonline.com/doi/abs/10.1080/13621718.2017.1381460.

Zhang, G. F., K. Zhang, L. J. Zhang, and J. X. Zhang, 2014, "Approach to disrupting thick intermetallic compound interfacial layer in friction stir brazing (FSB) of Al/Cu plates," *Science and Technology of Welding and Joining*, Vol. 19, No. 7, October 1, 2014, pp. 554–59, https://doi.org/10.1179/1362171814Y.0000000224.

References

Barker, E. I., P. Upadhyay, Y. Hovanski, and X. Sun, 2017, "Predicting lap shear strength for friction stir scribe joining of dissimilar materials," *Friction Stir Welding and Processing IX*, The Minerals, Metals & Materials Series, Springer, Cham. pp. 261–267.

Hovanski, Y., P. Upadhyay, S. Kleinbaum, B. Carlson, E. Boettcher, and R. Ruokolainen, 2017, "Enabling dissimilar material joining using friction stir scribe technology," *JOM*, Vol. 69, No. 6, pp. 1060–1064.

Kattner, U. R., and T. B. Massalski, in: H. Baker (Ed.), 1990, *Binary Alloy Phase Diagrams*, AMS International, Material Park, OH, p. 147.

Upadhyay, P., Y. Hovanski, S. Jana, and L. S. Fifield, 2016, "Joining dissimilar materials using friction stir scribe technique," *Journal of Manufacturing Science and Engineering*, Vol. 139, No. 3.

Upadhyay, P., Y. Hovanski, B. Carlson, E. Boettcher, R. Ruokolainen, and P. Busuttil, 2017, "Joining dissimilar material using friction stir scribe technique," *Friction Stir Welding and Processing IX*, The Minerals, Metals & Materials Series, Springer, Cham. pp. 147–55.

Wang, K., Y. Wang, J. Li, and U. Piyush, 2017, "Investigation of interfacial layer for friction stir scribe welded aluminum to steel joints," manuscript under preparation.

II.3.D High-Strength, Dissimilar Alloy Aluminum Tailor-Welded Blanks (Pacific Northwest National Laboratory)

Piyush Upadhyay, Principal Investigator
Pacific Northwest National Laboratory
902 Battelle Blvd.
Richland, WA 99352
Phone: 509-375-6591
E-mail: piyush.upadhyay@pnnl.gov

Sarah Kleinbaum, Technology Manager
E-mail: sarah.kleinbaum@ee.doe.gov

Start Date: November 1, 2014 End Date: September 30, 2018
Total Project Cost: $2,400,000 DOE share: $1,200,000 Non-DOE share: $1,200,000

Executive Summary

The purpose of this project is to further develop high-speed FSW joining to accommodate dissimilar Al alloy combinations in both linear and curvilinear geometries. This includes combinations that accommodate mixtures of work-hardenable alloys that demonstrate deep drawing capabilities, with precipitation-hardenable alloys that can be hardened after joining and forming to develop the high strengths required for body skins and structural supports. This work will develop the novel material coefficients needed to support formability modeling of dissimilar alloy structures that have properties ranging from strain hardening to heat-affected zone (HAZ) property degradation across a fixed panel. These material coefficients will be combined with properties of the base materials to allow for simulation of forming dissimilar alloy and dissimilar thickness Al tailor-welded blanks (TWBs). Simulated results will be validated on prototypical parts produced by the supplier to demonstrate production deployability within the duration of the three-year effort. In FY 2017, the project completed process robustness and production readiness tests at a Tier 1 supplier facility demonstrating production deployability for high-speed FSW of TWBs. Additionally, Barlat anisotropy coefficients for FSW Al alloys were determined and used to refine formability model.

Accomplishments

- Developed welding parameter sets to produce dissimilar thickness/alloy FSW joints between: (1) AA7075-T6 (2 mm) and AA5182-O (1.1 mm), (2) AA6022-T4 (2 mm) and AA5182-O (1.1 mm), and (3) AA7085-T6 (2 mm), AA5754 (3.0 to 3.8 mm), and AA5182-O (1.1 mm) (FY 2016 and FY 2017).
- Completed production repeatability (1000+ welds) study for linear dissimilar material (0.8 mm thickness differential) joint at Tier 1 supplier that simulated the number of welds produced in a single automated shift (FY 2017).
- Completed process repeatability for dissimilar material, dissimilar thickness in curvilinear path at a Tier 1 supplier facility for five different combinations of dissimilar thickness, dissimilar alloy combinations (FY 2017).
- Developed Barlat anisotropy parameters/coefficients for FSW material in AA6022 and AA5182 material (FY 2017).
- Expanded formability model to include weld metal properties of dissimilar thickness and dissimilar alloy combinations (FY 2017).

- Provided onsite and offsite support to the TWB Company to enable transfer of the developed high-speed dissimilar welding method to a fully automated assembly line, which came online in August 2017 (FY 2017).

Project Introduction

This project is targeted towards developing high-strength, high-speed FSW of dissimilar Al alloy combinations in linear and curvilinear geometries. The alloy combinations considered in this project include work-hardenable alloys (i.e., 5xxx series) capable of deep drawing and precipitation-hardenable alloys (i.e., 6xxx and 7xxx series), which can be hardened post-joining and post-forming to yield high strength for application in outer body panels and structural supports of automobiles. FSWs made at welding speeds greater than 1 m/min are considered high speed for this work. Figure II.3.D.1 shows a comparative chart that includes many Al FSWs reported in literature over the last 15 years (Zhang 2016). Welding speeds already implemented in the current project are also shown.

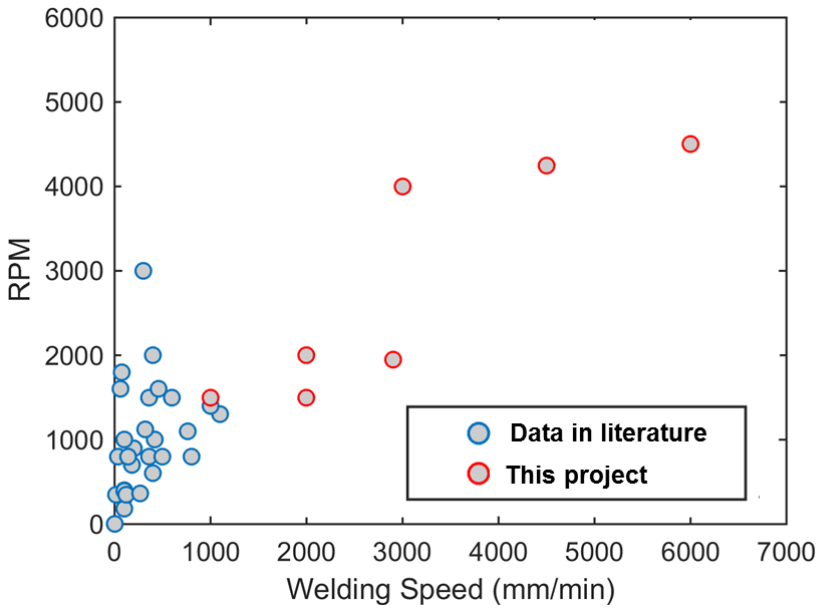

Figure II.3.D.1. Comparative chart showing welding speed in revolutions per minute and tool translation per minute used by many Al alloy FSW reported in literature. Parameters used so far in the current project are also shown (Zhang 2016).

The current project intends to significantly increase the welding speed, thus enabling high-volume application of FSW in TWB applications. The effects of high welding speed and the resulting weld properties were investigated. In addition, ways to exploit the high-speed FSW to the advantage of strength and ductility enhancements will be defined. This research will develop material coefficients required to support formability modeling of dissimilar alloy combinations with different hardening mechanisms (i.e., strain hardening in 5xxx series and precipitation hardening and HAZ property degradation due to coarsening in 6xxx and 7xxx series). The resulting material coefficients will be used to develop a formability model capable of simulating combinations of dissimilar alloys and dissimilar thicknesses of TWBs. Ultimately, the formability model will be validated against formability performance of welds made at the supplier's facility.

Approach

The work scope is divided into four main tasks. The first task is concerned with obtaining relationships between the weld parameters, process conditions, and weld properties. The second task focuses on developing high-speed parameter sets to produce sound welds in dissimilar alloy combinations for Aluminum Association (AA) 5xxx to 6xxxx and 7xxx series alloys in similar or dissimilar thicknesses. The third task pertains to

production readiness and deployability, including a FSW repeatability and tool durability study. The fourth task concerns weld formability modeling and validation, including development of material and weld region constitutive coefficients and simulation of sheet formability in dissimilar material and thickness of TWBs.

The FY 2017 focus was to further transition the laboratory-developed high-speed FSW technique into implementation and eventual commercialization by a Tier 1 supplier (TWB Company) and an automotive OEM. To this end, a large portion of the project work in FY 2017 was concentrated on assessing process robustness and tool durability at the supplier's facility. This required work on developing process parameters and tool design to provide effective joints between a specific dissimilar material set chosen by the supplier with the highest probability of commercialization. Because of this effort, the TWB Company now has a fully operational FSW assembly line with capability of producing dissimilar thickness, dissimilar material joints at a competitive process speed, as shown in Figure II.3.D.2. Additionally, this year, we obtained anisotropy coefficients for friction-stir-welded materials and used the coefficients in the developed formability model.

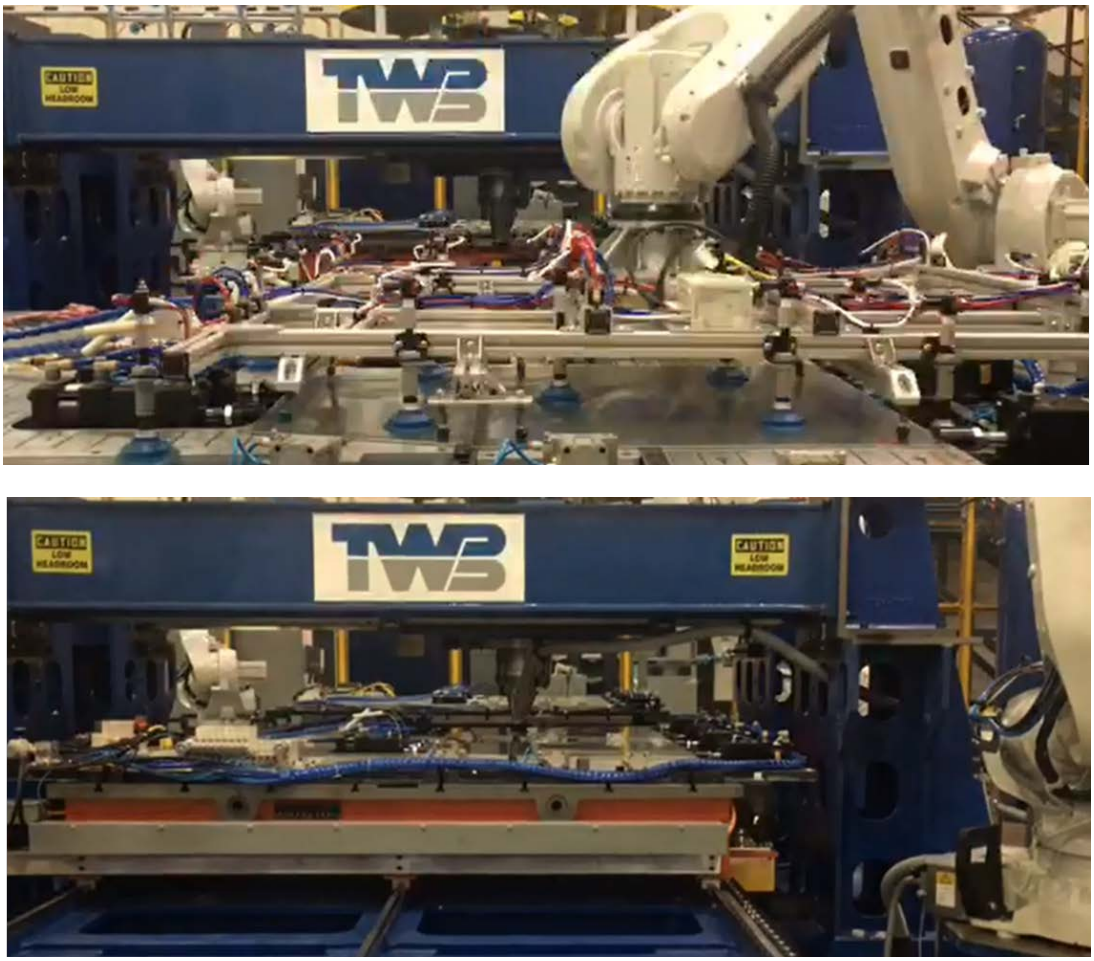

Figure II.3.D.2. Assembly line recently added at TWB Company showing six axis robotic material feeder and FSW gantry head ready to make a welding pass. The assembly line can make 95 blanks/hour including shearing, loading, welding, unloading, defect scanning, and stacking of blanks. Source: TWB Company.

Technology Transfer Path

Technology transfer has been made directly through the project participants (i.e., GM, TWB Company, and Arconic), who are the implementers of the technology. The TWB Company (i.e., a Tier 1 supplier to the automotive industry) will be able to use the joining technology developed during the project to address a wide

range of automotive market lightweighting needs by implementing tailor welded blanking for dissimilar Al alloys. As of August 2017, the TWB Company began high-volume production of TWBs using high-speed FSW because of collaborative work performed in this project.

Results

Dissimilar thickness joining of AA5754 (3.0 to 3.8 mm) was chosen as a viable candidate to assess production readiness and process robustness by the TWB Company. Since most of the developmental work thus far in the project was focused on relatively thin sheets of Al mostly in the range of 1 to 2 mm, development of tooling and welding parameters with several welding trials was performed at a TWB Company facility for the thicker sheets involved. This developmental work allowed us to obtain qualifying welded joints. Based on the design guideline that was generated earlier in the project, the thicker sheet (3.8 mm) was placed on the advancing side of the joint. The process conditions were evaluated in the range of 1 to 3 m/min, and 1000 to 3000 rpm. One of the factors that affected the propensity of defect formation in the nugget areas was the tilt angle of the FSW head. Usually for thinner gage sheets (1 to 2 mm), the tilt angle of 0.5 to 1 degree has been observed to provide sufficient forging at the wake of the FSW tool. For the relatively thick sheets that we worked on, the tilted angle needed to yield a defect-free weld was close to 4 degrees. Examples of welded panels of AA5754 are shown in Figure II.3.D.3.

Figure II.3.D.4 shows a comparison of a joint cross-section with a lead angle of three degrees versus that of four degrees. Larger compliance associated with greater planar forces for thicker sheet and strain hardening material is likely the reason behind the need for a greater tilt angle.

Having evaluated welding speed, tool head tilt angle, and tool and fixture design, the process development progressed to assessing stamping trials of welded joints. For this purpose, 150 parts were successfully stamped from dissimilar thickness TWB joints. The outside and inside portion of a door hinge reinforcement component is shown in Figure II.3.D.5.

Subsequently, as a part of the process robustness test for the FSW process, 1000+ linear welds were made at the TWB Company facility. This task was accomplished by stretching over several days with significant support from engineers and technicians at the TWB Company facility. The repeatability study was carried out such that it simulated a typical number of welds to be expected in a single automated shift. The welded linear panels shown in Figure II.3.D.3 were tested and characterized. Samples for tensile tests, micro hardness tests, and metallographic cross sections were extracted every 200th weld. In addition, properties of each weld along its length were also evaluated from near the start, middle, and end of the weld. Figure II.3.D.6 and Figure II.3.D.7 show representative engineering stress versus strain datasets for three American Society for Testing and Materials International (ASTM)-E8 samples extracted from the start, middle, and end of the weld. For the sake of brevity, data pertaining to only the 200th and 1000th welds only are shown in Figure II.3.D.6 and Figure II.3.D.7, respectively. In addition, fractured welded samples, all of which broke on the thin side in the base material, are shown. Representative joint cross-sections, the weld nugget, and root appearances (that exceeded the surface finish requirement) are also shown.

(a)

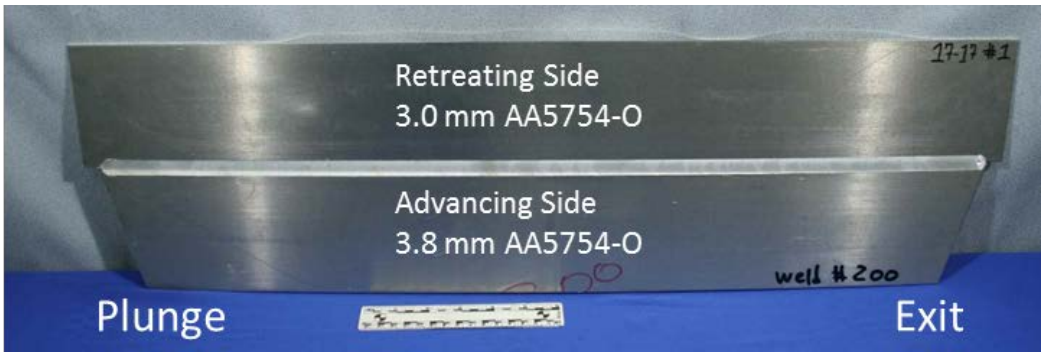

(b)

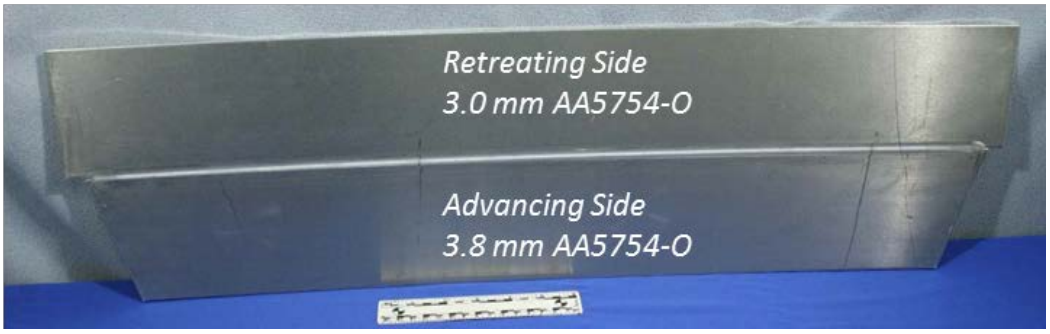

(c)

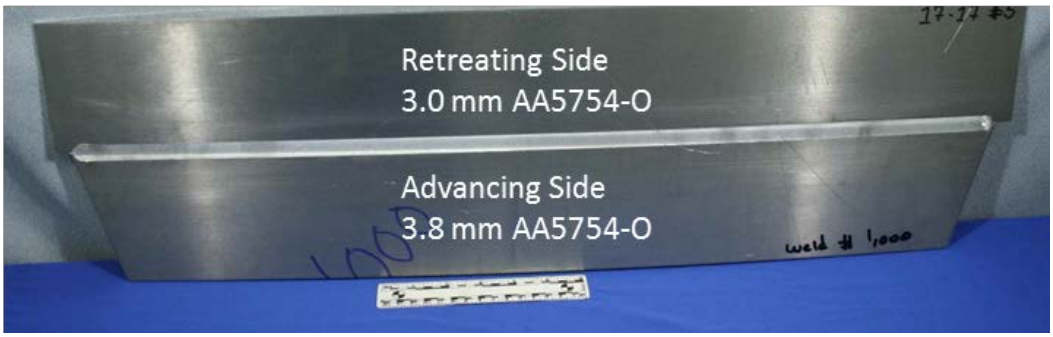

(d)

Figure II.3.D.3. Example of welded panels as a part of the repeatability study. Both the (a) root and (b) face sides of the welds are shown. (c) 200th weld, and (d) 1000th weld. Source: TWB Company.

(a)

(b)

Figure II.3.D.5. Door hinge reinforcement part stamped from dissimilar thickness TWB joint as a part of weld development in TWB. Outside of stamping is shown on the left; inside of stamping is shown on the right. Source: TWB Company.

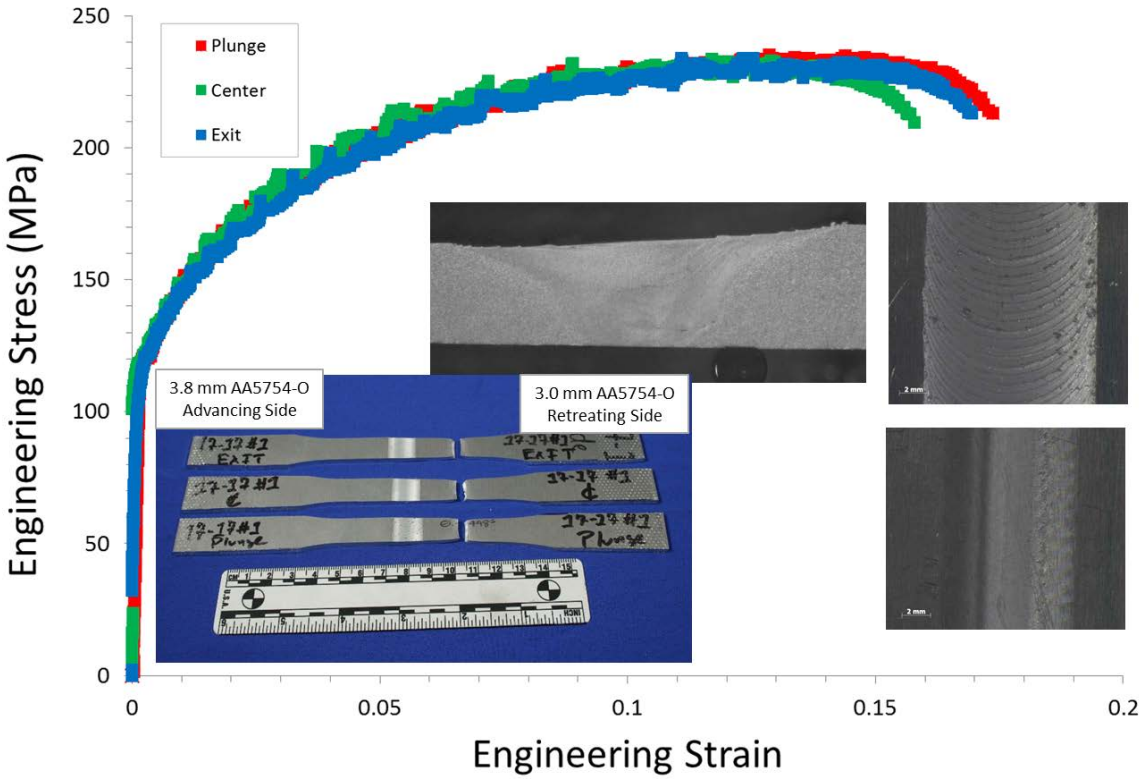

Figure II.3.D.6. Engineering stress versus strain data obtained from 200th welded joint in the repeatability study. The fracture samples and representative joint cross sections are shown. Weld crown and root surfaces are also shown. Source: TWB Company.

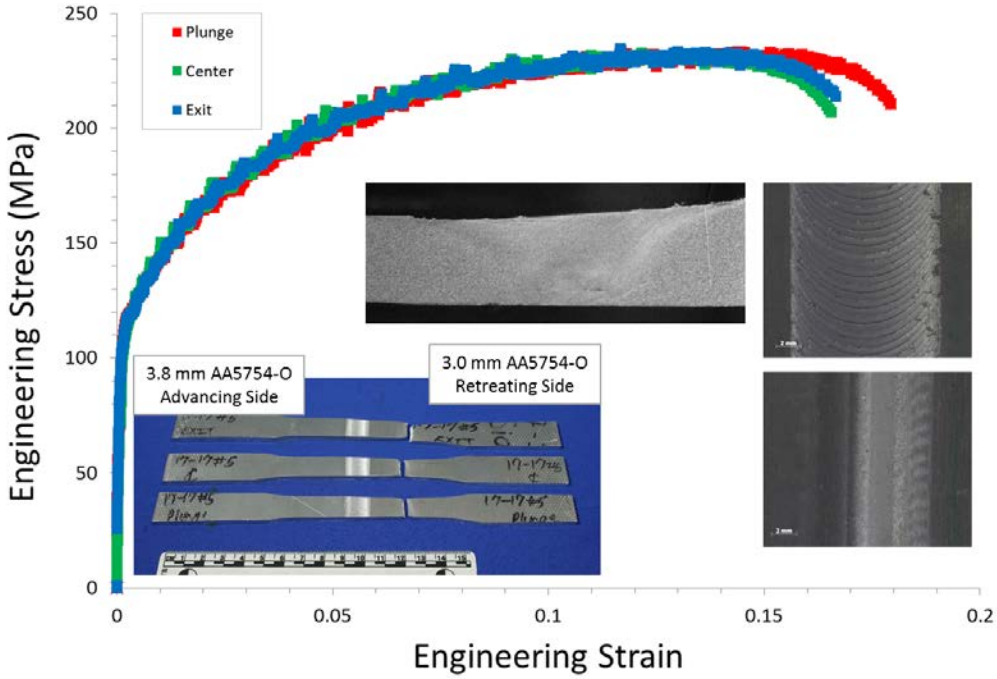

Figure II.3.D.7. Engineering stress versus strain data obtained from 1000th welded joint in the repeatability study. The fracture samples and representative joint cross sections are shown. Weld crown and root surfaces are also shown. Source: TWB Company.

The linear repeatability tests were also performed with the intent of assessment of tool durability as one of the project milestones. Tools made of heat-treated H13 were used for the study. Two color-coded tools (yellow used for 300 m and purple used for 500 m of welds) as shown in Figure II.3.D.8 (left side) exhibited no change in the length of pin after the weld runs. The tool cleaned up after the repeatability study is also shown in Figure II.3.D.8 (right side).

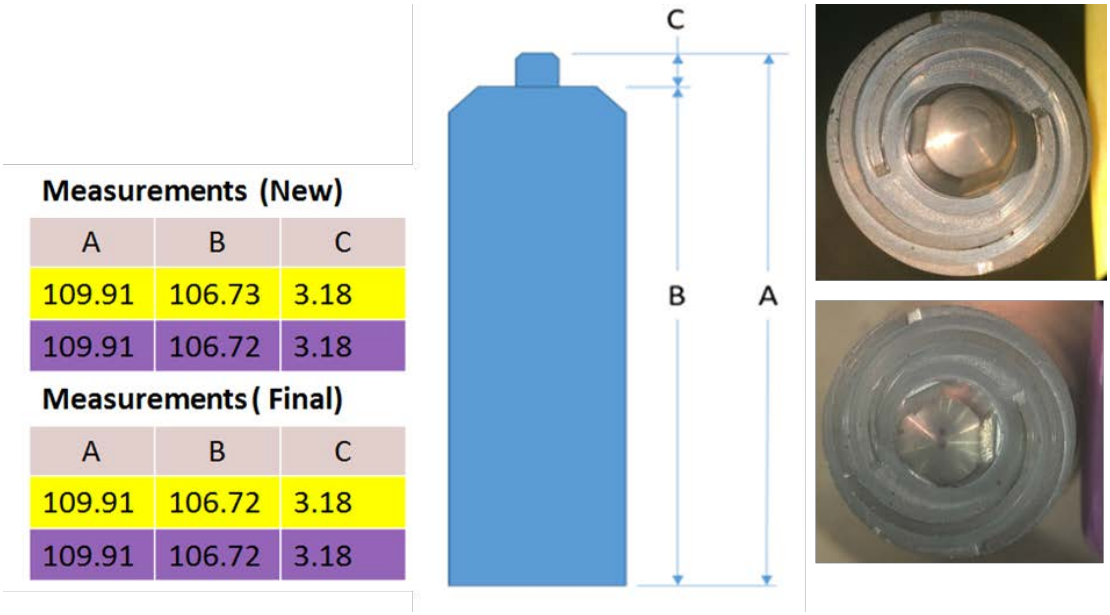

Figure II.3.D.8. Tool pin length, measured in millimeters, before and after welding. The cleaned tools after 500 m of welding are shown to the right (Top - yellow, bottom - purple). Source: PNNL.

In addition to production-like repeatability in linear FSW, several sets of dissimilar thickness, dissimilar alloy combinations were also joined at the TWB Company facility. The details of curvilinear joints made in the project are shown in Table II.3.D.1. While most of the welding parameters from linear runs were transferrable to curvilinear geometry, the control and parameter settings across curved surfaces had to be adapted by trial and error. Ultimately, effective welds were made such that the root and crown bend test criteria established in FY 2016 within the project was met.

Table II.3.D.1. A List of Dissimilar Alloy Combinations that Were Joined in Curvilinear Geometry at TWB Facility.

Advancing Side (1.3mm)	Retreating side (2.0mm)
AA5182	AA6022
AA5182	AA7085
AA6022	AA6022
AA6022	AA7085

Characterization of Dissimilar Joints

Results of some advanced characterization work pertaining to high-speed joining of dissimilar thickness, dissimilar alloys are shown in Figure II.3.D.9. Figure II.3.D.9(a) shows the preferred setup of joining dissimilar material such that the work-hardening AA5182 is on the advancing side while the precipitating-hardening AA6022 (thicker sheet) is on the retreating side. Metallographic examination of joint cross sections is shown by the etched optical micrograph of Figure II.3.D.9(b). The darker material (1) is the AA6022 and the lighter material (2) is the AA5182. Figure II.3.D.9(c) shows the crystal orientation map colored with respect to

the welding direction and Figure II.3.D.9(d) shows the grain misorientation map with a 2-degree threshold. The misorientation map defines two distinct regions with preferred crystal orientations. The area closest to the tool shoulder has texture oriented towards the advancing side (thin sheet), which indicates that AA6022 material flows towards the thin sheet due to shoulder interaction filling up the gap caused by sheet thickness differential. The lower region showed strong texture out of the plane of the paper/screen indicating that material flow near the root is highly favored towards the welding direction as the FSW pin pushes the material forward at high speed. The root region flow hypothesis is also strongly corroborated by the periodic material flow observed in the longitudinal cross section shown in Figure II.3.D.9(e). This also shows that while the crown region at the weld seam mostly consists of material from the thick sheet (AA6022, precipitation hardening), the root region at the seam is mostly thin sheet material (AA5182, strain hardening). Details of the characterization work is currently being prepared for a peer review journal for publication. Some of the results were presented at the Material Science and Technology 2017 Technical Meeting and Exposition (Zhang 2017).

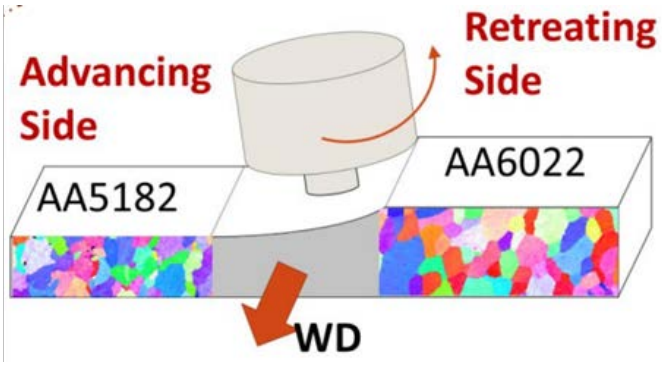

(a)

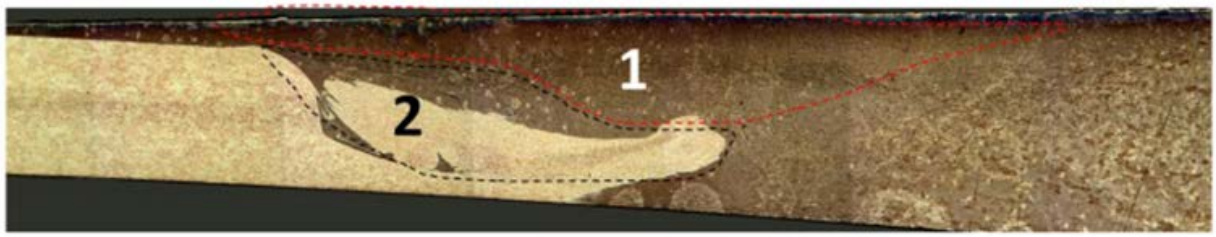

(b)

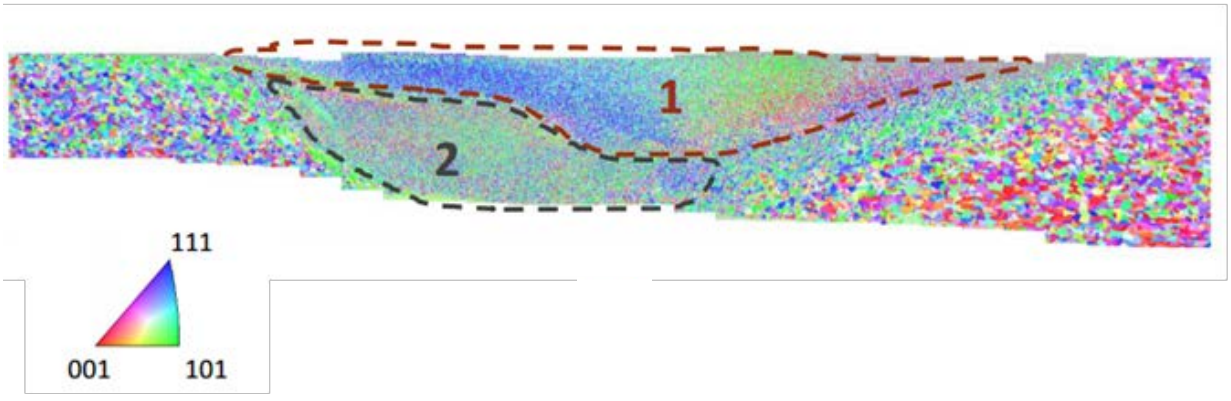

(c)

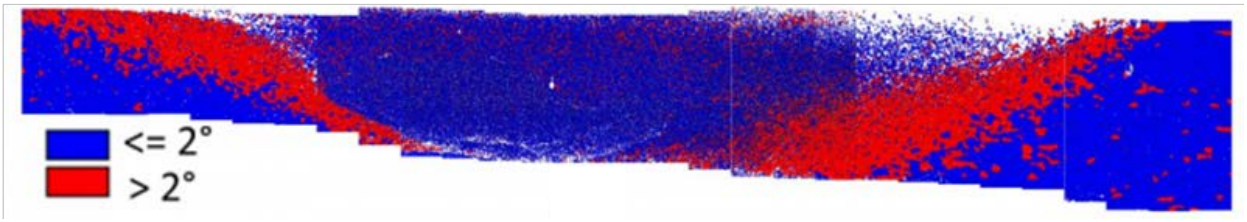

(d)

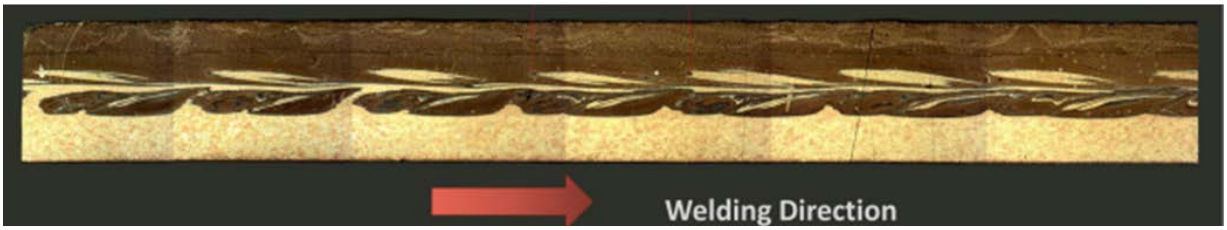

(e)

Figure II.3.D.9. (a) Dissimilar joining setup and (b) etched joint cross-section between AA5182 (1) and AA6022 (2) sheet. (c) Crystal orientation map with respect to welding direction and (d) grain boundary misorientation map with 2-degree threshold. (e) Etched joint top-view between AA5182 (1) and AA6022 (2) sheet.
Source: PNNL and Washington State University.

Development of Anisotropy Coefficients for Welded Material and Formability Model

Barlat 2000 model parameters for AA5182 and AA6022 Al alloys were obtained using a large set of micro-tensile and bulge tests for both the base material and FSW region. The Barlat 2000 model (Barlat 2003) requires eight parameters to account for material anisotropy, which subsequently serves as a critical input in the formability model in commercial codes such as LS-DYNA. These eight parameters for a specific material were obtained from four r-values and four yield strengths obtained from miniature tensile testing along the rolling direction, transverse to the rolling direction, and two 45-degree diagonal directions. This was done in close association with our GM partners. Waterjet-cut patterns on the welded and base material are shown in Figure II.3.D.10. The experimental setup used to test the mini tensile samples are also shown. The miniature samples were speckle patterned and DIC was used for localized strain measurement. In addition, several bulge tests with DIC were used to obtain biaxial strain values because the measured “normal” value of yield strength and r-values cannot be directly used as they change with plastic strain. A method (Min 2017, Pourboghrat 2013) was used to obtain strength and r-values for calibrating the Barlat 2000 model. The resulting Barlat coefficients for AA6022 base metal and FSW are shown in Table II.3.D.2.

We used the limiting dome height (LDH) simulation model developed in FY 2016 to investigate dome heights of TWB sheets using the discretized blanks with the newly obtained material properties (Barlat coefficients) for the base metal and the welded region. Simulation results are presented in Figure II.3.D.11 (left side). Onset of necking is determined in the simulations using two methods: (1) experimentally obtained forming limit diagrams (FLD) as failure criteria in LS-DYNA, and (2) using a limit strain value from tensile tests as a failure criterion. Simulation results for both methods are plotted against experimental data in Figure II.3.D.11 (right side). Dome heights for dissimilar thicknesses of TWB AA6022 sheets are plotted and it is clearly seen that the limit strain method is quite conservative and under-predicts the dome heights when compared to experimental data. The FLD-based failure criteria combined with the Barlat model accurately predict the dome heights.

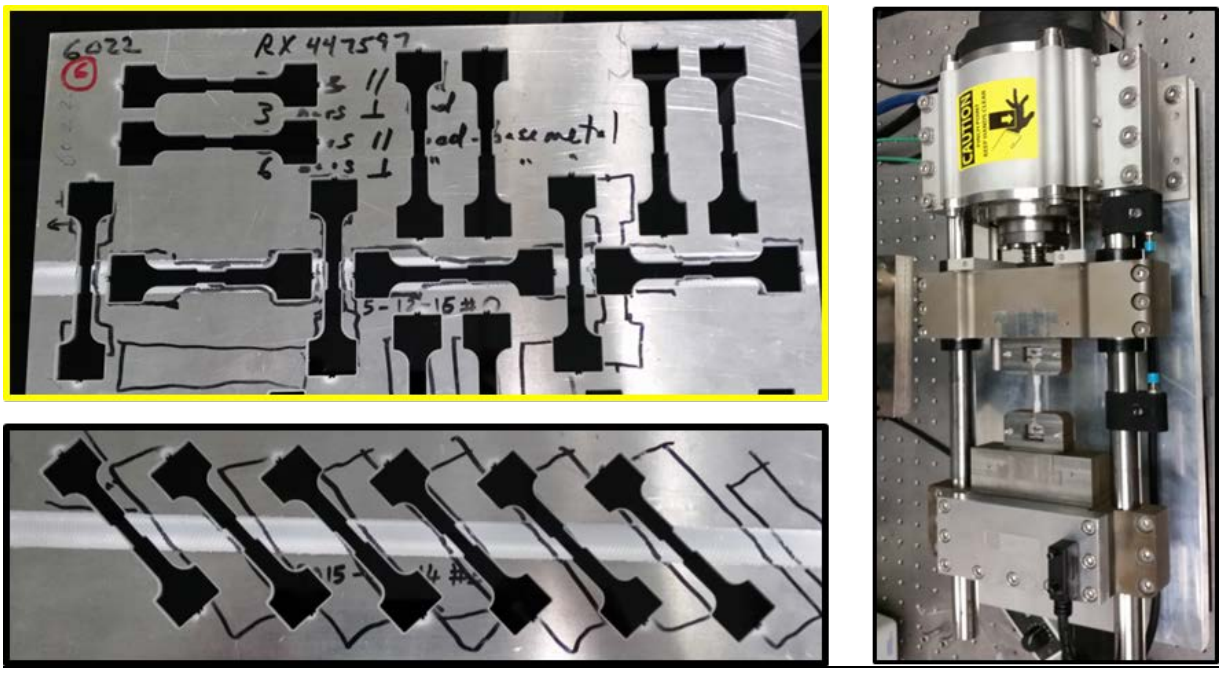

Figure II.3.D.10. Waterjet-cut location for mini tensile testing used to obtain Barlat coefficients (left) and Psylotech mini tensile testing machine equipped with DIC (right). Source: General Motors.

Table II.3.D.2. Barlat Coefficients for AA6022-T4 Aluminum Alloy (Base Metal and Weld).

Alloy	Barlat Coefficients							
	α_1	α_2	α_3	α_4	α_5	α_6	α_7	α_8
AA6022 base	0.938	1.049	0.890	0.991	1.006	0.962	1.02	1.07
AA6022 weld	0.892	1.01	0.975	1.042	0.977	0.974	0.922	1.09

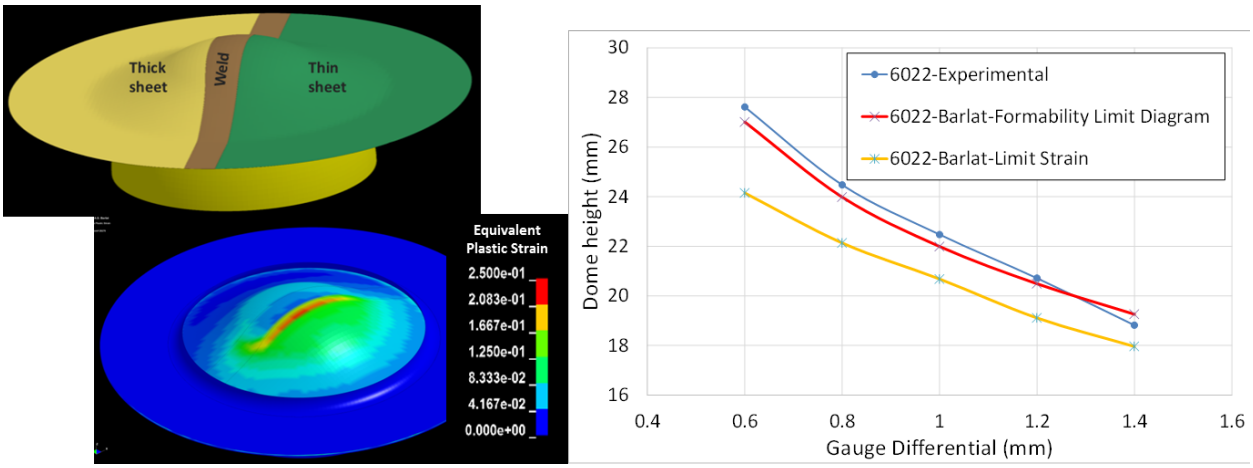

Figure II.3.D.11. Simulations showing equivalent plastic strain distribution in LDH geometry (left) and predicted and experimental dome height for AA6022 welded sheets as a function of gauge differential (right). Source: PNNL.

Conclusions

The development of optimized welding conditions, tools, and design guidelines for high-speed dissimilar joining that meets industrial formability requirements enabled commercialization of a FSW process from laboratory to industry floor at a Tier 1 automotive supplier. The project provides continued support to engineers and technicians in industry to ensure that FSW technique is successfully implemented. As a result, in late FY 2017, the TWB Company has fully integrated the developed joining technique into their assembly line capable of producing dissimilar thickness and dissimilar alloys at high speed. Additionally, for the first time, this project has provided Barlat coefficients of FSW Al alloys that serve as an input to many commercially-available formability codes. Moreover, fundamental advanced characterization of dissimilar joints at high speed has resulted in a large knowledge base that enhanced our understanding of material flow, microstructure, and weld properties.

Key Publications

Davies, R. W., M. T. Smith, M. A. Khaleel, S. G. Pitman, and H. E. Oliver, 2000, "Weld metal ductility in aluminum tailor welded blanks," *Metallurgical and Materials Transactions A*, Vol. 31, No. 11, pp. 2755–2763.

Hovanski, Y., P. Upadhyay, J. Carsley, T. Luzanski, B. Carlson, M. Eisenmenger, A. Soulami, D. Marshall, B. Landino, and S. Hartfield-Wunsch, 2015, "High-speed friction-stir welding to enable aluminum tailor-welded blanks," *Journal of Materials*, Vol. 67, No. 5, pp. 1045–1053.

Hovanski, Y., P. Upadhyay, A. Soulami, B. Carlson, M. Eisenmenger, and B. Landino, 2015, "Enabling high volume production of aluminum tailor welded blanks," *The 4th International Conference on Friction Stir Welding and Processing*, October 2015, Ordizia, Spain.

Hovanski, Y., J. Carsley, B. Carlson, M. Eisenmenger, S. Hartfield-Wunsch, and B. Landino, 2014, "Aluminum tailor welded blanks – Preparing for high volume production," *2015 TMS Annual Meeting and Exhibition*, March 16, 2015, Orlando, FL, USA.

Hovanski, Y., P. Upadhyay, B. Carlson, T. Luzanski, D. Marshall, and R. Szymanski, 2015, "FSW of aluminum tailor welded blanks across machine platforms," *2015 TMS Annual Meeting and Exhibition*, March 16, 2015, Orlando, FL, USA.

Mishra, R. S., and Z. Y. Ma, 2005, "Friction stir welding and processing," *Materials Science and Engineering Reports*, Vol. 50, No. 1–2, pp. 1–78.

Murr, L. E., 2010, "A review of FSW research on dissimilar metal and alloy systems," *Journal of Materials Engineering and Performance*, Vol. 19, No. 8, pp. 1071–1089.

Threadgill, P. L., A. J. Leonard, H. R. Shercliff, and P. J. Withers, 2009, "Friction stir welding of aluminum alloys," *International Materials Reviews*, Vol. 54, No. 2, pp. 49–93.

Zhang, J., M. Jamalian, P. Upadhyay, Y. Hovanski, and D. P. Field, 2017, "A microstructural approach to study that material flow features in FSW between AA5182 and AA6022 blanks in different thickness," *Material Science and Technology*, poster presentation, October 2017.

Zhang, J., P. Upadhyay, Y. Hovanski, and D. P. Field, 2017, "High-speed FSW aluminum alloy 7075 microstructure and corrosion properties," *In Friction Stir Welding and Processing IX*, The Minerals, Metals & Materials Series. Springer, Cham. pp. 125–35.

References

Barlat, F., J. M. Ferreira Duarte, J. J. Gracio, A. B. Lopes, and E. F. Rauch, 2003, "Plastic flow for non-monotonic loading conditions of an aluminum alloy sheet sample," *International Journal of Plasticity*, Vol. 19, No. 8, pp. 1215–1244.

Min, J., T. B. Stoughton, J. Carsley, B. Carlson, J. Lin, and X. Gao, 2017, "Accurate characterization of biaxial stress-strain response of sheet metal from bulge testing," *International Journal of Plasticity*, Vol. 94, pp. 192–213.

Pourboghrat, F., S. Venkatesan, and J. E. Carsley, 2013, "LDR and hydroforming limit for deep drawing of AA5754 aluminum sheet," *Journal of Manufacturing Processes*, Vol. 15, No. 4, pp. 600–615.

Zhang, J., M. Jamalian, P. Upadhyay, Y. Hovanski, and D. P. Field, 2017, "A microstructural approach to study that material flow features in FSW between AA5182 and AA6022 blanks in different thickness," *Material Science and Technology 17 Technical Meeting and Exposition*, poster presentation, October 9–12, 2017, Pittsburgh, PA, USA.

Zhang, J., P. Upadhyay, Y. Hovanski, and D. P. Field, 2016, "Quantitative microstructure study of high speed FSW aluminum alloy," *Material Science and Technology 2016*, October 23–27, 2016, Salt Lake City, UT, USA.

II.3.E Assembly of Dissimilar Aluminum Alloys for Automotive Application (Pacific Northwest National Laboratory)

Piyush Upadhyay, Principal Investigator
Pacific Northwest National Laboratory
902 Battelle Blvd.
Richland, WA 99352
Phone: 509-375-6591
E-mail: piyush.upadhyay@pnnl.gov

Sarah Kleinbaum, Technology Manager
E-mail: sarah.kleinbaum@ee.doe.gov

Start Date: July 1, 2017 End Date: June 30, 2019
Total Project Cost: $1,000,000 DOE share: $500,000 Non-DOE share: $500,000

Executive Summary

The purpose of this project is to develop joining technology needed to enable wider use of lightweight Al sheets in automotive assemblies. The objective of the proposed work is to mature FSLW technology geared towards high-volume applications. In collaboration with an automotive OEM and a material supplier, this project will develop FSLW technology in relevant alloys, thicknesses, and geometries. Specifically, the work will develop process techniques, tools, and control parameters needed to advance the FSLW method using experimental trials, testing, and validation at the laboratory scale and transition this work for integration into a production-like environment in association with the collaborating partner. The resulting body of work and knowledge base will enable automotive OEMs to effectively move towards commercialization of the joining technology for lightweight Al sheets. The project began in mid-FY 2017, with all the necessary agreements between the two partnering companies and PNNL in place.

Accomplishments

- Selected and established sourcing of three specific material stack-ups consisting of several combinations of 5xxx, 6xxx, and 7xxx materials (e.g., thicknesses, alloy types, and temper) for the life of the project in association with the partnering OEM and material supplier (FY 2017).
- Received and sized a large set of material from a partnering material supplier in preparation of weld development, characterization, and validation (FY 2017).
- Established and tested initial welding parameters, tool design, and process specifications to produce an FSLW joint between required stack-up of 5xxx, 6xxx, and 7xxx series of material (FY 2017).
- Established parametric tool design setup for weld configuration in the project, and procured initial FSLW tools with 24 different designs (FY 2017).

Technology Assessment

- Target: Establish testing and performance criteria for linear joints.
- Gap: While testing criteria for point joints (like rivets and other fasteners) already exists, a similar testing criterion for a continuous joint in Al assembly is not available.
- Target: Develop high-speed welding parameters in dissimilar lap welding of Al alloys.

- Gap: Commercially relevant welding speeds are higher than demonstrated at the research scale and robust processing parameters need to be developed that produce quality parts.

Project Introduction

While many successful demonstrations of the FSW process have been made in butt-joint configurations over the years, it is mostly lap joints that enable assembly of the modular components in the automotive industry. Assembly techniques used at present include rivets and adhesives; however, each has specific challenges when applied to join dissimilar alloy Al components. Assembly via high-speed FSLW would enable greater versatility in the integration of dissimilar Al sheet components, since it avoids surface issues associated with the use of adhesives and point assembly using rivets. Furthermore, assembly of body structures could be done without the need for rivets penetrating the outside surface with the use of FSLW.

A considerable amount of process development and some commercial adoption of FSW technologies have been made over the years. Similar to FSW, FSLW allows for solid-state assembly of a common joining geometry needed in the automotive industry. In FSLW, two or more sheets of different thicknesses, alloying elements, surface treatments, and/or strengths are stacked in desired order with required overlap. A rotating tool, plunges into the material stack-up extending through the bottom of the top sheet and into the bottom sheet creating a continuous linear bond between the faying surfaces of the sheets. Unlike butt-joint FSW, the lap joint interface is oriented perpendicular to the axis of tool rotation. Because of this, FSLW has a tendency for inadequate mixing of the multi-sheet stack-ups. Furthermore, undispersed surface oxide at the interface can lead to undesirable material upturn on either side of the nugget, often referred to as “hooks.” These hooks are formed adjacent to the tool and are detrimental to the joint performance.

Certain combinations of welding control parameters and tool geometries have been shown to perform better in the literature (Cederqvist and Reynolds 2001, Song et al. 2014, Soundararajan 2007); however, these parameters are highly specific to a chosen material stack-up. The reported strength values have large scatter and can range anywhere between 20 and 60% of the base metal. In addition to reported variation in weld strength, welding speed is another important issue that persists as a primary obstacle to commercialization. The welding speeds reported are relatively low (most of the welds are performed at around 0.3 to 0.6 m/min while only a few show capabilities up to 1 m/min) and do not justify commercial investment nor a switch to FSLW technology unless a significant improvement in welding speed can be demonstrated. Using and expanding the knowledge base from our earlier efforts, this project will develop FSLW up to a speed of 3 m/min.

A comprehensive series of weld trials will be conducted on material combinations that are most relevant to Honda R&D America (HRA) using a wide variety of welding parameters and tool designs. These trials are designed to help build functional relationships between several identified critical factors like the effective sheet thickness, interface morphology, tool geometry, control parameters and the joint morphology and resulting lap shear strength. Having developed these fundamental relationships, HRA will be able to more effectively move towards commercialization by understanding characteristics such as the effect of material stack-up with strong material on the top versus the bottom, placement of the advancing or retreating side in relation to the loading direction, interfacial coatings, etc.

Approach

In order to advance FSLW technology necessary to enable mainstream commercialization of dissimilar Al assembly and mitigate the technological gaps discussed in earlier sections, a systematic project plan is proposed. The project is divided into three main task areas and several milestones to ensure risk mitigation and successful completion. Task 1 focuses on the initial FSLW development and characterization. This task concludes with a performance milestone that enables continued development and process improvements. Task 2 expands upon work to be accomplished in Task 1, by optimizing the tool design; introducing stationary shoulder; and demonstrating applicability across additional alloys, thicknesses, and material combinations.

This task will ultimately lead to a decision gate for use of the process in the prototypical demonstrations associated with Task 3 by providing the information necessary to justify capital investments and product design for technology commercialization. Task 3 is divided into two subtasks that will prepare the process for commercialization and ultimately demonstrate the process in a production-like environment.

Technology Transfer Path

Technology transfer will be made directly through the project participants (i.e., HRA and Arconic), who will be the implementers of the technology. PNNL will support technology transfer of the developed FSLW technique in the selected dissimilar Al assembly for demonstration at PNNL and functional validation at HRA's facility in a specific production concept. This will include integration of FSLW tooling, parameters, and fixtures integrated with HRA's anticipated product development equipment.

Results

This project began in mid-FY 2017. No substantial experimental results are available at present.

Conclusions

During FY 2017, the project started with all the necessary agreements in place for effective information and material sharing between the partnering entities. Arconic and HRA provided input into material sourcing and material stack-up necessary to demonstrate the FSLW process for commercialization efforts. We have received the first batch of material for process development and characterization. Initial welding parameters, tool design, and process specifications have been established. A series of welding schedule and process development are underway.

References

Cederqvist, L., and A. P. Reynolds, 2001, "Factors affecting the properties of friction stir welded aluminum lap joints," *Welding Journal-New York*, Vol. 80, No. 12, pp. 281–287.

Song, Y., X. Yang, L. Cui, X. Hou, Z. Shen, and Y. Xu, 2014, "Defect features and mechanical properties of friction stir lap welded dissimilar AA2024–AA7075 aluminum alloy sheets," *Materials & Design*, Vol. 55, pp. 9–18.

Soundararajan, V., E. Yarrapareddy, and R. Kovacevic, 2007, "Investigation of the friction stir lap welding of aluminum alloys AA 5182 and AA 6022," *Journal of Materials Engineering and Performance*, Vol. 16, No. 4, pp. 477–484.

II.3.F Corrosion Protection of Dissimilar Material and Joining for Next Generation Lightweight Vehicles (Arconic)

Donald J. Spinella, Co-Principal Investigator
Arconic Technical Center
100 Technical Dr.
New Kensington, PA 15069
Phone: 724-337-2284
E-mail: DJ.Spinella@arconic.com

Sandeep S. Karwa, Co-Principal Investigator
Arconic Technical Center
100 Technical Dr.
New Kensington, PA 15069
Phone: 724-337-2831
E-mail: Sandeep.Karwa@arconic.com

Sarah Kleinbaum, Technology Manager
E-mail: sarah.kleinbaum@ee.doe.gov

Start Date: October 1, 2016 End Date: September 30, 2019
Total Project Cost: $2,395,295 DOE share: $1,764,331 Non-DOE share: $630,964

Executive Summary

The automotive industry is being driven to improve the fuel economy of the U.S. fleet. This is required by the stepped target improvement in the Corporate Average Fuel Economy (CAFE) Standard from 2012–2025 and customer demands for better fuel economy. Honda and other automotive OEMs have needs for higher levels of lightweighting beyond the increased use of Al in closure panels. As a result, multi-material solutions within the BIW are rapidly increasing to meet these requirements when a full Al BIW structure is not required. Multi-material structures require material isolation to prevent galvanic corrosion and a reliable joining method capable of joining all steel grades to Al or Al to carbon fiber composites.

The goal of the project is to demonstrate the use of resistance spot rivets (RSRs) to join steel to Al and Al to CFRP on a prototype scale. Prototype structures will be built to simulate specific joints in a multi-material vehicle. These RSR joints will be tested for strength and corrosion against baseline joining methods used today, such as self-pierce rivets (SPRs) and flow-drill screws (FDSs). The goal is to achieve an additional 10–20% weight reduction over high-strength steel. The resulting total weight savings will provide a 1.5–3% total improvement in fuel efficiency for vehicles that incorporate RSR for multi-material joining.

Accomplishments

- Defined target part and performance requirements for RSR joints (i.e., Al and steel sheet coatings and thickness, CFRP layup and thickness, joint adhesives, electrocoating [E-coat] and paint-bake, test coupon geometry, and testing standards).
- Created stack-up matrix for steel, Al, and carbon fiber RSR joints that includes top and bottom layers, pilot or non-piloted holes, with and without adhesives, and a sample quantity for each test.
- Ordered and procured material to produce multiple RSR test sample stack-ups (i.e., Al high-form alloy, Al alloy 6013, Aural2 Al alloy, Usibor® 1500 high-strength steel, JAC 980MPa galvannealed steel, and CFRP).

- Procured structural adhesives and steel fasteners to produce steel RSR samples.
- Developed weld process parameters for steel RSR with a piloted hole (with and without adhesives).
- Planned manufacturing details and produced around 1000 steel RSR test samples for electrode life (EL), mechanical, and corrosion testing. Produced RSR samples both with and without pilot holes.
- Planned, defined, and produced baseline (i.e., SPR and FDS) samples. Approximately 100 samples of each were produced.
- Completed EL tests on steel RSR samples. Measured and recorded tensile strength across 200 RSR samples.
- Started corrosion testing (e.g., ASTM B117 specification—continuous neutral salt spray) on baseline SPR and FDS samples. Also, B117 corrosion tests for steel RSR have been started.
- Achieved target EL, corrosion performance and mechanical properties for steel RSR joints.

Technology Assessment

- Target: Produce RSR joints for Al to steel and CFRP to Al material combinations that exceed minimum TSS specimen and CTS specimen requirements with resistance welding equipment.
- Gap: Conventional resistance spot-welding of Al to steel has low joint strength. Currently, there is no way to join CFRP to Al using resistance spot-welding equipment.
- Target: Achieve at least 100 consecutive RSR joints above minimum-strength targets.
- Gap: Confidence in the RSR process robustness must be established for production applications. EL of the process must be in line with existing tip-dressing frequency to be viable.
- Target: Integrate and demonstrate RSR process in a pilot robotic resistance welding station.
- Gap: Confidence in the RSR process for high-volume manufacturing. RSR has only been demonstrated on a pilot station.
- Target: Assess RSR corrosion baseline and develop mitigation techniques to improve the overall corrosion performance for multi-material combinations.
- Gap: Corrosion behavior of other multi-material joining technologies are well understood. RSR needs to have a baseline established to compare to other technologies, and if necessary, improve the corrosion performance to meet end-customer needs.

Project Introduction

The goal of the project is to demonstrate the use of RSR to join steel to Al and Al to CFRP on a prototype scale. This new technology is being developed by Arconic to leverage the existing automotive resistance spot welding infrastructure for high-performance joining of steel to Al and Al to CFRP.

When using this process to join an Al sheet to a steel sheet, a steel rivet is fed to a spot-weld gun. The initial spot-weld cycle heats the steel rivet, which is then forced through the Al sheet. Upon contact with the steel sheet, a resistance spot weld is made between the steel sheet and the rivet. An alternative is to use a pilot hole in the Al sheet and directly weld the rivet to the steel sheet while simultaneously mechanically locking the Al sheet.

In this project, the joint strength and corrosion performance will be documented with and without adhesives between steel and the Al sheet and Al and the CFRP sheet. The weld quality will be evaluated under different process conditions. The production viability will be evaluated with the feed system and integration of the feed system onto a robotic system.

Approach

During the first year of this program the focus was on weld process development and baseline characterization. The team (e.g., Arconic, Honda, and OSU) collectively developed the target multi-material combinations, including the Al alloys, steel grades, and CFRP layup orientations, along with gauges and orientations. Performance targets were identified for the manufacturing and testing conditions, including minimum tensile-shear and cross-tensile performance during an extended EL run. Weld process development and joint characterization was conducted on Arconic's RSR pilot equipment and corrosion performance of baseline technologies (e.g., SPR and FDS), along with RSR joints, were initiated.

Technology Transfer Path

The goal of this program is to demonstrate that the RSR technology enables high-performance joining in multi-material structures with existing resistance spot-welding infrastructure and knowledge base, offsetting billions of dollars in capital that other technologies would require. This project serves as a means of developing the joint requirements with Honda and the information needed to demonstrate the feasibility of the process. Corrosion performance will be evaluated by both Honda and OSU, and the results will guide optimization of the process, materials and coatings employed in the RSR fastener and joint materials. The RSR process will be demonstrated in a robotic station, providing guidance to future high-volume production applications. Arconic Fastening Systems and Rings will produce products for this contract (and for future production), rivets, and rivet feed systems. The rivets will be fabricated and the feed system manufacturing coordinated through their facility in Waco, TX. In addition to rivets and feed systems for this contract, Arconic Fastening Systems and Rings will manage all sales and marketing efforts to all potential automotive customers.

Results

Table II.3.F.1 shows the test plan developed by the team to evaluate the process parameters and performance of RSR versus baseline joining technologies employed in multi-material assembly today. The test plan matrix consists of three broad categories for RSR—joining Al to steel with a steel-based fastener and joining both steel to Al and CFRP to Al with an Al-based fastener. In terms of the steel RSR fastener, the process can accommodate both a piloted (hole through the top sheet where the fastener is inserted prior to welding) and a self-pilot (rivet heats and pushes through the Al top sheet prior to welding) mode. The Al RSR fastener is only applied in piloted mode for this program. It should be noted that MMHF denotes Arconic's MicroMill™ high form Al sheet.

Table II.3.F.1. Test Plan Matrix for Preliminary Electrode Life, Mechanical, and Corrosion Tests.

Joint Stackup Description							Team Member Test Type			Budget Period
Rivet	Pilot	Top	Adh.*	Mid	Adh.*	Bottom	Arconic	Honda	OSU	
Steel Resistance Spot Rivet	Y	AURAL2 3.0mm	Y			JAC980 1.2mm	E	C	C	1
	Y	AURAL2 3.0mm	N			JAC980 1.2mm	M		C	1
	Y	AURAL2 3.0mm	Y	JAC980 1.2mm	N	JAC980 1.2mm	E	C	C	1
	Y	AURAL2 3.0mm	N	JAC980 1.2mm	N	JAC980 1.2mm	M		C	1
	N	MMHF-T4 1.0mm	Y	Usibor® 1500 1.2mm	Y	JAC980 1.2mm	E	C	C	1
	N	MMHF-T4 1.0mm	N	Usibor® 1500 1.2mm	Y	JAC980 1.2mm	M		C	1
	Y	AA6013-T4 2.0mm	N			JAC980 1.2mm	M		C	1
	Y	AA5754-0 2.0mm	N			JAC980 1.2mm	M		C	1
	Y	AA7055-T76 2.0mm	N			JAC980 1.2mm	M		C	1
	Y	AA6013-T4 2.0mm	N			JAC590 1.2mm	M		C	1
Aluminum Resistance Spot Rivet	Y	JAC980 1.2mm	Y			AURAL2 3.0mm	E	C	C	2
	Y	JAC980 1.2mm	N			AURAL2 3.0mm	M		C	2
	Y	JAC980 1.2mm	N	JAC980 1.2mm	Y	AURAL2 3.0mm	E	C	C	2
	Y	JAC980 1.2mm	N	JAC980 1.2mm	N	AURAL2 3.0mm	M		C	2
	Y	JAC980 1.2mm	Y	Usibor® 1500 1.2mm	Y	MMHF-T4 1.0mm	E	C	C	2
	Y	JAC980 1.2mm	N	Usibor® 1500 1.2mm	N	MMHF-T4 1.0mm	M		C	2
	Y	Semi-iso CFRP 4.0mm	Y			AA6013-T4 2.0mm	E	C	C	2
	Y	Semi-iso CFRP 4.0mm	N			AA6013-T4 2.0mm	M		C	2
	Y	Semi-iso CFRP 4.0mm	Y			AA6013-T4 3.0mm	E	C	C	2
Aluminum Self- Pierce Rivet	N	JAC590 1.2mm	Y			AA6013-T4 2.0mm	M		C	1
	N	JAC590 1.2mm	N			AA6013-T4 2.0mm	M		C	1
Steel Flow Drill Screws Baseline	Y	JAC980 1.2mm	Y			AA7055-T76 2.0mm	M		C	1
	Y	JAC980 1.2mm	N			AA7055-T76 2.0mm	M		C	1
Adh* - Adhesive between sheets				Test Code:		Electrode Life	Mechanical Testing		Corrosion	

In addition to rivet materials, two thickness (2T) and three thickness (3T) stack-up combinations were evaluated. The effect of the Honda-supplied adhesive (Dow 5055C) between the Al and steel interfaces on both the joint and corrosion performance was also considered in the test matrix. Al, steel, and CFRP materials and thickness combinations were selected as target conditions and represent a broad class of applications that could be employed by the industry to achieve weight savings over today's baseline steel structure. A complete battery of tests (e.g., EL at Arconic followed by various corrosion tests at Honda and OSU) were either completed or are currently in progress for these target conditions. Other material combinations were also produced, not only for RSR, but baseline technologies such as SPR and FDS as well. These will undergo both mechanical testing at Arconic and corrosion testing at OSU. The purpose of these joints is to establish a baseline understanding of the impact of a broad range of Al alloys and the effect of adhesive on the corrosion

performance. Only the steel RSR along with the baseline SPR and FDS specimens were produced during BP1. The remaining joints, which include the Al fastener, will be completed in BP2.

Prior to samples being produced for EL and corrosion testing, each combination was tested at several weld settings, establishing the operating parameters to produce joints with sufficient strength. Weld process parameters were optimized through a series of cross-sectioning and peel-testing with the goal of establishing a weld diameter between the RSR and steel sheet that was roughly 3–5 times the square root of the sheet gauge. Once the parameters were optimized for a combination, a series of joints would be produced at that setting without changing the weld equipment settings and electrodes. EL conditions joining through 3mm AL employed the R4-6GA (e.g., 4 mm length, 6 gauge diameter) rivet while the 1 mm AL trials used the R4-3GA (e.g., 4 mm length, 3 gauge diameter).

Figure II.3.F.1 shows the two types of samples (with dimensions) employed during this program—TSS and CTS. TSS samples were produced for all combinations, but CTS samples were only produced for the EL evaluation.

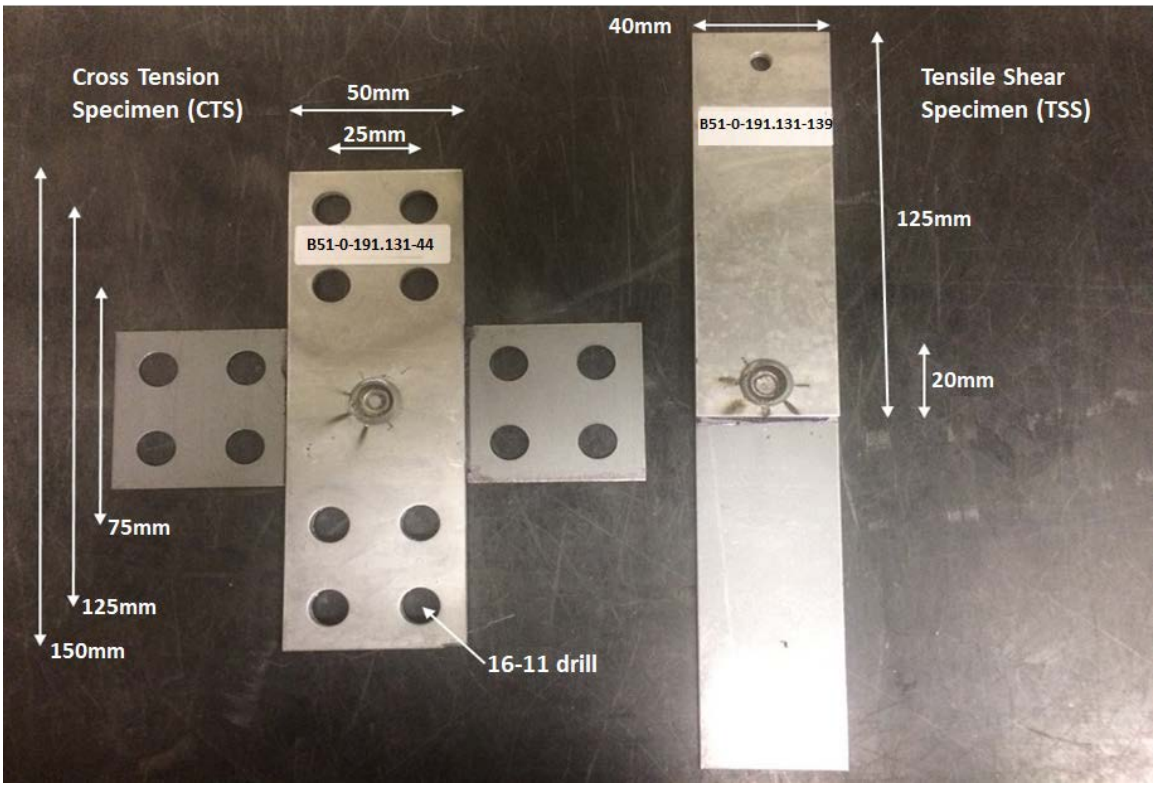

Figure II.3.F.1. CTS and TSS resistance spot rivet test samples for EL tests. Source: Arconic.

EL performance is an important metric in understanding the production robustness of the process. Typical production applications will dress the electrodes after a few hundred welds to maintain tight process control. A special EL procedure was developed in this program such that all members of the team would have access to samples through various stages of electrode wear. Table II.3.F.2 shows how the samples were divided among the team. The Go/No-Go decision for BP1 was based on EL performance, with the targets shown in Table II.3.F.3. The goal was to demonstrate at least 100 consecutive RSR joints whose TSS and CTS values exceeded the targets. An electrode life of 100 was selected since it is representative of electrode dressing values as seen in production resistance spot welding of an Al sheet. The TSS and CTS minimum strengths were established by internal Honda models that consider the material properties, gauges, and joint geometry.

Table II.3.F.2. Electrode life specimen description.

Weld Number Start	Weld Number End	Weld Number Total	Specimen Type	Post Weld Test Location	Post Weld Paint-Bake	Post Weld E-Coat
1	6	6	TSS	Arconic	N	N
7	7	1	TSS - section	Arconic	Y	N
8	19	12	TSS	OSU	Y	N
20	25	6	TSS	Arconic	N	N
26	34	9	CTS	Arconic	N	N
35	50	16	CTS	Honda	E-coat	Y
51	56	6	TSS	Arconic	N	N
57	57	1	TSS - section	Arconic	Y	N
58	65	8	TSS	Honda	E-coat	Y
66	72	7	TSS	OSU	Y	N
73	78	6	TSS	Arconic	N	N
79	79	1	TSS - section	Arconic	Y	N
80	84	5	TSS	OSU	Y	N
85	93	9	TSS	Honda	N	Y
94	94	1	TSS - section	Arconic	E-coat	N
95	100	6	TSS	Arconic	N	N
101	106	6	TSS	Arconic	N	N
107	107	1	TSS - section	Arconic	Y	N
108	116	9	TSS	Honda	E-coat	Y
117	121	5	TSS	OSU	Y	N
122	122	1	TSS - section	Arconic	Y	N
123	128	6	TSS	Arconic	N	N
129	135	7	TSS	OSU	Y	N
136	143	8	TSS	Honda	E-coat	Y
144	144	1	TSS - section	Arconic	Y	N
145	150	6	TSS	Arconic	N	N
151	167	17	CTS	Honda	E-coat	Y
168	175	8	CTS	Arconic	N	N
176	181	6	TSS	Arconic	N	N
182	193	12	TSS	OSU	Y	N
194	194	1	TSS - section	Arconic	Y	N
195	200	6	TSS	Arconic	N	N
Total		**200**				

Table II.3.F.3. BP1 Strength Target Criteria for Go/No-Go Condition.

Target Parameter	Unit	Governing Gauge and Alloy		Comments
		1.0 mm MMHF-T4	3.0 mm Aural 2-T7	
EL Minimum	Number of Welds	100	100	Consecutive welds achieved before TSS or CTS drops below minimum.
TSS Minimum	kN	1.51	3.38	Honda — formula based on parent material properties and gauge.
CTS Minimum	kN	0.60	1.35	Honda — formula based on parent material properties and gauge.
Corrosion	Visual	Qualitative	Qualitative	BP1 — currently, only visual inspection is required until enough corrosion cycles are completed in BP2.

The Go/No-Go evaluation was based on the as-welded RSR joints produced by Arconic with no additional paint-bake operations. Samples undergoing corrosion testing were either paint-baked (for OSU) or E-coated (for Honda), which subjects the samples to an elevated cure temperature. Paint-bake and E-coat followed guidelines established by Honda. Since the samples have not completed significant exposure to corrosion, it was decided by the team to visually note any issues at this phase.

The EL test results can be seen in Figure II.3.F.2 through Figure II.3.F.7 for the three target combinations. TSS was monitored at 10 different intervals over 200 welds. At each test interval, six consecutive welds were evaluated. CTS was monitored at two different intervals with either eight or nine consecutive welds. Figure II.3.F.2 shows the static strengths for the 1.2 mm 980 MPa steel to 3.0 mm Aural2 Al joint stack up. Welds were also sectioned, polished, and etched during the EL, as seen in Figure II.3.F.3, with weld sizes ranging between 4.8 mm to 5.1 mm.

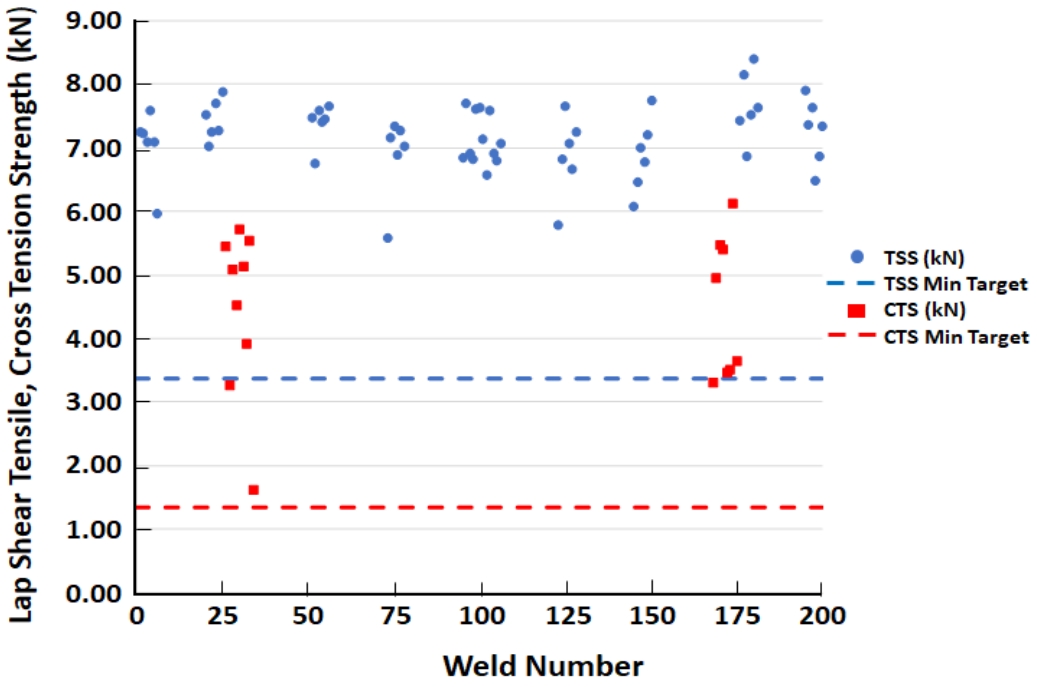

Figure II.3.F.2. Results from the EL Trial – 1.2 mm 980 MPa to 3.0 mm Aural 2 (e.g., 6 mm pilot) – through the Dow 5055-C with R4-6GA-V rivet.

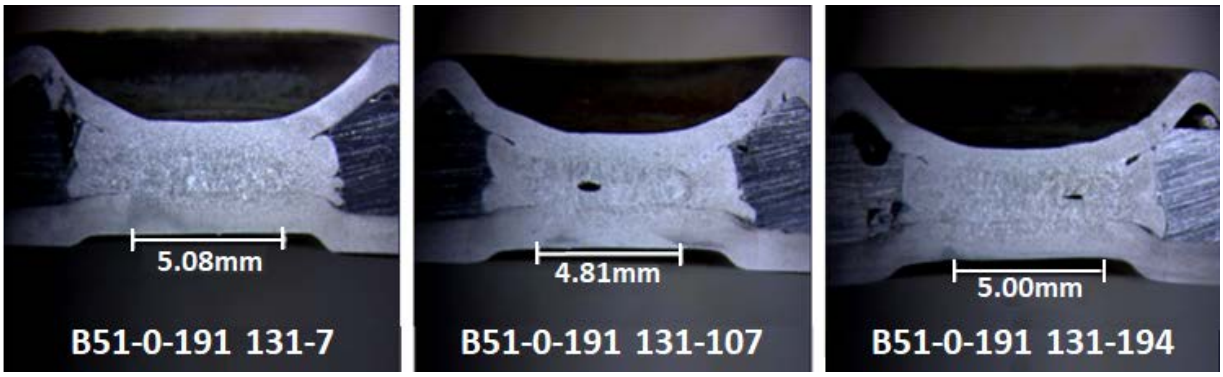

Figure II.3.F.3. Results from the EL Trial – 1.2 mm 980MPa to 3.0 mm Aural 2 (6 mm Pilot) – through the Dow 5055-C with R4-6GA-V rivet (left to right): Weld #7 Section, Weld #107 Section, and Weld #194 Section. Source: Arconic.

Figure II.3.F.4 and Figure II.3.F.5 show the EL performance of a 3T joint that employs a pilot hole through the Al sheet. The strength performance of this joint showed excellent stability over 200 welds, especially in the CTS results as compared to the first joint combination. Similar results are shown for the self-pilot 3T stack-up combinations seen in Figure II.3.F.6 and Figure II.3.F.7. The failure mode for the 3T joints was predominantly a fracture in the Al sheet. A few of the low CTS values observed in the 2T combinations, as seen in Figure II.3.F.2, were attributed to interfacial fractures. The process parameters require additional optimization to reduce this failure mode.

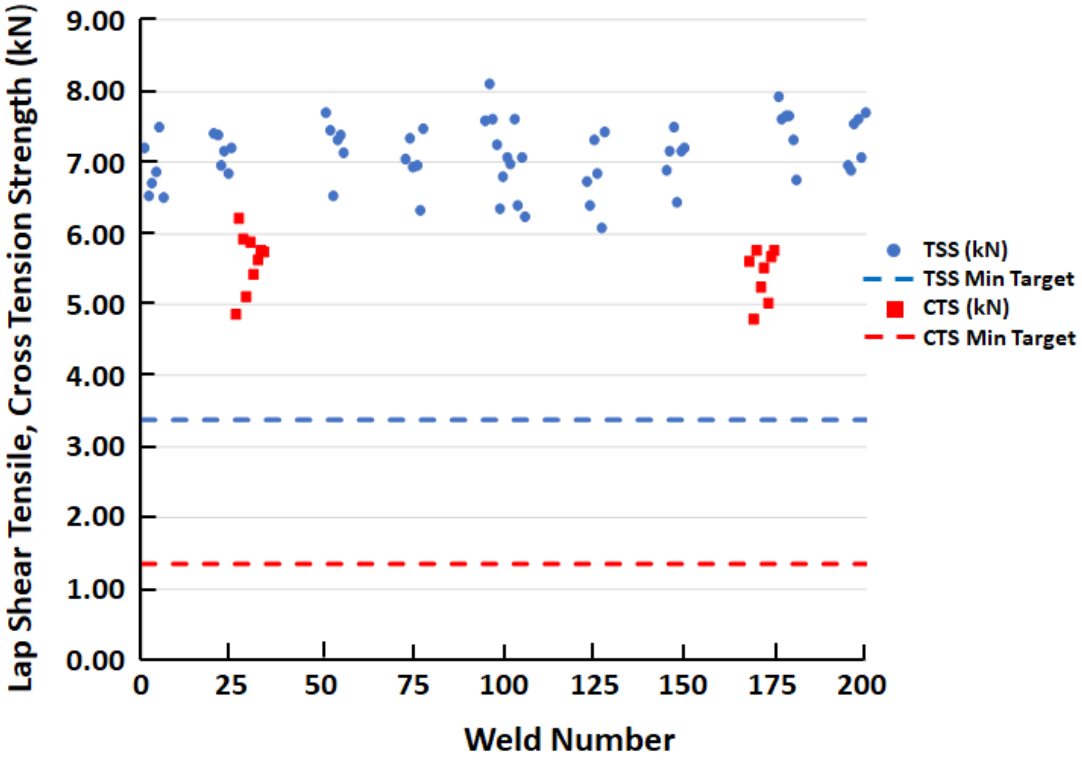

Figure II.3.F.4. Results from the EL Trial – 1.2 mm 980 MPa to 1.2 mm 980Mpa to 3.0 mm Aural 2-T7 (6 mm pilot) – through the Dow 5055-C with R4-6GA-V rivet.

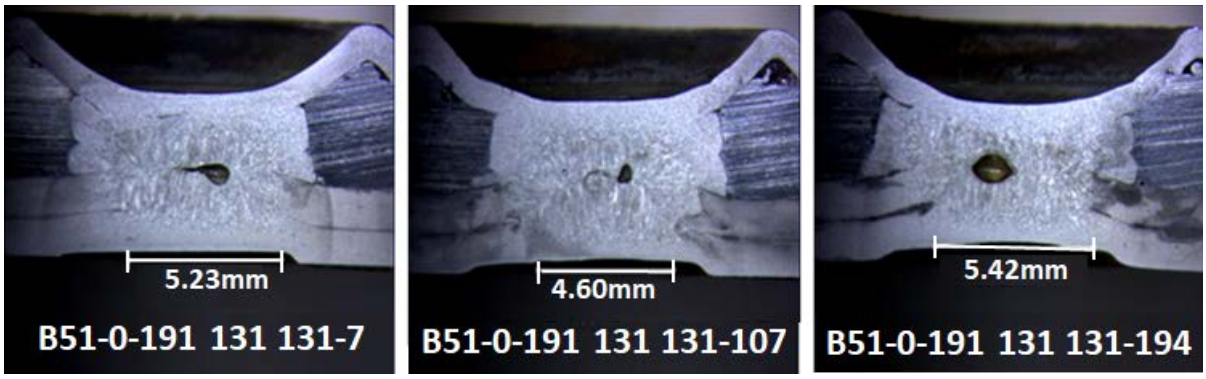

Figure II.3.F.5. Results from the EL Trial – 1.2 mm 980MPa to 1.2 mm 980MPa to 3.0 mm Aural 2-T7 (6 mm pilot) – through the Dow 5055-C with R4-6GA-V rivet (left to right): Weld #7 Section, Weld #107 Section, and Weld #194 Section. Source: Arconic.

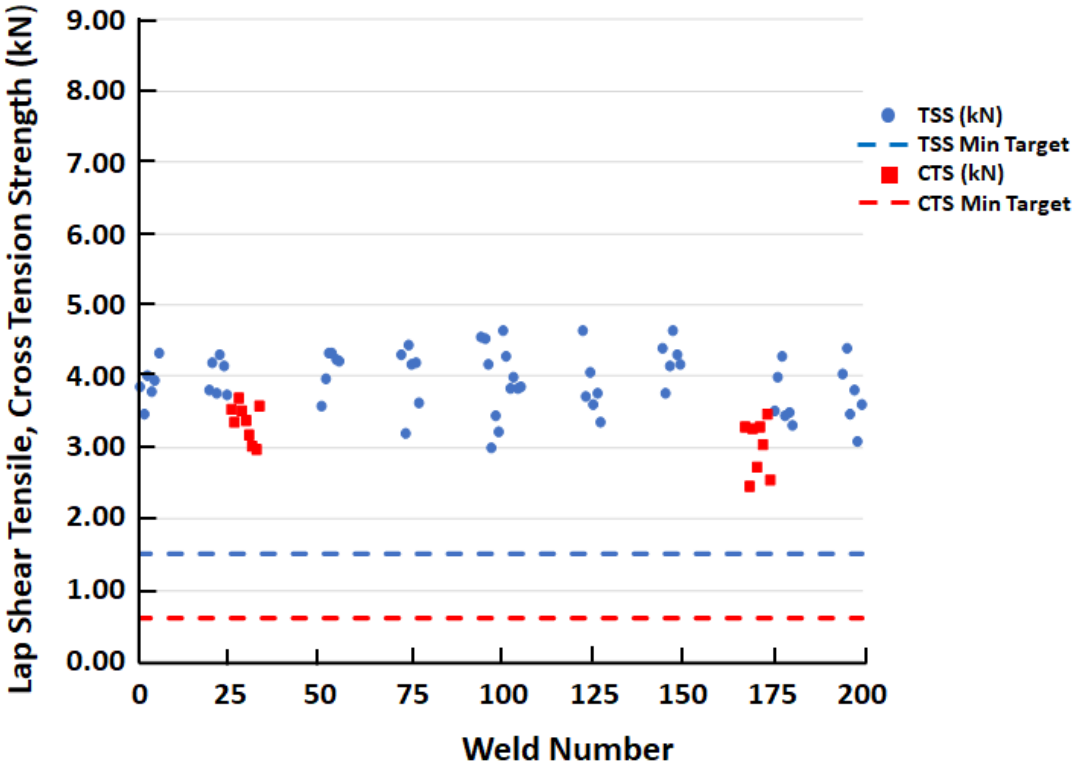

Figure II.3.F.6. Results from the EL Trial – 1.2 mm 980 MPa to 1.2 mm Usibor® 1500 to 1.0 mm MMHF-T4 (self-pilot) – through the Dow 5055-C with R4-3GA rivet.

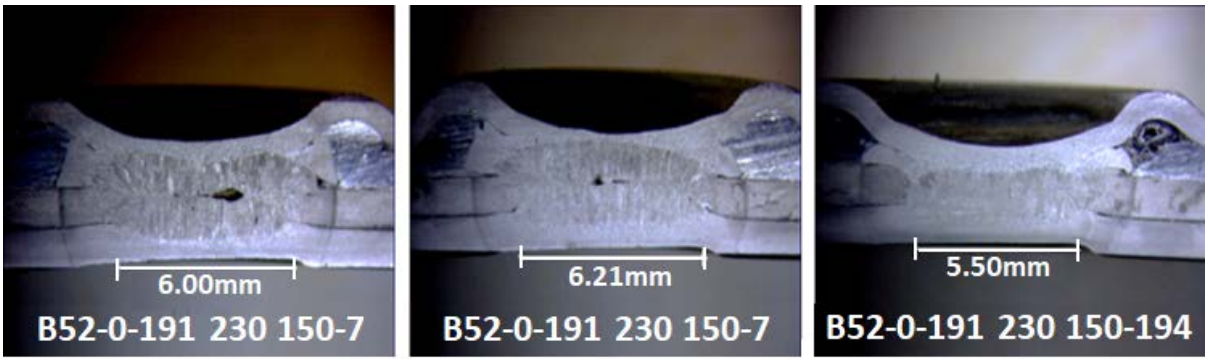

Figure II.3.F.7. Results from the EL Trial – 1.2 mm 980MPa to 1.2 mm 980MPa to 3.0 mm Aural 2-T7 (6 mm pilot) – through the Dow 5055-C with R4-6GA-V rivet (left to right): Weld #7 Section, Weld #107 Section, and Weld #194 Section. Source: Arconic.

The results of EL testing can be seen measured against the team targets in Table II.3.F.4. The testing exceeded both the strength and EL targets for all three target joint combinations.

Table II.3.F.4. BP1 Go/No-Go Target Criteria versus Actual Results.

EL Joint Stack-up Description							TSS Minimum, kN		CTS Minimum, kN		EL, # Welds	
Rivet	Pilot	Top	Adh	Mid	Adh	Bottom	Target	Measured	Target	Measured	Target	Measured
Stl RSR	Y	AURAL2 3.0 mm	Y			JAC 980 1.2 mm	3.38	5.57	1.35	1.61	100	200
	Y	AURAL2 3.0 mm	Y	JAC 980 1.2 mm	N	JAC 980 1.2 mm	3.38	6.08	1.35	4.79	100	200
	N	MMHF-T4 3.0 mm	Y	USIBOR 1500 1.2 mm	Y	JAC 980 1.2 mm	1.51	2.99	0.60	2.46	100	200
						Color Code	Target		Below Target	Met Target	Above Target	

Dr. Jenifer S. Locke, with the assistance of her graduate student, Mr. Paul Krell, OSU, is characterizing and quantifying the galvanic corrosion performance. The plan for the first budget period included assessing baseline technologies (e.g., SPR and FDS) for comparison and beginning corrosion characterization of RSR joints to understand worst case galvanic corrosion scenarios and any benefit that can be provided by adhesives. Evaluation methods planned were accelerated corrosion specifications ASTM B117, ASTM G85, and the Nissan underbody corrosion test.

This first budget period focused largely on characterizing the SPR and FDS conventional joining technologies and comparing performance to RSR. To accomplish this goal, accelerated cabinet corrosion exposure in ASTM B117 (e.g., neutral sodium chloride solution applied in continuous salt spray) followed by optical examination, macro-photographic documentation, and mechanical testing after corrosion, was performed. For initial testing and comparison, three different B117 corrosion exposure times were conducted 2.7, 10.7, and 32.4 days. These times were chosen based on visual appearance of the first round of an exposed joint with the aim of producing light, moderate, and severe corrosion.

For RSR versus SPR, AA6013-T4 to 590 MPa steel joints were examined. Figure II.3.F.8 shows macro-photographs of the RSR and SPR joints after testing in ASTM B117 after 2.7, 10.7, and 32.4 days. No obvious

difference in the corrosion performance of the RSR and SPR joints can be identified from these macro-observations. For RSR versus FDS, AA7055-T76 to 980 MPa steel joints were examined. Figure II.3.F.9 shows macro-photographs of the RSR and FDS joints after testing in ASTM B117 after 2.7 and 10.7 days. No obvious difference in the corrosion performance of RSR and FDS joints can be identified from these macro-observations.

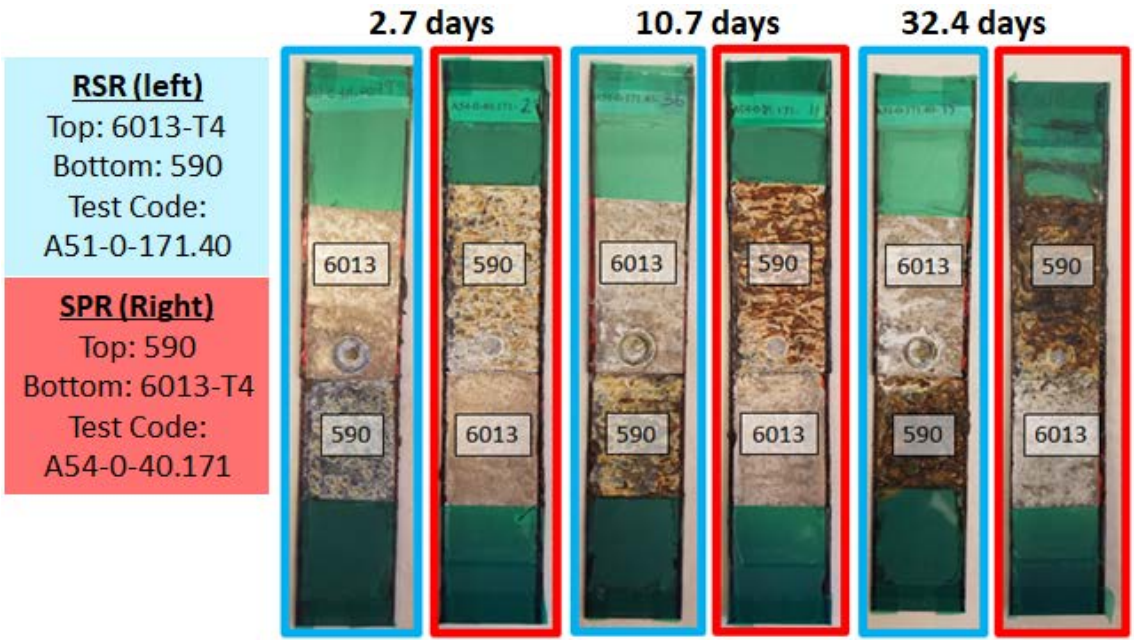

Figure II.3.F.8. RSR and SPR joints between AA6013-T4 and 590 steel after ASTM B117 exposure after 2.7, 10.7, and 32.4 days. Source: Arconic.

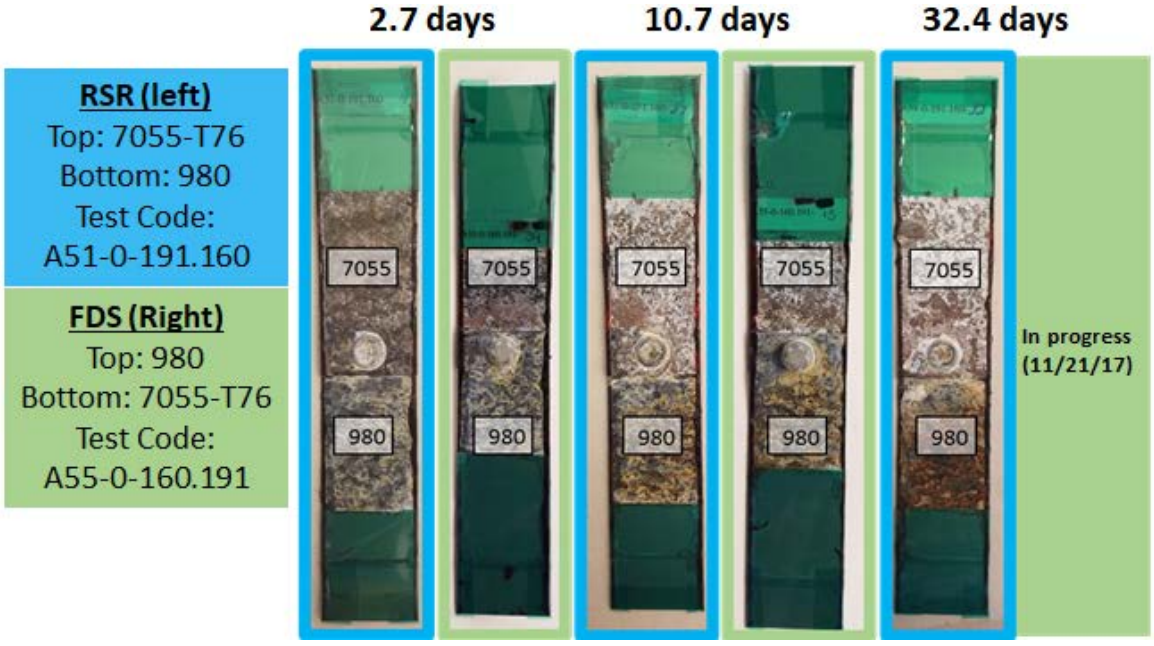

Figure II.3.F.9. RSR and FDS joints between AA7055-T76 and 980 steel after ASTM B117 exposure for 2.7 and 10.7 days. The RSR joint was also tested up to 32.4 days, but the FDS sample will not be pulled until 11/21/17. Source: Arconic.

Results from ASTM B117 testing for SPR joints between 590MPa steel and AA6013-T4 with and without an adhesive are shown in Figure II.3.F.10. FDS joints between 980MPa steel and 7055-T76 with and without an adhesive are shown in Figure II.3.F.11. The macro-photographs in Figure II.3.F.10 and Figure II.3.F.11 do not show any obvious difference in corrosion performance due to the addition of adhesive.

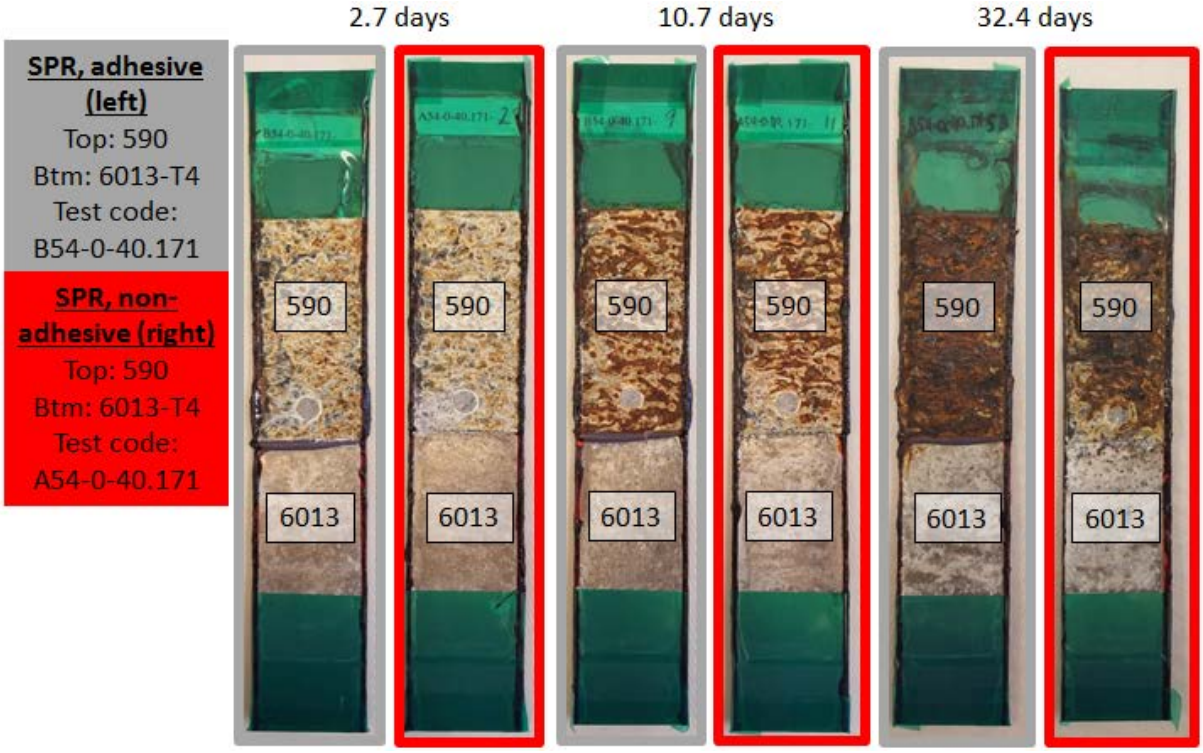

Figure II.3.F.10. SPR joints between 590 steel and AA6013T6 with (gray) without (red) adhesive after ASTM B117 exposure for 2.7, 10.7, and 32.4 days. Source: Arconic.

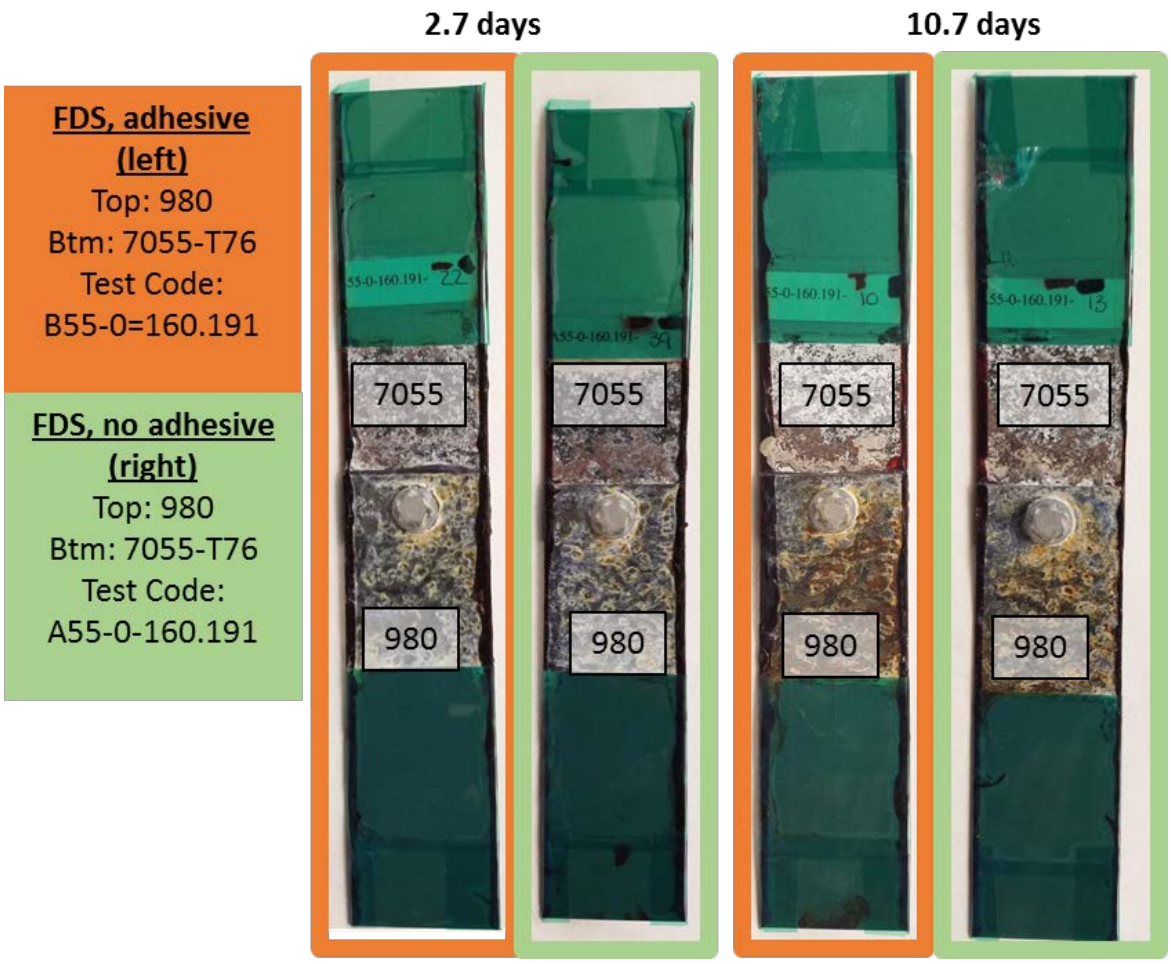

Figure II.3.F.11. FDS joints between AA7055-T76 and 980 steel with (orange) and without (green) adhesive after ASTM B117 exposure for 2.7 and 10.7 days. Source: Arconic.

After ASTM B117 testing, the most severely corroded sample from each exposure time and joint type was mechanically tested to failure to determine the ultimate load sustainable and failure mode. The sample types and exposure times tested to date are shown in Table II.3.F.5. Three different failure modes were observed during mechanical testing. SPR joints all failed by SPR pull out, while RSR joints experienced failure by either deformation around RSR or fracture of the RSR rivet itself. Comparison against the uncorroded counterpart is underway and is necessary to assess the impact of corrosion on mechanical failure.

In addition to mechanical testing, it is critical to also perform post-corrosion analysis that will quantify the type and depth of attack. Due to the nature of the mixed material joints, it was decided that optical profilometry would not be utilized. The rivets that rise above the surface would preclude any near rivet topographic investigation. Therefore, serial cross-sectional analysis is planned and will start in BP2. Preparation for this analysis has occurred during BP1.

Table II.3.F.5. Mechanical Testing Data Post Corrosion Exposure.

Joint Type	Sample #	Adh	Top Sheet	Middle Sheet	Bottom Sheet	Exposure, Days	Max Load, kN	Failure Mode
RSR	19	N	6013-T4		590MPa Steel	2.7	8.82	RSR Fracture
	36	N	6013-T4		590MPa Steel	10.7	10.48	Material deformed around RSR*
	15	N	6013-T4		590MPa Steel	32.4	9.07	RSR Fracture
	16	N	5754-0		590MPa Steel	2.7	6.72	Material deformed around RSR*
	15	N	5754-0		590MPa Steel	10.7	6.73	Material deformed around RSR
	37	N	5754-0		590MPa Steel	32.4	6.70	Material deformed around RSR
	11	N	7055-T76		590MPa Steel	2.7	11.47	RSR Fracture
	27	N	7055-T76		590MPa Steel	10.7	12.50	RSR Fracture
	32	N	7055-T76		590MPa Steel	32.4	11.86	Material deformed around RSR
	8	N	MMHF-T4	Usibor® 1500	590MPa Steel	2.7	5.99	Material deformed around RSR*
	12	N	MMHF-T4	Usibor® 1500	590MPa Steel	10.7	6.02	Material deformed around RSR
	17	N	MMHF-T4	Usibor® 1500	590MPa Steel	32.4	5.58	Material deformed around RSR
SPR	28	N	590MPa Steel		6013-T4	2.7	9.19	SPR Pullout
	11	N	590MPa Steel		6013-T4	10.7	9.16	SPR Pullout
	25	N	590MPa Steel		6013-T4	32.4	8.84	SPR Pullout
	5	Y	590MPa Steel		6013-T4	2.7	11.19	SPR Pullout
	9	Y	590MPa Steel		6013-T4	10.7	17.79	SPR Pullout
	53	Y	590MPa Steel		6013-T4	32.4	11.17	SPR Pullout*

* Mechanical testing not carried out to complete separation.

Conclusions

In year one of this project, the team defined target part and performance requirements for RSR joints (i.e., Al and steel sheet coatings and thickness, CFRP layup and thickness, joint adhesives, E-coat and paint, test coupon geometry, and testing standards). The test plan matrix was developed for these materials that included top and bottom layers, pilot or non-piloted holes, with and without adhesives, and a sample quantity for each test.

Materials were ordered and procured to produce multiple RSR test sample stack-ups (i.e., Al high-form alloy, A6013 Al alloy, Aural2 Al alloy, Usibor® 1500 high-strength steel, JAC 980MPa galvannealed steel, and CFRP) in addition to the structural adhesive and steel fasteners.

Weld process parameters for the steel-based RSR with and without adhesives were also developed. After optimizing the process parameters, approximately 1000 coupons were manufactured as part of the EL and corrosion assessments. EL testing was conducted on three different material combination conditions and all static strength (both TSS and CTS) and EL targets were achieved. Additionally, samples of baseline multi-material technologies (SPR and FDS) were manufactured for corrosion assessment. OSU began corrosion testing (ASTM B117 continuous neutral salt spray) on baseline SPR and FDS in addition to steel-based RSR.

The team partners (e.g., Arconic, Honda, and OSU) had a successful technical review on November 9, 2017. We reviewed the EL and mechanical properties for steel RSR joint, corrosion test performance on baseline SPR and FDS joints, and the RSR joint. Based on the test results, the team has met the “GO” criteria and the project will proceed into BP2.

II.3.G Friction Stir Scribe Joining of Carbon Fiber Reinforced Polymer to Aluminum (General Motors)

Blair E. Carlson, Co-Principal Investigator
General Motors Global R&D
m/c 480-106-RL2
30470 Harley Earl Blvd.
Warren, MI 48092-2031
Phone: 586-864-7698
E-mail: blair.carlson@gm.com

Sarah Kleinbaum, Technology Manager
E-mail: sarah.kleinbaum@ee.doe.gov

Start Date: January 1, 2016 End Date: June 30, 2018
Total Project Cost: $3,217,374 DOE share: $1,608,687 Non-DOE share: $1,608,687

Executive Summary

The purpose of this project is to develop and demonstrate the capability of multi-material joining techniques for friction stir scribe (FSS) joining of CFRP to Al on light-duty vehicle BIW joints. The project is also intended to overcome the major obstacles of implementing FSS technology in a fully 3D production robotic work cell and demonstrate the required CFRP/AL joint strengths in industrially relevant light-duty, BIW components. Specifically, the project will develop the critical process technology, models, and tools necessary to advance the FSS method through experimentation, validation at the laboratory scale, and integration into a production-like robotic environment. The FSS process has been developed to include integration of the FSS tool with a stationary shoulder, which has been shown to be required to achieve the desired surface quality (i.e., crown flash level). However, the targeted joint strength has not been achieved because the resulting stirred CFRP microstructure does not provide similar performance as the as-molded composite leading to low fracture strengths despite our efforts investigating various unique alternative approaches. In support of the experimental work, a process-structure model was developed and validated for the friction stir scribe joining (FSSJ) process using surrogate materials (steel and Al).

Accomplishments

- Integrated stationary shoulder with FSS technique and initiated implementation of FSS and stationary shoulder for 3.0-mm CFRP PlastiComp Velocity® long carbon fiber 45-polyamid 6 (LCF45-PA6) to 2.2-mm AA6111-T4 dissimilar joining application (FY 2016).
- Identified CPM (10V)/AISI A11 tool material as preferred over conventional H13 tool steel for the application of the FSSJ pin tool based on its pin tool tip diameter loss of 0.12% versus 1.6%, respectively (FY 2017).
- Developed computational model of CFRP-Al FSS joint and investigated effects of scribe geometry and relative location of the pin tool on hook morphology (FY 2017).
- Measured temperature-dependent CFRP mechanical properties (e.g., 25, 150, and 200°C, respectively) as input to modeling (FY 2017).
- Identified best practice to fiber length measurement, which resulted in entirely reasonable fiber orientation measurements of the PlastiComp Velocity® LCF45-PA6 plaques using microcomputer tomography techniques (FY 2017).

- Characterized weld zone CFRP microstructure (i.e., fiber length as a function of RPMs and translation speed) and measured weld zone tensile strengths (FY 2017).
- Produced super lap and super coach peel joints of FSSJ with CFRP on top as well as Al on top and compared the mechanical properties to alternative joining methods such as adhesive only, SPR only, SPR plus adhesive and blind rivets with adhesive. FSSJ was unable to achieve the targeted strength levels (FY 2017).

Technology Assessment

- Target: The joint strength of a dissimilar CFRP/Al joint joined by the FSSJ process is to meet or exceed the joint strength from a self-pierced riveted with adhesive dissimilar CFRP/Al joint.
- Gap: FSSJ of a CFRP-on-top, CFRP/Al stack-up produces a stir zone with fiber attrition wherein the stir zone strength is significantly lower than the base CFRP substrate. Furthermore, the scribe produces an in-situ upsetting of the Al at the faying interface, which creates a hook feature. This hook feature, intended to mechanically couple the layers, initiates fracture within the CFRP stir zone, which progresses through the lower strength stir zone and limits the ability of this process to achieve the desired strength targets.
- Target: Develop and apply a process-structure model of the FSSJ process for the dissimilar material CFRP/Al joint.
- Gap: Process-structure model validation was completed for the FSSJ process using surrogate materials steel and Al. Application of the coupled Eulerian-Lagrangian FSSJ process-structure model to predict CFRP/AL joint properties remains to be done and requires increased understanding of temperature and strain rate-dependent CFRP material stress-strain behavior as model input.
- Target: Demonstrate the FSS technique in a 3D robotic application.
- Gap: FSS has yet to be demonstrated in a 3D robotic application as it is imperative to achieve the targeted joint strength before allocating time and resources to this endeavor.

Project Introduction

This project addresses the joining aspects of lightweight dissimilar material structures made with carbon fiber-reinforced thermoplastics and Al with the aim of achieving DOE's goal of increasing the efficiency of vehicle transportation by enabling more efficient multi-material solutions. Project collaborators include PNNL, who is the originator of the FSSJ method (Hovanski et al. 2012) and provided unique expertise related to the specific hybrid joining process and process-structure modeling competencies; Alcoa (now Arconic) and PlastiComp, who are providing experimental materials and material structure-property expertise; Autodesk, Inc. and LSTC, who are providing software and modeling expertise necessary to develop the tools required for technical implementation; and KUKA Robotics Corporation, who is an automotive supplier and robotic integrator and provided robotic implementation of the FSS technique in the automotive supply chain. Upon successful completion of the development at the laboratory scale, the project will demonstrate a proto-typical application using the FSS process applied in a robotic 3D application.

Implementation of FSS technology for joining polymer composites to metals will enable greater use of lightweight materials by providing technology capable of joining linear configurations without the use of adhesives or other third-body fasteners by creating an in-situ joint from the parent materials. As FSS technology provides the capability to join multi-material structures on robotic platforms using linear configurations, the development of this technology for use on the BIW will impact a great diversity of CFRP joints within the vehicle; thus, allowing a greater reduction in vehicle mass through more specifically designed structures.

Approach

The objective of this project is to develop and demonstrate the capability of multi-material joining techniques for FSSJ of CFRP to Al on light-duty vehicle BIW joints. The project will also overcome the major obstacles of implementing FSS technology in a fully 3D production robotic work cell and demonstrating the required CFRP/AL joint strengths in industrially relevant light-duty, BIW components. Specifically, the project will develop the critical process technology, models, and tools necessary to advance the FSS method through experimentation, validation at the laboratory scale (see Figure II.3.G.1 for an example of a test specimen), and integration into a production-like robotic environment. The ultimate goal is to demonstrate the technology on industrially relevant components based on process development and numerical simulation performed at scale. The approach is summarized in Figure II.3.G.2.

Figure II.3.G.1. Four-point bend hat section test specimen. Source: General Motors.

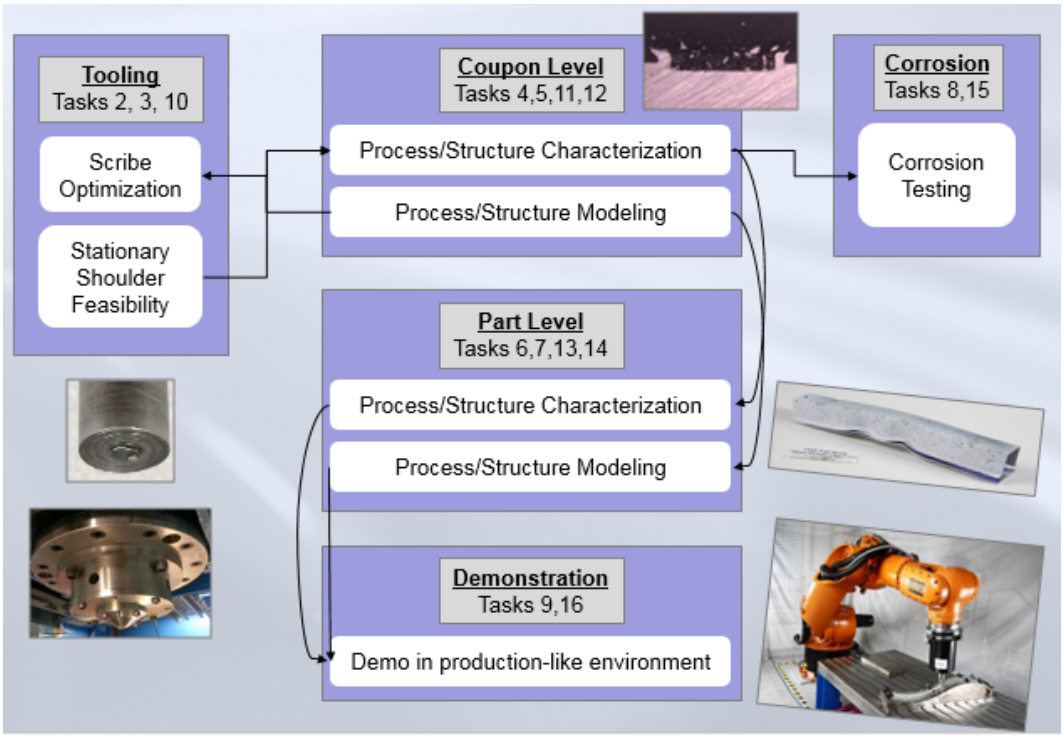

Figure II.3.G.2. Project approach strategy to address the technological roadblocks to friction stir scribe joining of CFRP/Al. Source: General Motors.

The project is to be conducted in two BPs wherein each period has specific tasks with a go/no-no decision gate after BP1:

- BP1: Coupon Level Optimization. Develop the FSS tooling and address the scribe tool/stationary shoulder integration issues in addition to developing the necessary process window parameters and process-microstructure-property model. This work will be based upon process development and numerical simulation performed at scale, wherein the models themselves are based upon experimental characterization of both base materials and joints as well as rigorous initial development of a process-structure model. The Go/No-Go gate is based upon achieving a defined minimum level of FSSJ CFRP to Al joint strength.
- BP2: Proto-typical Part Demonstration. Apply and optimize the coupon process window parameters to the hat section assembly and further develop/validate the process-structure model necessary to achieve optimized joint performance. This period will also demonstrate the technology on industrially relevant components in an integrated production-like environment at a production-like facility and investigate potential corrosion issues related to the dissimilar material joint.

Having shown that a stationary shoulder cannot only be integrated with the FSS tool but that it is required for achieving reasonable joint surface quality, several FSS process optimizations were attempted in the material set desired and supplied by participating partners in FY 2016. However, the desired joint strength was not achieved. Efforts in FY 2017 began with continued process optimization of the CFRP to Al stack-up. Several innovative alternatives were brought forward and pursued to achieve target strength. Furthermore, the original target was changed to better align the Go/No-Go target with joint strengths achievable with commercial-off-the-shelf technology solutions. This led to a broad comparative study of various joining approaches. In parallel to these experimental joining activities, the coupled Eulerian-Lagrangian FSSJ process-structure model was developed using tool geometry and process parameters as an input and weld interface (i.e., hook geometry) as a model output. This was validated based on Al/steel and applied to investigate scribe/pin geometries and their effect on the resulting joint interlock. Finally, a corrosion study was initiated, which is currently ongoing.

Technology Transfer Path

As one of the primary goals of this project, transferring the FSS process to the industrial participants is part of the everyday project execution. First, the team brings together the entire value chain from material suppliers, part manufacturers, engineering numerical tool providers as well as a robotic equipment integration supplier who will supply the technology as an off-the-shelf option, and finally the OEM who will ultimately integrate the dissimilar joining solution into their products. The project team develops the welding process and provides mechanical testing and characterization throughout the development to demonstrate how the technology is applied starting with coupons and maturing to an industrially relevant assembly, which includes a 3D robotic FSSJ path along the flange. Monthly calls bring together the team to evaluate the process, provide opportunities to educate and discuss the nuances of the process, and provide updates on the latest development. This forum provides design guidelines that establish a methodology for applying the FSS process across a more diverse set of materials and ultimately strengthens the ability for the industrial partners to make informed decisions regarding where and how to implement the FSSJ process for optimized multi-material designs.

Results

FSSJ Process Development

Figure II.3.G.3 is a photo of the initial work on the CFRP plaque using linear FSSJ with a conventional rotating shoulder. Channeling and excessive flash is obvious in the photo at several points. This is a result of too much heat being generated by the conventional rotating shoulder and the tool not being able to contain the heated material beneath the shoulder despite a convex shoulder design and tilting of the tool. This creates a situation of excessive flash and extremely low joint properties. This led to the conclusion that a stationary shoulder design is necessary.

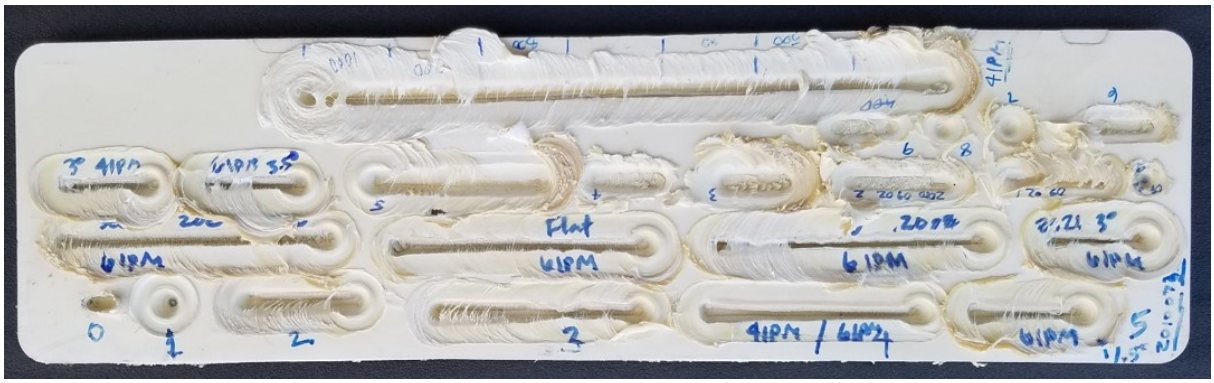

Figure II.3.G.3. Photo of a CFRP plaque following attempted linear FSSJ using a conventional rotating shoulder. Note the channeling and excessive flash. Source: PNNL.

Towards initial weld optimization a series of welds were made with CFRP plaques using the friction stir tool with and without a scribe feature and using the developed stationary shoulder shown in Figure II.3.G.4(a) and (b) in a developed design of experiments.

(a)

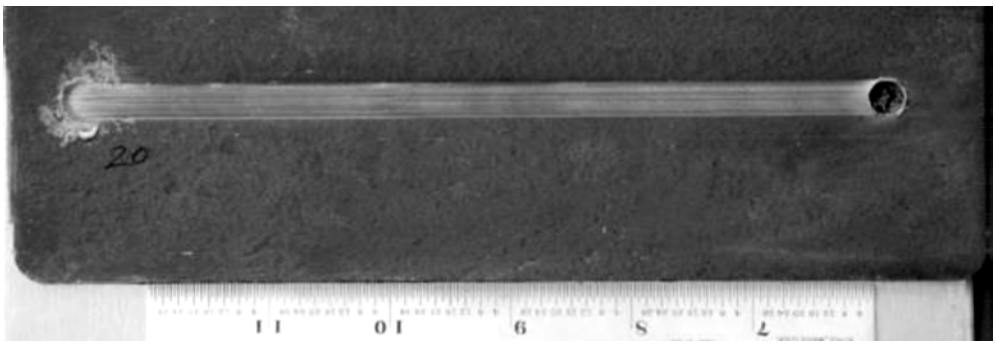

(b)

Figure II.3.G.4.(a) Stationary shoulder FSS setup; and (b) high-quality surface finish of FSS joint after welding with stationary shoulder. Source: PNNL.

These initial trials helped develop an understanding of the effects of welding parameters such as welding speed, tool rpm, pin length, plunge depth, and tool forces for specific tool designs. However, excessive wear in the pin region of the H13 steel FSS tool became apparent after approximately 20% of the design of experiment trials had been completed. Increasing the tool H13 material hardness to HRC55 improved wear performance slightly though the hardened H13 tool still showed sign of wear after approximately two to three welds. The primary concern of tool wear during FSS process optimization is the uncertainty in understanding the effect of welding parameters on weld quality when the tool geometry is continually changing as tool wear progresses.

An initial examination of wear performance using a pin tool fabricated from an alternative material, CPM (10V)/AISI A11 tool material, was completed. A11 tool steel is a powder metal tool steel with high vanadium content (9.25 to 10.25%) known to be wear resistant compared to other tool steels in cold work tooling applications. Comparison of tool wear characteristics between H13 and A11 tools using high-magnification images before and after FSS welds are detailed in Figure II.3.G.5 and Figure II.3.G.6. High-magnification images of tools before and after the FSS weld of around 24 in. are shown Figure II.3.G.5(a) and (b) for as-received H13 (HRC 45), and Figure II.3.G.6(a) and (b) for A11 (e.g., HRC 58). While after 24 in. of weld, the as-received H13 and doubled-tempered heat-treated H13 measured around 1.6% of tip diameter loss, a reduction of ~0.12% (very small change) in tip diameter was measured in the A11 tool. Visual observation of threads around the circumference of the tools shows significant wear performance improvement with the use of the A11 tool compared to the H13 tool. Thus, it was decided that A11 would replace H13 as the pin tool material in this study.

While wear resistance was observed to increase with the A11 tool relative to the H13 tool in initial welding trials, it was noted that there was loss of high-temperature toughness. An A11 tool used with a relatively new stationary shoulder (tight clearance) resulted in premature failure and breakage of the tool. This only occurred with an A11 tool used with a shoulder of relatively tight tolerance (clearance for tool shaft). When used with a shoulder with slightly lower tolerance (Δ=0.05mm), no excessive heating or premature tool failure were observed. This contrasts with the H13 tool where tight tolerance between the shoulder and the tool has not presented any problem, as shown in Figure II.3.G.7.

Through a rigorous process optimization, it was found that the use of a 5.5 mm diameter pin tool with an 18 mm diameter shoulder provided better weld surface quality given the CFRP as the top sheet and consequently, a set of welds were completed with different welding parameters. However, a relatively low joint strength was achieved because fracture in a lap-shear coupon easily initiated at the tip of the hook, as seen in Figure II.3.G.8(a), and then propagated through the stir zone within the CFRP, as shown with the white line in Figure II.3.G.8(b).

(a)

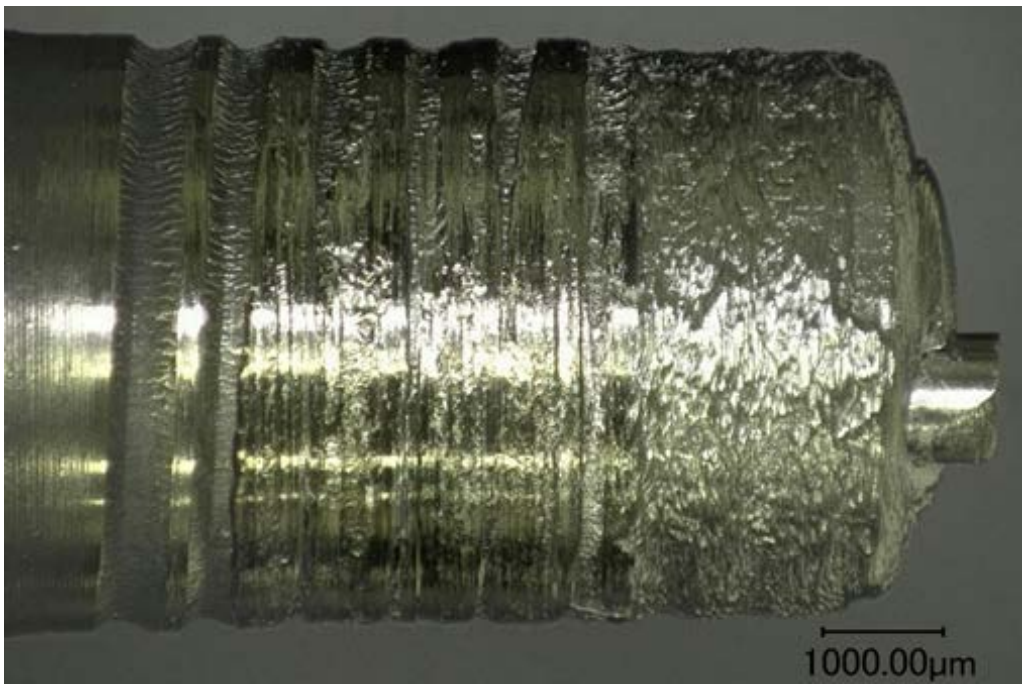

(b)

Figure II.3.G.5. H13 FSSJ tool material with hardness HRC45 (a) as-received with diameter of 4.99 mm and thread depth of 0.12 mm and (b) after 24 in. of welding with diameter of 4.91 mm and thread depth of 0.04 mm. Source: PNNL.

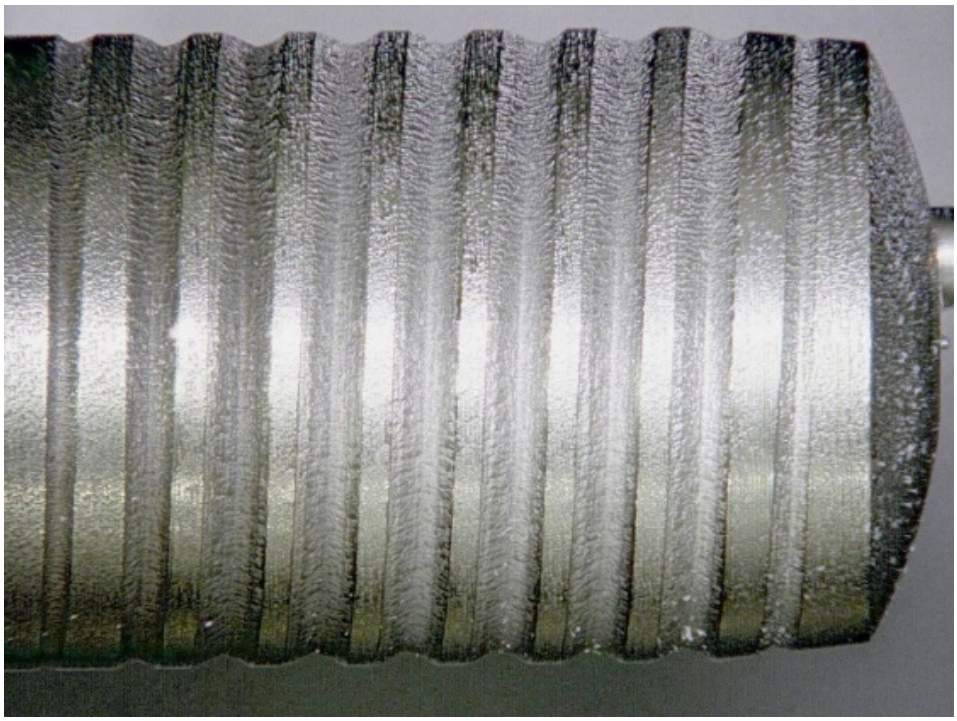

(a)

(b)

Figure II.3.G.6. A11 FSSJ tool material. (a) As-received with diameter of 7.87 mm. (b) After 24 in. of welding with diameter of 7.86 mm. Source: PNNL.

Figure II.3.G.7. Fractured A11 tool because of tight clearances. Source: PNNL.

(a)

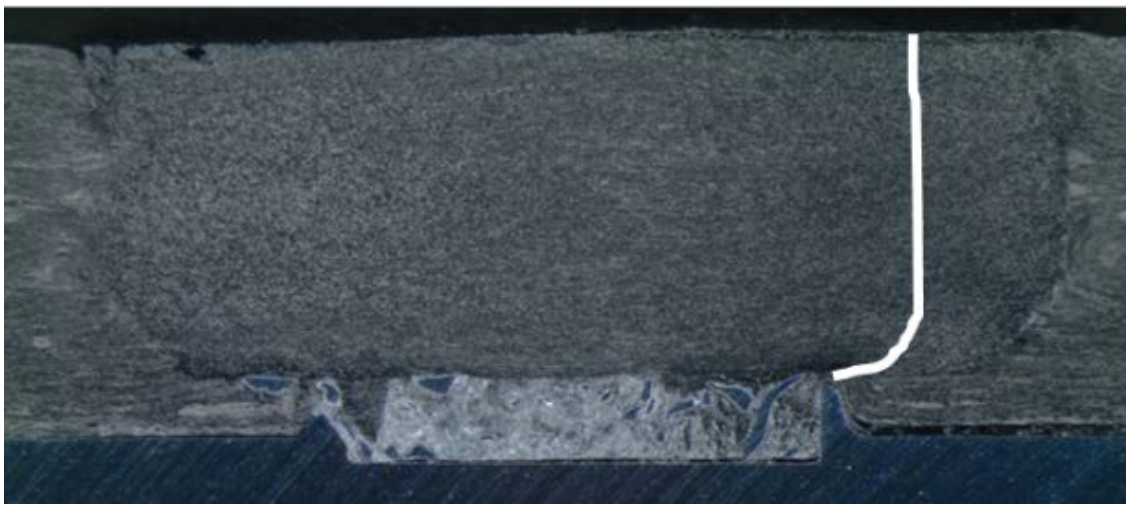

(b)

Figure II.3.G.8.(a) Fractured CFRP/Al FSSJ lap-shear coupon with the fracture initiating at the tip of the Al "hook;" and (b) proposed crack propagation path indicated by white line progressing through CFRP stir zone. Source: PNNL.

Fiber Length and Orientation Measurements

Because crack growth was through the CFRP stir zone, it is necessary to be able to model this region and to do so, the fiber orientation and length are required to determine the base CFRP material properties. The most significant effect on microstructure is the mechanical chopping or attrition of carbon fibers by the friction stir tool as the nylon matrix simply melts and solidifies during the welding process. CFRP plaques were welded to nylon plaques at PNNL to examine the effect of welding on fiber characteristics. Two welding speeds—20 and 30 mm/min—and two tool rotation speeds—1650 and 1950 rpm—were used. Figure II.3.G.9(a) shows an image taken from the as-molded CFRP plaque. When compared to Figure II.3.G.9(b), which is an image taken from the CFRP sample welded at 1650 rpm and 20 mm/min, it is apparent that the carbon fibers have undergone severe chopping—the fraction of the fine fibers has increased.

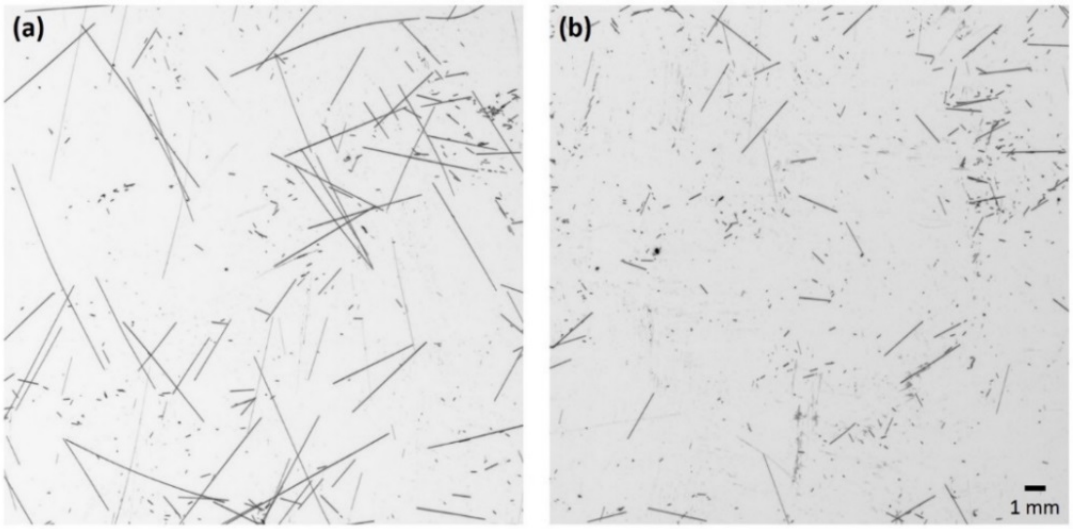

Figure II.3.G.9. Scanned images of fiber length samples taken at Virginia Tech: (a) as-molded CFRP plaque; and (b) welded CFRP (1650 rpm, 20 mm/min). Source: General Motors.

The number average value of the fiber length in the as-molded samples is 0.52 mm. For the samples taken from the weld nugget, the fiber length varies between 0.2 and 0.3 mm depending on the FSSJ process parameters—approximately a factor of two in number average length reduction. Table II.3.G.1 lists the measured values of the fiber lengths in the samples for the various combinations of the welding parameters. Stirring rotations per minute and translation speed are found to have a secondary effect on the fiber length. Fiber length decreased with increasing weld speed, and increased with increasing rpm. The reason for this can be attributed to the fact that CFRP material at a higher temperature (when rpm is high, or weld speed is low) is more compliant resulting in lower stress values transferred to the fibers during mixing.

Table II.3.G.1. Measured Fiber Lengths at Different Combinations of Welding and Tool Rotation Speed.

	1650 rpm	1950 rpm
20 mm/min	0.262 mm	0.310 mm
30 mm/min	0.189 mm	0.244 mm

Work with Pascal Pinter from the University of Waterloo and Karlsruhe Institute of Technology was successful in obtaining entirely reasonable fiber orientation measurements of the PlastiComp Velocity® LCF45-PA6 plaques using microcomputer tomography techniques. This has not been possible previously based on insufficient contrast between the carbon fibers and nylon matrix. It is not clear what aspect of their

algorithm is the enabling technology. Figure II.3.G.10(a) shows the plaque with the analysis locations indicated and Figure II.3.G.10(b) summarizes the major components of the orientation tensor for each slice in the z-direction along with a 3D view of the sampled section, which exhibits a dominance of the shell layers to be aligned in the y-direction.

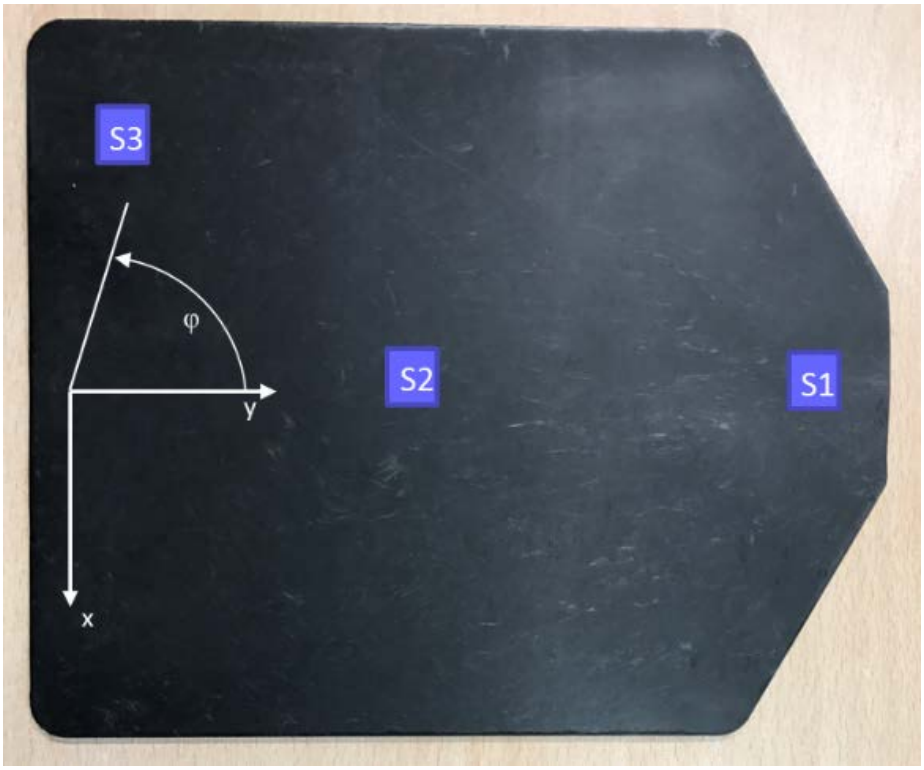

(a)

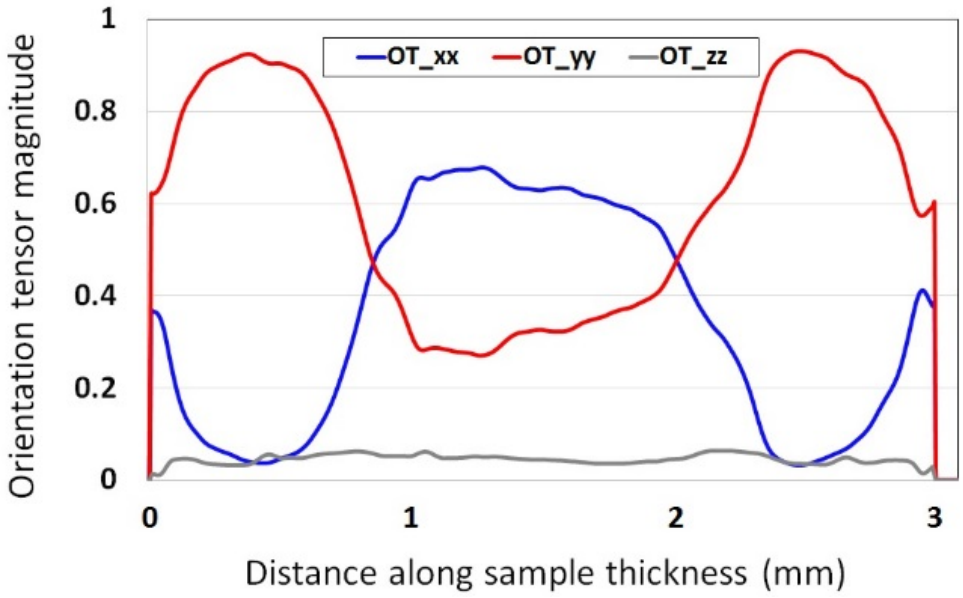

(b)

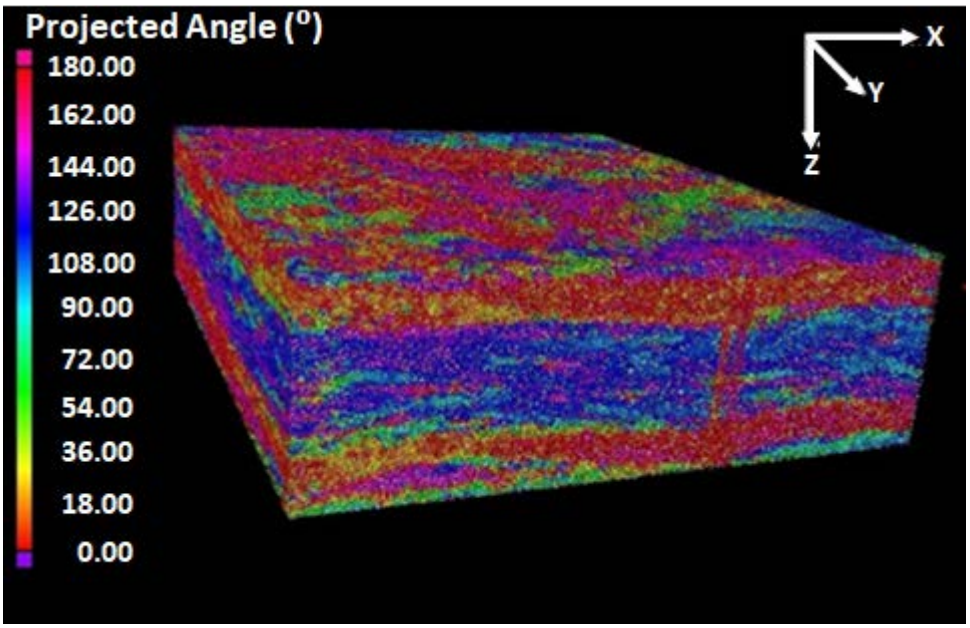

(c)

Figure II.3.G.10.(a) PlastiComp Velocity® LCF45-PA6 plaque with sample locations indicated by S1, S2, and S3; note in-gate located on the far right-hand side near position S1; (b) Orientation tensors of the 2nd order through the thickness of the plaque; and (c) a 3D plot of sampled volume. Source: General Motors.

"Aluminum on Top" FSSJ

The conventional approach to FSSJ of CFRP to Al is to position CFRP as the top sheet in a layup and to penetrate the friction stir pin through the CFRP and disrupt Al from the lower sheet using the scribe to create a mechanical Al hook up into the CFRP. A reverse "metal-side" layup with Al on top of the CFRP, however, was attempted with the same tool, as seen in Figure II.3.G.11(a) (Upadhyay et al. 2017). This approach was attempted to avoid issues related to attrition of the carbon fibers within the stir zone. The process produced some upsetting of the CFRP into the Al, as seen in Figure II.3.G.11(b), although in some cases the CFRP migrated to the top of the Al top sheet, as seen in Figure II.3.G.11(c). Modification of the pin tool geometry is ongoing to encourage the upsetting of the faying interface while discouraging the CFRP migration from the bottom sheet to the Al top sheet surface.

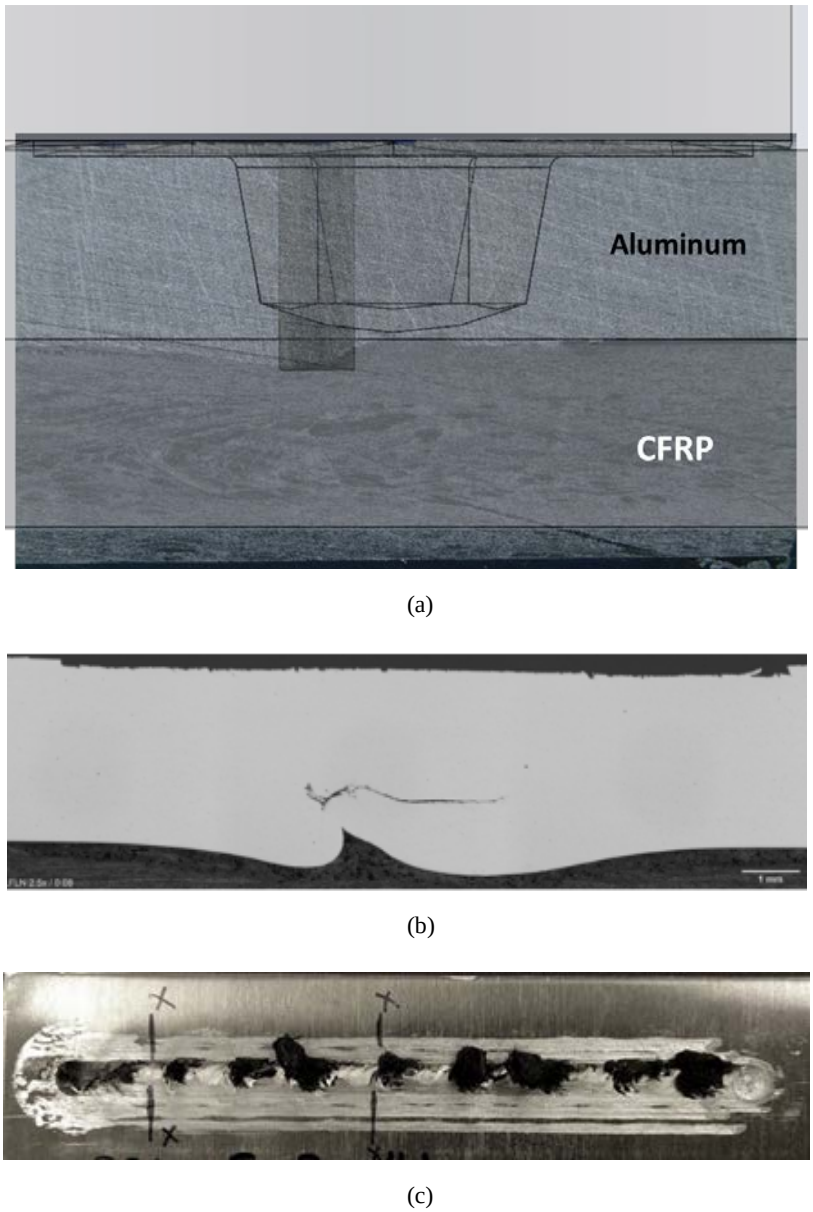

(a)

(b)

(c)

Figure II.3.G.11. Al-on-top super lap-joint sample: (a) schematic of metal-side FSSJ; (b) cross section of weld showing flow of CFRP (bottom sheet) into Al (top sheet); and (c) as-welded surface exhibiting tufts of carbon fiber extending above the Al sheet surface. Source: PNNL.

One of the major advantages of going through the metal side is a dramatic increase in the welding process speed compared to the FSSJ from the CFRP side. Preliminary results show that a welding speed ranging from 0.5 to 2.0 m/min can be used, which is 10 to 40 times faster than currently used when penetrating through the CFRP sheet. While a significant increase in the lap-shear strength has not yet been demonstrated we are optimistic that the Al-side FSSJ can improve the joint strength. Because the tool does not penetrate the CFRP through the thickness, fiber attrition is expected to be limited in the Al-side FSSJ. Nevertheless, some extent of fiber attrition near the interface is expected. We are currently preparing relevant tool modifications to join 2 mm-thick Al to CFRP. We also plan to use stationary shoulder that can provide flexibility in the pin length and allow for greater welding parameter changes without overheating the crown surface.

Comparative Study of Mechanical Properties

During FY 2016, all the Al/CFRP joint assessments were made by lap-shear testing of waterjet cut coupons joined together with the measured load-bearing capacity of the joint compared to the base CFRP material strength value. To make a more direct comparison of the FSSJ technique to other available joining methods, super lap-joint and super coach peel configurations were employed, as shown in Figure II.3.G.12. Both the CFRP and Al sections of the joints are independently reinforced with 1.9-mm DP590 steel (using adhesives) in the neck area to force fracture in the joint. Use of super lap-joint samples thereby minimizes the variation in test configuration effects between different joining methods.

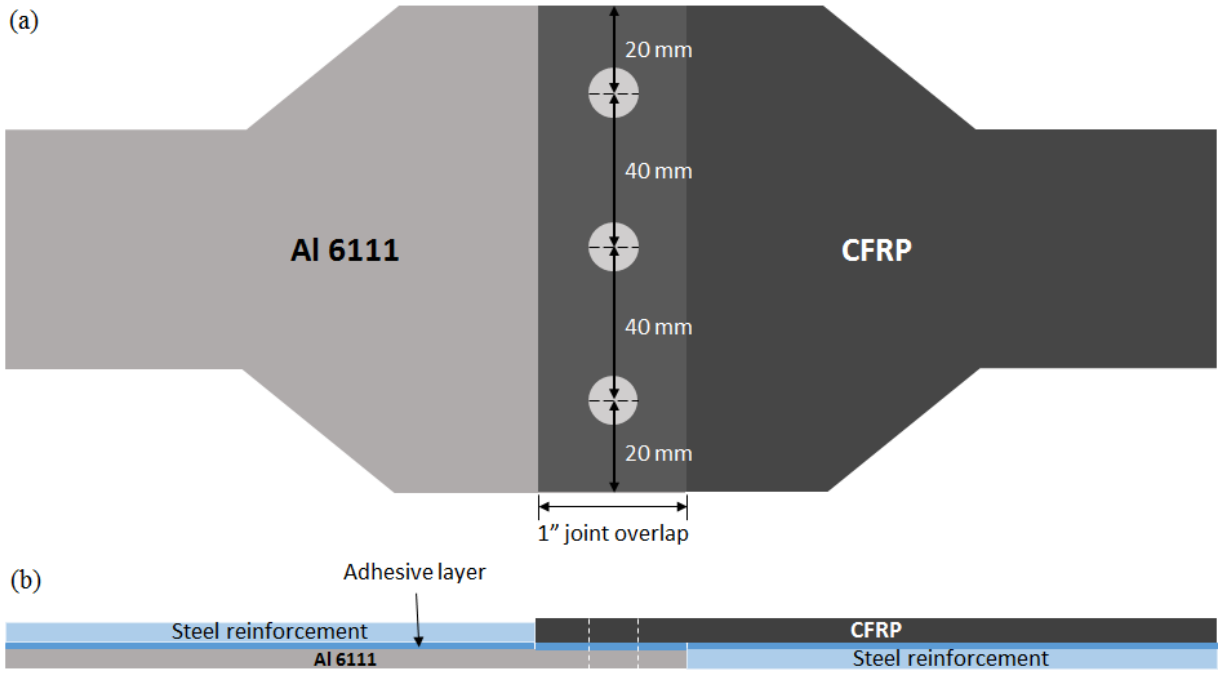

Figure II.3.G.12. Super lap-joint shear test specimen schematic: (a) top view showing the rivet positions (the steel reinforcements are not shown in this view); and (b) view of the sample edge-on showing all the components of the specimen.

Both Al-side and CFRP-side FSSJ, with and without adhesive, were tested. For comparison, adhesive only, SPR + Adhesive, and blind rivets + adhesive joints were tested. Seven samples were tested for each joint type, as shown in Figure II.3.G.13. In these joints, the adhesive served to provide joint strength while the FSSJ or rivets served as peel stoppers. The FSSJ – CFRP on top + adhesive exhibited higher strengths than FSSJ-Al on top for lap-shear testing (coach peel welding and testing are not complete at this time). However, the FSSJ – CFRP on top + adhesive coupons achieved only 70% and 44% of the comparable lap-shear and coach peel strengths of the targeted SPR + Adhesive. Once the FSSJ-Al on top coach peel testing is completed, a full analysis of the relative mechanical performance and fracture modes will be performed.

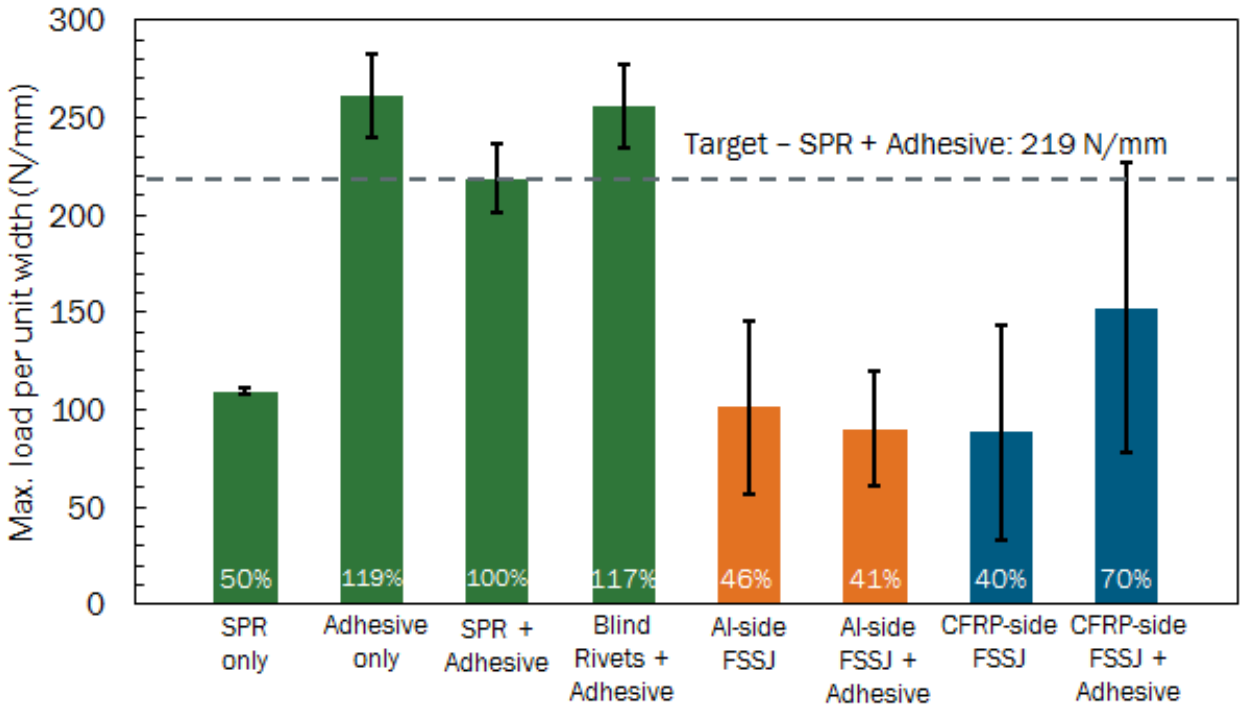

(a)

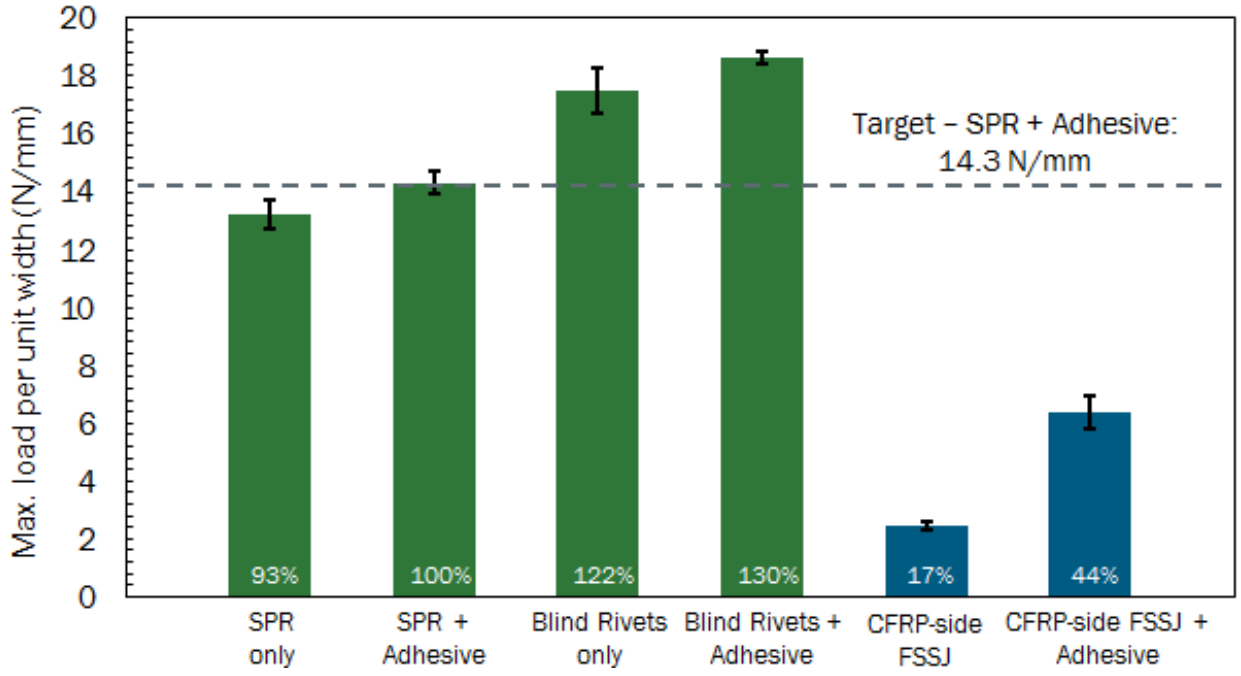

(b)

Figure II.3.G.13. Peak load plots as a function of joining method: (a) super lap joint test results; and (b) super coach peel test results. Targeted strength is that for SPR plus adhesive.

Process–Structure Model

A coupled Eulerian-Lagrangian FSSJ process-structure model for the FSS welds was developed (Gupta et al. 2017) and used to understand the interlock morphology for different scribe lengths and scribe engagement in the bottom plate. This type of parametric study can help in identifying optimal geometric and process parameters for the FSS welding process.

The FSSJ process subjects the material to large strains, high strain rates, and elevated temperatures. Therefore, it is necessary to use a material model that can adequately represent the deformation response during high rate loading and the resulting strain hardening or softening due to large changes in strain rate and temperature. The Johnson-Cook model is a popular material model widely used in such applications. The developed FSSJ process-structure model was validated using experimental data from FSSJ of two dissimilar metal alloys—mild steel and 6061-T6 Al—with well-known Johnson-Cook model parameters (Johnson and Cook 1983). The goal of performing this validation on well-understood material sets is to remove the uncertainties associated with CFRP behavior under such extreme thermo-mechanical conditions that, for example, lead to fiber attrition. The strategy is that with a validated framework, it is a matter of plugging in the material parameters for CFRP and Al and comparing to the experimental output to have a predictive CFRP/AL FSSJ process-structure model.

Figure II.3.G.14 shows a series of optical micrographs of polished joint cross sections (top row of images) and images of the corresponding joint structure predicted from simulations (bottom row of images) at different lengths along the weld. The simulation exhibits comparable variation in the joint structure along the length of the weld as also seen in the experiments.

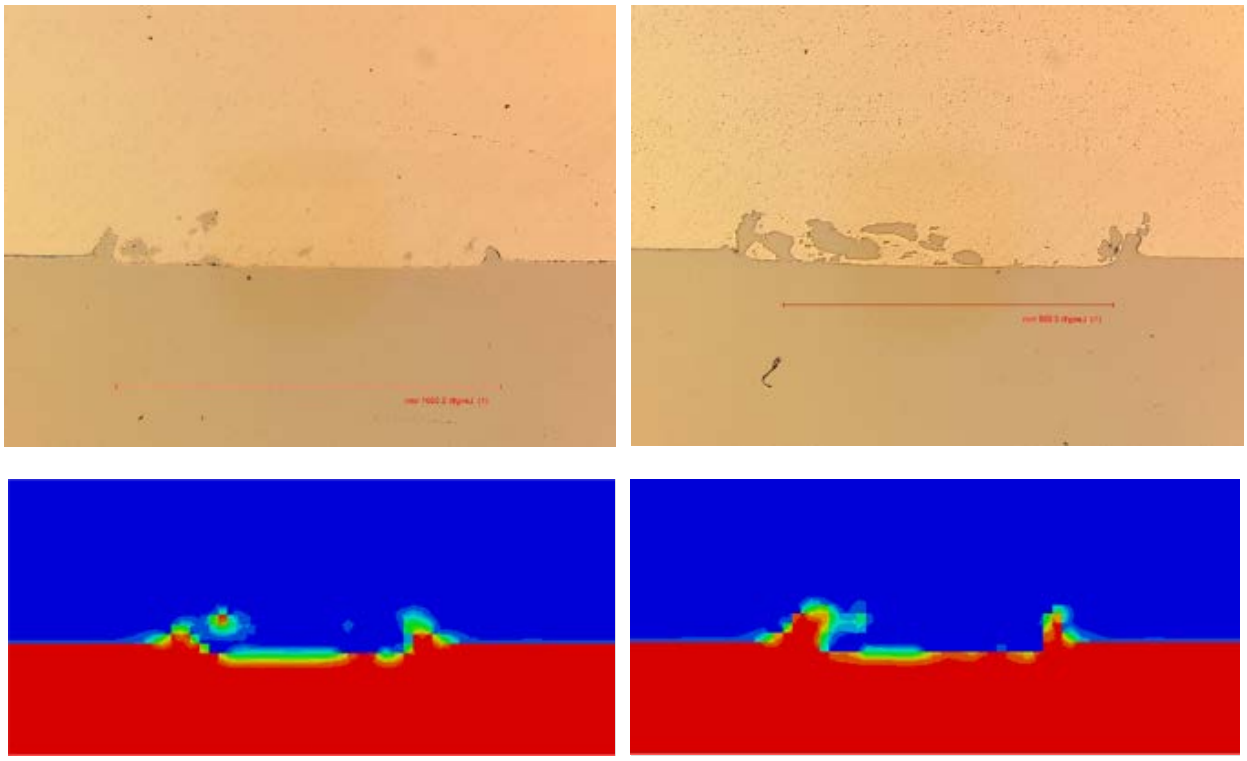

At x = 40 mm

At x = 100 mm

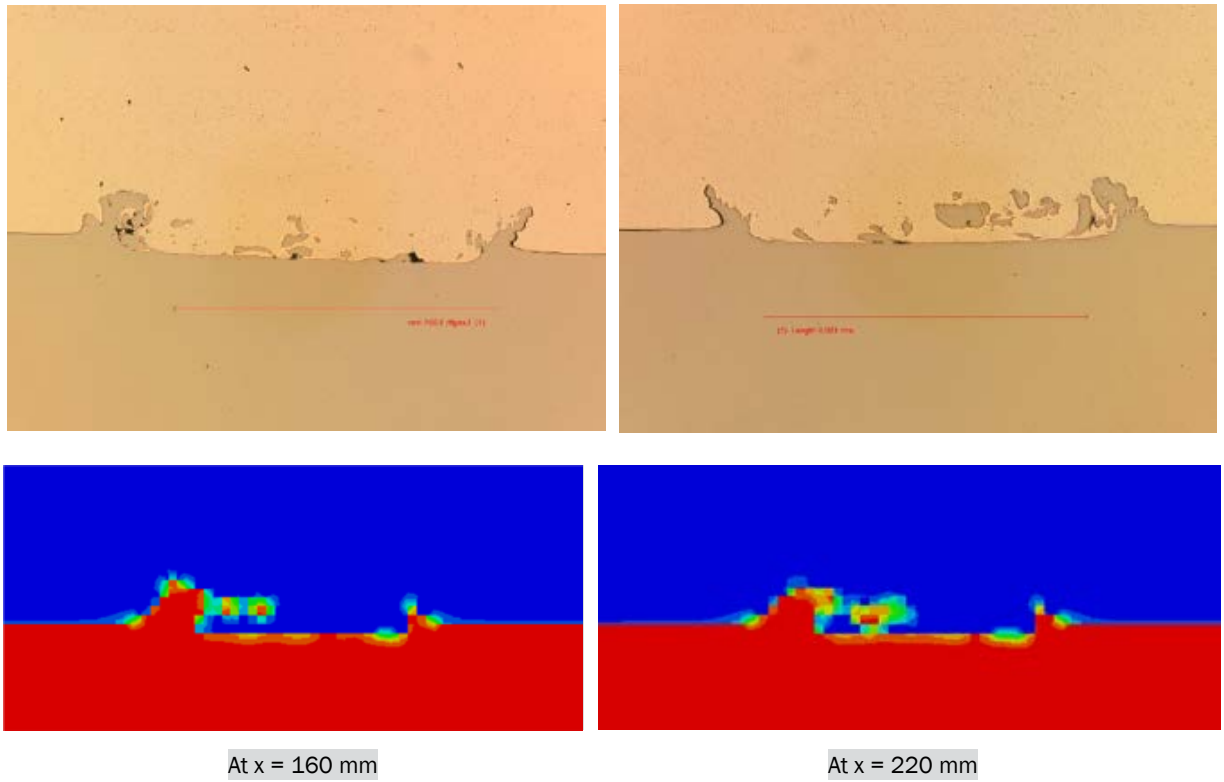

Figure II.3.G.14. Comparison between the experimentally obtained joint microstructure images and the predicted joint structure from simulations. Contour plot indicates the volume fraction of steel. Source: PNNL.

Conclusions

Early in the project, FSSJ of CFRP to Al was shown to require a stationary shoulder to meet the surface quality requirements. Integration of the scribe tool into a stationary shoulder was completed and joints with high surface quality were produced. However, the carbon fiber content of the thermoplastic was very abrasive causing the conventional H13 tool material to exhibit excessive pin tool wear. An alternative tool material, A11, was shown to provide significantly improved tool wear to the point where process development could continue. However, additional investigations into high wear-resistant/high toughness tool materials are recommended. The high tool wear is also indicative of the fiber attrition that occurs within the CFRP stir zone. Thus, fiber length and orientation data are desirable and new best practices for both fiber length and orientation measurements have been identified. The concept of the FSS joint is to create a hook feature to provide mechanical interlocking of the dissimilar materials. However, the tip of the hook in the FSSJ – CFRP on top is positioned within the CFRP stir zone, which exhibits nearly an order of magnitude reduction in fiber length and results in significantly reduced stir zone properties compared to the CFRP substrate base properties. Since the crack both initiates and propagates within the CFRP stir zone, it has not been possible to date, to achieve comparable strengths as with a self-piercing rivet and adhesive (the Go/No-Go target) for either super lap-shear or super coach peel test configurations. Modeling efforts have developed predictive capability to ascertain the resulting FSSJ structure based on process conditions and validated this for a dissimilar Al/steel couple. For the CFRP/Al couple, it would be beneficial to input the material properties as a function of temperature that have been measured in this project and validate the model predictions with experiments on CFRP/Al welds. Corrosion couples have been fabricated and are currently undergoing environmental exposure. Testing equivalent to 15-years of corrosion will be completed by the end of calendar year (CY) 2017.

Key Publications

Friction Stir Process

Andre, N. M., S. M. Goushegir, J. F. dos Santos, L. B. Canto, and S. T. Amancio-Filho, 2016, "Friction spot joining of aluminum AA2024-T3 and carbon-fiber reinforced poly(phenylene sulfide) laminate with additional PPS film interlayer: microstructure, mechanical strength and failure mechanisms," *Composites Part B: Engineering*, Vol. 94, pp. 197–208.

Kang, J., H. Rao, R. Zhang, K. Avery, and X. Su, 2016, "Tensile and fatigue behaviour of self-piercing rivets of CFRP to aluminum for automotive application," *IOP Conference Series: Materials Science and Engineering*, Vol. 137, No. 1, pp. 012025.

Khan, H. A., J. Li, and C. Shao, 2017, "Analysis of friction stir riveting processes: A review," *Journal of Manufacturing Science and Engineering*, Vol. 139, No. 9, pp. 090801.

Khodabakhshi, F., M. Haghshenas, J. Chen, B. Schalchi, J. Li, and A. P. Gerlich, 2017, "Bonding mechanism and interface characterization during dissimilar friction stir welding of an aluminum/polymer bi-material joint," *Science and Technology of Welding and Joining*, Vol. 22, pp. 182–190.

Upadhyay, P., L. Fifield, G. Grant, and K. Mattlin, 2017, U.S. Application No. 62/465,273, "Metal side friction stir scribe joining of metal and reinforced polymers, (March 1)." IPID: 31044-E PROV.

Upadhyay, P., Y. Hovanski, B. Carlson, E. Boettcher, R. Ruokolainen, and P. Busuttil, 2017, "Joining dissimilar material using friction stir scribe technique," In: Hovanski, Y., R. Mishra, Y. Sato, P. Upadhyay, and D. Yan (eds.). *Friction Stir Welding and Processing IX*, Ch. 15, pp. 147–155, John Wiley & Sons, Inc., Hoboken, NJ, USA.

Upadhyay, P., Y. Hovanski, S. Jana, and L. S. Fifield, 2016, "Joining dissimilar materials using friction stir scribe technique," *Journal of Manufacturing Science and Engineering*, (October) Vol. 139, No. 3, pp. 034501.

Yusof, F., M. Muhamad, R. Moshwan, M. Jamaludin, and Y. Miyashita, 2016, "Effect of surface states on joining mechanisms and mechanical properties of aluminum alloy (A5052) and polyethylene terephthalate (PET) by dissimilar friction spot welding," *Metals*, Vol. 6, pp. 101.

Friction Stir Process Modeling

Gupta, V., P. Upadhyay, X. Sun, E. I. Barker, L. Fifield, and B. Carlson, 2017, "A thermo-mechanically coupled model to predict joint properties in friction stir scribe welding of dissimilar materials," In: *4th World Congress on Integrated Computational Materials Engineering (ICME 2017)*, May 2017, Ypsilanti, MI, USA.

Fiber Length and Orientation Measurement

Goris, S., T. Back, A. Yanev, D. Brands, D. Drummer, and T. A. Osswald, 2017, "A novel fiber length measurement technique for discontinuous fiber-reinforced composites: A comparative study with existing methods," *Polymer Composites*, doi:10.1002/pc.24466.

Sharma, B. N., S. A. Kijewski, L. S. Fifield, Y. Shin, C. L. Tucker, and M. D. Sangid, 2017, "Reliability in the characterization of fiber length distributions of injection molded long carbon fiber composites," *Polymer Composites*, doi:10.1002/pc.24571.

Sharma, B. N., D. Naragani, B. N. Nguyen, C. L. Tucker, and M. D. Sangid, 2017, "Uncertainty quantification of fiber orientation distribution measurements for long-fiber-reinforced thermoplastic composites," *Journal of Composite Materials*, (September), http://journals.sagepub.com/doi/abs/10.1177/0021998317733533.

CFRP/Al Corrosion

Hakansson, E., 2016, "Galvanic corrosion of aluminum/carbon composite systems," *Electronic Theses and Dissertations*, pp. 1120, http://digitalcommons.du.edu/etd/1120.

References

Gupta, V., P. Upadhyay, X. Sun, E. I. Barker, L. Fifield, and B. Carlson, 2017, "A thermo-mechanically coupled model to predict joint properties in friction stir scribe welding of dissimilar materials," In: *4th World Congress on Integrated Computational Materials Engineering (ICME 2017)*, May 2017, Ypsilanti, MI, USA.

Hovanski, Y., G. J. Grant, S. Jana, and K. F. Mattlin, 2013, "Friction stir welding tool and process for welding dissimilar materials," US8434661 B2, filed June 14, 2012, and issued May 7, 2013, http://www.google.com/patents/US8434661.

Johnson, G. R., and W. H. Cook, 1983, "A constitutive model and data for metals subjected to large strains, high strain rates and high temperatures," *7th International Symposium on Ballistics*, Hague, The Netherlands, pp. 541–547.

Upadhyay, P., L. Fifield, G. Grant, and K. Mattlin, 2017, U.S. Patent Application No. 62/465,273, "Metal side friction stir scribe joining of metal and reinforced polymers," March 1, 2017, IPID: 31044-E PROV.

II.3.H High Performance Computing Tools to Advance Materials Joining Technology (General Motors)

Blair E. Carlson, Co-Principal Investigator
General Motors Global R&D
m/c 480-106-RL2
30470 Harley Earl Blvd.
Warren, MI 48092-2031
Phone: 586-864-7698
E-mail: blair.carlson@gm.com

Zhili Feng, Co-Principal Investigator
Oak Ridge National Laboratory
1 Bethel Valley Rd.
Oak Ridge, TN 37831-6064
Phone: 865-576-3797
E-mail: fengz@ornl.gov

Sarah Kleinbaum, Technology Manager
E-mail: sarah.kleinbaum@ee.doe.gov

Start Date: March 6, 2017 End Date: March 5, 2018
Total Project Cost: $380,000 DOE share: $300,000 Non-DOE share: $80,000

Executive Summary

Welding is a critical manufacturing technology that underpins nearly every corner of the modern industry from energy production and conversion to conservation. GM and Electric Power Research Institute (EPRI) representing two major U.S. manufacturing industry sectors (i.e., automotive and nuclear energy), are working with ORNL to advance HPC weld modeling tools for broad industrial applications. Welding simulation is extremely time consuming with today's computers. It often takes weeks or months for a detailed welding simulation of auto-body parts or nuclear reactor components that has sufficient fidelity for design and manufacturing optimization. This project aims at new HPC-based weld modeling tools that can complete a high-fidelity weld simulation within several hours and enable effective optimization of welding technology to minimize dimensional distortion and proactively mitigate the detrimental impact of weld-induced residual stresses. The current progress to date is the development of a novel acceleration scheme that has been tested on arc welding of steel pipes (nuclear application) and laser welding of thin plate (automotive application). Initially, several acceleration approaches based on the novel concept were developed using an in-house code, as well as implemented with commercial software, Abaqus. These different acceleration approaches were evaluated for accuracy and efficiency of calculations.

Accomplishments

- Developed and implemented a novel acceleration scheme in both the commercial (Abaqus) and in-house finite element codes (FY 2017).
- Evaluated the new acceleration scheme (under patent filing) for stress analysis for simulating a coupon level laser welding process in addition to a single-pass pipe welding model, which has already demonstrated the potential for major computational time reductions (FY 2017):
    - Laser welding: initial speed-up was in the range of 20 to 100 times.
    - Arc welding: initial speed-up was in the range of 15 to 50 times.

- Produced representative automotive laser welded subassemblies under four conditions to induce distortion that has been experimentally scanned for eventual comparison to simulated results (FY 2017).

Technology Assessment

- Target: Develop an HPC-based integrated computational welding engineering simulation tool with an approximate 100 times order of magnitude increase in computational performance, compared to today's commercial welding process simulation tools.
- Gap: Welding simulation is very time consuming with today's computers. It can take weeks or months to perform a detailed simulation with sufficient fidelity to achieve design and manufacturing optimization.

Project Introduction

Computational welding simulation tools are increasingly needed in nearly all industry sectors to improve understanding and prediction of the performance and properties of welded structures, as well as to drive welding manufacturing technology innovations. However, the multi-disciplinary nature of welding manufacturing and the complicated interactions between the highly localized welding heat source and the welded material makes high-fidelity welding simulations extremely demanding of computational resources. This high demand stems from some unique requirements of welding simulation: (1) the highly nonlinear thermal-mechanical responses of materials; (2) the fine mesh ($\sim 10^{-3}$ m) and short time increment ($\sim 10^{-2}$ second) necessary to capture the transient and extremely high temperature, stress, microstructure, and property gradients in the weld region; (3) the large number of elements representing the welded components, such as an auto-body structure (with 10^6 to 10^8 degrees of freedom to solve); and (4) the relatively long welding fabrication time (in hours to weeks) of complex structures such as an automotive body structure or the construction of a nuclear reactor component. Today, the industry only uses welding process modeling tools in limited cases that generally require considerable simplification to obtain solutions in a reasonable amount of time. For example, it is not possible to simulate the welding assembly of an automotive body structure or the welding construction of a nuclear reactor.

Inadequate Scalability of Today's Welding Codes on HPC

Today, industry uses several computer codes for welding simulations; the most common include Abaqus, ANSYS, SYSWELD, MSC-Simufact, VrWeld, virtual fabrication technology (VFT), and WARP3D. They typically are used on workstations and small cluster computers as they do not scale well on massively parallel HPC clusters. For example, in a 2015 benchmarking study by ORNL and EPRI (Feng et al. 2015), Abaqus, perhaps the most widely used code for welding simulations in the industry (including GM and EPRI), has poor scalability on HPC computers. As shown in Figure II.3.H.1 on two different types of multi-core computers (labeled as MJG and Jorvik), a 3D simulation of a simple one-pass pipe welding using the latest Abaqus (Version 6.14) did not scale up well over 32 to 64 nodes. In fact, the scalability of Abaqus started to "fall off" beyond 64 nodes. It is noted that Abaqus scaled quite well for certain other types of benchmark problems unrelated to welding in our study. However, WARP3D, an open source code, had similar scalability for the welding simulation as compared to Abaqus (Brust 2013). VFT uses Abaqus or WARP3D as its solid-mechanics solver and has a similar scalability issue. Another notable code is VrWeld from Goldak Technologies. VrWeld is intended for massively parallel HPC. However, the recent version of VrWeld is usually about five times faster although potential improvement is possible with improved Compute Unified Device Architecture (CUDA). Our experience with other welding simulation codes such as SYSWELD, ANSYS, and MSC-Simufact also resulted in similar scalability issues. This is not surprising as they all use implicit finite element formulations. In summary, today's welding simulation codes are limited to 10 to 50 times speed-up, best achieved on computers with less than 100 cores. They run poorly on HPC systems with 1,000 to 100,000 cores.

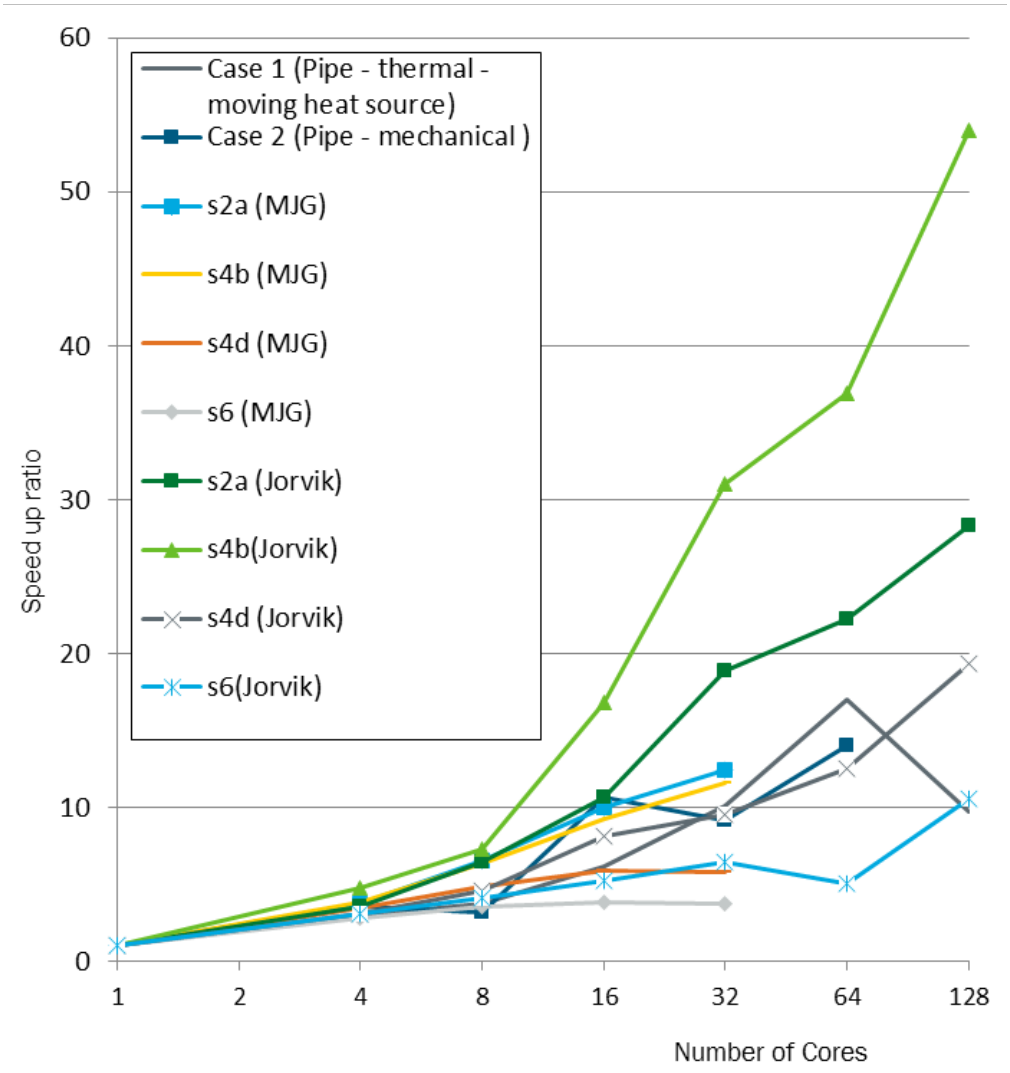

Figure II.3.H.1. Scalability study of Abaqus. Cases 1 and 2 are the respective thermal and stress runs of a 3D pipe weld simulation. Others are Abaqus stress benchmark cases used as comparison. Source: ORNL (Feng et al. 2015).

Approach

This high-performance computing for manufacturing (HPC4Mfg) project is an initial effort aimed at developing and demonstrating the potential of a novel modeling scheme specifically designed for broad welding simulation applications. The novelty will include efficient use of explicit FEM codes that generally have better scalability on massively parallel HPC systems. The broad application potential of our HPC weld modeling tool will be demonstrated with two representative but very different welded structural components, as shown in Figure II.3.H.2.

(a)

(b)

Figure II.3.H.2. Illustrative real-world examples taken from: (a) automotive laser brazing/welding of trunk lid; and (b) nuclear power industries for which HPC welding simulation would make a major impact. Source: (a) General Motors R&D, (b) EPRI.

The selection of these two cases also aim to support the immediate welding manufacturing needs: (1) high-fidelity prediction of welding-induced dimensional changes and stresses during laser welding assembly of a complex auto-body closure panel with required product features made of high-strength lightweight materials; and (2) high-fidelity prediction of arc weld residual stresses in the critical dissimilar welds that connect the nuclear reactor vessel to the piping systems. For this initial effort, a measurable technical goal is to demonstrate a substantial increase in computational performance on cluster HPC with 500 to 2000 cores, on the order of 100 times compared to workstation-based welding simulations today. This means a reduction of wall clock time of computation for a welding simulation from over 12 to 15 weeks on today's workstation computer to less than 24 hours using a HPC system and computational codes in this project. To the industry members of the project, such computational performance improvements means that the HPC welding process modeling tools could be realistically used to effectively analyze various welding fabrication options/scenarios to minimize dimensional distortion, or proactively mitigate the detrimental impact of welding-induced residual stresses within a timeframe such that expensive and time-consuming iterative physical trial and error can be avoided. A secondary objective is, through this research, to identify critical barriers and gaps in HPC codes that, once solved in the future, would lead to further major breakthroughs in application of HPC for welding simulations.

Our project plan focuses on the development of a novel weld simulation scheme that takes full advantage of a massively parallel HPC system. Both GM and EPRI will provide actual experimental results of representative welded structures to assist the model development and validation.

A sequentially coupled approach will be used to simulate the heat transfer and mechanical responses in the welding process in order to substantially speed up the simulations. In our past investigations, the thermal and mechanical solvers in a code package may not necessarily have the same scalability on HPC. Further, high-fidelity simulation of the molten metal flow in the weld pool, which is essential for both the weld pool shape prediction in laser welding of the car roof panel and the dilution prediction in dissimilar metal weld of nuclear reactors, will require the use of a computational fluid dynamics method instead of the common heat-conduction-based FEM. Thus, a key effort in this project is to identify and use the most efficient and appropriate thermal and mechanical solvers that may not be from the same code package. This would in turn require development of the capability for robust and seamless data transfer/communication between different HPC computational codes that are best suited for different aspects of welding process simulation.

For mechanical (thermal-plasticity stress) simulation of the welding process, we plan to use explicit FEM solver, accelerated by a novel time scaling scheme to be developed in this project. Generally speaking, explicit FEM has better scalability on HPC than the implicit FEM commonly used for weld stress modeling. This is particularly true when the number of processing cores increases from workstations to cluster computers with several hundred cores or more, as is the case of this project. However, the time increment in explicit FEM has an upper limit: $dt < L_e/c$, where dt is the time differential, L_e is the element length and c is the speed of the stress wave in material. As the element size in the weld region is typically less than 1 mm, the upper limit of the time increment is on the order of 10^{-7} seconds (whereas the time increment in implicit FEM is on the order of 10^{-2} to 10^{-3} seconds). This means that a simulation of a 1000-second welding fabrication would require 10^{+10} time increments in explicit FEM. As such, at the workstation level (up to tens of processing cores), there is no benefit to use explicit FEM for welding stress simulations although it is computationally much more efficient than implicit FEM.

In this project, we have successfully completed the initial development and testing of a novel accelerated time scaling scheme to speed up FEM for welding simulation on HPC. This scheme uses some unique physical features of the welding process, to drastically reduce the computational time. The new acceleration scheme is under patent filing, so the details are omitted in this report. By combining this novel time acceleration scheme with the use of cluster HPC with 500 to 2000 processing cores, 100 to 500 times improvement in performance would be highly likely.

Technology Transfer Path

Regular calls bring together the team to evaluate the process, provide opportunities to educate and discuss the nuances of the process, provide updates on the latest development, and develop external publications (Huang et al., 2017). This forum provides opportunities for cross-fertilization of ideas across industries that create a more diverse set of requirements for the project team and ultimately strengthens the ability for the industrial partners to make informed decisions regarding where and how to implement the HPC weld modeling tools for advanced materials joining applications. Both GM and EPRI have plans to implement HPC weld modeling tools for specific immediate applications that require HPC capability. GM plans to demonstrate the capability of HPC welding process simulation tools to potential users at GM, including dimensional analysis engineers and manufacturing engineers. Upon approval, the tool is to be installed in GM HPC clusters available to all GM users. The dimensional analysis team is expected to use the tools to speed up welding process simulations that enable consideration of necessary process details for improved accuracy. The manufacturing engineers are expected to use the tools to verify their design of welding processes. Building upon past partnerships on welding simulations and related research, both GM and EPRI are expecting ongoing work with ORNL to continue advancing HPC modeling tools for welding manufacturing through private funding and/or government and private collaboration.

Results

New Acceleration Approach

Two benchmark welding simulation cases—laser welding in the auto-body welding scenario in Figure II.3.H.3(a) and (b) and arc welding in the nuclear repair scenario in Figure II.3.H.4(a) and (b), including both heating and cooling cycles—were studied. The simulations were performed using the commercial finite element code, Abaqus Version 6.14. For those using the new acceleration approach, the implementation of the new approach was realized by Abaqus user subroutines. Comparison was made between the results with the new acceleration approach and those without. Figure II.3.H.3 and Figure II.3.H.4 present the contour of Mises stress after the welded components cooled down to room temperature. Figure II.3.H.5 and Figure II.3.H.6 plot the Mises stress and equivalent plastic strain distribution along a transverse line, as depicted in Figure II.3.H.3(b) and Figure II.3.H.4(b). The profiles calculated by the new scheme follow quite well with those calculated using the commercial model. Table II.3.H.1 summarizes the speedup ratios with respect to the results obtained by the conventional approach. The speedup ratio reached 92 times in one of the arc weld simulations.

Table II.3.H.1. Improvement of Computational Performance.

	Laser		Arc	
Number of elements	126,080		95,565	
Speed-up factor	Case A	Case B	Case C	Case D
	48.5x	43.1x	92.3x	68.0x

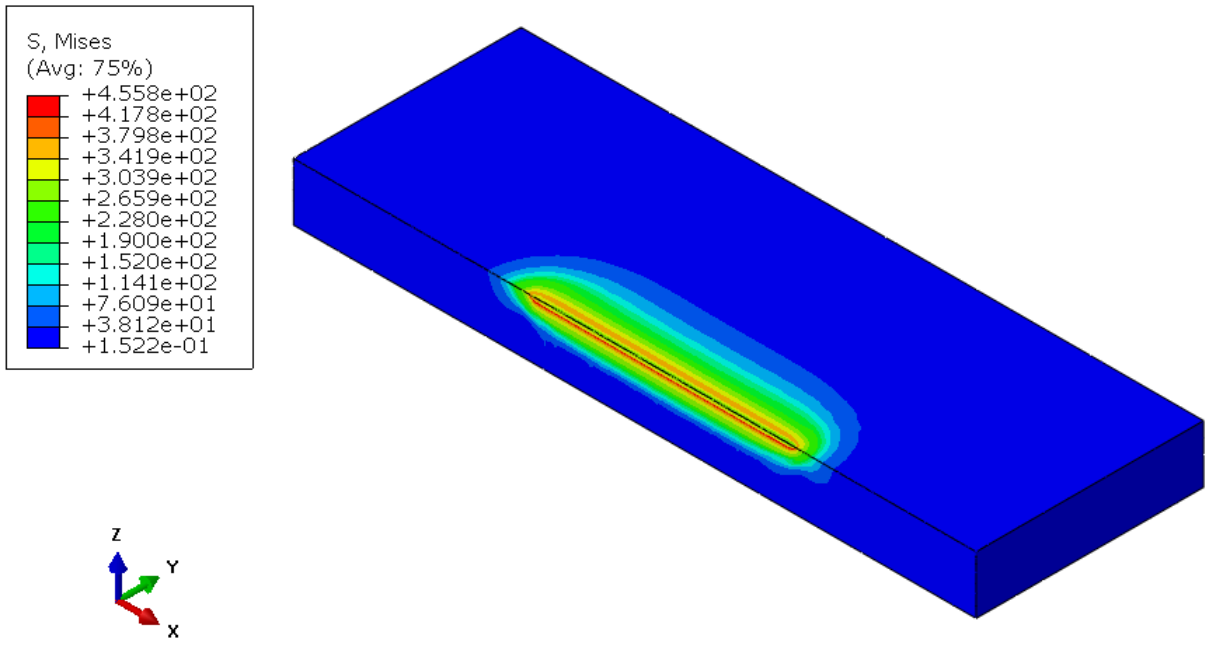

(a)

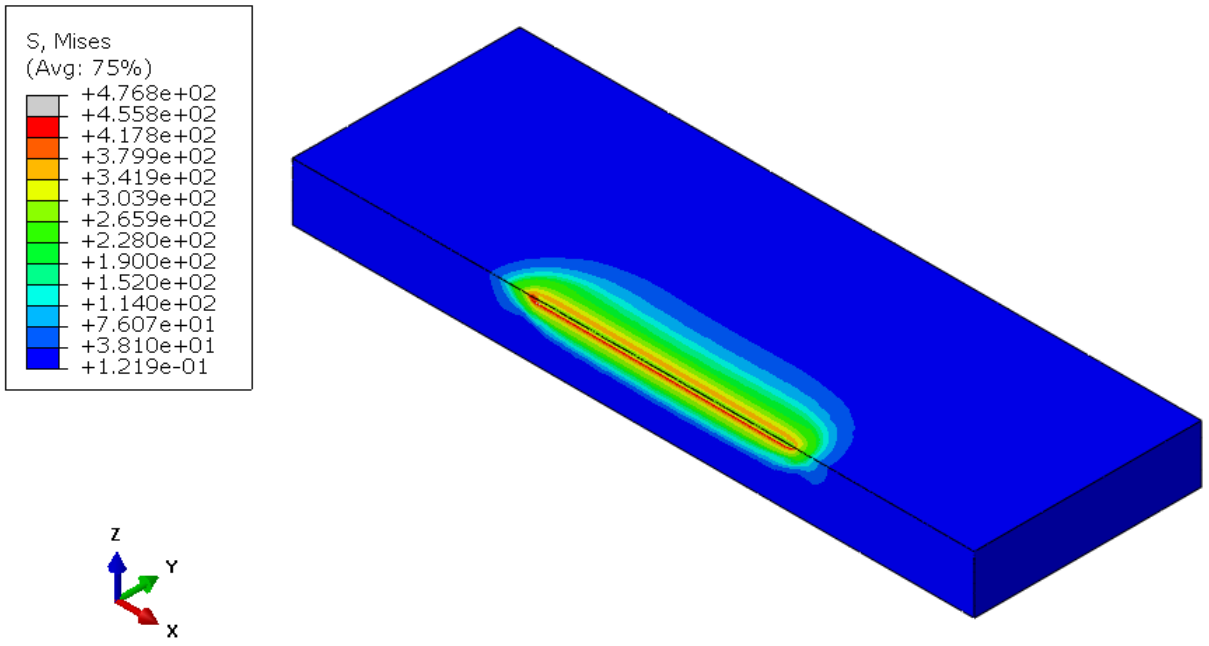

(b)

Figure II.3.H.3. Comparison of Mises residual stress in short stitch laser welding (auto-body welding scenario) calculated using: (a) commercial weld model; and (b) application of the new scheme. Source: ORNL.

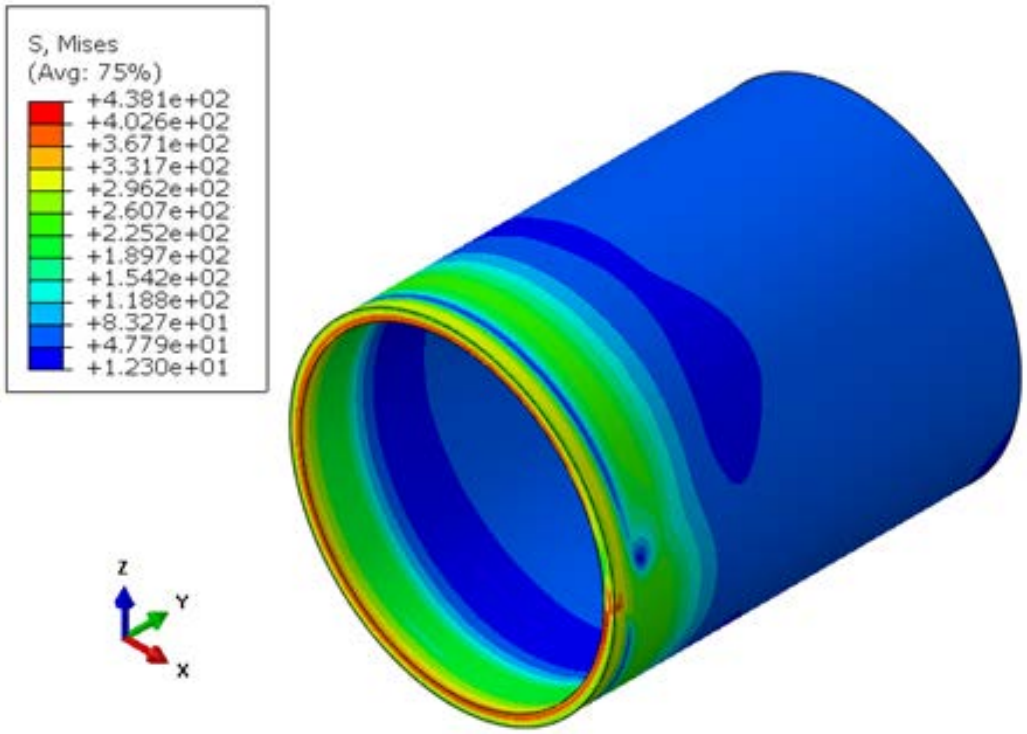

(a)

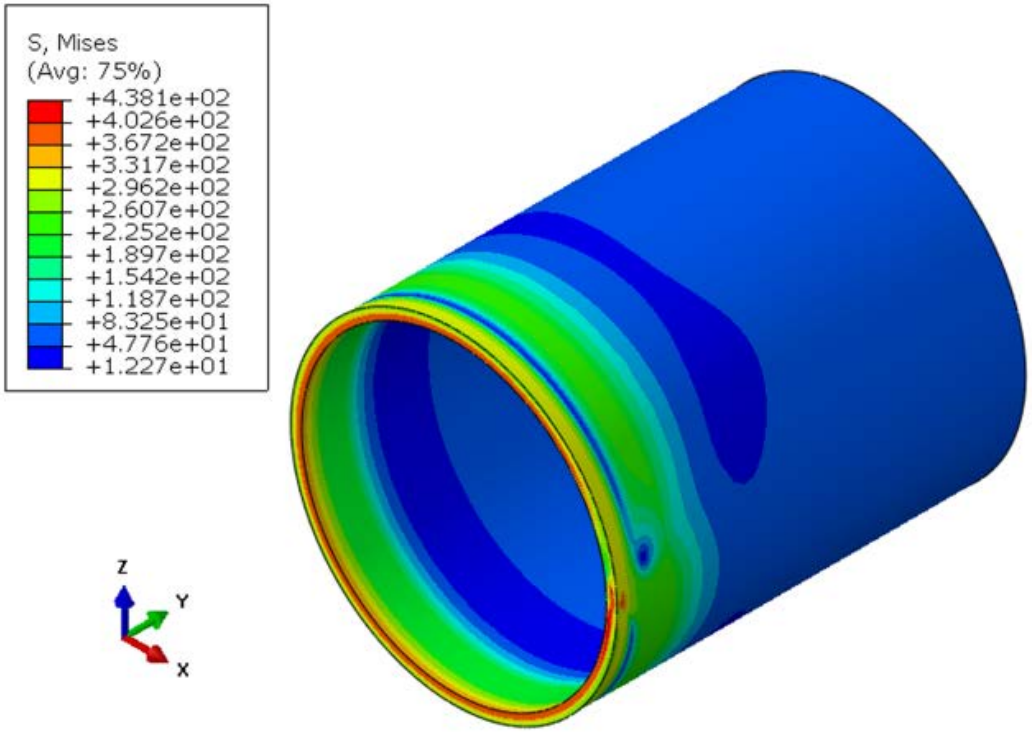

(b)

Figure II.3.H.4. Comparison of Mises residual stress in arc welding of steel pipe girth weld (nuclear reactor repair scenario) calculated using: (a) commercial weld model; and (b) application of the new scheme. Source: ORNL.

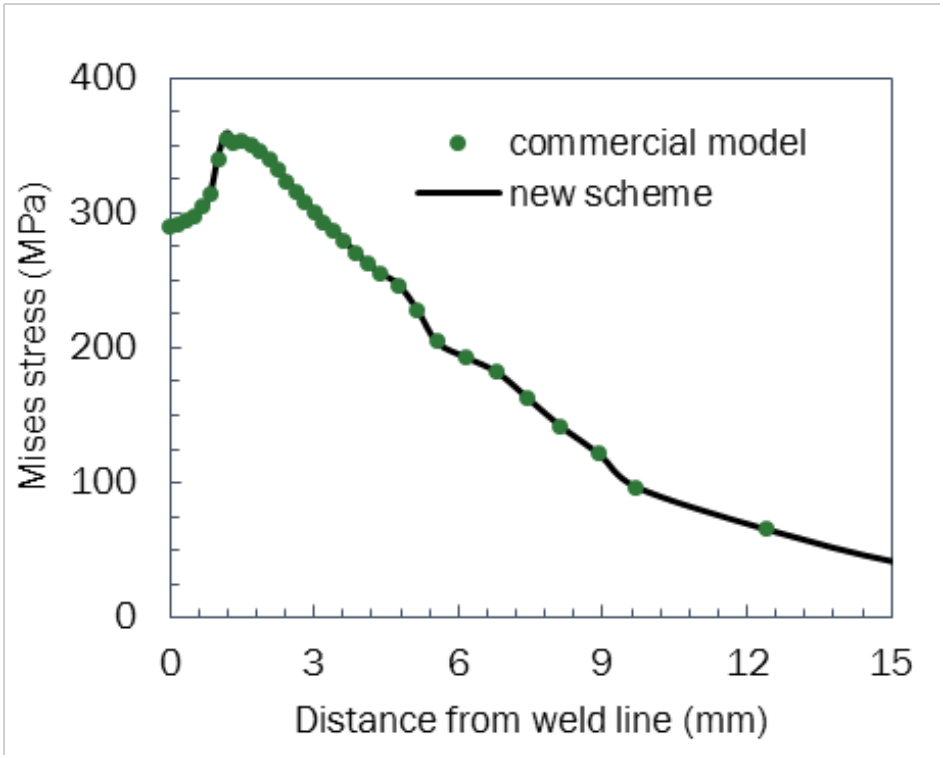

(a)

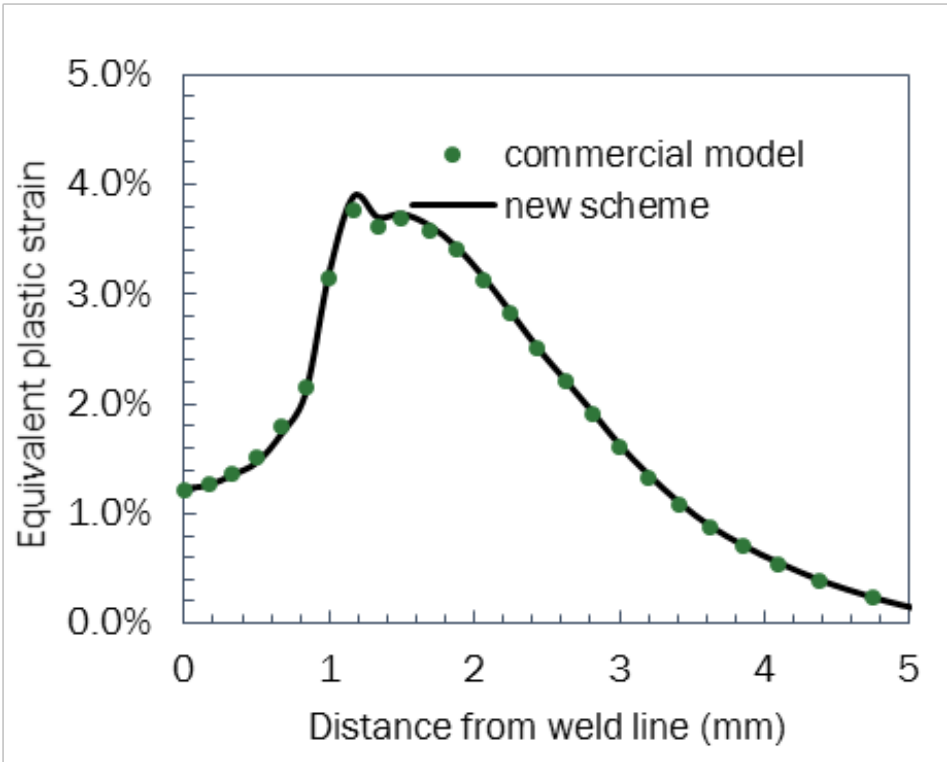

(b)

Figure II.3.H.5. Comparison of laser weld simulation results along a transverse line, as shown in Figure II.3.H.3(b), between application of a commercial model and the new scheme for: (a) Mises stress; and (b) equivalent plastic strain.

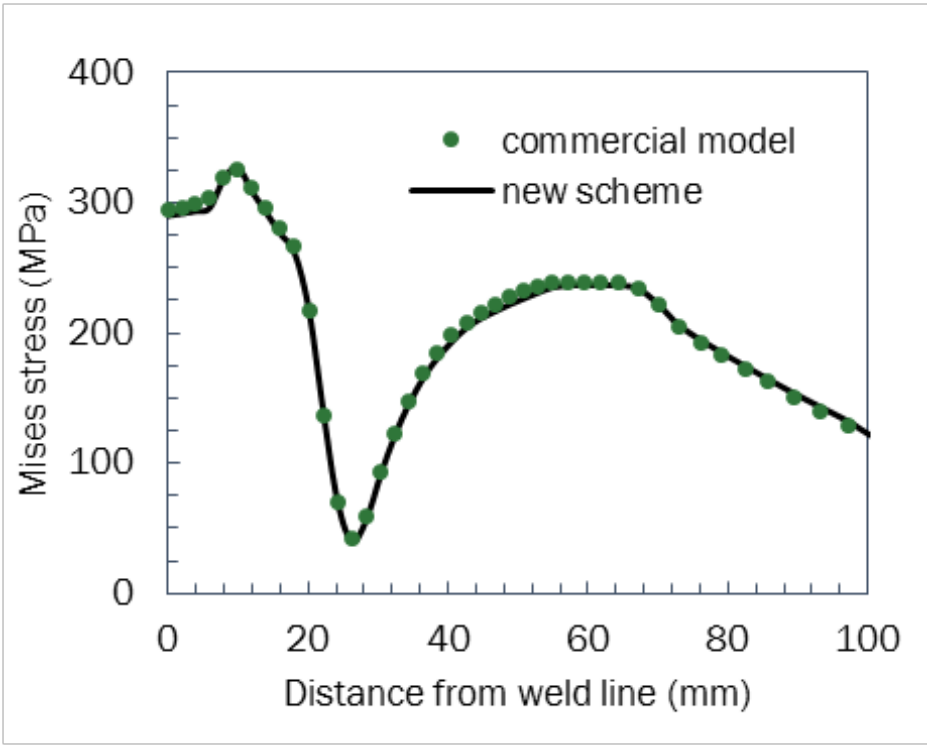

(a)

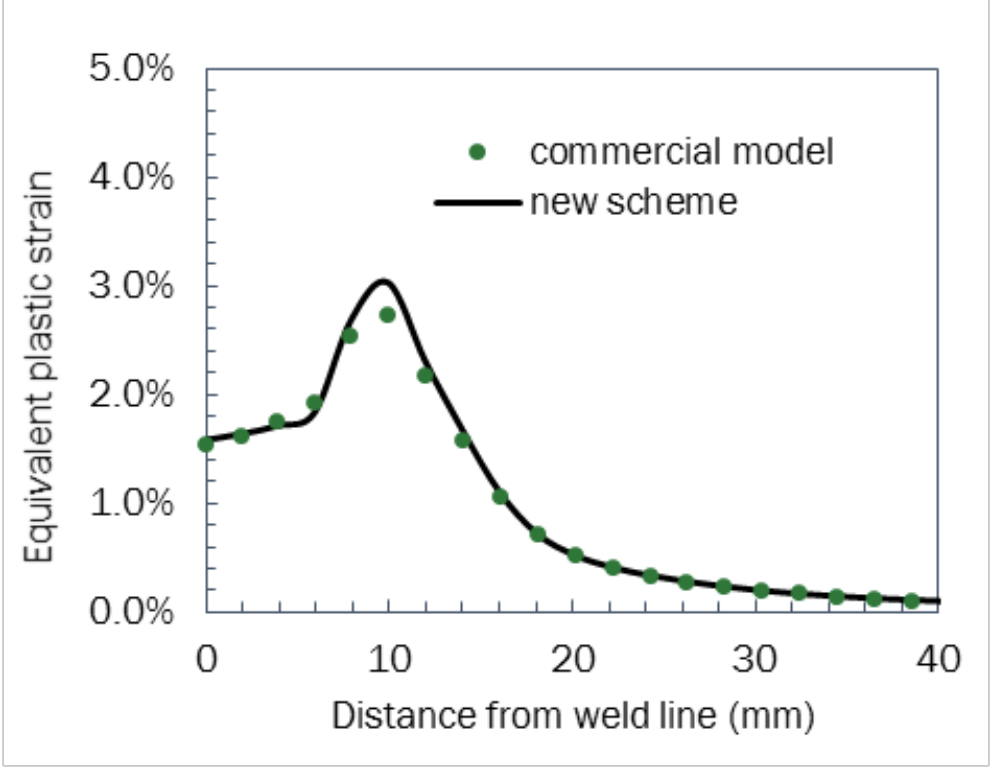

(b)

Figure II.3.H.6. Comparison of arc weld simulation results along a transverse line, as shown in Figure II.3.H.4(b), between application of a commercial model and the new scheme for: (a) Mises stress; and (b) equivalent plastic strain.

Experimental Case Study

As a step towards a demonstrative example, subassemblies composed of two components were welded/brazed under four different clamping conditions with three repetitions per condition to create differing conditions of laser welding-induced distortion, as shown in Figure II.3.H.7. These subassemblies were then three-dimensionally scanned and will be compared to the nominal dimensional data of the single parts positioned in the fixture. This experimental data will then be used to compare the numerical simulation of the distortion using both the commercial weld modeling tool as well as the new scheme developed within this project.

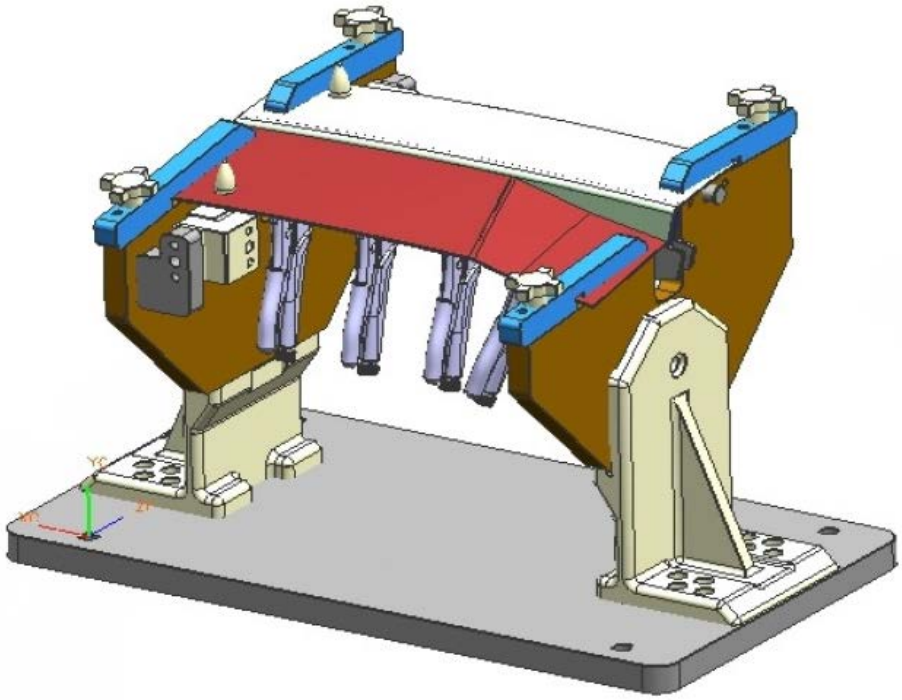

(a)

(b)

Figure II.3.H.7. Illustrative automotive laser welding/brazing example representing a lift-gate seam: (a) computer-aided engineering image of a welding fixture containing two parts to be laser welded/brazed along the seam; and (b) actual laser welding/brazing along the seam. Source: General Motors R&D.

Conclusions

Based on insight of unique physical features of welding processes, a novel acceleration scheme is developed to speed up welding simulation with an approximate 50 to 90 times speedup ratio compared to today's commercial welding process simulation tools. Simulations of laser welding and arc welding processes using the new scheme are demonstrated. The stress and deformation results agree well with those obtained by the commercial simulation tools, and the new modeling scheme allows for much faster simulation of welding fabrication scenarios. Furthermore, an in-house code is being implemented on HPC clusters such as multi-core central processing unit workstation and Graphics Processing Unit (GPU) accelerator to further reduce computation time and achieve an overall acceleration ratio on the order of magnitude of 100 times. Experimental studies are being carried out to validate the simulation results. The new method would have significant impact on energy savings, productivity, manufacturing cost reduction, reducing product development cycle, and the overall competitiveness of the U.S. welding industry.

Key Publications

Chen, J., H. Huang, Z. Feng, B. Carlson, H. Wang, P. Crooker, and G, Frederic, 2017, " High Performance Computing Tools for Advancing Materials Joining Technology," *HPC4Mfg Industry Engagement Day*, March 2–3, 2017, San Diego, CA, USA.

Huang, H., J. Chen, and Z. Feng, 2017, "High Performance Computing of Welding Thermal-Mechanical Process by a GPU-Based In-House Code," Presentation at American Welding Society 2017, Chicago, IL, USA.

Huang, H., J. Chen, B. Carlson, H. Wang, P. Crooker, and G. Frederick, 2017, "An Explicit FEM Approach for Accelerating Welding Stress and Distortion Analysis," Presentation at American Welding Society 2017, Chicago, IL, USA.

Lin, R., H. Wang, F. Lu, J. Solomon, and B. Carlson, 2017, "Numerical study of keyhole dynamics and keyhole-induced porosity formation in remote laser welding of Al alloys," *International Journal of Heat and Mass Transfer*, Vol. 108, Part A, pp. 244–256.

Yang, G., J. Ma, B. Carlson, H. Wang, and R. Kovacevic., 2017, "Effect of laser beam configuration on microstructure evolution and joint performance in laser joining AA 6111 panels," *Materials & Design*, Vol. 123, pp. 197–210.

Yang, G., J. Ma, H. Wang, B. Carlson, and R. Kovacevic, 2017, "Studying the effect of lubricant on laser joining of AA6111 panels with the addition of AA4047 filler wire," *Materials & Design*, Vol. 116, pp. 176–187.

References

Brust, B., 2013, "Distortion and Residual Stress Control in Welded Structures with Application to Oil Rig Platforms," *Residual Stress Summit 2013*, October 7–10, 2013, Idaho Falls, ID, USA.

Feng, Z., J. Chen, G. Chen, and P. Crooker, 2015, "Program on technology innovation: High-performance computing for weld residual stress modeling—A feasibility evaluation." EPRI, Palo Alto, CA 3002006526.

Huang, H., J. Chen, and Z. Feng, 2017, "High Performance Computing of Welding Thermal-Mechanical Process by a GPU-Based In-House Code," Presentation at American Welding Society 2017, Chicago, IL, USA.

Huang, H., J. Chen, B. Carlson, H. Wang, P. Crooker, and G. Frederick, 2017, "An Explicit FEM Approach for Accelerating Welding Stress and Distortion Analysis," Presentation at American Welding Society 2017, Chicago, IL, USA.

II.3.I Corrosion Control in Carbon Fiber Reinforced Plastic Composite-Aluminum Closure Panel Hem Joints (PPG Industries)

Brian Okerberg, Principal Investigator
PPG Industries, Inc.
Coatings Innovation Center
4325 Rosanna Dr.
Allison Park, PA 15101
Phone: 412-492-5292
E-mail: okerberg@ppg.com

Sarah Kleinbaum, Technology Manager
E-mail: sarah.kleinbaum@ee.doe.gov

Start Date: October 1, 2016 End Date: March 31, 2020
Total Project Cost: $2,950,025 DOE share: $2,212,519 Non-DOE share: $737,506

Executive Summary

The purpose of this program is to achieve vehicle weight reduction by developing technologies to enable the use of lightweight outer closure panels, based on a carbon fiber reinforced polymer inner panel and aluminum outer panel (CFRP/Al), and joined by a hem flange. This has the potential to reduce vehicle weight by up to 40 kg, but significant technical barriers exist that must be addressed prior to deployment. These barriers include the corrosion potential for the CFRP/Al joint, CTE mismatch, and CFRP instability at bake temperatures required for current paints and adhesives. During the first year of this program, significant progress was made in characterizing the extent of the galvanic corrosion of the CFRP/Al joint using morphological studies, potential measurements, and accelerated vehicle corrosion testing. SCC assessments were also started. Development of electrodeposition coatings (E-coats) and adhesives was also undertaken, and candidate formulations, which cure at temperatures compatible with CFRP (150°C), have been identified.

Accomplishments

- Developed a CFRP/Al overlap test coupon and completed accelerated corrosion cabinet testing (Ford CETP 00.00-L-467) and full vehicle corrosion testing (R-343, also known as MPG testing) of a matrix of variables, including CFRP type and Al alloy type, both coated and uncoated. These are Ford's standard corrosion test methods and have been shown to correlate very well (much better then more popular methods such as ASTM B117 Salt Fog or J2334 Cyclic Corrosion, which do not work well for Al) with real-world performance on vehicles. Test results indicated that galvanic corrosion and not simple crevice corrosion is the prime electrochemical degradation mode occurring during exposure.
- Identified, through E-coat development and characterization, at least two candidate formulas exhibiting the required level of cure at the target cure conditions of 10 minutes at 150°C metal temperature.
- Formulated prototype adhesives for hem flanges that were: (a) capable of crosslinking when cured at 10 minutes at 150°C; and (b) exhibited desirable cure response and lap-shear strengths, which surpass Ford Motor Company's specification, WSS-M2G575-A, and outperform the existing 175°C cure technologies.
- Submitted a presentation proposal entitled, "Impact of substrates and environmental aging on adhesively bonded lightweight joints," to the 41st Annual Meeting of the Adhesion Society and the 6th World Congress on Adhesion and Related Phenomena Meeting.

- Developed a technique to identify conductive regions on the CFRP surface. Cu is galvanostatically deposited from an electrolyte onto the conductive sites on the CFRP surface. CFRP-Twill was found to have nearly double the deposition site density of CFRP-random.

Technology Assessment

- Gap: The CFRP/Al couple has not been studied.
- Target: Characterization of the CFRP/Al couple for its corrosion and SCC properties.
- Gap: Conductive primers used on composite materials have not been used on galvanic couples.
- Target: Develop a conductive primer balancing the conductivity needed for E-coat application with the electrical isolation needed to prevent galvanic corrosion.
- Gap: When heated, the CFRP/Al hem joint will have mismatched CTE.
- Target: Develop an adhesive for use in the CFRP joint that will have the proper balance of flexibility and stress durability to maintain the integrity of the joint.
- Gap: Automotive E-coats currently require a cure temperature that would compromise the structural integrity of the CFRP matrix.
- Target: Develop an E-coat that will cure in 10 minutes at a metal temperature of 150°C.
- Gap: Galvanic corrosion concerns have prevented the use of hem joints between dissimilar materials.
- Target: Develop a novel hem joint geometry with enhanced isolation characteristics and the ability to manage differences in CTE between the dissimilar materials.
- Gap: The ability of current accelerated testing protocols to predict long-term corrosion performance is unknown.
- Target: Develop a fundamental understanding leading to new predictive testing correlations between accelerated tests and field performance for lightweight CFRP/Al closure panels.

Project Introduction

This program seeks to develop new coatings and adhesives, new joint geometries, and establish and validate corrosion characterization techniques that enable CFRP/Al hem flange joints. The CFRP/Al closure panels will save over 40 kg per vehicle compared to a vehicle with all Al closure panels. The CFRP/Al hem will meet current specifications for mechanical performance, corrosion resistance, and appearance when cured between 150–180°C. Critical success factors to achieve this goal include the development of novel coatings, adhesives, and/or joining geometries to fully isolate the inner panel from the outer panel in the joint while maintaining the ability to electrostatically paint the inner in the paint line. These materials must cure at a lower temperature and be designed to mitigate the CTE mismatch while enabling processing through a standard paint shop. Extensive electrochemical and stress corrosion cracking testing will be conducted to evaluate the corrosion performance of the new solutions and determine the appropriate accelerated test methods. Outdoor on-vehicle exposure testing will be conducted to verify the proper laboratory accelerated corrosion test method for CFRP/Al hem joints.

Approach

The project has been divided into three project/budget periods. The focus of BP1 has been to understand the nature and extent of the corrosion problem resulting from the CFRP/Al joint. The susceptibility to galvanic corrosion and SCC is being determined. An investigation is being made into the level of conductivity needed to promote electrostatic painting, but not galvanic coupling. Development of adhesives and coatings that develop the required cure and corrosion-preventive characteristics in the required temperature range is underway.

During BP2, prototype conductive primers, adhesives, and E-coats will be developed based on the learnings from BP1. Hem geometries, which mitigate galvanic coupling and CTE mismatches, will also be identified.

Finally, the solutions developed during BP2 will be optimized and developed during BP3. A surrogate Al-outer/CFR-inner closure capable of passing Ford's specifications and being processed through a typical paint shop operation will be constructed and tested.

Technology Transfer Path

Technology transfer and marketing of the technology developed under this project will depend on the successful demonstration of the prototype closure panel, which is the final milestone of the project. Successful completion of this milestone will demonstrate to PPG and Ford that the project risk has been effectively reduced to the point where self-financing of the activities needed to scale and implement the new solution will be viable. Once on-vehicle testing is passed, two years is sufficient to conduct the remaining testing and validation activities to enable commercial launch. Ford will need all materials to complete submission testing for traditional engineering and process robustness attributes, which normally includes numerous Design of Experiments (DoEs) to ensure process interactions are fully understood. Any new vehicle structures are both modeled and tested to ensure vehicles meet all applicable safety standards. In addition, purchasing agreements must be negotiated for any new materials.

The target market for this technology includes all vehicles produced by Ford, as there are severe fuel economy pressures on all product lines. Implementation would likely be prioritized for those products and geographical markets where this pressure is most intense. In particular, the growth of the sports utility vehicle and crossover utility vehicle market in North America and Europe makes initial implementation likely in those regions.

Although all automotive manufacturers are under the same regulatory pressures to improve fuel economy and reduce weight, individual manufacturers are taking different approaches, not all of which are focused on CFRP structures. Nevertheless, PPG's role as a supplier to all automotive manufacturers should increase the likelihood of CFRP's adoption, once low-cure coatings and adhesives are made available.

Product marketing and distribution would be according to existing channels used by PPG and Ford. New, lightweight vehicles would be marketed in the usual way, via commercials, the annual auto shows, and dealer literature. Similarly, PPG would market new low-cure products through product literature and communicate through typical sales channels both inside and outside of the automotive industry.

Results

The work performed under BP1 is divided into three primary tasks:

- Task 1.1 Benchmark Corrosion Performance and Electrochemical Testing of Target Substrates and Simple CFRP/Al Joints
- Task 1.2 Screening of Low-Cure E-coats, Adhesives, and Conductive Primers
- Task 1.3 Determine the Impact of CTE Mismatch

The details of the work performed in each of these tasks and their respective subtasks, is provided in the sections that follow.

Subtask 1.1.1: Prepare and Test Corrosion Samples (PPG/Ford)

A test matrix was formulated and agreed upon by all project parties. Corrosion testing of CFRP/Al joints via overlap coupons was completed using both accelerated corrosion cabinet testing (Ford 00.00-CETP L-467) and full vehicle corrosion testing (R-343, also known as MPG testing). A schematic is shown in Figure II.3.I.1.

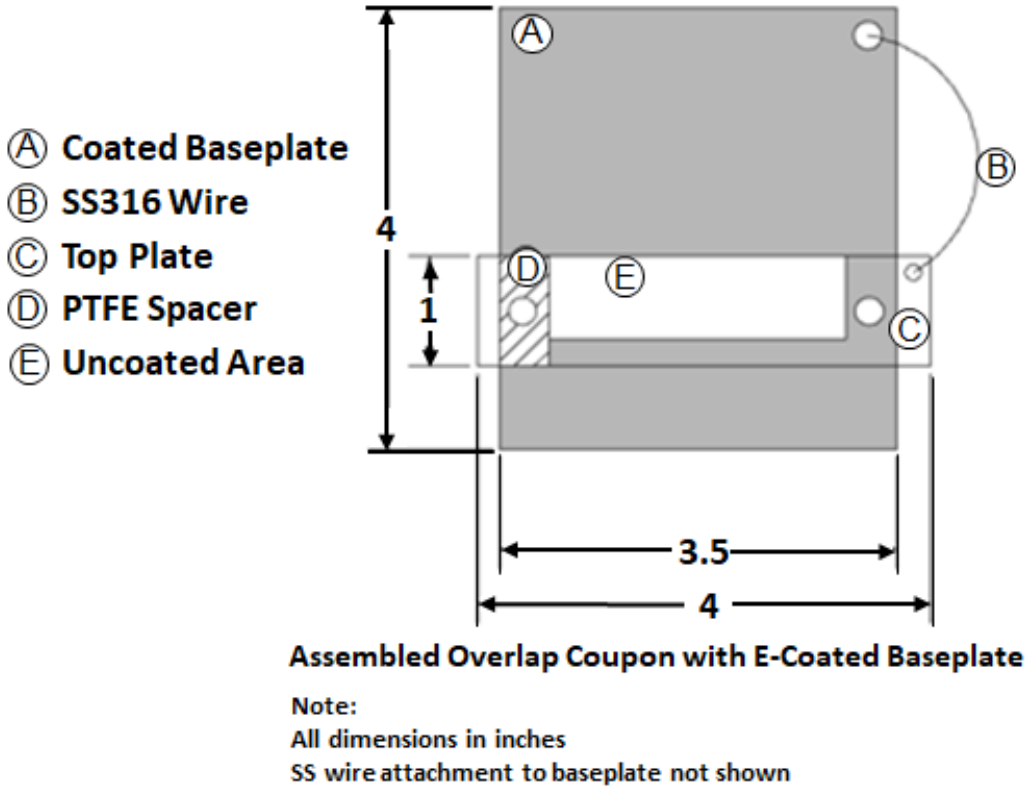

Figure II.3.I.1. Schematic of mixed material overlap coupons.

For full vehicle corrosion testing, the specimens were mounted to the exterior of the vehicle, as shown in Figure II.3.I.2. Two types of CFRP materials were utilized: (1) random chopped fiber composites; and (2) a carbon fabric (Twill). These composite top plates were joined to Al (6111 and 6022) substrates. In addition, coupons with fiberglass and Al top plates were used as control samples to separate out galvanic effects from crevice corrosion effects. Examples of the corrosion seen in both R-343 and L-467 are shown in Figure II.3.I.3 and Figure II.3.I.4, where the undercutting and blistering of the coating is shown at the leading edges of the test coupon for samples with both types of CFRP top plates. No corrosion is observed for samples with the Al or fiberglass top plates. The extent of undercutting has been quantified, as shown in Figure II.3.I.5, and agrees with the generally observed results (i.e., corrosion is extensive when CFRP is coupled to Al and is largely absent when fiberglass or Al is coupled to Al). While both the length (e.g., linear measurement away from the cover plate edge) and area of corrosion were measured, the area approach provides additional resolution and differentiation that the length measurement does not. Therefore, the area approach will be used for future evaluations.

Figure II.3.I.2. Mounting of corrosion specimens on vehicle for R-343 full vehicle corrosion testing. Source: Ford.

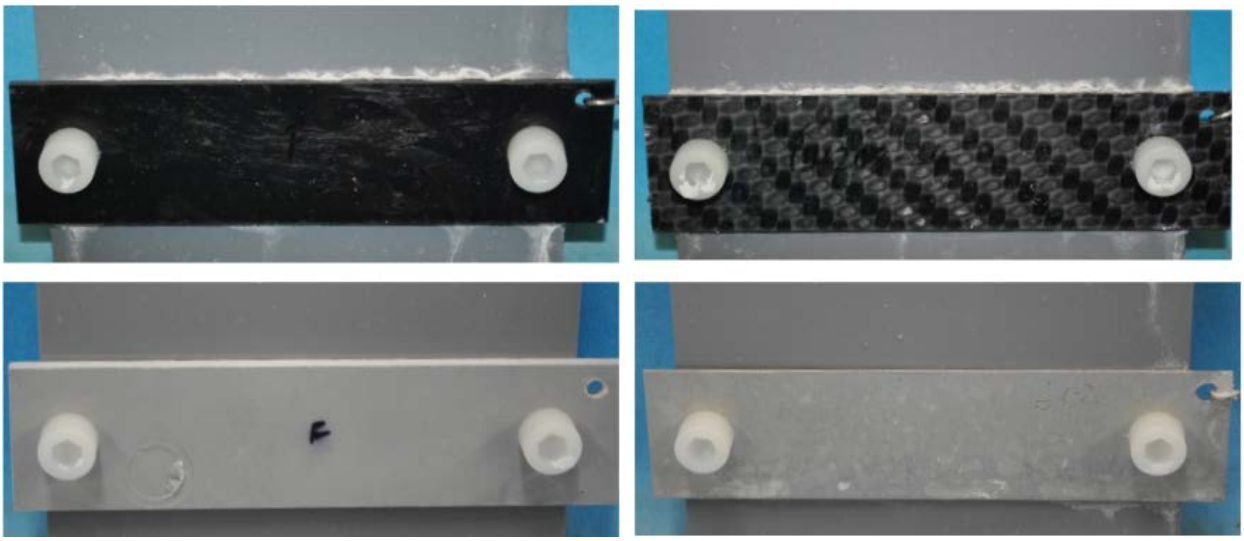

Figure II.3.I.3. Corrosion of test coupons after six weeks of L-467 accelerated corrosion testing. Note the undercutting/blistering of E-coat observed on AA-CFRP coupons in full vehicle corrosion testing at the top of both CFRP coupons (top) and the lack of corrosion on the E-coated Al and fiberglass coupons (bottom). Source: Ford.

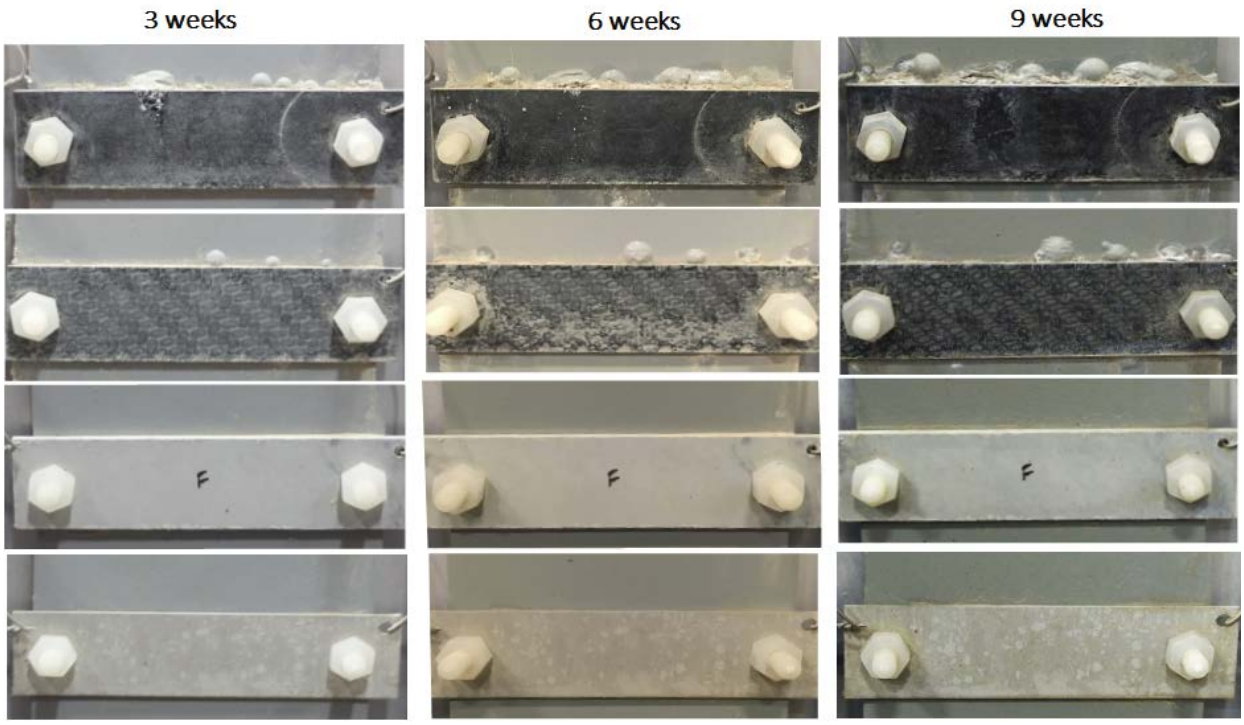

Figure II.3.I.4. Test coupons after indicated time periods in R-343 full vehicle corrosion testing. Coupons were affixed to the side of a vehicle during test protocol. Note the increase in undercutting/blistering of E-coat observed on AA-CFRP coupons (top two rows) over time and lack of corrosion on Al and fiberglass coupons (bottom two rows). Source: Ford.

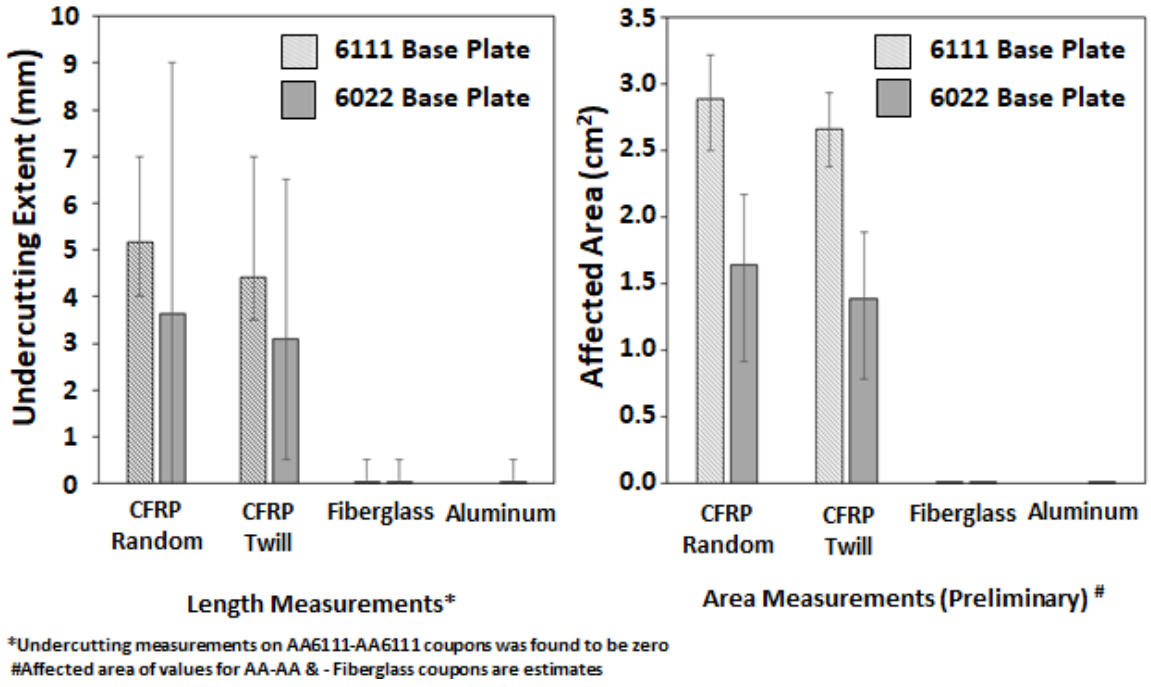

Figure II.3.I.5. Extent of undercutting/blistering on Al bottom plate when coupled to various cover plate materials. Area measurements provide a more robust and accurate means for differentiating performance than length measurements. A larger affected area occurred for the AA6111-CFRP than for the AA6022-CFRP coupons. Al only and Al-fiberglass showed minimal to no signs of undercutting.

After disassembling the samples, extensive corrosion was seen to occur under the baseplate for both types of CFRP samples, but little to none was observed when the Al or fiberglass top plates were used. This indicates that galvanic corrosion and not simple crevice corrosion is the prime electrochemical degradation mode occurring during exposure, as shown in Figure II.3.I.6 and Figure II.3.I.7. For this round of testing, we chose to only use mechanical fastening. In the next round of testing, similar coupons will be used, but those coupons will also include different adhesive types and conductive primers.

Figure II.3.I.6. Corrosion of AA6111 baseplate exposed to nine weeks of R-343 full vehicle corrosion testing. Note the extensive corrosion of the baseplate under both CFRP top plates (higher for AA6111-CFRP Random). AA6111-AA6111 and AA6111-fiberglass coupons show signs of bare shiny metal with traces of dirt. Source: Ford.

Figure II.3.I.7. Corrosion of AA6022 baseplate exposed to nine weeks of R-343 full vehicle corrosion testing. Note the extensive corrosion of the baseplate under both CFRP top plates. Corrosion was higher for AA6022-CFRP Random. AA6022-AA6022 shows signs of dirt accumulation and AA6022-fiberglass shows signs of bare metal. Source: Ford.

Subtasks 1.1.2—1.1.4: Galvanic Corrosion Susceptibility Assessment, Effect of Galvanic Coupling on SCC susceptibility, and Accelerated Corrosion Test Procedure Analysis/Development (OSU)

Preliminary characterization, which includes morphological studies and potential measurements on CFRP-Twill and CFRP-Random samples, was one goal of this performance period. Morphological studies of the polished top surface and the cut edges were carried out using optical microscopy and SEM to characterize the fiber shape, cross-section, distribution, and orientation for these two composite materials. Potential measurements were performed using scanning Kelvin probe (SKP) and scanning Kelvin probe force microscopy (SKPFM). Several attempts were made, but the results were not reproducible, and the analysis was difficult. According to the literature and input from the manufacturer, potential measurements on such non-conducting or poorly conducting materials, primarily the epoxy regions, using SKP/SKPFM would merely be an artifact.

In an attempt to understand the nature of the epoxy cover on the top surface, an electrodeposition technique was developed. In this technique, Cu is deposited from an electrolyte onto the conducting regions/areas of the substrate. If a small amount of material is deposited, the deposit indicates the locations and numbers of the active sites on the CFRP surface. Initially, potentiostatic deposition was attempted, but control of the extent of deposition was better using galvanostatic electrodeposition. Deposition was carried at 50 mA/cm^2 for 10 sec. In the end, we were successful in depositing Cu and locating and counting the number of active sites on the surface. The number of active sites on CFRP-Twill and CFRP-Random were $6240/cm^2$ and $3200/cm^2$, respectively. Currently, we are performing serial sectioning by focused ion beam (FIB)/SEM to image the interface between Cu deposit and epoxy/fiber and generate a better understanding of the structure of the defects on the surfaces of the composites.

Electrochemical measurements were performed on CFRP-Twill, CFRP-Random, and AA6XXX in aerated 5 wt% sodium chloride solution measured with a saturated calomel electrode (SCE) as the reference electrode, as shown in Figure II.3.I.8. Cathodic and anodic polarization curves were performed separately. The corrosion potentials of CFRP and AA6XXX were 1 volt (V) apart, CFRP being more noble, and their corrosion current densities differed by five orders of magnitude. The cathodic current density of CFRP-Random was 10x larger than that of CFRP-Twill at low potentials. This is in contrast to the higher number of active sites on CFRP-Twill determined by Cu deposition. The potentiodynamic polarization results could be understood by considering the nature of active sites on CFRP-Twill. It is possible that, although the number of Cu deposition sites is higher in Twill, these sites do not behave as active cathodic sites when coupled with AA6XXX. Furthermore, the physical distribution of the active sites might affect their efficiency as cathodes. The sites on the CFRP-Twill samples are concentrated along lines, whereas those on CFRP-Random are distributed across the surface. Modeling and the FIB/SEM analysis will provide insight in understanding this behavior better.

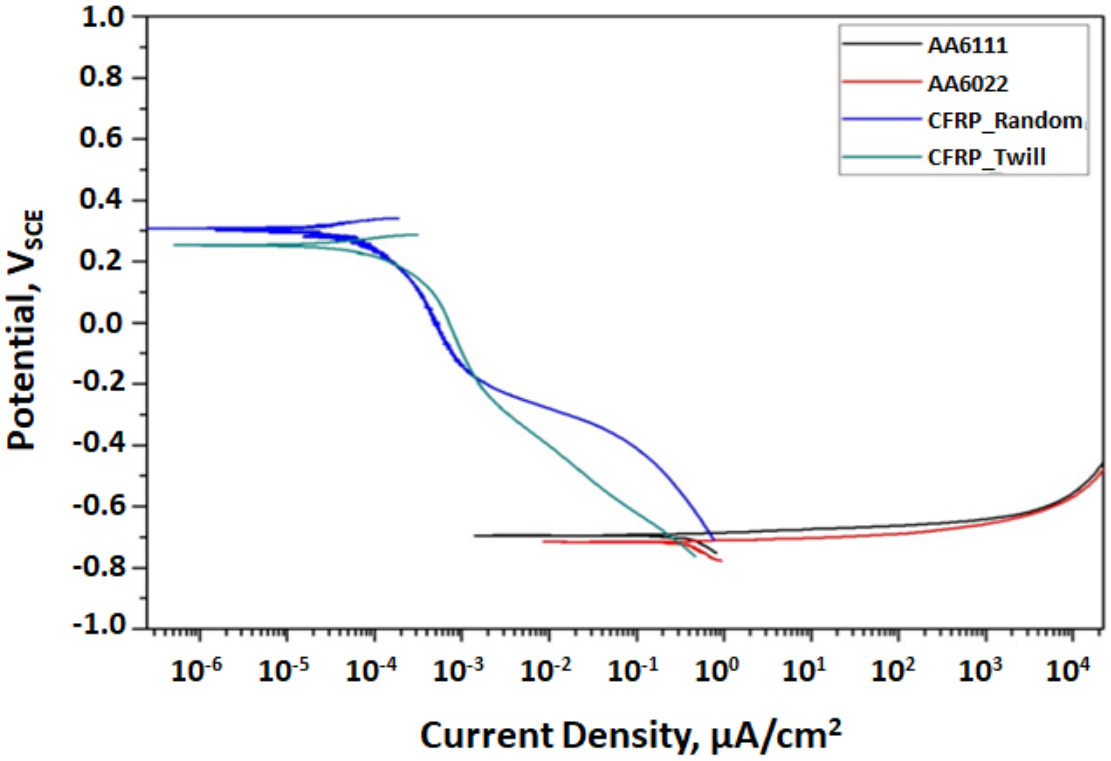

Figure II.3.I.8. Polarization curves of CFRP-Random, Twill, AA6022, AA6111 in 5% sodium chloride.

The determination of galvanic corrosion susceptibility is being carried out using accelerated corrosion testing in a 5 wt% sodium chloride environment in a salt fog chamber. As per Ford, this test should run for 12 weeks. Testing will be conducted on the CFRP-Twill and CFRP-Random couples individually with AA6XXX E-coated and without E-coat. Based on the results so far, the coupons comprising AA6XXX without E-coat coupled with CFRP-Random exhibited galvanic currents almost three to five times higher than the currents observed in AA6XXX-Twill consistently, as shown in Table II.3.I.1. This supports the inference drawn from the deposition study of Cu on CFRP-Twill that the active sites do not behave strongly as cathodes. These tests are continuing and will be repeated on more samples.

Table II.3.I.1. Summary of the Galvanic Current Measurements.

Time / Sample	Galvanic Current, µA								
	0 h	24 h	48 h	72 h	96 h	120 h	144 h	168 h	192 h
Uncoated 6022-Random (62RNC6)	500	800	820	790	880	1000	800	750	400
Uncoated 6111-Twil (61TNC8)	140	170	200	240	250	260-200	250	142	670
Coated 6022-Twil (62TC8)	40	30	50	100	120	130	225	270	400
Coated 6022-Random (62RC6)	250	300	–	–	–	–	–	–	–
Uncoated 6022-Random (62TNC6)	0	700	650	625	750	815	620	580	660

During this first performance period, Ford provided OSU with AA6111-T4 material for SCC investigation. AA6111 was chosen over AA6022 due to material thickness considerations (i.e., AA6111 is used as a thicker product, which makes machining of valid fracture mechanics samples easier) and likely performance considerations (i.e., AA6111 has more Cu, which leads to increased intergranular susceptibility). The AA6111-T4 sheet material was received from Ford in the second quarter of FY 2017. In the third quarter, an aging thermal treatment to simulate the Ford paint-bake process was applied by heating samples in a 171°C oven for 20 minutes (oven time, not metal temperature time) with a subsequent air cool. Thermal profiles were generated for each sheet during the aging process by using a thermocouple to measure metal surface temperature at 1-minute intervals. The thermal profile summary is shown in Figure II.3.I.9. The average final metal temperature in the oven was 161.5°C. It is important to note that no pre-stretch was applied to the sheet material prior to the aging process. The commercial product would undergo a pre-stretch to induce deformation substructure that assists with optimal strengthening precipitate formation. Not providing pre-stretch can lead to lower strength levels, which have been observed here. For this reason, the material will be referred to as T8-like.

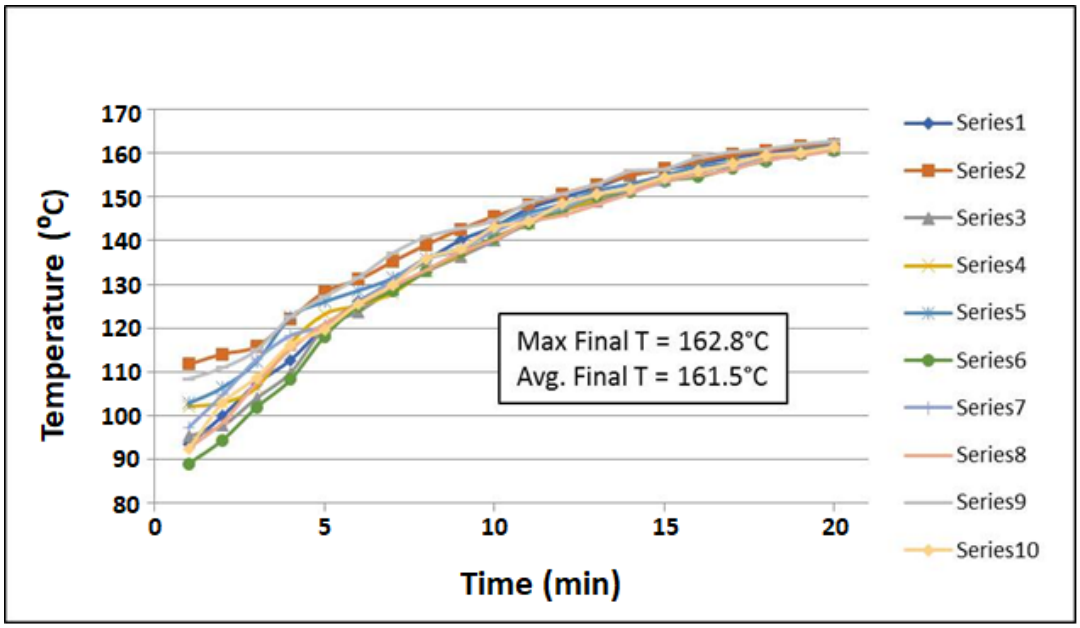

Figure II.3.I.9. Temperature profiles of AA6111 sheet material during paint bake-like thermal treatment.

Tensile testing was performed on the aged AA6111-T8-like sheet on five tensile specimens loaded in the L direction and tested at a constant strain rate of 0.5 mm/min. The stress-strain curves generated are shown in Figure II.3.I.10. The average ultimate tensile strength (σ_{UTS}) was 288 MPa and average offset yield strength (σ_{ys}) was 170 MPa. The σ_{UTS} measured for the T8-like temper is comparable to Arconic reported values for the commercial T81 temper, 290 MPa. The σ_{ys} is lower than the Arconic reported σ_{ys} value of the commercial T81 temper, 214 MPa, but higher than the Arconic reported T4 temper, 154 MPa. This implies that some aging was achieved in the T8-like thermal treatment, but the lack of a pre-stretch reduced the strength achievable in 20 minutes. It was decided by Ford and OSU that a second thermal treatment would not be performed. The T8-like temper is sufficient to understand and quantify the effect of anodic polarization on SCC. Should an adverse effect be found, later studies can confirm the effect on commercial product.

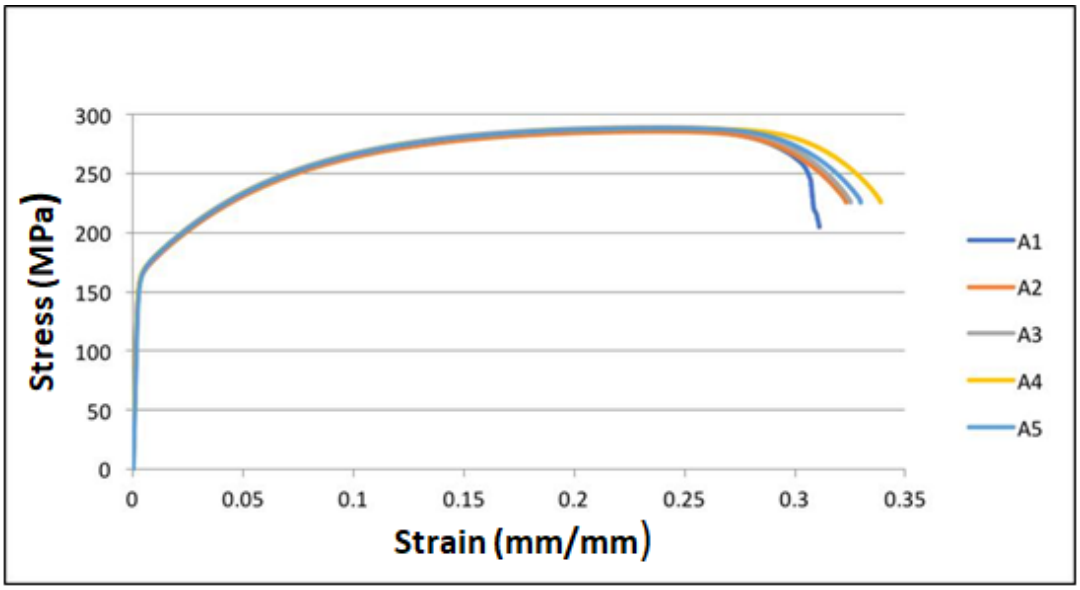

Figure II.3.I.10. Stress-strain curves of aged AA6111-T8-like sheet on 5 tensile specimens (A1 through A5) loaded in the L direction tested at a constant strain rate of 0.5 mm/min.

The eccentrically loaded single edge notch tp.376ension (ESE[T]) specimen geometry was chosen for SCC testing and a specimen drawing with appropriate dimensions for the AA6111-T8-like material was created. The drawing is shown in Figure II.3.I.11. Aged material for SCC specimens were sent out for machining. Round one of testing will be completed by the extended end of BP1.

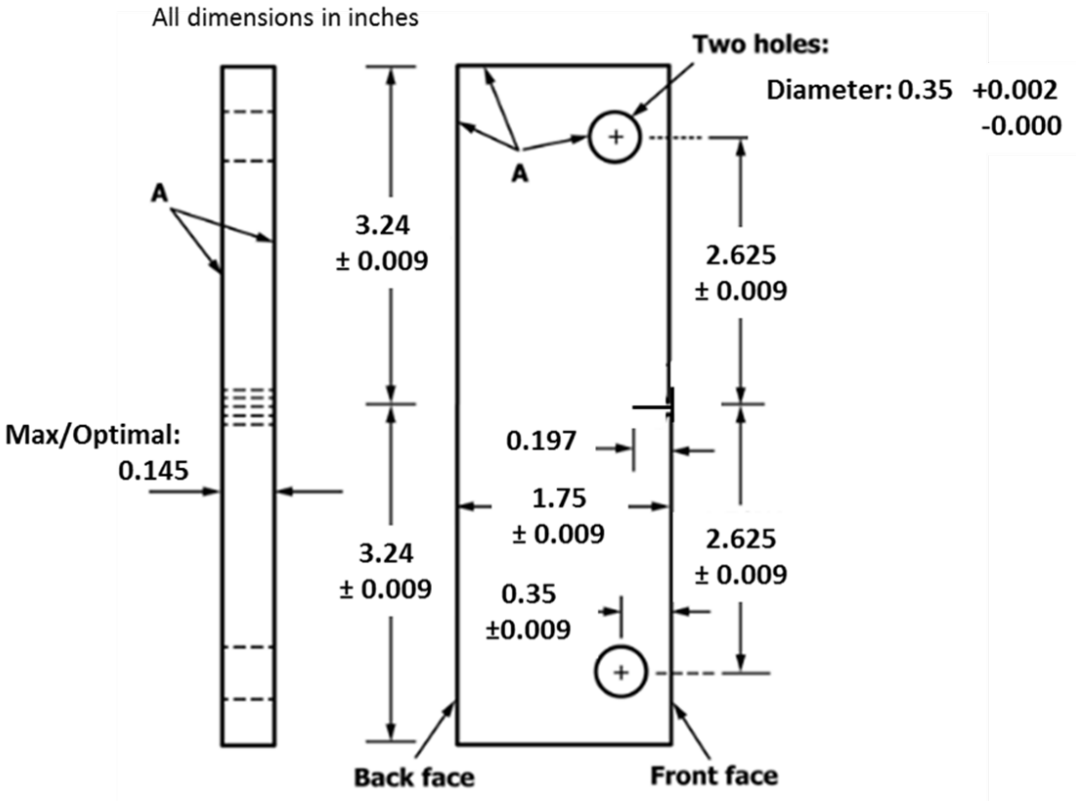

Figure II.3.I.11. ESE(T) SCC specimen drawing with dimensions.

The OSU campus bus system has agreed to allow us to utilize the campus buses for hanging outdoor exposure racks. The racks will have to be hung downward-facing as they need to be fully attached to the under-body structure of the bus. This is because the buses must reduce height for disability rider entrance, which prohibits hanging samples in an outward-facing manner. A rack was fabricated and is ready for use in on-vehicle on-road exposure testing once final selection of test samples has been made. This task is slightly behind since it was decided to wait and deploy a down-selected set of coupons.

A Q-fog cabinet capable of relative humidity control has been purchased and is in the process of being installed in the lab area at the OSU Fontana Corrosion Center. This frame will be used for the relative humidity control needed to run the Ford standard accelerated cabinet corrosion test. When all parts, including the chiller component, are delivered, the equipment will be experimentally validated so that SCC testing can be performed.

Subtask 1.2.1: Screening of E-coat (PPG)

Low-cure E-coat formulations were screened to identify formulations for hem joints comprised of CFRP and Al. A DoE approach was applied to systematically evaluate seven E-coat formulations, consisting of six prototype formulations with two polymer backbones and three crosslinkers. A control E-coat formulation was also prepared and evaluated in the study. The coat-out conditions were first optimized to generate the target thickness (i.e., 0.60 mils) for the E-coat within the target film build time of three minutes. The E-coat samples were baked at two different bake conditions, 150°C/10 min (metal) and 175°C/20 min (metal) followed by evaluation for cure, appearance, and corrosion. The details of the seven DoE formulations are summarized in Table II.3.I.2.

Table II.3.I.2. Formulation Details for Low-Cure E-coat Screening.

Sample ID	Formulation Variables			
	Resin	Crosslinker (XL)	Additive	Catalyst
P1B	A	XL 1	C	E
P2B	B		D	
P3	A	XL 2	C	
P4	B		D	
P5	A	XL 3	C	
P6	B		D	
C1	A	XL 3	C	E

(P1–P8: prototype formulations, C1: control formulation, XL1-XL4: crosslinkers)

The initial focus of the project was to evaluate cures at the target temperature (150°C/10 min). The metal temperature during the oven-bake cycle was measured by attaching a thermocouple directly onto an Al substrate, as shown in Figure II.3.I.12. The results allowed for precise determination of oven temperature and time for the baking process.

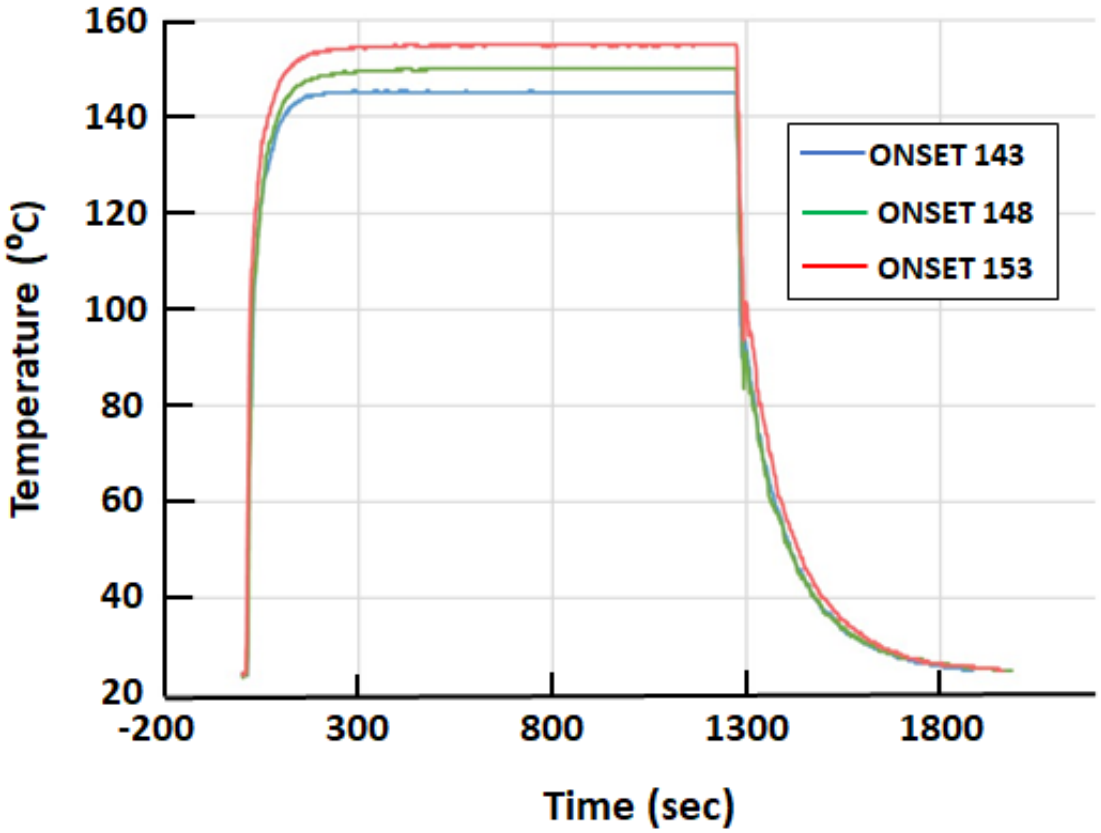

Figure II.3.I.12. Al panel temperature profiles at different oven set temperatures.

To characterize cure as a function of formulation type, thermogravimetric analysis (TGA) and rheology characterization was performed. TGA measures the weight loss of the blocking groups in crosslinkers that directly relate to the crosslinking reaction of E-coat. Rheology testing measures the viscoelasticity change of an E-coat upon baking, which is also directly related to the E-coat crosslinking reaction. To directly compare the results from each measurement, simple constant ramping with 10°C/min was used. The ramping condition can distinguish the various thermal behaviors (i.e., weight loss and viscoelasticity) of the E-coat with respect to temperature and allows a direct comparison between different E-coat formulations.

As shown in Figure II.3.I.13(a), the derivative of the weight loss of blocking groups from TGA measurements show very distinct profiles in terms of peak temperature and breadth for the prototype E-coats. The storage modulus (G') determined from rheology measurements also indicates that the viscoelasticity profiles are very distinct with respect to formulation variation. The initial drop of G' at temperatures around 70°C is due to enhanced mobility of the E-coat around its glass transition temperature (T_g). Temperatures higher than T_g lead to flow and leveling of the E-coat until the crosslinking reaction occurs. As shown in Figure II.3.I.13(b), the crosslinking reaction of the E-coats takes place in the wide temperature range of 130–190°C, which turns out to be primarily dependent on the crosslinker type. The trend of viscoelasticity change from rheology is consistent with the weight loss trend from TGA, strongly suggesting that the weight loss of the crosslinker blocking group and crosslinking reaction occurs simultaneously.

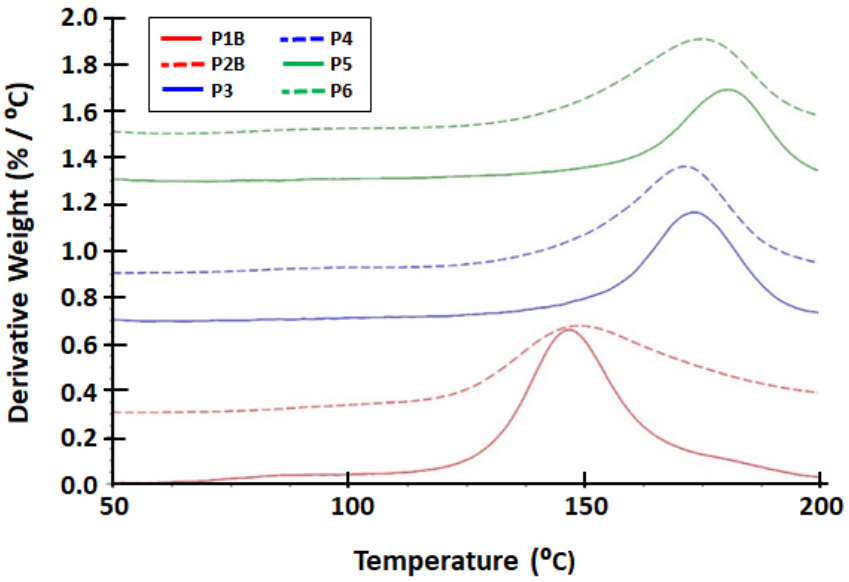

(a)

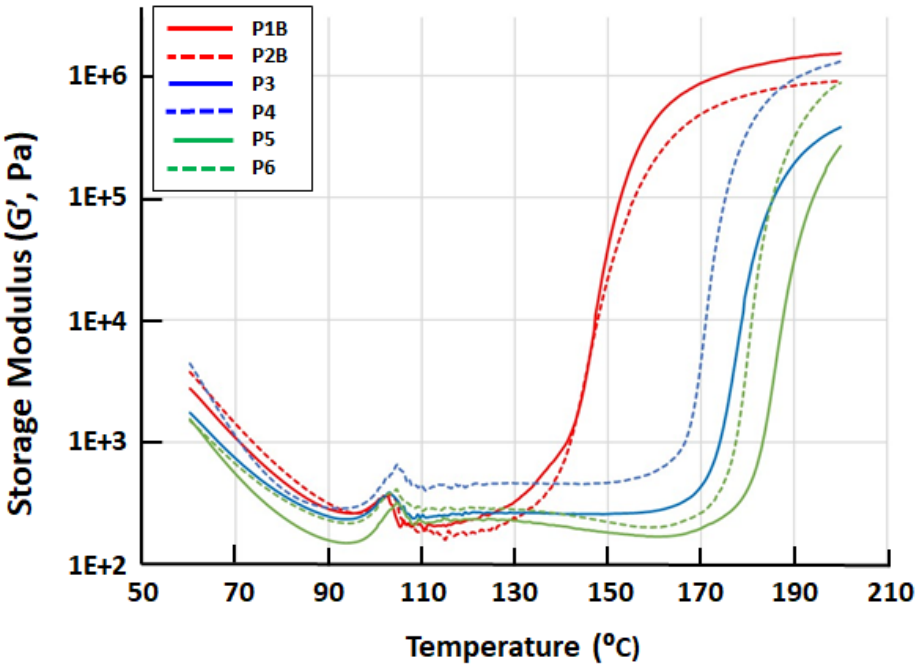

(b)

Figure II.3.I.13. (a) TGA weight loss derivatives; and (b) rheology data measured at a constant ramp of 10°C/min.

The cure of all E-coats on Al panels was evaluated separately by double acetone rubs (DAR), which is widely used in the industry to evaluate E-coat cure. The number of DAR was precisely measured with respect to the physical damage of the surface, such as coating removal and marring. As shown in Figure II.3.I.14, distinct DAR numbers are observed for the E-coats baked at 150°C/10 min (metal). All the E-coats exhibited promising cure upon baking at 175°C/20 min (metal).

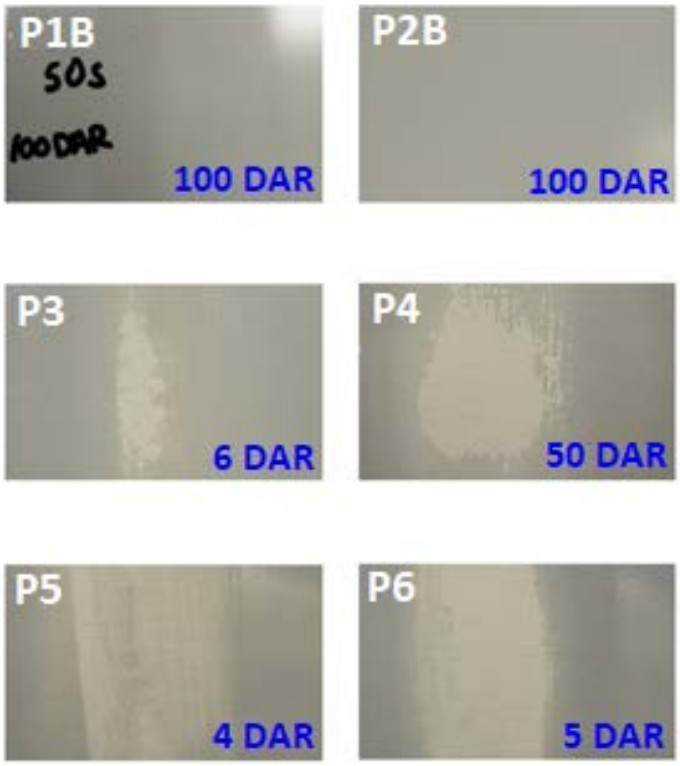

(a)

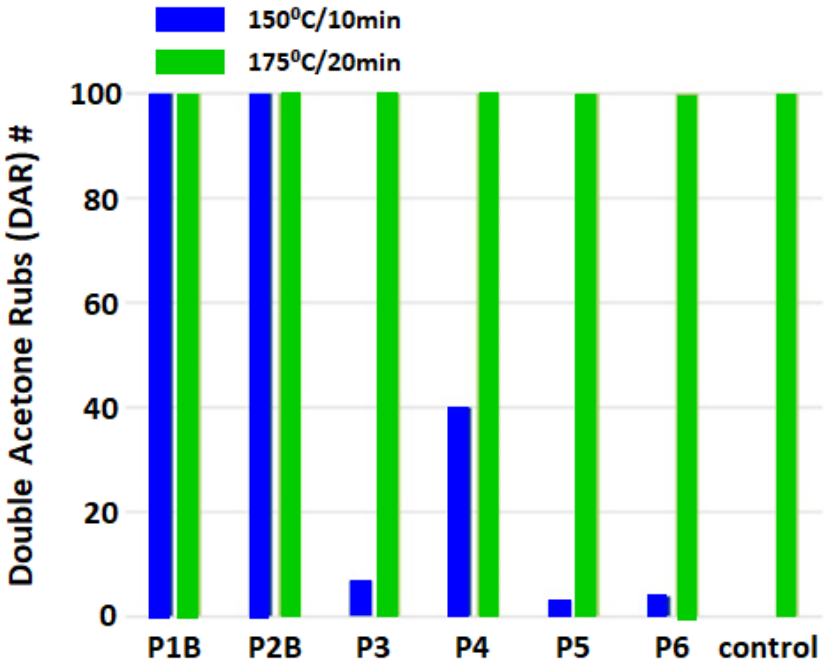

(b)

Figure II.3.I.14. (a) The images of E-coat formulations on Al panel after DAR. The formulations were baked at 150°C for 10 min (metal). (b) The number of DAR to reach the Al substrate panels. The E-coats were baked at both 150°C/10 min and 175°C/20 min. The DAR of 100 implies no physical damage of E-coats after DAR 100 times.

DAR results agree well with both TGA and rheology results in terms of predicting the crosslinking reaction temperature and order. Hence, we utilized both TGA and rheology measurements for fast and accurate screening in this study. The main formulation variation in the prototype E-coats are crosslinker and backbone type. Both TGA and rheology data strongly suggest that the crosslinker type plays a dominant role in determining the crosslinking reaction temperature. The data also suggest that backbone type also influences the profile in a smaller degree compared to the crosslinker type. The E-coat formulations with XL1 and two distinct backbone types (i.e., P1B and P2B) clearly result in a satisfactory cure upon processing at the target bake condition of 150°C/10 min (metal).

The appearance of E-coats baked at two different conditions (i.e., 150°C/10 min and 175°C/20 min) were evaluated by a contact profilometer. As shown in Figure II.3.I.15, all the prototype E-coats exhibited slightly higher W_b (surface structure parameter) values compared to the control. The value for P4 was determined as much higher than the rest of the samples. The reason for the abnormally high appearance value for P4 is not clear, but may be a result of poor E-coat bath stability.

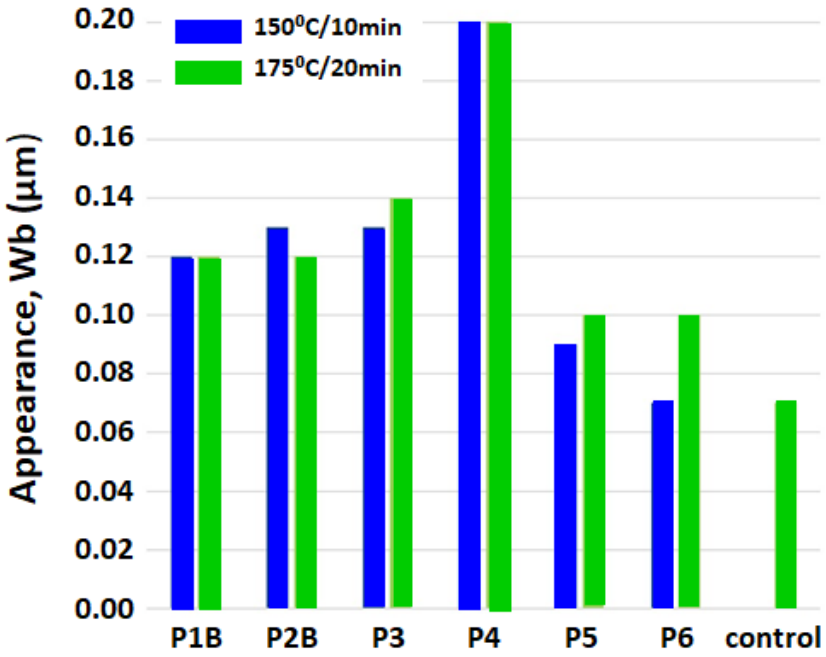

Figure II.3.I.15. Appearance (W_b) of E-coats determined by profilometry. Two bake conditions (i.e., 150°C/10 min and 175°C/20 min) were applied for prototype E-coats. The control was baked at 175°C/20 min.

Another key property of corrosion was evaluated by an ASTM G-85 A2 test. The test was performed for three weeks and six weeks to evaluate corrosion behavior over time. As shown in Figure II.3.I.16, improved corrosion resistance was observed for all the prototype E-coats baked at both 150°C/10 min and 175°C/20 min compared with the control sample that was baked at 175°C for 20 min. For the E-coats baked at 150°C for 10 min (metal), a strong inverse correlation between DAR result and corrosion resistance was observed. The E-coat with the lower DAR number (i.e., lower degree cure) exhibited better corrosion resistance, as shown in Figure II.3.I.17).

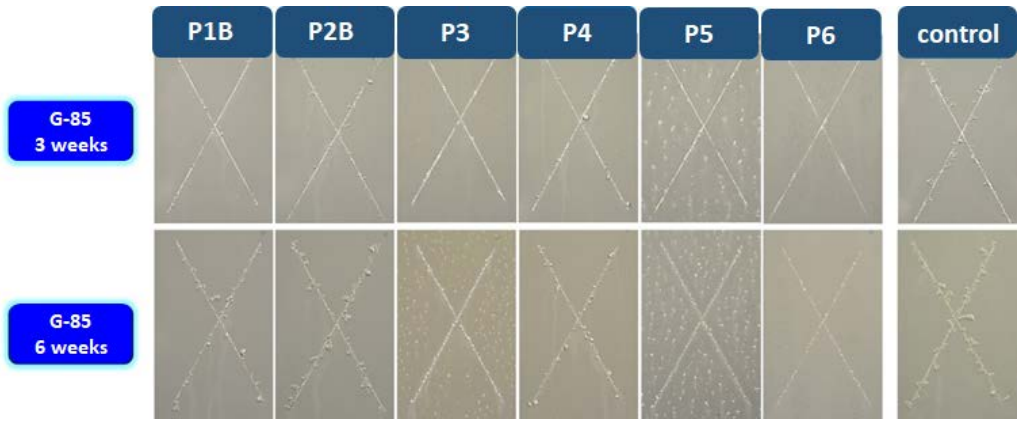

Figure II.3.I.16. Corrosion test (i.e., ASTM G-85 A2) results for E-coats on Al 6111 substrates for three and six weeks. The prototype E-coats were baked at 150°C for 10 min (metal) and the control sample was baked at 175°C for 20 min (metal).

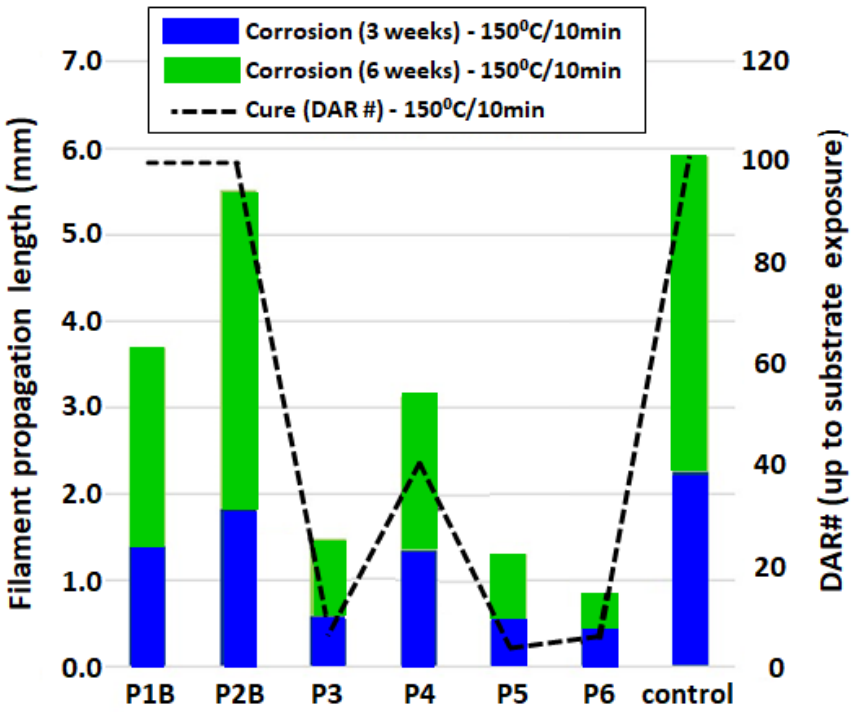

Figure II.3.I.17. Corrosion test (i.e., ASTM G-85 A2) results for E-coats on Al 6111 substrates for three and six weeks. The prototype E-coats were baked at 150°C for 10 min (metal) and the control sample was baked at 175°C for 20 min (metal).

The key observations from the initial testing are as follows:

- Several E-coat formulations were identified with satisfactory cure at the project specification (e.g., 150°C for 10 min, metal).
- The blocking group type and catalyst loading were the primary contributors to the crosslinking reaction temperature.
- Polymer backbone type also played a smaller but significant role in determining the cure temperature.
- Strong correlation of the cure degree of E-coat and corrosion resistance was observed (i.e., a better corrosion resistance is observed from the E-coat with a lower degree of cure).

Subtask 1.2.2: Screening of Adhesives (PPG)

Adhesive joint performance was measured in terms of cure response and lap-shear strength. The cure response was characterized using DSC to measure the onset of reaction and exothermic peak temperatures. A specimen of weight 20 mg ± 1 mg was sealed in an Al hermetic pan and scanned twice in a TAI Discovery DSC from 25–250°C at a heating rate of 5°C/min.

Lap-shear strengths were quantified using single lap-shear joints, which were manufactured by bonding two rectangular AA6022 (101.6 mm × 25.4 mm) together with an overlap length of 13 mm. The Al substrates were purchased from ACT Test Panels, LLC. In addition, some lap-shear tests were also performed on AA6022 and AA6111 Al alloy provided by Ford. All Al substrates were coated with a thin layer of dry film lubricant (Quaker DryCote®290) prior to adhesive application. Figure II.3.I.18 shows the schematic representation of a single lap-shear joint. The bonded lap-shear joints were baked in a convection oven at 150°C for 10 minutes metal time. To ensure the joints reached the intended temperature and baked for the required duration, a thermocouple was inserted as close as possible to the adhesive layer to monitor its temperature during the bake cycle. The actual cure time was then determined from the moment the adhesive reached the intended temperature. The specimens were allowed to equilibrate at room temperature for 24 hours prior to testing. The specimens were tested under ambient conditions according to SAE J1523 using an Instron testing machine at a nominal crosshead speed of 13 mm/min. The peak loads were recorded, and average or apparent shear strengths were calculated by normalizing the peak load with the bonded overlap area.

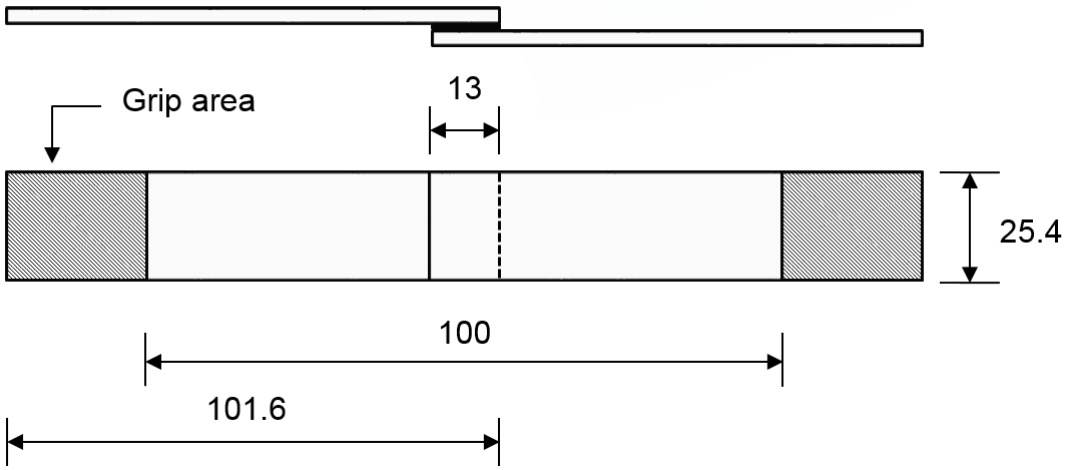

Figure II.3.I.18. Schematic representation of a single lap-shear joint. All dimensions are in millimeters.

Adhesive formulation variables including polymer resins, toughenners, curatives, and additives for cure response and lap-shear strengths were investigated to design and formulate low-cure prototype adhesives with a performance: (a) equal to existing 175°C cure technologies; and (b) that meet Ford's WSS-M2G575-A specification in terms of cure response and lap-shear strength. In this report, two existing 175°C cure technologies were denoted as C1 and C2. The results for two specific developmental prototype adhesives (denoted as D1 and D2) are also presented in this report. D1 was a developmental adhesive optimized for cure response, while D2 was a developmental adhesive optimized for both cure profile and lap-shear strength. Our studies demonstrated that the lap-shear strengths and cure profiles were markedly impacted by the formulation variables.

The cure response of adhesives was characterized by the onset of adhesive curing and exothermic peak temperature as determined from DSC heat flow curves. The onset of curing was defined as the temperature at the onset of the exothermic peak, which indicates that the adhesive resin-curing agent starts reacting. The peak temperature corresponds to the temperature at the exothermic peak, reflecting the maximum curing rate of the

adhesives. Table II.3.I.3 summarizes the DSC findings. The onset temperatures of curing for C1 and C2 were measured to be 132°C and 131°C, respectively, while the prototype adhesive D1 registered an onset reaction temperature of 99°C. The exothermic peak temperatures for C1, C2, and D1 were 174°C, 173°C, and 141°C, respectively. The relatively low onset and exothermic peak temperatures of D1 as compared to those of C1 and C2 are indicative of the capability of the developmental prototype adhesive to crosslink at 150°C for 10 minutes. Indeed, as will be shown later, this notion will be borne out by the results from the lap-shear tests.

Table II.3.I.3. Onset Curing Temperatures and Peak Temperatures for Various Adhesives.

Sample	Onset of Curing (°C)	Peak Temperature (°C)
C1	132	174
C2	131	173
D1	99	141
D2	TBD	TBD

Figure II.3.I.19 and Figure II.3.I.20 depict the lap-shear strengths for the adhesive joints manufactured using either AA6022 or AA6111 provided by Ford. All adhesive joints baked at 175°C exhibited relatively high lap-shear strength exceeding Ford's specification (i.e., 13 MPa). In the case of the 150°C bake condition, the lap-shear strength for the developmental prototype adhesive D1 was comparable to that of the 175°C bake counterparts. However, the two existing 175°C cure technologies, C1 and C2, did not cure completely at 150°C, as evidenced by their significantly lower lap-shear strengths as compared to the 175°C bake conditions and the lap-shear strength values fell short of the Ford specification target. The results were expected as C1 and C2 were not designed to fully cure at 150°C due to the inadequacy of their crosslinking agent and catalyst package, which led to either partial or incomplete network formation. Conversely, the high lap-shear strength of D1 clearly suggests the capability of the developmental low-cure adhesive to crosslink at 150°C for 10 minutes for both AA6022 and AA6111 provided by Ford.

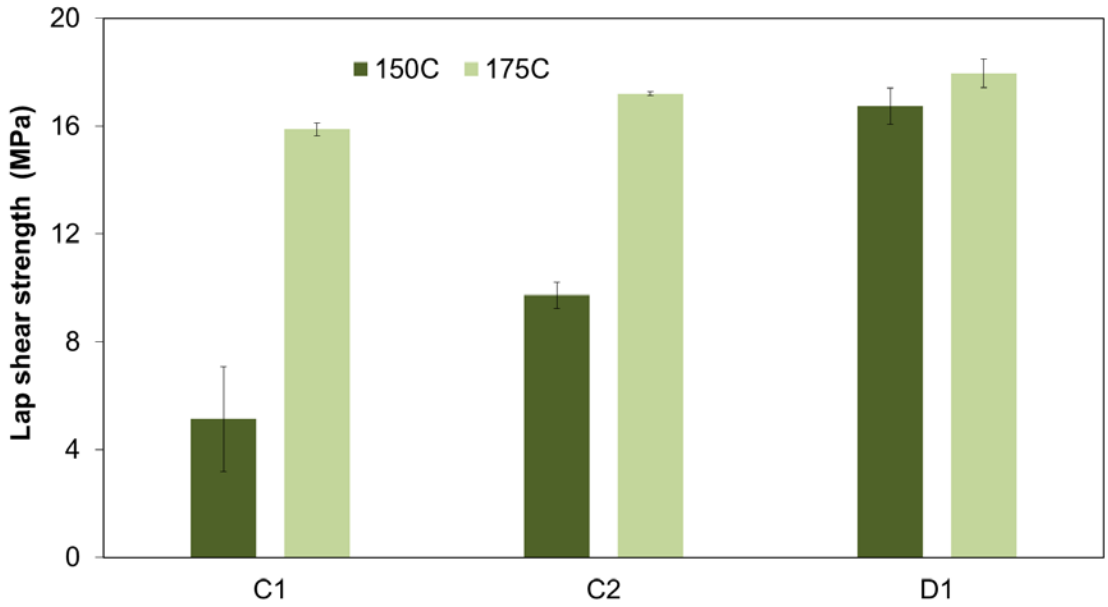

Figure II.3.I.19. Lap-shear strengths for C1, C2, and D1 adhesive joints manufactured using Ford Al 6111. The bake condition was either 150°C or 175°C for 10 minutes. The error bars represent one standard deviation.

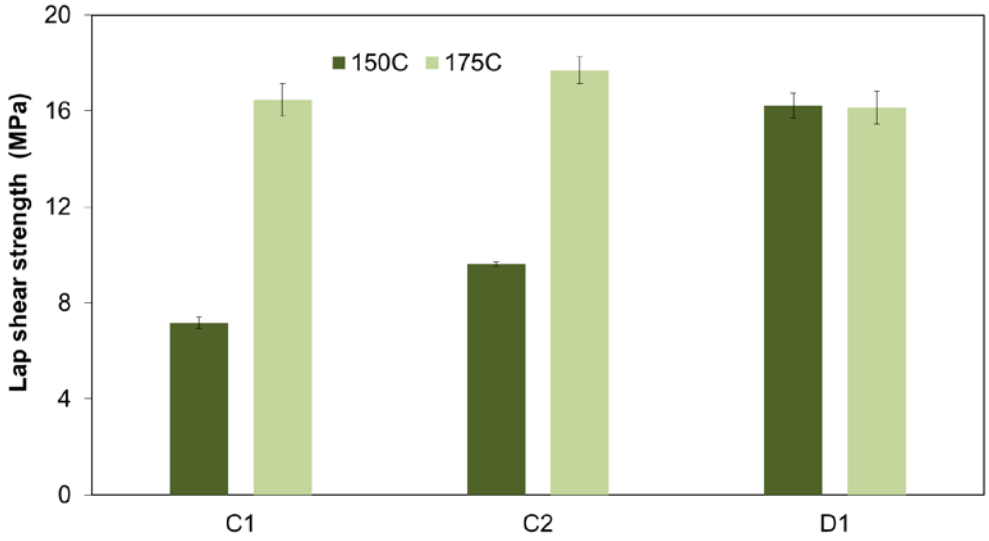

Figure II.3.I.20. Lap-shear strengths for C1, C2, and D1 adhesive joints manufactured using Ford AA6022. The bake condition was either 150°C or 175°C for 10 minutes. The error bars represent one standard deviation.

In addition, the adhesive performance was also evaluated using AA6022 from ACT. The lap-shear strengths for C1, C2, D1, and D2 are shown in Figure II.3.I.21. The influence of AA6022 from Ford and ACT on lap-shear strength is visible, which may be attributed to substrate surface properties and mechanical properties of the Al alloy. The former plays a critical role in dictating the degree of interfacial interaction between the adhesive and the substrate, while the latter may influence the stress distribution within the overlap bonded area (Kinloch 1987, da Silva et al. 2008). Consistent with the AA6022 studies from Ford, Figure II.3.I.21 shows that C1 and C2 exhibited relatively low lap-shear strengths, further corroborating the insufficient cure under 150°C for 10 minutes. Contrary to the existing 175°C cure technologies, D1 and D2 were capable of crosslinking under the low-bake condition, which was evident from their high lap-shear strengths compared to other adhesives. In particular, the lap-shear strength of D2 was eight times higher than that of C1. The joint failure for D1 and D2 was predominantly cohesive within the adhesive layer.

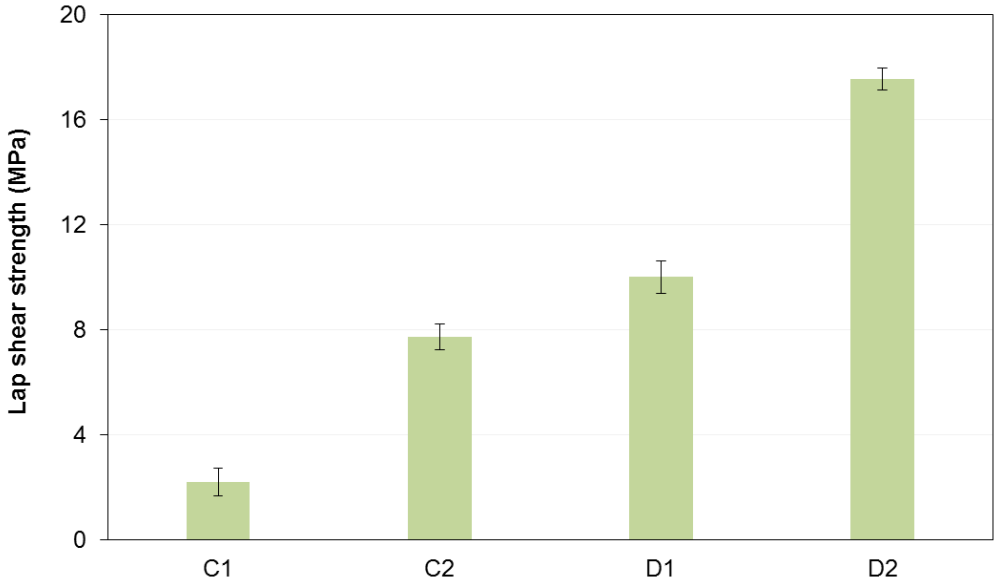

Figure II.3.I.21. Lap shear strengths for C1, C2, D1, and D2 adhesive joints manufactured using ACT AA6022. The bake condition was 150°C for 10 minutes. The error bars represent one standard deviation.

In summary, formulation variables including polymer resins, tougheners, curatives, and additives had an important influence on the cure response and lap-shear strength. Optimization of the formulation variables for the critical requirements enabled us to formulate prototype adhesives for hem flanges that: (a) were capable of crosslinking when cured at 10 minutes at 150°C; and (b) exhibited desirable cure response and lap-shear strengths, which surpass Ford's WSS-M2G575-A specification and outperform the existing 175°C cure technologies.

Subtask 1.2.3: Screening of Conductive Primers (PPG)

Two primer formulations were selected to vary the resultant conductivity in a systematic way. Optimization of the primer formulation is in progress, including conductivity, viscosity, and volatility at the target spray-out condition.

Task 1.3: Coefficient of Thermal Expansion Mismatch Impact (Ford)

The test methodology and simulation tools for this task have been developed. When appropriate adhesive formulations have been developed by PPG, Ford will begin to assess the effect of adhesive formulation and geometry on residual stress numerically and via experimentation. It is anticipated that a lower modulus adhesive will be advantageous for these applications.

Conclusions

The work performed on this project during FY 2017 explored the corrosion issues associated with the CFRP/Al couple. Galvanic corrosion was confirmed to be the prime electrochemical degradation mode occurring during both accelerated corrosion cabinet testing and full vehicle corrosion testing (also known as MPG testing). An electrochemical technique was developed that shows promise for providing a better understanding of the structure of the defects on the CFRP surfaces. Substantial progress was made to develop E-coats and adhesives, which provide the desired performance properties, while being cured at the reduced temperatures required by the presence of the CFRP material.

References

da Silva, L. F. M., J. C. das Neves, R. D. Adams, and J. K. Spelt, 2008, "Analytical models of adhesively bonded joints – Part I: Literature survey," *Inter. J. Adhesion Adhesives*, Vol. 29, pp. 319–330.

Kinloch, A. J. 1987. Adhesion and Adhesives: Science and Technology, Springer Science & Business Media, London. DOI 10.1007/978-94-015-7764-9.

II.3.J Brazing Dissimilar Metals with a Novel Composite Foil (Johns Hopkins University)

Timothy P. Weihs, Principal Investigator
Department of Materials Science and Engineering
Johns Hopkins University
3400 North Charles St.
Baltimore, MD 21218
Phone: 410-516-4071
E-mail: weihs@jhu.edu

Sarah Kleinbaum, Technology Manager
E-mail: sarah.kleinbaum@ee.doe.gov

Start Date: October 1, 2013 End Date: March 31, 2018
Total Project Cost: $595,520 DOE share: $595,520 Non-DOE share: $0

Executive Summary

Reactive brazing is a novel technique in the joining industry that uses reactive materials to produce substantial amounts of heat locally to join components. In this project, we create mechanically processed dilute thermite (reduction-oxidation [redox]) foils that upon ignition self-propagate to produce molten metal capable of joining dissimilar metal combinations. Due to the transient nature of the reaction, there is limited thermal damage to the base materials. Also, novel component combinations that cannot be joined via traditional furnace brazing, such as Mg alloys to steel, can be produced. Redox foils are produced by mechanically processing and consolidating constituent powders. By adjusting the fabrication pathway and chemistry, the reaction products can be tailored to join specific material combinations. In addition to producing mechanically processed foils, we produce vapor processed foils with controlled microstructures to understand some of the mechanisms of the reaction.

This FY, we worked to identify the length scale ratio of thermite to diluent versus the length scale of thermites to determine the degree of heterogeneity in the local composition. Furthermore, FEM heat transfer simulations predicted the length scale that suppresses Cu gas formation during propagation. Gas generation is detrimental to resulting bond strengths because it can cause mass ejection out of the bond area. This ejection creates pores in the resulting braze. We also investigated the use of one-part titanium to two-parts boron (Ti:2B) reactive scaffolds that provide a heated framework to enhance braze flow and minimize porosity. However, ball milled (BM) Ti:2B powders suffered ~8% mass loss due to surface adsorbed water resulting in porous and weak bonds.

As an alternative solution, we are currently developing a Ti-C-Cu based reactive braze system that relies on titanium carbide (TiC) formation reactions to melt the Cu braze material. In this system, we do not have components that produce gas/vapor that is detrimental to bond strengths. During the preliminary investigation, we observed TiC formation for a poorly incorporated Ti-C-Cu composite system. Initially, consolidated pellets have poor theoretical maximum density (TMD) and mechanical integrity. TMD is the theoretical weighted average of pure solid densities of the different reactants that make up the mixture. Typically, when consolidating powders to create compacts, we have trapped air pockets which reduces the overall density of the system. When TMD is below 100%, we express the degree of deviation from an ideal density of the mixture devoid of air pockets. However, these pressed fragments react easily when initiated with an electrically heated filament forming the desired TiC products.

Accomplishments

- Investigated the use of a Ti:2B reaction system to produce hot, molten scaffold to minimize porosity and enable braze to flow (FY 2017).
- Characterized the effect of milling parameters on the microstructure of a Ti:2B system (FY 2017).
- Microstructurally analyzed length scales of redox foils to compare with FEM heat dissipation models (FY 2017).
- Reduced mass loss in Cu_2O via heat treatment (FY 2017).
- Investigated use of a Ti-C-Cu system as an alternative to an Al:Cu2O diluent thermite system (FY 2017).

Technology Assessment

- Target: Bonds with a lap shear strength of 20 MPa.
- Gap: Current bonds fabricated with redox foil are on the order of 10 MPa; the shear strength can be increased by decreasing the porosity of the bond area and improving wetting of the samples during reaction.
- Target: Gasless propagation of redox foils.
- Gap: Current bonds fabricated with redox foil show significant porosity, likely due to the evolution of gases upon reaction and heating.

Project Introduction

Reactive materials have been used to join metals for over 100 years ever since Hans Goldschmidt discovered that reactive Al and iron oxide could produce molten iron capable of joining railroads (Goldschmidt 1903, Wang et al. 1993). This was called the thermite process, where the Al reduces a metal oxide creating molten metal, alumina, heat, and often gaseous products. Initial joining use of these chemistries involved powdered mixtures and a mold so that the molten braze created can flow into joints. More recently, reactive multilayer foils using intermetallic formation reactions have been used as a heat source (Wang et al. 2004, Duckham et al. 2004, Weihs 2014). These joints do not produce their own braze, and therefore require pre-wetting of solder or braze layers to enable joining. Reactive joining provides a fast, efficient bonding approach, allowing one to use high-temperature brazes that cannot be used on certain alloys.

This project aims to combine the concepts of the two types of reactive joining described above. By using a thermite composition, the exothermic reaction can create its own braze without requiring any pre-coated solder or braze layers on the components. Further, by creating a fully dense foil, the joint can be formed without any mold or complicated fixture. The braze is created at the location of the joint, as shown in Figure II.3.J.1, and does not need to flow into the joint area, as is the case with typical thermite joining. To reduce the amount of gas produced by thermite reactions, the mixture is diluted with excess metal. Adding diluent decreases the reaction velocity, decreases the total amount of heat, and decreases the reaction temperature. Adding diluent also has the benefit of increasing the quantity of molten metal braze in the products as compared to undiluted thermites (Kinsey 2016).

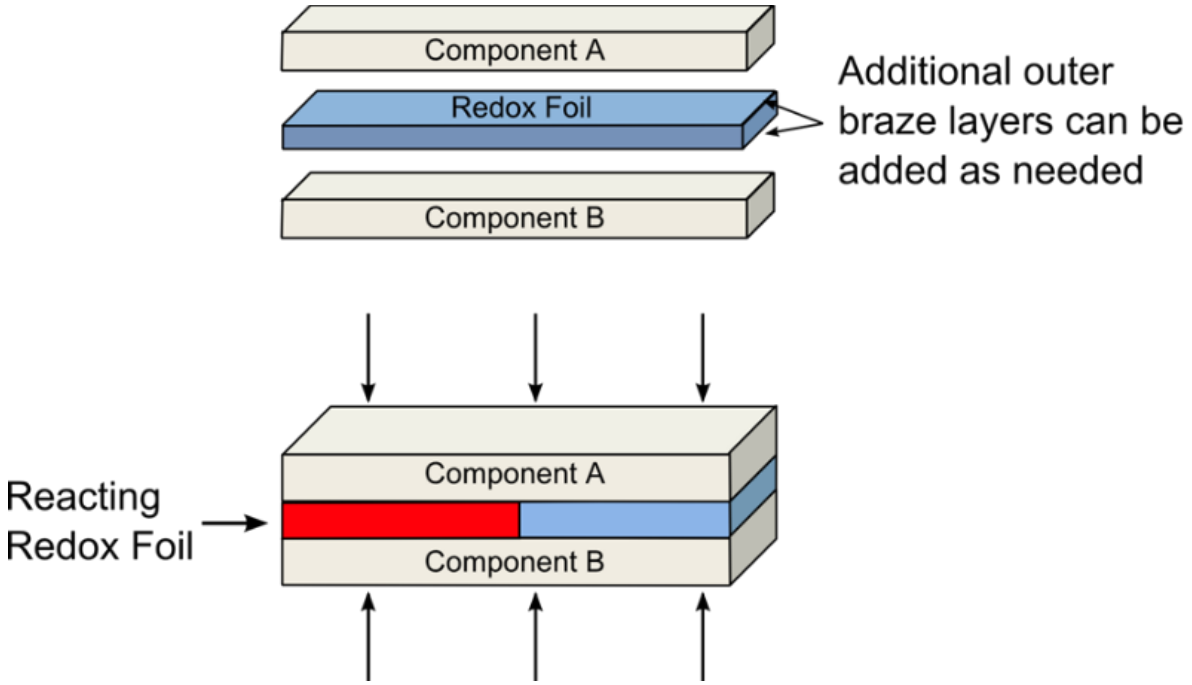

Figure II.3.J.1. Schematic of the joining process with redox foil. As the reaction propagates molten braze is produced. Source: Johns Hopkins University.

The chemistry and microstructure of the redox foil determines how the reaction will propagate. The chemistry also determines the characteristics of the braze that is formed. By engineering the reaction properties of the foil, we can tailor the reaction to join many dissimilar metal combinations. Because the reactions propagate quickly (on the order of 1 m/s), the heat is produced for a short period of time, and very locally. This allows for brazing of dissimilar combinations that cannot be joined with traditional furnace brazing, such as joining steel to Mg alloys.

Approach

To develop a redox foil capable of joining dissimilar metals, we have produced two different types of foils. The first foil is made by mechanically processing constituent powders (e.g., redox foil) (Kinsey et al. 2016, Woll et al. 2016), and the other by physical vapor deposition (PVD). The redox foil is the economical solution that can be easily scaled for automotive applications. PVD foils, on the other hand, have well-defined geometries for scientific inquiry. These ideal microstructures are critical for understanding the processes that occur during propagation, and aid in engineering the necessary microstructure that we emulate in the redox foils. In the past FY, we determined that the Al:Cu_2O system is the most promising system for joining, with the diluent typically Cu, but some silver dilutions have been prepared, as will be described.

The redox foil fabrication process involves three steps. First, constituent powders are BM to produce nanocomposite powders. This step was added in FY 2015 to reduce the reactant spacing between the Al fuel and the oxide. Initially, only the Al and metal oxide were milled together producing thermite composites (these foils are labeled BM). However, due to analysis from the PVD foils in FY 2016, it was determined that the diluent needs to be more uniformly incorporated into the final structure; therefore, the diluent was added to the BM process (BM+D). After milling, the powders are packed into a tube and then compacted by swaging, a radial reduction technique. Finally, the swaged tubes are rolled flat and the tube encasing removed leaving the fully dense redox foil.

The PVD foils are made using magnetron sputtering. The sputtering chamber contains three targets, Al, Cu_2O-Cu, and Cu. Inside of the chamber, substrates are rotated past each target producing layered foils of a planar geometry.

A variety of techniques were employed to analyze the materials. High-speed videos allow us to determine propagation velocity, a key metric for how fast the reaction is producing heat. Emission spectroscopy is used to identify if vapor species are produced by the reactions, as well as to approximate reaction temperatures. Slow heating experiments, including differential scanning calorimetry and thermogravimetric analysis (TGA), were also used to characterize the thermal properties of reactive materials and resulting braze. Finally, the redox foils were used to join Al AA3003, Mg AZ31, and hot stamped boron steel, and the shear strengths of resulting bonds were tested.

Technology Transfer Path

Patent application of reactive material has been submitted to the United States Patent Office and is under review. We will look to license the patent as the technology becomes viable.

Results

Thermite Length Scale Analysis

Image analysis was performed on micrographs of Al:Cu_2O:Cu BM redox foils to understand the length scales present in the microstructure. The results are summarized in Figure II.3.J.2 where the ratio of thermite to diluent is plotted versus the thermite length scale. Larger ratios correspond to smaller levels of dilution. The size of the circle corresponds to the area fraction of length scales within a given ratio. The blue color circles represent the length scales that have dilution levels that do not cause gas generation while the red color circles represent length scales with poor dilution levels that facilitate local gas generation. In addition, FEM heat transfer simulations were used to determine the critical thermite lengths and ratios that are required to suppress Cu gas formation during propagation, as summarized in Figure II.3.J.3. Based on these simulations, it was determined that for foils with 20 and 30 wt% diluent over half of the foil area was capable of producing vapor. This matches experimental observations in which redox foils with this level of dilution showed mass ejection and high levels of porosity. The 40 wt% sample, with fewer dangerous microstructural length scales, did not produce any vapor in experiments. Therefore, to produce gasless propagation, only BM+D foils, which have a finer spacing and more homogenous distribution of diluent in the microstructure, should be used moving forward.

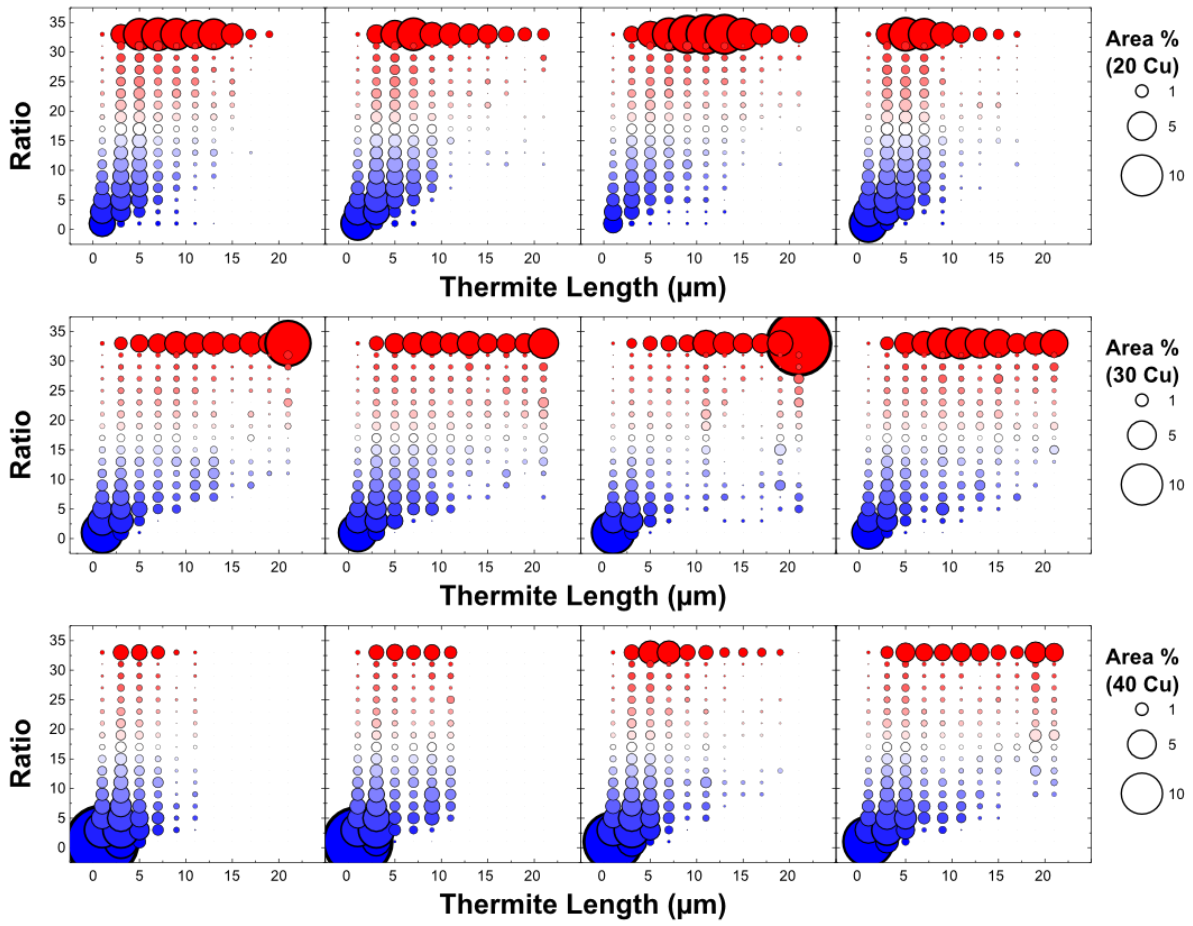

Figure II.3.J.2. Microstructural analysis of BM redox foils. Each graph represents analysis on a different region of foil. Top row is 20wt% Cu, middle row is 30wt% Cu, and bottom row is 40wt% Cu. Source: Johns Hopkins University.

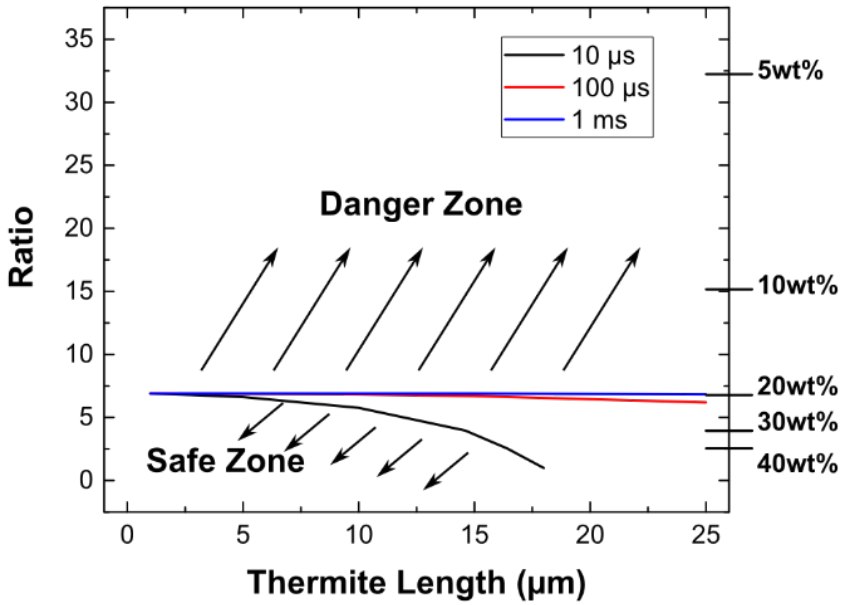

Figure II.3.J.3. Results from FEM simulations determining what ratio and length scales are required to suppress gas formation.

Evaluation of Ti:2B Scaffolds

Ti:2B BM powders have the advantage of a higher adiabatic temperature than thermites and higher melting temperatures for the final TiB_2 compound product that forms. This means that these powders quickly enter the solid phase after reaction. We combine the Ti:2B pellets with our traditional thermite powder systems and leverage the best qualities of both reactive systems. The Ti:2B has a high heat output upon reaction, forming TiB_2, which creates a hot, porous, and solid matrix. The thermite acts as an additional heat source while providing molten braze material that solidifies at temperatures approximately 2000ºC below the melting point of TiB_2. These metallic products (Cu and Ag) can flow into the hot pores of the TiB_2 matrix, decreasing porosity and increasing the degree of connectivity of the metal braze throughout the bond thickness. More molten metal is contributed from the local heating of the substrates (AA3003), which allows for further pore filling. We fabricated tri-layer pressed pellets with thermite outer layers and a Ti:2B core, as depicted in Figure II.3.J.4(a) and have demonstrated the ability to produce joints with such tri-layers as shown in Figure II.3.J.4(b) and Figure II.3.J.4(c).

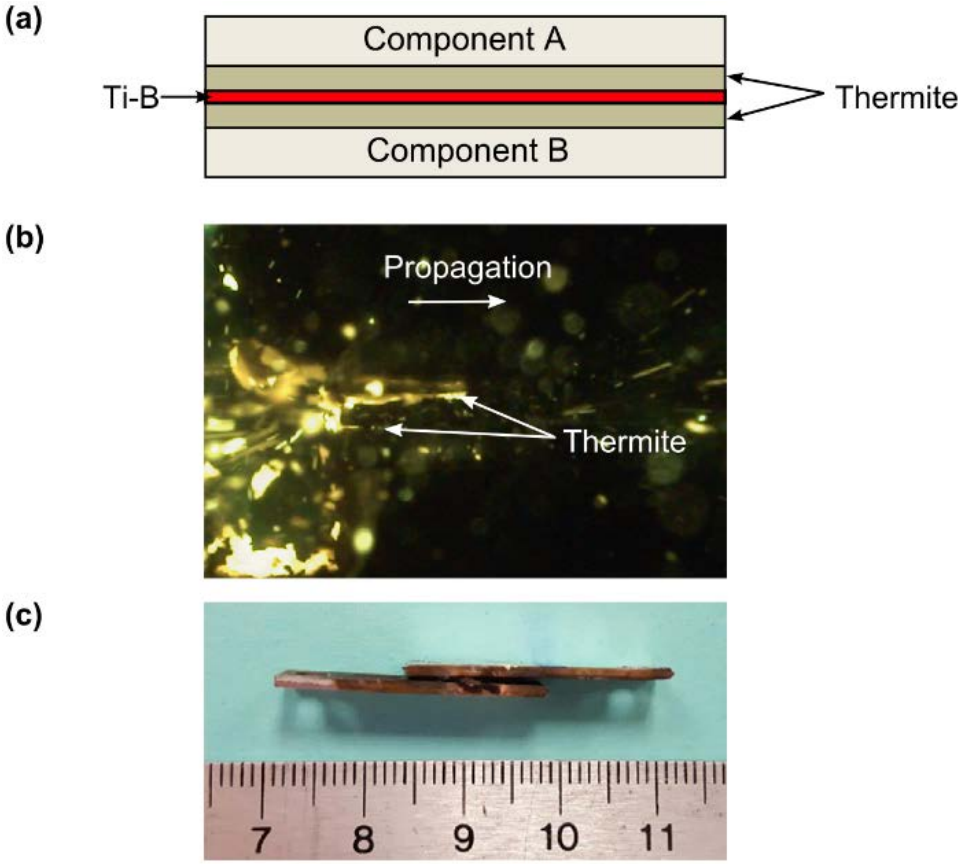

Figure II.3.J.4. (a) Schematic representation of bonding with a tri-layer pellet and (b) video of such a pellet propagating between two AA3003 substrates producing the joint shown in (c). Source: Johns Hopkins University.

Mass losses were observed for the Ti:2B BM powders that we fabricated. TGA scans of the elemental starting powders, as shown in Figure II.3.J.5, showed that the boron powder experiences a mass loss of nearly 8% within the first 150°C of heating. This mass loss is attributed to water vapor adsorbed to the boron surface as boron has well known hygroscopic properties. The release of this vapor upon reaction is in competition with the infiltration of molten metal into the porous TiB_2 structure as seen in the SEM image and the energy dispersive analysis x-ray (EDAX) image in Figure II.3.J.6. Therefore, it is advantageous to process the boron powder prior to being BM. The powders were annealed in an inert atmosphere to remove the adhered water, as well as packed into BM vials in an inert atmosphere to avoid the possibility of re-adsorption of water.

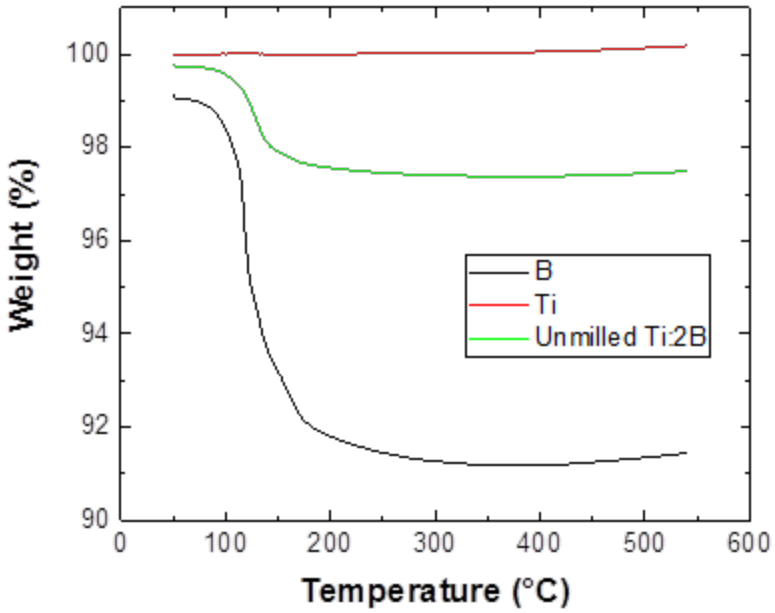

Figure II.3.J.5. TGA signals showing the mass loss associated with elemental starting powders comes solely from boron.

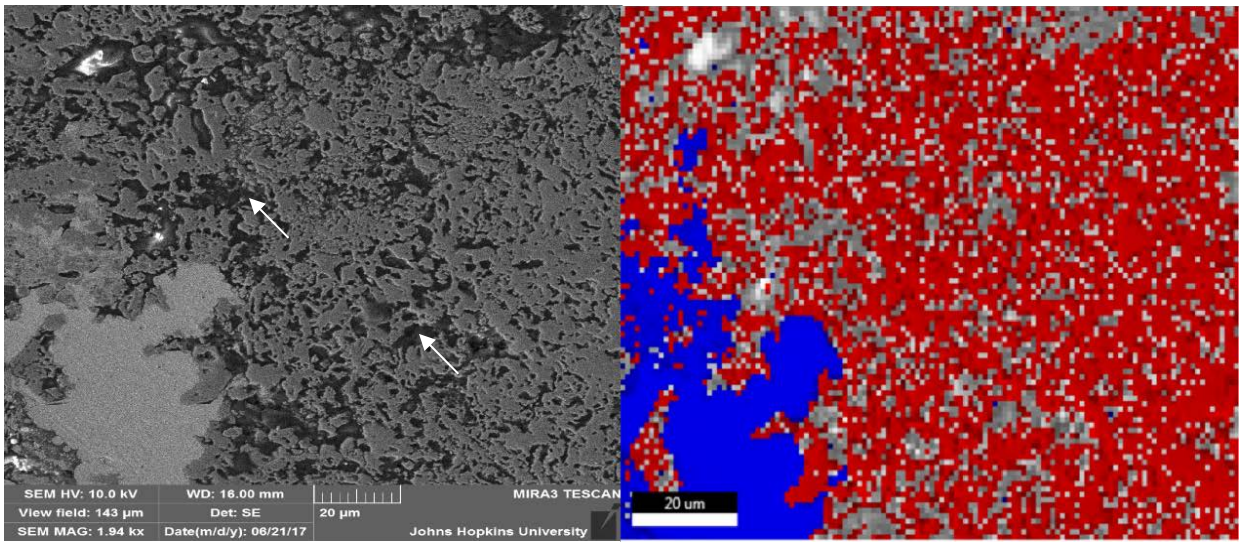

Figure II.3.J.6. (Left) SEM image of reacted Ti:2B/Al:Cu2O pellet. White arrows indicate porosity in TiB2. (Right) EDAX scan of area revealing TiB_2 region (red) and Cu region (blue). Source: Johns Hopkins University.

Bonding of Al and steel substrates was attempted using various combinations of thermite and Ti:2B powders. Bonding trials using annealed Cu_2O thermite have yielded low bonding strengths, as shown by the red dots in Figure II.3.J.7. This has been attributed to use of sub-optimal Ti:2B powder (i.e., over-milled or in need of further processing) leading to an inability to provide effective wetting of the substrate metal surface. The wide variation for the other points is attributed to the variation in TMD of the consolidated pellets. Additions of diluent metal in various stages of processing, annealing of boron powder to reduce vapor generation, and variation of the thickness and distribution of thermite and Ti:2B layers were investigated to improve bond strengths without success.

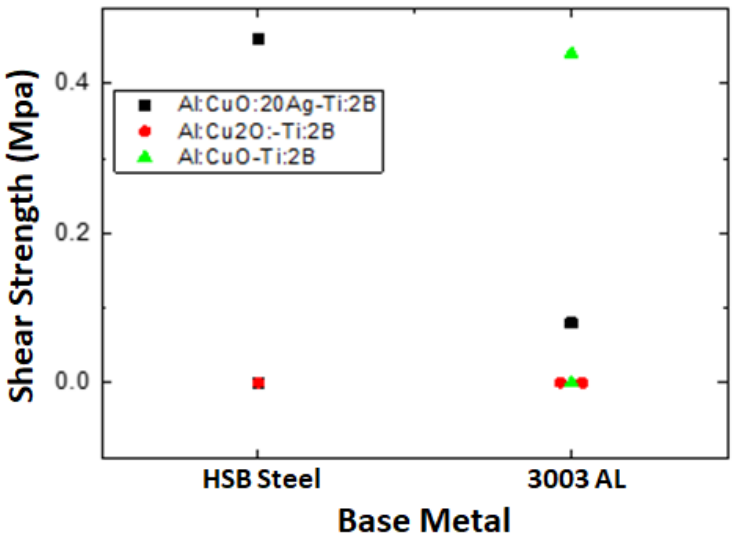

Figure II.3.J.7. Preliminary bonding results for various combinations of thermite and Ti:2B powders on high-strength boron steel and AA3003.

Investigation of Ti-C-Cu System

New Ti-C-Cu powders were synthesized using BM as an alternative to the Al:Cu2O:diluent thermite system. To understand the effect of braze dilution, we synthesized a Cu-rich 0.63CuTiC and a Cu-lean 0.44CuTiC composition. Table II.3.J.1 indicates the atomic percentages of the individual elements for each composition. For initial testing, we milled 60 g of powder with 1/4-in. stainless steel balls with a ball to powder mass ratio of three and milling time of 90 min using a Retsch Planetary Mill PM400.

Table II.3.J.1. Atomic Composition of the Milled Powders.

Composition	Ti at%.	C at%.	Cu at%.
0.63CuTiC	38	38	24
0.44CuTiC	41	41	18

To understand the effect of milling, we mounted the BM powders in epoxy and obtained back-scattered SEM images to determine the degree of incorporation of Ti and C into the Cu matrix as shown in Figure II.3.J.8. The contrast in the SEM images is due to the difference in the atomic number of the elements, heavier elements like copper are brighter when compared to Ti or C. The atomic number for carbon is significantly lower than that for both Cu and Ti; as a result, imaging C inclusions with the back-scattered detector is challenging. The SEM images show poor incorporation of Ti into the Cu matrix for both the compositions. Also, these images show that the milled powders are flake-like and elongated. We gauged the reactivity of the BM powders by heating them to 1400°C at 20°C/min using a simultaneous TGA and differential thermal analysis (DTA) system under argon. Figure II.3.J.9 depicts the typical heat flow versus temperature for the milled powders. Both the BM powders have poor heat release below 600°C, followed by a large heat flow spike. Though the net heat from the formation reaction is high, the poor low-temperature heat release is indicative of poorly milled powders. With better incorporation, we expect the sub-600°C heat release to improve significantly.

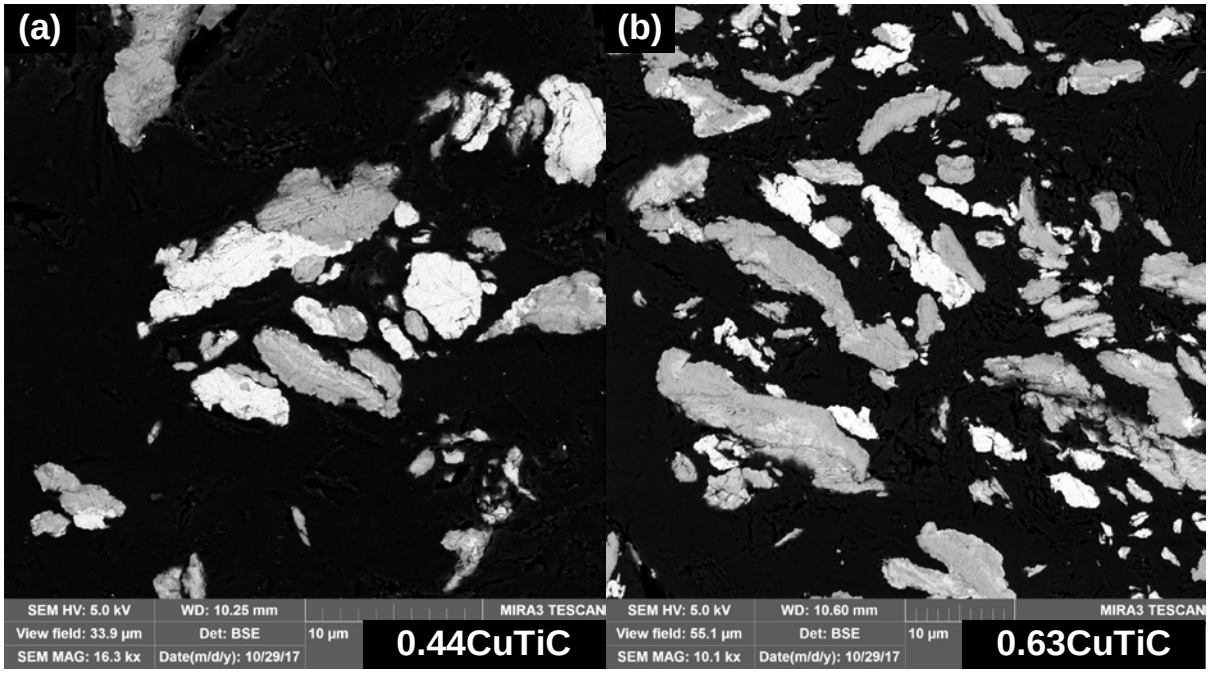

Figure II.3.J.8. Cross-sectional back scatter SEM images of (a) 0.44CuTiC and (b) 0.63CuTiC powders BM for 90 min. The dark (black) background is the epoxy, the grey particles are "Ti" and the higher atomic number "Cu" is depicted by the light grey particles. "C" with its low atomic number is hard to image and obtain a contrast of in SEM images. Source: Johns Hopkins University.

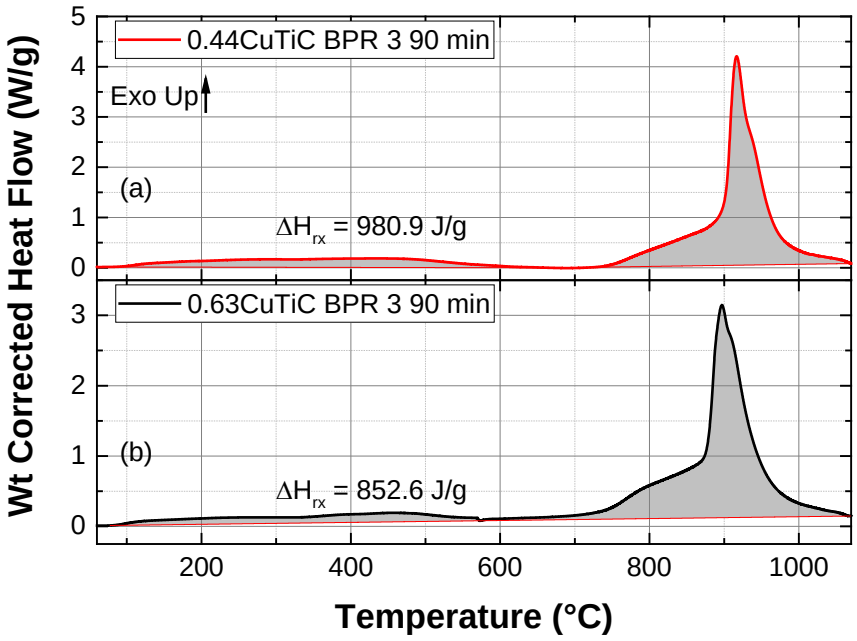

Figure II.3.J.9. DTA traces of (a) 0.44CuTiC and (b) 0.63CuTiC BM powders heated at 20°C/min up to 1400°C in Argon.

The Cu-rich 0.63CuTiC BM powders were pressed into 1/2 in. diameter by 1 mm pellets using a Carver press. With a maximum load value of 15,000 lb, we obtained pellets with an average TMD of 40%. These pellets have poor integrity and de-laminate with relative ease upon handling. However, the consolidated fragments ignite when initiated by an electrically heated coil. Figure II.3.J.10(a) through (c) show the ignition and propagation of the reaction front, while Figure II.3.J.10(d) depicts the long-time cooling of the fragment. Even

with a poorly incorporated composite, we observe powder compacts to be reactive. For the Ti-C-Cu system, the formation of Cu-Ti intermetallics is undesirable. We used x-ray diffraction to identify the composition of the reaction products that formed during low heating rate DTA experiments and faster heating during fragment ignition. The x-ray patterns show peaks for the TiC and Cu products from both modes of heating as shown in Figure II.3.J.11. Even with a poor incorporation of Ti/C in Cu, we observe the formation of TiC and not Cu-Ti intermetallics.

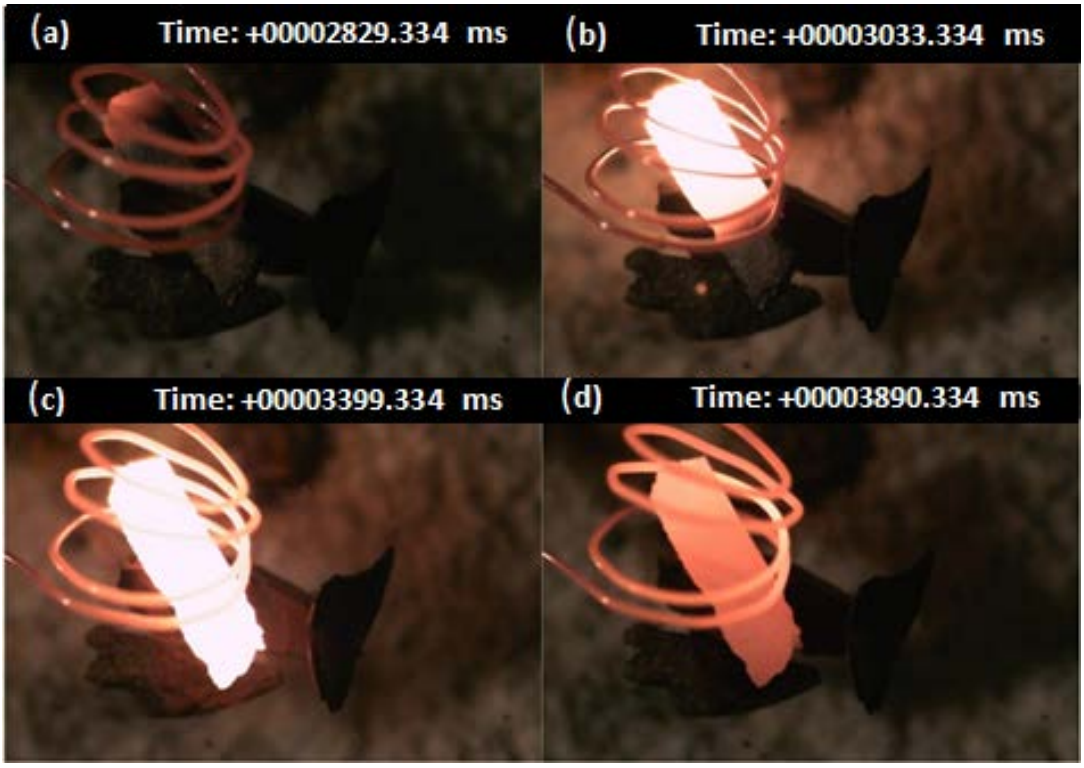

Figure II.3.J.10. Ignition and propagation of consolidated 0.63CuTiC fragment with a heated coil: (a) through (d) depict the propagation and cooling of the reactive braze. Source: Johns Hopkins University.

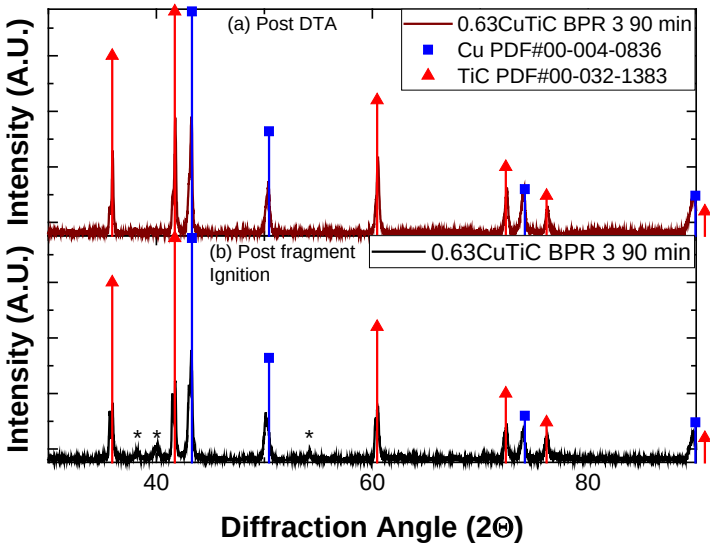

Figure II.3.J.11. X-ray diffraction scans showing peaks for the Cu and TiC products formed: (a) post DTA heating; and (b) post consolidated fragment ignition. Intensity is in arbitrary units.

Conclusions

To produce strong joints, the braze produced by propagating redox foils should have low porosity and mass ejection. Our efforts in FY 2017 focused on identifying the length scales present in the microstructure of BM and swaged Al:Cu2O:Cu system. The length scale ratio of thermite to diluent versus thermite length scale determines the degree of homogeneity in a given region of a BM foil. Large ratios correspond to smaller levels of dilution resulting in thermite-rich regions that are prone to produce hot spots that are the source for gas evolution and mass ejection. For different synthesized compositions, the volume fraction of these poorly mixed regions determines the degree of porosity in the bonds. FEM heat transfer simulations identified the critical thermite lengths and ratios that are required to suppress Cu gas formation. Using this insight, we determined that the thermite system with 40% dilution had fewer poorly mixed zones resulting in less porous bonds.

To overcome the gas evolution and enhance braze flow, we investigated the use of Ti:2B reactive scaffolds to provide a heated framework to improve bonding strengths. Early efforts focused on optimizing the milling parameters to obtain reactive Ti:2B composites. While optimizing the synthesis, we observed ~8% mass loss during TGA/DTA scans. We attributed the weight loss to the loss of adsorbed water on the surface of boron. This volatile mass enhances porosity and mass ejection during bonding, resulting in reduced mechanical strengths. Due to these powder processing hurdles, we decided to leverage the carbide formation reactions to melt the braze instead of a redox-reaction-based reactive braze. Our preliminary effort focused on synthesizing a Ti-C-Cu-based reactive braze wherein the TiC formation reaction results in melting the braze. Current efforts are underway to optimize the milling conditions and identify the braze volume fraction that will provide us with higher bond strengths than the previous systems.

Key Publications

Kinsey, A., K. A. Slusarski, K. Woll, and T. P. Weihs, 2017, “Gas suppression via Cu interlayers in magnetron sputtered Al:Cu2O multilayers,” presented at the European Materials Research Society Conference in Strasbourg, France, June 2017.

References

Duckham, A., S. J. Spey, J. Wang, M. E. Reiss, T. P. Weihs, E. Besnoin, and O. M. Knio, 2004, “Reactive nanostructured foil used as a heat source for joining titanium,” *J. Appl. Phys.*, Vol. 96, No. 4, Art. 2336.

Goldschmidt, H., 1903, Process of Joining Metal Pieces, US729573 A, June 2, 1903.

Kinsey, A. H., K. Slusarski, K. Woll, D. Gibbins, and T. P. Weihs, 2016, “Effect of dilution on reaction properties and bonds formed using mechanically processed dilute thermite foils,” *J. Mater. Sci.*, Vol. 51, No. 12, pp. 5738–5749.

Wang, J., E. Besnoin, A. Duckham, S. J., Spey, M. E. Reiss, O. M. Knio, and T. P. Weihs, 2004, “"Joining of stainless-steel specimens with nanostructured Al/Ni foils,” *J. Appl. Phys.*, Vol. 95, No. 1, pp. 248–256.

Wang, L. L., Z. A. Munir, and Y. M. Maximov, 1993, “Review thermite reactions: Their utilization in the synthesis and processing of materials,” *J. Mater. Sci.*, Vol. 28, pp. 3693–3708.

Weihs, T. P., 2014, Fabrication and Characterization of Multilayer Films and Foils, Metallic Films for Electronic, Optical and Magnetic Applications—Structure, Processing and Properties, pp. 160–243. https://doi.org/10.1533/9780857096296.1.160.

Woll, K., J. D. Gibbins, K. Slusarski, A. H. Kinsey, and T. P. Weihs, 2016, “The utilization of metal/metal oxide core-shell powders to enhance the reactivity of diluted thermite mixtures,” *Combust. Flame*, Vol. 167, pp. 259–267.

II.3.K High Strength Steel-Aluminum Components by Vaporizing Foil Actuator Welding (The Ohio State University)

Glenn Daehn, Co-Principal Investigator
Department of Materials Science and Engineering
The Ohio State University
141 Fontana Laboratory, 116 W. 19th Ave.
Columbus, OH 43210
Phone: 614-292-6779
E-mail: daehn.1@osu.edu

Anupam Vivek, Co-Principal Investigator
Department of Materials Science and Engineering
The Ohio State University
348 MacQuigg Labs, 105 W. Woodruff Ave.
Columbus, OH 43210
Phone: 608-332-4892
E-mail: vivek.4@osu.edu

Sarah Kleinbaum, Technology Manager
E-mail: sarah.kleinbaum@ee.doe.gov

Start Date: October 1, 2016 End Date: September 30, 2020
Total Project Cost: $2,750,000 DOE share: $2,475,000 Non-DOE share: $275,000

Executive Summary

The objective of this project is to develop the vaporizing foil actuator welding (VFAW) technology to near-commercial readiness by prototype scale integration of a multi-material component (henceforth, referred to as prototype component) that is 20% lighter than the incumbent all-steel design at a cost premium of three dollars per pound saved. This is accomplished by introducing Al extrusions, stampings and castings into the prototype component, which is currently an all-steel design. The dissimilar material joining aspect is executed with VFAW instead of the incumbent solutions such as self-piercing rivets, structural adhesives and FSW. Joints will be evaluated with static and dynamic mechanical testing, microstructural characterization as well as corrosion testing. VFAW, being an impact welding technique, maintains the solid state of the metals being welded and avoids or reduces the formation of brittle intermetallic compounds, which are identified through advanced microscopy. Welding parameters viz. impact angle, impact velocity and standoff gap, are designed with the help of validated numerical models capable of predicting the structure as well as the mechanical properties of the welded interface. The joint evaluation data helps CAE of the prototype component by the Tier 1 supplier, who also produces the subcomponents before assembly. The welding of dissimilar material subcomponents is conducted with a pedestal-style system built by an automotive equipment builder. The assembled prototype components are then subjected to all the mechanical and corrosion tests specified by the original equipment manufacturer. To assess process cycle times and manufacturing robustness, a robotic welding head is also implemented. The project aims to transition the technology to a state that can be adopted at a pilot plant or a research and development facility of a Tier 1 supplier.

The main goal of the FY 2017 work was to determine Al-steel material combinations that can be welded successfully and used in the design and build of the prototype component in the next budget period. This goal has been accomplished and three material combinations have been selected for further testing and design.

Accomplishments

- Screened Al-steel combinations relevant to chassis and body side components in FY 2017. These combinations were successfully welded.
- Selected four combinations for corrosion testing, extensive mechanical testing, and CAE of the prototype component in the next budget period.
- Welded 6 mm-thick Al flyer plates with input energies less than 12 kJ. Welded 3 mm-thick samples routinely with a low input energy of only 6 kJ.
- Achieved weld shear strengths that matches the interlayer material (i.e., 100 MPa). Welded coupons are able to sustain up to 20 kN of shear force prior to failure. In pry testing, the welded samples fail in the parent Al and not in the weld area.
- Successfully welded high-strength low-alloy (HSLA) 340 steel to Aural 2 Al without removing the galvanized coating. The weld had a failure load of 15 kN.
- Subjected welded samples with and without an adhesive sealant to 30 cycles of ASTM B-117 salt-spray testing. Greater than 80% of the initial strength was retained in the corroded samples.
- Built and tested pedestal-style welding system with automated feeding of the consumable foil, and contained it within an environmental chamber for noise suppression.
- Demonstrated the implementation of built-in standoff gaps through pre-forming and pre-machining of interlayers and target plates.
- Recorded the temporal evolution of the velocity of the flyer sheet and interlayer sheet using 4-channel photonic doppler velocimeter (PDV). Impact velocities in excess of 700 m/s were observed.
- Validated the process-to-structure numerical model with a coupled Lagrangian-Eulerian model that works with copper-titanium as well as Al-steel combinations. The wavy morphology and temperatures at the welded interface were predicted with this model.

Technology Assessment

- Target: Predict weld morphology and composition within 80% of experimental observation and use the model to design the optimal weld geometry.
- Gap: The high-strain rate constitutive data on the materials being used in this project are not available in open literature. Therefore, surrogate materials such as 4130 steels must be used. Even for such materials, the fidelity of the data may be low for the strain rates >105/sec experienced during impact welding.
- Gap: The process parameters used for modeling, impact angle, and impact velocity can be measured with high resolution with PDV; however, the first order variables in the process are input energy and foil shape, the interaction of which has not been modeled thus far and is outside the scope of this project.
- Target: Keep the thickness of the intermetallic compound (IMC) layer below 2 µm.
- Gap: From the numerical modeling work thus far, it has been shown that the temperature can rise above the melting point of Al due to plastic work and adiabatic heating at the impact weld interface in small pockets. IMC layers thicker than 2 µm can be seen intermittently distributed along the interface. However, the welds do perform quite well in mechanical testing. Therefore, the criteria for the tolerable IMC layer will have to be revised.
- Target: Meet or exceed the mechanical properties of the baseline prototype component.

- Gap: Most incumbent designs are steel-intensive and use traditional fusion welding techniques, such as spot- and arc-welding. With a multi-material design, only FSW has been used and the data on those welds is not publicly available. CAE of our prototype component will rely on coupon-scale testing, while benchmarking will be done against the existing data on fusion welds. Our simple target is that the sample, at coupon or prototype scales, fails in parent material during pry testing so that the designer can design based on geometry and the property of the base metal rather than the weld interface.
- Target: Create 1,000 welds without system stoppage.
- Gap: While the feeding of consumable foils has been implemented on the pedestal style welding system, the automatic removal of debris and maintaining clean electrode surfaces is yet to be resolved. Reduced foil and insulation material and different alloys for the electrode material will be tested to solve this issue.

Project Introduction

This project aims to address the challenge of effectively welding dissimilar materials—steel and Al for creating lightweight, multi-material automotive components. Traditional fusion-based welding between dissimilar combinations of Al and steel is difficult due to starkly disparate melting points and usually leads to the formation of brittle IMCs at the weld interface. Such joints are weak and cannot be implemented in crash-sensitive components. Structural adhesives and mechanical fasteners of various types including self-piercing rivets, flow drilled screws, friction element welds, and RIVTAC® are currently being utilized for addressing this issue. Solid-state welding techniques, like friction stir and impact welding, offer an elegant alternative solution for joining dissimilar metals without the use of a third body such as rivets. This project utilizes VFAW, an impact welding method developed at OSU (Vivek et al. 2013).

VFAW is driven by a thin, consumable dogbone-shaped Al foil, as shown in Figure II.3.K.1(a), about 100 µm-thick, which is replaced inexpensively after each welding cycle. The foil actuator is insulated with a polymer coating, but the ends are exposed for electrical connection to the output end of a capacitor bank. The foil actuator is constrained between the flyer sheet and a massive steel anvil, as shown in Figure II.3.K.1(b).

The target is set up parallel to the flyer at some fixed standoff distance apart using spacers. When the capacitor bank is discharged, a high-magnitude, short-duration pulse of electrical current passes through the foil and causes the foil to rapidly vaporize due to Joule heating, as shown in Figure II.3.K.1(c). This phenomenon, often referred to as electrically exploding foils, creates a high-pressure pulse that propels the flyer sheet to the necessary high speeds for impact welding. As the flyer advances, it bends around the standoff spacers and eventually collides with the target at an angle, which is necessary for weld creation. The impact angle and velocity are key parameters that determine the quality of the weld (El-Sobky 1983). The standoff gap can also be created by pre-forming a dimple in the target and/or the flyer. Between the two metals to be welded, typically the one with the lower areal density is chosen to be the flyer. Flyer sheet thickness typically ranges from 0.2–3 mm. Target plates can be as thick as needed because they are stationary during welding. Welds of different dimensions, as shown in Figure II.3.K.1(d), can be created with this method. This process has demonstrated much success in welding a wide range of alloys including Mg-Al, Al-Cu, Ti-Cu, bulk metallic glass-Cu and Ni-Ti. In this project, the focus is on welding specific grades of steel and Al that are relevant to automotive sub-frames and developing the technology to a level where it can be transitioned to an automotive supplier or an original equipment manufacturer. Besides the research on weldability of different material combinations and determining the ideal parameters through experiment and simulation, the project also includes design, production, and testing of a prototype sub-frame component. Robustness of the process for application in a serial production setting is demonstrated via robotic implementation.

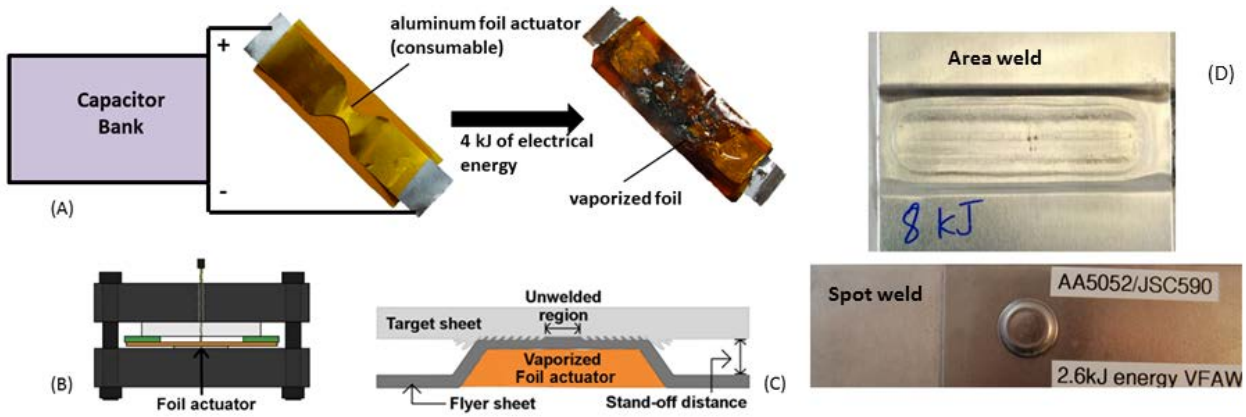

Figure II.3.K.1. Schematics of VFAW: (a) foil consumable, before and after being used; (b) typical welding assembly; (c) welding event; and (d) different weld geometries possible with various foil actuator shapes. Source: OSU Impulse Manufacturing Lab.

Work during FY 2017 focused on screening material combinations, validating a numerical model for the process-structure relationship, and developing a semi-automated pedestal style welding system that can be used for coupon as well as prototype production.

Approach

The main tasks of FY 2017 consisted of materials screening work conducted at OSU and the validation of a numerical model for the prediction of process and structure relationships performed via collaboration between OSU and PNNL. Additionally, the design of a pedestal-style VFAW machine was developed by OSU and Coldwater Machine Company; its fabrication was completed by Coldwater Machine Company. Collaborative tasks were accomplished by mutual visits and video conference calls throughout the year.

Material Screening

The material combinations selected for initial screenings are shown in Table II.3.K.1. Combinations 1-9 are applicable to the prototype component, while combinations 10-16 are primarily for body-side applications. The latter combinations were selected mainly as a risk mitigation strategy in case the thicker materials were not able to be welded successfully. Magna and Arconic provided the HSLA and 22MnB5 steels, 5xxx, 6xxx, and cast Al alloys. The thicknesses of the materials supplied were close to those mentioned in Table II.3.K.1.

Table II.3.K.1. Materials Selected for Initial Screening.

Combination Number	Steel	Thickness	Aluminum	Thickness
1	340Mpa yield HSLA sheet	2.5 mm	6061-T6 extrusion	3.5 mm
2	340Mpa yield HSLA sheet	2.5 mm	5754-0 sheet	4.6 mm
3	340Mpa yield HSLA sheet	2.5 mm	Aural 2 – T5 high-pressure coating	3.0 mm
4	340Mpa yield HSLA sheet	2.5 mm	A356-T6 low-pressure casting	5.0 mm
5	340Mpa yield HSLA sheet	2.5 mm	Crash-toughened Arconic 6xxx	3.0 mm
6	420Mpa yield HSLA sheet	2.5 mm	6061-T6 extrusion	3.5 mm
7	420Mpa yield HSLA sheet	2.5 mm	5754-0 sheet	4.6 mm
8	420Mpa yield HSLA sheet	2.5 mm	Aural 2 – T5 high-pressure casting	3.0 mm
9	420Mpa yield HSLA sheet	2.5 mm	A356-T6 low-pressure casting	5.0 mm
10	DP780 with 60G galvanizing	1.8 mm	6061-T6 extrusion	3.0 mm
11	DP780 with 60G galvanizing	1.8 mm	5182-0 sheet	2.0 mm
12	DP780 with 60G galvanizing	1.8 mm	Aural 2 –T5 high-pressure casting 3	3.0 mm
13	22MnB5 with AlSi coating	1.6 mm	6061-T6 extrusion	3.0 mm
14	22MnB5 with AlSi coating	1.6 mm	5182-0 sheet	2.0 mm
15	22MnB5 with AlSi coating	1.6 mm	Aural 2- T5 high-pressure casting	3.0 mm
16	22MnB5 with AlSi coating	1.6 mm	5052-0 sheet	2.0 mm

For the initial screening, small coupon welds were created using the bench top welding fixture and pry tested. If the combination passed the pry test (i.e., failure occurred in the parent material rather than the weld interface), then 40 mm x 125 mm coupons were welded together, and instrumented lap-shear testing was performed. The lap-shear tests were conducted on a MTS Systems Corporation 831.10 load frame at a crosshead speed of 0.1 mm/s.

To create tough welds between alloyed Al and steel, explosive welding companies utilize soft Al alloy sheets as interlayers. This method was also utilized here with VFAW, which requires a standoff gap between the three layers to be welded. The two standoff methods in this work were spacers placed between the sheets, referred to as Type 1, and pre-deformed targets and interlayers, referred to as Type 2. Samples of Type 1 were created with the method shown in Figure II.3.K.2. In this, sheets of G10 fiberglass composite were inserted between the layers to create a standoff. After welding, the G10 sheets were removed and the samples flattened before mechanical testing. Samples of Type 2 are created as shown in Figure II.3.K.3. In this method, the target and interlayer sheets are formed before the experiment to create the requisite air-gap in the stack-up. All samples

were created with an input energy level of less than 8 kJ from a 426 µF Maxwell Magneform™ capacitor bank that can be charged up to 8660 V to give a maximum output energy of 16 kJ. Current and discharge voltage histories were measured in each experiment with a 50 kA:1 V Rogowski coil and a 1000:1 voltage divider, respectively. These measurements were mainly used to check for characteristic discharge waveforms and diagnose any arcing that may result in an inefficient discharge.

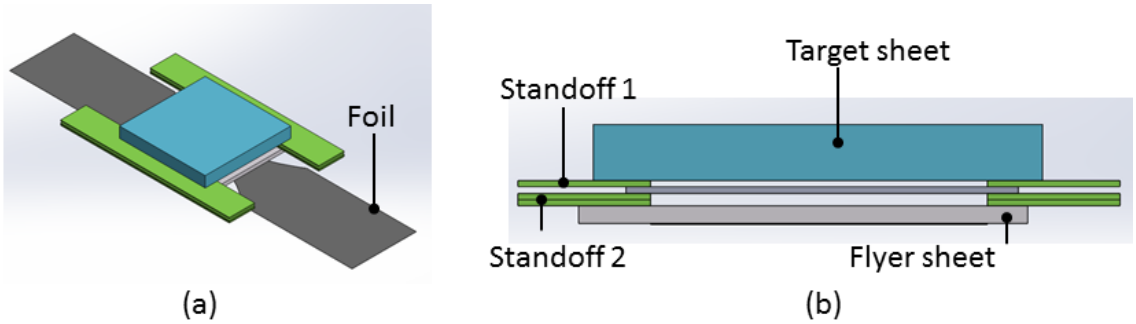

Figure II.3.K.2. Stack up procedure of Type 1 samples: (a) isometric view, (b) front view. Source: OSU.

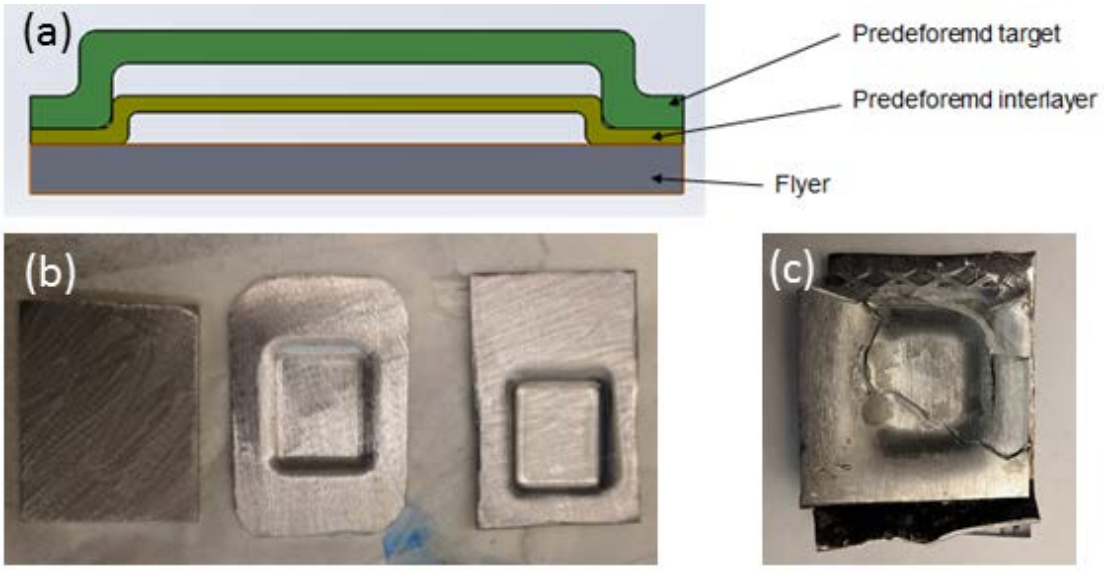

Figure II.3.K.3. Stack up procedure of Type 2 samples: (a) schematic of welding set up; (b) the flyer (left), pre-deformed interlayer (middle), and pre-deformed target (right); and (c) pry-tested weld coupon showing failure in Aural 2. Source: OSU.

All the material combinations were first tested with Type 1 samples. Welded samples of similar Al alloys were also created to assess the ideal lap-shear strength of the joint in the same geometry as the Al-steel joint, even if the test does not leave the weld nugget behind on the base metal. ASTM B117 corrosion testing for 32 days was also implemented on the following Type 1 samples (thickness):

- Aural 2 (2 mm)-HSLA 340 (2 mm)
- Aural 2 (2 mm)-HSLA 420 (2.5 mm)
- AA6061 (3.2 mm)-HSLA 340 (2 mm)
- Aural 2 (2 mm)-Aural 2 (2 mm)
- AA6061 (3.2 mm)-AA6061 (3.2 mm).

Weld samples created and tested in the Type 2 configuration (thickness) are:

- Aural 2 (3 mm)-HSLA 340 (2 mm)
- Aural 2 (3 mm)-HSLA 420 (2.5 mm).

These samples were also sectioned and observed under optical and electron microscopy to detect interfacial wave patterns and the formation of IMCs.

Model Validation

A dynamic thermo-mechanically coupled process-structure model for impact welding was developed. The large deformation and high-deformation rates in the impact welding process lead to severe mesh distortion issues in the purely Lagrangian approach, typically used in finite element method simulations. Therefore, to avoid such issues, an Eulerian framework is adopted to simulate the material flow in this process, as shown in Figure II.3.K.4. In the Lagrangian framework, the mesh is attached to the material points, so the mesh deforms as the material undergoes deformation. In an Eulerian analysis, the mesh acts as a background grid, which allows the material to deform (or flow) through the elements that do not deform. In this model, the Eulerian implementation is based on the volume-of-fluid method, in which the material is tracked by computing its volume fraction within each element. The constitutive response for each element is obtained by combining volume fraction data to create element averaged values. Eulerian elements can accommodate multi-materials as well as the void space.

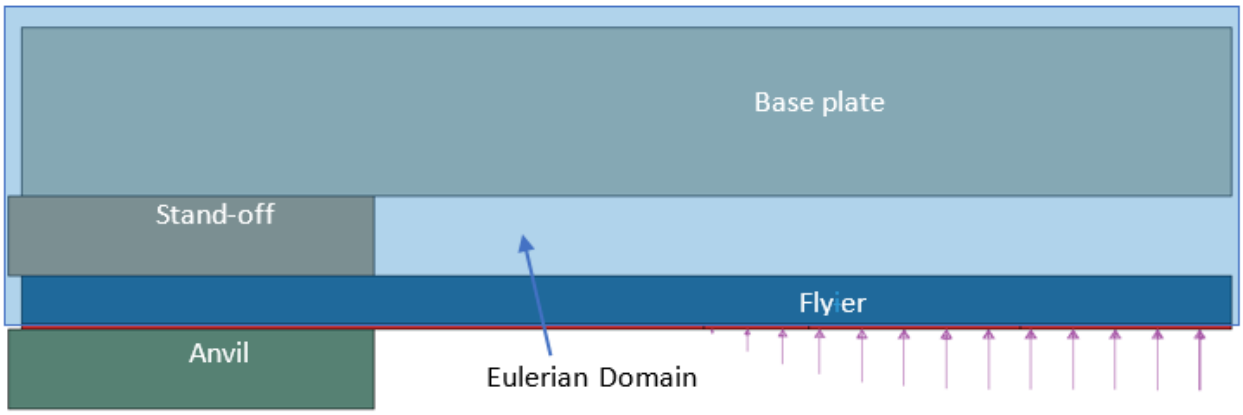

Figure II.3.K.4. Coupled Eulerian Lagrangian model set-up for the patch configuration weld between steel and Al. Source: PNNL.

For the validation of process-structure modeling framework, the impact welding is performed on the plates of two dissimilar materials—AA6061 and Steel 4130. These materials were selected based on resource availability and an extensive literature search such that the high temperature and high strain rate data for the two materials were available.

In terms of the input data for modeling purposes, the velocities at four different points along the length of the flyer are measured during the experiments using PDV (Strand et al. 2006). In the actual VFAW process, these velocities are the response of the flyer due to the pressure exerted on it by the expanding vapor. In the model, prescribing velocity (or displacement) at specific points of the flyer will constrain the deformation of the flyer leading to an unrealistic interface pattern. Most of the recent literature on modeling the impact welding process describe using a constant impact angle and prescribing terminal velocity profile to the flyer (Raoelison et al. 2016, Grignon et al. 2004). This approach is suitable for the weld set-ups resulting in a constant impact angle, like the ones involving grooved targets. However, it is to be noted that this kind of approach will not be able to capture the dynamic impact angle in the current weld set up resulting from the bending deformation of flyer. Therefore, it is important the model accurately captures the deformation and velocity response of the flyer

plate, at least, for the length of the weld. Due to the lack of any pressure measurements in the welding experiment, we adopted an inverse approach where the pressure profile on the flyer plate is predicted by a trial and error approach, such that the chosen pressure profile results in a velocity profile matching the velocities measured during experiments using PDV.

The pressure profile, applied on the flyer, was predicted by a trial and error approach. It is a combination of constant and cubic profiles for certain distances along the length. The experimentally measured velocity histories and the simulated output are plotted in Figure II.3.K.5. Attempts were not made to match the velocity data from Spot 4 because that would require temporal variation in the pressure profile, and moreover, it is not as important because the weld interface does not extend that far from the center.

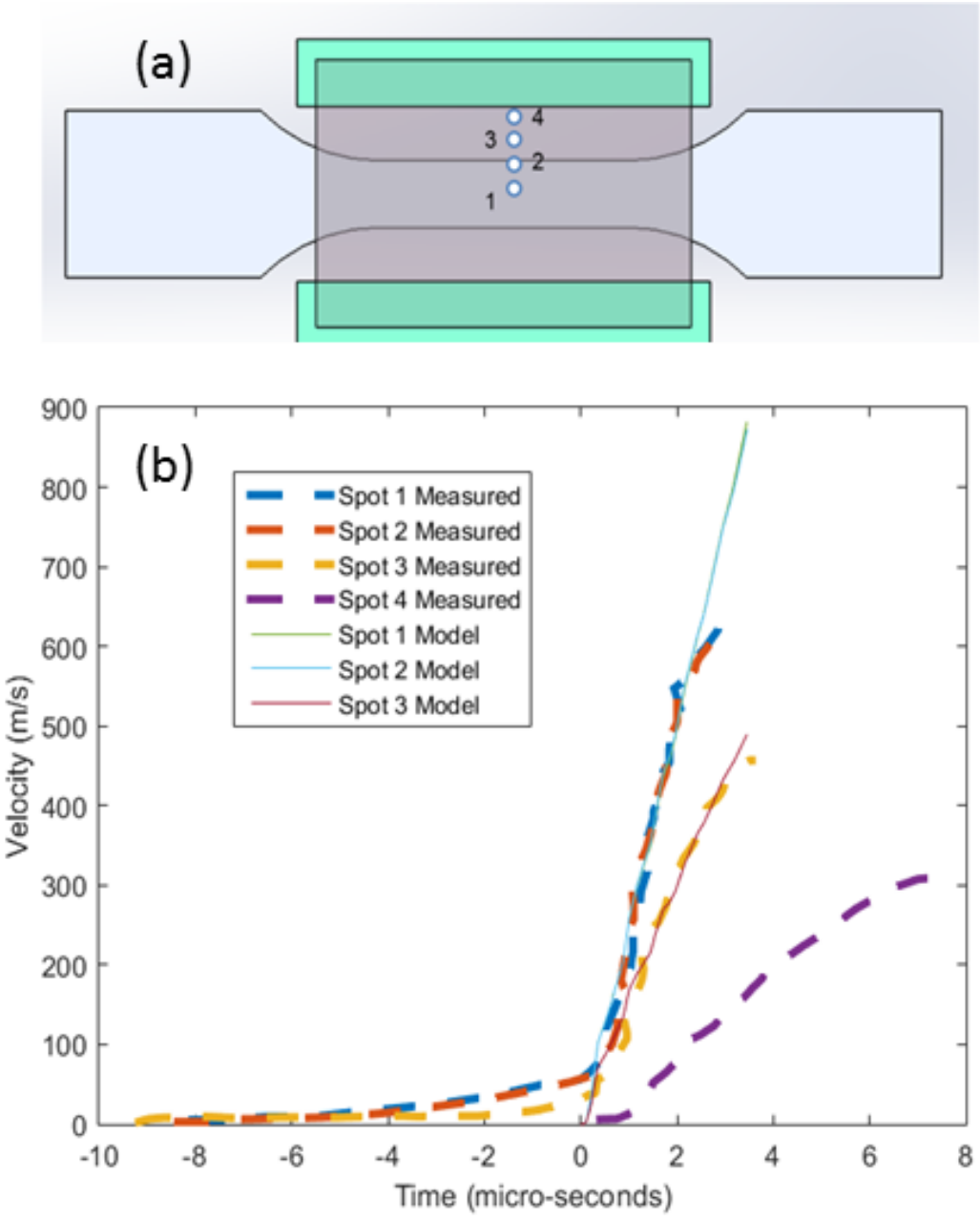

Figure II.3.K.5. PDV of different spots on the flyer sheet: (a) location of measured locations; and (b) measured and fitted PDV traces. Source: PNNL.

Standardization

While VFAW is an early-stage technology, from the beginning it has struggled with issues related to part-to-part reproducibility. It is postulated that this is due to dimensional imprecision in hand-location of foils, parts, and dies. Going forward, efforts will be made to utilize precise locating holes and dowel pins on all components for precise alignment. A typical, manual VFA fixture with location features is shown in Figure II.3.K.6. Standard foils will be mass produced by reproducible die-cutting to adapt to this fixture. It is planned that these will be made available to a broad community of research collaborators.

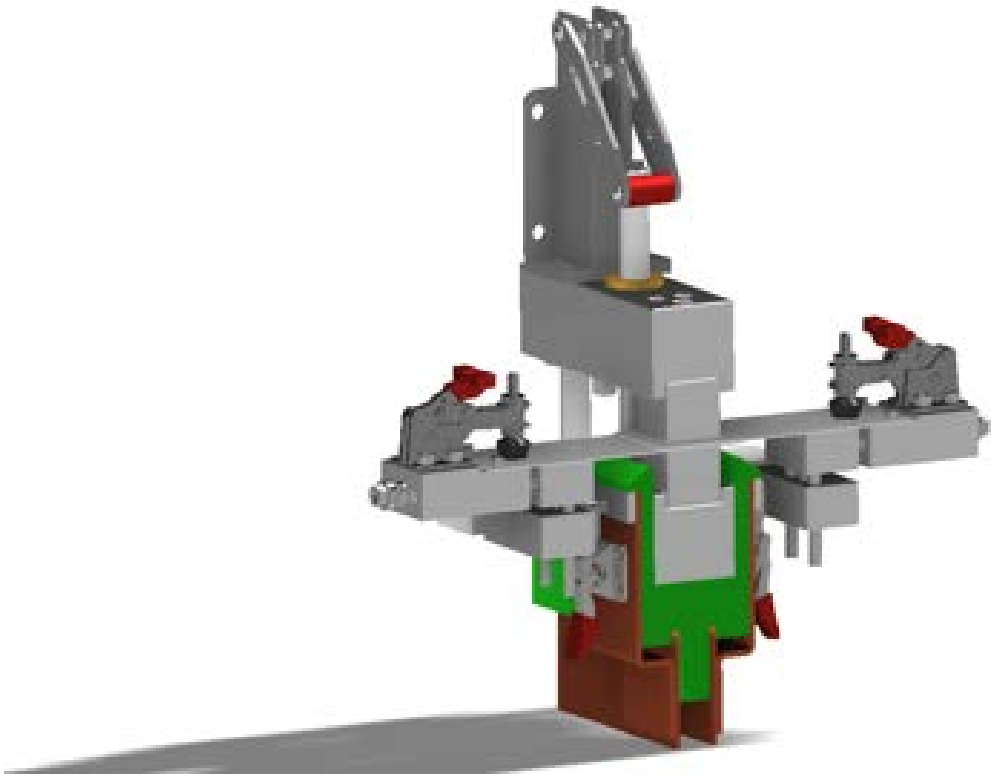

Figure II.3.K.6. VFA actuator head in development for precise, manual manufacturing operations. Source: OSU.

Equipment Availability

Both the AMP and MRI grants require equipment to be built. The MRI grant is optimized for data-gathering using PDV. The AMP grant will provide equipment to both Coldwater that can be used in customer evaluation and to Tri-Rivers Career Academy and their Robotics and Advanced Manufacturing Technology Education Collaborative center for training welding students. This equipment will harness the standard designs and provide beta-test equipment for further commercial deployment. The equipment will be designed for facile prototyping, as well as material weld testing and parameter development. Feedback from the Tri-Rivers Career Academy will be essential in evolving the designs to develop accepted equipment.

Validation

As equipment becomes more standard and available, more data on joining specific material pairs should become available as well. These data are expected to be available in commercial contexts and in published literature. This will assist in the validation of these methods. Efforts to develop formal standards and accepted parameters will be pursued through technical societies, including the International Impulse Forming Group (i2fg.org).

Training

As standard equipment and methods evolve, OSU will also actively develop training programs for both engineers and practitioners. The technical and organizational infrastructure of the partner Center for Design and Manufacturing Excellence (cdme.osu.edu) should represent an excellent organization from which to lead this effort.

Technology Transfer Path

The broad project team has a strong commitment to the difficult task of fully commercializing this technology and is leveraging the results from this grant with other grants and activities to transfer VFA-driven impact welding into a commercial application. The team understands traditional academic publications and presentations will not be sufficient to drive commercialization. Further, automotive manufacturing, with its need for low-cost and assured manufacturing and product reliability is possibly the most challenging technical sector in which to launch a new technology. To drive commercial acceptance for large scale manufacturing, the potential customers must feel confident about the cost, reliability, performance, availability, and adaptability of the technology. While all indicators are that these aspects can be developed, a base of user-experience likely must first exist in higher-value, lower-volume applications.

Leveraging this grant with other sponsored work, the team is attacking the key problems in advancing and diffusing the technology. These have been defined as: Standardization, Equipment Availability, Validation, and Training. Two other grants are leveraged heavily in this regard—a State of Ohio Advanced Manufacturing Program (AMP) grant, which is designed to drive commercialization, and a National Science Foundation Major Research Instrumentation (MRI) award. The activities and strategy that will drive the diffusion of the technology forward are briefly described under the following four pillars.

Results

Only the combinations that passed pry testing by showing parent metal failure, as shown in Figure II.3.K.7, were candidates for instrumented lap-shear testing and corrosion testing with Type 1 or Type 2 configuration samples. A summary of the material screening tests is provided in Table II.3.K.2.

Figure II.3.K.7. AA6061-HSLA 340 weld with AA3003 interlayer showing parent material (AA6061) failure during pry testing. Source: OSU.

Table II.3.K.2. Screening Tests Summary.

Material Combination	Pry testing result (Failure mode)	Type 1 pre-corrosion lap testing done?	Type 1 post corrosion lap testing done?	Type 2 pre-corrosion lap testing done?
AA6061-HSLA 340	Parent	✓	✓	✓
AA5754-HSLA 340	Interface	×	×	×
Aural 2- HSLA 340	Parent	✓	✓	✓
A356- HSLA 340	Parent	×	×	×
6061-HSLA 420	Interface/Parent	×	×	×
5754- HSLA 420	Interface	×	×	×
Aural2- HSLA 420	Parent	✓	✓	×
A356- HSLA 420	Interface	×	×	×

Various failure modes observed in mechanically tested pre-corrosion Type 1 samples are depicted in Figure II.3.K.8. One sample of a similar weld of AA6061 failed in mode (a). All AA6061-DP340 welds failed in mode (b). One Aural 2-DP340 sample failed in mode (c). All the other welds of Aural 2-DP340, Aural 2-DP420, and the similar weld of Aural 2 failed in mode (d). When visible, the image of the fractured weld surface was utilized to estimate the welded area, and with that the strengths of welds of various combinations. The shear strength of the AA6061-HSLA 340 weld was estimated as 57 MPa, that of Aural 2-HSLA 340 weld was 97 MPa, and that of Aural 2-HSLA 420 was 96 MPa. Attaining weld strengths as close to the shear strength of the interlayer AA3003 material, 83 MPa, is ideal. To assess the ideal weld strength here, the comparisons were made with failure loads of similar material weld combinations, and those comparisons are reflected in Figure II.3.K.9.

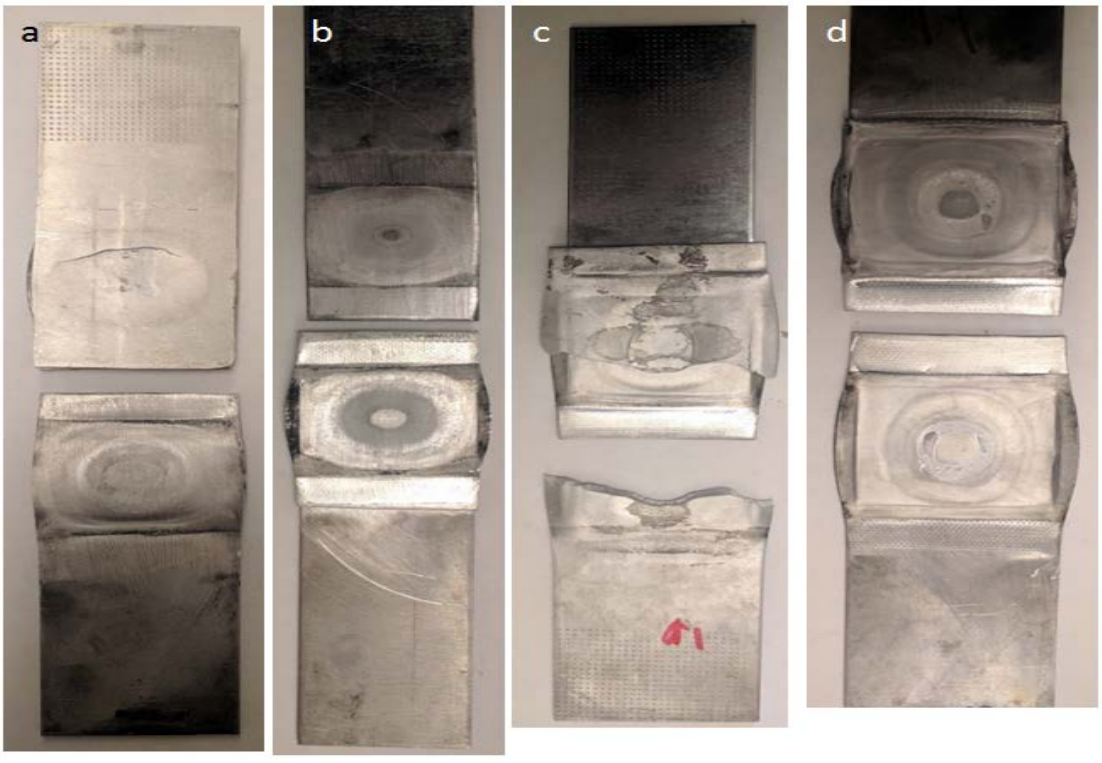

Figure II.3.K.8. Failure modes of the samples: (a) flyer cracking; (b) target peeled off from interlayer; (c) flyer failure; and (d) interlayer sheared. Source: OSU.

Figure II.3.K.9 also illustrates the results of instrumented lap-shear testing of Type 1 samples after corrosion. All material combinations had a pre-corrosion failure load of 70% or more as compared to those of similar material welds. Furthermore, the threshold of retaining 80% of pre-corrosion strength in the corroded samples was cleared in each case, even without the use of an adhesive. Figure II.3.K.10 shows an Aural 2-HSLA 340 sample corroded and mechanically tested. Parent material failure at 12 kN was observed.

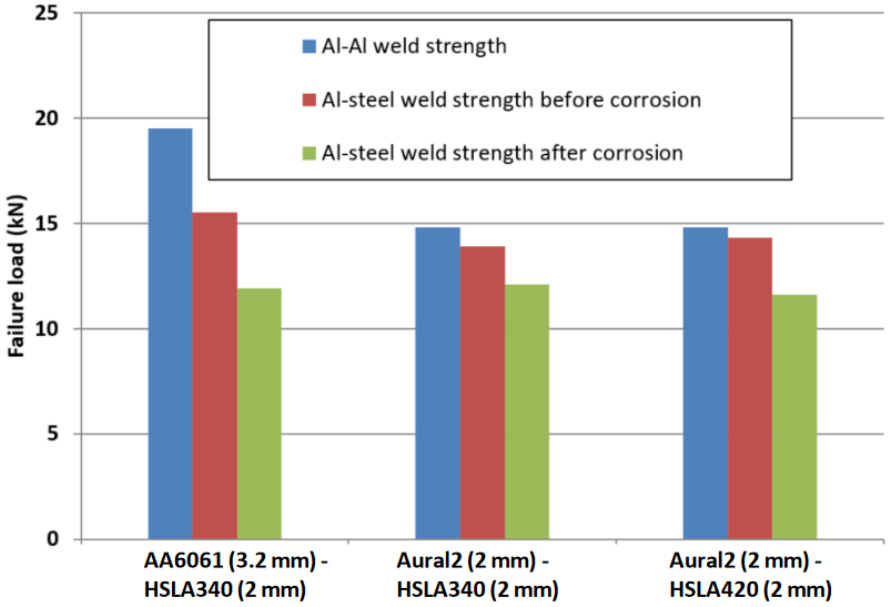

Figure II.3.K.9. Lap shear testing results of Type 1 samples before and after corrosion. Source: OSU.

Figure II.3.K.10. Result of a lap shear test on an Aural 2-HSLA 340 welded and corroded sample. Source: OSU.

The stacking procedure for Type 1 samples is rather cumbersome with manual placement and removal of standoff inserts and flattening of welded samples. Besides the issue of reproducibility, such a procedure will be difficult to implement in serial production. However, Type 2 samples used pre-formed dimples in the target, as well as the interlayer sheets, which are self-aligning and can be formed within the subcomponent flanges during stamping or casting process prior to assembly. Figure II.3.K.11 shows the results of lap-shear testing of welds created with 3 mm thick Aural 2 flyer sheets and uncoated HSLA 340, uncoated HSLA 420, and galvanized HSLA 340 target sheets. This is the first time coated steel has been successfully welded with cast Al using VFAW. It should be noted that the Aural 2 material used with the Type 2 samples was thicker than that used in the Type 1 samples reported earlier due to material availability. Figure II.3.K.11(a) shows a tested sample. The failure was in the interlayer material and the weld strength was estimated to be 95 MPa based on the failure load and welded area.

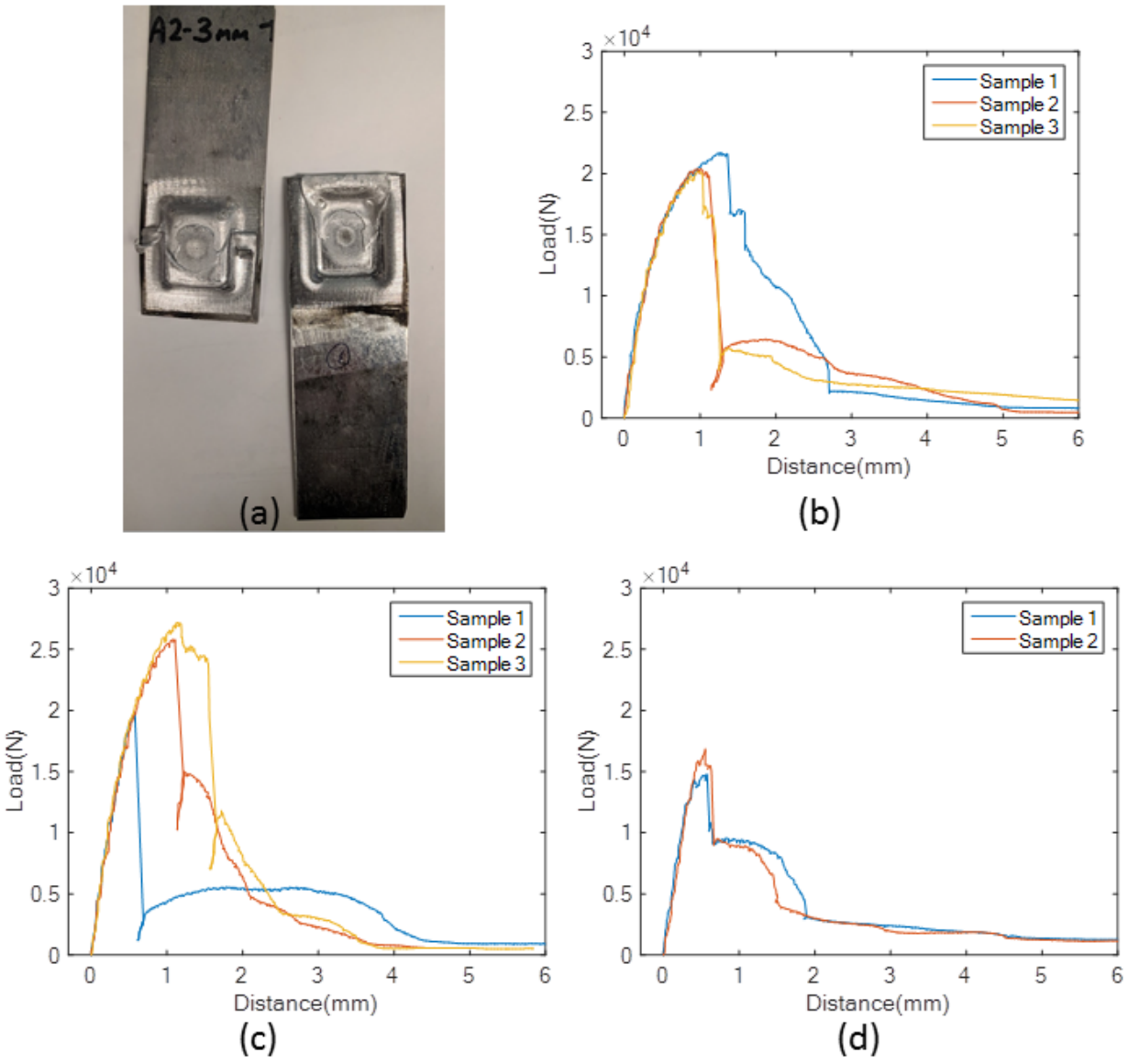

Figure II.3.K.11. Mechanical test results from Type 2 samples: (a) Aural 2-HSLA 420 tested sample; (b) load-displacement plot for Aural 2-HSLA 340; (c) Aural 2-HSLA 420; and (d) Aural 2-galvannized HSLA 340. Source: OSU.

We have also started the characterization of the welded interface to detect the formation of IMC and investigate the changes in the microstructure in the weld zone. Figure II.3.K.12 illustrates the hierarchical microstructure of Aural 2-HSLA 340 welds made with and without the coating removed prior to welding. In both cases, the Aural 2-AA3003 interface showed a wavy pattern. The Al-steel interface contained an intermittent layer of IMC in the weld made with uncoated material, whereas the coated material showed mostly an IMC-free interface, although the zinc coating remained in most parts of the interface. This is probably the reason why the welds made with coated HSLA material had slightly lower strength, as the zinc coating has a lower shear strength than the interlayer AA3003 material, indicating that the shearing likely happened in the zinc itself during testing.

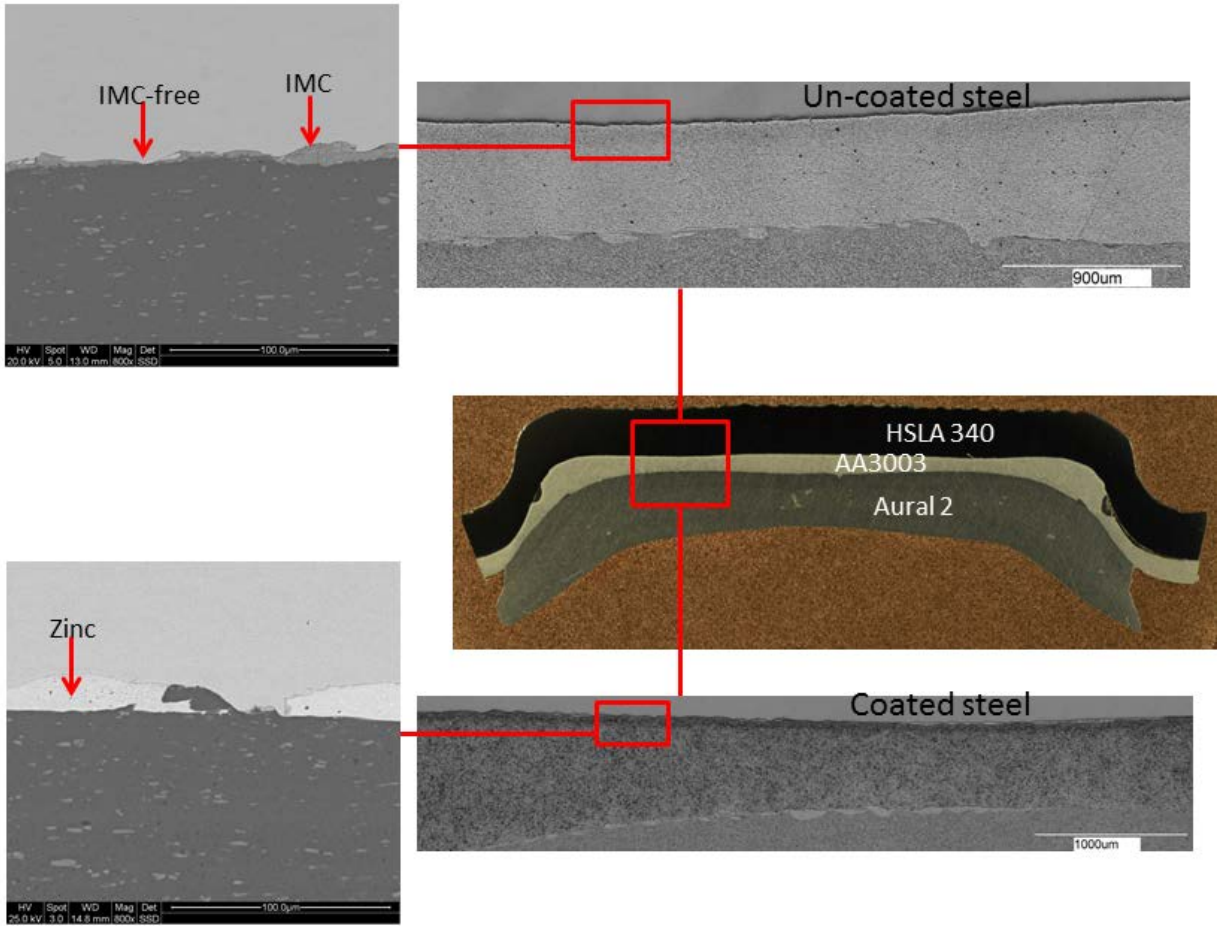

Figure II.3.K.12. Hierarchical microstructure of the Aural 2-interlayer-HSLA 340 weld interface. Source: OSU.

Model Validation

Figure II.3.K.13 shows the simulation results for the flyer deformation indicating the weld interface structure. It shows some jetting in front of the collision front, but no distinct interfacial waves are observed. This agrees with the micrograph of the weld-cross-section obtained experimentally, as shown in Figure II.3.K.14.

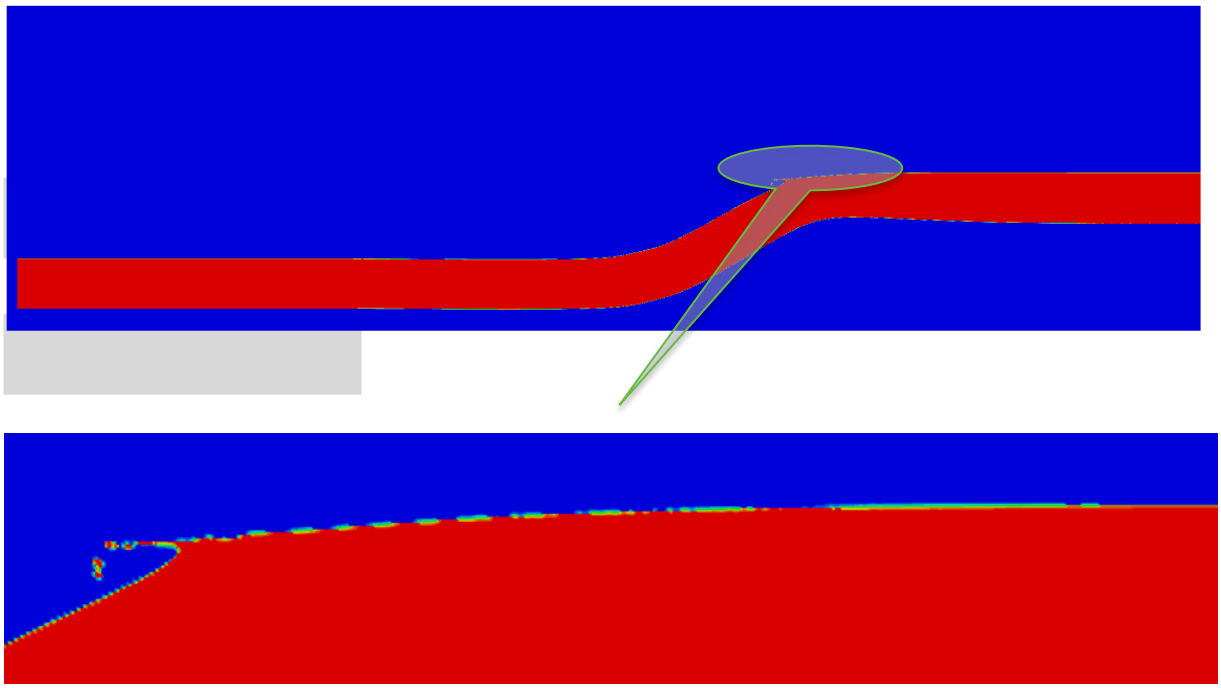

Figure II.3.K.13. Deformation of the flyer and interfacial structure. The contour plot represents the volume fraction of the flyer material (Al 6061-T6). Source: PNNL.

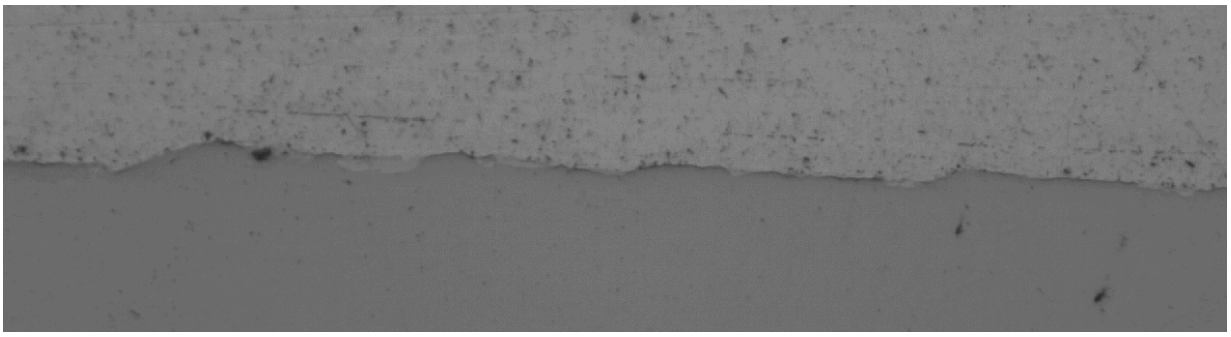

Figure II.3.K.14. Weld cross-section obtained between AA6061 and Steel 4130. Source: OSU.

To further validate the fidelity of the developed process-structure model, the coupled Eulerian-Lagrangian model was applied to a different material system consisting of Cu 110 and commercially pure Ti, for which the experimental results were already available (Vivek et al. 2014). Figure II.3.K.15 shows the schematic of the system that was used to conduct the experiments. The grooved target allows for obtaining a constant impact angle (β) of 20° between the flyer and the target. The flyer travels at a prescribed velocity (V_p). Translational motion in the x direction (u_x) and rotational motion in the y and z directions (θ_y and θ_z, respectively) are fixed to define the boundary conditions.

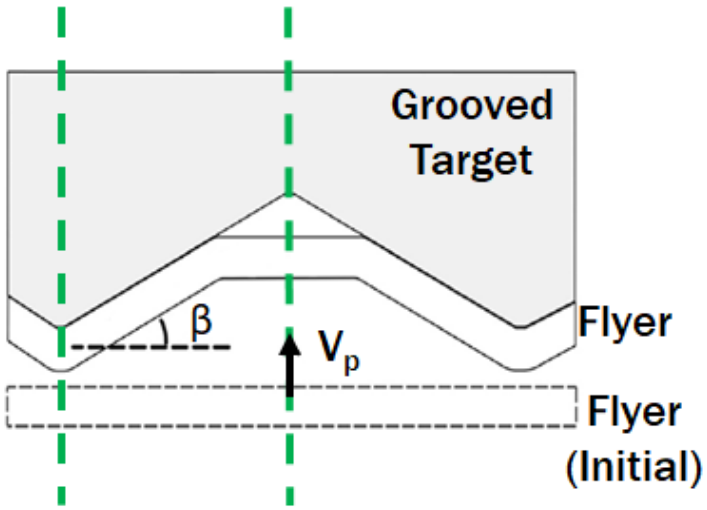

(a)

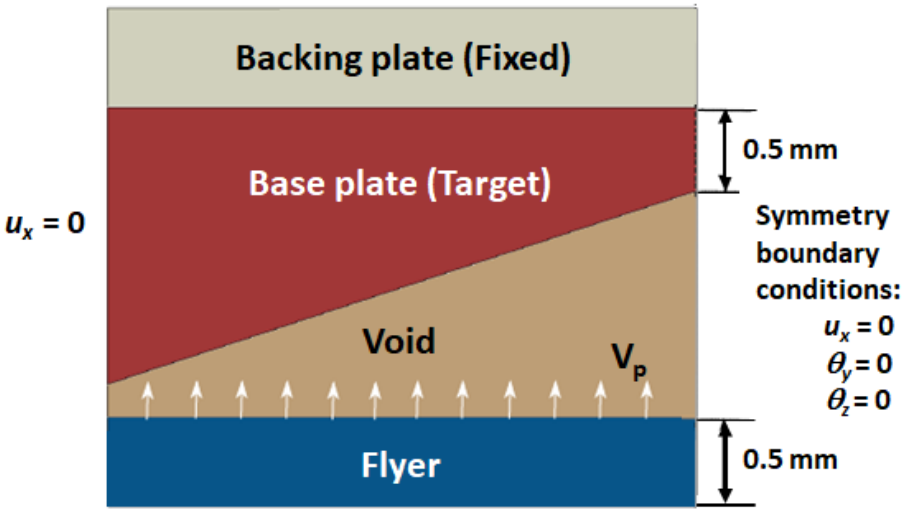

(b)

Figure II.3.K.15. Schematic of the impact welding system with (a) grooved target; and (b) the corresponding model set-up. Source: PNNL.

Figure II.3.K.16 shows the simulation results alongside the experimentally obtained micrographs for welds between Cu 110 and Ti for different impact velocities. As is evident from this figure, there is good quantitative agreement between the numerical simulations and experiments in terms of interfacial morphology. The numerical simulations were also performed using an AA6061 flyer and the steel 4130 target in the same configuration. Figure II.3.K.17 shows the predicted interfacial morphology with much shallower waves as compared to the Cu-Ti system. It is noted here that the impact angle in this groove configuration stays constant at 20°, whereas a dynamic impact angle exists for the flat-flat configuration shown previously in Figure II.3.K.2. In the flat-flat configuration, the impact angle is 0° in the center and increases as the weld progresses away from the center towards the ends. This could be another reason why the interfacial waves are not easily seen in the AA6061-steel 4130 weld.

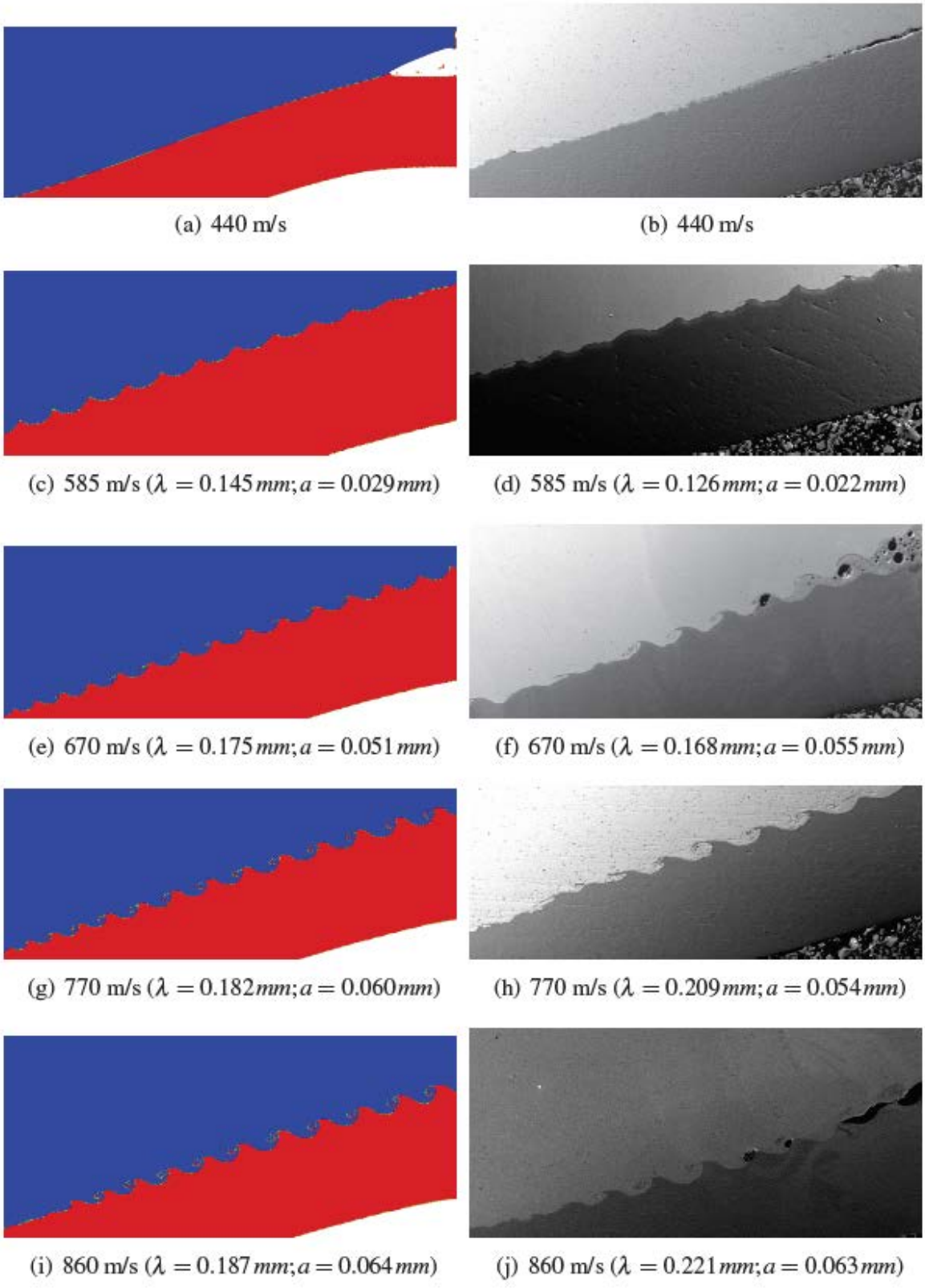

Figure II.3.K.16. Weld interface for Ti-Cu welds. Note that the simulation and experimental images are not at the same scale. λ is the wavelength and *a* is the amplitude of the waves. Source: PNNL.

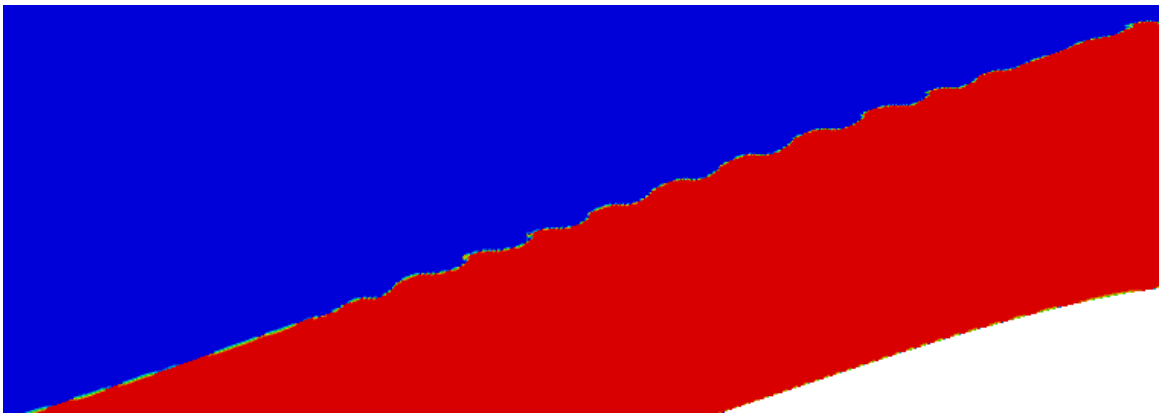

Figure II.3.K.17. Weld interface obtained for steel 4130-AA6061 welds in groove configuration with constant impact angle. Source: PNNL.

In the experiments, the structural Al and steel do not result in strong and repeatable welds in a flat-flat patch weld configuration. Therefore, a softer Al alloy interlayer is used to help produce robust joints. Therefore, the validated process-structure model will now be used to simulate the Al-steel weld using an interlayer. The preliminary simulation results for the set-up with interlayer is shown in Figure II.3.K.18. Going forward, a new set-up for the interlayer system is proposed in which the dimples in the target and interlayer are made such that the angle of impact is kept constant.

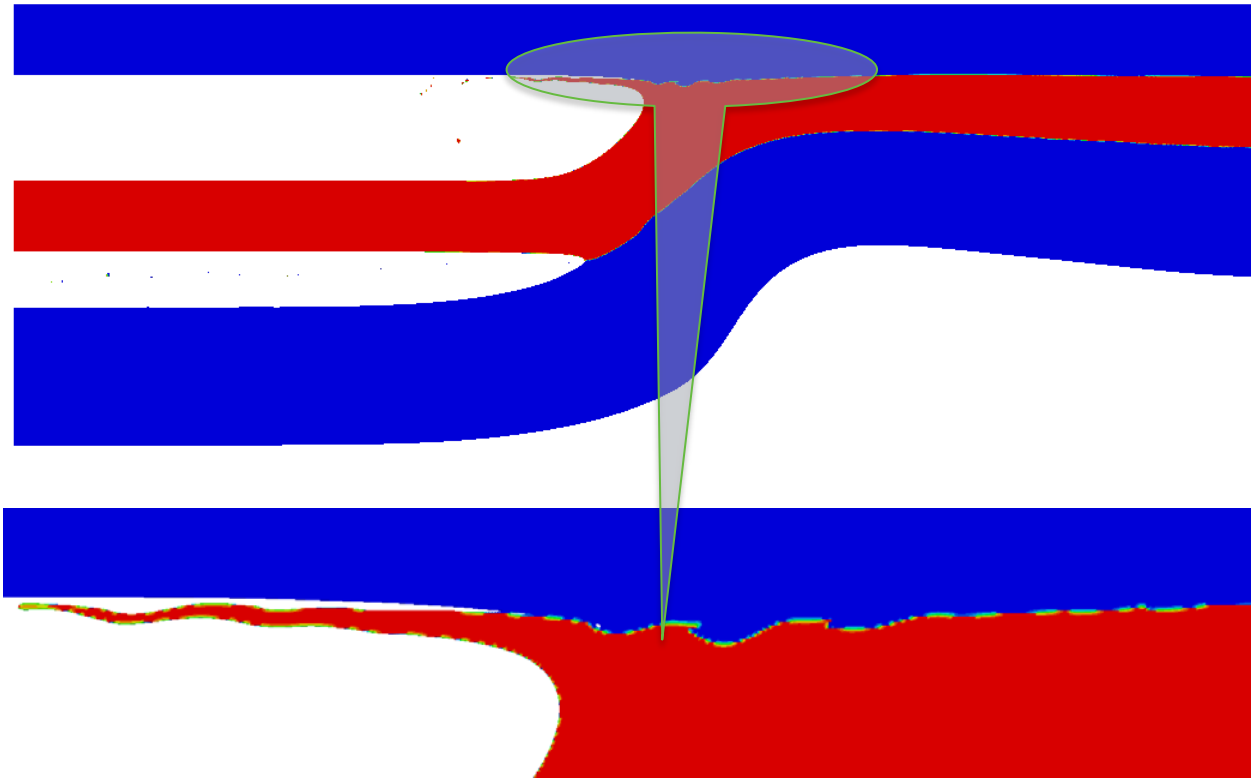

Figure II.3.K.18. Simulation results for the impact between Al and steel with a softer Al interlayer. Source: PNNL.

Welding System Development

In association with Coldwater Machine Company, a pedestal style VFAW coupon machine, as well as prototype scale welding, was developed. It will have the capability to feed the foil actuator automatically into the weld area where the plates to be welded will be positioned with alignment fixtures. Sound suppression is provided by a composite chamber built around the welder. An image of the machine in its enclosure and the human-machine interface is shown in Figure II.3.K.19. Test welds, which were made between AA3003 and DP 590 steel, were strong enough to result in base metal failure during pry testing.

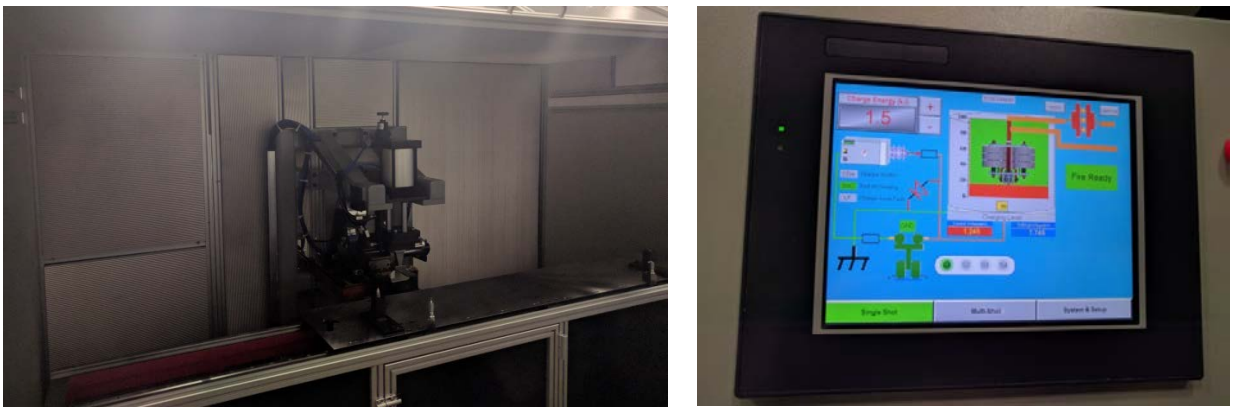

Figure II.3.K.19. Pedestal welding machine. The welder and fixture table (left) and human-machine interface (right). Source: OSU.

Conclusions

During FY 2017, the focus of the project was to screen for VFAW weldability of Al/steel combinations recommended by industry for potential application in a multi-material front subframe. Three material pairs, namely cast Al grade Aural 2/HSLA 340, Aural 2/HSLA 420, and wrought Al grade AA6061/HSLA 340, passed the screening criteria. The criteria include: (1) failure in parent material rather than weld interface during pry test, (2) greater than 70% joint efficiency and (3) retaining greater than 80% of the pre-corrosion mechanical strength in welded samples put through a standard salt-spray corrosion cycle. In each case, an interlayer of AA3003 was utilized, which resulted in tough welds. It was shown that impact welding of relatively thick (>3 mm) Al sheets to HSLA steels can be successfully implemented with input energy levels below 8 kJ.

A method for maintaining a standoff gap between the various layers of the weld stack up by preforming the target and interlayer sheets was developed and tested. This obviates the need for standoff inserts and makes the process more feasible for serial production. Process reproducibility needs to be improved by reducing reliance on manual alignment of foils and workpieces. The pedestal-style VFAW machine, which feeds foils automatically and has built-in fixture plates, will help reduce shot-to-shot variance. Welding through a galvanized coating is also possible with this method, although the coating did not get fully removed during the welding process through jetting. Therefore, the welds made with coated HSLA steels had a lower shear strength than the ones made with uncoated material. Furthermore, while VFAW is a solid-state process, a small amount of melting due to adiabatic heating resulting from severe plastic deformation may occur. This resulted in intermittent regions along the interface that contained brittle IMCs.

Besides the material screening work, high resolution diagnostics including measurement of flyer velocity with multi-channel PDV was also performed. The data from such measurements were fed into a dynamic thermo-mechanically coupled process-structure model, which simulated the generation of the impact welded interfaces. The model was validated for a flat AA6061/4130 steel interface and wavy Cu/Ti interfaces. The verified model is being adapted for triple-layer welds being developed in this project and will help improve the design approach to obtain ideal weld geometries, which presently is empirical to a large extent.

References

El-Sobky, H., 1983, "Mechanics of explosive welding," In: *Explosive Welding, Forming and Compaction*, pp. 189-217. Springer Netherlands.

Grignon, F., D. Benson, K. S. Vecchio, and M. A. Meyers, 2004, "Explosive welding of aluminum to aluminum: Analysis, computations and experiments," *International Journal of Impact Engineering*, Vol. 30, No. 10, pp. 1333–1351.

Raoelison, R. N., T. Sapanathan, E. Padayodi, N. Buiron, and M. Rachik, 2016, "Interfacial kinematics and governing mechanisms under the influence of high strain rate impact conditions: Numerical computations of experimental observations," *Journal of the Mechanics and Physics of Solids*, Vol. 96, pp. 147–161.

Strand, O. T., D. R. Goosman, C. Martinez, T. L. Whitworth, and W. W. Kuhlow, 2006, "Compact system for high-speed velocimetry using heterodyne techniques," *Review of Scientific Instruments*, Vol. 77, No. 8, Art. 083108.

Vivek, A., B. C. Liu, S. R. Hansen, and G. S. Daehn, 2014, "Accessing collision welding process window for titanium/copper welds with vaporizing foil actuators and grooved targets," *Journal of Materials Processing Technology*, Vol. 214, No. 8, pp. 1583–1589.

Vivek, A., S. R. Hansen, B. C. Liu, and G. S. Daehn, 2013, "Vaporizing foil actuator: A tool for collision welding," *Journal of Materials Processing Technology*, Vol. 213, No. 12, pp. 2304–2311.

II.4 Crosscutting

II.4.A Assessment of NTHSA's Updated Analysis of the Relationship between Fatality Risk, Mass, and Footprint in Model Year 2003-2010 Light-Duty Vehicles (Lawrence Berkeley National Laboratory)

Tom Wenzel, Principal Investigator
Environmental Technologies Area
Lawrence Berkeley National Laboratory
90R2000, 1 Cyclotron Rd.
Berkeley, CA 94720
Phone: 510-486-5753
E-mail: TPWenzel@lbl.gov

Carol Schutte, Technology Manager
E-mail: carol.schutte@ee.doe.gov

Start Date: March 1, 2010 End Date: September 30, 2017
Total Project Cost: $2,126,500 DOE share: $2,126,500 Non-DOE share: $0

Executive Summary

Using data for model year 2003 to 2010 light-duty vehicles from 2005 to 2011, Lawrence Berkeley National Laboratory (LBNL) completed an updated Phase 2 analysis of the relationship between vehicle weight, size (e.g., footprint or wheelbase times track width), and the two components of societal fatality risk per vehicle miles of travel (VMT): crash frequency (crashes per VMT) and crashworthiness/crash compatibility (fatality or casualty risk per crash). The analysis uses police-reported crash data from the 13 states that provide vehicle identification numbers; because of the relatively small number of fatalities in these 13 states, the analysis looks at both societal fatality and casualty (fatality plus severe injury) risk. The results of the current analysis are comparable to those from the 2012 LBNL Phase 2 analysis: 1) mass reduction is associated with increased crash frequency in all five vehicle types; 2) mass reduction is associated with decreases in both societal fatality and casualty risk per crash in all vehicle types; 3) footprint reduction is associated with an increase in crash frequency only for light trucks, and does not have a statistically-significant effect on fatality risk per crash, but an increase in casualty risk per crash for cars; and 4) the estimated effects for the 13-state fatality risk per VMT are similar to the effects the National Highway Traffic Safety Administration (NHTSA) estimated for U.S. fatality risk per VMT, with mass reduction associated with increases in fatality risk per VMT in cars, and decreases in light trucks and crossover utility vehicles (CUVs)/minivans, in both the U.S. and the 13-state analyses.

It is unclear why the 2012 and 2017 Phase 2 analyses both found that lower vehicle mass is associated with higher crash frequency, but lower risk per crash, and why some of the other control variables are statistically significant or have an unexpected positive or negative effect. Adding five control variables, both individually and together, to account for differences in vehicle design and driver behavior does not change the general result of mass reduction being associated with an increase in crash frequency. These results suggest that other, more subtle, differences in vehicles and their drivers may account for the unexpected finding that lighter vehicles have higher crash frequencies than heavier vehicles. And re-running the regression models including only severe crashes, to control for crash severity, does not change the sign on estimated coefficients for some of the control variables in the crash frequency or risk per crash regressions to the expected direction. We therefore conclude that not accounting for crash severity in the baseline model is not the reason why many control variables have unexpected associations with crash frequency or risk per crash.

We continued to develop a model to estimate the effect of mass reduction over time on the number of fatalities in two-vehicle crashes, as recommended by the 2015 National Academy of Sciences (NAS) committee report (NAS 2015). A preliminary analysis indicates that the relationship is u-shaped; that societal fatality risk increases as mass disparity, expressed either as the difference in the mass of the two vehicles or as the case vehicle mass as a percentage of the combined mass of the two vehicles, increases. A simulation of the effect of this relationship on mass disparity, and fatalities, over time suggests that, after an initial increase in fatalities, overall fatalities decline and result in a net decrease in fatalities over the long term.

NHTSA provided the updated public database for model year 2004 to 2011 vehicles from 2006 to 2012, which is to be used to update the Phase 1 analysis for consideration in the Final Determination/Final Rule in 2018, in September 2017 (over 6 months late). LBNL will use the updated database to update its Phase 1 analysis in FY 2018.

Accomplishments

- Participated in monthly discussions by the interagency working group (e.g., DOE, NHTSA, Environmental Protection Agency [EPA], and California Air Resources Board [CARB]) on updating the research on the relationship between vehicle weight/size and safety, in support of federal agency rulemakings on fuel economy/greenhouse gas emission standards for new light-duty vehicles.
- Completed an analysis of the relationship between mass and footprint reduction and the two components of fatality risk per VMT: (1) crashes per VMT (crash frequency) and (2) fatality risk once a crash has occurred (crashworthiness). This Phase 2 analysis involves analysis of police-reported crash data from 13 states.
- Continued developing a model to simulate the effect over time of mass reduction from the standards on the mass difference between two vehicles involved in a crash, and the resulting estimated change in societal fatalities. Began incorporating NHTSA comments on the methodology used in the model.

Project Introduction

Reducing vehicle mass is perhaps the easiest and least-costly method to reduce fuel consumption and greenhouse gas emissions from light-duty vehicles. However, the extent to which government regulations should encourage manufacturers to reduce vehicle mass depends on what effect, if any, lightweight vehicles are expected to have on societal safety. As part of an interagency analysis effort between NHTSA, EPA, and DOE, LBNL has been examining the relationship between vehicle mass and size and United States societal fatality and casualty risk, using historical data on recent vehicle designs. This research effort informs the agencies on the extent to which vehicle mass can be reduced to meet fuel economy and greenhouse gas emissions standards, without compromising the safety of road users.

In FY 2017 LBNL completed its updated Phase 2 analysis of the two components of risk per VMT (crash frequency and risk per crash) and continued analyzing the effect of mass reduction scenarios on the mass disparity of vehicles involved in two-vehicle crashes and the resulting fatalities. These analyses are described below.

Approach

Phase 2 Analysis of Two Components of Societal Fatality Risk per VMT

In its Phase 2 analysis, LBNL examined the relationship between vehicle weight, size (e.g., footprint, or wheelbase times track width), and the two components of societal fatality risk per VMT: (1) crash frequency (crashes per VMT); and (2) crashworthiness/crash compatibility (fatality or casualty risk per crash). For the updated Phase 2 study, LBNL used police-reported crash data from 13 states for model year 2003 to 2010 vehicles between 2005 and 2011. For the crash frequency regressions, induced exposure cases were derived from the non-culpable vehicle in a two-vehicle crash, taken from police-reported crash records from 13 states.

The induced exposure cases were then weighted by the number of vehicle registrations and average annual mileage by vehicle age and make/model, developed by NHTSA in their 2016 analysis, so that the models estimate the effect of changes in the control variables on the number of police-reported crashes per VMT. For the crashworthiness/crash compatibility (societal fatality/casualty risk per crash) regressions, analyses were run for both fatal crashes and crashes involving at least one severe injury (casualties), because of the relatively small number of fatalities in the 13 states.

In both sets of analysis, LBNL followed the methodology of the baseline regression model in 2016 NHTSA report (Puckett and Kindelberger 2016). Separate logistic regression models were run for each of three vehicle types (e.g., passenger cars, comprised of two- and four-door models; light trucks, comprised of pickup trucks and truck-based sport utility vehicles [SUVs]; and car-based CUVs and minivans), and for each of nine crash types, for a total of 27 regressions. Crashes with another light-duty vehicle were categorized into four types based on the type and weight of the crash partner: a car, CUV, or minivan lighter or heavier than average (3,157 lb), and a pickup or truck-based SUV lighter or heavier than average (4,303 lb). Because all of the fatalities/casualties in the crash were used, the crashworthiness risks reflect societal risk, rather than just the risk to the occupants of the case vehicle. As in the NHTSA's 2016 analysis, records where the case vehicle was one of three types of cars (models used as sports cars, police cars, and models with all-wheel drive [AWD]) or a full-size passenger or cargo van were excluded from both the crash frequency and crashworthiness regression analyses.

For cars and trucks, two variables (e.g., UNDRWT00 and OVERWT00) were used for vehicle weight, allowing the relationship between mass and risk to vary for lighter and heavier cars and trucks. The determination of the two weight classes was based on the median weight for each vehicle type: 3,197 lb for cars and 4,947 lb for light-duty trucks. Because there are fewer CUVs and minivans in the database, a single variable, LBS100, was used for CUV/minivan weight. Control variables were included for vehicle types (two-door cars, SUVs, HD pickups, minivans), vehicle technologies (AWD, antilock braking system [ABS], electronic stability control [ESC], two methods to make light trucks more crash-compatible with cars), eight variables for driver age and gender, crash circumstances (whether the crash occurred in a rural county, at night, on a high-speed road, or in a high-fatality state), vehicle age, and CY.

A single weighted average of the coefficients from the regression models was run for each of the nine crash types, based on the expected distribution of fatalities after 2012 when all vehicles were required to have ESC installed. The assumptions used for this adjustment were taken from an updated NHTSA study that found that ESC reduced fatal rollovers by 60% in cars and 74% in light trucks; fixed-object impacts by 31% in cars and 45% in light trucks; and other non-pedestrian crashes by 7% in cars and by 6% in light trucks (Kahane 2014). The "post-ESC" distribution of fatalities by crash type was multiplied by the regression coefficients for each crash type to create the weighted average effect of each variable on risk.

LBNL ran five sets of regression models, examining the effect of mass or footprint reduction on the frequency of police-reported crashes per VMT, societal fatality risk and casualty risk per crash, and societal fatality risk and casualty risk per VMT.

Effect of Mass Reduction Scenarios on Vehicle Masses in Two-vehicle Crashes and Fatalities over Time

The 2015 NAS committee on light-duty fuel economy recommended that NHTSA estimate the effect mass reduction scenarios have on annual fatalities as the fleet transitions to a lighter fleet, with a narrower distribution of weights and a smaller difference in the masses of two vehicles involved in two-vehicle crashes (NAS 2015). LBNL first estimated the relationship between the difference in the mass of the case vehicle with that of its crash partner, rather than just the mass of the case vehicle, for four types of crashes (with a heavier or lighter car, or with a heavier or lighter light truck) for each of the three types of case vehicles. LBNL then simulated the change in mass of the case vehicle and its crash partner over a 27-year period. The mass of the case vehicle was decreased to simulate mass reductions undertaken by manufacturers to comply with the fuel

economy/greenhouse gas emission standards, while the mass of its crash partner was changed in each simulation year based on the historical change in average vehicle mass. Finally, LBNL simulated the change in societal fatalities over time, by applying the estimated relationship between the differences in vehicle masses to each two-vehicle crash in the 2016 NHTSA public database, after adjusting the mass of each vehicle over a 27-year period. The simulation indicates that large reductions in vehicle mass, on the order of those recommended by the NAS 2015 committee report, will lead to an initial increase in fatalities in two-vehicle crashes, but no change after nine years, and a relatively large decrease in fatalities after 27 years. Based on this simulation, we conclude that mass reduction targeted toward heavier vehicles (i.e., light trucks, CUVs, and minivans) will not lead to increases in fatalities in two-vehicle crashes over the long term.

In FY 2017, NHTSA provided comments on this preliminary analysis, and recommended several changes. NHTSA pointed out that the NHTSA baseline method, which LBNL adopted, compares the mass of the case vehicle with that of its crash partner in the induced exposure database; however, the crash partner is the at-fault vehicle in the induced exposure crash, and may not be representative of all vehicle/driver combinations on the road at any given time, and may therefore bias the regression estimates. NHTSA recommended using the mass of another randomly selected case vehicle for the crash partner, as was done in Section 6 of NHTSA's 2003 analysis.

Results

Phase 2 Analysis of Two Components of Societal Fatality Risk per VMT

Figure II.4.A.1 compares the estimated effect of mass and footprint reduction on the two components of risk—the number of crashes per VMT (e.g., crash frequency, which is shown in orange) and the fatality risk per crash (e.g., crashworthiness/compatibility, which is shown in light red)—with the estimated effect on fatality risk per VMT (shown in dark red) from the 13-state crash data. For all five vehicle types, mass reduction is associated with an increase in crash frequency (shown in orange), but with a decrease in fatality risk per crash (shown in light red); the effects from the two components roughly add together to result in the overall estimated effect on fatality risk per VMT (shown in dark red).

For cars and light trucks, mass reduction is associated with larger increases in crash frequency as the mass of the case vehicle increases (i.e., mass reduction in heavier-than-average cars and light trucks is associated with a larger increase in crash frequency than mass reduction in lighter-than-average cars and light trucks). For cars, mass reduction is associated with an increase in crash frequency, a decrease in risk per crash, and an increase in risk per VMT, as car mass increases. For light trucks and CUVs/minivans, mass reduction is associated with progressively larger increases in crash frequency, which are offset by progressively larger decreases in fatality risk per crash, resulting in relatively small reductions in fatality risk per VMT. Figure II.4.A.1 indicates that a smaller footprint in light trucks is associated with a large increase in crash frequency and a small increase in fatality risk per crash, while smaller footprint in cars and CUVs/minivans is associated with decreases in crash frequency, essentially no change in fatality risk per crash for cars, and a relatively large increase in fatality risk per crash for CUVs/minivans. Figure II.4.A.2 shows similar estimates for the two components of casualty risk per VMT; the estimates for crash frequency (orange columns) in Figure II.4.A.2 are identical to those in Figure II.4.A.1.

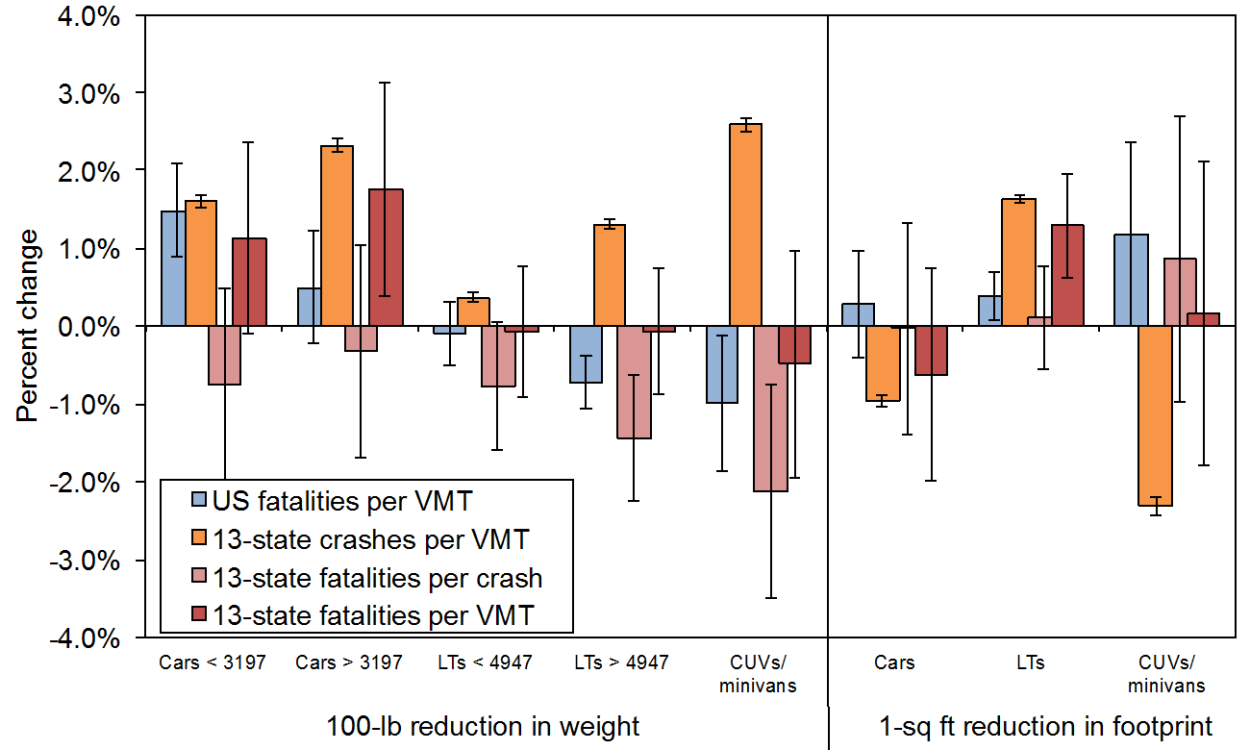

Figure II.4.A.1. Estimated effect of mass or footprint reduction on crashes per VMT (vehicle crash frequency), fatalities per crash (vehicle crashworthiness/compatibility), and fatalities per VMT, by vehicle type. Source: LBNL.

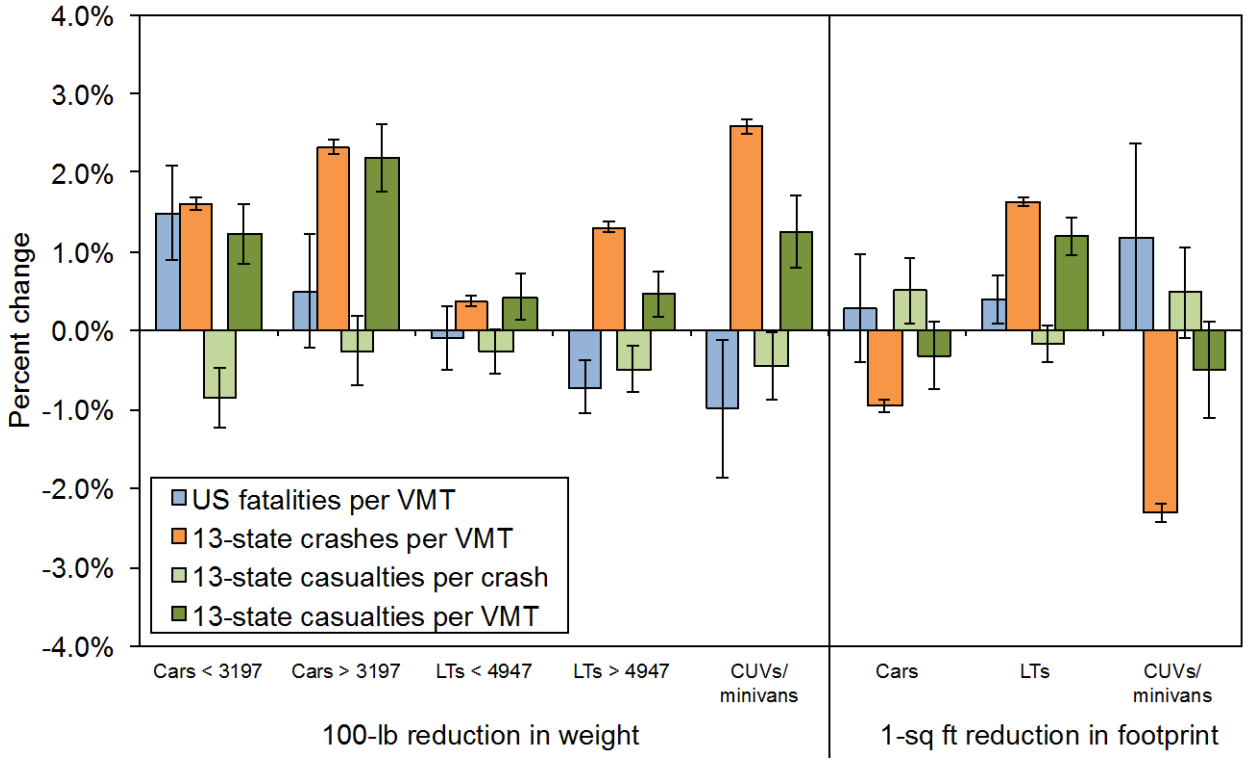

Figure II.4.A.2. Estimated effect of mass or footprint reduction on crashes per VMT (vehicle crash frequency), casualties per crash (vehicle crashworthiness/compatibility), and casualties per VMT, by vehicle type. Source: LBNL.

Casualty risks per crash are comparable to fatality risks per crash for cars, whereas casualty risks per crash are substantially lower than fatality risks per crash for light trucks and CUVs/minivans.

The results from the current analysis show the same general trends as the 2012 analysis—mass reduction is associated with statistically significant increases in crash frequency, small decreases in casualties per crash, and on net statistically significant increases in casualty risk per VMT, for all five types of vehicles. These results are unexpected: one would expect that lighter vehicles, with better maneuverability and shorter braking distances, would have lower crash frequency than heavier vehicles; and that heavier (or larger) vehicles would have lower risk once a crash has occurred than lighter vehicles. It is possible that including variables that more accurately account for important differences among vehicles and driver behavior would reverse this relationship, as discussed below.

Table II.4.A.1 shows the estimated effect of seven alternative regression models that test the sensitivity of the relationship between mass or footprint reduction and crash frequency to five additional vehicle or driver variables, and dummy variables for 15 vehicle makes, as well as all five variables plus the manufacturer dummy variables combined: initial vehicle purchase price, average household income, vehicle make, average "bad driver" rating, whether the driver was using alcohol or drugs, and whether the driver was using a restraint properly. Coefficients shown in red are statistically significant, based on the Chi-square value output by the logistic regression model.

For the most part, the estimated effect of the additional five vehicle and driver variables, and the dummy vehicle make variables, on crash frequency is similar when all variables are included in Model 7 as when only one of the five, or the make dummy variables, is included (Models 1 through 6). However, there are some exceptions: initial vehicle purchase price gets very small for cars in Model 7 (from a 0.70% decrease in crash frequency in Model 1 to a 0.01% decrease in crash frequency in Model 7), and changes sign for CUVs/minivans (from a 0.28% decrease to a 0.73% increase in crash frequency); average household income changes sign for light trucks (from a 0.31% decrease to a 0.66% increase in crash frequency); and bad driver rating changes sign for CUVs/minivans (from a 2.4% increase in crash frequency to a 4.1% decrease in crash frequency). The association of driver restraint use with crash frequency decreases substantially when the other variables are added to the regression models, from a 21 to 29% reduction in crash frequency to a 10 to 17% reduction in crash frequency, depending on vehicle type.

Including the five additional variables, as well as the dummy variables for vehicle makes, either individually or including all in the same regression model, does not change the general results of the baseline NHTSA regression model—that mass reduction is associated with an increase in crash frequency in all three types of vehicles, while footprint reduction is associated with a decrease in crash frequency in cars and CUVs/minivans, but with an increase in crash frequency in light trucks. The results for lighter-than-average light trucks is least stable under these alternative models, mostly because lighter light trucks are associated with only a small increase in crash frequency under the baseline model. The alternative regression model with the biggest effect is Model 3, which adds dummy variables for 15 vehicle makes, and substantially increases the estimated increase in crash frequency from mass reduction in the baseline model for all five vehicle types. These results suggest that other, more subtle, differences in vehicles and their drivers may account for the unexpected finding that lighter vehicles have higher crash frequencies than heavier vehicles.

Table II.4.A.2 shows the estimated effect of the vehicle, driver, and calendar year control variables on the two components of fatality risk per VMT: crashes per VMT (or crash frequency) and fatality and casualty risk per crash. Variables with estimates in the expected direction are highlighted in green, whereas estimates in the

unexpected direction are highlighted in yellow; only estimates that are statistically significant, which are shown in red, are highlighted. Table II.4.A.2 shows several unexpected results:

- Bumper height compatibility measures in light trucks, and some types of side airbags in cars and CUVs/minivans, are associated with decreases in crash frequency
- AWD is associated with an increase in crash frequency
- ESC and ABS are associated with decreases in risk once a crash has occurred
- AWD, male drivers, young drivers, and driving at night, in a rural county, or on a high-speed road are all associated with increases in risk once a crash has occurred.

Table II.4.A.1. Effect of Mass and Footprint Reduction on Crash Frequency under Alternative Regression Model Specifications. Source: LBNL.

Variable	Case Vehicle Type	NHTSA baseline model (crashes per VMT)	1. Including initial vehicle purchase price ($000s)	2. Including median household income ($000s)	3. Including 15 variables for vehicle make	4. Including average 'bad driver' rating	5. Including whether driver was using alcohol or drugs	6. Including whether driver was properly using restraint	7. Including all additional variables
Mass Reduction	Cars< 3106	1.60%	0.99%	1.55%	2.91%	1.66%	1.60%	1.67%	2.36%
	Cars> 3106	2.33%	0.82%	1.66%	3.84%	2.56%	2.34%	2.40%	3.23%
	LTs < 4594	0.36%	-0.56%	0.37%	1.32%	-0.20%	0.27%	0.37%	0.05%
	LTs > 4594	1.31%	0.01%	1.19%	2.36%	0.89%	1.21%	1.27%	1.00%
	CUV/mvan	2.59%	2.29%	2.07%	3.90%	2.62%	2.62%	2.57%	4.36%
Footprint Reduction	Cars	-0.95%	-0.75%	-0.23%	-1.87%	-1.00%	-0.89%	-0.98%	-1.33%
	LTs	1.63%	1.50%	1.66%	0.67%	1.81%	1.66%	1.62%	0.83%
	CUV/mvan	-2.31%	-2.27%	-1.79%	-3.81%	-2.32%	-2.33%	-0.08%	-3.74%
Initial Purchase Price	Cars	—	-0.70%	—	—	—	—	—	-0.01%
	LTs	—	-1.39%	—	—	—	—	—	-0.99%
	CUV/mvan	—	-0.28%	—	—	—	—	—	0.73%
Average Household Income	Cars	—	—	-1.70%	—	—	—	—	-0.83%
	LTs	—	—	-0.31%	—	—	—	—	0.66%
	CUV/mvan	—	—	-1.24%	—	—	—	—	-0.74%
'Bad Driver' Rating	Cars	—	—	—	—	6.38%	—	—	3.37%
	LTs	—	—	—	—	-7.74%	—	—	-8.19%
	CUV/mvan	—	—	—	—	2.37%	—	—	-4.08%
Driver Alcohol or Drug Use	Cars	—	—	—	—	—	251%	—	243%
	LTs	—	—	—	—	—	245%	—	236%
	CUV/mvan	—	—	—	—	—	236%	—	225%
Driver Properly Restrained	Cars	—	—	—	—	—	—	-21.3%	-9.95%
	LTs	—	—	—	—	—	—	-29.0%	-16.6%
	CUV/mvan	—	—	—	—	—	—	-24.7%	-11.8%

Estimates in red are statistically significant at the 95% level.

Table II.4.A.2. Estimated Effect of Variables on Crashes per VMT Fatalities per Crash and Casualties per Crash Using Data from 13 states. Source: LBNL.

Variable	Cars			Light Trucks			CUVs/Minivans		
	Crash/ VMT	Fatality/ Crash	Casualty/ Crash	Crash/ VMT	Fatality/ Crash	Casualty/ Crash	Crash/ VMT	Fatality/ Crash	Casualty/ Crash
UNDERWT	1.60%	-0.74%	-0.84%	0.36%	-0.77%	-0.27%	–	–	–
OVERWT	2.33%	-0.32%	-0.26%	1.31%	-1.43%	-0.49%	–	–	–
LBS100	–	–	–	–	–	–	2.59%	-2.12%	-0.44%
FOOTPRINT	-0.95%	-0.03%	0.51%	1.63%	0.10%	-0.17%	-2.31%	0.87%	0.48%
TWODOOR	6.48%	14.7%	-1.26%	–	–	–	–	–	–
SUV	–	–	–	7.06%	-1.34%	1.49%	–	–	–
HD	–	–	–	-2.28%	20.4%	4.24%	–	–	–
BLOCKER1	–	–	–	-3.72%	-0.89%	0.29%	–	–	–
BLOCKER2	–	–	–	-7.01%	-5.41%	-2.62%	–	–	–
MINIVAN	–	–	–	–	–	–	-2.66%	-0.58%	8.51%
ROLLCURT	0.00%	0.20%	0.34%	–	–	–	-0.08%	-0.43%	-0.45%
CURTAIN	3.43%	2.17%	-3.06%	–	–	–	2.29%	-10.06%	-2.38%
COMBO	7.49%	-0.91%	2.34%	–	–	–	-5.92%	1.51%	8.33%
TORSO	-7.14%	-11.2%	-6.69%	–	–	–	-8.59%	3.57%	-5.66%
ABS	-14.2%	-1.57%	-5.54%	–	–	–	-14.4%	-11.8%	-4.75%
ESC	-8.80%	-1.40%	-7.09%	-11.3%	-10.3%	-9.59%	-5.59%	-18.6%	-6.56%
AWD	–	–	–	36.3%	7.29%	0.51%	13.6%	-0.50%	-0.43%
VEHAGE	0.93%	2.35%	0.79%	1.87%	2.58%	1.53%	1.61%	1.02%	1.10%
BRANDNEW	3.44%	3.08%	2.70%	-0.23%	11.9%	3.56%	-1.13%	5.12%	-2.60%
DRVMALE	5.49%	21.8%	-0.79%	-3.28%	22.3%	-0.07%	1.97%	22.8%	4.54%
M14_30	4.10%	1.84%	0.43%	3.93%	1.25%	0.47%	4.74%	-0.04%	0.28%
M30_50	0.51%	0.18%	-0.15%	0.49%	-0.20%	-0.24%	0.23%	0.22%	-0.39%
M50_70	-0.01%	3.45%	1.26%	0.35%	2.20%	1.22%	0.38%	2.54%	1.15%
M70_96	3.60%	4.28%	2.17%	3.79%	4.09%	1.89%	3.15%	4.53%	1.93%
F14_30	3.36%	0.97%	0.38%	3.72%	-1.49%	-0.16%	3.59%	0.12%	0.56%
F30_50	0.26%	-1.22%	-0.68%	0.09%	0.06%	-0.22%	0.11%	-0.57%	-0.44%
F50_70	0.62%	2.71%	0.89%	0.95%	2.95%	1.14%	0.90%	2.73%	1.19%
F70_96	4.00%	5.36%	1.90%	3.05%	-4.16%	0.83%	3.85%	4.11%	1.33%
NITE	20.2%	81.9%	23.5%	28.6%	68.4%	20.8%	19.9%	68.3%	17.4%
RURAL	10.6%	53.7%	30.1%	15.0%	43.8%	26.7%	13.51%	49.2%	23.2%
SPDLIM55	33.1%	104%	55.5%	25.1%	107%	63.9%	19.2%	113%	63.4%
CY2005	-0.12%	25.9%	19.1%	3.13%	27.4%	24.1%	-4.34%	29.2%	17.2%
CY2006	0.14%	24.9%	14.3%	2.11%	20.2%	19.0%	-5.65%	16.7%	17.3%
CY2007	2.80%	18.8%	7.82%	4.96%	12.0%	11.3%	-1.06%	8.80%	11.5%
CY2008	-0.27%	10.1%	4.47%	1.32%	10.8%	7.90%	-1.93%	5.83%	6.20%
CY2010	2.82%	-4.88%	-11.3%	0.42%	-7.40%	-9.75%	2.14%	-4.69%	-1.88%
CY2011	7.04%	-16.0%	-20.8%	0.46%	-6.63%	-23.0%	4.63%	-11.1%	-17.3%
AL	95.1%	-103%	-24.2%	79.7%	-111%	-36.2%	104%	-112%	-40.6%
KS	56.1%	-124%	-161%	60.3%	-133%	-167%	81.7%	-131%	-146%
KY	114%	-129%	-156%	113%	-133%	-169%	141%	-153%	-173%

Variable	Cars			Light Trucks			CUVs/Minivans		
	Crash/ VMT	Fatality/ Crash	Casualty/ Crash	Crash/ VMT	Fatality/ Crash	Casualty/ Crash	Crash/ VMT	Fatality/ Crash	Casualty/ Crash
MD	14.4%	-55.0%	-58.2%	1.46%	-80.6%	-61.3%	6.19%	-73.8%	-58.2%
MI	94.9%	-199%	-203%	92.2%	-224%	-211%	102%	-187%	-206%
MO	83.7%	-109%	-127%	64.0%	-119%	-131%	88.0%	-116%	-136%
NE	80.8%	-155%	-134%	74.3%	-156%	-140%	86.6%	-201%	-145%
NJ	100%	-146%	-281%	101%	-172%	-283%	110%	-168%	-304%
PA	-22.5%	-27.5%	-154%	-13.6%	-40.2%	-143%	-7.2%	-22.5%	-154%
WA	37.3%	-125%	-194%	53.8%	-127%	-190%	73.4%	-129%	-201%
WI	46.5%	-124%	-144%	45.8%	-148%	-155%	54.5%	-125%	-149%
WY	84.3%	-164%	-188%	41.4%	-169%	-182%	79.9%	-172%	-176%

Estimates in red are statistically significant at the 95% level.

In some cases, these unexpected results apply to all three vehicle types; in other cases, to only one or two. The results suggest that the regression models may not fully account for all of the variables that influence crash frequency or risk per crash. In particular, they may not account for why risky or unskilled drivers select certain vehicle types, or even particular makes and models. Not accounting for these associations may be biasing the relationships the models estimate between vehicle mass or footprint and crash frequency and risk per crash.

In its 2012 report, the NHTSA (Kahane 2012) suggested that not accounting for crash severity might explain the unexpected results from the 2012 LBNL Phase 2 report (Wenzel 2012). We tested this by re-running the regression analyses focusing only on the most severe crashes (i.e., after excluding crashes in which no vehicle was reported as being disabled, or was towed from the crash scene). Because Washington does not report either of these crash severity measures, all crashes in Washington had to be excluded from the analysis. Of the crashes involving a casualty, 95% occurred in states other than Washington; of these, 42% were severe. Of the total casualties, 98% occurred in states other than Washington; of these, 84% occurred in severe crashes. In some cases, excluding non-severe crashes reduces the unexpected results from the baseline model; however, in none of the estimates does excluding the non-severe crashes change the sign on the estimated coefficient to the expected direction. We conclude that not accounting for crash severity in the baseline model is not the reason why many control variables have unexpected associations with crash frequency or risk per crash.

Effect of Mass Reduction Scenarios on Vehicle Masses in Two-vehicle Crashes and Fatalities over Time

In a draft report, LBNL simulated what effect the change in the masses of both vehicles involved in a two-vehicle crash has on societal fatality risk per VMT, over both the short and long term. The simulation involves three steps, using NHTSA's 2016 public database. First, new regression models are run, which estimate the relationship between the mass disparity between the case vehicle and its crash partner on societal fatality risk. Second, the mass of both vehicles is simulated annually, based on assumed mass reduction in the case vehicle because of the standards, and mass reduction in its crash partner based on historical trends in the average mass of the fleet. Finally, the estimated relationship between mass disparity and societal fatality risk is applied to the simulated fleet to estimate the change in total fatalities as the mass disparity changes over time.

LBNL ran several regression models to estimate the relationship between mass disparity and societal fatality risk. Figure II.4.A.3 indicates that the relationship is u-shaped; societal fatality risk increases as the mass of the case vehicle moves further away from the mass of its crash partner (the mass of the case vehicle equals that of its crash partner where the case vehicle mass equals 50% of the combined mass). Car-to-car crashes are least sensitive to the disparity in masses, followed by car-to-light-truck crashes and light-truck-to-light-truck crashes. The relationship between mass differential (i.e., case vehicle mass minus crash partner mass) and societal fatality risk has a similar shape to that shown in Figure II.4.A.5. The R^2 values in Figure II.4.A.3 indicate the degree to which the data fit the trend lines shown, with an R^2 of 1.00 signifying perfect correlation.

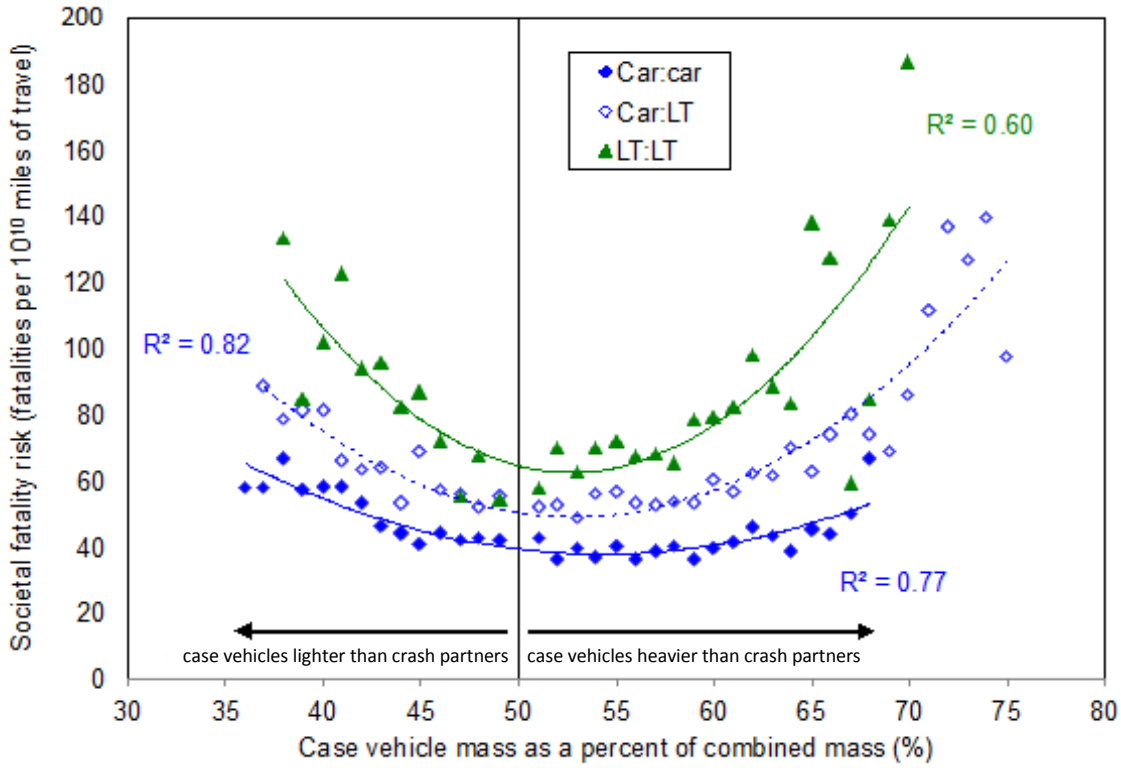

Figure II.4.A.3. Average societal fatality risk per VMT, by partner vehicle mass as a percent of combined mass, by crash type. Source: LBNL.

Table II.4.A.3 compares the results from several regression models: Model 1 only accounts for the difference in vehicle masses in hundreds of pounds, while Model 5 accounts for the case vehicle's mass as a percentage of the combined mass. The signs on most of the coefficients in Model 5 are the same as those of Model 1. However, the estimated coefficients on the case vehicle's mass as a percent of combined mass for either light trucks or CUVs/minivans in crashes with lighter light trucks are both negative (-6.26 and -0.60%, respectively), although the coefficient for CUVs/minivans is not statistically significant. Figure II.4.A.5 indicates that the relationship between case vehicle mass as a percent of combined mass and societal fatality risk is roughly symmetrical, for all three types of crashes (car-to-car, car-to-light-truck, and light-truck-to-light-truck crashes); Models 6 and 7 in Table II.4.A.3 introduce a polynomial term to Models 1 and 5 for the mass difference (in Model 1) and the crash partner mass as a percent of combined mass (in Model 5).

Models 6 and 7 in Table II.4.A.3 also collapse the 12 crash types into six: whether the crash partner is a car or a light truck, regardless of whether the crash partner is heavier or lighter than the case vehicle. The signs for the coefficients for the mass difference in Model 6 are positive when the crash partner is a car (i.e., 3.9% in car-car crashes, 8.0% in light truck-car crashes, and 8.8% in CUV/minivan-car crashes) and negative when the crash partner is a light truck (i.e., -15.7% in car-light truck crashes, -6.6% in light truck-light truck crashes, and -11.3% in CUV/minivan-light truck crashes), while the signs for the coefficients for case vehicle mass as a percent of combined mass in Model 7 are almost always positive; the exception is in light truck-light truck crashes, where an increase in the case vehicle mass as a percent of combined mass is associated with a 4.3% decrease in risk per VMT. The signs for the coefficients for the mass squared term in Models 6 and 7 are always negative. Based on the different regression models estimated, we decided to use the coefficients from Model 7 in our simulation of the change in societal fatalities as the distribution of vehicle mass changes over time, because, as Figure II.4.A.3 indicates, the relationship between mass disparity and fatality risk is not linear.

Table II.4.A.3. Estimated Effect of Mass Difference and Combined Mass on Societal Fatality Risk per VMT, by Case Vehicle and Crash Partner Type. Source: LBNL.

Case Vehicle Type	Crash Type*	Model 1	Model 5	Model 6		Model 7	
		Mass diff / 100	Pct case veh mass of total mass	Mass diff / 100	Mass diff^2	Pct case veh mass of total mass	Pct mass^2
Cars	5: w/heavier car	-0.95%	-3.11%	3.9%	-0.19%	34.0%	-28.3%
	6: w/lighter car	15.8%	19.0%				
	7: w/heavier LT	-10.2%	-19.9%	-15.7%	-0.23%	6.0%	-27.3%
	8: w/lighter LT	8.73%	10.6%				
Light Trucks	5: w/heavier car	-6.28%	-11.9%	8.0%	-0.05%	25.4%	-13.2%
	6: w/lighter car	7.02%	10.8%				
	7: w/heavier LT	-14.4%	-28.3%	-6.6%	-0.02%	-4.3%	-7.7%
	8: w/lighter LT	-3.12%	-6.26%				
CUVs/ Minivans	5: w/heavier car	-4.10%	-8.39%	8.8%	-0.18%	50.9%	-38.3%
	6: w/lighter car	9.34%	12.6%				
	7: w/heavier LT	-12.4%	-24.6%	-11.3%	-0.16%	4.9%	-22.6%
	8: w/lighter LT	0.38%	-0.60%				

* Crash types 5 and 6 include crashes with a CUV or a minivan.
Note: Estimates that are statistically significant at the 95% level are shown in red; estimates in the unexpected direction are highlighted in yellow.

Figure II.4.A.4 shows the average mass of the crash partner, by the model year and type of the crash partner, from the 13-state crash data. Figure II.4.A.4 indicates that, on average, the mass of cars/CUVs/minivans and light trucks declined by 2.2% each year between model year 1981 and 1987; the average mass of cars/CUVs/minivans then increased by 0.5% each year until model year 2009, whereas the average mass of light trucks increased 2.2% annually until 2009.

LBNL constructed a model to estimate the curb weight of vehicles involved in two-vehicle crashes over the next 27 years, using the induced exposure vehicles from the state crash data weighted by the VMT weights developed by NHTSA. We assumed that the distribution of crash partners by vehicle age, and all their attributes except their weight, remains the same over time. Following the method of Puckett and Kindelberger (2016) and Kahane (2012), only crashes involving case vehicles from model years 2007 to 2011 in calendar years 2007 to 2011 are included. In the first simulation year the mass of the case vehicle is reduced to reflect compliance with the standards, using the mass reductions recommended by the 2015 NAS report: 5% for lighter-than-average cars, 12.5% for heavier-than-average cars, and 20% for light trucks, CUVs, and minivans. We assume that the mass of the case vehicle is unchanged in every successive simulation year. The mass of the crash partner changes in each simulation year, based on the average change in curb weight by model year shown in Figure II.4.A.4. The model year of each crash partner is increased one year in each simulation year, to maintain the same age as in the baseline. For example, a crash partner that is a model year 1997 in the baseline is 10 years old; in simulation year 1 it is assumed to be a model year 1998, in simulation year 2 a model year 1999, etc. so that it remains 10 years old in each simulation year. The weight of each crash partner is then adjusted in each simulation year according to the trends in Figure II.4.A.4; vehicles decrease their mass 2.2% in each simulation year until they become a model year 1988; starting in model year 1988 cars, CUVs, and minivans increase their mass by 0.5%, and light trucks by 2.2%, each simulation year. When the crash partner becomes a model year 2007 vehicle its mass is reduced by 5% if a lighter-than-average car, 12.5% by if a heavier-than-average car, or 20% if a light truck, CUV, or minivan, which becomes the estimated effect of the standards on vehicle mass.

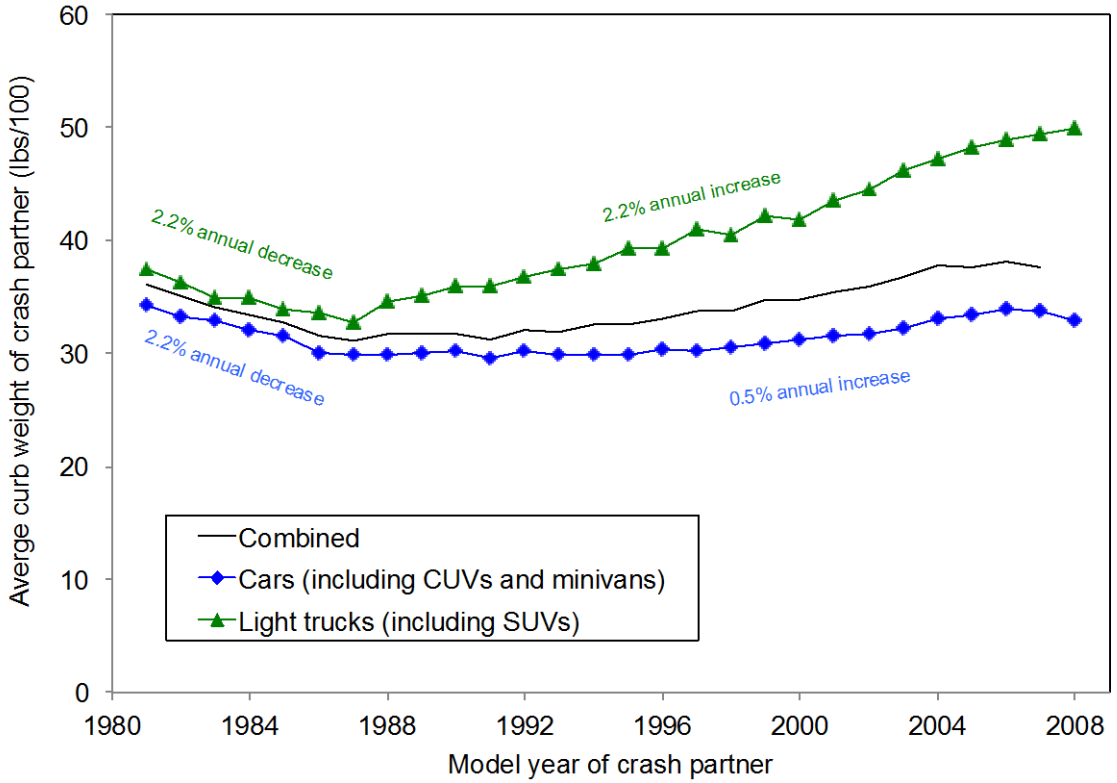

Figure II.4.A.4. Average curb weight of crash partner in 13-state crash data, by model year and type of crash partner. Source: LBNL.

Figure II.4.A.5 shows the change in the cumulative distribution of the mass of the case vehicle as a percent of combined mass, before and after the estimated reduction in case vehicle mass due to the standards, for all two-vehicle crashes. The solid lines show the cumulative distributions of mass differences in the baseline, the dashed lines show the cumulative distributions of mass differences after the assumed reduction in mass of the case vehicle due to the standards in simulation year 1, and the small dashed lines show the distribution 27 years later after all the crash partners have been subject to the assumed mass reductions from the standards. Figure II.4.A.5 indicates that the assumed mass reductions to the case vehicles in simulation year 1 shifts the distribution of crashes where the case vehicle mass is both less than and greater than 50% of combined mass; however, by simulation year 27, when all the crash partner masses have been reduced by the standards, the distribution of crashes where the case vehicle mass is less than 50% of combined mass is similar to that of the baseline, while the distribution of crashes where the case vehicle mass is greater than 50% of combined mass is shifted much closer to 50%. Figure II.4.A.5 shows that the assumed mass reductions to the case vehicles in simulation year 1 reduces the mass disparity across all crash types: the fraction of case vehicles with mass between 42 and 58% of the combined mass increases from 57% in the baseline to 64% after year 1. Once the masses of all crash partners are also reduced by simulation year 27, the fraction of case vehicles with mass between 42 and 58% of the combined mass increases to 68%, or 11 percentage points higher than in the baseline.

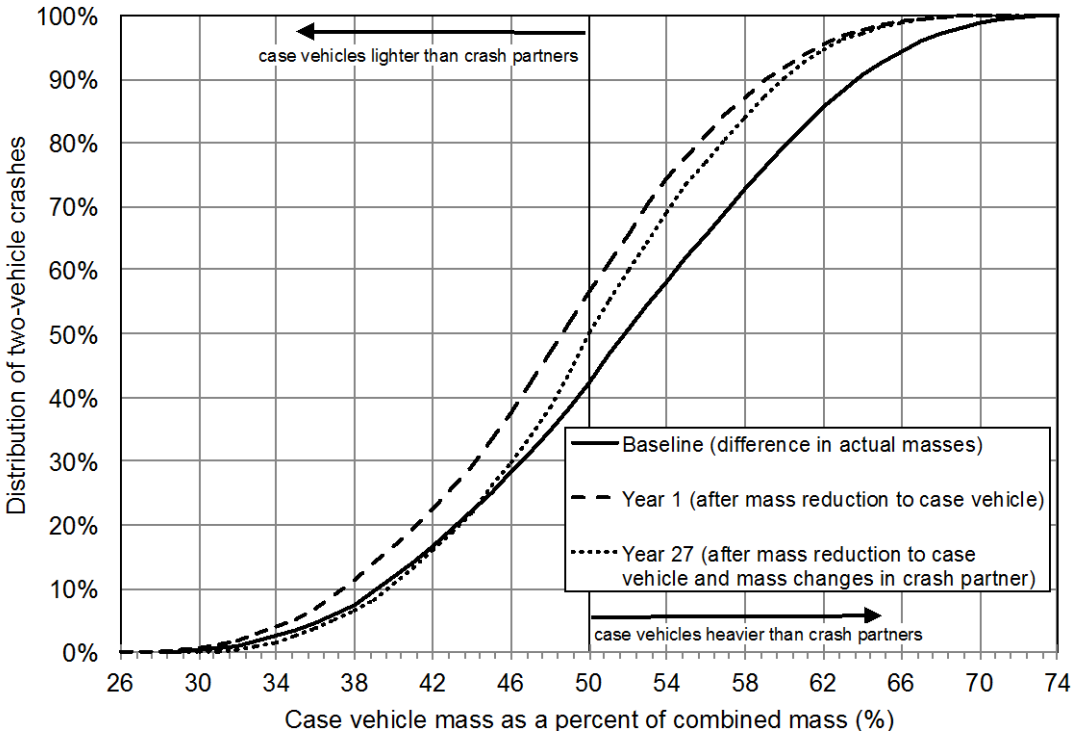

Figure II.4.A.5. Simulated change in the distribution of case vehicle mass as a percent of combined mass. Source: LBNL.

Figure II.4.A.6 shows the simulated average mass disparity over time using case vehicle mass as a percent of combined mass, by type of case vehicle. The mass of all case vehicles decreases from 51 to 48% of combined mass from the baseline to simulation year 1, but then increases gradually to 50% of combined mass by simulation year 27 (shown in heavy black line). Figure II.4.A.6 indicates that the mass disparity in crashes where the case vehicle is a light truck (shown in green) or CUV/minivan (shown in orange) decreases over time: the mass of light trucks declines from 58% of combined mass in the baseline to 53% of mass in simulation year 1, and then increases gradually to 55% of combined mass by simulation year 27, while the mass of CUVs/minivans declines from 53 to 48% of combined mass in simulation year 1, and then gradually increases to 50% of combined mass by year 27. In crashes where the case vehicle is a car (shown in blue), the mass disparity is essentially unchanged: while the disparity declines from 48% of combined mass in the baseline to 46% of combined mass in simulation year 1, it gradually increases back to 48% of combined mass by simulation year 27.

The final step is to use the coefficients from the regression models in Table II.4.A.3 to estimate the change in fatalities over time as the mass difference changes. We calculated the predicted risk for each induced exposure vehicle from the 13 state crash databases by multiplying the regression coefficients from for all driver, crash, and vehicle variables in Model 7 by the characteristics of each induced exposure vehicle, to obtain the predicted fatalities per vehicle. We then multiplied these fatalities by the VMT weighting each induced exposure vehicle represents, to obtain the number of total predicted fatalities and summed across vehicle type. Figure II.4.A.7 shows the simulated change in fatalities for all two-vehicle crashes, using the coefficients for case vehicle mass as a percent of combined mass from Model 7 in Table II.4.A.3, and the mass reduction scenario recommended in the 2015 NAS subcommittee report for case vehicles: 5% for lighter cars, 12.5% for heavier cars, and 20% for light trucks, CUVS, and minivans. Under these assumptions, fatalities in two-vehicle crashes are up to 2% greater than the baseline between simulation years 1 and 8, are the same as the baseline in simulation year 9, and are lower than the baseline starting in simulation year 10 until they reach nearly 5% below the baseline fatalities by simulation year 27. Figure II.4.A.7 indicates that fatalities in crashes where a car is the case vehicle (shown in blue) increase by a maximum of 7% after two years, and then decline to no

change in fatalities after 16 years and to 1% fewer fatalities after 27 years. Where the case vehicle is a CUV (shown in orange), fatalities increase by a maximum of 2% after four years, and then decline to no change in fatalities after 9 years and to 6% fewer fatalities after 27 years. For light trucks (shown in green), the mass reductions recommended in the NAS report result in an initial 5% decrease in fatalities and continue declining to 10% fewer fatalities after 27 years.

In the NHTSA baseline regression model, the effect of mass reduction on societal fatality risk is estimated as a function of the type of case vehicle and whether the mass of its crash partner is lighter or heavier than the median mass, but not the relative difference in the masses of the two vehicles. In Wenzel (2016), we estimated the following changes in annual fatalities in two-vehicle crashes, using the NHTSA baseline regression model coefficients and the NAS assumptions for mass reduction: 4.2% increase in fatalities when the case vehicle is a car, 13.4% decrease when the case vehicle is a light truck, and a 3.2% increase when the case vehicle is a CUV/minivan, for a 1.4% overall decrease in fatalities in all two-vehicle crashes (this simulation results in a 0.8% decrease in fatalities in one-vehicle crashes, and a 1.4% decrease in 3 plus vehicle crashes, for a 1.1% overall decrease in all crashes). The dashed lines in Figure II.4.A.7 indicate the point estimate of the change in fatalities from under this scenario from Wenzel (2016). Figure II.4.A.7 indicates that, while the NHTSA baseline regression coefficients estimate that the levels of mass reduction recommended in the NAS report result in a 4% increase in annual fatalities in two-vehicle crashes with a car as the case vehicle (shown in blue), LBNL's simulation based on changing vehicle masses over time estimates that the recommended mass reductions result in a 4% or larger increase in annual fatalities in years 1 to 9, a smaller than 4% increase in fatalities in years 10 to 15, and a reduction in annual fatalities after 16 years. Similarly, for two-vehicle crashes where the case vehicle is a CUV/minivan (shown in orange), the NHTSA baseline coefficients estimate a 3% increase in annual fatalities, whereas the LBNL simulation estimates a smaller than 3% increase in years 1 to 8, and a reduction in annual fatalities after 10 years. Both the NHTSA baseline regression coefficients and LBNL's simulation estimate that annual fatalities in two-vehicle crashes where the case vehicle is a light truck will decrease (shown in green), but the decrease is much larger using NHTSA's baseline coefficients than the LBNL simulation. For all vehicle types combined (shown in black), the LBNL simulation estimates increases in fatalities in two-vehicle crashes in years 1 to 8, but larger decreases in annual fatalities in years 12 to 27 than estimated using the NHTSA baseline coefficients (a 1% decrease in fatalities).

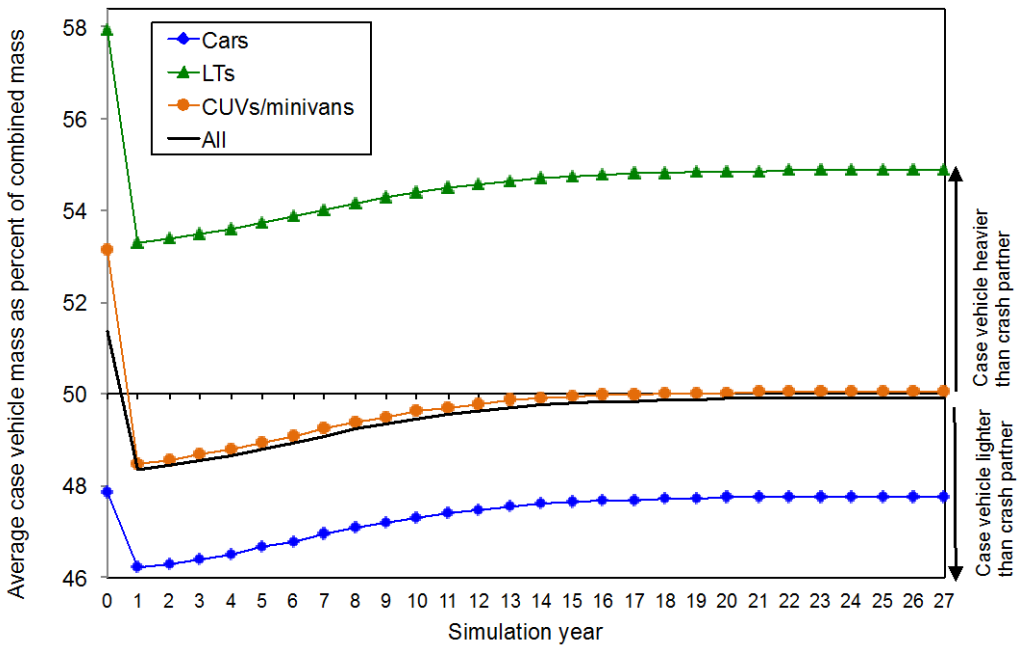

Figure II.4.A.6. Simulated change in average case vehicle mass as a percent of combined mass, by type of case vehicle. Source: LBNL.

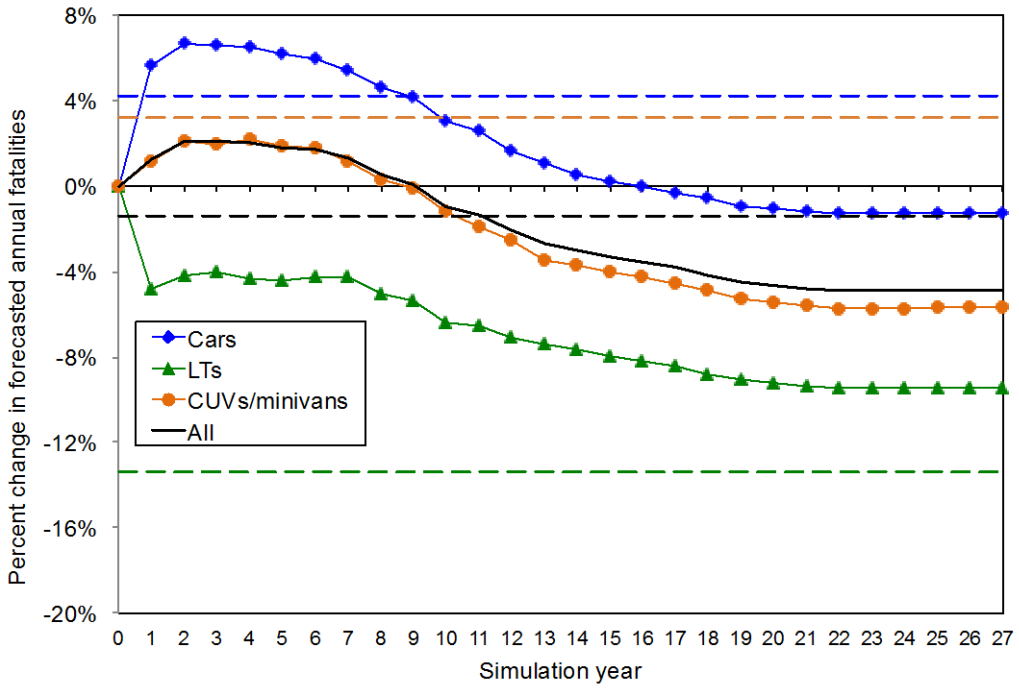

Figure II.4.A.7. Simulated change in fatalities from changes in partner mass/combined mass (Model 7 in Table II.4.A.3), assuming mass reductions in 2015 NAS report by type of case vehicle. Source: LBNL.

As noted above, NHTSA provided comments on the preliminary analysis. LBNL will work to incorporate these comments in a revised report in FY 2018.

Conclusions

Our analysis of the two components of risk per VMT, crash frequency, and risk per crash, indicates that much of the estimated detrimental effect of mass or footprint reduction on risk can be attributed to the tendency for crash frequency, rather than crashworthiness/compatibility (risk once a crash has occurred), to increase as vehicle mass or footprint decreases. It is unclear why lower vehicle mass is associated with higher crash frequency, but lower risk per crash, in the regression models; sensitivity analyses that included five additional variables, as well as vehicle make, to account for differences in specific vehicles and driver behavior did not reverse this relationship. It is possible that over 30 years of improvements in vehicle design to achieve high crash test ratings have enabled manufacturers to use clever vehicle design to mitigate the hypothetical safety penalty of vehicles with low mass. And restricting our analysis to only severe crashes did not change the sign on the coefficients for certain control variables whose sign was in the unexpected direction in the baseline model.

Our simulation of how mass reductions induced by the fuel economy/emission standards may change the mass disparity, and societal fatalities, in two-vehicle crashes over time suggests that fatalities may increase initially, and then decrease over time, relative to the number of baseline fatalities. However, these results are preliminary; more work needs to be done in FY 2018 to better characterize the relationship between the masses of two vehicles involved in a crash and societal fatality risk.

References

Kahane, C. J., 2012, Relationships Between Fatality Risk, Mass, and Footprint in Model Year 2000-2007 Passenger Cars and LTVs, Final Report, DOT HS 811 665, Washington, D.C., USA, National Highway Traffic Safety Administration.

Kahane, C. J., 2014, Updated Estimates of Fatality Reduction by Electronic Stability Control, NHTSA Evaluation Note No. DOT HS 812 020, Washington, D.C., USA, National Highway Traffic Safety Administration.

National Academy of Sciences, 2015, Cost, Effectiveness and Deployment of Fuel Economy Technologies for Light-Duty Vehicles, final report prepared by the Committee on the Assessment of Technologies for Improving Fuel, Economy of Light-Duty Vehicles, Phase 2, Board on Energy and Environmental Systems, Division on Engineering and Physical Sciences, Washington, D.C., USA, National Research Council.

Puckett, S. M., and J. C. Kindelberger, 2016, Relationships Between Fatality Risk, Mass, and Footprint in Model Year 2003-2010 Passenger Cars and LTVs, preliminary report prepared for the National Center for Statistics and Analysis, Docket No. NHTSA-2016-0068, Washington, D.C., USA, National Highway Traffic Safety Administration.

Wenzel, T., 2012, An Analysis of the Relationship between Casualty Risk per Crash and Vehicle Mass and Footprint for Model Year 2000-2007 Light-Duty Vehicles, final report prepared for the Office of Energy Efficiency and Renewable Energy, United States Department of Energy, LBNL-5697E, Berkeley, CA, USA, Lawrence Berkeley National Laboratory.

Wenzel, T., 2016, Assessment of NHTSA's Report "Relationships Between Fatality Risk, Mass, and Footprint in Model Year 2003-2010 Passenger Cars and LTVs", final report prepared for the Office of Energy Efficiency and Renewable Energy, United States Department of Energy, LBNL-1005177, Berkeley, CA, USA, Lawrence Berkeley National Laboratory.

II.4.B Ultralight Door Design, Manufacturing and Demonstration Project (Magna)

Tim Skszek, Principal Investigator
Magna International, Inc.
750 Tower Dr.
Troy, MI 48098
Phone: 248-631-5375
E-mail: tim.skszek@cosmaeng.com

Carol Schutte, Technology Manager
E-mail: carol.schutte@ee.doe.gov

Start Date: December 1, 2015 End Date: September 30, 2018
Total Project Cost: $8,444,583 DOE share: $4,222,291 Non-DOE share: $4,222,292

Executive Summary

During FY 2016 and FY 2017, Magna International Inc. (Magna), through a cooperative agreement with DOE and partners Fiat Chrysler Automobiles U.S. LLC (FCA US LCC), Grupo Antolin North America, and Magna Closures Inc., completed design/engineering, manufacture of prototype component parts, and component-level testing, as described in the Statement of Project Objectives. The project team commenced assembly of prototype component parts to manufacture complete door assemblies, integration of complete door assemblies with vehicles, and full vehicle testing. The ultralight door is 15.2 kg or 40% lighter than the 2016 baseline door assembly. Project completion, including full vehicle testing and reporting of the ultralight door assembly, will be completed by September 30, 2018.

Accomplishments

- Production Design & Analysis – Finalized the driver's side door design based on the results of CAE analysis and component-level test results.
- Prototype Door Components – Manufactured tooling, door component parts, and door assemblies required for component-level and vehicle-level testing.
- Door Assembly – Assembled twenty-two driver's side door assemblies, integrating the door structure with the glass, door module, and interior trim and latch components required for component and vehicle-level testing.
- Vehicle Integration – Integrated the lightweight driver's side door assemblies with 2016 production vehicles required for full-vehicle testing and management evaluation of the vehicles.
- Component Testing – Conducted noise, vibration, and harshness testing associated with the chemically toughened drop glass and door beam component-level testing.
- Life Cycle Analysis – Completed a peer-reviewed comparative life cycle analysis of the driver's side door, which was conducted by a third-party life cycle analysis expert, documenting an environmental benefit of a 6-gram carbon dioxide equivalent per kilometer environmental benefit associated with a 49.5 kg full-vehicle mass reduction and appropriate engine downsizing, thereby maintaining the performance specification of the baseline vehicle. The 49.5 kg full-vehicle mass reduction assumes that all four doors of a four-door C-segment passenger vehicle were lightweighted.

Technology Assessment

- Target: 120% of the Federal Motor Vehicle Safety Standards (FMVSS) Static 214 specified average reaction force value. Initial FMVSS Static 214 tests resulted in 99% of the specified average reaction force.
- Gap: Dimensional characteristics associated with the door components and door assembly significantly impact test results. The dimensional characteristics of the door assembly need to be validated prior to testing. The test will be repeated in 2016-2017 to demonstrate compliance to the OEM specification of 120% of the FMVSS threshold value.

Project Introduction

Magna, through a cooperative agreement with DOE and partners FCA US LLC and Grupo Antolin North America, has developed a lightweight door architecture that will further enable automakers with the means to achieve the proposed legislation regarding passenger vehicle emissions and fuel consumption regulation. The current lightweight is 15.21 kg, or 40% lighter than the 2016 baseline equivalent.

Magna's advanced engineering team—a collaborative effort between the company's corporate R&D, body and chassis, closures, and exteriors groups—combined its unique, full-vehicle perspective on the design of a driver's side door with an inventive mix of materials and technology to tackle the challenge of achieving a significant weight reduction, in a cost-effective manner, while maintaining all of the safety, durability, and functionality aspects relative to the 2016 baseline driver's side door. Grupo Antolin North America, a global Tier 1 manufacturer of automotive interior trim, agreed to design and manufacture lightweight interior trim assemblies. FCA US LCC will conduct safety, durability, and corrosion testing of the lightweight door assemblies.

Approach

The project proposal included the selection of a baseline "frame behind glass" door architecture, applicable to 70% of the lightweight vehicle market. Initial activities included characterization of the mass and performance characteristics associated with the baseline door and the development of a performance target matrix to achieve a functionally equivalent Ultralight Door, 42.5% lighter than the baseline driver's side door.

The Ultralight Door design realized the target performance and mass reduction objectives through functional integration of the various door components and subsystems, using various forms of aluminum, advanced molding processes, and innovative joining methods.

The significant mass reduction associated with the Ultralight Door is the result of a holistic design approach, enabling integration of the glass run channels with the module, application of advanced joining technologies to minimize the length of the flange, and the application of chemically toughened glass, local interconnect network (LIN) bus communications, advanced molding technologies, and innovative joining technologies. The materials associated with the Ultralight Door are commercially available and suited for use in high-volume/low-cost manufacturing applications. The manufacturing and joining technologies are compatible with existing manufacturing processes and can be commercialized, without significant increase in production costs or changes in body-shop infrastructure. The project plan includes a prototype build of thirty prototype door assemblies, component-level testing, and full-vehicle testing by FCA US LLC. Table II.4.B.1 provides details of the project test plan.

Table II.4.B.1. Project Test Plan.

Project Test Plan	
Corrosion	Full Vehicle
Safety	20 mph side pole 50th male
	38 mph side deformation (SINCAP)
	31 mph IIHS side impact
	20 mph side pole 5th female
	40 mph IIHS 25% small overlap frontal impact
	FMVSS 214 static
Structure/Durability	Hardware Slam
	Dynamic Over Check
	Sag-Set
	Anti-theft
	Static Over Check
	Window Cycle
	Water Testing
	Denting and Oil Canning
Fit and Finish	Appearance
	Noise, Vibration and Harshness

Technology Transfer Path

The direct participation of FCA US LLC, a global OEM, and Tier 1 suppliers Magna, Grupo Antolin North America, and Corning Glass provide a direct path to technology transfer and commercial application. Cost-effective mass reduction of automotive passenger car assemblies, which are compatible with existing manufacturing and assembly operations, are needed to meet Corporate Average Fuel Economy (CAFE) and EPA legislation. The project includes both component- and vehicle-level testing conducted by the OEM, which reduces the risk and timeline of the commercial application.

Results

During FY 2016, the Ultralight Door project team executed the design of a complete driver's side door assembly, which weighs 15.61 kg or 40.35% less than the 2016 baseline production door assembly. The Ultralight Door is based on materials and manufacturing technologies that are commercially available or have been demonstrated for high-volume production applications. The project team continues to evaluate material, process, and design alternatives to achieve the remaining 0.83 kg required to achieve the 42.5% mass reduction objective, as defined in the FOA.

The incremental cost per pound saved associated with the Ultralight Door design is estimated to be $2.59 per pound saved, well below the $5 per pound saved objective also defined in the FOA. Table II.4.B.2 shows the mass characteristics associated with Baseline and Ultralight Door systems.

Table II.4.B.2. Mass Characteristics Associated with Baseline and Ultralight Door systems.

Test Plan	Baseline front door mass (kg)	Ultralight front door mass (kg)	Front door mass reduction (kg)	Front door mass reduction (%)
1. Door-in-white (DIW)	16.95	9.32	7.6	45%
2. Window system/door module	2.85	1.80	1.0	37%
3. Interior Trim	4.31	2.65	1.7	38%
4. Glass	4.12	2.15	2.0	48%
5. Mirror	1.42	1.01	0.4	29%
6. Seals	2.18	1.99	0.2	8%
7. Exterior Handle	0.65	0.12	0.5	82%
8. Latch	0.81	0.50	0.3	39%
9. Speaker	0.96	0.50	0.5	48%
10. Electrical Components	1.27	1.07	0.2	16%
11. Carry over parts (no change)	0.66	0.66	0.0	0%
12. Other	0.46	0.23	0.2	49%
13. Fasteners	0.46	0.41	0.1	12%
14. Adhesives	0.95	0.45	0.5	52%
Total front door	38.03	22.86	15.2	40%

The engineering design effort included several CAE activities associated with structural performance, safety, and durability relative to the baseline production door. Other assessment activities included closing effort, manufacturing feasibility, and cost. Table II.4.B.3 gives the performance results of the Ultralight Door relative to the Baseline production door.

Table II.4.B.3. CAE Performance Results of the Ultralight Door Relative to the Baseline Production Door.

Design Performance Parameters		Status
Structural	Modal	Pass
	Stiffness	Pass
	Strength	Pass
	Abuse	Pass
Safety	Dynamic 214	Pass
	Static 214	Pass
Durability		Pass
Closing Effort		Pass
Manufacturing Feasibility		Pass

The key Magna innovations associated with the development of the Ultralight Door includes functional integration of the DIW assembly, SmartLatchTM, carrier module, glass, hinges, speakers, and interior trim:

- The lightweight carrier module is the result of the unique design and assembly process enabled by the bolt-on Beltline Inner and Beltline Outer structural components.
- Integration of the SmartLatch™ eliminated the need for mechanical hardware and enabled LIN bus control.

- The unique design of the Window System/Door Module resulted in an 11% reduction in glass area and integration of the glass run channels, providing mass reduction and assembly benefits.
- Material selection and design optimization of the design DIW components resulted in an 8.11 kg mass reduction of the door assembly, approximately 52% of the total mass reduction.

Grupo Antolin North America leveraged its know-how relative to the design and manufacture of interior trim components, integrating the additional functional requirements imposed by the electronic latch and lightweight door module. Their application of advanced molding technologies, polymers, and joining technologies contributed approximately 10% to the total mass reduction associated with the driver's side door.

The FCA US LLC engineering team collaborated with the Magna team throughout the development process to insure compatibility with existing assembly operations:

- FCA US LLC developed lightweight cast aluminum door hinges and lightweight neodymium magnet speaker components, which resulted in a 0.76 kg mass reduction.
- FCA US LLC conducted CAE durability, fatigue and safety analysis associated with the Ultralight Door to insure functional equivalence to the Baseline door.
- FCA US LLC conducted component- and vehicle-level testing of prototype door assemblies and full vehicles to validate the results of the CAE predictive simulation.

The DIW construction includes various grades and forms of aluminum, including a vacuum die-cast A-Pillar Support, extruded Upper Support, and stamped Inner Panel, Outer Panels, and Door Beam. Material grade, gauge, and cross-section geometry were optimized to achieve structural, safety, and durability requirements. Figure II.4.B.1 shows the schematic details of the DIW subsystem.

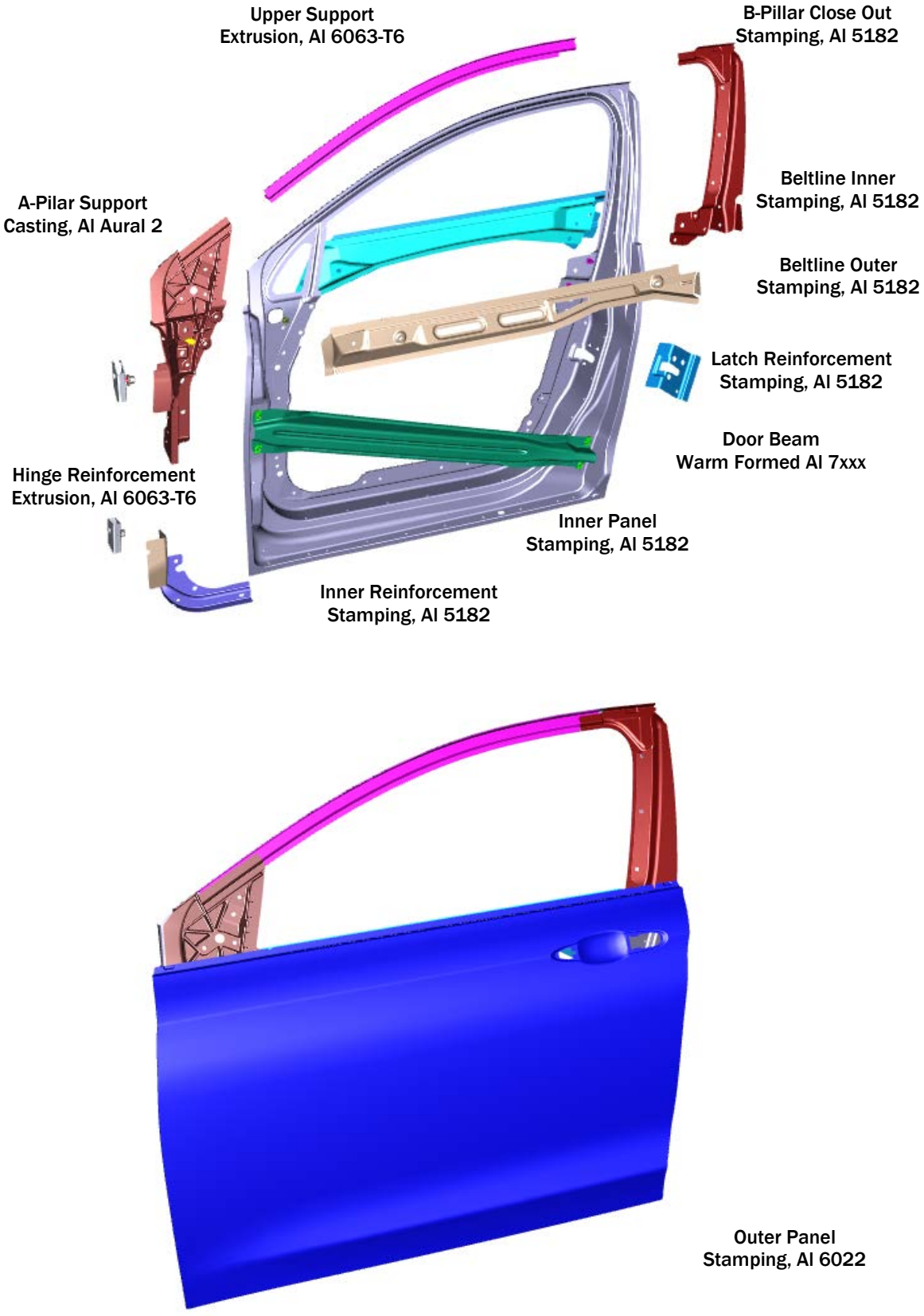

Figure II.4.B.1. DIW subsystem resulted in 8.11 kg mass reduction. Source: Magna International.

The Interior Trim subsystem, as shown in Figure II.4.B.2, was developed by Grupo Antolin North America. Lightweighting was achieved through part integration and the application of advanced molding technologies and materials. The interior trim includes functional integration of the SmartLatch™, Door Module, and DIW subsystems.

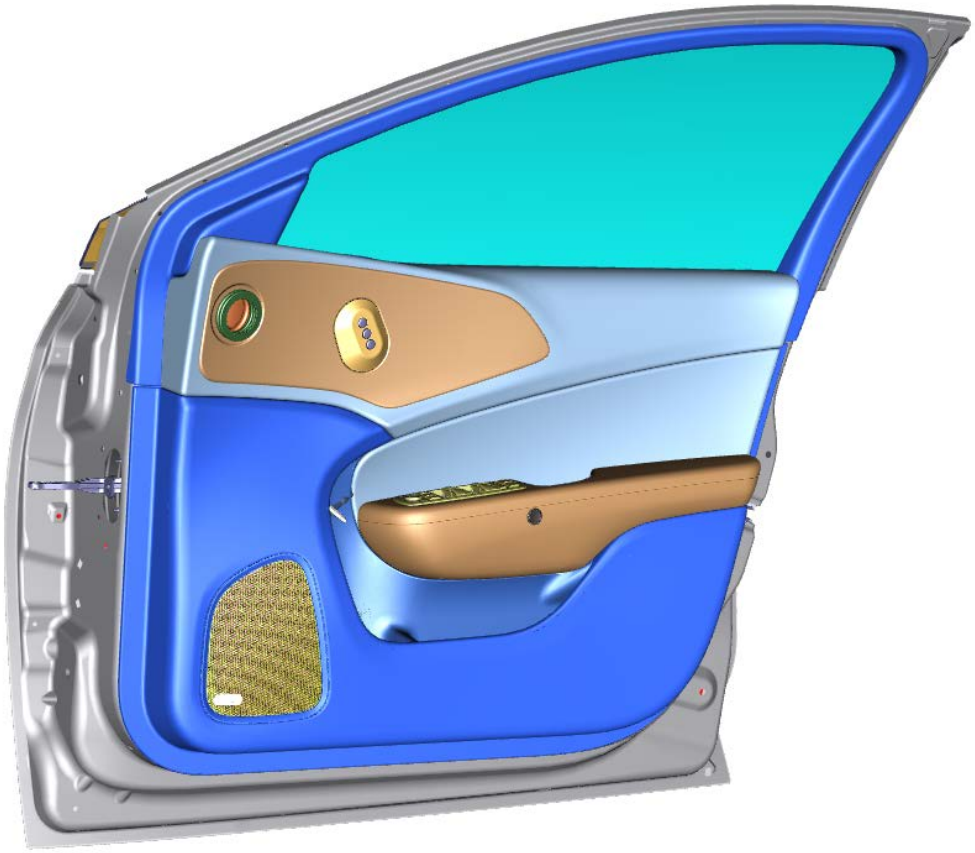

Figure II.4.B.2. Interior trim subsystem resulted in 1.57 kg mass reduction. Source: Magna International.

The side glass developed by Magna includes the application of a Corning® Gorilla® Glass laminate, as well as a 11% reduction in surface area enabled by the Carrier Module, as shown in Figure II.4.B.3. The SmartLatch™ developed by Magna includes the application of an electronic latch and lock, as shown in Figure II.4.B.4. The elimination of replacing the mechanical latch hardware enables application of the Carrier Module. The entire lightweight door assembly is shown in Figure II.4.B.5.

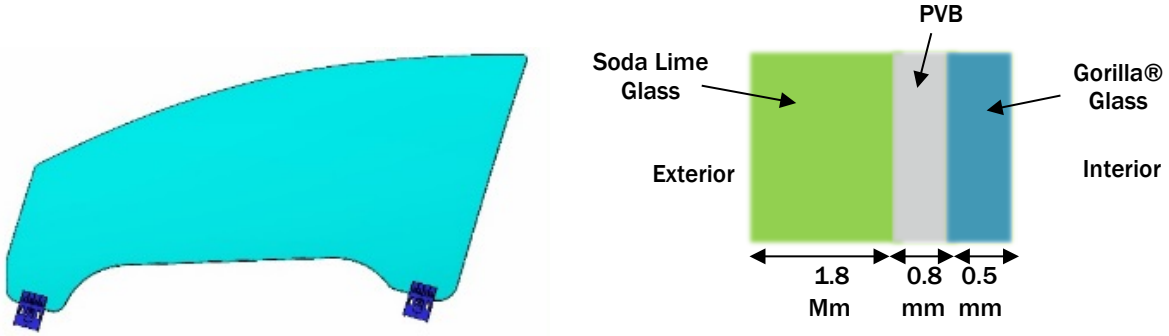

Figure II.4.B.3. Side glass resulted in 1.97 kg mass reduction. Source: Magna International.

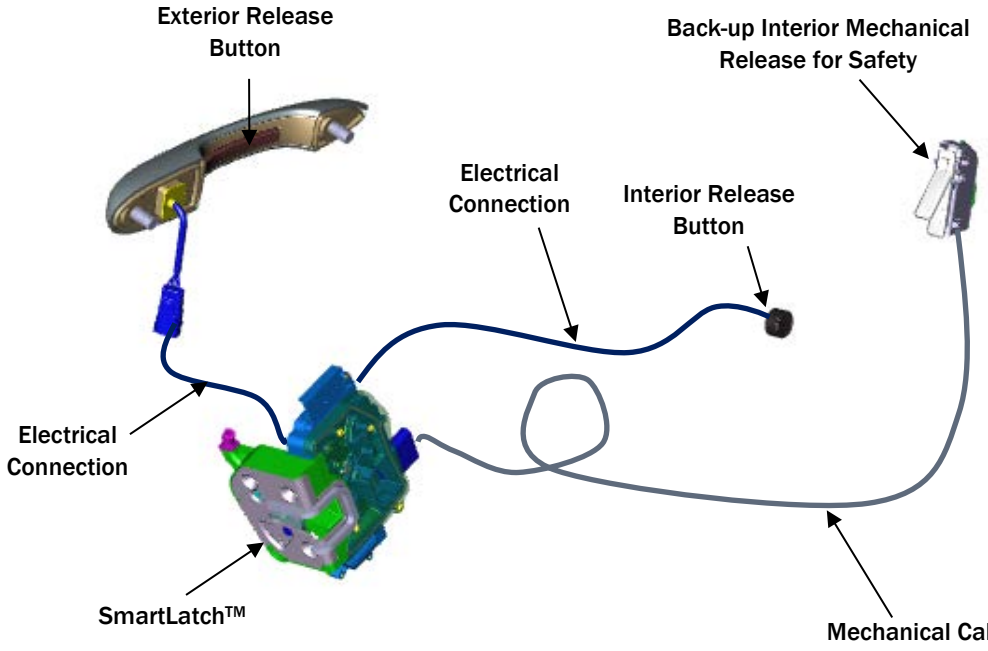

Figure II.4.B.4. SmartLatch™ and Exterior Handle resulted in 0.86 kg mass reduction. Source: Magna International.

Figure II.4.B.5. Entire lightweight door assembly. Source: Magna International.

Conclusions

The Ultralight Door development conducted by Magna's advanced engineering team, FCA US LLC, and Grupo Antolin North America in FY 2016 and FY 2017 demonstrates the feasibility of reducing the mass associated with a driver's side door by over 40% relative to a 2016 Baseline production door. During FY 2017 through FY 2018, the project includes full-vehicle safety, durability, and corrosion testing to enable high-volume commercialization of the technologies at a known cost and relatively low risk.

II.4.C Ultra-Light Hybrid Composite Door Design (TPI Composites, Inc.)

Nathan P. Gravelle, Principal Investigator
TPI Composites Inc.
373 Market St.
Warren, RI 02885
Phone: 401-247-4071
E-mail: ngravelle@tpicomposites.com

Carol Schutte, Technology Manager
E-mail: carol.schutte@ee.doe.gov

Start Date: December 1, 2015 End Date: November 30, 2018
Total Project Cost: $5,974,505 DOE share: $2,969,193 Non-DOE share: $3,005,312

Executive Summary

This project is developing a comprehensive systems approach for designing, manufacturing, and demonstrating an ultra-light hybrid composite automotive door. Composite structural components are integrated with other functional systems to reduce part count and full-system weight by a minimum of 42.5%. The approach will be demonstrated on a driver's side front door and will consider all fit, functional, safety, and cost requirements. Materials (i.e., fast-curing infusible epoxies developed by Hexion, non-crimp fabrics by Saertex, and acoustic foam/sealants/adhesives by Creative Foam) and processes (i.e., high-pressure resin transfer molding [HP-RTM] implemented by Krauss Maffei) will be demonstrated to meet the production rate and performance requirements established by the vehicle's OEM (i.e., an approximate four to five-minute cycle-time is required to meet annual production rate). TPI's expertise in system design and as a Tier 1 supplier will be complemented by the University of Delaware Center for Composite Materials (UD-CCM)'s modeling and simulation capabilities for HP-RTM, material response, and side-impact crash modeling of composites. Our team will use a systems approach for establishing door requirements, including geometry, environmental, structural, durability, and crash performance; assembly to vehicle structure; consumer preference (i.e., noise, vibration, and harshness); and weight and cost to meet or improve the metallic door. Concepts will be developed and include material selection and composite layups, geometries, light alternative glazing materials, and integration approaches to meet all requirements. These concepts will be evaluated using structural and crash simulations and linked to a manufacturing feasibility study, resulting in producible designs of an integrated door system. A cost model will evaluate part of the cost for the various designs and will ensure the cost target of less than $5 per pound of weight saved is met. Hybrid composites consisting of carbon, glass, and metal components will be included in our trade-off studies to satisfy these cost and performance goals.

The front-side driver's door consists of about 50% structural steel components (i.e., outer and inner sheet-metal panels, window frame, local steel reinforcement, fasteners, and hinges). Non-structural plastic molded panels and trims (about 15% of total weight) are attached and allow integration of subsystems such as speakers and controls. The remainder of the weight is the side window and mirror system (about 20%) and other components (e.g., sealants, lock, speaker, and others). Replacement of the steel parts and molded panels with carbon fiber-reinforced composites offer between 60 to 70% weight reduction potential over steel (i.e., 20–30% for glass fiber-reinforced composites will be designed to meet total weight reduction goals (Sloan 2012). A hybrid glass/carbon composite at 48% weight reduction could reduce the cost of the composite structure and meet the FOA goal through additional part consolidation and another component lightweighting. Geometries will need to be optimized to allow manufacturing feasibility and other materials can be strategically incorporated to allow improved structural performance coupled with other functionality (such as noise or vibration control). Fastener weights can be reduced through parts consolidation, co-molding, and adhesive bonding while improving durability and reducing secondary assembly steps that add to cost.

Accomplishments

- Requirements for the door were agreed upon.
- Computer-aided design data transferred.
- Finite element analysis model generated, both steel baseline and composite models.
- Laminate optimization completed.

Technology Assessment

- Target: Reduce part count and full-system weight by a minimum of 42.5%.
- Gap: Current materials and methods utilize steel as the main structural component, adding mass to the overall structure, thereby reducing the vehicle fuel efficiency.
- Target: Cost increase will not exceed $5 per pound of weight saved.
- Gap: One of the major lightweighting materials at our disposal—carbon fiber—is upwards of $10-15/lb. This material must be used judiciously to meet cost targets.
- Target: Materials and processes will be demonstrated to meet the production rate and performance requirements (an approximate four to five-minute cycle-time is required to meet annual production rate).
- Gap: Standard composite manufacturing processes can process these parts at a cycle time of about one hour per part. New injection technologies and resin formulations have opened the possibility of faster cycle times.

Project Introduction

New CAFE regulations require improved fuel efficiency of the future vehicle fleet. Weight reduction is key to achieving these targets. Replacing metallic body and chassis components with carbon fiber-reinforced composites offers the most weight reduction potential at up to 70%. Introduction of the BMW i3 and i8 in 2014 required mass production processes to meet 20,000+ units per year. Preforming with HP-RTM has been implemented and meets rate, cost, and performance requirements. Our team members, Krauss Maffei, Hexion, and Saertex were extensively involved in technology development (i.e., manufacturing, materials, and preforming) with BMW and brought this experience to our team, led by TPI, the vehicle OEM, and UD-CCM. We will advance these technologies to develop an ultra-light driver's side door for the vehicle with production rates of 80,000 units annually per plant in Detroit, MI.

TPI has over 40 years of experience in the design, testing, prototyping, and production of lightweight composite structures and is leading the team of industry and academic partners with knowledge in all aspects of vehicle design and composite materials. The OEM will provide system requirements, integrate the ultra-light door into the vehicle, and validate the design during vehicle testing. Krauss Maffei, Hexion, Saertex, and Creative Foam will demonstrate their next-generation material and process solutions, while UD-CCM is world-renowned for their composite expertise in all aspects of composites research and development. The team will implement the new composite door design and evaluate integration and manufacturing challenges to meet automotive rate and cost targets.

Approach

Development of a vehicle BIW is a very complex and time-consuming process because various, often-conflicting, functional requirements must be considered. Introducing new designs to reduce vehicle weight requires a systems approach where new designs can be quickly iterated and refined to evaluate their performance. This is particularly true when metals are replaced with composite materials because composite

materials have significant potential to reduce weight when designs are fully optimized for parts consolidation and engineered properties using a variety of available material, fiber layups, and processing choices.

A typical automotive door is made from a combination of materials, including steel, plastic, and glazing. The structural materials are heavy, while the non-structural components do not contribute significantly to structural performance. Elements are joined together, increasing manufacturing and assembly cost and weight. We propose to replace all structural parts of the front-side driver's door with continuous reinforced composites (with a weight savings of up to 60%), reduce part count and system weight through part consolidation, and evaluate alternative glazing materials. This approach has the potential to meet and exceed the goals of 42.5% system weight reduction as compared to the steel door baseline and to meet cost targets of $5 per pound weight saved. The team will take a systems approach to meet the targets, as seen in the flow diagram in Figure II.4.C.1.

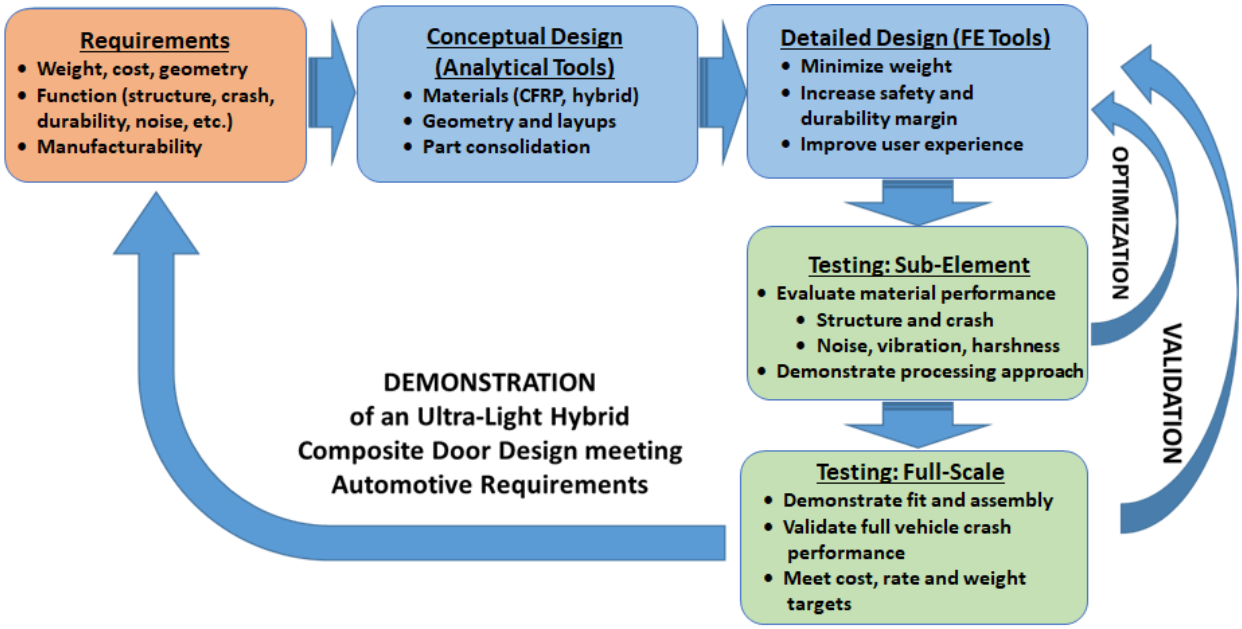

Figure II.4.C.1. Systems approach for reducing weight in complex automotive structures.

This approach relies on the use of computational engineering analysis and simulation tools combined with sub-element testing to rapidly develop and evaluate design changes while full-scale testing is used to proof out the final design. The program will define the design requirements (such as weight and cost targets), functional and topology constraints, and consider the ability to manufacture the door at the required rate and performance. Cost; structural; crash; noise, vibration, and harshness; and manufacturing simulations exist and will be utilized. These individual simulation tools are state-of-the-art, commercially-available, and have been validated on numerous occasions. Conceptual designs will be evaluated at the sub-element level to evaluate material performance (i.e., structure; crash; and noise, vibration, and harshness) and to demonstrate that the processing approach meets rate and quality targets. Full-scale test articles will be manufactured to validate form, fit, function, and cost of all integrated structural and non-structural components. A small number of design iterations may be required to optimize the various configurations. The approach will allow: (1) a shortened design cycle, resulting in reduced development time and costs; (2) elimination of trial-and-error process and part trials reducing tooling and manufacturing costs; and (3) an optimum door configuration at minimum weight leading to a more cost-competitive product. The overall approach will be demonstrated on a composite door solution for the vehicle, but it is also applicable to a wide variety of automotive components. The comprehensive systems approach for designing, manufacturing, and validating a complex ultra-

lightweight composite automotive component using a validated, multi-disciplinary design tool with a small number of manufactured components for validation will reduce risk to convert metal structures to composites.

Predictive engineering tools guide material and design down-selection and are critical for eliminating trial and error and reducing cost and time. Figure II.4.C.2 shows the design environment the team will employ to evaluate the composite door structure.

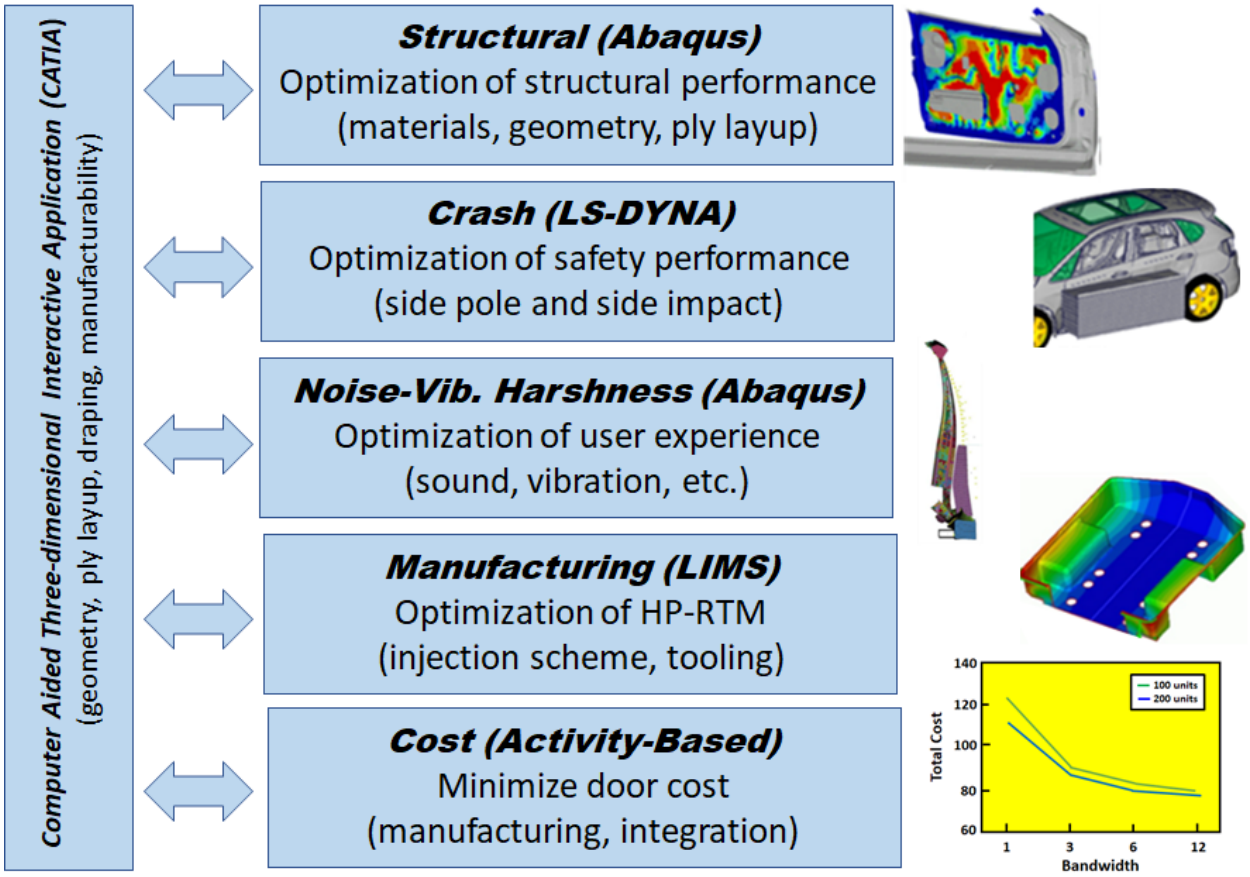

Figure II.4.C.2. Integrated predictive engineering environment. Source: University of Delaware.

Dassault System's computer-aided three-dimensional interactive application (CATIA) product design solution is our product development platform that easily communicates with other simulation tools. This enables multiple disciplines to share geometry, ply layup, and manufacturing-induced fiber orientations. Thus, designs are developed in one environment and then evaluated in the specialist applications across all phases of the product development process. For example, an important aspect of composite manufacturing is the effect of draping the fiber layer onto the mold surface, resulting in changes of the local fiber orientation. This can affect the infusion behavior during resin injection and the structural and crash performance of the final part. Our approach captures manufacturing-induced variations in the design and feeds these properties into all sub-models. Another example is potential sandwich constructions where the design not only improves structural stiffness, but also noise attenuation (improving ride experience) with novel foam solutions. Integration of other non-structural functional door items (e.g., speakers, glazing, and electronics) are captured in the design and are fed into the appropriate models and concepts.

The existing vehicle steel door is used as a baseline and the ability to reduce part count with a composite structure will be investigated. Part consolidation reduces weight and cost because a smaller number of parts

must be manufactured. Assembly time and associated labor costs can be significantly reduced as well. The HP-RTM process allows complex geometry part fabrication, which enables integration of features into one component. Figure II.4.C.3 illustrates the potential part count reduction of a steel door with an equivalent composite structure. Part count reduction alone will not be able to meet our weight reduction goals of 42.5%, but in combination with hybrid and/or carbon fiber-reinforced composites material replacement and lower weight window solutions, it will reduce the weight of the door structure to the required levels.

Figure II.4.C.3. Composites allow part consolidation, which further reduces cost and weight (Sloan 2012).
Source: http://www.compositesworld.com/articles/auto-composites-quest-one-minute-cycle-time.

Our hybrid solution will evaluate a variety of material solutions, including glass and carbon fibers. Fiber modulus and strength depend on the fiber selection with specific properties being the highest for carbon fibers. Design solutions without cost consideration will use 100% carbon fibers and provide the best structural performance at the lowest weight. A hybrid design will incorporate alternative fiber solutions at a lower cost and meet structural performance. Our optimal design will consider all options and will meet structural requirements and cost and weight targets.

Lower-density glazing (such as polycarbonate glazing) has been recently developed for automotive applications. Transparent polymers can be easily molded into complex shapes, and it offers a 50% weight savings compared to standard glass solutions. The new materials have been demonstrated in both concept and production cars, including the Chevrolet Volt, Hyundai European Design concept cars, the Mercedes SMART, and Toyota V (station wagon version of the Prius) vehicles (Motavalli 2011). New window solutions also address the requirement for improved cabin comfort. Because glazing thicknesses have been reduced to save weight, the noise level within the car has increased. Integrating transparent acoustic layers within the glazing can be used to increase damping performance and thinner and lighter-weight glazing can be employed without compromising cabin comfort or safety. Polycarbonate glazing enables new design concepts because complex geometry windows can be fabricated. Polycarbonate glazing with integral ribs lock the parts onto the vehicle or support other features. This program will evaluate a polycarbonate solution, which should not only impact the weight of the glazing, but the overall design of the composite door solution. This will simplify assembly and have the potential to lower the cost and weight of the total door solution.

All considered concepts will be evaluated at the component and full-door level using structural finite element analysis tools. The composite laminate structure can be varied and will change the anisotropic stiffness and strength behavior of the part. The selection of fiber materials will impact performance and cost. Optimization of the layups, materials, and geometries needs to result in a manufacturable design at minimum weight while meeting all design requirements. The team has significant experience in design and analysis using

commercially available structural static and dynamic finite element analysis tools for vehicle structures that will be key for evaluating and optimizing the designs.

Crashworthiness will be evaluated using LS-DYNA, allowing simulation of the door and full vehicle under dynamic conditions. We will consider the crash performance under side impact meeting FMVSS 214's protection requirements (other FOA crash scenarios will be considered). The simulation will evaluate inward deflection as a function of time during impact for the baseline steel door and our composite solution. A conservative design goal would require the composite solution provide a deflection profile that stays below the transient intrusion levels of the steel baseline door. This would ensure the safety mechanisms (such as the side airbag) are able to be deployed in time and space and the passenger is protected in case of a side collision. UD-CCM has significant experience with crash predictions and under a current NHTSA program evaluates composites for a steel B-pillar replacement. Strain-rate-dependent material properties for composites are available; however, additional properties for the HP-RTM resins and fibers may have to be determined using coupon and sub-scale element testing. The test data will provide the programs with a database of material properties for crash designs.

The program will implement the HP-RTM process to fabricate sub-elements and full-size components. The process has been proven to produce Class A finished structural components at automotive rates. Cycle times of less than ten minutes have been demonstrated in production on the BMW i3 and i8; this program will further reduce cycle-time and performance using the most recent advances in resins and reinforcements developed by our team members (i.e., a four to five-minute cycle-time would meet current vehicle production rates). Our partner, Krauss Maffei, has implemented a production cell to automate the process. Structural components, sidewall panels, floor pans, front-end carriers, crash boxes, and carbon fiber design components are applications that have been implemented via HP-RTM. Fiber mats or fabrics are preformed and then positioned in the mold. A variety of low-viscosity polymers (such as polyurethane, epoxy, and polyamide) can be used as matrix material. The material components are mixed and heated in a metering system and injected into the heated mold. The resin quickly cures in the closed tool and the part can be demolded. Trimming occurs onsite. The HP-RTM process can produce parts with fiber content up to 70%. The process allows reuse of scrap material, improving material yield. Components manufactured using high-pressure RTM exhibit Class A surface quality and can produce high-quality (low-defect) parts with an aesthetically pleasing carbon appearance. The procedure has been fully automated and is suited for series production from the manufacturing of preforms up to post-mold processing. The program will use the existing HP-RTM as the baseline process, evaluate opportunities to reduce cycle time through innovative new materials (Saertex and Hexion), and evaluate new process improvements (Krauss Maffei, UD-CCM, and TPI).

New resin materials are currently being developed at Hexion and will be optimized for this program. These resins (e.g., EPIKOTE™ 05475) and appropriate curing agents have low initial viscosity (below 100 centipoise) and allow rapid infusion of reinforcement during the injection phase of the HP-RTM process (Hillermeier et al. 2012). The rheology of the EPIKOTE resin with three different curing agents is discussed in Hillermeier et al. (2012) and shows the ability to control the viscosity profile, while ensuring rapid cure without significant exothermic reaction of the polymer. Recent advances show full property translation and rapid (i.e., snap) cure in less than two minutes at elevated temperature. The low viscosity profile allows reduced injection pressure throughout the infusion cycle, relaxing the requirements of the preform, tool, mixer, and press. This, in turn, reduces preform distortion, cycle-time, and capital cost.

Non-crimp fabrics provide the best fiber property translation and, using multi-axial systems, can be combined in a preform used in the production of large series vehicle components. These preforms are manufactured to the correct geometry and fiber layup, allowing rapid placement of the reinforcement into the HP-RTM tool. This enables minimum cycle-time during the process, paired with the high quality of the final product. It is important to optimize the preform to reduce scrap material and lower material cost. Our partner, Saertex USA,

is the worldwide leader in tailor-made non-crimp fabric materials and they will support development of low-cost preforms for this program.

A key challenge of the HP-RTM is design of the mold and preform to ensure full infusion of the polymer into the reinforcement. Tooling cost is a significant capital expense because applied pressures are high, and the tool is expected to last over the entire production run. UD-CCM is an expert in modeling the infusion behavior in liquid molding of hybrid preforms with complex geometry. The permeability and drapability of the reinforcement, as well as the rheology of the resin, are key material properties and are needed to allow optimization of the injection port locations and resin pressure cycle during infusion processing. We will evaluate the feasibility of the proposed designs to be manufactured and optimize the mold features for successful infusion, eliminating any required tool changes due to resin infusion issues. The program will ensure manufacturability of the proposed concept with HP-RTM and use virtual process tools to optimize tooling and infusion approaches. Tooling cost for HP-RTM is a significant investment and can only be amortized over a large production run. Conventional RTM processing of prototypes with equivalent part properties will be conducted as part of our risk reduction strategy.

The performance of our designs will be evaluated at the coupon, sub-element, and full-door component level. This will include structural performance testing (i.e., static and crash) and other functionalities such as durability to environmental exposures and noise, vibration, and harshness. Our team has existing testing capabilities in these areas and a comprehensive test plan will be developed as part of the program. Coupon testing is needed to characterize the mechanical and micro-structural (i.e., void content and fiber volume fraction) properties of the hybrid composite design made with the Hexion resin and HP-RTM process. Other data (such as durability, acoustical damping, and environmental performance) may need to be generated and may require larger component testing.

Technology Transfer Path

This HP-RTM technology and associated automation, demonstrated by European automakers, can be directly applied to U.S. manufacturers to reach and exceed 100,000 units per year.

Injection technology is the first step, part preforming is the second, and automation the third to ensure good takt times (the average time between the start of production of one unit and the start of production of the next unit) are reached to make this process and its associated capital expenditure worthwhile.

Results

Analysis – Optimization of Design

The designs were started by setting a baseline with an existing steel model, as provided by the OEM for the door. The driving load cases: Vertical Load Rigidity, Check Load Rigidity, Header Loads, and Torsional Loads were set as benchmarks for the design performance, as shown in Figure II.4.C.4.

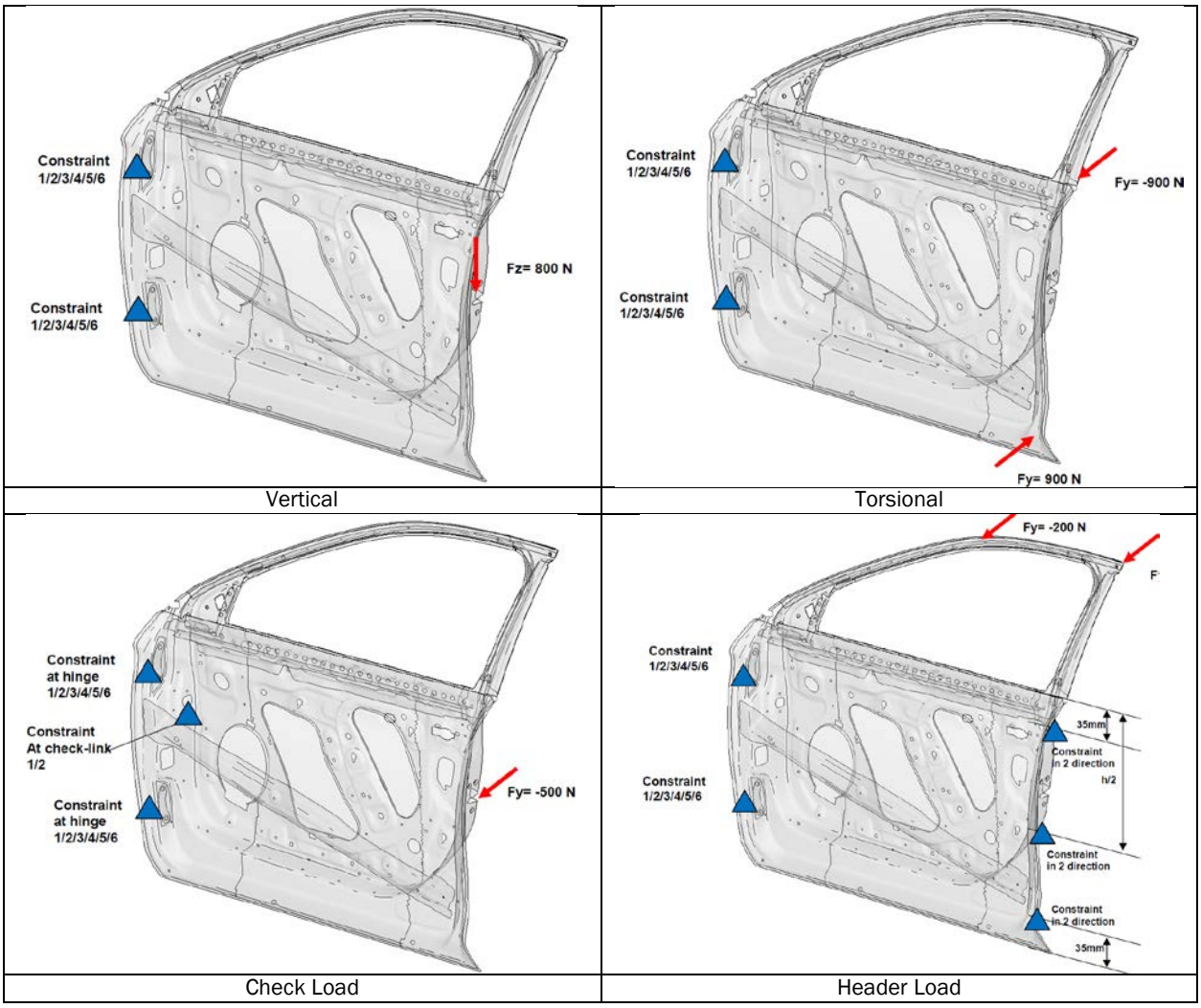

Figure II.4.C.4. Driving load cases. Source: Forward Engineering.

Initially, the design of the door was a stiffness-based design, set to match the maximum deflections of the steel baseline door for each of the driving load cases. This yielded a design that matched the steel design deflection, as shown in Table II.4.C.1, 8.69 kg mass (before adhesive) or a 54% reduction in mass over the steel. Figure II.4.C.5 provides details on the safety factor of the stiffness-based design.

Table II.4.C.1. Stiffness-based Solution.

Load Case	Applied Load	Steel Baseline Deflection	Stiffness-Based Composite Design Deflection Mass: 8.69kg
DIW Vertical Rigidity	800N	-3.3mm	-3.1mm
DIW Torsional Rigidity	900N	-36.6mm	-34.6mm
Check Load Rigidity	500N	-34.0mm	-34.0mm
Header Load	250N	-5.2mm	-4.9mm
	+200N	-5.7mm	-5.5mm

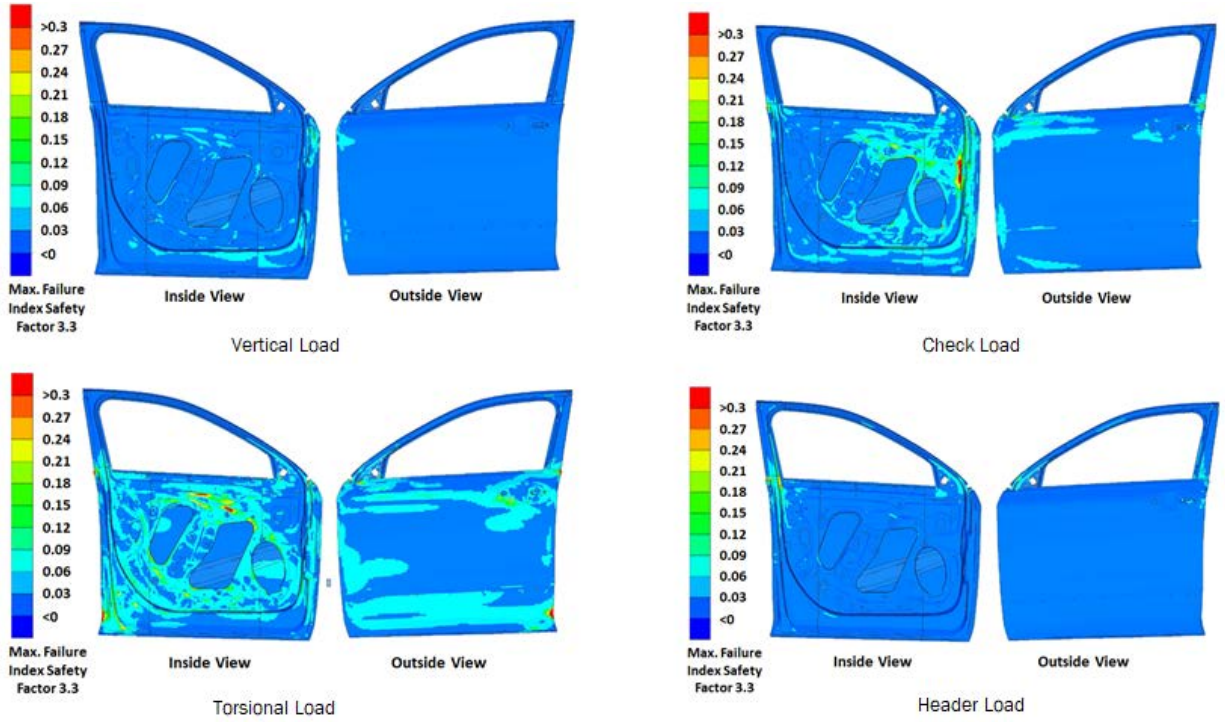

Figure II.4.C.5. Stiffness-based design showing puck failure criteria and safety factor. Source: Forward Engineering.

Looking to further reduce the mass in the design, we questioned the validity of the approach to mimic the steel deflections in the composite design. After some investigation with the OEM, it was determined that there are permanent deflection requirements of the door after loading, not while actively under the load. Therefore, it was determined that an analysis should be completed looking at purely a strength-based approach. First, ply failure criteria for composites was utilized for the analysis review as this considered within the elastic region of a composite. This design yielded a lighter door, 7.26 kg or 65% lighter than steel, but allowed considerably higher deflections, as shown in Table II.4.C.2. Figure II.4.C.6 provides details on the safety factor of the strength-based design.

Table II.4.C.2. Strength-based Design.

Load Case	Applied Load	Steel Baseline Deflection	Stiffness-Based Composite Design Deflection Mass: 8.69kg	Strength-Based Composite Design Deflection Mass: 7.26kg
DIW Vertical Rigidity	800N	-3.3mm	-3.1mm	-5.4mm
DIW Torsional Rigidity	900N	-36.6mm	-34.6mm	-69.6mm
Check Load Rigidity	500N	-34.0mm	-34mm	-81.4mm
Header Load	250N	-5.2mm	-4.9mm	-12.1mm
	+200N	-5.7mm	-5.5mm	-16.9mm

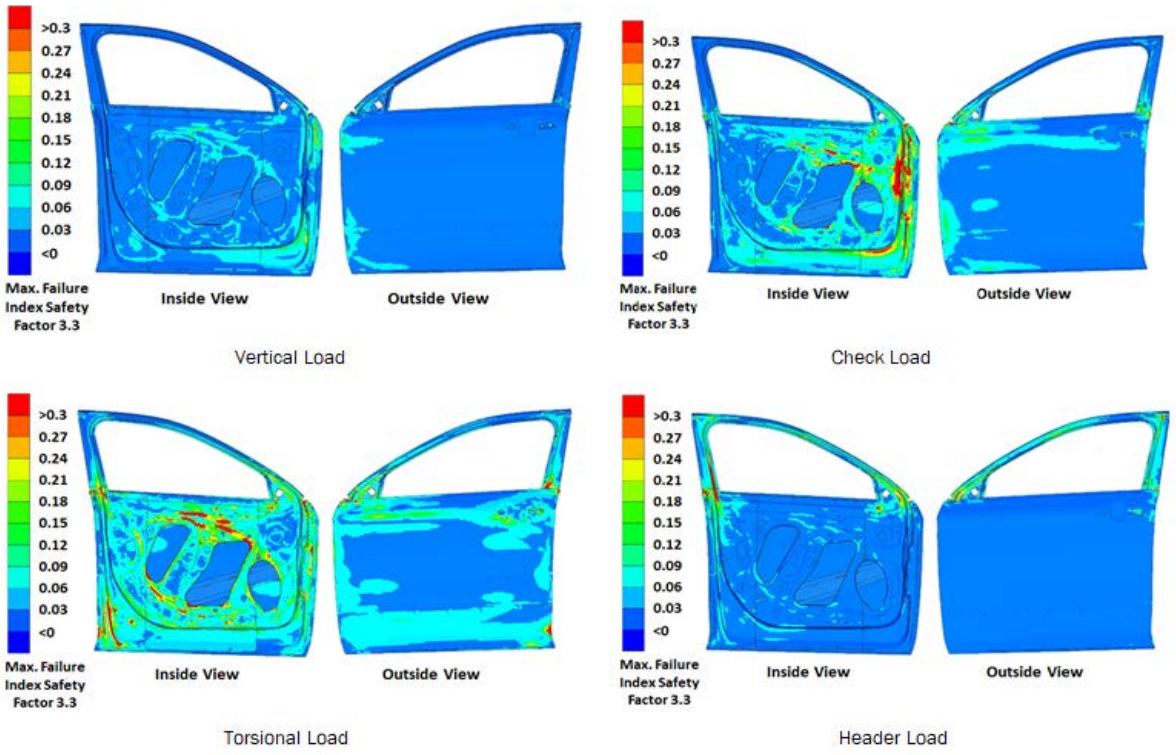

Figure II.4.C.6. Strength-based design showing puck failure criteria and safety factor. Source: Forward Engineering.

These two approaches created "bookends" for the analyses. The stiffness-based approach is considered conservative, while the strength-based approach is considered anti-conservative.

We then decided to take a scientific approach and "split the difference" by targeting an 8-kg solution. During the review of the results, it was noted that the ply overlap mass, as well as the adhesive bond lines, were omitted in the original stiffness- and strength-based summaries. These approaches were included in the next analyses, as shown in Table II.4.C.3. Figure II.4.C.7 provides details on the safety factor of the strength-based design.

Table II.4.C.3. Optimized Composite Design.

Load Case	Applied Load	Steel Baseline Deflection	Stiffness Based Composite Design Deflection Mass: 8.69kg	Strength Based Composite Design Mass: 7.26kg	Optimized Design Mass:8.22kg
DIW Vertical Rigidity	800N	-3.3mm	-3.1mm	-5.4mm	-3.2mm
DIW Torsional Rigidity	900N	-36.6mm	-34.6mm	-69.6mm	-39.1mm
Check Load Rigidity	500N	-34.0mm	-34mm	-81.4mm	-32.4mm
Header Load	250N	-5.2mm	-4.9mm	-12.1mm	-4.4mm
	+200N	-5.7mm	-5.5mm	-16.9mm	-5.5mm

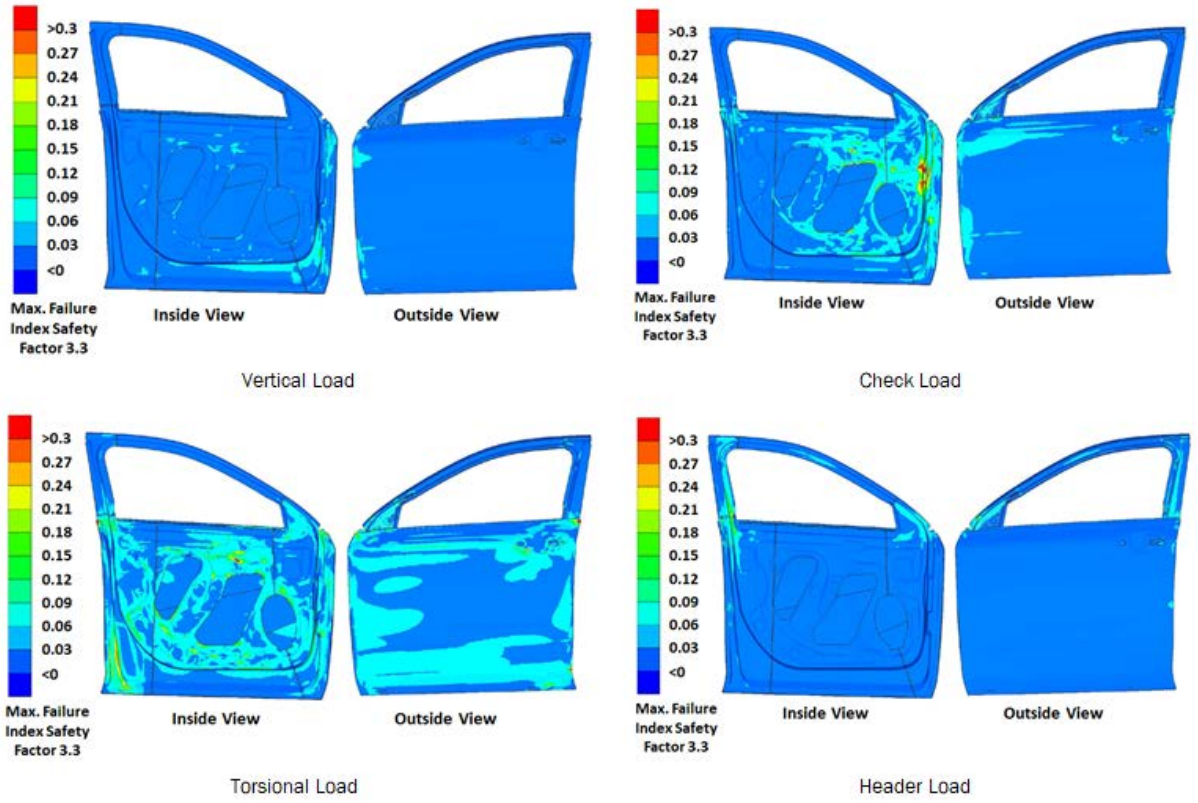

Figure II.4.C.7. Optimized composite design showing puck failure criteria and safety factor. Source: Forward Engineering.

Preform Design

The door inner assembly was segmented into five preforms to ease the drapability of the material over the contours of the door without wrinkling, as shown in Figure II.4.C.8.

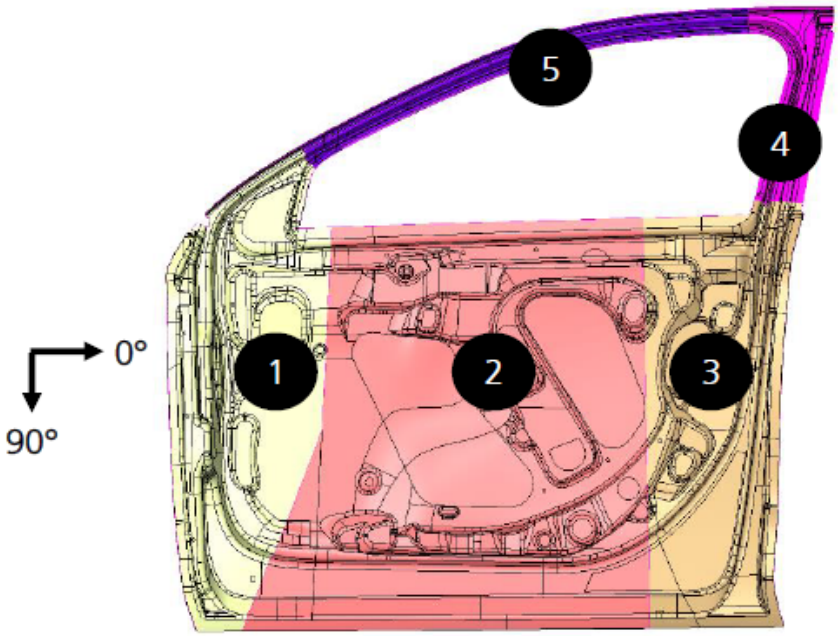

Figure II.4.C.8. Preform separation. Source: Forward Engineering.

This process of validating the manufacturability of a preform is completed using software known as Fibersim. This software simulates the drapability of a fabric to conform to complex curvatures and corners. In this software, a warning and limit angle is set to determine the shear ability (conformability) of the material as it is generally unique for each material. The Fibersim simulation in Figure II.4.C.9 shows the deformation of fiber angles through yellow (warning) and red (limit) angles for each preform.

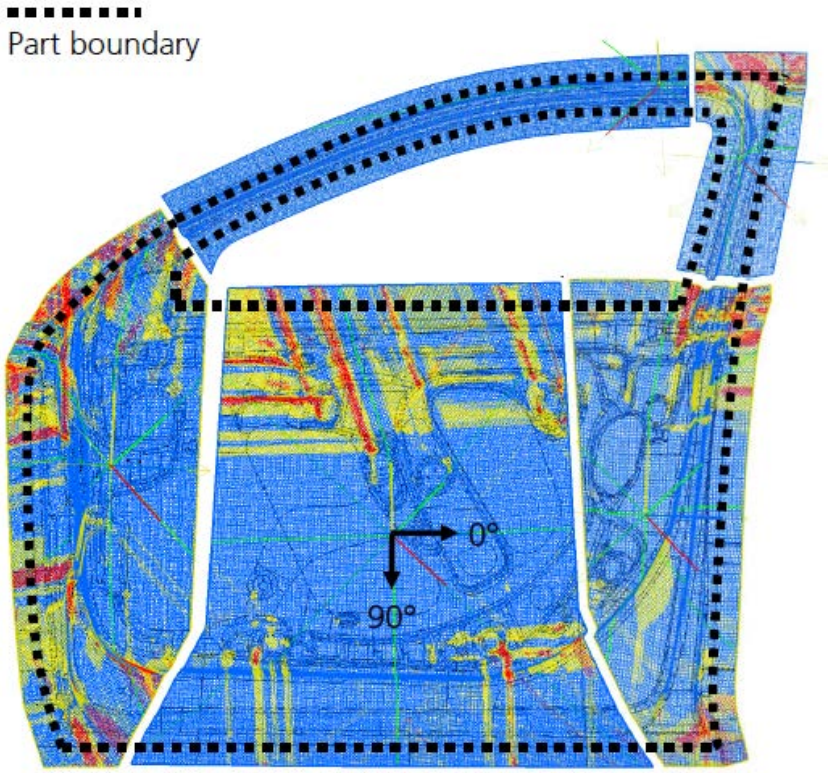

Figure II.4.C.9. Fibersim result. Source: Forward Engineering.

The areas of the preforms with large areas of red prediction require some geometric redesign of the door to reduce those red areas. Figure II.4.C.10 shows a critical area of concern.

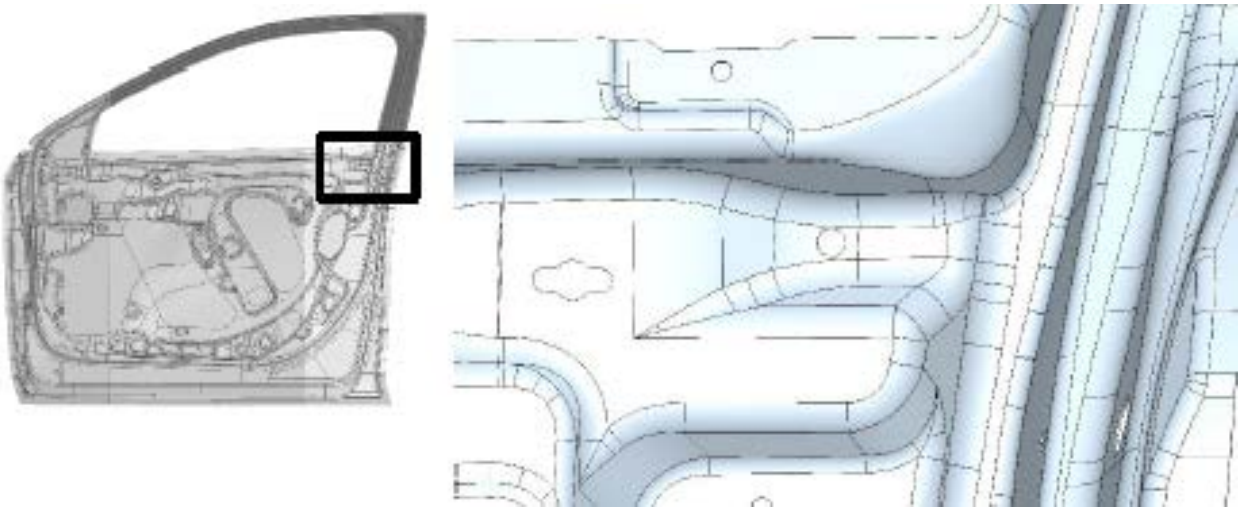

Figure II.4.C.10. Critical corner area. Source: Forward Engineering.

These areas can be smoothed out to reduce the red areas in the simulation, as shown in Figure II.4.C.11.

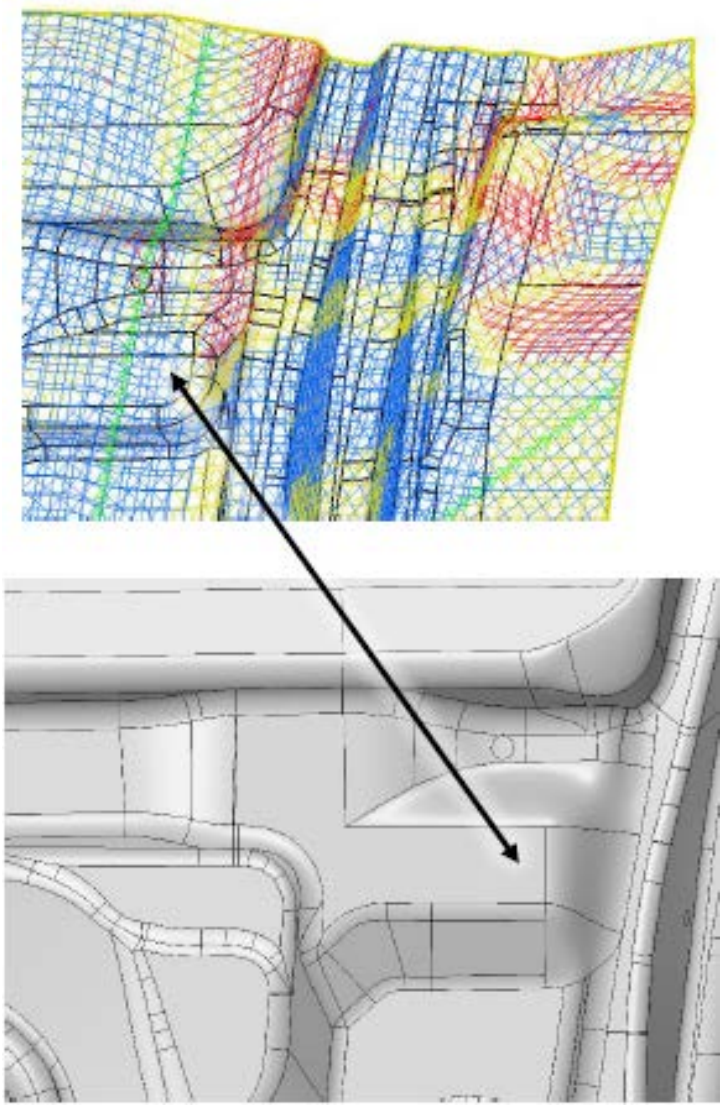

Figure II.4.C.11. Improved geometry for better draping. Source: Forward Engineering.

The analysis results defined the laminate structure for each preform, as seen in the next section.

Dynamic Analysis

The existing door was analyzed in a side pole impact situation for baseline energy absorption requirements. This result plus the cabin intrusion distance for a side pole impact set the requirements for our composite design, as shown in Figure II.4.C.12, Figure II.4.C.13, and Figure II.4.C.14. The hip intrusion point is defined in Figure II.4.C.14, while the deflection in this area for the steel beam is shown in Figure II.4.C.15.

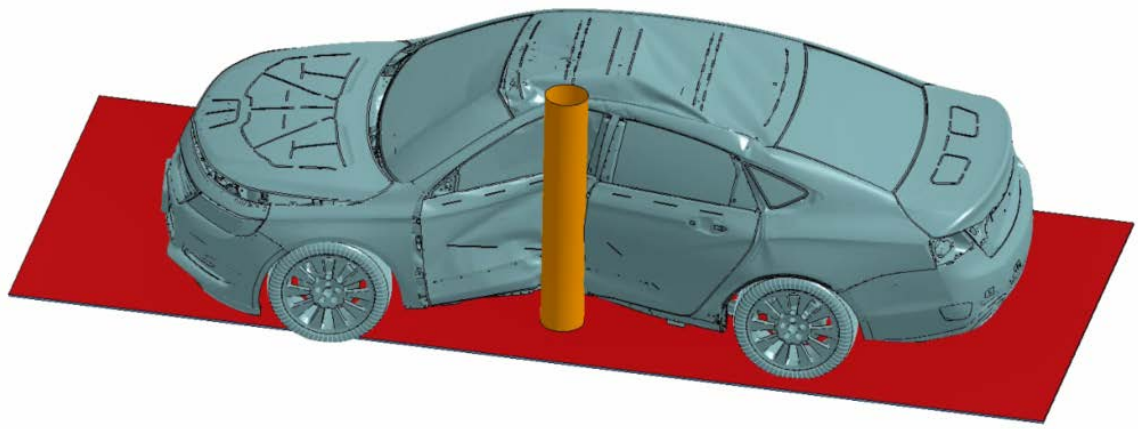

Figure II.4.C.12. Steel door baseline dynamic impact. Source: OEM.

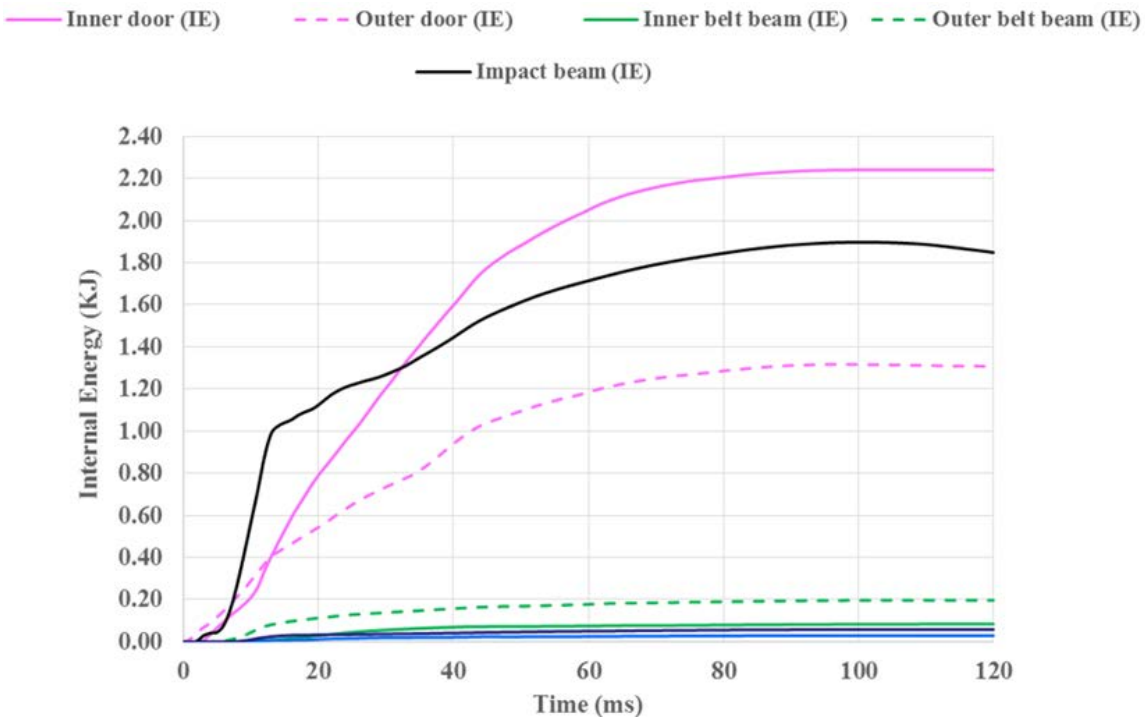

Figure II.4.C.13. Tests of energy being absorbed in the steel door (IE =internal energy).

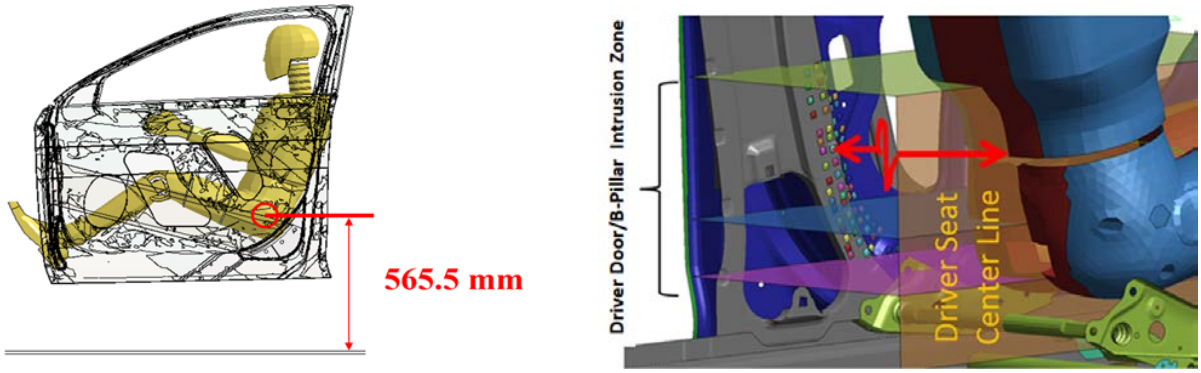

Figure II.4.C.14. Hip intrusion point. Source: Forward Engineering.

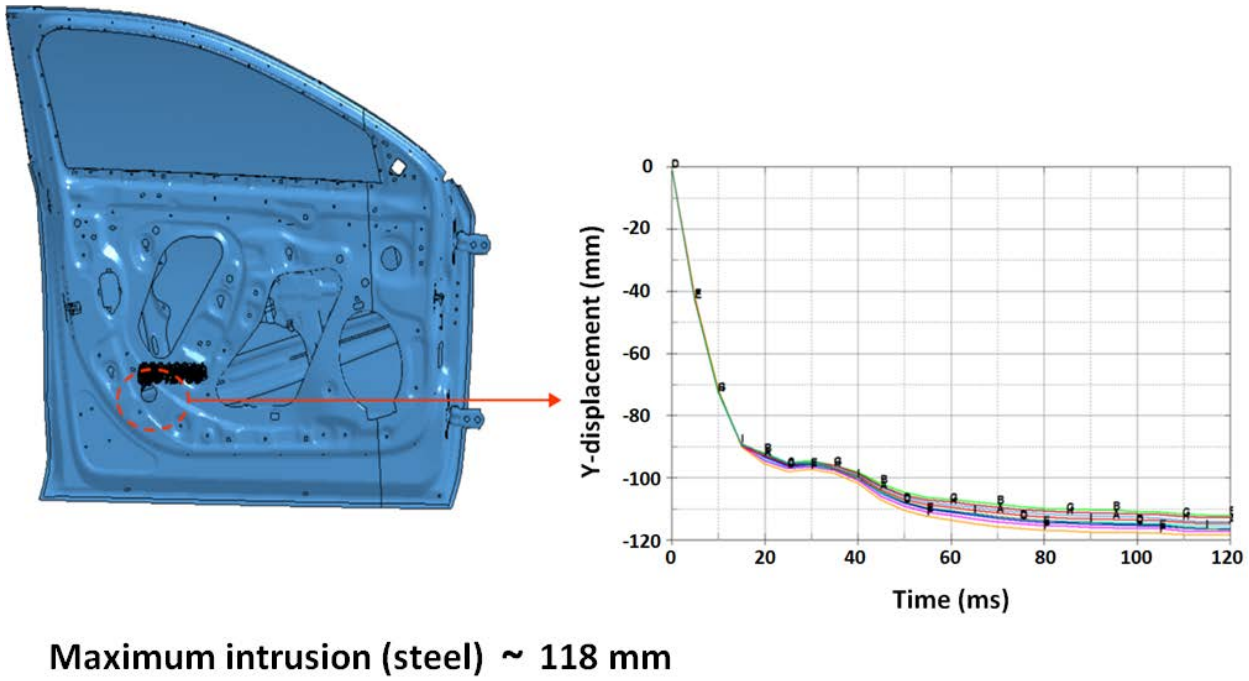

Figure II.4.C.15. Steel door deflection into cabin. Source: Forward Engineering.

Material Model

A predictive material model for composites failure is required to estimate the energy absorbed for each design. A matrix of testing was prescribed, both static and dynamic, to understand the behavior of these materials. The material properties needed for this model are shown in Table II.4.C.4. These test results will feed into the definition of the LS-DYNA Implicit Finite Element code for Dynamic Modelling Material Card to define the progressive damage of the part. The static tests prescribed were conducted on unidirectional coupons made of Saertex Uni Fabric and Hexion Snap Cure Epoxy.

Table II.4.C.4. Material Properties Needed.

Property
Longitudinal Tensile
Longitudinal Compressive
Intralaminar Matrix Tensile
Intralaminar Matrix Longitudinal Shear
Intralaminar Matrix Transverse Shear

Tests were then conducted in a three-point bend manner, as shown in Figure II.4.C.16. Then, a model simulation was created to emulate this behavior, as shown by the blue line in Figure II.4.C.16. The next step from the coupon level is to investigate the behavior in a sub-element model under three-point bending conditions. These trials utilized a hat section with a closeout on the back side, as shown in Figure II.4.C.17.

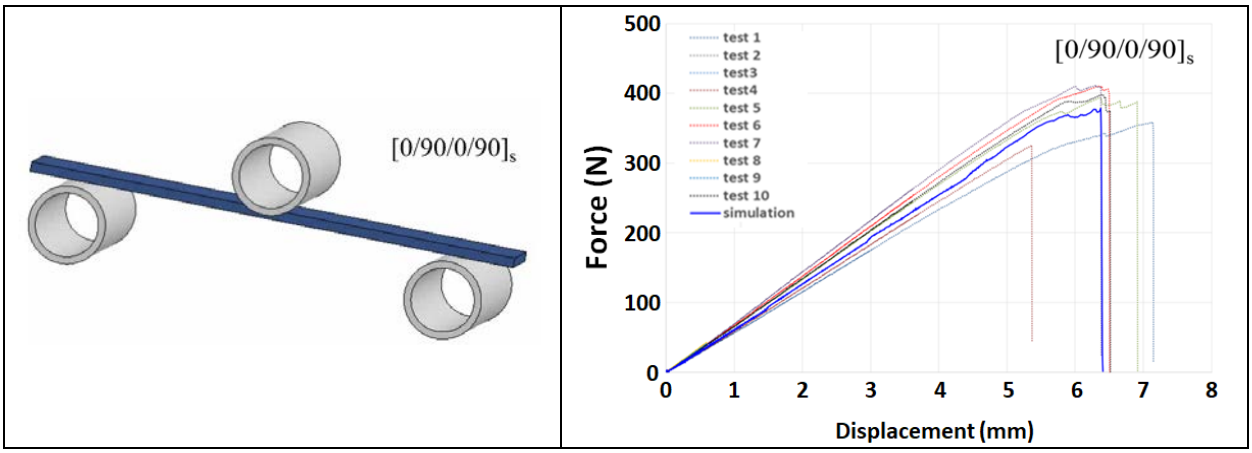

Figure II.4.C.16. Three-point bend test.

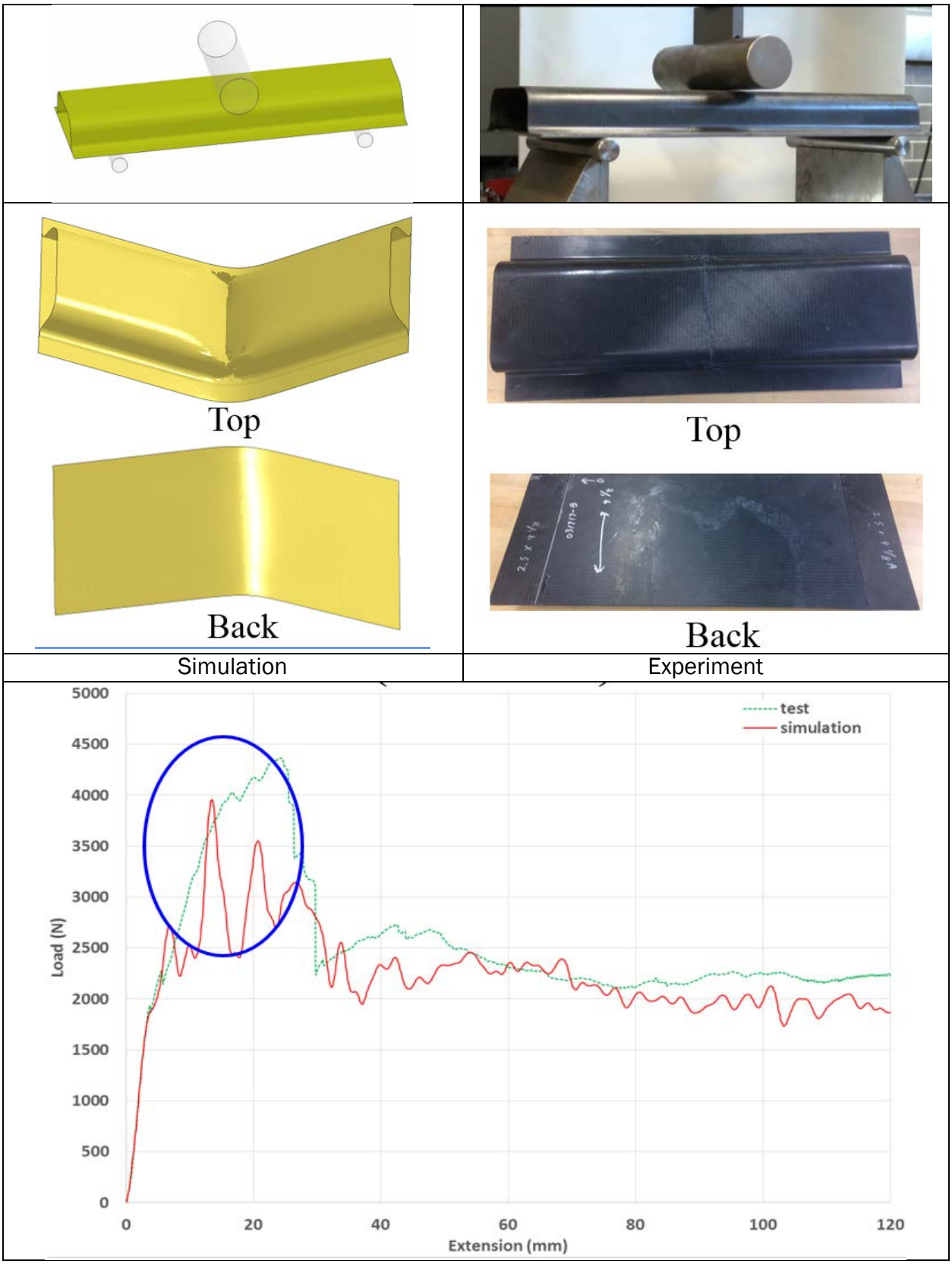

Figure II.4.C.17. Sub-element three-point bend coupons. Source: OEM Partner.

The chart in Figure II.4.C.17 shows decent correlation in the total area under the curves, but it also reveals that some improvement could be made regarding the initial loading/failure. These sub-element coupons laid the ground work for the creation of a fixture to test the full-size intrusion beam prototypes, as shown in Figure II.4.C.18.

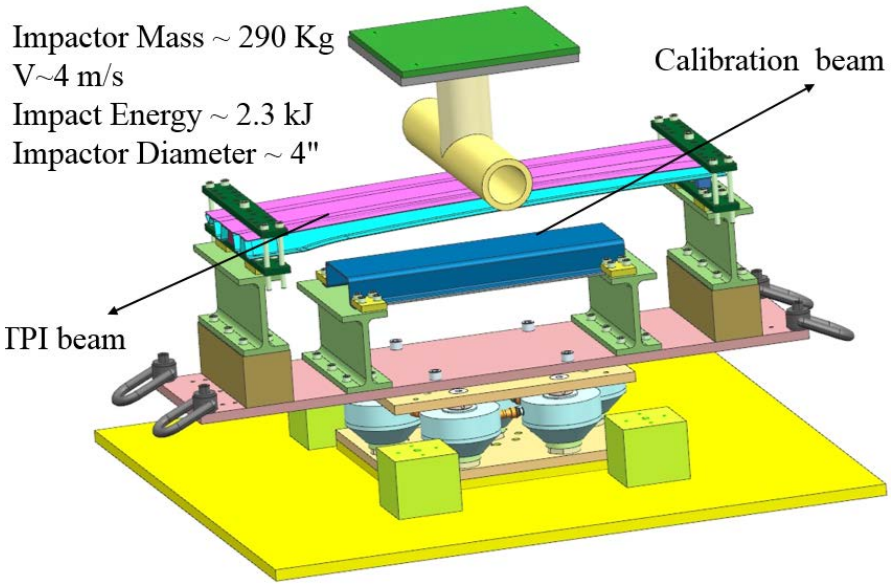

Figure II.4.C.18. Impact test fixture. Source: OEM Partner.

When this fixture was tested, it was determined that the “I beam” supports were not designed for this type of test. The ends of the beam, which are clamped and through-bolted to the fixture, need to rotate to prevent a local failure of the beam at the grips. However, before this fixture, as shown in Figure II.4.C.19, could be tested, the drop tower lab was closed for reasons outside of our control.

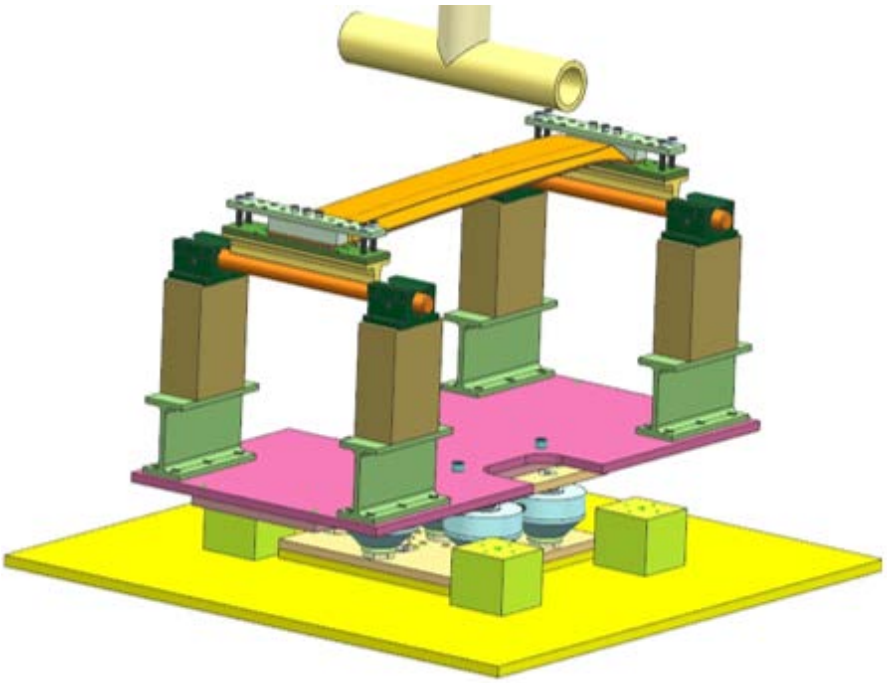

Figure II.4.C.19. Drop tower fixture. Source: OEM Partner.

This brought us to our current fixture-on-a-sled-test-fixture, as shown in Figure II.4.C.20, where a "pole" is attached to a sled and translated with high velocity into the beam. These tests were conducted throughout the month of October, but the results were not available at the time of the writing of this report. Three geometric variants each with two different layups will be tested and compared to the steel baseline.

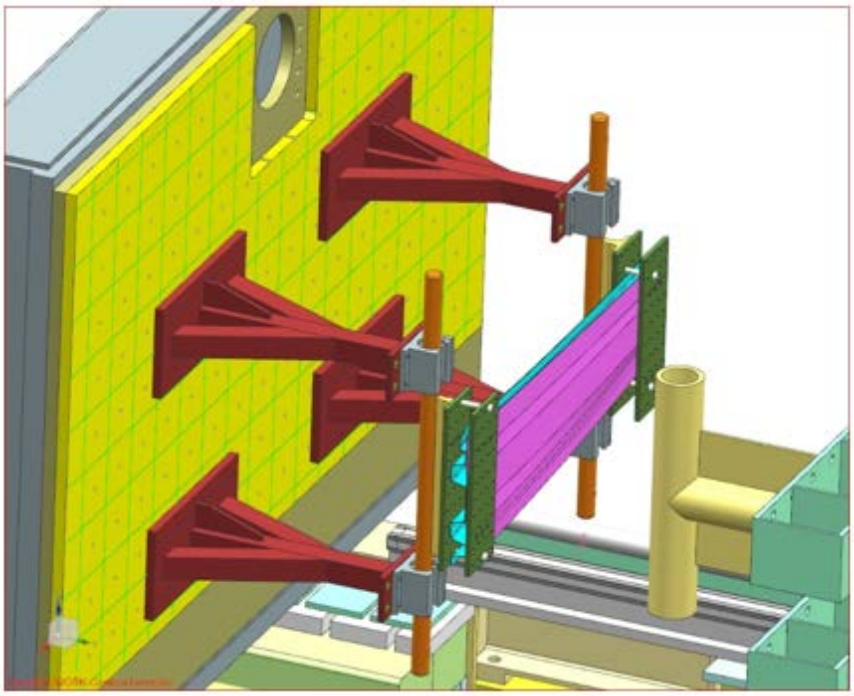

Figure II.4.C.20. Sled fixture to test intrusion beams. Source: OEM Partner.

After these trials are complete, the results and video will be used to further calibrate the material model in LS-DYNA to more accurately predict the behavior of a composite in a dynamic impact.

Design Summary to Targets

The original targets laid out to the program were to save 42.5% of the total mass and to increase the cost by no more than $5/per pound of weight saved, as shown in Table II.4.C.5, Figure II.4.C.21, and Figure II.4.C.22. The design solutions presented in this report represented a cost of $715 per door at a mass of 22.8 kg (or 50.2 lb.). This is a savings of 30 lb. over the existing baseline door design. The cost increase of $138 per part and 30 lb. mass save yields a $4.58 cost increase per pound of weight saved, beating the program target. The total mass saved is 38% going from 36.5 kg to 22.8 kg. This target proves to be more difficult as the total mass of the door is included in this calculation. The window track/motor, latch, hinges, and other sub-assemblies represent 56% of the total mass of the door and they are harder to lightweight than the structure.

Table II.4.C.5. Target Summary.

Property	
Weight reduction	30.12 lb
Percent reduction	38%
Cost increase	$138.33
Dollars/pound saved	$5.48

Component	Cost
Door Structure	$ 50.78
Inner Panel	$ 67.08
Door Mechanism	$ 57.33
Window system	$ 122.37
Sealing System	$ 21.92
Hinges	$ 9.92
Power System	$ 25.00
Molding System	$ 25.69
Mirror System	$ 46.45
Other	$ 150.00
TOTAL	$ 576.54

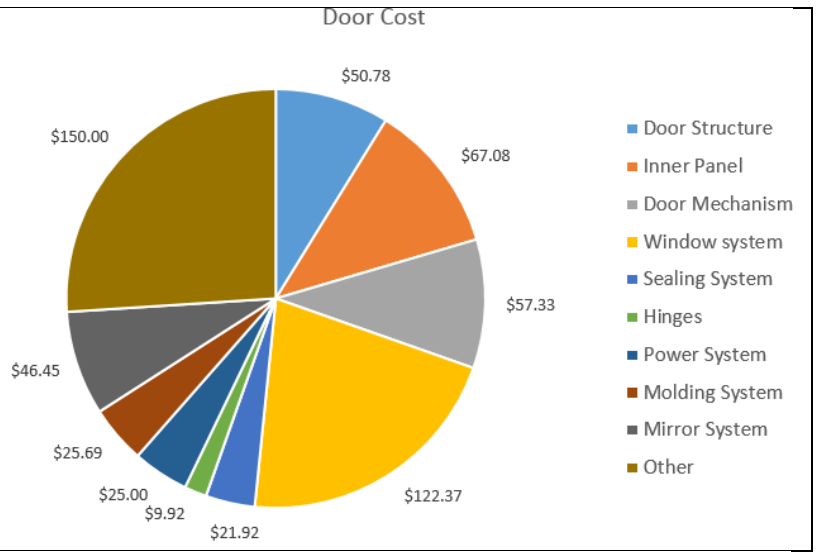

Component	Current Mass [kg]
Door Structure	16.2
Inner Panel	4.1
Door Mechanism	1.7
Window system	5.7
Sealing System	2.6
Hinges	1
Power System	1.1
Molding System	0.9
Mirror System	1.6
Other	1.6
TOTAL	36.5

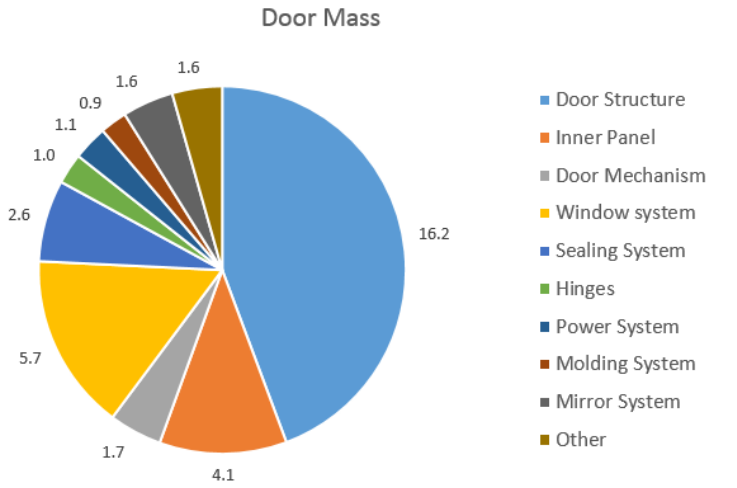

Figure II.4.C.21. Baseline door cost and mass.

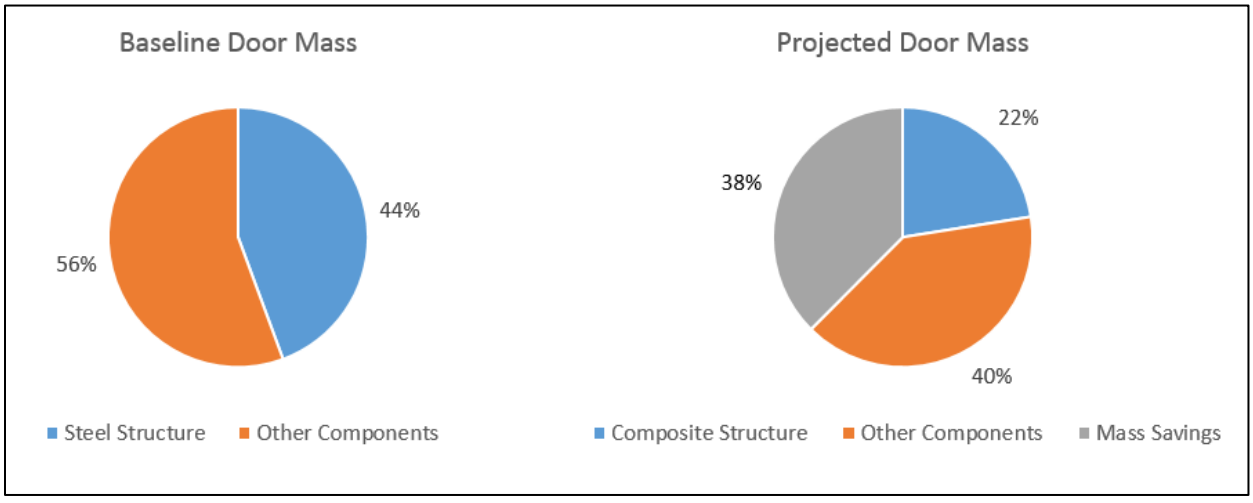

Figure II.4.C.22. Door mass breakdown.

Should the local reinforcement solution presented be realized and the low-cost carbon fiber be commercialized, these numbers could improve to 41.5% mass save and $4.27/ per pound saved.

Conclusions

Year one of this three-year program is nearly completed. We have achieved our major goals of defining the technology gaps and performance requirements. Computer-aided design, loading, and testing requirements (both static and dynamic) were transferred from the OEM and a preliminary design review was completed.

References

Hillermeier, R., T. Hasson, L. Friedrich, and C. Ball, 2013, "Advanced Thermosetting Resin Matrix Technology for Next Generation High Volume Manufacture of Automotive Composite Structures," SAE Technical Paper 2013-01-1176, https://doi.org/10.4271/2013-01-1176.

Motavalli, J., 2011, "Shattering Glass: Low-weight Plastic Car Windows are Coming," *CBS Money Watch* (July), http://www.cbsnews.com/news/shattering-glass-low-weight-plastic-car-windows-are-coming/.

Sloan, J., 2012, "Auto composites quest: One–minute cycle time?," *Composites World* (August), http://www.compositesworld.com/articles/auto-composites-quest-one-minute-cycle-time.

II.4.D Functionally Designed Ultra-Lightweight Carbon Fiber Reinforced Thermoplastic Composites Door Assembly (Clemson University)

Srikanth Pilla, Principal Investigator
Department of Automotive Engineering
Department of Materials Science and Engineering
Clemson University
4 Research Dr., Suite 340
Greenville, SC, 29607
Phone: 864-283-7216
E-mail: spilla@clemson.edu

Carol Schutte, Technology Manager
E-mail: carol.schutte@ee.doe.gov

Start Date: December 1, 2015 End Date: January 31, 2020
Total Project Cost: $5,367,754 DOE share: $2,249,994 Non-DOE share: $3,117,760

Executive Summary

One of most promising routes for achieving the 2025 CAFE standards involves decreasing vehicular weight through the incorporation of lightweight materials, coupled with component redesign to improve overall fuel efficiency. Indeed, one recent study indicates that the simple replacement of current metallic door frames with carbon fiber-reinforced plastic composites can reduce overall weight of the component by nearly 58% (Kelly et al. 2015). The objectives of this project are to achieve a weight reduction of at least 42.5%, as compared to the baseline door structure, at a cost of less than $5/lb while saving energy without compromising the fit, function, crash, noise, vibration, and harshness requirements. The strategy for achieving these targets involves a holistic systems approach through the integration of unique designs, novel materials, manufacturing technologies, and joining/assembly of subsystems to ensure the developed technologies are ready for commercialization.

Accomplishments

- The principal investigators (PIs) arrived at an optimal design via the merging of proposed concepts based on FEA and optimization (FY 2017).
- 150 test coupons of chopped and long fiber thermoplastic composites were manufactured (FY 2017).
- The PIs identified and investigated additional structural requirements for the door under static and quasi-static conditions representing daily use and the FMVSS 214 S test via FEA simulations (FY 2017).
- Based on discussions with the OEM, the team developed cost models to account for manufacturing forms and processes to achieve a production of 20,000 doors per year.

Technology Assessment

- Target: To design, build, and test a complete driver's side front door with all the trim, glazing, and other baseline features at a total weight of 42.5% less than the baseline structure.
- Gap: All current programs for lightweighting door assemblies approach this challenge by focusing on the structural frame with no emphasis on door sub-assemblies, which are approximately 50% of a door's overall weight. The PIs are approaching the 42.5% lightweighting target for the entire door as a holistic module.

- Target: To demonstrate via physical testing that the light door meets or exceeds baseline door performance with respect to noise, vibration, and harshness; fit/finish; structural performance; and performance of creature comforts like speakers and automatic windows (specific metrics are company confidential).
- Gap: As higher mass corresponds to better noise, vibration, and harshness performance, conventional approaches for noise insulation and vibration damping may be inapplicable, thus requiring innovative solutions to manage these deficiencies.
- Target: To demonstrate via cost modeling that the door assembly meets the indicated weight reduction for less than $5/lb of weight saved.
- Gap: Neither OEM's current cost-prediction models for baseline metallic doors, nor conventional cost prediction tools for composite-intensive closure systems, are effective, because production of the lightweight door involves non-traditional manufacturing systems and layouts.

Project Introduction

The objective of this project is to reduce the weight of a door assembly by at least 42.5% as compared to a baseline driver's side front door with an expected cost increase of less than $5/lb in weight saved. A 2013 mid-sized sport utility vehicle's door from our OEM partner with an assumed production volume of 20,000 vehicles annually was the basis for the design. These criteria will either meet or exceed the fit, function, crash, noise, vibration, and harshness requirements of the baseline door.

The intent of the project is to: (1) enable the radical redesign of the baseline door via a holistic systems approach through the integration of unique designs; (2) use novel materials that render the door 100% recyclable; and (3) investigate manufacturing technologies and joining/assembly of subsystems to ensure the developed technologies are ready for commercialization. The partner organizations listed in Table II.4.D.1 are providing highly leveraged knowledge expertise to ensure the success of this effort.

Table II.4.D.1. Project Participants.

Universities	Industry Partners	Computation Partners
Clemson University	Original Equipment Manufacturer (OEM)	Altair Engineering
	Continental Structural Plastics (CSP)	Core-Tech Systems (Moldex 3D)
	International Mold Corporation (IMC)	MSC Software (Digimat)
University of Delaware	BASF, Polyone	LS-DYNA
	Krauss Maffei, Trexel Inc.	
	Corning	

Approach

The project uses a systems-level approach that began with the systematic evaluation and benchmarking of the door and its subassemblies. In collaboration with our partnering companies and commercial suppliers, researchers are evaluating a variety of carbon fiber thermoplastic material forms for structural components (i.e., novel unidirectional and fabric prepregs, co-mingled fabrics, high aspect ratio discontinuous fibers, performance thermoplastic resins, novel fiber architectures, and localized reinforcements) and alternative solutions for glazing, trim, and other subcomponents. The initial focus is on creating the structural component and a materials database for all the parts of the door structural assembly (i.e., outer shell, inner panel, carrier, and anti-intrusion beams).

A two-phase integrated design and manufacturing optimization approach is being adopted to obtain the optimal manufacturing process parameters of the thermoplastic materials and the optimal structural design parameters of the door. The PIs also conducted a top-level trade study to determine at least two candidate designs for optimization. The design parameters will incorporate: (a) thermoforming and injection molding parameters (e.g., pressure and temperature); (b) fiber parameters (e.g., material, length, diameter, and volume fraction); (c) matrix parameters (e.g., material and volume fraction); (d) structural wall thickness; and (e) material density distribution. The research team will use four analysis tools—Moldex3D, Digimat, and LS-DYNA Implicit and Explicit—to construct the manufacturing-to-response analysis pathway (Mi et al. 2013, Chang and Cheon 2006, Yu et al. 2013). The team will fabricate a door based on this optimal design for testing in accordance with OEM performance requirements.

Technology Transfer Path

The design optimization process, coupled with a manufacturing-to-response pathway for computational analysis of proposed thermoplastic composite structures, serves as a conduit for ensuring developed technologies are market-ready to our OEM and different project partners.

Results

Historical Progression of Conceptual Designs

From a conceptual design perspective, the team undertook an iterative process of designing and evaluating several options based on their performance in FEA simulations, weight, scalability, and cost. Figure II.4.D.1 illustrates the different phases that were traversed until the end of year 2. Phase 1 and 2 comprised of basic models that were designed prior to our OEM partners sharing a virtual model of the baseline door. Phase 3 entailed understanding and analyzing the current door geometry and sealing planes culminating in a design workshop comprising all academic partners where seven concepts were hypothesized. Phase 4 involved the development of three distinct designs that encompassed the design ethos of the seven concepts; these were then modelled using computer aided design and were compatible with the current door sealing planes, class A surfaces, and within the current door envelope. These designs were subsequently evaluated based on their performance in FEA simulations, lightweight potential, anticipated cost, and ease of manufacturing.

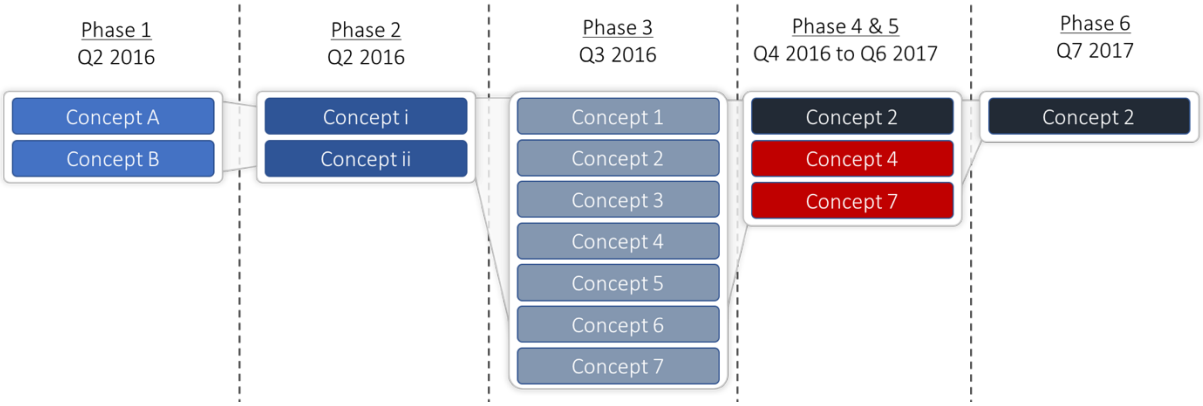

Figure II.4.D.1. Concept development history. Source: Clemson University.

Concept 2 had the entire structural part of the door frame as a single component. Although this made manufacturing a complex process, the quality, ease of assembly, and time required for the door assembly were all vastly improved. The other advantages of this design were the very tight tolerances given that the door frame could be manufactured in a single mold. The lightweighting potential for this door concept was quite high as there were very few lazy parts. In particular, parts like the door trim and the door module were integrated into the door frame, as shown in the Figure II.4.D.2.

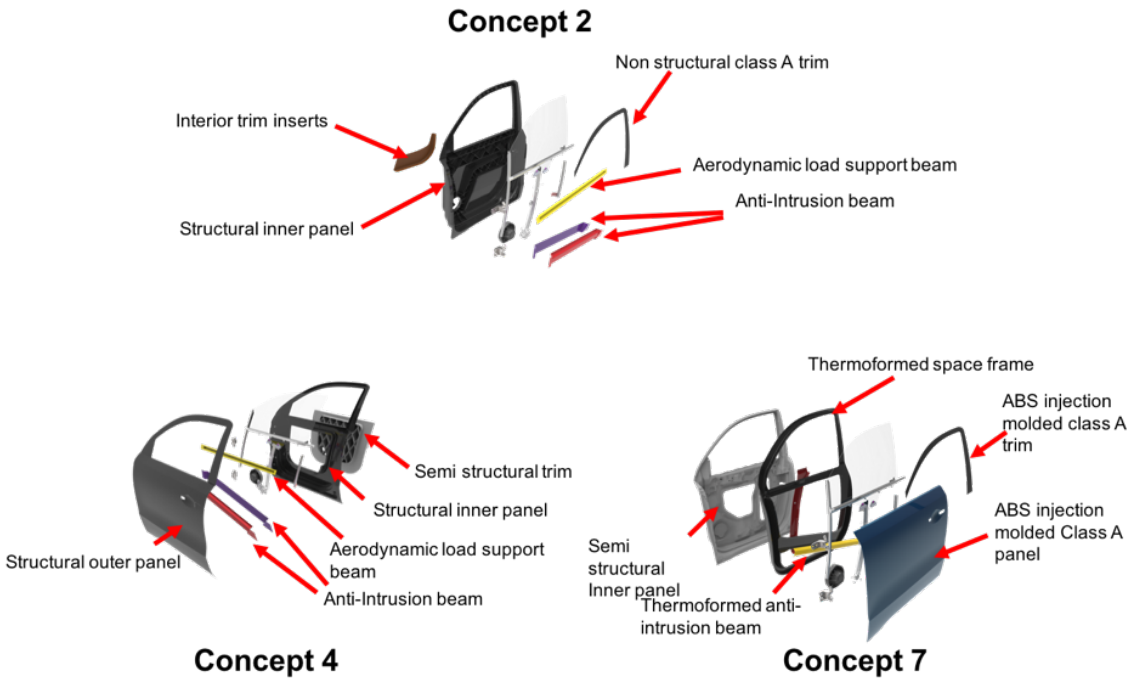

Figure II.4.D.2. Concepts 2, 5, and 7 exploded view. Source: Clemson University.

Concept 4 was a two-piece structural design that consisted of the door frame manufactured from a two-shell structure, which could be later bonded together to form the door frame—very similar to the baseline steel door design. The advantage of this concept was its relative simplicity for manufacturing as both the inner and outer panels could be thermoformed from endless fiber thermoplastics tapes, while the interior trim constituted a semi-structural member. The trim that was attached to the frame provided an additional in-plane stiffness to the inner panels, thus contributing to overall door frame stiffness. The semi-structural trim could be manufactured from injection-molded long/short fiber reinforced thermoplastics. A major issue with this concept was the high number of lazy parts, high estimated cost, and low lightweight potential.

Concept 7 was a space frame-inspired design where the major structural loads are carried by a space frame structure. This space frame structure consisted of an open hat section around the periphery of the door frame as shown in Figure II.4.D.2. Key load points, such as the hinges and latch, were directly attached to the space frame. A semi-structural inner panel was mechanically fastened to this frame, while access to the door's internals were from the exterior of the vehicle, using a removable class A panel.

From Phase 4 onwards, the team focused on the detailing of Concept 2 and to satisfy all geometry requirements (e.g., sealing planes), which were interfaced with all sub-assemblies/door internal components. Concept 2, as shown in Figure II.4.D.3, was incorporated with a ribbed structure, such as an injection-molded Long Fiber Thermoplastics (LFT), on the inner panel that acted as the main load bearing structure of the door frame with anti-intrusion beams to prevent intrusion during side impact. The full geometrical integration of door sub-assemblies (i.e., window regulator, latch/hinges hardware, electronics, and door stopper) to the inner panel is also shown in Figure II.4.D.3. The key advantages of this iteration of Concept 2 was that components with negative drafts and complex details, such as the hand rest and door pocket, could be attached via snap fit to the frame. This panel could be later covered with foam laminated leather or fabric for a premium feel. A removable class A was mechanically attached to the door assembly after all internal components were attached. The high functional integration of the inner panel and minimization of fiber distortion during the thermoforming process were the primary challenges associated with this concept. Minimizing the complex geometry, such as the compound curves surface and aggressive bend radius, was the primary method for resolving such problems.

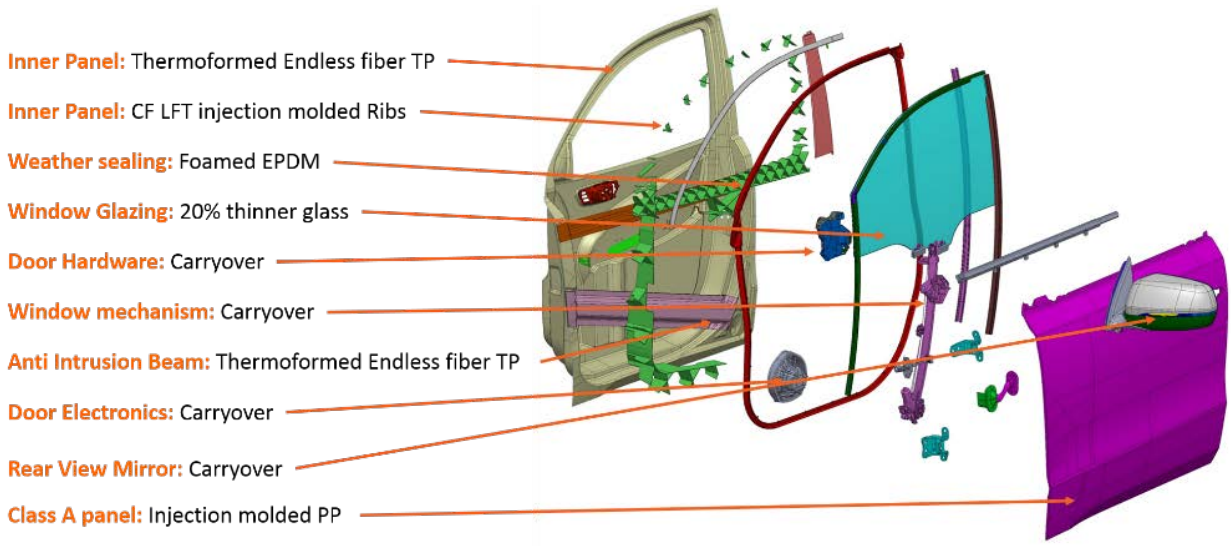

Figure II.4.D.3. Concept 2 exploded view (TP = thermoplastic, CF = carbon fiber, EPDM = ethylene propylene diene monomer, PP = polypropylene). Source: Clemson University.

A detailed computer aided design of Concept 7 with the window hardware (including window, guide rails, and hardware), non-structural trim, door limiter, and hinge/latch hardware was developed as shown in Figure II.4.D.4. Key features include the injection-molded nonstructural inner trim and outer panel, with the same method used to snap-fit the space frame and the inner trim geometry identical to that in Concept 2. The outer panel could be snapped into both the space frame and the inner panel to ensure the maximum access area for assembly. The complex curvature of the inner panel presented challenges during thermoforming, while the intrusion beam position also posed concerns in terms of both impact and crash performance.

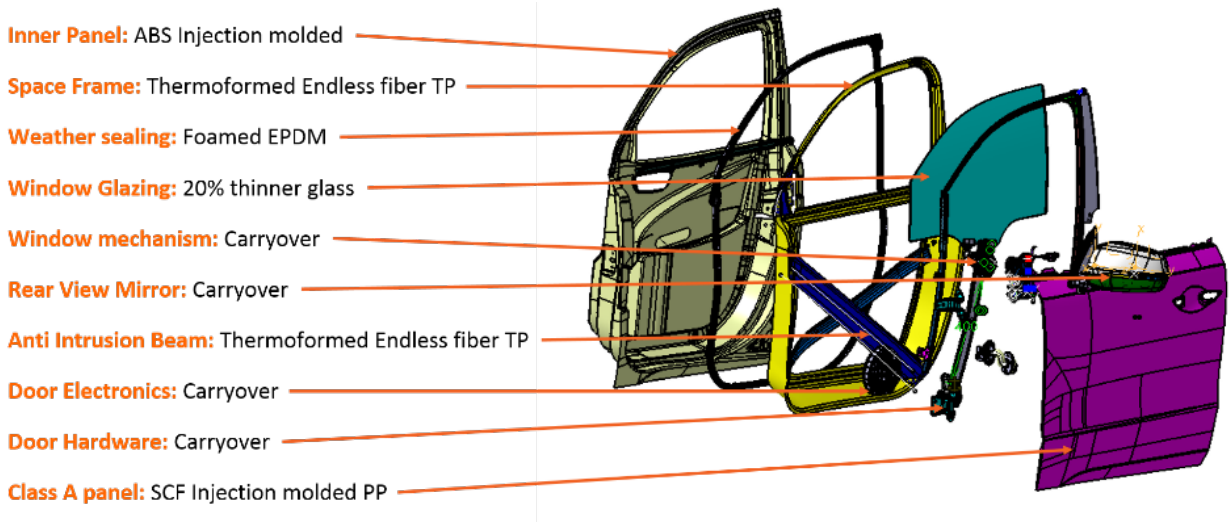

Figure II.4.D.4. Concept 7 exploded view (ABS = Acrylonitrile butadiene styrene, TP = thermoplastic, EPDM = ethylene propylene diene monomer, SCF = supercritical fluid; PP = polypropylene). Source: Clemson University.

Phase 5 focused on optimizing the mass of Concept 2 by exploring different reinforcing geometries for the inner frame in addition to optimization. Additionally, detailing the door design to interface with all sub-assemblies was a priority. The addition of this reinforcement member (shown in green in Figure II.4.D.5), mounting interfaces for the rear-view mirror, window regulator, and interior door release were accommodated without any additional brackets or secondary structures, thus preventing lazy parts. In addition to the prior

benefits, this new member (shown in green in Figure II.4.D.5) acts as local reinforcement for multiple point loads, thus aiding in better performance in the rear-view mirror mount stiffness, window regulator stiffness, and door sag by reinforcing the upper hinge and forming a load path between the upper hinge and latch.

As these geometric changes in the structural frame were finalized, composite-ply optimization was conducted to further minimize the mass. Geometry optimization and parametric studies were also conducted to minimize the weight of Concept 7, while meeting the static requirements. Door sag was chosen as the primary requirement for parametric studies with several parameters and geometric variations on the concept evaluated. These results were used to further refine Concept 7, which is shown in Figure II.4.D.5.

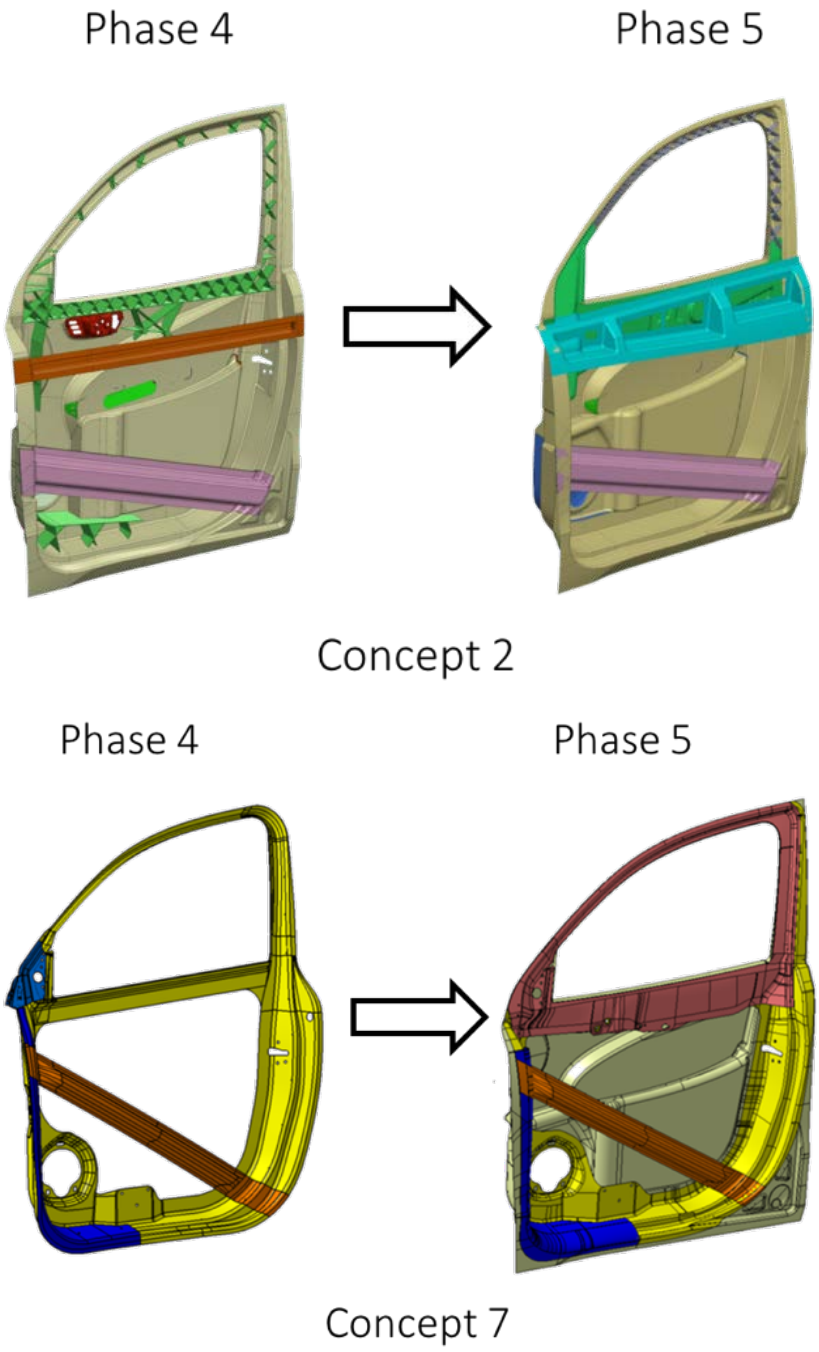

Figure II.4.D.5. Design Update to Concept 2 and Concept 7. Source: Clemson University.

In Phase 6, the team carefully evaluated both designs and determined that both concepts were converging in many ways to the same fundamental load-bearing design. Hence, research continued with Concept 2 to which key findings from Concept 7 were added. This unified design, shown in Figure II.4.D.6, included a revised inner panel design, a modified outer beltline support beam, and the integration of class A panel and interior trim development. The inner panel was redesigned to accommodate several mounting features and simplified geometry for easier manufacturing. The outer beltline support beam was designed to interface with the door handle mechanism.

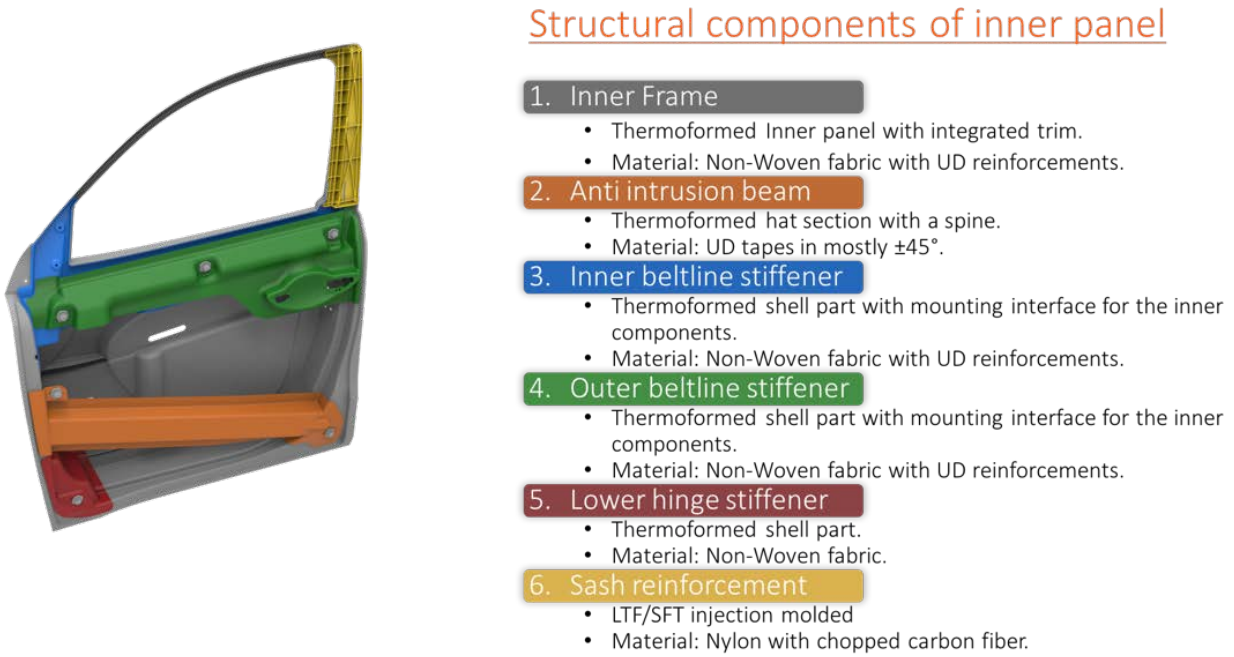

Figure II.4.D.6. Design Update to Concept 2 and Concept 7. Source: Clemson University.

Summary of FEA Results

Static analyses were performed on the composite door concepts to assess their performance. The main purpose of these analyses was to determine an initial thickness for the components that can satisfy the prescribed load cases and for performing an optimization to reduce the mass of the door. The load cases were: (1) door sag (DS); (2) opening frame stiffness; (3) door over opening; (4) beltline stiffness; and (5) torsional stiffness. In addition, the OEM partner specified the updated load cases of DS and sash rigidity (SR), each of which had two subcases. For each of the door concepts (after a failed initial static analysis for the aforementioned load cases) an optimization problem was developed to minimize mass and satisfy DS and SR load cases simultaneously.

The initial concepts during Phase 4 of our conceptual design were evaluated for all three concepts based on the five load cases defined above, with three of these presented in Table II.4.D.2. The optimization results of Concept 2 indicated a similarity of the thickness distribution of the inner panel for both cases with a greater thickness around the hinge bolts and at the intersection of the window frame with the door (red regions of Figure II.4.D.7. The thickness of the lower part of the inner panel was reduced to the minimum allowable value in all cases, indicating the possibility of further reducing mass if thinner laminates can be manufactured. Moreover, the thicknesses of the outer panel, part of the inner panel, and the ribs without a window frame were reduced to the minimum allowable value. As such, our findings created other possibilities for further weight reduction, such as in the partial removal of ribs. The optimized mass was 5.31 kg (65.6% mass reduction) for the nearly closed door position and 5.21 kg (66.2% mass reduction) for a fully open door, which was below the target value of 9.42 kg (only structural mass). Note that this value includes 3.24 kg trim mass, since this

concept had a built-in trim design. The optimization results for Concept 4 shows a reduction of the whole frame and outer panel thicknesses to the minimum allowable value of 1.2 mm, except for the thickness around the hinge bolts. These findings clearly indicated the possibility of excess material in these components if thinner laminates could be manufactured. The optimized masses of 7.62 kg and 7.63 kg for nearly closed and fully open door positions, respectively, were less than Concept 2 when only the inner panel is optimized. However, Concept 4 could not satisfy the mass reduction requirement of the project, since the target weight did not include the trim. The initial optimization for Concept 7 performed with just the frame demonstrated a high potential of weight reduction with a total structural weight of 3.28 kg, thus fulfilling those requirements. A plastic trim and outer panel was added to compare the results with the other concepts. The estimated weight for the total design is approximately 8.36 kg which is below the target mass of 9.42 kg. Based on initial static analysis, Concept 4, which failed to meet target mass, was eliminated.

Table II.4.D.2. Optimization Results of the Three Door Concepts.

		Concept 2		Concept 4		Concept 7
Door Sag Load Case		Nearly Closed	Fully Open	Nearly Closed	Fully Open	Nearly Closed
Mass Optimized Components		Inner Panel, Outer Panel, Ribs		Frame, Outer Panel		Frame
Optimized mass (kg)		5.31	5.21	7.62	7.63	3.28
Optimized response vs. requirement (mm)	**DS**	5.98<Req	4.98<Req	5.99<Req	4.99<Req	4.28<Req
	SR_A	3.49<Req	3.49Req	3.12<Req	3.12<Req	2.9<Req
	SR_B	2.51<Req	2.52<Req	3.06<Req	3.06<Req	1.6<Req
Target mass (kg)		9.42		6.18		6.18
Baseline mass in (kg)		18.1		15.6		15.6
Mass reduction (%)		70		51		79

DS = door sag, SR_A = sash rigidity location A, SR_B = sash rigidity location B.

In Phase 5, a detailed analysis of Concepts 2 and 7 involved adding a new updated set of load cases provided by our OEM partner. Several variations of Concept 2 were developed and optimization and static analysis was performed. Altair software was used for this three-step optimization process of free-size, size, and shuffle. Regarding free-size optimization, the total thickness of each of the finite elements in a component was reduced from its initial to a feasible value to satisfy the load cases and manufacturing constraints. In the second step, size optimization was performed to assign discrete thickness values to each component ply. In the third step, shuffle optimization was used to optimize the stacking sequence of the plies in laminates to improve the stiffness.

In the earlier version of Concept 2, the value of masses for the nearly closed door position and fully open door position after size optimization was 6.115 kg and 5.834 kg, respectively. The number of obtained plies was 25 for the closed position and 22 for the fully open position. Shuffle optimization, however, had no effect on the mass given its use in optimizing the stacking sequence of the plies for optimized stiffness. In addition to the three-phase optimization, rib structure optimization was performed to determine the optimum location and shape for the ribs. A design space was first defined for the ribs to ensure no interference with access to the internal door components. The topology of this design space was then optimized to determine a three dimensional rib structure, while a free-size optimization was conducted on the inner and outer panels. The door over opening and beltline stiffness were also considered in this rib structure optimization. The obtained optimized mass was 6.33 kg, which was slightly heavier than the previous designs and was expected given the imposition of more constraints on this design.

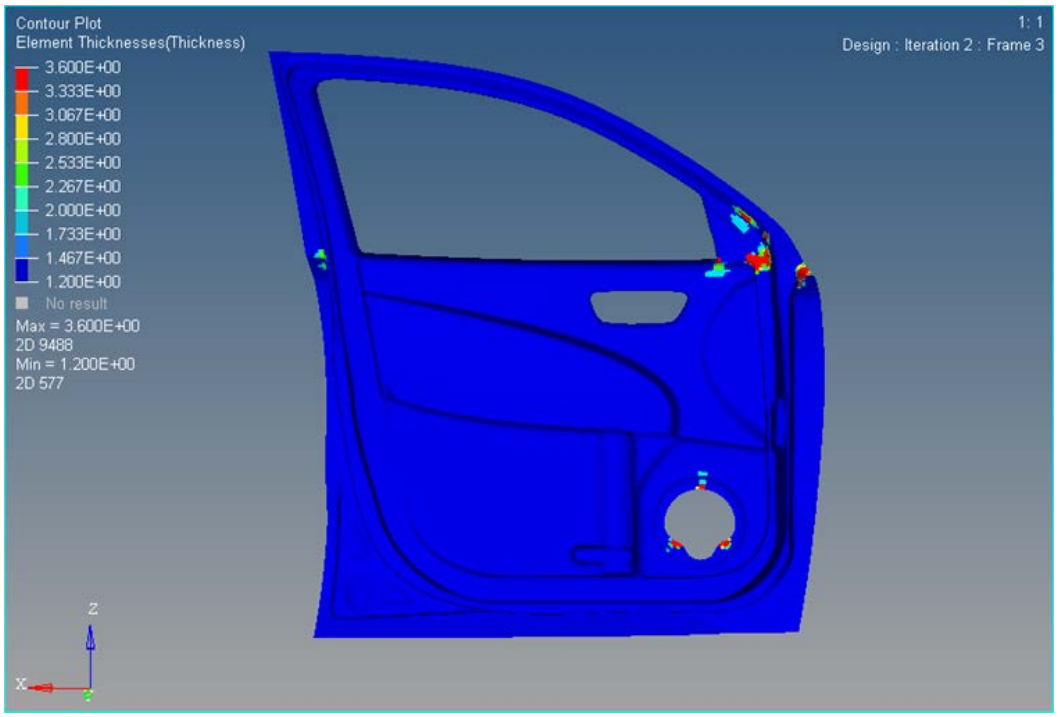

(a)

Iteration 0	Iteration 1	Iteration 2	Iteration 3	Iteration 4	Iteration 5
19	22	25	25	25	25
20	21	21	21	21	21
21	19	23	23	23	23
22	20	19	19	19	19
23	26	22	22	22	22
24	25	26	26	26	26
25	23	20	20	20	20
26	24	24	24	24	24

Legend
90.0 degrees
45.0 degrees
0.0 degrees
-45.0 degrees

(b)

Figure II.4.D.7. Thickness distribution for (a) inner panel after size optimization; and (b) stacking sequence after shuffle optimization. Source: Clemson University.

To further ensure both global and local stiffness of the composite door, a set of design constraints and load cases during design development was added, since there are no specific requirements from the OEM for the added design constraints (e.g., beltline stiffness, door over opening, and mirror mount stiffness). Such requirements were obtained by applying the same load cases on the baseline steel door. In the optimizations performed, although not used for computational efficiency, the effect of the body-in-white deformation was considered by adjusting the DS requirement by considering body-in-white deformation at the hinges. Based on the previous analysis results and manufacturability considerations, a newer version of the Concept 2 design was developed with an integrated beltline support. To assess the performance of the new design, specifically in

terms of beltline support, two analyses/optimizations with and without that support were performed. The door mass with and without the beltline support after free-size (step 1) optimization was 6.68 kg and 7.16 kg, respectively, given that the minimum allowable thickness is 1.2 mm. This result showed a decrease in the overall weight from this beltline support, since the beltline and upper hinge regions require a much larger thickness (>3.2 mm) without that support. An additional analysis with the beltline support determined that a reduction in the minimum allowable thickness to 0.9 mm decreased the optimized mass to 5.97 kg, with a corresponding weight savings of more than 10% as compared to the 1.2 mm sample.

Following the same analysis schema outlined above, multiple variations of the Concept 7 geometries were analyzed and optimized for additional load cases and for necessary geometry for attachments of the window regulator and other sub-components. A local stiffener on the hinge side and a closed head section at the beltline location were also added. All linear static load cases were satisfied with a total structural weight of 3.28 kg. The optimization shows that the regions around the hinges, review mirror, and latch were locally reinforced with a maximum lamina thickness of 2.75 mm, which in the other regions was minimized to 1.5 mm. Any further weight reduction in this concept depends on the sub-components, such as the trim and the outer panel.

In Phase 6, Concept 2 and Concept 7 were merged into a modified version of Concept 2 with beltline support and an additional upper section. The mass of the door after size optimization was determined to be 7.19 kg when the minimum allowable thickness was 1.2 mm. The thickness distribution of the inner panel in Figure II.4.D.7(a) shows that the panel is thicker (3.6 mm) around the part on which the mirror is mounted, and at the edges on the frame where the speaker is mounted, shown by the red regions in Figure II.4.D.7(a). The thickness in the other regions of the inner panel is reduced to 1.2 mm, which is the minimum manufacturing constraint. Shuffle optimization was then performed on the modified Concept 2. The thickness of plies was redefined based on the thickness distribution results after size optimization with two distinct minimum manufacturing constraints used (i.e., 0.15 mm and 0.3 mm). The final stacking sequence obtained for the inner panel and the beltline support is shown in Figure II.4.D.7(b). This modified version of Concept 2 was found to satisfy all static requirements.

Quasi-static and Dynamic Load Cases

Adhering to the FMVSS 214 standard, preliminary quasi-static crush tests were undertaken for Concept 7 using LS-DYNA. These initial FMVSS 214 quasi-static door crush requirements, listed in Table II.4.D.3, show that the average crushing force for the first 6 inches is 2264.4 N, far below the required value of 12011 N.

Table II.4.D.3. FMVSS 214 Static Door Crush Requirements and Results.

Item	Range (mm)	Requirement (N)	Baseline (N)	Concept 2 (N)
Initial Resistance	0–152	12011	11413	2264.4
Intermediate Resistance	0–304	18683	30745	N/A
Peak Load	0–457	37366	61769	N/A

Figure II.4.D.8 shows the comparison between the baseline and the Concept 7 force-displacement curve for crush test simulation. Simulations for Concept 2 only ran for a stroke of 235 mm, after which there was excessive deformation in the map pocket.

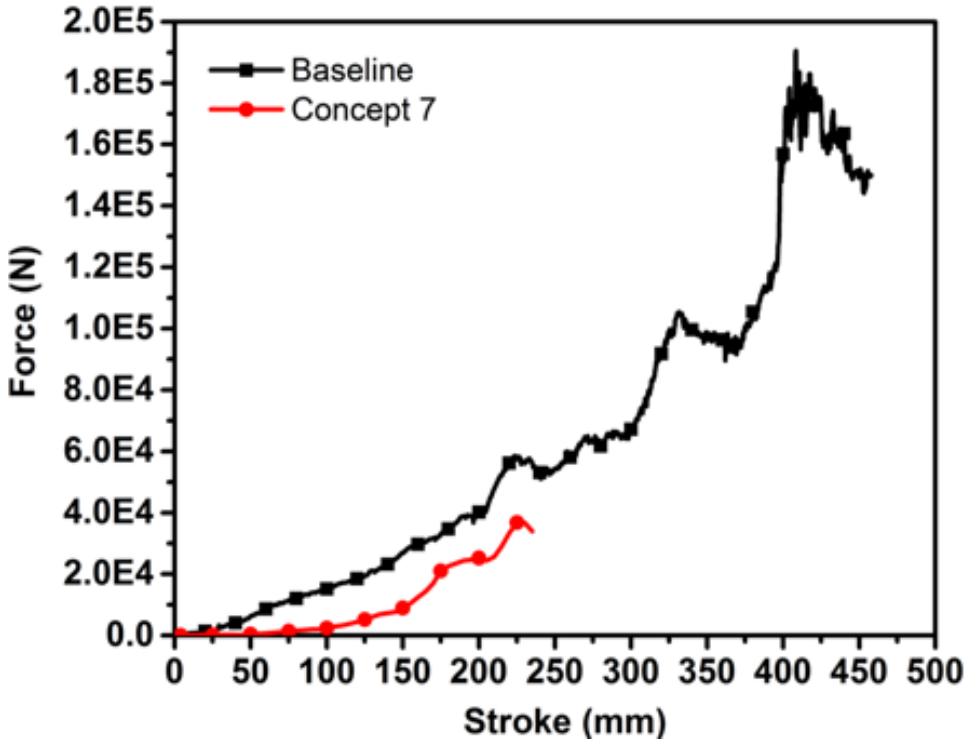

Figure II.4.D.8. Force-displacement curve for crush test for baseline and Concept 2 door.

The sectional view of collision and deformation at three states t = 0, t = 0.09s and t = 0.229s is shown in Figure II.4.D.9. Note the excessive deformation in one of the components (see Figure II.4.D.9c, map pocket) after termination of the simulation.

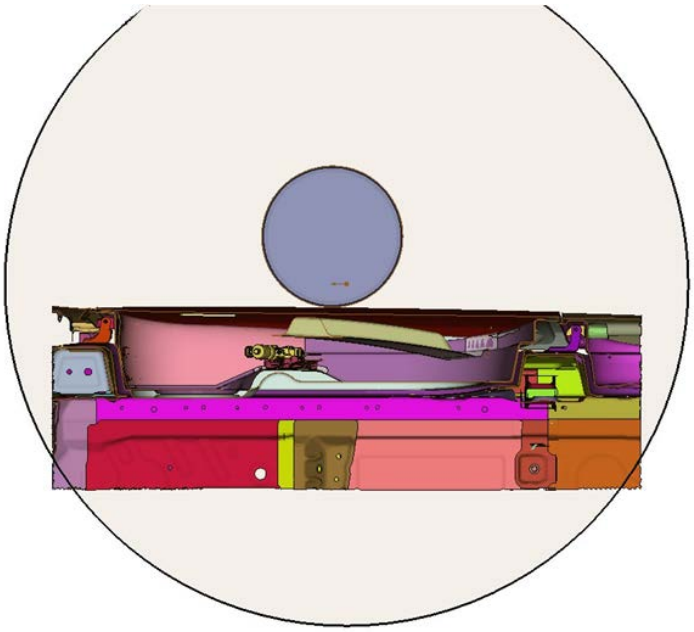

(a)

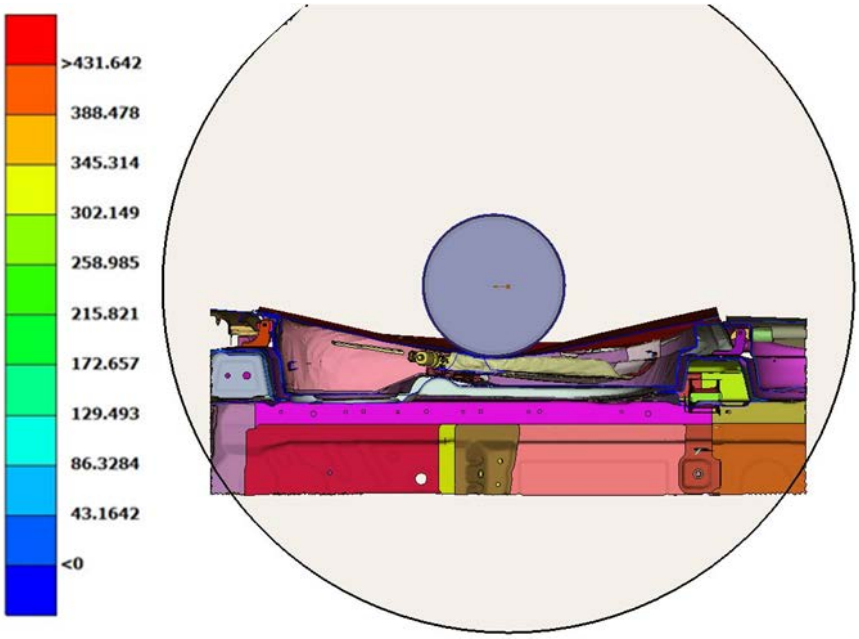

(b)

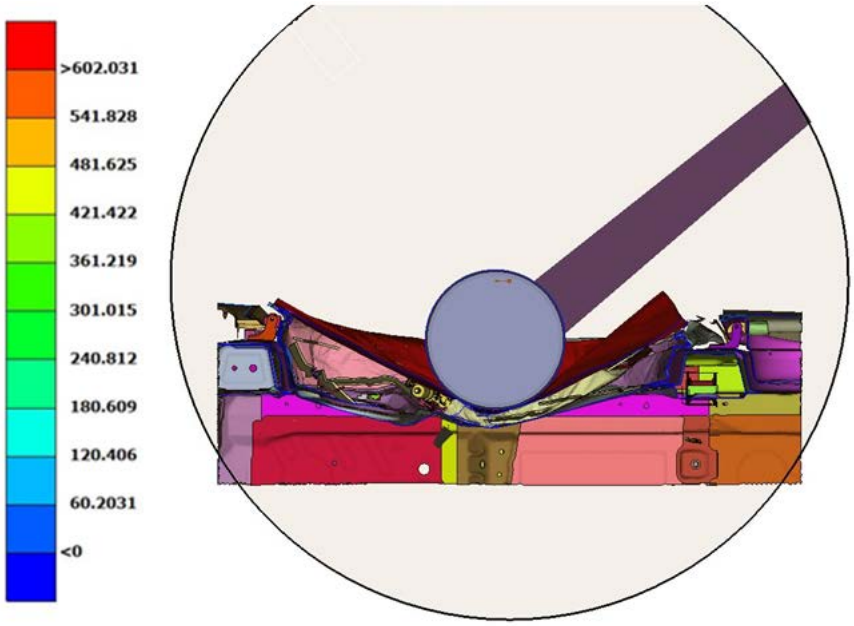

(c)

Figure II.4.D.9. Section view of the collision of Concept 7 door with a barrier at different states: (a) t = 0s; (b) t = 0.09s; and (c) t = 0.229s. Source: Clemson University.

A magnified version of this excessive deformation is shown in Figure II.4.D.10 at t = 0.229s. The initial crush test run for Concept 7 indicates that the composite door failed to meet the requirements, possibly because of an ill-defined FEA problem (e.g., incorrect boundary conditions). It was also determined that within a large initial travel distance, no resistance of the anti-intrusion beam was placed upon the rigid barrier, indicating that the anti-intrusion beam was located too far from the outer panel. Therefore, the FEA model must be redefined correctly via further testing prior to determining any conclusions.

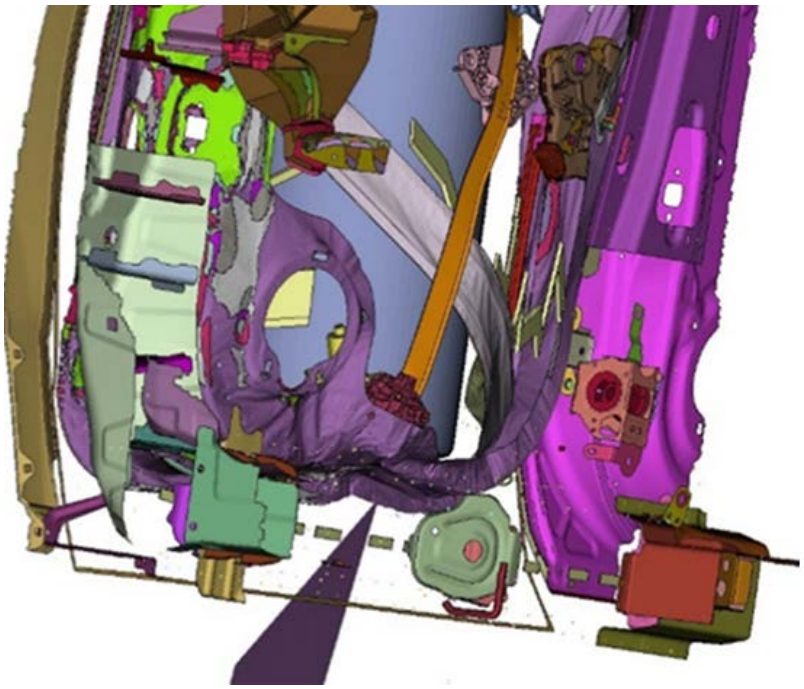

Figure II.4.D.10. Excessive deformation in map pocket at t = 0.229 s. Source: Clemson University.

Cost Modelling

The goal of the project is to achieve at least 42.5% weight reduction as compared to the baseline structure at a cost of less than $5/lb. of weight saved. The cost of the baseline structure was approximately $800, which gave us the latitude of adding $145 to the baseline structure cost. The overall cost estimating process is divided into three phases: (1) generative cost modeling; (2) parametric cost modeling; and (3) model refinement.

A generative cost model was prepared in which material, tooling, equipment, labor, energy, building, maintenance, overhead, and capital were all considered, and was developed for all the conceptual designs. These cost factors were also applied to those parts manufactured in-house and the cost for carry-over parts was estimated in consultation with our partners. In this model, the material cost incorporates part weight, raw material price, and material scrap rate, and labor cost includes labor wage, cycle time of machine, and number of labors working as important factors. Equipment cost was estimated by factoring equipment cost, equipment life, and production volume per year, and the tooling cost was estimated by considering tool cost, mold life, and production volume per year. Energy costs were calculated by considering power rating of the machine, cycle time, and electricity cost per unit. Four important assumptions of this model were considered while calculating the cost: (1) material scrap rate of 4%; (2) labor costs of $35/hour, (3) equipment and mold life with a seven-year life span; and (4) an overhead rate of 20%.

This generative cost model developed in Phase 4 was then applied for all concepts: for Concept 2, the cost was $848.74; for Concept 4, the cost was $976.97; and for Concept 7, the cost was $865.47. Concept 2 was the least expensive in that the proposed design consolidated both parts and assembly times, which thereby decreased manufacturing costs. Concept 4 was the highest in price given the use of a conventional door design that required a greater number of parts to be manufactured. The cost distribution for all three concepts, as shown in Figure II.4.D.11, clearly indicates that the greatest impact on the total cost for all three concepts was the materials (roughly 50%). Concept 4, which was the heaviest, was eliminated. In subsequent discussions, the team determined that Concept 2, with a few innovations added from Concept 7, would serve as the final design.

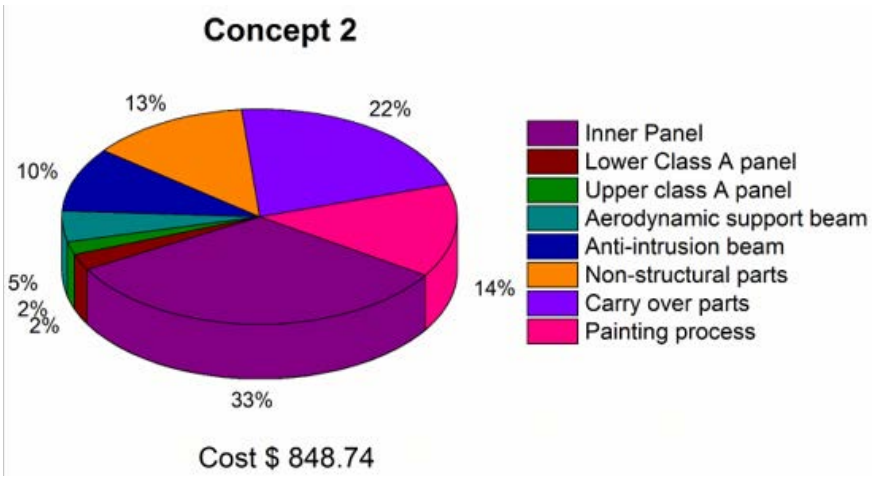

(a)

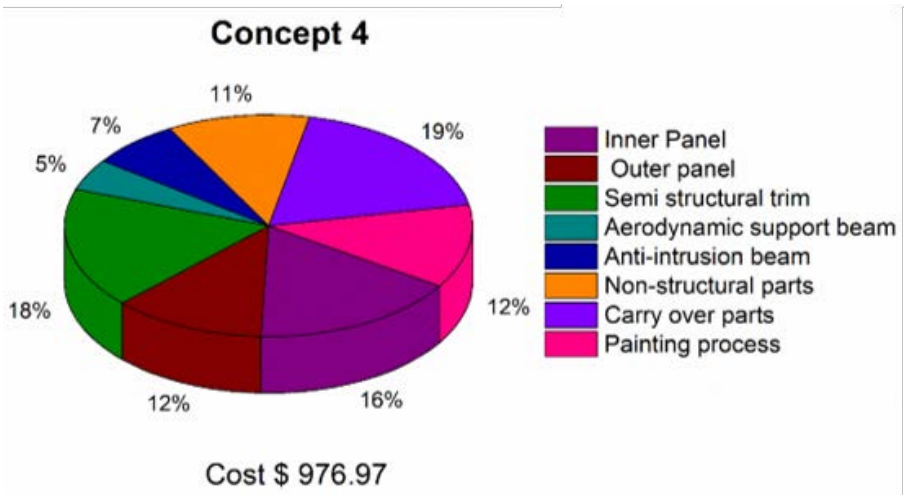

(b)

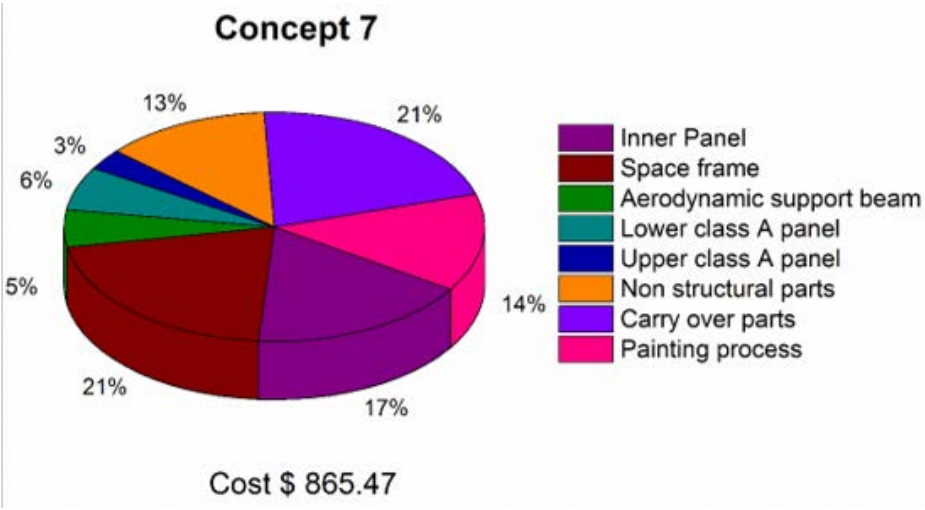

(c)

Figure II.4.D.11. Cost distribution of Concepts 2, 4, and 7. Source: Clemson University.

In Phase 6, the team converged on a modified design for Concept 2, in which the generative cost model mentioned above was applied at a cost of $915.45, the cost distribution of which is shown in Figure II.4.D.12.

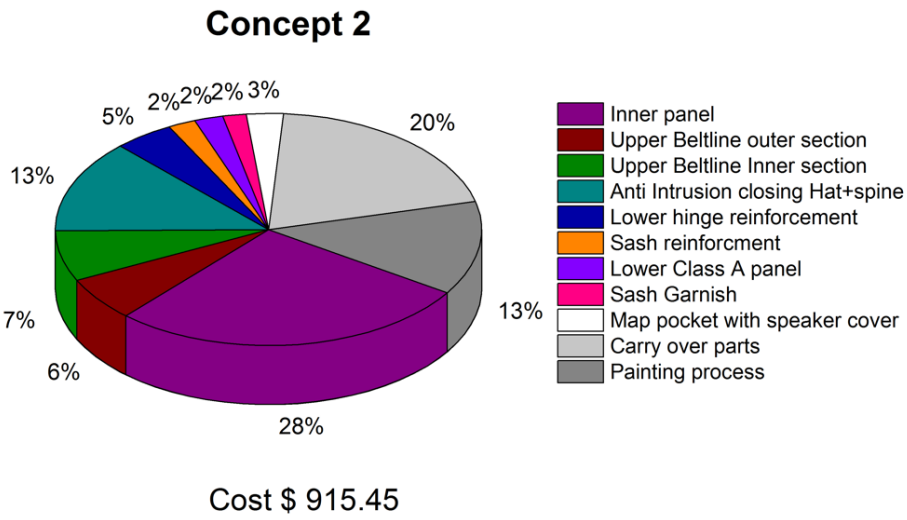

Figure II.4.D.12. Cost distribution of Concept 2. Source: Clemson University.

The next stage in cost modeling involved developing a parametric cost model for the finalized concept. These models are derived by applying the statistical methodologies and by expressing cost as a function of its constituent variables. We intend to integrate this concept with either the existing activity-based cost model or the feature-based cost model.

Conclusions

The research focus during this FY involved the converging of different proposed concepts into a single ideal concept based on their performance in FEA simulations, weight, scalability, and cost. Static and quasi-static FEA simulations, incorporating additional load cases, were used to better evaluate and optimize our final design to meet the weight and structural target criteria. A generative cost model was then used to evaluate cost and scalability in to meet our cost targets.

Key Publications

Journal Publication

Yerra, V. A., and S. Pilla, 2017, "IIoT-enabled production system for composite intensive vehicle manufacturing," *SAE International Journal of Engines*, Vol. 10, No. 2.

Conference Presentations

Kothari, A., I. B. Ozsoy, A. Yerra, G. Li, and S. Pilla, 2017, "Design optimization of a carbon fiber reinforced thermoplastic composite vehicle door assembly for weight reduction," *Fiber-reinforced Composites, International Symposium on Materials from Renewables*, Fiber Society's Fall 2017 Technical Meeting and Conference, Athens, GA, USA (November).

Pradeep, S. A., T. Zheng, N. Brown, and S. Pilla, 2017, "Advancements in the prediction of mechanical behavior of supercritical foamed short fiber thermoplastic composites," *Fiber-reinforced Composites, International Symposium on Materials from Renewables*, Fiber Society's Fall 2017 Technical Meeting and Conference, Athens, GA, USA (November).

Shah, P., C. Gandra, G. Li, and S. Pilla, 2017, "Factory layout design and cost modeling of a carbon fiber reinforced thermoplastic composite vehicle door assembly," *Fiber-reinforced Composites, International Symposium on Materials from Renewables*, Fiber Society's Fall 2017 Technical Meeting and Conference, Athens, GA, USA (November).

Yerra, A., and S. Pilla, 2017, "Design and optimization of carbon fiber reinforced closure systems," *Fiber-reinforced Composites, International Symposium on Materials from Renewables*, Fiber Society's Fall 2017 Technical Meeting and Conference, Athens, GA, USA (November).

Awards

Third Place in Graduate Student Poster Competition – Kothari, A., V. Yerra, I. Ozsoy, G. Li, and S. Pilla, 2017, "Design optimization of a carbon fiber reinforced thermoplastic composite vehicle door assembly for weight reduction," *Society of Plastics Engineers ACCE Conference*, September 6–8, 2017, Novi, MI, USA.

References

Chang, S. H., and S. S. Cheon, 2006. "In-plane directional mechanical properties of carbon fabric skins in sandwich structures after thermoforming," *Composite Structures*, Vol. 75, pp. 577–581.

Kelly, J. C., J. L. Sullivan, A. Burnham, and A. Elgowainy, 2015, "Impacts of vehicle weight reduction via material substitution on life-cycle greenhouse gas emissions," *Environmental Science Technology*, Vol. 49, pp. 12535–12542.

Mi, H.-Y., X. Jing, J. Peng, L.-S. Turng, and X.-F. Peng, 2013, "Influence and prediction of processing parameters on the properties of microcellular injection molded thermoplastic polyurethane based on an orthogonal array test," *Journal of Cellular Plastics*, Vol. 49, pp. 439–458.

Yu, Y., J. Ye, Y. Wang, B. Zhang, and G. Qi, 2013, "A mesoscale ultrasonic attenuation finite element model of composites with random-distributed voids," *Composites Science and Technology*, Vol. 89, pp. 44–51.

U.S. DEPARTMENT OF
ENERGY

Office of
ENERGY EFFICIENCY &
RENEWABLE ENERGY

For more information, visit:
energy.gov/eere/vehicles

DOE/EE-1711 ▪ May 2018